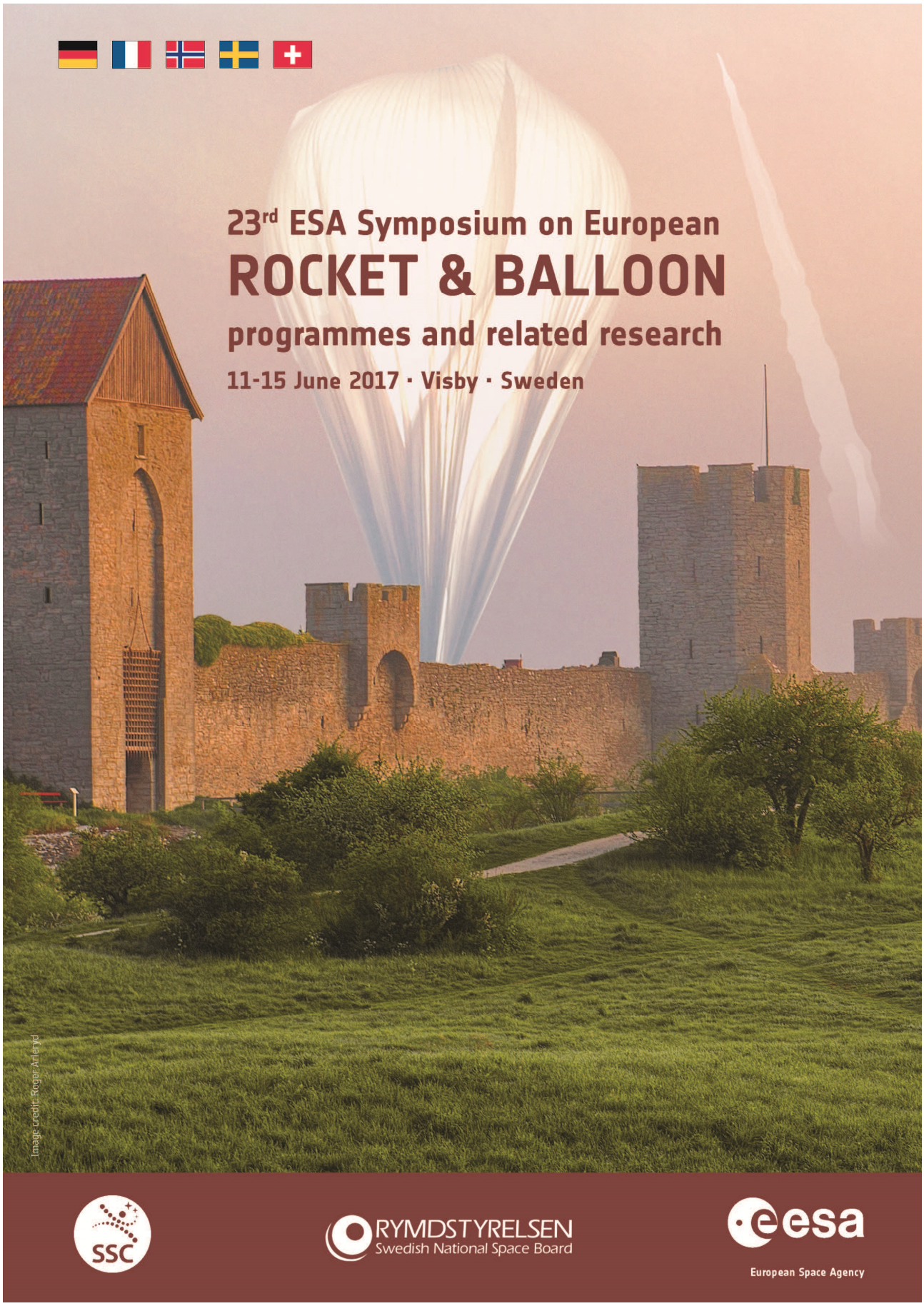
23rd ESA Symposium on European
ROCKET & BALLOON
programmes and related research
11-15 June 2017 · Visby · Sweden
Image credits: Roger Arleryd
SSC
RYMDSTYRELSEN
Swedish National Space Board
esa
European Space Agency

23RD ESA SYMPOSIUM ON EUROPEAN ROCKET AND BALLOON PROGRAMMES AND RELATED RESEARCH

11 – 15 June 2017

Visby - Sweden

Symposium Programme Committee

Chair

K. Dannenberg	SNSB, SE

Members

K. Boen	ASC, NO
V. Dubourg	CNES, FR
M. Egli	HSLU, CH
F-J. Lübken	IAP Kühlungsborn, DE
J. Moen	University of Oslo, NO
M. Pearce	KTH, SE
M. Viertotak	SSC, SE
A. Verga	ESA

Symposium Organising Committee

Chair

S.Kemi	SSC, SE

Members

A-K. Grenevall	SSC, SE
M-P. Havinga	ESA
U. McCabe	SSC
L. Poromaa	SSC

23RD ESA SYMPOSIUM ON
EUROPEAN ROCKET AND BALLOON PROGRAMMES
AND RELATED RESEARCH
VISBY, SWEDEN
11-15 JUNE 2017

PROGRAMME MONDAY 12 JUNE (AM)

OPENING EVENT - ROOM: WISBY

09:00 SYMPOSIUM CHAIR: K. DANNENBERG
09:05 CITY REPRESENTATIVE
09:20 DIRECTOR GENERAL SWEDISH NATIONAL SPACEBOARD: O.NORBERG
09:30 EUROPEAN SPACE AGENCY: M.N. DE PAROLIS
09:40 LOCAL ORGANISING COMMITTEE: S.KEMI

AGENCIES' REPORTS – CHAIR K.DANNENBERG

09:45 SWEDEN – K. DANNENBERG

10:05 GERMANY – O.JOOP

10:25 FRANCE – V. DUBOURG

10:45 – 11:15 COFFEE BREAK

11:15 NORWAY – P. BREKKE

11:35 SWITZERLAND - M. EGLI

11:55 CANADA – S. MONTMIGNY

12:15 JAPAN - T. ABE

12:35 USA – P. EBERSPEAKER

13:00 – 14:15 LUNCH BREAK

MONDAY 12 JUNE AFTERNOON SESSION		**PROGRAMME**
14:15	PLENARY INVITED LECTURE: [A-171] SHEDDING NEW LIGHT ON THE CRAB AND CYGNUS X-1 WITH POGO+ - M. PEARCE - ROOM: WISBY	
	ASTROPHYSICS, ASTRONOMY & COSMOLOGY Room: Wisby - Chair: M. Pearce	***RANGES FACILITIES*** Room: Lojsta 2 - Chair: S. Kemi
14:45	[A-061] R.M. Millan Highlights from the Barrel Balloon Experiment	[A-036] A. Rathsman Esrange Space Center – Meeting Future Needs for Advanced Space Services
15:00	[A-071] J-P Bernard & PILOT Team In Flight Performances and First Results of the PILOT Experiment	[A-023]T. Kristiansen Upgrade of Andoya Space Center's Launch Base at Svalbard – New Opportunities for the Space Science community
15:15	[A-038] J. Stahn CPT-Scope : Compact particle radiation monitor technology demonstration aboard TEXUS20	[A-159]R.Kirchhartz MORABA Activities in Retrospect
15:30	Withdrawn	[A-087] J. Idivuoma Andoya Space Center Trajectory and Position System (TPS)
15:45	Coffee Break	
	ATMOSPHERIC PHYSICS & CHEMISTRY Room: Lojsta 2 - Chair: J. Gumbel	***TECHNOLOGY & INFRASTRUCTURES FOR SR*** Room: Wisby - Chair: K. Boen
16:15	[A-002] F.J. Lübken Mesopause Jumps: Observations and Explanations	[A-024] S. Nonaka Technical Demonstrations and the Next Steps for Reusable Sounding Rocket
16:30	[A-039] B. Strelnikov Gravity Wave Signatures in Densities of Different Species in MLT as Measured during the WADIS Sounding Rocket Project	[A-015] O.Drescher Cork Based Thermal Protection System for Sounding Rocket Applications – Development and Flight Testing
16:45	[A-053] R. Song Test of a remote Sensing Michelson-interferometer for Temperature Measurements in the Mesosphere on a REXUS Rocket	[A-044] O. Verberne In Space with NAMMO's Hybrid Motors: Results and Achievements of the Nucleus Program.
17:00	[A-089] J. Hedin Atomic Oxygen and Temperature in the Lower Thermosphere from the O-States Sounding Rocket Project	[A-055] K.W.Naumann A Modular Sounding Rocket Concept with Green, Safe and Affordable Gelled Propellant Rocket Motors
17:15	[A-172] J. Stude ROMARA: the ROcket-borne MAss spectrometer for Research in the Atmosphere	[A-026] M. Uitendaal Recent Steps in the T-minus Dart Vehicle Development
17:30	[A-048] J. Fiedler Variability of Noctilucent Clouds as Observed by the Alomar RMR-Lidar	[A-157] M. Wittkamp Ethernet for Sounding Rocket
17:45	[A-178] H. Asmus Charge Balance of the Night Time D-Region Ionosphere Inferred from In-situ Measurements during the WADIS-2 Sounding Rocket Campaign	[A-183] S. Westerlund The development of a Rocket Motor Test Facility at Esrange
18:00	Withdrawn	Withdrawn
19:00 Ranges Night		

TUESDAY 13 JUNE MORNING SESSION			**PROGRAMME**
09:00	PLENARY INVITED LECTURE: [A-184] THE PROSPECT OF THE GRAND CHALLENGE INITIATIVE CUSP ROCKET PROGRAMME- J. MOEN - ROOM: WISBY		
	MAGNETOSPHERE & IONOSPHERE Room: Wisby - Chair: J. Moen		***TECHNOLOGY & INFRASTRUCTURES FOR SR*** Room: Lojsta 2 - Chair: M. Viertotak
09:30	[A-009] K. Blix The Grand Challenge Inititiative Cusp Project		[A-148] D.Krause NASA Sounding Rocket Program and Orbital Sciences Corporation - NSROC
09:45	[A-119] C.A.Kletzing Rocket Missions for Cusp Electrodynamics		[A-174] F.Garcia ARION1: The Next European and Reusable Sounding Rocket
10:00	[A-114] N. Ivchenko First Results from the Spider Sounding Rocket		[A-095] P.Caldas-Pinto Stage Concept for a Hovering Thermosphere Probe Vehicle with Green, Safe and Affordable Gelled Propellant Rocket Motors
10:15	[A-113] L. Jahan A Case Study of Sounding Rocket based GPS Signal Reception during Active Auroral Conditions		[A-122] M.Schelim Fields Validation of a Slant Range System at Rio Verde Campaign
10:30	[A-081] G.Giono Langmuir Probes Multi-points Measurements of the Plasma Properties inside an Auroral Electroject Recorded by the Spider Sounding Rocket		[A-050] L.Dawei Well-extensible and Configurable Image Monitor System Onboard Sounding Rocket
10:45	Coffee Break		
	MAGNETOSPHERE & IONOSPHERE Room: Viklau: 3 - Chair: K. Blix	***UTILISATION OF BALLOONS FOR RESEARCH APP.*** Room: Lojsta 2 - Chair: V. Dubourg	***RANGES FACILITIES*** Room: Wisby - Chair: L. Poromaa
11:15	[A-040] J. Moen Kelvin Helmholtz and Gradient Drift Instabilities in Ionosphere Cusp Flow Channels	[A-020] P. Maier ORISON, a Stratospheric Project	[A-084] K. Nehrman The New Old Process of Rocket Wind Weighing
11:30	[A-018] T. Abe On the Estimation of Ion Drift Velocity from Electrostatic Probe Data Obtained during ICI-4 Campaign	[A-182] – F. Piette / I. Wagner Albedo Measurement using Photodiodes on a High Altitude Balloon	[A-088] J. Idivuoma Orientation Calculations using 3-Axis Magnetometer
11:45	[A-149] Y.Kyzyurov Features of Sporadic-E Layer below the Turbopause	[A-162] V. Dubourg CNES Super Pressure Balloons Upgrade for Strateole-2 Campaign	[A-124] W. Jung EUROLAUNCH – A cooperation in change
12:00	[A-082] T.Sergienko BROR – Barium Release Optical and Radio Rocket Experiment	[A-134] E.F.Young Status of NASA's GHAPS Project; Gondola for High-altitude Planetary Science	[A-120] H. Eriksson Esrange Space Center – New Telecommand System
12:15	[A-133] P.A.Bernhardt Results from the Second Charged Aerosol Release Experiment (CARE II) Rocket Experiment	[A-126] M. Abrahamsson POGO+ - The Swedish National Transatlantic Balloon Mission	[A-060] H.Oliveira da Mata Artificial Neural Network for Range Flight Safety
12:30	[A-068] C-F. Enell Eiscat Incoherent Scatter Radar Facilities for Ground-based Atmospheric and Solar-terrestrial Science in the Northern Auroral Oval	[A-177] M-P. Zorzano The Packman Radiation and Environmental Instrument for Space Studies	[A-121] K. Larsson Esrange Space Center – New Telemetry Station at Esrange Space Center
12:45	[A-115] X.Zhou Development of a Balloon-borne NIR Camera for Auroral Observations under the Sun		[A-156] M. Abrahamsson Esrange Space Center – Latest Highlights and Future Plans
13:00 – 14:15 Lunch			

TUESDAY 13 JUNE AFTERNOON SESSION		**PROGRAMME**
14:15	PLENARY INVITED LECTURE: [A-129] NEW SYNERGIES OF SR AND REMOTE SENSING IN THE UPPER MIDDLE AND LOWER UPPER ATMOSPHERE - J. GUMBEL - ROOM: WISBY	
	ATMOSPHERIC PHYSICS & CHEMISTRY Room: Wisby - Chair: B. Strelnikov	***TECHNOLOGY & INFRASTRUCTURES FOR SR*** Room: Lojsta: 2 - Chair: O.R. Enoksen
14:45	[A-076] R.Latteck Characteristics of Polar Mesosphere Summer Echoes during the Maxidusty Campaign at Andenes, Norway in Summer 2016	[A-154] A.Thurswaldner Making the Case for Sounding Rocket Guidance System
15:00	[A-028] K.Schütze Collection of Stratospheric Aerosols Particles during the BEXUS20 Balloon Campaign by Team COSPA	[A-074] T.Lauritsen Gronas Design and Qualification of a Novel Pyrotechnical Release System for Sounding Rockets
15:15	[A-042] T.Antonsen / O.Havnes Estimates of the Size Distribution of Meteoric Smoke Particles from In Situ Measurements with Dust Impact Probes	[A-097] J-E Ronningen NAMMO Space Products and Activities
15:30	[A-086] T.Staszak A New Rocket-borne Meteor Smoke Particle Detector (MSPD) for D-Region Ionosphere	[A-110] B.Klein / L.Stamat Horizon Acquisition for Attitude Determination using Image Processing Algorithms – Results of PATHOS on REXUS20
15:45	Coffee Break	

TUESDAY 13 JUNE AFTERNOON SESSION			PROGRAMME
16:15	***PICO SESSIONS*** Room: Wisby - Chair: A. Kinnaird		
	MAGNESTOSPHERE & IONOSPHERE		
	[A054]	O.Brekhov	Balloon Gradient Magnetic Measurements and Satellite Magnetic Surveys Synergy
	ASTROPHYSICS, ASTRONOMY & COSMOLOGY		
	[A-145]	G.Roudil	Mechanical Design and Thermo-elastic Analysis of the PILOT Instrument
	LIFE & PHYSICAL SCIENCES		
	[A-047]	F.Meyer	Experimental Findings on Flame Propagation along PMMA Samples in Reduced Gravity on REXUS20 (UB-FIRE)
	SPACE-RELATED EDUCATION		
	[A-066]	C. Van Moll	Secondary School Students Designing, Testing and Flying Equipment to Study the Quality of µGravity on Drop Tower Tests, Parabolic & Suborbital Flights
	[A-107]	M.Kossagk	LOTUS-D – Light Optical Transmission-experiment of University Students
	[A-123]	A.L.Duarte	Signon from BEXUS23
	[A-065]	D. Buggenhout	Secondary School Students Designing, Testing and Flying Geiger Counter Equipment to Study Atmospheric Gammas over Europe and Svalbard
	[A-043]	O.Brekhov	Engineering Satellite Model as a Tool for Satellite Design, its Exploitation and Student Education
	[A-169]	L.Klicker	SLED Failure Analysis: How to Fail when you are Destined to Succeed.
	UTILISATION OF BALLOONS FOR RESEARCH APPLICATIONS		
	[A-057]	L.Wang	Command Filtered Back-stepping Integrated Guidance and Control for Hypersonic Glider based on Extended State Observer
	UTILISATION OF ROCKETS FOR RESEARCH APPLICATIONS		
	[A-032]	R.Gardi	MINI-IRENE: Design of a Capsule with Deployable Heat Shield for a Sounding Rocket Flight Experiment
	[A-179]	C.Bian/C. Liu	The Payload Service System of Kunpeng-1B Sounding Rocket
	TECHNOLOGY & INFRASTRUCTURES FOR SOUNDING ROCKETS		
	[A-010]	R.Lu	Deisgn and Flight Results of a Non-polluting Cold-separation Mechanism for TY-3F Sounding Rocket
	[A-027]	H.Otlhof	Recent Steps in the T-Minus Dart Motor Development
	[A-139]	S.Haas/H. Zöllner	REXUS19 – LIME (Link Made Early) – Investigation of an Attitude-dependent Satellite Communication Scheme
	[A-140]	A.Zaghdane	UB-Space on REXUS21: Test Data Acquisition for Relative Navigation with a Camera System for a 360 Degree Round View from a Sounding Rocket
	TECHNOLOGY & INFRASTRUCTURES FOR BALLOONS		
	[A-022]	X.Deng	Properties of a Gas-compression based Pressure Control System for Stratospheric Airship
	[A-166]	J-B Béhar	Coriolis Mass-Flowmeter for Aerostatic Gas Amount Determination in Zero Pressure Stratospheric Balloons
	[A-058]	G.Xu	Research on High Power Stacked Boost Converters for the Power Supply of Stratospheric Airship
	[A-180]	T-T. Liu	The Influence of the Solar Cells on Thermal Characteristics of Stratospheric Airship

WEDNESDAY 14 JUNE MORNING SESSION			**PROGRAMME**
09:00	PLENARY INVITED LECTURE: [A-175] HUMAN CELLS IN MICROGRAVITY – D. GRIMM - ROOM: WISBY		
	ASTROPHYSICS, ASTRONOMY & COSMOLOGY Room: Lojsta: 2 - Chair: J-P. Bernard		***LIFE & PHYSICAL SCIENCES*** Room: Wisby - Chair: M. Egli
09:30	[A-170] M. Kiss Design and 2016 Flight Performance of POGO+ - A Balloon-borne Hard X-ray Polarimeter		[A-011] M.Knie First Insights on the Influence of Altered Gravity on the Gene Expression in Daphnia Magna – A Sounding Rocket Experiment (TEXUS52)
09:45	[A-128] Y. Longval PILOT Optics and its in-flight performance		[A-003] S.L.Wuest Electrophysiological Measurements during a Sounding Rocket Flight, Results from the CEMIOS Experiment on REXUS20
10:00	[A-077] L. Dorman Forward to Automatic Forecasting of Radiation Hazards from Solar Cosmic Rays for Experiments on Long-lived Baloons, for Aircrafts and Spacecrafts		[A-001] S.Kopp Thyroid Cancer Cells in Space – Results of the TEXUS53 Mission
10:15	[A-105] B.Mot Characterisation and Performances of the PILOT Instrument		[A-090] M.Krüger Life-cell Imaging of F-actin Changes Induced by 6 Min of Microgravity on a TEXUS Sounding Rocket Flight
10:30	Withdrawn		[A-051] T.J.Corydon Alterations of the Cytoskeleton in Human Cells in Space Proved by Life-Cell Imaging
10:45	Coffee Break		
	ATMOSPHERIC PHYSICS & CHEMISTRY Room: Lojsta: 2 - Chair: F-J. Lübken	***LIFE & PHYSICAL SCIENCES*** Room: Viklau - Chair: A. Verga	***TECHNOLOGY & INFRASTRUCTURES FOR BALLOONS*** Room: Wisby - Chair:M. Abrahamsson
11:15	[A-091] T.Kuhn Comparison of In-situ Balloon-borne and Lidar Measurement of Cirrus Clouds	[A-080] B. Pröbster FOKUS II – A Vacuum Compatible Dual Frequency Comb System	[A-130] E.Carlsson Sjöberg BOOSTER – BallOOn for Science and Technology from Esrange
11:30	[A-085] T.Antonsen Simultaneous In Situ and Remote Observations of Dust in the Polar Summer Mesosphere : an Overview of the Maxidusty Campaign	[A-037] M.Podgorski DREAM – Drilling Experiment for Asteroid Mining	[A-143] J.Hruby Development of Ultra-sensitive Portable 3D Magnetometer based on Diamond NV-centers for OSCAR (BEXUS23)
11:45	[A-144] V.Wolf Properties of Ice Particles in Arctic Cirrus from Balloon-borne in-situ Measurements at Different Meteorological Conditions	[A-158] A.Schütte/G.Florin Size Matters – MAXUS9 Sounding Rocket Mission	[A-019] S.Rückerl TDP-3 Vanguard : Verification of a New Communication System for Cubesats on BEXUS 22
12:00	[A-059] J. Söder Measuring Wave Generated Stratospheric Turbulence with a Lightweight Balloon-borne Instrument	[A-125] Y.Houltz XRMON-SOL Microgravity Experiment Module on MASER13	[A-079] K.Garg Design, Verification and Validation of a Simulation Tool for High-Altitude
12:15	[A-108] E.J.Young Prospects for Improved Infrasound Detection from Balloon-borne Platforms	[A-152] G.Florin MASER13 Sounding Rocket Mission – Worth Waiting for	[A-014] J. Peeters Thermal Analysis of Components for Stratospheric Experiments using Finite Element Model Updating of the BEXUS20: HACORD Mission
12:30	[A-165] H.Oelhaf 25 Years of Atmospheric Science with MIPAS-B	[A-106] H.Oltmann Flumias and Perwaves : Two Exciting New Experiment Modules	[A-006] Q.Liu An Experimental Investigation into the Thermal Performance of Sphere Balloon
12:45	Withdrawn	[A-160] A.Vaerneus Roots in Space – The BIM-3 Microgravity Experiment Module	[A-004] J.Cai Analysis of Transient Surface Temperature and Aerodynamic Heating for Space Exploration Balloon
13:00 – 14:15 Lunch			
14:15 Excursions			

	THURSDAY 14 JUNE MORNING SESSION		PROGRAMME
09:00	PLENARY INVITED LECTURE: [A-031] 10 YEARS OF THE GERMAN-SWEDISH REXUS/BEXUS STUDENT PROGRAMME – A. KINNAIRD/M. BECKER - ROOM: WISBY		
	SPACE-RELATED EDUCATION 1 Room: Wisby - Chair: K. Dannenberg		***UTILISATION OF ROCKETS FOR RESEARCH APPLICATIONS*** Room: Lojsta 2 - Chair: R. Kirchhartz
09:30	[A-030] K.Schüttauf The STERN Project – Hands on Rockets Science for University Student		[A-041] M.Yang The Recent Development of China Sounding Rocket Space Exploration Activities and the Internal Cooperation
09:45	[A-173] Jean Oswald PERSEUS		[A-045] K.Sjölander O-STATES & SPIDER/LEEWAVES, a new Era of National Sounding Rockets from Esrange Begins
10:00	[A-100] C.Stausland Fly a Rocket ! A Norwegian-ESA Educational Programme – PILOT Cycle Report and Conclusions		[A-046] T.Gansmoe Development of New Payload Module for 4D Measurements
10:15	[A-109] S.G.Bilen Developing Student Leadership in Space Systems Engineering via the G-chaser Student Rocket		[A-131] M.Siedorf MIRKA2-RX – An Educational Precursor Mission for a Re-entry based Cubesat Mission
10:30	[A-056] B.Jensen STARBUST – A New, Unique Student Project in Maritime Surveillance from Space		[A-049] B.Tester Experimental Results from the Testing of the Prototype Inflatable Conical Antenna – REXUS Deployment on REXUS Flight RX19
10:45	Coffee Break		
	UTILISATION OF BALLOONS FOR RESEARCH APP. Room: Viklau - Chair: V. Dubourg	***SPACE-RELATED EDUCATION*** Room: Wisby - Chair: M. Becker	***UTILISATION OF ROCKETS FOR RESEARCH APP.*** Room: Lojsta 2 - Chair: W.Jung
11:15	[A-005] Z.Qu High Altitude Balloon Launched Micro Glider: Design, Manufacturing and Flight Test	[A-064] D.Nilsson SALACIA – A Study of Martian Brines with REXUS21	[A-136] A.Schütte TEXUS – Latest Developments and New Perspectives
11:30	[A-073] S.Wlach DLR ELAHA – Current Development State of an Unconventional Stratospheric UAV	Withdrawn	[A-033] P.Vernillo MINI-IRENE: The First European Flight Experiment of a Deployable Heat Shield
11:45	[A-078] M.Laabs Results from the Inflatable, Textile and Rigidisable Antenna (INTEX) Experiment on the BEXUS21 Mission	[A-093] D.Geeroms Using a Habduino for Telemetry in Arctic Atmospheres as a Hands-on Space Education Project for Secondary School Students	[A-135] K.Roed Miniaturised Sub-payload for Multi-point In-situ Measurements on the G-chaser Student Rocket
12:00	[A-101] S.Nagels BEXUS23 OSCAR: Solar Cell I-V Monitoring System for Space Environments	[A-112] A.Buzdugan WOLF REXUS Experiment	[A-083] G.Giono Detailed Photocurrent Characterisation for Meteor Smoke Particle Detectors Onboard the PMWE Sounding Rocket
12:15	[A-147] J.Lukacevic Findings of the PREDATOR Experiment – BEXUS23	[A-067] E. de Schrijver Bifrost Parabolic Flight: A New Recurrent Hands-on Space Education Programme for Secondary School Students	[A-092] J.Breitinger Launch Campaign of the Hybrid Sounding Rocket HEROS
12:30	[A-151] G.Florin Balloons and Sounding Rockets – Platforms for Drop Tests	[A-052] L.Frezza Assessment of the VHF Omnidirectional Range (VOR) Performance in the Stratosphere: STRATONAV on BEXUS22	[A-070] G.Lindahl Recent and Future Norwegian Sounding Rocket Projects conducted by Andoya Space Center
12:45	[A-062] T.A.Mis Balloon Micro Lifeform-and-Meteorite Assembler (BULMA) Experiment for BEXUS22 Launch Campaign	[A-094] F.Hertel Trajectory Analysis of the Hybrid Sounding Rocket HEROS	Withdrawn
	13:00 – 14:15 Lunch		

THURSDAY 14 JUNE AFTERNOON SESSION		**PROGRAMME**
14:15	PLENARY INVITED LECTURE: [A-153] IN SITU X-RAY STUDIES OF METAL ALLOY SOLIDIFICATION IN MICROGRAVITY CONDITIONS – THE XRMON PROJECT- H. NGUYEN-THI - ROOM: WISBY	
	LIFE & PHYSICAL SCIENCES Room: Wisby - Chair: A. Verga	***TECHNOLOGY & INFRASTRUCTURES FOR SR*** Room: Lojsta 2 - Chair: D.Krause
14:45	[A-025] L.Maywald REXUS22 GRAB: Assessment of the Adhesive Properties of Gecko-inspired Materials under Space-like Conditions	[A-008] A.Kolbe Design of Hybrid Lightweight Fins for Sounding Rockets
15:00	[A-150] A.Vaerneus The XRMON-DIFF2 Diffusion Experiment on MAXUS9 Mission	[A-102] M.Friedrich On the Calibration of Plasma Probes on the Maxidusty Mesospheric Rocket Payloads
15:15	[A-021] A.Cartasi U-PHOS Experiment: Thermal Response of a Large Diameter Pulsating Heat Pipe On Board REXUS22 Rocket	[A-111] A.Jegatheesan Low Cost Navigational Data Recording Payload for SERA Sounding Rocket
15:30	[A-069] T.Trittel Thermally Induced Material Flow in a Two-dimensional Liquid Crystal Film	Withdrawn
15:45	Coffee Break	
	LIFE & PHYSICAL SCIENCES Room: Wisby - Chair: M. Egli	***TECHNOLOGY & INFRASTRUCTURES FOR SR*** Room: Lojsta 2 - Chair: K.Blix
16:15	[A-029] L. Sturz Multiple Equiaxed Dendrite Interaction Investigated on MASER13	[A-116] F.Wolf / M.Engert RACOS – A Cold Gas Rate Control System On Board of REXUS 22
16:30	[A-034] J.Grosse Lessons Learned from the First Flight of an Atom Interferometer Payload on a VSB-30 Sounding Rocket Payload	[A-104] E.Zakutin Overview of the Dipole Inflatable Antenna Experiment (DIANE) within the REXUS21 Mission
16:45	[A-117] D.Becker Sounding Rocket Mission MAIUS-1: Creating the First Bose-Einstein Condensate in Space	Withdrawn
17:00	[A-035] G.Zimmermann Columnar-to-equiaxed Transition in the Transparent Alloy System NPG-DC for Different Gravity Levels – The Experiment "TRACE-3"	
	20:00 Gala Dinner	

ELECTROPHYSIOLOGICAL MEASUREMENTS DURING A SOUNDING ROCKET FLIGHT, RESULTS FROM THE CEMIOS EXPERIMENT ON REXUS 20

Simon L. Wuest[1,2], Tobias Plüss[1], Christoph Hardegger[1], Mario Felder[1], Aaron Kunz[1], Benno Fleischli[1], Carlos Komotar[1], Lukas Rüdlinger[1], Andreas Albisser[1], Thomas Gisler[1], Daniela A. Frauchiger[2], Marcel Egli[1]

[1] Lucerne School of Engineering and Architecture, Lucerne University of Applied Sciences and Arts, CH-6048 Horw, Switzerland, Email: simon.wueest@hslu.ch, marcel.egli@hslu.ch
[2] Institute for Surgical Technology & Biomechanics, University of Bern, Bern, Switzerland

ABSTRACT

It is still not fully understood how cells detect external mechanical forces. It is believed that mechanosensitive ion channels, among other structures, play an important role in detecting and translating physical forces into a biological response (mechanotransduction). In the framework of the REXUS/BEXUS program, we have developed an experiment with the goal to conduct electrophysiological experiments aboard a flying sounding rocket. The aim of such an experiment was, first, to assess whether electrophysiological measurements of *Xenopus laevis* oocytes on sounding rocket flights are possible, something that has never been done before. The second aim was to examine the gating properties of ion channels under microgravity conditions, if possible. The experiment was conducted in March 2016 on the REXUS 20 rocket. The post-flight analysis showed that all recording chambers were empty as the rocket reached the microgravity phase. A closer analysis of the flight data suggests that the oocytes were ripped apart a few seconds after the launch of the rocket. This first attempt at using sounding rockets as a research platform for electrophysiological recordings thus showed the method's limitation.

This paper has been submitted in a similar version elsewhere.

1 INTRODUCTION

Biological cells continuously sense and respond to their mechanical environment. To date, several mechanisms have been proposed for detecting mechanical forces and inducing a corresponding intracellular signal (mechanotransduction) [1]. As an omnipresent force, gravity has a major impact on evolution and the daily life of living organisms. Even though gravity becomes a very small force at the cellular level, it was astounding for many scientists to find that gravity variation has profound effects on many cells [2]. Among other structures, the cell membrane [3] and the embedded ion channels (membrane proteins) [4, 5], have been shown to respond to variable gravity.

Oocytes from the species *Xenopus laevis* are widely used for electrophysiological experiments. Since they are relatively easy to maintain, do not require a sterile environment and are quite large (ca. 1 mm in diameter), oocytes are easy to manipulate. In addition, the oocytes can heterologously overexpress specific membrane proteins by microinjection of either RNA or DNA. Due to their robustness, these oocytes have been used successfully in parabolic flights [6, 7]. Native oocytes as well as oocytes that overexpress Epithelial Sodium Channels (ENaC) demonstrated reduced membrane conductivity under microgravity and increased conductivity under hypergravity (parabolic flights) [6, 7]. In this study, we assessed whether oocytes are also suitable for electrophysiological measurements during sounding rocket flights. For this experiment, we further developed our previously introduced "OoClamp" for use during parabolic flights [7].

2 MATERIALS AND METHOD

2.1 Recording Principle and System Overview

The hardware was based on a previously published principle [7]. However, it had to be built from scratch, in order to meet the specific requirements for sounding rocket flights and the high integration demands. The recording principle can be thought of as an adapted patch clamp technique [7]. The voltage-dependent transmembrane currents of overexpressed or native oocytes were measured in specific recording chambers, with each holding one oocyte. By pressing the oocyte against an aperture, a patch of the cell's membrane was electrically isolated (Fig. 1). The recording chamber was divided into two compartments separated by the membrane patch. Both compartments were filled with culture medium (see below) and were equipped with two electrodes that allowed for the simultaneous application of a defined voltage (V_c) across the cell patch and measurement of the corresponding voltage-dependent current. The particular current from the ion channels of interest that were overexpressed in oocytes could be isolated by the subtraction method. Thereby, the total current (I_{leak}) could be reduced mathematically by the current recorded in a situation where the overexpressed ion channels were blocked pharmacologically (I_{patch}). As compared to conventional patch clamp technique, the oocyte was not impaled with micro-electrodes, which simplified experiment design and handling significantly. As a consequence direct control and measurement of the cytosolic potential was not possible. The contact quality of the oocyte with the aperture, was mon-

itored by determining the seal resistance. This was measured by applying one or more (trans-oocyte) voltage steps and simultaneously recording the corresponding currents. The slope of the current-voltage-relation represented the seal resistance and was typically around 100 kOhm.

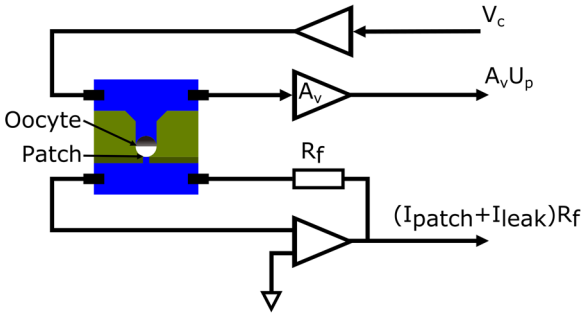

Figure 1: Schematic of the recording principle. An oocyte was placed in a cavity of a silicone chip (light green) and pressed against a small aperture at the lower end. This electrically isolated a patch of the cell membrane. The silicone chip was stabilized with a glass slide (dark green). With the help of four electrodes, a defined voltage was applied across the membrane patch and the corresponding current was measured. The medium in the lower compartment was exchangeable in order to apply various media or drugs.

The medium exchange in the recording chamber, required in order to apply and remove a specific ion channel blocker, was driven by air pressure. By means of a pressure controller, medium containers were pressurized such that the medium was pressed out through capillaries and into the recording chambers. The capillaries determined the hydrodynamic resistance and defined the flow rate together with the perfusion pressure. Valves before the recording chamber allowed for the medium flow to be controlled. The used medium was collected in a waste bag. To prevent oocytes from being displaced and to ensure good electrical isolation of the membrane patch from the remaining cell's membrane (seal), gentle pressure was applied to the upper compartment. Through a valve, the top pressure could be turned on and off as well. This allowed for the isolation of a recording chamber from the remaining system in case of malfunction. The voltage and current signals were generated, measured and digitized in close proximity to the recording chambers.

In total, six recording chambers, each accommodating one oocyte, were installed and operated in parallel. The recording chambers were mounted in two so-called late access modules, each of which had three recording chambers. These late access modules also hosted the electronics necessary for taking measurements, as well as the tubing, the capillaries and the valves. From the measurement electronics, the data were sent to the board computer, where they underwent preliminary processing before being stored on a nonvolatile memory device. Figs. 2 and 7 illustrate schematic overviews of the system.

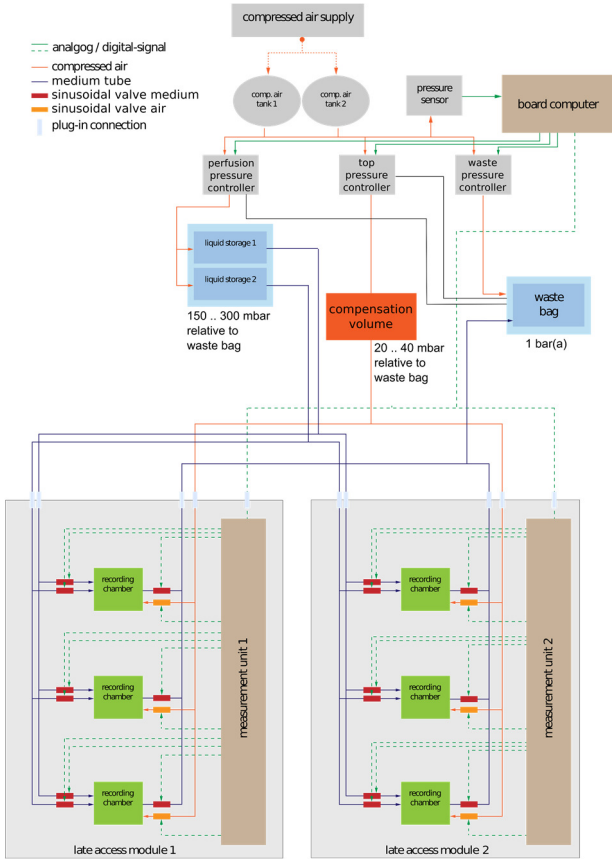

Figure 2: Schematic of the air and liquid system. Air pressure from the reservoir was reduced and regulated to the appropriate level by three pressure controllers: perfusion, top and waste pressure. The perfusion pressure was used for the flow of the medium through the recording chambers. The top pressure ensured the proper placement of the oocytes. The third pressure controller released the pressure from the waste container as medium was transferred into it. Fresh medium was distributed from its container to the two late access modules. In the late access module, the medium lines were split further, which then led to valves controlling the flow of the medium through the chambers. The medium passed through capillaries before it reached the recording chambers, which ensured a constant flow (not shown in the illustration). After the recording chamber, the medium passed through a waste medium valve and was finally collected in a waste medium bag. The vales were closed during launch and in case of malfunction.

2.2 Mechanics

The structure organized the experiment across four decks (Fig. 3). Two gas cartridges as well as pressure controllers and containers for fresh and waste medium were mounted on the lowest deck. The gas cartridges contained pressurized air (2.4 bar(a)), which was required to drive medium through the recording chambers. The two middle decks were designed to hold the two previously mentioned late access modules. The board computer and associated electronics were installed on the top deck.

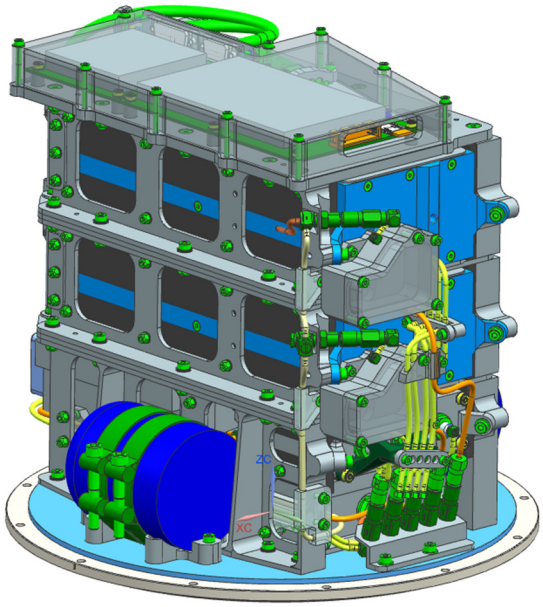

Figure 3: Structure of experiment. The structure organized the experiment across four decks. Two gas cartridges, pressure controllers and containers for fresh and waste medium were mounted on the lowest deck. Two late access modules were placed on the two middle decks. Three recording chambers were placed in each of them. The board computer and associated electronics was mounted on the top deck.

2.2.1 Recording chambers

The core measurements of the experiment were conducted in the recording chambers. Each recording chamber accommodated one oocyte and allowed the exchange of medium that was in contact with the patch of the cell membrane (Figs. 1 and 4). Furthermore, the recording chamber was designed to provide mechanical support for the electrodes and connecting tubes. The oocyte was held in a cavity of a silicone chip that featured a tiny hole that was 0.25 mm in diameter at the far end (Fig. 4). By applying top pressure, the oocyte was pressed against this hole and electrically isolated a patch of the cell's membrane. The conductivity was measured across this patch. Because the silicone was too soft to support such a tiny hole reliably, the chip was reinforced with a glass slide. To avoid sharp edges, a ruby bearing (originating in the watchmaking industry) was used to form the hole. The bearing was glued into a pre-drilled glass slide before casting the silicone around the glass slide. The introduction of the silicone chip holding the oocyte was the major modification on the recording chamber since previous publications [7].

The exchange of fluid in contact with the membrane patch was accomplished using a micro-fluidic chip, which was also cast in silicone. The two silicone chips were placed in a polymethyl methacrylate (PMMA) housing (Fig. 4), which held the two silicone chips, the electrodes and the tubing for the fluids in place. Each recording chamber was additionally equipped with a temperature sensor.

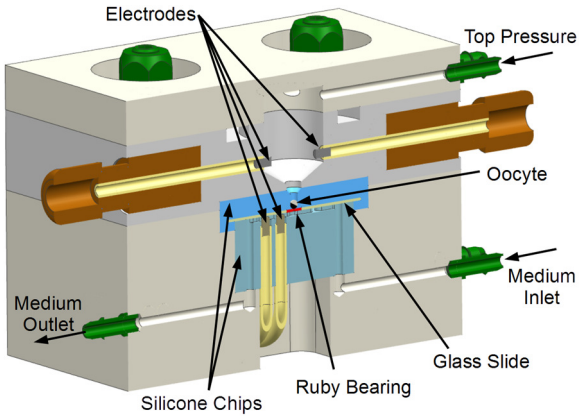

Figure 4: Cut open view of the recording chamber. The recording chamber accommodated one oocyte. It allowed the medium in contact with the patch of the cell membrane to be exchanged and provided the mechanical support for the electrodes and connecting tubes. The oocyte (black and white) was pressed in a cavity of a silicone chip (light blue), which had a tiny hole at the lower end. The chip was reinforced with a glass slide (gray), and the tiny hole was formed by a ruby bearing (red). The exchange of the medium in contact with the membrane patch was accomplished with a micro-fluidic chip (dark blue). A PMMA housing held the two silicone chips, the electrodes and the tubing for the fluids in place.

2.2.2 Late access module

The late access module accommodated three recording chambers, as well as valves and capillaries and the measuring electronics (Figs. 2 and 6). Two late access modules were operating in parallel during the experiment. The recording chambers were not fixed; instead, they were embedded in the module in a soft foam in order to decouple the vibration transfer from the module to the recording chambers. The foam was designed in multiple layers, so the tubes and cables could be laid in-between these layers.

The measurement electronics' printed circuit board (PCB) was mounted right next to the recording chambers. The valves, tubes and capillaries to regulate the medium in the recording chambers were installed on the bottom. Four valves were installed for each chamber. Among these four, two normally closed valves allowed for the flow of two different media to be controlled. The top pressure could be switched off by a normally-open valve. A third normally closed valve controlled the media flow through the waste tube. The valves for the top pressure and the waste media were only closed during launch and in case of malfunction (e.g. death of the oocyte). This allowed for a recording chamber to be isolated from the other chambers. The late access module was closed with bottom and top covers. The late access modules were made out of aluminum and thus also provided electrical shielding for the sensitive measurements.

2.2.3 Fluid system

As described above, the measurements in the recording chambers required first to set up a top pressure to the oocytes and then switching between two different media (Fig. 2). The media exchange was driven by air pressure. The supply air pressure, which was stored in two gas cartridges, was reduced and regulated to the appropriate pressure levels by three pressure controllers: perfusion pressure, top pressure and waste pressure. The perfusion pressure was responsible for the medium exchange in contact with the cell membrane patch. The top pressure kept the oocytes in place and ensured an adequate seal at the membrane patch. Since the experiment was exposed to vacuum conditions during the flight, it had to be implemented as a closed system. As liquid got transferred from the fresh medium container through the recording chambers into waste medium container, the pressure in the fluid system gradually increased. Therefore, a third pressure controller released the pressure from the waste container. The waste pressure also acted as the reference pressure for the entire fluidic system and was controlled by an absolute pressure controller (referring to absolute pressure). The pressure controllers for the top and perfusion pressure were relative pressure controllers, which adjusted the pressure so that it was always relative to the pressure in the waste container. This design made it possible to purchase all pressure controllers in the smallest possible working range, thereby providing the highest accuracy. It also ensured that the pressure differences in the recording chambers (between top and waste pressure and between perfusion and waste pressure) were always accurately regulated. The nominal top pressure was 30 mbar, and the nominal perfusion pressure was 150 mbar. The waste pressure was kept at 1 bar(a).

The fresh and waste medium containers had custom made plastic bags mounted inside. Medium could be pushed in and out of the bags by controlling the pressure of the gas phase outside of the bags. Fresh medium was pushed by the perfusion pressure out of its container and subsequently distributed via silicone tubes to the two late access modules (Fig. 2). In each late access module, the medium lines were split again, which then led to the valves that controlled the flow of medium through the chamber. In order to ensure a constant flow, the medium then passed through a 40 cm-long capillary with an inner diameter of 0.18 mm. After the medium passed through the recording chamber, it continued to run through a short tube to the waste medium valve, which was closed during launch and in case of malfunction. Directly after the recording chamber, a 5 mm-long capillary was placed in the tube, generating a small amount of back pressure. From the waste medium valve, the waste medium was brought to an intermediate waste medium container that was mounted on the front side of the late access module. From there, the medium was finally collected in the waste medium container.

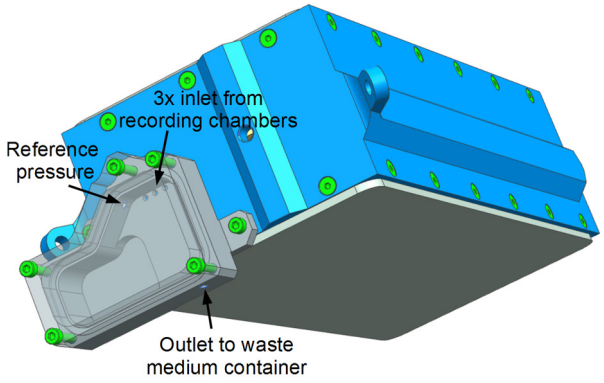

Figure 5: Intermediate waste medium container. In order to ensure a constant pressure at the recording chamber's outlet, an intermediate waste medium container was mounted on the front side of the late access module. In the upper part of this container, the waste lines from the recording chambers entered. Under normal operation, the exits of these tubes are always in contact with the gas phase. A further connection enabled fast pressure equilibration to the waste medium container (reference pressure). At the lower end, a tube was connected to the waste medium container, allowing the medium to drain.

The pressure in the recording chamber's outlet had to be kept constant and equal to the pressure in the waste medium container (reference pressure). Due to the hydrostatic pressure difference, large elevation drops from the recording chamber to the waste medium container had to be avoided. However, the limited availability of space

forced the installation of the waste medium container at the bottom of the experiment hardware. This issue was solved by introducing an intermediate waste medium container that was mounted on the front side of the late access module (Fig. 5). The waste lines from the recording chambers entered the upper part of this container. This ensured that the exit of these tubes was always in contact with the gas phase but never with the liquid phase (under normal conditions). A further connection located in the upper part ensured that the pressure in the container was constant and independent of the filling level. This connection enabled fast pressure equilibration to the waste medium container, which was the reference pressure for the entire fluidic system. Under normal conditions, pressure was only equilibrated through the gas phase. Finally, at the lower end of this intermediate waste medium container, a tube connected to the waste medium container, allowing the medium to drain.

2.2.4 Late access

In order to keep the living oocytes as fresh as possible, the oocytes were inserted into the rocket shortly before launch. This required a so-called late access hatch in the rocket through which the two late access modules and the fresh medium container were inserted. These three elements were prepared in the laboratory before launch and then combined into a single unit with a removable handle (Fig. 6). The handle was removed after insertion into the rocket. The connection of the liquid tubes was realized by quick-dry connectors, and the electrical connections were made using standard D-sub connectors, which made electrical contact automatically when the late access module was inserted.

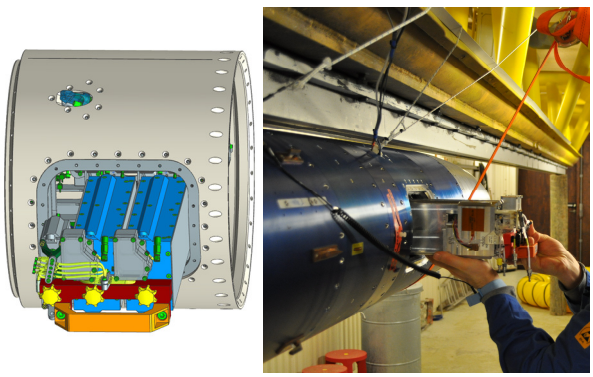

Figure 6: Late access insertion. In order to keep the oocytes as fresh as possible, the oocytes were inserted into the rocket shortly before launch. Left: Computer model showing how the late access was inserted into the rocket module. Right: Photography of the late access.

2.3 Electronics and Software

The electronics were distributed across four PCBs: one main board for the computer, two data acquisition units and one power supply unit (Fig. 7). For the interconnection of these PCBs, a Controller Area Network (CAN bus) was used due to its insensitivity to electromagnetic interference and its high reliability.

The board computer was the controlling unit for the experiment, and it was responsible for correctly executing the experiment protocol, controlling the pressure regulators, saving the measured data on two redundant nonvolatile storage devices (SD-card and Flash) and communicating with the rocket's service module. The measurement units were controlled through the CAN bus by the board computer. In addition to the electrophysiological readings, the acceleration was measured and recorded by two 3-axis accelerometers with a range of 24 g and 2 g, respectively.

The measurement units controlled the applied voltages and measured the corresponding current as well as the effective applied voltage. It also switched the valves controlling the media flow and the top pressure. In addition, it recorded the temperature in the recording chambers. While still on the ground, the units could also switch on heat foils under the recording chambers in case the temperature of the recording chambers dropped. The measurement units were directly mounted in the two late access modules in close proximity to the recording chambers. Commands from the board computer were received via the CAN bus and processed by a microcontroller. Measurement data was continuously transmitted over the CAN bus back to the board computer where they were saved. The microcontroller on the measurement units mastered three digital-to-analog converters (DACs), while the measured voltages and currents were digitized by six analog-to-digital converters (ADCs). The temperature in the recording chambers was acquired with a digital temperature sensor in each of the three chambers. These temperature readings were sent to the board computer and were also used to control heating foils under the recording chambers.

The rocket's service module provided the experiments with power, inflight signals and an RS422 serial communication interface. The 28 V power supply from the service module was converted by the power supply unit to the various voltage levels required. In addition, three signals were submitted during countdown and the flight. They were used to synchronize the procedures executed by the board computer with the major flight events. The first signal, "Start of Data Storage" (SODS), was submitted two minutes before liftoff and prepared the experiment for launch. The second signal, "Liftoff" (LO), signaled motor ignition, as the name implies. After receiving the LO signal, the board computer reset the timer. The

last signal, “Start of Experiment” (SOE), was submitted after motor separation and indicated the start of the microgravity phase. The serial communication interface enabled the data downlink during the flight. Due to the limited bandwidth, the acquired data was down-sampled by the board computer. While the rocket was still on the ground, the experiment could also be commanded via uplink. This allowed for final system level checks during the countdown. The successful insertion of the late access module could also be confirmed via uplink commands.

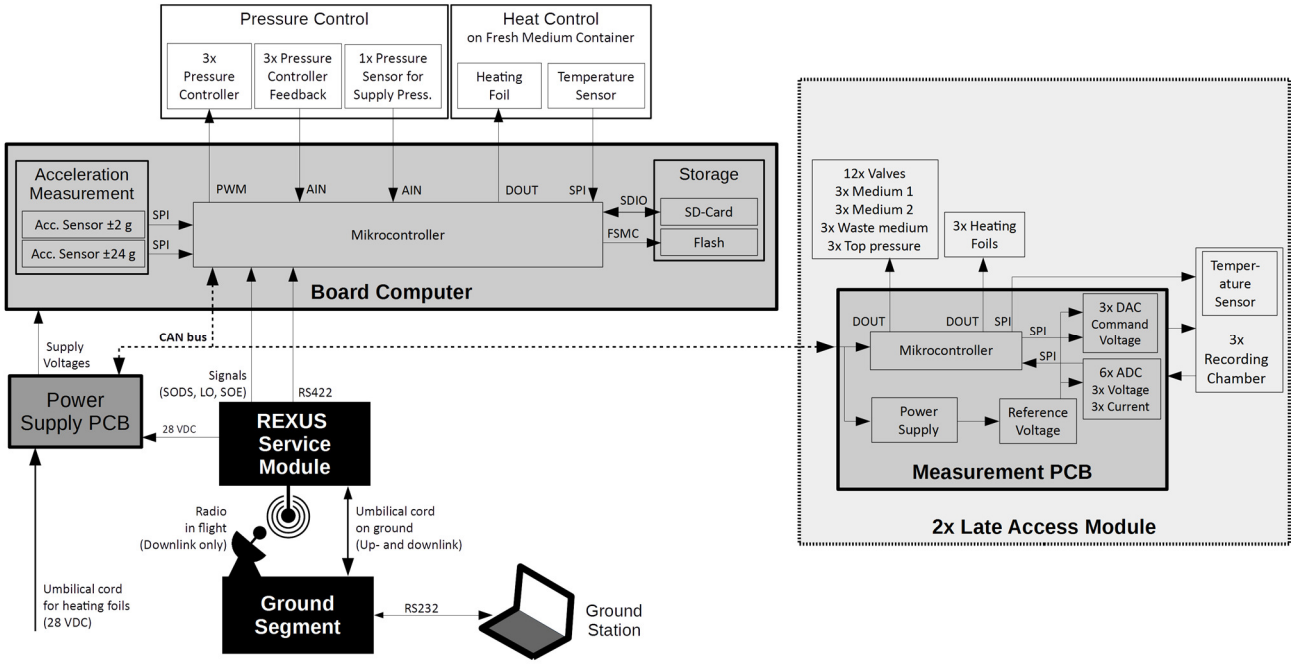

Figure 7: Schematic illustration of the electronics. The electronics were distributed across four PCBs: one main board for the board computer, two measurement units and one power supply unit. The PCBs were interconnected by a CAN bus. The board computer was the controlling unit of the experiment and was responsible for (1) the correct execution of the experiment protocol, (2) saving the measured data (on two nonvolatile storage devices), (3) controlling the pressure regulators, (4) recording the acceleration and (5) communicating with the rocket’s service module. The measurement units controlled the voltages applied to the oocytes and measured the effective applied voltage and the corresponding current. Further, they switched the valves and recorded the temperature in the recording chambers. While still on the ground, they also controlled heating foils under the recording chambers should the chambers become too cold. The rocket’s service module provided the experiments with power, inflight signals and an RS422 serial communication interface. The 28 V power supply from the service module was converted by the power supply unit to the various voltage levels required. Three signals were submitted during the countdown and the flight to synchronize the board computer with the major flight events. The serial communication interface allowed for data downlink during the flight and commanding via uplink while the rocket was still on the ground.

2.4 Heating System and Thermal Design

In order to keep the living oocyte healthy, the temperature had to be between 10 °C and 20 °C, but most favorably at 17 °C. In addition, the air temperature inside the module had to stay above 0 °C in order to prevent the medium from freezing inside the thin transporting tubes. The walls of the module were covered with an insulation layer and a polycarbonate plate to separate the aluminum structure from the bulkhead. Heating foils were installed under each recording chamber as well. The polyimide heating foils were glued on to the aluminum late access module. An additional foil was placed on the fresh medium container. Each heating foil provided 10 W of heating power. Three control loops were implemented, one in each late access module and one for the fresh medium container. A two-position controller was implemented in the software of the measuring units and the board computer. The power for heating was provided on the ground by an umbilical cord that automatically disconnected during launch. Thereafter, heating was no longer possible. Because the rocket’s surface heated up during ascent and due to the short flight duration, no additional heating was necessary.

2.5 Chemicals and Oocytes

Native oocytes were obtained from the University of Zürich (Switzerland) and Ecocyte (Castrop-Rauxel, Germany). The oocytes were prepared by the respective organizations and transported fresh to the launch site at ESRANGE (Kiruna, Sweden). The oocytes were kept at 17 °C in modified Barth medium, containing in mM 88 NaCl, 1 KCl, 0.41 $CaCl_2$, 0.82 $MgSO_4$, 2.5 $NaHCO_3$, 2 $Ca(NO_3)_2$ and 7.5 HEPES-TRIS, adjusted to a pH of 7.5.

To demonstrate a quick exchange of medium that was in contact with the cell membrane patch, either 100Na or 100Ch was used. The 100Na contained 100 mM NaCl, 2 mM $CaCl_2$, 1 mM $MgCl_2$, 2 mM KCl and 10 mM HEPES-TRIS (pH buffer). In contrast, the 100Ch contained 100 mM Choline-chloride (ChCl), 1 mM Ethylenediaminetetraacetic acid (EDTA) and 10 mM HEPES-TRIS. When switching from the more usual 100Na medium (which was also the bath medium in the upper compartment of the recording chamber) to the 100Ch, native oocytes showed a small and unspecific reaction, since 100Ch has a very small amount of cations.

2.6 Sounding Rocket and Flight

The REXUS 20 rocket was equipped with an "improved Orion" motor and had four experiments on board. REXUS 20 weighed 545.8 kg and measured 5.96 m in length, which is particularly long and heavy in comparison to usual REXUS rockets. Therefore, at 77.5 km, the apogee was lower than under normal conditions. The late access module was prepared shortly before launch and was inserted into the rocket just before arming. The successful insertion was checked via the uplink/downlink communication. Oocyte integrity was checked again only minutes before liftoff.

3 RESULTS

The CEMIOS experiment was developed and conducted within the REXUS/BEXUS program [8], which is realized under a bilateral agreement between the German Aerospace Center (DLR) and the Swedish National Space Board (SNSB). It was conducted in March 2016 on the "REXUS 20" rocket under almost optimal conditions. As the flight was scheduled for early morning, the late access modules were prepared during a night shift and were completed in time. All the systems of the experiment operated as planned during the flight. The temperature in the recording chamber was stable in the range between 15 ° and 18 °C. The temperature recorded on the fresh medium container increased during the flight but remained in an acceptable range between 14 ° and 17 °C. Also, no significant pressure drop was recorded, which would have indicated a major leak. Furthermore, we assessed if the medium in contact with the membrane patch was exchanged by switching between the different media (100Na and 100Ch) as explained previously. This test worked well during the test run shortly before launch.

However, all of the recording chambers appeared to be empty as the rocket reached the microgravity phase. Data from the launch period show a sharp drop in the applied voltage accompanied by a sharp rise in the current signal just a few seconds into the flight (Fig. 8). This indicates a sudden short circuit between the upper and lower compartments (or electrodes) in the recording chamber. These events likely indicate the time points when the oocytes were ripped. Inspection of the hardware after the flight showed that the waste compartments were full of oocyte debris, which is in agreement to the assumptions stated above. Because of this issue, no electrophysiological recordings were possible under the microgravity conditions.

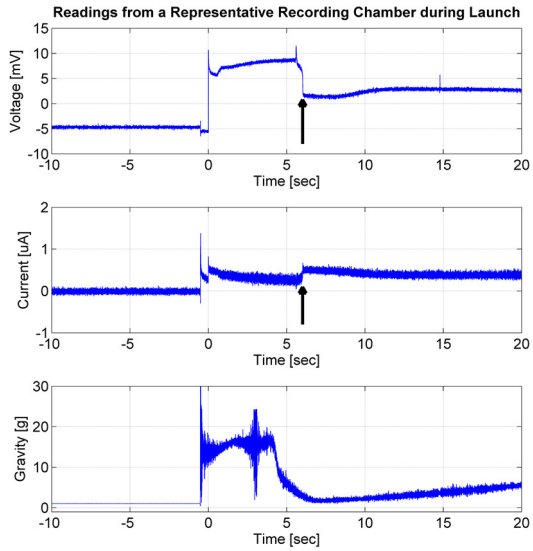

Figure 8: Representative reading of a recording chamber during launch (liftoff at 0 seconds). The voltage jump at liftoff was triggered by the board computer, to asses (1) if liftoff-signal was received and (2) obtaining a measurement of the seal resistance. A sharp drop in the applied voltage accompanied by a sharp rise in the current signal can be seen just a few seconds into the flight (arrow). Since the recording chambers all appeared to be empty as the rocket reached the microgravity phase, this event likely indicates the time point when the oocyte was ripped.

4 DISCUSSION AND CONCLUSION

Since all recording chambers were empty as the microgravity phase was reached, we were not able to demonstrate the feasibility of the proposed electrophysiological

experiments. The voltage and current readings during the launch suggest that the oocytes were ripped a few seconds into the flight. We believe that the vibrations that occurred at launch were the main cause of this. Ground tests, performed during the experiment validation phase, have demonstrated that the survival rate of the oocyte is critical during vibration (random vibration along a single axis at 12.7 g_{RMS}). Although the recording chambers were damped by foam, it appeared that this measure was not sufficient. It is thus possible that the linear acceleration during the launch compressed the foam and thereby reduced its damping properties.

In addition, there were several critical issues attached to this electrophysiological experiment: (1) Although the recording chamber was designed to provide optimal conditions for the oocytes, some died within an hour, while others survived several hours. We were not able to predict whether or not the oocytes would do well in the recording chambers by visual inspection for morphological specifications alone. Even though the flight duration was just around 10 minutes, the preparation and late access took several hours during which the oocytes had to survive in the recording chamber. (2) Due to the high level of integration of the experiment hardware, replacing a lost oocyte took up to 30 minutes, which is a long time when you are close to launching the sounding rocket. (3) For safety and operational reasons it was often not possible to perfuse and monitor the oocytes, which reduced their survival chances. (4) The late access had to be inserted while the rocket was in a horizontal position. This bears the risk of oocytes being displaced during late access and the following arming procedure. For these reasons, three oocytes were already lost after arming, despite extensively practicing and simulating the loading procedure.

In conclusion, electrophysiological measurements aboard a sounding rocket are difficult to perform given the conditions we presented in this paper. Further improvements on the experiment design and operations need to be implemented before a reflight. Unfortunately, some questions remained unanswered after our REXUS 20 flight and have to be clarified before the next flight: (1) What vibrations (frequency and magnitude) can oocytes tolerate? (2) What kind of stress (acceleration and/or vibration) caused the final rupture of the oocytes at launch? (3) What is a more suitable oocyte screening method that would ensure the recording chamber gets equipped with only the fittest eggs. It should also be possible to apply this method at the launch facility. (4) A general challenge, however, was the fact that the insertion of the late access module had to be done while the sounding rocket was still in a horizontal positon. This made the design of the module, including the recording chamber, more complicated. It would help a lot if the late access could be performed after the erection of the rocket.

5 ACKNOWLEDGEMENTS

We acknowledge our internal supporters, namely Ralf Baumann and Marcel Joss. We thank Ian Forster and Eva Hänsenberger from the University of Zürich for providing us with oocytes and helping us with their expertise. We also thank Benjamin Gantenbein from the University of Bern and the Gebert Rüf project # GRS-X028/13 for supporting this project. A special thanks goes to the supporters from the industry, namely Ruag Thun, Plastika Balumag AG and Plüss AG. We furthermore thank the Swiss Space Office for financing this project. Ultimately, we thank the REXUS/BEXUS program and its supporting agencies, namely the German Aerospace Center (DLR), the Swedish National Space Board (SNSB) and the European Space Agency (ESA) for making this project possible.

6 REFERENCES

1. Eyckmans, J., et al., *A Hitchhiker's Guide to Mechanobiology.* Developmental Cell, 2011. **21**(1): p. 35-47.
2. Pietsch, J., et al., *The effects of weightlessness on the human organism and mammalian cells.* Curr Mol Med, 2011. **11**(5): p. 350-64.
3. Sieber, M., W. Hanke, and F.P.M. Kohn, *Modification of Membrane Fluidity by Gravity.* Open Journal of Biophysics, 2014. **Vol.04No.04**: p. 7.
4. Meissner, K. and W. Hanke, *Action potential properties are gravity dependent.* Microgravity - Science and Technology, 2005. **17**(2): p. 38-43.
5. Goldermann, M. and W. Hanke, *Ion channel are sensitive to gravity changes.* Microgravity Science and Technology, 2001. **13**(1): p. 35-38.
6. Richard, S., et al., *A Semi-automated Electrophysiology System for Recording from Xenopus Oocytes Under Microgravity Conditions.* Microgravity Science and Technology, 2012. **24**(4): p. 237-244.
7. Schaffhauser, D.F., et al., *Microfluidic platform for electrophysiological studies on Xenopus laevisoocytes under varying gravity levels.* Lab on a Chip, 2011. **11**(20): p. 3471-3478.
8. Callens, N., et al., *REXUS/BEXUS – Rocket and Balloon Experiments for University Students*, in *21st ESA Symposium on European Rocket & Balloon Programmes and Related Research* 2013, European Space Agency: Thun, Switzerland. p. 561-568.

ANALYSIS OF TRANSIENT SURFACE TEMPERATURE AND AERODYNAMIC HEATING FOR SPACE EXPLORATION BALLOON

VISBY, SWEDEN
11-15 JUNE 2017

Jingjing Cai [(1)], Yanchu Yang [(1)], Qiang Liu [(1)], Yuanping Zhang[(1)], Dongbo Shi [(2)], Xinying Wang [(2)]

[(1)] Acdemy of Opto-Electronics, Chinese Academy of Sciences, Beijing 100094, China.,
Email: caijingjing@aoe.ac.cn
[(2)] National Space Science Center, Chinese Academy of Sciences, Beijing 100190, China,
Email:liangfuxin@iccas.ac.cn

ABSTRACT

A thermal analysis model for the balloon was proposed, with the solar radiation, the long-wave radiation of the surrounding environment and convective heat transfer with the environment considered, and the heat transfer mechanism between the balloon and its environment was described in detail. The finite element method was employed to analysis the temperature distribution of the balloon surface, with the complementation of the user's defined functions.

The effects of the aerodynamic heating due to the high initial velocity were inspected with the classic Ray-Riddell formulation, the aerodynamic heat flux on the windward and the stagnation temperature of the balloon was simulated numerically.

The results suggest that the release altitude and the initial ascending velocity may exert great influence on the surface temperature and aerodynamic heating of the balloon, and can provide quantity data support for the space exploration balloon design and mission planning.

1. GENERAL SPECIFICATIONS

The space exploration balloon can be used in the in-situ detection of the plasma, electric and magnetic properties of ionosphere in the near space, or carry out space physics experiment in the upper atmosphere. It has superiority over the conventional space exploration system in respects of light weight, high load, low launch cost and high reliability.

The space exploration balloon is carried into the near space or upper atmosphere by a sounding rocket. During the ascending process, the balloon is folded and confined in the narrow chamber of the rocket. When the rocket reaches its designed altitude, the balloon will be released and instantaneously filled with isopentane. Then the balloon quickly reaches its fully deployed status with the expansion of the isopentane. The exploration missions then would be conducted throughout the balloon flight process.

The balloon was endowed with high initial ascending velocity while released from the sounding rocket. After the departure from the rocket, the balloon will confront complicated thermal environment with complex heat fluxes and affected by the resulting heat loads. The thermal environment of the balloon mainly comprises the radiation heat from the sun, the earth and the space, the convective heat transfer between the balloon and the atmosphere and isopentane, and the aerodynamic heating due to the high initial ascending velocity.

Here, the major assumptions for the exploration balloon are as follows:
(1) The balloon will not be out of shape during the ascending and descending.
(2) The inner gas is totally transparent, and it does not absorb any energy.
(3) The balloon will be instantaneously filled with the gas as soon as it is released from the sounding rocket.

2. ATMOSPHERIC MODEL

During the ascent and descent phase, the temperature and density variation at the flight altitude is important. Based on 1976 standard atmosphere, the temperature and density are modeled as curve:

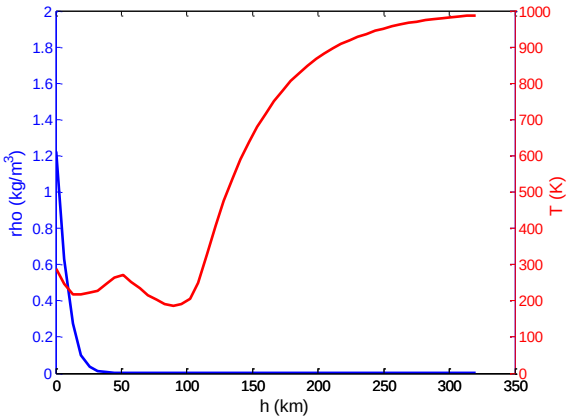

Figure 1: 1976 standard atmosphere model between 0~320km

3. DYNAMIC MODEL

The net buoyancy of the balloon is

$$F = \rho_a V g - \left(m_g + m_f + m_{pay}\right) \qquad (1)$$

Where ρ_a is the density of the ambient atmosphere, V is the volume of the balloon, m_g is the mass of inner gas, m_f is the mas of the film, m_{pay} is the mass of the payload, and g is the gravitational acceleration.

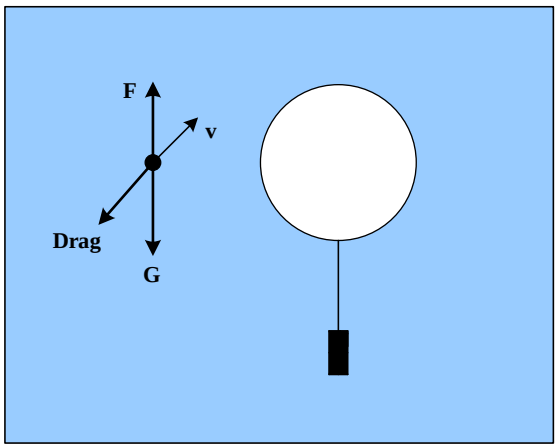

Figure 2: dynamic analysis in vertical direction

The governing differential equation of the vertical force balance on the balloon is:

$$\frac{d^2z}{dt^2} = \frac{F+D}{m_{total}+m_{add}} \quad (2)$$

Where m_{total} is the total mass of gas, film and payload:

$$m_{total} = m_g + m_f + m_{pay} \quad (3)$$

The m_{add} is the virtual mass, it can be calculated by

$$m_{add} = C_{add}\left(\rho_a V\right) \quad (4)$$

Where C_{add} is the virtual mass coefficient, it always be assumed 0.25~0.5 for sphere.

The drag force of the balloon D can be calculated by

$$D = \frac{1}{2}\rho_{air}\cdot v^2 \cdot C_d \cdot A_{top} \quad (5)$$

Where C_d is the drag coeffient, A_{top} is the top projected area of the balloon.

4. THERMAL MODEL

The heat-balance equation of the balloon film may be expressed as

$$m_{film}c_{film}\frac{dT_{film}}{dt} = Q_{sun} + Q_{albedo} + Q_{IR-earth} + Q_{IR} + Q_{conv-air} + Q_{conv-g} \quad (6)$$

The heat-balance equation of the inner gas may be expressed as

$$T_{gas} = \frac{Q_{conv-g}}{m_{gas}c_{gas}} \quad (7)$$

The direct solar radiation and the diffuse radiation absorbed by the film is given by

$$Q_{sun} = \alpha\frac{I_{sun}}{e^{b/\sin\beta}}\cdot\tau_{atm}\cdot A_{project} \quad (8)$$

Where α is the solar absorptivity of the film, β is the included angle between the horizontal plane and the solar irradiation, τ_{atm} is the atmosphere transmissivity, $A_{project}$ is the project area, I_{sun} is the solar radiation constant, 1367w/m^2.

The reflected solar radiation by the earth is expressed as

$$Q_{albedo} = \frac{1}{2}\alpha\cdot\gamma\cdot\frac{I}{e^{b/\sin\beta}}\cdot\sin\beta\cdot A_{surf} \quad (9)$$

Where γ is the reflectivity of the earth;

The external infrared radiation includes earth and atmospheric infrared. It can be calculated using the following equation

$$Q_{IR} = \varepsilon A_{surf}\sigma\left[\varphi\left(T_g^4 - T_f^4\right) + (1-\varphi)\left(T_{sky}^4 - T_f^4\right)\right] \quad (10)$$

Where ε is the emissivity of the film material, φ is the view factor from the film to the earth, σ is the Stefan-Boltzmann constant, 5.67×10^{-8}W/(m K).

The external convection heat transfer between the film and ambient air can be expressed as

$$Q_{conv-air} = h_{film-air}A_{surf}\left(T_{air} - T_{film}\right) \quad (11)$$

Where $h_{film-air}$ is the heat transfer coefficient.

The internal heat transfer between the film and inner gas is given by

$$Q_{conv-air} = h_{g-film}A_{surf}\left(T_g - T_{film}\right) \quad (12)$$

Where h_{g-film} is the heat transfer coefficient.

5. AERODYNAMIC HEATING MODEL

Based on the prandtl boundary layer theory, the process of estimating the process of hypersonic pneumatic heat is estimated by dividing the flow field into the viscous flow field outside the boundary layer and the viscous dominance region in the boundary layer. When the speed of the aircraft reaches highest, the highest heat flux density in the stagnation is the most severe point of aerodynamic heating, so this calculation is only for the stagnation temperature.

The surface thermal environment of the aircraft is closely related to the aerodynamic parameters (velocity, pressure et.) of the outer boundary of the surface boundary layer. For complete gas, as long as two of the state parameters (pressure, density, temperature, enthalpy, velocity of sound, entropy, velocity, viscosity coefficient) are independent, the other variables can be obtained from the thermodynamic relationship. For the blunt body hypersonic vehicle, the head produces a positive shock wave.

For the complete gas boundary layer outer edge parameters, the air pressure and density after shock wave can be obtained by the positive shock front and back relations:

$$p_2 = p_\infty\left(\frac{2\gamma Ma_\infty^2}{1+\gamma} - \frac{\gamma-1}{\gamma+1}\right) \quad (13)$$

Where p_∞ is the Flow pressure; Ma_∞ is the flow of Mach number; γ is the specific heat ratio of the complete gas;

The outer boundary density of the boundary layer can be calculated by using the isentropic relation:

$$\rho_e = \left(\frac{p_e}{p_2}\right)^{\frac{1}{\gamma}}\rho_2 \quad (14)$$

The outer edge enthalpy of the boundary layer can be calculated by using the ideal gas equation of state:

$$h_e = \frac{\gamma}{\gamma-1}\frac{p_e}{\rho_e}\times10^{-3} \quad (15)$$

The boundary layer outer edge velocity can be calculated by using the energy equation:

$$u_e = \sqrt{2\times10^3\left(h_s - h_e\right)} \qquad (16)$$

Enthalpy of stagnation

$$h_s = 1.0084T_\infty + 10^{-3}V_\infty \qquad (17)$$

Where T_∞ is the flow temperature, V_∞ is the flow velocity.

There are many formulas available in the project estimation, and the most common is the Fay-Riddell formula for the stagnant heat flow of the hypersonic blunt body.

The dimensionless parameters related to the aerodynamic property and the transport characteristic are assumed as a series of constants: $\Pr = 0.71$, $\rho_s\mu_s/\rho_w\mu_s = 0.17 \sim 1.0$, $Le = 1.0 \sim 2.0$, By saterland law of viscosity, if the total enthalpy is in the range $h_s = (1549 \sim 24158)\,KJ/kg$ and the surface temperature within $T_w = 300 \sim 3000K$, the empirical formula calculating the flux of the stagnation can be summed up as the follow empirical formula, the error between the empirical formula and numerical method is within 3%.

$$q_{ws} = 0.763\,\Pr^{-0.6}\left(\frac{\rho_w\mu_w}{\rho_s\mu_s}\right)^{0.1}\sqrt{\rho_s\mu_s\left(\frac{du_e}{dx}\right)_s} \times\left[1+\left(Le^{0.52}-1\right)\frac{h_D}{h_s}\right]\left(h_s - h_w\right) \qquad (18)$$

Where ρ_w, μ_w represents the density and viscosity of the surface, ρ_s, μ_s represents the density and viscosity of the stagnation point, h_D is the air average dissociation enthalpy。

6. RESULT

According to the mission requirements, the maximum flying height of the carrier missile is 320km, the exploring balloon can be released during the whole flight process. The parameters of the exploring balloon are shown in the following table:

Table 1: parameters of the exploration balloon

parameters	Values
Diameter	1m
Total mass	0.6kg
Material of the balloon	Polyimide
Inner gas	Isopentane

The speed trajectory of the sounding rocket as shown:

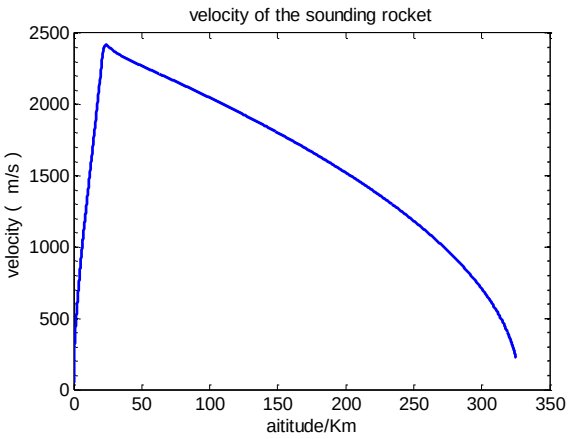

Figure 3: velocity of the sounding rocket

It can be seen that the sounding rocket reach the maximum speed 2417m/s at 24km, then the speed gradually reduce till to the 320km.

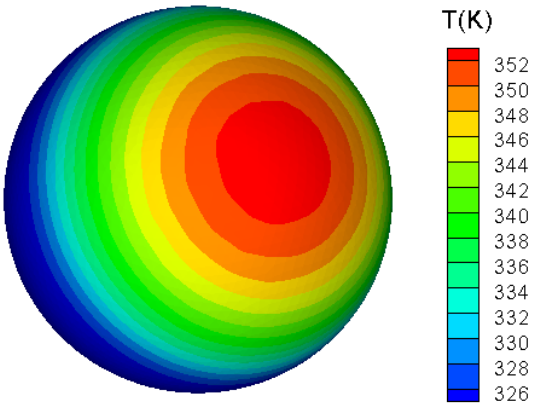

Figure 4: temperature of the exploration balloon on the top film

After the release, contribute to the action of the integrated thermal environment, the surface transient temperature distribution of the sounding balloon is shown in the figure. Because the air in the high-altitude is extremely thin, the solar radiation intensity and the surface convective heat transfer coefficient are almost unchanged from 68km ~ 100km. The temperature distribution on the surface is very close. The highest temperature on the surface is 80℃。

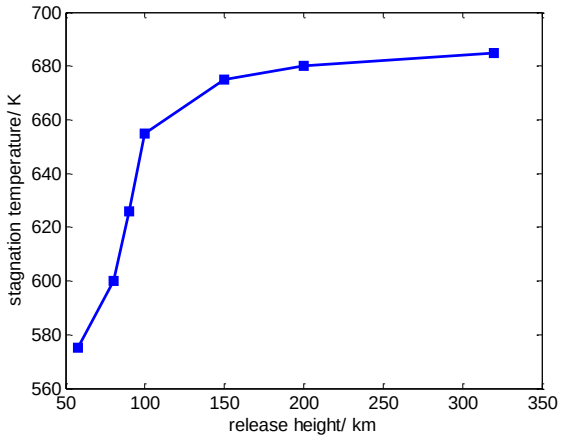

Figure 5: maximum stagnation temperature at different released altitude

According to the method of aerodynamic thermal engineering, the graph shows the maximum stagnation temperature during the flight of the sounding balloon at

typical heights. It can be seen that the lower the release height, the lower the highest stagnation temperature, once the release high is higher than 100km, the stagnation temperature changes tend to be smooth.

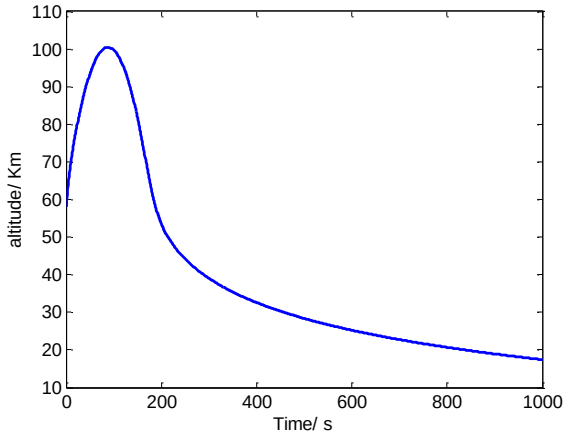

Figure 6: altitude trajectory after released at 58km

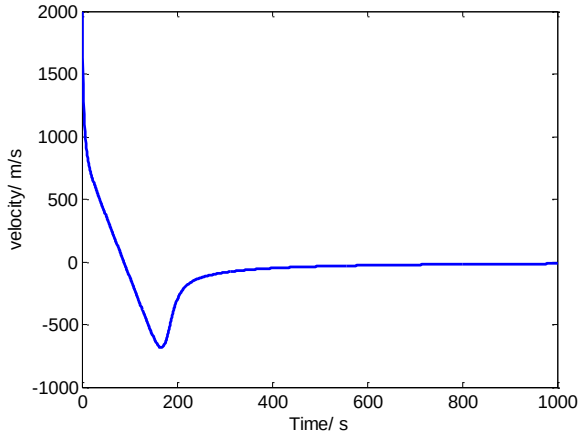

Figure 6: velocity trajectory after released at 58km

The figure shows the height and velocity of the exploration balloon after it is released at 58km. You can see that the flight height can reach 100km to meet the mission. After 1000s, for the intuition of the graph, only the previous part is intercepted. After 1000s, the velocity is less than 10m/s and gradually decrease to zero, no further aerodynamic heat, so for the intuition of the graph, only the previous part is intercepted.

7. RESULT

（1） To meet the task that covering a height of 100km, the release height cannot lower than 58 km. And that the aerodynamic analysis shows that the lower the release height, the lower the maximum stagnation temperature. Therefore, 58 km is chosen for the release.

（2） After released at 58km, the exploration balloon continues to rise with the initial velocity, then descends to complete the flight process. Under the action of gravity, the velocity reaches the maximum during the descent, meanwhile, the stagnation temperature caused by the aerodynamic heat also reaches the maximum.

（3） The aerodynamic maximum stagnation flux is generated during the falling process that is on the lower surface of the exploring balloon, and the thermal flux caused by the environment on the upper surface of the balloon, so the two are not coupled.

（4） The maximum temperature on the upper surface is 80 ℃, and 300 ℃ on the lower surface, the property of the balloon film must meet the temperature tolerance.

8. REFERANCE

1. Lv Lili, Febrery 2005.Engerering method for aerodynamic heating of hypersonic aircrafts, northwestern polytechnical university for the degree of master.
2. Batenin V M. et al. advanced reusable space transportation system for horizontal launch of air-space plane powered by pulsed MHD generators. AIAA-2001-0495.
3. Anderson E.C. lewis C H, laminar or turbulent boundary-layer flow of perfect gased or reacting gas mixture in chemical equilibrium, NASA CR-1893, October 1971
4. Zoby E V, J N moss, K sutton, approximate convective heating equations for hypersonic flows, journal of spacecraft and rocket, vol.18, NO.1, 1981, pp64-70
5. Jiang Youdi, Calculation of aerodynamic heating and transient surface temperature for hypersonic aircraft. shanghai jiao tong university for the degree of master. Februrary 2008.
6. Li X, Fang X, Dai Q, Zhou Z, Modeling and analysis of floating performance of stratospheric semi-rigid airships. Adv Space Res 2012, 50(7):881-890.
7. Farley RE, BalloonAscent: 3-D simulation tool for the ascent and float of high-altitude balloons. In: AIAA vol. 2005-7412; 2005
8. Xia XL, Li DF, Sun C, Ruan LM. Transient thermal behavior of stratospheric balloons at float conditions. Adv Space Res 2010, 46:1184-1190.

High Altitude Balloon Launched Micro Glider: Design, Manufacturing and Flight Test

Zhengyu Qu [(1)], Cuichun Li [(1)] , Yong Hao [(1)] , Feng Yan [(1)] , Yumei Qin [(1)] , Yanchu Yang [(1)]

[(1)] Academy of Opto-Electronics, Chinese Academy of Sciences, Dengzhuang South Road, 100094, Beijing, China, Email: zqu@aoe.ac.cn

ABSTRACT

This paper presents the design details, manufacturing and flight test data about high altitude launched micro glider. In design part, it is divided into three sub-parts which are aerodynamic design, electronic layout design and control law design to explain the design idea. In manufacturing part, an overall assembly process including material and components selection is presented. The low temperature experiment for the micro glider and the launcher is also discussed. In the final, the flight test data and the reason for the failure is analyzed.

1. INTRODUCTION

High altitude balloon platform as an important near space load carrier has been widely used in many areas. For recent years, a new application that to launch aircrafts from near space has been studied by many countries. A Swiss group launched a new shape gilder Smartfish from a balloon at 32000 m [1]. Their experiment shows an excellent result of the new shape design. The group Flying Robots in DLR launched a 3 m wingspan glider from near space in 2015. The flight campaign shows the feasibility for the small aircraft to fly at high altitude [2]. In 2012, the NRL of Unite States firstly proposed the concept of close-in covert autonomous disposable aircraft (CICADA). The prototype has been launched from a mother glider for stabilizing its initial attitude at the altitude 9000 m and validated the feasibility of precise landing [3] [4].

For expanding the potential application of this concept and studying the high altitude launch technology for large scale aircraft in the future, our group decides to develop the micro glider technology.

In concept design, we would like to design an aircraft that could be launched a great number at one time from a balloon. The aircraft could have the ability of stable glide, precise landing and data collection and transmission. The application concept of the micro glider is shown in Fig.1. After the balloon flight to the nearby region around the target spot, the gliders are launched from the balloon and autonomously flight to the target spot. Then the balloon will stay within a certain range around the target spot. The data collected by the glider is transferred back to the communication relay carried by the balloon and then transfer again to the satellite so that the people could finally achieve the data.

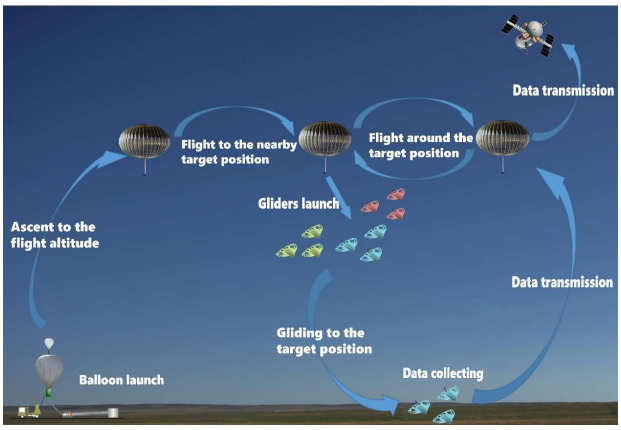

Figure 1. Application concept of the micro glider

2. MICRO GLIDER DESIGN AND SIMULATION

For meeting the design demands, the dimension of the glider should small enough. The wingspan length and chord length are decided not to be longer than 35 cm. Due to the small wingspan length, the tradition configuration with one main wing and one elevator will decrease effective wing area, which mean the wing loading will be very large and the glide speed will be fast. Hence, we adopt flying wing as the aerodynamic configuration to increase the wing area. From the manufacturing point of view, due to the glider is disposable, the structure of the glider must be simple and the cost should not be high. We decide to use printed circuit board as the material to manufacture the wing because it is easy to cut and the electronic components could be welded directly to the wing. Due to first prototype is only for validating the control law and some new designs, the mission sensor will not be included in design process.

2.1. Aerodynamic Design

As described in overall design, the micro glider will adopt flying wing as the aerodynamic configuration. Due to the PCB is selected as the wing material for the simple structure demand, the airfoil could be classified as flat-plate airfoil. For designing an optimal wing planform, the maximum lift-to-drag ratio is selected as the criteria due to we hope the aircraft could glide as far as possible. Okamoto and Azuma [5] and Torres and Mueller [6] studied various wing planforms of flat-plate airfoil at low Reynolds number. Based on their conclusion, with the same aspect ratio, the inverse-Zimmerman shows the highest lift-to-drag ratio. Considering the limits of the span length and the wing area, the inverse-Zimmerman planform with an aspect ratio 2 is decided as the final wing geometry dimension.

The maximum lift-to-drag ratio of inverse-Zimmerman planform at aspect ratio 2 is 6.9 based on the experimental results. Note that the maximum aspect ratio 6.9 is just the ideal wing planform. With the fuselage disturbance, elevon deflection and flying condition variation, the real maximum-to-drag ratio should be lower than the ideal condition. The final maximum lift-to-drag ratio considering the fuselage is decreased to 4.8 based on the CFD result.

In the design process, we find that the PCB material is much heavier for the inverse-Zimmerman planform to adjust the center of gravity, which means a balancing weight is needed to trim the glider. Hence we modified the leading edge of the planform by adding a small extra area for the balancing weight position to adjust the center of gravity.

The elevon dimension is another key parameter that affect the gliding performance. Generally the maximum elevon deflection angle should be able to reach to ±20°. The dihedral of the elevon would lead to an increasing of the balance angle of attack. Due to the stalling angle of attack is only about 12° for the flat-plate inverse-Zimmerman planform, over larged elevon dimension would lead to an over-sensitive response for the servo motors to constrain the elevon deflection angle for limiting the angle of attack less than 12°. For selecting an appropriate elevon dimension, the aerodynamic analysis is carried out in panel method software Xflr5. We tested various elevon dimension, the analysis results show an appropriate elevon dimension is that the width is one third of semi-span length and the elevon length is 7% of the local chord length. Due to the characteristics of the flat-plat airfoil flying wing configuration, the elevon should keep a 2° dihedral angle for longnitude stable flight and the trimmed angle of attack is 5°. Note that the elevon dimension is only from the aerodynamics point of view. The effectiveness of this elevon dimension still need to be tested by the flight control algorithm. The micro glider concept design is shown in Fig. 2.

For analyzing the stability and response of the micro glider, an aerodynamic model is developed based on the panel method (for solving static derivative) and CFD method (for solving dynamic derivative). Mechanical parameters are estimated in the CAD software. The results of longitudinal response and lateral-directional response are given in Fig.3. As can be seen, the step responses for both direction are stable. However, the gliding angle in longitudinal response is very slow. This may due to the dimension of the elevon is too small to control the pitch motion. The sideslip angle response velocity in lateral-direction only needs 2 second to recover to stable level, which shows the effectiveness of the elevon for controlling the roll moment.

2.2. Electronic components design

Due to the simple and low-price demand of the structure, all the electronic components should be easy to obtain. The electronic components used in the micro glider includes an U-blox GPS and a 9-axis IMU integrated in the STM32 SCM (CPU) as the whole flight control computer. The communication link component is removed from a weather sonde to transmit data (down link) including the position and control parameters to the ground station. PWM micro servo motor is selected for controlling the elevon. One main 4.2V lithium battery powers the electronic components and two small 4.2V lithium batteries for powering the heating film to heat the main battery. The circuit layout on the wing planform is

shown in Fig. 4. All components are placed along the root chord. Due to the batteries is heavier, they are placed on the front for adjusting the center of gravity.

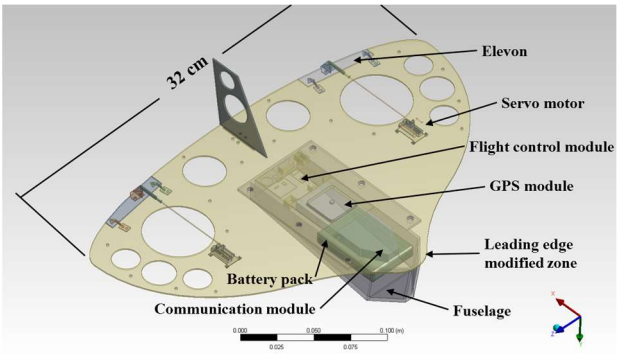

Figure 2. Micro glider concept design

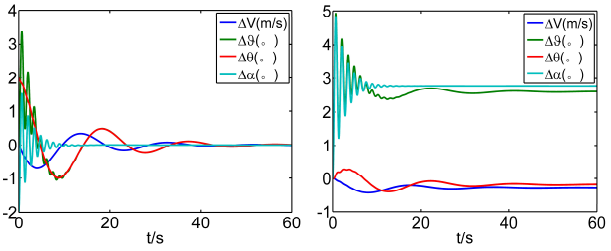

(a) Longitudinal: zero-input response (left) and zero-stat response (right)

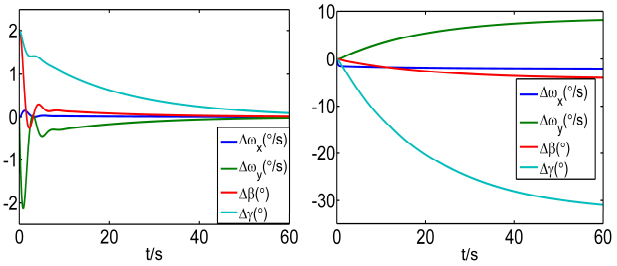

(b) Lateral-directional: zero-input response (left) and zero-stat response (right)

Figure 3. Dynamic response for the aerodynamic model

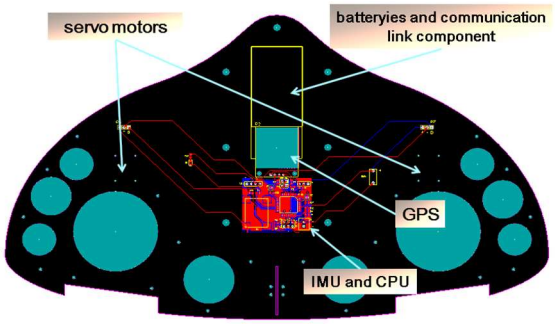

Figure 4. Electronic components design

2.3. Flight Control Design and Simulation

2.3.1. Guidance Law Design

The micro glider keeps stable gliding in longitudinal plane and the maneuver flight is in the horizontal plane. Therefore, the minimum turning radius is selected as the key performance index. The transient maneuver flight and the g-load equation could be expressed in Eq. 1 and Eq. 2:

$$\dot{\psi} = V_g \cos\theta / R \tag{1}$$

$$\tan\gamma = -V_g \dot{\psi} / g \tag{2}$$

Substituting Eq. 2 to Eq. 1 and neglecting cosθ, the turing radius R could be expressed in Eq. 3:

$$R_{\min} = \frac{V_a^2}{g \tan \bar{\eta}\gamma} \tag{3}$$

Where $\bar{\gamma} = \eta\gamma$ and η here is designed to equal to 0.7 for limiting the maneuver ability. γ is the roll angle.

The guidance law for the micro glider is divided into two modes:

- Pursuit guidance law: if the line of sight distance is large enough, the micro glider pursuits the target position. In this process, the velocity bearing angle ψ_V always equal to the angle of sight $\psi_{\lambda\mu}$. ψ_V and $\psi_{\lambda\mu}$ are obtained from the GPS data.

The error $e = \psi_{\lambda\mu} - \psi_V$ is limited under the range of $(-\pi, \pi]$. For eliminating the error e, PI control method is adopted, which could be expressed in Eq. 4:

$$\dot{\psi} = K_{GP2} \cdot e + K_{GI2} \cdot \int e dt \tag{4}$$

Where K_{GP2} and K_{GI2} need to be estimated by the designer. Based on the error-eliminated $\dot{\psi}$, the guidance law export the required roll angle:

$$\begin{cases} \gamma_{des} = \text{atan}\left(-V_g \dot{\psi} / g\right) \\ \gamma_{cmd} = \text{sat}\left(\gamma_{des}, \pm\bar{\gamma}\right) \end{cases} \tag{5}$$

Where the function sat is the limiting function

- Spiral descent guidance law: if the line of sight distance is small enough, the micro glider descend spirally around the target position. In this process, based on the error e, guidance law decides which side of the circle the micro glider needs to enter, which is shown in Fig. 5.

For condition of $e > 0$, firstly calculating the ψ_0 and $\Delta\psi_0$:

$$\psi_0 = \text{modangle}\left(\psi_{\lambda\mu} + \pi/2\right) \tag{6}$$

$$\Delta\psi_0 = -K_0\left(D - R\right) \tag{7}$$

Where the function modangle is the limiting function.
Then calculating the guidance command angle ψ_{cmd}:

$$\psi_{cmd} = \text{modangle}\left(\psi_0 + \Delta\psi_0\right) \tag{8}$$

Next step calculating the nominal spiral angular velocity:

$$\dot{\psi}_* = \frac{-V_g \cos\theta}{R} \approx \frac{-V_g}{R} \tag{9}$$

Based on the Eq. 8 and Eq. 9, the guidance command angular speed $\dot{\psi}$ could be expressed in Eq. 10:

$$\dot{\psi} = K_{GP3} \cdot \text{modangle}\left(\psi_{cmd} - \psi_V\right) + \dot{\psi}_* \tag{10}$$

Where K_{GP3} needs to be estimated by the designer as well. In the final, calculating the required roll angle, which is as same as Eq. 5.
For the condition of $e < 0$, only the ψ_0 and $\Delta\psi_0$ in the calculation is different compared to the condition of $e > 0$:

$$\psi_0 = \text{modangle}\left(\psi_{\lambda\mu} - \pi/2\right) \tag{11}$$

$$\Delta\psi_0 = K_0\left(D - R\right) \tag{12}$$

2.3.2. Control Law Design

The linear PID control method is adopted for the micro glider. The command for the actuator is divided into two parts: nominal command and deviation control command. Therefore, the control parameters are determined to control the flight path angle θ (gliding angle) in longitudinal channel and the roll angle γ in lateral-directional channel.

- Longitudinal channel: the command flight path angle θ_{cmd} is only decided by the glider lift-to-drag ratio K and the real flight path angle θ is estimated by the assumption that the glider dynamic pressure is constant during glide. The θ_{cmd} and θ are expressed Eq. 13 and Eq. 14:

$$\theta_{cmd} = -\text{atan}\left(1/K\right) \tag{13}$$

$$\theta = \text{asin}\left(V_U/V_0\right) \tag{14}$$

Where K is lift-to-drag ratio, V_U is the vertical speed obtained from GPS and V_0 is true air speed.
Due to there is only one parameter θ is available for the longitudinal channel, the PI control method is still used:

$$\begin{cases} e = \theta_{cmd} - \theta \\ \Delta\delta_{z,des} = K_{CP1} \cdot e + K_{CI1}\int edt \\ \Delta\delta_z = \text{sat}\left(\Delta\delta_{z,des}, \pm\Delta\overline{\delta}_z\right) \end{cases} \tag{15}$$

Where $\Delta\delta_{z,des}$ is the designed elevon deflection angle (symmetric) for controlling the pitching moment. K_{CP1} and K_{CI1} are the parameters estimated by the designer.

- Lateral-Directional Channel: the command rolling angle γ_{cmd} is needed for maneuvering flight. Based on the sensor ability, the rolling angular speed ω_x could be measured and the rolling angle is obtained by integrated ω_x. The PID control method for controlling the rolling motion are expressed below:

$$\begin{cases} e = \gamma_{cmd} - \gamma \\ \dot{e} \approx -\omega_x \\ \Delta\delta_{x,des} = K_{CP2} \cdot e + K_{CD2} \cdot \dot{e} + K_{CI2}\int edt \\ \Delta\delta_x = \text{sat}\left(\Delta\delta_{x,des}, \pm\Delta\overline{\delta}_x\right) \end{cases} \tag{16}$$

Where $\Delta\delta_{x,des}$ is the designed elevon deflection angle (anti-symmetric) for controlling the rolling moment.
In the final, the actuator compound command of the elevon is expressed below:

$$\begin{cases} \delta_R = \delta_{x0} + \Delta\delta_x + \delta_{z0} + \Delta\delta_z \\ \delta_L = -\delta_{x0} + \Delta\delta_x + \delta_{z0} + \Delta\delta_z \end{cases} \tag{17}$$

Where δ_{x0} and δ_{z0} is the nominal elevon deflection angle.

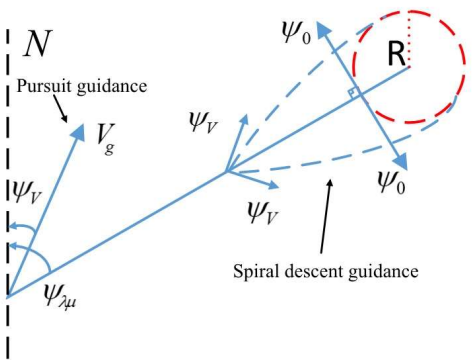

Figure 5. Two modes of the guidance law

2.3.3. Simulation Results

For validating the control law design, the most difficult situation that the initial heading direction is on the contrary of the landing position is tested. The result is shown in Fig. 6. The low initial velocity lead to an oscillation at the initial phase. After gliding a certain distance, the micro glider turns around and heads to the designed landing position. The simulation results validated the feasibility of the control law design.

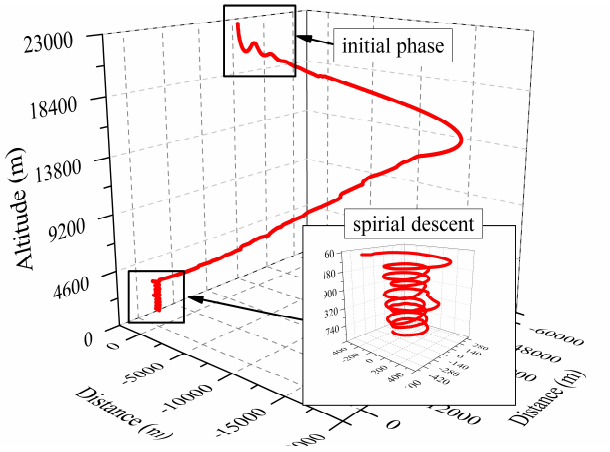

Figure 6. Simulation results for the control law design

3. MANUFACTURING AND ENVIRONMENTAL TEST

3.1. Micro Glider Manufacturing

The printed circuit board shown in Fig. 7(a) is cut based on the micro glider planform dimension. The material of the PCB is RF-4 and the thickness is 1 mm for the strength demand. If the thickness is smaller than 1 mm, the board would be flexible in high dynamic pressure. All electronic components shown in Fig. 7(c) are welded to the PCB manually.

The mechanical structure of the micro glider only includes the elevon control system, which is shown in Fig. 7(b). The elevon and the servo motor is connected by an aluminum-made push-pull rod. The elevon could have a maximum 20° dihedral angle and a maximum 10° anhedral angle with full strokemm 10 mm of the servo motor arm. Through the test, the geometrical relationship between the strokemm of the servo motor and the elevon deflection angle is linear.

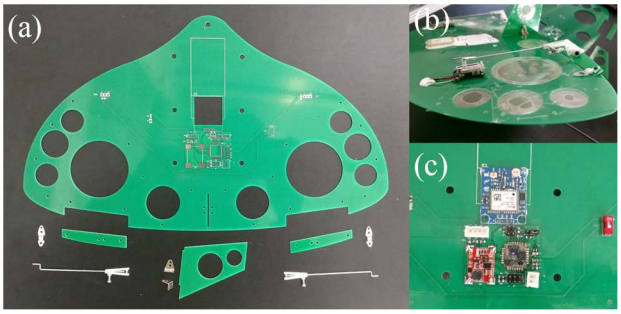

Figure 7. Components of the micro glider

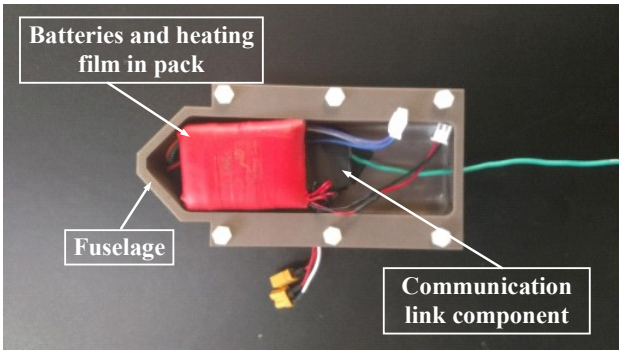

Figure 8. Batteries, communication link component and the fuselage

3.2. Launcher Manufacturing

The launcher consists of four main parts, which are slide rail, spring, slider and solenoid switch. The effective length of the slide rail is 420 mm. During the ascent of the balloon, the launcher is mounted on the gondola. The launcher could provide a stable initial attitude and an initial velocity about 10 m/s. Even though it is not a low velocity for micro air vehicle, it is still difficult to make the glider into equilibrium glide at the initial phase at high altitude due to the low air density effect, which means the glider will accelerate for a while at the initial phase to get into the equilibrium glide state.

3.3. Environmental Test

The high altitude low pressure and low temperature effect on the micro glider and the launcher are conducted in the environment simulation chamber, which is shown in Fig. 9. For testing the glider, the temperature is decreased from 0°C to -60°C gradually and keep the micro glider in the chamber for 2 hours for testing the electronic components, battery and elevon performance in low temperature. The

results show that the servo motor could withstand a lowest -50℃ temperature. If the temperature is lower than -50℃, the response of the servo motor will become very slow. The electronic components including CPU and GPS seem could work normally with the lowest tested temperature -60℃. This is due to the protection of the fuselage that prevent the forced convection effect. However, for the battery performance, we find that the temperature is very sensitive to the discharge capacity. Based on the test, when the temperature is lower than -20℃, the battery will lose more than 85% of its discharge capacity and this will lead to an abnormal working condition for other electronic components. For solving this problem, we decided to use a heating film to heat the main battery and meanwhile, the heating film will also heat the batteries that powers for it, as shown in Fig. 8. As for the experimental evaluation of the launcher, one big problem is that if the air humidity is high, low temperature will result in a condensation of the moisture around the magnetic valve, which will delay the time of open.

Figure 9. Environmental simulation chamber

4. FLIGHT TEST

The flight test of the micro glider as a sub-payload of the super pressure balloon was conducted on 11th, September (shown in Fig 11). The launch of the micro glider is activated at two altitudes, which are 9000 m and 21000 m, shown in Fig. 10. At 9000 m, due to the higher control effectiveness (higher air density compared to the high altitude), the micro glider is designed to activate the control system immediately after launching from the balloon. At 21000 m, the micro glider is designed to glide at the initial phase without control and when the altitude descend to lower than 18000 m, then activate the control system.

The flight trajectory is shown in Fig. 13. Unfortunately, the flight test cannot be said successfully. At the two launching altitudes 9000 m and 21000 m, the micro glider seems to lose its gliding state after being launched from the balloon. The trajectory indicates the motion is free falling. From the positive point of view, the roll angle control data shown in Fig. 12 indicates the control system could operate normally. The calculated roll angle is the real roll angle of the micro glider after losing attitude. It is calculated by integrating the angular velocity. The required roll angle is very large due to the control system try to correct the free falling motion of the glider and the command roll angle is small due to the limit function limits the roll angle within a small range. Furthermore, the insulation method for the batteries and the electronic components are proved to be effective.

(a) Launch at 9000 m

(b) Launch at 21000 m

Figure 10. Screenshot of the launch at the two altitude

The failure of the flight at the two launching altitudes are attributed to different reasons.

At 9000 m, we can see from Fig. 10(a) that the micro glider turns over immediately after being launched. The specific reason of the turn-over is not quite sure. One possible reason may due to the wind speed is high so that the glider is blow over by the gust. Another possible reason may due to the different initial deflection angle of the two elevens.

21000 m, we can see from the Fig. 10(b) that the initial attitude of the micro glider after being launched is very stable. However, the micro glider still fails to get into glide path after the initial acceleration. One possible reason could be attributed to the difference between the aerodynamic model and the real flight performance. The aerodynamic model is calculated only with the numerical method. In simulation, it shows the possibility of the stable glide and precise landing even in the worst condition. However, in real flight environment, the weight of the glider after being assembly is beyond the estimation, which is increased to 360 g (only 160 g total weight in the estimation). Furthermore, the dimension of the elevon may be designed too small. Both of the over weight problem and the small elevon problem lead to the slow response in the longitudinal direction so that the velocity path angle could not be controlled in time. Another possible reason may due to the poor aerodynamic performance of the flat-plate airfoil. For specific, the stall angle of attack of the flat-plate is very small, which means it is very easy to lose its lift under a gust.

Figure 11. Balloon and the gondola before launching

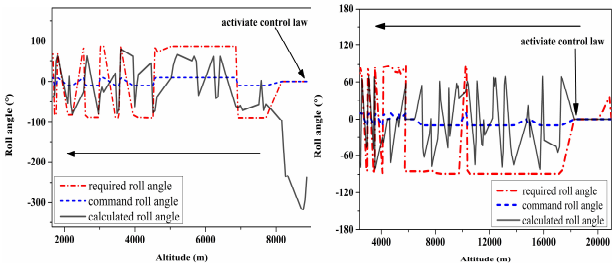

Figure 12. Roll angle control data of the micro glider: launch at 9000 m (left) and launch at 21000 m (right)

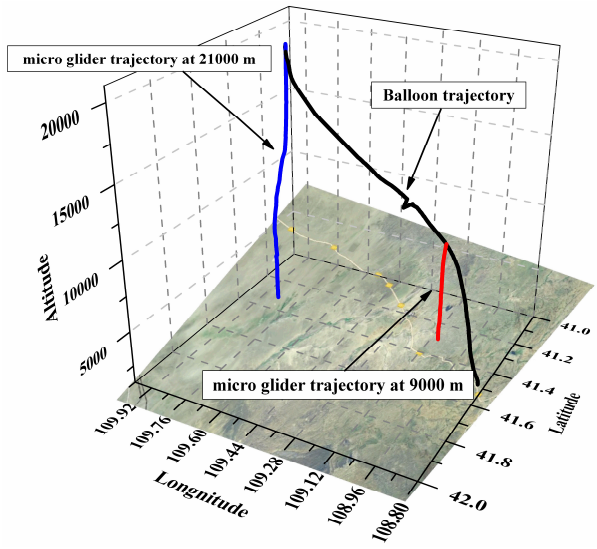

Figure 13. Trajectory of the balloon and the glider

5. CONCLUSION

The aerodynamic design and the control law design in the simulation show the possibility for stable glide and the precise landing. However, the real flight test performance is far from the simulation results and our expectation. There are several reasons for the failure of the flight test, which still need to be analyzed deeply.

We are still very confident for the potential application of the micro glider concept. For the next step, several concept need to be developed and re-design including the material, electronic components and the launching method. Particular for the launching method, the launcher is proved not helpful for stabilizing the initial attitude and is also difficult to offer an enough initial velocity at high altitude environment. The best launch method for the current configuration still need to be studied.

6. REFERENCE

1. Steenari, D., Kuhn, T. & Wlach, S. (2013). VEXREDUS: A Student High Altitude Glider Project to Demonstrate the Capabilities of a Blended Wing Body Concept. In Proc. '21st ESA Symposium on European Rocket and Balloon Programmes and Related Research', ESA SP-721, ESA Communications, European Space Agency, Thun, Switzerland, pp. 225-232.

2. Wlach, S., Schwarzbach, M. & Laiacker, M. (2015). DLR HABLEG–High Altitude Balloon Launched Experimental Glider. In Proc. '22nd ESA Symposium on European Rocket and Balloon Programmes and Related Research', ESA SP-730, ESA Communications, European Space Agency, Tromsø, Norway, pp. 385-392.

3. Kahn, A.D. & Edwards, D.J. (2012). Navigation, Guidance and Control for the CICADA Expendable Micro Air Vehicle. In Proc. 'AIAA Guidance, Navigation and Control Conference', AIAA 2012-4536.

4. Edwards, D.J. & Kahn, A.D. (2012). Design Evolution of a High Packing Density Micro Air Vehicle for Local-Area Seeding. In Proc. 'AIAA Atmospheric Flight Mechanics Conference', AIAA 2012-4735.

5. Okamoto, M. & Azuma, A. (2011). Aerodynamic Characteristics at Low Reynolds Number for Wings of Various Planforms. *AIAA Journal*, 49(6): 1135-1150.

6. Torres, G.E. & Mueller, T.J. (2004). Low Aspect Ratio Aerodynamics at Low Reynolds Numbers. *AIAA Journal*, 42(42): 865-873.

THE GRAND CHALLENGE INITIATIVE CUSP PROJECT

KOLBJØRN BLIX

Andøya Space Center
Andenes, Norway
Tel: +47 97151864
Email: kolbjorn@andoyaspace.no

JØRAN MOEN

University of Oslo
Oslo, Norway
Tel: +47 22855666
Email: joran.moen@fys.uio.no

The Grand Challenge Initiative (GCI) is a large-scale international collaboration effort targeting advancement in specific, fundamental issues in space and earth science. The GCI concept was conceived and developed over the past two years by the Andøya Space Center (ASC) and the University of Oslo. Their work has culminated in the first GCI project - "GCI Cusp" - to determine the multi-scale physics of heating and charged particle precipitation in the ionosphere specific to the geomagnetic cusp region.

GCI mission patch

"With 6 NASA sounding rocket missions now manifested for the trilateral (USA, Norway and Japan) "Grand Challenge Initiative – CUSP project", the GCI launch campaign in December 2018 and January 2019 will be a historic event. Consisting of 3 Black Brant XII's, 2 Black Brant X's, 1 Terrier Improved Malemute (G-CHASER student rocket), a SS-520 from ISAS/JAXA and 1 S30/Improved Malemute ICI-5 from Norway, this collaboration will be one for the books on sounding rocketry in terms of the amount of major scientific rockets in one launch campaign, the complexity in telemetry and the complexity in launch criteria for the two simultaneously used launch sites at Andøya, Norway and Ny-Ålesund, Svalbard." The statement comes from Dr. J. Daniel Moses, NASA SRPS, SMD, NASA Hq, Jan. 2017

The GCI Cusp Project, now grown to 11 sounding rockets from US, Japan and Norway, is designed to advance the common understanding of cusp region space physics through coordinated experimental and theoretical research using ground based instruments, modelling, sounding rocket investigations, and satellite based instruments. International student participation through space plasma model development and a dedicated student rocket is an essential aspect of the GCI concept. Strategic use of public outreach, particularly via the tools of social media, is also a vital component of the GCI Cusp Project.

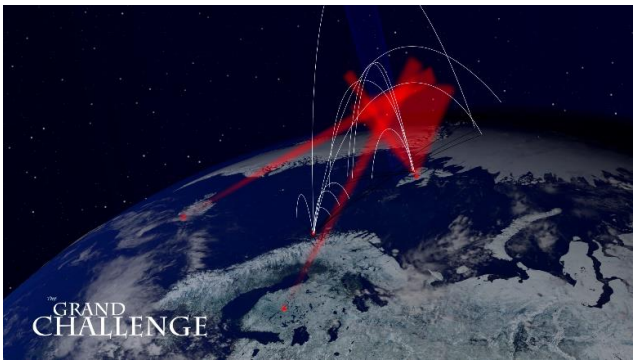

GCI 2017-2020: 11 sounding rockets from Andøya and Svalbard

The core of the GCI Cusp Project is a series of sounding rocket missions independently conceived and developed through the respective space exploration agencies of the US, Norway and Japan. The rockets will be launched in conjunction with observations of the cusp from an aggregate of state-of-the-art ground-based scientific instrumentation, including incoherent and coherent backscatter radars, all-sky cameras, meridian scanning photometers, magnetometers, and other instruments, which will operate continuously throughout the launch window.

The main GCI Cusp observational activities will be conducted in the high northern latitude region surrounding the Svalbard archipelago in late 2018 and early 2019. Additional observational activities

related to the GCI Cusp topic during other time intervals - such as a sounding rocket mission currently scheduled for 2017 – can also contribute to the overall GCI Cusp project. The GCI Cusp sounding rocket missions will be launched from ASC's Andøya and Svalrak launch sites while data are simultaneously gathered from the ground-based scientific instrumentation available to study the targeted Cusp and related phenomena. Further participation in this exciting new "Challenge" is encouraged and anticipated. A second rocket launcher is required at SvalRak to enable the VISIONS-2 dual Black Brant X launch (2 minutes separation). These two rockets are to be launched as close as possible to the launch of the TRICE-2 dual Black Brant XII launch from Andøya Space Center. A major achievement, and unprecedented in sounding rocketry if performed as described. Optimal science and weather for both launch sites/projects is mandatory.

DESIGN AND FLIGHT RESULTS OF A NON-POLLUTING COLD-SEPARATION MECHANISM FOR TK-31 SOUNDING ROCKET

Rui Lu , RongHui Wang, Jun Yang

The 41st Institute of the Fourth Academy of China Aerospace Science And Technology Corporation
169# mail box, Xi'an, China. Email: lr113132@163.com

ABSTRACT

In Apr.2016, TK-31 sounding rocket was firstly launched successfully from the Hainan Sounding Rocket Launch Site, China. The rocket accomplished a series of actions during its flight, such as the separation of the head and the body, the separation of the bow cap and the fairing, which creating conditions for the scientific payloads of the rocket detecting space ionosphere. During the separation of the head and the body, the separation technology of module interface without pollution is made for avoiding detection sensor pollution, which contains 'explosive bolts + compression springs + guide mechanism'. This technology not only meets requirement of extreme clean environment for rocket detection sensor, but also offers no less than 2m/s of the velocity of separation of the head and the body. This paper introduces the working principle, design idea and the flight results of the non-polluting cold separation technology.

1. INTRODUCTION

TK-31 sounding rocket is developed as general purpose vehicle platform by the 41st Institute of the Fourth Academy of Aerospace Science and Technology Corporation. The rocket is a two-stage solid propellant engine vehicle. The rocket delivered scientific payloads to the intended space area to execute space physics test and probe mission.

Rocket main technical requirements:

a) Vehicle total length 9337mm
b) Ⅱ-stage rocket length 6924mm
c) Ⅰ-stage rocket length 2413mm
d) Ⅱ-stage module outside diameter Φ398mm
e) Ⅰ-stage module outside diameter Φ400mm
f) Ⅱ-stage tail wingspan 1456mm
g) Ⅰ-stage tail wingspan 1420mm
h) Payload quality ~170kg
i) Apogee ~320km

The rocket should accomplish the separation of the head and the body during its ascent phase flight, which creates the conditions for the scientific payloads detecting space ionosphere. The rocket head-body separation mechanism main technical requirements:

a) Separation velocity: ≥2m/s;

b) Scientific loads in the module should not be destroyed and polluted during the separation process.

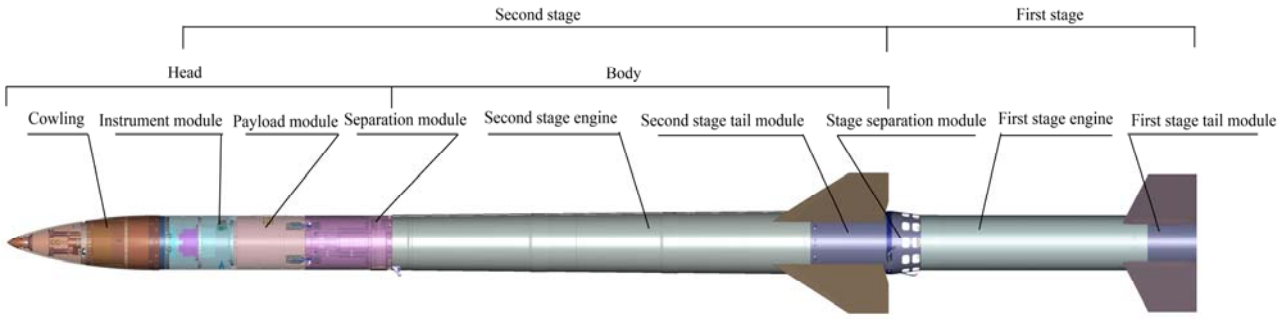

Figure.1 TK-31 sounding rocket

2. SEPARATION MECHANISM DESIGN

2.1 Principle of separation mechanism

The interface separation technology which contains 'unlocking device + separation springs + guide mechanism' is used for head-body separation. The connection and unlock between the head and the body can be accomplished by explosive bolts. The springs are compressed in the docking between the head and the body. After the explosive bolts are detonated, springs are unlocked. The compression displacement of the springs cause relative movement of the head and the body which provides not less than the relative separation velocity of 2m/s.

2.2 Module unlocking device

The separation interface between the head and the body is the connection interface between the payload module and the separation module. The payload module and the separation module are connected by 4-M16 explosive bolts. The diameter of the bolts axis circle is Φ350mm. Main performance of the explosive bolts is shown in Tab.1.

Table 1 Main performance of the explosive bolts

Ultimate load	50kN ~ 756kN	Installing form	M16×1
Detonation way	Electric detonating	Bridge form	Dual bridge
Firing current per bridge	≥5A	Bridge resistance	4 ~ 6Ω

For avoiding pollution on the detection sensors of scientific load on the rocket, 'clean' explosive bolts which work without soot pollution are chosen. At the same time, there is a protective structure on the inside of the module which ensure that the separated explosive bolts will not affect equipments in the module.

2.3 The head and the body motion analysis

Assumed conditions of throwing hood motion analysis are shown as below:

a. Separated body should only take plane motion of rigid body, ignore the effect of tilt on separation;

b. The effect of gravity acceleration on the relative motion of the separation is ignored.

When separating, the force on the head and the body is shown in Fig.2.

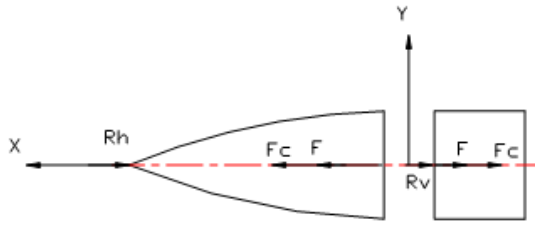

Figure.2 Head-body separated calculation model

Equations of motion are shown as Eq.1:

$$\ddot{X} = \frac{1}{m}(F - R_h - F_c) + \frac{1}{M}(F + R_v - F_c) \qquad (1)$$

Among them, m M --the quality of the head and the body;

F --ejected separation force ;

F_c --separation friction ;

R_h R_v --aerodynamic drag of the head and the body ;

X --relative movement of the head and the body.

Necessary conditions for separation :

$$\ddot{X} > 0 \qquad (2)$$

that is

$$F > \frac{MR_h - mR_v}{M + m} + F_c \qquad (3)$$

In order to separate reliably, separation force should be increased appropriately so that the head and the body can be separated at enough relative speed.

$$\Delta V = \sqrt{\frac{2(M+m)}{Mm}AF - \frac{2(MR_h - mR_v)}{Mm}l_0 - \frac{2(M+m)}{Mm}F_c l_c} \qquad (4)$$

Among them, ΔV —relative separation velocity;

l_0 —ejected separation device length

AF is the work done by ejected device, F_0 is the spring force at the initial compression position.

$$AF = \frac{1}{2}kl_0^2 = \frac{1}{2}F_0 l_0 \qquad (5)$$

Separation is done at a high altitude, air resistance can be ignored. If the effect of separation friction can not be considered, then

$$\Delta V = \sqrt{\frac{2(M+m)}{Mm}AF} \tag{6}$$

From Eqs.5-6

$$F_0 l_0 = \frac{Mm}{(M+m)}\Delta V^2 \tag{7}$$

2.4 Compression springs parameter calculation

The diameter of spring D_2, free length and compression length l_0 can be determined depending on the size of space. The maximum load of the spring F_0 can be got from Eq.8, then the diameter of the spring material can be got as Eq.8:

$$d \geq \sqrt[3]{\frac{8F_0 D_2 K}{\pi \tau_p}} \tag{8}$$

K --curvature coefficient, C --spring index, which can be calculated form the following equations

$$K = \frac{4C-1}{4C-4} + \frac{0.615}{C}$$

$$C = D_2 / d$$

Spring effective wraps:

$$n = \frac{Gd^4 l_0}{8F_0 D_2^3} \tag{9}$$

Spring stiffness:

$$k = \frac{F_0}{l_0} = \frac{Gd^4}{8D_2^3 n} \tag{10}$$

The relative movement velocity can be not less than 2m/s after separation of the head and the body. Spring parameter is shown in Tab.2.

Table 2 Head-body separation spring parameter

Material diameter d	5mm
Spring pitch diameter D_2	45mm
Spring stiffness k	2.71 k/N.mm^{-1}
Effective wraps n	25
Maximum load F_0	554.6N
Ejected length l_0	204.6mm

Calculate from the selected spring, the relative velocity is 2.2m/s when the head and the body are separated.

3. FLIGHT TEST CONDITION

At 2:00 in Apr.2016, TK-31 sounding rocket was firstly launched from the Hainan Sounding Rocket Launch Site, China. During the test, the two-stage solid propellant engine, head-body separation and rocket scientific loads all worked normally. The rocket debris fell to the predetermined safe area accurately. Ground telemetry equipment obtained entire test parameter. The test was successful.

Figure.3 TK-31 sounding rocket launched

Head-body separation process recorded by rocket camera is shown in Fig.4.

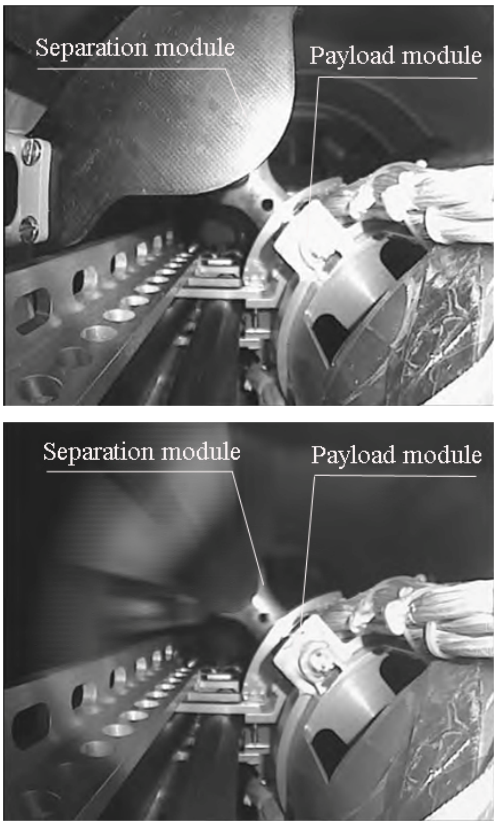

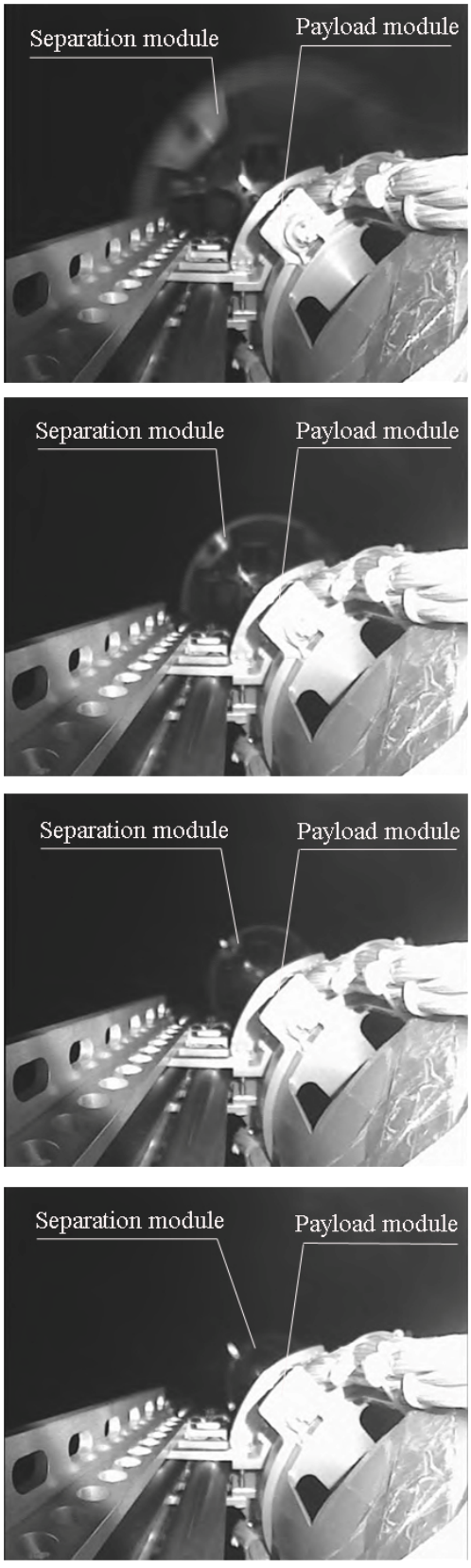

Figure.4 Head-body separation process recorded by rocket camera

4. CONCLUSIONS

Head-body separation mechanism which contains 'explosive bolts + compression springs + guide mechanism' has many advantages such as high separation velocity, high reliability and good synchronicity. It also meets particular installation requirements which is non-polluting and non-knocking. Through ground test and flight test, the mechanism is verified that it is designed appropriately, has a simple structure and can be separated reliably. The mechanism has been used for head-body separation in several kinds of sounding rockets.

Suitability of the sounding rocket TEXUS 52 to analyse the impact of microgravity on the gene expression in *Daphnia magna*

Miriam Knie[(1)], Kathrin Schoppmann[(1)], Christian Laforsch[(1)]

[(1)] Animal Ecology I, University of Bayreuth, Universitätsstr. 30, 95447 Bayreuth, Germany, miriam.knie@uni-bayreuth.de, kathrin.schoppmann@googlemail.com, christian.laforsch@uni-bayreuth.de

ABSTRACT

The waterflea *Daphnia* is a promising candidate for bioregenerative life support systems (BLSS), because of its essential role in the aquatic food web and its mode of reproduction. However, the effects of altered gravity on *Daphnia* have to be investigated, especially on the molecular level, to evaluate the suitability of *Daphnia* for BLSS in space. The experiment aboard the sounding rocket TEXUS 52 was designed to test whether this vehicle is suitable to elucidate the influence of altered gravity conditions on gene expression in *Daphnia magna*. Three consecutive time points were chosen during the flight to compare differentially expressed genes with a 1g reference: Directly at the onset of microgravity (µg), to discriminate the effects of the launch and despin (hypergravity/ accelerations); at 180 s µg and at 360 s µg. RNA extraction revealed sufficient levels for further gene expression analysis using microarrays.

Keywords: microgravity, gene expression

SCIENTIFIC BACKGROUND

The exploration of mankind into space started almost 60 years ago with Juri Gagarin to be the first human to cross the Kármán line. Nowadays capabilities are designed and build to send humans farther into the solar system than ever before, including Mars [1]. To enable such missions it is necessary to reduce or even overcome the dependency on regular supply with essentials like food, water and oxygen. A solution to create more independency from regular delivery is the development of bioregenerative life support systems (BLSS), such as the controlled ecological life support system (CELLS) developed by NASA [2]. BLSS consist of organisms from different trophic levels to mimic natural ecosystems and establish a stable biomass production. When selecting organisms for this artificial ecosystems, the absence of gravity in space has to be taken into account. This microgravity environment for example impairs the embryonic development in model organisms like *Drosophila melanogaster* [3] and mice [4]. Similarly it was shown that the growth and reproduction of terrestrial plants are dependent on gravity to some extent [5, 6, 7]. Therefore, aquatic systems are of relevance, since aquatic systems may react less sensitive to weightlessness given the increased viscosity compared to terrestrial systems [8, 9].

In our research, we focus on herbivorous zooplankton, as it plays an essential role in the aquatic food web as a link between oxygen-producing microalgae and higher trophic levels such as fish [10], which in turn may serve as protein source for humans. Among those organisms are small crustaceans commonly termed as water fleas (*Daphnia*, Branchipoda: Cladocera). *Daphnia* is able to produce a large amount of biomass in a very short time frame [11], due to its parthenogenetic mode of reproduction, its high reproduction rate (up to 80 neonates per clutch) and its short generation time of less than 10 days. Furthermore, *Daphnia* is able to produce desiccation resistant resting eggs [12], which would enable a quick revival after a population breakdown. This renders *Daphnia* an ideal organism to introduce into BLSS. It has previously been shown aboard the MIR space station that daphnids are able to survive and reproduce in microgravity for a period of four months [13, 14], although they show an abnormal swimming behaviour (loop swimming). Though, still a lot of questions remain open, regarding the impact of microgravity on daphnids, especially on the molecular level.

It was shown earlier that diminished gravity leads to changes in gene expression in different model organisms like *Arabidopsis thaliana* [15] and *Drosophila melanogaster* [16], as well as in cell culture experiments [17]. Subsequent translation of such transcripts may result in an equally altered abundance of the corresponding proteins, which in turn may have consequences on the survival and / or reproductive output of the respective organisms during long-duration missions in space. Whether this also holds true for *Daphnia* has yet to be analysed.

Apart from the use of satellites and space stations, real microgravity conditions can also be achieved by research platforms like parabolic flights and sounding rockets, which are more easily accessible. Already short-time exposure to microgravity, as in parabolic flights, may have an influence on gene expression [18]. However, as each parabola is preceded by a hypergravity phase (between 1.8 and 2 *g*) of equal length [19], the possibility cannot be ruled out that gene expression in these experiments is biased by the hypergravity phase. The launch of a sounding rocket also comprises a hypergravity phase due to the motor thrust and the YoYo despin (total duration ca. 60 sec), though the subsequent microgravity phase is approximately six times longer (about 360 sec). Beside the prolonged microgravity

phase, a further advantage of sounding rockets compared to parabolic flights is the microgravity quality. While the microgravity level achieved with parabolic flights is in the range from 10^{-2} to 10^{-3} *g*, sounding rockets provide a guaranteed microgravity level of 10^{-4} reaching normally up to 10^{-6} *g*.

Therefore, we decided to use this research platform to carry out an experiment on the impact of microgravity on the gene expression in *D. magna*.

EXPERIMENTAL SETUP

Maintenance of animals

To ensure the availability of neonate individuals of *D. magna* on a daily basis, age-synchronized individuals of a laboratory cultured clone ($K_3$4J) of *Daphnia magna* were kept in 1.5 L glass containers, filled with oxygenated "Volvic" mineral water (Danone Waters, Germany) at 21.5 ± 0.6°C under fluorescent light at a constant photoperiod (15 h day : 9 h night) in the biological laboratory at ESRANGE. As soon as offspring was present, the neonate daphnids were transferred in fresh glass containers, to a maximum of 20 animals each. The daphnids were fed ad libitum with green algae *Acutodesmus obliquus* every other day.

Flight implementation plan

The TEXUS 52 payload consisted of three different experiment modules and the total payload mass was 402.3 kg. Our Module TEM 06-31 consisted of three experimental platforms and an experiment service subsystem. Two platforms were used for behavioural experiments and one platform was dedicated to the analysis of gene expression (fixation experiment).

The fixation experiment is comprised of three temperature controlled (23 ± 1°C) late access units with two culture dishes each, mounted on a temperature controlled (23 ± 1°C) platform. Another fixation unit was kept at ground at the biological laboratory at ESRANGE (Swedish Space Cooperation's launch facility, Kiruna, Sweden) to serve as 1 *g* reference. To increase the number of replicates, each culture dish was separated in two compartments with a volume of approximately 5 ml each. Each compartment had a dedicated sealing, but a common supply for filling and fixation. The in- and outlets were covered with gauze (300 µm porosity). The fixative (RNAlater) was contained in two spring loaded syringes per fixation unit, which were mounted beneath the culture dishes and connected to the culture dishes by silicone tubes and valves which could be opened at the dedicated time points by a timer sequence. If the valve is opened, the fixative flows into the culture dish. Both valves of the fixation unit are opened at the same time.

Preparation of the late access units started at 3:30 hrs prior to launch. Insertion of the animals was completed at 1:30 hrs prior to launch and handover and integration of the late access units into TEXUS 52 took place.

TEXUS 52 mission profile

The sounding rocket TEXUS 52 was successfully launched on April 27th, 2015 from the Swedish Space Cooperation's launch facility ESRANGE Space Center near Kiruna. The rocket performed a ballistic flight and reached its ceiling at 255.6 km height. Thereby a microgravity phase of 366 sec was achieved. After 1:35 h the payload was recovered and back at ESRANGE. Launching time was 6:54 a.m., and the first thrust acceleration (first stage) was maximal 8.1 *g* (mean 5.5 *g*) at 2.2 sec with motor burnout at 12 sec. The second thrust acceleration (second stage) was maximal 11.4 *g* (mean 6.6 *g*) at 35 sec, followed by motor burnout at 43.3 sec, YoYo despin at 56 sec and motor separation at 59 sec. Start of zero-*g* was at 74 sec. Reentry deceleration was from 448.8 sec until 482.0 sec with a maximal load of 17.2 *g*.

Experimental procedures

To ensure for a sufficient amount of tissue for subsequent RNA extraction and gene expression analysis with microarray, 30 neonate individuals of *D. magna* were inserted in each of the compartments of the culture dishes of the fixation units and closed with the respective sealings. Subsequent, the syringes were loaded with 25 ml RNAlater each, and connected to the valves and the culture dishes with silicone tubes. After checking for leaks, the fixation units were completely assembled and handed over for the integration into the payload of TEXUS 52.

For the analysis of the impact of microgravity on the gene expression and to discriminate them from the effect of the acceleration occurring during the launch, three different time points for fixation during the flight were chosen. The valve of the first fixation unit was opened 70 sec after launch, shortly after the YoYo despin. The second time point for fixation was set at 250 sec after launch (approx. half of the microgravity phase) and the third valve was opened 430 sec after launch, at the end of the microgravity phase. The valve of the 1 *g* reference sample was opened manually after reentry of TEXUS 52 to compensate for the effect of a possible oxygen shortage within the compartments of the culture dishes, due to the small volume.

After payload recovery to ESRANGE, the late access units were dismounted. Subsequent, the samples were collected from the culture dishes and stored in reaction

tubes at 8°C until return to the laboratory at the University of Bayreuth.
Back at the University of Bayreuth, total RNA was extracted from the replicate samples, each containing 30 neonate individuals of *D. magna*, using the RNeasy Microarray Tissue Kit (Quiagen GmbH, Hilden, Germany) as recommended by the manufacturer with the following modification: The initial tissue lysis step was facilitated by homogenization of the animals at 5 m/sec for 40 sec using 0.5 mm glass beads in a benchtop homogenizer (Fastprep-24, MP Biomedicals, Heidelberg, Germany). Total RNA was quantified using a Qubit 3.0 fluorometer (ThermoFisher Scientific, Dreieich, Germany).

RESULTS

The infrastructure and conditions at the biological laboratory at ESRANGE allowed for a continuous rearing of *D. magna*, thereby it was possible to cover several delays of the rocket launch.
The design of the fixation units proofed to facilitate a fast and smooth insertion of the animals during the experiment preparation before the flight. Therefore, hand-over for integration of the late access units into the payload of TEXUS 52 was performed well within the time schedule. The in-flight fixation at the three dedicated time-points worked excellent, as all of the RNAlater containing syringes were completely drained and no daphnids got lost during the medium exchange. The design also allowed a quick and loss-free recovery of the preserved samples.

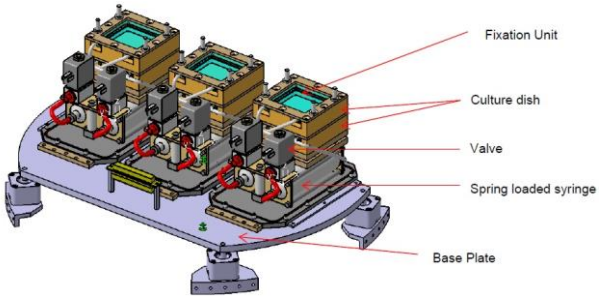

Figure 1. Schematic draft of the fixation experiment, from flight implementation plan, TEX52-RIBRE-PL-0001 (Airbus Defence & Space, Bremen, Germany).

RNA extraction back at the laboratory at the University of Bayreuth showed a sufficient RNA yield for further analysis using a costume made high-density microarray (Agilent Technologies, Ratingen, Germany) (Tab. 1).

Table 1. RNA yield per replicate (30 neonate *D. magna*). G1 – 1 *g* reference; 1- first fixation; 2 – second fixation; 3- third fixation; A- D – numbering of the replicates

probe	RNA in ng/ µl	Probe	RNA in ng/ µl
G1-A	200.1	2-A	231.3
G1-B	240.5	2-B	188.8
G1-C	193.1	2-C	188.8
G1-D	256.5	2-D	212.0
1-A	231.9	3-A	246.9
1-B	247.7	3-B	236.7
1-C	298.9	3-C	245.8
1-D	226.5	3-D	241.1

CONCLUSION

In conclusion, sounding rockets within the TEXUS programme launched from the ESRANGE Space Center, have proved to be highly suitable tools to analyse gene expression changes in *D. magna* which are induced by altered gravity. Not only do they provide a quite long microgravity phase of approximately six minutes, but they also offer a good microgravity quality which is otherwise only achieved by drop towers or aboard space stations and research satellites.
A further advantage for experiments like the one carried out in this study, is given by the laboratory infrastructure at ESRANGE, with well-equipped laboratories for biological research.

REFERENCES

1. Board, S.S. & National Research Council (2014). *Pathways to Exploration: Rationales and Approaches for a U.S. Program of Human Space Exploration.* National Academies Press.

2. Wheeler, R.M., Mackowiak, C.L., Stutte, G.W., Sager, J.C., Yorio, N.C., Ruffe, L.M., Fortson, R.E., Dreschel, T.W., Knott, W.M. & Corey, K.A.(1996). Nasa's biomass production chamber: a testbed for bioregenerative life support studies. *Adv. Space Res.* **18**(4-5). 215-224.

3. Vernos, I., Gonzales-Jurado, J., Calleja, M. & Marco, R. (2002). Microgravity effects on the oogenesis and development of embryos of Drosophila melanogaster laid in the Spaceshuttle during the Biorack experiment (ESA). *Int. J. Dev. Biol.***33**(2), 213-226.

4. Ma, B. H., Cao, , Y.J., Zheng, W.B., Lu, J.R., Kuang, H.B., Lei, X.H., Lv, Y.H., Zhang, T. & Duan, E.K. (2008). Real-time micrography of mouse preimplantation embryos in an orbit on SJ-8 satellite. *Microgravity Sci. Technol.*, **20**(2), 127-136.

5. Hallstead, T.W. & Dutcher, F.R. (1984). Status and prospects. *Ann. Bot.*, 3-18.

6. Hallstead, T.W. & Dutcher, F.R. (1987). Plants in space. *Annu. Rev. Plant Physiol.* **38**(1), 317-345.

7. Musgrave, M.E., Kuang, A. & Matthews, S.W. (1997). Plant reproduction during spaceflight: importance of the gaseous environment. *Planta* **203** 177-184.

8. Bluem, V. & Paris, F. (2001). Aquatic modules for bioregenerative life support systems based on the CEBAS biotechnology. *Acta Astronautica* **48**(5). 287-297.

9. Slenzka, K. (2002). Life support for aquatic species-past; present; future. *Adv. Space Res.* **30**(4), 789-795.

10. Tollrian, R., & Dodson, S.I. (1999). Inducible defences in cladocera: constraints, costs, and multipredator environments. In *The ecology and evolution of inducible defenses* (Eds. R. Tollrian & C. D. Harvell), Princeton University Press, Princeton, New Jersey, USA, pp 177-202.

11. Lampert, W., & Sommer, U. (2007). *Limnoecology: the ecology of lakes and streams*. Oxford university press, Oxford, UK.

12. Doma, S. (1979). Ephippia of Daphnia magna Straus-a technique for their mass production and quick revival. *Hydrobiologia* **67**(2), 183-188.

13. Ijiri, K., Mizuno, R., Narita, T., Ohmura, T., Ishikawa, Y., Yamashita, M., Anderson, G., Poynter, J., & MacCallum, T. (1998). Behavior and reproduction of invertebrate animals during and after a long-term microgravity: space experiments using an Autonomous Biological System (ABS). *Biol Sci Space,* **12**, 377-388.

14. Ishikawa, Y., Kobayashi, K., Mizutani, H., Kawasaki, Y., Koike, J., Ijiri, K., Yamashita, M., Sugiura, K., Poynter, J., MacCallum, T., & Anderson, G. (1998). Concluding remarks of aotonomous biological systems (ABS) experiments. *Biol. Sci. Space* **12**(4), 394-399.

15. Martzivanou, M., Babbick, M., Cogoli-Greuter, M., & Hampp, R. (2006). Microgravity-related changes in gene expression after short-term exposure of Arabidopsis thaliana cell cultures. *Protoplasma* **229**, 155-162.

16. Taylor, K., Kleinhesselink, K., George, M. D., Morgan, R., Smallwood, T., Hammonds, A. S., Fuller, P. M., Saelao, P., Alley, J., Gibbs, A. G., Hoshizaki, D. K., von Kalm, L., Fuller, C. A., Beckingham, K. M. & Kimbrell, D. A. (2014). Toll Mediated Infection Response Is Altered by Gravity and Spaceflight in Drosophila. *PLOS ONE* **9**, e86485.

17. Ma, X., Pietsch, J., Wehland, M., Schulz, H., Saar, K., Hübner, N., Bauer, J., Braun, M., Schwarzwälder, A., Segerer, J., Birlem, M., Horn, A., Hemmersbach, R., Waßer, K., Grosse, J., Infanger, M. & Grimm, D. (2014). Differential gene expression profile and altered cytokine secretion of thyroid cancer cells in space. *The FASEB Journal* **28**, 813-835.

18. Paul, A.L., Manak, M.S., Mayfield, J.D., Reyes, M.F., Gurley, W.B., & Ferl, R.J. (2011). Parabolic flight induces changes in gene expression patterns in Arabidopsis thaliana. *Astrobiology* **11**(8), 743-758.

19. Pletser, V. (2004). Short duration microgravity experiments in physical and life sciences during parabolic flights: the first 30 ESA campaigns. *Acta Astronautica* **55**(10), 829-854.

20. Thiel, C.S., Tauber, S., Schütte, A., Schmitz, B., Nuesse, H., Moeller, R. & Ullrich, O. (2014). Functional activity of plasmid DNA after entry into the atmosphere of earth investigated by a new biomarker stability essay for ballistic spaceflight experiments. *PLoS one* **9**(11), e112979.

SOUNDING ROCKET AND BALLOON RESEARCH ACTIVITIES WITHIN THE GERMAN SPACE PROGRAM 2015-2017

VISBY, SWEDEN
11-15 JUNE 2017

Otfried Joop, Michael Becker, Christian Gritzner

DLR, German Aerospace Center, Space Administration,
Koenigswinterer Str. 522-524, D-53227 Bonn (Germany),
Email: Otfried.Joop@dlr.de, Michael.Becker@dlr.de, Christian.Gritzner@dlr.de

ABSTRACT

Sounding (suborbital) rockets and stratospheric balloons currently play a major role in the following research disciplines of the German space program: Space Science, Life and Physical Sciences under Microgravity, Space Technology development, and Education. In its role as space administration DLR manages these activities and promotes the related experiments by grants and contracts.

In its role as a research establishment DLR also executes flight projects. The DLR Mobile Rocket Base (MORABA) provides launch services for rockets and balloons. The DLR Institute of Materials Physics in Space develops and conducts own microgravity experiments in the frame of the MAPHEUS research rocket missions. Further DLR institutes participate in flights with rocket technology experiments or support the STERN program.

1. INTRODUCTION

In the Space Science discipline the research focus was the middle atmosphere of the Earth using stratospheric balloons, lidars, and DLR FALCON flights, e.g. during the LITOS concerted campaign. Further, in-situ measurements of atmospheric parameters up to 140 km are planned to be conducted by sounding rocket campaigns (e.g. PMWE) from the Andøya Space Center (ASC) in Norway. The scientific coordination of these missions is performed by the Leibniz Institute of Atmospheric Physics at the University of Rostock (IAP) in Kuehlungsborn. 3-dimensional measurements are targeted for the near future by releasing three daughter payloads from a single rocket.

Biological, physical, and chemical phenomena under microgravity conditions were studied by German scientists using ESA's MAXUS 9 as well as national TEXUS, MAPHEUS, and MAIUS missions on parabolic trajectories.

Within the German-Swedish REXUS/BEXUS student program further sounding rocket and balloon missions have been performed successfully. A wide range of scientific and technological experiments such as atmospheric physics, satellite communication, and test of space equipment was addressed by the selected student teams. Other German educational programs like STERN, D-CanSat, or StratoSAT have been continued or initiated during the last two years.

In the field of Rocket and Re-Entry Technology the German Space Program supported three projects during the last two years, namely ROTEX-T launched from Esrange, Improved Malemute launched from Andoya, and the HIFIRE flights in Australia. In all of them either DLR MORABA or EUROLAUNCH, a joint venture of SSC and MORABA, have been responsible for the preparation and the flight of the rockets.

The paper reports on activities supported by the German Space Program and implemented by the DLR Space Administration and DLR research institutes in the period June 2015 to June 2017.

2. SPACE SCIENCE: AERONOMY

Scientific studies of the middle atmosphere of the Earth can be performed using stratospheric balloons, lidars, radar arrays, and DLR FALCON flights, but only sounding rockets allow for in-situ measurements. Therefore, in-situ measurements of atmospheric parameters up to 140 km are conducted by sounding rocket campaigns from the ASC launch site in Norway.
The scientific coordination of German activities of these missions is performed by the Leibniz Institute of Atmospheric Physics at the University of Rostock (IAP) in Kuehlungsborn in partnership with the Institute of Space Systems (IRS) at the University of Stuttgart, and the Munich Meteorological Institute, Ludwig-Maximilian University of Munich (LMU) with contributions from the DLR Institute of Atmospheric Physics (IPA), Oberpfaffenhofen, Germany, the Graz University of Technology (TUG), Austria, and the Department of Meteorology at Stockholm University (MISU), Sweden. Financial support for the German partners is provided by DLR Space Administration, Bonn, Germany.
The current research project PMWE (Polar Mesospheric Winter Echoes) is dedicated to the analysis of the phenomenon of strong Radar echoes in the middle atmosphere at about 55 to 85 km in the polar region in winter time. Dynamic processes (turbulence) as well as meteoritic dust particles and negative ions are assumed as their starting point but their formation mechanism is still under debate. Understanding the basic physics of these Radar echoes will lead to use PMWE as a tracer for long-term observations of small-scale dynamic processes in the Mesosphere. This will result in a better knowledge of the Earth's atmosphere.

The PMWE sounding rocket campaigns aim at measuring all the key parameters simultaneously both in-situ and by ground based instrumentation. Thereby, the main goal of the project is to gain an experimental basis for the theoretical explanation of the PMWE phenomenon.
To conduct in situ measurements eight proven or newly developed instruments are combined as the scientific payload for each of the two PMWE sounding rocket campaigns. For example, the CONE sensor has been already used in several former campaigns (e.g. WADIS, ECOMA, MIDAS) and steadily optimized and updated.
The launch window for the first PMWE campaign is October 1st to 10th, 2017. The ASC launch site in Norway will be used for the campaigns as before and DLR MORABA will provide the launch services. The launcher will be an Improved Malemute rocket stage. The payload mass will be about 250 kg and the altitude up to 130 km. The launch campaigns will be accompanied by lidar measurements from the Alomar Observatory and the MAARSY radar array. A second PMWE campaign is planned but the launch window still has to be determined.

3. MICROGRAVITY RESEARCH: LIFE AND PHYSICAL SCIENCES

Microgravity Research is another large field where the German Space Program in general employs sounding rockets – or a better term in this case might be „suborbital or research rockets“ – which can provide scientists with up to 12 minutes of high quality microgravity conditions on their parabolic flights, serving investigations in the Physical and Life Sciences.
In the timeframe 2015 to 2017 two rocket missions within the TEXUS and MAIUS programs, respectively, have been performed, both of them contracted by the German Space Administration with funds provided by the German Federal Ministry for Economic Affairs and Energy.
In addition, the MAPHEUS program led by the DLR Institute of Materials Physics in Space (Cologne) has been continued successfully with two other missions, and German scientists contributed with three experiments to ESA's MAXUS 9 flight in April 2017.
All of these microgravity missions have been launched from Esrange Space Center (ESC) close to Kiruna (Sweden).

3.1. TEXUS 53

The ESA/DLR TEXUS program uses the two stage solid propellant VSB-30 research rocket of Brazilian origin since 2005. Since then, 12 successful missions have been launched from ESC within the German TEXUS program, the most recent one being TEXUS 53 on January 23, 2016. TEXUS 53 reached an apogee of 253 km, corresponding to a little more than six minutes of high quality microgravity conditions, and carried five experiments of German scientists into space, investigations in the fields of technology, materials science, and gravitational biology (Tab. 1).

Table 1: Experiments on TEXUS 53

TEXUS Module	Principle Investigator	Experiment
TEM 06-36	R. Holzwarth MPQ Munich	Fiberlaser-based optical frequency comb in zero gravity (FOKUS-1B)
TEM 06-33	R. Hampp Univ. Tuebingen	Fluorescence-based analysis of signaling molecules involved in plant gravity sensing (CAMELEON)
	A. Peters Humboldt Univ. Berlin	K-Laser experiments in microgravity (KALEXUS)
TEM 06-37	D. Grimm Univ. Magdeburg	Influence of micro-gravity on human endothelial cells (THYROID)
TEM 02-3	J. Friedrich Fraunhofer Institute Erlangen	Determination of the critical capture velocity of particles during directional solidification of solar silicon in space (ParSiWal-2)

The experiment THYROID studied biochemical mechanisms within isolated human cancer cells and investigated their genome and proteome. Earlier experiments with this cell type already proved, that short microgravity phases influence the cell structure as well as its genome, while longer exposure to zero gravity changes cell growth and mitigates the malignancy of cells. These results show, that cancer cell research in microgravity can lead to scientific findings, which might help to develop new anti- cancer drug therapies.
In another biological experiment, scientists from Tuebingen University investigated how plant cells sense gravity. In all organisms, calcium ions (Ca^{++}) are an essential component of regulatory and signal chains. Experiments on parabolic flights already showed increases in Ca^{++} concentration within *Arabidopsis thaliana* cells during 20 seconds of microgravity conditions. The CAMELEON experiment investigates the course and duration of the calcium response in the six minutes microgravity phase of a TEXUS flight.
The materials science experiment ParSiWal-2 intends to optimize the efficiency and quality of photovoltaic cells. During directional solidification of solar silicon, the incorporation of certain particles like silicon nitride (Si_3N_4) impairs the crystal quality. Conditions and parameters how to reduce or avoid this incorporation have been studied during the experiment.
In many scientific areas optical laser systems are being applied, e.g. in climate research to determine trace gases in the atmosphere, or in astrophysics. The experiment FOKUS-1B on TEXUS 53 tested a new optical laser (frequency comb) for space applications recently developed in the Max Planck Institute of Quantum Optics (Munich).

To investigate the characteristics of special miniaturized potassium spectroscopy laser systems, scientists from the Humboldt University in Berlin sent the KALEXUS experiment into space. Results from this first qualification mission on a research rocket will be an important prerequisite for other applications of this technology on future space flights.

3.2. MAPHEUS 5 and 6

MAPHEUS (the German acronym for Materials Science Experiments in Microgravity) is a research rocket program of the DLR Institute of Materials Physics in Space conducting annual launches of science payloads initially dedicated only to materials studies. During the first four flights of this program between 2009 and 2013, smaller rockets have been employed, providing just three to four minutes of microgravity conditions. On MAPHEUS 5 successfully flown on June 30, 2015, the VSB-30 two stage rocket combination was introduced into the program. The four experiments on this mission covered a wide range of scientific topics such as granular dynamics in 3D, thermophysical properties of metals using an electrostatic levitation facility, the chemical diffusion and the solidification of Al-alloys using X-ray radiography in real time, and – for the first time on MAPHEUS – also a biological experiment from the DLR Institute of Aerospace Medicine in Cologne. MAPHEUS 5 reached an apogee of 256 km corresponding to more than six minutes under microgravity conditions.
Almost two years later, on May 13, 2017, MAPHEUS 6 has been launched into space, attaining a peak altitude of 254 km above ESC (Fig. 1). This mission again carried four experiments from DLR scientists, three material science investigations, and one experiment in gravitational biology from the DLR Institute of Aerospace Medicine in close cooperation with scientists from the University of Hohenheim, which dealt with changes of the fluidity of artificial lipid membranes under microgravity conditions.

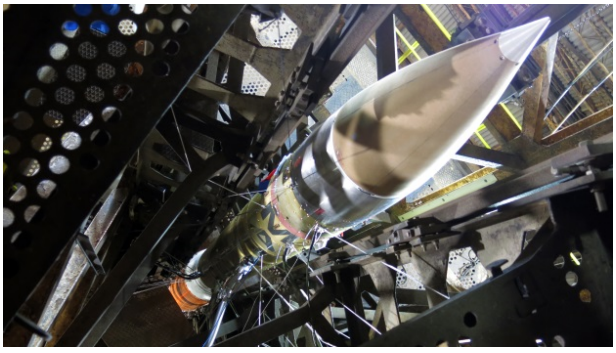

Figure 1: MAPHEUS 6 in the ESC launch tower

Topics of the three material science experiments were, for example, to study the demixing of undercooled copper-cobalt samples, as well as reflights of the electrostatic levitation facility and the X-RISE module of MAPHEUS 5 with different samples and changed experimental parameters. Launch support within the MAPHEUS program is being provided by DLR MORABA and SSC.

3.3. MAIUS 1

On January 23, 2017, exactly one year after TEXUS 53, another VSB-30 carried the MAIUS-1 payload into space. MAIUS is the German acronym for Materiewellen-Interferometer unter Schwerelosigkeit, meaning matter wave interferometer in microgravity. Within the more than six minutes of microgravity on this flight up to an altitude of 243 km, for the first time a Bose-Einstein-Condensate (BEC) has been generated in space.
MAIUS-1 is certainly one of the most complex experiments ever flown on a research rocket, and to accomodate the large and sensitive hardware, a slightly larger payload diameter than on a usual VSB-30 flight has been employed. Compared to earlier VSB-30 missions, and in addition to the necessary high quality µg,
this experiment required a modified rocket nosecone and a constant attitude with respect to the nadir vector during the microgravity phase.
The MAIUS experiment was developed and performed by scientists of the so called QUANTUS consortium, consisting of seven German universities and a research institute. The matter wave interferometer has been the main scientific payload on this flight, enabling the investigation of atom optical methods in a parameter range inaccessible to experiments on ground (Fig.2).

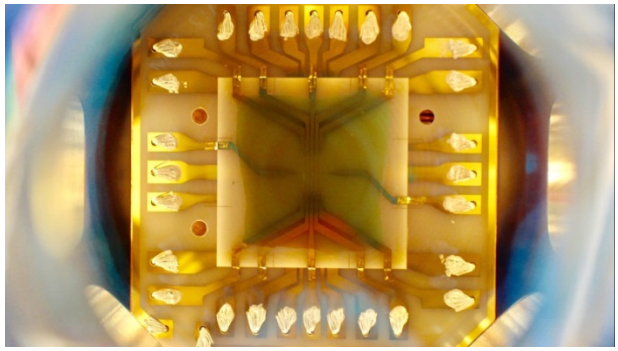

Figure 2: MAIUS atom chip (ca. 3x3 cm)
Credit: MAIUS project team, J. Matthias

Basically, the flight should prove the feasibility of experiments with ultra-cold quantum gases in microgravity, which is an essential requirement for long duration precision measurements with quantum sensors in space. Generally speaking, quantum technology in space shall enable innovations in areas as precision metrology, geodesy, earth observation, GPS-independent navigation, satellite platform technology, and fundamental physics. The German Space Administration funds the MAIUS program and plans to continue it with further rocket flights during the next years.
The Micro Inertial Measurement Unit (Micro IMU) experiment, developed by engineers from DLR/GSOC, has been an additional payload on the MAIUS 1 flight. One aim of this experiment was to enhance the robustness of global navigation satellite system (GNSS) receivers – like GPS or Galileo - for sounding rockets and other launch vehicles.

3.4. MAXUS 9

The MAXUS microgravity research rocket program has been established by Airbus DS and SSC in 1990 as an industrial joint venture. Since then, ESA has been the single user of this program, financed through the European Program for Life and Physical Science in Space (ELIPS). Being the tenth MAXUS mission in total, MAXUS 9 was launched from ESC on April 7, 2017, powered by the large Castor 4B motor up to an apogee of 678 km. On its trajectory, four of the five experiments on board experienced high quality microgravity conditions for almost 12 minutes (Tab. 2). SUPERMAX, the fifth experiment, a supersonic parachute test, was released from the payload prior to microgravity conditions.

Table 2: Experiments on MAXUS 9

MAXUS Module	Principle Investigator	Experiment
GRADECET	U. Hecht ACCESS Aachen	Gravity dependence of CET in peritectic TiAl alloys
EUGRAPHO	M. Lebert Univ. Erlangen	Determination of the gravitactic threshold in *Euglena gracilis* after previous microgravity phases An assay to determine the role of cAMP in phototaxis and gravitaxis of *Euglena gracilis*
XRMON-Diff 2	F. Kargl DLR Cologne	In-situ X-Ray monitoring of advanced metallurgical processes under microgravity and terrestrial conditions
PERWAVES	A.J. Higgins McGill Univ. of Montreal	Percolating reactive waves in particulate suspensions
SUPERMAX	J. Longo L. Ferracina ESA ESTEC	Supersonic parachute experiment ride on MAXUS

German prime investigators contributed three of the five experiments on MAXUS 9, their preparatory work funded by the German Federal Ministry for Economic Affairs and Energy via the German Space Administration. In addition to the scientists, the MAXUS 9 team consists of ESA, Airbus DS, SSC, OHB, RUAG, and DLR MORABA.

4. EDUCATION

4.1. REXUS/BEXUS

REXUS/BEXUS (Rocket and Balloon EXperiments for University Students) is a German-Swedish student program to acquire practical experience in real space projects on a regular basis. The program is realised under a bilateral Agency Agreement between the German Aerospace Center (DLR) and the Swedish National Space Board (SNSB). The Swedish share of the payload has been made available to students from other European countries through a collaboration with the European Space Agency (ESA). EuroLaunch, a cooperation between the Esrange Space Center of SSC and MORABA of DLR, is responsible for the campaign management and operations of the launch vehicles. Experts from DLR, SSC, ZARM and ESA provide technical support to the student teams throughout the project. REXUS and BEXUS are launched from Esrange Space Center in northern Sweden. By annual calls for proposals the flight experiments are selected after evaluation by the agencies DLR and SNSB/ESA.

The Agreement between DLR and SNSB for cooperation in student rocket and balloon activities was signed in 2007 during the 18th ESA Symposium on European Rocket and Balloon Programmes and Related Research in Visby, Sweden. Now, existing for 10 years in its current form, the program has launched 147 student built experiments with over 1,200 direct participations.

In the past two years, the REXUS missions 19, 20, 21, and 22 were accomplished. On 18 March 2016 REXUS 19 was successfully launched with the German experiment MIKRA2-RX. A student team from the University of Stuttgart tested and validated a mock-up of the MIRKA2 micro return capsule, a free-falling unit ejected from the rocket with autonomous systems sensors and transceiver.
The LIME team from the University of Applied Science in Jena proposed a dynamic scheme for the communication of CubeSats, ejecting free-falling units only transmitting data with high data rates, when pointing towards the ground station.

Two German payloads flew on REXUS 20 on 15 March 2016. Students of the University Würzburg tested with experiment PATHOS a system for the horizon acquisition for altitude determining of a rocket, using image processing algorithms. The horizon of the earth and its curvature was processed via optical data coming from a camera and was used to calculate a 2D vector to the center of the earth, offering information of the spacecraft's altitude.
The UB-FIRE module was provided by students of the University of Bremen. The team investigated the concurrent flow of flame propagation of different PMMA rods during reduced gravity. By means of an infrared camera, pyrolysis of the different shaped material was observed and compared to ground-based experiments and a NASA standard test.

Figure 3: Launch of REXUS 20 from Esrange on 15 March 2016

On REXUS 22 three German experiments were flown on 16 March 2017.
The AtmoHIT team of the University of Wuppertal, FZ Jülich and Erlangen tested a remote sensing Michelson-Interferometer. The instrument was developed to measure temperatures in the mesosphere/lower thermosphere and consists of a highly miniaturized Spatial Heterodyne Spectrometer, measuring the oxygen atmospheric band emission.

The objective of the GRAB experiment from students of the Technical University Braunschweig was to assess the adhesive properties of Gecko-inspired materials under space conditions. The main objective was to observe how gecko-materials behave in space in comparison to the laboratory environment and to what extent they can be used for active space debris removal performed by robotic spacecraft.

The experiment of team RaCoS from the University of Würzburg had the purpose to reduce and control the angular rate of the REXUS rocket in the roll axis by cold gas propulsion. Therefore the angular rate of the roll axis was measured and used by the control algorithm to calculate the opening times of the valves. The RaCoS experiment helped to improve the milli-gravity environment of the REXUS flight.

Two German experiments flew on REXUS 21 on 15 March 2017. Students of the Technical University of Dresden conducted an experiment with an inflatable dipole antenna. The team developed a 7 m long antenna for the application in miniaturized satellites like a CubeSat. During the REXUS flight, a CubeSat mockup, including the whole antenna with its storage compartment, deployment mechanism, gas generating system, transmitter and control board, was deployed and the inflation of the nylon fabric coated TPU antenna was recorded by two cameras. The experiment provides a set of data for the dynamical behavior and transmitted a test signal that was received by amateur radio operators.
The UB-SPACE experiment was developed by students of the University of Bremen and is based on a method for a relative navigation of satellites with the purpose of removing space debris. A free falling unit was ejected and observed via a 360 degree camera view, together with an IMU and sun sensors for attitude determination. By means of image processing, a pose estimation of the FFU relative to the rocket can be determined. The experiment provides test data of an uncooperative object in the space environment for camera based relative navigation of space vehicles.

In the reporting period the four balloon missions BEXUS 20, 21, 22 and 23 were conducted from Esrange with German student payloads. Typical float times of the balloons were 2 to 4 hours at an altitude up to 30 km.

BEXUS 22 was launched on 5 October 2016 with the Lotus-D experiment. The students from the Technical University of Dresden conducted an experiment that established an optical communication link with the BEXUS balloon from ground. By means of a modulated LED, a predefined data sequence was sent to the balloon gondola. The purpose was to show a relation between determined factors and the achieved bit error and data rates.
The team TDP-3 Vanguard from the Technical University of Munich conducted an experiment to verify the correct operation of a new communication system for CubeSats in a space environment. Two transceivers based on FPGA-architectures were tested over a large distance using a software-defined radio station and the DLR MORABA telemetry station at Esrange.

BEXUS 20 and 21 were launched on October 10 and 7, 2015, respectively. The experiment of team COSPA from the Technical University Darmstadt on BEXUS 20 collected stratospheric aerosol particles with a Micro Inertial Impactor. Particles were impacted on boron grinds for scanning electron microscopy and Ni-Transmission Electron Microscopy. Information on size, chemical composition, and morphology was obtained and compared to samples from different layers of earth's atmosphere.

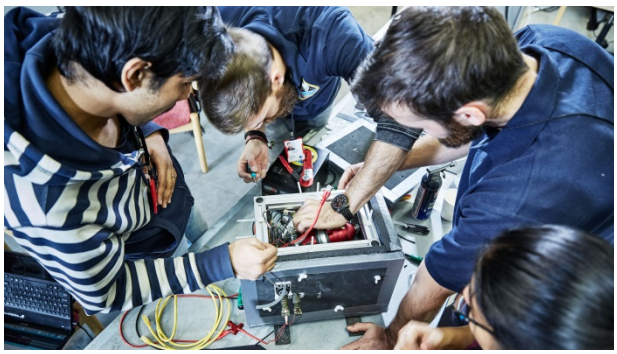

Figure 4: Team COSPA preparing its experiment for the flight with BEXUS 20

Team InTex of BEXUS 21 developed and tested a novel approach for inflating antenna structures in space by using a hybrid material from cotton fabric coated with a PVC layer, applying a UV cured epoxy rigidization. The antenna became inflated and the epoxy cured due to UV irradiation by sunlight. The successful stabilization approach was proofed by an enforced leakage.

4.2. STERN

STERN – which stands for Studentische Experimental-Raketen or Experimental Rockets of Students - is another educational program for university students, initiated in 2012 by the DLR Space Administration and funded by the German Ministry for Economic Affairs and Energy. Compared to REXUS, where the rocket payloads have to be developed, here the rockets themselves or critical parts of them are being designed, developed, and launched by the student teams (Tab. 3).

Table 3: STERN Launches in 2015 and 2016

Project	Team	Launch Date
FAUST	TU Braunschweig	October 22, 2015
HEROS	Univ. Stuttgart	October 22, 2015
DECAN	TU Berlin	October 27, 2015 October 29, 2015
AQUASONIC	IAT Hochschule Bremen	April 14, 2016
ZEpHyR	Univ. Bremen ZARM	April 16, 2016
HEROS2	Univ. Stuttgart	October 31, 2016
HEROS3	Univ. Stuttgart	November 8, 2016

During the campaign at ESC in October 2015, the three teams from Braunschweig, Stuttgart, and Berlin performed four missions in total with boosters of various sizes and propellant types, reaching heights of up to 6 km. As a remarkable add-on to their success during the campaign, in 2017 the FAUST team received the Science Award of the German State Lower Saxony for their professional achievements and social engagement.
In 2016, the STERN program evolved further with two launches each in a spring and an autumn campaign in Esrange. During these missions, the three teams from Bremen and Stuttgart employed self-developed hybrid motors, with paraffin, polyethylene, nitrous oxide, or LOX as propellants. During their second flight on November 8, the rocket of the HEROS team from Stuttgart reached an altitude of almost 33 km, being the current European record for rockets developed by students.
The student teams are being supported by SSC, DLR MORABA, DLR Lampoldshausen and Trauen. The program will be continued with further campaigns during the next years.

4.3. CanSat

Another educational activity - meanwhile also supported by the German Space Program - addresses younger students (of ages 14 years and older). The so called CanSat program has been initiated by ESA in 2010. It is a yearly competition for high school students from ESA member states to build and fly a can-sized rocket payload, using small available commercial rockets, which can fly up to 1 km altitude.
Meanwhile, there are 14 national qualifying competitions, and the winners of each country can participate in the following European competition. At the end of June 2017, the ESA competition is being hosted by ZARM in Bremen.
The German CanSat program receives support by a large number of mainly national institutions, schools, and companies.

4.4. SatTec/StratoSAT

In 2016, analog to D-CanSat, another German high school project for students of 14 years and older has been initiated, called SatTec/StratoSat.
This is a competition between 10 student teams to develop, build, and fly scientific payloads for aeronomy or earth observation on stratospheric balloons to be launched at the end of June 2017.
Special H/W as the balloon, a GPS tracking device, batteries, a parachute, and a data logger is being provided for the teams, but it also belongs to the specifics of this competition, that the teams have to find a suitable launch site by themselves, and to evaluate and follow the special rules and regulations for launching a stratospheric balloon.
The project is being managed by the Faculty of Physics of the University of Munich on behalf of the German Space Administration. It remains to be determined, whether this educational project will also be continued during the next years.

5. ROCKET TECHNOLOGY

5.1. ROTEX-T

ROTEX-T – short for Rocket Technology Experiment – has been launched successfully from ESC on July 19, 2016 to an apogee of 182 km. For the first time, this combination of Terrier Mk12 and Improved Orion rocket stages has been employed here to measure laminar and turbulent flow over the rocket surface and collect additional data on temperature, pressure, and accelerations during flight. ROTEX-T was an unguided solid propellant rocket reaching more than Mach five and a peak acceleration of 21 g. The experiment has been conducted by engineers from the DLR Institute of Aerodynamics and Flow Technology and the RWTH Aachen, supported by SSC and DLR MORABA.

5.2. Improved Malemute

In a second rocket technology project, an ex-military Patriot missile has been modified and tested in two successful qualification flights from Andøya Space Center (ASC) in Norway on June 30 (Fig. 3) and July 8, 2016.

Figure 5: Launch of Improved Malemute in Andøya (Credit: ASC)

The Improved Malemute is a single stage 3-fin rocket type about 2.4 m long with a mass of 100 kg and lift-off thrust of 57 kN, reaching an apogee of up to 120 km. Participants in this project were ASC, DLR MORABA, and the University of Stuttgart, as well as the University of Tromsø (Norway), which used the qualification flights to perform the MaxiDusty experiment, investigating dust particles in the middle atmosphere.

6. CONCLUSION

Suborbital rockets and stratospheric balloons have been in the past and will keep to be in the future valuable and indispensable flight opportunities for research in all of these fields: For example in space science, where balloons complement ground based investigations and satellite observations to probe the middle Earth atmosphere; in microgravity research and life sciences, where research rockets like the VSB-30 or new developments, e.g. the upcoming suborbital Recoverable Launch Vehicles (sRLV), provide flight opportunities with microgravity times in the medium range; or in educational programs for high school or university students. The German Space Program will continue to support all of these activities in the future.

7. ACKNOWLEDGEMENT

The authors thank all DLR colleagues, who contributed to the mentioned projects, as well as the scientists from universities and other research entities in Germany for the provision of information material used in this paper. The activities were funded by the German Federal Ministry for Economic Affairs and Energy, according to a resolution of the German parliament.

THERMAL ANALYSIS OF COMPONENTS FOR STRATOSPHERIC EXPERIMENTS USING FINITE ELEMENT MODEL UPDATING OF THE BEXUS20: HACORD MISSION

Jeroen P. Peeters[1], J. Van Houtte[2], A. Martinez[2], J. Van Muiden[2], J. Dirckx[3], and G. Steenackers[4]

[1]*(University of Antwerp, Op3Mech, Groenenborgerlaan 171, B-2020, Antwerp Belgium*
[2]*University of Antwerp, Elementary Particle Physics research group, Groenenborgerlaan 171, B-2020, Antwerp Belgium*
[3]*University of Antwerp, Biomedical Physics Lab, Groenenborgerlaan 171, B-2020, Antwerp Belgium*
[4]*(University of Antwerp, Op3Mech, Groenenborgerlaan 171, B-2020, Antwerp Belgium & Vrije Universiteit Brussel, Acoustics & Vibration Research Group, Pleinlaan 2, B-1050, Brussels, Belgium*

ABSTRACT

In general, it is difficult to analyse equipment for space applicability due to the fact that realistic tests on Earth are technically difficult and expensive. To prove the reliability of space systems, a combination of numerical analysis and expensive pre-flight tests is used. However, this paper discusses a new methodology in which a combination is made of low-budget ground tests with a newly developed finite element model updating technique which can deliver a time efficient added value or alternative to the expensive and time-consuming pre-flight tests during thermal analysis. In addition, this contribution shows the influence of several design parameters on the accuracy of thermal simulations for space applications and discusses how this accuracy can be optimised. The methodology is verified within the HACORD project of the REXUS/BEXUS programme.

Key words: Finite element model updating; thermal analysis; inverse problem; material characterization; REXUS/BEXUS.

1. INTRODUCTION

The thermal design of spacecraft or balloon experiments is vitally important due to the extreme environmental conditions and zero-failure tolerances [1–3]. In general, thermal designs of balloon experiments are based on a combination of knowledge gained through previous experiments, empirical data and numerical simulations. Occasionally extra information is found by interpolating the environment at high altitude [1, 3, 4]. The use of accurate numerical models is essential to perform accurate simulations and to be able to design insulation techniques [5, 6].

Finite element (FE) models, as explained in section 2.3, are widely used for virtual modelling and the prediction of the dynamic and the thermal behaviour of materials and lightweight structures [7, 8]. These predictions are essential in the preparation of atmospheric balloon experiments [2, 9, 10]. Since atmospheric and space experiments are generally very expensive, it is important to have an excellent knowledge of the interaction between the experiment and its environment in advance, which is efficiently gained through reliable simulations. In general until now, these simulations are made only in steady state conditions and are mapped to a structural analysis [5, 8]. Recent research compares these models manually with complex ground experiments which simulate the space environment as for example the NIRVANA facility, but these experiments are expensive to perform [8].

Next to its importance for predicting the response of the system, simulations are also crucial to increase confidence in advanced experiment set-ups operating in extreme conditions present in the upper atmosphere [6]. All material parameters and

thermal loads of the experiment should be known in order to generate accurate estimations of the thermal behaviour [1].

Recent research, as performed by Liu et al. [11] tries to further improve these numerical models by using transient, time-dependent simulations in which the temperature and time-related parameters during the flight are approximated more accurately. The next step to improve the accuracy of the numerical models and predict the behaviour of balloon experiments is the combination of the numerical models with experimental measurements using numerical updating techniques like finite element model updating, known of system dynamics [12] and recently adapted to use for thermal models by Peeters et al. [13]. For example, one of the important parameters in thermal radiation simulations which is essential to estimate correctly is the emissivity. This parameter is difficult to approximate correctly due to the influence of complex geometrical shapes [14].

The combination of an FE model of the structure with experimental data has major benefits because the experimental criteria can be relaxed due to the integration of the numerical model. Simple and fast to perform ground tests deliver enormous potential for FE updating, as part of a structural condition assessment program to use for correct approximate behaviour at extreme conditions. To ensure accurate numerical simulations the finite element updating technique introduced in [13] is used for non-destructive evaluation. The technique is adapted for more general 3 dimensional thermal problems. The prediction results are validated using the real experimental data retrieved by thermal sensors during flight. The goal of this contribution is to validate if it is possible to better predict experimental device behaviour in space by using a straightforward thermal load and freezer experiment, performed in atmospheric conditions as input for an FE model updating routine. The described methodology can be used to accelerate the design process of atmospheric balloon experiments [3] and helps to improve the design process of future spacecraft [1]. This contribution contains minor corrections to an earlier published contribution with respect to this research [15].

2. MATERIALS & METHODS

2.1. Experimental device description

The HACORD experiment consists of four Geiger-Muller tubes for the detection of cosmic ray particles and a PCB with an ARM® mBed™ microcontroller, a digital and analogue thermal sensor, three pressure sensors and the necessary power and communication electronics. The full system is packed in a polycarbonate box containing 8-20 mm of Styrofoam insulation and a reflective space blanket on the inside of the box to encapsulate the thermal heat of the PCB. The experimental components are shown in Fig. 1.

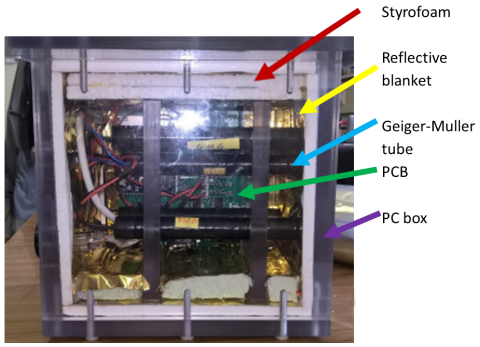

Figure 1. Side view inside the experiment with in white the Styrofoam and in gold the reflective blanket.

2.2. Description measurements

Three different types of measurements are performed: thermal load tests using a thermal imaging camera, a freezer test of the experimental box and finally the balloon flight.

Thermography of electronics The thermal load monitoring test is performed using a thermal camera (Xenics Gobi 640Gige). The temperature increase of the PCB is monitored in a stabilised environment at an ambient temperature of 25.5°C and atmospheric pressure starting from steady state disconnected to steady state under power. The temperature profile is measured during 30 minutes. After five minutes the temperature profile is stabilised to a steady state temperature.

The temperature distribution of the PCB over time is used after post-processing [16, 17] with the up-

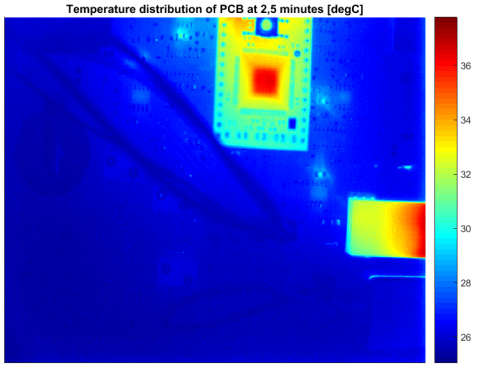

Figure 2. Thermal image of the PCB during the thermal load test after 2.5 minutes.

dating routine of section 2.4. To calculate the thermal loads of all the PCB components, the finite element updating techniques described in [13] is used. A frame of the PCB is shown in Fig. 2. An emissivity map is used to perform accurate thermal measurements and to extract the true temperature for each component during the heating phase.

Freezer test Within this test, the thermal insulation capacity is measured from the retrieved thermal loads of the thermography test of section 2.2. The data of the two temperature sensors on the PCB were used: one NTC resistor below the ARM® mBed™ microcontroller and one digital sensor close to the DC/DC converters which are used to convert the supply voltage from the gondola to the needed high and low voltage for the PCB. Furthermore, four thermocouples have been placed in the experimental box:

- one on the High Voltage DC/DC converter;
- one in the centre of the box;
- one on the side wall above the reflective blanket;
- one below the reflective blanket, which is used to keep the heat radiation inside the box, on the same side wall.

For the test, the following procedure was followed. First, the experiment is switched on for 30 minutes inside the experimental box at room temperature to preheat the full system as in pre-flight conditions. Next, the box is placed in a freezer at a stable temperature of -80°C for more than two hours, which is a simulation of the floating time in the balloon experiment. In this test the thermal isolation of the box could be tested for worst case scenarios where convection and radiation dissipation are considered.

Experimental flight BEXUS 20 The BEXUS 20 balloon with on board the HACORD experiment is launched from the balloon launch area of the Esrange space centre from SSC above the Arctic circle in Sweden. The BEXUS 20 atmospheric balloon reached an altitude of 28.2 km where it remained for 2h and 10min floating. During this flight, the temperature is measured at different locations on the PCB and in the experimental box:

- an NTC thermal resistor below the mBed™ controller on the PCB;
- a digital temperature sensor close to the DC/DC converters;
- a thermocouple type T on the outside wall of the polycarbonate box, shielded from cold air, wind and sunshine which measures the true temperature of the polycarbonate box;
- a thermocouple type T outside the gondola which measures the outside temperature.

The thermal and pressure data are logged at a rate of 1 measurement per second for the data from the PCB and 10 measurements per second for the external thermocouples. A representation of the temperature data is shown in Fig. 3.

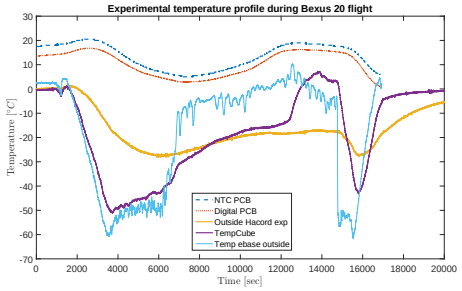

Figure 3. Experimentally measured temperatures for all thermocouples during BEXUS 20 flight.

2.3. Description numerical models

There is made use of the finite element method (FEM) to perform the numerical simulations, which is a computational technique used to approximate complex boundary value problems by

subdividing the large structure in a mesh of connected calculation elements. These mesh elements have dependent variables which must satisfy the standard heat equation and specific boundary conditions within the known domain of the experiment, described by the independent environment variables. This problem will be approximated by iteratively solving the describing differential equations with its boundary values for each element on each time step until the problem converges [5, 18].

Finite element model The numerical simulations are performed in the commercial Siemens NX 10 finite element software which solves the FEM using the NX Thermal solver, which is based on the I-deas^{TM} TMG solution which uses a conservative, element-based control volume formulation [19]. There is made use of specifically adapted meshes with in total 154 774 non-linear tetrahedral elements and 235 438 nodes with thermally dependent material properties as shown in Fig. 4. The calculation time for the full model was approximately 330 minutes on a desktop PC with 32GB ram and a 3.2GHz octa-core CPU approximately 330 minutes. A representation of the meshed in-

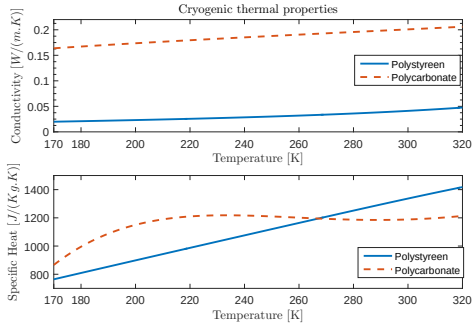

Figure 4. Temperature dependent material properties of the polycarbonate box and the Styrofoam insulation.

ternal structures with the loading on the PCB is shown in Fig. 5.

Physics & boundary conditions The ambient pressure and temperature are related to the local ambient temperature according to the flight profile. The results of the numerical model, with the thermal profile measured outside, are used to compare the standard data and the updated simulation data. As shown in the simplified formula of Eq. 1 to Eq. 3, the convective heat transfer varies equivalent with the air pressure or density as shown in Eq. 3 derived in [20].

$$Nu = C(Gr.Pr)^n = CRa^n \tag{1}$$

with typically n = 1/4 for laminar flow and n = 1/3 for turbulent flow.

$$h = \frac{k}{L}.C(\frac{g_c C_p \rho \beta \Delta T L^3}{\nu \cdot \kappa})^n \tag{2}$$

or

$$h \sim \rho^n \tag{3}$$

The thermal loads are updated using information from the thermal load test of the PCB. Hemicubes and view factors are used to calculate radiation by dividing each mesh element into three parts in such a way that the thermal coupling between the different components inside the box and the radiation to the outside of the polycarbonate box. The reflective blanket is implemented in the thermo-optical parameters of the mesh. The literature on this subject shows that the IR reflectance of these thermal space blankets equals 0.95 and the emissivity/absorbance of solar radiation is 0.05 [21]. From the experimental data shown in Fig. 3, one

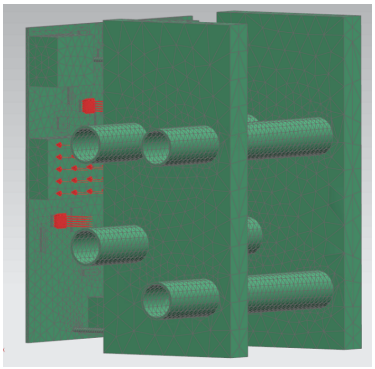

Figure 5. Simulated internal structure with tetrahedral mesh

can see that the solar radiation causes a significant temperature drift during the float stage which influences the temperature profile of the electronic components. This can be deduced from the temperature rise between 6000 and 14000 seconds where the balloon remains floating at its maximum altitude. In contrast to what is expected, the measured temperature rises, first starting in the outside thermocouples. This proves that the influence is coming from outside the box. The irradiation due

to the current solar flux can be predicted using the geometrical coordinates, altitude, date and time considering the inclination of the sun for an east-bound balloon flight. Besides an Albedo factor[1] of 0.15 is considered typical for the forest vegetation of Lapland and a clear sky factor of 1 is chosen as visual contact remains over approximately 100 km. The solar flux is calculated for each time step considering the solar time and the altitude of the gondola. A plot of the time variance of the solar flux is shown in Fig. 6.

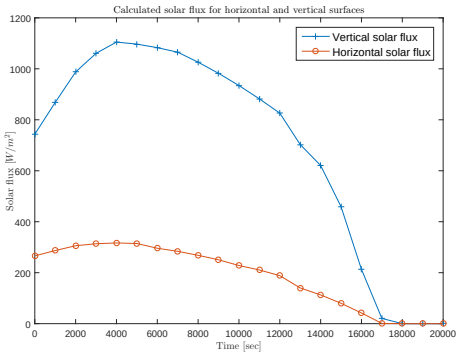

Figure 6. Evolution of the solar fluxes during the flight in the East direction.

2.4. Updating algorithm

The updating algorithm works in two different stages where the targets are set to update the numerical model of the BEXUS 20 flight simulation:

1. The experimental data of the thermal load test is used as a target to estimate the thermal loads on the PCB.
2. The experimental data of the freezer test are used as a target to estimate the insulation properties of the full assembly.

The optimisation uses the relative temperature differences $\vartheta = T_{numerical} - T_{target}$ as objective function to accurately estimate the thermal behaviour in a near-space environment. The algorithm has no fixed amount of iterations, in contrast to the method described in [23], and is based on the methodology described in [13]. The parameter *stability control* is increased even for the use of dependent parameter sets and the use of multiple initial values for each parameter set, in contrast to the method described in [13]. In a first stage, a meta-model is created of a response surface built out of $2 * n - 2$ data points for $n > 2$. This surface is retrieved from numerical simulations that are randomly distributed across the design space. The design space is built out of the physical boundary values for each parameter of the objective function. This meta-model is built out of n-dimensional polynomials, each dimension representing an unknown parameter and forming one single n-dimensional response surface together with all the other dimensions. The optimisation algorithm searches for a global minimum of the objective function in the meta-model which results in estimated values for each parameter. The estimated parameter values are the input of a new numerical model, called the updated numerical model. The results of this updated numerical solution have a higher correlation with the experimental target values and deliver new input that could replace the least accurate data point inside the meta-model with the more accurate data point of the last solution. This iterative process reforms the response surface locally in the region of the global minimum. The local conversion of the response surface is a local solution of the optimisation problem. The simultaneous use of different values delivers a conversion to a global minimum. This process continues until convergence is achieved for the error value between the experimental values and the minimum of the meta-model. The optimiser is a least square curve fitting optimiser following the trust region regression algorithm conform to [13]. In [13] this is explained as the most efficient.

[1] Reflection factor due to the Earth surface. It represents the fraction of solar energy reflected from the Earth back into space.[22]

3. RESULTS & DISCUSSION

In the following section, the results of the two different updating routines will be discussed and the influence of the updating on the numerical simulation will be shown. Finally, both the updated and the normal numerical model will be compared with the retrieved experimental data of the BEXUS 20 flight.

3.1. Comparison thermal load PCB

In a first stage, a comparison was made between the numerical model of the thermal load test and the experimental thermography data. As the com-

position of the PCB is well known and the ambient conditions are controlled as explained in section 2.2, the only difference between the numerical model and the experimental data are the effective thermal loads of the components and the heat distribution over the PCB. Using the updating routine of section 2.4, the thermal load values in Tab. 1 are retrieved. It is clearly shown that the overall thermal load is a little bit higher than the assumed thermal loads derived from data sheets: $1.68W$ instead of $1.4W$ which is verified by the true power consumption of $0.06A$ at $28V$ of the PCB. To perform the updating process, the temperature response is compared for the different components during the start of the experiment until steady state conditions are achieved. From these results, we can conclude that the overall power consumption can be predicted from data sheet information in combination with a global power test. However, if the power distribution over the PCB is important to balance the heat distribution or adapt the thermal insulation to the local power consumption, an accurate simulation with accurate values is necessary. Tab. 1 shows that after updating the thermal loads the distribution over the PCB is more precise and the summation is accurately close to the global power consumption.

3.2. Comparison Isolation parameters

In a second stage, after the thermal loads on the PCB are updated correctly, the heat transfer parameters must be made more accurate. The most important parameters are the heat transfer coefficients of the experimental box, the conductivity of the PCB, the specific heat of the PCB and the emissivity of the box. The emissivity map of the PCB is already known from the thermal load test of section 2.2, discussed in the previous section and the conductivity and specific heat of the Styrofoam and polycarbonate are calculated analytically as a function of the temperature as described in section 2.3. To update the numerical model of the freezer test, the temperature sensors were used as described in section 2.2 as target data and the updating routine of section 2.4. A comparison of the experimental temperature profile and the updated profile is shown in Fig. 7 for the thermocouple of the high voltage DC/DC converter and ambient temperature in the centre of the box. As could be seen in Fig. 7, the thermal behaviour of the numerical model of the freezer test corresponds with the experimental data. The largest error is seen

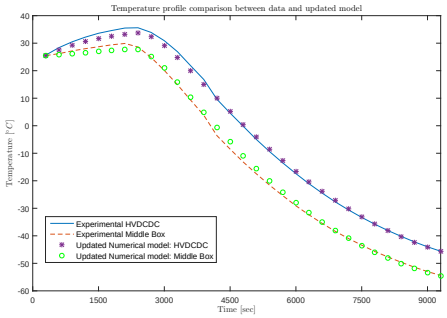

Figure 7. Comparison of the temperature evolution of the numerical model and the experimentally measured data from the thermocouples.

when the box is placed from the ambient climate into the freezer. This little time instance, however, has a limited effect on the characterisation of the isolation parameters.

3.3. Prediction thermal flight data using updated model

After the updating of the thermal load parameters in section 3.1 and the material parameters in section 3.2, the same numerical model is used to simulate the balloon flight with the decrease of convection depending on the altitude and the insolation as described in section 2.3. In the results, shown in Fig. 8, a comparison has been made between the experimental data, the numerical model before and after updating the parameters. The temperature profile of the different measurement spots, including the imposed ambient temperature is shown as discussed in section 2.2. Fig. 8 shows that the thermal parameters have a major influence on the temperature evolution of the PCB components. Without updating the numerical model, a major drift in the heat dissipation caused by insolation during float can be detected by looking at the two sensors inside the box. After updating the thermal loads and thermal properties the numerical model predicts the experimental measurements with an improved accuracy. The root-mean-square error for the difference between the numerical and experimental data improves by a factor 2.2 to 7.6 for each time interval due to the updating. The major discrepancy is seen around 16000 seconds. At this time step, the balloon is cut and the gondola encounters a brief free fall back to earth before the parachute opens. It is assumed that the fast move-

Table 1. Comparison thermal loads on PCB assumed from datasheets and after updating from the thermal load test.

Component	**Assumed** $[W]$	**Updated** $[W]$
High Voltage DC/DC Converter	0.3	0.17
Voltage Comparator	0.2	0.07
DC/DC Step Down Converter	0.3	0.42
mBed microcontroller	< 0.1	0.84
Remaining components	< 0.01 (total ≈ 0.1)	total ≈ 0.18
Summation global Power consumption	1.4	1.68

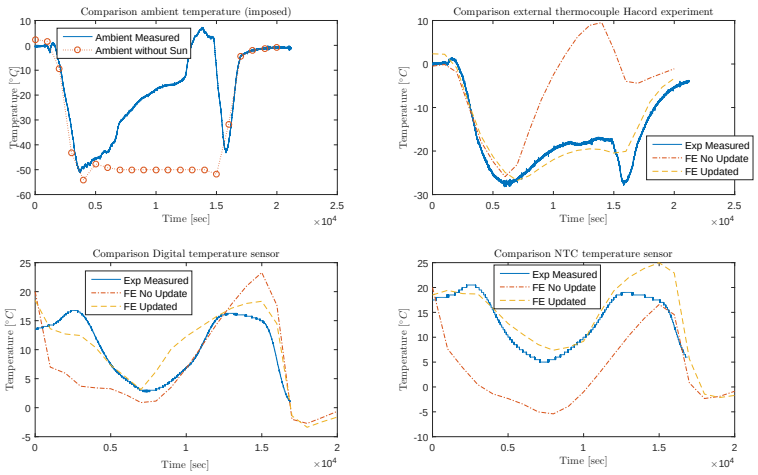

Figure 8. Comparison between the temperature evolutions of the numerical model and the experimentally measured data from the flight data.

ment of the gondola and the fast temperature and pressure gradients cause the divergence as this dynamic movement of the gondola is not considered in the simulation model.

4. CONCLUSIONS

A numerical model, used to predict the thermal behaviour of stratospheric balloon experiments, can be updated through a limited number of ground tests. When the environmental conditions are well described, but contain a number of uncertain parameter values, the updating routine delivers a major accuracy improvement by a factor of 2.2 to 7.6. This method can also be used for other well-known complex environment estimations as a replacement for expensive, long duration and/or dangerous experiments. The boundary conditions of the method are that the uncertain parameter values are independent of the experiment environment. Moreover, the methodology can be used to validate experimental designs for space applications and determine the failure risk of different components or design versions in a fast and cost-efficient way.

REFERENCES

[1] D Swanson. Spacecraft Thermal Control Systems. Technical report, NASA, 2001.

[2] A Vargas, C Tarrieu, J-P Lepage, P Mauroy, and C Sirmain. Mars balloon simulator. *Acta Astronautica*, 26(8):697–706, 1992.

[3] Yajima Nobuyuki, Izutsu Naoki, Imamura Takeshi, and Abe Toyoo. *Scientific Ballooning: Technology and Applications of Exploration Balloons Floating in the Stratosphere and the Atmospheres of Other Planets*. Springer, 2009.

[4] Frank Kreith. Thermal design of high-altitude balloons and instrument packages.

Journal of Heat Transfer, 92(3):307–332, 1970.

[5] Sadanand Wachche, Aniket Marne, Sumit Singare, Pranjal Naik, Ojas Bhide, Gitesh Chaudhari, Prathamesh Vartak, Saloni Pendse, and Chinmay Tadwalkar. Thermal modeling and simulation of a Pico-satellite using Finite Element Method. In Lynn Ferguson, Robert Goldstein, Scott MacKenzie, and Rozalia Papp, editors, *5th International Conference on Thermal Process Modeling and Computer Simulations*, pages 65–74, Orlando, 2014. ASM International.

[6] S Lapensée and C Alary. Development and analysis of the surface thermal environment for the ExoMars lander mission. *40th International Conference on Environmental Systems, ICES 2010*, pages 1–22, 2010.

[7] Ali Abdul-Aziz. Assessment of crack growth in a space shuttle main engine first-stage high-pressure fuel turbopump blade. *Finite Elements in Analysis and Design*, 39:1–15, 2002.

[8] P. Vialettes, J. M. Siguier, P. Guigue, M. Karama, S. Mistou, O. Dalverny, S. Granier, and F. Petitjean. Experimental and numerical simulation of super-pressure balloon apex section: Mechanical behavior in realistic flight conditions. *Advances in Space Research*, 37(11):2082–2086, 2006.

[9] E. S. Seo, H. S. Ahn, S. Beach, J. J. Beatty, S. Coutu, M. A. DuVernois, O. Ganel, Y. J. Han, H. J. Kim, S. K. Kim, M. H. Lee, L. Lutz, S. Nutter, S. Swordy, and J. Z. Wang. Cosmic-Ray energetics and mass (CREAM) balloon experiment. *Advances in Space Research*, 30(5):1263–1272, 2002.

[10] Dinesh Balagangadhar and Subrata Roy. Design sensitivity analysis and optimization of steady Fluid-thermal systems. *Computer Methods in Applied Mechanics and Engineering*, 190, 2001.

[11] Q. Liu, Z. Wu, M. Zhu, and W. Q. Xu. A comprehensive numerical model investigating the thermal-dynamic performance of scientific balloon. *Advances in Space Research*, 53(2):325–338, 2014.

[12] Tshilidzi Marwala. *Finite-element-model Updating Using Computational Intelligence Techniques*. Springer, 2010.

[13] Jeroen Peeters, G. Arroud, Bart Ribbens, J.J.J. Dirckx, and G. Steenackers. Updating a finite element model to the real experimental setup by thermographic measurements and adaptive regression optimization. *Mechanical Systems and Signal Processing*, 64-65:428–440, 2015.

[14] J. Peeters, B. Ribbens, J.J.J. J J Dirckx, and G. Steenackers. Determining directional emissivity : Numerical estimation and experimental validation by using infrared thermography. *Infrared Physics & Technology*, 2016.

[15] J Peeters, J. Van Houtte, A Martinez, J. van Muiden, J.J.J. Dirckx, and G. Steenackers. Determination of stratospheric component behaviour using Finite Element model updating. *Aerospace Science and Technology*, 56:22–28, sep 2016.

[16] XPV Maldague. *Theory and practice of infrared thermography for nondestructive testing*. Wiley, New York, 2001.

[17] M. Vollmer and KP Möllmann. *Infrared thermal imaging: fundamentals, research and applications*. Wiley-VCH, Berlin, 2010.

[18] O C Zienkiewicz and R.L. Taylor. *The Finite Element Method*, volume 1-3. Butterworth Heinemann, Oxford, 5 edition, 2000.

[19] (Siemens). I-DEAS TMG Thermal Analysis, 2015.

[20] Theodore L Bergman, Adrienne S Lavine, Frank P Incropera, and David P. DeWitt. *Fundamentals of Heat and Mass Transfer*. John Wiley & Sons, Incorporated, 7th edition, 2011.

[21] Laurence Viennot and Nicolas Décamp. Which side to put the survival blanket? Analysis and suggestions for activities with students. Technical Report July, Physics Education Division (PED) of the European Physical Society (EPS), 2014.

[22] J. P. Holman. *Heat Transfer*. McGraw-Hill, 6th edition, 1990.

[23] G. Steenackers, F. Presezniak, and P. Guillaume. Development of an adaptive response surface method for optimization of computation-intensive models. *Computers & Industrial Engineering*, 57(3):847–855, oct 2009.

CORK BASED THERMAL PROTECTION SYSTEM FOR SOUNDING ROCKET APPLICATIONS – DEVELOPMENT AND FLIGHT TESTING

Oliver Drescher[(1)], Marcus Hörschgen-Eggers[(2)], Grégory Pinaud[(3)], Maxime Podeur[(4)]

[(1)] Deutsches Zentrum für Luft- und Raumfahrt (DLR)/Oberpfaffenhofen, Mobile Raketen Basis, Münchener Straße 20, 82234 Weßling, Germany, E-mail: oliver.drescher@dlr.de

[(2)] Deutsches Zentrum für Luft- und Raumfahrt (DLR)/Oberpfaffenhofen, Mobile Raketen Basis, Münchener Straße 20, 82234 Weßling, Germany, E-mail: marcus.hoerschgen-eggers@dlr.de

[(3)] ArianeGroup, Rue du Général Niox, 33165 Saint-Medard en Jalles Cedex, France, E-mail: gregory.pinaud@airbusafran-launchers.com

[(4)] ArianeGroup, Rue du Général Niox, 33165 Saint-Medard en Jalles Cedex, France, E-mail: maxime.podeur@airbusafran-launchers.com

ABSTRACT

The application of aerospace thermal protection systems (TPS) is not limited to orbital flight and re-entry vehicles. Although less critical in terms of the thermal load's magnitude, it is also an essential part of sounding rocket primary structures.
For a large variety of launch vehicles, DLR's Mobile Rocket Base (MORABA) uses thermal protection systems on primary structures such as fin, nose cone, conical adapter and heat shield assemblies. Hereby, an ablative, epoxy based, two component thermoset coating has been the material of choice over several decades. Using relatively simple manufacturing methods, it can be sprayed onto almost any geometry. However, its noxious fumes released during the spraying process, its limited shelf life, its extensive storage requirements and above all, its residues polluting adjacent payload components during the ablation phase, are the key drivers for the development of a new thermal protection system using a special cork material.
This paper presents the development and manufacturing process as well as flight testing and post-flight analyses for different cork protected structural components flown on recent scientific missions (e.g. MAIUS 1, MAPHEUS 6, etc.). Results are discussed and a future outlook is given.

1 MOTIVATION

Aerospace thermal protection systems (TPS) are an essential part of sounding rocket primary structures such as fin, nose cone, conical adapter and heat shield assemblies; see also Fig. 1. Until recently the Mobile Rocket Base (MORABA) of the German Aerospace Centre (DLR) used an ablative, epoxy based, two component thermoset coating as TPS material.

Figure 1. IMPROVED MALEMUTE (IM) vehicle with cork based TPS on fin and motor adapter assemblies.

However, its noxious fumes released during the spraying process, its limited shelf life, its extensive storage requirements and above all, its residues polluting adjacent payload components during the ablation phase, are the key drivers for the development of a new thermal protection system.

2 TPS MATERIAL SELECTION

Besides the main functionality as a TPS material, the following additional requirements are considered as stringent for the selection of the new TPS material:

- Easy to apply on various shaped geometries,
- low mass,
- environmentally friendly (REACH, pollution of adjacent structures),
- low procurement and process costs,
- easy to store,
- easy to repair,
- good availability,
- preferably "Made in the European Union (EU)",
- no or less export restrictions.

From these outlined specifications resin infiltrated cork has been selected as the most potential TPS substitute. ArianeGroup (AG) 40 years of experience in the design, manufacturing and integration of cork based TPS for several space flight vehicles is a further key asset in selecting especially NORCOAT® LIÈGE HPK FI as the most promising semi-finished product available on the EU market.

NORCOAT® LIÈGE HPK FI is a low density thermal insulator based on cork granules mixed with phenolic resin as matrix; it is manufactured by LIÈGE HPK and marketed by AG. It is currently used on Ariane 5 launch vehicles, on M 51 French deterrence force missiles and has been successfully operated on the Atmospheric Re-entry Demonstrator (ADR) back cover as well as on the front heat shield of the BEAGLE 2 space probe of the European MARS EXPRESS mission. Furthermore, the successful operation on the latest Mars re-entry capsule Schiaparelli (EXOMARS mission, Fig. 2) proved the robustness of the material.

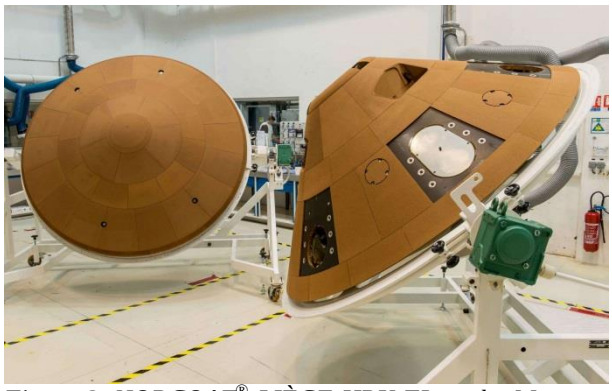

Figure 2. NORCOAT® LIÈGE HPK FI on the Mars re-entry capsule Schiaparelli; source: ESA.

NORCOAT® LIÈGE HPK FI is produced in form of flat plates of various thicknesses from 1.5mm to 19.0mm and can be further processed by e.g. machining (e.g. cutting, milling, etc.), hot-press forming, adhesive bonding and outgassing treatment for special space applications.

3 THERMAL ANALYSIS

In order to pre-assess the minimum TPS material thickness required as well as the charred layer thickness, a one-dimensional thermal analysis has been performed, considering a stacking of material and thermophysical phenomena as shown in Fig. 3.

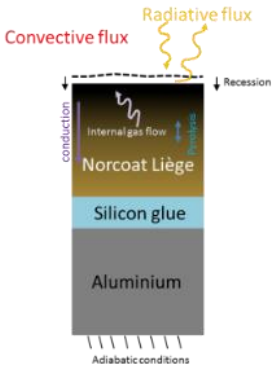

Figure 3. Schematic view of material and thermophysical phenomena stacking.

The simulation has been carried out on the VSB-30 aluminium forward nose cone (FNC) structure, laminated with 1.5mm as well as 2.0mm sheets of NORCOAT® LIÈGE HPK FI, using the commercial code AMARYLLIS (part of the SAMCEF code suite).

3.1 Method and Material Response Modelling

NORCOAT® LIÈGE HPK FI is a so called charring material, which decomposes when subjected to high temperatures, followed by a decrease in the material's density. Since this material consists of different constituents, its degradation can occur over different temperature ranges. To account for this type of behaviour, a multiple species Arrhenius definition can be used. However, for the herein described simulation only a single species Arrhenius law has been applied, due to available material model; Eq. 1.

$$\frac{\partial \rho}{\partial t} = -A\rho_v^{1-N}(\rho - \rho_c)^N e^{-\frac{E}{RT}} \quad (1)$$

The above described degradation results in the production of gaseous products, which diffuse through the material. Therefore the steady state gas mass balance equation is used; Eq. 2.

$$\frac{\partial \rho}{\partial t} + \nabla . \dot{\overline{m}}^g = 0 \quad (2)$$

Assuming an ideal gas law, and introducing Darcy's law to relate the pressure of the gas to the gas mass balance, Eq. 3 can be formulated.

$$\dot{\overline{m}}^g = -K_P \nabla P$$
$$K_P = \frac{M^g \beta P}{\mu^g \overline{R} T} \tag{3}$$

By introducing the pressure as a variable, a three-dimensional gas flow can be defined, using a scalar degree of freedom. Thus a direction of gas mass flow has not to be imposed beforehand. The heat balance equation reflects the time variation of enthalpy (both solid and gas), the heat conduction and the presence of gas in the pores of the solid parts. The model is set up with a local thermal equilibrium, assuming the gas and the solid parts having the same temperature at microscale. With the assumption of linear enthalpy variation, the following heat balance equation is obtained, Eq. 4.

$$-\frac{\partial \rho}{\partial t} H_p + \rho c \frac{\partial T}{\partial t} = -\nabla . \lambda \nabla T - \dot{\overline{m}}^g . \nabla h^g \tag{4}$$

All temperature dependent material properties (ρ, λ, c_p) are obtained by interpolation between the virgin and the charred state.

3.2 Loads and Boundary Conditions

The VSB-30 vehicle's ascent velocity, altitude and heat flux over flight time are applied and taken from TEXUS 43 nominal trajectory data; see also Fig. 4 and Fig. 5.

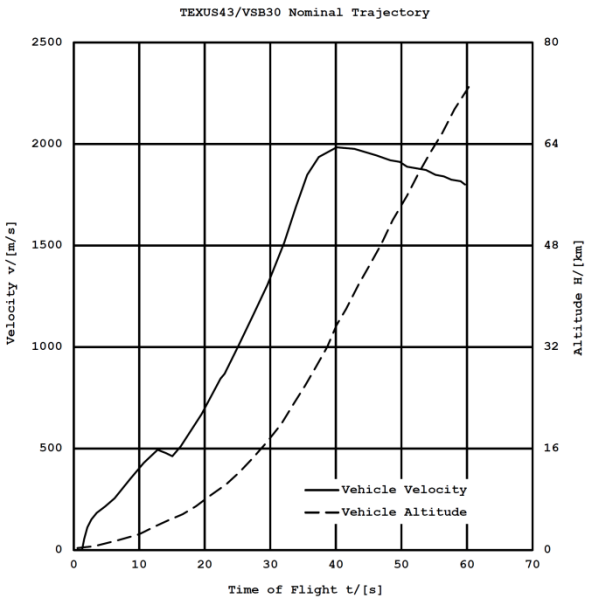

Figure 4. TEXUS 43 nominal vehicle velocity and altitude data.

Since the VSB-30 FNC structure is ejected after approximately T+60s the simulation is only carried out within this time frame.

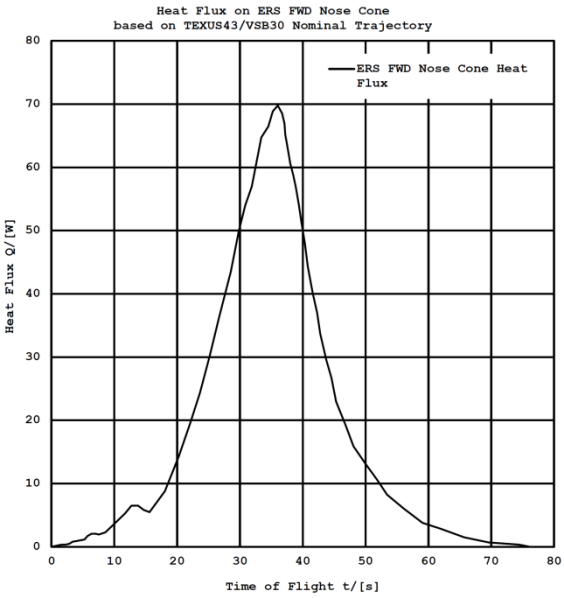

Figure 5. Heat flux on VSB-30 FNC base on TEXUS 43 nominal trajectory data.

The predicted cold wall heat flux is tabulated for different wall temperatures based on the trajectory data and is then rebuilt in an iterative loop.

In total three types of boundary conditions are applied to the model:

- The outer surface pressure, representing the aerodynamic pressure (Eq. 5),
- the outer wall temperature, dependent on the applied heat flux (convective and radiative term, Eq. 5),
- the imposed temperature dependent ablation speed (Eq. 6).

$$-\lambda \frac{\partial T}{\partial \overline{n}} = q(T_w, \overline{x}, t) + \epsilon \sigma (T_r^4(\overline{x}, t) - T_w^4) \tag{5}$$

$$\dot{s} = \dot{s}(T_w) \tag{6}$$

The surface ablation is implemented by a moving ablation surface and a deforming volume.

3.3 Results

Fig. 6 shows the calculated FNC's inside wall temperatures for the different NORCOAT® LIÈGE HPK FI layer thicknesses (1.5mm and 2.0mm) and

typical inflight measured temperatures for a 1.0mm layer of the traditional epoxy based thermoset coating.

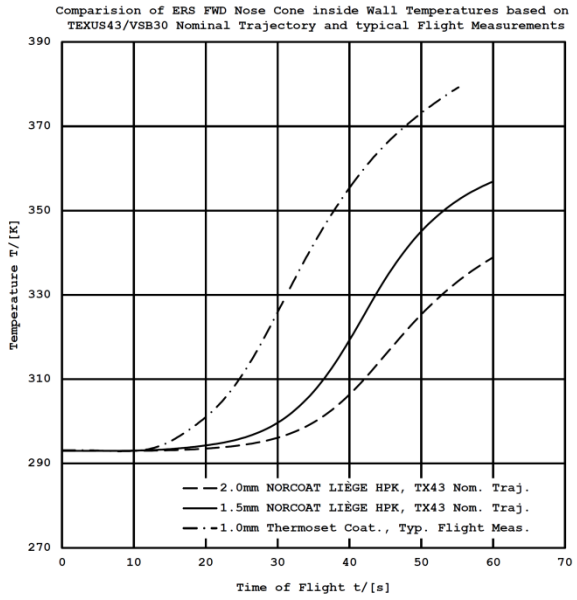

Figure 6. Comparison of predicted inside wall temperatures.

After T+60s, maximum inner wall temperatures of ~357K (84°C) for 1.5mm and ~338K (65°C) for 2.0mm of cork are reached. The resulting temperatures can be rated as non-critical compared to the measured temperature for the traditional epoxy based thermoset coating and to the maximum service temperature of the aluminium structure. However, a direct comparison of the cork and epoxy based thermoset TPS is not possible due to the different layer thicknesses applied.

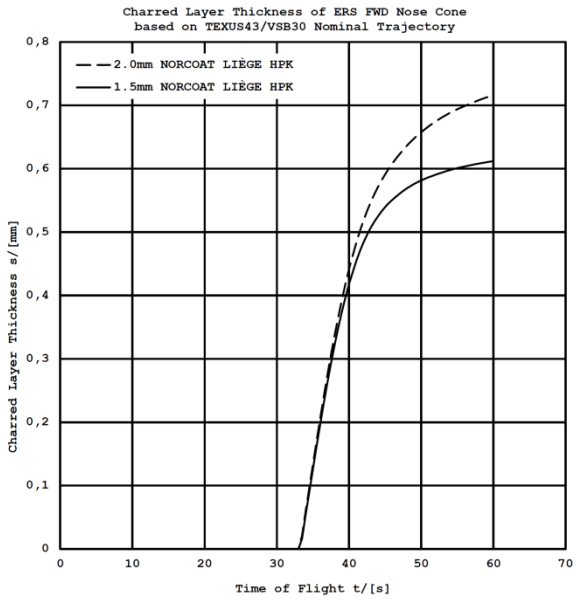

Figure 7. Comparison of TPS charred layer thicknesses.

Fig. 7 shows the calculated NORCOAT® LIÈGE HPK FI charred layer depth for virgin layer thicknesses of 1.5mm and 2.0mm. During the ascent phase the pyrolysis is expected to start from approximately T+30s and the TPS external surface to be fully charred. After T+60s the pyrolysis front can reach a depth of ~0.6mm for 1.5mm and ~0.7mm for 2.0mm virgin cork layer thicknesses.

Showing non-critical wall temperatures and non-sensitive insulation behaviour, a layer of 2.0mm NORCOAT® LIÈGE HPK FI has been selected as the VSB-30 FNC's TPS substitute for further manufacturing trails as well as inflight testing. Considering a 2.0mm coating and the respective adhesive layer, the total aerial mass at lift-off for this TPS solution would be less than 1.5kg/m^2.

4 MANUFACTURING PROCESS AND HARDWARE

Another major part of the TPS substitution has been the development and establishment of a suitable manufacturing process by fulfilling the following main needs: Low process costs, less lead time, environmentally friendly, applicable to all TPS related structures, performable by 1-2 workers.

The essential process steps (Fig. 8) can be named in the right order as: Surface preparation, structural adhesive application, TPS layer application, vacuum bagging and curing, finishing.

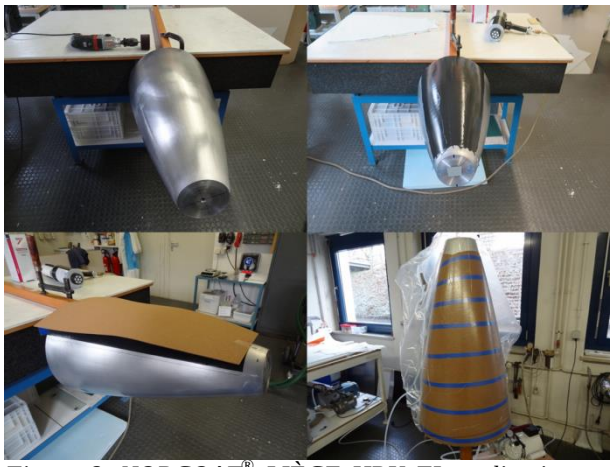

Figure 8. NORCOAT® LIÈGE HPK FI application on VSB-30 FNC structure.

After the successful manufacturing process development, performed on a VSB-30 FNC structure (Fig. 8), it has been adopted to other TPS related structures such as fin, motor adapter and heatshield assemblies (Fig. 9).

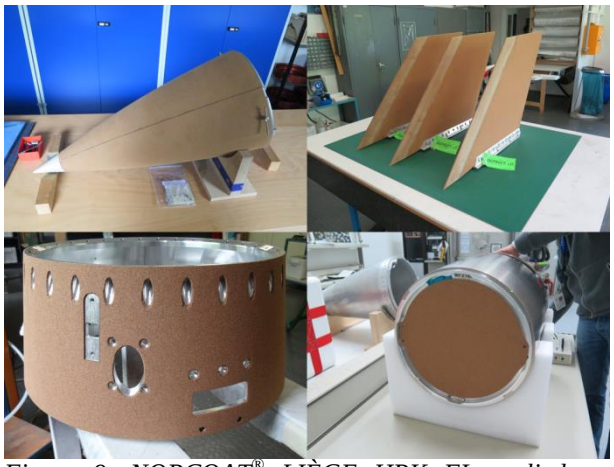

Figure 9. NORCOAT® LIÈGE HPK FI applied on various primary and secondary sounding rocket structures.

Up to present, this process is object of a continuing iteration loop of certain process parameters and thus of further improvements for serial production.

5 FLIGHT TESTING

With several flight hardware items coated using the cork based TPS, flight testing has been imminent.

The first NORCOAT® LIÈGE HPK FI coated structures tested during flight were fin and motor adapter assemblies for IM sounding rocket vehicles, launched for the MAXI-DUSTY missions in July 2016 from Andøya Space Centre in Norway. Due to the tight time schedule for the preparation of these missions none of these structures were instrumented with temperature or other sensors. However, measured trajectory as well as inflight video footage showed non-critical, nominal vehicle behaviour and thus the first operation of the new TPS material is considered as a success.

During the two follow-up missions MAIUS 1 in January 2017 and MAPHEUS 6 in May 2017, both launched from ESRANGE in Sweden, two cork coated FNC and heat shield assemblies were successfully flight tested on the VSB-30 vehicle. Each of the FNC assemblies was equipped with two PT100 temperature sensors.

Figure 10. MAPHEUS 6 in the Skylark tower (left), payload (mid) and cork coated FNC recovery (right).

Fig. 10 shows the cork coated FNC assembly launched on the MAPHEUS 6 mission, which could be fully recovered after the re-entry.

6 POST FLIGHT ANALYSES

The measured flight data from MAIUS 1 and MAPHEUS 6, as well as the recovered FNC structure flown on MAPHEUS 6, have been used for further post flight investigations described in the following subchapters.

6.1 Comparison of Flight Data

Before comparing the MAIUS 1 and MAPHEUS 6 measured temperature data, a closer look on the underlying trajectory data as well as the PT100 temperature sensor position and mounting technique is necessary.

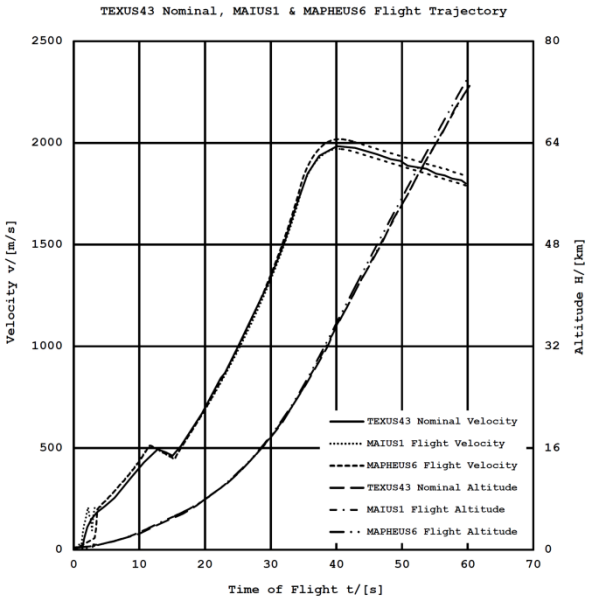

Figure 11. Comparison of TEXUS 43 nominal, MAIUS 1 and MAPHEUS 6 flight trajectory data.

Fig. 11 shows a comparison of the measured MAIUS 1 and MAPHEUS 6 trajectory data from lift-off until FNC separation (T+60s). The related measured vehicle velocity and altitude is plotted together with the TEXUS 43 nominal trajectory data, taken for the pre-asset thermal analysis. Apart from some minor deviations shortly after lift-off, the graphs show a good accordance and thus representing a reasonable basis for the temperature comparison.

Fig. 12 shows the standard positions and mounting technique of the two PT100 sensors (T1 & T2) on the inside of the FNC structure as integrated on the MAPHEUS 6 flight hardware. The sensor itself was casted inside an aluminium casing (Fig. 12, bottom, left)

and bonded on the respective position on the inside of the aluminium structure (Fig. 12, bottom, right) using a high temperature conductive resin.

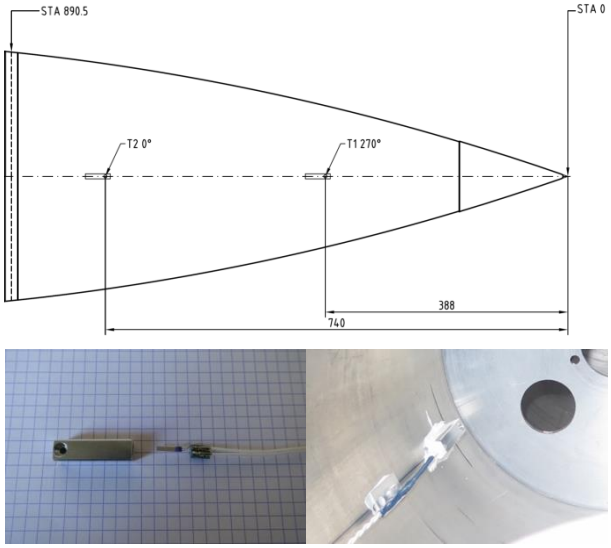

Figure 12. Position and application of PT100 sensors.

In contrast to MAPHEUS 6, the MAIUS 1 FNC was of a spherically blunted geometry (90mm tip radius) and ~200mm shorter in length. Both PT100 sensors were mounted close together at the T2 position (measured from the separation interface STA 890.5). The reason for this application was to evaluate the influence of one sensor mounted with and one sensor without the aluminium casing.

Fig. 13 shows the measured inside wall temperatures of MAPHEUS 6 and MAIUS 1 together with the predicted temperatures from the pre-asset analysis over the first 60s in flight. In general, the measured temperatures are clearly below the predicted ones. The MAIUS 1 T2 sensor without the aluminium casing measured the highest and the closest values to the prediction (~14% max. deviation). Because of its higher thermal mass, all sensors casted in the aluminium casing showed a clear delay and thus ending up with much lower magnitudes at the point of nose cone separation (~50% max. deviation). Due to the different ambient temperature conditions at launch, a clear difference of the measured values between MAIUS 1 and MAPHEUS 6 is detected. However, assuming a similar heat capacity for both nose cone structures, a comparison of the various temperature differences from lift-off until nose cone separation is feasible.

By comparing the MAPHEUS 6 T1 sensor to its T2 sensor only a marginal difference (<10% max. deviation) can be detected resulting from the different sensor positions.

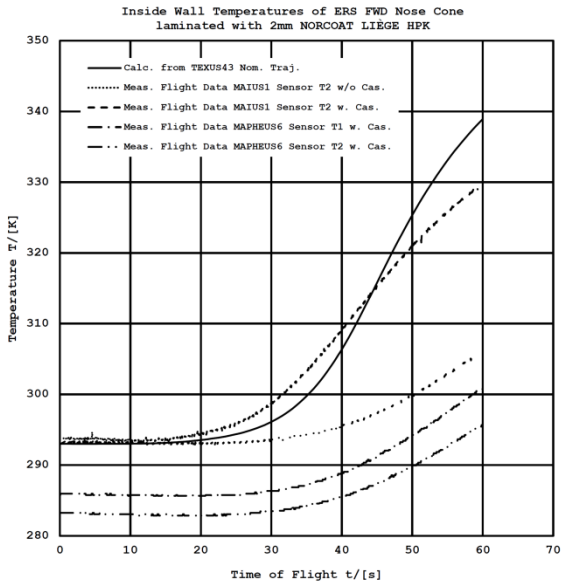

Figure 13. Comparison of measured and calculated inside wall temperatures.

Negligible, small deviations can be found by comparing the T2 sensor of MAIUS 1 to the T2 sensor of MAPHEUS 6, implying only small deviations at T2 position due to the different nose cone geometries.

6.2 Recovered Flight Hardware Inspection

In addition to the post flight analysis of measured data an investigation of the recovered MAPHEUS 6 FNC structure has been performed. Besides the first visual inspection, five samples have been cut out from various nose cone positions (including the T1 and T2 positions), prepared and inspected under a light microscope.

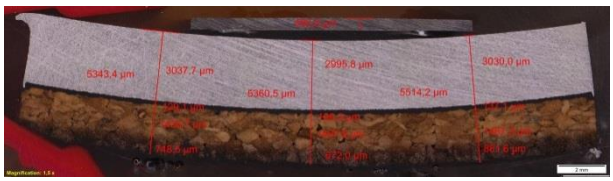

Figure 14. Light microscopic investigation of MAPHEUS 6 FNC cut-out samples.

Fig. 14 shows the light microscopic picture of the sample cut out at 650mm from the nose cone separation plane. For all samples the stacking has been measured and the average thicknesses can be summarised as follows:

- Adhesive layer 0.15mm,
- virgin cork layer 1.80mm,
- charred cork layer 1.10mm,
- total cork layer 2.90mm.

From the original and measured total cork layer thickness an approximate swelling of ~45% can be calculated.

In addition to the material thicknesses, the microscopic pictures also revealed a very high porosity of the sensor casting inside the aluminium casing as well as of the bonding layer between the nose cone structure and the aluminium casing.

6.3 Thermal Analysis Validation

In order to get a better insight of the deviation between calculated and measured temperatures, a validation of the thermal simulation has been carried out and is described in this subchapter. Furthermore, this validation has been only performed on the example of the MAPHEUS 6 flight hardware, since the FNC geometry flown on the MAIUS 1 mission is not representing the standard tip geometry.

6.3.1 Actual Trajectory and Atmospheric Data

The measured MAPHEUS 6 main trajectory parameters together with the actual atmospheric profile have been used to rebuild more realistic aerothermal loads for the heat flux calculation. Since all weather balloons, launched during the countdown, were measuring exclusively wind speed and wind direction, only forecasted atmospheric profiles have been used.

6.3.2 Aerothermal Loads Assessment

For the assessment of the aerothermal heat flux the software ARPEGE, coded by Airbus, has been selected. ARPEGE (Aérothermodynamique de Rentrée pour PrédirE la fraGmentation d'Etages) is a fast computer programme designed to predict surface pressure, shear stresses, aerodynamic forces, coefficients and heat transfer distributions of an arbitrary shaped geometry at hypersonic speed. Below 40km (until T+40s) the VSB-30 vehicle is not strictly in a hypersonic regime, however for a first quick assessment the tool is considered as sufficiently accurate.

The MAPHEUS 6 FNC geometry has been used to create a three-dimensional surface mesh. Furthermore, a zero degree angle of attack is assumed all along the trajectory leading to an axisymmetric heat flux distribution.

Fig. 15 shows the resulting cold wall aerothermal heat flux distribution at T+35s for a uniform initial temperature of 300K. At high Mach numbers the heat flux profile decreases rapidly after a few centimetres measured from the nose tip.

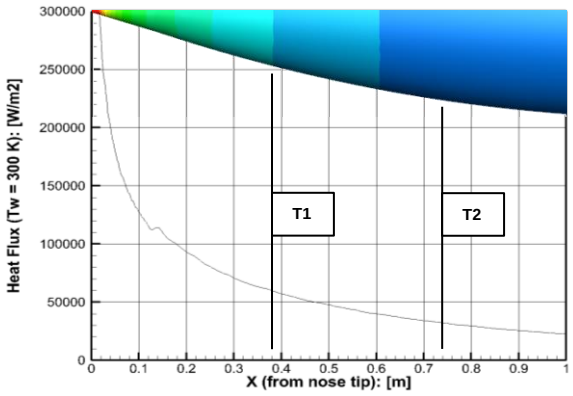

Figure 15. MAPHEUS 6 calculated cold wall aerothermal heat flux profile at T+35s.

At each point of the recorded trajectory, steady state runs provide the time profile of the heat flux on any location of the FNC.

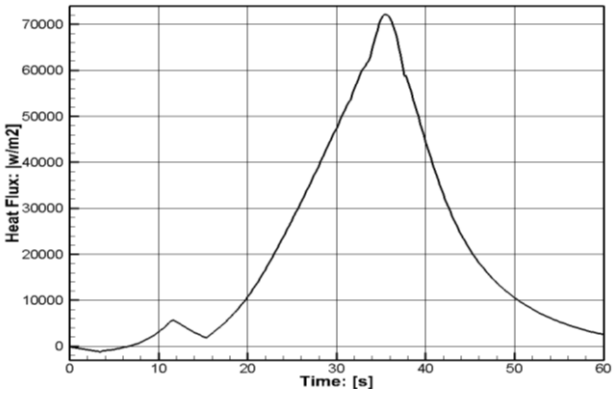

Figure 16. MAPHEUS 6 calculated cold wall aerothermal heat flux time profile (300mm from the nose tip).

Fig. 16 shows the time profile of the aerothermal heat flux at the exact location of the temperature sensor T1, which is similar to the initial heat flux taken for the pre-asset analysis (Fig. 5). However, an over prediction in the subsonic and low supersonic regime must be considered due to the described limitations of the ARPEGE programme.

6.3.3 Thermal Response Assessment

Based on the microscopic investigations, as well as on the PT100 sensors actual integration and mounting situation, a more realistic material stacking has been taken into account. Therefore, a three-dimensional model, including a numerical thermocouple with aluminium casing, has been created. The simulation has been performed using the same software (AMARYLLIS), method and boundary conditions as used for the one-dimensional pre-asset analysis described in chapter 3. Finally, for the calculation of the temperatures at the T1 and T2 positions the previously

calculated time-dependent aerothermal heat fluxes of these respective locations have been applied. For the material input the actual parameters of all materials used have been taken from corresponding technical data sheets.

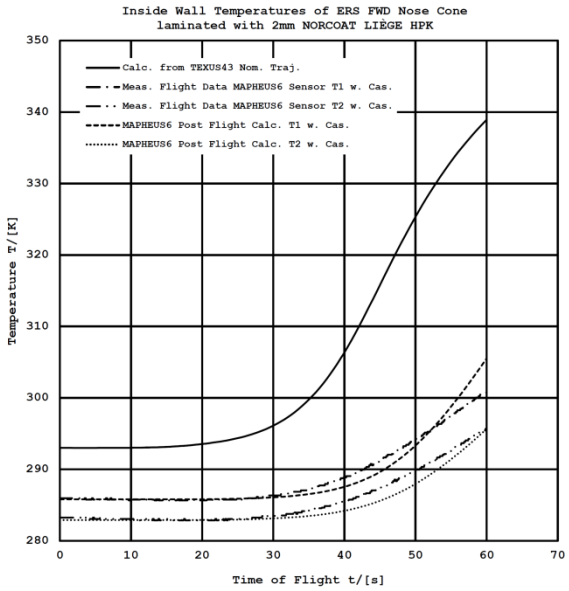

Figure 17. Comparison of measured, calculated and validated inside wall temperatures.

Fig. 17 shows the inside wall temperatures of the pre-asset calculation as well as those measured during the MAPHEUS 6 flight and those from the validation runs. Although the initial temperature of the pre-asset calculation is slightly higher, a comparison of the various temperature differences from lift-off until T+60s is feasible. Thereby, the validated results show a clear trend towards a more accurate temperature prediction. However, their steeper gradients are still indicating a different behaviour and thus the data shall be handled with care. One major aspect concerning the different temperature gradients is linked to the pour quality of the casting and mounting of the respective temperature sensors.

The predicted charred layer thickness resulting from the pyrolysis (Fig. 18) has been compared to the cut-out samples from the recovered MAPHEUS 6 FNC (Fig. 14) and has been proved as consistent with the observations.

Because of the relatively low convective heat flux during the vehicle's ascent phase, the simulated temperatures remain below the ablation threshold. Consequently, the simulation did not predict any surface recession.

Due to the model's simplifications, swelling is not directly considered. Instead, the apparent diffusivity is corrected on the basis of a comprehensive infra-red and plasma internal test.

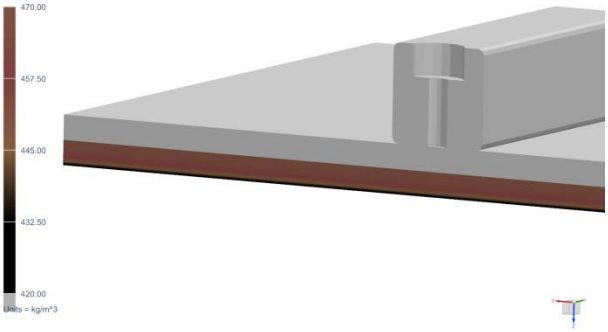

Figure 18. Simulated charred layer thickness after the VSB-30 ascent phase.

7 SUMMARY AND LESSONS LEARNED

The herein described work can be summarised as follows:

- NORCOAT® LIÈGE HPK FI has been pre-selected as a suitable cork based TPS substitute for various sounding rocket primary and secondary structures.

- A pre-asset one-dimensional thermal analysis has been performed for the VSB-30 FNC using 1.5mm and 2.0mm thick NORCOAT® LIÈGE HPK FI layers. Non-critical structural heating has resulted from this investigation.

- A suitable manufacturing process using 1.5mm and 2.0mm thick NORCOAT® LIÈGE HPK FI layers has been established for various sounding rocket primary and secondary structures.

- Various sounding rocket primary and secondary structures such as fin, motor adapter, nose cone and heat shield assemblies have been flight tested on four different missions.

- A post flight investigation of on-board measure-ments and recovered hardware has been performed for the VSB-30 FNC structure.

- A post flight validated three-dimensional thermal analyses has been carried out, leading to an improved predictability of the structural heating as well as the ablation process of the cork based TPS.

For a more detailed understanding of the phenomena and a more accurate prediction of the structural heating as well as the TPS ablation the following lessons learned can be named:

- In order to enlarge the set of flight data, future comparable flight hardware items should be equally

equipped with temperature sensors and data should be monitored.

- The temperature sensor mounting technique should be improved to ensure a reliable data acquisition, especially without the sensor's aluminium casing and a professional sensor bonding technique.

- A complete atmospheric profile should be measured by atmospheric balloons during the countdown and thus providing better input for the post flight analysis.

- A full uncertainty analysis of the input parameters should be performed to understand the sensitivity of the simulated results.

- A more adequate analysing method for the computation of the heat flux, especially for the subsonic and low supersonic regime, should be applied.

- The ablation and swelling behaviour should be investigated more deeply. Therefore, a more advanced hardware recovery and sample preparation procedure is necessary (e.g. charred layer fixation after landing).

ACKNOWLEDGEMENTS

Special acknowledgements are addressed to:

- Grégory Pinaud and Maxime Podeur from AG for their great and enduring contribution in the field of thermal analysis, which formed an important part of the cork based TPS development and last but not least of this paper.

- DLR Systemhaus Technik, especially Jean Werner Dequet, for his marvellous work in establishing the manufacturing process of the cork coated hardware items; they all are truly handcrafted master pieces.

- Tobias Ruhe from DLR MORABA for the processing of the raw flight data.

REFERENCES

[1] A.J. van Eekelen, J.-M. Bouilly, S. Hudrisier, J.-M. Dupillier and Y. Aspa. Design and Numerical Modelling of Charring Material Ablators for Re-entry Applications. In 6th European workshop on Thermal Protection Systems and hot structures, April 2009, Stuttgart.

[2] G. Pinaud, Thermo-chemical and mechanical coupled analysis of swelling charring and ablative materials for re-entry application, 5th AF/SNL/NASA Ablation Workshop, Lexington (KY), 2012

[3] G. Pinaud, Thermo-chemical and mechanical coupled analysis of swelling charring and ablative materials for re-entry application, 5th AF/SNL/NASA Ablation Workshop, Lexington (KY), 2012

NATIONAL REPORT

CAPABILITY DEMONSTRATION – CSA PROGRAM FOR INCREASING SPACE READINESS OF SPACE SCIENCE AND TECHNOLOGY WHILE TRAINING THE NEXT GENERATION

VISBY, SWEDEN
11-15 JUNE 2017

Steeve Montminy[1], Wanping Zheng[2]

[1]*Canadian Space Agency, 6767 route de l'aéroport, St-Hubert, Canada, J3Y 8Y9*
Email: steeve.montminy@canada.ca
[2]*Canadian Space Agency, 6767 route de l'aéroport, St-Hubert, Canada, J3Y 8Y9*
Email: wanping.zheng@canada.ca

ABSTRACT

Canada has a strong national strategic interest in space. Space will be used as a way to drive a broader economic growth and leveraged for the benefits of Canadians. Canada's future in space relies on innovation, advancement of science and technology, and future generation of highly educated and skilled space scientists and engineers. A strong Canadian space capability demonstration program is needed for maintaining Canada's leading edge in space and developing new capabilities for the future. The Canadian Space Agency (CSA), in response to the needs expressed by Canadian space industry, academia, and the government, and to better prepare Canada to capture future mission and commercial opportunities, is in the process of developing a capability demonstration program, which includes both pre-space demonstration and space demonstration. Demonstration in space on board a satellite or a space platform (e.g. ISS) is the most desirable method to demonstrate new technology, scientific approach or capability. However, there are only a limited number of opportunities for space demonstration flights and the associated cost is usually high. Suborbital platforms, such as balloons and rockets, remain popular for the academia and industry engaging in space science and engineering to test their hardware and approaches as they provide near-space environments with low cost and easy access. Suborbital platforms are also often used to conduct science in Canada's priority areas such as study of climate changes and validation of satellite data (ex. atmospheric data).

This paper discusses the needs for a capability demonstration program and its overall objectives, and provides greater details on demonstration activities using suborbital platforms, including on-going stratospheric balloon flights, parabolic flights, and possible rocket flights in the future for Canada.

1. INTRODUCTION

Canada has a strong national strategic interest in space. Canadian satellites enable us to protect our national sovereignty, and security and safety; Space systems become crucial to our daily essential services, including banking, internet, weather forecast, environmental monitoring, natural resources management, natural disaster warning and response, border security, and military surveillance; Participation in space activities has created a world leading vibrant space industry in Canada, which provides innovative products and services to the world; Space also captures the imagination of the humankind and inspires and motivates young Canadians to pursue careers in science, technology, engineering and mathematics to produce a highly educated and skilled workforce required for an advanced and prosperous Canada.

Since the earliest days of spaceflight, Canada has been at the forefront of space technology and space exploration. We have built enormous space capacity in earth observation and remote sensing, satellite communication, space robotics and space science. These capabilities have enabled Canada to make remarkable achievements in space science and space technology.

The space sector is entering a period of tremendous dynamism, and the future will present both the private sector and government with a range of opportunities to advance national security, resource development, and a broad range of public and private services using space assets, technologies, and applications. To continue to explore space for the benefits of Canadians and the mankind, to sustain and grow its

space industry, and to capture emerging space opportunities and markets, Canada needs not only to remain excellent in its current key capabilities, but also to develop new capabilities, especially in emerging space technologies and services, through technology development and innovation. The ability and opportunities to test or demonstrate these capabilities are crucial to the development of Canada's future space capacity, including innovative space technologies and services. A well-structured demonstration program is required to provide frequent and responsive opportunities to test new technologies, new scientific approaches, new concepts and space applications, and new space capabilities.

The Canadian Space Agency (CSA), in response to the needs expressed by Canadian space industry, academia, and the government, and to better prepare Canada for future space missions, is in the process of developing a capability demonstration program, which includes both pre-space demonstration and space demonstration. This paper discusses the capability demonstration program with a focus on the pre-space demonstration activities.

2. CAPABILITY DEMONSTRATION

Space capability refers to the ability to conduct science in space, to explore space, to do human space flights, to develop and launch space asset, or to provide services using space asset such as weather forecast, telecommunications, remote sensing, positioning and navigation, and etc. Capability demonstration, for the purpose of the demonstration program, is to demonstrate these capabilities in a relevant environment or expected operational environment. The capability for demonstration could be a new science experiment, a new technology, a new product, a new instrument, a new service, a new application, new operations of space asset, or a new space system. It could also be a student experiment payload.

Depending on the purpose and requirements of each demonstration, it could fall into one of the following categories: a ground demonstration, a suborbital flight demonstration, or a space flight demonstration. The ground demonstration makes use of lab facilities, ground stations, analogue sites and/or terrestrial rovers to demonstrate the capability, while the suborbital demonstration uses drop towers, UAVs, aircrafts, balloons, or sounding rockets. The ground demonstration and the suborbital demonstration constitute the pre-space demonstration. The space flight demonstration can use an orbital platform, such as the International Space Station (ISS), a cubesat/nanosat, a small/micro satellite, or a host satellite to conduct an in-orbit demonstration or an interplanetary spacecraft for demonstration of space exploration capability.

The overall objective of the capability demonstration program is to support Canadian innovation in space and the development of Canada's future space capacity by providing opportunities to demonstrate Canadian space capabilities. Specifically, through capability demonstration, the CSA intends to achieve the following:

- Gain flight heritage for Canadian space products or services to pursue world-wide commercial opportunities;
- Increase Canadian space technology's TRL level to help Canadian space industry to compete in global market;
- Position Canadian industry, academia, and the government to respond in a timely manner to space mission opportunities, including international missions;
- Raise technology and science maturity to reduce risks of future government-sponsored space missions;
- Maintain and advance Canadian global science leadership and excellence in space science;
- Provide flight opportunities to test new concepts or new space applications for demonstration of feasibility in support of space innovation;
- Train HQP to prepare highly educated and skilled workforce for future space missions and business;
- Inspire and motivate young Canadians to pursue careers in STEM by providing hands-on demonstration opportunities and funding.

3. PRE-SPACE DEMONSTRATION

Launching a payload onboard a satellite or space platform (e.g. ISS) is the most desirable method to demonstrate new technology, scientific approach, space operations, or capability. However, there are only a limited number of opportunities for demonstration on space platforms and the associated cost is usually high. As such, using space platforms to train next generation space scientists and engineers or to quickly demonstrate a new concept is often beyond the financial capacity of academia and small industry. Therefore, pre-space platforms (rovers, UAVs, aircrafts, balloons, and sounding rockets) remain popular for the academia and industry engaging in space science and engineering to test their hardware and approaches. Although these platforms don't give the full in-space "flight heritage," they reproduce some aspects of it and are equally effective in training university students and postdoctoral fellows (PDF). The flight data obtained in the near-space environment provide preliminary scientific data and more importantly, allow identification of problem or deficiency in the experiment or prototype. All these are possible because pre-space flights are low cost and readily available. Many needs can be fulfilled by pre-

space demonstration, such as validation of user requirements for future missions; calibration and cross validation of satellite downlinked data; proof-of-concept for new applications, operations, or services; validation of scientific experiments in reduced gravity environments; validation of new scientific instrument; increase of TRL levels for new technologies; training of HQPs for future space missions; and inspiring youth in STEM.

With this in mind, the Canadian Space Agency (CSA) started the pre-space demonstration activities with focus on stratospheric balloon flights and analogue missions.

4. STRATOSPHERIC BALLOON FLIGHTS

Canada has a long history of scientific ballooning, dating back to airglow measurements made in 1960. A series of pioneering measurements were made through the 1960s and 1970s, including measurements of hydroxyl emission and the 1.27-micron O2 band. A variety of early instrumentation was flown, including infrared spectrometers, Michelson interferometers, and filter photometers. In the 1970s and 1980s, the Atmospheric Environment Service of Canada led the Stratoprobe series of balloon flights that included measurements of NO2 and HNO3 that predate the onset of stratospheric ozone depletion. These campaigns contributed to our understanding of the stratosphere and included early estimates of the northern hemisphere mid-latitude odd-nitrogen budget. The MANTRA (Middle Atmosphere Nitrogen TRend Assessment) series of four high-altitude balloon flights, which carried instruments to measure vertical concentration profiles of a suite of stratospheric trace gases, built on these earlier Stratoprobe efforts. The first MANTRA launch, in 1998, was the first Canadian large high-altitude balloon mission in 15 years, and was followed by three more late summer campaigns, in 2000, 2002, and 2004. Due to the lack of a sustainable program, the funding to upgrade and maintain the launch capability was not possible. The 2004 campaign was the last launch in Canada until the CSA/CNES collaboration.

In 2007 and again in 2010, scientists have recommended that CSA establish an active and sustainable Canadian balloon program with regular yearly flight opportunities. This is achieved through the agreement that was signed in 2012 between the Centre National d'Études Spatiales (CNES) and the Canadian Space Agency (CSA) for an international collaboration for the launch of stratospheric balloons. The CNES, with their 3500 flights of heritage and 50 years' experience in ballooning, brought to the table the flight hardware, including a newly developed control system for aerostat known as NOSYCA (New Operational System for the Control of Aerostat), as well as all associated ground support equipment. On the other hand, CSA provides a mid-latitude launch base located in Timmins, a low populated area of northern Ontario, aerostats recovery services as well as interfaces with all national authorities needed to carry heavy stratospheric balloons safely within Canadian airspace. In exchanges of these services, Canadian payloads are to be flown yearly by CNES from its worldwide network of sites[1].

The Timmins Stratospheric Balloon Base is located next to the Victor M. Power Airport, 11 km north from the city of Timmins. The base is composed of 3 main buildings and the launch area as shown in Fig. 1. The first building is called the Flight train Hall. Its main feature is a 35 m x 10 m high bay designed for the integration and preparation of the flight train. The second building is 335 m² in size and is dedicated to the integration of payloads. The third building is a storage area and is also used as a garage for some of the operational vehicles. The launch area is located at the east end of the Timmins airport runway. It consists in a wide stabilized area offering no less than 400m in diameter. Access to the runway is done through a gate controlled by the airport personnel.

Fig. 1: The Timmins Stratospheric Balloon Base

CNES balloon flight system NOSYCA, as shown in Fig. 2, is used for the balloon flights.

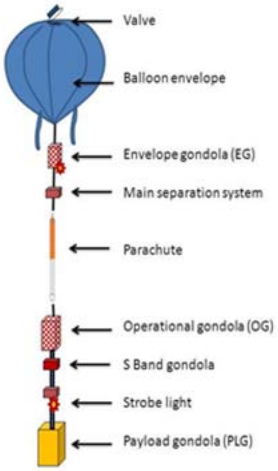

Fig. 2: The NOSYCA flight segment

The 2013 campaign was a qualification campaign with only a few small payloads on board the gondolas as the two flights were meant to test and validate the NOSYCA flight system and payloads were accepted on a no interference basis only. Time of launch and flight profiles were selected for the different qualification scenarios and the full bandwidth of the communication system was dedicated to the tests being performed.

Fig. 3: A stratospheric balloon being inflated

The Strato-Science 2014 campaign was the first real test with more than 90 scientists and a team of almost 40 persons to coordinate and perform the launches. A total of 17 instruments were flown with 24 laboratories and universities being involved. The campaign lasted 41 days with an operational phase of 30 days during which 7 balloons were launched. The smaller balloons were 100,000 m3 in size (3.5 million ft3) while the larger ones were 400,000 m3 (14 million ft3). Flights lasted between 4 hours and 19 hours and landed at distances varying between a 100km (60 miles) and 350km (215 miles) from their starting point.

The Strato-Science 2015 campaign only had 6 flights, but two of these were with 800,000 m3 (28.25 million ft3) balloons, the largest launched by CNES. Two telescopes were flown: BIT from University of Toronto, Canada, which aimed at qualifying some of its components toward a long duration flight with NASA; and PILOT, a French telescope whose purpose is to study the polarized emission in far-infrared of the interstellar medium dust grain. The flight for PILOT lasted almost 24 hours (23h54m) and landed only 290 km (180 miles) east north east of Timmins. The remaining four flights included technology demonstration, a complete set of camera for a 360 degree documentary movie, 12 atmospheric chemistry instruments and 5 spectrometers

Fig. 4: Balloons launched during the Strato Science 2015 Campaign

In September 2016, the CSA participated in the KASA 2016 balloon flight campaign in Kiruna, Sweden. There were three Canadian payloads on board the CNES BANA gondola: a Fabry-Perot spectrometer, an attitude determination module (ADM), and small probe called “Lightning”. The Fabry-Perot spectrometer was jointly developed by York University in Toronto and MPB Communications Inc. This instrument can obtain very high spectral resolution measurements related to atmospheric particulates and greenhouse gases. This novel technology was demonstrated during the stratospheric balloon flight to assess the readiness of its components and its overall performance. Built by a group of students from the École de technologie supérieure in Montreal, the ADM is a multi-purpose electronics box. Its goal is to record and provide real-time data about the location and attitude of the gondola as well as other useful information during the entire flight. The last payload, the “Lightning” probe, was entirely developed by a group of high school students from Sir Wilfrid Laurier School in Calgary. It measured the temperature and pressure during the stratospheric flight.

Fig. 5: Canadian payloads integrated on BANA gondola

In April 2017, the CSA participated to the AUSTRAL 2017 balloon flight campaign in Alice Springs, Australia. Six Canadian payloads flew on board the CNES pointed gondola called CARMEN: an Imaging Fabry-Perot Spectrometer (IFPS), an Aerosol Limb

Imager, a suite of three Optical Particles Counters (OPCs), two payload gondola subsystem prototypes and a collection of art pieces. In the case of the Fabry-Perot spectrometer, it has been a re-flight of an adapted version of the 2016 instrument. The Aerosol Limb Imager (ALI V2) developed by the University of Saskatchewan is an atmospheric monitoring tool that can measure the concentration of aerosols—tiny dispersed particles in the upper atmosphere using a unique optical device. The instrument is an improved version of a prototype designed and constructed by the University of Saskatchewan that was successfully deployed on a stratospheric balloon in 2014. The upgraded version of ALI can detect a wider range of optical wavelengths, allowing it to more precisely measure the size of aerosol particles.

The OPC package was used to sample the stratospheric air from the balloon platform and measure aerosol size and concentration. The objectives were to provide validation of satellite limb scattering observations, enable synergistic and corroborative aerosol measurements for use with the Aerosol Limb Imager (ALI) measurements, and contribute to the scientific record of in-situ size-resolved stratospheric aerosol measurements to further understanding of volcanic influence and aerosol formation and transport. This project is carried out by the University of Saskatchewan, in collaboration with the University of Colorado and the University of Wyoming.

The RumbleSat Art in Space Mission was also added to this flight, a University of Calgary research project, the first RumbleSat I mission payload consists of 64 small works of art. The payload will begin a cross-Canada tour starting in September 2017, as part of the 150 Artists Celebrating Canada 150: the "RumbleSat Art from the Edge of Space Exhibition". Finally, a prototype of generic and reusable power subsystem for payloads and a prototype of a multi-purpose electronics box for recording and providing the location and attitude of the gondola during the flight were mounted on the gondola for this flight. In addition, this instrument also called Payload Remote Interface & Support Module (PRISM) has monitored, through various sensors, the health of other components on board the gondola. This instrument has an on board storage capacity for telemetry data and two high-definition cameras. This instrument is an improved version of a technology developed by a group of students from École de technologie supérieure, which was successfully tested on a stratospheric balloon in 2016.

Fig. 6: Canadian payloads integrated on CARMEN gondola

So far, 30 Canadian payloads from Industry and Academia were flown under STRATOS balloons for supporting the development and demonstration of new space technologies, for Science and for training of the next generation of engineers and scientists in Canada and to attract and inspire young people to pursue careers in the areas of STEM. More than hundred participants have attended each of the launch campaign in Timmins and between 40 and 50 students and young engineers have been trained annually on STRATOS balloon flights from Canada and abroad.

With the 2018 STRATOS Balloon launch campaign planned for August-September 2018 in Timmins, CSA aims to provide suborbital flights for ten Canadian payloads currently in the STRATOS portfolio of payloads. The CSA and CNES plan to launch and operate between three and five balloon flights. Two of these flights will be dedicated to Canada using CNES payload gondolas as host platforms for payloads. It is expected that approximately 45 Canadian engineers, scientists and students will be involved in the field activities and an additional 10 to 16 undergraduate students will be trained via the SEDS-STRATOS Pan Canadian Student Design challenge. The 2018 STRATOS Balloon Launch campaign will also provide good opportunities for outreach and support the local economy in a Northern Ontario region (i.e. Timmins).

Fig. 7: Balloon launched during KASA 2016 Campaign

5. ANALOGUE MISSIONS

An analogue mission is a field activity set in a remote location with extreme characteristics that resemble the challenges of a space mission. Analogue missions prepare us for near-future exploration to asteroids, Mars, and the Moon. Demonstration or test through an analogue mission plays a significant role in problem solving for spaceflight research. It helps the real mission to reduce technical risks, validate and optimize operations, and validate technologies and scientific experiments. Analogue missions enable testing at a fraction of the cost of a planetary mission, enhancing future mission success. Analogue sites can provide planet appropriate environments to understand planetary process. Analogue-based missions also provide high-fidelity HQP training.

Mars Sample Return (MSR) is one of the highest priority goals of the international scientific community. Returning samples with known geological context from Mars for analysis using the best laboratory techniques on Earth is seen as a crucial step in advancing knowledge of Mars. In addition to scientific interest, MSR will address important knowledge gaps and may aid in demonstrating key capabilities needed for human exploration.

The Canadian Space Agency, in partnership with Western University and MacDonald Dettwiler and Associates, conducted a field deployment in the Utah desert in November 2015 to emulate portions of the first steps of a Mars Sample Return mission: the identification and acquisition of scientifically interesting samples[2]. The site was selected because of its scientific relevance to certain regions on Mars, being predominantly of sedimentary nature and preserving evidence of a previous aqueous environment. Equipment being tested at the site included the CSA's Mars Exploration Science Rover (MESR), as shown in Fig. 8, equipped with a mini-corer and a 3D microscope mounted on a robotic arm, a suite of cameras, and a LASER range sensor.

In November 2016, the Canadian Space Agency will return to the Utah analogue site to have a CSA-led Mars Sample Return Analogue Deployment, in collaboration with JPL, DLR, and UK Space Agency. This analogue mission is expected to produce the following outcomes and benefits to Canada:

- Positioning of Canadian scientific and industrial expertise to contribute to an international Mars Sample Return mission.
- Demonstration of advanced Canadian capacities in robotics and sciences.
- Collaboration with international experts in planetary research.
- Maintenance, leveraging, and advancement of Canadian niche expertise in robotics, in particular in the development of autonomous vehicle, arm and sensors.
- Advancement of Canadian niche expertise in science instruments and optics through demonstration of Canadian instruments side by side with NASA instruments.
- Training of Canadian HQP (technology development – AIT - operations – application development) within areas of Canadian strength (robotics, optics, scientific instruments, and planetary sciences).
- Precursor activity to enable future space mission (lessons learned, risk mitigation; validation of technology development with operations concepts and science).

Fig. 8: MESR rover deploying mini-corer and microscope

Analogue missions will continue to be an important element of the CSA capability demonstration program and play a critical role to prepare Canada for future space exploration missions.

6. SPACE EXPLORATION DEMONSTRATION FACILITIES

In order to facilitate the ground testing and demonstration of planetary exploration technologies, and to support analogue missions to prepare Canada for future planetary exploration missions, the Canadian Space Agency has developed an infrastructure and facilities for testing, integration and operations of exploration systems and equipment such as rovers and scientific instrument, in a "mission-like" planetary analogue environment. The facilities include integration labs, test facilities, a planetary analogue site, a control center and the communications infrastructure necessary to connect various facilities.

The Space Exploration Demonstration Facilities consist of ExDOC, the Exploration Development and Control Center; AT, the Planetary Analogue Terrain; PCSS, the Portable Command & Control Shelter; RIF, the Rover Integration Facility; ESF, the Exploration Storage Facility; and RIW, the Rover Indoor Workspace.

Fig. 9 shows the planetary analogue terrain AT, located at the CSA headquarter in the suburb of Montreal. This is a 60 X 120 meter outdoor facility offering various surface features and topographies to simulate the planetary surface, such as rock bed, crater, summit, and flag stone patch. This facility is also equipped with situation awareness cameras and WIFI network for the needs of rover and payload testing, deployment and demonstration.

Fig. 9: CSA AT planetary analogue terrain

The Exploration Development and Control Center ExDOC, as shown in Fig. 10, provides centralized command and control for various technology and science resources deployed at local or remote analogue sites. It also provides re-distribution of voice, video, and data & control functions to other participating organizations and international partners. It can generate time delay to simulate the communications with Mars and other planets. ExDOC also provides secured VPN link with the NASA Space Network Research Federation (SNRF network).

The CSA Space Exploration Demonstration Facilities have been used extensively in supporting the development of science and technologies for Canadian planetary exploration endeavour, especially the technology development of planetary rovers and scientific payloads by facilitating the integration, testing, and operations. These facilities have been opened to industry and universities. In addition to supporting the Canadian university students to test their rovers for international competition, these facilities have also supported the International Space University (ISU) for their Robotic Planetary Exploration Analogue Mission.

Fig. 10: CSA ExDOC control center

7. CONCLUSIONS

Canada's future in space relies on innovation, advancement of science and technology, and future generation of highly educated and skilled space scientists and engineers. A strong Canadian space capability demonstration program is needed for maintaining Canada's leading edge in space and developing new capabilities for the future.

Pre-space demonstration has proved to be, in complimentary to space demonstration, an effective way to achieve some of the objectives of the CSA capability demonstration program. In the past, the CSA pre-space demonstration activities have focused on stratospheric balloon flights and analogue missions, which successfully fulfilled the needs of Canadian industry and academia and government. Based on these successful programs, the CSA capability demonstration program will expand to include more platforms for pre-space demonstration such as aircrafts, UAVs, and sounding rockets, in addition to space demonstration flights.

REFERENCES

1. Lafrance, S., Montminy, S., and Louvel, S., "CSA's Stratos Program: bring a New Mid-latitude Stratospheric Balloon Base," 2016 IEEE Aerospace Conference, Big Sky, Montana, USA, May 5 - 12, 2016.

2. Dupuis, E., Picard, M., Haltigin, T., Lamarche, T., Rocheleau, S., and Gingras, D., “Results from the CSA’s 2015 Mars Analogue Mision in the Desert of Utah,” The International Symposium on Artificial Intelligence, Robotics and Automation in Space (i-SAIRAS 2016), Beijing, China, June 19-22, 2016.

TDP-3 *VANGUARD*: VERIFICATION OF A NEW COMMUNICATION SYSTEM FOR CUBESATS ON BEXUS 22

Nicolas Appel[1], Andreas Kimpe[2], Karl Kraus[1], Martin Langer[1], Martin J. Losekamm[3], Michael Milde[3], Thomas Pöschl[3], Sebastian Rückerl[1], Felix Schäfer[1], Anke Stromsky[2], and Korbinian Würl[1]

[1]*Technical University of Munich, Department of Mechanical Engineering, Germany*
[2]*DLR MORABA, Germany*
[3]*Technical University of Munich, Department of Physics, Germany*

ABSTRACT

CubeSats are evolving from simple, low-cost satellites built solely for education purposes to ever more powerful platforms capable of supporting scientific experiments. Among the technologies required for the operation of scientific instruments are communication systems that can transmit all relevant data to its operators. We have developed two such systems for the MOVE-II satellite, a single-unit CubeSat being built at the Technical University of Munich (TUM). Slated for launch in late 2017, MOVE-II shall demonstrate several new technologies supporting the operation of scientific instruments in successive missions. We conducted the TDP-3 (Technology Demonstrator Platform 3) *Vanguard* experiment aboard the BEXUS 22 stratospheric balloon to verify the correct operation of the communication systems in a near-space environment and at large distances between the transceivers and the receiving ground station.

Key words: CubeSat, MOVE-II, communication, data handling, REXUS/BEXUS.

1. INTRODUCTION

TDP-3 *Vanguard* is a technology demonstration platform that was built by students of the Technical University of Munich (TUM) as part of the REXUS/BEXUS program. The near-space environment during the flight of the BEXUS 22 stratospheric balloon was used to verify the communication and command & data handling subsystems of the MOVE-II nanosatellite. The said environment approximates two important aspects of the environmental conditions of a satellite mission: A fairly long distance between the experiment and the ground station and the reduced air pressure and temperatures in Earth orbit. This allowed us to test and operate the satellite subsystems under realistic conditions.

Initially, we planned to include a prototype of the Multipurpose Active-target Particle Telescope (MAPT) as scientific payload (Losekamm et al., 2016). A first prototype of MAPT was flown on BEXUS 18 in 2014 (Losekamm et al., 2015). However, due to a mismatch in development schedules, the MAPT prototype was replaced by a payload simulator providing comparable scientific data as expected during regular operations of the experiment.

We give an overview of the MOVE-II satellite in Sec. 2 and a detailed description of the TDP-3 mission in Sec. 3. We summarize our findings and results in Sec. 4 before concluding with a summary of what we achieved in Sec. 5.

2. THE MOVE-II SATELLITE

The MOVE-II satellite is a single-unit (1U) CubeSat currently under development at the Technical University of Munich (TUM). The MOVE (Munich Orbital Verification Experiment) satellite program was initiated in 2006 with the objective of building a single-unit CubeSat verification platform called First-MOVE (Czech et al., 2010). First-MOVE was launched in late 2013 and operated in space for about a month.

Since then, the main purpose of the program has been the hands-on education of undergraduate and graduate students. Funded by the German Aerospace Center (DLR) as an educational project, the objectives of MOVE-II are to build and operate a 1U CubeSat capable of supporting a scientific payload, to enhance the subsystems that were developed for First-MOVE, and to apply the lessons learned from the First-MOVE project (Langer et al., 2015b). The mission's scientific objective is to measure the current-voltage characteristics of novel multi-junction solar cells in orbit (Rutzinger et al., 2016).

We had to enhance several subsystems of First-MOVE to achieve the objectives of the MOVE-II project (Langer et al., 2015a). The new attitude determination and control system (ADCS) uses magnetic actuators and allows a pointing accuracy of better than $\pm 10^{\circ}$. An advanced solar panel deployment mechanism uses shape memory alloy technology, enabling repeated tests with the flight

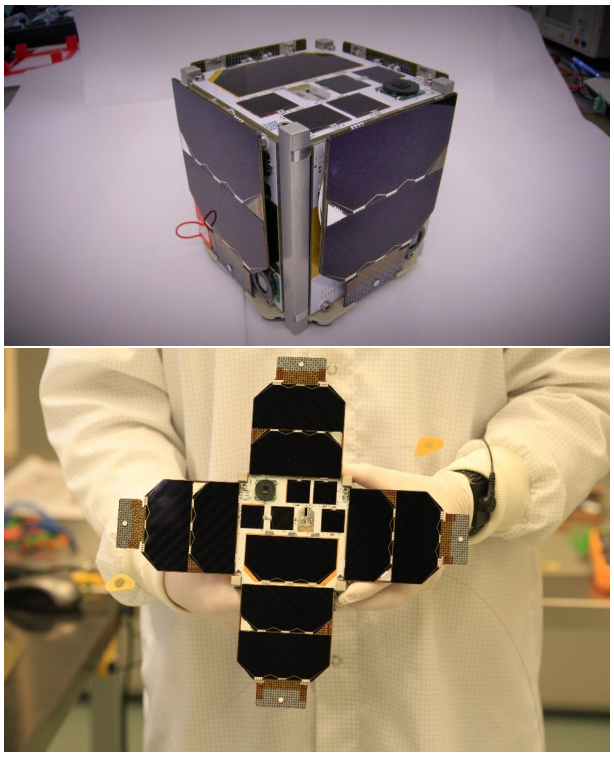

Figure 1. The MOVE-II nanosatellite in launch (top) and deployed configuration (bottom).

unit without compromising its performance (Figure 1 shows the satellite in its launch and deployed configuration). A UHF/VHF transceiver ensures a reliable transmission of telemetry and scientific data. An experimental S-band transceiver will provide a bandwidth of more than 1 Mbit/s for a high-rate downlink of payload data. Both transceivers use the TUM-developed Nanolink protocol (Appel et al., 2016). The launch of the satellite is currently expected in early 2018.

3. THE TDP-3 *VANGUARD* EXPERIMENT

The TDP-3 platform demonstrator experiment consists of a flight segment and a ground segment. The ground segment simulates the ground station and mission operations center of the MOVE-II mission. It provides the capabilities to monitor and remote-control the flight segment via the BEXUS E-Link communication system. The flight segment is the demonstrator platform itself, comprising the satellite subsystems to be tested and support systems for power supply and monitoring purposes.

3.1. Flight Segment

The flight segment of TDP-3 consists of four main components: The communications (COM) system comprising the UHF/VHF and S-band transceivers, the command & data handling (CDH) system, a scientific payload, and support systems. As the MAPT detector was replaced by a payload simulator, it is considered as part of the support systems in this paper. Figure 2 shows the flight segment shortly before installation into the BEXUS 22 gondola.

3.1.1. Command & Data Handling

The CDH system of TDP-3 is a development board based on an Atmel SAMA5D2 system-on-a-chip, designed and produced by Hyperion Technologies[1] for the MOVE-II project. It is equipped with all the interfaces required for the final MOVE-II CDH system, as well as a number of additional interfaces only used for connections to the TDP-3 support systems and for evaluation purposes. The main interface of the CDH system is a board-to-board SPI[2] connection to the communication system. An additional Ethernet interface is used for communications with the support systems—including the payload simulator—using the TCP/IP and UDP/IP protocols.

The software of the CDH system is running on a custom Linux distribution. This choice of operating system enables us to use of a variety of software modules available for standard Linux distributions. A custom SPI driver is used to communicate with the COM system's transceivers. The CDH system is the bus master for all SPI communications. As SPI slave devices cannot initiate communications, the interface uses an additional interrupt pin to signal a communication need from the COM system.

3.1.2. Communication

The COM system of TDP-3 consists of two radio transceivers, one of them operating within the UHF/VHF bands, the other within the S-band. These transceivers were developed for the MOVE-II project in cooperation with Multimedia Studio Rolf-Dieter Klein[3]. Table 1 lists the basic properties and parameters of the transceivers.

Software-Defined Radio Transceivers Both COM system transceivers are software-defined radios. A Xilinx Spartan-6 field-programmable gate array (FPGA) is used for data handling and baseband signal processing. The generated baseband I/Q signal is converted to an analog signal and fed to a quadrature mixer through a chain of filters and amplifiers.

For the UHF/VHF transceiver, a similar approach is used for the receiver. The received signal is amplified and filtered, fed to a quadrature demodulator, and directly converted to a digital representation. All further signal processing is done on the FPGA. The receiver part of the S-

[1] www.hyperiontechnologies.nl
[2] Serial Peripheral Interface Bus
[3] www.rdklein.de

Figure 2. The TDP-3 flight segment.

Band transceiver was not used during the BEXUS flight. Figures 3 and 4 show functional diagrams of the analog signal processing chains of both transceivers.

Data Flow Data is transferred to and from the transceivers using a SPI-based custom protocol. SPI is a master-slave protocol in which only the master can initiate the communication, in our case the SPI bus master is the CDH system. To avoid active polling an additional interrupt line is used. The SPI-based protocol itself was designed to reduce the risk of errors due to erroneous communication. Checksums are used to detect these errors, and a simple acknowledge mechanism informs the communication partner. This reduces the risk of invalid states due to single event upsets or other disturbances.

The data received via SPI is embedded in Nanolink frames. Nanolink is a versatile data link layer protocol for radio links with low bandwidth-delay product. Nanolink utilizes type-I hybrid ARQ, and provides eight virtual channels for qualitiy of service. Additional protocol features can be used by means of extension headers. All these features are designed with low overhead for efficient use of the communication link (Appel et al., 2016). Nanolink frames are serialized and embedded in larger blocks of data with a preceding sync marker. The sync marker is used to align the bit stream at byte boundaries at the receiver side.

The whole data, including the sync marker, is encoded with a forward error correction code. The resulting bit stream is modulated and filtered in the baseband, before converting it to an analog signal. The setup allows reception and decoding of the code blocks by CCSDS compatible receivers. Thus, the transceiver downlink can be decoded by virtually any satellite telemetry station operating within the S-band.

The receivers' structure is quite similar regarding the data flow. The digital baseband signal is filtered, its frequency error is corrected and the symbols are recovered. These symbols are decoded and the resulting bit stream is byte-aligned. Nanolink frames are extracted from the resulting byte stream and are subsequently decoded. The payload data itself is then transmitted to the CDH system via the SPI interface.

Antennas The flight segment antenna of the UHF/VHF transceiver is a radial-free monopole antenna. Other than for the MOVE-II satellite, only a single dual-band antenna with additional diplexer to remove the transmitted signal from the receiver and vice versa is used. A ground plane is used for S-band transmissions. As the S-band transceiver was used as transmitter only during the TDP-3 mission, no diplexer or additional antenna was needed in

		UHF/VHF	**S Band**
TX	Frequency	144 MHz	2323 MHz
	Power	< 30 dBm	< 30 dBm
	Modulation	DBPSK	OQPSK
	FEC	-	Viterbi
RX	Frequency	435 MHz	-
	Modulation	DBPSK	-

Table 1. Properties and parameters of the UHF/VHF and S-band transceivers.

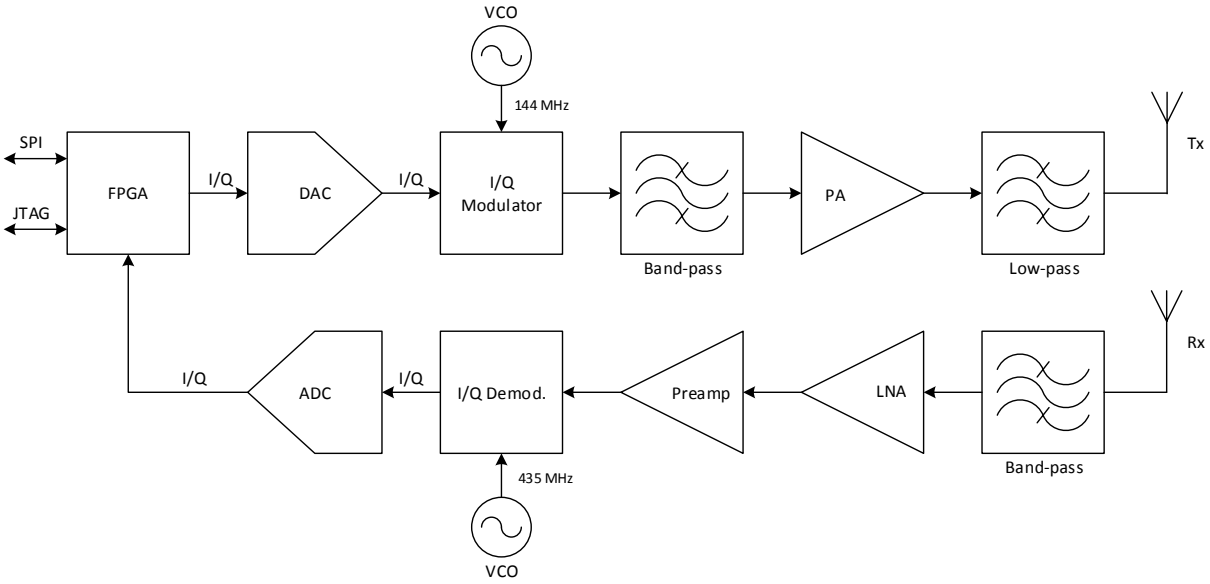

Figure 3. Functional diagram of the UHF/VHF transceiver.

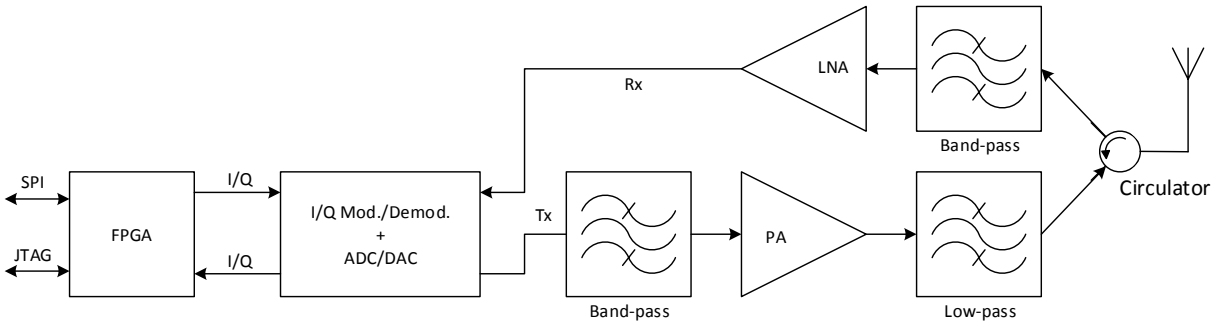

Figure 4. Functional diagram of the S-band transceiver.

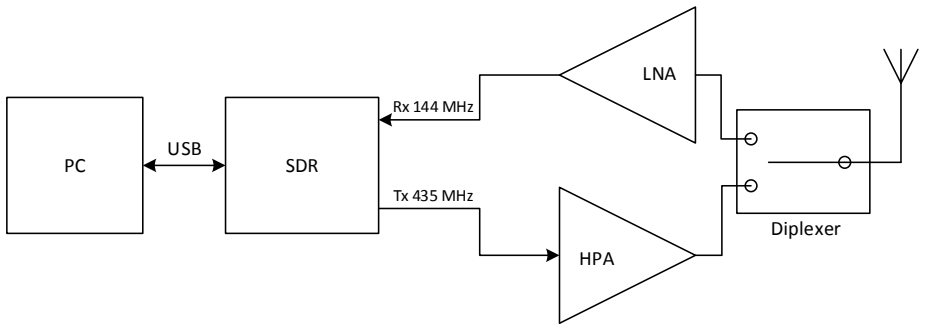

Figure 5. Functional diagram of the UHF/VHF ground station.

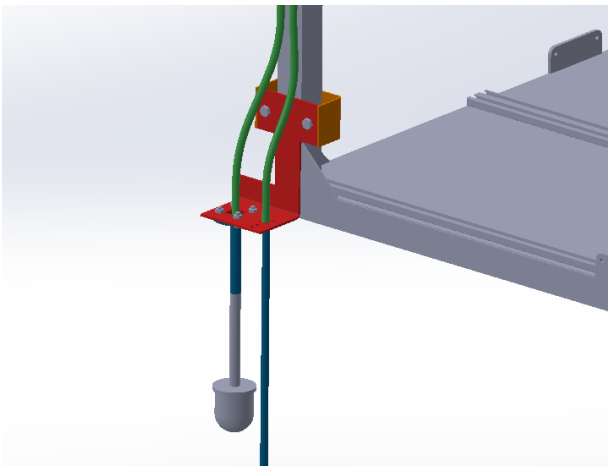

Figure 6. Antennas mounted to the gondola. The longer one is the UHF/VHF antenna, the shorter one is the case of the S-band ground plane antenna.

this case. Figure 6 shows how the antennas were mounted to the gondola.

3.1.3. Support Systems

The support systems of TDP-3 are responsible for the power and network interface of the experiment, the payload data simulation, and the supporting structure to mount the experiment to the gondola.

Power Supply Module The power supply module provides power to all other systems of the TDP-3 flight segment. It converts the 28 V supplied by the BEXUS battery system to the voltages required by each system. We us commercially available DC-DC converters that have been proven to operate reliably during previous balloon flights (Losekamm et al., 2015). Each power bus is monitored by the module's central microcontroller and is switched off in case of out-of-limits sensor readings. The controller is connected to the BEXUS E-Link system via the flight segment's network E-Link interface and can be accessed and controlled from the ground segment using the TCP/IP protocol.

Network Interface The network interface is a standard 100-Mbit network switch that is connected to the BEXUS E-Link communication system via an Ethernet connection. The flight segment's systems are connected to the switch using industrial M12 Ethernet connectors. The E-Link system supports the TCP/IP and UDP/IP protocols.

Payload Simulator The payload simulator consists of a Raspberry Pi single-board computer running a standard Linux distribution. It is directly connected to the network interface and communicates with the CDH system via UDP/IP. The data stream generated by the simulator closely resembles the one generated by the MAPT payload and can thus be used to assess the CDH system's performance and stability when operating as the intermediary between a payload and the COM system. The payload simulator can be accessed and controlled from the ground segment through the E-Link system.

3.2. Ground Segment

The ground segment of TDP-3 simulated the ground station of the future MOVE-II satellite mission and supported the operations of the experiment during the BEXUS 22 flight. The ground segment consists of three main components: a UHF/VHF ground station, a S-band ground station, and a control and data storage server.

3.2.1. UHF/VHF ground station

Figure 5 shows a functional diagram of the UHF/VHF ground station. It consists of widely available amateur radio components. The antenna is a dual band ground plane and the digital signal processing was done with GNU-Radio. It included the modulation and demodulation of the signal, handling of the blocks to synchronize the bit stream, and the Nanolink frame handling. The resulting byte stream was then forwarded to the control and storage server.

3.2.2. S-band ground station

The S-band ground station service was provided by the MORABA telemetry station at Esrange Space Center. It is capable of tracking signals automatically, decoding them, correcting bit errors with forward error correction, and synchronizing the bit stream. These tasks were performed by a Cortex RTR-XL radio telemetry receiver. The byte stream output of the Cortex modem was forwarded to the control and storage server. The byte stream contained the Nanolink frames, which were decoded by the central control server.

3.2.3. Control & Storage Server

The central control and storage server collected all important data generated by the UHF/VHF and S-band ground stations. It also interpreted the Nanolink frames of the S-band transmissions and visualized the status of the COM system. This visualization was combined with the control interface to switch the system into different states of operation and to control the flight segment's CDH components remotely.

3.3. Verification Strategy

The high floating altitude of the BEXUS 22 balloon gave us the unique opportunity to test the MOVE-II communications hardware with a moving, long-range transmission path. Although the balloon appears stationary when compared to the velocity of a satellite, other aspects of the radio link are quite similar to an orbital link. The most important common features are the high slant range and decreasing elevation angle. They are also encountered in the last minutes of a pass, when the satellite approaches the horizon. During that time, the worst signal conditions of a pass are experienced. Moreover, since the balloon is moving, signal conditions change rapidly and deep fading can be observed. A characterization of these features is important for a satellite mission. The BEXUS 22 flight gave us a good opportunity to test the capabilities of the COM system under worst-case conditions.

4. FLIGHT & RESULTS

The BEXUS 22 balloon was launched on 05 October 2016 at 13:34 UTC from Esrange Space Center in northern Sweden. The COM system's transceivers were switched on 30 minutes before release of the balloon. The VHF baseband signal and the extracted data frames from both links were recorded.

The balloon reached its floating altitude of about 32.5 km 110 minutes after launch. The gondola was separated from the balloon at 17:41 UTC, resulting in a floating phase of about 2 hours. From launch until touchdown, the balloon traveled a ground distance of 270 km. The recording stopped after 301 minutes, when the radio connection to the gondola was lost.

4.1. VHF Flight Results

The user data rate of the VHF downlink can be derived from the VHF frames recorded by the ground segment. Figure 7 shows the VHF data rate over the duration of the flight. Values are averaged over a window of 60 seconds. The green horizontal line marks the maximum possible total data rate of 1562.5 bits per second (bit/s).

The data rate graph is complemented by Figure 8, which illustrates the signal-to-noise ratio (E_b/N_0, SNR) of the baseband signal. The x axis is given in samples, since restarts of the GNURadio software rendered a temporal assignment imprecise. We used GNURadio's built-in *MPSK SNR Estimator* block and the *2nd and 4th Moment* method for the E_b/N_0 measurement. The green line in Figure 8 marks the signal level that corresponds to a bit error rate (BER) of 10^{-6}.

During the flight, the ground station software had to be restarted seven times. Restarts of the ground station software and the resulting communication dropouts are marked in Figure 7 as red vertical lines. Please note that due to the time needed to restart the ground station software there is some discrepancy in time between the two graphs in Figures 7 and 8.

The data rate remained high and stable for the most part of the flight. From the beginning of the recording up to minute 39 it was stable at about 1065 bit/s, with only one small dropout happening after about 30 minutes. The reason for this lower but stable value was an incorrect setting in the frame synchronizer, which resulted in the loss of a part of every transmitted block. We detected this issue after about 39 minutes and restarted the ground station. An analysis of the baseband data with an updated GNURadio flow graph revealed a steady transmission with an average data rate of 1490 bit/s.

Short-term increases in data rate above this value were likely caused by the storage software, since timestamps were generated when the data was stored, not when it was received. At minute 56, frames with a repetitive pattern with a size of 990 bit were transmitted for 240 seconds. At the same time, we observed a sharp decline in the data rate (see mark 1 in Figure 7). This may have been due to a lack of bit transitions in the transmitted pattern, which caused the receiver's timing recovery to fall out of lock.

Sharp declines in the SNR in minutes 89 and 96 resulted in frame losses, which in turn caused drops in the data rate (see marks 2 and 3 in Figure 7). It is likely that these were caused by interference from nearby hand-held radio devices. We observed these devices to significantly increase the noise level at the receiver and thus deteriorate the SNR.

At events 4 and 5, frames with a size of 1000 bit were transmitted for 100 seconds each, leading to a local increase in the data rate with a global maximum of 1545 bit/s. This increase reflects the increase in efficiency of larger payload data compared to the shorter telemetry frames sent otherwise.

A noteworthy feature of the SNR graph in Figure 8 is the high fluctuation which can be observed between samples 2000 and 4000. The magnitude of the fluctuation is up to 5 dB. This fast fading stems from a multi-path propagation of the transmitted signal. It travels along different paths and is received at the ground station with a phase difference, resulting in destructive or constructive interference. This effect is expected and its magnitude is an important parameter for the MOVE-II mission.

The link remained very stable until minute 168, but the SNR graph reveals a gradual decrease of the signal quality. Afterwards, the signal continued to deteriorate strongly as a result of the increasing distance between the flight and ground segments. Objects in the vicinity of the ground station began to block the signal as they obstructed the line of sight. As a remedy, we relocated the receiver antenna, which improved reception for a short period of time and kept the data rate at a tolerable level of more than 1000 bit/s.

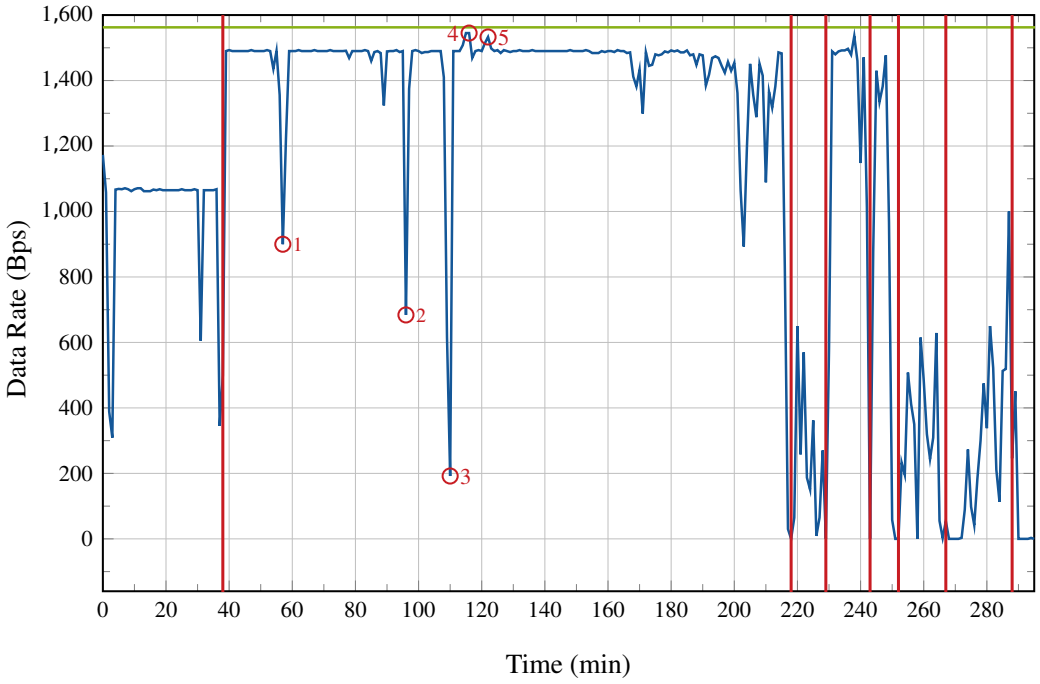

Figure 7. VHF data rate during the BEXUS 22 flight.

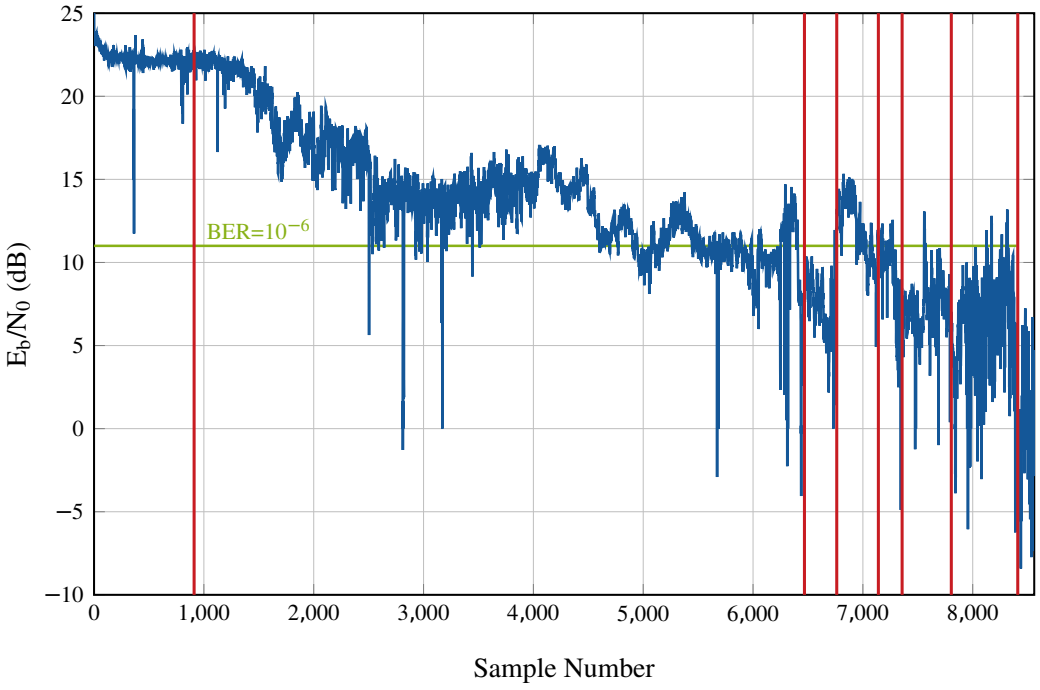

Figure 8. VHF signal-to-noise ratio during the BEXUS 22 flight.

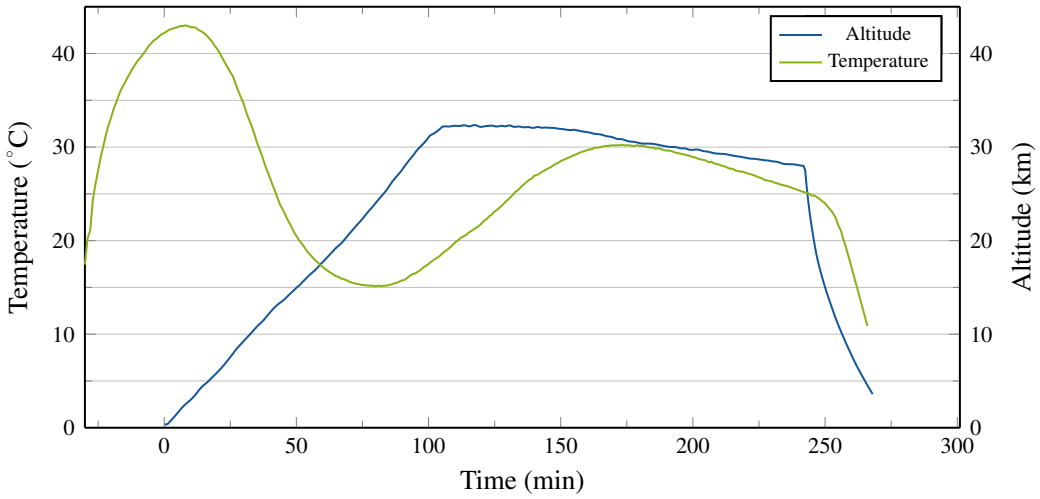

Figure 9. Temperature of the UHF/VHF transceiver during the BEXUS flight.

At this period, the GNURadio software could not recover from low signal levels and loss of synchronization. These cases required a restart of the entire ground station software to resume operation. In minute 218, the ground station was restarted due to loss of synchronization. When the signal was lost a second time, we manually elevated the antenna to about 2 m above the ground. This improved the SNR by about 10 dB for roughly 10 minutes. Figure 7 reveals the sharp increase in data rate as a result of this action.

At minute 276, the gondola was separated from the balloon. As the balloon approached the horizon, effects of signal scattering and multi-path transmission increase. No more frames could be decoded after minute 289 and the experiment was concluded.

Another interesting aspect of the experiment was the observation of the transceiver temperature during the flight. The readings of a temperature sensor placed below the transceiver's power amplifier was transmitted as part of the telemetry packages. The readings are shown in Figure 9. Before launch, there was a steep increase in temperature with a maximum of 48 °C reached shortly after launch. During ascent, the temperature gradually decreases to a minimum of 15 °C at about 80 minutes into the flight. Afterwards, the it slowly increases again to a maximum of 30 °C at 173 minutes. Subsequently, the temperature begins to fall again with very constant rate of about 0.08 $^{\circ}C/_{min}$. After cutoff, the temperature drops rapidly with about 0.16 $^{\circ}C/_{min}$, most likely due to an increased air flow during the free fall.

4.2. S-Band Flight Results

Regrettably, the data from the S-band transceiver received by the ground station was lost and could not be recovered after the flight. An analysis of the S-band telemetry was therefore not possible.

Figure 10 shows the SNR of the S-band signal as received by the MORABA ground station. The measurement was performed at the automatic gain control (AGC) of the ground station. The figure shows the calculated signal strength according to the link budget. This calculation was performed using the data from the balloon's GPS tracking device. The green line at the bottom of the graph indicates the approximate SNR required for a BER of 10^{-6}. The first observation that can be made from the figure is an extreme variation of the signal quality in the first 30 minutes prior to launch. There are several causes of this. First, the attenuation is partly due to partial or total occlusion of the line of sight by nearby trees. Second, the antenna did not point at the gondola the entire time, so that the signal may been received through a side lobe of the antenna. Lastly, the movement of the balloon by the launch vehicle may have also introduced some signal level variance.

Another observation is a signal variance of about 10 dB during the ascent phase. The signal becomes more stable as the balloon enters the floating phase. The same observation has already been made from the VHF signal, therefore it can be assumed that there is a common source which causes this effect.

During the flight, a defective contact in the CDH system disabled the SPI slave-select line. At 170 minutes into the flight, the S-band transmitter was restarted in an attempt to resolve this issue. This can be seen in the SNR graph as short spike. As the attempt was unsuccessful, no further experiments were conducted with the transmitter.

The SNR graph reveals a steep decline of the SNR at about 275 to 280 minutes after launch. At this time, the gondola was in free fall, resulting in a very low elevation angle. The automatic pointing mechanism directed the antenna to a negative elevation, which was corrected manually. This showed an improvement of the signal quality. However, as the graph shows, the signal began to quickly fade soon after. Since the gondola's altitude

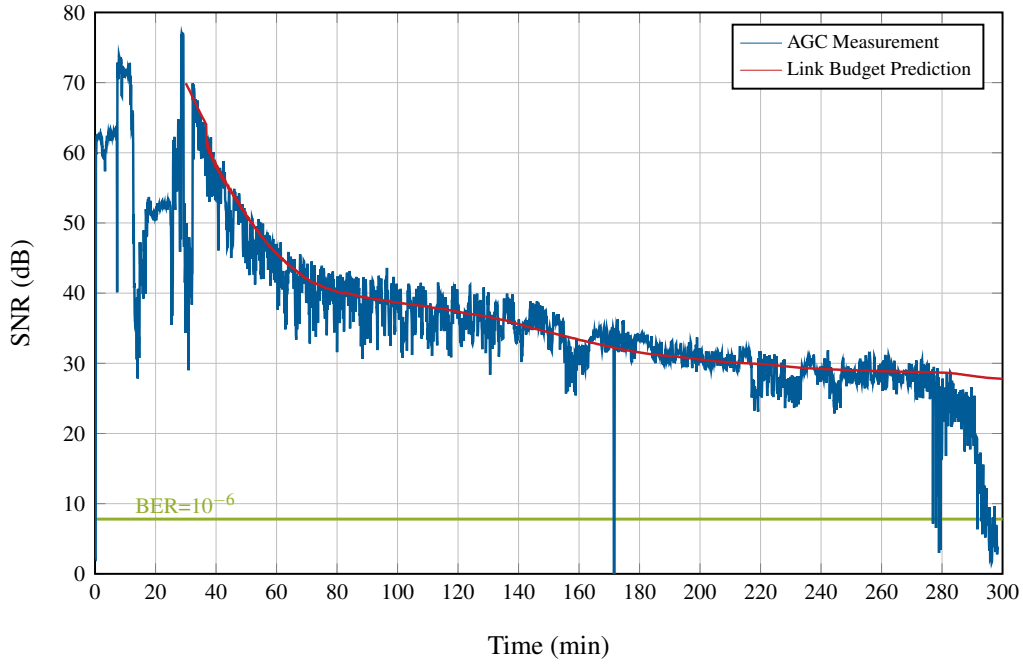

Figure 10. Signal-to-noise ratio of the S-band transmission during the BEXUS flight.

decreased quickly, it is very likely that the signal did not travel via line of sight but rather by diffraction at the horizon. Moreover, occlusion by foliage and trees around the location very likely amplified this effect. The signal was lost entirely when the gondola was at a height of less than 3 km above the ground. At this point, all other communication systems on the gondola had already lost connection.

When comparing the measured and calculated SNR graphs in Figure 10, it can be seen that apart from the smaller variations, the calculation yields a good approximation of the actual signal levels. Therefore, these results can be transferred to the satellite model. At the farthest point in an overpass of MOVE-II, the satellite is about 2800 km away from the ground station. This is about ten times more than the maximum distance of the BEXUS 22 balloon to the MORABA ground station. By the inverse square law, this results in 20 dB higher free-space path loss. The ground station at TUM that will be used for MOVE-II has a gain of approximately 30.6 dBi and the satellite antenna has a gain of 5 dBi. Also, a stronger LDPC 1/2 code will be used instead of the convolutional code, resulting in a coding gain of about 2.7dB. In total the additional attenuation of the MOVE-II setup is about 22.7dB. This leaves only a very thin link margin of about 3dB for the system. However, this margin increases during an overpass.

5. CONCLUSION

From the analysis of the VHF transmission, we can see that the TDP-3 setup was sensitive to bad signal conditions. This is a result of the uncoded transmission: Single-bit errors void the checksum of a frame, which leads to high data losses. When the SNR fell below 10 db, severe frame losses occured and the data rate degraded quickly. This may be a result of a suboptimal implementation in GNURadio. When the SNR was above 10 dB, the performance was very high, with an efficiency of 95%.

We observed that the transceiver is able to dissipate excess heat well despite the lack of air for convection. It remained comparatively cool and far from the limits of the operating temperature of its commercially available components, which typically lies between -40 C and +85 °C.

The experiment showed the S-band link to be very stable. The transmitter hardware and software operated flawlessly in near vacuum for more than four hours. The observed margin for signal fading of about 5 dB is reasonable for future satellite missions. The long duration of continuous transmission proves that the thermal design of the system is sufficient. When translating the results of the SNR measurement to the MOVE-II mission, it becomes clear that the link may not operate optimally at low elevations at the beginning of a pass, but should be stable through most of it.

ACKNOWLEDGMENTS

The REXUS/BEXUS program is realized under a bilateral agency agreement between the German Aerospace

Center (DLR) and the Swedish National Space Board (SNSB). The Swedish share of the payload has been made available to students from other European countries through a collaboration with the European Space Agency (ESA).

This research was supported by the DFG Cluster of Excellence *Origin and Structure of the Universe*. The authors acknowledge the funding of MOVE-II by the Federal Ministry of Economics and Energy, following a decision of the German Bundestag, via the German Aerospace Center (DLR) with funding grant number 50 RM 1509.

REFERENCES

Appel, N. M. E., Rückerl, S., & Langer, M. (2016). Nanolink: A robust and efficient protocol for Small Satellite radio links. In *4S Symposium*, Valetta, Malta.

Czech, M., Fleischner, A., & Walter, U. (2010). A First-MOVE in Satellite Development at the TU-München. In *Small Satellite Missions for Earth Observation*, pages 235–245. Springer.

Langer, M., Appel, N. M. E., Dziura, M., et al. (2015a). MOVE-II—der zweite Kleinsatellit der Technischen Universität München. In *Deutscher Luft-und Raumfahrtkongress (DLRK)*, Rostock, Germany.

Langer, M., Olthoff, C., Harder, J., et al. (2015b). Results and lessons learned from the CubeSat mission First-MOVE. In *Small Satellite Missions for Earth Observation*. Springer.

Losekamm, M. J., Milde, M., Pöschl, T., Greenwald, D., & Paul, S. (2016). Real-Time Omnidirectional Radiation Monitoring on Spacecraft. In *AIAA SPACE 2016*, AIAA SPACE Forum. American Institute of Aeronautics and Astronautics.

Losekamm, M. J., Pöschl, T., Gaisbauer, D., Greenwald, D., & Paul, S. (2015). AFIS: A New Instrument for Cosmic Radiation Studies on BEXUS 18 and Future Nanosatellite Missions. In *22nd ESA Symposium on European Rocket & Balloon Programmes and Related Research*, Tromsø, Norway.

Rutzinger, M., Krempel, L., Salzberger, M., et al. (2016). On-orbit verification of space solar cells on the CubeSat MOVE-II. In *Photovoltaic Specialists Conference (PVSC), 2016 IEEE 43rd*, pages 2605–2609. IEEE.

U-PHOS EXPERIMENT: THERMAL RESPONSE OF A LARGE DIAMETER PULSATING HEAT PIPE ON BOARD REXUS 22 ROCKET

A. Catarsi[1], M. Anichini[1], L. Barsocchi[1], G. Becatti[1], L. Buoni[1], F. Celi[1], P. Di Giorgio[1], P. Fattibene[1], E. Ferrato[1], P. Guardati[1], E. Mancini[1], G. Meoni[1], P. Nannipieri[1], F. Nesti[1], S. Piacquadio[1], E. Pratelli[1], L. Quadrelli[1], A.S. Viglione[1], F. Zanaboni[1], M. Mameli[1], F. Baronti[1], L. Fanucci[1], S. Marcuccio[1], C. Bartoli[1], P. Di Marco[1], S. Filippeschi[1], N. Bianco[2], and M. Marengo[3]

[1] *University of Pisa, Largo Lucio Lazzarino 2, 56122 Pisa, Italy.*
[2] *University of Naples Federico II, Corso Umberto I 40, 80138, Naples, Italy.*
[3] *University of Brighton, Lewes Rd, Brighton BN2 4AT, United Kingdom.*

ABSTRACT

A Pulsating Heat Pipe (PHP) is tested on board REXUS 22 sounding rocket in order to obtain data over a relatively long milli-gravity period (120s). The device is made of an aluminum tube bent in a serpentine staggered configuration, closed in a single loop and partially filled with FC-72. Despite the 3mm internal diameter is greater than the capillary threshold in ground conditions, in milligravity the slug flow pattern is maintained as well as the thermally driven self sustained oscillation of the working fluid.

The possibility to build PHPs with big diameters, with increased heat transfer rates and reduced overall thermal resistances, is an interesting step forward in the fast developing space industry, always craving for greater performances at a reduced weight and cost.

The experiment is the natural improvement of the PHOS project, launched on REXUS 18 but only partially successful due to a failure in the de-spin system of the rocket. All the components have been improved, especially the test cell geometry, the data acquisition system -now employing 24 Fiber Bragg Grating optical sensors for a more accurate temperature detection- and the heat sink -now composed by a combination of paraffin wax and metal foams for an enhanced thermal conductivity. The thermal response of the device is given under a constant heat power supply at the evaporator.

Figure 1. The U-PHOS Experiment

1. INTRODUCTION

The space industry is probably the field that has been interested above all in the reduction of weight and cost of the various components. The progressive miniaturization of electronic components has been a natural path to follow and resulted in great advantages, but at the same time the thermal management has become more and more complex and demanding. Right now, two-phase heat transfer devices are becoming the predominant solution, in particular sintered wick Heat Pipes (HP) and Loop Heat Pipes (LHP). Thanks to their reliability, lightness and, most of all, their capability to operate without the assistance of any acceleration field (*Gilmore*, 2002 [1]). The latter is obtained thanks to a wick, which is also the most complex and expensive element inside the system, enhancing capillarity.

With space applications in mind and not to reduce costs, *Akachi* (1990 [2], 1993 [3]) introduced the concept of Pulsating Heat Pipe (PHP), which is basically a wickless two phase loop, consisting in a small diameter capillary tube bent in several turns.

In this particular configuration (Fig. 2), the fluid resides inside the tube as an alternation of liquid slugs and vapor bubbles: when the vapor formed in the heated zone expands, it pushes the adjacent fluid to the condenser zone where heat is released and a part of the vapor condensed.

The cooled fluid returns then to the evaporator to begin the cycle anew. Generally, in literature, the static critical tube diameter - *i.e.* evaluated not considering the fluid's viscosity and inertia- is estimated using the correlation by *Kew and Cornwell* (1997) [4]:

$$d_{cr} = 2\sqrt{\sigma/(g(\rho_l - \rho_v))} \quad (1)$$

where σ is the liquid surface tension, ρ_l and ρ_v are respectively the liquid and vapor density and g is the gravitational acceleration. From equation 1, it is evident that a reduced g gives back a bigger critical diameter and consequently a higher thermal flux that can be dissipated.
Actually, *Gu et al.* [5] and *Mameli et al.* [7] asserted that viscous and inertial effects always play a significant role in the definition of the flow pattern within the device that cannot be discounted. All things considered, with respect to the new dynamic confinement criterion based on Weber and Garimella numbers (*Harichian & Garimella*, 2010 [8]), it seems that a two-phase loop may still work as a PHP in reduced gravity conditions with a tube's inner diameter larger than the one evaluated on static ground conditions.

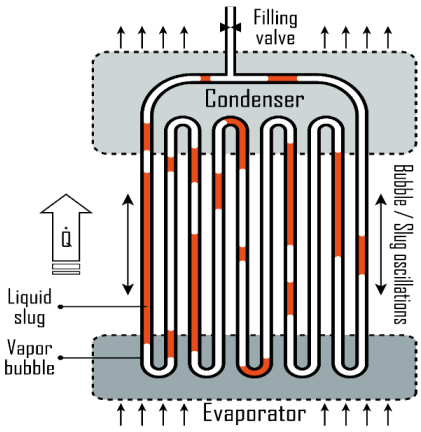

Figure 2. PHP working principle

Many experiments in milli-gravity condition (*i.e.* by means of parabolic flight or sounding rockets) have been carried out on capillary PHPs (*Gu et al.*, 2004 [5], 2005 [6]; *Mameli et al.*, 2014 [7]; *De Paiva et al.*, 2010 [9], 2013[10]; *Taft et al.*, 2015 [11]; *Ayel et al.*, 2015 [12], 2016 [13]) and most of them clearly revealed a self-sustained two-phase flow motion in milli-gravity, though only a few experiments have been performed with a bigger tube diameter than the threshold one on ground. The Space PHP concept has been already successfully tested by *Mangini et al.* (2015 [14], 2017 [15]), who tested a PHP with an inner diameter of 3mm filled with FC-72 both on ground and on milli-gravity condition during ESA 61 and 63 Parabolic flight campaigns. They noticed that a sudden transition of the flow pattern from stratified to slug flow appears as the reduced gravity condition kicks in, showing that the device is able to work as a PHP. Yet, the reduced gravity environment experienced during the parabolic flight (about $20s$) was not long enough to reach a steady state condition, which would be useful to characterize the thermal performances of the device.
In light of the above, the first experiment of the Space PHP on board a sounding rocket was performed within the REXUS-BEXUS Programme (REXUS 18) in order to obtain data on a longer milli-gravity duration ($120s$) but it failed due to a problem in the rocket de-spinning system (*Creatini et al.*, 2015 [16]).

Hence, the idea of a re-flight of an optimized experiment on sounding rocket REXUS 22, again with the REXUS-BEXUS Programme: the U-PHOS mission (Fig. 1) has been successfully launched from Kiruna Esrange Space Center in March 2017. Many improvements have been made for the U-PHOS design with respect to the previous experiment, to maximize the reliability of the system and the scientific output. The idea is essentially the same, but the hardware has been redone, as well as the software, designed with the experience gained from the previous flight. It certainly cannot be discounted the improvements to the data-acquisition system and on the heat sink employed, that will be discussed throughly in the next paragraphs.

Finally, the data obtained are very promising and they lead the way for further investigations.

2. EXPERIMENT SET-UP

The experiment set-up consists of:

- A PHP test cell;
- A heat sink realized by means of a Phase Change Material (PCM) -paraffin wax- doped with a metallic foam in order to increase the overall heat sink thermal conductivity;
- A heat source, realized by means of two ceramic heaters, also used during the pre-launch operations in order to maintain the wax as close as possible to the melting point (27°C);
- A Power board to distribute power to the heaters;
- An eight-cells (MP 176065 by SAFT) lithium-ion battery;
- A Battery Management System to monitor the State of Charge of the cells and to control the power flux;
- A Main Control Unit (MCU) to control in real time all the processes and responsible for the on-board data handling system, measuring the necessary values in order to obtain the thermal resistance of the device;
- A Single Board Interrogator (SBI) to realize the temperature measurements in 24 fixed points of the PHP via Fibre Bragg Grating (FBG) sensors;

- A pressure transducer and two resistance thermometers, in order to characterize the PHP together with the aforementioned optical sensors;

- A system interface with the REXUS rocket to provide the power supply to all the electronic devices.

2.1. Test cell

The PHP test cell is a single loop aluminum tube (6060 alloy) folded in a staggered configuration with fourteen U-turns at the evaporator and thirteen U-turns at the condenser. On the PHP are mounted a total of 24 temperature sensors, realized by means of a FBG (Fiber Bragg Grating) system, as shown in Fig. 3.
The device has been emptied through a two-stage turbo

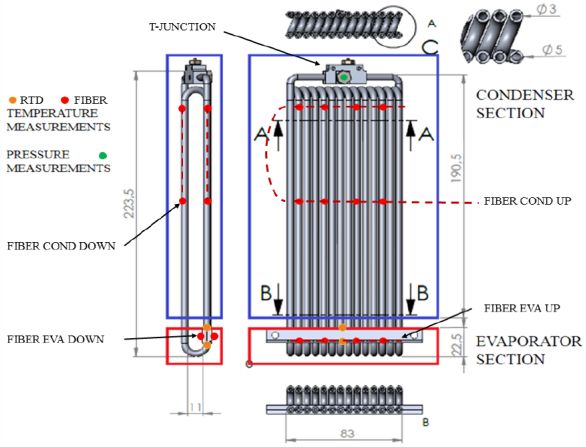

Figure 3. Test cell overview

pump down to 0.3 mPa and then partially filled with the working fluid (perfluorhexane, C_6F_{14} commercial name FC-72) at a volumetric ratio of 0.5 ± 0.025 (corresponding to 22 ml), via a T-junction.
The PHP condenser section is embedded into a heat sink, consisting of a PCM (Octadecane paraffin wax) doped with an aluminum metallic foam (40 Pores Per Inch, 88% void). In order to avoid any leakage, this ensemble is contained inside an airtight box (the Experiment Box), made of a 6060-T66 aluminum alloy, in which the heat sink and the condenser section of the PHP are kept in mutual thermal contact for all the experiment duration.
The heaters are placed on an aluminum flat surface brazed on the PHP. They are sized in order to allow a constant heat flux even with increasing resistors' temperature. The heating elements are powered up to 200W (corresponding to a radial wall to fluid local heat flux of $12.6 \frac{W}{cm^2}$) by a battery.
The model of the setup is shown in Fig. 4.

The experiment procedure is divided in four main parts, as shown in Fig. 5.

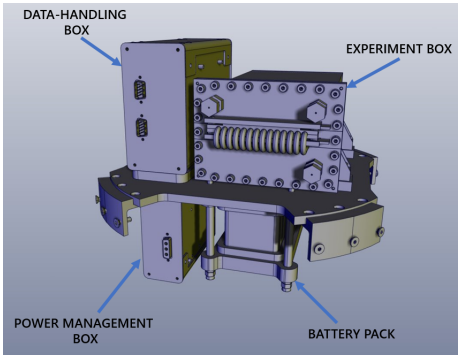

Figure 4. CAD illustration of the experiment assembly

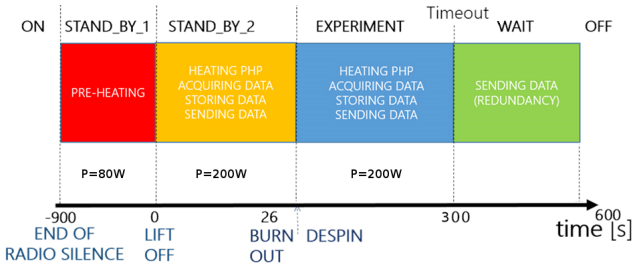

Figure 5. Experiment timeline with power profile at the heaters

2.2. The electronic system and the on-board software

The electronic system (Fig. 6) has the following tasks:

- Control the experiment timeline;
- Provide a controlled power flux to the heaters;
- Collect data provided by the sensors for the characterization of the PHP;
- Send data to the ground station.

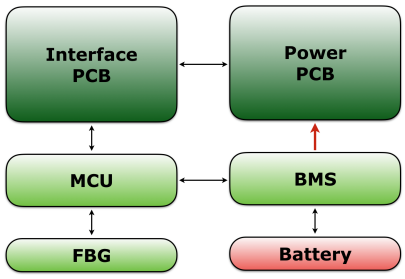

Figure 6. Block diagram of the electronic system

The MCU is realized by a commercial board from Embedded ARM (TS7200): it is a programmable board hosting a LINUX distribution with on board memory and peripherals, such as ADC channels and a RS-485 port. The software running on the MCU controls of the experiment

and its timeline. In addition, it collects all the data provided by the sensors and the power supplied measurement system, placed on the Power PCB. In particular, the MCU interacts through the PC104 bus with the Single Board Interrogator (SBI) which performs temperature measurements by the FBG sensors.
The collected data are sent to the Ground Station through the Interface board, which hosts digital transceivers for the conversion from RS-485 to RS-422. In addition, the Interface PCB contains all the DC/DC converters which allow to provide power supply with different voltages to all the electronic devices of the experiment, guaranteeing the DC-isolation from the Rexus Module power supply.
In order to provide a controlled amount of power to the heaters, the Power PCB embeds an isolated DC/DC (DCM24AP480T320A50 VICor), able to fix its output voltage to 48V independently on the variations of the input battery voltage, due to the discharge process.
In addition, a dedicated circuit measures the power provided to the heaters and realizes a Pulse Width Modulation control on the output voltage of the DC/DC. The PWM operates a close-feedback loop control which allows to maintain the temperature of the paraffin near the melting point before the launch (Preheating control).
Finally, in order to prevent the battery from dispensing power when not necessary, a Battery Management System (BMS) is implemented. It interacts through a dedicated interface board with the MCU which enables and disables the power flux from the battery depending on the experiment timeline. Moreover, the BMS performs measurements on the current and voltage of the single cells and interrupts the power supply from the battery if not appropriately discharged.

3. DATA ACQUISITION SYSTEM: FIBER BRAGG GRATING OPTICAL SENSORS

In the former PHOS experiment, flown as part of the REXUS 18 sounding rocket, the temperature acquisition system consisted of 32 T-type thermocouples; a number of issues arose during the integration process and this convinced the team to upgrade to a more compact and straightforward solution. This lead to the U-PHOS temperature acquisition system based on a Fiber Bragg Grating (FBG) system that acquires temperatures in 24 points by means of optical sensors, with an accuracy of 0.1 K (*Nannipieri et al.* [17]). This new system has many technological advantages such as the intrinsic immunity to electromagnetic interference, compactness, easy integrability and accuracy.

A Bragg sensor is realized by permanently modulating the refraction index of the core in a specific point of an optical fibre, which becomes a reflection mirror. If stimulated by light source, *e.g.* a super-luminescent led, the signal back-reflected has a typical Gaussian-type narrow band spectrum located at the wavelength specified by the following equation:

$$\lambda_B(T_0) = 2n\Lambda \tag{2}$$

where λ_B is the characteristic Bragg wavelength, n is the effective refractive index of the core, Λ the grating pitch and T_0 is the reference temperature. A temperature variation ΔT from T_0 causes a variation on the λ_B according to the relationship:

$$\Delta\lambda_B = \alpha\Delta T + k\Delta\varepsilon \tag{3}$$

where α and k are the coefficients that consider the temperature (T) and strain (ε) dependence respectively.

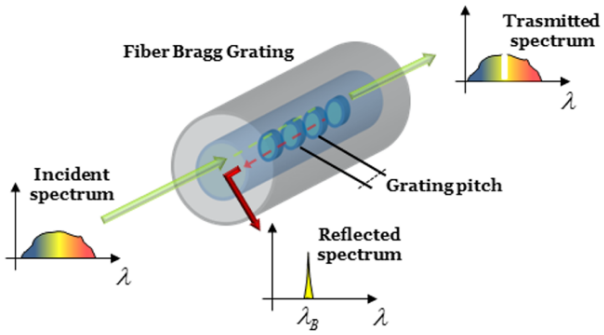

Figure 7. FBG working principle

In our setup the FBG sensors are interfaced with a COTS board from the SmartScan series realized by Smart Fibres and Infibra Tec. This Interrogator board is linked through a PC 104 interface to an MCU, in our case a TS-7200 running Linux Kernel 2.6.32 and powered by an ARM9 processor clocked at 200 MHz; this solution has an operating temperature range of -20 °C to +75 °C and a maximum scanning frequency of 2.5 kHz for all sensors simultaneously, while the fiber sensors, depending on the external coating, can withstand up to 150 °C.

In order to achieve good accuracy and reliability, the experiment features 12 locations where temperature is sampled and implements a double redundancy approach. In fact, four fibres -two pairs of identical FBG arrays- are used connected to an independent channel of the interrogator, providing 24 simultaneous temperature measurements. The arrangement of the fibres is shown in Fig. 3.

A comparative analysis points out the following advantages of FBG based temperature sensor systems with respect to conventional electronic sensors:

- FBGs can be easily used in highly explosive and high electromagnetic radiation environments.
- FBGs are lightweight and typically less invasive making easier to embed the sensors into complex structures.
- due to their multiplexing capabilities, a monitoring system with a large number of sensors can be easily implemented and many point sensors can be inscribed along only one optical fibre in a so-called array of FBG sensors.

4. HEAT SINK: PARAFFIN WAX AND METALLIC FOAMS

In order to be on a certain degree independent of the cooling section thermal inertia, a stable temperature would be desirable in the condenser section. Heat dissipation at constant temperature may be obtained using a phase change material in close contact with the condenser section. The material chosen is Octadecane paraffin wax, because of its melting temperature and its high latent heat as shown in table 1.

Density	814 (s), 774 (l)	kg/m^3
Specific Heat	2160	$J/(kgK)$
Melting Point	28.0	^{o}C
Boiling Point	317.9	^oC
Heat of Fusion	244	kJ/kg
Thermal Conductivity	0.15	$W/(mK)$

Table 1. Octadecane paraffin wax thermophysical properties

Unfortunately it is a very poor thermal conductor meaning that, once the paraffin starts melting, the liquid layer around the tube is heated faster than the melting front propagation, resulting in a strong condenser temperature variation in time. This behaviour was found during the mission of the experiment on REXUS 18 (*Creatini et al.*, 2015 [16]).

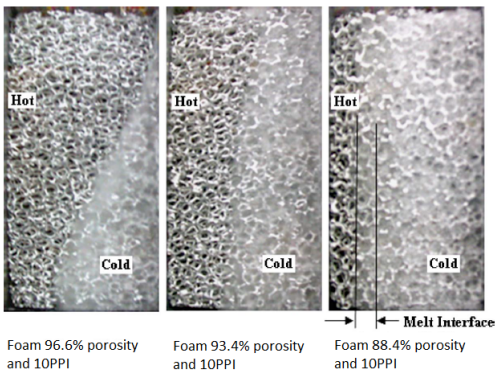

Figure 8. Melting interface at various relative densities and constant PPI (10) of the metallic foam (Lafdi et al. [18])

To avoid this effect, the paraffin thermal conductivity may be enhanced by integrating it with a metallic foam. Furthermore, since the metallic foam is highly porous the overall mass of the PCM/ metallic foam assessment does not increase too much. Several studies in literature calculate an overall thermal conductivity more than 10 times higher than the paraffin alone (*Lafdi et al.*[18]) using copper foams.

Metallic foams are characterized by two main parameters: porosity is defined as the ratio between the foam weight and the weight of the same solid volume composed of the same material, while pore density indicates the number of pores in a linear inch (PPI). We are interested in the combination of these two parameters that leads to the lowest condenser temperature increase for the same thermal flux.

The porosity affects the melting process: in fact the interface region for a high density foam (88% of porosity) is thicker, while with a lower density foam (96% and 94% of porosity) it is thinner, as shown in Fig. 8. This is due to the high thermal conductivity of this foam: the temperature difference between the paraffin wax and the metallic foam is not negligible, and a relatively thick layer of the foam is above the melting temperature.

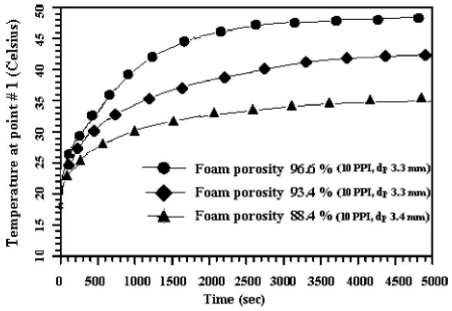

Figure 9. Heater plate temperature variation for three different foam densities (Lafdi et al. [18])

Increasing foam density would imply higher thermal conductivity and so lower temperature variations at the condenser interface, as shown in Fig. 9.

For this reason, the best solution seems to be a relatively high density foam (88% porosity). No information about the pore density can be gathered from the literature because, as seen before, it influences the convective heat transfer inside the porous medium that does not occur in micro-gravity.

The final set-up of the metallic foams system is shown in Fig. 10.

Figure 10. Metallic foams set-up: system brazed on PHP

The Aluminium foams are brazed on the PHP, in the con-

denser zone, in order to create a perfect thermal contact.

5. RESULTS

The flight and the experiment were successful and all the data were collected properly. The 3 main parameters, (evaporator temperature, condenser temperature and pressure) are plotted against time in Fig. 11, 12, 13.

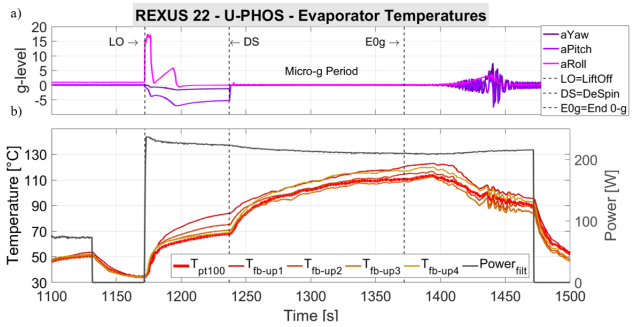

Figure 11. a) Accelerations during the different phases; b) Evaporator temperature trends (left y-axis) and Heating power (right y-axis)

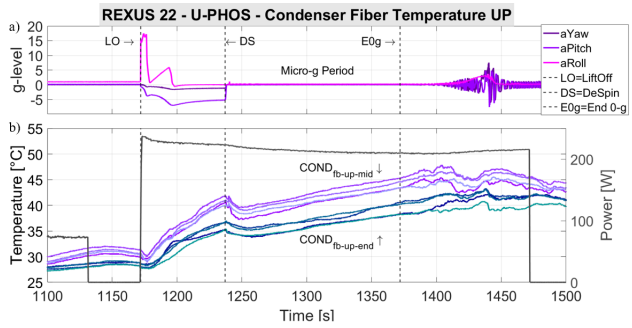

Figure 12. a) Accelerations during the different phases; b) Condenser temperature trends on the upper tube rank (left y-axis) and Heating power (right y-axis)

With respect to the experiment timeline (Fig. 5, Pag. 3), we can divide the analysis in 4 main section.

Before Lift Off The experiment is pre-heated and the paraffin is successfully maintained near its melting point (28°C) as shown in Fig. 12. In this phase the PHP does not work and the heat is transferred only by conduction of the aluminum tube. The evaporator temperature, indeed, rises homogeneously (Fig. 11) and the pressure does not vary (Fig. 13).

Between Lift Off and De-Spin The experiment receives the full power (200 W) and experiences nearly 20g of vertical acceleration due to the motor thrust and up

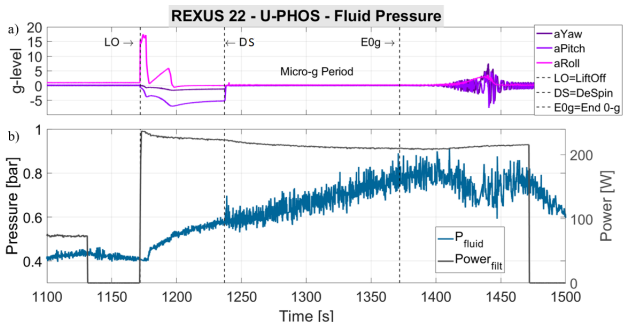

Figure 13. a) Accelerations during the different phases; b) Local fluid pressure trend (left y-axis) and Heating power (right y-axis)

to 6g of centrifugal acceleration due to the rocket spinning: the first is perpendicular to the flow path direction pushing the liquid phase in the lower tube rank; the latter pushes the liquid phase on the two ends of the device. The effect of this acceleration field on the thermo-fluidic behavior is unpredictable but, overall, it seems to assist the fluid motion. This is clear by comparing the temperature trends in the subsequent milli-gravity period.

Between rocket De-Spin and End of Og The three acceleration components approach the milli-gravity condition. During this period, the fluid motion is only related to thermocapillary effects so the evaporator temperature exhibits a sudden increase while condenser temperature decreases. Therefore, the PHP experiences a sudden drop of the overall heat transfer performance with respect to the previous period.
It is reasonable to assess that the acceleration field during the launch phase has a positive effect on the fluid motion and consequently on the device heat transfer rate. On the other way, even if the device performance seems to degrade during the milli-gravity period, both the temperature and fluid pressure trends show that the fluid exhibits still some sort of motion inside the device. Both the evaporator and condenser temperatures and -more evidently- the fluid pressure (Fig. 13) oscillate for the whole zero gravity duration and this is one the most important outcome of the present work since it basically confirms that a multi-turn two phase loop is able to work as a PHP in milli-gravity conditions. Unfortunately, it was not possible to reach a pseudo-steady state, stressing the fact that a longer term milli-gravity period is needed in order to infer about the actual heat transfer performance.

After the End of the 0g period The rocket experiences a complex acceleration field that, once again unpredictably, assists the fluid motion: the evaporator temperatures indeed decrease.

6. CONCLUSION

The U-PHOS Project aims at characterizing the thermal behaviour of a large diameter Pulsating Heat Pipe (PHP), a promising device for the thermal management in space applications. The experiment is an upgrade of a previous one (PHOS) that was launched on board REXUS 18 sounding rocket (*Creatini et al.*, 2015 [16]). The main differences with respect to PHOS consist of: a new optimized staggered geometry; the enhancement of the heat sink thermal conductivity using a metal foam directly brazed on the PHP tubes and filled with a paraffin wax; the implementation of a temperature measurement system based on optical fibres, characterized by a better accuracy, reliability and integrability. The experiment has been launched in March 2017 from the ESRANGE Space Center (Sweden) on board of REXUS 22 sounding rocket. The flight was nominal and the experiment succeeded in all of its objectives. Immediately after the milli-gravity condition ensued, all the temperature signals both in the evaporator and condenser exhibited an oscillating component for the whole zero gravity duration. The amplitude of the fluid pressure signal was evidently increased under the occurrence of the milli-gravity period, proof of a change in behaviour. Unfortunately, it was not possible to reach a pseudo-steady state because of the thermal inertia of the heat sink, emphasizing the fact that a longer milli-gravity period is still needed in order to measure the potential heat transfer performance. Anyway, it is clear that the perspective of having a hybrid device that works effectively on ground as a thermosyphon and switch to a PHP in zero gravity conditions is promising. Furthermore, aside the potential applications, the complexity and variety of the physical phenomena inside a PHP under varying gravity conditions, together with the challenge to be able to model the device, are an excellent opportunity for a further, deeper understanding of the thermodynamics of two-phase systems and liquid/vapour interfaces.

ACKNOWLEDGMENTS

We would like to thank the many colleagues who supported us, even if they were outside of the team, just for the love of scientific research. We would also like to acknowledge ESA, DLR and SNSB, the ESA MAP INWIP project for funding the project, the International Scientific Team on Pulsating Heat Pipes, the school of engineering and AAVID Thermalloy, especially Marco La Foresta and Lorenzo Caporale, for the crucial help in the test cell manufacturing. We also would like to thank Alessandro Signorini and INFIBRA Technologies for the great help.

REFERENCES

[1] Gilmore G., 2002. Spacecraft Thermal Control Handbook, Fundamental Technologies, The Aerospace Press, El Segundo California.

[2] Akachi H., 1990. Structure of a heat pipe, US Pantent 4.921.041.

[3] Akachi H., 1993. Structure of a micro heat pipe, US Patent 5.219.020.

[4] Kew, P.A. and K. Cornwell 1997. Correlations for the prediction of boiling heat transfer in small-diameter channels. Applied Thermal Engineering, Vol. 17, pp. 705715.

[5] Gu, J., Kawaji, M., and Futamata, R., 2004. Effects of gravity on the performance of Pulsating Heat Pipes, Journal of Thermophysics and Heat Transfer, Vol.18, pp. 370-378.

[6] Gu, J., Kawaji, M., Futamata, R., 2005. Microgravity performance of micro pulsating heating pipe, Microgravity Science and Technology, Vol.16, pp. 179-183.

[7] Mameli, M., Araneo, L., Filippeschi, S., Marelli, M., Testa, R., Marengo, M., 2014. Thermal performance of a closed loop pulsating heat pipe under a variable gravity force, International Journal of Thermal Science, Vol. 80, pp. 11-22.

[8] T. Harichian and S. Garimella. A comprehensive flow regime ap for microchannel flow boiling with quantitative transition Criteria. International Journal of Heat and Mass Transfer, 53, 2010.

[9] De Paiva, K. V., Mantelli, M. B., H., Slongo, L. K., Burg, S. J., 2010. Experimental tests of mini Heat Pipe, Pulsating Heat Pipe and Heat Spreader under microgravity conditions aboard suborbital rockets, Proc. of the 15th International Heat Pipe Conference, Clemson, South Carolina, USA.

[10] De Paiva, K., Mantelli, M.B.H., Florez, J.P.M., Nuernberg, G.G.V., 2013. Mini Heat Pipe Experiments under Microgravity Conditions. What have we Learned?, Proc. of the 17th International Heat Pipe Conference, Kanpur, India, 2013.

[11] Taft, B. S., Laun, F.F., Smith, S., 2015. Microgravity Performance of a structurally Embedded Oscillating Heat Pipe, Journal of Thermophysics and Heat Transfer, Vol. 29(2).

[12] Ayel, V., Araneo, L., Scalambra, A., Mameli, M., Romestant, C., Piteau, A., Marengo, M., Filippeschi, S., Bertin, Y., 2015. Experimental study of a closed loop flat plate pulsating heat pipe under a varying gravity force, International Journal of Thermal Sciences, Vol. 96, pp. 23-34.

[13] Ayel, V., Araneo, L., Marzorati, P., Romestant, C., Bertin, Y., Marengo, M., 2016. Visualizations of the flow patterns in a closed loop flat plate PHP with channel diameter above the critical one and tested under microgravity, Proc. of 18 International Heat Pipe Conference and 12 International Heat Pipe Symposium, South Korea.

[14] Mangini, D., Mameli, M., Geourgoulas, A., Araneo, L., Filippeschi, S., Marengo, M., 2015. A pulsating heat pipe for space applications: Ground and milli-gravity experiments, International Journal of Thermal Sciences, Vol. 95, pp. 53-63.

[15] Mangini D., Mameli M., Fioriti D., Araneo L., Filippeschi S., Marengo M., 2017. Hybrid Pulsating Heat Pipe for Space Applications with Non-Uniform Heating Patterns: Ground and Microgravity Experiments, accepted for publication by the Applied Thermal Engineering.

[16] Creatini F., Guidi G.M., Belfi F., Cicero G., Fioriti D., Di Prizio D., Piacquadio S., Becatti G., Orlandini G., Frigerio A., Fontanesi S., Nannipieri P., Rognini M., Morganti N., Filippeschi S., Di Marco P., Fanucci L., Baronti F., Manzoni M., Mameli M., Marengo M., Phos Experiment: Thermal Response Of A Large Diameter Pulsating Heat Pipe On Board Rexus 18 Rocket, 22nd ESA PAC Symposium, 7-12 june 2015, Tromso, Norway.

[17] P. Nannipieri, G. Meoni, F. Nesti, E. Mancini, F. Celi, L. Quadrelli, E. Ferrato, P. Guardati, F. Baronti, L. Fanucci, A. Signorini, T. Nannipieri, 2017, Application of FBG sensors to temperature measurement on board of the REXUS 22 sounding rocket in the framework of the U-PHOS project, IEEE Metrology for Aerospace 2017.

[18] K. Lafdi, O. Mesalhy, and S. Shaikh. Experimental study on the influence of foam porosity and pore size on the melting of phase change materials. (102), 2007.

UPGRADE OF ANDØYA SPACE CENTERS LAUNCH BASE AT SVALBARD – NEW OPPORTUNITIES FOR THE SPACE SCIENCE COMMUNITY

Preben Hanssen [(1)], Kjell Bøen [(2)], Tore Kristiansen [(3)]

[(1)] Andøya Space Center, Norway, preben@andoyaspace.no

[(2)] Andøya Space Center, Norway, kjell@andoyaspace.no

[(3)] Andøya Space Center, Norway, tore@andoyaspace.no

Figur 1 - Andøya Space Center

Figur 2 - "SvalRak" ASC's launch base in Ny-Ålesund

ABSTRACT

Andøya Space Center (ASC) is in the process of upgrading the installations at SvalRak - ASC's launch base for sounding rockets in Ny-Ålesund at Svalbard. The upgrades include new wind measurement system, new intercom, communication system, and a new launcher with a protective shelter to protect the rocket and payload to weather and environment until shortly before launch. ASC has now several mobile telemetry stations in its inventory. Thus, future campaigns in Ny-Ålesund will have complete redundant telemetry systems. The upgrade also means that now it will be possible to implement parallel rocket campaigns at Andøya and Svalbard, as well as simultaneous launches from both bases.

The most significant upgrade is however a new launcher. Two modern launchers with protecting

shelters in Ny-Ålesund provides new opportunities for the scientific community.

1. INTRODUCTION TO ANDØYA SPACE CENTER

ASC is located on the island Andøya, 2 degrees north of the Arctic Circle, in northern Norway. Andøya has its own airport capable of handling all sizes of aircrafts. Several daily connections to Tromsø and Bodø makes it convenient traveling to/from Oslo.

ASC supports sounding rocket and balloon operations both at Andøya and at Svalbard, and is host to a large array of ground based scientific instruments. ASC also owns and operates the ALOMAR lidar observatory located at the top of the nearby mountain. Our clients include ESA, NASA, JAXA, DLR as well as national and international universities and institutes.

ASC operates two sounding rocket launch bases; at Andøya and at Ny-Ålesund on Svalbard. Combined, these bases offer a variety of rocket trajectories and access to all layers of the atmosphere. Due to the increased interest of launching sounding rockets from Svalbard, ASC is now in the proses of upgrading the launch base in Ny-Ålesund.

1.1. History of "SvalRak"

Planning of a launch site in Ny-Ålesund started in 1993, a location chosen because of its ideal location to study the polar cusp. Construction of the site started in the summer of 1997. By November, the launch base was finished and a test rocket was launched 15 of November. The first proper launch was a Norwegian rocket, *Isbjørn 1*.

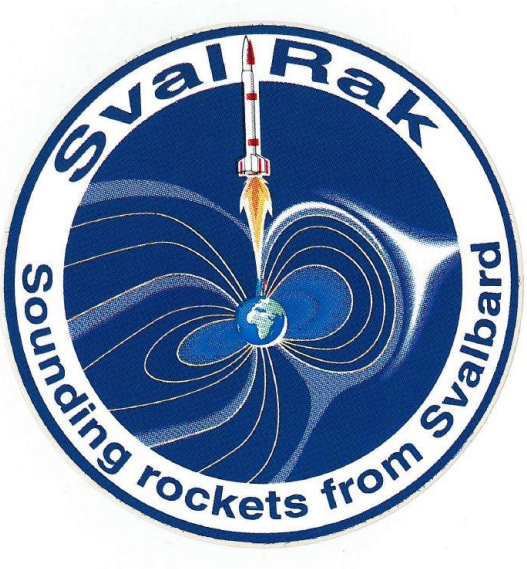

Figur 3 - Old patch from 1997 showing rocket launched trough the cusp, from SvalRak.

2. WHY SVALBARD

Svalbard has a unique location for space research. The archipelago is located right below what is called the polar cusp. Nowhere else in the world do we have the fortuitous combination of geography and ground-based instrumentation that enables sounding rocket experiments to be launched directly into the Earth's magnetic cusp. The cusp is the only place where the energy of the solar wind can directly influence the upper atmospheric dynamics. And that is what makes Ny-Ålesund the perfect location for these kind of missions.

3. INCREASED SCIENTIFIC INTEREST

Due to increased, scientific interest of launching sounding rockets from Svalbard, and knowing that major scientific discoveries typically require multiple rocket launches, either as a part of a single investigation, or as separate, complementary investigations. For example, both NASA TRICE-2 and VISIONS-2 missions require a pair of rockets launched within a short timeframe, from two separate launchers, and this is likely to become a more common mode of operation in the future.

Therefore - ASC has decided to expand the launch capabilities in Ny-Ålesund, by adding another rocket launcher, upgrade of telemetry systems and other support systems.

4. NEW SOUNDING ROCKET LAUNCHER

ASC is now in the proses of planning installation of a new rocket launcher in Ny-Ålesund. The new launcher will be in the same category as the existing launcher at SvalRak, supporting sounding rockets up to 45 ton meters. This is equivalent to a Black Brant 10 configuration.

The launcher will be covered with a protective shelter mounted on rail systems, which makes it easy to remove during launch operations. Two heating systems, temperature control and monitoring will be installed to secure the environment for the rocket and payload. These systems are remotely controlled from the Block House.

In addition to the new launcher, we have decided to install a brand new 120 feet tall telescopic wind mast

with four 3D wind sensors. Together with wind balloons, the new wind mast gives us the opportunity to provide very accurate launcher settings during operations.

Regarding connections and cabling the plan is to have both copper and fiber cables available. Not to mention pipelines for the different types of gases needed.

Figur 4 - Installation of the U4 launcher in Ny-Ålesund in 2008

5. TELEMETRY AND COMMUNICATION

For the last few years ASC has invested in new telemetry equipment.

Our telemetry park consist of six telemetry tracking antennas, all fully rigged with the latest technology in receivers and recorders for wide band telemetry. ASC has telemetry over IP for transferring data over wired or wireless networks, as well as decom equipment suitable for viewing data remotely in real time (over internet if necessary).

In 2004 Svalbard (Longyearbyen) was connected to the rest of the world with fiber optics internet access, and in 2015 the fiber cable was extended to also cover Ny-Ålesund. That means any communication whether it is voice over IP or any other bandwidth consumable technologies works flawlessly.

Figur 5 - New 7.3 meter TM antenna at ASC

6. COMBINED OPERATIONS FROM ANDØYA AND SVALBARD

ASC has through several years expanded capability for combined operation, both with respect to competence, personnel and technical systems.

Thus, ASC can now have full crews and setup of systems, both at Andøya or SvalRak, and operate both bases as a combined operation.

7. NEW OPPORTUNITIES FOR THE SPACE SCIENCE COMMUNITY

With years of experience from sounding rocket operations, we felt it was time to take it to the next level.

Our skilled and trained launch personnel, together with the latest range improvements, gives us the ability to operate from two launch bases at the same time.

ASC now offers possibilities for doing simultaneous measurements in different parts of the atmosphere. Not only from Andøya, but from both Andøya and Svalbard at the same time.

And of course now ASC invites the science community to take the advantage of these new capabilities.

Recent steps in the T-Minus DART vehicle development

M. Uitendaal [(1)], H.W. Olthof[(2)]

[(1)]T-Minus Engineering B.V., Molengraaffsingel 12, 2629 JD, Delft, the Netherlands, m.uitendaal@t-minus.nl

[(2)]T-Minus Engineering B.V., Molengraaffsingel 12, 2629 JD, Delft, the Netherlands, h.w.olthof@t-minus.nl

ABSTRACT

The T-Minus DART rocket system is specially designed for scientific research in the middle and upper atmosphere as successor of the unavailable Viper and Super Loki rockets previously used. The higher projected altitude performance of the DART compared to its predecessors, in combination with robust and durable active payloads, enables a completely new way of performing research.

In May 2016, a new test flight of the T-Minus DART, TF-02, was carried out. The test flight was performed at ASK ‘t Harde in The Netherlands. Building on conclusions drawn from previous tests, the test vehicle was launched from the T-Minus Mobile Launch Tower, equipped with a helical Viper II rail that was borrowed from DLR MORABA (Mobile Rocket Base). The test vehicle was designed as a shape-representative of the production model. A miniaturized deployable payload was implemented for analysis and reconstruction of the flight. The flight was completely successful, and valuable data was gathered.

1. INTRODUCTION

The T-Minus DART system is currently under development by T-Minus Engineering. The vehicle is specially designed for scientific research to altitudes of 120 km.

The system is designed for ejectable payloads. These can be:

- Active payloads, with sensors, data processing and telemetry
- Passive payloads such as chaff release and falling spheres

For the test flights of this rocket system a similar approach has been chosen. A small ejectable payload can be used on the up-leg of the flight to perform measurements on acceleration, rotation, temperature and altitude. At apogee these test-payloads are ejected and able to transmit their instantaneous position via telemetry. After that they are able to transmit maximum values. After the test-payload has landed, the system can be located via the telemetry link and a high bandwidth dataset can be downloaded from its on-board storage.

The test-payload can also be equipped with a small amount of chaff to enhance its radar signature for external verification.

The second test-flight of the DART system at ASK ‘t Harde in the Netherlands was called TV-02 or TestVehicle-02. The vehicle was launched at May 20th 2016 to an altitude of 2500 meters.

The aim of this test flight was to validate several technologies:

- Active spin stabilisation: a defined spin-rate was induced by the helical Viper launch rail. Mechanical compatibility between the rail and the vehicle was validated;
- Flight dynamics: improved vehicle stability during flight and the absence of pitch-roll coupling due to active spin stabilization was validated. Simulation software was validated for low altitude flights;
- Separation dynamics: data on dynamics during the separation of booster and dart was collected by means of an on-board Inertial Measurement Unit (IMU).
- Aerodynamics: the aerodynamic characteristics of the vehicle were determined based on flight data, enabling the validation of the aerodynamic model, and comparison between CFD data, wind tunnel data and flight data;
- Electronics and payload ejection mechanism: the full prototype of the flight electronics of the dart, including the new payload ejection system was tested;
- Operations: the operations of TV-02, made identical for the future production of the T-Minus DART, were validated.

2. DESIGN

The design of the TV-02 vehicle is almost identical with the T-Minus DART vehicle, with the exception of the rocket motor. Due to altitude restrictions on ASK ‘t Harde the vehicle needs to be underpowered. Therefore the system is equipped with a standard TM-80 rocket motor of T-Minus. This in-house design uses approximately 4 kg of rocket propellant to propel the TV-02 vehicle to approximately 1900 meters. The downside of this test approach is that the mass distribution throughout the flight is not identical with the real vehicle, due to the fact that only 4 kg of propellant is expelled. Care is taken that at least the first part of the flight has similar inertia and Centre of Gravity (Cg).

The aerodynamic outline of TV-02, as well as the mechanical interface with the launch tower is identical with the T-Minus DART.

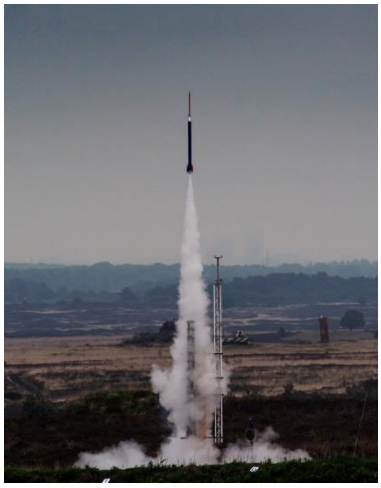

Figure 1. The launch of the TV-02

TV-02 was launched from a Viper rail provided by DLR MORABA, which T-Minus could borrow for testing purposes. The interface between the vehicle and the rail was a part of the validation of this flight, therefore the fin span and motor casing diameter were fixed by the rail. The pitch of the rail is fixed to the original VIPER construction, which leads to restrictions in the design of the DART.

The predecessor of TV-02 was TV-01. This flight was only an aerodynamic outline test with a straight rail. This lead to a flight without spin-up by the launch rail. Instead, canted taps on the booster fins provided rudimentary spin to the system on this vehicle. Unfortunately some pitch roll resonance was observed during this flight due to the variable spin rate. This phenomenon was the primary reason to test active spin by heritage hardware of VIPER the flight of TV-02. The TV-02 flight validated compatibility with the VIPER hardware as well as the launch equipment of T-Minus Engineering.

The payload of TV-02 was equipped with an Inertial Measurement Unit or IMU, which sampled at 62.5 samples per second. A couple of parameters were recorded:

- Accelaration (x, y, z)
- Rotation (x, y, z)
- Magnetic field strengh (x, y, z)
- GPS position
- Pressure
- Temperature

Unfortunately due to software constrains only the first four items were recorded in the on-board storage. The GPS position was used as telemetry output as well, in order to speed up recovery of the payload. The payload was equipped with a very small parachute to limit the descent speed of the total dart to 30 m/s. The payload itself was positioned in the parachute train such that the impact speed was less than 10 m/s.

3. FLIGHT OF TV-02

Part of the operational validation of the system is about performing the same procedures as a normal full-scale launch. These procedures were tested and timed. A normal operation (untrained) is timed at 6.5 minutes, including raising the launch tower to its launch settings.

Figure 2. The preparation of the DART system in combination with the T-Minus Engineering multi-rail mobile launcher

The test flight of TV-02 itself was unfortunately not completely visible during the entire flight, due to cloud cover at approximately 800 meters. Therefore the

rocket motor was not completely spent when the rocket was entering the clouds. The rest of the flight can only be deducted from the data from the test payload. Wind situation during the flight was around 2 m/s from the northwest. This was taken into account for launcher settings for the ballistic impact point as well as the recovered impact point.

4. RESULTS

It is deducted from the fact that the rocket motor is found separately from the dart that the 2 items were separated during flight. The dart was equipped with sensors (the test payload) but the motor casing is not. However it can be seen from the data in the graph of Figure 3 that separation between the dart and the motor casing occurs at 6.2 seconds after ignition.

The motor performance of the flight, based on the total accelerations are nominal.

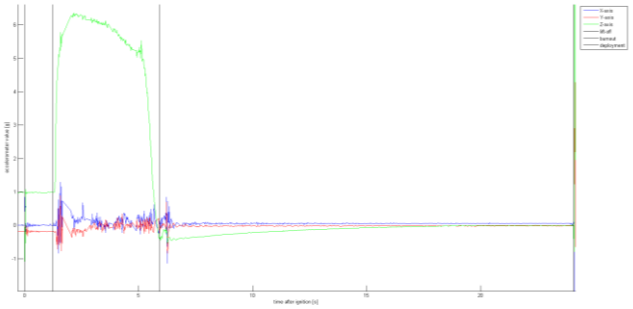

Figure 3. Body fixed accelerations of TV-02

The rotation of the vehicle has been recorded by the gyroscopes and the magnetometers on the vehicle. In this respect, only the data in X and Y axis is relevant, since the Z axis is defined as the direction of flight (negative is up). The two graphs are shown in Figure 4 and Figure 5. The maximum spin rate of the vehicle can be derived from this data which is around 2,2 Hertz at rail exit in the Boosted Dart part of the flight and 0.6 Hertz after separation of dart and booster, which is slightly lower than expected.

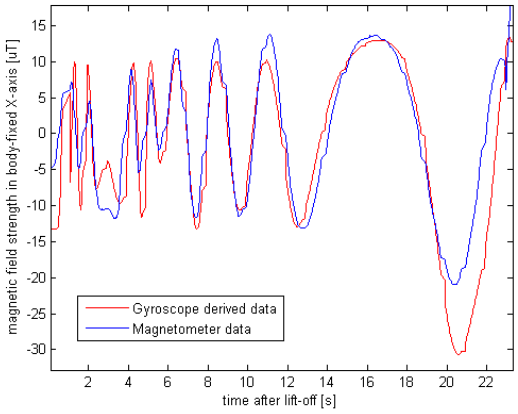

Figure 4. Gyroscope and magnetometer data in X axis

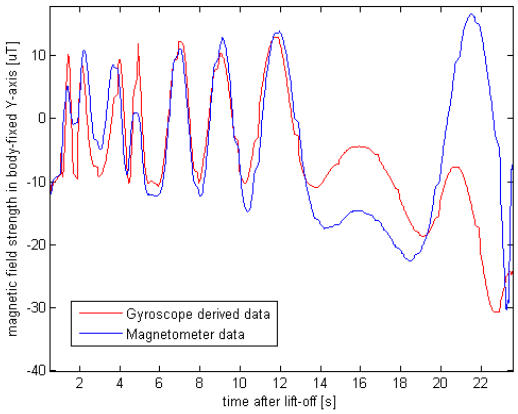

Figure 5. Gyroscope and magnetometer data in Y axis

The simulation software used in this flight is an in-house developed 3DOF simulation which predicts flight trajectory and impact points in ballistic and recovered situation. The burnout mass of booster of the vehicle is significantly bigger that the realistic situation, since it also carries a dummy mass which represents unburned propellant. The flight trajectory in the low altitude case is therefore not the characteristic small parabola normal for boosted dart situations.

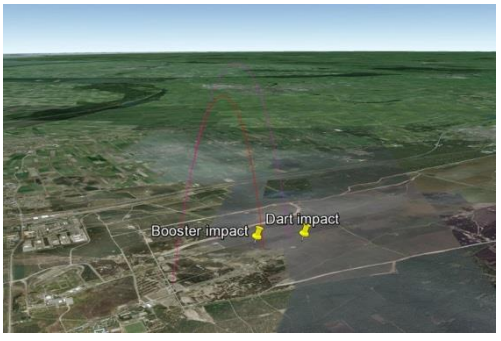

Figure 6. Simulated flight trajectory in combination with the impact points of the vehicle (as flown)

It can be seen in Figure 6 that the calculated impact point are slightly less downrange than the actual points, indicating a slightly lower elevation angle or a small kick-angle in the fly-out trajectory. This needs to be investigated further.

5. CONCLUSION

The test flight of TV-02 validated the T-Minus DART in operation, dynamics, electronics, simulations and aerodynamics. The flight proved that the system is fit for flight, once the full-scale rocket motor has been validated. Certain factors, such as supersonic aerodynamics and thermodynamics are only possible to test on full-scale and will be dealt with during the first full scale test flights, which are expected in end 2018.

Recent steps in the T-Minus DART motor development

H.W. Olthof[1], M. Uitendaal [2]

[1]T-Minus Engineering B.V., Molengraaffsingel 12, 2629 JD, Delft, the Netherlands, h.w.olthof@t-minus.nl

[2]T-Minus Engineering B.V., Molengraaffsingel 12, 2629 JD, Delft, the Netherlands, m.uitendaal@t-minus.nl

ABSTRACT

The T-Minus DART rocket system is specially designed for scientific research in the middle and upper atmosphere as successor of the unavailable Viper and Super Loki rockets previously used. The higher projected altitude performance of the DART compared to its predecessors, in combination with robust and durable active payloads, enables a completely new way of performing research.

To reach the desired altitude performance with a small and compact vehicle, it is essential that the solid propellant rocket motor, or Booster, is mass- and volume efficient. Next to that, safety and ease-of-use, and limited manufacturing cost are important requirements. The Booster design is developed in-house by T-Minus Engineering, and several innovative concepts are applied, such as use of light weight composite materials.

A test campaign was conducted to validate the most important concepts, materials and construction techniques. Next to that, a propellant development program is being conducted, wherein the formulation and production process are adjusted to the requirements.

1. INTRODUCTION

T-Minus Engineering is developing the DART system s a cost-effective and easy-to-use rocket system for performing in-situ measurements in the middle atmosphere and lower thermosphere. A key element of this system is the multifunctional booster: a small-diameter solid rocket motor with a high propellant fraction, containing a composite propellant with high specific impulse.

The motor is designed for adequate performance and a low manufacturing cost. A holistic optimization approach of the complete vehicle and infrastructure is used in the design process, taking into account all facets in the production- and operation cycle of the DART, from propellant formulation, to flight performance, assembly procedure, logistics and operations.

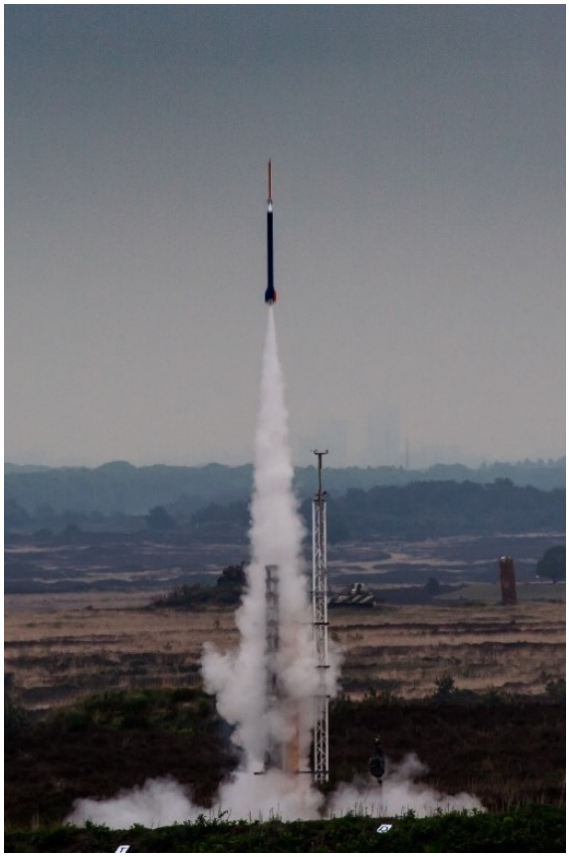

2. DESIGN REQUIREMENTS

System-level considerations have led to a number of requirements on the design of the DART booster motor, affecting the design of the various motor elements.

Ground infrastructure compatibility – The DART rocket shall be compatible with existing infrastructure, notably the Viper helical launch rail that is widely available. This limits the motor outer diameter and fin configuration

Performance – The motor is to provide sufficient impulse to launch the payload dart to the target apogee altitude of 120+ km. This is verified by means of validated flight simulation software. Depending on parameters such as propellant density, vehicle dry weight, dart diameter and burn time, a total impulse of approximately 50 kNs is needed.

Thrust profile – A burn time of 5 seconds is aimed for. This limits the acceleration of the payload to 60 g's, which is deemed the lower limit for electronic payloads to survive the launch.

Minimal production cost – this affects mainly the propellant configuration, as this is the highest cost element of the rocket system. Also the dry mass of the motor is an important parameter, as a lower dry mass leads to a lower propellant mass and therefore lower cost.

Ease of operation – Operation of the rocket system is a major cost driver. For this reason, simple (ground) operations have been be aimed for.

3. MOTOR ELEMENTS

The complete motor consists of various elements, the design considerations of which are elaborated in this chapter.

Propellant and ballistics

The thrust profile and operating pressure of the motor are determined by the propellant composition and -geometry. As the propellant production is the most cost-intensive part of the vehicle value chain, a simple propellant geometry is chosen: the multi-bates grain configuration. This consists of a number of propellant grains with a cylindrical core, stacked in axial direction in the motor casing. The burning surfaces of the grains are the inner perimeter as well as the grain ends. By choosing the dimensions of the grains, the burn profile can be altered. The number of grains then determines the thrust that is produced. This concept has two advantages. Firstly, the motor is multifunctional: various versions with different thrust levels can be made with the same grains, and at minimal design effort. Next to that, because the length of the grains is small and the shape of the core is simple, the production process is much simpler, and the chance of defects is smaller. The concept also has a disadvantage: due to the fact that the end faces of the grains are burning, the casing is subjected to a significant heat load. This problem is solved in the casing design, as explained in a later section.

As the propellant grain burns radially outward, the burn time of the motor is dependent on the web thickness, as depicted in Figure 1, and the regression rate of the propellant

$$t_b = \frac{\tau_w}{r} \qquad (1)$$

The web thickness is defined by the outer diameter and core diameter of the grain.

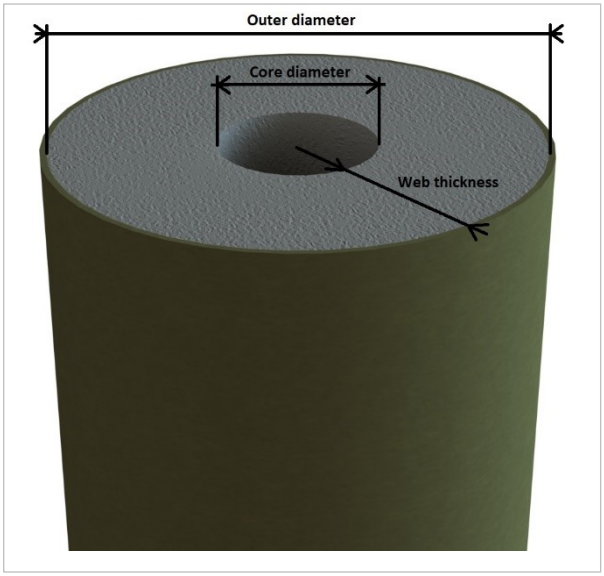

Figure 1: Definition of web thickness

The outer diameter is restricted by the maximum diameter of the motor, driven by the launcher compatibility requirement. The core diameter is limited by the nozzle throat diameter: it must be substantially larger in order to avoid excessive erosive burning of the propellant. The throat diameter determines, in combination with the ballistic parameters of the propellant, the operating pressure of the motor. With these restrictions in mind, it follows that only a relatively slow-burning propellant will be suitable for the DART motor. More details on this are given in Chapter 5. An ammonium perchlorate composite propellant is chosen, for its high specific impulse and density, and extensive knowledge base. The formulation is optimized for use in the DART motor.

Casing

The casing of the motor fulfils four functions:

- Containment of the propellant and combustion gasses
- Containment of combustion heat
- Transfer of the aerodynamic loads
- Interface with the launch rail

For the DART motor, carbon fibre composite is chosen as casing material, for its high specific strength and, more prominently, stiffness. This is manufactured in a filament winding process, which is highly efficient for pressure vessel geometries. In common rocket motor casings, the components for the first two functions are separated: the outer casing is designed to carry the

internal pressure, while a separate liner is included to shield the outer casing from the internal combustion temperatures. In this case, it is decided to incorporate both functions in the same part, by adding layer of ablative material on the inside of the tube in the filament winding process. This is possible because of the relatively short burn time of the motor. The ablative layer absorbs the radiation energy of the combustion, which causes a chemical endothermic reaction. The heat is thus not transferred to the load-carrying outer layer, leaving the pressure vessel intact. The high specific stiffness of the carbon fibre material is needed to withstand the aerodynamic moment caused by the booster fins, without bending to the extent that aeroelastic phenomena occur.

Forward closure
The interface between the motor and the payload dart is formed by the forward closure. This is a rotationally symmetric, metal part, which also forms the closure of the motor pressure vessel. The interface is formed by two cylindrical faces with precise tolerances, providing the sliding connection necessary for a smooth payload separation.

Nozzle
The nozzle of the rocket motor is exposed to the combustion temperature of approximately 3500 K. For this reason, the flow channel is made of isostatic graphite, which is able to withstand this load. Because of its brittleness, the flow channel is inserted in an aluminium holder. The problem of difference in thermal expansion between the two materials is solved by a layer of flexible rubber adhesive between the parts.

Igniter
As a safety-critical interface with the ground infrastructure, the igniter is designed for maximum simplicity of operation. Instead of being connected to the forward closure, as is most common, the igniter is inserted via the nozzle side of the motor. This enables the operator to perform the mating of motor and igniter, a safety risk increasing operation, to an as late as possible moment in the countdown procedure. This keeps the vehicle in a relatively safe state until the last operational phase. The igniter consists of a squib and a container with a small amount of hot-burning pyrogen ignition pellets. The squib has a no-fire condition compliant with regulations on launch sites: 1 amp, 1 W for 5 minutes.

4. MATERIAL TESTS

The technical feasibility of several key concepts of the rocket motor construction has been verified in a number of proof-of-principle tests.

Firstly, the concept of the linerless motor casing was investigated. To this end, several composite materials were subjected to a heat flux, and their ablation characteristics investigated. The chosen materials were carbon fibre/epoxy and glass fibre/epoxy. For the latter material, also the use of alumina flame-retardant filler was investigated.

Two test setups were used. In the first test series, a sample of material of defined thickness was clamped into a frame and an acetylene flame was impinged on it. The temperature of the cold side was monitored and logged until burn-through was observed.

In the second test series, a small-scale rocket motor was used in which several material samples were placed downstream of the propellant in the combustion chamber. A defined thickness of ammonium perchlorate propellant, with similar burn characteristics of the DART propellant was ignited, providing a heat flow and pressure over a defined period of time.

It was found that the performance of the carbon fibre materials was superior to that of glass fibre, and that the addition of alumina lead to lower ablation and better heat resistance. The ablation was sufficiently slow for the material to be used in the DART rocket motor, during its 5-second burn time. Both of these materials can be accommodated in the manufacturing process. Further details on the tests and their results are provided in [1].

The overall construction concept of the motor was investigated by means of tests as well. A small-scale motor was developed, containing up to 350 grams of commercially available ammonium perchlorate composite propellant. The casing consisted of liner material, wrapped with epoxy-impregnated 45/45 glass fibre as pressure vessel. Three tests were conducted, at different burn times and heat fluxes. A pressure transducer was connected to the combustion chamber and a standalone datalogger used to store the pressure measurements.

For test 1, a standard single bates-grain was used. Two spacer rings were included, separating the propellant from the forward closure and the nozzle, as these are the problem areas expected in the design of the real motor. A non-metallized propellant was used in this case, causing less slag build-up, offering better post-flight

inspection possibilities. This lead to a decreased combustion temperature, of approximately 2250 K. Because of the limited propellant mass and motor diameter, burn time and operating pressure of the full-scale design could not be achieved. The pressure curve that was recorded is given in Figure 2. Post-test analysis shows no burn-through of the casing, only minor charring of the carbon fibre liner and no visible damage to the nozzle area. No signs of leakage were found in the seal areas.

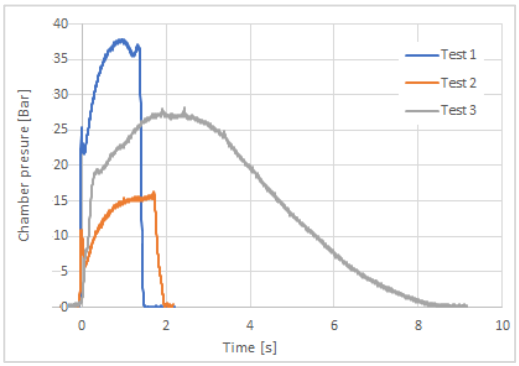

Figure 2: Time-pressure traces of burn tests

Tests 2 and 3 were conducted in a similar way, with a different propellant geometry. In this case, metallized propellant was used, yielding a combustion temperature of 3180 K. The propellant was shaped in slot-burner geometry, such that one strip of the casing was exposed to the heat of the combustion throughout the burn. For test 2, a small slab was used, leading to a burn time of 2 seconds, at a maximum pressure of 15 Bar, as shown by the graph in Figure 2. Post-test inspection reveals some charring of the casing in the downstream area of the nozzle, as displayed in Figure 3. The affected depth is estimated approximately 0.3 mm. At other areas, no apparent damage was found.

Figure 3: Slight deterioration of casing after test 2

Test 3 was conducted with a larger slab of propellant, leading to a burn time of approximately 7.5 seconds at a maximum pressure of 27 Bar. As in previous tests, no burn-through was observed. In the post-test inspection, extensive deterioration of the liner material was discovered, as shown in Figure 4, but not throughout the complete thickness of the liner material. No extensive degradation was found in the slot area, indicating that the ablation process speed is higher with an increasing flow velocity.

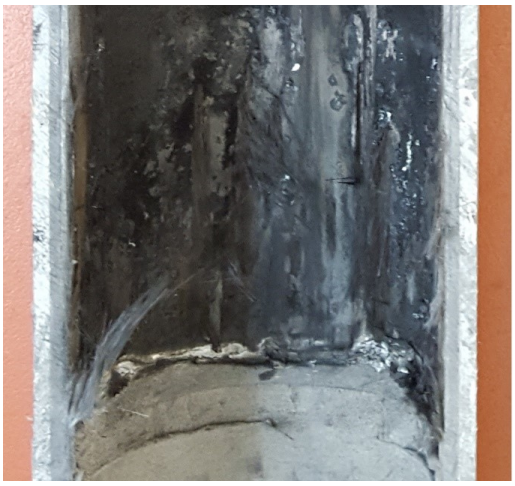

Figure 4: Deterioration of casing after test 3

5. PROPELLANT DEVELOPMENT

As mentioned before, a metalized ammonium perchlorate composite propellant (APCP) is chosen for the DART booster. Reasons for this are its high density, high performance and well-documented knowledge base. A project was started to develop a propellant formulation with suitable characteristics for use in the DART vehicle. Important parameters are:

- Performance
- Ballistic parameters (regression rate)
- Manufacturability, availability and cost

The performance requirement has been identified as being the least stringent: the majority of known APCP formulations were found to have adequate performance. For the ballistic parameters, it was found that the required regression rate is low, because of the small available web thickness and desired long burn time. The regression rate of a formulation can be steered with both the particle size distribution of the oxidizer and the solid load: coarse oxidizer particles and a low solid load lead to a low regression rate. As an added benefit, it increases the manufacturability. A low solid load generally leads to lower performance, both in terms of propellant density as well as specific impulse, but these

requirements are less stringent, as indicated before. Also a lower combustion pressure leads to a lower regression rate. This can be altered with the propellant geometry and nozzle design.

The mechanical properties of the propellant also have to be sufficient to withstand the handling- and launch loads. Although the acceleration of the vehicle is relatively high, with 60 g's, the vibrations at low frequencies, where the propellant is most sensitive, are low because of the small size of the vehicle. Next to that, the actual loads on the propellant are also relatively low because of its small mass.

Additional considerations are the availability and cost of the propellant. Also here, the choice for coarse particle oxidizer is beneficial: it decreases the handling safety risk of the chemical, and therefore its price. Next to this, the use of export-restricted chemicals is avoided.

Several propellant samples have been prepared and a number of combustion- and mechanical tests have been performed successfully. The detailed results of these tests are classified.

6. CONCLUSIONS

A feasible design for the DART solid rocket booster has been made, with focus on suitability, manufacturability and price. The functionality of several key design concepts has been verified by means of small-scale tests. The detailed design will be completed in the near future, and validated in a number of full-scale static tests, in which the performance of the motor will be evaluated. When these are successfully concluded, it is deemed qualified for flight. A production plant will be established where the motor can be manufactured efficiently. The first real flight use of the DART motor will be in the validation campaign of the complete DART vehicle, planned in the end of 2018.

7. REFERENCES

[1] S. Westerlund, *Design of ablative insulator for solid rocket booster*, 2015, M.Sc thesis , KTH school of engineering technology and management

MULTIPLE EQUIAXED DENDRITE INTERACTION INVESTIGATED ON MASER-13

Laszlo Sturz, Martin Hamacher, Janin Eiken, Gerhard Zimmermann

ACCESS e.V., Intzestrasse 5, 52072 Aachen, Germany, Email: L. Sturz@access-technology.de

ABSTRACT

Nucleation, crystallographic orientation, growth and interaction of equiaxed dendritic solidification structures have been investigated experimentally, and by microstructure modelling. Experimentally, this was achieved by solidifying the organic transparent analogue material Neopentylglycol-30.0wt.-%(d)Camphor, which crystallizes with a dendritic morphology similar to metallic alloys. The experiment was carried out onboard the sounding rocket MASER-13 under about six minutes of reduced gravity conditions, where convection of the melt and sedimentation of the solid crystals are negligible. The experimental conditions (thermal gradient, cooling-rate) in the sample were adapted to obtain multiple equiaxed dendritic structures, which interact via their solutal fields at later stages of the experiment. The structures have been observed with two different optical systems to analyze the global and microscopic features of solidification. Here, we complement some previous experimental results and compare the first stages of equiaxed dendritic solidification to microstructure simulation. As one highlight, we find that the favorable crystallographic orientation of the dendrites deviates from the regular case and causes equiaxed growth with eight instead of six arms. The phase-field simulations validate this result, where the changed crystallographic orientation is devoted to a significant change in the anisotropy of interface properties.

1. INTRODUCTION

Equiaxed dendritic grain structures are very common to solidification of technologically relevant alloys from their molten state. Equiaxed growth with equivalent growth directions of the dendritic arms occurs often for isolated dendrites and at experimental conditions of low thermal gradient and high cooling-rate imposed on the material. Starting from heterogeneous nucleation on a substrate, inoculant or impurity the solid phase is forming in the surrounding liquid phase, increases in volume and tends to protrude needle-like arms into the undercooled liquid, the primary dendrite arms. The directions of primary dendrite arm growth relate to the crystal structure of the solid solution phase. In solids with underlying cubic crystal structure, these preferred crystallographic orientations are often normal to the six faces of the unit cell, leading to a microstructure composed of six equivalent primary arms ({100}-family), growing perpendicular to each other and with higher order side arms growing perpendicular to and originating from the lower order arms. The selection of crystallographic orientation in this specific, regular case is mostly due to a minimum in surface tension along the {100}-directions. Nevertheless, it is well known experimentally and from modeling, that in some systems with cubic unit cell other crystallographic orientations are preferred, like {110} or {111}, due to composition (or other) related changes in the surface-tension anisotropy distribution and leading to different equiaxed structures with more than six arms and different angles than 90° between the arms [1]. For some technical applications, the properties of the material are strongly dependent on the crystallographic orientation, i.e. creep-deformation in some turbine blades [2] and magneto-striction [3], motivating studies on the orientation selection.

Following a first stage of isolated growth with a certain selected crystallographic orientation, thermal or solutal interaction between growing equiaxed dendritic structures arrests their growth and is a key phenomenon, determining the final grain structure [4,5]. In addition, gravity may impose settling or floatation of the equiaxed crystals, transportation of crystals or advection of heat and mass by convective motion and the presence of a metallostatic pressure [6]. Reduced gravity solidification experiments avoid many of these complicating aspects and serve as benchmarks for numerical modelling of crystallization on multiple length scales under conditions dominated by diffusion for heat and mass transport, as well as negligible relative motion. The ESA microgravity application program CETSOL (Columnar to equiaxed transition in

solidification processing) investigates columnar and equiaxed grain formation and their transition (CET) in different alloy systems during transient solidification experimentally and by modelling [7,8]. MEDI (Multiple Equiaxed Dendrite Interaction) is a sounding rocket experiment performed on MASER-13 within the CETSOL project and focuses specifically on equiaxed dendrite nucleation, growth, crystallographic orientation and interaction via solutal fields in the transparent organic model alloy Neopentylglycol-(d)Camphor (NPG-DC).

A summary of the alloy properties, the experimental set-up and procedure, as well as first experimental results and analysis are given in [9] and are referred to in this paper. The analysis includes investigations on interaction between a pair of equiaxed dendrites, leading to their deceleration, an analysis of the thermal evolution, the kinetic law for isolated equiaxed growth and the temporal evolution of number of equiaxed dendrites and their average projected area. Many of these results are important input parameters to modelling from microscopic to macroscopic (container size) length scale. Here, we recall very briefly the main experimental features in section 2, complement with some experimental results in section 3 and focus on the comparison of crystallographic orientation and kinetic law with microstructure simulation in section 4 to conclude in section 5.

2. EXPERIMENTAL PART

The core part of the experiment is shown in Figure 1, see also [9]. The experimental volume has dimensions of height of about x=10 mm, depth of y=3 mm and width of z=13 mm. The volume size was selected to allow for 3D growth of sufficient equiaxed crystals under precise experimental control within the available microgravity period of about six minutes.

To control the experiment, Peltier elements were employed on the top (hot, +x) and bottom (cold, -x) side. After melting and thermal mixing by temperature inversion, a small thermal gradient of G_x=(0.3±0.1) Kmm^{-1} is applied and stabilized on ground. This small gradient increases experimental control, when compared to a purely isothermal case. Later and before lift-off of the rocket, constant cooling-rates of 0.75 Kmin^{-1} at hot and cold side are applied simultaneously at t=- 235 s (before lift-off=LO). This time was selected to have crystallization appearing only in the microgravity period, where all effects of rocket launch, payload separation and rotation can be neglected or have been faded away.

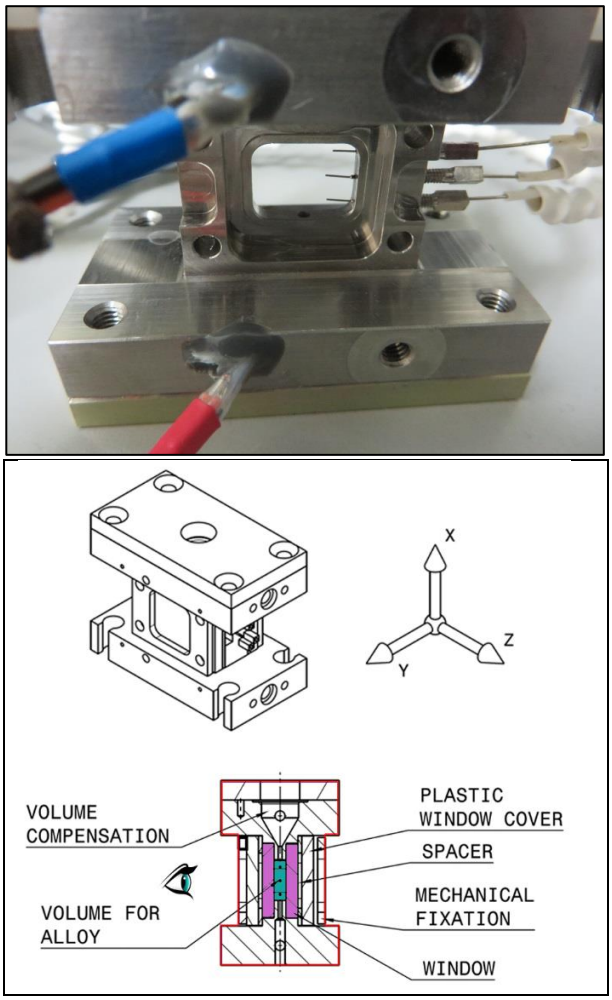

Figure 1: Experiment container (top) and schematic drawing with coordinate system (bottom), experimental volume filled with the alloy (cyan).

Figure 2 shows the phase diagram and relevant phase-transitions of the NPG-DC system, taken from [10]. For MEDI, a NPG-0.30 wt.-fraction DC was selected and equiaxed dendritic growth occurs in the undercooled melt at some degree Celsius below the liquidus-temperature of 79.3°C, the latter taken from the DSC-measurements [10]. The material is solid below the eutectic temperature of about 53°C.

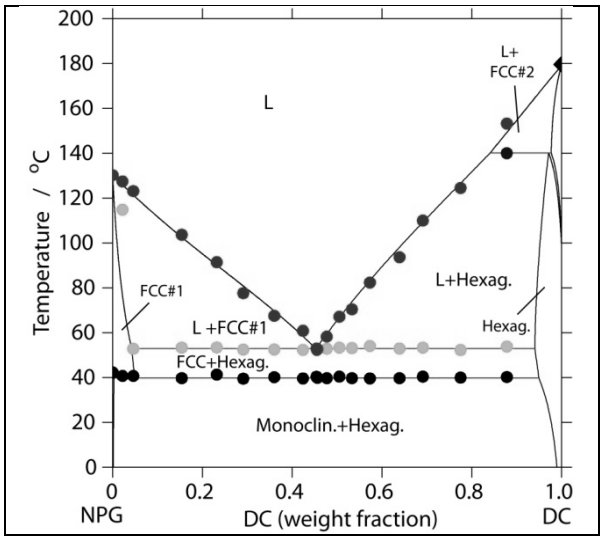

Figure 2. Phase-diagram of NPG-DC. Alloy chosen for MEDI is NPG-0.30 wt.-fraction DC. L=Liquid, FCC = face-centred cubic (phases).

3. RESULTS

Figure 3 shows a series of 8-Bit greyscale overview CCD-images obtained from the side-view camera with field of view of 13.6 mm width, 10.625 µm/pixel optical resolution and depth-of-field covering the full depth of the sample. Three thermocouples have been inserted into the bulk sample and measure the thermal evolution in-situ; details are discussed in [9]. As can be seen, no crystals are present at the beginning of the low-gravity period and the sample is liquid completely. Small dark spots are dust particles outside of the experimental volume. Fraction solid increases in time and the mushy zone is developing. Equiaxed dendrites coalesce and form a network developing from the bottom of the cell.

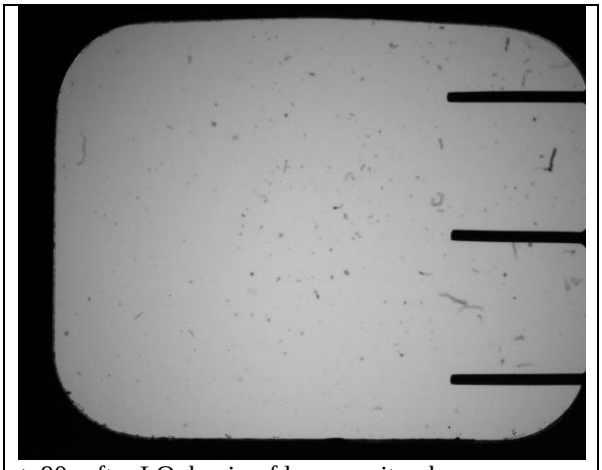

t=90s after LO: begin of low-gravity phase.

t=370s after LO.

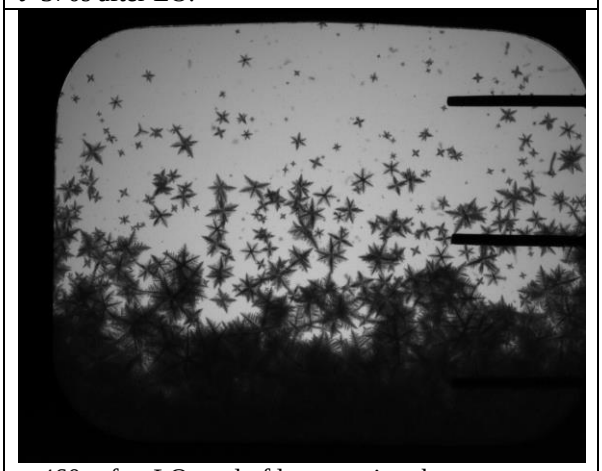

t=460s after LO: end of low-gravity phase.

Figure 3. Overview images of multiple equiaxed dendritic growth during the reduced gravity period.

From the images shown in Figure 3, the number of equiaxed dendrites and their average projected area have been determined, the results are summarized in [9]. Furthermore, the nucleation temperatures were analysed during the complete microgravity period, leading to a cumulative distribution, shown in Figure 4, with an average (standard deviation) of 8.39 K (0.60 K) for a total number of N=456 equiaxed crystals [9].

We point out, that the measured distribution in Figure 4 is related to the application of a cooling-rate of 0.75 $Kmin^{-1}$. This may represent a subset of all available nucleation temperatures, if some of them at higher undercooling have not been activated, since the cooling-rate is not high enough to obtain sufficient undercooling in the melt. In addition, the distribution is not at steady-state, as is shown for the temporal evolution of the average and standard deviation values of the nucleation undercooling during the low-gravity period in Figure 5.

The later were calculated from all nucleation events within a time-interval of 10 seconds.

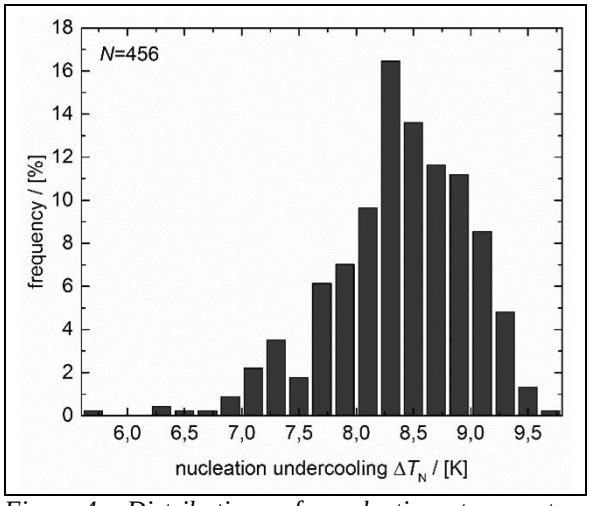

Figure 4. Distribution of nucleation temperatures during transient nucleation after application of the cooling-rate of 0.75 Kmin^{-1}.

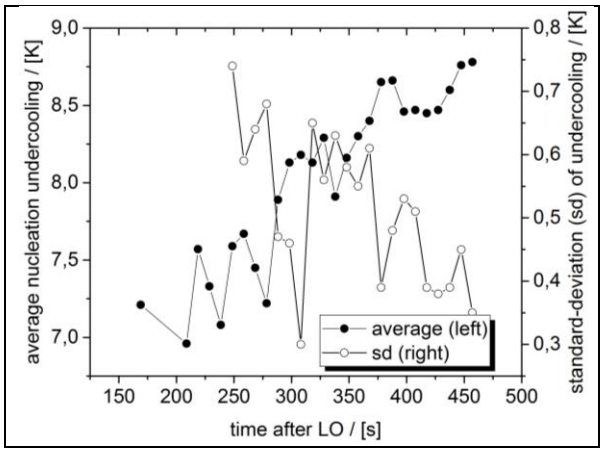

Figure 5. Temporal evolution of average and standard-deviation of the nucleation undercooling distribution after application of the cooling-rate of 0.75 Kmin^{-1}.

The crystallographic orientation of the experimental dendrites is identified to be close to {111}, in which the eight primary dendrite arms grow along the diagonals of the face-centred cubic unit cell of the NPG solid-solution crystal. The dendrite tips have a trigonal symmetry and side arms grow at some angle against the primary arm, which is different from 90°. This is shown as an example in an image in Figure 6, which was recorded using the microscopic optics. The field-of-view (FoV) is 1.44 mm wide with an optical resolution of 0.9 µm/pixel. The position of the FoV (x- and z-coordinates) can be selected manually by telemetry from ground. A sequence of images was then recorded automatically at equally spaced focal positions (in y direction) with focal distance of about 6 µm. Figure 6 is thus one image of such a sequence, where some parts of the dendrite appear to be focused and some other are out of focus.

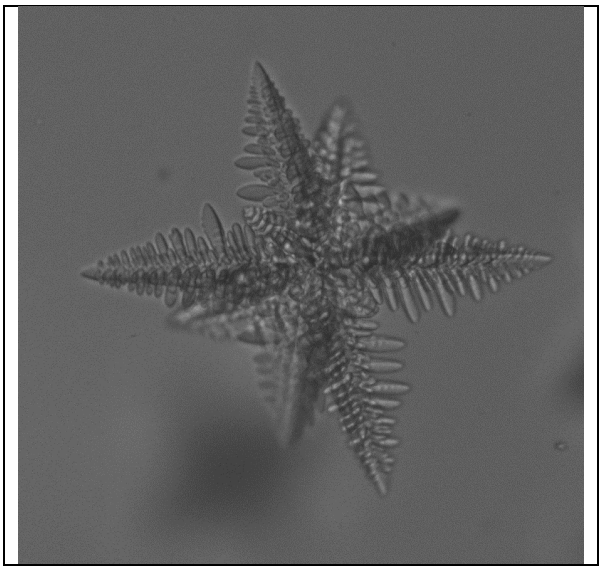

Figure 6. Microscopic image of an equiaxed dendrite taken during a focal scan through the depth of the sample. Image width is 1.44 mm.

4. PHASE-FIELD SIMULATIONS

Phase-field simulations of solidification compute the microstructure evolution for a given set of thermodynamical and thermophysical properties, here taken from [9], and shown in Table 1.

Table 1: Alloy properties of NPG-30.0 wt.-%DC

Liquidus-slope m_L	-1.59±0.10 K/wt.-%	[10]
Partition coefficient k	0.072±0.01 wt.-/wt.-%	[10]
Liquidus temperature T_L	79.3±1.0 °C	[10]
Eutectic temperature T_E	52.9±0.5 °C	[10]
Solute diffusion coefficient liquid D_L	97±15 µm^{2}s^{-1}	[11][(a)]
Gibbs-Thomson-coefficient Γ	(7.5±0.7) 10^{-8} Km	[12][(a)]
Entropy of fusion ΔS	(1.08±0.06)10^5 JK^{-1}m^{-1}	[12]

(a) For eutectic liquid at c_E=45.3 wt.-% DC and T=T_E

The evolution of the complex solid-liquid interface follows basic thermodynamic principles, obeys mass conservation at the interface and takes into account solute diffusion in the liquid. Here, heat diffusion, release of latent heat and chemical diffusion in the solid were neglected. Furthermore, as basic ingredient, the anisotropies of solid-liquid interfacial energy and of

kinetic attachment need to be specified. Without better knowledge, a typical value of 1 pct. was assumed for both. The anisotropy functions were defined such, that the minima correspond to the {111}-directions. Mathematically, the anisotropies then change sign from positive to negative, when describing the change from {100} to {111} directions and using the same set of basic functions (spherical harmonics). As first approach, the simulations were carried out with the parameters given above, zero thermal gradient (as opposed to the small thermal gradient used experimentally) and without application of a cooling-rate. We assume that the influence of these changes on the final results are of second order. The numerical grid resolution of 0.3 µm was selected to be smaller than the estimated final tip radius. A constant undercooling of 6.5 K was applied corresponding to an experimental dendrite tip velocity of about 1.2 μms^{-1} (taken from a fit of the kinetic law) see [9]. Thus, we aim to compare one data point from the fitted kinetic law curve [9] to the simulations.
Figure 7 shows the result of the phase-field simulation for a selected time-step at steady-state conditions, where only the solid-liquid interface is shown without the concentration field of (d)Camphor in the liquid outside the solid dendrite.

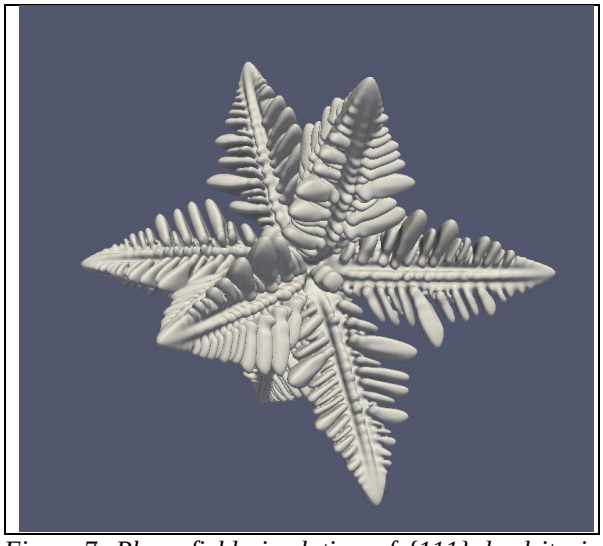

Figure 7. Phase-field simulation of {111}-dendrite in 3D.

Very close agreement is found to the experimental result (Figure 6), regarding the dendrite morphology. This is taken as indication, that the a-priori selection of {111} crystallographic orientation is correct, although higher order anisotropy functions and parameters may have some minor influence, too. Nevertheless, with respect to kinetics, the dendrite tip velocity is about 5 times larger in the phase-field simulations. Possible reasons for this deviation can be devoted to (a) an incorrect choice of too large anisotropy-parameters (b) a virtually too high chemical diffusion coefficient. The value selected for the latter was taken from indirect measurements of the lamellar spacing in eutectic growth, but for different composition and temperature [11]. More detailed simulations will be carried out to cross-check and validate these assumptions.

5. CONCLUSIONS

Multiple equiaxed dendritic growth has been investigated within the organic alloy NPG-30.0 wt.-%DC on-board the sounding rocket MASER-13 with emphasis on nucleation and growth of dendrites. Following conclusions can be drawn from the results:

- Multiple equiaxed dendrite growth was achieved in the reduced gravity period of the sounding rocket and the hardware worked nominally.
- Interaction between the dendrites was clearly observed as deceleration of approaching dendrite arms [9].
- The nucleation temperature distribution was determined for the cooling-rate of 0.75 $Kmin^{-1}$ and found to be slightly changing within the low-gravity period due to approach to steady-state conditions.
- Dendrite morphology of isolated dendrites is found to be close to {111}, which is revealed by assuming negative anisotropy coefficients in a phase-field model.
- Phase-field simulations validate the dendrite shape, but kinetics were overestimated in a first approach, mostly due to incorrect assumptions for the input-parameters.

As outlook, we intend to perform more detailed phase-field simulations and a re-determination of the chemical diffusion coefficient.

ACKNOWLEDGEMENTS

This work was financially supported by the German Space Agency DLR under BMWi/DLR grant no. FKZ 50WM1443 and ESA funding under CETSOL-contract AO-99-117, which is gratefully acknowledged. The

authors appreciate the Team of Airbus D&S for the hardware development and support during the preparatory and final experiments. SSC, DLR-Moraba and OHB System AG are acknowledged for mission support at Esrange/Sweden.

REFERENCES

1. Haxhimali, T., Karma, A., Gonzales, F., Rappaz, M. (2006), Orientation selection in dendritic evolution, *Nat Mater*. **5**, 660-664.
2. Pollock, T.M., Tin, S (2006), Nickel-Based Superalloys for Advanced Turbine Engines: Chemistry, Microstructure, and Properties, *J. Propul. Pow*er **22**, 361-374.
3. McKnight, G.P., Carman, G. P. (2002) [112]-oriented Terfenol-D composites, *Mat. Trans.* **43**, 1008-1014.
4. Martorano, M.A., Beckermann, C., Gandin, C.-A. (2003) A Solutal Interaction Mechanism for the Columnar to-Equiaxed Transition in Alloy Solidification *Met. Mat. Trans. A* **34A**, 1657-1674.
5. .Bogno, A., Nguyen-Thi, H., Reinhart, G., Billia, B., Baruchel J. (2013) Growth and interaction of dendritic equiaxed grains: In situ characterization by synchrotron X-ray radiography, *Acta mat.* **61**, 1303-1315.
6. Jarvis, D.J., Minster, O. (2006) Metallurgy in Space, *Mat. Sci. For.* **508**, 1-18.
7. Sturz L. et al. (2012) ISS—Experiments of Columnar-to-Equiaxed Transition in Solidification Processing, Proceedings of a symposium held at the 141st TMS 2012 Annual Meeting and Exhibition, Orlando, Florida, March 11–15, 56-62.
8. Zimmermann, G. et al. (2014) Columnar-to-Equiaxed Transition in Solidification Processing of AlSi7 alloys in Microgravity – The CETSOL project, *Mat. Sci. Forum* **790-791**, 12-21.
9. Sturz, L., Hamacher, M., Zimmermann, G. (2017) In-situ observation of equiaxed dendritic growth and interaction in microgravity, Proceedings of the 6th Decennial International Conference on Solidification Processing, 25th-28th July 2017, Beaumont Estate, Old Windsor, UK, 300-303.
10. Witusiewicz, V.T., Sturz, L., Hecht, U., Rex, S. (2004) Thermodynamic description and unidirectional solidification of eutectic organic alloys: III. Binary systems neopentylglycol-(D)camphor and amino-methyl-propanediol-(D)camphor, *Acta Mater.* **52**, 5519-5527.
11. Vitusevych, V.T., Sturz, L., Hecht, U., Rex, S. (2014) Lamellar coupled growth in the neopentylglycol-(D)camphor eutectic, *J. Cryst. Growth* **386**, 69-75.
12. Bayram, U., Aksoz, S, Marasli, N. (2012). Solid-liquid interfacial energy of neopentylglycol solid solution in equilibrium with neopentylglycol-(D) camphor eutectic liquid, *J. Cryst. Growth* **338**, 181-188.

THE STERN PROJECT – HANDS ON ROCKETS SCIENCE FOR UNIVERSITY STUDENT

Schüttauf, Katharina [(1)], Stamminger, Andreas [(2)], Lappöhn, Karsten [(3)]

[(1)] Mobile Rocket Base (MORABA), German Aerospace Center (DLR), Oberpfaffenhofen, 82234 Wessling, Germany, Email: Katharina.Schuettauf@dlr.de
[(2)] Mobile Rocket Base (MORABA), German Aerospace Center (DLR); Oberpfaffenhofen, 82234 Wessling, Germany, Email: Andreas.Stamminger@dlr.de
[(3)] Space Administration, German Aerospace Center (DLR), Königswinterer Str. 522-524, 53227 Bonn, Germany, Email: Karsten.Lappoehn@dlr.de

ABSTRACT

In April 2012, the German Aerospace Center DLR initiated a sponsorship program for university students to develop, build and launch their own rockets over a period of three years. The program designation STERN was abbreviated from the German "STudentische Experimental-RaketeN", which translates to Student-Experimental-Rockets.

The primary goal of the STERN program is to inspire students in the subject of space transportation through hands-on activities within a project structure, to motivate universities to supervise and support the student projects with the help of financial support and to increase the lecture activities in the field of launcher and propulsion systems. The STERN program incorporates a space mission project life cycle, including preliminary, critical, integration and acceptance reviews, a thorough integration and testing campaign, launch and follow up activities.

The program is funded by the German Federal Ministry of Economics and Technology (BMWi) and managed through the DLR Space Administration.

The first STERN cycle is now almost finished. During the first cycle more than 460 students (status: February 2016) have been involved in the program. Furthermore eight rockets have been launched during three campaigns. The paper presents an overview of its hands-on activities, highlights technical results and the operational improvements over the years.

INTRODUCTION

This document provides an overview about the first STERN cycle and the three launch campaigns at ESRANGE near Kiruna Sweden. The following section introduces the STERN program, the used rockets with their hybrid and solid rocket motors as well as the operational activities during the campaign.

STERN PROGRAM

The aim of the STERN program is to inspire students in the subject of space transportation through hands-on activities, and to motivate universities to supervise and to give financial, infrastructure and laboratory support and to increase the lecture activities in the field of launcher and propulsion systems. This will ensure the availability of highly educated professionals in launcher systems for the future also taking into account Germany`s crucial part in the Ariane program.

In April 2012, the German Aerospace Center DLR launched the STERN program, which is supported by funds from the German Federal Ministry of Economics and Technology (BMWi) and conducted by the DLR Space Administration. Three DLR institutions at Oberpfaffenhofen, Lampoldshausen and Trauen, together with the space administration, supervise work and launch campaigns and hold reviews and conducting workshops.

Figure 1: Logo of STERN

The program is open for all German universities which offer aerospace engineering lectures and offer students the possibility to develop, build, test and launch their own rockets in university teams. The focus is on the development of the complete vehicle system within three years.

The student's should develop their knowledge in the following disciplines:

- Rocket propulsion and testing
- Aerodynamics,

- Flight dynamics (e.g. flight stability, loads, trajectory calculation and optimization, etc.)
- Mechanics and lightweight structures
- Telemetry, data acquisition
- Testing of the rocket and its subsystems
- Application of professional tools (e.g. CAD, CFD, FEM)
- Project Planning and organization (time, budget, technical risks, etc.)
- Launch preparation and operation
- Soft skills (different disciplines and customers)

From the beginning of the project until the launch of the rocket, the students have to conduct several reviews in which they will have to present the current status of their work to a review team consisting of DLR Space Administration, DLR experts from Mobile Rocket Base (MORABA) and the DLR Institute of Space Propulsion, but also further external experts if required. This aims to increase the chance of achieving the mission goal of the student teams and improve safety during development and launch of the vehicle. At Lampoldshausen the M11.5 Student Test Field has been set up and it is available for performing motor test campaigns under the supervision of engineers and scientists.

The requirements for participation in the STERN program are

1. Formal requirements
   - German universities focusing on aerospace, particularly on launcher aspects. Teaching content at the university must be linked to the project.
   - Conduct of reviews including the participation of a minimum of one reviewer from DLR MORABA, DLR Institute of Space Propulsion and the DLR Space Administration, respectively
2. Technical requirements
   - The rocket shall reach a minimum apogee of 3 km and reach a supersonic velocity
   - The rocket shall have recovery system, and
   - The rocket shall have a telemetry unit to transmit the most important trajectory data (acceleration, velocity, altitude and GPS-position) during its trajectory.

2.1 Overview of the student rockets

Eight teams are participating in the STERN I program. Five of them launched their rockets in the last two years. Due to the expected flight altitude, the launches took place at the SSC ESRANGE Space Center in Kiruna, Sweden. An overview of the rockets is given in the following:

TU Berlin, DECAN

"DECAN – Deutsche CanSat-Höhenrakete" is the designation of the two-stage sounding rocket project of the Technical University of Berlin. However it was decided to launch only the Engineering and Qualification Model (EQM) and Flight Model (FM) of the upper stage at ESRANGE. Both rockets were identical except that one contained a telemetry payload and the other one a dummy payload. The predicted apogee of the DECAN "SHARK" rockets was 6.5 km. ("SHARK" is the name of the rocket) The solid rocket motor is a commercially available class N motor for high power rocketry with level 3 certification. Its propellant is an aluminum / ammonium perchlorate composite (AL + APCP). The project was performed under professional supervision based on ECSS standards and was supported by the Aerospace Institute of the Technical University of Berlin. Detailed information about the development of the rocket and the motor is given in reference [1].

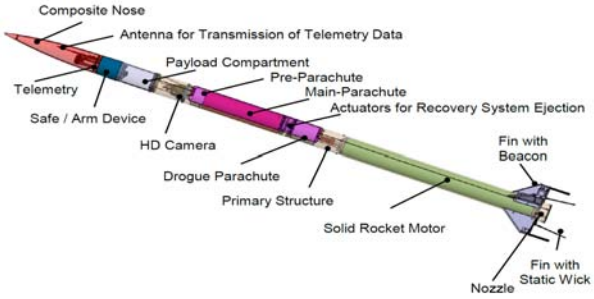

Figure 2: System of the SHARK rocket

DECAN SHARK I was launched from the Medium Range Launcher (MRL) at 13:55UTC on October 27, 2015 and DECAN SHARK II was also launched from the MRL at 08:55UTC on October 29, 2015. For safety reasons a launch elevation of 80° was set by the launcher. If the elevation angle is an acute angle the rocket leaves the launch side faster as with a rectangular elevation angle. Before lift-off of SHARK I, an unexpected long ignition delay of approximately 8 seconds of the rocket motor was observed. The reason for this was the low temperature of the rocket motor resulting from the low ambient temperature during the extended countdown. The gas generator inside the combustion chamber needed more time to generate the required hot gas in order to provide the ignition temperature for the propellant grain. After the ignition of the solid motor, the rocket left the launcher and a stable flight trajectory was observed. It can be assumed that the integrity of the rocket structure was ensured during the entire flight. Furthermore, telemetry data was received during the flight and a maximum altitude of 5,556 m was reported. Moreover, a maximum velocity of 401 m/s (Mach 1.2) was measured by the sensors of the telemetry system. The triggering of the drogue parachute was confirmed by the telemetry system. However, the recovery system malfunctioned. It was

observed that the rocket descended without any parachute and crashed into the ground.

The DECAN SHARK II rocket had a stable flight trajectory as well and reached an altitude of 5,703 m. A maximum velocity of 414 m/s (Mach 1.2) and an acceleration of 103 m/s^2 (10 g) were measured. The triggering of the drogue and main parachute was reported from the telemetry system. It was observed that the drogue parachute was ejected; however the main parachute malfunctioned. Thus, the vehicle crashed into the ground as well. [2]

TU Braunschweig, ERIG:
The ERIG is an association at the Technische Universität Braunschweig. As an in the STERN participating team, the ERIG is developing a research hybrid rocket and a new hybrid rocket engine. The rocket named Faust was powered by a hybrid rocket motor called HYDRA3X. The HYDRA3X engine consists of a solid HTPB (Hydroxyl-terminated polybutadiene) / aluminium powder mixture and liquid oxidizer (nitrous oxide) and was planned to deliver 1.25 kN of thrust, which should allow the rocket to reach altitudes in the order of about 5 km. The rocket FAUST was used with external helium pressurization. Furthermore, ERIG was designing a telemetry platform containing of an inertial measurement unit (IMU) and navigation data via GPS, as well as a new proprietary flight simulation tool called ExRaS (ExperimentalRaumfahrt-Simulation). This allows an individual simulation run with different configurations and the estimation of key parameters such as the maximum altitude and velocity. By including online wind data, it is possible to perform a complete flight simulation and thus predict where the vehicle will impact.

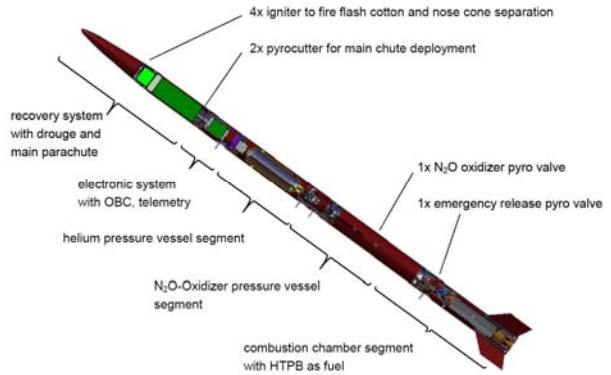

Figure 3: System of the FAUST rocket

Detailed information about the development of the rocket and the motor is given in reference [3].

FAUST was launched from the team´s own launcher at 08:45UTC on October 22, 2015 (see Figure 4) with an elevation of 80°. The launch went well but the recovery system did not work as expected. According to the flight data analysis it is assumed that the drogue chute deployed as planned, but the high velocity of 100 m/s due to the launch angle caused higher aerodynamic loads than expected. Even the integrated damper was not able to alleviate this and the drogue chute ripped off and was unable to pull out the main chute. This theory is supported by the recovered parts. The main chute was found inside the rocket while the drogue chute was missing. Later analysis and pull tests show that the rod between the rocket and drogue chute was weakened by knots. In conclusion the failure was caused by several reasons. A lower than planned launch angle inducing higher loads, a weakened rope by knots and furthermore, a wrong load calculation.
Nevertheless, the propulsion system and the electronics performed as planned. No anomalies were detected during launch sequence and flight. However, due to the harsh impact, no flight data could be recovered from the on board memory. Only data transmitted during flight was available. [2], [3]

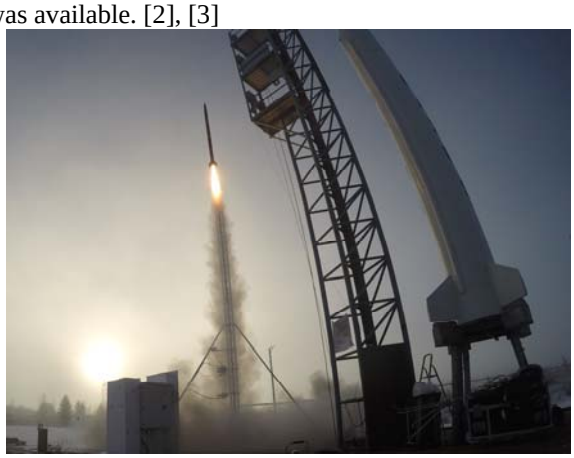
Figure 4: Launch of FAUST

HS Bremen, AQUASONIC
The project AQUASONIC, aimed to develop a two-stage sounding rocket transporting a 2 kg payload to a ceiling altitude of 6 km while reaching a velocity of at least Mach 1. Concept, design and realization of the optimized, lightweight rocket system was performed by graduate and undergraduate Aerospace and Aviation students of Bremen City University of Applied Sciences, during their final phase of studies. The hybrid propulsion system is based on Polyethylene as fuel and Nitrous Oxide as oxidizer. The engine was pressure-fed using a regulated Helium pressurization system. Moreover a two-stage parachute based recovery system was foreseen. Recovery parachute ejection was initiated by the on-board computer, based on barometric altitude, acceleration and rocket attitude. A redundant activation system with independent sensors, microcontroller, telemetry link and power supply was also foreseen. Detailed information on the rocket is given in reference [5]

The launch campaign at Esrange took place from April 4, 2016 until April 14, 2016. Everything went according to the schedule, until the first launch attempt on April 8, 2016. Due to a technical problem, the AQUASONIC rocket had a misfire and did not leave the launcher. Conclusion of detailed analysis was that the ignition material (rocket-candy) was not kept at the desired place inside the engine. Intensive testing including reproduction of the failure, lead to the decision to use an additional holding plate made of PLA, which would have a minor impact on the flow field in the rocket motor because it would burn completely away during motor operation. Additionally, the time delay between ignition of the rocket candy and activation of the pyro valve was reduced to create a longer overlap time between igniter operation and oxidizer flow.

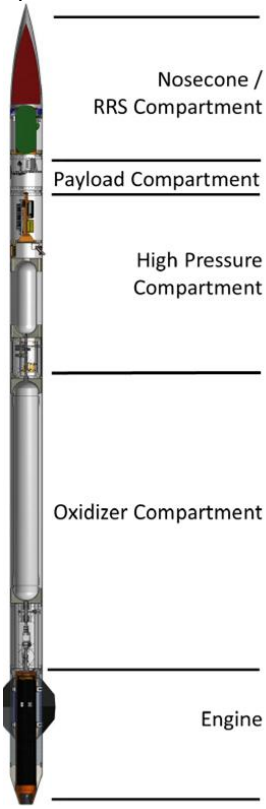

Figure 5: System of the AQUASONIC rocket

The second launch attempt was set for April 14th. The rocket was launched at 04:00 UTC with a launcher elevation of 80°. Around nine seconds after lift-off, no telemetry data was received, because the link margin decreased below its minimum required threshold. According to Mission Analysis, the rocket should have reached an apogee of about 6,5 km after 40 s of flight. The malfunction of the primary telemetry system resulted in a lack of information about flight performance and the function of the recovery system. After extrapolating the trajectory the rocket was found on July 16, 2016. The on-board data was destroyed by the harsh impact of the rocket. [4], [5]

U Bremen/ ZARM, ZEpHyR

The ZARM Experimental Hybrid Rocket, ZEpHyR for short, which is a contribution of the University of Bremen, was powered by a hybrid rocket motor. The engine utilised paraffin as a fuel and liquid oxygen as an oxidiser, which was produced by their own liquefier. The pressurant was Helium. The engine is designed to develop 1,8kN of thrust for thirty seconds, resulting in a total impulse of about 54kNs. The recovery system included a two stage parachute system. Moreover the telemetry system, which is part of the rocket payload, features OBC, GPS, IMU and pyro-modules. Detailed information on the rocket is given in reference [6].

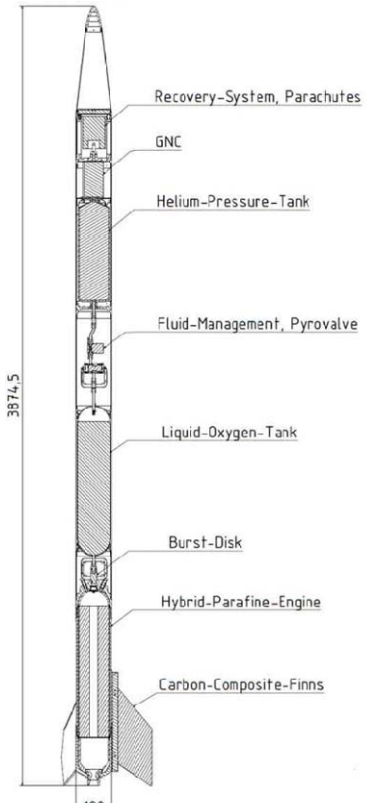

Figure 6: System of the ZEpHyR rocket

ZEpHyR was launched from the MANII launcher at 08:57UTC on April 16, 2016 and was the first paraffin/LOX hybrid sounding rocket to be launched in Europe (to the knowledge of the authors). Due to the low acceleration during lift off, the launch elevation was set to 75° by Esrange.

A first analysis of the flight indicates that the burning time of the engine was lower than predicted, resulting in a significantly reduced performance of the vehicle. A malfunction of the Functional Propulsion System could be excluded shortly after the flight. Video and telemetry data show clearly nominal engine behaviour. Most likely the oxidizer tank was not filled with enough liquid oxygen during the fuelling process. Due to technical complexity, a rising pipe inside the LOX-tank was used to check the filling level instead of cryogenic sensors or a scale. Filling operation is completed as

soon as drops of LOX are visible and there is no significant vapour of gaseous oxygen at the outlet of the rising pipe. The latter was monitored by a camera to observe the filling process from the control room. On the launch day, the sky was clouded with a light snow fall and the camera pointed against this white background, make it difficult to see vapour or drops and resulted in a lower fuelling level.

As with previous flights a malfunction of the recovery system occurred. The recovered debris of the rocket indicates that the drogue parachute was deployed but was unable to handle the forces during deployment. The wreckage indicates that the main line connecting the drogue to the rocket ruptured, leading to non-deployment of the main chute and loss of the vehicle. This coincides also with telemetry data. Due to the hard impact of the rocket the storage card with high sampling data rates was damaged and only the telemetry data with 1Hz and the video material from the outside cameras are available. [4], [6]

U Stuttgart, HyEnD

The student team Hybrid Engine Development (HyEnD) of the University of Stuttgart has developed a hybrid rocket called HEROS (Hybrid Experimental Rocket Stuttgart) with a design thrust of 10 kN, a total impulse of over 100 kNs and a lift off mass of up to 175 kg. The major subsystems are the rocket engine, propellant management, telemetry unit, a recovery system and ground support equipment. During flight the telemetry unit sends trajectory data to the ground station. Additionally a flight computer stores telemetry data, tank pressure and combustion chamber pressure to a disk. The flight computer also triggers the recovery system, which consists of a braking parachute, which is ejected at apogee, and a main parachute, which is deployed at a fixed altitude. After the successful and safe landing of the rocket, HEROS is tracked with last GPS data and a radio transmitter. HEROS is reusable to a high degree.

HEROS has been launched in the DLR educational program STERN the first time at 14:45UTC on October 22, 2015 from the MRL launcher. However combustion instabilities occurred during lift-off, due to low oxidizer temperature. This led to a failure of the combustion chamber in the flight after ~7s and the rocket did not reach the targeted altitude. The propulsion system uses a paraffin-based solid fuel and Nitrous Oxide (N_2O) as the liquid oxidizer. The launch has been analysed in detail and a Failure Analysis Review was performed in order to find the root cause of the malfunction. It could be shown, that these instabilities appeared also in ground tests, when the N_2O temperature and corresponding vapour pressure was not high enough to maintain an adequate differential pressure over the injector.

An extension of the project for a 2nd campaign was granted by the DLR Space Administration, with a launch in October, 2016. Small improvements in the rocket design were made for another launch including an improved heating system and increased number of sensors.

HEROS 2 was launched on October 31, 2016 at 1200UTC. During the launch, a failure occurred in the on-board electronics. Everything worked nominally during the countdown, the electronics worked nominally until launch. Exactly at T-0, the telemetry was lost completely. It was not possible to regain reception. Since both units failed simultaneously at T-0, when mechanical loads are small, a failure due to mechanical reasons is highly unlikely, so the failure was presumably caused by an electrical issue. In an array of tests, it was shown that an electromagnetic interference from the firing line induced a voltage in the on-board computer connection line and thereby a shut-off command for the computer. All improvements were implemented before the launch of HEROS 3. The third rocket was launched on November 8, 2016 at 0930UTC. HEROS 3 was very successful. The maximum flight altitude was 32300 m. This sets a new record for European student and amateur rocketry. The maximum velocity of HEROS 3 was 2600 km/h with a Mach number of 2.3. The parachute system deployed at apogee and the rocket landed softly without any damage in 20 km distance to the launch pad.

The other student teams are described shortly below:

- SMART (TU Dresden): Single stage, liquid propellant using ethanol and liquid oxygen (LOX), fed by pressurized nitrogen (N_2). Engine tests with increased thrust from 500 to 700N in 2017.
- HyComet (FH Augsburg): single stage rocket, lift-off mass 25 kg, hybrid motor (polyethylene (PE) + liquid oxidizer (nitrous oxide (N_2O), flight altitude 3-5 km, planned launch: 2017
- Hyper (TU München): Single staged rocket, hybrid: cryogenic propellant using liquid oxygen (LOX) and hydroxyl-terminated polybutadiene (HTPB), flight apogee 15km, battle ship engine test: 2017

2.2 Overview of the campaigns

Three Campaigns were conducted during STERN I-October 2015, April 2016 and October 2016-. All launches took place at the SSC ESRANGE Space Center in Kiruna, Sweden. Five student groups (Technical University of Berlin, University of Applied Sciences of Bremen, Technical University of Braunschweig, University of Stuttgart, and ZARM/ University Bremen) could successfully launch their rockets under supervision of DLR scientists and engineers.

Three of the university teams (TU Braunschweig, U Stuttgart and TU Berlin) attended the launch campaign in October 2015, with four rockets in total. All rockets, i.e. two hybrid rockets and two identical solid rockets, could be launched within the scheduled two weeks campaign.

The second STERN campaign was from 03.04 till 15.04.2016 with two rocket launches. HS Bremen and ZARM University Bremen launched their hybrid rockets.

Up to now the last STERN campaign was from 24.10 till 09.11.2016. The University of Stuttgart launched two rockets. The second flight had an apogee of more than 32 km and is the European record for student rockets.

For the launch preparation and operations phase, the responsibility for each mission resided with the STERN teams. MORABA coordinated and managed the mission activities at the launch site.

3. Lessons Learned

All an all, there are points which could be better performed in the next project but making mistakes is the best way of learning. The following lessons learned is done by MORABA to determine and analyse elements of the project that were successful or unsuccessful. The list is applicable for all different project organizations (DLR Space Administration, DLR Institute of Space Propulsion, University, SSC and DLR MORABA).

3.1 Organizational

Points regarding project management, which should be improved in future projects or which were positive and should be done again in future projects:

- Regular project meetings and splinter meetings between the different project organizations
- Requirements should always be achievable within the scope of the project. If they are not, then this can lead to unnecessary diversions of resources which in turn may compromise progress.
- Fileserver that is easy to operate and accessible for all project members
- English language during meetings and for documentation
- All different project organizations should visit the students at their test facility

3.2 Technical

The following subchapters should give an overview on the main technical lessons learned of STERN program. These lessons learned, should help future teams to design, build and fly their rockets.

General

- Try to use components that could be replaced. The design of the system should be constructed that parts could be replaced. The complicated part on having spare parts is the balance from cost and need. A campaign could be over without a spare part but which one do you need during a campaign.
- Try to use components that come with a datasheet and/or a manual including all necessary information
- Where possible, design should attempt to include COTS components to reduce lead times in manufacturing. It can also be prudent to simplify designs such that the students themselves can fabricate many of the parts. This will reduce mechanical workshop costs and lead-times.
- Accurate vibration tests are absolutely essential to ensuring the payload will function correctly on the launch day
- In case of a harsh rocket impact, it is recommended using a black box to protect the rocket flight data.

Propulsion

- All further STERN rocket motors will be full scale tested
- Do intensive testing under representative conditions (e.g. temperature)
- The engines (or even the entire propulsion subsystem) should be tested in (almost) vertical position. At least a vertical ignition test shall be performed.

Communication

- External standalone system to localise the rocket (for example an Iridium system from SSC)
- Use an independent “beacon” for location of the rocket
- Do intensive testing under representative conditions (e.g. modems inside rocket)

Recovery System

- Recovery system is electrically independent of the communication system
- Intensive testing under almost realistic conditions
- More education about recovery system, selection, construction, handling/ packing of a parachute
- Recovery system should be improved for high horizontal velocities during apogee.

Operation/ campaign

- A communication solution between blockhouse and launcher → for example headset solution
- More spare parts at the range:
    - gas bottles connections
- Grounding concept should be discussed in advance with SSC and MORABA experts
- Working hours needs to be shorter for students during a campaign
- Handling of pyrotechnics: Always one person from

SSC should be supervising the students
- The duration planning of a STERN Campaign should be increased because of weather, daylight- or other technical issues.

4. Conclusion & Outlook

The experience and results from the STERN campaigns demonstrated a very good performance of the student rockets and the good approach for student support by the STERN program strategy. The challenging and extensive task of the preparation and conduction of a launch campaign is an excellent opportunity for a large gain of hands-on experience for the students.

The STERN program supports the universities in the education of the students by the intense knowledge gain in designing, building and testing of rockets in the scope of ambitious projects. A second funding period (STERN II) will start within 2017 currently planned with four universities.

REFERENCES

1. *Schmid M, Fleischer P., Sliwowski F.,DECAN (Deutsche CanSat-Höhenrakete) – A Sounding Rocket Project at TU Berlin, in: EUCASS Book Progress in Propulsion Physics; Bonnal, C.; Calabro, Galfetti, L. & Maggi, F. (Eds.), 2015, submitted for publication*
2. *Töyrä M., "STERN Campaign Report", REK221-E66, 2015*
3. *May S., Poppe G., Pöppelmann M., Sültrop H. P., Vörsmann P., Development of a Supersonic Research Rocket with Hybrid Rocket Engine , in: EUCASS Book Progress in Propulsion Physics; Bonnal, C.; Calabro, Galfetti, L. & Maggi, F. (Eds.), 2015, submitted for publication*
4. *Töyrä M., "STERN Campaign Report", SCIENCE-61-7582, 2016*
5. *Apel U., Baumann A., Dierken C., Kunath T., "AQUASONIC – A Sounding Rocket Based on Hybrid Propulsion", Applied Mechanics and Materials, Vol. 831, pp. 3-13, 2016. submitted for publication*
6. *Rickmers P., Drinkewitz M., Orlowski F.; The propulsion system of the ZEpHyR - ZARM Experimental Hybrid Rocket: A contribution to the DLR STERN Project by the University of Bremen in: EUCASS Book Progress in Propulsion Physics; Bonnal, C.; Calabro, Galfetti, L. & Maggi, F. (Eds.), 2013, submitted for publication*
7. *Kobald M., Petrarolo A., Schmierer C., Fischer U., Tomilin K., Flight Analysis of the Hybrid Sounding Rocket HEROS, submitted for publication*
8. Schüttauf, K., Stamminger, A., Lappöhn, K. Ciezki, H., Kitsche, W., 2016, *Operation of solid rockets in comparison with hybrid rockets during the STERN project.* 14th International Conference on Space Operations. SpaceOps 2016, submitted for publication
9. Schüttauf, K., Stamminger, A., Lappöhn, K. Ciezki, H., Kitsche, W., 2015 *STERN - Educational Benefit for the Space Industry.* In: Proceedings 22nd ESA Symposium on European Rocket and Balloon Programmes and Related Research, SP-730, 22nd ESA Symposium on European Rocket and Balloon Programmes and Related Research, ISBN 978-92-9221-294-0 ISSN 1609-042X, *submitted for publication*
10. Stamminger, A., Ciezki, H., Kitsche, Kobald, M, Lappöhn, K. Schmidt, A., 2013, *STERN – A Rocket programme for German Students.* In: Proceedings of the 21st ESA Symposium on European Rocket and Balloon Programmes and Related Research, *submitted for publication*

10 YEARS OF THE GERMAN-SWEDISH REXUS/BEXUS STUDENT PROGRAMME

Michael Becker [1], Alexander Kinnaird [2], Kristine Dannenberg [3], Maria Roth [1], Armelle Frenea-Schmidt [2], Maximillian Nürmberger [2]

[1] DLR Space Administration, Königswinterer Str. 522-524, 53227 Bonn, Germany Email: Michael.Becker@dlr.de; rexusbexus@dlr.de
[2] ESA Education Office, ESTEC Keplerlaan 1, PO Box 299 NL-2200 AG Noordwijk, The Netherlands Email: Alexander.Kinnaird@esa.int; rexus-bexus@esa.int
[3] SNSB, Box 4006, SE-171 04 Solna, Sweden, Email: Kristine.Dannenberg@snsb.de

ABSTRACT

The German-Swedish Rocket/Balloon Experiments for University Student (REXUS/BEXUS) programme has existed in its current form for 10 years, and with over 1200 direct participations has launched 147 student built experiments.

Prior to the formalisation of the programme in 2007 a number of test rockets and balloons were launched by both SSC and DLR MORABA, both individually and in the form of EuroLaunch.

This paper explores the development over the 10 years of the programme, including the development of the programme itself as well as trends in experiments, teams and payload composition.

A discussion also summaries the programme 'reach' in terms of student numbers, academia and the public and looks at the participation satisfaction and programme effectiveness through the comparison of three 'alumni surveys'.

1. WHAT IS REXUS/BEXUS?

The REXUS/BEXUS programme is realised under a bilateral Agency Agreement between the German Aerospace Center (DLR) and the Swedish National Space Board (SNSB). The Swedish share of the payload has been made available to students from other European countries through a collaboration with the European Space Agency (ESA). EuroLaunch, a cooperation between the Esrange Space Center of SSC and the Mobile Rocket Base (MORABA) of DLR, is responsible for the campaign management and operations of the launch vehicles. Experts from DLR, SSC, ZARM and ESA provide technical support to the student teams throughout the project. REXUS and BEXUS are launched from SSC, Esrange Space Center in northern Sweden.

The REXUS/BEXUS programme allows students from universities and higher education colleges across Europe to carry out scientific and technological experiments on research rockets and balloons. Each year, two rockets and two balloons are launched, carrying up to 20 experiments designed and built by student teams.

2. BEFORE THE PROGRAMME: BX I-V & RX I-IV

The celebration of 10 years of the REXUS/BEXUS programme coincides with REXUS 24/25 and BEXUS 23/24 as the programme was actually initiated with REXUS 5/6 and BEXUS 6/7. The first BEXUS (I-V) balloons were launched prior to the formation of the programme through a cooperation between SSC Esrange and the Department of Space Science at Kiruna Space and Environment Campus with technical high school programs from Umeå and Luleå University of Technology. Annually, from 2002, students were offered a flight-opportunity with a stratospheric balloon. The programme was named BEXUS (Balloon Experiments for University Students). From 2002 to 2007, five BEXUS (I-V) balloons were launched with experiments entirely designed and built by students.

The first REXUS flight took place in 1995. SSC Esrange invited students from the Swedish Institute of Space Physics in Kiruna to use the empty space in a test-rocket to be used in preparation for the MAXUS 2 launch. The students renamed the GPS-Orion-rocket to REXUS (Rocket Experiment for Upcoming Students), inspired by the MAXUS and TEXUS programmes. In 2003, the EuroLaunch cooperation between DLR MORABA and SSC Esrange was established to consolidate competencies and improve their efficiency and capabilities (Kemi 2004) . EuroLaunch planned to continue using test flights of rockets and therefore had a vested interest in the continuation of REXUS.

Nine years after the first student rocket, the first EuroLaunch project, REXUS 2 (Rocket-borne Experiments for University Students) (Inga 2005, Persson and Hörschgen 2005) was launched in 2004. The payload capacity was shared between Swedish and

German students and was comprised of 7 experiments.

REXUS 2 was followed by REXUS 3 and REXUS 4 in 2006 and 2008, respectively. However, all pre-programme flights were primarily test-flights where student experiments could fly 'piggyback'. It could have taken several years until an experiment had the chance to fly. By then, students sometimes already left University. This changed with the realisation of the REXUS/BEXUS programme.

3. A GERMAN-SWEDISH PROGRAMME – THE CREATION OF A PROGRAMME

The realisation of the REXUS/BEXUS programme is based on a German-Swedish Agreement between DLR and SNSB for cooperation in student rocket and balloon activities, signed in 2007 during the 18th ESA Symposium on European Rocket and Balloon Programmes and Related Research in Visby, Sweden. The purpose of the programme is to offer students, particularly in Germany and Sweden, experiment opportunities using sounding rockets and balloon flights, to get young people into space research and the space business and to inspire them about space. For the Swedish half of the programme, a collaboration with the ESA Education office was quickly established to invite students from all ESA member states to participate as part of the Swedish 'quota'. The Agreement offers flexible, quick and regular access to execute student experiments, with DLR and SNSB providing two rocket and two balloon flights every year.

4. CYCLES 01 TO 10 –IMPROVEMENT

Immediately after signing the bilateral agreement, the first strategies and preparations with major improvements were initiated. The first call for proposals for students in Germany, Sweden and all ESA member states was issued in October 2007 by DLR and the ESA Education office. Therefore standard proposal forms and technical manuals with necessary information with respect to assessment, feasibility, safety aspects and composition of payloads were provided for the first time. In contrast to the pre-programme missions, a reliable schedule with two annual balloon flights in Autumn and two rocket flights in Spring in double campaigns was now provided along with a series of reviews to execute a full life-cycle of a "space" project.

As in that first cycle teams are selected based on the review of the student proposals and an oral presentation to a panel of experts at DLR Space Administration or ESA/ESTEC.

All experiments have to pass a Preliminary Design Review (PDR) in the frame of a newly established Student Training Week. The training week included (and continues to include) lectures in scientific and engineering topics, explanations of the launch vehicles and systems, "ask your expert" sessions, training, teambuilding events and tours of the facilities and is held by experts from DLR, ESA, SSC and ZARM, to ensure the teams receive the necessary information for their projects. The training week is hosted alternatively at Esrange Space Center by SSC Esrange or at DLR Oberpfaffenhofen by DLR MORABA and has been continuously improved and updated with respect to content and schedule, over the past 10 years.

The PDR panel, with experts from all partners, reviews the student teams, who have to demonstrate their experiment design is feasible and respects the experimental interface, operational and safety requirements. For the optimisation and support of the teams, experts provide constructive advice regarding the student's project, which are also provided as written 'minutes'.

Necessary information has to be provided by the students with the establishment of a Student Experiment Documentation (SED), including scientific, technical and operational requirements, as well as project management and outreach information. The SED reports the progress of the student experiments. Five different versions have to be delivered prior to major reviews and defined deadlines. For assistance, guidelines, user manuals and ECSS standards are provided. The execution of an outreach programme also became a mandatory part of the programme requiring teams to report about their projects in social media, blogs, on a project website, in presentations at their universities or in newspaper articles, for example.

Following the programme schedule, all teams have to pass the Critical Design Review (CDR) for the acceptance of their design. The CDR takes place in May for BEXUS at ESA/ESTEC and in June/July for REXUS experiments at DLR Oberpfaffenhofen. The detailed design has to be finalised, the fabrication and integration of the flight hardware should have begun and major issues identified at PDR should have been closed out. During the CDR, students also participate in lectures regarding the next steps and an interface discussion. "Ask your experts" sessions also allow individual questions to be addressed to relevant experts. One team member also gets the opportunity to participate in a soldering course for flight hardware.

The purpose of the CDR is primarily to prevent teams running into issues during, or after, manufacturing due to a poor design and to give expert approval before the main fabrication and testing phase beings. During the last 10 years, additional reviews have been implemented to gain more time for trouble shooting and avoid pushing problems into the campaigns. An Integration Progress Review (IPR) is held in July for BEXUS and

in August for REXUS at the student teams' institutes. The IPR was first introduced in Cycle 03 (2010) as a compliment to, the now defunct, Mid Term Report/Review (MTR). These reviews are performed by experts from ZARM, SSC and/or ESA, and formerly experts from DLR Bremen, to ensure, and to assess, the appropriate progress of fabrication and assembly. The experiment's design should be frozen and the majority of the hardware should be fabricated at this time. The IPR is followed by the Experiment Acceptance Review (EAR), during which the experiments are accepted for shipping to campaign and the fully integrated experiment should be presented and demonstrated to be operational. During the campaign a Flight Readiness Review is performed, which replaces the previous Flight Acceptance Reviews, Launch Acceptance Reviews and pre-campaign Flight Readiness reviews as trialled in Cycles 01, 02 and to extent 03.

For REXUS, an additional testing phase was implemented in cycle 04 (2011): the Scientific Payload Integration Week at the DLR Institute of Space Systems in the first years of the programme and now at ZARM's facility in Bremen. Here teams integrate and test their experiments including electrical interface and mechanical interface tests, functional testing, flight simulation of the integrated payload. and, in recent years, vibration testing of individual experiments. The creation of the Integration week necessitated the introduction of the REXUS Service System Simulator. The final event for the REXUS teams is the Bench Test at DLR Oberpfaffenhofen in January/February (first introduced in Cycle 05 – 2012) this is the final opportunity for modifications before the launch campaign. Individual check-outs are performed and the flight configuration is assembled together with the recovery system and service module of the rocket to test and fine tune the communication and flight timeline. The fully integrated payloads are then transported to Sweden for spin-balancing.

During the last 10 years many improvements have been made. Based on the pre-programme flights, reviews have been introduced and are continuously being improved. Schedules have been adapted and continuous support by experts has been established to provide technical, financial and organizational support for the students throughout their project. Changes in the programme organisation have had a great impact on the students' support and this has been intensified by introduction of a continuous student support by ZARM and SSC. Significant technical improvements (e.g. the simulators), the standardisation of electronic interfaces, use of recommended components (e.g. pyro-cutters, connectors and power converters) and the standardisation of the rail characteristics of the BEXUS gondola, were made. Together with technical improvements and the student organisational support, documents and forms were continuously adapted and upgraded. All improvements that have been made from the beginning of the programme have been aimed at aiding the students to have a higher chance of success with their experiments as well as improving the educational return of the programme.

5. PROGRAMME REACH

Over 1200 university students have being directly involved in the REXUS/BEXUS programme, with around 120 students participating in each cycle. In addition to these direct participants it is suspected that a small but significant number of students have been involved with experiment design/development in a part-time manner and have not been reported as direct participants.

In addition to the direct reach, an analysis was performed to determine the 'academic' reach of the programme. This was done using Google Scholar and searching for "REXUS", "BEXUS", "REXUS/BEXUS" and each of the experiment names, and then filtering for duplicate and irrelevant results. This method prevents an internal bias and any over reporting of publication by teams (see alumni survey section 7). Combining all these results shows that the programme and experiments have the following unique references.

Total Unique references	**318**
Book sections	5
Conference Papers	199
Peer reviewed journal articles	54
Publically available theses (at all levels)	60

Table 1: Google scholar results

It should be noted that this analysis was performed prior to the 23rd ESA PAC Symposium where a further 27 experiment results were presented. The alumni survey (see section 7), suggests that around $^{2}/_{3}$ of all respondents plan to present their results in conferences, with an average of 2.4 conferences each.

With regards to journal papers the survey suggests that an average current experiment team expects to, or has, published one peer reviewed journal article, with some experiments publishing up to 5 articles in renowned publications such as Physical Reviews Letters (Harth, Kornek et al. 2013), Acta Astronautica (Boesso and Francesconi 2013) and The International Journal of Astrobiology (Bérces, Egyeki et al. 2015). This number does not correspond to the much lower number of publications found, however this is partly explained by the lengthy process to publication following flight; at the time of this paper the average number of references for RX teams flying prior to 2016 is 4.47, compared to just 0.35 for the 26 'newer' teams.

In addition to academic reach, an attempt was made to

assess the reach to the wider public. This kind of outreach is achieved by the programme, but also by the teams. The programme has had a website (rexus-bexus.int) since 2008, as well a presence on social media with Facebook (2008), Twitter (2013) and on each of the organising institutions webpages. Through Facebook's insights tool it's possible to see the page has nearly 2500 regular followers and regular reaches around 10,000 users during peak activities such as launch campaigns.

The teams' outreach covers a large array of media including traditional media such as newspapers and radio as well as online. Teams regularly report Facebook reaches into the 10,000s, and through appearances on national media have estimated reaches into the millions.

6. STASTICS AND TRENDS

6.1. Experiment teams

The 147 experiments launched as part of the REXUS/BEXUS programme corresponds to the same number of teams however it should be noted that approx. 6% of individuals have participated in the programme twice, either through 're-flights' of their experiment e.g. Telescobe (REXUS 9) and Telescobe 2 (REXUS 11) (Keegan, Wylie et al. 2011), evolutions of their experiment e.g. CoCoRad (BEXUS 12) and Techdose (BEXUS 14) (Zábori, Apáthy et al. 2013), or through participation in entirely new experiments at their own or even different Universities. This retention of a small number of students has proved advantageous for the new teams and team members due to the knowledge and experienced gained through the students' initial participation.

Throughout the 10 cycles, the average size of a REXUS team has been 9.2, with a maximum of 24 (Daedalus, REXUS 23), and minimum of three (VIB-BIP, REXUS 5). In general BEXUS teams have had fewer members (avg. 7.02, max. 19 and min. 2), however in both cases there was a clear trend in the early cycles of increasing team size, leading to the current averages of 10 for REXUS and 8 for BEXUS (see *Figure 2*). Prior to the formalisation of the programme teams may have been only one student or up to 20 high school students.

In terms of geographical distribution (see *Figure 1*), as one may expect, the majority of students come from either Germany or Sweden. There is also notably a strong history of participation from Italy (the only other nation to have participated every year), the UK and Spain. 'Newer' ESA nations, in particular Hungary and Poland, can also be seen to be well represented.

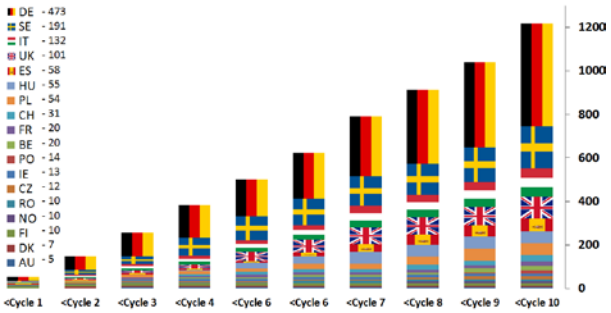

Figure 1: Cumulative geographical distribution of participants.

The size of the final version of the SED (see section 4) for each team was also analysed (see *Figure 2*), with the trends showing a general increase from around 100 pages (BEXUS) and 130 pages (REXUS) to an average of 240 pages (BEXUS) and 260 pages (REXUS). It is hypothesised this is due to: an increase in experiment complexity, increased access to modelling software allowing more detailed design and increased documentation demands from the SED guidelines.

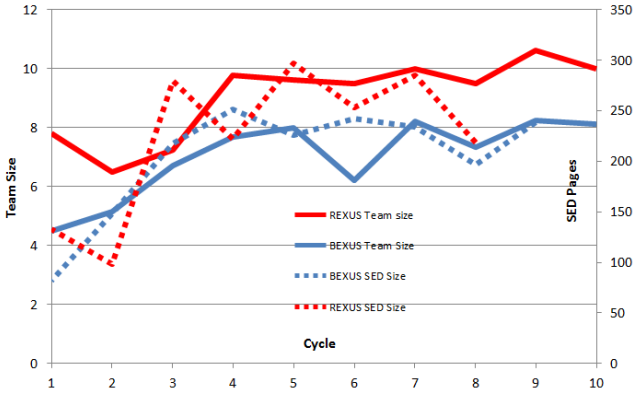

Figure 2: Team size and SED (Student Experiment Document) size trends

Finally the reported expenditure for each team was also examined, with the results showing a slight trend for increased expenditure, but with a very large range (min. €585, max. ~€90,000), and an approximate average of €17k (REXUS & BEXUS), rising from around €5k in early cycles to approx. €20k more recently. It should be noted that real experiment cost is very hard to estimate due, among other things, to teams frequent use of donated hardware, expertise and manufacturing facilities and that a higher budget or expenditure does not necessarily correspond to higher educational, technical or scientific return.

6.2. Areas of investigation

REXUS/BEXUS experiments are loosely grouped into one of 16 different categories, seven 'science' and nine

'technology demonstrators'. Categories have been added over time as new areas are in investigated e.g. 'Biology' in 2011 with the flight of BioDos (Grósz, Gorócz et al. 2013).

Analysis of the number of teams in each category has shown that approximately half of the experiments perform scientific investigations and half perform some kind of technology demonstrator (with a slight preference for science on BEXUS and technology on REXUS). The total break-down can be seen in *Figure 3*

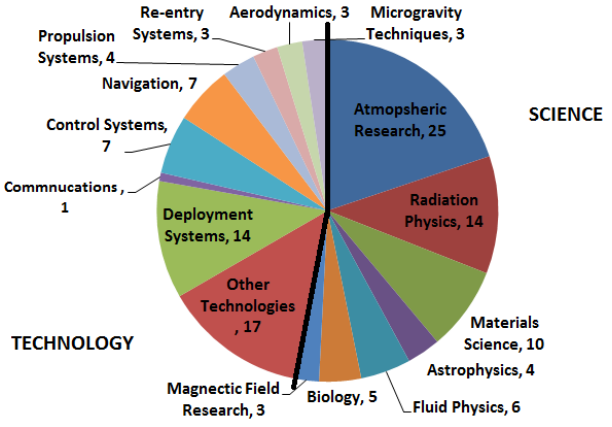

Figure 3: Areas of investigation

There are some minor trends apparent here, notably the frequent investigation of atmospheric research and deployment systems, as well as a historical strong interest in radiation physics.

Looking at REXUS vs. BEXUS it's also possible to see the discontinuation of aerodynamic and re-entry systems on BEXUS following Cycle 4, and, as one might expect, a much stronger preference for REXUS with regards to microgravity techniques, and perhaps a little more surprisingly materials science.

6.3. Experiment hardware trends

The key experiment metrics of mass, power consumption, data rate and volume were analysed across both platforms. The results do not show convincing trends, despite some expectations of increased mass and power consumption. Given that these metrics are largely constrained by the vehicle this result is not so surprising. It is however suspected that the data produced by the teams (and stored locally rather than transmitted) during the flight is increasing due to an increase in the use of high data rate devices, specifically cameras, as well as the availability of cheaper high capacity storage devices.

A typical REXUS experiment weighs between 1 and 30 kg (avg. 9.3 kg), with a volume between 0.0002 and 0.02 m^3, a power consumption of between 0.24 and 49.1 W (avg. 13.24 W) and a data rate between 0.2 kbit/s and 200 kbit/s (avg. 32.2 kbit/s).

BEXUS experiments are little heavier (1.4-39.8 kg, avg. 10.9 kg), larger (0.001-0.537 m^3) and consume between 0.92 and 62.7W (avg. 23.54 W) with data rates between 0 and 2000 kbit/s (avg. 346.6 kbit/s).

6.4. Payload and flight trends

Given the standardisation of the programme in terms of vehicle (see section 3), it is suspected, and confirmed by analysis, that the key payload metrics of: experiments per payload, total payload mass, apogee and float attitude (BEXUS only), have remained relatively stable – this is especially apparent when compared with the 'pre-programme' flights (for example REXUS IV, a dual-stage rocket, reached 175km, compared with the programme maximum of 93km).

The vast majority of REXUS rockets have been de-spun and often come in 'pairs', with one rocket focusing on higher quality microgravity with the other housing more mechanically 'noisy' experiments which may not require the reduced gravity environment at all (such as free-flyers), in which case some rockets have remained spinning (e.g. REXUS 17).

Since the creation of the programme a typical REXUS payload has consisted of between 2 and 5 experiments (avg. 3.85), with a total payload mass of 113 kg (95.1-127.2 kg). This corresponds to a typical vehicle mass of 525 kg. There is a slight trend towards an increased number of experiments/payload with typical REXUS now containing 4 or 5 experiments compared to 3 or 4 in the earlier cycles. The payloads have reached between 77.5 and 93 km, with an average of 83.2 km,

BEXUS payloads also contain between 2 and 5 experiments (avg. of 3.45), with a payload mass between 14 and 112.2 kg (avg. 47.16 kg). This corresponds to a total vehicle mass of around 320 kg. BEXUS payloads have reached between 24.2 and 33 km (avg, 27.85 km), and have maintained the 'float' altitude for between 1.2 and 5 hours (avg. 3.45). They have achieved this using 10,000 m^3, 12,000 m^3 balloons and in the case of BEXUS 22 and 23 two surplus 35,000 m^3 balloons were used (and thus achieved the programme record for float altitude).

7. ALUMNI SURVEYS

In order evaluate the effectiveness of the programme with regards to: motivating students into space related careers and further research, helping them achieve these career goals, tracking the status of the programme alumni and getting feedback over the longer term about the programme; three alumni surveys have been performed. Surveys were performed in 2011 (Fittock,

Siegl et al. 2011), 2013 (Callens, Kinnaird et al. 2013) and 2016 (presented here).

7.1. Survey 2016

The 2016 survey was sent to 439 alumni with valid email addresses as well as promoted in alumni groups and shared between alumni. 107 responses were received, roughly corresponding to a statically relevant 10% of alumni at the time. The gender ratio (approx. 20% female) and nationality distribution (high numbers from DE, IT, ES and SE) also suggest an approximately representative sample. Answers were received from all vehicles apart from BEXUS 12/13 (2011), 16 (2013), 18 (2014) and REXUS 8 (2010). At least one answer was received from every cycle.

With regards to effectiveness of the programme the survey produced the following results:

7.1.1. Project/programme satisfaction

- 95.3% were satisfied to highly satisfied with the results of their project.
- 99% were satisfied to highly satisfied with the their participation in the programme.

7.1.2. Publications

- 62% have presented their results at conferences, with a further 33% planning to, and with 73% personally having contributed to papers. The average number of conferences is 2.4.
- 27% have published in journals with a further 53% planning to, with the average number of publications of 1.24.

7.1.3. Career

- 92% have increased in their interest in a space-related career, with 79% saying they are 'more' or 'much more' likely to pursue a space-related career (see **Error! Reference source not found.**).

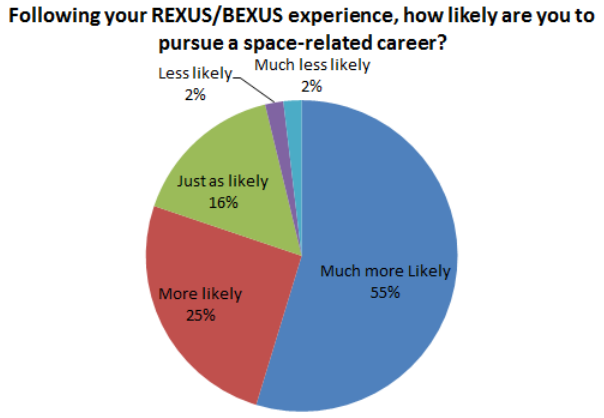

Figure 4: Survey result: increase in likelihood of pursuing space-related career (survey 2016)

- 88% say REXUS/BEXUS is relevant to their career and 78% say REXUS/BEXUS has been a 'springboard' for their career.
- Of those employed the largest areas of employment are 'Aerospace' (36%), 'Academia' (16%) and 'Space' (8%). 66% are engaged in self-identified 'space-related' employment.

An unintended result of the survey is the knowledge of current employment country vs. country of origin/study, with around 29% of alumni working abroad, with Germany, the UK and Sweden being the most popular countries for expat alumni.

7.1.4. Programme feedback and skills developed.

- All learning aspects in the programme are valued, but participants placed particular emphasis on the usefulness of the practical aspect of knowledge in design (88% very useful or useful) and in building/testing (89%) as well as contact with experts (77%) and 'self-learning' (86%).
- In particular the practical application of knowledge in building and testing and 'self-learning' were both consistently ranked as 'very useful' when considering current and future careers.
- Participants consistently report that the participation has increased their understanding of the space project life cycle (91%), space project processes (91%).
- Participants consistently report participation has increased their design skills (92%), practical skills (93%) and team work skills (93%).

Furthermore the survey received a lot of qualitative feedback, with a lot of praise for its effectiveness, but also a number of points which the programme could address within future cycles. The negative aspects which were often repeated focused on the large time commitment, problems with experiment funding, problems with support within universities, internal team conflicts and the documentation requirement.

The overall impression of the survey is one of very high satisfaction with the programme and a consistent message of appreciation of students for their participation.

7.2. Comparison with previous surveys

Comparison with the two previous surveys showed three interesting trends:

Firstly participants are increasingly reporting that they are using REXUS/BEXUS as part of their degree (up from 20% in 2011 to 54% in 2016), It is theorized that as the programme has become more established and teams are returning from the same universities both

students and professors see the value and reduced risk of using the REXUS/BEXUS project as either part of a module or the subject of a thesis.

Secondly students are increasingly delaying their graduation date as a direct result of participation in the programme, with an average delay of 5.5 months (modal delays of 6 and 12 months).

Thirdly an increased satisfaction with their project results. The Programme satisfaction question was only added in 2016, not allowing any assessment of change over time.

	2011	2013	2016
Part of degree?	20%	45%	54%
Delayed graduation?	.33%	43%	54%
Satisfaction with project results	66%	74%	85%

Table 2: Survey comparison

In terms of increase in interest in space-related career, relevance to career, and employment in space the percentage results have remained relatively steady.

8. CONCLUSION

The German-Swedish REXUS/BEXUS programme has been developed on the back of the concept of student experiments on sounding rockets and balloons initially developed by the EuroLaunch partners.

The creation of the programme added a significant degree of stability, regularity and standardisation to the programme which has so far allowed for 10 cycles of continuous improvement with key additions including new reviews and provision of standard parts.

Experiments have been performed in a wide range, and increasing, number of areas. With over 1200 direct participants and public reach greater than 10,000 the programme appears to be achieving its educational and inspirational goals.

Surveys of REXUS/BEXUS alumni show a broad appreciation for the programme, an increasing use for it as part of their university education and suggest strong positive results with regards to employment within the space industry.

In general the programme can be deemed to be performing well, and with a mind for continual improvement, consideration of participant and partner feedback along with a continued spirit of excellent collaboration the programme should continue to be a success.

9. REFERENCES

Bérces, A., et al. (2015). "The PUR Experiment on the EXPOSE-R facility: biological dosimetry of solar extraterrestrial UV radiation." International Journal of Astrobiology **14**(01): 47-53.

Boesso, A. and A. Francesconi (2013). "ARCADE small-scale docking mechanism for micro-satellites." Acta Astronautica **86**: 77-87.

Callens, N., et al. (2013). REXUS/BEXUS ROCKET AND BALLON EXPERIMENTS FOR UNIVERSITY STUDENTS. 21st ESA Symposium on European Rocket & Balloon Programmes and Related Research. E. C. L. Owehand. Thun, Switzerland, ESA Communications, ESTEC, Noordwijk, The Netherlands**:** 561-568.

Fittock, M., et al. (2011). REXUS/BEXUS Alumni-Looking at the Long-Term Personal Benefits of Participation in a Practical Student Programme. 20th Symposium on European Rocket and Balloon Programmes and Related Research.

Grósz, V., et al. (2013). Continuous measurement of the biological effects of stratospheric UV radiation.–BIODOS Experiment BEXUS-15. Proc. 21st ESA Symposium on European Rocket and Ballon Programmes and Related Research (ESA SP-721).

Harth, K., et al. (2013). "Granular gases of rod-shaped grains in microgravity." Physical review letters **110**(14): 144102.

Inga, M. (2005). REXUS II-rocket borne experiments for university students. 17th ESA Symposium on European Rocket and Balloon Programmes and Related Research.

Keegan, J., et al. (2011). Deployment and characterisation of a telescopic boom for sounding rockets. 20th Symposium on European Rocket and Balloon Programmes and Related Research.

Kemi, S. T., P.; Norberg, O. (2004). EUROLAUNCH - a cooperation between DLR, German Aerospace Center and SSC, Swedish Space Corporation in sounding rocket launches.
35th COSPAR Scientific Assembly, Paris, France.

Persson, O. and M. Hörschgen (2005). REXUS 2-the first EuroLaunch project. 17th ESA Symposium on European Rocket and Balloon Programmes and Related Research, Sandefjord, Norwegen, ESA.

Zábori, B., et al. (2013). CoCoRAD and TECHDOSE cosmic radiation experiments on board BEXUS stratospheric research balloons. Proceedings of the 21st ESA Symposium on European Rocket and Balloon Programmes and Related Research (ESA SP-721).

MINI-IRENE: THE FIRST EUROPEAN FLIGHT EXPERIMENT OF A DEPLOYABLE HEAT SHIELD

VISBY, SWEDEN
11-15 JUNE 2017

Paolo Vernillo [(1)], Alberto Fedele [(1)], Roberto Gardi [(1)], Raffaele Savino [(2)], Francesco Punzo [(3)], Florin Gunnar [(4)], Raphael Molina [(5)].

[(1)] CIRA, Italian Aerospace Research Center, via Maiorise 81043, Capua (CE), Italy.
E-mail: p.vernillo@cira.it, a.fedele@cira.it, r.gardi@cira.it.
[(2)] University of Naples, P.le v. Tecchio, 80, 80125 Napoli, Italy. E-Mail: rasavino@unina.it
[(3)] ALI S.C.ar.l., Via E. Gianturco, 31, 80146, Napoli, Italy. E-mail: francesco.punzo@aliscarl.it
[(4)] Swedish Space Corporation, P.O. Box 4207, SE-171 04 Solna, Sweden. E-mail: gunnar.florin@sscspace.com
[(5)] ESA, Kepleraan 1, 2201, AZ Noordkijk, The Netherlands. E-mail: rafael.molina@esa.int

ABSTRACT

MINI-IRENE is the Flight Demonstrator of IRENE, a new-concept capsule with a variable geometry, originally conceived by ASI to widen the range of available platforms to retrieve payloads and/or data from low Earth orbit. The main characteristics of IRENE is the "umbrella-like" deployable front structure that reduces the capsule ballistic coefficient, leading to acceptable heat fluxes, mechanical loads, stability and final descent velocity. This paper describes the roadmap of the IRENE concept, providing details concerning the heritage and past activities, together with the next qualifications tasks that will be performed in order to converge to the flight of MINI-IRENE.

1. INTRODUCTION

The feasibility study of the IRENE deployable re-entry system has been carried out in 2011. The TPS materials selected for the nose cone and for the flexible umbrella shield, have preliminarily been tested in the SPES hypersonic wind tunnel at the University of Naples, and in the SCIROCCO Plasma Wind Tunnel at CIRA. Such successful tests and the preliminary experimental results proved the concept feasibility and the viability of commercial materials for low-cost re-entry nacelles.
Based on the initial results, the European Space Agency supported a study to preliminarily address the main issues of a reduced-scale IRENE demonstrator, called MINI-IRENE, to be embarked as a piggy-back payload in a future mission of a sub-orbital Maxus sounding rocket.
After the preparation phases A and B were successfully completed, the European Space Agency funded the current phase of the program. The object is to design and built a Flight Demonstrator and a Ground Demonstrator to prove, with a suborbital flight and with a Plasma Wind Tunnel (PWT) test campaign, the functionality of the deployable heat shield. In order to face this challenge the Swedish Space Corporation (SSC) has joined the working group and the Centro Italiano Ricerche Aerospaziali (CIRA) has taken over the responsibility of the program.

2. PROJECT TEAM

A team of four groups shall carry out the activities. The team is composed by:

- CIRA - Centro Italiano Ricerche Aerospaziali is the prime contractor. It was founded in 1984 to manage PRORA, the Italian Aerospace Research Program, and uphold Italy's leadership in Aeronautics and Space. CIRA is a company with public and private sector shareholders.

- University of Naples "Federico II" is the Scientific Partner. Founded in 1224, it is one of the oldest public universities in the world, and is now organized in three main Schools (Polytechnic and Basic Sciences School, School of Medicine and School of Human and Social Sciences) and 26 Departments, which operate as semi-independent bodies for teaching and research activities management.

- ALI - Aerospace Laboratory for Innovative components is the Industrial Partner. It is a Consortium of 17 Companies operating within the fields of design, engineering, prototyping and realization of innovative aerospace subsystems for technological and scientific platforms

- Swedish Space Corporation (SSC) is in charge to provide support to launch. It is a comprehensive space company with more than 40 years of experience in helping space organizations, companies and research organizations with access to space.

3. IRENE MAIN FEATURES

IRENE, which stands for Italian Reentry NacElle, is a capsule concept, equipped with a deployable heat shield aimed at a drastic reduction of ballistic coefficient. Low ballistic coefficient turns into reduction of the peak heat flux and mechanical load. Because of this, commercial materials can be used for the main TPS.
The deployment is achieved with an umbrella like structure and a blanket able to resist at high temperature as shown in figure.

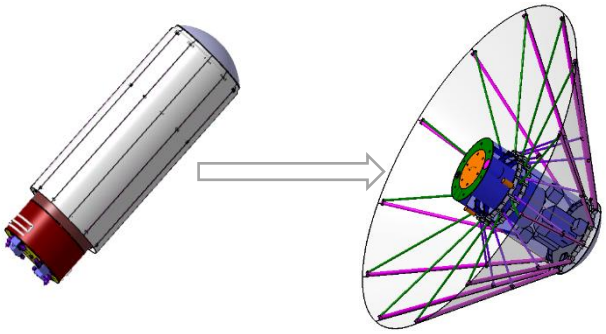

Figure 1. IRENE deployment early concept

One characteristic of the IRENE concept, is that the blanket is in contact only with the extremities of the rods (or struts) of the umbrella.
The diagrams in the next figures show how the reduction of the ballistic coefficient translate in a reduction of heat flux and stagnation pressure. It can be also noticed that the pressure and heat flux peaks occurs at higher altitude, when the atmosphere is more rarefied.

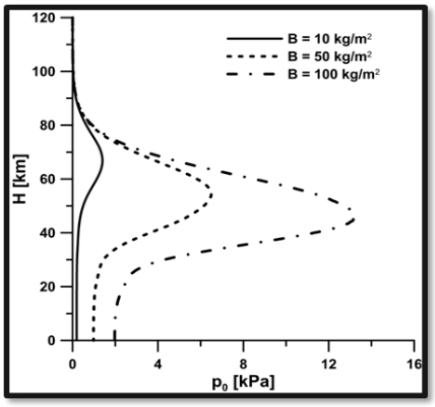

Figure 2. Stagnation pressure w.r.t. altitude for different ballistic coefficients capsules.

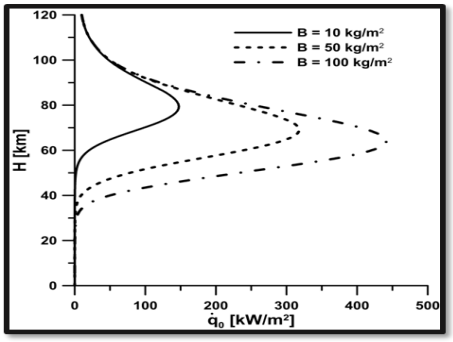

Figure 3. Heat flux w.r.t. altitude for different ballistic coefficients capsules

4. BACKGROUND AND CURRENT STUDIES

The deployable TPS idea is not new. Many inflatable and mechanical systems have been and are currently under development for several different mission typologies:

- Satellite deorbit.
- Landing large mass on planet with thin atmosphere (Mars).
- Entry planets with thick and dense atmosphere (Venus).

Italy has developed some activities in the field of the mechanically deployable heat shields since 2001. In that year, the Italian Space Agency funded a feasibility study for a deployable re-entry system. In the frame of this activity a flexible TPS material and complementary ceramic foam for the nose have preliminarily been tested in the SPES hypersonic wind tunnel at the University of Naples. Then a subsystem test, including both the nose and the flexible TPS material, has been executed in CIRA SCIROCCO plasma wind tunnel. The next figure shows two images acquired during the test campaigns.

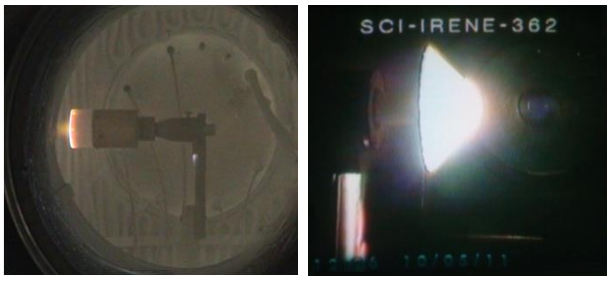

Figure 4. Material test on the left in SPES and subsystem test in SCIROCCO on the right.

Consecutive studies have been focused on the development of a scaled down prototype of IRENE, named MINI-IRENE, for suborbital flight on MAXUS sounding rocket and the current deployment logic has been conceived. During this phase a mock-up has been realized.

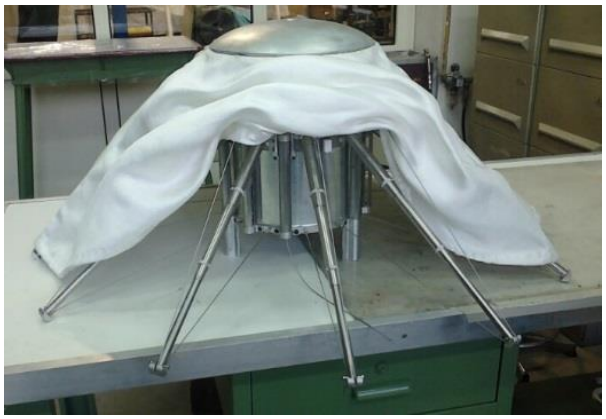

Figure 5. Mock-up of the MINI-IRENE MAXUS deployed capsule.

In the meantime, related research was carried out at the University of Naples Federico II: aerothermodynamics was studied, by means of CFD and DSMC tools, aerodynamic control capability during de-orbit trajectories was investigated, conceptual design of heat shields as end of life systems for cubesats was provided and drop tests were performed to study dynamic stability.

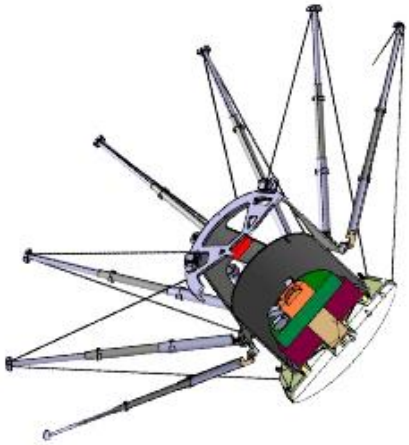

Figure 6. CAD model of the MINI-IRENE MAXUS deployed capsule.

For instance, the following figures show two velocity contours obtained, at different time instants, by means of an unsteady CFD simulation of the capsule aerodynamics in transonic regime, at high angle of attack. Such analysis showed that, in these flight conditions, the flow field is oscillatory and, a result of the pressure oscillations, also the aerodynamic loads acting on the capsule experience a periodic variation. This kind of analyses are meant to give input for the investigation of aerodynamic buffeting phenomena, related to excitation of the structural natural frequencies (vibration or resonance of the modes of the structure) due to external unsteady aerodynamic forces.

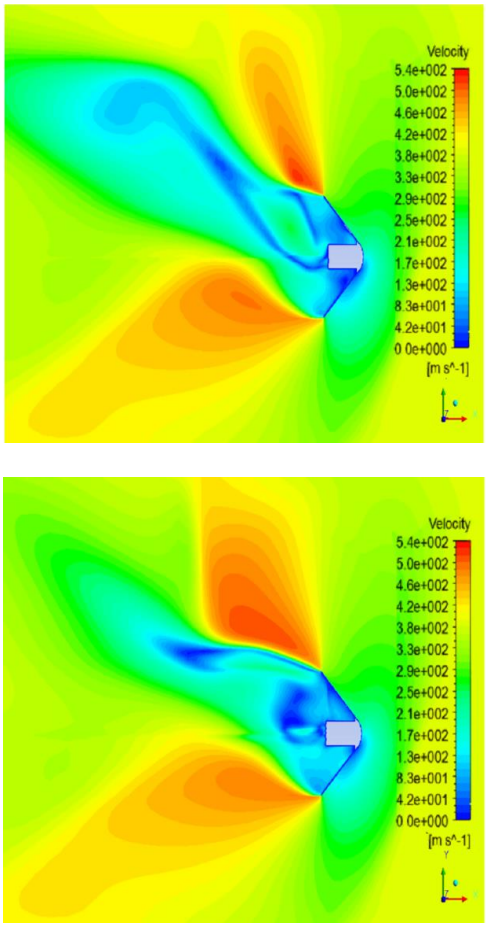

Figure 7. University of Naples activities: unsteady CFD analyses in transonic regime

The following pictures finally show a 3D printed test model that has proven the subsonic dynamic stability in several drop tests.

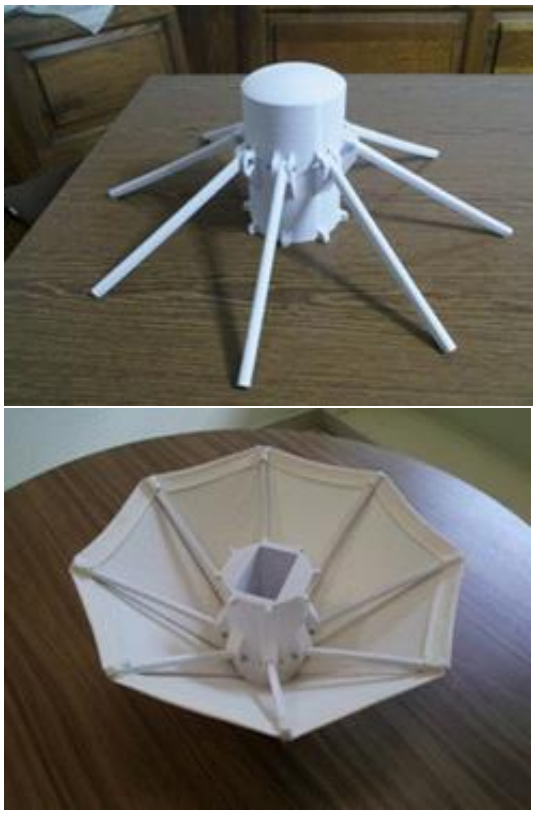

Figure 8. University of Naples drop test mock up.

5. CURRENT ACTIVITIES AND MISSION

The current phase of the program, that will bring the IRENE concept to flight, is articulated in the following main phases:

- Design and realization of a Flight Demonstrator (FD) for suborbital flight.
- Design and realization of a Ground Demonstrator (GD).
- Plasma Wind Tunnel test of the GD.
- Ground qualification of the FD.
- Flight test on VSB-30 rocket of the FD.
- Recovery and post flight analysis.

The FD shall be even more scaled down because the VSB-30 is smaller than MAXUS. The flight test shall be representative of the aeromechanical part of the flight but not of the thermal part of a LEO re-entry.
The GD shall be representative of the material and of the mechanisms of the FD in order to achieve an overall TRL equal to 6.
The capsule shall be dropped by the payload stage of an VSB-30 Rocket after the burn out of the second stage during the ascent, at 65 seconds from the lift off at an altitude close to 83km at a speed of about 1700 m/s.
The fight would continue up to a 250km altitude. The landing is scheduled 860 seconds after the separation from the Launcher.
The following diagrams below compare the dynamic pressure, the acceleration and the heat flux experienced by a capsule in a LEO re-entry trajectory, on a MAXUS flight test and on a MAPHEUS VSB-30 flight.

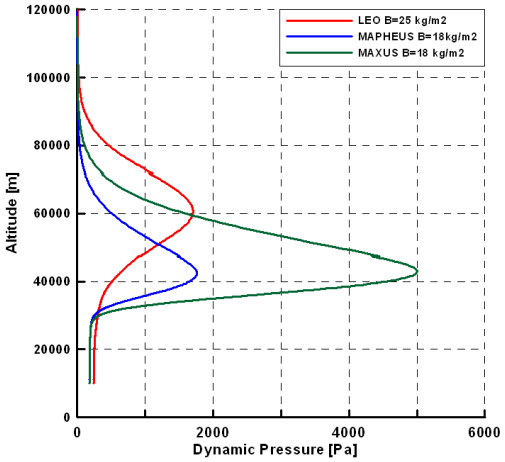

Figure 9. Dynamic pressure experienced by a capsule in a LEO re-entry trajectory, on a MAXUS flight test and on a MAPHEUS VSB-30 flight

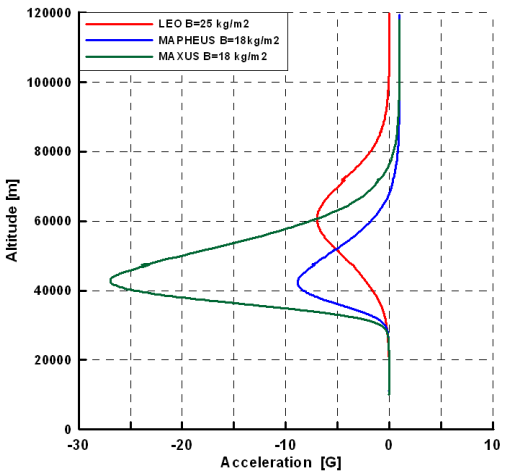

Figure 10. Acceleration experienced by a capsule in a LEO re-entry trajectory, on a MAXUS flight test and on a MAPHEUS VSB-30 flight

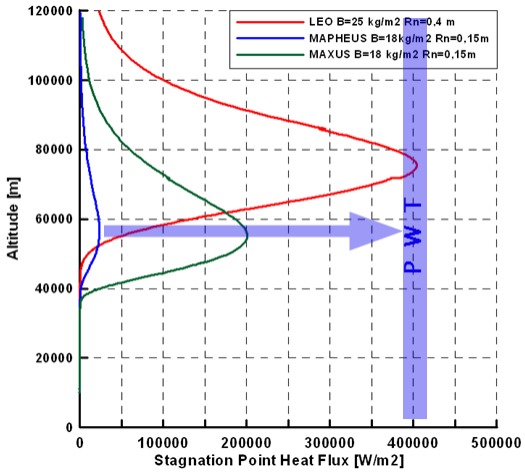

Figure 11. Heat flux experienced by a capsule in a LEO re-entry trajectory, on a MAXUS flight test and on a MAPHEUS VSB-30 flight

The VSB-30 sounding rocket flight is not sufficiently energetic for achieving significant heat fluxes on the TPS. Because of this, a PWT test is needed in order to achieve TRL 6 in a relevant environment. The Ground Demonstrator that will be tested in PWT will be representative not only of the materials, but also of the mechanisms of the flight model. While the PWT test carried on in 2001 was a test on the materials, the current test is a test on the TPS and deployment mechanisms subsystem and shall be executed for matching as much is possible the real LEO re-entry thermal environment. Even if not representative of the thermal part of the flight, the analyses show that the aerodynamic environment encountered in the VSB-30 flight is very close to the LEO entry. The flight will then prove the structural worthiness of the whole system and the aerodynamic characteristics. It is here important to underline that the previously planned MAXUS flight was less representative of the LEO entry because even if it is more energetic the LEO het fluxes are not matched, while the aerodynamic environment is excessively severe because the steepness of the trajectory.

6. VALIDATION AND VERIFICATION WORK LOGIC

In order to meet the required qualification needs for the qualifications of the two demonstrators the work approach proposed for the MINI-IRENE project is developed at two complementary levels:

- At system level, where it has impacts on the mission profile, on the overall architecture of the capsule, both on ground and in-flight operational constraints
- At subsystem level, where the innovative solutions proposed for some functions must be explored and validated.

At system level the main activities are:

- Identification of the technical challenges for cost-efficient independent access to space and adaptation of critical technologies (Deployable Structure, Thermal Protection) to the capsule. This project will provide guidelines for the future space application system.
- Definition of the qualification testing strategy.
- Development of a roadmap to actuate an exploitation plan, based on market analyses, competitive positioning, cost modelling and cost-benefits analyses.

At subsystem level the research activities will address the following domains:

- Deployable structure: umbrella like.
- Flexible Thermal Protection System: LEO thermal-mechanical re-entry environment resistant.
- Light weight avionic: miniaturized boards.

The following work logic is proposed:

- Design and Development of the relevant Bread-Boards for the emulation of the FD critical functions, i.e. structure deployment, umbrella deployment, stowing and initialization of the deployments after the release from the LV.
- Design and development of flight demonstrator and ground demonstrator.
- Qualification tests in representative environment of both FD and GD.

The relevant Bread Boards together with the qualification tests needed are illustrated in the following sections.

7. MINI IRENE TECNOLOGIES BREAD-BOARDS

7.1. Flexible Thermal Protection System

The target of the activity is the demonstration by testing of the suitability of the TPS fabrics to stand the thermal and mechanical stresses that are expected for the FD and GD. In particular, a tensile strength test campaign is supposed to be carried out on some samples of the TPS fabrics, which are prepared to be representative of the Demonstrators in terms of coupling and orientation of fabric layers, clamping methods, sewing typologies and edges reinforcements.

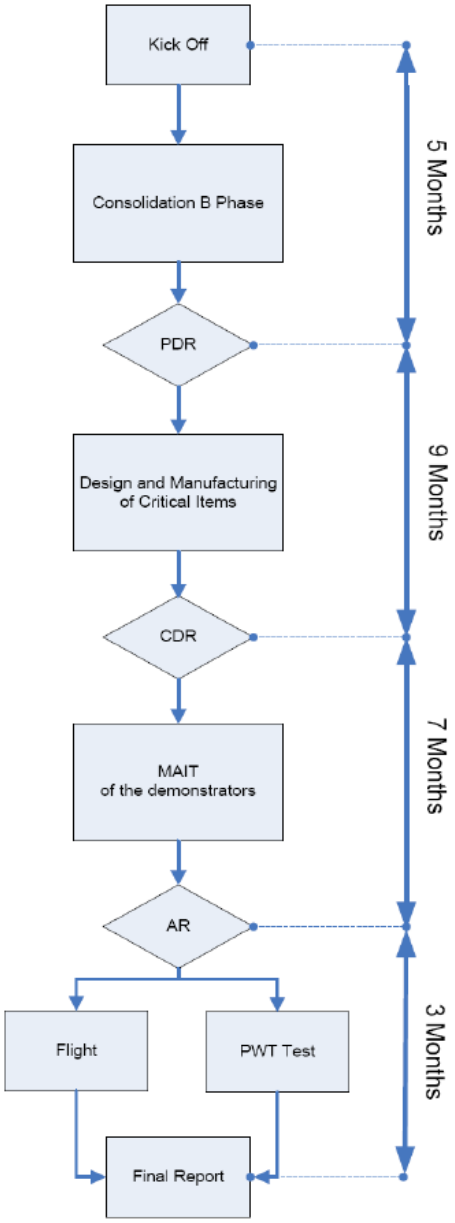

Figure 12. Work Logic

7.2. Integrated Test Equipment

Due to the complexity and amount of critical functions to be performed by the capsule for the deployment of the flexible TPS, an Integrated Test Equipment (ITE) has been designed with the purpose of demonstrating all the mechanical functions prior to finalize the design of the Flight Demonstrator.

In order to separate the critical functions analysis, the manufacturing and testing of the ITE has been split in three main parts with the objective of demonstrating their suitability to perform the required function in a laboratory environment:

- Capsule Body Deployment and locking;
- TPS Deployment and locking together with Integrated Deployment;
- Capsule Stowage System characterization.

The ITE testing activity shall provide fundamental information related to the following features:

- Proper displacement of the structure over its Linear Guides;
- Proper deployment of the TPS Fabric;
- Proper opening sequence for the two kinds of relevant actuators, based on gas springs;
- TPS fabrics fixation at the capsule Nose Plate and at the bottom side;
- Correct tensioning of the Flexible TPS between the Capsule nose and the bottom side;
- Proper functioning of every locking mechanisms.

Furthermore, the ITE also shall provide benefit for the consolidation of the design of the Avionic and S/S accommodation, the Stowage sequence and procedures and the AIT sequences and procedures.

7.3. Capsule Dummy Model

The activities aim to demonstrating the functioning of the separation mechanism that will expel the capsule from the launcher. For this purpose a Model of the capsule will be designed and built, which will be representative of the real capsule only in terms of mechanical interfaces, mass and (closed) shape. It will be used in separation and interface tests with the Launch Vehicle.

7.4. Deployment System Telescopic Pole

The target of the activity is to submit the gas springs to thermal and mechanical loads, in a laboratory environment, in order to demonstrate their suitability to the environmental conditions expected for the FD.

8. ENVIRONMENTAL TESTS AT THE SPACE QUALIFICATION LAB

The test campaign shall verify the MINI-IRENE capability to withstand operational loads encountered during launch and microgravity phases. After the measurement of the capsule mass properties the following tests shall be performed.

8.1. Deployment Test

The purpose of the test is to verify the functionality of deployment mechanism according to final chosen design requirement. A set of suitable physical parameters (strain, displacements, etc.) will be measured and compared with design values. The entire sequence of deployment will be monitored (elongation/extension,

tensioning phases, etc.). The motion of the deployment will be closely monitored and a final visual inspection will point out any presence of damage of the system or broken components or also parts becoming loose.

8.2. Static Acceleration Test

The test shall demonstrate and substantiate the design of FD to safely sustain the ultimate loading conditions due to launch phase. The FD will be subjected to centrifugal acceleration that will not exceed 8 g.

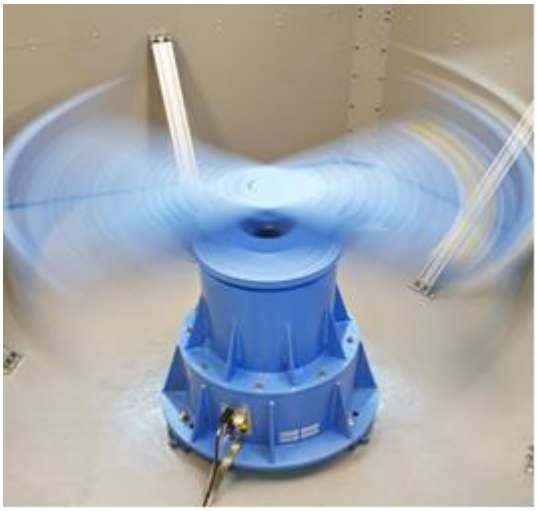

Figure 13. Centrifuge test for static acceleration

8.3. Vibrational Test

A low-level sine sweep will be applied to FD in order to identify main resonance frequencies. Furthermore, a resonance search test will be executed before and after each random and sine test to identify structural faults that could arise after the random and sine vibration runs, from the shift of the resonance frequencies and/or a change of the amplification factors value.
Sine vibration testing will subject the FD to excitation at all frequencies within a prescribed bandwidth, typically 10 to 2000 Hz, only on thrust axis. Actual vibration levels will be definitely identified after sounding rocket selection. FD, mechanical interfaces, EGSE, connectors and cables (to link FD – placed inside the chamber – to the EGSE – located outside the chamber-) will be provided and in charge of other project partner.
Random vibration test will subject the FD to excitation at all frequencies within a prescribed bandwidth, typically 20 to 2000 Hz, in the x, y, z directions as defined below.

8.4. Deployment in Vacuum Condition

A thermal vacuum test shall be conducted to demonstrate the ability of FD and of the electronic devices to perform in a thermal vacuum environment. Deployment test will be executed and the entire sequence will be monitored (elongation/extension, tensioning phases).
Before starting the Environmental Test Campaign, the FD shall be fully assembled, including the Separation System with the LV.

Figure 14. Thermal vacuum chamber

9. PLASMA WIND TUNNEL QUALIFICATION OF THE GROUND DEMONSTRATOR

In addition to the past qualification test performed at the Plasma Wind Tunnel, focused on the thermal qualification only of the flexible TPS in perspective of the IRENE mission, a further thermal qualification test in the PWT facility is also envisaged to be leaded. This test aims to the qualification of the integrated deployment mechanism, included the flexible TPS, and shall be representative of the IRENE mission profile, i.e. critical atmospherical reentry. Based on engineering formulas and the previous qualification test, the set of reservoir conditions will be defined, i.e. total pressure and total enthalpy. The test chamber free stream conditions will be obtained from the nozzle flow simulation.

Figure 15. SCIROCCO facility aerial view

10. CONCLUSION

The successful completion of all the validation steps and of the qualification test campaigns will allow the readiness to the final mission of the capsule, consisting in a suborbital flight after the launch with a sounding rocket. The readiness will be concurred in a dedicated project review, scheduled in advance to the planned launch window, named Test Readiness Review (TRR). In the TRR a special test review board (TRB) will review the preliminary results declaring potentially the tests completion by approving the test results at the end of test activities and reviewing the test results with respect to the testing specification.

11. REFERENCES

1. Savino, R., Aurigemma, R., Dell'Aversana, P., Gramiccia, L-, Punzo, F., Longo, J., Scolamiero, L. & Marraffa, L. (2015). European Sounding Rocket Experiment on Hypersonic Deployable Re-entry Demonstrator. In Proc. of the 8th European Symposium on Aerothermodynamics for Space Vehicles , IST Lisbon, Portugal.

2. Bassano, E., Savino, R., Lo Forti, R., Ferrarotti, A., Richiello, C., Russo, G., Aurigemma, R., Punzo, F. & Dell'Aversana, P. (2011) IRENE - Italian Re-Entry NacellE for Microgravity Experiments. In Proc. of the 62nd International Astronautical Congress. Cape Town, South Africa.

3. Savino, R. & Carandente, V. (2012). Aerothermodynamic and Feasibility Study of a Deployable Aerobraking Re-Entry Capsule. Tech Science Press, Fluid Dynamics and Materials Processing, Vol. 8, pp. 453-476.

4. Savino, R., Aurigemma, R., Carandente, V., Dell'Aversana, P., Gramiccia, L., Longo, J., Marraffa, L. & Punzo, F. (2014) Study and development of a sub-orbital reentry demonstrator. Journal of the British Interplanetary Society, Vol. 67(2), pp. 74-81.

5. Carandente, V., Zuppardi, G. & Savino, R. (2014) Study and development of a sub-orbital reentry demonstrator. Elsevier, Acta Astronautica, Vol. 93, pp. 291–303.

6. Gardi, R., Del Vecchio, A., Russo, G. & Marino, G. (2011). Shark-Maxus 8 Experiment: A technology demonstrator of the re-entry. In Proc. of the 20th ESA Symposium on European Rocket and Balloon Programmes and Related Research. Hyre, France.

7. Gardi, R., Vernillo, P., Fedele, A., Pezzella, G., Savino, R., Dell'Aversana P., Gramiccia, L., D'Aniello, G., Aurigemma, R., Cimminiello, N., Punzo, F., Florin, G. & Molina, R. (2017). MINI IRENE: Deployable heat shield for suborbital flight test. In Proc. of the 24th AIDAA International Conference. Palermo-Enna, Italy.

LESSONS LEARNED FROM THE FIRST FLIGHT OF AN ATOM INTERFEROMETER PAYLOAD ON A VSB-30 SOUNDING ROCKET

JENS GROSSE[1,2], STEPHAN T. SEIDEL[3,6], MAIKE D. LACHMANN[3], DENNIS BECKER[3], ANDRÈ WENSLAWSKI[5], VLADIMIR SCHKOLNIK[4], ALINE N. DINKELAKER[4], ORTWIN HELLMIG[8], HAUKE MÜNTINGA[1], HOLGER AHLERS[3], BENJAMIN WEPS[7], THIJS WENDRICH[3], ANDREAS STAMMINGER[6], MARKUS KRUTZIK[4], CLAUS BRAXMAIER[1,2], ERNST RASEL[3] AND THE QUANTUS TEAM[*]

[(1)] Universität Bremen, Zentrum für angewandte Raumfahrttechnologie und Mikrogravitation (ZARM), Am Fallturm, 28359 Bremen, Germany, Tel.: +49-421-24420-1228, jens.grosse@dlr.de
[(2)] Deutsches Zentrum für Luft- & Raumfahrt, Institute of Space Systems, Robert-Hooke-Str. 7, 28359 Bremen, Germany
[(3)] Institut für Quantenoptik, Leibniz Universität Hannover, Welfengarten 1,30167 Hannover, Germany
[(4)] Institut für Physik, Humboldt-Universität zu Berlin, Newtonstr. 15, 12489 Berlin, Germany
[(5)] Institute of Physics, Johannes Gutenberg University Mainz, Staudingerweg 7, 55128 Mainz, Germany
[(6)] Deutsches Zentrum für Luft- und Raumfahrt, Mobile Rocket Base, Oberpfaffenhofen, 82234 Wessling, Germany
[(7)] Deutsches Zentrum für Luft- und Raumfahrt, Simulation and Software Technology, Lilienthalplatz 7 38108 Brunswick, Germany
[(8)] Institute of Laser Physics, Universität Hamburg, Luruper Chaussee 149, 22761 Hamburg, Germany
[(*)] Refer Acknowledgments

ABSTRACT

The MAIUS-1 experiment is a pathfinder ultra-cold atoms experiment launched on a VSB-30 sounding rocket on the 23rd of January 2017. The scientific objective of the mission was to demonstrate the feasibility of creating a Bose-Einstein condensate (BEC) and performing atom interferometry aboard a sounding rocket with rubidium 87 atoms. This paper summarizes the design of the thermal control system, the payload sealing and the vacuum system. Moreover in-flight data for the hull temperatures, the vacuum and payload pressure are presented. This data is evaluated to verify the functionality of the thermal control system, the payload sealing and the vacuum integrity. The paper closes with the lessons learned from the MAIUS-1 mission and a brief outlook towards upcoming experiments with ultra-cold atoms in space.

1. INTRODUCTION

In order to create BECs, the atoms are cooled using laser light, magnetic fields and radio frequencies. The atoms are pre-cooled in an atomchip-based magneto optical trap (MOT) and finally brought below the critical temperature for the phase transition by evaporative cooling. These atoms are manipulated in a light-pulse interferometer sequence [1].

The two-staged VSB30 sounding rocket was operated by the DLR MORABA and launched from Esrange in the north of Sweden. The flight ticket for the MAIUS-1 mission includes all systems needed for rocket operation as well as the Brazilian S-30 and S-31 motors [2].

The motors lifted the payload to an altitude of 243 km providing 357.2 s of experimental time from T+93.0 (End of attitude and rate control - ARCS) to T+450.8 (Start Re-Entry) as shown in table 1.

During ascent the motors cause strong accelerations and vibrations. The maximum acceleration was approximately 12 g along the longitudinal axis. During re-entry the friction of the atmosphere caused accelerations of approximately 15 g in the lateral axis. Moreover the payload hull is heated up due to aerodynamic friction as discussed in chapter 3.

Time [s]	Alt [Km]	Event
T+ 0.0	0.33	Lift-Off
T+ 42.5	39.77	Burnout 2nd Stage (S30)
T+ 64.0	79.69	Start of ARCS Control 1st Cycle
T+ 76.2	100.23	Altitude > 100 km
T+ 93.0	126.29	End of ARCS Control 1st Cycle
T+ 252.2	242.55	Apogee
T+450.8	61.16	Re-Entry, Payload Spin Up by ARCS (TC)
T+ 468.0	60.93	Re-Entry Mode, Spin-Up by ARCS
T+573.2	4.07	Heat shield, Stab Chute Activation + Beacon Activation

Table 1. Excerpt of Time Events of MAIUS-1 Flight

The payload as presented in chapter 2 is designed to withstand these mechanical and thermal loads. The performance of the hull sealing, vacuum system and thermal control system during flight is discussed in chapter 3.

2. PAYLOAD DESIGN

The MAIUS scientific payload consists of five hull segments with an overall length of 2790 mm and a total mass of 309 kg. As shown in Fig. 1 the hull segments house four systems needed to perform atom interferometry.

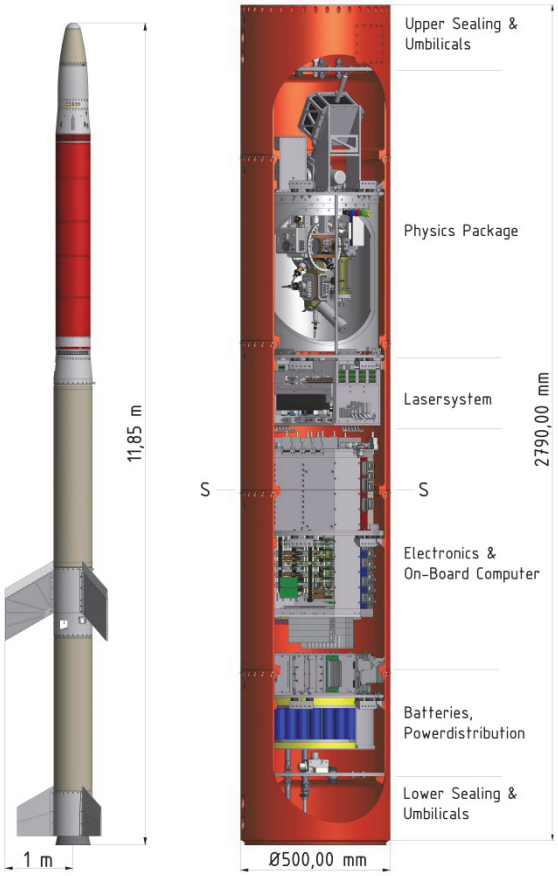

Figure 1. Overview of MAIUS-1 payload

The modules of the MAIUS-1 scientific payload are 500 mm in diameter with a wall thickness of 5 mm. The increase of the wall thickness from standard 3 mm to 5 mm reduces the impact of aero-thermal heating on the inside of the payload by increasing the thermal capacity of the outer structure.

2.1. Sealing of the Payload

During flight the scientific payload is sealed and pressurized. To limit the change in the alignment of the components inside the laser system, a pressure of more than 800 hPa is required during the entire flight.

For operation the enclosure is filled with synthetic air. The gas used for pressurization is a mixture of 20% oxide and 80% nitrogen, which ensures, that no carbon hydrates are remaining in the payload. The pressure was set to 1200 hPa to be able to detect leaks. For pressurization of the enclosure one ball tap each is installed in the top and bottom sealing plate.

Several data and power connections are fed through the sealing plate using hermetic (rubber sealed) DSUB and MIL-38999 circular connectors. Additionally four rubber sealed water feed through are installed.

The sealing of the structure is achieved by 3mm hydrogenated nitrile rubber o-ring seals. These o-rings are used at four radial seals between the modules and two axial seals at the top and bottom sealing plate as illustrated in Fig. 2.

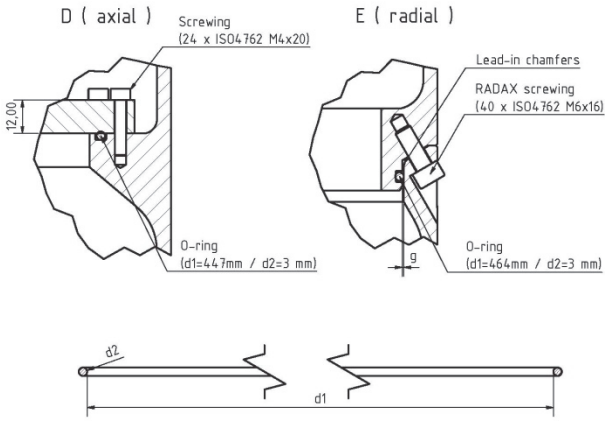

Figure 2. Detailed drawing of axial (D) and radial (E) sealing of the payload enclosure

For radial sealing a groove has been added to the MAIUS RADAX flanges. Moreover the tolerances and surface roughness properties have been changed compared to usual RADAX flanges. This minimizes the gap between the connected modules and ensures proper sealing between the modules.

2.2. Vacuum System

The vacuum system is an important part of the MAIUS-1 experiment. It comprises two vacuum chambers and the pumping system as shown in Fig. 3. In the experiment chamber the atoms are caught in a magneto optical trap.

Most connections in the vacuum system are using commercial con-flat (CF) seals or are brazed to minimize leakage rates of the apparatus. In the experiment and preparation chamber indium wire is used as an advanced sealing technique to mount and seal windows directly into the associated pockets in the chamber. The windows provide optical access to the atoms.

The vacuum system pressure is required to be below 5E-10 hPa to reduce perturbations from interactions with residual gas atoms. This pressure is maintained by

the pumping system mounted to the upper side of the chamber.

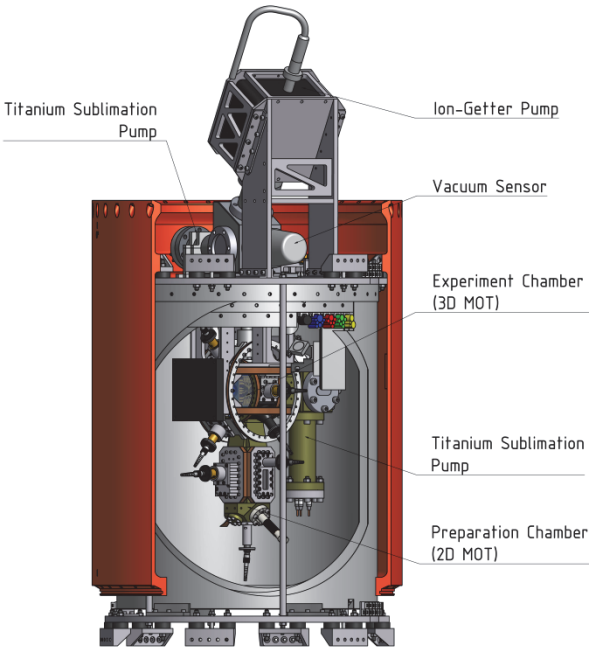

Figure 3. The Physics Package and components of the vacuum system of the MAIUS payload

This pumping system consists of a titanium sublimation pump and an ion getter pump. The pressure is monitored by a cold cathode vacuum gauge. An additional titanium sublimation pump is installed behind the atom chip.

2.3. Thermal Control System (TCS)

A stable thermal environment is needed for long-time operation in the lab as well as during the flight. The thermal control system of the payload uses different strategies to archive both. For long-term operation water cooling is used to extract the heat from the payload. Before lift-off it is provided by four umbilicals in two separate cooling cycles as depicted in Fig. 4.

Additionally the temperature sensitive hardware and high power electronics are placed in closed housings to reduce their heat exchange.

The water of the lower cooling cycle first cools the batteries and power distribution unit and then passes through the bottom and top electronic system heatsink. It is separated from the cooling cycle of the lasers to ensure that the high power that is dissipated at the electronic system does not disturb the temperature control of the laser system heat sink.

The temperature of the electronic system housing and heatsink is required to be in the range 0-50°C. This provides enough reserve to keep all electronic boards below 70°C. To minimize the drift in the coil current drivers, which results in a drift of the magnetic fields at the atoms, the temperature of the heat sink should not rise by more than 10 K during flight.

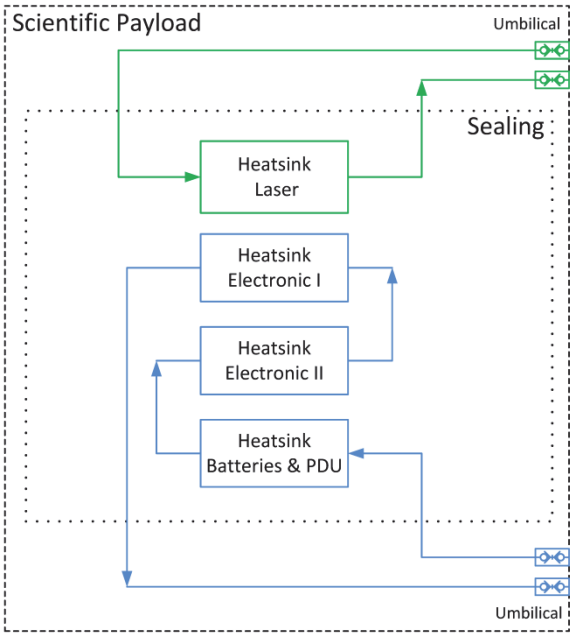

Figure 4. Schematic of the thermal control system of the MAIUS payload

During the flight electronic cards with power dissipation below 1 W store their heat in the printed circuit board, while cards with higher power are attached to the solid walls of the housing using copper heat pipes. During flight the average dissipated heat of 300 W is stored in the heatsinks and housing of the electronic system consisting of 29.8 kg of aluminum.

Special care has been taken to assure the temperature stability of the laser system. Its temperature requirements are driven by the laser modules installed within. Their temperature has to be controlled with an accuracy of +/- 0.1 K to maintain the frequency stability of the laser light. This is achieved by a two staged temperature control.

The first stage is the individual water cooling cycle of the laser system that controls the temperature of the laser heatsink with an accuracy of +/- 1° K during ground operation.

The second stage is formed by Peltier elements, which are placed below the laser modules to achieve the desired accuracy in temperature stabilization. In contrast to the water cooling, which is disconnected at launch, the Peltier elements operate during the entire flight. For reliable operation of the Peltier element, the temperature of the 7.3 kg aluminium heatsink should not rise by more than 5 K.

3. FLIGHT RESULTS

In the following the data of the MAIUS-1 housekeeping data for the payload pressure, the vacuum system pressure and the thermal control system are discussed.

3.1. Payload Pressure and Air Temperature

The payload pressure is measured using a *Freescale Semiconductor, Inc. MPXx6250A* absolute pressure sensor located close to the on-board computer at the lower side of the electronic system (compare Fig. 2). The payload was pressurized to 1230 hPa prior to launch.

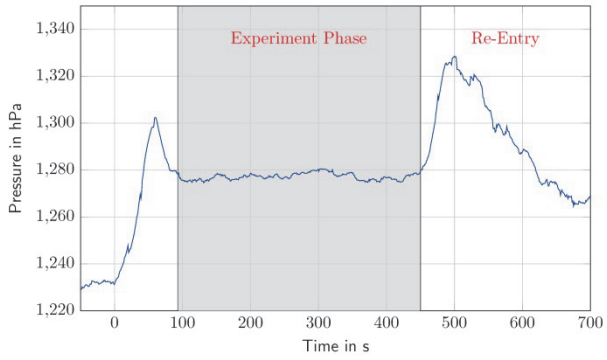

Figure 5. Payload absolute pressure during flight

As shown in Fig. 5 the payload pressure rises during ascent (T+0s to T+92s) and during re-entry (from T+468s) due to heating of the payload hull and the enclosed air respectively by aerodynamic friction with Earth atmosphere. During the experiment phase the pressure is constant. This is due to the negligible accelerations in this phase and the significantly reduced heat transfer coefficient between the hull and the enclosed air. This results in a reduced heating of the air.

The pressure profile during the flight suggests that no significant leak appeared during the flight of MAIUS-1. This statement is supported by a measured payload pressure of 1146 hPa after recovery on January 26th 2017 (3 days after flight)

3.2. Vacuum Pressure

The vacuum pressure was measured using a Pfeiffer IKR270 cold cathode gauge integrated in the pumping system as shown in Fig. 3.

The initial pressure of the vacuum system was measured to be 8.5E-11 hPa. During ascent the pressure rose to a maximum of 4E-10 hPa. This effect has also been observed during qualification of the vacuum system components [3]. The pressure rise is caused by micro leaks due to mechanical loads on the seals.

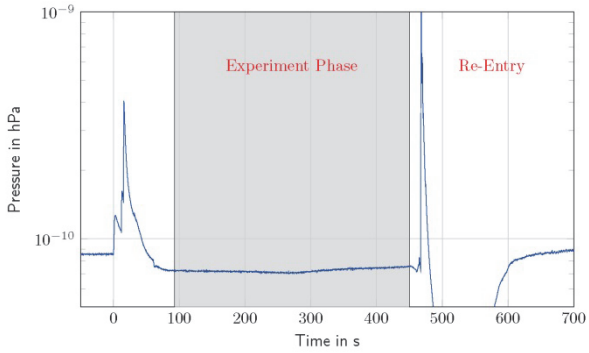

Figure 6. Vacuum system pressure during flight

After motor burn out at T+42.5s the pressure stabilizes within 24 s at a pressure of 7.2E-11 hPa. During re-entry the pressure reading rises to 8E-9 hPa before the sensor malfunctions. This behaviour has also been observed during testing of the sensor when strong vibrations or accelerations are applied [3]. However during these tests the sensor returned to reliable operation after a short deadtime. The same has also been observed during flight. After 130 s the sensor returns to a reliable pressure reading and stabilizes at 9E-11 hPa around T+700s. After touch-down (~ T+800s) all payload systems have been deactivated. Recovery was performed after 3 days. During this time the ion-getter pump was not active, yet the vacuum pressure after three days and recovery was 8E-09 hPa. Re-activation of the three pumps and half a day of pumping allowed to regain the initial pressure of 8.5E-11 hPa.

3.3. Hull and Heatsink Temperatures

A precise control of the heat sink temperature is crucial for a reliable operation of the experiment. The heatsink temperature is not only influenced by the dissipated heat of the payload instruments, but also by the heat flux from the hull which is affected by aerodynamic heating. The heat is transferred from the rocket hull to the different systems by conduction, radiation and convection [4].

To verify the numeric models used for the heat transfer from the hull to the system components and for the heat flux into the hull segments by aerodynamic friction [4] it is important to measure the hull temperatures. For this purpose four NTC temperature sensors have been mounted on the hull segments at 105° in the MAIUS coordinate system as shown in Fig. 7. The sensors have been mounted to the mounting flange of the battery, electronic and laser system as well as the physics package. The longitudinal distribution of the sensors can be identified from Fig. 1.

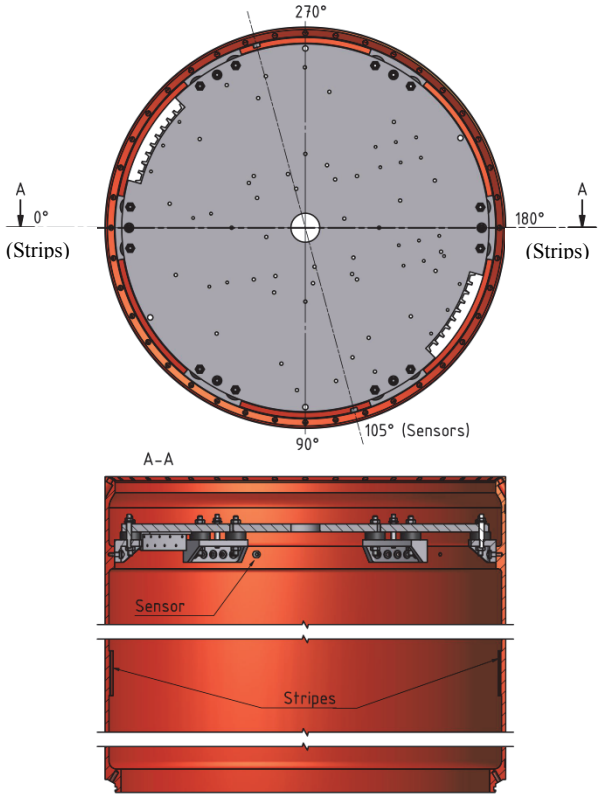

Figure 7. Position of temperature sensor across the MAIUS payload

In addition to these sensors a triplet of *testoterm* temperature strip has been applied to each hull segment at 0° and 180° of the MAIUS coordinate system as shown in Fig. 7. These strip measure the inside surface temperature of the hull. The strip change their color irreversibly when a certain threshold temperature is exceeded. The applied strip triplets cover a temperature range from 116°C to 260°C as shown in Fig. 9. The strip have been chosen as a redundant temperature indicator. As the measurement is passive it also delivers data through visible inspection after the flight if the house keeping data is not recorded.

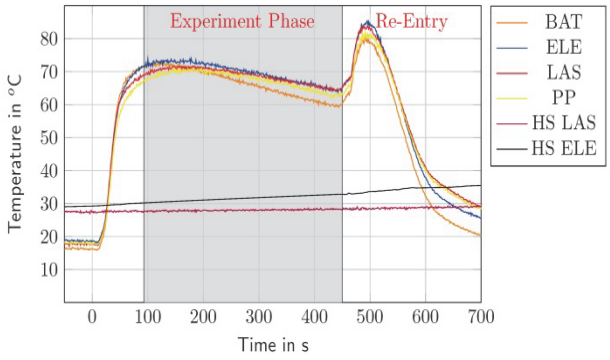

Figure 8. Temperature of 4 hull segments and two heatsinks (HS) during flight.

As shown in Fig. 8 the sensors recorded a maximum hull temperature of 73°C during ascent and 85°C during re-entry. Despite the temperature rise at the hull segments, the heatsink temperature of the laser system rose from 27.0°C to 28.3°C and the electronic system heatsink from 27.4 to 32.8 from lift off to the begin of re-entry. Thus both heatsink temperatures are within the requirements attesting a functional thermal design.

Figure 9. Temperature strips of the uppermost module (Umbilical Module) at 0° after flight. Black color indicates maximum hull temperature

Position	Temperature at 0°	Temperature at 180°
Umbilical	149°C - 154°C	< 116°C
Physics Pack.	143°C - 149°C	< 116°C
Laser System	143°C - 149°C	< 116°C
Elect. System	138°C - 143°C	< 116°C
Power System	127°C - 132°C	< 116°C

Table 2. Temperature strip measurements at 0° and 180° of the MAIUS coordinate system

The temperatures obtained from the strip (Table 2) show that the 0°-side of the payload was heated to temperatures between 149°C and 154°C at the top of the scientific payload and to temperatures between 127°C and 132°C at the bottom. The stripes at the 180°-side were not activated, indicating temperatures below 116°C. This is supported by recorded temperatures of 85°C as measured by the sensors.

The payload entered the atmosphere along the lateral axis. Before re-entry the payload was spun up along the longitudinal axis. The temperature difference between 0° and 180° indicates, that the payload was stabilized during re-entry with the 0°-side facing towards the atmosphere, while the 180°-side was shielded, which results in the lower hull temperatures.

4. SUMMARY & OUTLOOK

In the MAIUS-1 mission all systems presented herein functioned as required. However, there are several points that can be improved. For the three systems discussed in this paper lessons learned are presented as follows.

4.1. Lessons Learned

The sealing of the payload kept the pressure within the required range with no indication of a pressure loss during or after flight. Thus, the payload sealing does not require significant redesign.

However some of the commercial DSUB connectors leaked during testing and had to be replaced. Especially the high-current feedthroughs were not suitable for this application. These feedthroughs will be replaced by hermetic military grade connectors for the upcoming missions. Moreover it was difficult to separate the hull segments after assembly. A mechanism for separation will ease this procedure in future.

The vacuum system kept the vacuum pressure below the threshold of 5E-10 hPa even during launch. The performance has even been better than during testing [4]. For this reason the pumping speed is sufficient for this application and no design change is required.

Heatsink temperatures have also been in the required range despite the high thermal loads from the inside and the outside. The water cooling allowed for unlimited operation in the laboratory and on the launch pad. However the measured flow rates have been around 3 L/min, which is at the edge of what is required for a sufficient heat exchange. For this reason the chillers will be replaced by a model with a more powerful pump.

Additionally it is desirable to add more temperature sensors to be able to measure the radial temperature distribution in the hull segments as well. The measurement range of the temperature strips will be adapted to 71°C to 204°C to allow detection of lower temperatures as well.

4.2. Outlook

System and payload designs for realization of dual species interferometry with potassium and rubidium on a sounding rocket are currently being developed.

These designs already include improvements based on the lessons-learned in MAIUS-1 as described in chapter 4.1. The design phase will be completed with the critical design review scheduled for June 2018. Launches of the payloads MAIUS-2 and MAIUS-3 are scheduled for spring 2020 and summer / autumn 2021, respectively.

In parallel activities have been started to design a Bose-Einstein condensate and cold atom laboratory (BECCAL) for operation onboard the international space station based on the design and technologies of the MAIUS payloads.

ACKNOWLEDGMENTS

The QUANTUS project is a collaboration of LU Hannover, HU Berlin, U Hamburg, JGU Mainz, U Ulm, TU Darmstadt, FBH Berlin, U Birmingham, DLR RY Bremen, DLR MORABA, DLR SC and ZARM at U Bremen. It is supported by the German Space Agency DLR with funds provided by the Federal Ministry of Economics and Technology (BMWi) under grant numbers DLR 50WM 1131-1137.

REFERENCES

1. Seidel, S. T. (2015), *Atom Interferometry On Sounding Rockets*, Proceedings of the 22nd ESA Symposium on European Rocket and Balloon Programmes and Related Research, European Space Agency, Noordwijk, The Netherlands, pp. 309–312
2. Stamminger, A., et al. (2015), *MAIUS1 - Vehicle, Subsystems Design and Mission Operations*, Proceedings of the 22nd ESA Symposium on European Rocket and Balloon Programmes and Related Research, European Space Agency, Noordwijk, The Netherlands, pp. 183–190
3. Grossse, J. et al. (2016) Design and qualification of an UHV system for operation on sounding rockets. Journal of Vacuum Science and Technology A, 34 (3). American Vacuum Society. DOI: 10.1116/1.4947583 ISSN 0734-2101
4. Grosse, Jens (2016) Thermal and Mechanical Design and Simulation for the first high precision Quantum Optics Experiment on a Sounding Rocket. PhD Thesis, University of Bremen.

COLUMNAR-TO-EQUIAXED TRANSITION IN THE TRANSPARENT ALLOY SYSTEM NPG-DC OBSERVED IN THE LOW-GRAVITY AND NORMAL GRAVITY EXPERIMENT "TRACE-3"

Gerhard Zimmermann, Martin Hamacher, Laszlo Sturz

ACCESS e.V., Intzestrasse 5, 52072 Aachen, Germany, Email: G. Zimmermann@access-technology.de

ABSTRACT

The experiment "TRACE-3" (TRansparent Alloys in Columnar Equiaxed Solidification - 3) has been carried out onboard the sounding rocket TEXUS-51 in low-gravity environment in 2015. The experiment is a modification of the previous experiments "TRACE" and "TRACE+" flown on TEXUS-47 and TEXUS-49 missions, respectively.

The experiments aimed at investigating dendritic growth and the transition from columnar to equiaxed solidification (CET) in the transparent organic alloy system Neopentylglycol (NPG)-(D)Camphor (DC). To investigate the concentration effect on CET an alloy concentration of 22.5 wt.-% DC was chosen, being between the compositions selected for "TRACE" (37.5 wt.-% DC) and "TRACE+" (20.0 wt.-% DC).

Here we present the experimental results of the "TRACE-3" experiment, including a comparison with reference experiment REF carried out under terrestrial gravity conditions. The results will serve as precise benchmark data for a comparison with different theoretical models.

1. INTRODUCTION

Solidification of an alloy is often accompanied by the formation of dendritic microstructures at the propagating solid-liquid interface or in the melt pool. Such dendrites may undergo coarsening or phase transformations upon further cooling towards the final microstructure at ambient. The first microstructure and grain structure formation from the liquid is of fundamental importance for the mechanical properties of the solidified specimen, especially with respect to casting defects. Additionally, dendritic microstructures are interesting from a fundamental point-of-view as examples for pattern formation in non-equilibrium systems.

In general, columnar and equiaxed dendritic grains can be distinguished from their physics of formation and appearance in solidified materials. Columnar grains show primary dendrite stems growing continuously in a favourable crystallographic orientation towards the direction of an applied thermal gradient. The primary stems develop higher order side-arms and branches during growth. Interacting columnar grains thus have an elongated shape ("columns") in the primary stem growth direction. Equiaxed dendritic grains can form within a sufficiently undercooled melt having also a branched structure, but a generally more isotropic shape ("equiaxed").

Usually, for given alloy composition and thermophysical properties either columnar or equiaxed grain growth is favoured in dependence of the main experimental parameters, thermal gradient and cooling-rate. As an empirical formula, the grain structure tends to be equiaxed, when G/v is decreased, with G being the thermal gradient in growth direction and v the solidification velocity, respectively. This implies that with changing solidification conditions - like in typical casting - a mixed zone with columnar and equiaxed grains may exist simultaneously. This leads to a transition from columnar to equiaxed grain growth (CET), resulting in inhomogeneities of the microstructure and, as a consequence, in undesired mechanical properties. Therefore, it is essential to know the mechanisms and critical parameters for CET.

Besides the investigation of CET in metallic alloys [1-5], a few organic alloys can be used, having the same non-facetting but dendritic solidification behaviour like metals. Such alloys are often transparent to visible light and therefore allow for in-situ and real-time observation of microstructure and grain formation down to the micrometer scale using light microscope optics.

Gravity can have a significant influence on CET. On the one hand, it induces sedimentation or buoyancy of equiaxed grains depending on the density difference between them and the surrounding liquid. Furthermore, gravity can also cause convective motion with enforced heat and mass transport. But in low-gravity conditions these effects can be minimized and growth is dominated by diffusive conditions. This allows for simplified experimental boundary conditions. Such experiments serve as benchmarks for analytical and numerical dendrite growth and CET models under diffusive conditions [6-10].

Here, we present a comparative analysis of results obtained from a CET-experiment realized under low-gravity conditions and from the corresponding reference experiment on ground. The microgravity experiment "TRACE-3" was carried out on the sounding-rocket mission TEXUS-51 in 2015 using the transparent

organic alloy system Neopentylglycol - 22.5 wt.-% (D)Camphor (NPG-DC).
The experimental set-up, modifications and methods are explained in section 2, while results of low-gravity and reference experiment are summarized and discussed in section 3. Conclusions and an outlook are given in section 4.

2. EXPERIMENTAL PART

2.1. Alloy preparation and properties

Figure 1 shows the binary phase-diagram of the NPG-DC system [11]. The purified materials have been alloyed as NPG-0.225 wt.-fraction DC. The preparation and alloying of the organic materials have been described elsewhere [7, 8]. According to the selected composition in the solidification experiments primary dendrites of NPG will be formed Relevant thermodynamic and thermophysical properties for the NPG-22.5wt.-%DC alloy are given in Table 1.

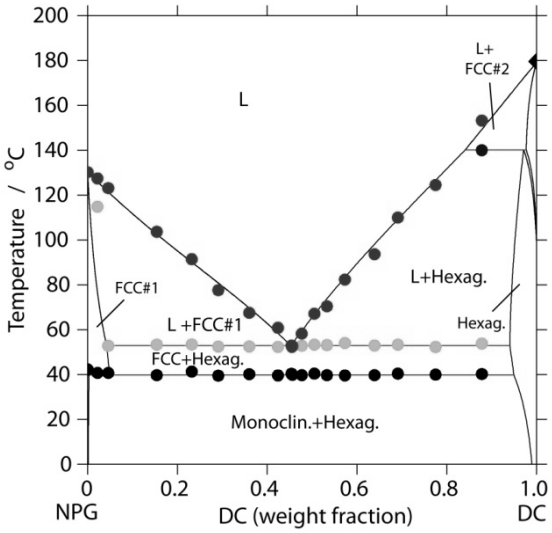

Figure 1. Phase-diagram of NPG-DC. Alloy chosen is NPG-0.225 wt.-fraction DC. L=Liquid, FCC = face-centred cubic (phases).

Table 1. Some relevant thermodynamic and thermo-physical properties of the NPG-22.5wt.-%DC alloy.

Property	Value
Liquidus-temperature T_L	91.2±1°C[(a)]
Solidus-temperature T_S	52.9±0.5°C[(a)]
Transfomation temperature (FCC-monocl.)	39.9±0.5°C[(a)]
Liquidus-slope m_L	-1.57 K/wt%[(a)]
Partition-coefficient k	0.064[(a)]
Gibbs-Thomson-coefficient Γ	(7.7±0.8)*10^{-8} Km[(b)]

(a): from thermo-dynamic CALPHAD-description [11];
(b): interpolated from [12].

2.2. Experimental set-up and procedure

The experimental set-up is based on previously used hardware developments by Airbus D&S for sounding rockets investigating solidification in transparent model alloys [8].
For the experiment "TRACE-3" on TEXUS-51 the experimental volume was contained in between a steel frame and two plates made from crystalline quartz glass having about 4-times the heat conductivity of normal quartz glass. The experimental volume size is 13 mm in width, about 10 mm in height and 3 mm in thickness. This thickness may allow for gravity driven convective flow on ground because of less viscous friction than in a thin, sheet-like cell. A bottom inlet and top outlet in the steel frame supports feeding of the pre-molten alloy and volume compensation during thermal and phase-change shrinkage and expansion to avoid bubble formation.
Five thermocouples type K of 0.25 mm diameter were inserted through holes at both sides of the frame to follow the temperature evolution during the experiment within the alloy. The three TC's at the left side (see Figure 4) are at y-positions of 1.41±0.025 mm, 4.91±0.025 mm and 8.39±0.025 mm, measured from the bottom of the experimental volume; the two TC's at the right side are at y-positions of 3.24±0.025 mm and 6.68±0.025 mm. The acquisition rate of the thermocouples was 5 Hz. Due to the small size of the thermocouples, their influence on the thermal field or the nucleation events is negligible.
A schematic drawing of the set-up is given in Fig. 2. The experimental volume was illuminated from one side with monochromatic LED-light and observed with two different optical systems: A beam splitter provided a microscopic observation of solidification details within a movable field-of-view of 2.25 mm width and 1.65 mm height, while in parallel an overview image with field-of-view of 18.2 mm width and 13.7 mm height was acquired. For both images a frame rate of 10 frames/sec was realized. The overall image is fixed showing the complete experiment cell. The position of the detail image can be shifted in x- and y- direction within the whole field-of-view.

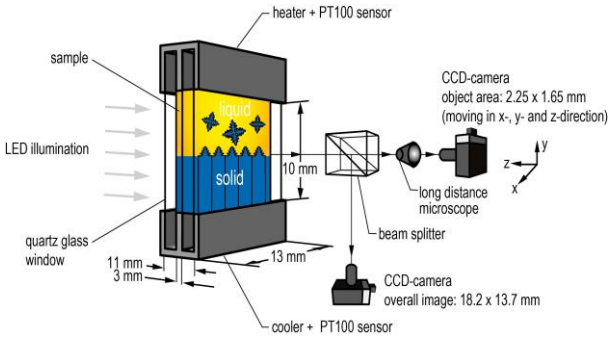

Figure 2. Schematic drawing of the main parts of the experimental set-up.

Additionally, moving in z-direction allows for focussing on objects solidifying in at different depths inside the experiment cell. The experiment cell temperature was controlled from the bottom with a Peltier-cooler and from the top by a resistance heater, both using PT-100 temperature sensors.

Table 2 summarizes the experimental procedure for "TRACE-3". Before lift-off the cell was oriented vertically upwards in the payload and in the gravity field. After complete melting of the alloy and a phase of thermal mixing induced by a horizontal temperature gradient due to an additional side heater, the initial vertical temperature gradient was applied. At heater and cooler temperatures of T_H = 121°C and T_C = 87°C the liquid state was equilibrated, with liquidus-temperature being at T_L = 91.2°C. Before lift–off cooling rates of - 1.5 K/min were applied at heater and cooler simultaneously to initiate columnar growth starting in the microgravity period. CET was triggered by increasing the cooling rates to - 3.0 K/min.

The images of both of the cameras, as well as the house-keeping data and thermal data from the thermocouples were transmitted during the complete experimental runs on ground and during flight, except small time-intervals after lift-off and re-entry of the rocket. Furthermore the detail images were stored digitally on-board with higher resolution than those transmitted to ground with standard video resolution. The corresponding reference experiment on ground was carried out after the flight experiment with the identical experimental procedure as given in Tab. 2 and solidification vertically upwards during the complete experiment.

Table 2. Experimental procedures for the low-gravity experiment (similar for reference experiments). The times refer to lift-off of the sounding-rocket at t=0 s.

Time	Action
	Complete melting of the alloy from room temperature
	Thermal mixing by convection; with side heater on
≅ - 50 min	Equilibration in liquid state: Heater temperature T_H = 121°C Cooler temperature T_C = 87°C
= - 146 s	Setting of bottom and top cooling rates to - 1.5 K/min.
0 s	Rocket lift-off, high accelerations.
< 60 s	Burn-out of rocket stages, de-spinning and stabilization of rocket.
> 72 s	Gravity level < 1 mg.
≅ 100 s	First crystals at the bottom, starting of columnar growth
320 s	Initiation of CET: Increase of the cooling rates from -1.5 K/min to -3.0 K/min.
442 s	Re-entry of rocket, end of low-gravity period

3. RESULTS AND DISCUSSIONS

3.1. Thermal data

Figure 3 shows the cooling curves measured at the five thermocouples T1 to T5 for the "TRACE-3" flight experiment and the 1g reference experiment (REF). The temperature evolutions during the first stages of melting, mixing and equilibration are not shown explicitly here. At t = -146 s the lower cooling rate is started resulting in a general decrease of the temperatures.

In the flight experiment the temperatures measured at the thermocouples between lift-off (t=0 s) and beginning of the low-gravity period (t=72 s) show a significant deviation from nominal decrease. This is attributed to the controlled de-spinning of the sounding rocket at the end of the rocket boost phase and the inertia of the liquid in the cell reacting to the de-spinning and leading to a convective motion and partial thermal mixing. The CCD-images show that the convective motion in the melt was slowing down rapidly (~10 s), while the thermal field was rebuild at about t = 100 s when the first crystals start to grow.

In the low-gravity period the temperatures in the flight experiment ("TRACE-3") are slightly higher than in the reference experiment (REF). This is due to suppressed air convection in the experiment module during the flight, resulting in a reduced cooling of the windows of the experiment cell.

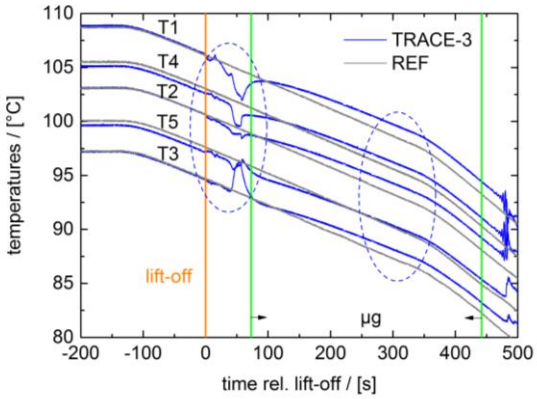

Figure 3. Temperatures T1 to T5 measured inside the experiment cell for µg ("TRACE-3") and 1g (REF)

3.2. CCD-images

Figures 4 & 5 show sequences of overview CCD-images obtained from the "TRACE-3" and the 1g reference experiment at selected time-steps. In the overview images 3 thermocouples are visible on the left-hand side and 2 TC's on the right-hand side. The first images at t = 270 s show the development of the columnar dendritic front from the bottom. Most of the columnar grains have a crystallographic orientations (i.e. <100> direction of the FCC crystal) close to the y-direction, but

also grains tilted up to about 30° (projected to the image plane) from the y-axis exist.
After increase of the cooling-rate to -3.0 K/min at t = +320 s a relatively small amount of equiaxed crystals occurs ahead of the columnar front, shown here at t = +360 s. Later on, more and more equiaxed dendrites nucleate and grow, leading to the columnar-to-equiaxed transition (CET). In the µg experiment a more cluster-like equiaxed dendritic structure are observed, whereas in the 1g experiment a more homogeneous distribution exists. In both cases CET is successfully initiated by the applied cooling conditions.

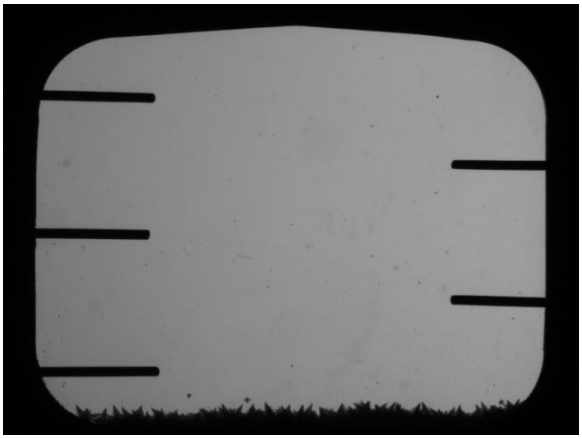

(a) t=270 s, columnar growth

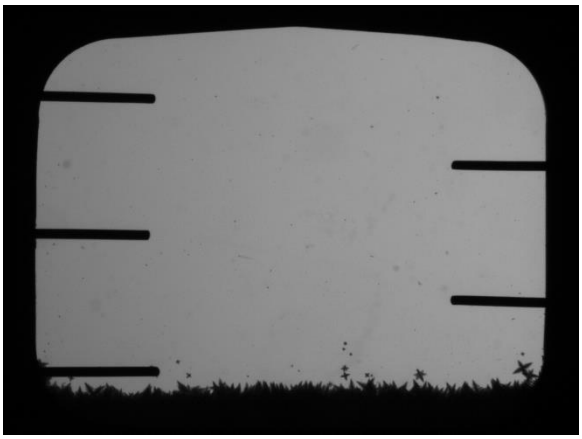

(b) t=360 s, formation of some equiaxed dendrites

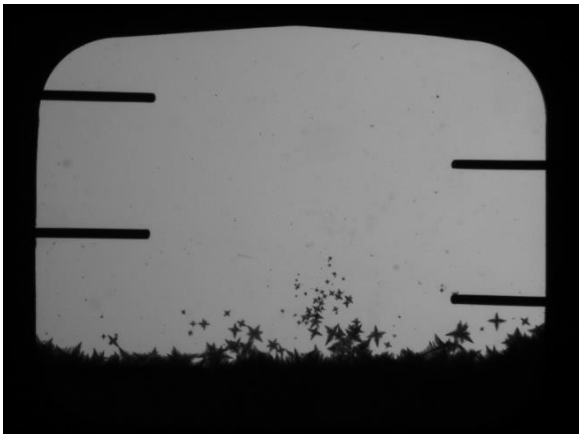

(c) t=430 s, equiaxed growth.

Figure 4. Selected overview images of the µg-experiment "TRACE-3". Times refer to lift-off (t=0 s).

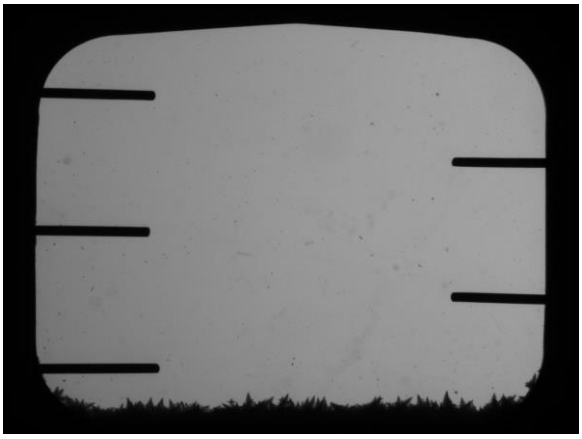

(a) *t=270 s, columnar growth*

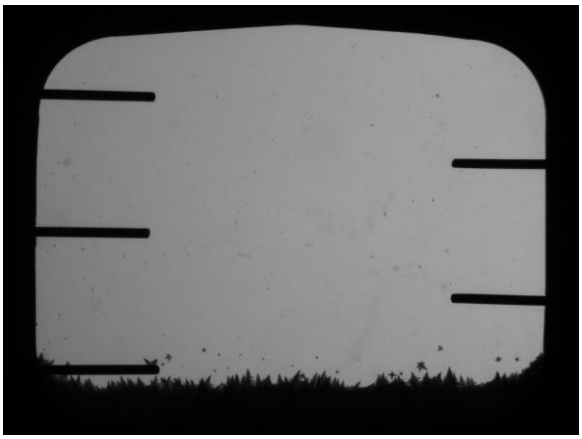

(b) *t=360 s, formation of some equiaxed dendrites*

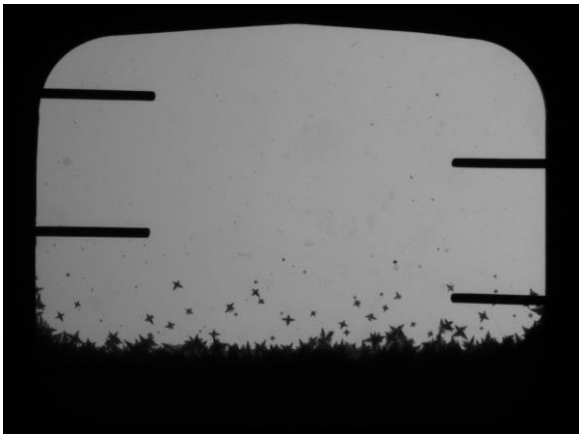

(c) *t=430 s, equiaxed growth*.

Figure 5. Selected overview images of the 1g-experiment "REF". All times refer to lift-off (t=0 s).

3.3. Front position, velocity and undercooling

The position of the front is obtained by automatic image processing from the overview CCD-images in the centred 8 mm of the 13 mm wide sample. The positions are averaged over the length of the sampling window and are shown in Fig. 6. The front velocities are derived from the point-by-point derivatives of the averaged front positions and are shown in Fig. 7. No considerable difference between the µg and 1g experiments is detected. In both cases a steady-state columnar growth with constant front velocity of about 7.5 µm/s was established at t=320 s. Then, after the increase of the cooling rate, the velocity of the columnar front increases significantly until blocking by the equiaxed dendrites.

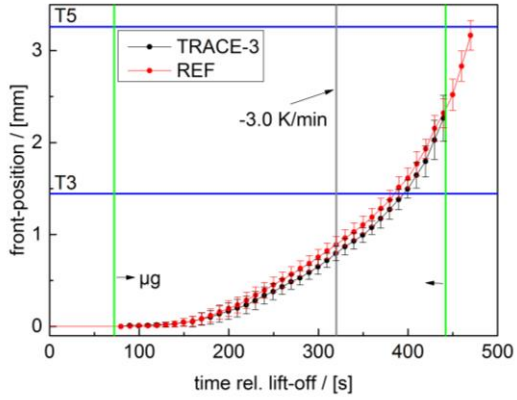

Figure 6. Averaged front positions for "TRACE-3" and reference experiment REF with T3/T5 positions of the thermocouples.

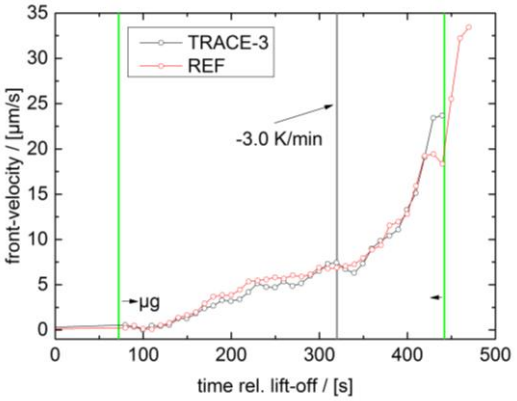

Figure 7. Front velocities for "TRACE-3" and reference experiment REF

The front temperatures are derived from the front positions and the local temperature, which is determined from a linear interpolation of the temperatures measured with the two thermocouples T3 and T2, and an extrapolation in the region below T3 using the average temperature gradient G = 1.7 K/mm. The front undercooling is calculated from the difference of the front temperature to the liquidus-temperature of T_L = 91.2 °C and is shown in Fig. 8.

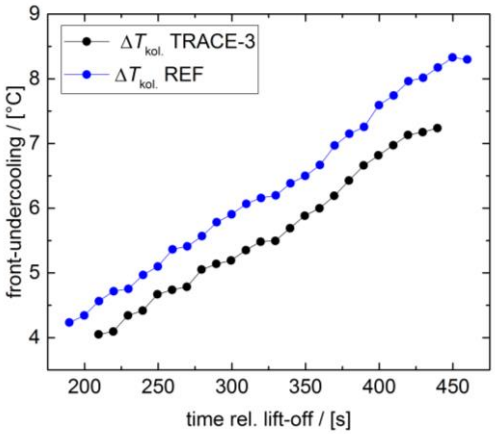

Figure 8. Front undercooling for "TRACE-3" and the reference experiment REF.

In both experiments the undercooling of the front rises continuously with the same rate. This holds for both cooling rates. The front undercooling in the µg experiment "TRACE-3" is about 0.5 – 1.0 K lower than the front undercooling in the 1g reference experiment. This effect on the one hand is due to the slight overall temperature differences shown in Fig. 3, and on the other hand due to a moderate melt flow in the 1g case. Such a flow reduces the solutal pile-up of (D)Camphor ahead of the columnar front and results in a higher position of the front.

3.4. Kinetic law for columnar growth

Figure 9 shows the columnar growth velocity as a function of the front undercooling. Both µg and 1g experiments show a similar behavior starting with nucleation of first equiaxed dendrites at an undercooling of about 4 K. For higher undercooling the front-velocity in the µg-experiment is slightly higher than in the 1g case.

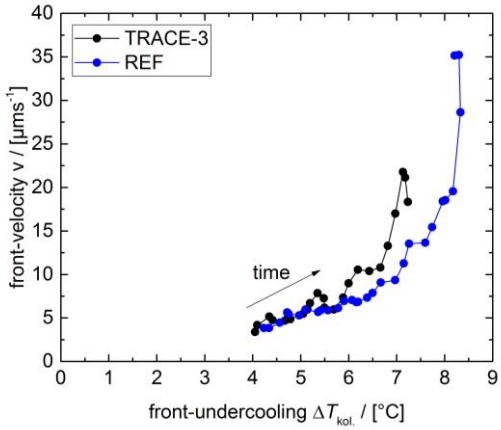

Figure 9: Kinetic law for columnar growth from experiments

3.5. Equiaxed dendrites

After increasing the cooling rate from -1.5 K/min to - 3.0 K/min equiaxed dendrites nucleate and grow in the melt ahead of the columnar front. The nucleation mechanism is heterogeneous nucleation on unknown substrates like in previous experiment [6–8]. From the overview images the number of equiaxed dendrites is determined using MATLAB© software. We recall that the pixel resolution in the observation plane is about 24 µm, thus dendrites/nuclei of smaller size cannot be detected. Equiaxed dendrites engulfed into the growing columnar front with more than about 50 area% were not taken into account in the analysis.

Figure 10 shows the number of equiaxed dendrites found in time intervals of 10 s for "TRACE-3" and the reference experiment REF. Both curves are similar and show a significant increase in the number of dendrites after increasing the cooling rate. Fig. 11 shows the cumulative total number of equiaxed dendrites for "TRACE-3" and REF.

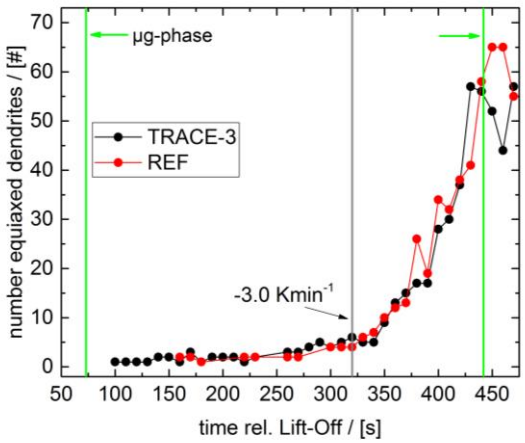

Figure 10. Number of equiaxed dendrites determined in time intervals of 10s for "TRACE-3" and REF

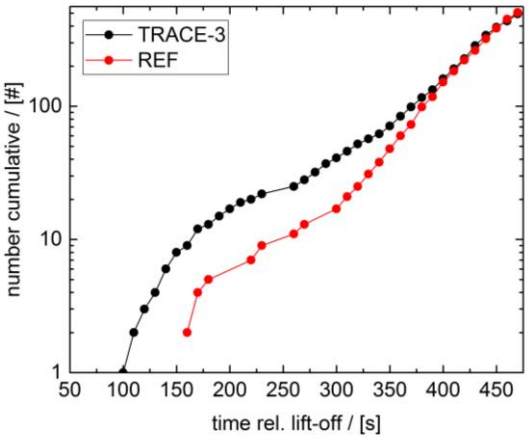

Figure 11. Cumulative total number of equiaxed dendrites for "TRACE-3" and REF

It can be found that in the µg experiment the growth of equiaxed dendrites starts about 50 s earlier than in the 1g experiment. This may be due to the fact that for the diffusive boundary conditions the undercooled region ahead of the columnar front keeps undisturbed. In the 1g experiment a moderate convective melt flow reduces the undercooled zone. Interestingly enough towards the end of the experiments the cumulative total number of equiaxed dendrites is nearly identical. This indicates different solidification paths leading to the same total number of equiaxed dendrites in the µg and 1g experiments.

Detail images of 2.25 mm width and 1.65 mm height in Fig. 12 show the growth and interaction of equiaxed dendrites in the µg-experiment "TRACE-3". The development of the arm lengths of a single dendrite marked with A1 to A4 is given in Fig. 13. Free growing arms are characterized by a nearly constant growth velocity of 7.5 ± 1.0 µm/s. In case of an interaction with neighbouring dendrites the growth velocity is decreased (see arm A3).

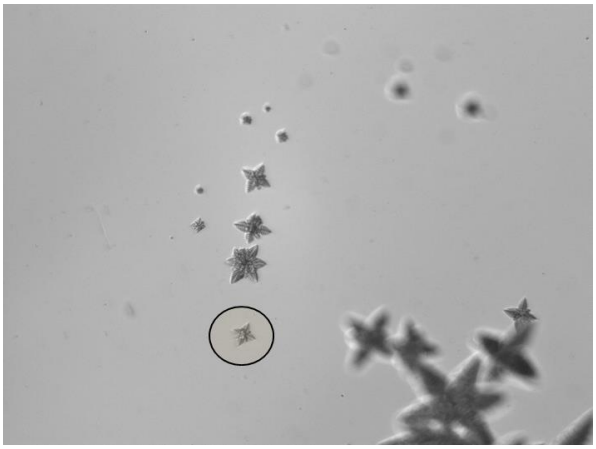

(a) t=405 s

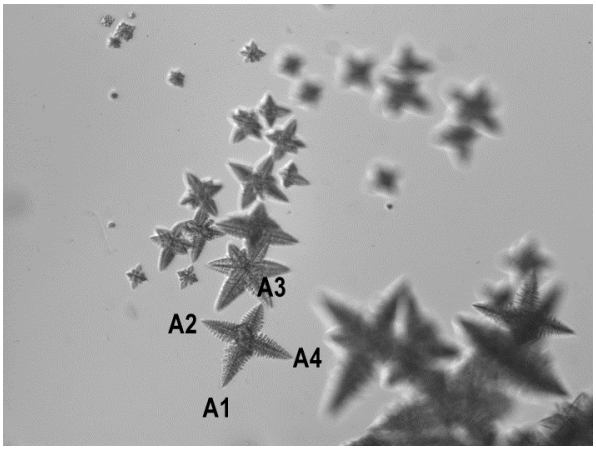

(b) t=425 s

Figure 12. Detail images showing the growth and interaction of equiaxed dendrites in the µg-experiment "TRACE-3". Times refer to lift-off (t=0 s).

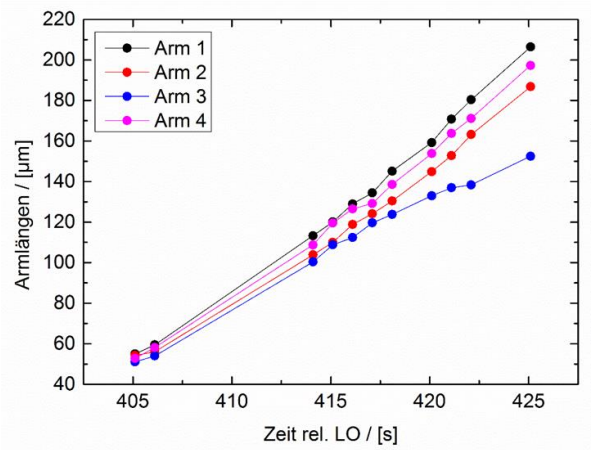

Figure 13. Development of the dendrite arm lengths A1 to A4 of the dendrite marked in Fig. 12.

3.6. Columnar-to-equiaxed transition CET

Figures 14 & 15 show overview images indicating the beginning and the end of the CET for the µg and the 1g experiments This CET time interval is determined by the area portion of the equiaxed dendrites close to the columnar front reaching about 30%.

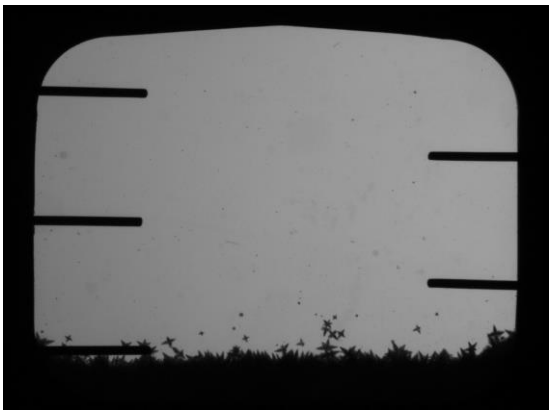

(a) t=390 s, start of CET

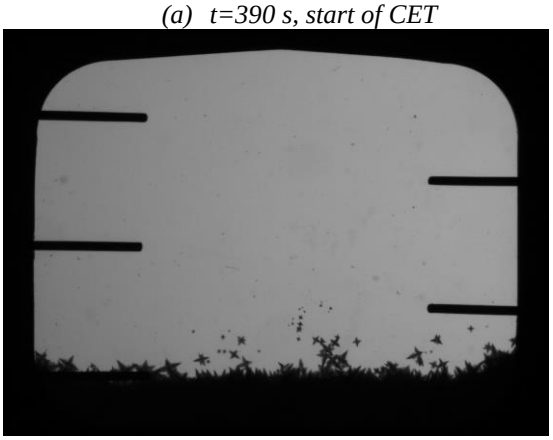

(b) t=410 s, end of CET

Figure 14. Overview images at CET for the µg-experiment "TRACE-3". Times refer to lift-off (t=0 s).

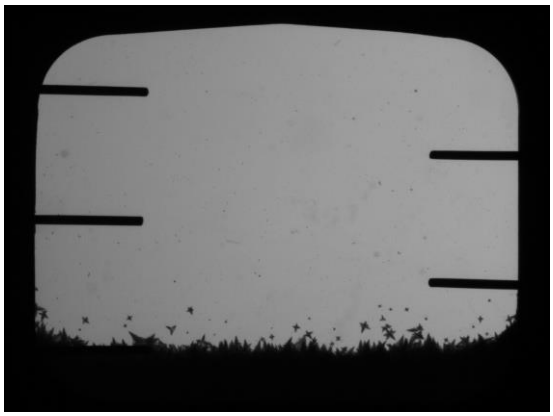

(a) t=400 s, start of CET

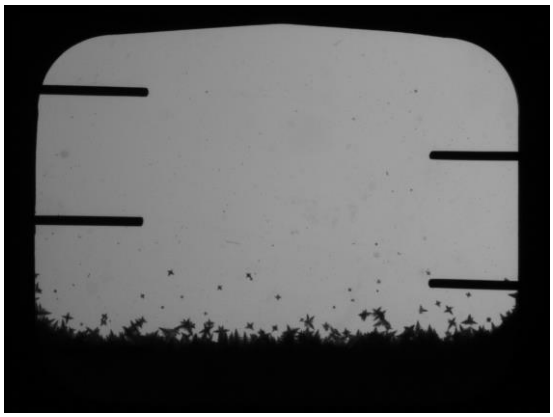

(b) t=420 s, end of CET

Figure 15. Overview images at CET for the 1g-experiment "REF". Times refer to lift-off (t=0 s).

The critical values for CET are summarized in Table 3. It is found that CET occurs about 10 s earlier in the µg experiment and the critical values of both µg and 1g experiment are quite similar. But, the spatial development of CET is different. Figs. 14 & 15 show that in the diffusive case ("TRACE-3") some accumulations of equiaxed dendrites occurs, whereas in the 1g case (REF) a more homogeneous distribution of equiaxed dendrites exists.

Table 3. Critical values of CET for the low-gravity experiment "TRACE-3" and the 1g reference experiment REF. The times refer to lift-off of the sounding rocket at t=0 s.

	„TRACE-3"	REF
Time *t*, s	390-410	400-420
Front position *z*, mm	1.40-1.65	1.63-1.93
Front velocity *v*, µm/s	11.1-15.5	13.1-19.2
Front undercooling Δ*T*, °C	6.7-7.0	6.8-7.2
Number of equiaxed dendrites, N	17-30	34-38
Temperature gradient G, K/mm	1.74-1.75	1.68-1.69

4. CONCLUSIONS

Dendritic growth and the transition from columnar to equiaxed growth regime were investigated within the organic alloy NPG-22.5 wt.-%DC onboard the sounding rocket TEXUS-51 and on ground. Following conclusions can be drawn from the results:

- The hardware and especially the optical diagnostics worked nominally to investigate the solidification in-situ.
- The microscope optics with focussing in depth allows for determination of the velocity of equiaxed dendrites arms growing freely or interacting with neighbouring dendrites.
- A columnar-to-equiaxed transition was triggered successfully both in the µg and 1g experiment. The critical parameters for CET are rather similar, but the in-situ observation showed, that the time-dependent spatial development of equiaxed dendrites in the undercooled region was different.

ACKNOWLEDGEMENTS

This work was financially supported by the German Space Agency DLR under BMWi/DLR grants no. FKZ 50WM1143 and FKZ 50WM1443, which is gratefully acknowledged. The authors appreciate the Team of Airbus D&S for the hardware development and support during the preparatory and final experiments. SSC, DLR-Moraba and OHB System AG are acknowledged for mission support at Esrange/Sweden.

REFERENCES

1. Hunt, J.D. (1984). Steady State Columnar and Equiaxed Growth of Dendrites and Eutectic, *J.Materials Science and Engineering* **65**, 75-83.
2. Zimmermann, G., Sturz, L., Billia, B., Mangelinck-Noël, N., Liu, D.R., Nguyen-Thi, H., Bergeon, N., Gandin, C.-A., Browne, D.J., Beckermann, C., Tourret, D. & Karma, A. (2014). Columnar-to-Equiaxed Transition in Solidification Processing of AlSi7 alloys in Microgravity – The CETSOL project, *Materials Science Forum* **790-791**, 12-21.
3. Liu, D.R., Mangelinck-Noël, N., Gandin, C.-A., Zimmermann, G., Sturz, L., Nguyen-Thi, H. & Billia, B. (2014). Structures in directionally solidified Al–7wt.%Si alloys: Benchmark experiments under microgravity, *Acta Mater.* **64**, 253-265.
4. Liu, R.D., Mangelinck-Noël, N., Gandin, C.-A., Zimmermann, G., Sturz, L., Nguyen-Thi, H. & Billia, B. (2015). Simulation of directional solidification of refined Al - 7 wt% Si alloys -Comparison with benchmark microgravity experiments, *Acta Mater.* **93**, 24-37.
5. Zimmermann, G., Sturz, L., Nguyen-Thi, H., Mangelinck-Noel, N., Li, Y.Z., Gandin, C.-A., Fleurisson, R., Guillemot, G., McFadden, S., Mooney, R.P., Voorhees, P., Roosz, A., Ronaföldi, A., Beckermann, C., Karma, A., Chen, C.-H., Warnken, N., Saad, A., Grün, G.-U. Grohn, M., Poitrault, I., Pehl, T., Nagy, I., Todt, D., Minster, O. & Sillekens, W. (2017). Columnar and equiaxed solidification of Al-7wt.%Si alloys in reduced gravity in the framework of the CETSOL project, *JOM* (2017) DOI 10.1007/s11837-017-2397-4
6. Sturz, L. & Zimmermann, G. (2011). Comparison of results from low-gravity and normal gravity experiment "TRACE" on the columnar-equiaxed transition in the transparent alloy system neopentylglycol-camphor. In *ESA **SP-700***, 459-466.
7. Sturz, L. & Zimmermann, G. (2011). In-situ and real-time investigation of the columnar-equiaxed transition in the transparent alloy system NPG-DC onboard the sounding rocket TEXUS-47, *Journal of Physics: Conference Series* **327**, p. 012002.
8. Sturz, L., Hamacher, M. & Zimmermann, G. (2013). Results from low gravity and normal gravity experiment 'TRACE+' on dendritic growth and the columnar-equiaxed transition in the transparent alloy system NPG-DC, In *ESA **SP-721***, 285-292.
9. Sturz, L., Wu, M., Zimmermann, G., Ludwig, A. & Ahmadein, M. (2015). Benchmark experiments and numerical modelling of the columnar-equiaxed dendritic growth in the transparent alloy Neopenthylglycol-(d)Camphor, In *IOP Conf. Series: Materials Science and Engineering* **84**, 012086.
10. Ahmadein, M., Wu, M., Sturz, L., Zimmermann, G. & Ludwig, A. (2016). Numerical investigation of solidification and CET of the transparent alloy NPG-37.5 wt.% DC in microgravity "TRACE" experiment, In *IOP Series: Materials Science and Engineering* **117,** 012011.
11. Witusiewicz V.T., Sturz L., Hecht U. & Rex S., (2004). Thermodynamic description and unidirectional solidification of eutectic organic alloys: III. Binary systems neopentylglycol-(D)camphor and amino-methyl-propanediol-(D)camphor, *Acta Mater.* **52**, 5519-5527.
12. Bayram, U., Aksoz, S. & Marasli, N. (2012). Solid-liquid interfacial energy of neopentylglycol solid solution in equilibrium with neopentylglycol-(D) camphor eutectic liquid, *J. Cryst. Growth* **338**, 181-188.

ESRANGE SPACE CENTER – MEETING FUTURE NEEDS FOR ADVANCED SCIENCE SERVICES

Anne Ytterskog[(1)], Anna Rathsman[(1)], Mattias Abrahamsson[(1)],

[(1)]SSC, Swedish Space Corporation, P.O. Box 4207, SE-17104 Solna, Sweden, Email:anne.ytterskog@sscspace.com, anna.rathsman@sscspace.com, mattias.abrahamsson@sscspace.com

ABSTRACT

Esrange Space Center has been used by the international scientific community, space agencies and commercial customers for the past 50 years. Over 550 sounding rockets for microgravity and atmospheric research and over 620 high altitude balloons for astronomy, atmospheric research and drop tests have been launched since Esrange was founded.
The requirements and driving forces have of cause changed during the past five decades, today there is still a demand for sounding rockets and balloons as important tools for science but there is also a need for extended service capabilities. Esrange Space Center is presently undergoing a major upgrade and expansion; project "New Esrange", to meet both the present and future needs for advanced science services. The project includes both modernization and upgrading of existing infrastructure as well as investments in new rocket launchers, technology and research platforms.

This paper presents the future plans for Esrange.

1. ESRANGE 1966-2017

Esrange Space Center, owned and operated by SSC, has been used by the international scientific community, space agencies and commercial customers for the past 50 years. Over 550 sounding rockets for microgravity and atmospheric research and over 620 high altitude balloons for astronomy, atmospheric research and drop tests have been launched since Esrange was founded in 1966.

Figure 1. Rocket on launcher from the past

2. TRENDS & DRIVING FORCES

The requirements and driving forces have of cause changed during the past five decades, today there is still a demand for sounding rockets and balloons as important tools for science but there is also a need for extended service capabilities.

Figure 2. Present and future services

3. NEW ESRANGE

Esrange Space Center is presently undergoing a major upgrade and expansion; project "New Esrange", to meet both the present and future needs for advanced science services. The project includes both modernization and upgrading of existing infrastructure as well as investments in new rocket launchers, technology and research platforms.

The aim is to be able to offer cost effective launch services and more frequent launch opportunities for sounding rockets and balloons, improved possibilities to perform coordinated measurements from ground based instrumentation, balloons, sounding rockets and satellites as well as new capabilities for affordable and easy access to space. The new services will include full scale testing of reusable space vehicles, technology tests for space exploration by means of re-entry and landing tests, robotic rover tests in a Moon and Martian like environment and SmallSat Express, a European launch capability for small satellites.

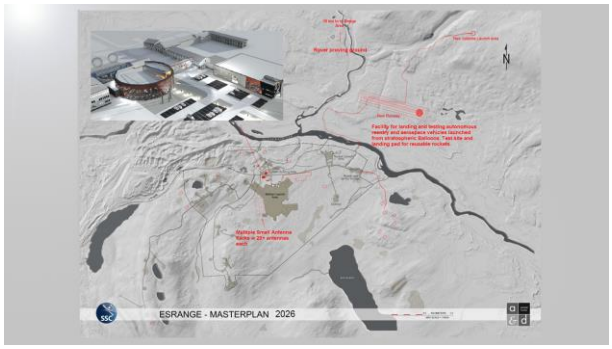

Figure 3. New Esrange masterplan

3.1. Combined measurements

SSC can already today offer combined measurements using sounding rockets, stratospheric balloons, ground based scientific instrumentation and satellite data. The plan is to increase the ground based instrumentation as well as to invest in infrastructure enabling multiple sounding rocket launches and balloon cluster launches.

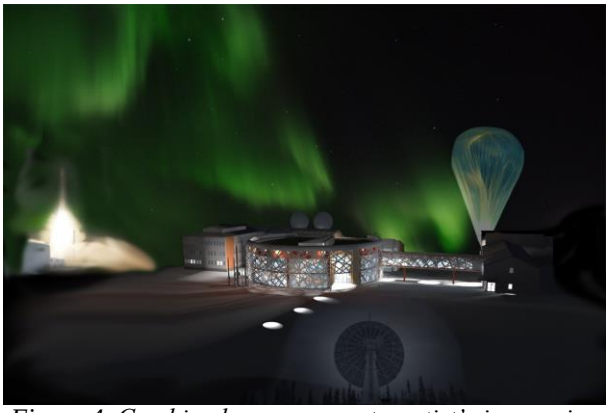

Figure 4. Combined measurements, artist's impression

3.2. Technology tests

Esrange's vast land impact area, its infrastructure and experienced staff enable all the requirements to perform technology tests within areas such as exploration, reusability and autonomous vehicles. The impact area can be used for creating Moon and Mars like surfaces for tests of of capsules, parachutes, rovers, habitats, balloons, preparing for interplanetary missions to Mars, Venus and the Moon. Test and demonstrations of reusable vehicles can be performed by means of implementing a runway at Esrange and as an example use large balloons to drop the vehicles. Besides, sounding rockets and balloons are excellent tools for in-flight tests and validation of satellite subsystems.

3.3. SmallSat Express

To meet the increasing demand for launch opportunities for small satellites and to contribute to Europe's space policy, "independent access to space", SSC has initiated "SmallSat Express". The intended launch service will enable a standardized orbit suitable for most small satellites; sun-synchronous, "dawn-dusk" orbit at 500 km altitude (inclination = 97.4°). By using the launch service on three consecutive launches a constellation of satellites covering every local time can be established. The launch periods, one to three per year, will be fixed. The goal is to launch the first satellite in 2021.

Figure 5. SmallSat Express, artist's impression

3.4. Big data from space

The increasing number of satellites in orbit, new space and constellations of Earth observation satellites or communication satellites generate a massive amount of data. Consequently, the infrastructure in space demands infrastructure on ground.
SSC owns and operates the world's largest network of multi-mission ground stations, SSC Universal Space Network, where Esrange is a hub. By placing agile antennas at current sites and in new future locations, the service SSC Infinity will provide sequential and frequent TT&C and data download at low latency.

Figure 6. Big data from space, artist's impression

4. ESRANGE IN 2026

Welcome to Esrange in 2026!

Figure 7. Esrange in 2026, artist's impression

DREAM – DRILLING EXPERIMENT FOR ASTEROID MINING

23RD ESA SYMPOSIUM ON EUROPEAN ROCKET AND BALLOON PROGRAMMES AND RELATED RESEARCH

VISBY, SWEDEN
11-15 JUNE 2017

Dorota Budzyń [1], Mikołaj Podgórski [2], Jędrzej Kowalewski[3], Kamil Sieciński [4], Konrad Pleban [5], Artur Błaszczyk[6], Maksymilian Żurman[7]

[1] Wroclaw University of Science and Technology (WUST), 27 Wybrzeże Wyspiańskiego st. 50-370 Wrocław, Poland, Email: dorota.h.budzyn@gmail.com
[2] WUST, 27 Wybrzeże Wyspiańskiego st. 50-370 Wrocław, Poland, Email: mikolaj.podgorski@gmail.com
[3] Scanway sp. z o.o., Duńska 9, 54-427 Wrocław, Poland, Email: j.kowalewski@scanway.pl
[4]) WUST, 27 Wybrzeże Wyspiańskiego st. 50-370 Wrocław, Poland, Email: siecinski.kamil@gmail.com
[5] Scanway sp. z o.o., Duńska 9, 54-427 Wrocław, Poland, Email: k.pleban@scanway.pl
[6]) WUST, 27 Wybrzeże Wyspiańskiego st. 50-370 Wrocław, Poland, Email: ablaszczyk3@gmail.com
[7]) WUST, 27 Wybrzeże Wyspiańskiego st. 50-370 Wrocław, Poland, Email: makzur@gmail.com

ABSTRACT

In present days space operations are not only measured in scientific and technical goals. Economical aims gain recently bigger influence in space industry.

One of the greatest opportunities for mankind space expansion is the asteroid mining. Although there is certainly a big gap between current human or robotic spaceflight operations and running space mining industry, scientists and engineers already work hard on simulating asteroid conditions for excavating ore such as platinum or nickel.

The DREAM project (DRilling Experiment for Asteroid Mining) took part in European international programme, led by European and German Space Agencies and Swedish National Space Board, called REXUS (Rocket Experiment for University Students). Organizers allow participants to take part in suborbital flight up to almost 100 kilometres on-board the sounding rocket launched from Esrange Space Center in Kiruna, Sweden. The DREAM project was launched on 15th of March 2017.

The experiments' scientific goal was to measure the conditions and aspects of drilling in space environment, especially to measure the output distribution and condition of output after excavation. These parameters were measured by the vision system equipment in measurement chamber during flight and the rest is the result of on-ground analysis which are still in progress. Such process has never been studied in the space missions before.

Most challenging part of designing space equipment was to ensure that it will survive both harsh conditions of delivery and work in the outer space. The technical goal of the experiment was to design the robust equipment able to perform drilling operations in space.

One of the most innovative parts of the experiment is the measurement chamber for drilling. The chamber have the functionality to capture the drilled outcome saving its distribution vector for the post-flight data analysis. With the use of the laser triangulation techniques and the fast camera acquisition the DREAM project is able to provide information about the 3D position of almost every rock fragment excavated during the drilling procedures in the reduced gravity.

1. EXPERIMENT OBJECTIVES

Primary Objectives:

- Scientific goal was to measure the conditions and aspects of space excavating using drilling techniques and compare it with results obtained from on-ground tests.
- Technical goal was to design the Measurement Chamber for drilling with main task to capture the drilled output.

Secondary Objectives:

- Design the robust equipment able to perform drilling operations in space.
- To train young scientists and engineers and give them a possibility to earn a space-related experience.
- To increase the awareness of the educational and scientific potential of space-related projects within the Wroclaw University of Science and Technology and beyond.

2. EXPERIMENT DESCRIPTION

Experiment fits into REXUS 220 mm module – it is 348 mm in diameter and 188 mm height. It was connected to the rocket module by dampers which enabled experiment to move 4 mm vertically and horizontally. The mass of the experiment is 5,024 kg.

The experiment module in general is a drilling machine with set of sensors used to monitor the drilling outcome distribution and the experiment performance. The main sensor set is vision system which basic components are shown in the Figure 1. As it is shown on the picture main camera records the drilling output particles that cross the line laser plane. There is also another camera which was connected to the REXUS TV Channel and enabled the experiment operators to see the process in real time.

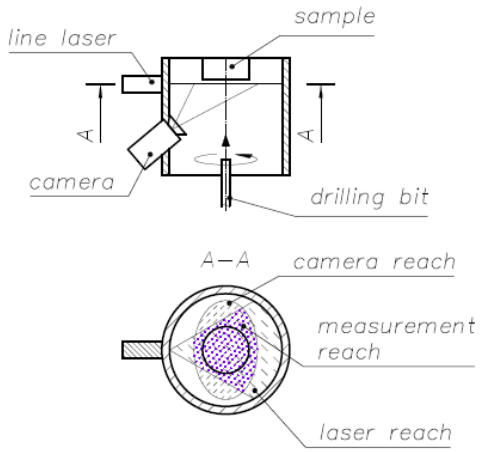

Figure 1. Basic components of measurement subsystem

The experiment started after receiving signal SOE (Start Of Experiment) form REXUS Service Module. That was the time when the whole payload should be in microgravity state. Experiment start was the start of drilling machine – the two motors turned on, one of them pushed the platform with drilling bit towards the sample while the other one rotated the drilling bit. The drilling output particles was moving in the Measurement Chamber while being recorded by two cameras and after the drilling bit reached its maximum position of 30 mm it was pulled back to position 0 ending the experiment.

Next paragraphs describe in details the experiment architecture and design.

2.1. Mechanical Design

The mechanical design consists of Experiment Frame, Moving Platform and Measurement Chamber. Chamber and Platform are connected to the Experiment Frame, which is a structure that provides mechanical interface with the rocket module.

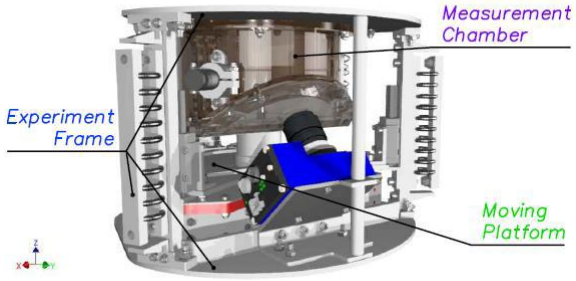

Figure 2. Basic mechanical subsystems

The main principal of the experiment from mechanical point of view is drilling 5 mm hole in the sample while the whole process is observed by vision system. The depth of drilling was 22,5 mm. Figure 2 shows all the components that were required to fulfill that task. There is plaster sample attached to the Experiment Frame structure in the interior of Measurement Chamber. Most of the sensors are fixed in Measurement Chamber so they are stationary to the sample. Movement of the Moving Platform is conducted by stepper motor and a screw-nut mechanism. It pushes the platform with a speed of 0,3 mm/s towards the sample while drilling. For the drilling there is a drill bit rotated by a DC brushless motor. The RPM of the motor is 159, and the torque is 0,24 Nm.

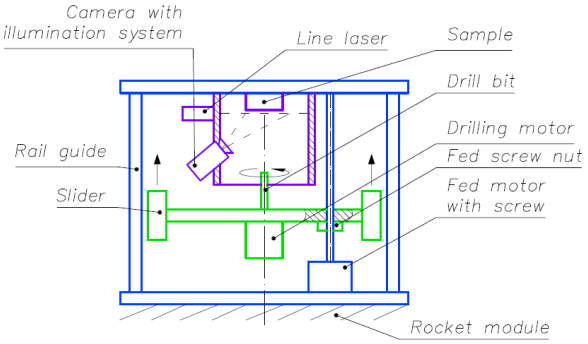

Figure 3. Basic mechanical subsystems

Figure 3 shows illustrative drawing of the experiment components. Figure 4 shows the 3D orientation of components that were crucial for monitoring the particles.

Most of the structure was EN AW-5754 and EN AW-2017A aluminium alloy providing the stiffness for the whole experiment. There were also 3D printed parts made by FDM (Fused Deposition Modelling) technology from PLA. The printed parts were: electronic boxes (also covered with 0,5 mm aluminium layer), Measurement Chamber and one mounting element.

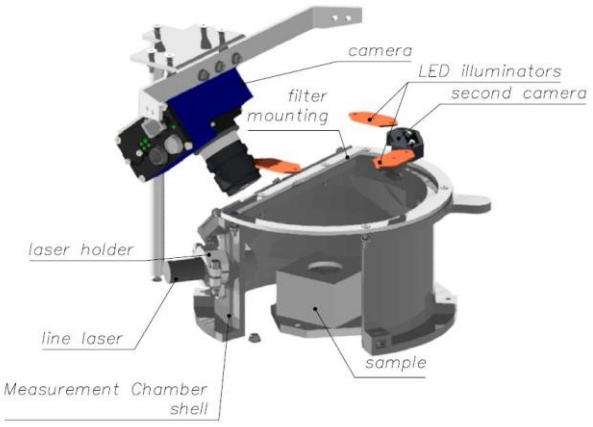

Figure 4. Measurement system basic components and its 3D orientation.

Key element that brings almost all of the scientific sensors together is the Measurement Chamber. The structure of this element is based on 3D printed PLA tube sealed with fabric material for the rock crumbles but not airtight. Measurement Chamber is responsible for the two matters of the whole experiment:

- Providing surface for the sticky substance collecting the drilling output,
- Keeping all of the drilling output inside for safety reasons.

The material fabric sealing was custom made and its main task was to prevent rock output from flowing out from the Drilling Chamber into the experiment environment. It provided free movement of the platform and was still able to keep the dust and rock fragments inside the chamber in every position. The Measurement Chamber interior was also covered with double-sided tape for the drilling output particles to glue to it after reaching the edge of the chamber.
The sample was positioned completely inside the chamber. The diameters of sample are: 35x40x40 mm and it was made of plaster. Sample mount was also filled with glue to equally fill all free space between sample holder and sample itself.

2.2. Electronics Design

Experiment electronic system was divided into two separate PCBs (Printed Circuit Boards) placed in separated boxes. One of the boards was PB (Power Board) responsible for power management and the other one was FCU (Flight Control Unit) board responsible for the control system and drilling procedure. Block diagram of general electronic system is presented in the Figure 5.
Power board consisted of DC-DC converters for power distribution and optocouplers used to connect signals between FCU and RXSM (REXUS Service Module). Signals SODS (Start Of Data Storage), LO (Lift Off) and SOE were implemented as OC (Open Collector) outputs, so the used optocouplers provided galvanic isolation between experiment and rocket (GNDs) grounds.

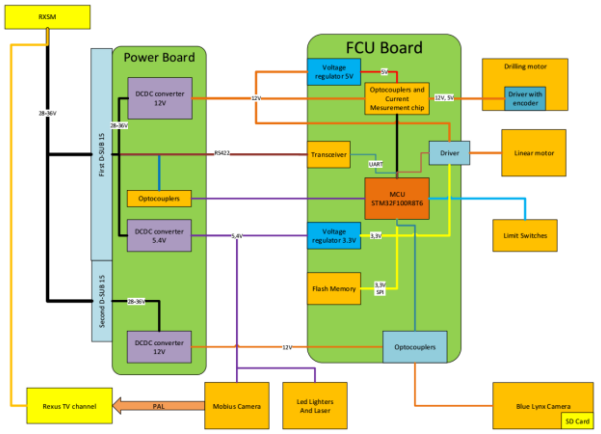

Figure 5. Block diagram of electronic system.

FCU board consisted of voltage regulators, MCU (Main Control Unit), flash memory, transceiver and motor drivers. Main chip on FCU was STM32F100 microcontroller which measured parameters of working system. All data was stored in external flash memory and sent to the GS (Ground Station) using RS422 communication interface. Microcontroller controlled also behaviour of motors and monitored status of Blue Lynx camera. Optocouplers were used for isolation between signals from microcontroller and motor or camera drivers.

2.3. Thermal Design

Thermal design mostly focused on determining whether conditions of pre-flight and flight phase will anyhow influence electronics of DREAM experiment and any other mechanical devices.
Several numerical analysis were performed in ANSYS CFX 14.0

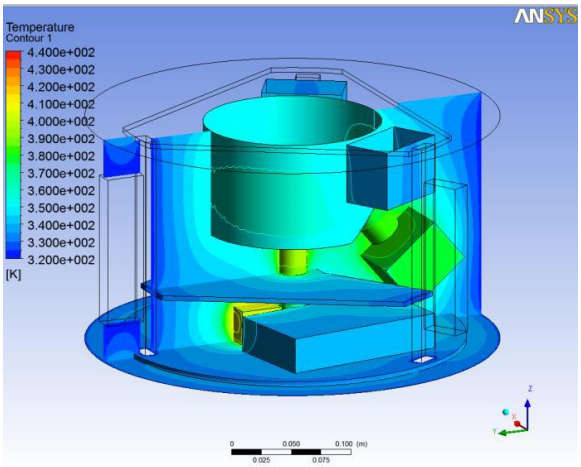

Figure 6. Surface temperature distributions of individual components

Analysis showed that the most endangered components were both motors and camera.
Following test campaign in climatic chamber and in vacuum chamber showed that there is no risk of overheating any component in DREAM experiment.
No heat dissipation nor radiators were implemented to the endangered components

2.4. Power System

Experiment had three electronic subsystems and all of them had their own DC-DC converter with additional LED diode for quick check whether the converters are operating or not.
Power supply lines in the range of 24-36 V DC (Direct Current) and signal lines from the RXSM were delivered to experiment using two cables with female D-SUB15 plugs connected directly to male D-SUB15 connectors on PB.
Power from the first connector was connected to 12 V DC/DC converter used to power drilling and linear motors and to the 5,4 V DC/DC converter used to power laser, LED illuminators, Mobius camera and FCU. LED illuminators and laser were powered directly from 5,4 V converter, FCU has their own voltage regulator because all used chips require a stable 3,3 V or 5,0 V power and Mobius camera is powered by diode which has reduced the voltage in the 0,2-0,4 V range.
Power lines from the second connector were connected to the second 12 V DC/DC converter used to power only Blue Lynx, which was the main camera used to capture images of plaster particles during drilling procedure.
12 V DC/DC converters design was based on LMR14030 chip in step down configuration with maximum output current up to 3,5 A. 5,4 V DC/DC converter design was based on LMR14020 chip in the same configuration, however with maximum current up to 2A.
DC/DC converters chips applied in PB system had internal overvoltage, overcurrent and overheating protection with additional thermal pad on the bottom side to dissipate heat. Rectifier diodes were used to prevent inverse polarity of power supply.
The power distribution in presented way allowed to turn on and off the main camera and control system independently. This was necessary due to the long starting and booting up of main camera. Table 1 presents calculated average power supply distribution from both power lines for each subsystem.

Table 1. Calculated average power supply distribution.

First line	Second line	Drilling motor	Linear motor	Vision system	Light system	Electronics
15 W	10 W	First RXSM Line	First RXSM Line	Second RXSM Line	First RXSM Line	First RXSM Line
		6 W	5 W	10 W	2 W	2 W

2.5. Software Design

Software consisted of two parts. One of them was embedded software implemented in C language for STM32 microcontroller and the other one was GS software implemented as desktop application in C++ language with Qt library.
Software for microcontroller was prepared as 3 layer application with FreeRTOS (Real Time Operating System) as task scheduler and its design is presented in the Figure 6. One of this tasks was application layer responsible for system behaviour management. The second task was board layer responsible for executing application commands and to manage external subsystems. The third task was communication layer responsible for exchanging data with GS and saving measured parameters in external flash memory.

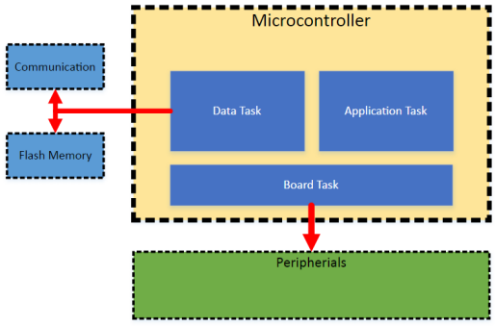

Figure 7. Embedded software divided into 3 tasks

Application layer was implemented as state machine with 4 states as presented in the Figure 8. Test Mode and Flight Mode states had internal microstates to divide state behaviour into small procedure parts.

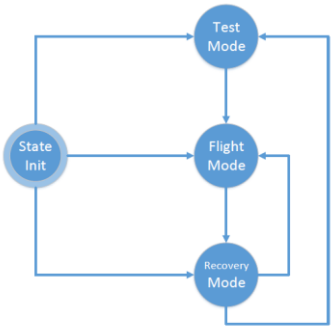

Figure 8. Embedded software divided into 3 tasks

When the system was started state machine was initialized as State Init. In this state system read experiment status from external flash memory and switched to last executed state. This procedure is necessary because of possible power problems during flight or system stability problems. Test Mode state was implemented to perform all subsystems tests remotely from GS. All internal microstates was responsible for

testing each subsystem separately. Algorithm for Test Mode state is presented in the Figure 9.

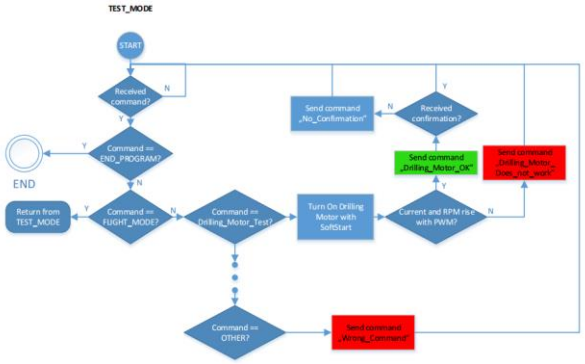

Figure 9. Algorithm for Test Mode state

Flight Mode state was implemented to manage experiment behaviour which was automatically based on signals from RXSM. All measured parameters and system status were sent to GS and stored in flash memory. Algorithm for this state is presented in the Figure 10.

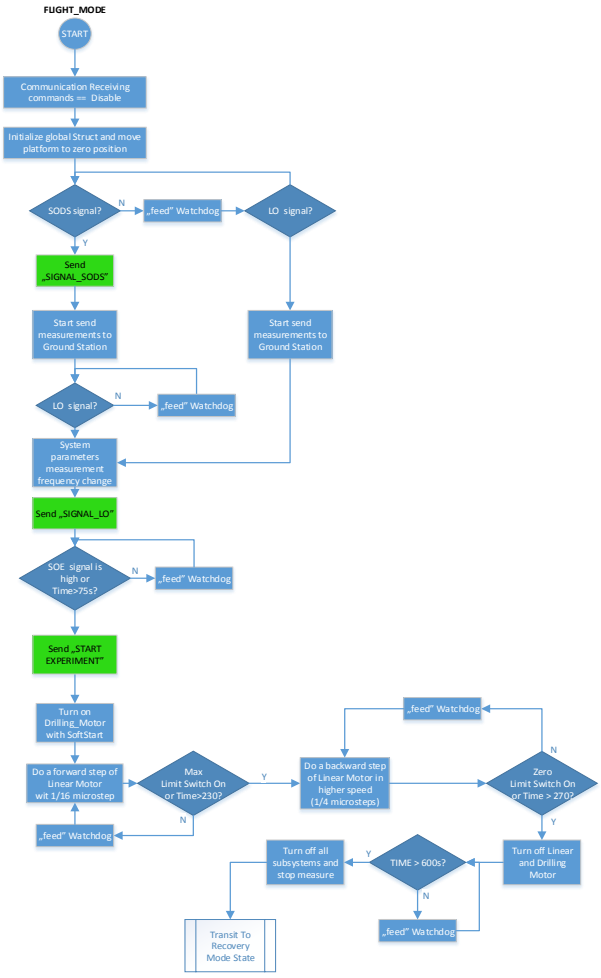

Figure 10. Algorithm for Flight Mode state

Ground Station desktop application was implemented to remotely control experiment behaviour during tests and flight. The application allows to configure appropriate communication port and then switches to control panel after successful connection. Configuration panel is presented in the Figure 11.

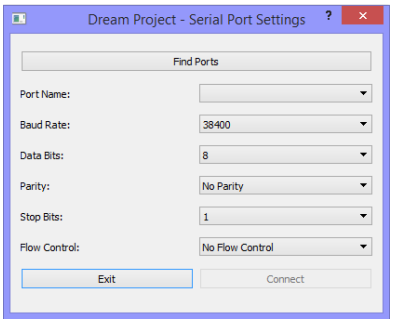

Figure 11. Configuration panel of communication port

Control panel contains indicators for determining the status of subsystems and signals from RXSM. The application allows to switch between states Test and Flight Modes and allows to test each subsystem in Test Mode separately. The application display results of tests and values of measured parameters received from experiment. Control panel window of GS application is presented in the Figure 12.

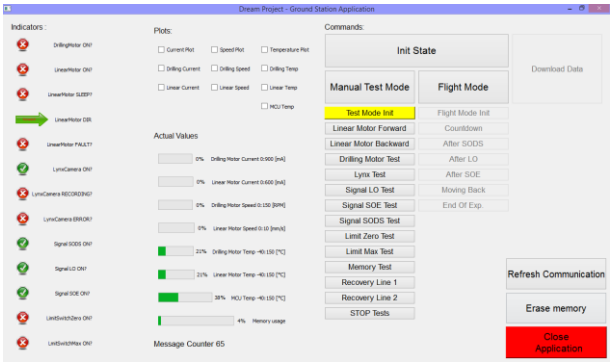

Figure 12. Control panel of Ground Station application

3. TESTING

Test campaign for DREAM experiment consisted of several phases which were finished by pre-flight tests during flight campaign.

Every component, such as electronics, linear motor, drilling motor, both cameras and LED diodes had to be tested in normal conditions, before being implemented to the experiment.

Fully assembled experiment withstood hundreds of individual tests which started mostly shortly before IPR (Individual Progress Review).

During months following IPR fully functional experiment was tested in climatic chamber and in vacuum chamber. Both of these tests were performed with an operating time of DREAM experiment several times more than during real flight.

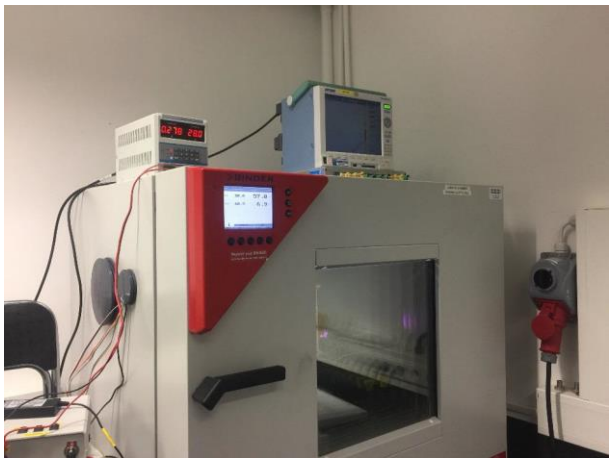

Figure 13. Climatic chamber

Climatic chamber, which can be seen in the Figure 13, allowed members of DREAM experiment to test the equipment in two phases:

a) cold phase with ambient temperature decreased down to -17°C – which was more than required in REXUS programme,
b) hot phase with ambient temperature increased up to almost 60°C – which was also more than required in REXUS programme.

In both of these phases components of the experiment performed in a nominal way, without any overheating or overcooling.

Next step in test campaign was a check of outgassing and experiment performance in vacuum chamber. Pressure in chamber was decreased down to 0,2 mbar and experiment was switched on.

There were small outgassing of 3D printed material, however it did not have any influence on creating any fog on camera lens.

During experiment being switched on, thermal behaviour of both engines were checked as well as fabric filter ability endurance and persistence to rapid pressure changes. Tests were declared as a full success.

Fig. 14. Vacuum chamber before tests with DREAM

After intensive test campaign in vacuum chamber experiment was brought to so-called Integration Week, during which the vibration test was performed. Because DREAM experiment used dampers to reduce vibrations this test did not show any issues. Moreover, during that test campaign several interference tests and mechanical fit check tests were performed. No problems occurred there.

After such actions experiment was brought to the flight campaign to Esrange Space Center in Kiruna, Sweden.

4. FLIGHT CAPMAIGN

Flight campaign for REXUS-21 rocket, with scientific payload of e.g. DREAM experiment, took place from 6th to 17th of March, 2017. REXUS-21 rocket was launched after intensive pre-flight test campaign, on second attempt at 11.43 AM, 15th of March.

During first week of flight campaign, several checks and tests were performed. Most of them focused on looking for interferences between scientific payload itself and between scientific payload and RXSM. Even though there were several issues found, all ended successfully.

Because of the nature of scientific payload, a lot of actions had to be taken prior to launch. It extended pre-countdown actions, but had no impact on actual launch.

Figure 15. Actual setup of REXUS-21 rocket during interference and bench tests.

Last actions performed during flight campaign were countdown tests, which aimed at increasing performance of scientific payload Ground Station operators during countdown and flight. These tests were performed with payload attached to the RXSM.

During these test there was small issue with REXUS TV channel connector in DREAM experiment. It occurred twice and in both cases required disassembly of DREAM and neighboring RXSM to disconnect and connect the connector. After second attempt there were no problems with that.

First launch was postponed due to the bad weather conditions. Finally, second attempt was successful.

Countdown for DREAM started at T-900 with powering

on experiment. It required one power cycle for main camera to boot up. All pre-flight tests during countdown were performed successfully. Start of Data Storage signal was received nominally at T-240.
Start of Experiment signal was received at T+78 and at this time drilling system started working. At T+162 limit switch maximum was triggered and it indicated that Moving Platform movement in direction of drilling was finished. Soon after system was reversed to zero state and experiment was prepared for reentry.
Landing itself was very delicate and nothing was damaged as rocket fell in vast snow field.


Figure 16. REXUS-21 scientific payload after recovery

REXUS-21 flight campaign, flight and recovery was declared by REXUS/BEXUS organizers as a total success. No major problems were encountered both with vehicle and with scientific payload.

5. PRELIMINARY RESULTS

Vision system data was recorded by two cameras. Low resolution camera (Mobius) images were analyzed without processing. High resolution camera images were processed with following algorithms:

a. Channel split:
- Splitting into Red, Green, Blue images,
- Selecting only Red channel,

b. Geometrical transformation:
- Lens distortion calibration with pre-flight obtained calibration matrix,
- Homography calibration with pre-flight obtained homography matrix,

c. Morphology, masking and measurement annotations:
- Median filter 5x5 node,
- Pixel value inversion,
- Binary threshold with 239 pixel value,
- Adding subtracting mask for drill shadow,
- Adding annotations with measurement scale,

d. Feature recognition and data parametrization:
- Canny filter 3x3 node,
- Contour finding based on Suzuki85 algorithm,
- Calculation of center of "mass" for every contour,
- Stacking all frames into one for whole process analysis,

All algorithm implementations were made in C++ with Intel OpenCV library.

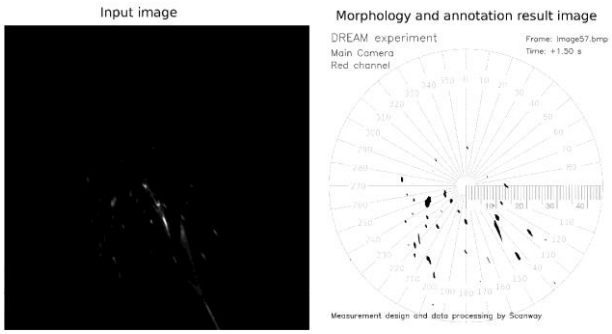

Figure 17. Result of performed algorithm from input image to resulted annotated image

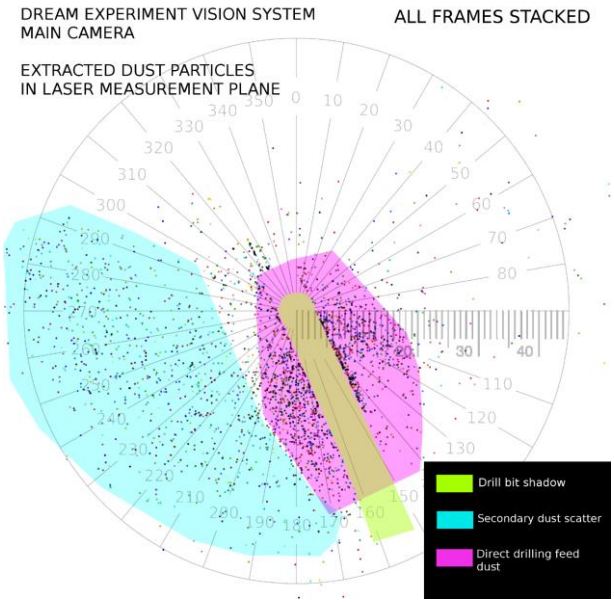

Figure 18. All detected particles stacked in one image

In the picture above one can clearly see two major groups of particles in the measurement area. First, more dense and circular group is the direct drilling feed dust, which comes from rock sample drilled entrance area. This group is circular which confirms the theory of stable dust cone formed from drill bit movement. One of the most important observations about the direct dust cone is its position shifted from the vision system center. This phenomenon is most probably the result of payload rotation after rocket motor separation, which was observed in the outer camera video from experiment UB-Space which was also part of the same payload. Calculated rotation speed is estimated at about 12 deg/s. This rotation caused shift in particles position because of constant movement of measurement chamber

with camera related to floating particles. Shift was not the result of centrifugal forces. Resulted offset was added to particles coordinates.
Another group is the secondary dust scatter which formed from particles bounced from measurement chamber surfaces not covered with sticky substance. This group partially is also created directly from drilling area, but investigation of whole 360 degree range confirms it is small population of particles.
Most important difference between pre-flight experiments compared to flight is that cone of dust is as expected forming around drill bit and is more spread than in Earth conditions.
Another observation is previously unseen sticking of drilling dust to outer surface of drill bit. This was clearly seen on low resolution camera and is shown in the Figure 19.
Reason of this phenomenon is not yet determined certainly. One of the most important thesis is that moisture left in rock sample or water extracted from plaster itself changed into gas state and then resublimed on drill bit causing rock particles to stick.
Another thesis is that electrostatic forces caused drilling dust to stick to drill bit and remain there during whole process.

Figure 19. Dust sticking to drill bit in space conditions.

During flight all other subsystems and components performed in a nominal way. There were no problems with executing software algorithms nor with the work of electronics system. Both motors behaved as expected and there were no differences in comparison with on-ground tests.
Maximum drilling current was 220 mA with drilling motor temperature equal to 23°C. Linear motor temperature was lower, around 18°C and MCU reached almost 44°C. There were no signs of any thermal problems during flight, firstly because time was too short to allow cooling via radiation to have major influence and secondly because heat bridges between experiment and rocket module had large heat capacity.

6. CONCLUSIONS

Project DREAM was first in the history attempt to drill a sample in microgravity. With its vision system and sample collection system it allowed to receive a complex data about how the drilling process looks like in space conditions.
Results of the DREAM experiment shows that it is possible to construct a numerical model of drilling with chosen drill bit and a sample. This is very important issue to be resolved in future if mankind want to acquire via drilling rare materials present on asteroid or comets.
Not only drilling itself is a challenge. Also capturing drilled output must be designed in a such way that particles are efficiently and safely collected.
From the technical side, the experiment showed that it is possible to obtain very precise information about dust distribution in space conditions, even in real time, if the right processing unit is implemented. This data can be used to improve drilling machines after every attempt of drilling in space or even during this process autonomously.
With this conclusions it is possible to say, that all technical and scientific goals of DREAM Project were met.

CPT-SCOPE: COMPACT PARTICLE RADIATION MONITOR TECHNOLOGY DEMONSTRATION ABOARD BEXUS 20

Timo A. Stein[*1,2], **Julian Petrasch**[3], **Anton Walter**[4], **Anastasiya Dykyy**[5], **Michael Beermann**[5], **Lucas Kempe**[6], **and Johannes Stahn**[6]

[1]*University of Oslo (UiO), 0371 Oslo, Norway.*
[2]*Integrated Detector Electronics AS (IDEAS), 0484 Oslo, Norway.*
[3]*Freie Universität Berlin, 14195 Berlin, Germany.*
[4]*Beuth Hochschule für Technik Berlin, 13353 Berlin, Germany.*
[5]*Norwegian University of Science and Technology (NTNU), NT-faculty, 7491 Trondheim, Norway.*
[6]*Technische Universität Berlin, 10587 Berlin, Germany.*

ABSTRACT

In October 2015, the Cosmic Particle Telescope (CPT-SCOPE) instrument was flight-tested from Kiruna, Sweden, aboard the BEXUS 20 balloon. The technology demonstrator was developed by Norwegian and German students with the objective to detect energetic particles in the mixed-field radiation environment of the tropo- and stratosphere at Northern latitudes. Based on a stack of silicon detectors and copper absorbers two redundant instruments were built combining radiation-hard integrated circuits with COTS components in a hybrid approach. The detector geometry was varied to expand the detectable range of particles. Housekeeping data such as position, temperatures and pressure were recorded. The science data was obtained from individual triggers of four detectors used in each instrument. The Pfotzer-Maximum was recovered from altitude-dependent count rate data. This paper outlines the final[1] results with additional efforts to recover coincidence triggers and discuss the obtained data. The science data is compared to instrument simulations using FLUKA of the atmospheric radiation environment modelled by MAIRE. The CPT-SCOPE data and instrument design is reviewed. The measurements are compatible with the Belgium BEXUS 20 HACORD instrument findings. We further elaborate lessons learnt, and present the outcome of CPT-SCOPE outreach and educational activities. The paper concludes with a description of follow-up developments targeting a miniature, CubeSat-ready radiation monitor for space and terrestrial mixed-field applications.

Key words: REXUS/BEXUS, radiation monitor, particle telescope, radiation-hard, VATA465, IDE3465.

[*]corresponding author, e-mail: t.a.stein@fys.uio.no

[1]Preliminary results were presented at the 1st Symposium on Space Educational Activities in Padova, Dec. 2015. Submitted papers are available online: http://www.esa.int/Education/ESA_Academy/Symposium_on_Space_Educational_Activities

1. INTRODUCTION

1.1. Motivation

The study of primary and secondary cosmic rays in the atmosphere and in space has been carried out over several decades [1, 2]. Nevertheless this field remains an active and dynamic research topic. Taking the space perspective it is important to follow the latest trend of highly miniaturised consumer electronics. Traditional space-rated electronics is of much older technology and usually larger, more expensive with less performance. The available state-of-the-art electronics should be utilised in space to serve emerging sectors involving nano- and picosatellites such as CubeSats [3]. These platforms have a radically different and simplified philosophy as compared to conventional larger satellites allowing for easier and rapid design and lower overall cost but providing less reliability.

Such inexpensive satellites may be used to build larger constellations. One application for such would be a space weather monitoring service in LEO with a few satellites also placed in other orbits. A first serious step towards space weather monitoring capabilities by CubeSats was taken in 2012 when the CSSWE mission was launched providing valuable scientific data to the community [4]. However, at present there are no standard compact radiation monitoring devices available off the shelf for CubeSats. Either these devices are too large e.g. SREM [5] or NGRM [6], not yet fully space-qualified (HMRM), have only a small number of channels (CSSWE) or are restricted due to export regulations. This project is intended to start a new design of a compact radiation monitor for CubeSats. This is done along-side other on-going European activities such as the HMRM [7, 8]. In the present approach an IDEAS rad-hard front-end integrated circuit (IC) is used in combination with consumer electronics to build a sufficiently miniaturised device capable of delivering valuable scientific data. Such device is becoming

increasingly relevant for more sophisticated space infrastructure is build and plans of human space exploration beyond LEO are at hand. An ultra compact radiation monitor may also be used for proposed interplanetary CubeSat missions or personal dosimetry.

When looking at Earth the interaction of cosmic rays with the atmosphere and its effect the our planet's climate is not well understood [1, 9, 10]. In particular the radiation fields and dynamics in the stratosphere lack observational data [11] and are subject to recent studies e.g. by the BARREL team [12].

The CPT-SCOPE project started with a single-channel lab prototype developed within a master thesis [13, 14]. This activity was a spin-off from the Norwegian NUTS CubeSat project [15, 16]. Based on the initial single channel design a team of Norwegian and German students developed a four channel technology demonstrator which is capable to withstand the harsh conditions associated with a stratospheric balloon flight while being able to study the particle precipitation in the tropo- and stratosphere.

The team was selected for the REXUS/BEXUS programme [17] for a flight aboard BEXUS 20, a stratospheric balloon, along-side the Belgium HACORD (directivity of cosmic rays) and German COSPA (microscopic particles) instruments. CPT-SCOPE is the first Norwegian participation for BEXUS. Other radiation detectors have flown previously aboard BEXUS or REXUS mission such as PERDaix [18] or other instrument examples [19, 20, 21, 22]. One common atmospheric feature studied by these missions concerning cosmic rays was the Pfotzer maximum [1]. In regard to CPT-SCOPE the focus of the project was technology development and testing while producing sound scientific data for cosmic rays in the lower atmosphere.

1.2. Instrument Description

The instrument is capable of measuring subatomic particles with energies ranging orders of magnitude of 0.1 MeV to 100 MeV and low-energetic gamma rays of 10 keV to 100 keV. This is achieved with four epoxy-covered, reversed-biased silicon detectors (First Sensor X100-7 THD, 250 μm thickness, 1 cm^2 active surface, biasing voltage: 35 VDC) arranged in an absorber-sensor-stack, also known as particle telescope. The sensors had a p-readout i.e. positive charges were injected into the front-end electronics.

Limited ability to determine the particle species and energy based on individual trigger patterns was planned. However, this feature had to be removed due to resource limitations. A trigger-based, as opposed to an analogue readout, approach was utilised in order to allow for high-count rates and reduced external hardware. The count rates for each channel was recorded instead of more advanced pattern recognition. Redundancy was provided by duplicating the hardware, running two devices independently called CPT-A and CPT-B. Each instrument was

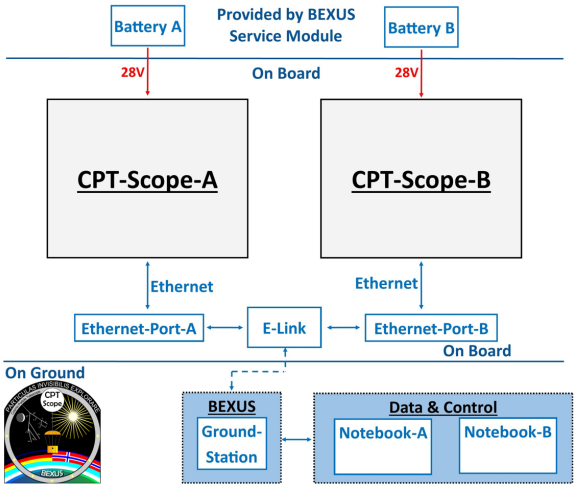

Figure 1. CPT-SCOPE main block diagram.

identical besides the used particle telescope geometry which was optimised for different energy ranges. CPT-A and CPT-B utilised 4 channels with each two triggers (A and B) per channel at different threshold values.

The device implementation used mostly commercial off-the-shelf (COTS) components to allow for rapid development and low cost. These were combined with specialised detector front-end electronics based on a radiation-hard IDEAS VATA465 integrated circuit (IC) [23, 24]. A custom power supply, reverse-bias generation board and two interface cards were designed. The block diagrams for the overall CPT-SCOPE and for the individual instruments CPT-A and CPT-B are shown in Fig. 1 and Fig. 2, respectively. CPT-SCOPE instruments CPT-A and CPT-B were each connected to a BEXUS 28VDC battery and the E-Link system for communication.

A FPGA was used as high-speed counter with a SPI interface. The counter received and processed trigger signals from the VATA465 IC. A Numato Lab Mimas board featuring a Xilinx Spartan-6 FPGA was used and programmed in VHDL. The science payload was configured and readout by an on-board computer (OBC), a Raspberry Pi model B+, running a Linux operating system and storing data on a SD card. In addition to particle count rates, telemetry data was collected by the OBC and telemetry unit such as external pressure and temperature at various locations and position information using a commercial modules. Telemetry modules were readout using either I2C or serial interfaces. Care has been taken to isolate and shield sensitive analogue electronics such as the sensor head from noisy digital electronics e.g. the OBC. Low-pass filtering has been employed on all sensor-related power rails. The total power consumption for CPT-SCOPE was 7 W. CPT-A and CPT-B (each 3.5 W) were powered from individual batteries and had their own E-Link connection.

The OBC was running multiple threads of Python scripts to control I/O operations, schedule and execute readouts

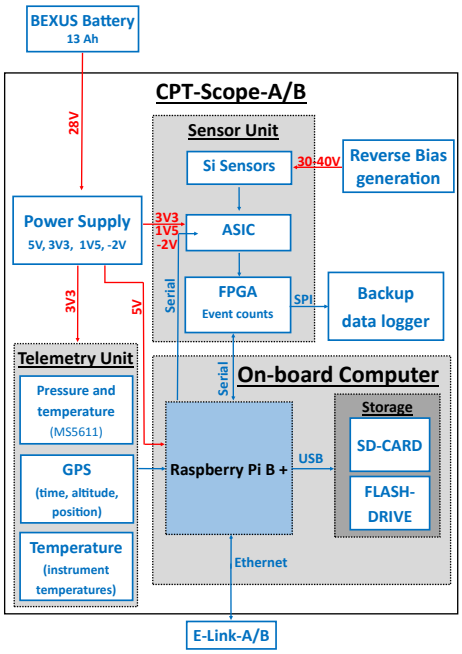

Figure 2. CPT-SCOPE individual instrument system block diagram.

Figure 3. CPT-SCOPE mounted inside the BEXUS 20 gondola. The black material is the thermal insulation and the red labelled places are access points. Gaffer tape was used to keep the insulation in place.

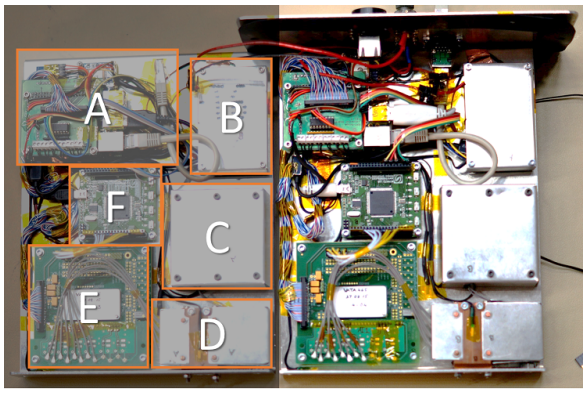

Figure 4. CPT-A (left, labelled) and CPT-B (right) with exposed subsystems before assembly: A - OBC and interface card 1, B - power supply, C - reverse-bias generation, D - particle telescopes, E - front-end electronics and interface card 2, F - counter FPGA.

Figure 5. GPS flight path of BEXUS 20 recorded by the CPT-A telemetry unit. Background map credit: OpenStreetMap.

and configurations of subsystems as well as communicating with a ground station control and monitoring software written in Python and Java. UDP was used for downstreaming sensor and telemetry data. Every UDP packet used a MD5 checksum to verify the packet integrity. Each packet received a unique identifier and system timestamp. The logging thread is controlled by a server thread. The server thread receives commands via E-Link. The commands are transferred with a self-written protocol based on TCP. The device can also run autonomously.

The finished device had dimensions of 27.9 cm x 29.0 cm x 32.2 cm (LxWxH, including mounting) and a total weight of 4.1 kg. The mechanical structure was made from aluminium sheets. Thermal insulation of approx. 1 cm thickness was used on all sides with the exception of two openings for the particle telescopes, cables and other access points. A picture of the final device mounted inside the gondola is shown in Fig. 3 while the opened CPT-SCOPE instrument exposing CPT-A and CPT-B along with labelled subsystems is provided in Fig. 4.

1.3. Flight Campaign

CPT-SCOPE was launched on October 10, 2015, 09:16:54 UTC from the European Space and Sounding

Rocket Range (ESRANGE) in Kiruna, Sweden (67.5° N, 20° E). The balloon was ascending for 1h 39m with 4.68 m/s till 28.2 km altitude. The float began around 10:54:35 UTC. Its duration was 2h 10min 5s and the float ground range was 171 km at approx. 28 km altitude with a slight decease towards the end. Cut-down occurred at 13:06:03 UTC. The ground was reached around 13:43:04 UTC over Finish territory. The mainly eastwards flight track is shown in Fig. 5.

The ground station was receiving telemetry and science data for the whole flight duration except the last 1,000 m of descend. It was not necessary to change the readout IC's configuration. Therefore, only ping commands were issued to the instruments to check the functionality of the command connection periodically and retrieve near-real time data. After the landing the instrument was running for an additional 19h 54min 28s until the batteries were empty. Hence, the total runtime of instrument CPT-A was 1d 1h 34min 45.41s and 1d 1h 31min 52.99s for CPT-B.

The instrument was returned to ESRANGE on Sunday, October 11, 2015. The instrument remained mounted in the gondola and was transported back from Finland by truck after being airlifted to the next street using a helicopter. The gondola had a hard landing bending the aluminium frame. From the detailed GPS altitude data the gondola has likely experienced at landing a rapid fall of at least 10 m after impact and shortly after experienced three more falls of at least 1 m each within a four minute window. However, since no separate acceleration data is available the exact events during the landing are not clear. In addition, the gondola was transported loaded sideways causing excessive mechanical stress on the instrument. This is important for our investigation into a minor mechanical failure at the end of this paper.

2. RESULTS AND DISCUSSION

The OBC unit recorded data continuously for over 25 hours 30 minutes starting on October 10, 2015, at 07:53:15 UTC until the supply batteries were drained. This resulted into 53489 and 53679 data packets for CPT-A and CPT-B, respectively. Of these were valid 53477 (>99.9%) for CPT-A and 53568 (>99.7%) for CPT-B and provided useful telemetry and science data. Each packet contained a unique ID, system time, ambient pressure, several temperature readings from in- and outside the instrument, GPS location and time, test register readings and the science data i.e. counter register values. The period between packets was 1723 ms and 1732 ms for CPT-A and CPT-B, respectively.

The data analysis was carried out using a Python 2.7 script in combination with libraries Numpy, Pandas and Matplotlib. The system time of instrument CPT-B had to be manually synchronised to the CPT-A GPS-time due to a failure of the CPT-B GPS-receiver. The science data was re-sampled using Pandas at 4 minute intervals to reduce noise by adding all events for the new time bins.

In the following paragraphs we will present the data and subsystem status retrieved from the recovered instrument CPT-A and CPT-B memories. The data correspondents with the down-linked data (not shown) which was obtained during the flight.

2.1. Technical Data

2.1.1. Subsystem Status

All subsystems have been found operational throughout the flight for both CPT-A and CPT-B. Minor technical issues were observed with the telemetry and on-board computer unit. The FPGA module has always returned proper test register values and was hence functioning properly the entire time. No power cycling was observed from the system indicating full functionality of the power supply. Science data was obtained pre-, during and post-flight. Although the observed noise levels were high at times for individual channels the overall function of the sensor unit (science payload) was complete throughout the entire run. The OBC reported stable core temperature, frequency and voltage (10 °C - 30 °C, 700 MHz, 1.2 V). Network communication through the E-Link system was available throughout the flight and data was recorded continuously. Nevertheless, a small number of packets were lost or corrupted, and several others written to memory delayed or duplicated likely due to internal buffering. This affected below 0.5% of all packets. The GPS-receiver for CPT-B failed before flight already, while unit CPT-A worked without any issue allowing for precise timing and positional data.

No data is available after the instruments shut down on October 11, 2015 at 09:37:24 UTC. When the instrument was taken apart for inspection back at ESRANGE it was observed that the aluminium cap protecting the sensitive readout IC for CPT-B was loose and damaged several wire-bonds. Due to the fact that CPT-B delivered proper science data even after the landing the damage must have occurred during the transport back to ESRANGE. A failed M2.5 screw thread inside the aluminium cap (not shown) in combination with the hard landing and mechanical stress during back transport was identified as cause of the failure.

2.1.2. Telemetry Data

The telemetry unit on both instruments functioned without significant failure. Telemetry data included instrument position and UTC time from GPS satellites, ambient pressure and several temperatures from the in- and outside. Units CPT-A and CPT-B recorded 8 temperature readings per cycle.

The temperature readings for CPT-A (top) and CPT-B (bottom) are shown in Fig. 6 for the duration of the flight.

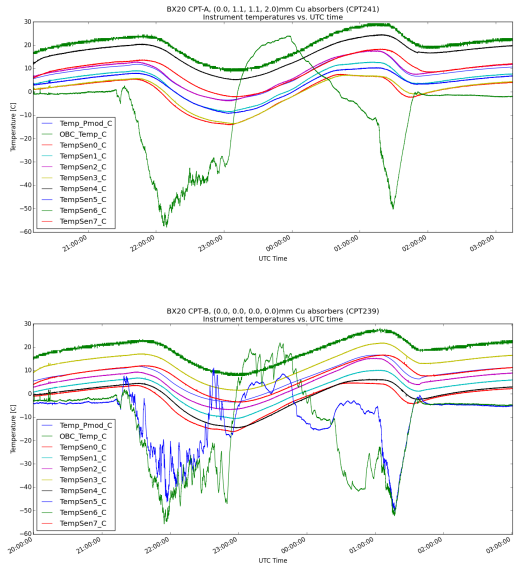

Figure 6. Temperature readings of CPT-A (top) and CPT-B (bottom) shown for the flight of BEXUS 20. The temperature range is from -60 °C to +30 °C (y-axis).

Internal temperatures: Note that the internal temperature was always within a range of -15 °C and +25 °C while external temperatures varied between approx. -58 °C and +25 °C. Temperature sensitive components such as the FPGA board where mounted close to components with higher heat dissipation to allow for higher operating temperatures. The placement of the external temperature sensors was also important as the gondola slowly rotated in and outside the sun causing variable heating.

External temperatures: The CPT-A ambient, external temperature (right) and pressure (left) profile for the ascend phase is shown in Fig. 7. The altitude is inferred from the GPS positional data collected by the telemetry unit. The ambient temperature on the ground was approx. -1 °C. The temperature decreased to -5 °C by the time an altitude of 1.2 km was reached. The balloon flew then through an inversion layer in the troposphere causing a rise in temperature to +2.5 °C at 2.1 km. The tropopause was reached at an altitude of 12.3 km with minimum temperature of -58 °C. The temperature then increased steadily within the stratosphere until the float altitude of approx. 28 km was reached with initial temperatures of -32 °C to -27 °C. The variation in the temperature is suspected to be caused by a slow rotation of the gondola in reference to the sun. The external sensor slowly started to warm up to +10 °C before cut-down due to heat dissipation of the instruments and solar irradiation. This leads to the suggestion that no thermal equilibrium was achieved, likely due to too strong thermal insulation. However this allowed to operate all components within tested temperature limits.

Pressure profile: The pressure profile (left) for the ascend of CPT-A as function of altitude is shown in Fig. 7. Note the logarithmic scale for the pressure. The ground temperature was -1 °C at an altitude of 322 m. The decrease in pressure follows approximately the expected exponential decrease over increasing altitude. However, the effect of the varying external temperature is visible as ”bending” away from the idealised standard atmosphere at constant temperature. The float altitude was around 28.2 km with external pressure of 11.9 mbar. The readings of the pressure sensor were used in the determination of the interaction depth X for the science data analysis but not for altitude determination.

Altitude profile and positioning: The telemetry unit of CPT-A was able to provide precise positioning data during the BEXUS 20 flight and helped to understand what happened during and after the landing. The altitude profile for the flight is shown in Fig. 8, while the flight path is shown projected onto a map in Fig. 5. The BEXUS 20 flight was already discussed above.

2.2. Science Data

At the heart of the CPT-SCOPE project was the development of a compact radiation monitoring device capable of measuring count rates for energetic subatomic particles in the energy range of several 100 keV to several 10 MeV. Each instrument hosted one particle telescope consisting of each four silicon (Si) detectors stacked on top of each other. While CPT-A had thin copper (Cu) absorbers between the inner sensors, CPT-B had none. Both instruments had the first sensor (D1) exposed facing the top towards the balloon. The thickness of the Cu absorbers for CPT-A were 1.1 mm in front of the second (D2) and third (D3) each and 2.0 mm before the last sensor (D4). The sensor separation within the particle telescope was approx. 4.0 mm. The particle telescopes were mounted within a 6 mm thick Cu housing closing all sides besides an opening for the PCBs and sensors facing the top. This acted as shield against lower to medium energetic particles. A rough estimate can be derived from tabulated ranges of NIST’s *estar*, *pstar* and *astar* database [25] yielding a minimum kinetic energy of approx. 8.5, 65 and 250 MeV for electrons, protons and alpha particles, respectively, to enter the shielding perpendicular and not considering the external aluminium housing.

Due to variable performance of the individual channels the threshold values of the readout IC were set to different values for each channel and A-/B-window trigger. The following values were used for CPT-A: A0 = 30 (110 keV), A1 = 30, A2 = 43 (150 keV) and A3 = 50 (175 keV); B0 = 1 (290 keV), B1 = 1, B2 = 2 (330 keV) and B3 = 2. While CPT-B was configured as follows: A0 = 30, A1 = 30, A2 = 30 and A3 = 30; B0 = 1, B1 = 1, B2 = 1 and B3 = 1. The bracket values indicate the minimum energy deposited in the Si diode to trigger the VATA466 front-end electronics, operated in double-gain mode of its high-gain channels, and assuming full charge transfer.

For every data packet the OBC requested from the FPGA the value for each channel’s current counter value. This

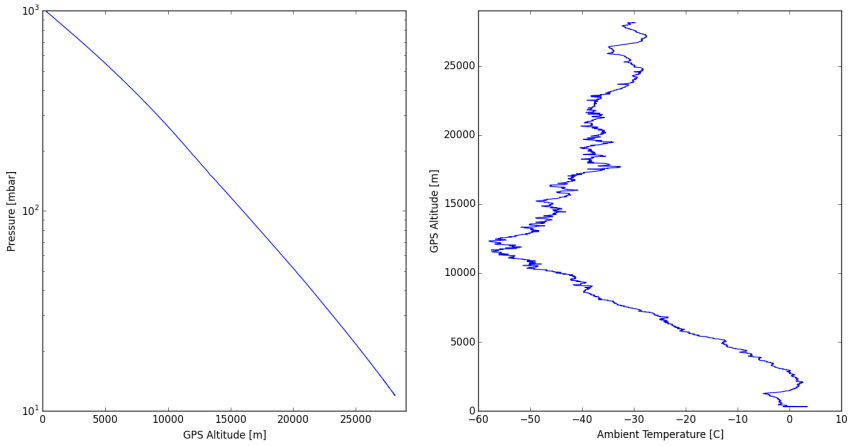

Figure 7. Relevant meteorological flight data for the balloon ascend provided by CPT-A: Logarithmic plot (left) of the ambient pressure over altitude. The external temperature profile (right) over altitude.

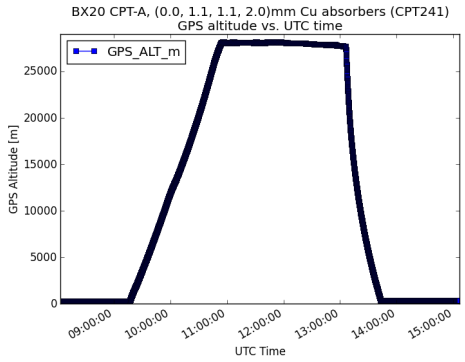

Figure 8. GPS altitude over UTC time for the BEXUS 20 flight.

data is available at relatively high time resolution of some 1.7 s. The readout device was automatically reconfigured every 1,000 packets resulting in erroneous counter readouts. These values were easily removed thanks to their repetitive nature as a first step. In the next step the previous counter value was subtracted in order to only deal with new triggers instead of their cumulative number relevant for dosimetry.

At the relatively high readout rate and small detector size only a few triggers are expected per reading. In order to increase the expected number of events, and therefore improving the counting statistics, the raw counter increase values were first summed for fixed time intervals of 240 s using the `resample()` function of the Pandas library in Python. This step does not influence the resulting data analysis but enables to improve noise performance at the cost of a lower temporal resolution, and to deal with missing data points or noise triggers.

In the last step the count rate is determined by dividing the counter increase over the integration time in order to obtain instrument count rates.

In order to display the data in a well-comparable manner the interaction depth X was chosen instead of the altitude. The interaction depth X, calculated from the ambient pressure p, is a measure of how much the air column atop the instrument weights per unit area. This is directly related with the number of possible interaction partners an energetic particle encounters along its path towards the ground. To first order it is assumed that all particles are coming vertically i.e. perpendicular to the ground. In this way the interaction depth X is easily evaluated as:

$$X = \frac{p}{g}.$$

The local[2] acceleration due to gravity was used for Kiruna, Sweden, namely $g = g_{\mathrm{Kiruna}} = 9.8227\,m\,s^{-2}$. The value of X was approx. 1,000 g cm^{-2} on the ground as compared to some 12 g cm^{-2} during the float phase, a decrease by a factor of almost 100. The resulting instrument count rates - in units of Hz cm^{-2} - are shown for the sensor A-trigger (top) and B-trigger (bottom) in Fig. 10 for CPT-A (Cu absorber) and in Fig. 11 for CPT-B (no absorber). Note that the threshold values for the channels was set to different values (see above). The scaling for these figures is as follows: Interaction depth from 10 to 1,010 g cm^{-2} logarithmic scale for all graphs, and instrument count rate in the range of 0 to 2 Hz cm^{-2} and 0 to 1 Hz cm^{-2} (linear) for the A- (top) and B-trigger (bottom) graphs, respectively.

The general picture is consistent with the expected behaviour [1]: The count rate is lowest but non-zero at ground level (X = 1,000 g cm^{-2}), less than 0.05 Hz cm^{-2} and 0.03 Hz cm^{-2} for A- and B-triggers of CPT-A and CPT-B, respectively.

[2]Obtained from the Gravity Information System of PTB: http://www.ptb.de/cartoweb3/SISproject.php.

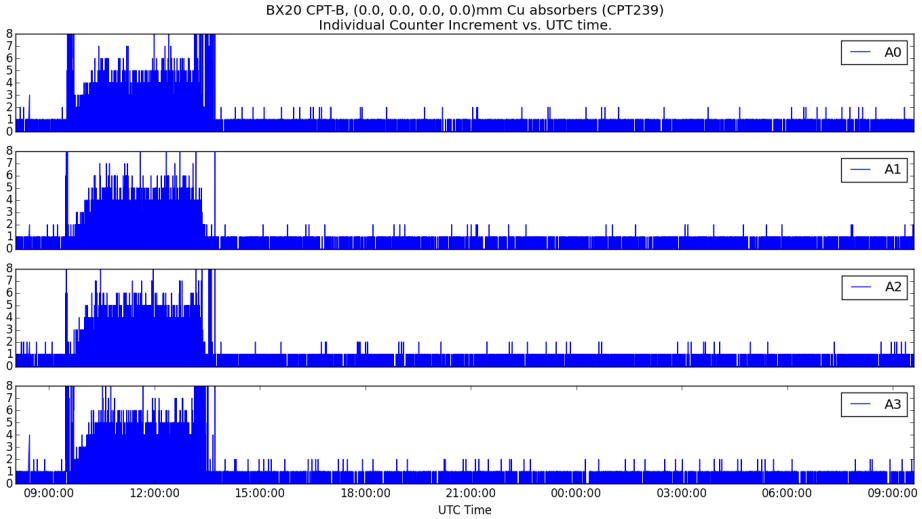

Figure 9. Increment of A-trigger counters for CPT-B (no absorbers) between consecutive packet readings as function of time. The data has the periodic erroneous readings due to the device configuration already removed. However, the original sampling rate and the full measurement duration of over 25 hours are shown. Clearly visible are the increased triggers due to increased number of particles at higher altitude during the BEXUS 20 flight (approx. 9:00 and 14:00 UTC). Strong transient noise triggers are are also visible in particular at ascend and descend in channel A0. Note that no significant change in the count rate is observed after landing indicating that the mechanical failure of the readout IC housing occurred during recovery and transport back to ESRANGE.

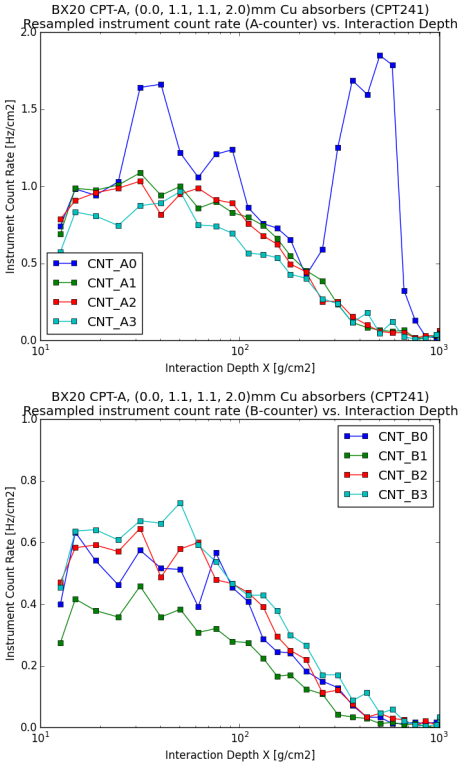

Figure 10. Instrument count rate as function of interaction depth X for CPT-A. The first graph shows the high-gain channel A-triggers, while the second one displays the B-triggers. Note that CPT-A has Cu absorbers between the inner sensors installed.

As the balloon climbs the count rate increases significantly until it reaches a broad maximum with 0.35-0.75 Hz cm^{-2} (0.10-0.60 Hz cm^{-2}) for the B-trigger and 0.80-1.00 Hz cm^{-2} (0.90-1.10 Hz cm^{-2}) for the A-triggers of CPT-A (CPT-B) around an interaction depth $X \approx 40$ g cm^{-2} (equivalent to $p = 39.3$ mbar, 21.6 km altitude). This likely constitutes the Pfotzer maximum which is to be expected at an $X < 100$ g cm^{-2} [1].

With higher altitude i.e. lower interaction depth X the count rate decreases but less pronounced to 0.30-0.50 Hz cm^{-2} (0.10-0.40 Hz cm^{-2}) for the B-trigger and 0.60-0.80 Hz cm^{-2} (0.55-0.65 Hz cm^{-2}) for the A-triggers of CPT-A (CPT-B).

Note that the broad spreed is due to the different response, threshold settings of the individual sensors and their placement within the particle telescope. Furthermore, several transient trigger events are visible in particular for the A0 triggers of both CPT-A and CPT-B, and in addition the A3 channel of the CPT-B. Such events are also visible in the long-term raw data shown in Fig. 9. The nature of these events is unknown but are likely caused within the instrument itself or due to pick-up from external interference as such behaviour was previously observed in the laboratory as well.

Further evaluation of the scientific data without detailed simulations and calibration measurements are not possible. It should be noted that CPT-SCOPE is due to time limitations a technology demonstrator and hence emphasis was placed on getting the detector system to work without full pre-calibration. Nevertheless, all channels

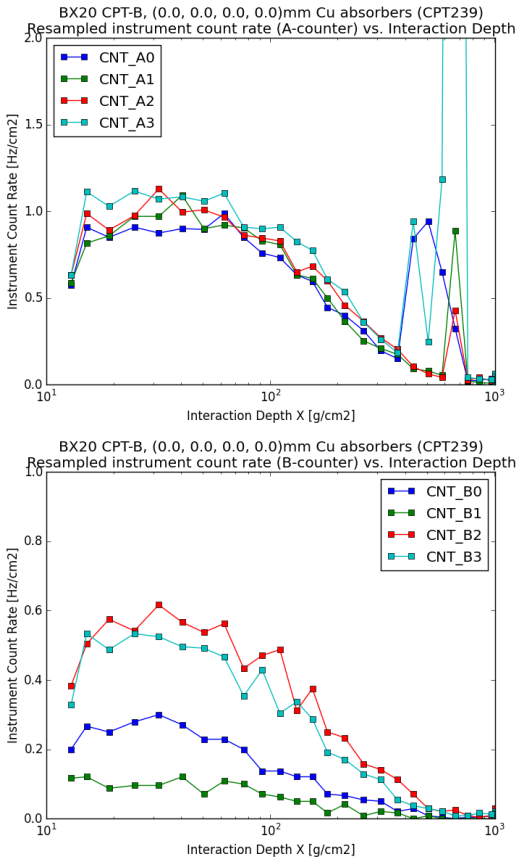

Figure 11. Instrument count rate as function of interaction depth X for CPT-B. The first graph shows the high-gain channel A-triggers, while the second one displays the B-triggers. Note that CPT-B has no absorbers installed.

produced scientific data and the overall shape of the measured instrument count rates follows the expected behaviour. The observed count rate graph is compatible with the preliminary findings of the HACORD instrument (data not shown), a Geiger-counter-based radiation detector developed by Belgium students also flying aboard BEXUS 20.

2.3. Particle Telescope Discussion

In order to resolve individual events, a particle telescope uses multiple sensors in coincidence. During the BEXUS 20 flight the FPGA firmware was not ready to detect coincidence but only the number of particles for each sensor was retrieved every 1.7 s. The sensors (D_1, D_2, D_3, D_4) were stacked one after other with D_1 being the first sensor. If the same particle was detected by multiple sensors, there must be a correlation between subsequent increased counts of different sensors. Therefore if a particle is detected by the $i+1^{th}$ sensor D_{i+1} at time t_j, the particle count on the previous, i^{th} sensor D_i around the same time should be higher than the particle count on D_i 1.7 s later at the time t_{j+1} if no event was detect by D_{i+1}.

We analysed all measurements where D_{i+1} detected at least one event at the time t_j and no events at $t_j + 1$ (1.7 s later). For theses measurements we checked if D_i had more counts at the time t_j than at time t_{j+1} (see column "$D_t > D_{t+1}$" in Tab. 1 and 2). We also counted how often the opposite happened (see column "$D_t < D_{t+1}$" in Tab. 1 and 2). Sensor D_i detected also particles when D_{i+1} was not hit. Therefore not every sensor detected every particle. If a sensor detected a hit the probability that another has been hit as well rises by 16% to 35% (see "Δ" column in Tab. 1 and 2). From this we deduce that in these cases a particle entered from the top and penetrated the stack. However, a significant portion of events also has an unexpected pattern in which not all subsequent sensors were hit. This may be caused by particles entering through the outer shielding, gamma rays or transient noise triggers e.g. caused by external interference.

Table 1. Number of (un)correlated hits for CPT-A.

	$D_t > D_{t+1}$	$D_t < D_{t+1}$	Δ
$D2_t > 0$	554	469	18.1%
$D3_t > 0$	555	469	18.3%
$D4_t > 0$	589	507	16.2%

Table 2. Number of (un)correlated hits for CPT-B.

	$D_t > D_{t+1}$	$D_t < D_{t+1}$	Δ
$D2_t > 0$	566	484	16.9%
$D3_t > 0$	527	416	26.7%
$D4_t > 0$	522	386	35.2%

In regard to the particle telescope data one recognises the limitation of using individual sensor-based count rates i.e. a statistical- rather than event-based approach. With CPT-A we observe the expected behaviour of increased count

rates for sensors closer to the opening i.e. less material is available to slow down or absorb the incident particle (Fig. 10). However, CPT-B shows a strange behaviour, namely that count rates do not follow such pattern (Fig. 11). It is not clear as to why this happens. Post-flight cabling and readout register order were checked and found to be correct. Further efforts to better understand the CPT-SCOPE data relied on simulating the particle telescopes in FLUKA [26, 27], a Monte-Carlo simulation package for particle transport and physics, and comparing the measured atmospheric count rates with values obtained from the MAIRE[3] tool by RadMod Research Ltd.

We find through the MAIRE tool that at float (28.2 km) the dominant particle species are protons, electrons and gamma rays. A cut-off rigidity of 0.3 GV is obtained for the Kp index during the flight of Kp = 2 - 3 using MAIRE with the GCR-ISO, IGRF 2000 and Tsyganenko 89 model options. In the following we will neglect other particle types due to their low expected flux. Gamma rays may cause a hit in any of the detectors without the need of another hit inside the detector stack. However, the utilised Si diodes are only effective in fully absorbing gammas of less than 50 keV. For higher energies, Compton scattering or pair creation in the active volume or any surrounding material contributes. The gamma spectrum is falling off towards higher energies with less than 10% integral flux at energies higher than 25 MeV. Electrons also have a falling off spectrum with less than 10% integral flux at energies higher than 150 MeV. Lastly, protons for a broad energy peak centred around several hundred MeV. Typical integral fluxes in the energy range of 0.1 MeV and 800 GeV are 1.45, 1.08 and 14.9 cm^{-2} s^{-1} for protons, electrons and gamma rays, respectively. In this way gamma rays dominate the integral flux in the above, wide energy range. However, the particle telescope will be inefficient such that it is expected to see a lower instrument count rate due to gammas. Overall the instrument count rates are on the order of 1 cm^{-2} s^{-1} which is similar to the values for the proton and electron population to which the device is most sensitive. Due to the small detector size of 1 cm^{-2} and multiple detectors stacked a low geometric factor is inevitable. This causes count rates to be lower and in fact we assume that a significant contribution is caused by higher energetic particles penetrating the outer shielding. These may also explain the above findings that most events may not show a hit in one or more detectors that are closer to the entrance opening.

Within FLUKA (version: 2011.2c.6) the particle telescope stack and outer shielding were build into a simplified geometry using the FLAIR tool. For the particle transport simulation the PRECISIO physics default in FLUKA was chosen. For each run 1 million, monoenergetic primary particles were impinged onto the particle telescope stack, and their deposited energy for each detector written into a histogram file using a custom routine by K. Røed (University of Oslo). We find that particles penetrate the sensor stack for defined threshold kinetic energies. For the CPT-A instrument with Cu absorbers in place we find these to be at approx. 40, 60 and 80 MeV for protons, while for electrons at 4, 10 and 16 MeV. With no absorbers installed we find for CPT-B these to be at approx. 30, 40 and 50 MeV for protons, while for electrons at 2, 4 and 5 MeV. Particles with larger energies behave similarly to minimum ionising particles (MIPS) e.g. for protons starting around 150 MeV. These particles deposit sufficient energy in all sensors to cause a trigger. In conclusion, we find through FLUKA simulations that for most protons and electrons that are expected at floating altitude and obtained using the MAIRE tool no particle energy or species distinction from each event can be inferred due to the low energy thresholds inherent to the existing design. These simulations would have been extremely useful and necessary during the instrument design phase. Unfortunately, these were not possible due to limited resources. On the upside, the count rates are thus higher. Lastly, simulation of muons with 3 GeV kinetic energy, that are typical and the dominant flux of cosmic rays on ground level, indicate that about 20% of events will deposit sufficient energy to trigger multiple sensors. The measured rate on ground level is compatible with reference values (data not shown). From the simulation we can further exclude that the different threshold settings for the triggers had a significant impact. This unfortunately adds confusion about the measured instrument count rates that not necessarily increased for detectors closer to the entrance opening. Both CPT-A/-B are still operational and may if the opportunity arises be tested in a mono-energetic particle beam to clarify the issue.

3. EDUCATIONAL AND OUTREACH PROGRAMME

Besides the technical and scientific objectives the CPT-SCOPE project had also a strong outreach component. Its main focus was on education with the development of a secondary and high school curriculum by two science teacher students in Norway. The program consisted of two building blocks for the respective age group. The first module was theoretical and the other practical in order to engage students directly. The goal of both modules was to motivate students for future studies within space research or other natural sciences disciplines. Educational material for teachers was also created and complemented with simple experiments such as floating weights on helium-filled balloons or visualising radioactivity with cloud chambers. Throughout the CPT-SCOPE school programme four sets of educational materials for the use in schools were developed. We also presented our material to some 150 secondary school pupils in seven different presentation at secondary schools in the Trondheim region, Norway. In addition, talks were given at conferences and science outreach days such as the Researcher's Night 2015 in Trondheim. Lastly, a web[4] and Facebook page ("CPTSCOPE-Team") were maintained in English, German and Norwegian.

[3]MAIRE: http://radmod.co.uk/maire

[4]CPT-SCOPE web page: http://www.cpt-scope.com.

4. OUTLOOK

Based on the experience made using an IDEAS VATA465 readout IC with CPT-SCOPE the development of a CubeSat-ready radiation payload is the next step. The instrument is called the Norwegian Radiation Monitor (NORM). For NORM an updated particle telescope geometry and the latest IDEAS VATA466 readout IC model, designed for the flight to Jupiter aboard the RADEM instrument [28] of the ESA JUICE mission, will be used. It is easier to interface, providing better performance and features such as built-in (anti-)coincidence counters. This will allow for the development of a functioning prototype within the next two years. Such device may also be useful towards operational space weather now- and forecasting, personal dosimeters for astronauts or for aircrews and passengers on polar routes.

5. CONCLUSIONS

The CPT-SCOPE instrument was successfully flight-tested aboard BEXUS 20. The two instruments CPT-A and CPT-B functioned with minor issues. Both telemetry and science data provided valuable information to determine the functionality of the compact radiation monitoring technology demonstrator and towards future improvement. The radiation monitoring payload was able to measure the instrument count rates due to particle precipitation as function of altitude. A clear increase of the count rate with altitude is visible from all radiation data aboard both instruments and channels. The Pfotzer maximum is visible peaking at some $X = 40$ g cm^{-2} (21.6 km altitude). Additional analysis was carried out using FLUKA simulations and the MAIRE tool. However, within the available resource no further radiation data could be retrieved. It is important to fully calibrate the radiation data and to carry out full simulations of the instrument design early on. Transient noise triggers, in addition to other minor issues in subsystems, have to be further investigated. The CPT-SCOPE project was done within a short life cycle of less than one year which provided valuable experience. The first Norwegian participation within the BEXUS programme was achieved and in collaboration with German students the project was a big success and important milestone towards our planned compact radiation monitor, NORM, for nano- and picosatellites.

ACKNOWLEDGEMENTS

CPT-SCOPE is a joint Norwegian-German student project. In addition to the authors, the following students contributed: F. Freyer, P. M. Schönberg, R. Wenzel and G. H. Wesenberg. We would like to thank the project's endorsing professor, I. Simonsen (NTNU), and the REXUS/BEXUS team and partners. We would like to thank our main sponsor the Integrated Detector Electronics AS (IDEAS). In addition, the project has been supported by Sparebanken Midt-Norge, the Anette og Brynjulf Skaugens Veldedige Stiftelse, NUUG, SNSB / DLR / ESA, NTNU, UiO, CONTAG, Corentium, Hirose Electric, Numato Lab, Ikalogic, Advanced Energy Industries, WIMA, First Sensor AG, Flexitron, Webspace-Verkauf.de, with additional contributions of other sponsors and partners to which we are all grateful. K. Røed (UiO) assisted in the FLUKA simulations and provided a custom routine to create energy deposition histograms. Special thanks go to our families for their patience and support, to our IDEAS co-workers for their help, to SNSB / DLR / ESA for giving us the opportunity to participate in the REXUS/BEXUS programme, to the ESRANGE flight and support crew which allowed us to have a successful flight and stay in Kiruna and to the other REXUS/BEXUS teams of Cycle 8 for the great time.

REFERENCES

[1] P. K. F. Grieder. *Cosmic Rays at Earth: Researcher's Reference Manual and Data Book*. Elsevier Science & Technology, 2001. ISBN 0444507108.

[2] L. Dorman. Discovery and Research of Cosmic Rays on Balloons. In *Proc. "21st ESA PAC Symposium", 9-13 June 2013, Thun, Switzerland (ESA SP-721, October 2013) - ISBN 978-92-9092-285-8*, pages 655–662. European Space Agency, 2013.

[3] P. Fortescue, G. Swinerd, and J. Stark. *Spacecraft Systems Engineering*. John Wiley & Sons, third edition, 2003. ISBN 978-0471619512.

[4] X. Li et al. First results from CSSWE CubeSat: Characteristics of relativistic electrons in the near-Earth environment during the October 2012 magnetic storms. *Journal of Geophysical Research: Space Physics*, 118(10):6489–6499, Oct 2013. ISSN 2169-9380. doi: 10.1002/2013ja019342. URL http://dx.doi.org/10.1002/2013JA019342.

[5] A Mohammadzadeh et al. The ESA Standard Radiation Environment Monitor program first results from PROBA-I and INTEGRAL. *IEEE Transactions on Nuclear Science*, 50(6):2272–2277, 2003.

[6] L. Desorgher et al. ESA Next Generation Radiation Monitor. In *14th European Conference onRadiation and Its Effects on Components and Systems (RADECS)*, pages 1–5, Sept 2013. doi: 10.1109/RADECS.2013.6937362.

[7] E. F. Mitchell et al. The Highly Miniaturised Radiation Monitor. 2014. URL http://arxiv.org/abs/1401.3533.

[8] N. Guerrini et al. Design and characterisation of a highly miniaturised radiation monitor HMRM. *Nuclear Instruments and Methods in Physics Research Section A: Accelerators, Spectrometers, Detectors and Associated Equipment*, 731:154–159, Dec 2013. ISSN 0168-9002. doi: 10.1016/j.nima.2013.06.073. URL http://dx.doi.org/10.1016/j.nima.2013.06.073.

[9] K. S. Carslaw, R. G. Harrison, and J. Kirkby. Cosmic rays, clouds, and climate. *Science*, 298 (5599):1732–1737, 2002. doi: 10.1126/science.1076964. URL http://www.sciencemag.org/content/298/5599/1732.abstract.

[10] L. Dorman et al. Cosmic Rays and other Space Weather Factors Influenced on the Earth's Climate. In *Proc. "22nd ESA PAC Symposium", Tromsø, Norway, 7-12 June 2015 (ESA SP-730, September 2015) - ISBN 978-92-9221-294-0*, pages 547–554. European Space Agency, 2015.

[11] G. Reitz. Radiation environment in the stratosphere. *Radiation Protection Dosimetry*, 48(1):5–20, 1993. URL http://rpd.oxfordjournals.org/content/48/1/5.abstract.

[12] L. A. Woodger et al. A summary of the BARREL campaigns: Technique for studying electron precipitation. *Journal of Geophysical Research: Space Physics*, 120(6):4922–4935, 2015. ISSN 2169-9402. doi: 10.1002/2014JA020874. URL http://dx.doi.org/10.1002/2014JA020874. 2014JA020874.

[13] T. A. Stein. Development of a compact radiation monitor for space application. Master's thesis, NTNU, 2015. URL http://hdl.handle.net/11250/2352104.

[14] T. A. Stein. CubeSat-ready Radiation Monitor Front-End Electronics. 2014. URL https://www.cubesatsymposium.eu/.

[15] O. Gutteberg and R. Birkeland. Overview of the NUTS CubeSat project. In C. Chappelletti and F. Graziani, editors, *Proceedings of the 2nd IAA Conference of University Satellite Missions & CubeSat Workshop*, volume 2 of *IAA Book Series*. International Academy of Astronautics, 2013.

[16] R. Birkeland, T. A. Stein, M. Tømmer, M. Beermann, J. Petrasch, and A. Gjersvik. The NUTS Cubesat Project: Spin-offs and Technology Development. In *Proc. "22nd ESA PAC Symposium", Tromsø, Norway, 7-12 June 2015 (ESA SP-730, September 2015) - ISBN 978-92-9221-294-0*, pages 649–656. European Space Agency, 2015. URL http://pac.spaceflight.esa.int/proceedings/.

[17] N. Callens et al. REXUS/BEXUS: Rocket and Balloon Experiments for University Students. In *Proc. "21st ESA PAC Symposium", 9-13 June 2013, Thun, Switzerland (ESA SP-721, October 2013) - ISBN 978-92-9092-285-8*, pages 561–568. European Space Agency, 2013.

[18] C. Mai et al. The PERDaix experiment. In *Proc. "20th ESA PAC Symposium", Hyere, France, 22-26 May 2011 (ESA SP-700, October 2011) - ISBN 978-92-9092-264-3*, pages 539–546. European Space Agency, 2011.

[19] M. J. Losekamm et al. AFIS: A New Instrument for Cosmic Radiation Studies on BEXUS 18 and Future Nanosatellite Missions. In *Proc. "22nd ESA PAC Symposium", Tromsø, Norway, 7-12 June 2015 (ESA SP-730, September 2015) - ISBN 978-92-9221-294-0*, pages 377–384. European Space Agency, 2015.

[20] S. Martensen et al. Angular Distribution of Charged Particles on the Atmosphere - Results of the ADAM Experiment on BEXUS 19. In *Proc. "22nd ESA PAC Symposium", Tromsø, Norway, 7-12 June 2015 (ESA SP-730, September 2015) - ISBN 978-92-9221-294-0*, pages 535–538. European Space Agency, 2015.

[21] T. Möller et al. Radiation Measurement on the Stratopsheric Balloon BEXUS13. In *Proc. "21st ESA PAC Symposium", 9-13 June 2013, Thun, Switzerland (ESA SP-721, October 2013) - ISBN 978-92-9092-285-8*, pages 637–640. European Space Agency, 2013.

[22] B. Zabori et al. REM-RED Cosmic Radiation Monitoring Experiment On-board the REXUS-17 Sounding Rocket. In *Proc. "22nd ESA PAC Symposium", Tromsø, Norway, 7-12 June 2015 (ESA SP-730, September 2015) - ISBN 978-92-9221-294-0*, pages 539–546. European Space Agency, 2015.

[23] D. Meier et al. VATA465 Datasheet (Rev. 1.5). 2015. URL http://www.ideas.no/.

[24] D. Meier et al. Development of an ASIC for charged particle counting with silicon radiation detectors. In *Nuclear Science Symposium and Medical Imaging Conference (NSS/MIC), 2013 IEEE*, pages 1–5, Oct 2013. doi: 10.1109/NSSMIC.2013.6829764.

[25] Martin J Berger, JS Coursey, MA Zucker, and J Chang. *Stopping-power and range tables for electrons, protons, and helium ions*. NIST Physics Laboratory Gaithersburg, MD, 1998.

[26] TT Böhlen, F Cerutti, MPW Chin, Alberto Fassò, Alfredo Ferrari, PG Ortega, Andrea Mairani, Paola R Sala, G Smirnov, and V Vlachoudis. The fluka code: developments and challenges for high energy and medical applications. *Nuclear Data Sheets*, 120:211–214, 2014.

[27] Alfredo Ferrari, Paola R Sala, Alberto Fasso, and Johannes Ranft. Fluka: A multi-particle transport code (program version 2005). Technical report, 2005.

[28] W. Hajdas et al. Development of radiation hard electron monitor RADEM for ESA JUICE mission. In *Geophysical Research Abstracts (EGU2015-11661)*, volume 17, 2015. URL http://meetingorganizer.copernicus.org/EGU2015/EGU2015-11661.pdf.

[29] T. Stein et al. Student Experiment Documentation (SED) for BEXUS: CPT-SCOPE, version 5.0. 2015.

THE RECENT DEVELOPMENT OF CHINA SOUNDING ROCKET SPACE EXPLORATION ACTIVITIES AND THE INTERNATIONAL COOPERATION

VISBY, SWEDEN
11-15 JUNE 2017

Yang Mingxing [(1)], Liu Bo [(2)]

[(1)] Xi'an Aerospace Solid Propulsion Technology Institute, No.1 Tian Wang Street, Ba Qiao District, Xi'an 710025, P. R .China, Email: yuhangrot@sina.com
[(2)] China Great Wall Industry Corporation, No.88 Nan Cai Yuan Street, Xi Cheng District, Beijing 100054, P. R. China, Email: liubo@cgwic.com

ABSTRACT

Sounding rockets played an important role in the early stage of China's space development, and laid a solid foundation for today's Chinese Long March family launch vehicles. By the end of last century, China has developed 18 types of sounding rockets, and has completed various sounding rocket space exploration activities. Entering 21st century, China has developed the fourth generation of TK series sounding rockets, and its performance reaches the international level. As of today, China's TK series sounding rockets include TK-20, TK-30, TK-40 and TK-50 etc.

China actively explores international cooperation in sounding rocket space exploration activities, promoting the peaceful use of space and sharing the achievements of the space development. Based on the development of China's space technology, it explores the different international cooperation models in the sounding rocket space exploration domain with the global partners. Regarding the characteristics of different latitudes of the current China's launch sites, both sides can collaborate in the manner of exchanging experiment payloads with other international sounding rocket launch services providers. Meanwhile, China can carry out space exploration missions with joint investment and development, or providing the sounding rockets and related testing equipments/experimental payloads to the relevant industry globally.

1. OVERVIEW

Sounding rockets played an important role in the initial stage of Chinese space development, and it laid an important foundation for today's Chinese Long March series rockets and satellites.

China started space exploration and testing activities of sounding rockets in the late 1950s, it is the auxiliary project born & developed to accompany with the development of China aerospace and other high-tech fields, which played an important role in the developing of the space environment verification and testing, along with finalizing the designing work of Chinese satellite, the Long March rocket, and space technology research programs in early stage. It also successfully conducted numerous space exploration activities, such as meteorological observation, sampling test, biological test, and unit technical testing of artificial satellite and carrier rocket. Currently, China's sounding rockets are still one of the most important testing & verification methods of China space science programs and China space development programs.

Figure 1. TK-32 sounding rocket

Figure 2. Electric field instrument

In recent years, China TK-Series sounding rockets conducted a series of space exploration and experiment activities in China, and making major breakthroughs in many fields. At the same time, AASPT (Academy of Aerospace Solid Propulsion Technology) and CGWIC (China Great Wall Industry Corporation) together are seeking technical exchange and cooperation with its

international counterparts, and expecting substantial cooperation in this area. AASPT and CGWIC are both subordinated to the state-owned China Aerospace Science and Technology Corporation.

2. THE DEVELOPMENT OF CHINA'S SOUNDING ROCKETS

Since 1958, there are four generations of China's sounding rockets developed.

The first generation of sounding rockets was developed and used during 1958-1969, while the first stage motor of rocket was powered by solid propellant(double base propellant), and the second stage motor was powered by liquid fuel. The main sounding rockets include the No. 7 sounding rocket (T-7) and the No. 7A sounding rocket (T-7A). During this period, it is the analysis and trial stage of the sounding rockets, the basic task is to explore the technical approach of sounding rockets, master the development law and methods of sounding rockets, and carry out the corresponding rocket sounding activities.

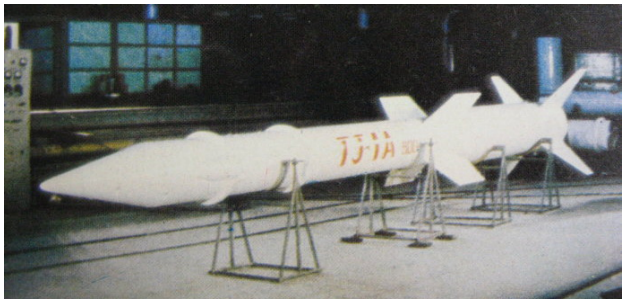

Figure 3. TJ-1A sounding rocket

The second generation of sounding rockets was developed and used during 1965-1987, and the rocket motors were both based on the double-base solid propellant. The typical representatives are the HP-2 meteorological rocket, HP-3 space test sampling rocket, HP-4 space test sampling rocket, HP-5 space test sampling rocket and the HP-8 test rocket.

The third generation of sounding rockets was developed and used during 1970-2012, using a composite propellant solid motor. The main sounding rockets are HP-6 meteorological rocket, ZN-1 meteorological rocket, TY-4 meteorological rocket, ZN-3 meteorological rocket, TJ-1space test sampling rocket, TJ-1A space test sampling rocket and TJ-2 space test sampling rocket, TY-3 microgravity test rocket.

During the development stage of the second & third generation of sounding rockets, it mainly improved the technical performance and detection level of sounding rockets, and gradually expanded the application field of sounding rockets.

Figure 4. ZN-3 sounding rocket

In order to strengthen international cooperation in space exploration activities, the fourth generation of sounding rockets was successfully developed by AASPT in 2013 under the background of China's "One Belt One Road" development strategy. On the basis of the third generation of TY-series sounding rockets, the fourth generation using the technology advantage on solid power and space detection, successful developed TK-20 series sounding rockets (medium and high altitude meteorological rockets), TK-30 series sounding rockets (50kg payload with 200km altitude), TK-40 series sounding rockets (260kg payload with 300km altitude), TK-50 series sounding rockets (500kg payload with 700km altitude). TK-series sounding rockets adopt the advanced high-performance solid rocket motor, the rockets have other advanced characteristics, such as the large payload mass, the high altitude, the long air time, advanced detection instruments, simple and practical ground equipment of launch vehicle, command and control, telemetry and tracking, data real-time receiving and processing and ground communication.TK series technology is an advanced technology with low cost and high reliability. Its technical level is at or near the level of its European counterparts.

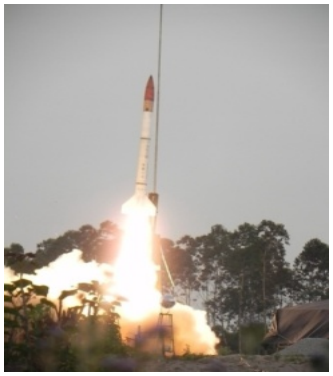

Figure 5. TY-3 sounding rocket

During this stage, it mainly optimize the sounding rocket performance significantly, synchronous improve rocket loading quality and higher altitude, improve the reliability of the rocket, and reduce cost, then realize the seriation, modularization and spectrum of TK-series sounding rockets.

After nearly 60 years of development, China's sounding rockets have been developed from early liquid rocket to today's high performance solid rocket. Exploration instruments have realized the miniaturization, and space exploration activities have become favourable methods to promote the development of China's space science and aerospace industry. But development of sounding rockets in 60 years is not balanced. In the late 1950s, along with the starting of China's carrier rockets and satellites development, its specific requirements for the space exploration became the demand tractions of all kinds of sounding rockets. Therefore T-Series, HP-Series and TJ-Series etc. were respectively developed. This period is the golden period among the development of China's sounding rockets. By the 1980s, the development of China's sounding rockets had slid to a trough and reached the bottom in the 1990s. This is mainly because the development of relevant fields of China's aerospace industry was matured, and there is no technological need for the sounding rocket exploration activities. Entering the 21st century, China's rapid economic development is a big push to the development of science and technology, many areas is in need of space demonstration and validation by sounding rockets, China's "One Belt One Road" development policy also strengthens the international cooperation in space exploration activities. Under such background, TK-series sounding rockets and its supporting system are developed accordingly, facing the new period of development of China's sounding rockets and space exploration activities.

3. TK SERIES SOUNDING ROCKET SYSTEM

Entering 21st century, China has developed the fourth generation TK series sounding rocket, and the performance of TK series rockets is close to or at the European technical level. China's TK series sounding rockets system include five subsystems: sounding rocket and exploration system, equipment of launch site, training support system, production and test system, civil construction design and implement system.

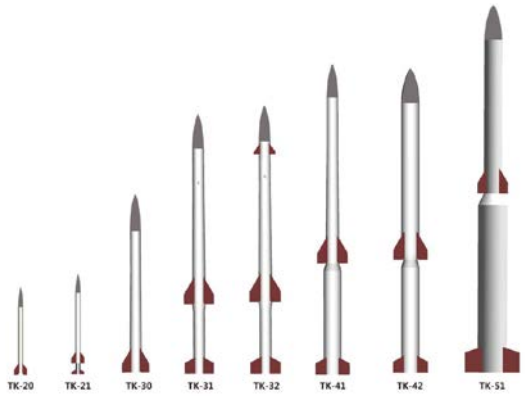

Figure 6. TK series sounding rocket

3.1. Sounding rocket and exploration system

TK series sounding rockets include TK-20 series, TK-30 series, TK-40 series and TK-50 series.

(1) TK-20 series

TK-20 series sounding rocket system is used for measurement of meteorological parameters, such as air temperature, pressure, density, wind speed, wind direction, at an altitude range of 20～100km. It can be applied for spacecraft research in high altitude meteorological environment, providing meteorological services for scientific research and spacecraft launch missions.

Figure 7. TK-20 sounding rocket

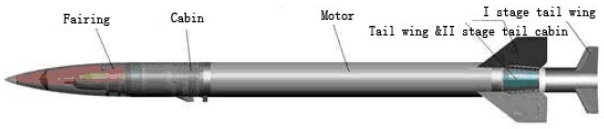

Figure 8. TK-21 sounding rocket

The performance of TK-21 sounding rocket is similar to Mini Texus sounding rocket of ESA.

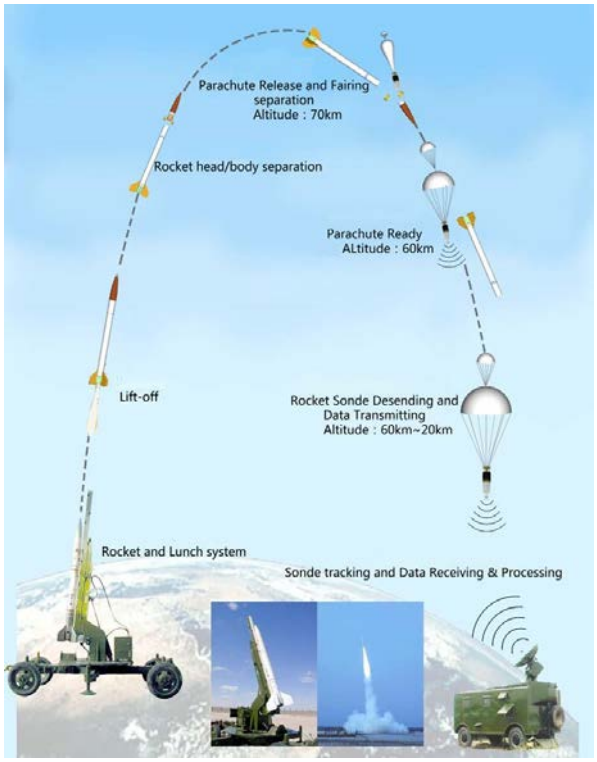

Figure 9. The typical working process of TK-20

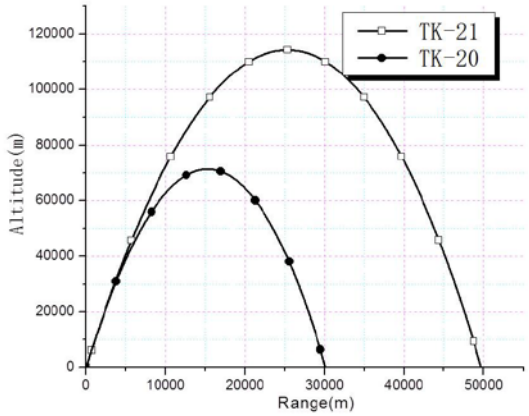

Figure 10. Main technical parameters of TK-20 series

Figure 11. The exploration system of TK-20

(2) TK-30 series

TK-30 series sounding rockets can carry 50 kg payload to an altitude of about 100～300km for aero-physical probe, meteorological research, environmental monitoring and micro-gravity test. Using de-spinning device, it can provide micro-gravity level of 10^{-4}. The microgravity test time is not less than 6 minutes.

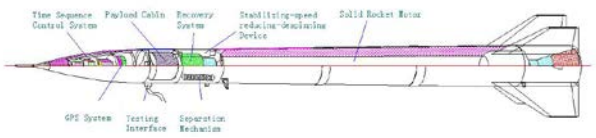

Figure 12. TK-30 sounding rocket

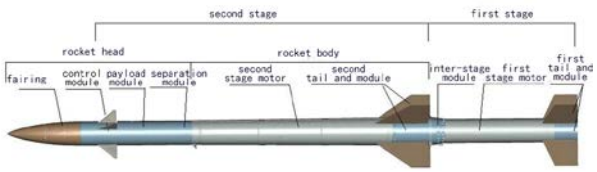

Figure 13. TK-32 sounding rocket

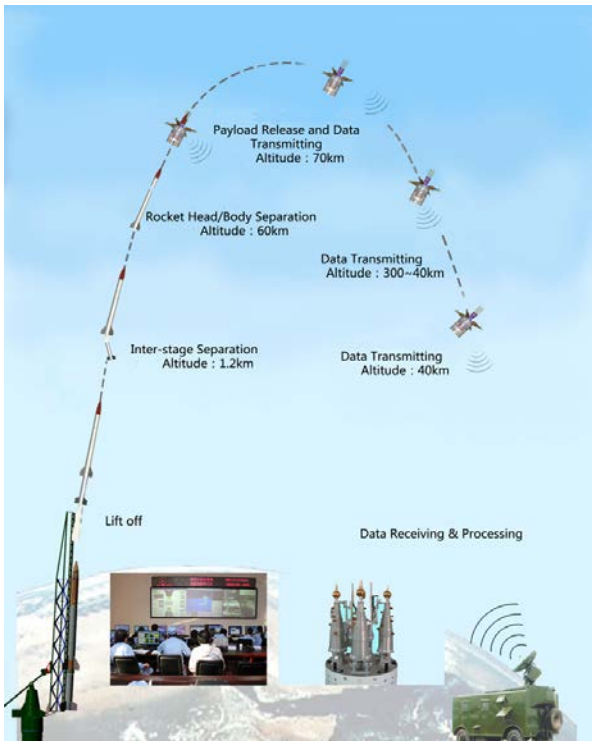

Figure 14. The typical working process of TK-30

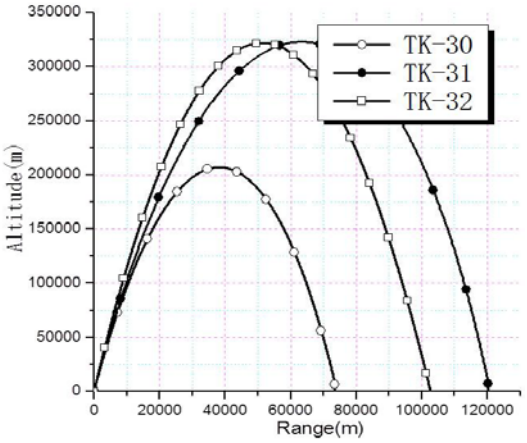

Figure 15. Main technical parameters of TK-30 series

Figure 16. The exploration system of TK-30/TK-32

(3) TK-40 series

TK-40 series sounding rockets is a type of microgravity experiment system of the larger carrying capacity, lower cost, high reliability and simpler launch preparations for meeting the requirement of space microgravity test.

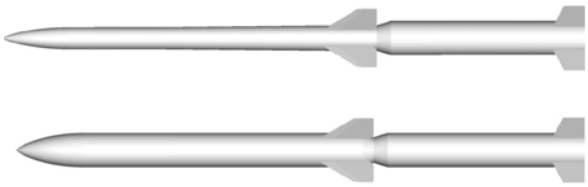

Figure 17. TK-41/42 sounding rocket

TK-40 series can carry 260kg payload (effective payload) to the 270km～330km high altitude, and it can provide microgravity level of 10^{-4} in payload cabin for various space scientific experiment missions. The microgravity test time is not less than 10 minutes.

The performance of TK-40 series sounding rockets is similar to Texus and Maser sounding rocket of ESA.

Table 1. Main technical parameters of TK-40 series

Item	TK-41	TK-42
Rocket diameter (mm)	Φ 605	Φ 605
Overall length (mm)	11500	10200
Stages	2	2
Launch mass (kg)	2880	3300
Payload type	micro-gravity equipment	micro-gravity equipment
Payload mass (kg)	260	260
Rocket head (kg)	460	510
Motor mass (kg)	1425/803	1425/1425
Apogee altitude (km)	270	330
Max. velocity (m/s)	2200	2300
Average thrust (KN)	116/92	116/116
Work time (s)	24/17.6	24/24

(4) TK-50 series

TK-51 sounding rocket can transport the effective payload of 200kg to the high altitude of 700km using for many experimental projects such as science exploration, geophysics, solar physics, astrophysics and space medicine.

Figure 18. TK-51 sounding rocket

The performance of TK-50 sounding rocket is similar to Maxus sounding rocket of ESA.

Table 2. Main technical parameters of TK-51

Item	TK-51
Overall length (mm)	13500
Max. diameter (mm)	Φ 1000
Launch mass (kg)	7350
Effective payload mass (kg)	200
Rocket head (kg)	500
Apogee altitude (km)	705
Max. velocity (m/s)	3380
Motor mass (kg)	5172/1425
Average thrust (KN)	150/116
Work time (s)	70/24

3.2. Equipment of launch site

Sounding rocket equipment of launch site include launch and control equipment, data receiving and processing equipment, launch vehicle, command and communication vehicle, telemetry station and related communication equipment etc.

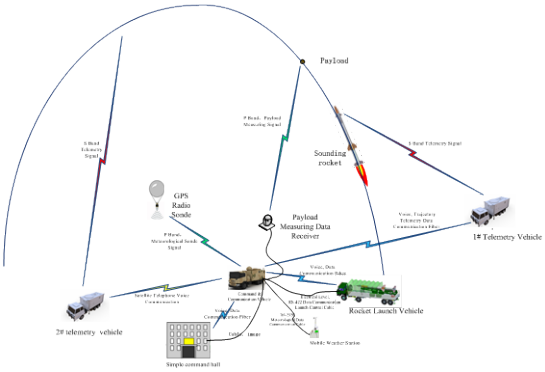

Figure 19. Sounding rocket system

Figure 20. Sounding rocket launch vehicle

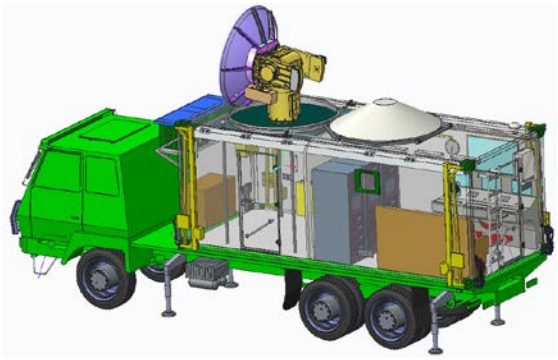

Figure 21. Sounding rocket mobile telemetry station

Figure 22. Command & communication vehicle

Figure 23. Portable Telemetry Station

Front end control box

Figure 24. Launch and control equipment

3.3. Training support

AASPT has a well-established training system. According to the needs of our customer, we can provide training on sounding rocket theory and design, production test technology, equipment operation etc.

3.4. Production and test system

Production and test system mainly accomplish the production, test and detection of the sounding rockets. It includes the rockets production center and the assembly & test center, which is shown in fig.25.

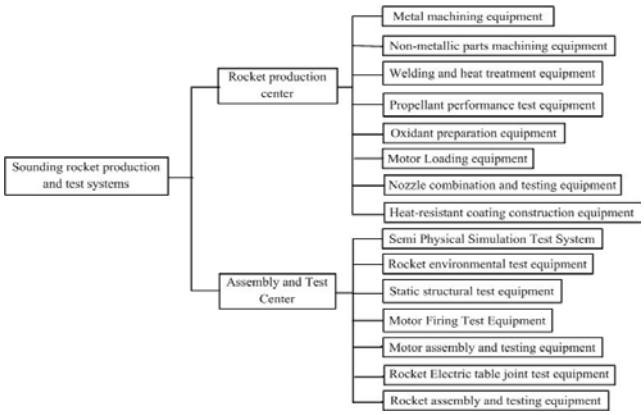

Figure 25. Production and test system

3.5. Civil construction design and implement system

AASPT has a special civil construction design team and civil construction implementation team. Within two years, AASPT can complete civil construction design, construction implementation, equipment installation and testing.

Figure 26. Sounding rocket production system

4. INTERNATIONAL COOPERATION OF CHINA SOUNDING ROCKET SPACE EXPLORATION

China actively explores international cooperation in sounding rocket space exploration activities, promoting the peaceful use of space and sharing space development. Based on the development of China's space technology, it actively explores the international cooperation model of sounding rocket space exploration activities. The Chinese side consider to explore technology and business operation model on sounding rocket launch service.

ESA and its member states have the strong technical strength and level in sounding rocket space exploration areas. CGWIC and AASPT have already conducted the preliminary communication with some European countries on possible cooperation at the early stage. Therefore, at the conference, CGWIC and AASPT suggest the following cooperation proposals about sounding rocket system and space exploration activities subject to the relevant international regulations：

(1) On the premise of peacefully using outer space and promoting the development of space science and technology, according to characteristics of different latitudes of the Chinese and partners launch site, both sides can explore the cooperation model of exchanging experiment payload.

(2) For the cooperation projects, Chinese side and its partners can jointly carry out space exploration activities in the manner of joint funding, or Chinese side providing sounding rocket and partners providing experiment payload and related testing equipment.

(3) For the sounding rocket space exploration activities, China is willing to provide sounding rocket or other related components for partners. Meanwhile, the Chinese partner can also provide experiment payload and relevant instrument and equipment as well.

Table 3. Item list

Sounding rockets and the relevant components	sounding rockets
	the rocket's electrical system
	sequential control computer
	the rocket structural components
	motor
	propellant raw materials
	experiment payload
The relevant instruments and equipments	metal parts and non-metal parts processing equipment
	propellant loading equipment
	ground fire test equipment of motor
	environmental testing equipments of sounding rockets and the relevant components
	the unit test and comprehensive test equipments
	launch and control equipments
	telemetry equipments
	the data receiving and processing equipments
	launch site environment monitoring equipments

(4) To providing the technology training and relevant technical services of sounding rockets

overall and subsystem design technologies
production and test technologies of sounding rockets
detecting technologies of sounding rockets
the data processing technologies of sounding rockets
technical training
technical consulting
technical guidance
technical exchange
quality assurance system
safety assurance system

(5) To provide the civil construction design and implementation of sounding rocket production and test system.

5. CONCLUSION

Based on the technical features of China and its cooperation partners in space exploration areas, on the principle of achieving a win-win result, China hope to jointly explore technology cooperation method and business operation model on sounding rocket and launch service with partners, and jointly promote the peaceful use of space and share space development.

6. REFERENCES

1. Wu Ke (1998). The Development Process of Chinese Sounding Rocket.
2. DaYao Li (1997). Development of the Third Generation Sounding Rockets in China.
3. DaYao Li, LinFan Li (2000). China Sounding Rocket Space Exploration in 20th Century.

ENGINEERING SATELLITE MODEL AS A TOOL FOR SATELLITE DESIGN, ITS EXPLOITATION AND STUDENT EDUCATION

Oleg Brekhov [(1)], Pavel Zhdanov [(1)]

[(1)] Moscow Aviation Institute (National Research University) (MAI), 125993, Volokolamskoe highway, 4, Moscow, Russia. Email: obrekhov@mail.ru, p.a.zhdanov@mai.ru

ABSTRACT

Traditional engineering model of the satellite is developed prior to the flight model. It is necessary to test and debug hardware and software systems, algorithms, operation modes, communication links, etc. This paper is devoted to the development of an Integrated Engineering Model (IEM) as a tool that has diversified usage at different phases of satellite creation. IEM can be used at the development phase as well as at the operation phase. Additionally it can be used in educational process. IEM consists of a common part (kernel) and additional hardware and software tools. The kernel consists of basic service subsystems necessary for the satellite operation. Hardware and software tools depend on the mission phase and usage of the IEM.

1. INTRODUCTION

The engineering model of the satellite is used for the designing the flight model (FM), to test and debug its hardware and software subsystems, operation modes communication capabilities. It is almost identical to the flight model and corresponds to FM in terms of power supply characteristics, external connectors, electrical circuitry and the composition of the components. Differences in the mechanical design and the category (military, industrial, aerospace) of components used are allowed.

2. INTEGRATED ENGINEERING MODEL

Here we consider the Integrated Engineering Model (IEM). It is a modular engineering model with diversified usage. It can be used for various pusrposes:

- As the usual enginnering model that is created before the flight model.
- Usage at the satellite operation phase in parallel with the flight model.
- The integration of the engineering model into the educational process.

3. ARCHITECTURE OF THE IEM

IEM (see Fig. 1) contains a common part (kernel), which is developed prior to the flight model and additional hardware and software tools required to solve the particular problems at different phases of the mission.

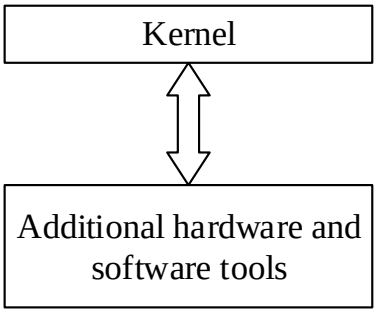

Figure 1. The architecture of the IEM

4. KERNEL OF THE IEM

Hardware and software tools of the kernel include basic service subsystems necessary for the satellite operation: thermal control system, electrical power system, attitude determination and control system, scientific complex, communication system. Each of these subsystems is represented as a set of related hardware and software (engineering or mathematical models), see Fig. 2. The mathematical models run on the personal computer that is a part of the Ground Control System. It is a technological computer that has all necessary interfaces and software to communicate with the onboard communication system and onboard computer (OBC) of the engineering model. The software of the technological computer contains the following components:

- Mathematical models of the sensors and actuators of the attitude determination and control system.
- Onboard software (OBSW) image that has to be loaded to OBC.
- OBSW image loader - program that control the loading of OBSW image into OBC memory.

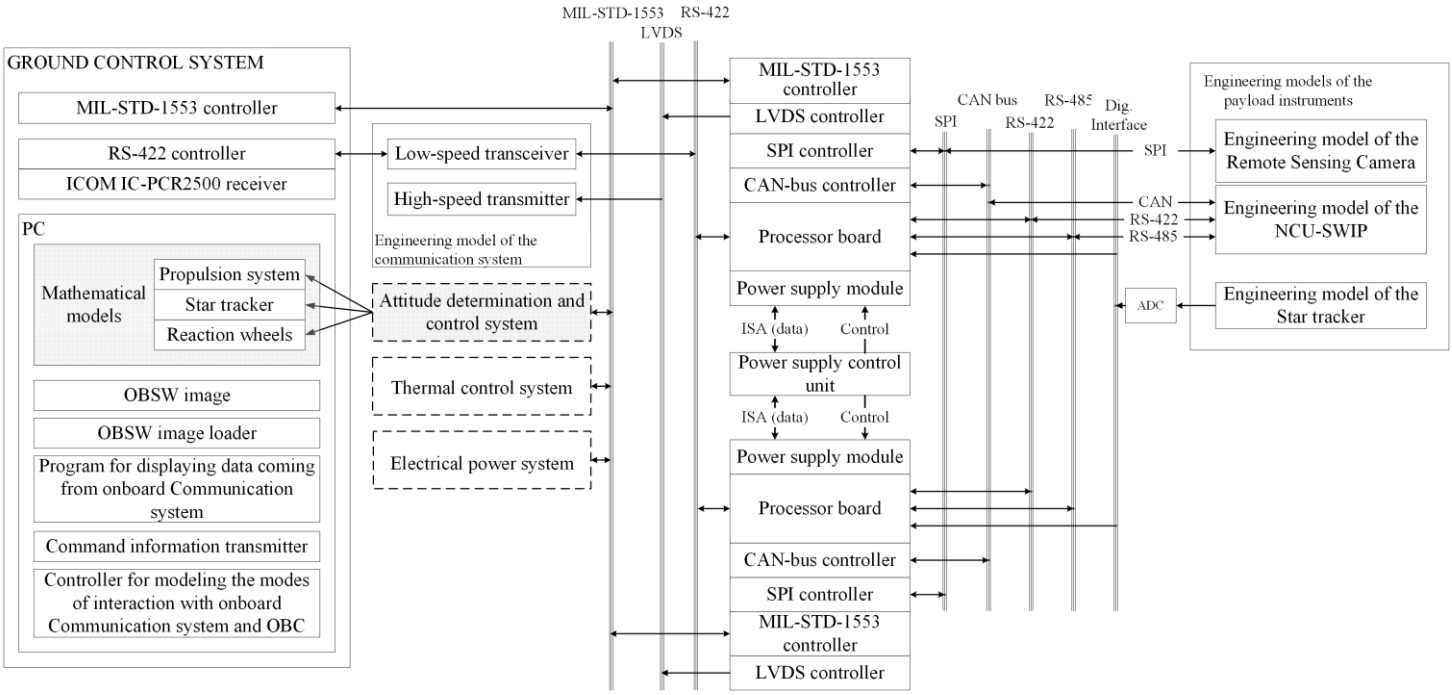

Figure 2. The kernel of the IEM

- Command information transmitter - program for transfer the command information to OBC via technological RS-422 and Mil-STD-1553 channels.
- Controller for modelling the modes of interaction with onboard Communication system and onboard computer.

Other parts of the kernel are the redundant onboard computer described in [1] and engineering models of the payload instruments.

5. ADDITIONAL TOOLS

The additional hardware and software tools depend on the purpose for which IEM is used:

- Usage at the development phase.
- EM and FM cooperation at operation phase.
- Usage of IEM in educational process.

6. IEM AT THE DEVELOPMENT PHASE

At the development phase the IEM is used to test all subsystems, flight software, satellite operation modes, to debug operation algorithms that will be used onboard the flight model. In this case, the additional tools are the simulators of external influences for different platform subsystems (for example, sun exposure) and for the scientific equipment. The communication media simulators are used to simulate noise and inject errors into the traffic between the ground control segment and the satellite. It is necessary to test the error detection and correction algorithms used.

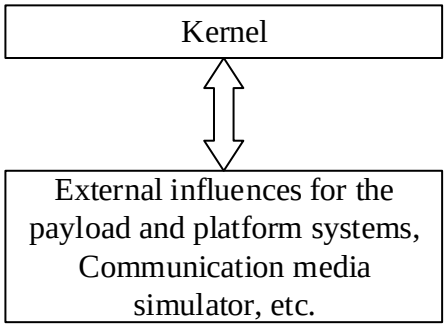

Figure 3. IEM at the development phase

7. IEM AT THE OPERATION PHASE

At the operation phase the engineering model is used for the testing of the new developed software, debugging new algorithms and new operation modes before they are applied to real conditions on flight model. Engineering model also can be used for testing in parallel with the flight model. Co-operation of engineering and flight models in real time provides a synergistic effect and allows to:

- Control the correctness of the payload as well as the scientific and telemetry data received.
- Model and predict the behavior of the satellite, using different environment simulators (solar simulators, ADCS testbeds, dedicated simulators for payload instruments), telemetry and payload data obtained and performing ground modeling. It is is extremely important in case of emergency situations.

- Display the real-time position and orientation of the satellite, using a special ADCS testbeds.

At the operation phase the additional hardware and software (along with simulators) include specialized tools that allow to obtain the original influences on the instruments on the base of the obtained scientific and telemetry data. These influences serve then as the inputs for the engineering models of the IEM payload. Comparison of data obtained from flight model and data generated by the IEM instruments allows to make conclusions about the availability and correctness of on-orbit payload (see Fig. 4).

Another tool that can be used at the development and operation phases is a special testbed that allow to change the position of the engineering model according to the satellite position.

8. IEM IN EDUCATION

During the educational process the engineering model is used in the laboratory and practical training during the teaching of students (bachelors, masters) in relevant areas (see Fig. 4). The main area is the information processing on board the satellite or within a ground segment, the hardware-software implementation of new technologies, data processing algorithms in order to increase the performance of satellite systems or ground segment infrastructure. It can be used to improve electrical power and communication systems design, satellite tracking and data acquisition algorithms. So the IEM can be used as a base for the next missions.

Another challenge is teaching and training the operators of ground control stations in conditions close to real.

The kernel of the IEM in this case is supplemented with special software tools to analyze the satellite behavior and to assess the feasibility of new technologies and algorithms (compression, protection, error detection and correction, security). Additionally IEM is connected to the computer network. This allow students and ground control personnel to get an access to the received payload and telemetry data generated by the IEM as well as to the communication system.

9. CONCLUSIONS

The IEM considered here was developed during the project aimed at the creation of spacecraft for solving various scientific, technical and educational tasks. The main scientific goals of the project are remote sensing and integrated observation of ionosphere, which provide new fundamental results in the field of geophysics and space physics. Subsequently, the obtained data can be used for the prediction of earthquakes.

10. REFERENCES

1. Brekhov, O.M., Tse-Liang Yeh, Shyh-Biau Jiang, & Zhdanov, P.A. (2016). Design of the scientific payload complex for the international university satellite “CONDOR”. In Proc. ‘Living Planet Symposium 2016’ (Ed. L. Ouwehand), ESA SP-740, ESA Communications, ESTEC, Noordwijk, The Netherlands.

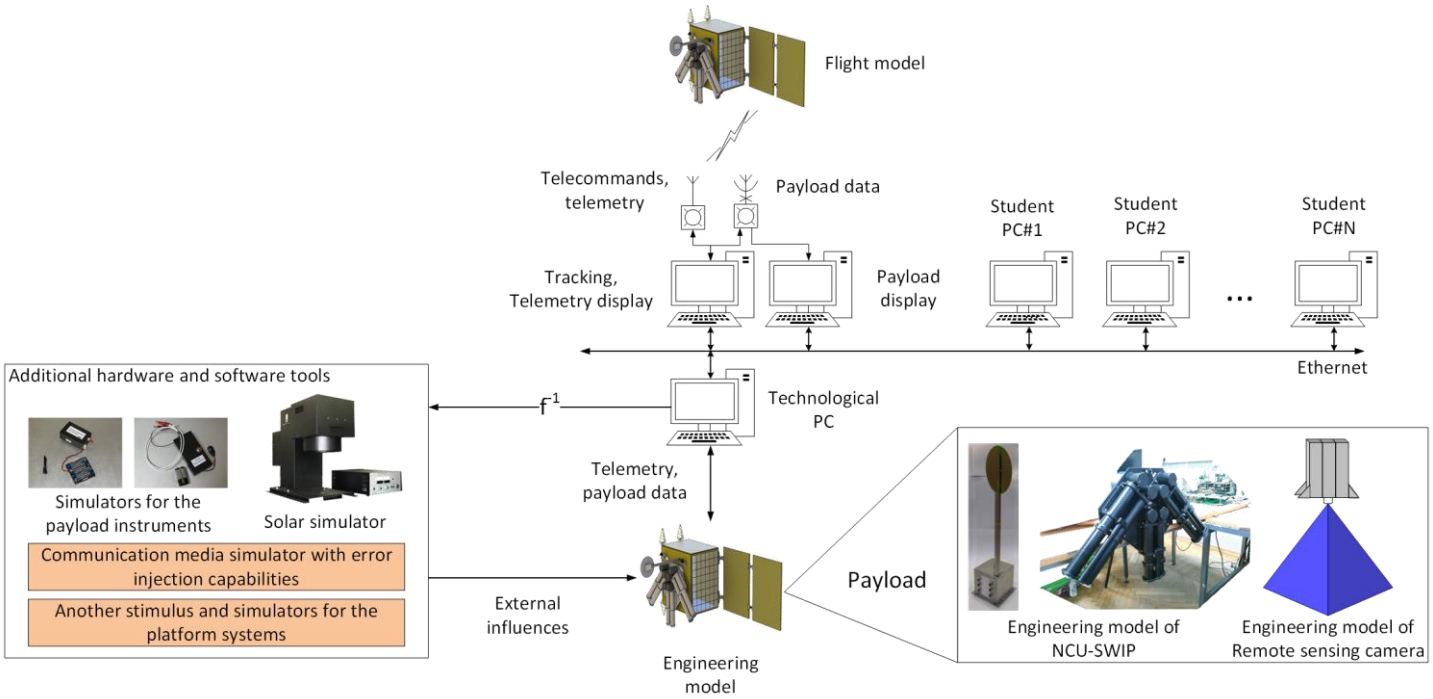

Figure 4. Usage of the IEM in cooperation with the flight model and in educational process

IN SPACE WITH NAMMO'S HYBRID MOTORS: RESULTS AND ACHIEVEMENTS OF THE NUCLEUS PROGRAM

Bastien Haemmerli[(1)], Adrien J. Boiron[(1)], Martina G. Faenza[(1)], Lennart Solli[(1)], Onno Verberne[(1)], Terje Vesterås[(1)]

[(1)] Nammo Raufoss AS, P.O. Box 162, NO-2831 Raufoss, Norway, Email: bastien.haemmerli@nammo.com

ABSTRACT

In the framework of ESA FLPP, Nammo is working on the development of the Unitary Motor (UM), a 30 kN hybrid rocket motor based on 87.5% H2O2 - HTPB, and the Nucleus, a sounding rocket propelled by UM and to be launched from Andøya Space Center to reach over 100 km altitude. The Nucleus is conceived as a demonstrator of the hybrid technology and its possibility of being upscaled whilst maintaining competitive performance. UM went through two development phases, successfully concluded in early 2017 with great propulsive performance demonstrated. The development of the Nucleus is ongoing and static test campaign is planned to be completed during fall 2017. This article provides the status of Nammo's activities on its large scale hybrid in order to get ready for Space.

1. INTRODUCTION

The space market sees nowadays an evolution towards nano- and micro-satellites, that are more and more performant for all kind of purposes. The need for a dedicated launch service for these satellites is becoming quite clear to everybody in the space community ([1]). The challenge lies in their limited launch mass, which represents the low-end of the satellite mass range for which no institutional launchers have been developed. In response to this need, several commercial space companies have already claimed that they will soon be ready to offer to the market their own version of such a new launch service, i.e. Virgin Galactic's LauncherOne, Rocket Lab's Electron, to name but the most matured ones, with dozen others at different level of development.

The Norwegian initiative, or NorthStar, with Nammo, Andøya Space Center (ASC) and the Norwegian Space Center (NSC) as main contributors, is moving along a path leading to a solution which will provide this emerging market a dedicated launch service.
ASC, in Northern Norway, operates a launch site for sounding rockets and scientific balloons. The site has been operative since 1962 and has launched around 1200 sounding rockets. Andøya Space Center however does not manufacture rocket motors and therefore depends on acquiring rocket motors on the open market or on their customers to provide their own rocket motors. Increasing difficulties in acquiring suitable rocket motors for their customers has made them approach Nammo, as being rocket motor manufacturer, for a solution to this need.
In 2008, ASC and Nammo, with NSC support, conceived the vision to cooperate on the realization of a family of rockets based on hybrid rocket propulsion, thanks to its appealing features, such as simplicity, low cost, safety and fast responsiveness. The family of rockets created was called the NorthStar Rocket Family.
The NorthStar Rocket Family is based on a modular concept of Nammo's hybrid rocket motors clustered together. The initiative is conceived for maturing the propulsive technology and enhancing the system complexity according to a step by step approach that keeps both risks and costs as low as possible. The first market to be addressed is the sounding rockets one, where microgravity flights remain an active and appealing sector for scientific and technological application of reasonably sized rocket motors. Ultimately, the operational flight experience and technology matured on this market can be implemented as well for a future affordable dedicated space transportation system for small to very small satellites.

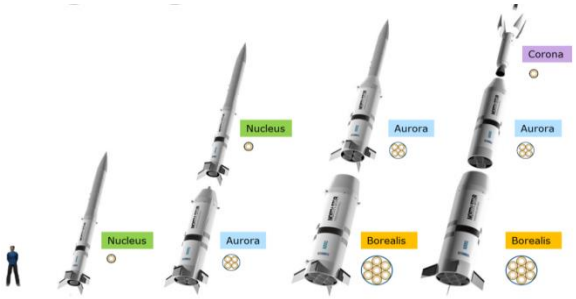

Figure 1: The North Star Rocket Family

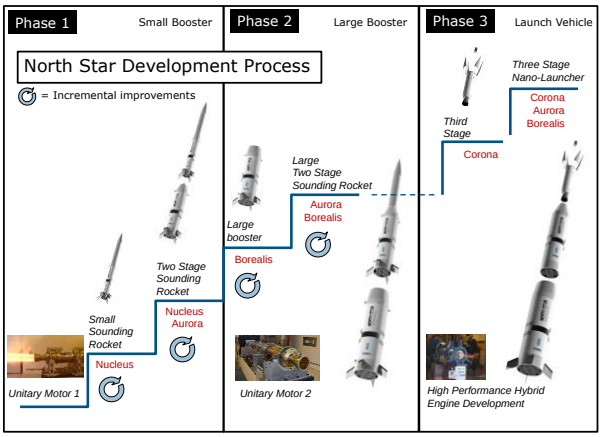

Figure 2: The North Star Development logic

For full details about the NorthStar initiative, the reader is referred to [2] and [3].

Two main factors have motivated the Norwegian space activities: first of all in order to stimulate growth and innovation in Norway's high-tech economy; secondly because of its very unique geography. Norway is an elongated country, reaching far to the north, with a sea area more than six times larger than its land area. With a scattered population, rugged topography, long distances to cover and harsh climatic conditions, space is an attractive place from where to monitor its own territory. In addition, Norway's economy includes heavy elements of natural-resource extraction and maritime transport. There is a priority towards the use of navigation, communication and earth observation satellites to address needs related to ship traffic, fisheries, agriculture, offshore petroleum and search and rescue in the north.

All these priorities and the will to exploit the geographic and territorial advantages of Norway have led to considerable investments in space infrastructure. Norwegian infrastructures are located in Svalbard and in northern Norway (Figure 3), in addition to Antarctica, and this has made Norway an attractive space partner for international cooperation.
As a coastal island far from major settlements, Andøya's launch location is a competitive advantage for launching rockets: there is a vast sea area, no air restrictions and it is situated at high latitude, away from most international airline corridors, with a year-around access, which makes it the ideal place for launching into polar or Sun-Synchronous Orbits. Moreover Andøya Space Center is located at 2 degrees north of the Arctic Circle in northern Norway, making it ideally situated for scientific research in the auroral oval. With the SvalSat satellite station in Svalbard and the TrollSat station on Antarctica, Norway can offer launch, orbit insertion and multiple download and control points of a nanosatellite from Norwegian territory. It can offer an around-the-globe service.

Figure 3: Space infrastructures in Norway.

1.1 Hybrid Rocket Technology at Nammo's

The conception of the NorthStar Rocket Family is based on the know-how which Nammo has acquired since 2003 on hybrid rocket propulsion technology. Nammo Raufoss began working on hybrid motors strong of its consolidated experience from solid motor design and production for defense (Exocet, NSM) and space applications (FE/FA Ariane 5 boosters).
Several research and technology programs have been completed since, either nationally or in cooperation with partners like Lockheed-Martin, ESA, SAAB Dynamics, and ONERA to name a few ([4], [5] and [6]). Nammo started its development on lab scale motors investigating initially different kind of oxidizers (N2O, GOX, LOX, H2O2) and fuels (HTPB, HDPE, plus additives). Since 2008, high concentration hydrogen peroxide and HTPB has been the core which Nammo has built its strong expertise around, a combination which is both friendly to the environment and cost effective. The motors developed at Nammo combine the environmental friendliness and cost effectiveness of a H2O2-HTPB hybrid rocket motor, with a high regression rate and an excellent overall combustion efficiency (up to 98%).
2010 saw the beginning of the support, still lasting today, from the Norwegian Space Center and the European Space Agency in developing Nammo's hybrid propulsion technology. Firstly within ESA TRL Improvement program and lately in ESA FLPP (Future Launchers Preparatory Program), Nammo has performed more than 100 small-scale successful hybrid rocket tests exploring many different motor and flow configurations, and has afterward moved to upscaling the technology, in order to demonstrate the feasibility of using hybrid propulsion for sounding rocket and nano-launcher applications.
In order to support the development of the hybrid technology Nammo has invested in 2014 in the

construction of a state-of-the-art test facility for green propulsion, with the capacity to test the first stage of a nano-launcher with a sea level thrust up to 500kN (see ref. [7]).
FLPP aims at fostering new promising technologies for future European access to space. The objective of the Future Launchers Preparatory Programme (FLPP) is to determine and ensure how Europe maintains and strengthens its independent access in space into the mid to long-term. The Programme has been investing in development of technological and industrial capabilities in all main space transportation areas since 2003, including in the propulsion field (see ref. [8]).

2. THE UNITARY MOTOR

With the support of ESA FLPP, Nammo is developing the Unitary Motor (UM1), which represents the first building block to design a clustered architecture potentially applicable both to the sounding rocket and the nano-launcher market.
The Motor belongs to the 30 kN thrust class and is based on a novel concept of hybrid rocket engine technology developed by Nammo. It uses high concentration hydrogen peroxide (87.5% H2O2) as oxidizer and hydroxyl-terminated polybutadiene (HTPB) rubber as fuel.
It was 2014 when Nammo successfully tested the battleship configuration for a burning time of up to 25 seconds. The upscaling factor with respect to the previous phase of lab-scale testing was above 20 and the performances achieved have been beyond expectations, in terms of stability, efficiency and high regression rate. This achievement promoted the go-ahead towards flight weight optimization of the UM1.

Figure 4 shows the working principle of UM1. The incoming liquid oxidizer, with a mass flow of about 11 kg/s, is decomposed passing through a catalyst into hot steam and gaseous oxygen at a typical temperature of 670°C. It is then injected into the combustion chamber in hot gaseous form, where ignition of the hybrid combustion occurs instantly without any dedicated ignition device due to the sole high temperature which is sufficient to vaporize the solid fuel. The vortex flow-field in the chamber generated by the injector helps in maintaining a high heat flux towards the fuel surface and in achieving appropriate mixing of the reactants. Ultimately, this allows sustaining high combustion efficiency. The hot combustion gases are then expelled through a standard nozzle, generating close to 30 kN of thrust.

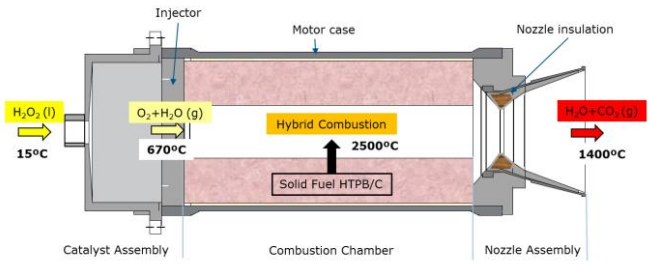

Figure 4: Schematic Showing the Working Principle of the Unitary Motor.

Compared with solid rocket motors, the hybrid technology developed by Nammo has a rich set of attractive features, which are:

- self-ignition (no dedicated igniter needed) increasing engine start reliability and enabling and unlimited restart capability;
- wide range throttling with limited performance losses;
- green life cycle and exhaust properties;
- solid inert fuel and high-density green storable oxidizer;
- high engine combustion efficiency, performance and stability;
- simplicity of a single circular port and single feedline configuration;
- low development and operational costs.

Most of these properties are shared with the inherent properties of other hybrid propulsion technologies, but some of them are unique for the H2O2 based technology perfected by Nammo. Some of these features are as well common with liquid rocket engines, but compared with liquid engines, the architecture of the Unitary Motor is much simpler and the same features are obtained for a fraction of the cost.

2.1 Development Logic

As previously mentioned, in the last years Nammo has been developing its hybrid technology with the support of ESA and the FLPP program. The primary objective of the FLPP hybrid demonstration is to increase the TRL of hybrid propulsion while demonstrating it at a significant scale; that is at a thrust level above 100 kN.
As illustrated in Figure 4, the program started with lab-scale motors which notably investigated combustion processes and the use of different fuel additives. After the completion of more than 100 lab-scale motor tests across many projects, Nammo was ready for upscaling. This upscaling occurred within FLPP Hybrid Phase 1, which was completed after the first two firings of the Heavy-Wall Unitary Motor (HWUM) in autumn 2014.
Phase 2 of the project continued the HWUM test campaign until completion, and then moved on to the

design and manufacturing of the next motor evolution, the Flight-Weight Unitary Motor (FWUM). Phase 2 was concluded in spring 2017 by the FWUM Post Test Review after a successful test campaign which confirmed the performance of the HWUM on a flight optimized design.
Phase 3 focuses on two different further utilizations of the FWUM, displayed in Figure 4: the Cluster Demonstrator, a bundle of 4 FWUMs expected to deliver a sea-level thrust of the order of 120 kN; and the Nucleus demonstrator, a flying vehicle that will lead to a flight test of the FWUM and of Nammo's hybrid rocket technology. The rocket is planned to be launched from Andøya's Space Center in Northern Norway and to reach an altitude above 100 km. This flight has to be considered as a technology demonstration of the propulsive system (motor and feed system) in a representative environment: all the main motor parameters in flight will be measured and thus the performance assessed. More details will be provided on the Nucleus in the last section of the article.

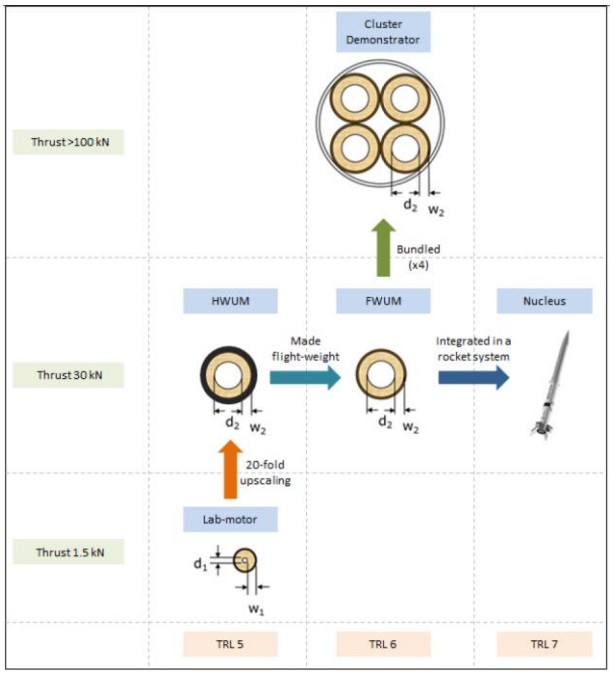

Figure 5: Development logic of Nammo's hybrid propulsion technology within ESA FLPP.

2.2 Motor Evolution

The FWUM is an evolution of the HWUM in terms of mass, with 3 times less dry mass, but not only: it is also an evolution in terms of capability. Through discussions with actors of the sounding rocket industry on the UM and Nucleus sounding rocket payload and altitude capabilities, the preference for a larger total impulse capability of 1000 kNs was expressed on numerous occasions. This need furthermore coincided with the fact that a 1000 kNs impulse UM would have an outer diameter of 14 inches, which is the standard sounding rocket payload diameter in use in Europe and at Andøya Space Center in northern Norway.
The decision was then taken by Nammo and ESA to increase the UM outer diameter to 14 inches, applying this change directly on the FWUM. Within the demonstration program, this evolution means not a higher thrust level for the motor, but a longer burn time, which was increased from 25 seconds to more than 35 seconds.
From the analysis of the HWUM firing test data, the project actors were able to conclude that this increase in motor capability and diameter was feasible and to be pursued within the framework of the FLPP hybrid demonstration program.
Table 1 shows an overview of the differences between the HWUM and the FWUM, while Figure 6 and Figure 7 show the two motors during testing at Nammo Raufoss premises.

Table 1. Differences between FWUM and HWUM

	HWUM	**FWUM**
Total impulse at ground level	700-750 kNs	1000 kNs
Outer diameter	334 mm	356 mm (14 in)
Burn duration	25 s	>35 s
Motor dry mass	> 280 kg	< 100 kg
Consumed fuel mass	< 50 kg	> 60 kg
Consumed oxidizer mass	270 kg	400 kg

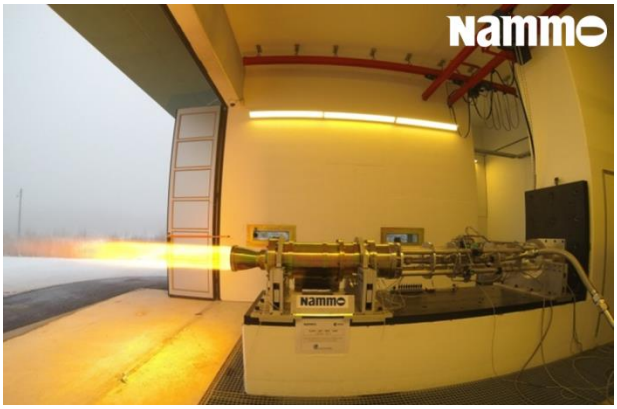

Figure 6. HWUM during static testing.

Figure 7. FWUM during static testing.

2.3 Test Campaign of the Unitary Motors

2.3.1 Heavy Wall

Within FLPP Phase 1, the HWUM was designed, manufactured and first fired during the sole year 2014. The HWUM campaign then continued in FLPP Phase 2.
The HWUM ground tests were concluded with the delivery of a very satisfactory motor design yielding the performance desired for the next stage in the program.

The reader is referred to ref. [9] for a complete overview about the results of this test campaign.

2.3.2 Flight Weight

The design of the FWUM occurred within the first 8 months of 2015, with the completion of its Preliminary Design Review in June 2015 and its Manufacturing Readiness Review in September 2015. The manufacturing phase then followed on during the fall of 2015, leading to the first catalyst tests at the end of November 2015.
During the FWUM test campaign, and after a preparatory phase of GSE (Ground Support Equipment) validation with water tests, both monopropellant and hybrid tests were performed.

The former consisted of catalyst functional tests whose results have been already presented in the past: the reader is referred to ref. [10] for a complete overview on the results of this part of the campaign.
Since the last monopropellant test, the project has worked on preparing for the hybrid firing. Several tests have been performed with the targeted goal of ramping up the burn duration towards the same duration achieved during the HW campaign.
In performing this part of the campaign an additional achievement has been demonstrated: the capability of Nammo's engine to stop and restart, feature very appealing for hybrid rocket based propulsion systems. One of the hybrid firings, with a targeted cumulated burning time of 15s, has been split in two pulses: a first one lasting 5 s and a second one, lasting 10 s. The second pulse has been performed 2 hours and 35 minutes after the first pulse. Ignition, stability and performance of the engine confirmed very satisfactory in the stop-restart tests as well.

At the end of this static test campaign, burning time duration of 25 s was demonstrated and the performance confirmed at the expected level. It is remarked that 25s is the maximum duration allowed and tested during the HWUM test campaign. It was therefore an important milestone to achieve again the same burning time duration, but this time on the flight weight configuration.

The flight weight UM demonstrated great and stable performances for the full burn duration, delivering a specific impulse in line with the expectation and a stable thrust in the order of 28 kN. Figure 8 shows typical frames of the motor during testing while Figure 9 shows the thrust curve as recorded during the test. One can really appreciate the stability and neatness of the produced thrust, thus suggesting a well performing motor.

This firing is currently the longest 30 kN firing performed by Nammo which demonstrated a long and stable burn time of the FWUM without any major issue encountered. This result together with a delivered overall average motor efficiency of the order of 95% clears the way to proceed to longer firings as part of the Nucleus ground test campaign.

Figure 8: FLPP-UM-016-HRE during the various stage of the firing

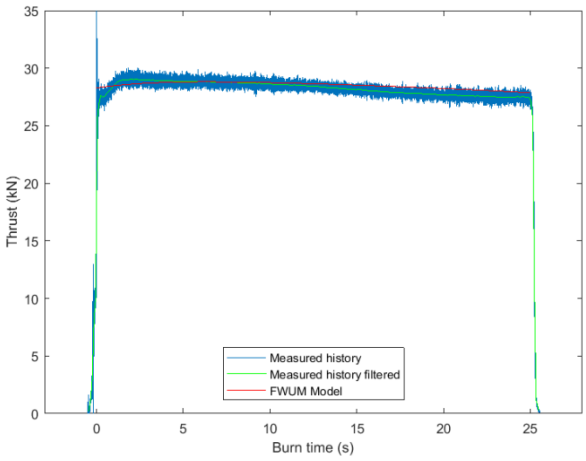

Figure 9. Experimental unfiltered thrust curve in comparison with model prediction.

3. NUCLEUS

With both a Cluster Demonstrator and a Flight Demonstrator (the Nucleus rocket) on the Nammo

roadmap of future hybrid activities, the Nucleus is currently the one on which most focus is placed. That is primarily because of the pressing sounding rocket market needs, with ASC ready to propose those vehicles on the commercial market as soon as available.
As already mentioned, the Nucleus is the prototype sounding rocket developed by Nammo, with the flight weight UM1 as propulsive unit. This vehicle will be a flight demonstrator for Nammo's hybrid rocket technology, and will include the entire life cycle at system level, with tanks and valves, electronics, launch pad GSE and operations, etc. It will be used to demonstrate at full scale the Concept of Operations (CONOPS) associated with rocket launches based on hydrogen peroxide powered hybrid rockets.

The design activities started in Nammo Raufoss and ASC in November 2015 with the three actors, ESA, Nammo and ACS working closely together. Manufacturing Readiness Review (MRR) with ESA has been successfully passed in December 2016 and manufacturing is now ongoing and well underway.

3.1 Specifications

Table 2 summarizes the main features of the Nucleus rocket according to specifications.

Table 2. Nucleus specifications.

Parameter	Specification
Motorization	One FWUM fitted with a flight nozzle (AR 8.5)
Apogee altitude (with 82° launch rail elevation)	> 100 km
Body outer diameter	356 mm
Total length	9 m
Total mass	820 kg (of which 70kg for the ASC payload)
Hybrid motor burn time	>35 s
Total impulse	> 1000 kNs
Average delivered specific impulse in flight	> 250 s
Peak acceleration	7 Gs
Oxidizer tank material	Aluminum
Helium tank material	Carbon-composite
Airframe structures	Aluminum

3.2 Architecture

The Nucleus is a single stage spin-stabilized sounding rocket. In order to reduce the complexity and the cost of this prototype, no active control of the rocket is foreseen during the flight and no recovery is planned.
Nucleus architecture can be divided in 4 main sections, as shown in Figure 10: the FWUM, the oxidizer feeding section, the pressurizer feeding section and the payload.
The main components of the rocket can be separated in 4 categories, depending on their role:

- Propulsion;
- Structure;
- Aerodynamics;
- Instrumentation and telemetry.

Except for the payload section, developed by Andøya Space Center, and the fins, developed by DLR Stuttgart, the rest of the rocket has been entirely designed within Nammo and all the manufacturing is either carried out in house or outsourced to local companies in the Raufoss industrial park.
As the "scientific" payload of this launch is the propulsion system itself, the payload sections are limited to what is necessary for the flight: housekeeping (battery, accelerometers and magnetometers,…), telemetry system (transmitter and antennas) and nose cone. Several types of sensors are located along the rocket and especially in the FWUM section (pressure probes, thermocouples and accelerometers) and signals are carried to the nose cone where they are handled by ASC payload.

The propulsion is covered by the FWUM section, where one FWUM is fitted with a flight adapted nozzle to maximize the flight performances. A boat-tail is mounted around the nozzle in order to reduce the base drag and provide interface for the attachment of the DLR fins, responsible of the stability of the rocket. The motor housings carry the loads: thrust, G forces, dynamic pressure and aero-heating. The motor is operated in blow down using helium as pressurizing gas.

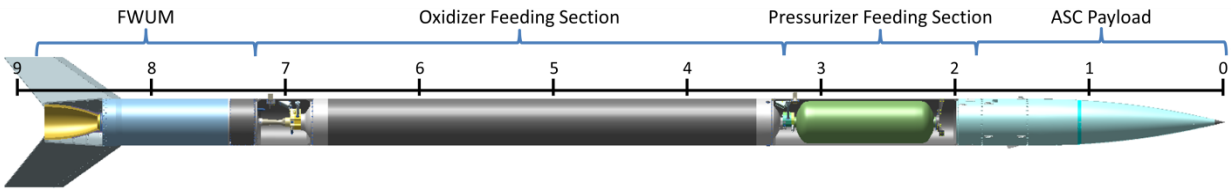

Figure 10. Simplified CAD model of the Nucleus Prototype Rocket.

3.3 Tanks and Valves

The Oxidizer Feeding Section mainly consists of the structural oxidizer tank filled with about 400 kg H2O2. The design and qualification of the tank is carried out by Nammo with the support of a Norwegian company experienced in friction stir welding for the manufacturing. A Propellant Management Device (PDM) has been developed in order to limit the formation of free surface vortex in the liquid due to spin and to avoid premature ingestion of gas in the motor. Nammo has also developed a customized oxidizer valve assembly with different functions embedded in one single body in order to significantly decrease mass and size of the fluid system. The assembly performs the filling/draining of the oxidizer tank, as well as the catalyst priming and the firing of the motor, all in one structure. A cavitating venturi is used to calibrate the mass flow rate given to the FWUM. Figure 11 shows a schematic representation of the main items included in the Oxidizer Feeding Section.

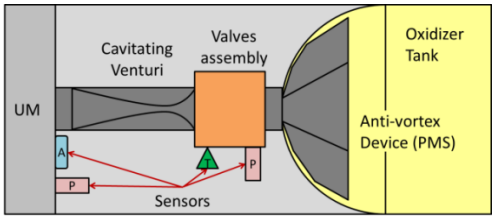

Figure 11. Sketch of the Oxidizer Feeding Section.

The Pressurizer Feeding Section has a structure similar to the Oxidizer one: a composite non-structural cylinder filled with Helium at 400 bars, a purpose-built and multifunction valve assembly designed for the pressure level and all the operations needed (filling/draining of the cylinder, pressurization of the oxidizer tank and flow regulation) and a flow restrictor to ensure a good pressurization level in the oxidizer tank all throughout the propulsive phase. Helium is selected as pressurizing gas due to its low mass. In this section, the loads are carried by a dedicated aluminium airframe structure around the pressurizer tank. Figure 12 shows a schematic representation of the main items included in the Pressurizer Feeding Section.

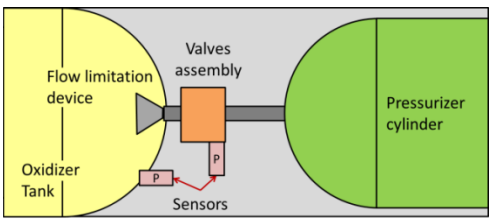

Figure 12. Sketch of the Pressurizer Feeding Section.

In order to further reduce the dry mass of the rocket, the actuators for both valve assemblies are installed on the launch rail and planned to remain on the ground at rocket take-off.

3.4 Ground Support Equipment

ASC has launched over 1200 sounding rocket since its foundation in 1962, but so far only one hybrid rocket. The launch pad has thus to be adjusted to accommodate this technology. The Nucleus will be launched from the main launch pad, the U3 launcher, capable of launching all kind of sounding rockets. The upgrades of the U3 facility concern mainly the safe handling and storing of H2O2, for which dedicated ground support equipment is designed and installed. This GSE will be used to fill the oxidizer tank and the pressurizer cylinder, to control and operate the rocket system from the bunker while on ground and to ensure the safety in the launch area. Figure 13 shows an overview of ASC site and launch pad.

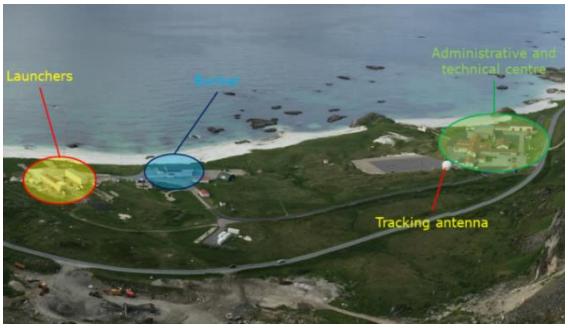

Figure 13: Global view of ASC

3.5 Launch Pad

In order to accommodate the Nucleus rocket on the U3 launcher some extra hardware has been developed by Nammo: it consists of a set of two retractable launch lugs and a guiding rail specifically designed for guaranteeing the simultaneous release of the rocket at take-off. The guiding rail is connected to the U3 launch rail and the Nucleus is suspended on it through the mentioned lugs (Figure 14). At rocket release, the lugs design guarantees them to retract inside the rocket body in order to minimize aerodynamic drag. Figure 15 shows a schematic representation of the lugs design and connection to the guiding rail.

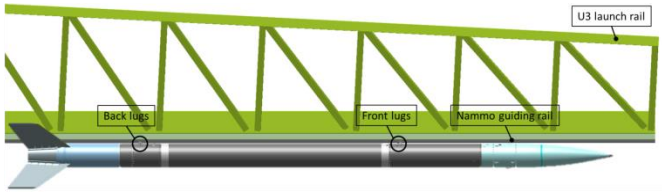

Figure 14. CAD model of the Nucleus suspended on the U3 .

Figure 15. Schematics of the lugs.

3.6 Flight Performance

Trajectory analysis and safety assessment are performed by Nammo in collaboration with Andøya Space Center.

A numerical tool for rocket design was developed by Nammo to help the design process. This tool allows the user to define all parameter of interest (size of the motor, oxidizer total mass, Helium initial pressure, etc.) and gives the corresponding rocket preliminary design. This design can then be used as input to the second part of the code that is a flight simulator. It includes physical models for the motor operation, for the aerodynamic forces acting on the rocket and for the resulting trajectory. The expected trajectory calculated with this tool is shown in Figure 16.

Figure 16. Simulated trajectory of Nucleus flight.

3.7 Ground Testing

Before being cleared to launch the Nucleus, the full propulsion system is being validated through an ongoing ground test phase in Nammo's Test facility in Raufoss (ref. [7]).
This test campaign has two main goals:

- test the FWUM functioning in blow-down and for the full burn duration (>35 s);
- introduce all the flight components (tanks, valves, sensors) in the test assembly in order to qualify filling, testing and draining operations on ground before flight.

These goals are being pursued progressively adding step by step complexity to the test assembly. Several hybrid tests will be needed in the next months to reach the ground system test objectives and proceed to rocket final assembly and flight.

4. CONCLUSIONS

Between 2014 and 2017, Nammo has upscaled and matured its hybrid technology to a scale and technology readiness level relevant for sounding rockets and nano-launcher applications. Those developments have so far culminated with the design, the manufacture and the testing of the Unitary Motor 1, a 30 kN class hybrid motor which showed all along the test campaigns exceptional performances and behaviour. In parallel to the motor development, Nammo has worked on the design and the manufacturing of the Nucleus, a single stage sounding rocket, seen as a demonstration platform for the Unitary Motor 1. The design has been finalized, manufacturing is ongoing and the project is currently occupied with the ground testing of the full propulsion system, with a flight that has the goal to bring Nammo's technology above 100 km altitude.

Ultimately, the work done so far by Nammo demonstrates its capability of mastering the hybrid technology with a dedicated work oriented towards continuous improvement; moreover it paves the way with the support of Andøya Space Center, the Norwegian Space Center and ESA for the use of its hybrid technology for heavy-lift sounding rockets and potentially nano-launcher application, where the Nucleus represents the first and smallest building block of the NorthStar rocket family.

5. ACKNOWLEDGMENTS

This project is supported by funding from ESA under the Future Launchers Preparatory Programme.

6. REFERENCES

[1] http://spacenews.com/launch-woes-diminish-demand-for-small-satellites/. Foust J., "Launch Woes Diminish Demand for Small Satellites". Article on spacenews.com, February 2017.

[2] Haemmerli B., Boiron A. J. and Verberne O., "The Norwegian Initiative for a Satellite Nano-launcher". Proceedings of the 29th AIAA/USU Conference on Small Satellites, Logan, Utah, August 2016.

[3] Verberne O., "The North Star Rocket Family". Proceedings of the 12th ReInventing Space Conference, London, Great Britain, November 2014.

[4] Verberne, O., Rønningen J. E. and Boiron A., "Development and Testing of Hydrogen Peroxide Hybrid Rocket Motors at Nammo Raufoss". Proceedings of AIAA 50th Joint Propulsion Conference, Cleveland, Ohio, July 2014.

[5] Rønningen J.-E. and Husdal J., "Nammo Hybrid Rocket Propulsion TRL Improvement Program". Proceedings of the 48th Joint Propulsion Conference, Atlanta, Georgia, August 2012.

[6] Rønningen J.-E., "The HTR Program – An Overview of the Rocket System and Program Achievements". Proceedings of the 18th ESA Symposium on European Rocket and Balloon Programmes and Related Research, Visby, Sweden, June 2007.

[7] Verberne O., Boiron A.J. and Vesterås T., "Green Propulsion Rocket Test Stand". Proceedings of the 4th Space Propulsion Conference, Cologne, Germany, May 2014.

[8] Underhill, K., Caruana, J-N, De Rosa, M. & Schoroth, W. (2016). Status of FLPP Propulsion Demonstrators – Technology Maturation, Application Perspectives. Proceedings of the Space Propulsion Conference 2016, Rome, Italy, May 2016.

[9] Boiron J.B, Faenza M.G, Haemmerli B and Verberne O., "Hybrid Rocket Motor Upscaling and Development Test Campaign at Nammo Raufoss". Proceedings of the 51st AIAA Joint Propulsion Conference, Orlando, FL, July 2015.

[10] Boiron, A.J, Faenza M. G., Haemmerli B., Verberne O., Vesterås T., Caruana J.N., Schoroth W., "Demonstration of 30kN-Thrust Hybrid Rocket Propulsion at Nammo Raufoss within ESA FLPP". Proceedings of Space Propulsion 2016, Rome, Italy, May 2016.

O-STATES & SPIDER/LEEWAVES, A NEW ERA OF NATIONAL SOUNDING ROCKETS FROM ESRANGE BEGINS

VISBY, SWEDEN
11-15 JUNE 2017

Krister SJÖLANDER[(1)]

[(1)]*SSC, Swedish Space Corporation, P.O. box 4207, 17104 Solna, Sweden, Email:krister.sjolander@sscspace.com*

ABSTRACT

In the autumn of 2015 and beginning of 2016 the three first rockets within the Swedish national balloon and rocket programme, initiated by the Swedish National Space Board (SNSB) in 2012, were successfully launched from Esrange. From the 1960's to the end of the last millennium one or two Swedish national sounding rockets were launched each year, not accounting for any of the many meteorology rockets. These latest three rockets launched over the past two years mark the beginning of a new era for advanced research by rockets from Esrange, available for Swedish scientists.
This paper reports on the O-STATES 1 & 2 and SPIDER/LEEWAVES missions and flights, focusing on the related technical solutions and results.

1. BACKGROUND AND HISTORY

There is a long history of Swedish sounding rocketry that started in the early 60's from Nausta and Kronogård. But in 1968 the first national rocket from Esrange, K68, was launched on the 24th of October marking the start of an almost 30 year era of high launch rate of national rockets.
In the first 30 years of operation, an average of almost two national rockets per year for research on atmospheric physics, plasma physics and research on aurora borealis were launched from Esrange.

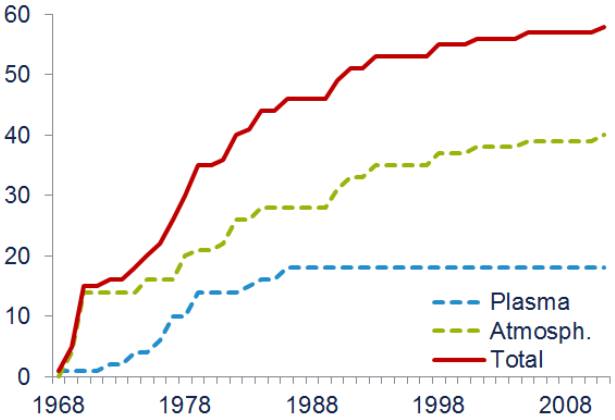

Figure 1. Number of national rockets from Esrange

By the turn of the millennium, as can be seen in Fig. 1, more than 50 major national rockets and numerous smaller meteorology rockets had been launched from Esrange while in the first 15 years of the new millennium only three national rockets were launched, Hygrosond-2, MAGIC and PHOCUS.
But then in 2012 the Swedish National Space Board (SNSB) initiated, with an annual budget, the "Swedish national balloon and rocket programme" dedicated to the Swedish science and research community.

2. THE NEW ERA OF NATIONAL ROCKETS

In the first call for ideas under the new "Swedish national balloon and rocket programme" three rocket missions were picked in the selection process. The three missions selected were one plasma physics research mission, SPIDER and two atmospheric physics research missions, O-STATES and LEEWAVES. SSC was contracted to realize the three rocket projects.

2.1. O-STATES mission description

Figure 2. O-STATES

O-STATES 1 & 2 (Oxygen Species and Thermospheric Airglow in The Earth's Sky), is an atmospheric physics research mission by the Meteorological Institute at Stockholm University (MISU).
The payload was developed by SSC and MISU and this single payload was launched twice in one single campaign, in October 2015, with on-site refurbishment between flights, for time and fund efficiency.

The O-STATES rocket project idea is about quantifying the relationship between various oxygen species in the

thermosphere and the airglow emissions that they cause. Spectral analysis was suggested as a measurement technique for thermospheric atomic oxygen and temperature. These parameters are essential in describing the state of the thermosphere.
A central part of this project is an evaluation of this technique and its potential use in remote sensing applications like Global Oxygen And Temperature (GOAT) mapping and verifying this with in-situ measurements between 100 km and 250 km altitude

The on-board instrumentation used on O-STATES were a photometer based, actively cooled, spectrograph (developed by MISU/SSC) for day-glow spectroscopy, an active optical system (MISU's O-probe) for oxygen resonance fluorescence of atomic oxygen, FIPEX (IRS) electrolytic oxygen probes and also electron and ion density of ionosphere were measured using faraday rotation, Langmuir and ion/electron probes (TUG). The front looking optical instrumentation is exposed by releasing the nose cone (developed by SSC) and the side looking instrumentation by ejecting two hatches.

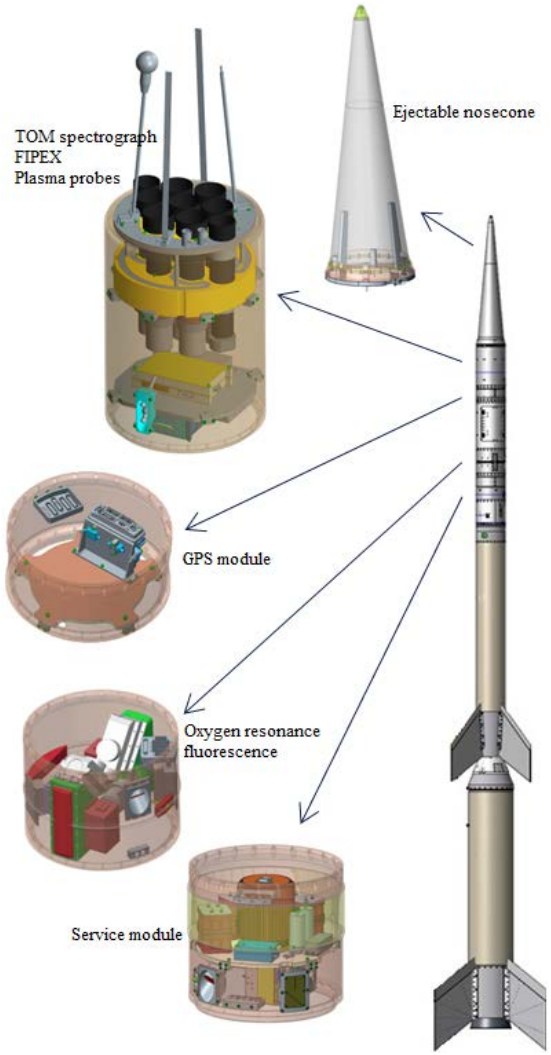

Figure 3. O-STATES payload and vehicle

Also background measurements were made using EISCAT radar as well as the ODIN satellite Osiris instrument.

The requested launch requirements were to launch the same payload configuration twice into different geomagnetic conditions. One launch into quiet conditions (< 1 kp index) and one launch into mildly disturbed condition (~ 2 kp index). The launch should also be in twilight or dusk/dawn conditions (sun at +5°) giving a launch window of ~ 10 minutes in the morning and ~10 minutes in the evening. The desired apogee was > 235 km and measurements starting from 70 km.

The core instrument on the O-STATES payload is the TOM spectrograph. This instrument was developed by SSC and MISU. MISU improved the design of their photometers that have a great flight heritage and SSC provided the data collection system and developed the new cooling system needed for the PMT's to minimise noise levels and increase sensitivity. During flight the PMT's were kept at -6°C and within 0.1°C.

The service module flown on O-STATES was the SM14 system initially developed by SSC for the PHOCUS mission in 2011. This versatile and modular system is the core for the Swedish national 14-inch payloads but can also be adapted for diameters like 17-inch or other.

Some examples of major functions this system provides:
- Switched power for H/K as well as instrumentation,
- Instrument data collection,
- Position and attitude determination,
- Pyro control,
- Ground-link for H/K and instrument data,

Selected features of O-STATES SM14 configuration:
- 2 x CCSDS telemetry interface (1.25 to 10 Mbit/s),
- 1 x 2.5 Mbit, 5W, S-band, FM downlink,
- Internal H/K,
- System and power control,
- 15 x 1A LCL power switches for external users,
- 1 x 3.5A LCL power switch for external users,
- 8 x galvanically isolated full duplex RS422,
- 8 bit parallel output,
- 2 x SpaceWire interfaces,
- GMSK cmd input,
- GMSK bitsychronizer output,
- OCXO for slant range,
- Local H/K storage (SD),
- COCOM GPS receiver,
- Time synchronization,
- 6 pyro control channels,
- 3 x 3200 mAh, NiMh batteries,
- 90 x Analog I/O, 16 bit, up to 1600 Hz sample rate,
- 3 x Digital I/O, 16 bit inputs / 8 bit output,
- 12 LVDS pulse counters, up to 40 MHz,
- DMARS-R, Roll Isolated INS,

2.2. O-STATES launch

Launching the same payload individual twice within one single campaign was one of the challenges of the O-STATES mission. There was no actual requirement to use the same payload and no constraint on time between launch dates. However, it was found that in this case it would by far be the most cost efficient way to achieve these two flights and make funding possible. The risks of having two flights planned for the same hardware within such a short period were mitigated, by being well prepared with spares and personnel, and found acceptable.

The first launch attempt of O-STATES #1 was on the 2nd of October 2015. The payload and two stage S31-Improved Orion rocket were launched from the Esrange MAN-2 single rail launcher at 07:39:00 local time. It was launched in miserable but acceptable weather conditions into mildly active geomagnetic conditions.

Figure 4. O-STATES #1 lift-off

The lift off and flight was nominal. All instruments were powered and delivering data and an apogee of 246.6 km was reached after 251 seconds.
The recovery operations had to be postponed to the following day due to weather conditions and the payload was back at Esrange with helicopter on the 3rd of October at mid-day.

On-site refurbishment started immediately on the payload that was more mechanically damaged than anticipated. This was due to the landing site being full of stones and boulders. Additional hardware had to be shipped to the launch site. The payload was despite all damage ready for launch within the budgeted time and O-STATES #2 was ready on the launch pad on the 10th of October only 7 days after recovery of O-STATES #1.

O-STATES #2 was launched on the fourth attempt (waiting for weather and scientific conditions) on the 19th of October at 16:09:00 local time. It was launched in perfect weather conditions into quiet geomagnetic activity.

Figure 5. O-STATES #2 lift-off

Both O-STATES flights were a success. This was the first time this motor combination, with an S31 and Improved Orion, had been launched and it performed very well and within predictions. The service system performed nominally and provided uninterrupted data from the instrumentation as well as attitude data for instrumentation correlation. The MORABA recovery system safely landed the payload, both times, for recovery.

Figure 6. O-STATES campaign team

2.3. SPIDER/LEEWAVES

Figure 7. SPIDER/LEEWAVES

SPIDER (Small Payloads for Investigation of Disturbances in Electrojet by Rockets)
LEEWAVES (Local Excitation and Effects of Waves on Atmospheric VErtical Structure)
This was a collaboration project of two missions shared between two institutes, SPIDER from the department of Space and Plasma physics at the Royal Institute of Technology (KTH) and LEEWAVES from the department of Meteorology at Stockholm University (MISU). These two missions were launched as a combined payload in February 2016.

2.4. SPIDER mission description

The SPIDER rocket project idea is about studying the physics of the electromagnetic fields and plasma density irregularities related to ion acoustic turbulences (Farley-Buneman instabilities) in the auroral electrojet and pre-breakup aurora. These irregularities and instabilities affects and disturbs the propagation of radio waves and causes disturbances in transmissions of for instance satellite communication, media transmissions etc.

This study is done by in-situ multi point measurements using a set of 10 small payloads, Free Falling Units (FFU's), ejected into the auroral electrojet in the ionosphere e-region (90 to 130 km) with relative separation of tens of meters to several kilometres. These FFU's measure spatial distribution and time evolution of electric fields, electron densities and currents inside the active aurora in relation to the auroral luminosity.

The on-board scientific instrumentation was all contained in the self-sustainable FFU's consisting of electric field probes on deployable wire booms, Langmuir probes on deployable wire booms, SMILE magnetic field instrument, GPS L1 raw RF logger and a star camera. All scientific data collected were stored locally in the FFU's for extraction after recovery. The FFU's all had individual systems with parachutes and GPS positioning. During re-entry the parachutes automatically deploys and GPS data is acquired and sent to ground via VHF and satellite link. 4 out of 10 FFU's were required for scientific success.

Also background measurements were made using ALIS (Auroral Large Imaging System by IRF-K), all-sky cameras in Trömsø, IRF-K and Esrange, IRF-K magnetometer as well as EISCAT radar.

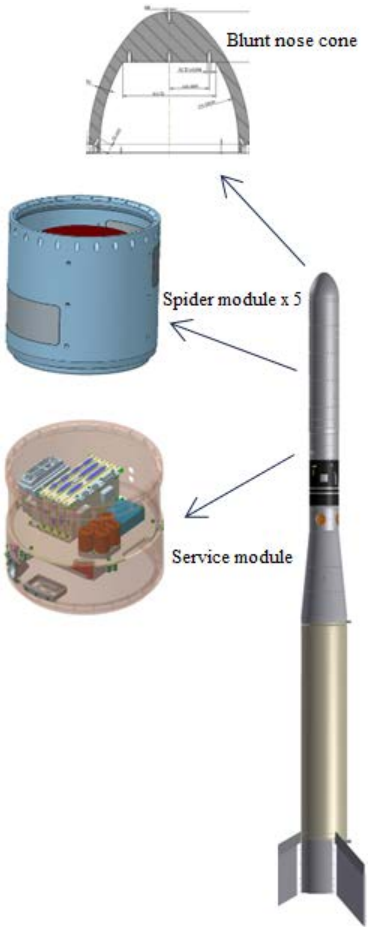

Figure 8. SPIDER payload and vehicle

The requested launch requirements were to launch the payload into an active slowly moving discrete auroral arc close to the rocket trajectory and apogee. It also required darkness and clear skies to determine the scientific launch conditions optically. This gives a two week window twice in the early winter and twice shortly after New Year with the best possibilities around pre-midnight aurora conditions. The very specific scientific launch conditions require launch operations with extensive hold periods during night hours and extremely short notice to launch (~ 2 minutes). Due to recovery constraints for the FFU's, launch conditions also required no precipitation between launch and recovery operation as well as good helicopter weather conditions. FFU recovery is required within 24 hours of launch. The desired apogee was 125 km with FFU ejection at 60 km.

2.5. LEEWAVES mission description

The LEEWAVES rocket and balloon project idea is about studying and characterizing the properties and interactions of gravity waves and particularly mountain waves as they propagate through the atmosphere. Little is known about the details of the gravity wave life cycle.

The LEEWAVES mission is executed is close collaboration with the GW-LCYCLE (Gravity Wave Life Cycle) programme by DLR. This is a comprehensive campaign in northern Scandinavia, north Atlantic and east coast of Greenland with two research aircrafts at its core, the HALO and the Falcon.

The LEEWAVES contribution to the GW-LCYCLE programme is providing the Esrange based ground measurements and data with focus on LIDAR measurements as well as providing rocket- and balloon-borne data on horizontal wind vectors.

A major aim of the LEEWAVES rocket and balloon project is to resolve the questions posed by providing wind, pressure and temperature data from the upper atmosphere regions not covered by the GW-LCYCLE instrumentation. The radiosonde balloons providing data from lower stratosphere and the rocket borne instrumentation higher up in the atmosphere. This paper only covers the rocket borne part of LEEWAVES.

The study is done by in-situ multi point measurements using a set of 4 small payloads, active rigid falling spheres, ejected from the rocket. Ejection is provided at 10 m/s relative the rocket achieving a separation of more than 1 km in the down leg. The falling spheres record data using MEMS based inertial sensors as well as GPS L1 raw RF data receivers. This data is then used to reconstruct their trajectory of the falling spheres and thus provide the possibility to study horizontal gradients in the gravity waves. All scientific data collected were stored locally, in the falling spheres, for extraction after recovery. The falling spheres all had individual systems with parachutes and GPS positioning. During re-entry the parachutes automatically deploys and GPS data is acquired and sent to ground via VHF and satellite link. 2 out of 4 FFU's were required for scientific success.

Also background measurements were made using Esrange LIDAR, ESRAD MST radar, AMTM, ALIS (Auroral Large Imaging System by IRF-K), Skyimet meteor radar and the ALOMAR facility.

The LEEWAVES rocket mission was included as a piggyback on the SPIDER mission as can be seen in Fig. 9. Due to the significant launch condition requirements from the SPIDER payload, LEEWAVES did not add to them and accepted being launched based on the SPIDER conditions.

The LEEWAVES falling sphere deployment was set to an altitude of ~75 km to provide good separation from the SPIDER FFU's being released at 60 km altitude.

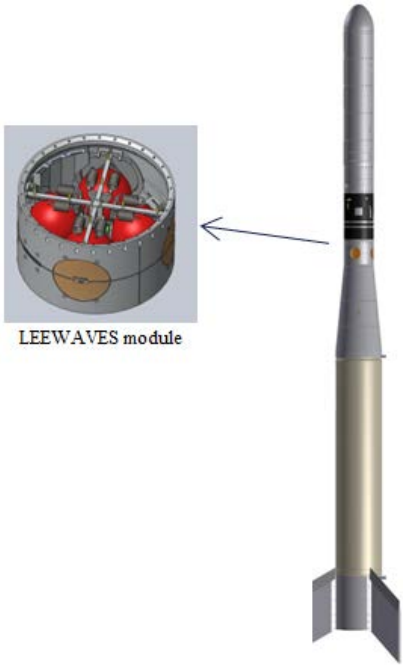

Figure 9. LEEWAVES payload and vehicle

The SPIDER/LEEWAVES service module was a stripped version of the SM14 system flown on the PHOCUS and O-STATES missions.
Some examples of major functions this system provides:

- Switched power for H/K as well as instrumentation,
- Position determination (GPS),
- Pyro control,
- Ground-link for H/K and instrument data,

Selected features of SM14 configuration:

- 2 x CCSDS telemetry interface (1.25 to 10 Mbit/s),
- 1 x 1.25 Mbit, 5W, S-band, FM downlink,
- Internal H/K,
- System and power control,
- 8 x 1.4A LCL, MB power switches,
- 3 x 3/6 W LCL, 12V power switches
- 1 x 4W LCL, 5.1V power switch
- 1 x 60W 30V switch
- 10 x galvanically isolated full duplex RS422,
- 8 bit parallel output,
- 2 x SpaceWire interfaces,
- GMSK cmd input,
- GMSK bitsychronizer output,
- OCXO for slant range,
- Local H/K storage (SD),
- Local H/K storage (USB)
- COCOM GPS receiver,
- Time synchronization,
- 6 pyro control channels,
- 1 x 6800 mAh, LiIon battery,

- 2 x CAN-bus,
- 4 x PT100 inputs,
- 2 x BW interface,
- 1 x 1-wire port,
- 1 x Ethernet port,
- 20 x event inputs,
- 4 x analog inputs,

2.6. SPIDER/LEEWAVES launch

SPIDER/LEEWAVES was launched on the second launch attempt (the first was cancelled due to lack of scientific conditions) on the 2nd of February 2016. The payload and single stage S30 rocket were launched from the Esrange MRL single rail launcher at 22:08:59 local time. It was launched into an active aurora, a westward travelling surge of a sub-storm preceding the launch.

Figure 10. SPIDER/LEEWAVES lift-off

The lift off and flight was nominal. All systems were powered and delivering data. An apogee of 138.4 km was reached after 183 seconds and all 10 FFU's and 4 active rigid falling spheres were successfully ejected at their desired altitudes.

The recovery operation was performed the following morning, on the 3rd of February as planned, using four helicopters and crews. 6 out of 10 FFU's and 4 out of 4 falling spheres were recovered after which the main payload was picked up and brought back to Esrange.

The SPIDER/LEEWAVES flight was a success. However, the single stage S30 motor had more performance than necessary for this payload and therefor additional mass, as well as a blunted nose cone, had been implemented for apogee correction. Nevertheless, the vehicle still overshot the desired apogee of 125 km. The post flight analysis showed that an unlucky combination of aeromodelling, wind situation, normal dispersion and unusual atmospheric condition all added on the plus side of performance causing this anomaly. The service system performed nominally and provided uninterrupted data from the payload as well as the correct FFU release sequence. The MORABA recovery system safely landed the payload for recovery and provided the correct release sequence for both the main payload as well as the LEEWAVES falling spheres.

Figure 11. SPIDER/LEEWAVES flight track

3. CONCLUSIONS

The Swedish science and research community need an affordable platform and foundation for performing their research in space. This applies for atmospheric physics, plasma physics as well as micro-gravity research etc. Keeping a program alive and dedicated for this community, with continuity in the calls for proposals as well as the funded missions, will be the basis for a healthy and active science community. A healthy and active community will also create a greater interest and stimulate growth in new scientists and P.I.'s that will apply to this program. It will also promote the development of technology and the possibilities to keep the technology and its operators active as well as up to date. This also provides for efficiency in the projects and by that efficiency the cost per science data generated can be lowered.

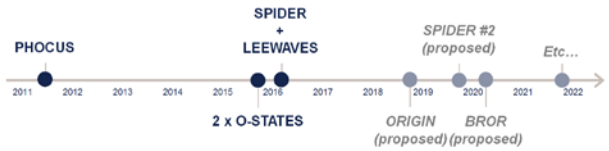

Figure 12. Swedish sounding rockets from 2011

The latest call for proposals within the Swedish national balloon and rocket programme has generated three really interesting proposed rocket missions for the next period of the program.
The momentum has to be kept, and even increased, to make this the great success it has already taken steps to become by the launches of the O-STATES, SPIDER and LEEWAVES rockets. This is the opportunity to start a new era of high Swedish science presence and activity in the sounding rocket research field operating from Esrange.

DEVELOPMENT OF NEW PAYLOAD MODULE FOR 4D MEASUREMENTS

VISBY, SWEDEN
11-15 JUNE 2017

Thomas Gansmoe [(1)], Geir Lindahl [(1)], Trond Aksel Olsen[(1)], Torgeir Grønås[(1)], Kolbjørn Blix [(1)]

[(1)] Andøya Space Center, Bleiksveien 46, 8480 Andenes, Norway, Email: thomasg@andoyaspace.no

ABSTRACT

Traditionally the sounding rocket carries a payload in which all instruments are mounted in a payload section on the main rocket body. A nosecone and/or doors protects the payloads' instruments during the rockets' ascent until the area of interest has been reached and nosecone and doors are ejected to expose the instruments.

Although the sounding rocket can reach areas of the atmosphere to perform in-situ measurements that balloons and satellites cannot, it only performs such measurements during a very brief moment in time and at particular place governed by the ballistic trajectory of the rocket.

To be able to determine the dynamic properties of a particular phenomenon or the scale of such phenomena, it must be possible to perform measurements covering a larger area as well as over an extended time interval than what is possible with a single sounding rocket payload.

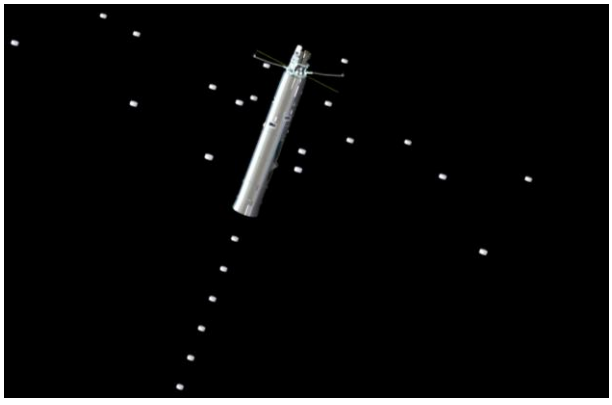

Figure 1. Swarm of daughter payloads

In order to allow researchers to see a bigger picture of the phenomenon that is being investigated, Andøya Space Center (ASC) has initiated a development of a new payload module for sounding rockets that will allow for 4 dimensional (4D) measurements (3D space and time). The purpose of the new development is to be able to eject a large number of miniaturized payloads in different directions at predefined times during the ascent of the rocket. The miniature payloads carries the identical instruments and sensors, which then allows for measurements to cover a much larger area and thus form a 3D mapping. Depending on the direction the miniaturized payload is ejected, a measurement of the same position at different times during the flight of the rocket is possible. As such, the free flying miniature payloads can be seen as forming a cloud. While they propagate along the ballistic path of the sounding rocket the fourth dimension, time, is realized.

The first phase of the project is to flight qualify a module that fits on a 14 inch payload. The module will release several daughter payloads into one plane, making 3D measurements (2D space through time). The system is easily scalable to fit larger payloads and to add more daughter payloads as necessary.

The development of the new payload module are done in close collaboration with the University of Oslo and their 4DSpace initiative.

THE 4D-SPACE MODULE

The module contains six daughter payloads, a deployment system and a communication unit for retrieving data from the daughter payloads.

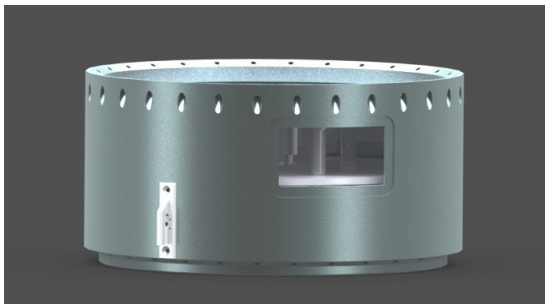

Figure 2. 4D-Space Module

Deployment system

After the doors have been ejected from the payload at a predefined altitude, the 4D-space module will start ejecting the daughter payloads in pairs of two, with a separation of 180 degrees. The daughters will activate after separation and transmit data collected from the on-board instruments. The speed of the daughters outwards from the payload after separation are determined by the spin rate of the main payload.

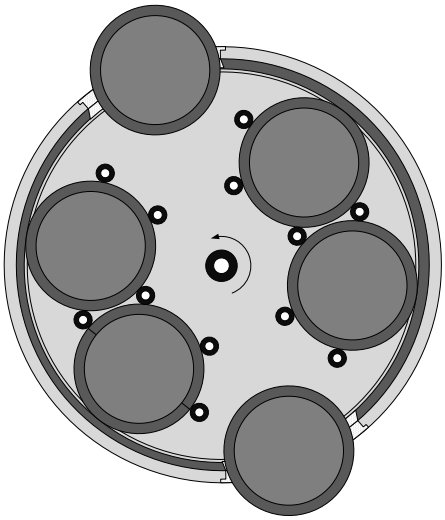

Figure 3. Ejecting daughter payloads

A stepper motor controls the ejection timing in the 4D-Space module. By adding a delay between each ejection of daughter payloads, the distance between each set of daughter payloads can be controlled for a desired pattern around the main payload.

In addition to gyro data from the main payload and timing data from the motor controller, there is also a set of optic sensors mounted on the door openings, for a more accurate measurement of the ejection speed while the daughter payloads leave the 4D-Space Module.

The Daughter Payloads

Fig.2 shows the top side of the electronics inside the daughter payload. The daughter payload contains:

- Power supply
- 9-Dof IMU
- Microcontroller
- Transceiver
- Connection for experiments

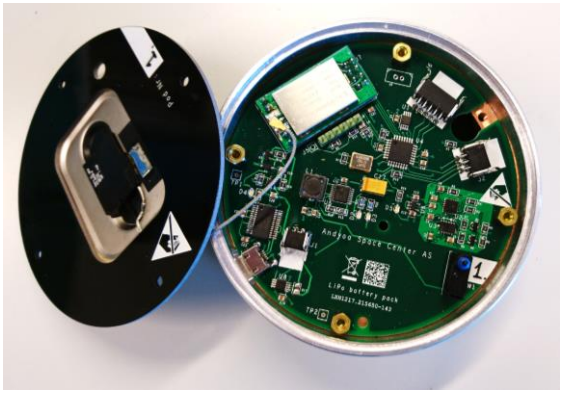

Figure 4. The Daughter Payload

In the bottom side, there is room for mounting of the main experiment. Fig.5 shows a cross section of the daughter payload from the side. In the qualification flight, two of the daughter payloads will contain a set of four Multiple Needle Langmuir Probe (mNLP) instruments from University of Oslo (UiO). The rest of the daughters will collect data from the on-board IMU and test the telemetry.

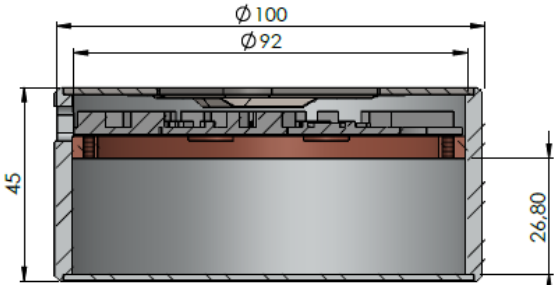

Figure 5. Cross section of the daughter payload

SCALABILITY

In the first launch, we will be testing a single module as a proof of concept, mainly testing deployment and telemetry, but also do measurements with UiO's mNLPs.

Further on, we will do a test with two 4D-Space Module in the ICI-5 rocket campaign. In this launch, the two modules will have an offset of 90 degrees. By synchronising the ejection of daughters from these two modules, we will be able to eject tree sets of four daughter payloads in a shape of a square expanding from the main payload.

Also in a parallel rocket campaign, G-Chaser, we will do a test in a different size payload, where we will demonstrate how the module easily can be scaled to a different size.

EXPERIMENTAL FINDINGS ON FLAME PROPAGATION ALONG PMMA SAMPLES IN REDUCED GRAVITY ON REXUS 20 (UB-FIRE)

Florian Meyer, Maximilian Ruhe, Tim Schwenteck, Patrick Bihn, Alex Freier and Christian Eigenbrod

ZARM – University of Bremen, Am Fallturm, 28359 Bremen, Germany
Email: florian.meyer@zarm.uni-bremen.de

ABSTRACT

Aiming for improvements on fire safety in human spaceflight, upward flame propagation, according to NASA-STD-6001B, is examined on five different cylindrical polymethyl methacrylate (PMMA, Plexiglas®) rods during the REXUS 20 sounding rocket mission within the University of Bremen – Fire Safety Research Experiment (UB-FIRE) project. The rods are of identical diameter of 15 mm and of identical length of 100 mm but differ in terms of surface structure or core material. Besides the smooth surface reference sample there are two surface structured samples. One sample features vertical grooves and one sample exhibits two vertical ribs. Two other samples feature a PMMA-metal compound structure with an aluminum and a stainless steel core respectively. The concurrent flow of air is identical for all five samples with 18 cm/s velocity which is comparable to air conditioning flow velocities in space habitats like the International Space Station (ISS). The leading edge of the pyrolysis front is observed by means of an infrared (IR) camera centrally mounted between the surrounding wind tunnels alternately looking to the individual samples. The UB-FIRE experiment, flown on REXUS 20 in a reduced gravity environment (~0.094 g), reveals a reduced pyrolysis front propagation velocity up to a factor of 0.28 compared to ground-based experiments with an identical test setup (NASA-STD-6001B test 1). However, the corrugation effect which affects the propagation velocity of structured samples is different in a reduced gravity environment compared to normal gravity. Possible reasons for this behavior along with a detailed evaluation of each sample are discussed in this paper.

1. INTRODUCTION

Fire is one of the greatest hazards in areas of human life. This applies not only to a fire on earth but all the more to human space flight. The main difference of a microgravity fire compared to normal gravity (1g) is the manner by which the oxidizing agent is provided. On Earth buoyancy-driven air flow can yield a sufficient oxygen supply for a self-sustained fire. Under microgravity conditions this buoyancy support is missing, which rapidly changes the appearance and the whole process of mass and heat transfer. However, due to the spacecraft's air conditioning systems, there is a forced convection present which can provide the needed oxygen supply for self-sustained fires. This air flow can be orientated in any direction and therefore enables fire spreading in any direction as well. As also exhaust gases and particulates may spread into any direction as well, it may become rapidly diluted and are hard to detect to distinguish from non-hazardous particulates of other origins. The possibility of a self-sustaining fire along with very limited means of escape and a complex cleaning process of toxic exhaust gases demonstrate the great hazard of fire in human space flight. [1]

In terms of fire safety there are many ground-based test procedures to determine the flammability characteristics of different materials under respective worst case conditions regarding pressure, temperature and oxygen concentration [2]. As a common test procedure the upward flame propagation test is defined in NASA-STD-6001B as test 1 [2] or similarly in ECSS-Q-ST-70-21C [3] and in an ISO standard 14624-1:2003 [4] under development. The purpose of this procedure is to determine whether a material is self-extinguishing, which then defines its applicability for manned space vehicles. For the size and the shape of a sample, the National Aeronautics and Space Administration (NASA) standard stipulates dimensions of 300 mm by 65 mm with a flat surface. The thickness of the specific sample shall reflect the "as applied" thickness to cover the worst case condition. The procedure defines the ignition of a material sample at the bottom edge with a standardized ignition source with either an electrical or a chemical ignitor. Principal evaluation indicators are the burning length and the possible ejection of burning debris. To meet the acceptance criteria, five samples have to show a burning length less than 150 mm and must not transfer burning debris. Thus a specimen simply passes or fails the test. [2]

Although the standard test procedure shall cover the worst case conditions of a possible application in a spacecraft, the test is performed in 1g and only considers a smooth surface. But previous experiments and simulations at the Center of Applied Space Technology and Microgravity (ZARM), according to NASA-STD-6001B, reveal a significant effect of different surface structures on the pyrolysis front propagation velocity of PMMA [5-12]. For example, a vertically grooved structure which was investigated during these experiments raises the propagation velocity up to a factor of ~3.4 compared to an unstructured

sample [5]. These findings demonstrate that not only the thickness of the sample, but also the sample's surface structure has a direct influence on the worst case criterion of the test procedure. A material sample, which will pass the standard test in an unstructured configuration, may fail the acceptance criteria in a structured shape. In real space applications components are often structured with regard to weight or functional performance. This leads to complex geometries which could affect the flammability characteristics under microgravity conditions as the 1g experiments demonstrate. [1]

As mentioned before, fires in 1g and microgravity/reduced gravity (µg) can be very different. The reason for this is that the very different flow situation alters the dominant oxygen and heat transport mechanisms. Unlike combustion processes in 1g, fires in a µg environment are not supported by buoyancy-driven oxidizer transport which can reach velocities from 20 to 100 cm/s [13]. The only self-generated flows are those which are caused by thermal expansion, production of gaseous species and fuel surface evaporation/blowing [13]. Under these conditions the molecular diffusion is the dominant oxygen transport mechanism. Also with regard to heat transfer the dominant mechanisms are radiative and diffusional heat transfer. The presence of a forced convective flow can enhance the transport of oxygen as well as local heat loss and gain [13]. This also in turn alters the shape of the flame under µg conditions. In contrast to the complex structure of the hot 1g flame, the different flow conditions can lead to a smoother and cooler flame under µg [14]. In most cases the flame spread is slower in a reduced gravity environment. Even though a microgravity fire is weaker in general, the local heating rate may be higher as in 1g. As this shifts the balance between heat production and heat losses towards heat production, it cannot be excluded that a material passing the 1g test may fail in µg.

Combustion science and fire safety are of interest to the microgravity research community, but only small, thin or smooth samples had been typically used in microgravity experiments [15-17]. Due to the lack of experimental data for structured thick samples a student team of the University of Bremen has developed a flammability experiment for a sounding rocket within the German-Swedish student program REXUS/BEXUS. The goal of the experiment was to perform an upward flame propagation test, according to NASA-STD-6001B, with several PMMA samples but under a reduced gravity environment. Two structured samples and one smooth reference sample as well as two compound samples provide insights into the corrugation effects and the ignition effects of compound samples under reduced gravity in contrast to the known effects under 1g.

The purpose of the Spacecraft Fire Safety Demonstration (SAFFIRE) project, as a NASA program with collaboration partners in Europe, Russia, Japan and also at ZARM, is to perform realistic large-scale fire experiments in a relevant environment. The experimental setup is integrated in several CYGNUS ISS-resupply vehicles which are used after their service missions and so ideal environmental conditions are provided [18]. So far, two SAFFIRE missions have been performed, both in 2016. The SAFFIRE II mission, performed in November 2016, revealed that the corrugation effects alter for thick PMMA samples under microgravity conditions compared to 1g experiments. Under 1g conditions the structured sample burned 70% faster than the flat sample. In contrast, this difference was reduced to only 32% under µg conditions [19].

2. EXPERIMENTAL SETUP

The starting position of the experimental design for the sounding rocket flight is the test chamber according to the upward flame propagation test (NASA-STD-6001B) at ZARM. This apparatus is used to perform 1g experiments for comparison purpose. Inside the chamber an infrared (IR) camera system is installed to evaluate the combustion process properly. The IR images enable a clear view through the luminous flame onto the sample's surface, which is used to determine the motion of the damage front on the sample's surface. This laboratory setup has been used successfully for many upward flame propagation experiments during the last years [5-12, 20]. The main design idea is to duplicate this apparatus into an experiment module for the sounding rocket to highlight the differences between 1g and µg. [1]

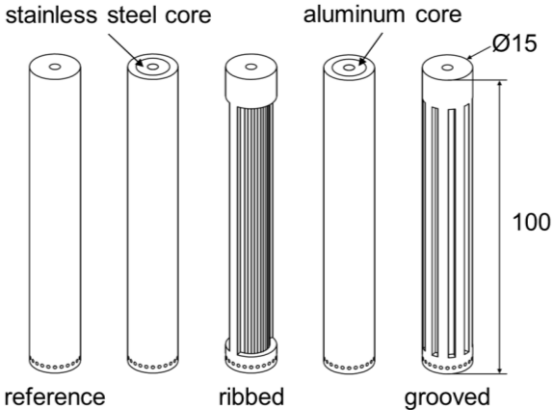

Figure 1. UB-FIRE sample design (dimensions in mm)

Fig. 1 shows the sample design for the University of Bremen – Fire Safety Research Experiment (UB-FIRE). All samples are made out of cast PMMA. The cylindrical samples are of identical diameter of 15 mm and of identical length of 100 mm. The advantage of the cylindrical shape is that no boundary effects, of e.g. air entrainment from the sides, occur in comparison to rectangular shapes. For the grooved shape there are 9 grooves with width and depth of 2 mm each. This results in an arc length of 3.23 mm for the 9 ribs. For

the ribbed sample there are only two ribs on opposite sides. The geometry of these ribs is exactly the same as for the ribs on the grooved sample. This leads to two different geometrical influence situations: two single ribs without any influence of a neighboring structure (ribbed sample) and many ribs with direct influence of the neighboring ribs (grooved sample). The two compound samples are made out of PMMA tubes with 1.5 mm thickness. Two metal cores were assembled into these two tubes by thermal shrinking. One sample was equipped with an aluminum core, the other with a stainless steel core. At the lower edge of all samples there are small drillings for threading of a Kanthal® gauge 29 wire for ignition purpose according to the NASA standard test [2].

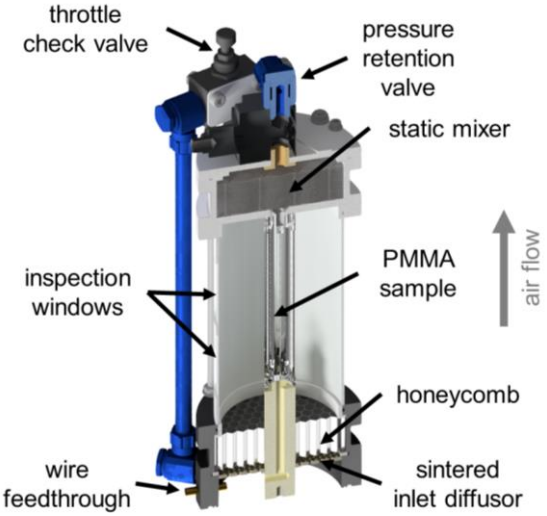

Figure 2. CAD sectional view through combustion chamber/wind tunnel

In the upward flame propagation test, defined in NASA-STD-6001B, the material samples are exposed to an air flow caused by natural convection only. However, for the sounding rocket experiment the samples are mounted concentrically in wind tunnels with a constant concurrent air flow along the sample's surfaces to compensate the strongly reduced natural convection due to the µg environment (Fig. 2). Ferkul et al. estimate the characteristic velocity at the bottom of the flame for air at normal pressure under 1g conditions to be 20 cm/s [21]. Therefore, the air velocity is set to this value for each individual combustion chamber. This flow velocity is also comparable to the air conditioning flow in human spaceflight systems like the ISS. The free volume of each chamber is about 360 ml. To ensure constant conditions during the experiment, each chamber is equipped with a throttle check valve and a pressure retention valve (Fig. 2). This combination allows the setting of the desired air flow velocity and the desired internal pressure which will be held constant during the combustion process. Sintered inlet diffusors and honeycomb structures straighten and stabilize the air flow to ensure a laminar flow. For the ignition process the Kanthal® wires are connected to a sealed feedthrough. As mentioned before an IR camera is used to observe the combustion process during the experiment. For this reason there are two IR transparent windows in the metallic sheath of the flow ducts.

Due to very limited space available in the experiment module, only one IR camera system is used to observe all samples sequentially. The individual combustion chambers and two high pressure air bottles are mounted at a circular arc on the lower bulkhead (Fig. 3 and Fig. 4). The IR camera system FLIR Tau® 2 640 (7-13 µm) is mounted on a turning drive on top of the flight computer housing. Both elements are mounted to the upper bulkhead. The turning drive is powered by a stepper motor and enables the camera to look to the individual PMMA samples alternately. After the ignition process, the camera images one sample for 1 s before the camera turns to the next sample. So during the experiment the camera repeatedly stores several short clips of every sample at different times onto a flash drive.

Figure 3. CAD view of UB-FIRE experiment without the module, upper bulkhead, one high pressure bottle and tubing

Figure 4. Integrated experiment module without upper bulkhead

On March 15th, 2016 the UB-FIRE experiment was flown onboard the sounding rocket REXUS 20 from Esrange, Sweden. The apogee was at ~80 km which enabled an experiment time in a reduced gravity environment of 122 s. The ignition wires were powered simultaneously for 20 s which reduced the unaffected experiment time. The reference sample ignited ~6 s after the ignition wire was powered. Due to some residual rotation along the roll axis and slight wobbling of the rocket after de-spin and motor separation the average acceleration during the burning time was $0.094\ ^{+0.05}_{-0.04}$ g. The acceleration level fluctuated slightly during the beginning and the ending of the experiment time. In between the accelerations were nearly constant. The absolute pressure inside the combustion chambers was $1.075\ ^{+0.02}_{-0.01}$ bar. The maximum pressure difference between the chambers was 31 mbar. The overall pressure drop of the two air reservoirs revealed that the average air velocity of each combustion chamber was at ~18 cm/s – a little bit lower than the set velocity of 20 cm/s.

3. EXPERIMENTAL RESULTS

In contrast to the test criterion in test 1, according to NASA-STD-6001B, PMMA samples are not self-extinguishing, so PMMA does not pass the test and the position of the damage front along the surface can't be measured after extinction as foreseen in the standard test. Instead the pyrolysis front has to be determined at any point in time during the experiment to identify the flame spread of different samples. Therefore an IR camera is used for the evaluation of the pyrolysis front position during combustion, which is represented in the IR images by the temperature range of 330±5°C on the sample's surface. The determination of the corresponding temperature range and the correction of the IR window's influence on the IR images are based on former calibration experiment series at ZARM [5, 9]. The evolution of the pyrolysis front position can be used to determine the pyrolysis front propagation velocity of the individual sample. In Fig. 5 composed IR images of three samples from the UB-FIRE experiment are shown within a temperature range from 175°C to 425°C.

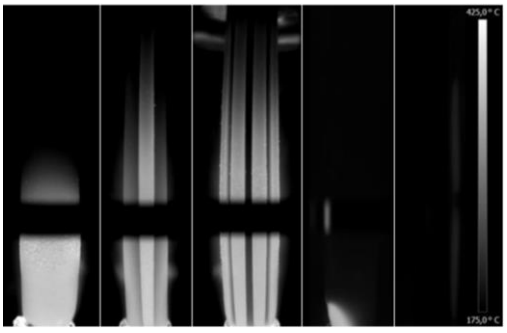

Figure 5. UB-FIRE IR images 85 – 91 s after ignition, left to right: reference, ribbed, grooved, stainless steel core & aluminum core sample

For the IR image processing the ZARM internal software tool "SeriesImageProcessor" is used. This tool filters the original temperature data of the IR images and recolors it in accordance with the defined temperature range to black and white pixels. With the manual determination of the lower and upper edge of the sample as well as the setting of a search area the tool computes the position of the pyrolysis front in this area and delivers the coordinates on the sample's surface for each image.

During the electric ignition phase of 20 s the reference sample as well as the grooved and ribbed samples were ignited. The two compound samples were not ignited. Thus there are no propagation data available for these two samples. The post flight analysis revealed that the sample with a core of stainless steel was ignited but extinguished after some seconds. The other sample with an aluminum core inside could not be ignited at all.

In Fig. 6 the pyrolysis front positions vs. time for three individual PMMA samples in a 1g environment with natural convection are shown. The computed position data reveal a linear slope for all samples which is typical for PMMA combustion in an upward flame propagation test as former experiments at ZARM have shown. As mentioned before the two structured samples propagate faster (along the edges) than the unstructured reference sample. The resulting propagation velocities varied from 1.271 mm/s for the reference sample up to 2.735 mm/s for the grooved one which is 115% faster. For each sample shape, three identical experiments were performed to test reproducibility [11]. Therefore, the final average propagation velocities are:

- reference sample: 1.286 ±0.01 mm/s
- ribbed sample: $2.602\ ^{+0.08}_{-0.07}$ mm/s (+102%)
- grooved sample: $2.701\ ^{+0.03}_{-0.02}$ mm/s (+110%)

Due to the fact that only one IR camera is used to observe all samples alternately and all samples are ignited at the same time to make use of the whole experiment time in reduced gravity, the observation of each individual sample is interrupted from time to time. This leads to a discontinuous data stream of the pyrolysis front position for the samples of the UB-FIRE experiment (Fig. 7). In addition the view of the camera is partly obstructed because of the wall section in between the two inspection windows in the sheath of the wind tunnels (Fig. 2 and Fig. 5). Thus, there are no data available for the area between the windows. The diagram reveals that the slope of the pyrolysis front positions is nearly linear and the two structured samples propagate faster than the reference sample. The propagation velocities for the samples in reduced gravity are:

- reference sample: 0.536 mm/s
- ribbed sample: 0.729 mm/s (+36%)
- grooved sample: 0.823 mm/s (+54%)

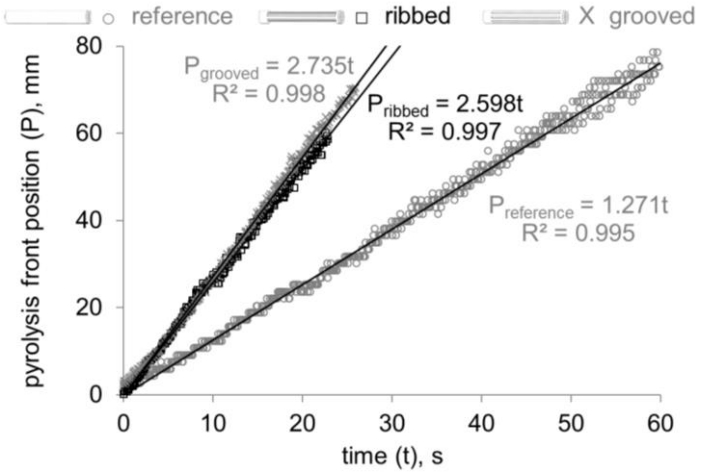

Figure 6. Evolution of the pyrolysis front positions under 1g (natural convection)

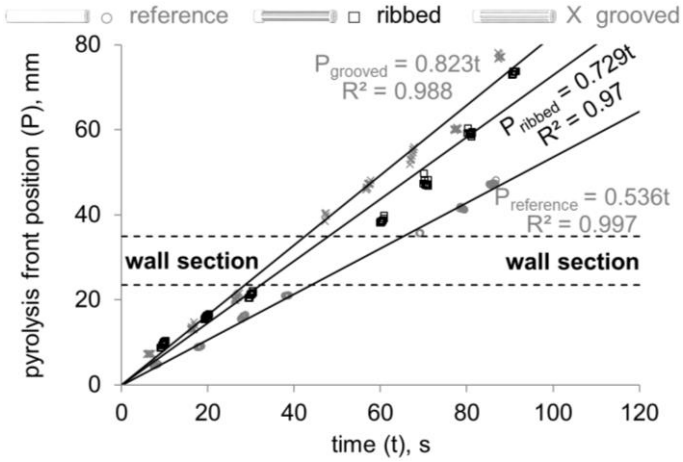

Figure 7. Evolution of the pyrolysis front positions under µg (18 cm/s concurrent flow)

4. DISCUSSION

A key factor for the comparison between the 1g and µg findings is the comparability of both environments to ensure that differences in the pyrolysis front propagation are only caused by the different gravity conditions. Therefore, the ambient temperature, the ambient pressure, the flow velocity and the composition of air have to be contrasted. The combustion experiments at ZARM as the 1g reference experiments are performed at room temperature (22°C) and normal pressure (~1000 hPa), whereas the UB-FIRE experiment is performed with a starting temperature of 13-15°C and an average pressure of 1075 hPa. In both cases the chamber temperature rises a little bit during the experiment, but this can be tolerated. The maximum difference in pressure between 1g and µg is 94 hPa. This should be considered when the results are compared. However, the average pressure difference between the single combustion chambers of 32 hPa can be tolerated. As mentioned before, the flow velocity of 18 cm/s is comparable to the characteristic incoming flow velocity under 1g conditions without forced convection. In both experiment setups the air contains 21% oxygen. Summarized, the small differences in the environmental conditions might lead to small deviations regarding the pyrolysis front propagation velocity solely. The main effect on the propagation velocity is gravity. [1]

The results of the 1g experiments reveal the effect of structured surfaces with regard to the accelerated pyrolysis front propagation along the edges. The geometrical difference between the ribbed and the grooved sample is the presence of a neighboring rib which leads to two burning edges side by side. But nevertheless the difference in the propagation velocities is very small under 1g as well as under µg conditions. A possible reason for this small effect in comparison to former experiments is the small diameter of the samples, particularly of the ribbed sample. The remaining diameter between the ribs is only 11 mm. Former experiments revealed that the pyrolysis front propagation along a cylinder with a diameter of 11 mm is accelerated by a factor of ~1.3 in relation to a diameter of 15 mm [10]. Therefore, the propagation along the edge of the rib can be supported by the propagation between the ribs. This leads to an increase of the propagation velocity for the ribbed sample.

As expected for the UB-FIRE experiments with a concurrent air flow of 18 cm/s, the pyrolysis front propagation velocity decreases under reduced gravity conditions. But the order of velocity of the three samples remains constant, i.e. in 1g and µg conditions the pyrolysis front propagates faster along the grooved sample than along the ribbed and the reference sample which is the slowest. The slowdown factor or the µg/1g-ratio of the pyrolysis front propagation velocities varies for each sample shape. For the unstructured reference sample the slowdown factor is 0.417 on average. The other structured samples are slowed down by a factor of 0.280 for the ribbed and by a factor of 0.305 for the grooved sample. With regard to the µg quality of ~0.094 g in average, which was achieved during the REXUS 20 flight, the decrease of the propagation rate for the unstructured sample with a factor of 0.417 is within the expectations. Due to the remaining accelerations there were still small buoyancy driven forces present during the experiment time. However, the structured samples must be subjected to other slow down factors than the unstructured reference sample. This indicates a different effect of surface structures under reduced gravity conditions in comparison to the known 1g corrugation effects in terrestrial experiments. The relation of the pyrolysis front propagation velocities of the fastest to the slowest sample supports this finding. Under 1g conditions the grooved sample propagates 2.1 times faster than the unstructured reference sample. Whereas under reduced gravity conditions the grooved samples propagates only 1.5 times faster than the reference sample. Therefore, the influence of surface structures under µg is decreased compared to 1g findings but still relevant. [1]

The SAFFIRE II mission revealed a faster flame spread of a grooved PMMA sample compared to a flat sample in µg conditions but also to a lesser degree than under 1g conditions. In 1g the structured sample propagates 1.7 times faster than the flat sample. However, under µg conditions this ratio is reduced to a factor of 1.3 [19]. Therefore the SAFFIRE II mission demonstrated similar results to the UB-FIRE experiment regarding the influence of gravity to the corrugation effects of PMMA samples.

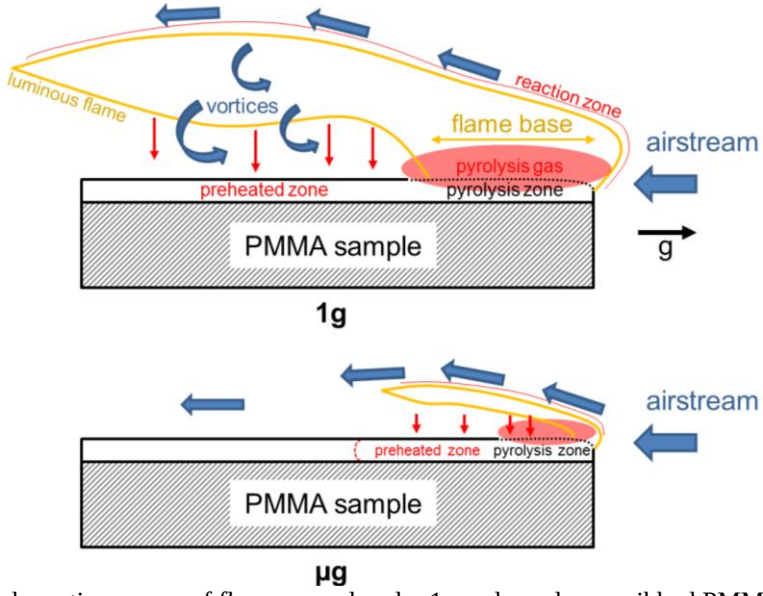

Figure 8. Assumed schematic process of flame spread under 1g and µg along a ribbed PMMA sample (cut view)

A possible explanation for this behavior under reduced gravity conditions is the shape and the position of the flame as well as the process of oxygen supply. In Fig. 8 the shapes of 1g and µg flames are qualitatively described. In case of 1g combustion the oxygen supply is enhanced due to the buoyancy driven flows that lead to lateral gas exchange in the shear layer. Due to that vorticity ahead of the flame base oxygen is transported to the sample's surface and pyrolysis gases off the surface. This enables the flame base propagation along the pyrolysis front of small structures far ahead of the sample's flame base. Thus, the pyrolysis gas can be burnt immediately. In case of µg conditions the flame appears very smooth and laminar across the surface. Therefore, the oxygen supply is reduced to the forced convective air stream, which provides oxygen mainly to the burnout end. This leads to a lack of oxygen along the sample's surface due to the shielding effect of the flame. As a result the flame base propagation is limited even though the pyrolysis front propagates according to the length of the flame, the related preheating process and the progress of the burnout end. The produced pyrolysis gas can't be burnt due to the lack of oxygen and is conveyed with the flow. In case of a reduced gravity environment with residual accelerations of ~0.094 g there are still some buoyancy driven flows which can transport oxygen to the sample's surface due to emerging vortices. The different oxygen supply along with different flow conditions also alter the shape, form and intensity of the µg flame, which affects the heat

transfer into the sample. Therefore, it is assumed that the propagation velocity is strongly dependent on gravity and the influence of surface structures is reduced under very low gravity conditions. The SAFFIRE II experiments which were performed at residual accelerations of $3x10^{-5}$ g revealed 7 times slower flame propagation velocities than these in the UB-FIRE experiment [19]. Hence, to transfer the results of the UB-FIRE experiment the magnitude of remaining accelerations has to be considered. [1]

Another finding from the UB-FIRE experiment is the effect of a shortened ignition delay time under reduced gravity conditions as described in earlier literature. Lautenberger et al. demonstrated with validated numerical simulations that the ignition delay times in microgravity at a low air flow velocity of 0.9 cm/s are much shorter than in a 100 cm/s normal gravity flow [22]. Other simulations by Fereres et al. verify this behavior also for a PMMA slab and quantify the change in ignition delay from 1g to µg to -22% for an ambient pressure of 100 kPa and a concurrent flow velocity of 40 cm/s [14]. For the 1g reference experiments at ZARM the ignition delay time is 10 s for the unstructured sample. During the UB-FIRE sounding rocket flight the ignition delay for the unstructured sample with a forced convective air stream of 18 cm/s is reduced to ~6 s. This corresponds to a change in ignition delay from 1g to µg of -40%. The reason for this acceleration is the reduced heat removal due to buoyancy driven flows which leads to a faster heating and a faster thermal decomposition of the fuel [14]. Another aspect is that less fuel vapor is carried away downstream due to weaker induced buoyancy flow. This leads to an enhanced accumulation of fuel vapor which can also lower the ignition delay in a reduced gravity environment [23].

Ground experiments at ZARM with compound PMMA-metal samples reveal an impeded ignition process due to the higher heat conductivity and heat capacity of the metal cores compared to pure PMMA. The metallic cores transport the heat away from the ignition zone. However, after ignition hot metallic cores can promote the burning process due to a preheating effect as already demonstrated in ground experiments [20]. Unfortunately there is no exploitable IR data from the UB-FIRE experiment available for the two compound samples. It is assumed that the electrical energy was too low to ignite the cold (13°C) compound samples. Another explanation could be that the heat production from the short ignition zone was not enough to outperform the heat losses into the metal core.

5. CONCLUSION

In this paper the experimental setup of the UB-FIRE sounding rocket experiment, as part of the REXUS/BEXUS program, and the appropriate 1g reference experiments at ZARM are presented. Both experiments are performed according to the upward flame propagation test, as defined in NASA-STD-6001B. During these experiments two differently structured cylindrical PMMA samples and one unstructured reference sample along with two compound samples with metallic cores were investigated. The goal of the experiments is the characterization of the corrugation and compound effects under 1g and µg. The determination of the pyrolysis front propagation velocity under 1g conditions by means of an IR camera reveals a significant influence of surface structures. Compared to the reference sample the propagation velocity is increased up to a factor of 2.1 due to the surface structure of the samples. In general the evaluation of the UB-FIRE experiment reveals a decelerated propagation velocity. A closer look at the propagation ratio of each sample shows a changed relation of the corrugation effects known from 1g experiments. Therefore, the comparison of the unstructured sample with the structured samples under µg conditions demonstrates a maximum acceleration factor of 1.5 for the propagation velocities. This behavior indicates a changed corrugation effect under µg. A possible explanation is that for gravity-driven buoyant flows, oxygen is transferred beneath the flame and is laterally entrained into the flame. In a µg environment these natural convective flows are strongly reduced so that the oxygen transport into the pyrolysis zone is hindered. These assumptions have to be verified by additional experiments and flow simulations under reduced gravity. The ignition of two compound samples failed under µg conditions.

6. ACKNOWLEDGMENTS

This research was supported by the REXUS/BEXUS program. We are very grateful for the opportunity to perform the UB-FIRE experiment within this program.

The REXUS/BEXUS program is realized under a bilateral Agency Agreement between the German Aerospace Center (DLR) and the Swedish National Space Board (SNSB). The Swedish share of the payload has been made available to students from other European countries through the collaboration with the European Space Agency (ESA).

Experts from DLR, SSC, ZARM and ESA provide technical support to the student teams throughout the project. EuroLaunch, the cooperation between the Esrange Space Center of SSC and the Mobile Rocket Base (MORABA) of DLR, is responsible for the campaign management and operations of the launch vehicles.

7. REFERENCES

1. Meyer, F., Schwenteck, T., Ruhe, M., Bihn, P., Freier, A. and Eigenbrod, C. (2017). UB-FIRE Experiment Results on Upward Flame Propagation along Cylindrical PMMA Samples

in Reduced Gravity. *47th ICES.* 2017-98, Charleston, SC, p. 2-3, 8-9.
2. NASA-STD-6001B (2016). Flammability, Offgassing, and Compatibility Requirements and Test Procedures. *NASA*.
3. ECSS-Q-ST-70-21C (2010). Space Product Assurance - Flammability Testing for the Screening of Space Materials. *ECSS*.
4. ISO 14624-1:2003 (2003). Space Systems - Safety and Compatibility of Materials - Part 1: Determination of Upward Flammability of Materials. *ISO*.
5. Nordmann, C. (2013). Comparative Investigations on the Flame-Propagation along Differently Surface-Structured Samples. University of Bremen, Bachelor Thesis, Bremen, (unpublished).
6. Meyer, F. (2013). Generation of a Numerical Model to Simulate the Radiative Heat Transfer onto a Surface-Structured Material Sample Including Execution and Evaluation of Parametric Studies. University of Bremen, Bachelor Thesis, Bremen, (unpublished).
7. Schwenteck, T. (2014). Experimental Investigation of the Flame Propagation along Surface-Structured PMMA-Samples. University of Bremen, Bachelor Thesis, Bremen, (unpublished).
8. Freier, A. (2014). Upward Flame Propagation Test (NASA-STD 6001): Investigation of the Interaction between Surface-Structures and Flame Propagation. University of Bremen, Bachelor Thesis, Bremen, (unpublished).
9. Würzburg, N. (2015). Experiments on the Vertical Flame Propagation along Surface-Structured PMMA-Samples; Influence of Sample Thickness. University of Bremen, Bachelor Thesis, Bremen, (unpublished).
10. Stein, A. B. (2015). Upward Flame Propagation Test (NASA-STD 6001): Experimental Investigation of the Flame Propagation along Cylindrical PMMA-Samples. University of Bremen, Bachelor Thesis, Bremen, (unpublished).
11. Meyer, F. (2016). Analysis of Experimental Findings to Investigate the Flame Propagation along Surface Structured PMMA Samples under Normal- and Microgravity. University of Bremen, Master Thesis, Bremen, http://nbn-resolving.de/urn:nbn:de:gbv:46-00106018-15.
12. Schwenteck, T. (2016). Analysis and Comparison of Experimental Investigations on the Flame Propagation along Cylindrical and Flat PMMA Samples under Normal and Microgravity Conditions. University of Bremen, Master Thesis, Bremen, (unpublished).
13. Ruff, G. A., Urban, D. L., Pedley, M. D. and Johnson, P. T. (2009). *Safety Design for Space Systems*, Butterworth-Heinemann, Burlington, Chapter 27 - Fire Safety, pp. 831, 834, 838, 840.
14. Fereres, S., Fernandez-Pello, A. C., Ruff, G. A. and Urban, D. L. (2012). Understanding Piloted Ignition of Solid Combustibles in Spacecraft Environments through Numerical Modeling. 5th IAASS Conference: A Safer Space for Safer World. Versailles (FRA), pp. 3, 5.
15. Olson, S. L., Hegde, U., Bhattacharjee, S., Deering, J. L., Tang, L. and Altenkirch, R. A. (2004). Sounding Rocket Microgravity Experiments Elucidating Diffusive and Radiative Transport Effects on Flame Spread over Thermally Thick Solids. *Combustion Science and Technology.* 176-4, pp. 557-584.
16. Shah, T. J., Miller, F. J., Olson, S. L. and Wichman, I. (2015). Modeling and Analysis of Intermediate Thickness PMMA Sheets Burning in Microgravity Opposed Flow. *Western States Section of the Combustion Institute - Fall 2015 Meeting.* Brigham Young University, p. 2.
17. Zhao, X., T´ien, J. S., Ferkul, P. V. and Olson, S. L. (2015). Concurrent Flame Growth, Spread and Extinction over Composite Fabric Samples in Low Speed Purely Forced Flow in Microgravity. *9th U. S. National Combustion Meeting.* Cincinnati, OH, p. 2.
18. Joomas, G., et al. (2015). Fire Safety in Space – Beyond Flammability Testing of Small Samples. *Acta Astronautica.* 109-2015, pp. 210-212, 214.
19. Eigenbrod, C., et al. (2017). Experimental Results on the Effect of Surface Structures on the Flame Propagation Velocity of PMMA in Microgravity. *47th ICES.* 2017-67, Charleston, SC, pp. 2-3, 7.
20. Ruhe, M. (2016). Investigation on Flammability and Flame Propagation of PMMA-Metal Composite Samples under Normal and Microgravity. University of Bremen, Master Thesis, Bremen, (unpublished).
21. Ferkul, P. V., Kleinhenz, J., Shih, H. Y., Pettegrew, R., Sacksteder, K. and T´ien, J. (2004). Solid Fuel Combustion Experiments in Microgravity Using a Continuous Fuel Dispenser and Related Numerical Simulations. *Microgravity Science and Technology.* XV-2, 3.
22. Lautenberger, C. W., Zhou, Y. Y. and Fernandez-Pello, A. C. (2005). Numerical Modeling of Convective Effects on Piloted Ignition of Composite Materials. *Combustion Science and Technology.* 177-5-6, pp. 1248-1249.
23. Liao, Y.-T. T. and T'ien, J. S. (2013). A numerical simulation of transient ignition and ignition limit of a composite solid by a localised radiant source. *Combustion Theory and Modelling.* 17-6, 1096-1124, p. 1120.

ASSESSMENT OF THE VHF OMNIDIRECTIONAL RANGE (VOR) PERFORMANCE IN THE STRATOSPHERE: STRATONAV ON BEXUS 22

Lorenzo Frezza [(1)], Paolo Marzioli [(1)], Alice Pellegrino[(1)], Federico Curianò [(1)], Federica Angeletti [(1)], Andrea Gianfermo [(1)], Tommaso Cardona [(1)], Marcello Valdatta [(2)], Fabio Santoni [(3)], Fabrizio Piergentili [(4)]

[(1)] *Sapienza Space Systems and Space Surveillance Laboratory (S5Lab), Department of Mechanical and Aerospace Engineering (DIMA), Sapienza – University of Rome, Rome, Italy. Email: stratonav.bexus2016@gmail.com*
[(2)] *Faculty of Aerospace Engineering, Department of Industrial Engineering, Alma Mater Studiorum – University of Bologna, Bologna, Italy*
[(3)] *Department of Astronautical, Electric and Energy Engineering (DIAEE), Sapienza – University of Rome, Rome, Italy*
[(4)] *Department of Mechanical and Aerospace Engineering (DIMA), Sapienza – University of Rome, Rome, Italy*

ABSTRACT

The VOR (VHF Omnidirectional Range) is an aircraft navigation system designed in the 1940s to safely navigateon pre-determined routes by giving an indication on the aircraft relative position to the destination airport. The system architecture is based on ground stations, transmitting a specific signal, and on airborne receivers able to decode it and to extract the "radial information", equal to the aircraft bearing with respect to the ground station magnetic North.Although newer positioning systems have been developed and implemented as primary navigation systems on every commercial aircraft, the VOR is still extensively used as a backup navigation system. Even though the VOR service volume usually extends to 185 km in range and 18 km in altitude, link budget estimates indicate that the system could correctly operate beyond these operational boundaries. There is no information available on the VOR performances above the service volume limit, due to the absence of civil aviation vehicles able to fly at those altitudes. However, the VOR could enhance the reliability of future stratospheric aircraft navigation systems, if used alongside other radio and inertial navigation systems. Moreover, the high altitude extended field of view could offer a larger number of ground stations in line of sight, allowing performing a VOR-stand-alone position determination.
The purpose of STRATONAV (STRATOspheric NAVigation) Experiment was to evaluate both the reliability and functionality of the VOR in the stratosphere. The experiment was selected for the REXUS/BEXUS (Rocket/Balloon-borne EXperiments for University Students) Programme Cycle 9 in December 2015 and it was launched on a stratospheric balloon from the Esrange Space Center in Kiruna, Sweden, on October 5th 2016. The experiment was developed by a joint student team from Sapienza - University of Rome and Alma Mater Studiorum - University of Bologna. The scientific project included the experiment concept, design, development, test, launch and post-flight data analysis. The aim was to receive the signal from the several VOR stations located in the Scandinavian area.
STRATONAV was entirely developed in the framework of the Sapienza Space Systems and Space Surveillance Laboratory (S5Lab) educational activities, that allow students from the Bachelor and Master courses of Aerospace Engineering, Space and Astronautical Engineering and Aeronautical Engineering at Sapienza – University of Rome to improve their skills and to widen their knowledge by participating in several hands-on educational activities.
The acquired data proved that the VOR maintains an adequate reliability at high altitude with the available ground stations architecture, without the need to upgrade existing systems. This establishes that the VOR can be used in the stratosphere as a low-cost standalone positioning system or as back-up for GNSS receivers.
This paper provides a detailed description of the STRATONAV Experiment concept, design and development. Moreover, an accurate flight report and a results overview will be presented.

1. INTRODUCTION

The VOR (VHF Omnidirectional Range) is an aeronautical Navaid (Navigational Aid) based on the transmission of a complex signal in VHF band. This is composed by two sine waves (sub-modulated at 30 and 9960 Hz from the carrier frequency) and an audio identification signal (at 1200 Hz from the carrier)[1]. The frequencies between 108 and 118 MHz are dedicated to the VOR, characterized by a channel spacing of 50 kHz. The system aims at indicating the bearing angle (with respect to the Magnetic North) between the signal source (the ground station, identified by the signal frequency and the audio identification tone) and the airborne receiver. The measure is often defined “radial”.
The VOR ground stations are disseminated throughout the world in order to provide complete coverage to every VOR-navigating aircraft. Each station is designed to

serve specific regions of the airspace, in terms of maximum service altitude and range distance.
The VOR contributed to the growth of the civil aviation after the World War II. Its passiveness and the relatively high performance rates (error below 4 degrees for the first version of VOR, used since the 1950s, below 1.4 degrees for its evolution implemented in the 1970s [2]) improved the accuracy of the navigational systems and the simple architecture of the receiver, when combined with the large presence of VOR ground stations on ground, increased its reliability to new standards [3].
Nowadays, VOR is still used alongside the other Navaids as back-up for Inertial Navigational Systems (INS) and Global Navigation Satellite Systems (GNSS) ([4], [5]).
In case of a GNSS systems outage (or an on-board receiver failure), aircraft still revert to VOR-to-VOR navigation in order to continue their mission([5], [6]).
The VOR service is guaranteed by the Terminal, the Low-Altitude and the High-Altitude VOR stations (indicated as TVOR, LVOR, HVOR). The latter are characterised by a service volume that spans from ground level up to the boundary of the controlled airspace (18000 m, 55000 ft, Flight Level 550), in stratosphere. The service is ensured between 0 and 40 degrees of elevation angles. the remaining region is often called “Cone of confusion” due to the radial oscillations that could be experienced while flying inside it. The correct operations are defined by a threshold power density level standardized by the International Civil Aviation Organization (ICAO), while the Standard Service Volume (SSV) boundaries are declared on each aeronautical chart or Aeronautical Information Publication (AIP) ([1], [8]). The AIPs related to the H-VOR stations always refer the height threshold of 18000 m and the range boundary of 185 km, while their declared radiated power rates (200 W) suggest possible implementations several kilometers above the predicted SSV end. Indeed, the vehicles in charge of verifying the VOR correct operations are mainly fixed-wing air-breathing aircraft [9], whose flight envelope has a limit altitude kilometers below the declared SSV boundary. Thus, a verification on the possible extension of the VOR SSV to stratosphere could be suitable for future stratospheric aviation navigation systems.

STRATONAV (STRATOspheric NAVigation experiment) is a scientific experiment proposed and selected for the REXUS/BEXUS (Rocket and Balloon-borne EXperiments for University Students) Programme cycle 9 in late 2015 and flown on-board BEXUS 22, a stratospheric balloon, on October 5th 2016 [10]. The project was aimed at testing two different VHF receivers in order to assess the performance and accuracy of the VOR systems for the whole balloon flight duration([11], [12]). STRATONAV was carried out by a joint team of Italian students of Aerospace Engineering both from Sapienza - University of Rome and Alma Mater Studiorum - University of Bologna. The payload was entirely designed, built and tested by the student team, with the support of endorsing professors from Sapienza - University of Rome and the space experts involved in the Programme from Swedish National Space Board (SNSB), German Aerospace Centre (DLR) and European Space Agency (ESA). Moreover, the technical operations were assisted by experts from Swedish Space Corporation (SSC) and from the German Center of Applied Space Technology and Microgravity (ZARM). STRATONAV was one of the educational activities promoted and carried out by S5Lab - Sapienza Space Systems and Space Surveillance Laboratory at Sapienza - University of Rome.

In this paper, an overview of the design of STRATONAV will be presented in Chapter 2. Then, the analyses on the link budget and the description of the on-board Radio-Frequency systems will be provided in Chapter 3, with an overview on the telecommunication system design and data collecting processes in Chapters 4 and 5. Finally, a detailed launch campaign report will be given in Chapter 6, with an overview on the achieved results in Chapter 7. As conclusion of the work, an analysis on the applicability, a list of the work outcomes and a summary of the work main features will be presented Chapters 8 and 9.

2. STRATONAV: SYSTEMS OVERVIEW

The STRATONAV mission objectives were to test the VOR radio-navigation system on-board a stratospheric balloon and to assess the precision rate of this system outside its nominal operational height limit. To this purpose, the STRATONAV experiment used two separate receivers: a Commercial Off The Shelf (COTS) receiver, the Yaesu FTA-550A ([13], [14]), and a Software Defined Radio (SDR), the SDRPlay [15]. The receivers were connected to a V-shaped antenna and to the experiment RF chain that will be described in paragraph 3. The COTS receiver was able both to operate automatically or to be manually controlled by the Ground Station. The communication with the Ground Station was ensured by the BEXUS telemetry system (“The E-Link”) [16]. When working automatically, the receiver was tuned on the closest VOR stations. The SDR was used to record the entire raw VOR frequency spectrum, for a more in-depth analysis of the VOR signal during the entire flight. These recordings were stored into a SSD (Solid State Drive).An in-house developed Power Control Board managed the power distribution from the BEXUS batteries to each component, by monitoring each component power and voltage in order to prevent eventual malfunctionings and damages. Moreover, the experiment also included several temperature sensors, an IMU and a GPS receiver. The whole experiment was managed by two On Board Computers (OBC), two Raspberry Pi 3 ([17]), which independently controlled

the two receivers. The main OBC communicated with the experiment Ground Station, managed the COTS receiver operations and collected current, voltage, temperature, position and attitude data. The secondary OBC controlled the SDRPlay. The usage of one separated subsystem per receiver allowed to improve the system reliability: in case of failure of one subsystem, the other could guarantee the fulfilment of all the mission objectives.
Both OBCs were designed to work automatically without input from the Ground Station, and to recover from most of the problems that could arise. An overview of the system can be seen in Figure 1.

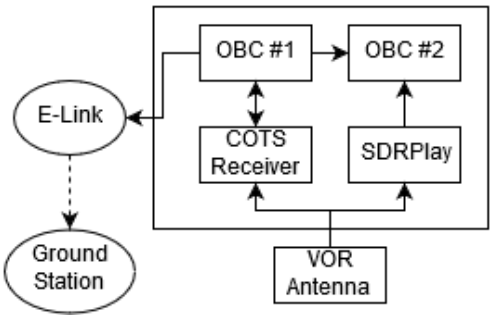

Figure 1. *STRATONAV System Overview*

Using the connection provided by the gondola, the E-Link, the data collected from the sensors were transmitted back to the Ground Station and it was possible to control various aspects of the system. All the components were mounted inside an in-house manufactured aluminium box of dimensions 340x340x550 mm on two separate levels (shown in Figure 2), while the antenna was mounted outside the gondola on a polycarbonate pole of 1.2 m, pointing downwards.

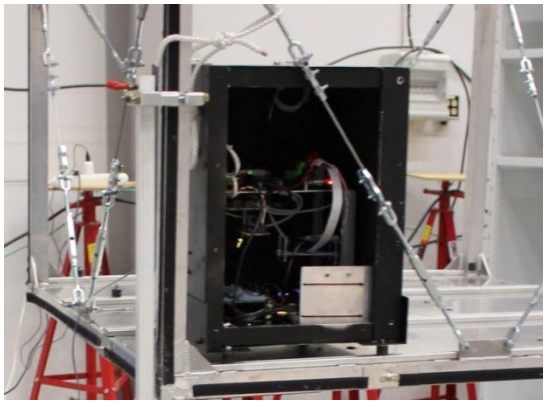

Figure 2. *STRATONAV Experiment box while mounted on the BEXUS payload vehicle.*

STRATONAV was provided with a 4 cm layer of plastazote, a high performance insulating foam, fixed on the experiment box inner edges, in order to protect the internal components.

All the components inside the experiment were thoroughly tested to survive in the harsh stratospheric environment, and to ensure the complete functionalities in order to achieve all the mission objectives.

4. TELECOMMUNICATION SYSTEM

The nature of the mission identified in a correct design of the telecommunication system the key to achieve all the mission objectives.
The telecommunication system design was aimed at replicating the typical design of a general aviation VOR navigation system and at testing it during a stratospheric flight.
The VHF antenna design merged the general aviation VOR antennas traditional shape to the usual manufacturing technique of CubeSat RF system. The antenna final configuration consisted in a V-shaped horizontal polarized antenna (equal to a common VOR antenna geometry [18]), composed of two measuring tape branches. The antenna is shown in Figure 3.

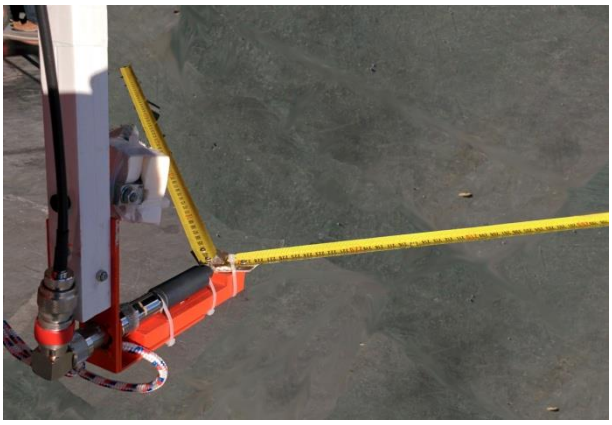

Figure 3. *Experiment in-house developed antenna.*

In order to ensure the complete functionality of this in-house developed component, the antenna pattern was analyzed with the aid of a Numerical Electro-magnetic Code (NEC) during the design phase, in order to validate the optimality of the experiment design and the possible interferences caused by the metallic structure of the BEXUS payload vehicle (the “gondola”). The analysis led to the antenna optimal distance calculation from the gondola floor plane and to the validation of the selected geometry. After the antenna manufacturing, its pattern was directly measured through a specific calibration test, performed by rotating the antenna on its azimuth and elevation plane and by measuring the VOR signal received power (the test was performed nearby Rome Ciampino airport VOR station) by means of an accurate SDR. The test confirmed the well-functioning of the antenna and its suitability for the STRATONAV mission. Finally, the antenna was tested while flying on a general aviation plane nearby the Campagnano HVOR station, 30 km North-West from Rome.

In order to evaluate the optimal RF system design, a link budget was estimated by only considering the high frequency HVOR stations transmitted power (200 W). The link budget indicated a gain margin of at least 6 dBs, even when considering the SSV edge (maximum service height, maximum service distance). The signal from the single antenna has been convoyed to the two receivers by means of a 3dB splitter: its overall losses have been directly measured in different operative condition in order to assure the complete well-functioning for the BEXUS flight. A 3dB splitter (in spite, for example, of an active signal switch) has been selected in order not to complicate excessively the experiment RF chain design and to ensure the possibility of continuously receiving the VOR signal, by admitting an acceptable signal loss.
In order not to suffer from possible interferences from other transmitting RF on-board equipment and to avoid the effects of possible inter-modulation of FM radio signals, a Band-Pass Filter designed for the VHF band[19] was added between the antenna and the 3dB splitter, with an additional signal loss of 0.5 dB. The experiment RF chain has been designed to allow several different configurations, aiming at eventually permitting the insertion of a stop-band filter in the described chain, to further minimize the effect of VHF transmissions on the experiment hardware.

5. DATA COLLECTING PROCESSES

The data from the COTS receiver were collected both by taking a picture of its screen from a fixed camera and by directly calculating the radial from the receiver motherboard. During the whole flight, the collected data were both stored on the on-board memory devices and down-linked to the experiment Ground Station. The receiver was controlled from the main OBC, which could manipulate the input line of the receiver processor to simulate keypresses. The frequency could therefore be commanded from the Ground Station, or automatically set by the OBC, allowing the VOR radial acquisition. The radial was directly extracted from the receiving RF chain circuits of the receiver, and it consisted in two 30 Hz digitized sine waves corresponding to the VOR reference and directional sine waves [14]. The radial was then calculated on the OBC as a phase difference of the two signals (as described in paragraph 1), stored on-board and sent to the GS. This method allowed a more accurate reading of the radial, by admitting inherent measure oscillations, directly filtered by the OBC by averaging arrays of 50 consecutive measures. The complete automatic capabilities of the system ensured the achievement of the mission objectives in case of an eventual telemetry system loss of signal, or a possible Ground Station malfunctioning. Indeed, the system was fully able to:

- Compute the optimal VOR frequencies, by evaluating the measured GPS position and by computing the distance from all the Scandinavian area stations;
- Tune the receiver, through the described key-pressing electric system;
- Acquire the radial measures by thoroughly evaluating the phase shift between the VOR sine waves
- Store the receiver screen pictures as back-up for the processed electric measures of the radial.

The SDRPlay stored all the recorded data into a SSD. The SDR OBC was not connected to the telemetry system and the great size of the VOR spectrum recordings did not allow to down-link the acquired SDR data during the flight. The data were therefore obtained after the balloon recovery, once retrieved the on-board memory devices. The files were raw dumps of the spectrum containing several VOR stations at once, switching periodically, every 35 seconds, between four spectrum bands of 2 MHz covering the 112-117.7MHz bandwidth of the possible flight area VOR stations. An SSD was the only possible choice, as the storage hardware had to survive both the atmospheric conditions of the stratosphere and a possible hard landing shock of 10 Gs, and to be able to continuously write the large amount of data that the SDR was outputting (around 1GB/minute). The stations were then band-pass filtered during post-mission analysis to get the spectrum of each station, to be analysed separately. The accurate radial reading was extracted from the files, as well as information on the Signal to Noise ratio and overall integrity of the signal. This could not be performed real time during the flight because the required computational power far exceeded the selected OBC maximum performance. Moreover, a real-time SDR data analysis was not needed to achieve the mission objectives.
An adequate time synchronization between the OBCs was essential to guarantee an accurate assignment of the radials to specific locations, which was performed with an internal LAN network, synchronizing GPS time and location periodically.
The time synchronization on the COTS receiver data was ensured by collectively store the acquired radial and GPS time and position. The receiver screen pictures were saved by indicating the OBC timestamp. The overall status of the data collecting processes was indicated by the Ground Station Graphical User Interface (GUI) by immediately comparing the measured and the “real” radials. The latter was computed on the base of the current VOR frequency, the VOR station position, the GPS position and AIP declared magnetic declination of the tuned VOR station.

6. LAUNCH CAMPAIGN AND BALLOON FLIGHT

The flight campaign took place between Oct 1st and Oct 9th at the Esrange Space Center in Kiruna, Sweden. The team started inspecting the experiment status on the first day and the next was spent integrating the experiment on the gondola. The Flight Compatibility Test took place on the morning of Oct 5th together with the Flight Readiness Review. The BEXUS 22 balloon lifted off at 13:33 UTC, and the STRATONAV COTS VHF radio started receiving data from the closest station, Kiruna, at 53 km from the launch site, within the first few seconds after lift-off. The balloon overcame the height threshold of the VOR SSV after one hour of flight: all the data collected afterwards (and before the balloon cut-off) were therefore used to assess the VOR accuracy rates in stratosphere. The balloon remained at an altitude above the SSV for three more hours with a peak altitude of 32.2km, flying inside the range of several VOR stations. The profile of the altitude, compared to the SSV threshold, is shown in Figure 4.

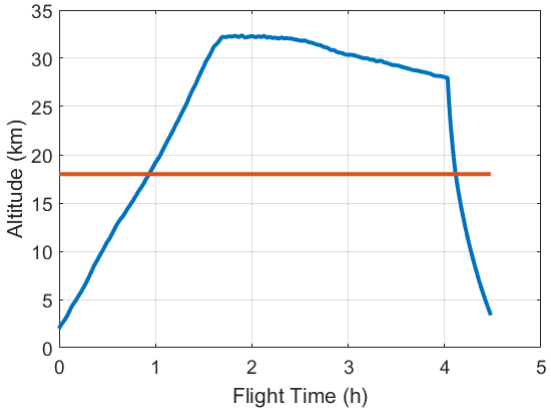

Figure 4. *Flight altitude evolution (blue) and SSV height limit (red).*

During the first half of the flight, the OBC mostly ran in automatic mode, automatically computing, by means of the GPS position data, the VOR stations nearby. The ground stations operator verified the accuracy of the acquired radials by validating the data visualized on the ground station GUI. The final part of the balloon floating phase was spent by manually operating the experiment and by forcing the receiver to tune farther frequencies, several km outside of the expected maximum range. The signal was received for several stations outside the SSV, with varying accuracies. An overview of the results is presented in paragraph 7.

The SDR receiver ran automatically the entire time, with the Ground Station checking sporadically that the system was working correctly by analysing the log file.

Temperatures and current data were monitored in real-time on the GS GUI, with its temporal trend, in order to continuously assess the system health status and to predict further possible manoeuvres to avoid, for example, reaching extremely cool temperatures or the premature discharge of the dedicated batteries. No value was found to be outside the safe range for the whole flight time. The GPS antenna showed a temporary malfunctioning shortly before the balloon cut-off, probably due to the extremely cold temperatures outside. The malfunctioning had no impact on the collected data, since the system was already in manual mode and the ground station operators continued to check the availability of the VOR service from the farthest stations of the Scandinavian area. The balloon was cut down at 17.41 UTC, starting the parachute descent phase. The telemetry connection was immediately lost by all the BEXUS 22 experiments, indicating a general telemetry system malfunctioning, not related to the experiment connection. The radio contact with the balloon was lost at 18.08 UTC, while the balloon was safely descending into the Finnish taiga, 250 km away from the Esrange Space Center. Shortly before landing, at circa 1000 m AGL (Above Ground Level), STRATONAV terminated its operations by executing the safe shut down sequence, deeply tested before the launch in order not to damage any component, with particular effort on the data storage devices.

The experiment was recovered a few days later. All the experiment components were checked, including the structure status. Every component survived to the flight and landing as expected. The experiment recovery concluded the successful launch campaign and all the collected data were backed up on multiple computers.

7. RESULTS OVERVIEW

The experiment managed to acquire more than 2000 radials from the COTS VOR receiver and more than 350 GB of raw VHF recordings from the SDR. Data from both the receivers were acquired during all the balloon flight phases.

The data collected during the ascending phase confirmed the well-functioning of the system, remaining highly below the declared ICAO standards for the VOR navigation system.

The on-board computer core connected to the BEXUS telemetry system (the "E-Link") managed to communicate with the experiment Ground Station up to the balloon cut-off. The descending flight phase was conducted by operating the experiment in automatic mode and by commanding a safe shut-down before landing.

The acquired data were processed in the month after the flight, by decoding and extracting the sub-modulated signals from the SDR data and by evaluating and extracting the COTS radials from the COTS VHF receiver data. The radials were compared to the experiment GPS data, whose correctness was verified by comparison with the BEXUS pilot unit GPS data (the "EBASS" data). The experiment demonstrated the

correct functionality of the VOR system in a stratospheric flight, by maintaining a high percentage of correct radial measures when flying over the SSV predicted end. The majority of the acquired data (almost 60%) are characterized by an error below 1.4 degrees (equal to the current ICAO standard for VOR). Almost the totality of the data (98%) has an error below 4 degrees (equal to the previous VOR functional standard).
The SDR data showed how, out of the eighteen VOR stations considered in the Scandinavian area, fourteen were received. Half of the stations were deeply outside their range limit. The closest approach above the SSV was Rovani (ROI) VOR station, coming as close as 60km, while the furthest station that was received was Storuman (SUM) at an average of 410km. The considered VOR stations are listed in Table **1**. Besides the stations name, the average distance from the BEXUS 22 ground track is provided, as long as the indication of the successfully received VOR signal (or not) for the two on-board receivers.

Table 1. *List of VOR stations*.

Station name	*Av. distance (km)*	*COTS*	*SDR*
Alta	296	*Y*	*Y*
Banak	304	*Y*	*Y*
Bardufoss	310	*N*	*Y*
Bronnoy	585	*N*	*N*
Evenes	345	*N*	*Y*
Kirkenes	345	*N*	*Y*
Kiruna	180	*Y*	*Y*
Lulea	240	*Y*	*Y*
Natta	163	*Y*	*Y*
Oulu	282	*N*	*N*
Rovani	119	*Y*	*Y*
Seida	353	*Y*	*Y*
Skagen	413	*N*	*Y*
Skelleftea	349	*N*	*Y*
Storuman	410	*N*	*Y*
Tromso	341	*N*	*Y*
Vardefjell	520	*N*	*N*
Vardo	426	*N*	*N*

Av. Distance: *Average distance from the balloon ground track.*
COTS/SDR: *Relative to the data collected by the COTS receiver or the SDR*
Y/N: *Signal received (Y) / not received (N) and radials collected (Y) / not collected (N) from the station.*
See [20]–[22] *for further information on the stations location and operational conditions.*

The BEXUS 22 path did not cross any "cone of confusion". It was therefore impossible to conduct analyses on the VOR precision oscillation while crossing the service limit elevation angles over the VOR limit height. The maximum measured elevation angle was 27.82 degrees (while the cone extends from 40 to 90 degrees), corresponding to the aforementioned closest approach to Rovani station, during the floating phase.

Finally, the acquired radials were combined in order to estimate the balloon ground track throughout the flight. Even if depending on the relative angle between the balloon heading and the stations couple conjugating line, an error standard deviation below 4 km in determining the balloon ground track was achieved both by the COTS and SDR data.

8. OUTCOMES AND APPLICABILITY

The success of the STRATONAV Experiment leads to new interesting scenarios in terms of possible experimental researches on new applications of the aeronautical Navaids. In particular, new tests can be conducted by stratospheric payloads able to record not only the VOR, but also the other traditional aeronautical signals, such as the NDB (Non-Directional Beacon) and the TACAN (Tactical Air Navigation system), in order to evaluate further possible improvements of the navigation systems reliability given by the usage of a multiplicity of traditional Navaids. Additional investigation could be also performed on the implementation of an active RF-equipment, possibly able to interrogate the DME (Distance Measuring Equipment) stations nearby, to simultaneously acquire the distance and the relative azimuth from the operative VOR-DME stations. Moreover, the investigation on the VOR can be extended by implementing a rotating antenna, able not only to receive the signal with an improved gain, but also to more precisely compute the balloon ground track and flight direction.
Further VOR and Navaid tests can also be conducted on-board sounding rockets, in order to precisely state the limit of the VOR SSV, which appears overcoming the stratospheric balloons usual floating altitude.

For what concerns the applicability of the research conducted with the STRATONAV experiment, various applications of VOR to stratospheric vehicles are feasible. First of all, the low-cost nature of VOR receivers could easily make this mature navigation system preferable to GNSS for non-retrievable payloads, such as meteorological balloons. The VOR receivers have a cost lower than high altitude GNSS receivers, allowing significant money savings for their development.
The VOR can also improve the reliability of stratospheric navigation systems, even when used as back-up for GNSS. Nowadays, there is large research and industrial interest on the usage of High Altitude Balloons (HABs) and High Altitude Platform Stations (HAPSs), due to the potential savings in terms of development and qualification costs([19], [20]). Indeed, these stratospheric platforms ensure a variety of potential applications that could revolutionize the Earth Observation (EO) field of research. Indeed, a stratospheric platform provides a Field of View (FOV) comparable to the LEO satellites view angle, by maintaining a greatly lower cost.

Moreover, a HAPS with low-power propulsion systems could also be commanded in order to steadily remain in the same position, due to the relatively low wind speed (up to 90 km/h) atmospheric layer[25]. HAPSs could be used, for example, to facilitate communications from areas just hit by natural catastrophic events, such as earthquakes or tsunamis, or permanently serve as radio link hotspot for remote zones, in order to provide wireless connections to these areas inhabitants.

Finally, the next decade could mark a significant milestone for suborbital manned vehicles. Indeed, the large effort dedicated in last years on developing suborbital vehicles able to reach the outer space boundaries (100 km) for touristic and scientific applications will probably lead to a significant growth of the space tourism sector([26], [27]). As for the aforementioned stratospheric vehicles, the VOR could improve the reliability rate of these vehicles navigation system, at least providing assistance for the stratospheric segment of their trajectories, but most probably for the entire flights.

9. CONCLUSIONS

The STRATONAV experiment was aimed attesting the functionality of the VOR navigation system at high altitude, above its service limit height of 18km. The experiment successfully conducted its analysis by flying on-board BEXUS 22 stratospheric balloon on October 5th, 2016, being launched from the Esrange Space Center in Kiruna, Sweden.

The system was carefully designed to withstand the harsh conditions of the stratosphere and to be completely automatic in case of loss of the experiment Ground Station connection. Several tests were performed to ensure the system reliability.

The telecommunication system was designed to replicate a typical general aviation navigation system. All the components have been tested in order to characterize their performances.

The experiment retrieved data from the VOR stations in the Scandinavian area with two independent receivers, a Commercial Off-The-Shelf device and a Software Defined Radio connected in parallel to the V-shaped antenna using a 3dB splitter.

All mission objectives were satisfied during the flight, collecting data by fourteen of the eighteen VOR stations. Data showed that most of the radials collected (~98%) have an error below 4 degrees, and that the majority (~60%) have an error below 1.4 degrees, which is equal to the current ICAO standard.

The successful results provide insight on the possible applicability of the VOR on stratospheric vehicles, as a low-cost alternative to GNSS. The system could also be used alongside current navigation methods to improve reliability of stratospheric or sub-orbital flights, such as meteorological balloons or other commercial and scientific applications.

ACKNOWLEDGEMENTS

STRATONAV project was proposed and accepted for the REXUS/BEXUS Programme in December 2015. The REXUS/BEXUS programme is realized under a bilateral Agency Agreement between the German Aerospace Center (DLR) and the Swedish National Space Board (SNSB). The Swedish share of the payload has been made available to students from other European countries through the collaboration with the European Space Agency (ESA). Experts from DLR, SSC, ZARM and ESA provide technical support to the student teams throughout the project. EuroLaunch, the cooperation between the Esrange Space Center of SSC and the Mobile Rocket Base (MORABA) of DLR, is responsible for the campaign management and operations of the launch vehicles.

The authors also wish to thank the companies that provided technical and financial support to the experiment team: Eggcelerate, Mediasoft, MEGATRON sensors and the Italian Amateur Radio Association (ARI) – Rome chapter.

REFERENCES

1. International Civil Aviation Organization (ICAO), “Annex 10 - Aeronautical Telecommunications, Volume I.” Mar-2001.
2. Anderson, W.G., “The Accuracy of the VHF Omni-Range System of Aircraft Navigation; A Statistical Study,” *Aeronautical and Navigational Electronics, IRE Transactions on*, vol. ANE-2, no. 1, pp. 25–37, Mar-1955.
3. R. B. Flint and E. R. Hollm, “VOR evolutionary system improvements in the United States,” *IEEE Transactions on Aerospace and Navigational Electronics*, vol. 12, no. 1, pp. 46–56, Mar. 1965.
4. European Space Agency (ESA), “What is Galileo?” Online at *http://www.esa.int/Our_Activities/Navigation/The_future_-_Galileo/What_is_Galileo*. (as of 23 January 2016).
5. “BeiDou Navigation Satellite System.” Online at *http://en.beidou.gov.cn/*. (as of 23 January 2016).
6. International Civil Aviation Organization (ICAO), “Navigation Roadmap,” presented at the Twelfth Air Navigation Conference, Montréal, Canada, 2012.
7. Ken Ward, “Discontinuation of VOR Service,” presented at the FAA Aeronautical Charting Forum, Apr-2012.
8. European Organization for Civil Aviation Electronics, EuroCAE, “ED-52: Minimum operational performance specification (MPS) for ground conventional and doppler very high frequency omni range (CVOR and DVOR) equipment.” 1984.
9. Italian National Agency for Flight Assistance, ENAV, “ENAV completes its flight inspection

fleet with the fourth aircraft Piaggio Aero P180 Avanti II 'Flight Inspections,'" 27-Nov-2013. Online at *http://www.enav.it/ec5/enav/en/comunication/press_office/press_release/pdf/2013/radiomisure_ing.pdf*. (as of 20 January 2016).
10. "REXUS BEXUS Programme Official Website: BEXUS projects," *Rexus/Bexus*. Online at *http://rexusbexus.net/bexus/*. (as of 19 January 2016).
11. P. Marzioli *et al.*, "Testing the VOR (VHF Omnidirectional Range) in the stratosphere: STRATONAV experiment," presented at the IEEE 3rd International Workshop on Metrology for Aerospace, Florence, Italy, 2016, pp. 340–345.
12. P. Marzioli *et al.*, "Testing VOR Performances in the Stratosphere: the STRATONAV Experiment," presented at the 67th International Astronautical Congress (IAC), Guadalajara, Mexico, 2016.
13. Yaesu Musen, "Yaesu FTA-750L/FTA-550A Operating Manual." Online at *http://www.yaesu.com/airband/indexVS.cfm?cmd=DisplayProducts&DivisionID=2&ProdCatID=204&ProdID=1777*.
14. Yaesu Musen, "Yaesu FTA-750L/FTA-550A Air Band Transceiver: Service Manual." .
15. SDRplay, "SDRplay datasheet." Online at *http://www.sdrplay.com/docs/SDRplay_datasheet_r1p4.pdf*. (as of 6 May 2016).
16. EuroLaunch, "BEXUS User Manual, version 6.12." 31-Oct-2014.
17. Raspberry Pi, "Raspberry Pi 3 Model B datasheet." Online at *http://www.farnell.com/datasheets/2020826.pdf*. (as of 9 May 2016).
18. COMANT, "VOR/LOC/GS (CI-157P) Datasheet." Online at *http://www.aircraftspruce.com/catalog/avpages/comant157p.php?recfer=14008*. (as of 4 September 2016).
19. Minicircuits, "BPF A-113+ Datasheet." Online at *https://www.minicircuits.com/pdfs/BPF-A113+.pdf*. (as of 26 June 2016).
20. LFV, "Aeronautical Information Publications (AIPs) for Instrumental Flight Rules (IFR) in Sweden." Online at *https://www.aro.lfv.se/*. (as of 20 January 2016).
21. Finavia, "Finland Aeronautical Information Publication (AIP)." Online at *https://ais.fi/C-en*. (as of 23 January 2016).
22. AVINOR, "Aeronautical Information Publications (AIPs) for Instrumental Flight Rules (IFR) in Norway." Online at *https://www.ippc.no/norway_aip/current/main_en.html*. (as of 20 January 2016).
23. T. Konefal, T. C. Tozer, J. Thornton, D. Grace, and C. Spillard, "Broadband communications from a high-altitude platform: the European HeliNet programme," *Electronics & Communication Engineering Journal*, vol. 13, no. 3, pp. 138–144, Jun. 2001.
24. T. C. Tozer and D. Grace, "High-altitude platforms for wireless communications," *Electronics & Communication Engineering Journal*, vol. 13, no. 3, pp. 127–137, Jun. 2001.
25. "Thales Alenia Space wins initial funding for high-altitude platform, plans 2018 demo," *SpaceNews.com*, 26-Apr-2016. Online at *http://spacenews.com/thales-alenia-space-high-altitude-platform-wins-initial-funding-plans-2018-demonstration/*. (as of 17 May 2016).
26. T. Brannen, "Private Commercial Space Transportation's Dependence on Space Tourism and NASA's Responsibility to Both," *J. Air L. & Com.*, vol. 75, p. 639, 2010.
27. Virgin Galactic, "Space tourism: Virgin Galactic vehicles." Online at *http://www.virgingalactic.com/human-spaceflight/our-vehicles/*. (as of 6 June 2017).

TEST OF A REMOTE SENSING FOURIER-TRANSFORM INTERFEROMETER FOR TEMPERATURE MEASUREMENTS IN THE MESOSPHERE ON A REXUS ROCKET

VISBY, SWEDEN
11-15 JUNE 2017

Michael Deiml[1,2], Rui Song[1,2], Denis Fröhlich[4], Björn Rottland[3], Friedrich Wagner[5,6], Jilin Liu[2], Oliver Wroblowski[1,2], Qiuyu Chen[1], Florian Loosen[5,6], Martin Kaufmann[2], Heinz Rongen[4], Tom Neubert[4], Herbert Schneider[3], Friedhelm Olschweski[1], Peter Knieling[1], Klaus Mantel[5], Brian Solheim[7], Gordon Shepherd[7], Ralf Koppmann[1], Martin Riese[2]

(1) University of Wuppertal, Gaussstraße 20, 42119 Wuppertal, Germany, E-mail: deiml@uni-wuppertal.de
(2) Research Centre Jülich, IEK-7, Wilhelm-Johnen-Straße, 52425 Jülich, Germany
(3) Research Centre Jülich, ZEA-1, Wilhelm-Johnen-Straße, 52425 Jülich, Germany
(4) Research Centre Jülich, ZEA-2, Wilhelm-Johnen-Straße, 52425 Jülich, Germany
(5) Max Planck Institute for the Science of Light, Staudtstraße 2, 91058 Erlangen, Germany
(6) Friedrich-Alexander-Universität Erlangen-Nürnberg (FAU), Staudtstr. 7/B2, 91058 Erlangen, Germany
(7) York University, 4700 Keele St, Toronto, ON M3J 1P3, Canada

ABSTRACT

The experiment AtmoHIT, the Atmospheric Heterodyne Interferometer Test, is a precursor mission with the goal to verify a small satellite remote sensing instrument under space conditions. The satellite instrument is developed to measure temperatures in the Mesosphere/ Lower Thermosphere. Temperature measurements allow the characterization of gravity waves, which have an increasing importance in the modelling of the climate system representing one of the larger uncertainties in this field. The instrument consists of a highly miniaturized and rigid Spatial Heterodyne Spectrometer (SHS), which measures the oxygen atmospheric band emission in the Mesosphere/ Lower Thermosphere. The instrument resolves individual rotational lines whose intensities follow a Boltzmann law, allowing for the derivation of temperature from the relative structure of these lines. This instrument is characterized by its high throughput at a small form factor to perform scientific remote sensing measurements with a CubeSat. The AtmoHIT experiment is part of the Rocket Experiment for University Students campaign (REXUS 22), realised under a bilateral agency agreement between the German Aerospace Centre (DLR) and the Swedish National Space Board (SNSB). This contribution focuses on the developed technologies, laboratory measurements, and rocket campaign results.

1. INTRODUCTION

1.1. Temperature Measurements in the Mesosphere/ Lower Thermosphere (MLT)

The Mesosphere/ Lower Thermosphere (MLT) is the region of the atmosphere in the altitude range from 60 km to 110 km [1]. The MLT is an interface region: on the one hand, the dynamics generated in the lower atmosphere affects the entire middle and upper atmosphere including space weather (bottom-up). On the other hand, the solar-terrestrial interaction affects the middle- and lower atmosphere (top-down). The MLT is strongly affected by solar variability, much more than the lower atmosphere. The general circulation in the MLT is driven by waves that are generated in the lower atmosphere [2]. These so-called gravity waves propagate from the lower atmosphere to the MLT and, when they break, deposit momentum and energy there, influencing the background flow. However, it is not even understood which part of the gravity wave spectrum is most important for the momentum deposition in the MLT. Either a few large sporadic waves or many small waves can potentially provide the momentum [1]. In addition, annual and inter-annual variations of the momentum flux need to be observed to understand the temporal effects of gravity waves [3].

Gravity waves can be observed in wind, temperature, and trace gas fluctuations. Their amplitudes are quite small in the lower atmosphere, but they increase with the altitude due to the decrease of atmospheric density. The horizontal wavelength of these waves varies from a few km to a few thousand km and the vertical wavelength is in the order of several hundred meters to a few km.

The only measurement technique to observe vertically resolved temperature and gravity wave parameters globally is limb sounding from Low Earth Orbit (LEO) satellites. Nearly the lifetimes of all MLT relevant satellites have come or will come to end within the next few years, as they have been measuring for more than a decade. It is conceivable that there will be a gap in the observation of this part of the atmosphere soon [4].

In addition, none of the existing instruments can perform measurements of atmospheric parameters relevant for characterizing gravity waves globally in three dimensions. New measurement strategies are needed to provide experimental data to the latest generation of climate models to adjust their model parametrizations.

1.2. The AtmoCube-1 CubeSat Mission

The AtmoCube-1 satellite mission has the goal to perform temperature soundings in the MLT to provide data for climate models and to characterize gravity waves [5, 6, 7]. It has also the objective to demonstrate miniaturized remote sensing instrument technologies and to serve as a pathfinder for atmospheric swarm observations. AtmoCube-1 shall use tomographic three-dimensional retrieval routines to increase the measurement sensitivity to a larger gravity wave spectrum [8]. The satellite, illustrated in Fig. 1, has a 3U-CubeSat formfactor with a deployable baffle to observe the atmosphere in the altitude range of 60 km to 120 km in a limb sounding configuration. The AtmoCube-1 instrument occupies 1.5 units in the stowed configuration and about 3 units with the deployed baffle.

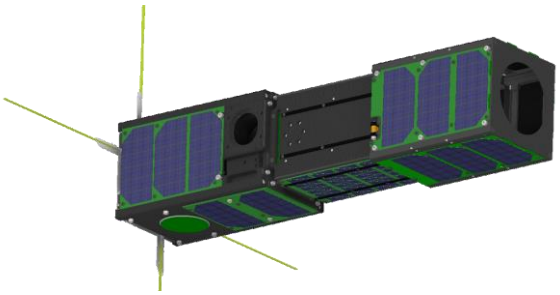

Fig. 1: Illustration of the AtmoCube-1 satellite.

1.3. The AtmoHIT Mission

The Atmospheric Heterodyne Interferometer Test (AtmoHIT) is the precursor mission for the AtmoCube-1 satellite with the goal to verify the instrument under near-space conditions from a sounding rocket within the Rocket/ Balloon Experiments for University Students Program (REXUS/ BEXUS). The AtmoHIT experiment flew on the REXUS 22 rocket from Esrange, Sweden, in March 2017. This paper summarizes the AtmoHIT experiment. First, the measurement principle is described, followed by an overview of the instrument technology and the verification/ calibration campaign prior to the actual rocket launch campaign. The discussion of the results from the rocket launch campaign conclude this contribution.

2. MEASUREMENT PRINCIPLE

2.1. Temperature Measurement in the MLT

AtmoHIT measures the fine-band structure of the oxygen atmospheric band (A-band) in the MLT. The A-band is generated by excited oxygen molecules that emit radiation around 762 nm during deactivation to the ground state ($O_2(b^1\Sigma, v = 0)$ to $O_2(X^3\Sigma, v = 0)$). The excited oxygen is created by six processes in the atmosphere during daytime, forming an emission layer in the atmosphere extending from 60 km to 120 km.

The rotational fine-band structure distribution of the oxygen emission can be used to derive the kinetic temperature in the MLT, because the intensity follows a Boltzmann distribution. Thus, individual lines have individual rotational temperature dependencies, which are measured to derive the rotational temperature by relative comparison of the line intensities. Hence, an absolute calibration is not necessary. In addition, the excited oxygen molecules are in thermodynamic equilibrium with the background state (lifetime approx. 12 s [9, 10]). Thus, the rotational temperature corresponds to the kinetic temperature in the atmosphere. Fig. 2 shows the normalized fine-band structure distribution. The six marked red lines can be used for temperature retrieval.

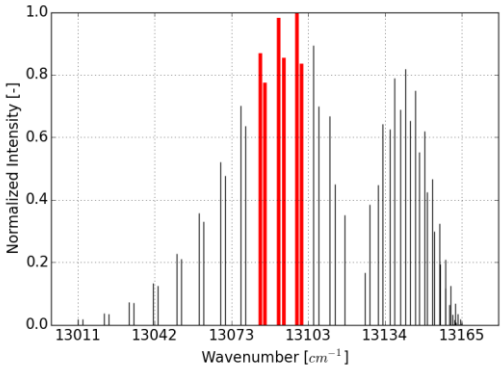

Fig. 2: Oxygen atmospheric band fine-band structure distribution. The six red marked lines are used for temperature retrieval.

2.2. Spectrometer Technology

The fine-band structure lines of the emission are measured with a Spatial Heterodyne Spectrometer (SHS), which is a relatively new type of spectrometer. Originally proposed by Pierre Connes in 1958 in a configuration that he called “Spectromètre interférential à selection par l’amplitude de modulation (SISAM)” [11], this was impractical to use until the development of imaging detectors. Afterwards, it was revisited by Harlander and Roesler at the University of Wisconsin [12] and called SHS. Following this concept, a space instrument was implemented by Christoph Englert in collaboration with Harlander by the Naval Research Laboratory in the USA [13] for the measurement of hydroxyl abundance, demonstrating the principal usage of this instrument type for space applications.
The SHS has the advantage that it can be built as a monolith, which makes it rigid and fault tolerant against external disturbances, two important properties for aerospace applications. Additionally, it can be temperature stabilized and field-widened, which increases the étendue (light-throughput) by approximately one to two orders of magnitude compared to a standard Michelson interferometer and by five orders of magnitude compared to a grating spectrometer. Thus, it is possible to build a small instrument which fits onto a

CubeSat, while still being able to provide data with high precision for scientific applications. Like a Michelson interferometer, the SHS is a Fourier-transform spectrometer, except that the mirrors in the two arms are replaced by gratings. Fig. 3 shows a basic schematic of an SHS with two gratings, a beam splitter, and a detector.

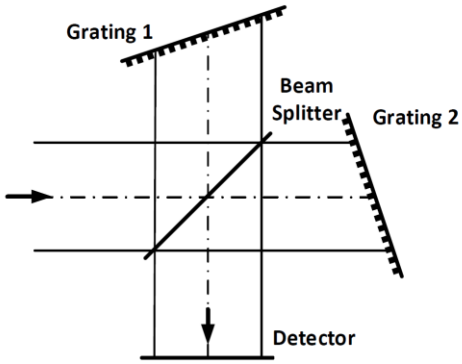

Fig. 3: Schematics of a basic Spatial Heterodyne Spectrometer (SHS) with two gratings, a beam splitter, and a detector.

Light from the left gets divided by a beam splitter and the two beams reach the gratings in both arms. There, the beams are diffracted back into the system. The beams traverse the beam splitter again and interfere at the detector. The gratings are tilted, so that for a specific wavenumber, the Littrow wavenumber σ_L, light which propagates parallel to the optical axis is diffracted back into itself and again propagates parallel to the optical axis. Thus, the wavefronts at the detector are parallel to one another and a constant illumination intensity is recorded by the detector. For emission lines with different wavenumbers, the gratings introduce tilts to the wavefronts that have the opposite direction for the two beams. Thus, the two beams exhibit an Optical Path Difference (OPD) relative to one another that increases approximately linearly with distance from the centre position of the detector. This changing OPD results in localized positive and negative interference between the two beams, creating a fringe pattern on the detector with a spatial frequency characteristic for the respective emission line. Since the spatial frequency for the Littrow wavenumber is zero, the spectrum is measured relative, heterodyned to the Littrow wavenumber. Thus, a Fourier-transformation allows to retrieve the spectrum of emission lines around the Littrow wavenumber.

3. INSTRUMENT TECHNOLOGY

The AtmoHIT experiment has the cylindrical volume of Ø35.6 cm x 17 cm and a total mass of 9.8 kg. A picture of the assembled instrument is shown in Fig. 4. Two windows are visible in the picture. The large window is used for the spectrometer and the small window for an additional camera in the visible spectral range (VisCAM). The VisCAM looks in the same direction as the spectrometer and it is used to help with the interpretation of the interferograms recorded by the spectrometer.

Fig. 4: Picture of the assembled AtmoHIT experiment.

Fig. 5 provides an overview of all subsystems within the AtmoHIT instrument. The VisCAM is a modified GoPro Hero 3 black camera. The spectrometer with the optics is located in the aluminium housing on the right. It is directed to the atmosphere via a straylight reducing baffle. The spectrometer electronics is located within the instrument housing and it connects to a Power Supply Unit (PSU). This unit builds the interface to the REXUS payload service module to provide power and communication.

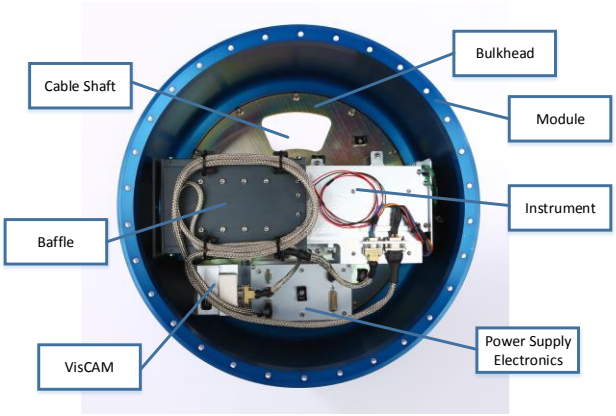

Fig. 5: Overview over the subsystems of the AtmoHIT experiment.

The experiment was located directly below the nosecone of the rocket. Thus, air friction heated up the module ring and the windows. The windows are made from Borofloat 33 glass to cope with the thermal loads. In addition, the spectrometer and baffle are mounted via wire-rope isolators to the bulkhead, reducing the conductivity between the outer structure and the spectrometer. However, the main functionality of the wire-rope isolators is to dampen vibrational loads during launch for the sensitive optical components.

3.1. The Spatial Heterodyne Spectrometer (SHS)

Possibly, the most sensitive optical component is the

SHS. The spectrometer consists of 13 glass parts that are glued together. Fig. 6 shows a picture of the assembled SHS. The gratings are clearly visible with their yellow and blue colours. Compared to the basic SHS schematics of Fig. 3, the built SHS includes also field-widening prisms to increase the light throughput. Effort was put into temperature stabilizing the SHS that it can operate within a temperature range of -10°C to +50°C.

Fig. 6: Picture of the assembled Spatial Heterodyne Spectrometer (SHS). The yellow and blue surfaces are the gratings.

Glass spacers between beam splitter, field-widening prisms, and gratings connect all components. The SHS was glued while being illuminated with laser light to align the components with interferometric accuracy and to monitor the gluing process. Two SHS have been assembled, where the achieved Littrow wavenumber always lay within the allowable tolerance around the design Littrow wavenumber. The properties of the SHS are summarized in Tab. 1. A detailed description of the SHS development is provided in [14, 15].

Tab. 1: Design parameter of the Spatial Heterodyne Spectrometer (SHS) of AtmoHIT.

Parameter	**Value**
Volume [mm³]	38.8 x 37.8 x 27
Grating groove density [lines/mm]	1200
Effective grating area [mm²]	7 x 7
Littrow wavenumber σ_L[cm^{-1}]	13,127
Theoretical resolving power (without apodization) [-]	16,800
Diffraction order	1

3.2. The Optical Assembly

The spectrometer is complemented with a fore-optics and a detector optics. The fore-optics images the scene in the atmosphere with a full FOV of 1.3° onto the gratings of the SHS. The intermediate image at the gratings is imaged onto the detector with a transfer optics having a design magnification of 1:1.66. The fore-optics has an entrance aperture of 66 mm that defines together with the FOV the étendue of the system, matching the étendue of the SHS. In front of the first fore-optics lens, an optical bandpass filter, with a bandwidth of 4 nm, transmits only the relevant fine-band structure lines of the oxygen A-band emission. The custom-made lenses are mounted in an aluminium housing and are held in place with brass rings. The lens mounting is designed that the lenses stay centred under the static loads during the rocket flight and within a temperature range of -10°C to +50°C [16]. The SHS is glued into its aluminium housing with a single compound low outgassing silicon and it is accessible from the top, which is necessary for calibration. Small shims between the fore-optics and SHS housing, between the SHS housing and the detector optics, and between the detector optics and the detector allow to align these parts relative to one another. The detector is a HWK1910A scientific CMOS detector with full HD resolution and 5 µm pixel pitch. A cut through the optical assembly is shown in Fig. 7.

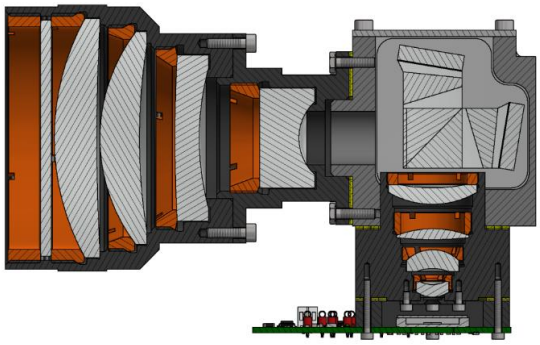

Fig. 7: Cut through the optical assembly with fore-optics, Spatial Heterodyne Spectrometer (SHS), detector optics, and detector board (PXE).

3.3. The Electronics

The electronics consists of four parts. The Power Supply Unit (PSU) is the interface between the rocket service module and the spectrometer electronics. The spectrometer electronics consists of the Front-End Electronics (FEE) that is connected to the PXE by a flexible board-to-board connector. The FEE includes an SD-card for data storage and a commercial System-on-a-Chip (SOC)-board with a Field Programmable Gate Array (FPGA) and a dual-core processor for data processing. The PXE houses the CMOS detector and is directly screwed onto the optical assembly. The VisCAM is connected to the FEE via an interface board. The interface board is necessary, because the grounding of the satellite instrument is floating to avoid any interferences with other instruments on-board the rocket. Fig. 8 shows the boards with the connections between them. All boards except the SOC-board have been developed in-house. Additional information can be found in [17].

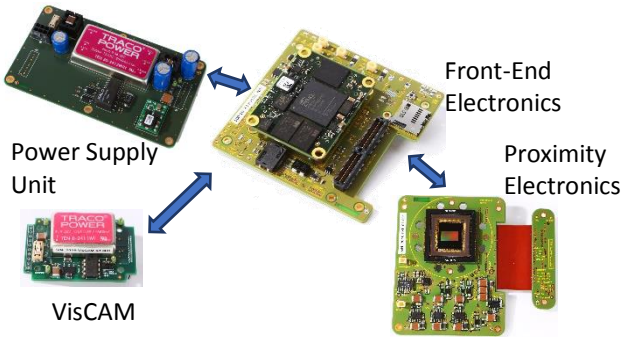

Fig. 8: Pictures of the four electronics boards and their interactions.

4. VERIFICATION AND CALIBRATION

The AtmoHIT instrument has been verified and calibrated prior to the rocket launch campaign. The spectrometer was continuously tested during assembly and alignment, because the gluing processes cannot be easily reverted. Three important tests are described in the following to show that the instrument characteristics are as defined.

4.1. Simulated A-band Emission Spectrum with a Tuneable Laser Light Source

The A-band emission spectrum was simulated with a tuneable laser light source. Thereby, the laser was tuned to eleven emission lines within the bandpass of the optical filter. A detector image (interferogram) was recorded for each emission line. In the post-processing, the interferograms have been summed up to simulate the interferogram from an oxygen A-band emission. This approach is possible because the line-shape function of the instrument is much broader than the Doppler-broadened lines of the oxygen A-band emission and the laser emission linewidths.
The Fourier-transformed spectrum is shown in Fig. 9. The six highest peaks are clearly distinct and can be used for temperature retrieval. The spectral peaks fit also well to the theoretical positions of the emission lines which are indicated by the green dashed lines.

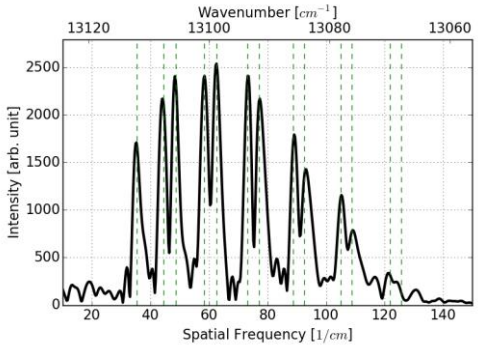

Fig. 9: Oxygen A-band emission spectrum of a synthetically generated interferogram by subsequent measurements of multiple emission lines with a tuneable laser.

4.2. Thermal Vacuum Chamber Tests

The AtmoHIT experiment was also tested in a thermal vacuum chamber to verify its survivability under near-vacuum conditions and within the operational temperature environment. Specifically, the instrument was tested in a temperature range from -21.7°C to 46.7°C and a pressure range from 15 mbar to 1013 mbar. The instrument was operational during testing and survived the tests without performance degradation. Additional objectives of the thermal vacuum chamber tests were the characterization of the temperature and pressure dependencies of the SHS. Thereby, it was shown that the temperature stabilized design of the SHS was successful with a Littrow wavenumber temperature gradient of $\frac{\partial \sigma_L}{\partial T} = (7.9 \pm 0.2) 10^{-3}\, cm^{-1}/K$ and the pressure dependence trend was verified to be $\frac{\partial \sigma_L}{\partial p} = (1.287 \pm 0.003) \cdot 10^{-3}\, cm^{-1}/mbar$. The Littrow wavenumber in vacuum conditions was calculated to be $\sigma_L = 13128.4\, cm^{-1}$, which is very close to the design Littrow wavenumber of $13127\, cm^{-1}$, and is within the acceptable tolerance.

4.3. Vibration Tests

Two SHS have been assembled and two instruments have been built up to mitigate risks. Both spectrometers have been tested on a vibration test bench. The first spectrometer was tested with the fully assembled AtmoHIT experiment and the second was tested separately. Both vibration tests confirmed that it can sustain sinusoidal vibration loads of 4.0g and random vibration loads of 6.0g RMS between 40 Hz and 2000 Hz. The instruments have been operational during these tests and performance degradation could not be monitored.

5. LAUNCH CAMPAIGN RESULTS

The AtmoHIT experiment was launched on 26th of March 2017 at 12:58 UTC. The rocket reached its ceiling altitude of 84.3 km 140 s after launch. The payload section landed nominally on a parachute and was recovered by a helicopter a few hours later. The instrument was fully intact after the flight. The REXUS rocket is a spin stabilized rocket and rolled with a rate of more than 1000°/s during the ascent phase. At T+66 s, a Yoyo-system was released that reduced the roll rate to 2 °/s. A low roll rate is very important for the AtmoHIT experiment, because the instrument needs to integrate over 1 s to collect enough photons for an acceptable signal-to-noise (S/N)-ratio. Unfortunately, an anomaly appeared during separation of the rocket motor from the service module that led to high spin rates of more than 100 °/s in all three axes. Another experiment lowered the roll-rate to low values again in the following 20 s. However, the pitch- and yaw rates stayed at their high values. Thus, the instrument looked often into the Sun or

towards the Earth´s surface and had the atmospheric limb only for short time periods in view.
Housekeeping data was recorded between T-480 and T+580. Voltages and currents of the PCBs, as well as the temperature at the SHS and detector were monitored. Interference with other experiments could not be observed in the data. During the whole flight period, every 17 seconds one detector image and the corresponding housekeeping data package was transmitted to the ground station as backup to the stored data on the SD-card.
The measurement time above 60 km altitude was 140 s. Of all collected detector images during this time, approximately 50% are saturated and cannot be further used. However, there are still a few useful images where an oxygen A-band spectrum could be measured. One of these scenes is analysed in the following.
The representative scene is shown in Fig. 10. The figure shows one image of the VisCAM, which was recorded at an instrument altitude of 84.3 km. The red rectangle in the centre illustrates the FOV of the spectrometer. Its exact position is not known, because co-alignment of the VisCAM and the spectrometer could not be performed. The figure shows also the limb tangential altitude range from 60 km to 120 km with a yellow line. This image shows only a snapshot of the scene during integration of the spectrometer image. Analysing the full 1 s integration time shows that the spectrometer views for approximately 0.25 s the Earth surface, then sweeps over the atmospheric limb and looks towards space for the remaining integration time. The Earth view increases the background light considerably so that the detector image is at approximately half its radiometric bandwidth.

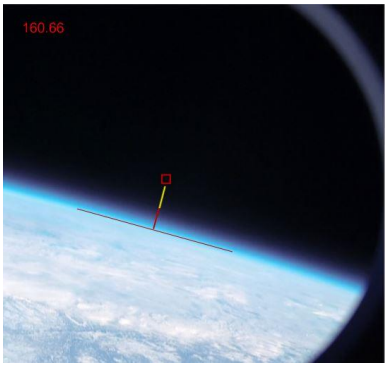

Fig. 10: Scene in the atmosphere at 83.4 km instrument altitude. The red rectangle shows the spectrometer field of view and the yellow line represents the altitude range from 60 km to 120 km.

The resulting interferogram is shown in Fig. 11. The interferogram is expressed in detector counts and the horizontal pixel coordinate is the spectral coordinate over which the Fourier-transformation is performed to calculate the spectrum. The vertical coordinate is the altitude coordinate over which an altitude dependent temperature value can be retrieved. However, due to the tumbling of the instrument, the altitude resolving property of the instrument is meaningless.
The grey spikes on top of the interferogram are artefacts from the gluing process of the SHS. The affected areas are removed for further analysis.

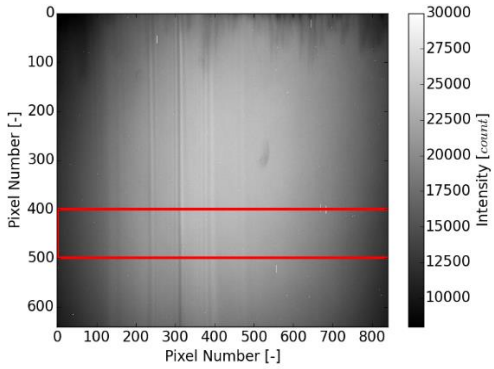

Fig. 11: Interferogram for the scene at 83.4 km instrument altitude. The red rectangular area is spectrally analysed.

Specifically, the red rectangular area in the interferogram of Fig. 11 is analysed in the post-processing. First, the bias is removed from the spectrum by fitting a 2D second order polynomial to get rid of flat-field effects, then the interferogram is apodized and zero-padded to reduce side-lobes and to increase the spectral sampling. The resulting spectrum is shown in Fig. 12. The effective resolution of the spectrum is lower than for the tuneable laser generated A-band spectrum. The main reason lies in the higher background level due to the Earth view during the image acquisition, which increased the shot noise of the interferogram, and the higher detector temperature, which increased the dark current.

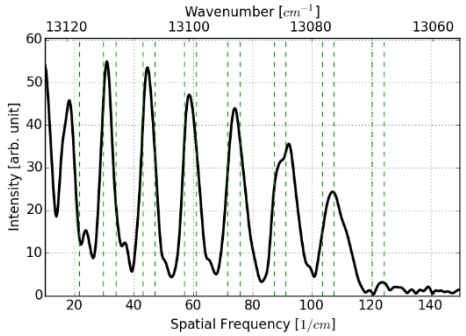

Fig. 12: Spectrum of the scene at 83.4 km instrument altitude.

Thus, individual fine-band structure lines could not be resolved and each line pair combines to a single spectral peak. The peak positions of these line pairs fit to the theoretical position of the emission line peaks. The combined emission peaks can still be used for temperature retrieval, because each line pair has a similar temperature dependence. However, the temperature retrieval is meaningless due to the tumbling of the payload.
The AtmoHIT experiment survived the rocket launch and could measure the oxygen A-band spectrum in the atmosphere in the near space environment. It increased

the maturity of the AtmoCube-1 satellite instrument, which allows to further proceed with this satellite mission.

6. CONCLUSION

This paper provides an overview over the AtmoHIT experiment that was developed within the REXUS/ BEXUS programme. The AtmoHIT experiment includes a miniaturized spectrometer that allows to derive temperature data from the oxygen A-band emission in the MLT. AtmoHIT is the precursor mission for the AtmoCube-1 remote sensing satellite with the mission to characterize gravity waves and to provide data for climate models.

The core of the AtmoHIT experiment is a highly miniaturized, temperature stabilized, monolithic, and light sensitive Spatial Heterodyne Spectrometer. It can be used in a variety of applications where high spectroscopic performance is required in a small volume and in a rugged environment, for example for the measurement of water vapour from satellites [18].

The AtmoHIT experiment was successfully launched on-board REXUS 22 from Esrange, Sweden, in March 2017. It survived the rocket launch and operated nominally during the whole flight. The instrument measured the oxygen A-band spectrum, but its scientific output was limited due to unforeseen circumstances during the rocket motor separation that led to a strongly tumbling instrument. Nevertheless, the AtmoHIT project is deemed successful as it verified the instrument technology in a demonstrative environment.

7. REFERENCES

[1] Vincent, R. A. (2015). The Dynamics of the Mesosphere and Lower Thermosphere: *A Brief Review*, *Progress in Earth and Planetary Science*, 2.

[2] Lindzen, R. S. (1973). Wave-Mean Flow Interactions in the Upper Atmosphere, *Boundary-Layer Meteorology*, 4, 327–343.

[3] Preusse, P., Schroeder, S., Hoffmann, L., Ern, M., Friedl-Vallon, F., Ungermann, J., Oelhaf, H., Fischer, H., and Riese, M. (2009). New Perspectives on Gravity Wave Remote Sensing by Spaceborne Infrared Limb Imaging, *Atmospheric Measurement Techniques*, 2, 299–311.

[4] Smith, A. K. (2012). Global Dynamics of the MLT, *Surv Geophys*, 33, 1177-1230.

[5] Deiml, M., Kaufmann, M., Knieling, P., Olschweski, F., Toumpas, p., Langer, M., Ern, M., Koppmann, R., Riese, M. (2014). DiSSECT – Development of a small satellite for climate research, *IAC-14 Tools and Technology in Support of Integrated Applications*.

[6] M. Kaufmann, M. Deiml, F. Olschewski, K. Mantel, F. Wagner, F. Loosen, D. Fröhlich, H. Rongen, T. Neubert, B. Rottland, H. Schneider, M. Riese, P. Knieling, J. Liu, R. Song, O. Wroblowski, Q. Chen, R. Koppmann, B. Solheim, J. Shan, G. Shepherd (2017). A miniaturized satellite payload hosting a spatial heterodyne spectrometer for remote sensing of atmospheric temperature, *Proceedings of the 11th IAA Symposium on Small Satellites for Earth Observation*, Berlin, Germany.

[7] Kaufmann, M., Olschewski, F., Mantel, K., Deiml, M., Wagner, F., Loosen, F., Fröhlich, D., Rongen, H., Neubert, T., Rottland, B., Schneider, H., Riese, M., Knieling, P., Liu, J., Song, R., Wroblowski, O., Chen, Q., Koppmann, R., Solheim, B., Shan, J., Shepherd, G. (2017), A highly miniaturized satellite payload for the measurement of atmospheric temperature in the mesosphere and lower thermosphere by means of a spatial heterodyne spectrometer, *Atmospheric Measurement Techniques*, in preparation.

[8] Song, R., Kaufmann, M., Ungermann, J., Ern, M., Liu, G., and Riese, M. (2017), Tomographic Reconstruction of Atmospheric Gravity Wave Parameters from Airglow Observations, *Atmospheric Measurement Techniques Discussions*, pp. 1–18,

[9] Bucholtz, A., Skinner, W. R., Abreu, V. J., and Hays, P. B. (1986). The Dayglow of the O2 Atmospheric Band System, *Planetary and Space Science*, 34, 1031–1035.

[10] Touzeau, M., Vialle, M., Zellagui, A., Gousset, G., Lefebvre, M., and Pealat, M. (1991). Spectroscopic Temperature Measurements in Oxygen Discharges, Journal of Physics D: *Applied Physics*, 24, 41.

[11] Connes, P (1958). Spectromètre Interférentiel à Sélection Par l'amplitude de Modulation, J. phys. radium, 19, 215–222.

[12] Harlander, J. M., Reynolds, R. J., and Roesler, F. L. (1992). Spatial Heterodyne Spectroscopy for the Exploration of Diffuse Interstellar Emission Lines at Far-Ultraviolet Wavelengths, *The Astrophysical Journal*, 396, 730.

[13] Harlander, J. M., Roesler, F. L., Cardon, J. G., Englert, C. R., and Conway, R. R. (2002). Shimmer: A Spatial Heterodyne Spectrometer for Remote Sensing of Earth' Middle Atmosphere, *Applied Optics*, 41, 1343.

[14] Deiml, M. (2017). Development of a Small Satellite Remote Sensing Payload for Passive Limb Sounding of the Atmospheric Oxygen Emission, *PhD Thesis*, University of Wuppertal, Research Centre Jülich.

[15] Wagner, F. (2017). Entwickeln und Testen eines „Spatial Heterodyne Spectrometer" für das AtmoHIT-Experiment, *Master Thesis*, Friedrich-Alexander-Universität Erlangen-Nürnberg.

[16] Rottland, B. (2016). Mechanische Konstruktion Zur Halterung Der Optischen Komponenten Eines Spektrometers Und Deren Anbindung An Eine Rakete, *Bachelor Thesis*, University of Applied Sciences, Aachen.

[17] Fröhlich, D. (2016). Entwicklung Der sCMOS-Detektor Ausleseelektronik Für Das AtmoHIT-Experiment Zum Einsatz Auf Der REXUS-Höhenforschungsrakete, *Master Thesis*, University of Applied Sciences, Düsseldorf.

[18] Deiml, M., Jimenez-Lluva, D., Arago-Higueras, N.,

Pavesi, S., Rourke, S., Bylund, O., Joblin, J., Karnthaler, A., Klingenberg, T. F., Link, M., Niemela, P., Paraiso, D., Pauna, C., Scheiblaue, S., Al Bitar, A., and Aguirre, M. (2017). WAVE-E: The WAter Vapour European-Explorer Mission, IAA-B11-0603, in: *Proceedings of the 11th IAA Symposium on Small Satellites for Earth Observation*, Berlin, Germany.

BALLOON GRADIENT MAGNETIC MEASUREMENTS AND SATELLITE MAGNETIC SURVEYS SYNERGY

Oleg Brekhov [(1)], YuryTsvetkov [(2)]

(1) Moscow Aviation Institute (National Research University) (MAI), 125993, Volokolamskoe highway, 4, Moscow, Russia. Email: obrekhov@mail.ru

(2) Pushkov Institute of Terrestrial Magnetism, Ionosphere and Radio Wave Propagation of Russian Academy of Sciences (IZMIRAN), 142190, Kaluzhskoe Hwy 4,Troitsk, Moscow Region, Russia. Email: tsvetkov@izmiran.ru

ABSTRACT

Using balloon magnetometer system provides data anomalous GMP in a limited amount of space than with the satellite measurements.The stratospheric balloon magnetic gradiometer has been developed at the IZMIRAN and the MAI. It has two-stage measuring base of 6 km general length, oriented along the vertical line by means of the gravity. Measuring the balloon base, located at the altitude of 30 km, allows obtaining the geomagnetic field gradients (GMP) from sources up to the lower boundary of the Earth's crust. Using balloon and satellite magnetic data provide a synergistic effect, allowing to refine the process of formation of satellite magnetic anomalies and investigate the deep structure of the Earth's crust in the global and local views, consider the representativeness of the main model GMP, a detailed examination of three-dimensional structure of the external GMP, which is important for type "Swarm" projects.

1. INTRODUCTION

In the process of exploring the surrounding world, the Earth and the cosmos, three main stages are historically distinguished: ground, stratospheric and cosmic observations. In the problems of geomagnetism, the use of stratospheric balloons has not yet been properly applied. Over the past decades, the world has created the prerequisites for obtaining qualitative aerostat geomagnetic surveys based on

- Global navigation system (GPS, GLONASS);
- a global data transmission system from anywhere in the world to the FTP server on the Internet (GlobalStar, IRIDIUM);
- global analytical models of the main GMF for satellite magnetic measurements (IGRF, EMM / 720, MF7, et all.);
- An aerostat magnetic gradiometer with a measuring base length of 6 km.

It is shown in [1] that even using the most modern measuring techniques it is impossible to obtain vertical gradients of the geomagnetic field from sources located near the base of the earth's crust. We have obtained such gradients by using the measuring base of a gradiometer of the order of several kilometers in length. Such measurements can be realized only on a stratospheric balloon [2].

Let's note the main advantages of balloon gradient geomagnetic surveys, performed at altitudes of 20-40 km, numerically comparable to the vertical thickness of the earth's crust:

- In the stratosphere on a vertically oriented measuring base 6 km long, at measurements at altitudes of flights of stratospheric balloons, it is possible to obtain and estimate the magnitudes of magnetic anomalies and their gradients from sources located up to the depths of the Curie isotherm. The indicated measuring base can be realized only on stratospheric balloons;
- According to aerostat measurements, under conditions of naturally smoothed local magnetic anomalies, it is possible to fully isolate the magnetic fields of deep sources. Smoothed magnetic fields from surface and deep sources at these altitudes of flights of balloons have values of the same order, since the remoteness of the measurement point from the earth's surface and from the sole of the earth's crust differs only by half and the fields of deep sources are fully allocated;
- When measuring three magnetometers spaced along a vertical line, it is possible to calculate true magnetic gradients from the obtained differentials along the measuring base of the gradiometer
- Due to the deep minimum separating the main and anomalous geomagnetic fields in the field of their gradients (differentials), it can be reliably divided into the main and anomalous parts of the geomagnetic field. We note that the differentials of the main geomagnetic field, obtained from analytical models for points spaced 6 km apart, do not contain a noticeable systematic error of these models, as well as models of the secular variation of the MPE. This follows from the fact that for sources located at depths greater than 3000 km at such a relatively small distance between the

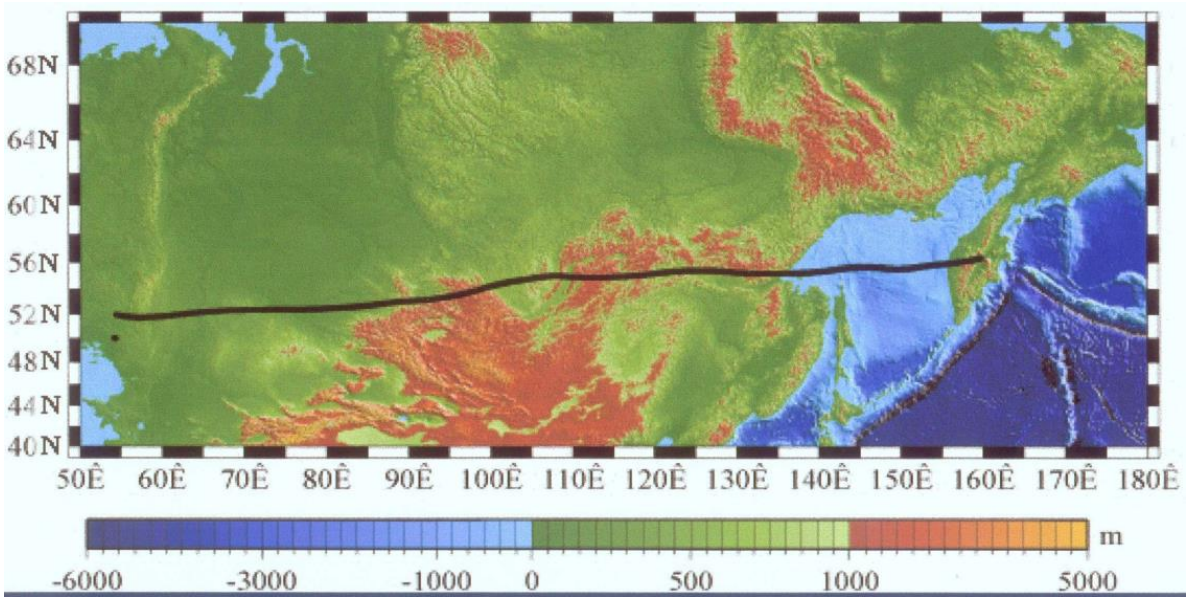

Fig. 1. One of the track of the balloon flight from Kamchatka to Ural Mountains (30 km height, ~6000 km length).

gradiometer sensors (6 km) these errors are almost identical and are excluded when calculating the differentials.

- Using geomagnetic data obtained on balloons, it is possible to estimate the errors of aeromagnetic data (maps (ΔF) a in the region of regional magnetic anomalies, and also to study the formation of satellite magnetic anomalies;
- Due to the presence of magnetic fields in balloon data created by the entire thickness of the earth's crust, the depth of occurrence of the centers of mass of magnetic anomalies is most correctly estimated from the possible variants. At the same time, the synergistic effect of satellite (for example, on the Swarm project) and aerostatic magnetic surveys allows to carry out a geological and geophysical interpretation of the data of both surveys on a global and local scale.

The Russian Federation occupies a unique position in the world for flights of Russian stratospheric balloons. Over the territory of Russia, the length of the route from east to west is 10,000 km, and for round-the-world flights of Russian balloons over the Arctic Ocean, there are practically no obstacles. Fig. 1 shows an example of one of the flights of balloons that we performed.

2. AEROSTAT MAGNETIC GRADIOTOMETER

The stratospheric balloon magnetic gradiometer has been developed at the Pushkov Institute of Terrestrial Magnetism, Ionosphere and Radio Wave Propagation of the Russian Academy of Sciences (IZMIRAN) and the Moscow Aviation Institute (MAI). It has a two-stage measuring base of 6 km. Measuring the balloon base, located at the altitude of 30 km, allows for the receipt of the geomagnetic field gradients (GMP) from sources up to the lower boundary of the Earth's crust.

The principle of constructing an aerostat magnetic gradiometer is given in [3]. AMG consists of three instrument containers, uniformly arranged in space along a vertical line within 6 km of the balloon suspension (the first container is located directly on the balloon). Each container contains a scalar proton magnetometer, a GPS navigation receiver, an on-board computer for collecting and packetizing information coming from the magnetometer and GPS receiver data storage units, a GlobalTel modem serving to transmit scientific and navigation information via satellite radio channels to the FTP Internet folder . Data from the FTP folder on a special computer program is read to the user's computer. The container, installed directly on board the balloon, contains controls for the automatic deployment of the gradiometer. Also on board the balloon there are cable cars with 6 km of cable (4 pieces of 1,5 km of capacity, one of the cable cars is shown in Fig. 2), actuators in the form of pyro-locks providing the beginning of the deployment process of AMG, braking and rescue parachutes.

Fig. 2. Magazine of the rope.

Schematic view of AMG on the starting position and in flight are shown in Fig. 3 and Fig. 4.

Fig. 3. AMG before the start

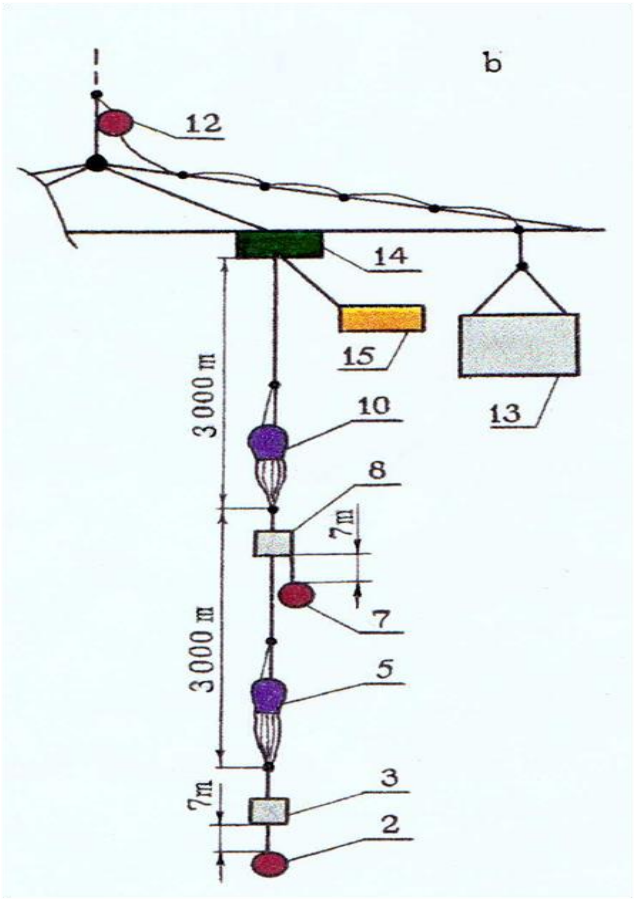

Fig. 4. Kind of the balloon systems.
3, 8, 13 – Magnetometers; 2, 7, 12 – Sensors of magnetometers; 5, 10, 15 – Parachutes

The process of mounting the gradiometer on the balloon suspension is shown in Fig. 5.

Fig. 5. Installation of a gradiometer on a suspension bracket of a balloon

Fig. 6 shows one of the three instrument containers gradiometer assembled in the process of testing for the transfer of scientific and navigational data to the FTP folder of the Internet system with subsequent reading of data on the client's computer.

Fig. 6. The instrument container in the collected kind on tests

The accuracy of the binding of magnetic measurements to time was 1 s. The cycle of magnetic measurements was 60 s. The operation cycle of the GPS navigation receiver was 1 second. The accuracy of measuring spatial coordinates was ~ 10 m (as the average for 60 s is the cycle of magnetic measurements). The problematic part of the gradiometer was the automatic deployment system, which is a long-length cable system. It serves to ensure reliable smooth descent of two instrument containers down from the balloon suspension to a distance of 3 km and 6 km, respectively. In our development, the principle of the honeycomb was used. Cells were filled with a supporting cable in such a way

that it would leave them consistently and completely. For the AMG deployment system, a synthetic cable from high-modular aramid yarns was used as the carrier cable. The cable loaded with a cable is rolled up into a roll and suspended on the side of the balloon.

The principle of deploying AMG is as follows. During the take-off of an aerostat at an altitude of 3 km from the barometric altimeter, the instruction arrives at the puff start of the container detachment at the beginning of the AMG deployment. The pyrolock of the detachment works, the lower garland container is separated from the main suspension of the balloon and starts to fall freely. In this case, the brake parachute is activated and the container is reduced at a speed of 5-7 m/s. When the balloon rises to a height of 6 km, the second pyrolock of the detachment works and unhooks the second instrument container, the descent of which is similar to the first one. When the cable leaves the second drive completely, the process of AMG deployment ends. When the balloon landed at an altitude of 6 km, a third piercing detachment works, which separates the whole garland of instrument containers from the balloon suspension. A garland of two instrument containers AMG lands on the parachutes used during the deployment of the gradiometer. The same parachutes are a protective means in the event of the termination of the supporting cable during deployment and flight.

An important issue is the estimation of the deviation in the flight of the lower magnetometer from the vertical line passing through the upper magnetometer (hodograph) under perturbations of the carrier air flow and its account when processing the experimental results. Deviations of up to 1500 m were recorded (at the base of a gradiometer with a length of 6 km) with a duration of 20-30 minutes. (Fig. 7). For such deviations, a correction calculated from the GPS receiver and the analytical model of the main geomagnetic field (IGRF) is introduced.

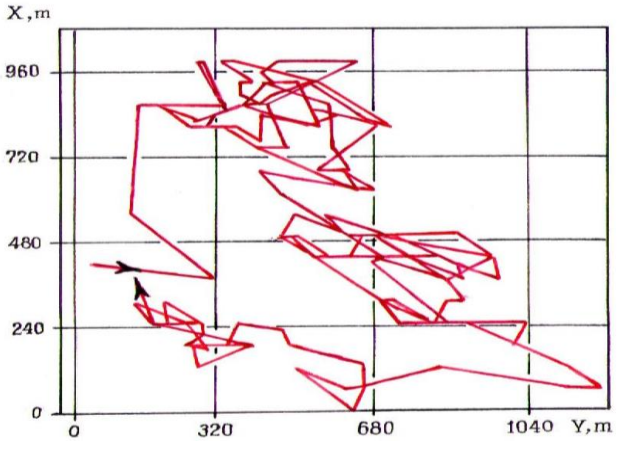

Fig. 7. Hodograph on the basis of 6 km

3. COMPUTER MODEL OF THE DYNAMICS OF THE PROCESS OF AUTOMATIC DEPLOYMENT OF THE HIGH-SPEED MAGNETIC GRADIENTOMETER

Reliable operation of long cable systems is a worldwide problem. As noted above, in our development, the principle of the honeycomb was used. When using such a drive to ensure the reliability of its operation, a computer model was developed for the process of deploying a gradiometer in the troposphere during the lift of an aerostat after the launch.

Instrument containers, each weighing 20 kg, under the take-off of the balloon during the deployment, one by one, are separated from the balloon ball and lowered by parachutes, remaining in series connected to the balloon by means of a supporting cable. An important requirement for such a gradiometer design is to ensure the strength of the supporting cable under dynamic loads, the maximum at the completion of the deployment process, and also to ensure a monotonic cable exit from the accumulator.

The mathematical apparatus of the gradiometer deployment process is given in [4]. The equations obtained were solved by the numerical Euler method. A computer model was developed and the damping factors, the rigidity of the cable, the pulling force of the cable, the horizontal velocity distribution of the wind along the height, the vertical speed of the balloon, the altitude of the flight at which the system was deployed, the integration step were varied. The results of the calculations were displayed on the computer display for visual analysis.

The problem of the work of the cable car is that when the weight of the released cable exceeds the force of the cable's adhesion to the walls of the drive (pulling force), the cable starts to be produced arbitrarily. The speed of the cable exit in this case exceeds the permissible value. Since the descent container is connected to the brake parachute and moves at a lower speed than the outgoing cable, in this case a sagging loop is formed in which the cable can overlap, and at the end of the deployment the cable on the nodes that have arisen at this node may break off. According to the computer model, the necessary binding force of the cable with the walls of the cable car was selected (the pulling force) in such a way that the observed effect was not observed and, as the cable exit, the cable was "smooth", as shown in Fig. 8.

4. EXPERIMENT

Our team carried out about 10 balloon flights with a magnetic gradiometer on board, since 1986 [5] (aerial magnetic surveys were carried out since 1972. [6] Experimental flights were carried out along the routes of the Kamchatka-Povolzhye and over the territory of Eastern Europe.

A detailed description of the experiments is given in [7,8].

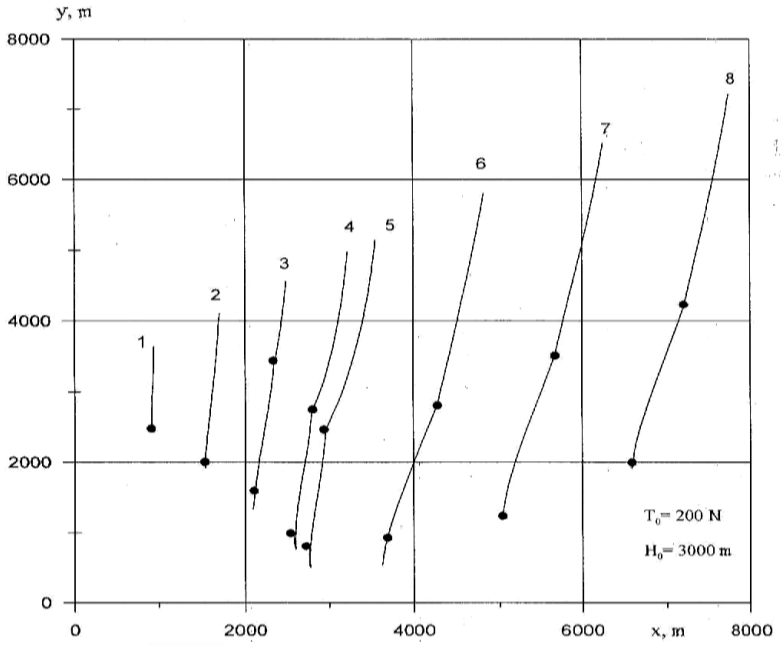

Fig. 8. Process of expansion of a gradiometer

5. OBTAINED RESULTS

In the flights of the balloon magnetic gradiometer over long trails (~ 6,000-8,000 km) from Kamchatka to the Volga region, the magnetic anomalies and their vertical gradients at an altitude of 30 km (50 nT and 2.5 nT, respectively) were obtained [9]. An analysis of various experimental data shows that these data contain magnetic fields of sources located in the entire thickness of the earth's crust. The obtained flight results allowed estimating the attenuation characteristics of magnetic anomalies with distance from the Earth's surface to show that satellite magnetic anomalies are formed by superposition of anomalous magnetic fields obtained in the stratosphere [8]. Gradient magnetic measurements in the stratosphere have shown the ability to best divide the geomagnetic field into main and anomalous components [10].

Note that ground data and methods for analyzing potential fields make it possible to obtain the values of the anomalous geomagnetic field at any altitude of near-Earth space, but the results of recalculating the field up from the Earth's surface do not satisfy the researchers. In confirmation, we give the phrase from the monograph [11]: "deep sources make a significant contribution to the anomalies of Marsat, but do not fully explain their intensity. This entails the assumption of unaccounted for more in-depth sources. "There is no reliable control over the separation of the interference field and the field of deep sources. To determine the reasons for the failure of the recalculation, a comparison was made between the initial data of the anomalous geomagnetic field represented by the map [12]. The map [12] is based on aeromagnetic survey data with a low flight altitude (the first hundreds of meters). The data of such a survey contain high-intensity local anomalies from near-surface sources. For this reason, the map [12] is distorted in the field of deep-field sources due to the loss of the fields of these sources when it is created, orders of magnitude smaller than local anomalies [7]. For a detailed study of the magnetic field of deep sources, magnetic surveys at altitudes of 20-40 km, numerically comparable to the vertical thickness of the earth's crust, in which an anomalous magnetic field is formed with natural averaging of local anomalies are fundamentally needed. At the same time, the smoothed magnetic fields from surface and deep sources at these altitudes have values of the same order, since the remoteness of the measurement point from the earth's surface and from the bottom of the earth's crust differs only by half and the fields of deep sources are fully allocated.

Spectral analysis of the data showed [8] that the map [12] does not contain components of over 130 km in length (this additionally indicates that fields of deep sources in the map data are unrepresentative [7]), whereas the data obtained at an altitude of 30 km contain the entire set of components [8].

The noticeable depth of the bottom edges of the magnetoactive layer of the earth's crust, obtained from aerostat data, [7], which determines the lower boundary of the magnetoactive layer of the earth's crust by thermal, rather than structural (Mohorovicic boundary) characteristics of the earth's crust.

6. CONCLUSIONS

1. The method of balloon gradient magnetic surveys on a measuring base 6 km long is considered and its implementation is given.
2. The method of gradient magnetic measurements on stratospheric balloons allows solving such pressing geophysical problems, such as the processes of attenuation of magnetic anomalies

in near-Earth space, the formation of satellite magnetic anomalies, and the separation of the geomagnetic field into the main and anomalous parts.

3. The importance and usefulness of the use of balloon magnetic data for estimating the vertical thickness of the magnetoactive layer of the earth's crust and the depth of its lower edge are shown.
4. The aeromagnetic data presented by the latest version of the map of the Earth's anomalous magnetic field does not contain any components of over 130 km in length (this additionally indicates that fields of deep sources in the data of this map are unrepresentative), whereas the data obtained at an altitude of 30 km contain the entire set of regional components of the anomalous magnetic field.
5. The noticeable heterogeneity of the lower edges of the magnetoactive layer of the earth's crust, obtained from aerostat data, determines the lower boundary of the magnetoactive layer of the earth's crust by thermal, rather than structural (the Mohorovicic boundary) characteristics of the earth's crust.

7. REFERENCES

1. Nelson, J.B., Marcotte, D.V., and Hardwick, C.D., Comments on “Magnetic field gradients and their uses in the study of the Earth’s magnetic field” by Harrison and Southam, J. Geomagn. Geoelectr., 1992, vol. 44, pp. 367–370.
2. Gorham, P.W., Particle astrophysics in NASA’s Long Duration Balloon Program, Proc. Nuclear Physics B, 2013, pp. 1–8.
3. Tsvetkov Yu., Filippov S., Brekhov 0., et all. Experimental estimations of errors of measurements carrying-out by the stratospheric balloon magnetic gradiometer. Proceeding SP-647 of the 18st ESA Symposium on European Rocket and Balloon. Visby, Sweden. 3-7 June 2007. pp. 577-579.
4. Brekhov O.M., Tsvetkov Yu. Balloon magnetometric complex. Proceeding SP-721 of the 21st ESA Symposium on European Rocket and Balloon Thun, Switzerland. 9-13 June 2013. pp. 703-707.
5. Tsvetkov Yu.P. Experimental studies of the Earth’s anomalous magnetic field (AMF) in the stratosphere. Dokl. Akad. Nauk SSSR, 323 (5), pp. 868-870 (1992).
6. Tsvetkov Yu.P. To an opportunity of measurement of elements of a magnetic field of the Earth onboard drifting balloons. Geomagn. Aeron. Vol. 14, No. 4, pp. 721-724 (1974).
7. Tsvetkov, Yu.P., Brekhov, O.M., Bondar, T.N., and Tsvetkova, N.M., Peculiarities of the geomagnetic field, revealed by gradient magnetic measurements at stratospheric altitudes, Geomagn. Aeron. (Engl. Transl.), 2015, vol. 55, no. 1, pp. 124–132.
8. Tsvetkov Yu.P., Ivanov V.V., Petrov V.G., et all. Spectral Analysis of the Multiple-Altitude Anomalous Geomagnetic Field. Geomagn. Aeron., 2016, Vol. 56, No. 6, pp. 774–780.
9. Tsvetkov Yu.P. Anomalous geomagnetic field study at stratospheric altitudes. Geomagn. Aeron., English Translation, Vol. 33, No. 6, June 1994, pp. 838-841.
10. Tsvetkov Yu.P., Rotanova N.M., Bondar T.N. Separation of a magnetic gradient field into normal and anomalous components. Transactions (Doklady) of the Russian Academy of Sciences/Earth Science Sections. Vol. 355, No. 5, 1997, pp. 712-715.
11. Petromagnetic Model of the Lithosphere. Pecherskii, D.M., Ed., Kiev: Naukova Dumka, 1994. 175 p.
12. Map of Magnetic Field Anomalies (□F)a of the Russia. Scale 1 : 5000000), Petrov O.V., Morozov A.V.,et all., Ed., VSEGEI, 2004.

A MODULAR SOUNDING ROCKET CONCEPT WITH GREEN, SAFE AND AFFORDABLE GELLED PROPELLANT ROCKET MOTORS

Karl W. Naumann[(1)], Helmut K. Ciezki[(2)], Pedro Caldas-Pinto[(3)], Jürgen Ramsel[(4)], Helmut Niedermaier[(5)], Sebastian Rest[(6)]

[(1, 3-6)] Bayern-Chemie GmbH, PO. Box 1131, D-84544 Aschau/Inn, Germany
[(1)] karl.naumann@mbda-systems.de
[(2)] DLR Istitute for Space Propulsion, Langer Grund, 74329 Hardthausen, Germany, helmut.ciezki@dlr.de,
[(3)] pedro.caldas-pinto@mbda-systems.de
[(4)] juergen.ramsel@mbda-systems.de
[(5)] helmut.niedermaier@mbda-systems.de
[(6)] sebastian.rest@mbda-systems.de

ABSTRACT

This paper presents the design concept of a 2-stage sounding rocket using green, safe and affordable gelled propellant rocket motors (GRM). A brief introduction describes the technology of GRM in general and the specific properties of the German GRM technology in particular. Essential properties with relevance to cost-driven sounding rocket business are low cost in production, transport, handling, safety and launch procedures. The main part of the paper describes the paradigms that drive the concept, the design of the stages, the mass and performance parameters. Calculations of the trajectory show that with the standard payload section (400 kg) of the VSB-30 rocket assembly the altitude of the apogee is about 340 km. The incorporated thrust vector control allows to eliminate cross-wind dispersion and provides longer µg-test phases even within a limited test range area.

1. SHORT INTRODUCTION INTO GELLED PROPELLANT ROCKET MOTOR TECHNOLOGY

The development of Gelled Propellant Rocket Motor (GRM) technology in Germany was initiated to create a controllable rocket motor that does not entail the hazard potential of liquid propellants. Particularly critical for military applications is the risk of fire if liquid propellants are set free, be it by an accident or damage by an impact: Liquids spill out of a leaking tank, create a large evaporation surface and have a high vapour pressure. Hence, the risk of fire is high and the consequences are severe:

- Polluting or poisonous products of an imperfect combustion
- Significant efforts needed to extinguish the fire, and
- The unburnt portion of the propellant soaks into ground or spills into waters

As a consequence, Liquid Rocket Motors (LRM) are no more part of military arsenals of NATO member states.
Another requirement was to develop a solution with such low toxicity and causticity that in case of an accident or destruction unprotected humans are not injured.

Known technologies at the time when the GRM development started were controllable Solid Rocket Motors (SRM) and Hybrid Rocket Motors (HRM).

Controllable solid rocket motors were ruled out because the mechanism that controls the throat cross section area needs a lot of energy, following the law $W = p\mathrm{d}V$. Moreover, it has to control the exhaust at the most adverse combination of gas state parameters p^*, ρ^*, T^*. In addition, interfaces and sealing of extremely hot structures in a transient heating scenario are challenging thermo-mechanical problems.

Hybrid rocket motors were ruled out because of the large volume needed, the low thrust density, caused by low regression rate of the propellant, and the fact that the combustion process is driven by many interacting physical phenomena (boundary layer, heat transfer, decomposition or melting of solid propellant, evaporation, mixing, turbulence, combustion, etc.) that vary along the combustor length and cannot be controlled directly, but just indirectly by the injection method and the initial shape of the solid propellant grain.

The technology of choice was to build a GRM that combines the advantages of an SRM and a LRM. Overviews on GRM technology are given in [1, 2]. The state of particularly the German Gel Propulsion Technology (GGPT) activities are reported in [3, 4, 5] and the perfect free-flight demonstration in [6], see Fig. 1. Aspects of hazard potential and environmental impact of GRM and other rocket motor technologies are discussed in [7, 8]. Hence, in this paper we just briefly outline specific properties of GRM technology that are needed to understand this paper. For scientific aspects and verification data the reader is asked to study the references and the literature cited therein.

Fig. 2 shows the principle of operation of a GRM. The

Gelled Propellant (GP) is solid in the tank and has to be delivered into the combustion chamber by pressure. The propellant mass flow rate is controlled by a valve in the feeding line. Upon injection into the combustion Chamber (CC) the gel structure of the GP is destroyed and the GP liquefies. The spray burns in the CC almost like a liquid propellant. Whereas monopropellants represent the current state of GRM technology, bi-propellants and hypergolic propellants are under investigation

Figure1. BC´s GRM demonstrator missile with smoke-free GRP-001 just after launch [6]

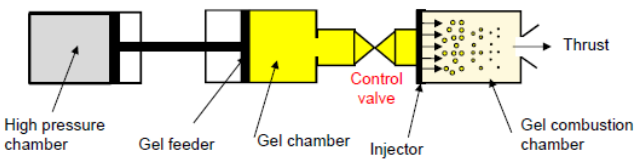

Figure 2. Principle of operation of a GRM [9]

The Gelled Rocket Propellants (GRP) consist of a blend of fluids, gelling agents, additives and if useful and tolerable, solid particles. This increases the density and the specific impulse and can be done because the nature of the GRP prevents sedimentation or buoyancy of incorporated small particles even over long storage times. Many monopropellant formulations for various applications have been tested [10]. An essential guideline of the GGPT program was to develop GP that have a minimum hazard potential to unprotected persons in case of an accident, a malfunction or some other kind of mishap. This has been achieved with respect to the monopropellant GP itself and equally for the combustion products [7, 8].

The pressurization of the GP tank can be done by compressed gas or (solid) gas generators if space is limited, or a combination of both. For GP tanks with high L/D and small *D* a piston is a good solution to separate GP and gas. Tanks with low L/D can separate GP and gas by a membrane or a bladder; the latter solution is also suitable for tanks with large diameter. Helpful in many respects is that GP shows no sloshing in the tank.

The CC is designed using materials and methods that are common in the design of exposed surfaces in SRM. The uncooled CC walls are protected by an ablative heat shield. This design method is comparatively easy and does not need very special materials. For short times of operation, the nozzle throat can be made conventionally from graphite. If a higher degree of resistance against erosion is required, Ceramic Matrix Composite (CMC) materials have shown already good performance in SRM. For long operation times, and if T_c is not too high, the entire CC with nozzle can be made of CMC.

Tests showed very good scalability of GRM in the range from 0.3 – 20 kN nominal thrust and there is no indication that further scale-up should create difficulties [11]. We also observe very stable combustion and very fast and stable thrust control characteristics. Fig. 3 shows unfiltered pressure curves of a test with GRP-006 that has a very wide combustion pressure range from 0.6 to more than 10.5 MPa.

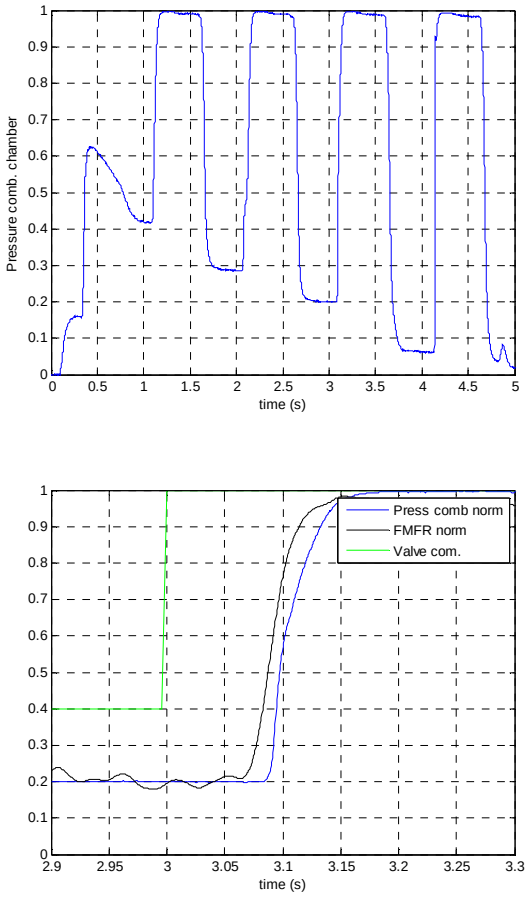

Figure 3. Normalized p_c over time for a test with 4 thrust level steps [12]. Left: complete test cycle, right: time-zoom of the sequence from t = 2.9 – 3.3 seconds. Yellow: GRP valve command, red: propellant mass flow, blue: combustion pressure

For tests with the Highly Controllable Combustion Chamber (HCCC) with variable injector head, variable nozzle and appropriate control algorithm see reference [12].

A GRM is inherently safe because three independent actions are needed to set a GRM into operation. At first, the tank is pressurized. The second step is to initiate the igniter. When p_{CC} exceeds a given threshold value, the GRP valve opens and the GRM starts to operate. Hence, no ignition safety device, essential for igniters of SRM, is needed.

By now, GRM and GGG technology have reached a maturity that allows to enter into demonstrators and developments for specific applications. Promising applications of the German GRM / GGG technology are expected where the following requirements drive the design:

- Low hazard potential, good insensitivity, strict safety requirements
- Affordable propellant
- Easy handling operations including launch, uncritical infrastructure and launch operations
- REACh-compatible propellant (over the entire life cycle) that produces environmentally friendly exhaust gas
- Particle-free exhaust gas if required
- Long operation times due to the separation of tank and CC
- No sloshing of propellant in the tank
- A limited number of operation cycles
- Controllable thrust

Some ideas about design trade-offs for the various applications and some exemplary generic concepts of space applications gives [13]. Concepts for impulse control systems like Divert and Attitude Control Systems (DACS) outline [14, 15].

2. CONCEPT OF MODULAR STAGES FOR SOUNDING ROCKETS WITH GRM

The following considerations on design trade-offs, performance and functional parameters of the sounding rocket concept are based on the results of the efforts described in the references given above.

Stages for sounding rockets are a reasonable first application of a novel propulsion technology because the specific performance requirements in terms of specific impulse and propellant mass fraction are relaxed. This allows designs with good margins. Data obtained from successful flights allow to assess the degree of "over-quality" and provide the base for further optimization. Generic concepts for stages of sounding rockets were outlined in [9, 13].

In this paper, we establish a design concept with the goal to match the ballistic performance of the VSB-30 sounding rocket. The SRM stages S-30 and S-31 are used as point of reference for the performance parameters of the GRM stages, particularly for thrust level, total impulse and total mass of the stage. The discussions with DLR-MoRaBa included calculations of the trajectory of the GRM Sounding Rocket (G-SoRo) by MoRaBa [16].

2.1. Premises and boundary conditions

The VSB-30 [17] carries a payload section of about 400 kg mass to an apogee of about 270 km what allows some minutes of microgravity experiments. VSB-30 consists of two SRM stages, S-31 as first stage and S-30 as second stage. S-30 and S-31 are quite conventional SRM with a steel case, a fixed nozzle and an aluminized HTPB-APC composite propellant what is common for launcher stages. Table 1 gives some key parameters for the two stages of VSB-30. S-31 is the first stage with higher thrust level and shorter burning time to exceed a minimum launch acceleration. This is important to minimize the impact of cross-winds on the impact point dispersion.

Table 1. Key parameters of S-31 and S-30 SRM [17]

		S-31	S-30
Diameter	[m]	0,56	0,56
Propellant mass	[kg]	616	861
Gross mass	[kg]	900	1200
Peak thrust	[kN]	240	102
Burning time	[s]	13.5	29

For the G-SoRo stages, the following data, functions and design features have been chosen a priori:

- Two stages, each with 1 ton of aluminized gelled propellant
- Initial thrust of stage 1: 180 kN at main sea level (MSL)
- Initial thrust of stage 2: 100 kN at altitude (90 kN at MSL)
- Operation time of stage 1: t ~15 s
- Operation time of stage 2: t ~30 s
- Diameter of the stage body: D = 582 mm, to allow accommodation in the space between the rails of the ESRANGE launch tower, state as of 2015
- The propellant chosen is GRP-002 which contains energetic solid particles. The specific impulse of GRP-002 is somewhat better than that of aluminized solid propellants (see Fig. 4). The density of GRP-002 is 1300 kg/m^3 which is a good value for liquid propellants but less than the 1800 – 1860 kg/m^3 of highly aluminized solid propellants. Taking also into account that the GRM needs devices for

pressurization and GRP mass flow control, and has separate tank and CC means that GRM stages need more volume for the same mass of propellant than SRM stages

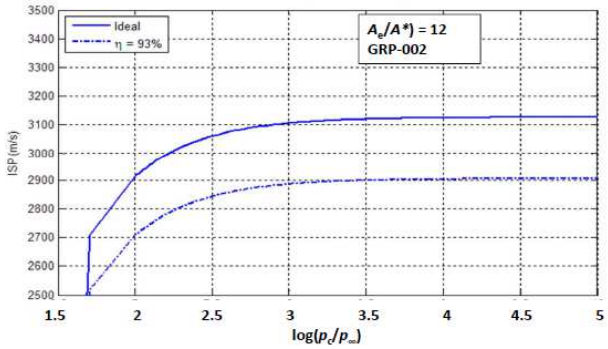

Figure 4. Specific impulse of GRP-002 over p_c/p_∞ for $A_e/A^* = 12$

2.2. The design of the G-SoRo stages

In order to reduce development cost, the two stages use identical parts and components as far as possible. This means that the design of each stage is a compromise that satisfies the requirements of both. Fig. 5 shows sketches of both stages.

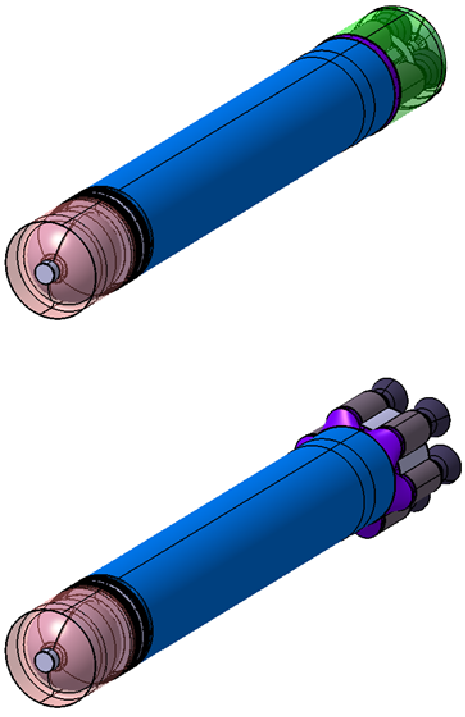

Figure 5. Picture of the modular 1st (below) and 2nd (above) stage of the G-SoRo

The main building blocks of both G-SoRo stages are the block of GRM as the aft section, the tank for the GRP as the main body and the high-pressure tank for the pressurizing gas as the front part.

The key design features of the main building blocks and components of the propulsion systems of the stages are:

- The GRP and gas tanks are also the body of the stages and carry the axial, lateral and bending loads
- The spherical high-pressure gas tank is the forward closure of the GRP tank and carries the front skirt of the stage
- The aft skirt of the GRP tank section carries the interface to the GRM blocks and is the interface to the rear skirt (stage 1) or intermediate section (stage 2)
- The load-carrying structures of both GRP and gas tank are made of Carbon Fibre Reinforced Resin (CFRR). CFRR allows to build light-weight high-pressure tanks with good bending stability if the interfaces are simple as is the case for the G-SoRo design
- The spherical gas tank has a liner of aluminium that provides the necessary tightness and serves as the liner for the winding process of the carbon filaments
- The GRP is held in a collapsible bladder within the tank. This separates the load-carrying tank structure and the GRP and eliminates any chemical compatibility problem of GRP and CFRR matrix resin. Another advantage is that no specific requirements address the properties of the inner surface of the CFRR tank structure, e. g. surface roughness or tight tolerances of the inner diameter. In total this reduces signi-ficantly the costs for production, verification and proof of the CFRR structures. The collapsible bladder has to be compatible with the GRP. Because the pressure difference over the wall of the bladder is very small, the bladder is subjected to negligible mechanical loads. This equally reduces the cost for verification and proof of the collapsible bladder
- The GRP tank is pressurized using a pressure reducer. The advantage is that the design pressure is very well defined and that uncertainty margins can be reduced to zero. The maximum operating pressure p_T = 10 MPa for the first phase of operation. After about half of the operation time the pressure in gas tank and GRP tank equilibrate. Subsequently, the pressure decreases with the expulsion of the GRP. In parallel, the combustion pressure has to be reduced to maintain the safe pressure ratio between p_T and p_{CC}. The p_{CC} is controlled by the controller and the control algorithm. The corresponding decrease of thrust corresponds to some degree to the decreasing mass of the

launcher and helps to reduce the peak acceleration

- All GRM CC with injector head and nozzle, in the following designated GRM, are identical for both stages; also with respect to the nozzle opening area ratio A_e/A^* = 12. This is sub-optimal for the low ambient pressure operation of stage 2, but cost-efficient in development and production. The injector head and the shells of the CC and nozzle are made of metal alloy. The CC shell and the nozzle structure are protected by an ablative heat shield. For operating times of about 15 and 30 seconds, respectively, the thickness and mass of the ablative heat shield is well tolerable. We use the aft closure and nozzle design methods and materials that are known from SRM
- The GRM blocks consist of 6 GRM for the first stage and 3 GRM for the second stage; the GRM are identical. The bundles of GRM are chosen because:
    - The development effort needed for the development of the smaller GRM is less than that needed for the development of a much bigger single GRM with 180 or 100 kN nominal thrust
    - The bigger number of identical GRM per launcher allows lower production cost due to higher production rate
    - The multiple GRM need significantly less length than a single GRM
    - Each individual GRM is thrust controlled by propellant mass flow rate control. This includes already a thrust vector control (TVC) capability by differential thrust of the individual GRM. No additional components like gimbal bearings, movable nozzles or actuators for these elements are needed. The only item to be adapted is the control algorithm
    - The exact number of GRM per stage depends on trade-offs that take into account not only the internal optimization, but also boundary conditions, e. g. of the launch infrastructure
- The GRM of the stage 1 block are placed in that way that the axis of the GRM is aligned with the rear skirt of the tank. This yields an optimum force transfer into the skirt structure. This arrangement allows also to place the GRP control valve and actuators in the space between the GRM what saves length. Of course a placement between tank and a GRM array that fits into the outer diameter of the stage is possible
- The GRM of the stage 2 block are placed within the outer diameter of the stage to allow a simple design of the interstage section. The GRP control valves and actuators care placed between the GRM
- The ancillary components needed are:
    - The filling assembly for the pressurizing gas
    - The valve that opens the gas pipe to the GRP tank. This can be a pyro-valve or a valve with an actuator.
    - The gas pressure reducer
    - The propellant flow control valves for each GRM with actuators
    - The propellant loading pipes with non-return valve
    - The emergency venting system for the GRP tank
    - The energy supply
- The standard configuration of the VSB-30 has no roll control device, but canted aft fins that produce a speed-dependent spin rate plus small thrusters that provide the initial spin rate because the fins are ineffective at low velocity. If roll control should be required, cold gas thrusters using gas tapped from the high-pressure gas reservoir would be an appropriate solution.

Figure 6 shows a longitudinal cut of the two stages with some details of the relevant components. Table 2 gives the mass breakdown. Whereas the GRM stages with L = 4.3 m are longer than the SRM stages S-31 with L = 3.0 m and S-30 with L = 3.3 m, the inert mass of the GRP stages (280 and 232 kg) is lower (S-31: 284 kg; S-30: 339 kg) despite the bigger propellant mass of the GRM stages.

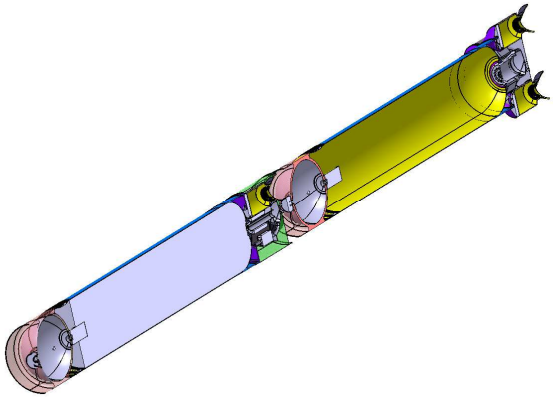

Figure 6. Longitudinal cut of the two stages

The trajectory calculations in [16] for a complete sounding rocket with the two GRM stages, interfaces, stabilizers, payload module and ancillary components yielded a good margin of about 70 km for the required

apogee altitude of 270 km.

Because the I_{sp} of GRP-002 has not been measured in a vertical test up till now, a very conservative estimate was used for the calculation, using $I_{sp,vac,GRP-002}$ = 2760 m/s or in US units: 281 s.

Table 2. Mass breakdown of stage 1 and stage 2 of the G-SoRo

	Stage 1	Stage 2
	[kg]	[kg]
GRM block, 6 or 3 GRM	87	50
GRP mass flow control and piping	33	20
GRP tank with skirts and GRM supports	70	70
He gas tank with skirt, pressure reducer and piping	63	63
Igniter, radiation shield, He gas, energy supply, electronic box	27	29
Total inert mass	280	232
GRP with energetic particles	<1060	<1060
GRP mass fraction with 1000 kg GRP	0,78	0,81

3. DISCUSSION

3.1. Complexity and modularity

The G-SoRo is more complex than the currently used SRM stages, but complexity is not just proportional to the number of parts or components:

- SRM have very few components, but each component is subjected to a combination of loads and requirements that can be severely contradictory. For example, the solid propellant grain has to simultaneously fulfil requirements on ballistic, mechanical, chemical, physical and geometrical requirements. Simultaneously it has to bond safely to the surface of the case. The integrity of the grain structure and the bonding is essential for the correct function of the SRM. Less relevant for SRM for sounding rockets is the change of all parameters due to ageing of the materials, because the expected life time of dedicated sounding rocket stages is limited and the storage conditions should be good
- GRM have many components, but the functions are well distributed to specific parts. Some examples are:
    - The requirements on the mechanical properties of the GRP are limited: The GRP has to keep the fine energetic particles in suspension
    - Variations in viscosity of the GRP with soak temperature are compensated for by the GRP flow control
    - Only the comparatively small GRM are exposed to high T_c. In contrast to the CC of a SRM, the GRM carry no external load.

Another aspect is that the components of a stage with GRM can be developed and tested on component level. Parts like the tanks and the GRP feeding and control assembly can be used for all development tests if the design has not to be changed as a result of these tests. This reduces the hardware cost for development articles and allows to separate the root causes for failurs more easily.

The modular nature of the GRM stages allows to integrate new components into the existing design. This may be necessary due to obsolescences of materials, or beneficial because progress in technology development offers improved solutions. In the same way, other GRP can be used if desired.

3.2. Performance and capability

The use of GRM blocks allows to integrate a Thrust Vector Control (TVC) with no additional development effort on the hardware side. The control software of the GRM blocks can be modified to generate a thrust vector by differential thrust of the individually controllable GRM. If the sounding rocket is equipped with a guidance and navigation device, the G-SoRo can follow a pre-determined trajectory.
The controllability of the GRM can also be used:

- To fly a given thrust (i. e. acceleration) profile
- To limit the peak acceleration if this is required by the scientific payload. With a TVC, the trajectory of the sounding rocket is not affected by cross-winds and a mild initial acceleration is possible without a detrimental increase of the impact area
- To shut down the GRM at a given point along the trajectory.

The compensation of cross-wind effects can also be done if the sounding rocket itself is not equipped with a guidance and navigation system. Using a gyro set allows to determine the momentary direction of the axis of the sounding rocket. A deviation from the desired direction is compensated by differential thrust of the GRM. This method does not compensate the lateral displacement caused by the cross-wind, but it prevents the rocket to turn into the wind. And this turning makes the much bigger contribution to the impact point dispersion than the lateral displacement. Hence, the GRM allow to launch at much stronger cross-wind, wind shear or turbulence conditions than stages with SRM without expensive TVC devices.

3.3. Safety, handling and environment

A GRM is inherently safe, because three independent inputs are needed to put it into action: pressure in the GRP tank, operation of the igniter and opening of the GRP valve. This low hazard potential eases handling significantly.

The filling procedure of the GRP tank can be chosen according to what is most practical. At a launch site with a high launch rate, a local production facility for GRP can be the best solution. At launch sites where only sporadic launches are carried out, the transport of the filled stages to the launch site might be preferred.

The environmental friendliness of GRM and GRP has already been outlined in the introduction.

4. SUMMARY

A sounding rocket using modular stages with GRM is well feasible. Whereas a stage with GRM needs more volume than a SRM stage with similar total impulse, the inert mass is rather lower than higher. Hence, a GRM stage provides a good ratio of propellant mass / inert mass and offers good ballistic performance.

Stages with multi-GRM propulsion block need just an adequate propellant mass flow control algorithm to provide TVC by differential thrust of the GRM. A simplified method allows to prevent the rocket from turning into the cross wind direction.

A key asset is the low environmental impact of GRM and GRP, the low hazard potential and the good handling properties.

5. ACKNOWLEDGEMTS

We highly appreciate the support of DLR MoRaBa in the definition of the GRM stages and for the calculation of the trajectory. Equally we thank all our collegues that work with endeavour within the GGPT working group.

6. REFERENCES

1. Natan, B. and Rahimi, S., "The Status of Gel Propellants in Year 2000" in: *Combustion of Energetic Materials*, pp. 172-194 (eds.: K.K. Kuo and L.T. DeLuca), Begell House, USA, 2002.
2. Ciezki, H.K., Naumann, K.W., Weiser, V., "Status of Gel Propulsion in the Year 2010 with a Special View on German Activities", *Deutscher Luft- und Raumfahrtkongress 2010*, Hamburg, Germany, August 31 - September 2, 2010.
3. Schmid, K., Ramsel, J., Naumann, K.W., Stierle, R.; Weiser V., "Raketenmotore mit Gel-Treibstoffen – Stand der Technologie bei Bayern-Chemie", *Deutscher Luft- und Raumfahrtkongress 2012*, Berlin, Germany, September 10-12, 2012.
4. Kirchberger, C., Ciezki, H. K., Hürttlen, J., Schaller, U., Weiser, V., Caldas-Pinto, P., Ramsel, J., Naumann, K.W., "An Overview of the German Gel Propulsion Technology Program", *AAAF Space Propulsion Conference*, Roma, Italy, May 2-6, 2016.
5. Ciezki, H.K., Kirchberger, C., Stiefel, A., Kröger, P., Caldas Pinto, P., Ramsel, J., Naumann, K.W., Hürttlen, J., Schaller U., Imiolek, A., Weiser, V., "Overview on the German Gel Propulsion Technology Activities: Status 2017 and Outlook", *7th European Conference for Aerospace Sciences*, Milano, Italy, July 2-6, 2017.
6. Stierle, R., Schmid, K., Ramsel, J., Naumann, K. W., "Free-Flight Demonstration of the Gelled Propellant Rocket Motor of MBDA-Bayern-Chemie", *4th European Conference for Aeronautics and Space Sciences*, St. Petersburg, Russia, July 4-8, 2011
7. Ciezki, H.K and Naumann, K.W., "Some Aspects on Safety and Environmental Inpact of Gel Propulsion", *Propellants, Explosives, Pyrotechniques*, invited publication for special issue "Insensitive Munitions", Vol. 41, pp. 539-547, 2016.
8. Ciezki, H.K , Naumann, K.W., Kobald, M., "A Short Discussion on Performance, Safety and Environmental Aspects of Gel and Hybrid Rocket Propulsion Systems", *31st International Symposium on Space Technology and Science*, Matsuyama, Japan, June 3-9, 2017.
9. Naumann, K.W., Ramsel, J., Caldas-Pinto, P., Niedermaier, H., Scheutzow, S., Thumann, A., "Rockets with Green Gelled Propellants – A Promising Technology for Sounding Rockets", *22nd ESA Symposium on European Rocket and Balloon Programme and Related Research*, Tromsø, Norway, June 7-11, 2015
10. Ramsel, J., Scheutzow, S., Caldas-Pinto, P., Naumann K.W., Thumann A., Kurth G., "Gelled Rocket Propellants – Development and Performance", *6th European Conference for Aerospace Sciences*, Krakow, Poland, June 29 - July 3, 2015.
11. Caldas-Pinto, P., Hopfe, N., Ramsel, J., Naumann, K.W., Thumann, A., Kurth, G., "Scalability of Gelled Propellant Rocket Motors", *7th European Conference for Aeronautics and Space Sciences*, Milan, Italy, July 2-6, 2017
12. Caldas-Pinto, P., Ramsel, J., Scheutzow, S., Naumann K.W., Thumann A., Kurth G. "Control Characteristics of a Gel Propellant Throttleable Rocket Motor", *6th European Conference for Aerospace Sciences*, Krakow, Poland, June 29 - July 3, 2015

13. Naumann K.W., Caldas-Pinto, P., Ramsel, J., Niedermaier, H., Risse, S., Thumann A., "Green, Highly Throttleable Gelled Propellant Rocket Motors – State and Application Potentials", *AAAF Space Propulsion 2016 Conference*, Rome, Italy, May 2-6, 2016
14. Naumann, K.W., Caldas Pinto, P., Ramsel, J., Scheutzow, S., Thumann, A., Niedermaier, H., Hopfe, N., Kurth, G., "Gelled Propellant Throtteable Rocket Motor and Gas Generator Technology at Bayern-Chemie", *6th European Conference for Aerospace Sciences*, Krakow, Poland, June 29 - July 3, 2015
15. Naumann, K.W., Tussiwand, G, Caldas Pinto, P., Hopfe, N., Ramsel, J., Eineder, L., Risse, S., Thumann, A., Niedermaier, H., Kurth, G., "Green Gelled Propellant Gas Generator for High-Performance Divert- and Attitude Control Systems", *51st AIAA/ASME/SAE/ASEE Joint Propulsion Conference & Exhibit*, Salt Lake City, UT, USA, July 25-29, 2016, AIAA 2016-4667
16. Scheuerpflug, F., Kirchhartz, R., Naumann, K. W., Weigand, A., Ciezki, H. K., Kirchberger, C., Gülhan, A., Eggers, T., Bosic, O., Weihs, H., "Study of a Rocket Motor Stage for Sounding Rockets", DLR, May 2017
17. https://en.wikipedia.org/wiki/VSB-30; May 17, 2017

7. NOMENCLATURE

7.1. Parameters

A	[m^2]	Area
D	[m]	Diameter
I_{sp}	[m/s]	Specific impulse
L	[m]	Length of a body
p	[Pa]	Pressure
T	[K]	Temperature
t	[s]	Time
V	[m^3]	Volume
W	[J]	Work
η	[1]	Efficiency
ρ	[kg/m^3]	Density

Superscripts

*	Value at nozzle throat, sonic condition

Subscipts

CC	Combustion chamber
c	Combustion
e	Condition at nozzle exit
GRP	Gelled rocket propellant
T	Tank
vac	Vacuum conditions
∞	Ambient condition

Abbreviations

APC	Ammonium perchlorate
BC	Bayern-Chemie
CC	Combustion chamber
CFRR	Carbon fibre reinforced resin
CMC	Ceramic matrix composites
DACS	Divert and attitude control system
GGG	Gelled propellant gas generator
GGPT	German gel propellant technology
G-SoRo	Sounding Rocket with GRM
GP	Gelled propellant
GRM	Gelled propellant rocket motor
GRP	Gelled rocket propellant
HCCC	Highly controllable combustion chamber
HRM	Hybrid rocket motor
HTPB	Hydroxyl terminated polybutadiene
LRM	Liquid propellant rocket motor
MSL	Main sea level altitude
NATO	North Atlantic Treaty Organization
REACh	Registration, evaluation, authorization of chemicals
SRM	Solid rocket motor
TVC	Thrust vector control

STARBURST - A NEW, UNIQUE STUDENT PROJECT IN MARITIME SURVEILLANCE FROM SPACE

BENTE JENSEN[1], CHRISTIAN HAUGLIE-HANSSEN[2], CHRISTOFFER STAUSLAND[3]

(1) NAROM, Norwegian Centre for Space-related Education (Norway), Tel: +47 76144662, E-mail: bente@narom.no

(2) KONGSBERG Defence and Aerospace AS, Kongsberg, Tel: +47 92060043, E-mail: christian.hauglie-hanssen@kongsberg.com

(3) NAROM, Norwegian Centre for Space-related Education (Norway), Tel: +47 76144661, E-mail: christoffer@narom.no

ABSTRACT

The STARBURST project is a new, unique national Norwegian project in maritime surveillance from space where 15 selected, motivated university students get the possibility to work with new space technology in Norwegian space companies.

The goal is to demonstrate new technologies and system architecture for small payloads and advanced data processing for maritime surveillance from space by establishing an end-to end surveillance system with payload, downlink and ground station.

The STARBURST project will introduce the students to a real industrial context, involving project management, design, development, integration, launch and release operations followed by results analysis, albeit in a very condensed timescale.

Figure 1: Student rocket launch at Andøya Space Center

1. INTRODUCTION

The STARBURST programme will provide practical project experience in direct interaction with professionals at KONGSBERG (The Kongsberg Group) [1], NAROM (National Center for Space Related Education) [2], ASC (Andøya Space Centre) [3] and other Norwegian space companies [4]. The project is partly sponsored by the Norwegian Space Center [5].

This project includes hands-on activity for university students, and aims to take students through a complex system integration project, which concludes with the release of a stratospheric balloon carrying the student payloads. In addition, the students will go through a full sounding rocket campaign at Andøya Space Center. The students will build, test and integrate a payload into a Mongoose 98 rocket before they will take central positions in the rocket launch operation and launch their rocket to approximately 9 km. During the rocket flight, the students will track the rocket and use telemetry to read flight sensor data for subsequent analysis.

During the spring 2017, the students went through an online introductory and training pre-course covering subjects related to space technology and maritime surveillance. During the whole STARBURST project period (January - August 2017) the students will be part of a social media based discussion group with the other participating students. During an 8 weeks' summer work period at one of the participating Norwegian Space Companies the students will develop contributions to a STARBURST Stratosphere balloon payload. The final test, integration and launch of the student payloads will take place at Andøya Space Center in July/August 2017.

Figure 2: The STARBURST Project logo

2. THE PARTICIPANTS IN THE STARBURST PROJECT

2.1 The participating companies

The project is organised by KONGSBERG and is a collaboration between KONGSBERG, NAROM, Andøya Space Center and other Norwegian space

companies which all are members of NIFRO (Norwegian Industrial Forum for Space Activities) [4]. There are six KONGSBERG-companies participating in the project representing capacities from all sectors within the Space & Surveillance domain; from launcher equipment to downstream services. The other participating NIFRO companies are complementary in technology and product niches, and were selected in order to provide the STARBURST project with a complete set of resources necessary to obtain the project's objectives.

T&G Elektro AS is a leading Norwegian supplier of electrical and fiber optical cable systems, harness solutions and connectors for defence, space, telecommunication and offshore applications.

EIDEL (Eidsvoll Electronics AS) designs and delivers products and control systems to the defence-, aviation - and space industry. System definition of hardware and software designs are covered. EIDEL provides standard products as well as custom designs.

CMR Prototech AS activities cover energy systems, mechanical structures and life support system components.

KONGSBERG Space Systems is Norway's leading supplier of equipment to scientific satellites, space probes and launchers, and is established as an important niche supplier to ESA and other European space operators.

KONGSBERG Norspace AS delivers satellite on-board electronics for Telecommunications, Navigation, Search & Rescue, Earth Observation and Scientific programs. Functions span from units for satellite remote control and telemetry, to frequency processing units.

KONGSBERG Spacetec AS has provided ground station equipment for earth observation satellites for more than 30 years, and is today one of the leading providers worldwide.

KONGSBERG Norcontrol AS is a provider of high-end, real time situational awareness, decision support and management solutions and services for optimum safety, efficiency and security within the maritime domain.

KONGSBERG Seatex is a marine electronics manufacturer with products for precision positioning and motion sensing for safe navigation and operations at sea. As part of Kongsberg Maritime they provide complete ship and offshore systems. Kongsberg Seatex is a supplier of AIS-payloads for satellites.

KSAT (KONGSBERG Satellite Services AS) (50% owned by the KONGSBERG GROUP) operates over 60 antennas optimally positioned for access to polar and geostationary orbiting satellites, with ground stations all over the world. KSAT provides satellite operation services, including telemetry, tracking and command of satellites, global data dump services, data dissemination and communication, earth observation services and LEOP Services (Launch and Early Orbit Phase).

2.2 The participating students

For this STARBURST project 15 Norwegian university students (6 female and 9 male) with a completed 2-4 year of master degree study, preliminary within the disciplines of engineering, physics, mathematics or other technical subjects, were selected individually by each company with respect to wanted and required qualifications for each vacant student position in the project. The 15 participating students were selected from approximately 250 applicants indicating a huge interest from master level students for participating in this type of space industrial related projects.

Figure 3: The 15 Students and supervisors/point of contacts in the STARBURST Project

3. THE BALLOON MISSIONS

The overall ambition of the STARBURST project is to demonstrate new technology and system architecture for small payloads and advanced downstream data processing and presentation for maritime surveillance from space. The students shall organise and execute a comprehensive system project. In order to succeed, knowledge and understanding of the challenges of such a complex project must be established. The students

shall understand and conduct a series of Work Packages that combined constitutes the STARBURST project.
The balloon used for the STARBURST-mission is a standard TOTEX 3000g balloon filled with Hydrogen. The use of Hydrogen demands special precautions, and the actual preparation and release will be performed by ASC.
The balloon will carry 4 different sub-payloads as illustrated in Fig. 4. Two of these are mandatory for ASC and NAROM and standard payloads as explained below. The remaining two payloads are the Aurora and the Borealis payloads that will be the central part of the students work during the summer period.
In order for the students to complete the development and integration of the student payloads, the Aurora and Borealis missions are organised in 9 sub-projects described in 25 work packages. Each work package defined by the participating companies describes the functions, input and output of a central part of the payload/mission together with information of responsibilities.

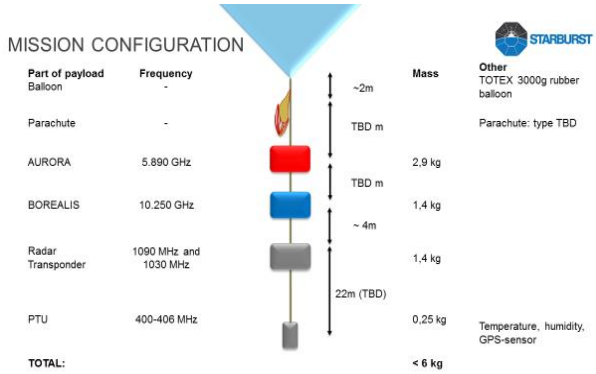

Figure 4: The STARBURST balloon mission configuration. There are four different payloads and a parachute attached to the balloon.

3.1 **PTU Telemetry pack**

The PTU Telemetry pack is a standard pack from Lockheed Martin. It is mandatory for all balloon releases by NAROM. The PTU Telemetry pack includes telemetry and sensors for measuring temperature, humidity and GPS-signal. The GPS-signal will be used in the Aurora mission as described below.

3.2 **Flight Radar Transponder**

The flight radar transponder is a standard transponder and will provide information that can be used by the national flight monitoring services to track and identify the balloon during flight. The transponder is mandatory for Andøya Space Center [5].

3.3 **The Aurora Mission Payload**

The Aurora mission payload will consist of dual cameras, video encoders, a marine broadband radio (MBR) and a battery unit.

The ground segment will consist of a receiving station, and a video decoding system with displays. Figure 5 shows the principle outline of the Aurora Mission payload and ground station. Both payload and ground segment will use phase-controlled antennas.

The goal of the Aurora mission is to transmit live video from the balloon during the complete mission and present live video on the operator station. Furthermore, to extract video images and present those in real time on a C-Scope map-application, together with synthetic-aperture radar (SAR)-imagery and 3D-tracking information from the GPS.

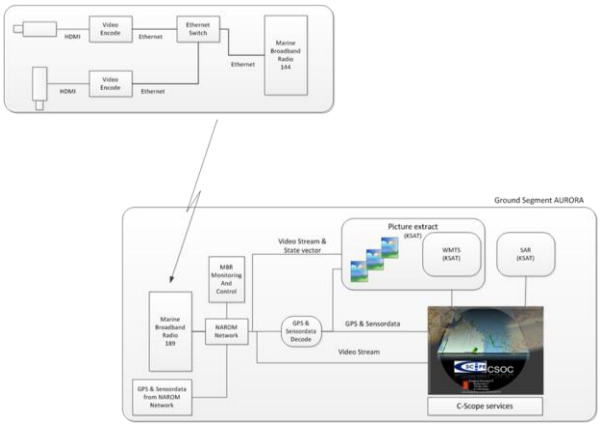

Figure 5: Principle outline of the Aurora mission. Payload and ground segment.

3.4 **The Borealis Mission Payload**

The payload for Borealis mission will consist of a data stream source, a crypto unit, a transmitter module, antenna and battery unit. The Borealis transponder will operate in X-band at a frequency of 10.3 GHz.
The ground segment will consist of a tracking antenna with X/Y-servo electronics, a receiver, a de-crypto unit and a tracking algorithm unit in a feedback loop.
The goal of the Borealis mission is to track the balloon during the flight and decrypt and present the received data-stream in real time. Figure 6 shows the principle outline of the Borealis mission payload and ground segment. As seen in the figure stated in the top of each

box, the different parts of the payload are of the responsibility to the participating student in different companies.

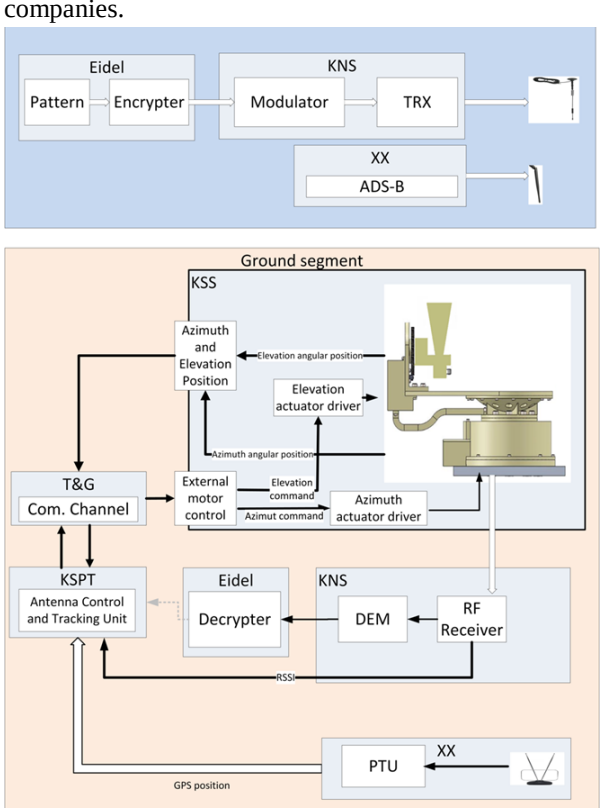

Figure 6: The Borealis mission, payload and ground segment

4. STATUS, RECOVERY AND FUTURE

The status of the STARBURST project at the time of writing is that the students have now been working on the balloon payloads in the participating space industry companies for a few weeks. Previously the students have completed the e-learning course and are now working towards the Camp STARBURST taking place from 30/7 to 6/8 2017 at Andøya Space Center.

The ambition is for the STARBURST Project to be a multi-year event, with a long term goal to make real contribution to the development of micro-satellite maritime surveillance in Norway. It is also an ambition to re-use and improve the developed hardware from one year to the next. The payloads will contain various functional modules, and of particular monetary value.

The STARBURST balloon will aim to be recovered at sea, as land recovery is often very hard, expensive and complicated. The boat shown in Figure 7, a Targa 37, will be used for this, and a small recovery team of students will join the recovery boat. The tracking of the balloon and payload during the descent is from signals from the marine broadband radio (MBR) in the Aurora payload. The payload structure design will, in order to maintain the tracking and enhance the chances for recovery, allow the MBR antenna to point upwards when the payload is floating in the sea after touch down.

Figure 7: Targa 37, the boat used for recovery of the balloon payloads

Social media updates during the project period and more information of the STARBURST project can be found in [6] and [7].

REFERENCES

1. https://www.kongsberg.com/
2. http://www.narom.no
3. http://andoyaspace.no/
4. http://nifro.no/en/
5. https://www.romsenter.no/eng
6. https://www.narom.no/aktiviteter/STARBURST/
7. https://www.facebook.com/kogSTARBURST/?fref=ts

BALLOON MICRO LIFEFORM-AND-METEORITE ASSEMBLER (BULMA) EXPERIMENT FOR BEXUS 22 LANUCH CAMPAIGN

Tomasz A. Miś [(1)], Paula Gajewska [(1)], Kamil Jasiński [(1)], Iwo Koryciński [(2)], Kacper Maciszewski [(2)], Patryk Mierzejewski [(2)], Adrian Nowakowski [(1)], Mateusz Płonka [(1)], Piotr Rugor [(1)], Emilia Węgrzyn [(1)]

[(1)] Students' Space Association, Warsaw University of Technology, Poland; ska.pw.pr@gmail.com
[(2)] Students' Microbiology Association, University of Warsaw, Poland; knmikro@gmail.com

ABSTRACT

The paper presents the Balloon micro Lifeform-and-Meteorite Assembler (BuLMA) experiment for the BEXUS 22 stratospheric balloon flight campaign belonging to the REXUS/BEXUS programme of DLR and SNSB with cooperation with ESA, SSC, ZARM and MORABA. The experiment employed a kinetic air-moving method (the Electric Ducted Fans, or EDFs) for in-situ particle recuperation, as well as instrumentation for stratospheric micro-lifeforms accumulation (mats and membrane filters). Its design employed 3D-printed elements; other mechanical subsystems unreachable in common trade were manufactured in the laboratory and workshops. The amount of electric power needed to run the experiment was taken from an own, non-BEXUS space-applicable battery pack. After the flight was completed, various samples were extracted from the experiments' instruments. Technical challenges and vast amount of samples induced a long analysis time – in this paper some of the preliminary results are presented (the analysis is still in progress).

1. INTRODUCTION

Often intercepted on ground using various methods (magnetic, optical-manual etc.), micrometeorites – space particles large enough not to burn completely during their entry into the Earth's atmosphere – as well as dust particles (anthropogenic or natural, i. e. volcanic) and micro lifeforms – can be recuperated in situ using air-moving (or moved-in-the-air) machines, i. e. the diaphragm pumps or plates placed outside an airplane travelling at high speed at ~20 km of altitude; the pumps flushes the air through a series of filters which intercept the particles, while the plate, covered with adhesive substance, accumulates the particles by their impacts [2-4] [7-8]. Created and designed in Students' Space Association, Faculty of Power and Aerospace Engineering of Warsaw University of Technology, Poland and in Student's Microbiology Association, Faculty of Biology of the University of Warsaw, the Balloon micro Lifeform-and-Meteorite Assembler experiment for the REXUS/BEXUS programme employed for the particles' recuperation a kinetic method of flushing the air – two highly efficient Electric Ducted Fans (EDFs) coupled with cyclone-like containers equipped with instrumentation able to intercept different types of particles. Two cyclones permitted the simultaneous use of various recuperating instrumentation.

The experiment itself was preceded with simpler stratospheric balloon experiments employing magnetic elements and deployable sails that caused the air to swirl onto the micrometeorite-intercepting elements – the PARTICULA experiment programme [5] [6]. Its outcomes showed promising results (small amount of different types of particles intercepted) on which the BuLMA experiment based.

2. MECHANICAL DESIGN

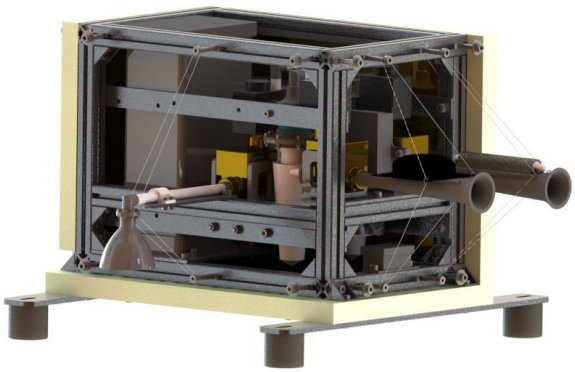

Figure 1. The overall view of the experiment's 3D model [1].

The experiment mechanically consisted of two cyclone assembly units (with two separate inlets and a common outlet) – see Figure 2, mounted together in a frame made of system profiles [1]. Inside the frame the electronic compartments and the battery box were also affixed. The external insulation was provided by a single-layer of dense styrodur with aluminized mylar coating on the inside. The entire set was mounted inside the BEXUS M-Egon gondola using thick plastic and rubber washers with supporting bars.

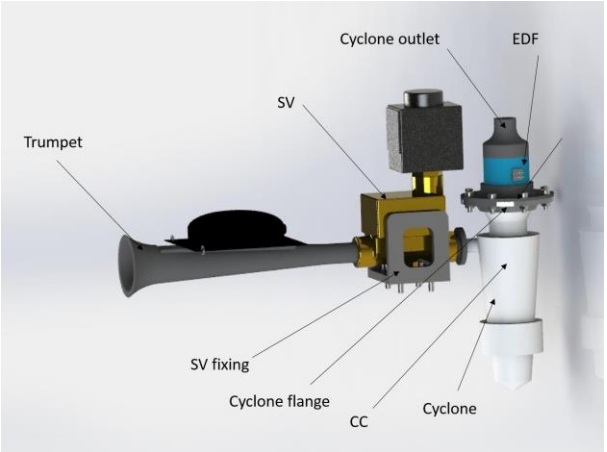

Figure 2. Fan unit assembly [1].

The cyclones themselves, EDF affixations, inlet trumpets, pipe connectors, solenoid valve (SV) bases, inlet trumpets, exhaust nozzle, electronic boxes and battery box were all 3D-printed from black ABS material [1]. The inlet trumpets and the outlet nozzle, protruding of the experiment – and therefore out of the M-Egon gondola – were calculated (FEA) in order to be provide enough stiffness to withstand the forces occurring in the beginning of the descent phase (high shock/acceleration).

The cyclones (see Figure 3) [1] were designed in a conical shape in order to maintain the peripheral air velocity of the swirl, which prevented it from disappearing (changing from swirl to straight flow). Inside the cyclones the particle-recuperating equipment was glued.

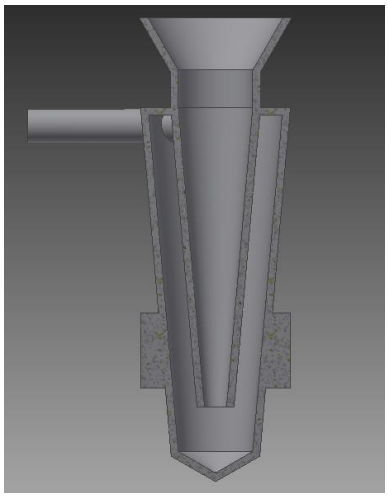

Figure 3. The cyclone cross-section [1].

As the Electric Ducted Fans were expected to create a lot of heat during their full-power working period, proper thermal analysis using the AnSYS software had to be made to define – with the help of Dr Philipp Hager from ESA – the possible ways of accumulating and dissipation of this heat. Finally, the internal parts of the EDFs were covered with aluminium foil and their external parts – with copper foil, increasing their heat capacitance. Some of the rotating elements of the motors were coloured black to increase the heat emissivity.

During the integration process of the experiment, the chosen solenoid valves have proven to be unreachable – new valves were designed by Mr Płonka at the Warsaw University of Technology (see Figure 4). The valves, driven by separately bought solenoids, had Teflon seals and all-machined brass carcasses; the pistons were positioned in a way which permitted the cyclones to decompress slowly during the ascent (so that there is no risk of destroying the cyclones by the air pressure).

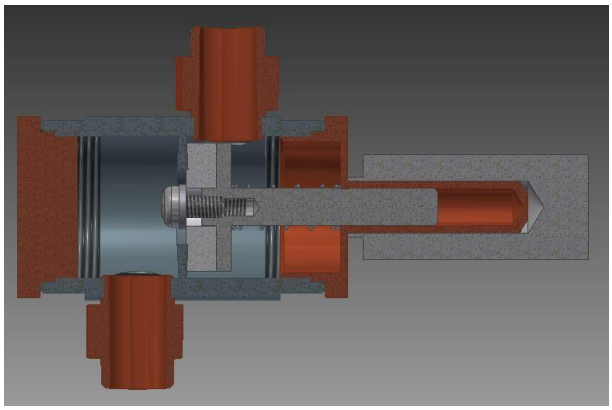

Figure 4. The cross-section of the new solenoid-driven valve with Teflon seal and brass carcass [1].

3. ELECTRONIC DESIGN AND SOFTWARE

The electronic design was divided into 2 main parts: 2 cyclone systems and the OBC (On-Board Computer) system [1].

The cyclone systems were in two copies from the electronic point of view – for the high level of redundancy needed. Every system included:

- EDF - BLDC motor which works as an air pump (see Figure 5),
- ESC - controller for that motor,
- cyclone driver - based on an Arduino which controls the temperature on the motor, proper time of opening and closing valves, controlling the speed of the motor, and sending information to the OBC,
- heater
- temperature sensor for the motor,
- tachometer
- batteries.

Figure 5. Botland's EDF 27.

The OBC system included:

- OBC - which controls the entire mission,
- Differential pressure sensors
- pressure sensor,
- temperature sensors,
- GPS receiver,
- GM counter (on the schematic – included in the voltage converter to 400 V).

The OBC (On-Board Computer) determined the moment to open the valves and to turn on the EDF's motors (approximately on 20-km. of altitude) with the basis on the GPS data and (as a redundancy) static pressure data.

Another task of the OBC was to collect data from all sensors (flowmeters, G-M sensor, pressure, temperature), save it on an external memory (SD card) and also send it to the GS via E-link. The OBC was connected with two cyclones' drivers via UART in order to get the status of the valves and motors and, if necessary, control them from the GS directly.

The power system (see Figure 6) of the experiment was divided into 3 main parts [1] :

- 1 system which will be powered by the BEXUS gondola power supply (OBC system),
- 2 systems (cyclone systems).

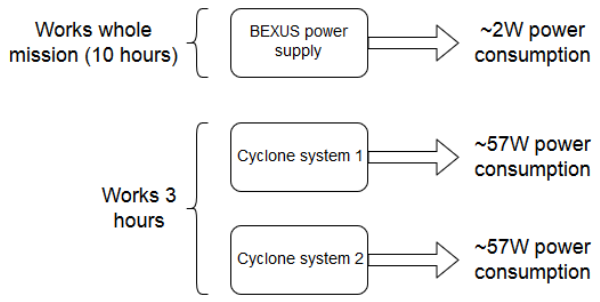

Figure 6. The power outline of the experiment. Max. 10-hour-long mission includes operation + ascend/descent + recovery [1].

The cyclone systems were powered by 18 batteries with high continuous current consumption (SAFT LO26SXC). These two systems worked at full power only for 3 hours of the entire mission (plus tests). The rest of the time power consumption was designed (and has proven to be) negligible. The SAFT LO26SXC batteries have low operating temperature (-60 degrees centigrade with low drop voltage). The experiment had its own power supply for both motors and valves employed because of high power consumption of this components (BEXUS power supply could not provide this amount of power).

The experiment's GS (Ground Station) [1] – see Figure 7 – provided the control of basic parameters of the motors, as well as the position of the valves, with the possibility of manual modifying the motor's speed and opening/closing the air system. The software was developed in C# for Windows platform.

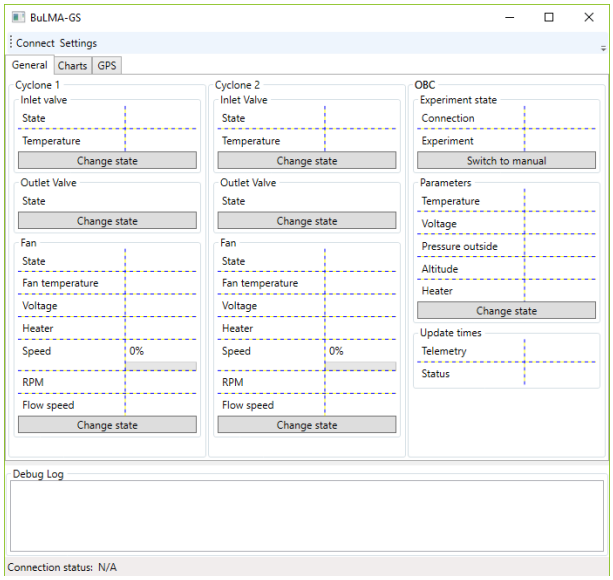

Figure 7. The GS layout screenshot [1].

4. SCIENTIFIC EQUIPMENT AND ANALYSIS PLAN

For intercepting the particles, two major methods (partially basing on the PARTICULA experiment programme outcomes) were chosen – the electric field and the magnetic field [1].

The electric field was provided by the use of an 'open-air capacitor' – a pair of aluminium electrodes placed inside one of the cyclones; the electric field between them would intercept the particles which show a dipole-like electric structure (or are not neutrally-charged). The 'open-air capacitor' was fed by a ~300-V. KEMET capacitor, mounted inside the experiment and discharged through a high-power resistor after the mission was complete and the M-Egon BEXUS 22 gondola was found.

The magnetic field method employed a neodymium-made constant magnet, affixed inside the second cyclone and wrapped with in a plastic foil. The foil would not affect the intensity of the magnetic flux, yet it would facilitate the separation of the intercepted particles (those magnetically susceptible, i. e. iron

spherules) from the magnet's surface for further analysis.

The micro-lifeforms were to be intercepted by a series of membrane filters (glued inside one of the cyclones) and mat filters (put inside the second cyclone) [1]. The collected microbiological material was to be analysed (mainly after grooming in a laboratory) using following methods:

- DAPI staining – on a non-groomed sample – detection of microbial cells in the sample,
- trypan blue staining – on a non-groomed sample; differentiation between living and dead cells,
- inoculation on different media – assessment of growth capabilities of the microorganisms in different nutritional conditions,
- microscopic observations (optical and confocal electron microscope),
- 16S rDNA isolation, amplification and sequencing – identification of systematic position of intercepted microorganisms,
- metagenomics (for the non-groomed microorganisms) – total DNA sequencing.

5. LAUNCH CAMPAIGN AND PRELIMINARY RESULTS

The experiment was assembled in a laminar chamber (with airflow curtain and UV sterilization) and successfully flown onboard the BEXUS 22 balloon mission from Esrange Space Centre, Sweden, on 4th October 2016 [1] – see Figure 8. After a nearly 3-hour-long flight, the gondola landed safely in Finland. The BuLMA experiment was switched onto stand-by mode during the least access events on the balloon pad, and operated actively (after being turned on manually in the Ground Station via the E-link connection) above the altitude of 22000 m.

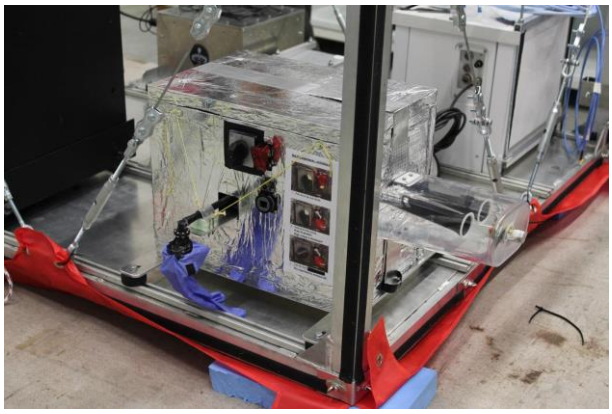

Figure 8. The experiment mounted onboard the M-Egon gondola during pre-launch testing. The inlets and the outlet are secured with plastic shields [1].

During the operation phase the experiment experienced a gradually-growing temperatures of both EDFs – the temperatures were measured using IR (infrared) and contact sensors. A great amount of heat was successfully radiated by the copper-covered casings of the fans, yet one of them must have experienced a previously undetected cable failure (breakage of some of the cable's thin wires) which led to increased electrical resistance resulting in significant heat losses (detected by the temperature sensors, both contact and IR) and, finally, burning the cables, immobilizing the EDF. The second EDF had worked without problems.

The samples from the experiment – mats, filters, a drop of the glue (for assessment of the equipment's sterility) and the foil-wrapped magnet were extracted in the laminar chamber, put into plastic containers and transported to the laboratories in Poland.

The foil, after removing the magnet, was placed under an optical microscope for initial, visual inspection (magnification: 45x) and then under a TM-1000 electron microscope for detailed imaging and spectroscopy of the particles. The electron ray, scanning the sample at 95 mA of anode current, generated a vast amount of heat on it (especially on high magnifications: 400x, 1200x) which caused the foil to melt. This distorted the image (the microscope went out of focus) and made the spectroscopy nearly impossible (as the small size of particles required a very high magnification and good focusing for effective spectroscopy).

The solution for the melting foil would be the use of a thin aluminium foil instead of a plastic one – being electron-microscope convenient (as it conducts electricity, making it a good anode for the electron ray) it presents lower adhesive capabilities than the foil, yet the magnetic flux distortion caused by it should not be significantly worse.

For the foil samples, the solution for the melting was to cover the entire sample with thin layer of conductive material, i. e. carbon, molybdenum, copper or gold. As the electron ray easily penetrates also the subsurface region of the sample, the intercepted particles would be visible; as the sample would not melt and wrinkle, the focusing of the microscope should remain good and constant and very high image resolutions should be accessible.

Figure 9 shows the test surface image of an intercepted particle; Figure 10 shows the test below-surface image of the same particle and the point in which the spectrum was collected. The spectrum itself is presented on the Figure 11. It is clear, as well as the photographs of the particle – the carbon-covering of the plastic foil have proven to be fully useful. The particle presented in the figures consists of iron almost in 100% (the calcium peak on the spectrogram is an indication error) which makes it probably not a space-coming particle (more likely a possible dust particle coming from the Kiruna Iron Ore mines), yet the amount of particles (and their small sizes) on the sample still

makes it probable to find space-coming micrometeorites. The searching of the sample in order to find suitable candidate for detailed imaging and spectroscopy is in progress (a long, manual process, depending also on the access to the electron microscope).

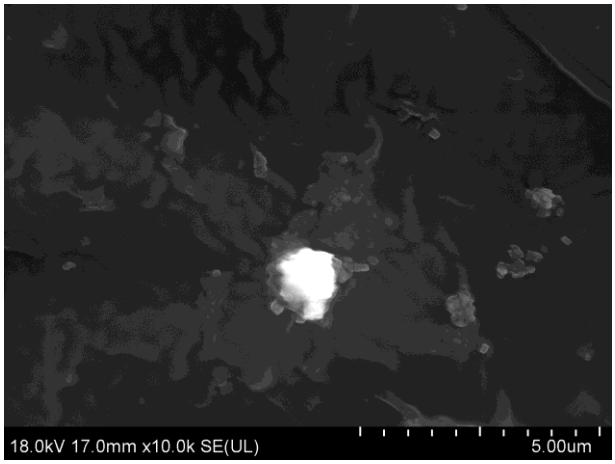

Figure 9. A surface view of an intercepted particle.

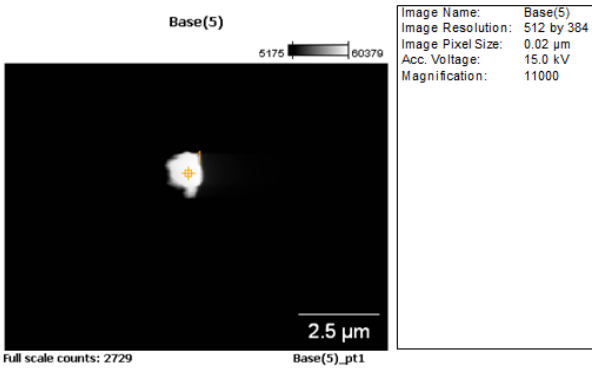

Figure 10. Subsurface view of an intercepted particle showing a point in which the spectroscopy was carried out.

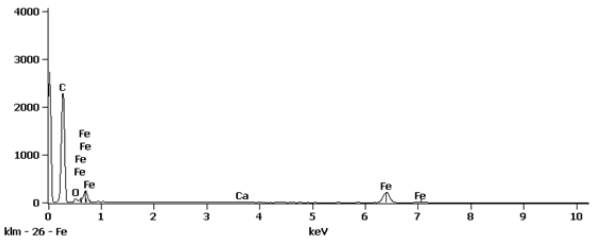

Figure 11. The spectrogram of in intercepted particle. Carbon peak indicates the sample coating, iron peaks indicate the particle.

The microbiological analysis began with the analysis of the glue (silicone-like sanitary glue) used to affix the membrane- and mat filters inside the cyclones – the glue has proven to be effectively sterile (not metabolism-supportive and not containing any colony-forming microbial units) [1]. The samples were carefully washed from their substrates (the filters) and their grooming was started. Before that, several pictures were taken under a confocal electron microscope, revealing that the comparative sample differs substantially from the flight samples (which definitely proves that the experiment's air duct system worked and collected stratospheric particles) and that much more particles are present on the sample taken from the cyclone's outer wall – this means that the centrifugal force pushed more particles in that direction, so the air actually rotated inside the cyclone (as it was designed). On the Figures 12-16 many putative bacteria-like forms can be visible. The varying colours are the effect of the DAPI test staining, which was mainly to define (by fluorescence detection) which of these particles actually possess DNA, yet a major part of the detected particles have shown autofluorescence in various sections of the light spectrum, including the wavelength of emission maximum for DAPI (~460 nm), which in this case made the DAPI method unreliable.

The grooming of the microorganisms has shown a microbiological contamination of the comparative sample – this was likely to happen in laboratory conditions; the analysis shall be modified (the contamination is going to be excluded from the flight sample to reveal the non-terrestrial organisms). In August 2017 the analysis was still in progress.

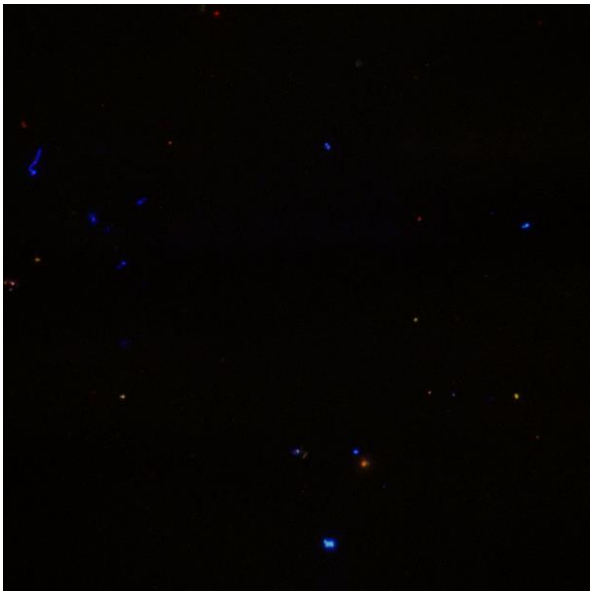

Figure 12. The comparative sample [1].

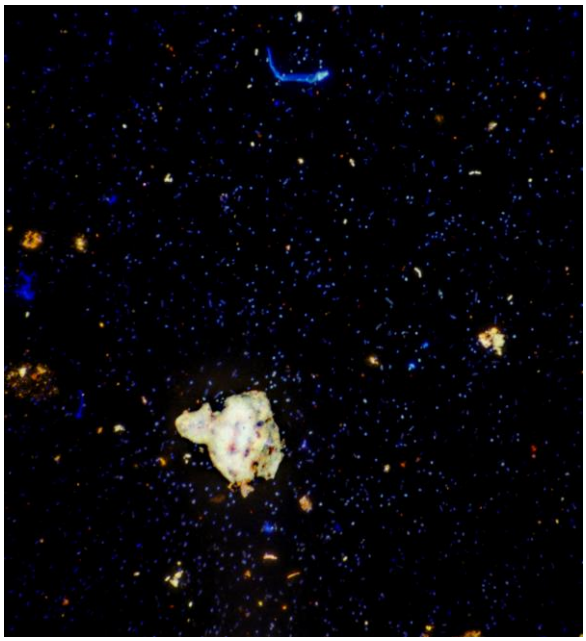

Figure 13. The mat filter sample [1].

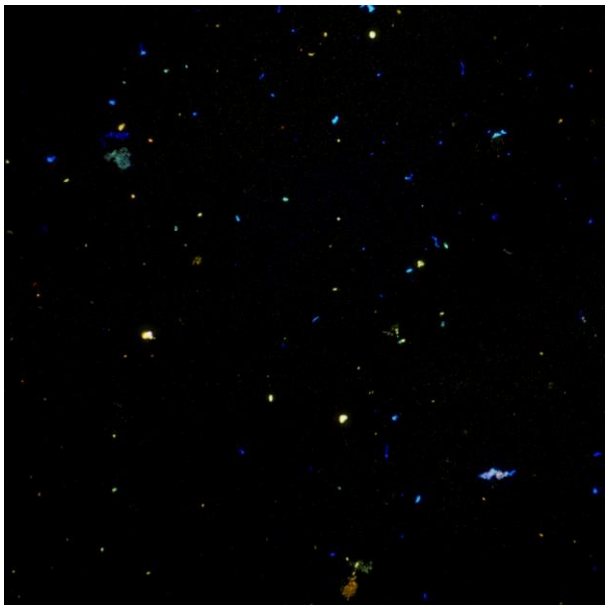

Figure 14. The membrane filter sample – filter mounted on the internal pipe of the cyclone [1].

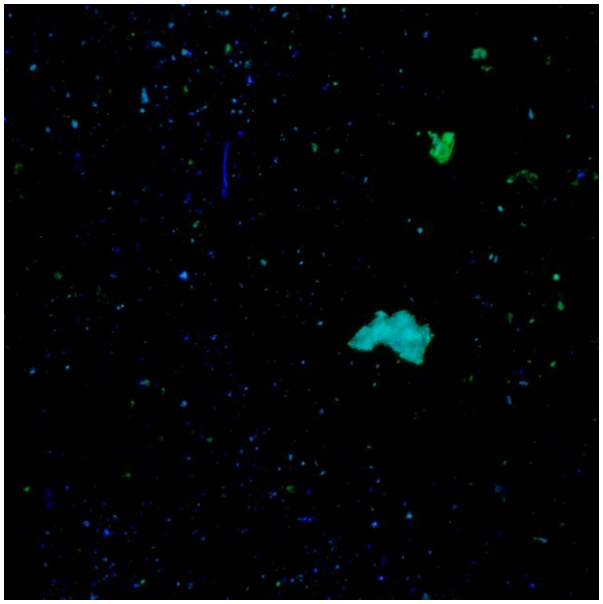

Figure 15. The membrane filter sample – filter mounted on the outer wall inside the cyclone [1].

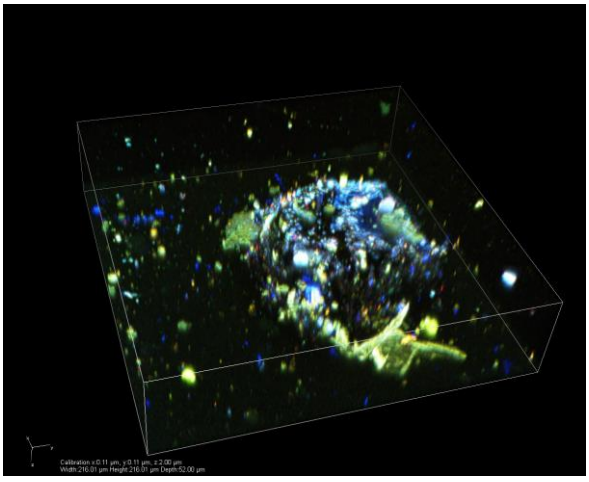

Figure 16. 3-dimensional image of a particle intercepted in the electric field on the cyclone's wall [1].

Developed since 2014 (with initial experiments carried out in 2013), the BX22 BuLMA experiment was the third BEXUS experiment built in Warsaw University of Technology (after BX06 Icarus and BX11 SCOPE 2.0); its developing process, the flight campaign and results were shown in various media affiliated with the University, inspiring next generations of students and young engineers to create their own ideas for stratospheric research. BuLMA Team members have gained (and are still gaining, as the analysis has not finished yet) a unique experience in participating in a real space project. This experience, cultivated in Students' Space Association's WUT Balloon Division, shall be exploited by the next generation of students taking part in the REXUS/BEXUS campaign.

6. REFERENCES

1. *BuLMA 2015 Student Experiment Documentation (SED) v5-0*. BEXUS 22 campaign. 2017

2. Souplet S. : *Des microméteorites dans le jardin (Micrometeorites in the garden)* [in:] Astronomie Magazine, number 155, april 2013 [In French]

3. Irion R. : *Na początku był chaos (In the beginning there was chaos)* [in:] National Geographic Poland, number 7 (166), july 2013 [In Polish]

4. *Odtworzyć kosmiczny pył… (To recreate the space dust…)* [in:] Astronomia, number 24, june 2014 [In Polish]

5. Miś T. A. : *Sonda stratosferyczna PARTICULA 1 (Stratospheric Probe PARTICULA 1) - final report*; Sekcja Balonowa SKA (Balloon Division - Student's Space Association) 2013 [In Polish]

6. Miś T. A. : *Sonda stratosferyczna PARTICULA 2 (Stratospheric Probe PARTICULA 2) - final report*; Sekcja Balonowa SKA (Balloon Division - Student's Space Association) 2013 [In Polish]

7. *Micrometeorites* [in:] Curry J. A., Holton J. R., Pyle J. A. Encyclopedia of atmospheric sciences, UK 2003

8. Maurette M.: *Micrometeorites and the Mysteries of Our Origin*. Berlin 2006

NORWEGIAN NATIONAL REPORT – ARCTIC ACCESS TO SPACE

Pål Brekke[(1)]
[(1)] Norwegian Space Centre, Norway, paal.brekke@spacecentre.no

ABSTRACT

Norway has long traditions as a space nation, much due to our northern latitude. Our space science activities are concentrated into relatively few areas. This concentration is necessary due to limited resources, both in funding and personnel. The main scientific activities are within Solar-terrestrial physics and cosmology.

The first field has been a priority since before the space age and is still the major priority. The usage of the ground infrastructure in Northern Norway and on Svalbard is essential in studying the middle and upper atmosphere and the interaction with the Sun. This includes the utilization of sounding rockets, both small and large, and ground based installations like radars, lidars and other optical instrumentation. The planned use of Svalbard as a launch site for large stratospheric balloons may allow the cosmology community access to our northern infrastructure. The solar physics community is also heavily involved in the HINODE and IRIS missions and Norway is supporting downlink of data via the Svalbard Station for these missions.

The sounding rocket program is in close collaboration with many countries like Germany, USA, France, Canada and Japan. Two scientific sounding rocket programs are currently being pursued: The ICI series (from Svalbard) and MaxiDusty (from Andøya). A series of scientific publications have recently appeared from the ECOMA campaign a few years ago.

A significant improvement of today's polar and ionospheric research infrastructure in Northern Norway and Svalbard has recently been put on the ESFRI roadmap for European research infrastructure through the SIOS and EISCAT 3D initiatives. The Norwegian government has recently decided to upgrade the VLBI facilities at Svalbard.

1. HISTORIC PERSPECTIVES

The early aurora and solar research led to the establishment of the rocket range on the island of Andøya in North Norway, where the first Norwegian research rocket was launched in 1962. Researchers from numerous countries now utilize this rocket range in their studies of the northern lights and the Earth's atmosphere and the facility is NASA´s most important launch facility for sounding rockets outside USA. More than 1000 rockets have been launched since 1962, the biggest being NASA's 15 meter long Black Brant XII, with an apogee of up to 1500 km.

Norwegian scientists participated in the solar telescope HRTS (High Resolution Telescope and Spectrograph) that flew on the space shuttle Challenger in 1985 and several times on sounding rockets. More recently they played a central role in the successful SOHO mission - a large satellite based solar observatory including 12 different telescopes and instruments launched in 1995, which is still operating. SOHO is a collaboration between ESA and NASA in which Norwegian industry provided equipment and services to the sum of 80 million Norwegian kroner.

Scientists at the Norwegian Defence Research Establishment (FFI) participated on Spacelab 1 flying onboard the space shuttle Challenger in 1983. They built the electron accelerator, which produced artificial aurora in space. Later Norwegian institutes participated in the European Space Agency's Cluster mission, a «space fleet» of four identical satellites flying in formation through the Earth's magnetosphere. The University of Oslo (UiO), The University of Bergen (UiB) and NDRE all delivered electronics and parts to three different instruments on Cluster.

2. OVERALL SPACE SCIENCE PRIORITIES

Due to its size and the resulting limited resources, Norway needs to concentrate efforts to compete with other space nations. Space related science in Norway can be divided into three major fields: research OF space, research FROM space and research IN space.

- "OF space"
  - Solar-Terrestrial physics (about 60%)
  - Cosmology
- "FROM space"
  - Ocean monitoring
  - Polar and climate research
  - Science leading to needed applications
- "IN space"
  - Plant physiology
  - Human psychology
  - Robotics and operations
  - Technology demonstrators

In this article, the main focus is science OF space and the other fields will just be mentioned briefly. Science OF space includes space physics with the emphasis on

the magnetospheric/-ionospheric physics and processes in the neutral middle atmosphere at high latitudes. Solar physics and cosmology and life sciences with a focus on plant physiology are also included.

Norway is participating in ESAs Space Situational Awareness program. The Norwegian Mapping Autority is contributing to monitoring space weather effects on the ionosphere and degradation of positioning systems. Tromsø Geophysical Observatory is monitoring deviations in the Earth's magnetic field. And the University of Oslo and EIDEL are developing miniaturized Langmuir-probes for space weather missions.

3. SOUNDING ROCKET PROGRAM

3.1 Andøya Space Center

Andøya Space Center (ASC) provides sounding rocket and balloon operations from Norway. ASC was established in the 1960s as Andøya Rocket Range and more than a thousand sounding rockets have been launched from Andøya since the first lift-off in 1962. Due to the increased and diversified activities, as well as the need for a modernisation of the company profile, the name was changed to Andøya Space Center in 2014. Both subsidiaries, Andøya Test Center (ATC) and NAROM were included in the modernisation of the profile program as well.

Figure 1. Andøya Space Center (ASC).

The sophisticated infrastructure includes a cluster of ground-based state-of-the-art instruments. The Norwegian Institute for Air Research (NILU), the Institute of Atmospheric Physics (IAP Kühlungsborn), ASC, the Norwegian Defence Research Establishment (FFI), University of Oslo, and eight other science groups from outside Norway run their instruments at ALOMAR (Arctic Lidar Observatory for Middle Atmosphere Research) and contribute to the running costs of the observatory. The instruments include five lidars, four atmospheric radars, and a number of passive instruments, such as an imaging riometer, all-sky camera, several spectrometers, microwave radiometers, and others. ASC has operated the observatory since 1994, celebrating its 20-years anniversary with a scientific symposium at ASC in 2014.

ASC offers the scientists the opportunity for in-depth studies of the Arctic atmosphere and ionosphere by both short- and long-term monitoring techniques which can be combined with in-situ measurements from rocket and/or balloons. The new Science Centre, located beside the ASC telemetry section, has replaced the former USOC and provides real-time monitoring of scientific parameters and other phenomena during operational campaigns.

ASC has recently ordered a new, mobile 23ft telemetry antenna to further enhance its telemetry services for NASA, DLR, JAXA and other customers. This procurement adds to the already fully updated ASC telemetry equipment featuring state of the art Cortex receivers, capable of 30Mb/s. Used together with the ATC telemetry, also of the same standard, ASC now is capable of serving the most demanding telemetry needs with a very high quality.

The high latitude location of ASC (69ºN), north of the Arctic Circle, is favourable because it is close to the southern boundary of the Polar Vortex and lies within the nightside auroral oval. The infrastructure gives the scientists the opportunity to exploit these advantages; the physics, chemistry and dynamics in all atmospheric layers can be investigated, thus both climate change and space weather parameters can be monitored.

In the context of Space Weather Services, there are several relevant ground-based instruments located at Andøya. In particular, the ALOMAR Imaging Riometer for Ionospheric Studies (AIRIS) is important because it can monitor the ionosphere and its response to particle precipitation. An All-sky camera will monitor the aurora and the cluster of radars have the capability to monitor the mesosphere and lower ionosphere and provide information on electron density, meteors, turbulence, wind field and tides.

The ALOMAR observatory provides measurements of the troposphere to the lower thermosphere and includes profiles of temperature, total density, wind speed and direction, certain trace constituents such as Na and O_3, atmospheric gravity waves and their momentum flux. Several of the scientific parameters that are monitored play an important role regarding the space weather. ASC also has the knowledge and expertise to build sounding rocket payloads, which can be used to study parameters relevant to the understanding of space weather phenomena.

Sounding rockets could either be launched from Ny Ålesund (78.92°N, 11.93°E) on Svalbard (SVALRAK) or at Andøya (69.28°N, 16.01°E). At Andøya two launchers are capable of launching large rockets such as Black Brant XII up to more than 1600 km in altitude. At Ny Ålesund the launcher can launch rockets to altitudes above 1100 km while from Longyearbyen (78.25°N, 15.47°E) long duration balloons are launched up to altitudes between 30 and 40 km.

So far in 2017 (and since late 2015) five sounding rockets have been launched from ASC. NASA CARE-2 (Sept 2015), NASA RENU-2 (Nov 2015), NASA CAPER (Dec 2015) and DLR/UiT Improved Malemute/MaxiDusty 1 and 1b (July 2016). The first launch of the NAMMO 28 kN hybrid rocket motor – NUCLEUS, is scheduled for September this year. The NUCLEUS payload, built by Space Systems dept. at Andøya Space Center, will also be used to test a new ASC developed pyro-system, version 2 of the ASC/UiO 4D-Space module and a Sensonor IMU unit.
As a major player in the upcoming Grand Challenge Initiative – CUSP project, NASA is having 9 out of the 11 sounding rockets scheduled for launch from ASC and SvalRak between December 2016 and November 2019. More about GCI – CUSP later.

The NUCLEUS, which will serve as the basic building block for the North Star series of rocket motors, has been undergoing full scale static testing at NAMMO's new hybrid test center at Raufoss since mid-2014. The NUCLEUS will serve as the second stage on two stage rockets from ASC, and will be complemented by the a bigger version – the AURORA booster, which will consist of a cluster of 4 NUCLEUS motors. The AURORA is expected to be ready for test in 2016, providing ASC and associated scientists with a hybrid, controllable and environmentally friendly alternative to the Brazilian S-30 booster and US Improved Orion.

3.2 ICI Rocket Programme

The Norwegian Investigation of Cusp Irregularities (ICI) rocket program, led by University of Oslo, takes full advantage of Svalbard's ideal geophysical location under the daytime part of the auroral oval to study solar wind interaction with the Earth's magnetic field and subsequent energy deposition into the upper atmosphere. There is world class space research infrastructure in place at Svalbard, and this is the only place in the world where we can continuously monitor the ionospheric response to magnetopause reconnection by auroral cameras and radars from ground, and simultaneously in-situ by rockets. Sounding rockets are however rare, but they are also the sharpest tool to conduct frontier research on waves, instabilities, and turbulence phenomena in the ionosphere. UiO has during the past 15 years built capacity in the ICI sounding rocket program, to facilitate studies of multi-scale physics in the daytime auroral ionosphere. The primary objective is to explore the physical properties of plasma turbulence in the F-region cusp ionosphere. This is grand challenge research motivated to deliver know ledge for physics based space weather models to predict disturbances in GPS navigation and communication systems .

UiO has invented a multi-Needle Langmuir Probe System (m-NLP) to make high-resolution density measurements along the rocket trajectory. However, such measurements along a single rocket trajectory being one dimensional and they do not allow us to determine the spatial extent of ionospheric plasma irregularities, nor do they provide any unambiguous answer regarding whether the observed structures are due to the linear superposition of decoupled normal modes (waves), or due to turbulent interactions across a wide range of scales caused by some plasma instability. The ICI-5 sounding rocket flight in January 2019 will be equipped with two 4DSpace modules, each containing 6 miniaturized sub payloads that each carries an m-NLP instrument. This new technique will provide the first 3D measurements of ionosphere plasma turbulence, and we will be able to determine the spatial scales of turbulence which will be pivotal to discriminate between plasma turbulence and plasma wave phenomena.

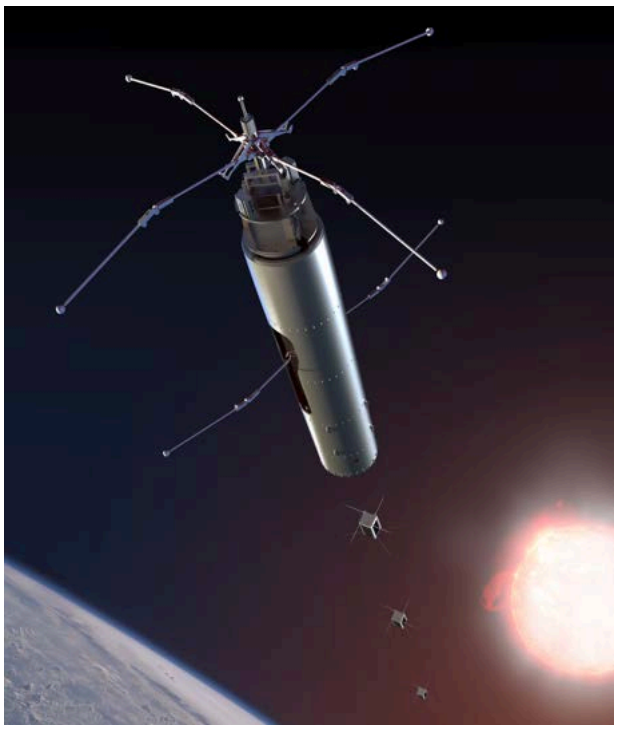

Figure 2. Artist concept of future ICI-4 (T. Abrahamsen, ASC)

ICI-2 was successfully launched from Ny-Ålesund in 5 December, 2008. It intersected 3 regions of HF radar backscatter targets. With UiO's new concept Langmuir probe system it measured absolute electron density at 5.7 kHz resolution, and for the first time it resolved decametre HF backscatter irregularities.

ICI-3 was launched from Ny-Ålesund in December 2011. The ICI-3 payload consisted of several instruments with contributions from University of Oslo (UiO), Japan Aerospace Exploration Agency/Institute of Space and Astronautical Science (ISAS/JAXA) and Laboratoire de Physique des Plasmas (LPP). University of Alberta, Canada contributes to the payload instrumentation of ICI-4 that will be launched in December 2013As illustrated in Figure 3 the ICI-5 rocket planned for December 2016 will include three or more sub payloads.

3.3 MUDD/MAXIDUSTY Rocket Programme.

The aim of the MAXIDUSTY (MXD) programme at the University of Tromsø, in cooperation with the University of Oslo, is to enhance our understanding of key physical and chemical processes in the Earth's mesosphere and of its coupling to other atmospheric regions. The project represent a continuation of the Norwegian rocket programme on the mesosphere, including the rocket projects TURBO, TURBO/DUSTY, MINIDUSTY, MIDAS, ROMA, and ECOMA. The MXD project has a particularly strong emphasis on the investigation of dust and aerosol particles, compared to earlier mesosphere projects. The first launch in this programme (MXD-1) was 30th June 2016 at 09:43:18 UTC, and the second (MXD-1B) on the 8th July 2016 at 13:01:00 UTC . The launches contained 11 different experiments with 6 aimed at measuring dust particles. There are two new instruments, the MUDD (Multiple Dust Detector, built by University of Tromsø - UiT) to measure the fragments produced by impacting icy particles near the mesopause and a mass spectrometer ICON (UiT). ICON looked for elements besides water vapour, for example meteoric metals. MXD-1 also contained a photometer. MXD-1B contained 6 daughter payloads to be released below the NLC/PMSE clouds, in addition to several plasma and dust detectors.

Instruments for a MXD-2 are being constructed. It will contain most of the instruments of MXD-1 in addition to a new instrument MESS (Meteoric Smoke Sampler - UiT). It works on the much the same principle as ICON, and icy particles are channelled into a collection chamber to be opened below and closed above the NLC/PMSE layers. The NLC icy particles should contain a large amount of meteoric smoke particles (MSP) and we expect that when the ice evaporates the MSP will remain. MESS will be recovered and the collection chamber inspected for MSP which will be analysed.

3.4 The Grand Challenge Initiative Cusp Project

The Grand Challenge Initiative (GCI) is a large-scale international collaboration effort targeting advancement in specific, fundamental issues in space and earth science. The GCI concept was conceived and developed over the past two years by the Andoya Space Center (ASC) and the University of Oslo. Their work has culminated in the first GCI project – "GCI Cusp" – to determine the multi-scale physics of heating and charged particle precipitation in the ionosphere specific to the geomagnetic cusp region.

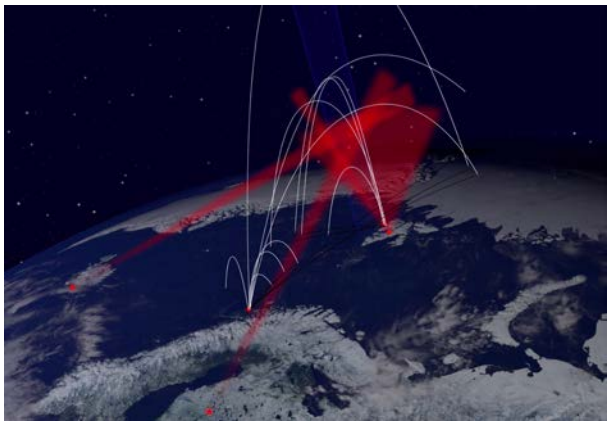

Figure 3. The Grand Challenge Initiative consist of a large number of coordinated observations (ASC)

The GCI Cusp Project is designed to advance the common understanding of cusp region space physics through coordinated experimental and theoretical research using ground based instruments, modelling, sounding rocket investigations, and satellite based instruments. International student participation through space plasma model development and a dedicated student rocket (G-CHASER (US/NOR/JAP)) is an essential aspect of the GCI concept. Strategic use of public outreach, particularly via the tools of social media, is also a vital component of the GCI Cusp Project.

The GCI CUSP project currently includes 11 sounding rockets from 8 separate projects. 9 rockets from NASA, 1 from ISAS/JAXA, plus ICI-5 from Norway. GCI Cusp scientific work will engage with the wider community and data will be shared through the Svalbard Integrated Arctic Earth Observing System (SIOS).

4. KJELL HENRIKSEN OBSERVATORY

The old Aurora Station in Adventdalen at Svalbard was built in 1978 but was in recent years outdated and hampered by increasing light pollution from Longyearbyen. The Kjell Henriksen Observatory is the largest of its kind with a gross total area of approximately 700 square meters, which includes a service section of approximately 200 square meters floor space and an instrument section with 30 instrument rooms with domes. The activity has been high since it was opened in 2008.

Figure 4. Kjell Henriksen Observatory (KHO) at Breinosa 12 km from Longyearbyen. View is from the roof of KHO towards South-West. Photo F. Sigernes (2010).

During the auroral winter season from November to the end of February, 28 optical instruments operate 24 hours a day. The 13 non-optical instruments run all-year-round 24 hours a day. 21 different institutions from 13 nations were present at KHO in 2016. KHO also serves as the main laboratory for hands on training and teaching of students in the Space physics group at UNIS.

The main task of KHO is in general to study processes associated with the Magnetospheric cusp and its connection to the Sun-Earth environment. The dayside aurora gives an open window to processes on the Sun and how they interact with our upper atmosphere. Studies of phenomena such as airglow and aurora are therefore essential for understanding of how energy is transported into the Magnetospheric Clefts down the whole vertical column of the atmosphere, and how it on a larger scale contributes to the climate

KHO was a central part of the Rocket Experiment for Neutral Upwelling 2 (RENU2) campaign launched in mid-December 2015 from Andøya Space Centre. KHO instruments together with the Eiscat Svalbard radar identified and tracked the target - the dayside aurora – successfully. KHO will support and play a vital role in the Grand Challenge Initiative (GCI).

Each instrument at KHO has its own scientific task and objective listed at the observatory's own home page: http://kho.unis.no.

5. EISCAT

EISCAT (European Incoherent Scatter) Scientific Association are currently operating 3 large radar systems, two at the Scandinavian mainland with transmitters and receivers located outside Tromsø, and external receivers in Kiruna, Sweden and Sodankylä, Finland. The third system is located on Svalbard, on the mountain Breinosa outside Longyearbyen, in close proximity to the Kjell Henriksen Observatory (KHO).

The EISCAT radars are capable of studying several fundamental processes in the Earths upper atmosphere and ionosphere, and, as it is using radar techniques, are not dependent on light of weather conditions.

A major upgrade of EISCAT's facilities on the Scandinavian mainland has been under investigation in recent years, through funds from the EU's 7th Framework Program and Horizon2020. Next generation radar - EISCAT-3D - will be a phased array radar system with main transmitter and receiver located outside Skibotn in Norway, with external receivers in Bergfors, Sweden and Karesuvanto, Finland. Smaller external receivers will be placed in the vicinity of the main transmitter, which will help resolve the very small structures in the northern lights. Such a phased array radar system with external receiver stations will be able to conduct continuous 3 dimensional measurements of processes in the Earth's upper atmosphere / ionosphere and will greatly contribute to the understanding of several important science questions, such as turbulence and coupling between processes on different scales.

Data from the EISCAT system, together with data from the worlds other Incoherent Scatter Radars, are openly available in the MADRIGAL database http://cedar.openmadrigal.org and can be used by researchers and educators from across the world – adhering to the EISCAT datapolicy.

6. SUPERDARN

The new Svalbard SuperDARN (Super Dual Auroral Radar Network) HF Radar is also located at the Breinosa mountain on Svalbard. The Svalbard SuperDARN radar (http://kho.unis.no/sd/sd.htm) is part of a network of over 30 radar facilities which continuously monitor the motion of plasma in the

Earth's ionosphere over both the Northern and Southern polar regions, utilizing the high frequency (HF) radio band between 8 – 20 MHz. This facility is owned and operated by UNIS and was built in 2016 and funded through industrial collaboration with ConocoPhillips and Lundin though their High North Research Program. It is the first of its kind to be built in the European high arctic sector and represents Norway's entry into the international SuperDARN radar community (which consists of 17 research groups from 10 countries.

A transmitted signal is reflected back to the radar from plasma structures allowing the location and motion of the ionosphere to be measured. The strength of the returned signal, combined with the speed of the structures is directly related to ionospheric turbulence and the coupling of the Earth's magnetic field to the Solar Magnetic Field. All SuperDARN radars operate in the same standard mode, using the same radar control software allowing data to be assimilated into a single database. Each radar has 16 contiguous pointing directions, yielding a 52 degrees angular coverage. Plasma structures can be observed over distances of between 180 km to ~3300 km away from the radar site, up to a resolution of 15 km. The database provides both real-time and archived observations of the global high altitude atmospheric circulation in the polar regions and is available to scientists from around the world where it has wide ranging applications from scientific research to educational outreach in addition to having possible industrial applications in the communications and navigation sector.

7. BIRKELAND CENTRE FOR SPACE SCIENCE

Named after the celebrated Norwegian space scientist and inventor Kristian Birkeland (1867-1917) the Birkeland Centre for Space Science (BCSS) is a centre of excellence established in 2013 to solve major outstanding puzzles related to the coupling of Earth with space. Following the tradition of Birkeland, the centre embraces a multi-disciplinary approach that combines observations of natural phenomena from ground and space, experiments done in the laboratory, theoretical analyses, and numerical simulations to deliver ground-breaking results. The centre also joins together expertise covering the atmosphere, ionosphere, magnetosphere, particle physics and astrophysics to form a unique team designed to tackle broad questions across traditional disciplinary boundaries. Current main topics of investigation include: understanding when and why the aurora in the southern and northern hemispheres are asymmetric, better understanding of the dynamic ionosphere, the effects of particle precipitation on atmospheric chemistry, weather, and climate, and understanding the production of energetic particles in thunderstorms.

BCSS is anchored at University of Bergen with contributions also from NTNU and UNIS and involving partners and collaborators worldwide. Building on significant investments in existing infrastructure for ground-based observations at Svalbard and in Northern Norway as well as UiB's well-established capability in space instrumentation, the centre serves as a natural focal point for space physics research in Norway and for ensuring the optimal utilization and leverage of these national assets. Having established itself firmly as a powerhouse for frontline space physics research, BCSS plays a crucial role in maintaining and strengthening the international recognition of the Norwegian space physics community.

The successful completion and delivery in 2016 by BCSS of the Modular X-and Gamma-ray Sensor (MXGS) to the ESA Atmosphere Space Interactions Monitor (ASIM) project constitutes the largest space instrumentation project ever undertaken by Norwegian academia. The ASIM payload will be launched in January 2018 and mounted on the International Space Station (ISS), to study the coupling of thunderstorm processes to the upper atmosphere, ionosphere and radiation belts. The engineering model from ASIM was also flown April-May, 2017 on an ER-2 aircraft at 20 km altitude above thunderstorms in Georgia, US to detect terrestrial gammaray flashes from lightning.

BCSS is also involved in the new SuperDARN radar wa on Svalbard. BCSS was also instrumental in the development and implementation planning for the proposed EISCAT-3D radar. Further, BCSS is involved in a new space mission by the name of SMILE, which is a collaboration between ESA and the Chinese Academy of Science aimed at imaging the entry of solar plasma into near-Earth space in both polar hemispheres. With the support provided to the ESA SWARM mission, BCSS is now in the unique position that it participates in all three major programs at ESA: Earth Observations (SWARM), Human Space Flight and Exploration (ASIM/ISS), and Space Science (SMILE).

8. TROMSØ GEOPHYSICAL OBSERVATORY

Tromsø Geophysical Observatory (TGO), is a small unit under the Faculty of Science and Technology at UiT – the Arctic University of Norway. The unit exist to continue and ensure the quality of the long time series of geophysical measurements performed in Northern Norway since the establishment of the Haldde observatory (1916) and the Auroral Observatory (1928).

TGO operates a network of 18 magnetometers in mainland Norway and Norwegian areas in the Arctic. Three of them - Bear Island, Tromsø and Dombås - are geomagnetic observatories, the remaining are stable

variometers with less accurate absolute calibration aimed to serve ionospheric physics and monitoring magnetic field variations for space weather purposes. Data from the stations are included in the IMAGE and SuperMAG databases.

Near real time data can be found at http://flux.phys.uit.no/geomag.html where they are displayed along with corresponding data from Finland, Denmark, Greenland, Alaska, Canada and Russia.

Additionally, TGO is operating an ionosonde near Tromsø; this instrument represents one of the world's longest time-series of ionospheric electron density soundings dating back to 1934. TGO also operates three meteor radars (jointly with Japanese institutions) at Tromsø, Alta and Longyearbyen, an MF radar (with Japan and Canada) at Tromsø, the SOUSY MST radar and an imaging riometer (with Denmark) in Longyearbyen. Recent new operations include single-beam riometers in Ny-Ålesund and Skibotn. TGO is also contributing to the operation of a sensitive, multispectral all-sky imager owned by UiO at Skibotn.

8. SPACEWEATHER SERVICES

9.1 Ionosphere monitoring service "seSolstorm"

The Norwegian Mapping Authority (NMA) has developed a publicly accessible service that displays an overview of the state of the ionosphere, as viewed from a GNSS perspective, in real-time. The service is primarily intended for users of the positioning service CPOS, but is open to everyone. The main parameters are the total ionospheric electron content (TEC) and the Rate-Of-TEC Index (ROTI), which is a measure of ionospheric turbulence level. These parameters are related to errors in GNSS positioning. The service can be accessed at http://sesolstorm.kartverket.no/.

9.2 Ionosphere monitoring service at ESAs space weather portal

As part of ESAs Space Situational Awareness program, the NMA has developed a service of the same kind as that described in the previous paragraph, but with additional products available. The additional data products are scintillation maps, and data files for all types of data displayed. The service is currently accessible at http://swe.ssa.esa.int/web/guest/rtim-federated. It requires the user to log in to the ESA space weather portal system. The only requirement for getting an account is that a valid email address is needed.

9.3 A service Supporting Resource Exploitation System

As part of the ESA SSA program preparatory phase project Provision of Space Weather Additional Services (SN-VI) led by Rhea Group, TGO and the NMA have developed a Service Supporting Resource Exploitation System Operators (RESSOS).

The RESSOS service provides near real-time information about geomagnetic disturbances which primarily affect directional drilling and aeromagnetic surveys, and ionospheric disturbances which primarily affect GNSS-based services. The RESOSS service provides these two independent service components as parts of a single service. RESOSS will be aimed at a broader user base, and introduces existing end users of the detailed service components to additional, available and related service components, which should be of interest and benefit to them.

9.4 The Norwegian Center for Space Weather

TGO has for many years supported the oil industry with real-time magnetometer data during directional drilling operations on the Norwegian continental shelf. The experience from this type of space weather related activity has gained TGO the role of Expert Service Center coordinator for geomagnetic conditions within the ESA Space Situational Awareness (SSA) program. TGO currently participates in many activities within this program. In light of the above and the increasing awareness of space weather in non-scientific areas as well as the increasing commercial activity in the auroral zone/Barents Sea, the Norwegian Center for Space Weather (NOSWE) was established as a unit under TGO during summer of 2014. The Norwegian Space Center is supporting the development of the center, which will be built around a physical forecasting room from where space weather will be monitored and forecasts issued. The main purpose of NOSWE is to act as a tool to enhancing Norwegian abilities to participate in the ESA SSA program, to be a national source for information and knowledge about space weather hazards and to provide means towards mitigation of these. An important aim of NOSWE is to establish contact with national directorates, industries and other activities that are vulnerable to or dependent on space weather, ranging from search and rescue and offshore drilling operations to the tourist industry and the amateur radio community. Already, collaboration with Norwegian power grid company, Statnett, is underway to increase preparedness for major space weather events.

10. GEODETIC RESEARCH

The Space Geodetic Research Facility of the Norwegian Mapping Authority in Ny Ålesund, Svalbard, is part of an international network of stations, which is crucial for society's satellite-based infrastructure and provides the basis for accurate climate monitoring in the far north. The observatory is the northernmost facility of its kind, and maps movements in the Earth's surface, planetary rotation, and the Earth's position in space. The Norwegian government appropriated funds for a new geodetic observatory with new technology in its revised national planning budget for 2012. Construction of the new geodetic observatory is under way after the first pile was driven in the autumn of 2014. The new observatory is due to be completed in 2018.

Figure 5. The twin VLBI antennas of the new observatory in Ny Ålesund, Svalbard (Photo: Norwegian Mapping Authority)

The upgraded observatory will combine several geodetic measuring techniques - very long baseline interferometry (VLBI), satellite laser ranging (SLR), global navigation satellite systems (GNSS) – including GPS – and doppler orbitography and radio positioning integrated by satellite (Doris), based on the standard set by the global geodetic network. Norway's Uninett group has laid fiber optic cables on the seabed between Longyearbyen and Ny-Ålesund. This link is important for the research community at the latter site. The cables were in operation for the first time on 9 May 2015. With this fiber optic link, the Norwegian Mapping Authority will be able to transmit real time data from its new observatory to such recipients as NASA in the USA and the international geodetic research network.

11. EGNOS AND GALILEO PERFORMANCE

Considering the limitations in available infrastructure in the arctic, there is a need for improved navigation services in this area. A good performance and coverage by satellite based navigation systems is therefore of great importance. Such systems are particularly vulnerable to space weather effects that are a regular occurrence in the arctic ionosphere. Independent monitoring of the performance of GNSS at high latitudes is therefore important.

The Norwegian Mapping Authority (NMA) is currently continuously monitoring the European EGNOS and Galileo (from 2017) system performance with a particular focus on the ionosphere and its impact on these systems. The results from the monitoring are part of the Norwegian contribution to the EU/GSA project "EGNOS Service Performance Monitoring Support" (SPMS).

Large parts of the Arctic are presently not covered by SBAS services (EGNOS), so improving this coverage would be a significant contribution to the navigation in the arctic. The ESA Arctic Testbed Project (ATB) is an important contribution to achieve this goal. The main objective of Arctic Testbed is to contribute to the evolution of EGNOS, with the focus on extending the secure satellite navigation in the Arctic region. Kongsberg Seatex is the prime contractor. The Norwegian Mapping Authority is responsible for the operation of the ATB Control Centre, as well as performing several experiments using the SPEED platform. The SPEED platform is a hardware and software platform implementing the EGNOS algorithms and design.

12. SOLAR RESEARCH

The solar research environment blossomed early in Norway and today Norway has one of the strongest solar research groups in the world. Today observations of the sun are carried out from large international observatories as well as from satellites. Norway is currently involved in several missions including the SOHO mission and the Japanese solar satellite Hinode. Data from the satellite are downloaded at the Svalbard archipelago and a European data centre at the University of Oslo is processing the raw material making it accessible for the entire European science community.

In addition, Norwegian scientist are involved in NASA's Solar Dynamics Observatory (SDO) launched in 2010. SDO is a super-telescope taking images with four times higher resolution than HD-TV quality every 10 seconds, transmitting 1500 Gb of data every single day. The NASA solar mission IRIS (Interface Region Imaging Spectrograph) was launched in June 2013 with a significant Norwegian contribution in modeling of the solar atmosphere as well as providing downlink of data via the Svalbard Satellite Station.

What has become increasingly clear is that a proper utilization of high quality satellite data requires extensive numerical modelling. This is needed in order to make the connection between observed quantities such as spectral lines and the physical conditions in the radiating atmosphere. The solar physics group in Norway has built up a considerable expertise in this area and is now, as one of the first groups in the world, producing three-dimensional models of the solar atmosphere, from the convection zone to the corona. These models include enough of the relevant physics so that synthetic observations from them can be compared directly with observations.

12.1 ROSSELAND CENTRE FOR SOLAR PHYSICS

The Rosseland Centre for Solar Physics is a centre of excellence established in 2017 that will push the boundaries of solar physics by exploiting and extending the unique combination of cutting edge expertise in observational data and numerical simulations at the Institute of Theoretical Astrophysics, University of Oslo. The overarching goal of the centre is understanding the workings of the energetic Sun. This is an ambitious goal and an important research focus for the international solar physics community. The proven track record in understanding and integrating simulations and observations into a coherent picture of the quiet solar atmosphere puts the centre in an excellent position to tackle the more complex challenges presented by the energetics of the active Sun and bring the field to a new level.

13. COSMOLOGY AND ASTRONOMY

A small cosmology group has existed at the University of Oslo since the 1960's, but in the last decade it has grown to become an internationally leading research group. Presently the most important research subject is the Cosmic Microwave Background, the group emphasizes the closest interaction between analysis of data from experiments and fundamental theory to further the understanding of the Universe.

The last decade has seen an enormous growth in cosmology, making it a leading branch of both astronomy and physics. While cosmology until one or two decades ago was a data-starved science, the opposite is the case today. The wealth of new data coming out of new large space- and ground-based experiments has made cosmology a data-rich science where one poses detailed questions and where simplified models are no longer sufficient. Already with NASA's Wilkinson Microwave Anisotropy Probe (WMAP), large classes of cosmological models are today ruled out, and a concordance model has been established.

The cosmology group concentrates its activities on studies of the cosmic microwave background through ESA's Planck mission and until recently the ground based QUIET experiment, and on research preparing for the Euclid space mission, which will be launched in 2021, concentrating on models that can explain the mysterious observed acceleration of the expansion of the Universe. The group's studies of large-scale anisotropies in the cosmic microwave background have caught world-wide attention. About 20 people at the University of Oslo have been involved in analyzing the results from Planck. The initial cosmological results from Planck were released in 2013, the next results, including the full set of observations, both in temperature and polarization, were released in 2015, and the final results from Planck are expected to be made public in 2017/2018. The UiO group has contributed strongly to separation of components, estimation of power spectrum, measurements of gaussianity of the fluctuations and of large-scale anisotropies. Research based on the results from Planck will continue for many years to come.

14. PLANETOLOGY

During the last years, a group working on comparative planetology has emerged at the UiO. This group mainly focuses on the dynamics and evolution of Earth and planets. Using the surface record of volcanic and tectonic features together with numerical modelling of the interior dynamics they try to decipher why Earth is the only planet, which shows active plate tectonics. For the temporal evaluation cratering statistics (spatial density of craters) is used.

The group is developing new cratering chronology models for the inner solar system, by improving the scaling relationships between impact crater and projectile (sizes) using numerical simulations of impact crater formation, by n-body simulations of the projectile populations (asteroids and comets) to describe the bombardment flux through time, and detailed characterisation of the surfaces of planetary objects. They also build and exploit a spectral library of planetary terrestrial analogues, for the characterisation of the mineralogical and geological evolution of terrestrial planets and small Solar System bodies using laboratory experiments under controlled conditions to gain in depth understanding of the rock and mineral alteration in different climatic and atmospheric conditions for example on Mars.

15. SPACE EXPLORATION

Svalbard offers a unique variety of geological sites in an Arctic dessert environment perfectly suited for planetary exploration. Mars analogue activities have been ongoing since 1997 when rocks in the Bockfjord Volcanic Complex (BVC) were discovered to be identical to the Martian meteorite ALH84001. The Arctic Mars Analog Svalbard Expedition project (AMASE) was initiated by Norway in 2003 and is funded by ESA and NASA to develop and test instruments onboard "Search for Life" missions to Mars including Mars Science Laboratory, ExoMars and Mars Sample Return. AMASE also provides training for mission scientists and engineers as well as field-testing of astronaut suites and robotic platforms and plays an important role in fostering collaboration between ESA and NASA teams.
The Norwegian Defence Research Establishment (FFI) developed and tested a prototype of the WISDOM georadar for the ESA ExoMars mission. WISDOM will chart ice, water and rocks to a depth of three meters on Mars and is being field tested on AMASE. FFI is now developing the ground penetrating radar RIMFAX for NASA's Mars 2020 rover mission. FFI was also responsible for the CAPS instrument designed to study plasma processes onboard the Cassini mission. The University of Bergen delivered components to the SIR-2 infrared spectrometer on the Indian Chandrayaan-1 lunar mission.

16. INTERNATIONAL SPACE STATION

The International Space Station (ISS) also contains a mini-greenhouse (EMCS - European Modular Cultivation System). All experiments in this mini-greenhouse are controlled and operated from the Norwegian User Support and Operation Centre at the CIRiS. Everything - water, nutrients, light, temperature - are controlled by commands from this centre. The first Norwegian experiment on the ISS called MULTIGEN-1 was performed in 2007 and the scientists are very satisfied with the results. One of the major results obtained solved a problem that has been a challenge since Charles Darwin asked the question about gravity and plant movements as they grow; Are circumnutations in plants dependent on gravity or will internal control mechanisms in plants also participate? The results from the ISS show clearly that both factors are required.

The Oslo branch of the research and technology group SINTEF has developed the Multi-Comcponent Trace Gas Monitor (ANITA) to monitor air quality on the International Space Station (ISS). The instrument was launched in 2007 on the space shuttle to detect whether the air might contain gases potentially hazardous to the astronauts. The instrument can trace gasses no other previous systems on ISS could detect. Only ANITA detected a leak in the cooling system in 2007. An operational instrument for the Space Station and in preparation of possible future missions, ANITA 2, is under development.

The University of Bergen is one of the key participants in the ASIM instrument to be installed externally on the International Space Station for observation of transient effects such as sprites, elves and blue jets. ASIM (Atmosphere- Space Interaction Monitor) is scheduled for launch in march 2017.

NORAIS-2, the second generation AIS receiver for the International Space Station, was successfully integrated on ISS in February 2015. The NORAIS-1 receiver has been successfully brought back to Norway for technical inspection and will be a valuable space-historic artefact.

17. ACCESS TO SATELLITE DATA

Norway has since the early 1980 been active in development of satellite based services for Marine situational awareness including oil spill. - ship and ice detection. The services are primarily based on data from polar orbiting radar satellites. This near real time operational services is used world-wide among others by the European Maritime Safety Agency. The services are being developed through various national initiatives and offered commercially by Kongsberg Satellite Services (KSAT).

KSAT also owns and operates the world¹s largest station for satellites in polar orbits (KSAT SvalSat) located at Svalbard Norway. Combined with the other KSAT ground stations daily contacts are made to about 100 satellites using more than 120 antennas world wide. Important Norwegian antenna installations are also located in Tromsø and at the Troll Station (TrollSat) in Antarctica. All the major space agencies are using Norwegian ground stations, including ESA, NASA and JAXA. KSAT services ensures easy access to high quality science data for Norwegian scientists.

Norway is therefore a significant operational user of remote sensing data from satellites, and Norwegian scientists are involved in many of ESA's Explorer satellites for earth observation research. We will not go into the details in this article.

17.1. Ship Detection from Space

In July 2010 Norway's first satellite for ship traffic monitoring was launched. AISSat-1 has been a big success, and a copy AISSat-2 was launched in 2013. A Norwegian built AIS receiver has also been placed on the ISS and is being used for anti-piracy operations in the Indian Ocean. Combined with the oil spill detection from radar satellites, the space based AIS system is a

unique system to detect and identify illegal release of oil or illegal fishing and even support monitoring of pirates.

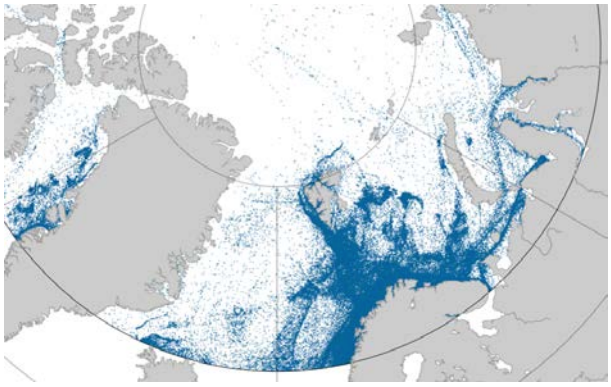

Figure 6. AISSat-1 has for the first time monitored all ship traffic in the Arctic and it is obvious that mots traffic is within Norwegian territories.

Norway has built two new small satellites called NORSAT-1 and 2 and they were launched in July 2017. The payload consist of a new generation Solar Total Irradiance monitor delivered by PMOC/WRC in Switzerland and is providing important data for the Sun-climate connection. A multi-Needle Langmuir Probe system by University of Oslo provides ionosphere space weather measurements while a new AIS receiver is being tested out.

Figure 7. NORSAT-1 was launched in 2017 and provides Sun-Earth connection observations as well monitoring ship traffic.

18. EDUCATION AND PUBLIC OUTREACH

NAROM (Norwegian Center for Space-related Education), partly funded by the Norwegian Government, offers educational programmes for teachers and students at many different levels to promote appreciation for the benefits of space activities, to facilitate recruitment in the space industry, and to stimulate an interest in science in general.

NAROM is co-located with Andøya Space Center (ASC). The close proximity to the facilities and personnel at ASC provides important advantages with respect to educational activities, and NAROM uses the unique technical facilities at ASC to provide an exciting educational experience. The Nordic European Space Educational Resource Office *ESERO* is established at NAROM . The office provides five different courses for teachers in upper secondary schools.

18.1 Student Satellite Program

NSC is actively sponsoring a student satellite programme in Norway, which is implemented together with NAROM and ASC. The aim is to plan, build, launch and operate three student satellites within three Norwegian Universities. One satellite has been launched, but attempts to obtain contact with it have not been successful. Two others are currently being built, for possible launch in the future. More than 230 students have participated in the program. These students have produced more than 4 700 ECTS credits related to the program. In 2017 NAROM did a survey of a list of 119 former students who had been active in the program. About 26% of these students was in February 2017 working in a space related company.

18.2 CaNoRock – a Canadian Norwegian Student Exchange & Rocket Programme

The Canada-Norway Student Sounding Rocket (CaNoRock) exchange program is a partnership between the Universities of Alberta, Calgary and Saskatchewan, the University of Oslo, University of Tromsø, Andøya Rocket Range and NAROM (Norwegian Center for Space Related Education) in Norway. Twice a year CaNoRock runs a one week hands on rocket campaign for 10 Canadian and 10 Norwegian BSc students. An International space mission training program (2017-2020) will run in parallel with CaNoRock, which includes NTNU and University of Bergen as additional partners. This space mission training program is funded by the Norwegian Centre for International Cooperation in Education (SIU) and is motivated to enhance mobility of students and to develop a joint curriculum. The plan is to develop an educational program around development of CaNoSat-1 to be launched in 2020.

In conjunction with the upcoming October visit to Andøya Space Center by the Canadian Ambassador to Norway (CaNoRock 14 launch), an international workshop will be held at ASC to further elaborate the plans for a Canadian/Norwegian CaNoSat-1.

18.3 European Space Camp

Each year a group of students (17-19 years old) from all over the world meet at Andøya Space Center to learn more about the Sun, the atmosphere, and the aurora. After a week they are among the few that can call themselves real rocket scientists.

The goal of Space Camp is to let the students take part in real science. They get to work with the same tools as real rocket scientists. Tutors guide the students while they construct their own instruments to take measurements in the atmosphere. The highlight of the Space Camp is the launch of a student rocket with self-built instruments and sensors.

18.4 Nordic ESERO

The European Space Education Resource Office (ESERO) project is ESA's main way of supporting the primary and secondary education community in Europe. ESERO Norway was established in 2009 and expanded in 2013 to Nordic ESERO, an office for the Nordic countries since Norway, Sweden, Denmark and Finland (01.01.2013 - 01.05.2017). Nordic ESERO in collaboration with ESA, NSC and several partners in the Nordic countries.

ESERO uses space related themes and the genuine fascination felt by young people for space to enhance school pupils' literacy and competence in STEM-related subjects. The ESERO project also highlights the associated applications from space and raises awareness of the large range of career prospects in the space domain.

By using the space context to make the teaching and learning of STEM subjects more attractive and accessible, pupils can feel more comfortable and familiar with sciences in general. The ESERO activities help bring STEM subjects within the pupils reach, demolishing the misconception that science is only for geniuses. Space, in particular, becomes not just a place of inspiration and future dreams, but also an everyday fact of modern life.

One of the main activities for Nordic ESERO is to provide teacher training courses for primary and secondary teachers. A total of 2586 Nordic teachers have in the period 2013 – 30.04.2017 attended these courses. Nordic ESERO will with the support from ESA and all partners continue for the next period 01.05.2017 – 31.12.2019 with Norway, Sweden and Finland.

18.5 Spaceship Aurora

Spaceship Aurora is a visitor-educational center connected to NAROM and Andøya Space Center. The main attraction, a virtual trip to space, serves as an entrance to a collection of exhibitions and films, all of which communicate the wonders of space science and especially aurora.

School students and private visitors alike can take part in scientific experiments, launch virtual rockets and get a glimpse of life at a space center. With its focus on education, Spaceship Aurora has suitable activities at every age and in different languages, Norwegian and English.

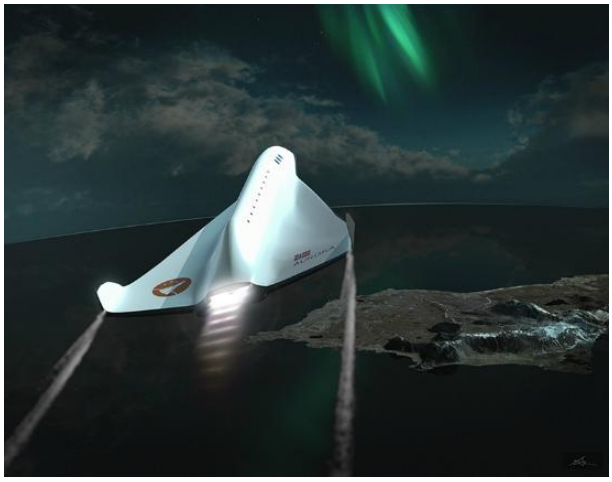

Figure 8: Spaceship Aurora is a visitor –educational center at Andøya Space Centre (NAROM)

Since its opening in 2014 by Norwegian prime minister Erna Solberg, over 5000 people have taken the virtual trip in the spaceship, starting at Spaceport Andøya and traveling halfway to the moon, in order to examine the aurora at close hold.

18.6 "Fly a Rocket" – ESA Student Rocket Campaign

«The Fly a Rocket program is a ESA program in cooperation with NAROM and the Norwegian Space Center which gathers students from all ESA countries to a five days long student rocket campaign at Andøya Space Center and NAROM. Before the campaign, the students go through an online pre-course where the students read up on rocket science and satellite orbits and delivers two reports prior to arrival at Andøya. This brings all students to a given level before the campaign, increasing the teaching output of the course and also helps on team building, as the students need to work together to solve the assignments in their reports. The

first campaign is now completed, and the program will be evaluated before initiating future campaigns."

18.7 Public Outreach

The Norwegian Space Centre is focusing on outreach and media activities to increase the interest in science and technology among young people and the general audience.

On the web sites romsenter.no and the more static version spacecentre.no is the main access to the target groups. NSC publishes stories on Earth observation, astronomy, industrial policy, ESA activities and space activities in general, all with a Norwegian hook or commented by the staff at the space center.

This pays off in media and NSC staff is a much sought after source for journalists writing stories on space. Last year the NSC was cited 600 times in papers, magazines, websites, TV and radio.

The NSC section for kids up till 12 years old, called Space for Kids, generates much traffic on the web site. The site is commonly in use by young students and schools as a source for information when they work on space related projects. Facebook and to a lesser extent Twitter are also important platforms for outreach.

In September 2016 the Norwegian Space Centre hosted the regional public citizen's debate on behalf of ESA in Norway. A general audience spent a Saturday immersed in discussions of space related issues. The feedback from the consultations in the 22 ESA member states showed that 98% think that space represents a universe of possibilities and opportunities, while 94% have full or a high level of trust in European space agencies. Summer 2017 there will be much focus on launch of two new, national micro satellites.

Presentations for schools, students and the general public are a priority as well. The staff of 40 employees makes more than 200 presentations every year.

SALACIA - A STUDY OF MARTIAN BRINES WITH REXUS 21

Daniel Nilsson[1], E. Krantz[2], J. Ekelund[2], F. Emmoth[2], J. Güttler[2], W. Höglund Leuf[2], L. Ingeström[2], A. Jafari[2], F. Jensen[2], V. Lidström[2], M. Lukanovic[2], P. Olsson[2], M. Persson[2], Á. Soria[2], M. Svensson[2], and J. Ågerlind[2]

[1]*Luleå University of Technology, 971 87 Luleå, Sweden, Email: adiino-2@student.ltu.se*
[2]*Luleå University of Technology, 971 87 Luleå, Sweden, Email: salacia@salacia.se*

ABSTRACT

The search for water on Mars has been ongoing for a long time. Following a discovery by the MSL in 2015 hydrates salts were being considered for a potential source of water on Mars. SALACIA is a REXUS/BEXUS project aimed at providing guidance to future missions studying brines on Mars. The experiment was flown on REXUS 21 and manage to provide visual images of the movements of the salts leading to conclusions about how the vessels should be designed.

SALACIA also manage to provide conductivity data from the salts to indicate hydration of the salt. From this data it was understood that the time the rocket is on the launch pad is a risk factor when some of the examined salts risk absorbing water from the humidity in the air. This should be considered before future missions to Mars with these salts.

Key words: SALACIA; REXUS; BEXUS; 2017; 21; BRINES; MARS; SALTS.

1. INTRODUCTION

Examining sources of water on Mars has long been of interest to the scientific community. Data from the Mars Science Laboratory (MSL) has indicated that there might be an active water cycle on Mars thought to be driven by chlorate and perchlorate salts commonly found on the Martian surface, see [1]. Students at Luleå University of Technology developed the SALACIA mission, a REXUS/BEXUS experiment designed to prepare future missions to Mars examining these salts.

Finding liquid water on Mars is challenging. The planet is associated with a low surface pressure combined with a highly varying temperature between night and day.[2] However, in April 2015 the MSL found indications of liquid water that was later confirmed by instruments on the Mars Reconnaissance Orbiter from NASA in October during the same year. This is thought to be made possible by brines on the surface and subsurface of Mars. Fig. 1 shows a laboratory experiment by SALACIA in which a salt with the ability to form brines is exposed to the water vapour in the air.

2. THE SALACIA MISSION

SALACIA, named after the roman goddess of salt water, is an abbreviation of Saline Liquids and Conductivity in the Atmosphere. The general mission of SALAICA is to investigate the dynamics of hydration and monitor the movements of certain hygroscopic salts to provide information for future Mars missions examining brines. The experiment primary objectives are as follows:

- By making continuous conductivity, temperature and pressure measurements throughout the flight of the REXUS 21 rocket, SALACIA shall provide an atmospheric profile displaying the variation of hydration levels over altitude for each respective salt.
- SALACIA shall show how the hygroscopic properties of the salts are affected by the characteristics of a real-world rocket launch.

For a total mission success, the following Secondary Objective should also be fulfilled:

- SALACIA shall by camera monitor the salts inside the REXUS 21 rocket throughout the whole flight.

The salts examined by SALACIA can all be found on the surface of Mars and they are: Sodium Perchlorate, Calcium Perchlorate, Calcium Chloride and Magnesium Perchlorate. These salts all have the ability to, through crystallization of water, absorb surrounding water and form different stages of hydration. Thus the salts can be thought to be prime contestants for participating in a water cycle on Mars.

It should be noted that conductivity is used as an indicator of hydration of the salts. In order to fulfil the objectives

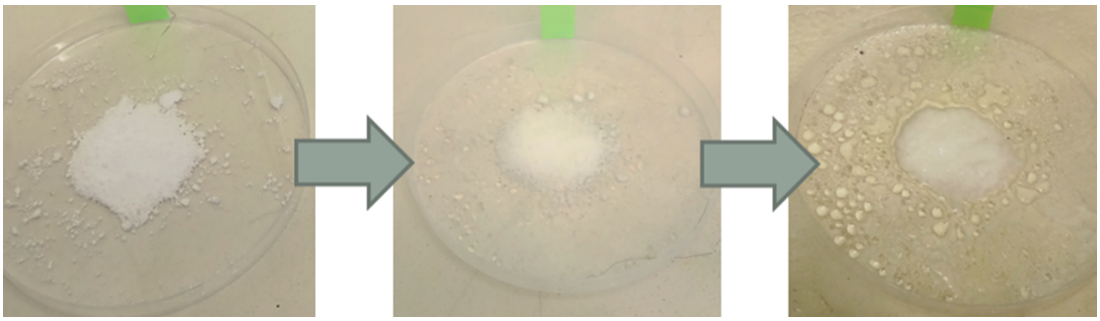

Figure 1. The salt is exposed to the water vapour in the air and forms a partially hydrated stage.

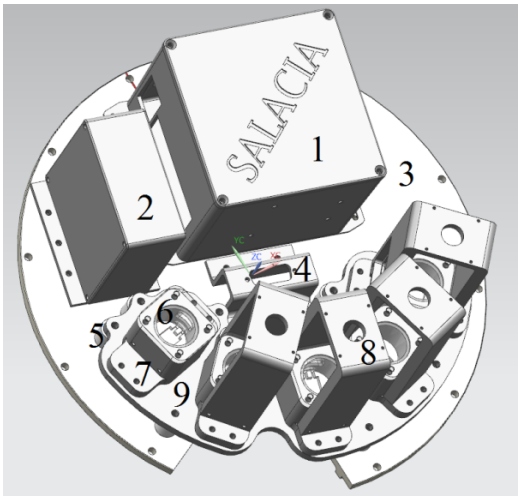

Figure 2. The main parts of the instrument can be seen in the following picture. 1: Bigger electronics box, 2: Smaller electronics box, 3: Bulkhead, 4: D-sub connector, 5: Teflon legs, 6: Polycarbonate, 7: Vessel, 8: Camera mount, 9: Platform.

an instrument was designed and the final instrument can be seen in Fig. 2. The main parts of the instrument are: the power unit, the electronics box and the five vessels in which the salts were placed.

Before launch each salt was completely dried and then measured and placed in a vessel. One vessel was left empty as reference. Below each vessel was a heater used to prevent the temperature from becoming too low in the vessels resulting in a frozen stage for the brines. On top of each vessel was a camera that was used to monitor the movements of the salts. At the side of each vessel was an opening of which a filter was placed in order to allow for a sufficient airflow while preventing the salt from escaping the vessel.

The following sensors where mounted on the SALACIA module in order to fulfil the objectives.

- 5 conductivity sensors designed by SALACIA
- 4 cameras. O-3000 Industrial Camera by Stettbacher Signal Processing

Figure 3. The conductivity sensors were printed on a flexible PCB and glued to the side and bottom of the vessels.

- 1 humidity sensor. HIH-4000-001 by Honeywell
- 2 pressure sensors. HSCDANN001BAAA3 by Honeywell
- 6 temperature sensors. MCP9700A by Microchip

2.1. Conductivity sensors

The conductivity sensors were used to give an indication of the hydration levels of the salts as a high hydration level should result in a high conductivity and vice versa. The sensors were designed to be able to cover the vessels entirely apart from the transparent top of the vessel needed for a clear image by the cameras.

The conductivity sensors consist of exposed conductive fingers in an even mesh. These sensors were printed on flexible PCB and glued on the side and bottom of the vessels and connected to the MCU. A picture of the sensor can be seen in Fig. 3.

3. RESULTS

On the 15^{th} of March 2017, the SALACIA instrument was successfully launched as part of the sounding rocket REXUS 21's payload. Further, the instrument was later recovered from the landing site and returned to the SALACIA team for inspection. The experiment mass with the bulkhead and module was 9.956 kg and reached its apogee, 86.068 km, at T+142s.

The cameras on the SALACIA module managed to record the flight and the full version can be found at the SALACIA Youtube Channel.[1] Note that in this video camera 1 recorded the sodium perchlorate, camera 2 the calcium perchlorate, camera 3 the calcium chloride and camera 4 the magnesium perchlorate.

Moving on, the other sensors at the module also managed to record data which have been processes and the following graphs produced. In Fig. 4 the measured conductivity can be seen. In Fig. 5 is the results from the temperature sensors and Fig. 6 visualizes the results from the humidity sensor. Finally, the results from the pressure sensors is shown in Fig. 7.

4. ANALYSIS

Fig. 4 shows relative small changes in conductivity for all the vessels, except for two. Sodium perchlorate had a clear decrease in conductivity which was not an expected behaviour. Before the mission is had been made clear that a concern for future missions examining brines on Mars were the risk of absorbing water during the flight through the atmosphere. The expected result was that a process like this would result in a higher conductivity.

However, during the preparations for the mission the SALACIA team could observe that the absorption process could take around 24 hours during launch conditions. The absorption time was also discovered to highly differ between the salts. Also parameters such as temperature and relative humidity affects the time significantly. A process that is this slow should then be expected to not have a clear impact on the hydration levels of the salts during a short flight. But the behaviour of the sodium perchlorate and calcium perchlorate was unexpected.

Based on post analysis it has been concluded that the decrease observed in Fig 4 should not be thought to indicate that the salt actually became drier during the flight. Instead, what most likely happened was that the sodium perchlorate was partially hydrated before the launch. As seen in Fig. 1, the first hydration of the salt when exposed to the humidity in the air is on the edges of the salt formation.

[1] https://www.youtube.com/channel/UCA1X8kEXI7TwepQhsNhzmSA

Before the launch, it was probably the case that crystals at the edge of the salt had been hydrated and, because of their location unproportionally triggered the sensor. At T-0 the vibrations then changed the distribution of the hydrated salt crystals more evenly resulting in a more realistic conductivity level for the level of hydration.

A similar strange behaviour is seen for calcium perchlorate with the two jumps right after lift off at T-0. This was investigated and the behaviour of the conductivity sensor has later been replicated in the lab. The observed behaviour is likely to have arisen from the movement of the salts due to the vibrations and accelerations during launch.

Again, for the vibrations and accelerations to have this effect on the salt it must have been partially hydrated. Before the launch, the likely scenario is that the salt was partially hydrated with some portion of salt being more hydrated compared to the general hydration level of the salt. After launch, the vibrations caused some of the hydrated salt to get better contact with the sensor observed as a spike. After a while however, the hydrations are more evenly distributed among the salt crystals as would be expected. The slight increase from T+400 to T+600 at Calcium perchlorate could indicate water being absorbed from the atmosphere.

Comparing this to the temperature measurements in Fig. 5 it should be noted that the heater for the calcium perchlorate malfunctioned during the flight. However, since both sodium perchlorate and calcium perchlorate is thought to have absorbed water before the flight and generally behaved in a similar fashion regarding the conductivity measurement it is concluded that this malfunction had a very limited, if any, effect on the final results.

Further, when the salts were put into the vessels they had been completely dried and pulverised. However, based on the obtained images from the cameras it can be observed that both sodium perchlorate and calcium perchlorate had formed large salt structures which is a clear indication of hydration. Thus, sodium perchlorate and calcium perchlorate were most likely hydrated through absorption during the time the rocket stood on the launch pad.

The result from these conductivity measurement is hence an indication that it is probably not the water vapour in the atmosphere during the flight that is the most crucial to consider. Instead, one should be aware that the time on the launch pad before the flight is probably when a substantial amount of water will be attracted.

Moving on, the salts movements were monitored using the on-board cameras. It could be observed that the rotation and movement of the rocket tended to push the salt against the filter. After recovery, it was also confirmed that the filters were almost fully saturated with salt. Further, due to the filters being the entry point for the humid air that was also a natural hydration area for the salt. It is possible to perform more detailed analysis of the movements of the salts. However, the current

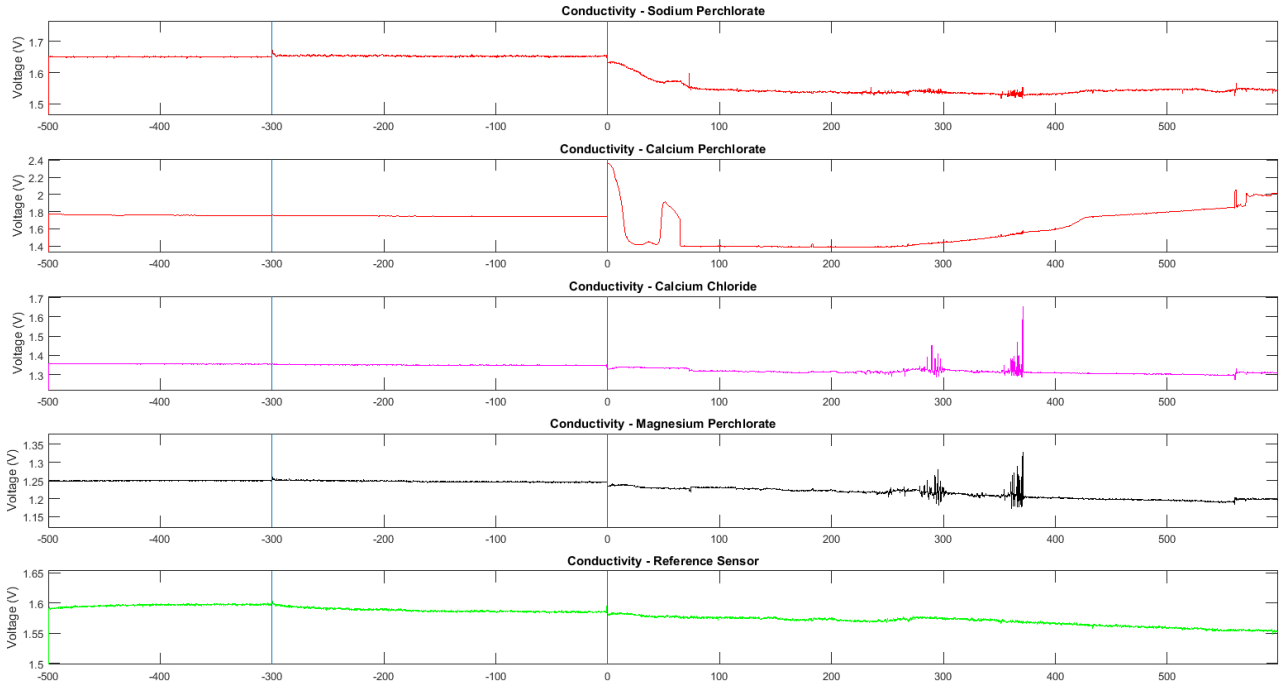

Figure 4. The conductivity measurements after filtering in Matlab. 3.3V indicated full saturation for the sensors. The first line at T-300s indicates the SODS signal and the second line at T-0 indicates lift-off.

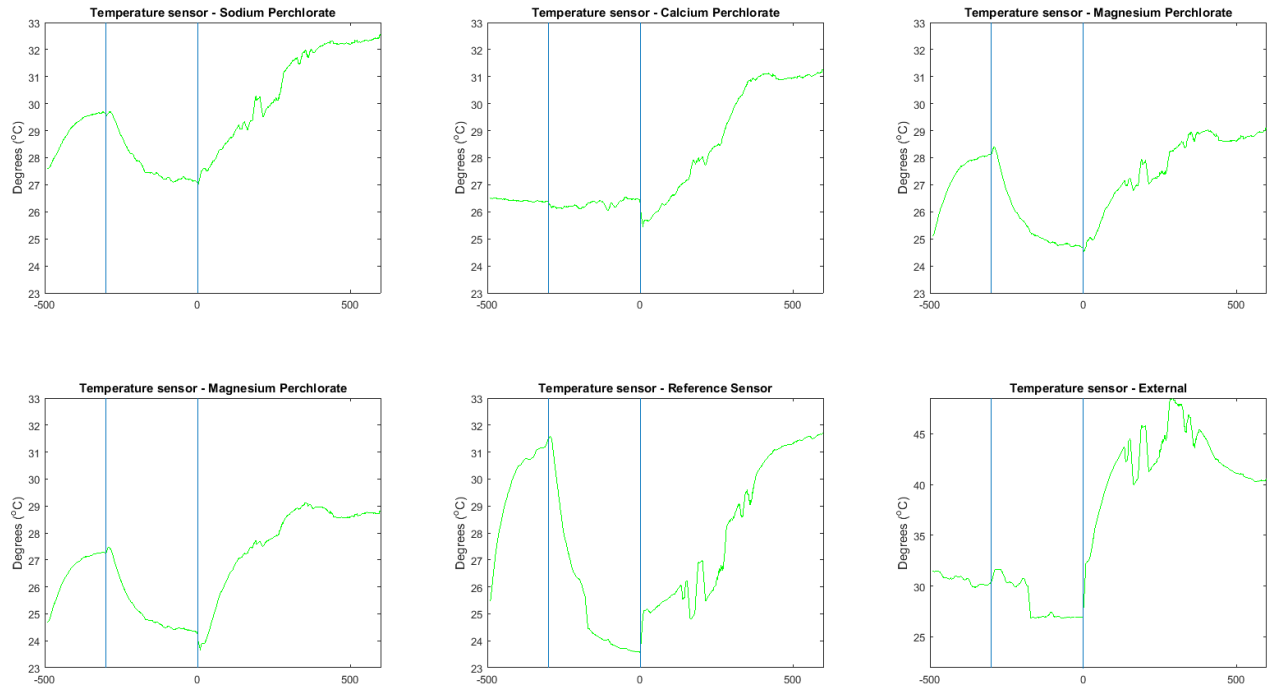

Figure 5. The temperature measurements from SALACIA. Heaters were used from T-500s until the SODS signal at T-300s.

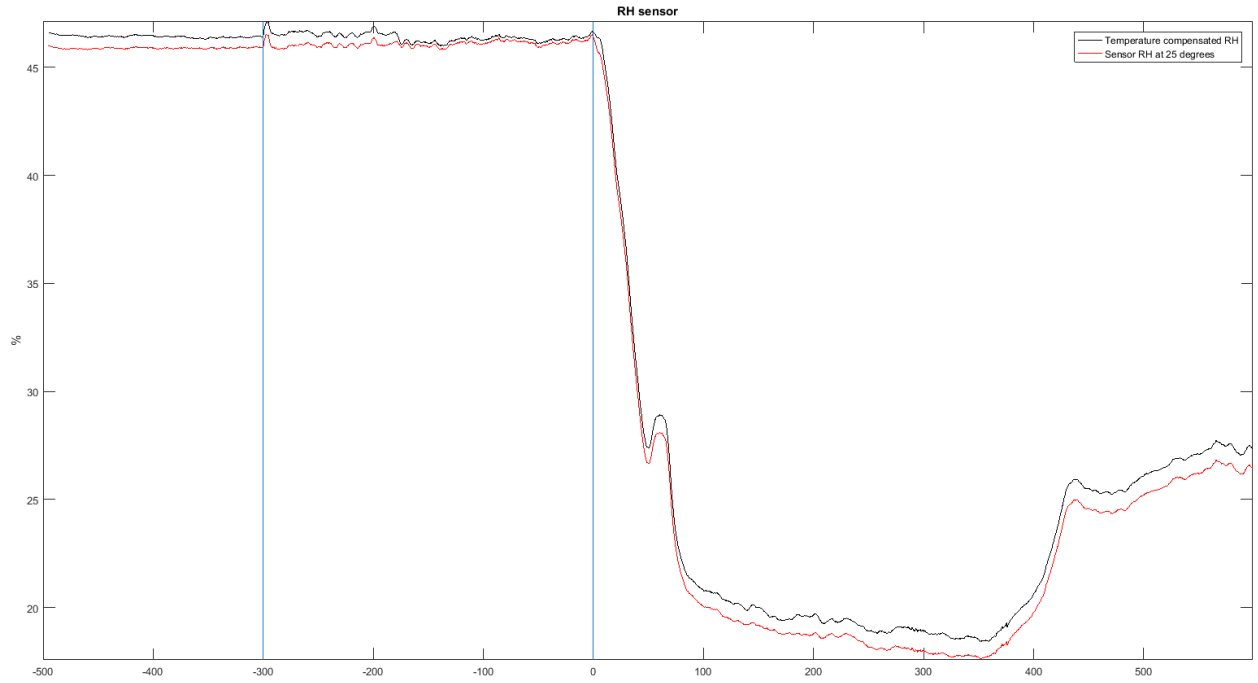

Figure 6. The realtive humidity plotted assuming 25 degrees Celsius, and relative humidity adapted to the measured temperature around the sensor..

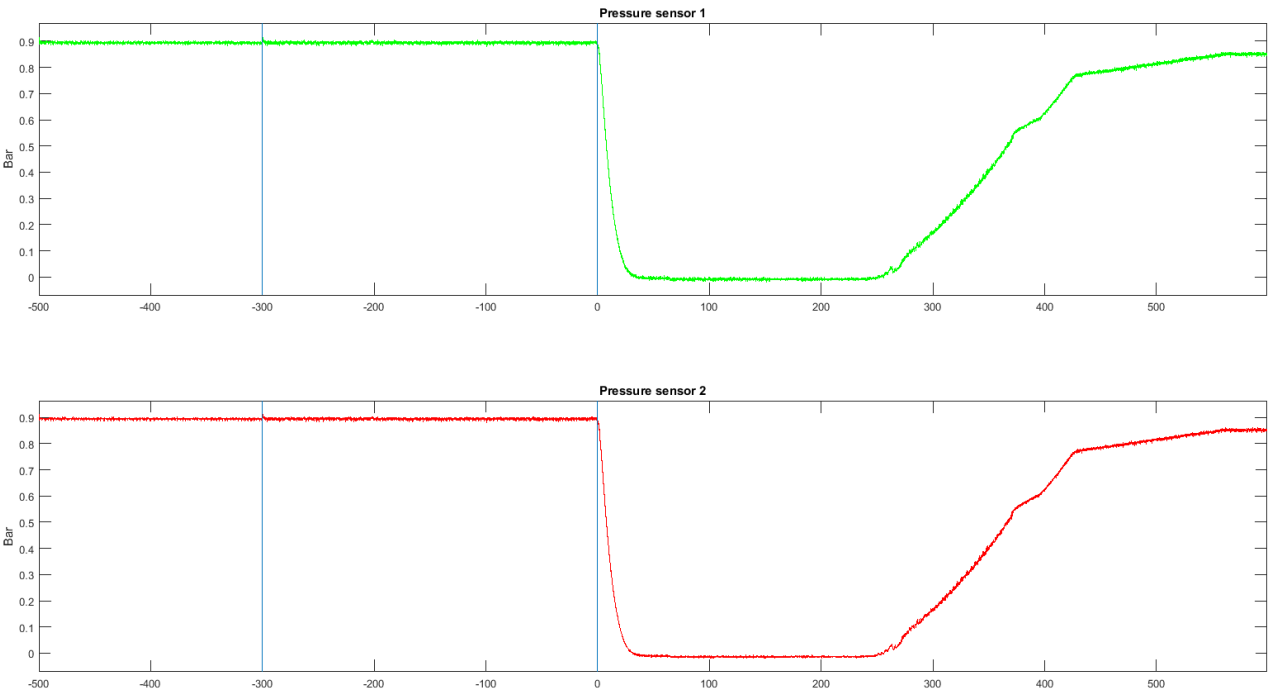

Figure 7. The pressured measurements performed by SALACIA.

results indicate that the filters and design of the vessels should be changed before performing future missions.

Finally, it can be noted that both the relative humidity in Fig. 6 and the pressure in Fig. 7 behaved as expected.

4.1. Objectives

Regarding the objectives, SALACIA did manage to partly fulfil its first primary objective. SALACIA did perform continuous conductivity, temperature and pressure measurements throughout the REXUS 21 flight. The data has been shown in Fig. 4-7. However, SALACIA did not produce an atmospheric profile displaying the variation of hydration levels over altitude. This was because of the fact that the hydration process for the salts were slow in comparison the the actual flight and the scientific value of a profile like this was deemed low. Instead, as was discussed above, it is probably more reasonable to consider the time before launch as important for hydration of the salts.

The second primary objective was the show the hygroscopic properties of the salts and how they were affected by the rocket launch. As mentioned above, the conductivity did most likely increase for the measurements of calcium perchlorate which is a clear indicator that the hygroscopic properties were not affected by the characteristics of the flight. Also, the properties of the used salts were tested in the lab at LTU Kiruna Campus soon after the launch campaign. The results showed that the salts acted as before, that is to say they did still absorb water from the air. Hence, the second primary objective was fulfilled and the conclusion is that the hygroscopic properties of the used perchlorates and calcium chlorate was not affected by the characteristics of this rocket launch.

Finally, SALACIA also managed to fulfil the secondary objective of monitoring the salts by camera. The result from the camera footage was an indication of how the design of the vessels should be adapted to prevent salt from getting stuck at the filter.

5. CONCLUSION

SALACIA managed to fulfil the majority of its objectives and provide a deeper understanding of how to study brines on Mars. From the results it was clear that the design of the vessel was not optimal as the salt tended to be pushed against the filters where they became attached. It was also argued that the risk of hydration before the flight is more valuable to consider compared the the hydration during flight.

ACKNOWLEDGEMENTS

We in the SALACIA team would like to give our thanks and appreciation to Olle Persson, Thomas Kuhn, Victoria Klippmark. Olle Persson is operations administrator at Luleå University of Technology and provided technical guidance though the project and provided contacts with experienced people at LKAB for the handling the the perchlorates. Thomas Kuhn is associate professor at Luleå University of Technology and supported SALACIA in moste areas including: management, technical and scientific guidance. Victoria Klippmark work with product development at LKAB Kimit and provided guidance regarding handling of oxidizer both at LKAB Kimit and at Kiruna Campus.

REFERENCES

[1] Pater, I. de, Lissauer, J. J., 2015, Planetary Sciences,Cambridge University Press, 81, 208

[2] Martin-Torres, J. F., 2015, Transient liquid water and water activity at Gale crater on Mars, Nature Geoscience 8, 357–361

SECONDARY SCHOOL STUDENTS DESIGNING, TESTING AND FLYING GEIGER COUNTER EQUIPMENT TO STUDY ATMOSPHERIC GAMMAS OVER EUROPE AND SVALBARD

VISBY, SWEDEN
11-15 JUNE 2017

Noham Behe, Dmitry Buggenhout, Zakaria Chentouf, Ines Dekock,
Agatha Smet, Corneel van Moll, Erwan Van Vreckom, Erik de Schrijver
Sint-Pieterscollege Jette, L. Theodorstraat 167, 1090 Brussels, BELGIUM, eds@sint-pieterscollege.be

ABSTRACT

A three-tube Geiger counter assembly was designed to investigate the angular distribution of atmospheric gamma-radiation in an (unspecified) vertical plane using AND-gates as coincidence circuit. The experiment was flown on an Asgard-balloon (a hands-on space education programme dedicated to giving secondary school students near-space research opportunities) in April 2016.
Furthermore, in order to determine if atmospheric gamma ray production is latitude-dependent, a single tube Geiger counter datalogger was flown from the site of the Kjell Henriksen Observatory near Longyearbyen, Svalbard in September 2016. Differences in the altitude of the Pfotzer maximum between Longyearbyen at 78°N and Brussels at 51°N, and in the altitude profile of gamma radiation intensity are discussed.

1. GEIGER COUNTER MODULES

The MightyOhm Geiger Counter Module was used, carrying a Russian SBM-20 tube. Producing 3,3V pulses in its standard configuration, it was converted to produce 5V pulses for compatibility with Arduino microcontrollers. A 2015 Asgard balloon flight over Brussels confirmed the suitability of this module for studies of atmospheric gamma radiation, corroborating reports in the literature of an increase with altitude up to about 17-20km (sometimes referred to as the Pfotzer maximum).

2. BALLOONS OVER BRUSSELS

2.1. Triple Geiger Counter with coincidence circuit

Three Geiger counter tubes (and associated circuitry) were arranged in parallel, their axes forming an isosceles triangle, with the equal sides at right angles to each other. The Geiger tubes' signals were connected both to an Arduino Uno microcontroller and – in pairs – to AND-gates to determine when two tubes would give off overlapping pulses. This would signal a single particle passing through two tubes, as a particle moving at the speed of light would cover the distance between two tubes in far less time (typically 0,2ns) than the duration of a pulse (100µs). The whole procedure would be repeated at 1 second intervals to ensure sufficient spatial resolution as the balloon carrying the experiment ascended at approximately 400 meters per minute.

2.2. Results

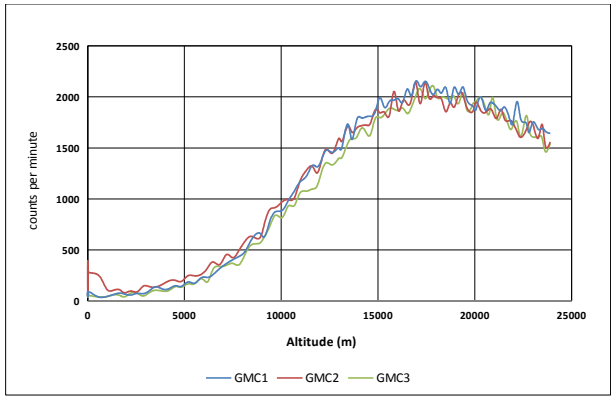

Figure 1. Gamma counts per minute (GCPM) vs altitude over Brussels in April 2016

Results from the triple Geiger counter flown on Asgard-6 in 2016 are shown in Figs. 1 and 2. All 3 tubes show similar results, as expected. A gradual increase leading up to a maximum of +/- 2000 counts per minute at an altitude of 18 km is observed, in agreement with the literature. Slight variations are observed, as is to be expected on short duration measurements.

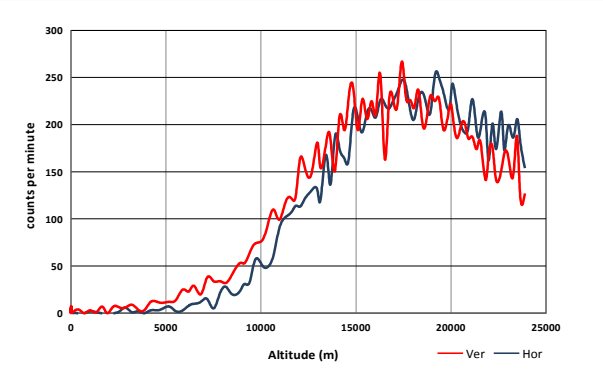

Figure 2. Coincidences per minute vs altitude over Brussels in April 2016.

Fig. 2 shows the data from the coincidence circuits for the horizontally (blue line) and vertically stacked tubes (red line). Clearly, only about 1/10th of the total number of detected particles transit through two tubes. Taking into account the diameters of the tubes and their separation, particles piercing both tubes must have paths separated by < 19°, about 1/10 of 180°.

3. SOUNDING OVER SVALBARD

In 2016, a single Geiger counter module was flown on a weather balloon from Kjell Henriksen Observatory near Longyearbyen, Svalbard. The initial decrease is attributed to radioisotopes in the rocky (sub)surface. Interestingly, the gradual increase with altitude observed over Brussels (and reported in the literature), is absent, and we see the gamma counts go to zero, except for a sudden but pronounced peak around 10000m. A glitch in the equipment is considered unlikely, as the software recorded gamma counts per second, and the increase was observed for several minutes, i.e. hundreds of seconds of sampling time.

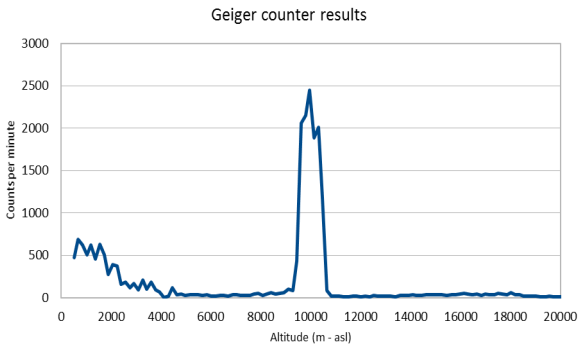

Figure 3. GCPM over Svalbard in September 2016

Moreover, the curve peaks at a gamma count quite similar to what was observed over Brussels (both in 2015 and in 2016). Once passed 11000m, the gamma count went back to zero. No satisfactory explanation was found, and no prior reports of this phenomenon could be found.

4. CONCLUSIONS

The 3-tube Geiger counter was equipped with an AND-gate circuit to detect the simultaneous passage of particles through two Geiger tubes (stacked either horizontally or vertically). The results show that beneath the Pfotzer maximum vertically moving particles are somewhat more abundant, whereas above the maximum, slightly more horizontally moving particles are observed. A statistical analysis was performed to determine the probability of 2 separate particles accidentally triggering the coincidence circuit by hitting both tubes within a single pulse duration (100µs). Chances are about 10% of signal magnitude, which seems to vindicate the validity of the conclusion above.

A single tube experiment over Svalbard also showed a maximum but both overall altitude dependence and altitude of maximum were very distinct from results obtained over Brussels. The reason for this discrepancy remains unclear and hence further investigations are planned.

5. FUTURE PROJECTS

Because particles moving parallel to a Geiger tube's axis face a far smaller tube cross section than particles moving perpendicular to the tube's axis, a Geiger counter's sensitivity is far greater perpendicular to its axis than it is in its axis. Hence an array of 3 Geiger tubes perpendicular to one another is also suitable for angular distribution studies. This approach avoids the decrease in signal incurred by using parallel tubes. Hence, this configuration has a significant sensitivity advantage, which increases the statistical significance of any finds. Therefore this configuration will be developed and flown over Brussels on the Asgard-8 balloon mission, and (TBC) over Svalbard, in order to confirm the findings of the 3-tube Geiger Counter over Brussels, and to further investigate the nature of atmospheric showering effects at both medium (Brussels, 51°N) and high northern latitudes (Longyearbyen, Svalbard, 78°N).

6. ACKNOWLEDGEMENTS

The authors wish to thank M. Steven Peterzén from the Istar Group, for his help and support in taking care of the logistics of the Svalbard Balloon Campaign.

SECONDARY SCHOOL STUDENTS DESIGNING, TESTING AND FLYING EQUIPMENT TO STUDY THE QUALITY OF MICROGRAVITY ON DROP TOWER TESTS AND PARABOLIC FLIGHTS

VISBY, SWEDEN
11-15 JUNE 2017

Noham Behe, Dmitry Buggenhout, Zakaria Chentouf, Ines Dekock,
Agatha Smet, Corneel van Moll, Erwan Van Vreckom, Erik de Schrijver
Sint-Pieterscollege Jette, L. Theodorstraat 167, 1090 Brussels, BELGIUM, eds@sint-pieterscollege.be

ABSTRACT

Different platforms used for microgravity research were studied and the quality of the microgravity environment was evaluated based on 3D accelerometer data. An Inertial Measurement Unit (IMU) was designed, developed, tested and flown to this end. The microgravity platforms studied were the ZARM Drop Tower in Bremen, Germany, parabolic flight on the Cessna Citation II flying laboratory of the Technical University of Delft, the Netherlands, parabolic flight on the Cap10 aerobatic aircraft and the short post-burst drop phase of a high altitude weather balloon

1. MEASUREMENTS

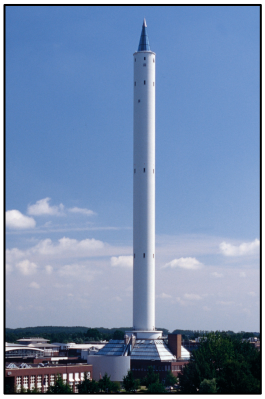

Fig. 1 shows the results from the ZARM tower. Equipped with a catapult exposing the payload to an acceleration of 35g, the payload rises and falls back in approx. 9,3 seconds. In vacuum and the absence of vibrations caused by engines, the quality of the µg environment is expected to be the very best that can be achieved at Earth's surface.

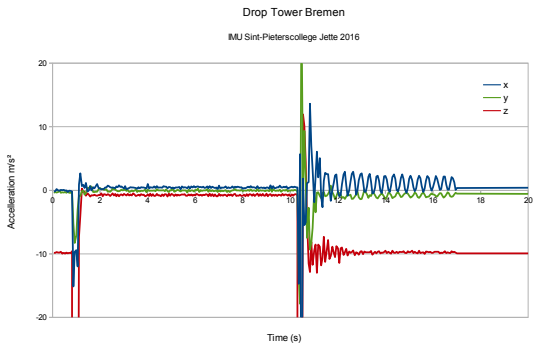

Figure 1. Acceleration on 3 axes during a drop test at ZARM. The z-axis is vertical. (The sensor had a maximum range of +/-16g, lower than the 35g imparted to the payload by the tower's catapult system, so peak values – not shown here – were inaccurate).

Fig. 2 shows the data obtained on the BIFROST parabolic flight campaign with the Cessna Citation II flying laboratory of the Technical University of Delft, the Netherlands in 2014. The duration of the µg phase is approximately 15 seconds.

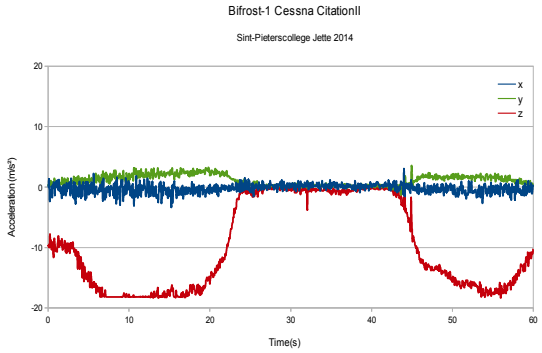

Figure 2. Acceleration on 3 axes during a parabolic flight with the Cessna Citation II. The z-axis is vertical.

Fig. 3 shows results from parabolic flights on the Cap10 aerobatic aircraft during the 2017 BIFROST-One parabolic flight campaign for secondary school students (organised by Innoviris for schools in Brussels with technical support from Sint-Pieterscollege Jette). On all flights discussed in this study, identical IMU units were flown.

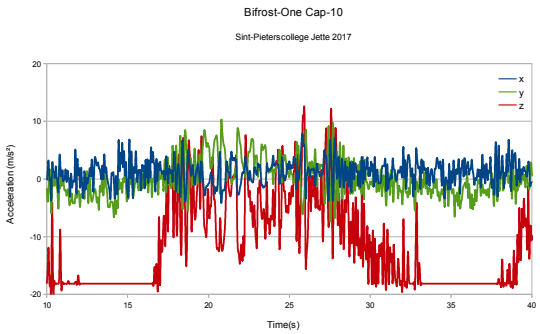

Figure 3. Acceleration on 3 axes during parabolic flight with the Cap10 aerobatic aircraft. The z-axis is vertical.

Fig. 4 shows data from the IMU that flew over Belgium on the Asgard-7 balloon carrying 13 high school experiments (from 3 different countries) in April 2017. The balloon burst at an altitude of 28,5 km and approximately 20 seconds of freefall were observed before parachute deployment.

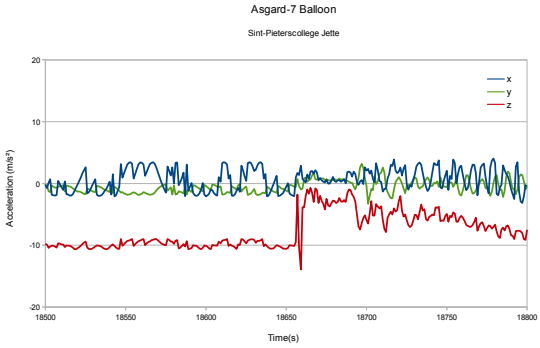

Figure 4. Acceleration on 3 axes during freefall after balloon burst on Asgard-7. The z-axis is vertical.

2. DISCUSSION

Whereas drop tower tests are very repeatable and all parameters are well in hand, parabolic flight is much more prone to suffering disturbances caused by weather conditions or human handling. The least repeatable conditions were expected during the freefall phase after balloon burst, as the gondola can fall down tumbling wildly, dragging behind it shreads of the balloon before the parachute opens.

In order to verify the validity of these assumptions the mean acceleration during the µg phase and the standard deviation from the mean were determined for all 4 flights.

Mean acceleration during µg-phase:

1) Drop Tower:	0,74 m/s²
2) Bifrost-1 (Cessna Citation II):	0,32 m/s²
3) Bifrost-One (Cap10):	3,31 m/s²
4) Asgard 7 freefall :	2,47 m/s²

Standard deviation:

1) Drop Tower:	0,13 m/s²
2) Bifrost-1 (Cessna Citation II):	0,35 m/s²
3) Bifrost-One (Cap10):	4,82 m/s²
4) Asgard 7 freefall :	0,95 m/s²

3. CONCLUSIONS

The data were collected with an ADXL345 3-axial accelerometer at a sampling rate of +/-20Hz. The bias level for this sensor is typically 80mg on the z-axis, which amounts to about 0,8m/s². Therefore, while the mean acceleration observed on parabolas flown with the Cessna Citation II show somewhat better values than on the drop tower, this is believed to be – at least in part - attributable to sensor offset. Moreover, positive and negative values partially cancel each other out in the Cessna data (the mean of the absolute values is 0,37 m/s²) but not on the drop tower data. It was to be expected that by its very nature, the µg environment in the plane is less stable than in drop tests, and this is confirmed by the standard deviation which is significantly better for the drop tower. From these data, it is also clear that parabolas flown on the CAP-10 aerobatic aircraft hardly qualify for the name 'zero-g' flight, as the mean acceleration is approximately 0,3g. The short freefall phase following 'burst' on high altitude weather balloon flights falls somewhere in between

4. FUTURE PROJECTS

The hardware used in this work is currently being upgraded, making it smaller through the use of SMD circuitry (as opposed to through-hole) and more performant.

The Oufti-2 cubesat currently being designed by the ULg (Université de Liège) and HEPL (Haute Ecole de la Province de Liège) will fly this upgraded IMU as a subsystem to investigate the performance of the satellite's passive stabilization system, and – possibly – the drag on the cubesat when it nears the end of its orbital lifetime.

5. ACKNOWLEDGEMENTS

We wish to thank Andreas Schütte, DLR, for his efforts to get the experiment to fly on the Drop Tower in Bremen, and Prof. Alexander in 't Veld, Technical University Delft, The Netherlands, for his assistance in the Bifrost project, making parabolic flight accessible to high school students.

BIFROST PARABOLIC FLIGHT: A NEW RECURRENT HANDS-ON SPACE EDUCATION PROGRAMME FOR SECONDARY SCHOOL STUDENTS

VISBY, SWEDEN
11-15 JUNE 2017

Erik de Schrijver[(1)], Sébastien Rush[(2)], Alexander in 't Veld[(3)]
[(1)] Sint-Pieterscollege Jette, L. Theodorstraat 167, 1090 Brussels, Belgium, eds@sint-pieterscollege.be
[(2)] Innoviris Brussels, 110 Chaussée de Charleroi, 1060 Brussels, Belgium, srush@innoviris.brussels
[(3)] Delft University of Technology, Kluyverweg 1, 2629 HS Delft, The Netherlands, A.C.intVeld@TUDelft.nl

ABSTRACT

A recurrent hands-on high altitude balloon space education programme called Asgard has been running succesfully since its inception in 2011. Now a new hands-on programme, involving parabolic flight, was initiated (after a precursor edition in 2014) along lines comparable to - though somewhat different from - those of a Cansat competition. Called Bifrost ('Brussels Initiative to provide Flight Research Opportunities to STudents'), this programme aims to motivate upper high school students for STEM studies (Science-Technology–Engineering-Mathematics) by offering the opportunity to fly an experiment (and possibly a team of 5 students plus a teacher!) on a parabolic flight, flown with Delft University of Technology's Cessna Citation II flying laboratory. Where Asgard offers access to the near-space environment, Bifrost offers a microgravity environment (a dozen 15s parabolas), bigger payload capabilities and possible in-flight human intervention.

1.RECURRENT HANDS-ON PROJECTS

Figure 1. Asgard balloon flights offer students a research opportunity at 30km altitude (so-called near-space)

Secondary school students worldwide can participate in the annual Asgard balloon programme, organized by Sint-Pieterscollege Jette, Brussels, ESERO-Belgium, KMI (the Royal Meteorological Institute of Begium), and other partners. Asgard selects about a dozen teams. Flight duration is about 2 to 3 hours, and the balloon's burst altitudes are typically around 30km.

Students from Brussels and the region of Wallonia can participate in the biannual Belgian Cansat Competition (participation of the region of Flanders has been under study for some time now). Typically, about a dozen teams are selected for the finals of the competition. Payload mass is limited to about 300 grammes per team, flight duration is on the order of 2-3 minutes, and altitudes are typically 1km.

Figure 2. The Cessna Citation II is the Technical University of Delft's flying laboratory. It is used (among other things) for microgravity research and technology development.

In recent years, a third hands-on project has been initiated, offering parabolic flight opportunities to high school students. Proof of concept was delivered in the Bifrost pilot edition in 2014 [1] and now in 2017 in the first full-scale 'Bifrost One' campaign. Whilst this campaign was open only to schools in the Brussels Capital Region (8 teams selected out of the initial 18 project proposals), the programme goal is to open the Bifrost Programme to all Belgian secondary schools.

Bifrost provides each team with several flight's worth of measuring time, each flight lasting for about 1 hour and encompassing 12 parabolas offering 15 seconds of microgravity each.

2. ASGARD AND BIFROST SIMILARITIES

Scientific balloons have been used by Nasa's NSBF, based in Palestine, Texas, USA, the French CNES and many others worldwide. Parabolic flight is performed by ESA through Novespace in Bordeaux, France, by Nasa in the US and others worldwide.

Now, with Asgard and Bifrost, such research platforms (high altitude balloons and parabolic-capable aircraft) are made accessible to secondary school students for hands-on education.

Both Asgard and Bifrost cover one school year, allowing students to go through all phases of a project (experiment inception, design, development, testing, flight and data processing/interpretation) in the course of a single year.

In both projects a call for proposals is issued and a jury of competent outsiders selects the most promising ideas. Once this selection made, there is no further competition between teams and mutual assistance becomes possible and is fostered by the organisers.

The number of teams (about ten) and team size (about 5 students) are comparable in both projects, as is the availability of a manual and of technical support. Also in both cases, teams are required to make presentations both before and after the flight, reporting first on their intentions and encountered problems, then on the results (or lack thereof).

3. ASGARD AND BIFROST DIFFERENCES

The Asgard balloon programme is annual and open to secondary schools worldwide. Bifrost parabolic flight campaigns on the other hand, are organised biannually in the years between national Cansat campaigns, and are only open to schools from the region or regions funding the project.

On Asgard, the jury selection is based solely on the team's project proposal and falls in November, early on in the project. For Bifrost, selection is a two-step process with a preselection early on (November), and final selection (annex flight assignments) later on, in March.

Balloon flights don't allow for in-flight human intervention and are severely limited in the total payload mass they can carry. Therefore experiment mass per team is limited to 200 grammes on Asgard, as opposed to 15kg on Bifrost. On Bifrost passengers must remain seated during parabolas so only lap-carried experiments allow for human intervention during the microgravity phase. Experiments that are too heavy or bulky to be lap-carried can be mounted in the rack at the rear of the plane, but must operate fully automatically or be designed for intervention in between parabolas only.

4. ASGARD AND BIFROST TIMELINES

September:	Announcement of opportunity
October:	Call for proposals
November:	Asgard selection / Bifrost preselection
January:	First progress report
February:	Second progress report
March:	Bifrost presentations & final selection
April:	Asgard & Bifrost: Flight& Presentations first results
May:	Asgard scientific poster

5. THE BIFROST ONE 2017 CAMPAIGN

5.1. The plan

A jury of academics (with professional activities related to microgravity research) selected 12 experiments from 18 applications early on. These 12 teams were then given several months (and a small budget) to develop the hardware for their experiment.

Late March, the teams then gave a final presentation (and, for some, a hardware demonstration) in front of the jury. Two categories of 'winners' were then selected: four schools would get the chance to fly their experiment and their team (5 students and a teacher), four others would fly only their experiment. This allowed to maximise the number of participants, while respecting the budgetary envelope, which called for 4 one-hour flights of the TU Delft's Cessna Citation II flying laboratory.

5.2. Aircraft qualification issues

Due to changing regulations in The Netherlands, the Cessna Citation II was not available for parabolic flight at the scheduled dates, and an alternative programme had to be put in place. Within the constraints of availability and budgetary margins emerged a campaign with considerably larger numbers of flights, though with smaller and less capable aircraft.

Figure 3. One of the Cap10 acrobatic aircraft used for the Bifrost One parabolic flight campaign in March 2017. Three aircraft performed a total of 250 parabolas, carrying 27 students and 4 teachers from 8 different schools in the Brussels Capital region.

The aerobatic airplane Cap-10 is a two-seater with a small storage area behind passenger and pilot. It was decided to offer the 'flight' teams their full number of six flights (5 students and 1 teacher), and the others one flight each. Some extra flights were added last minute so that in total no less than 27 students and 4 teachers, from 8 schools would experience microgravity. A grand total of 250 parabolas were flown (against 48 originally planned), lasting about 9s each.

5.3. Quality assessment

In order to determine the quality of the microgravity phase in the Cap10 aircraft, an IMU (Inertial Measurement Unit) datalogger was flown, identical to the one flown on the Bifrost pilot edition in 2014. The results are shown in Figs. 4 and 5. Clearly, the signal from the Cessna Citation II is far less 'noisy' and shows good quality µg while the Cap10 signal hardly goes to zero.

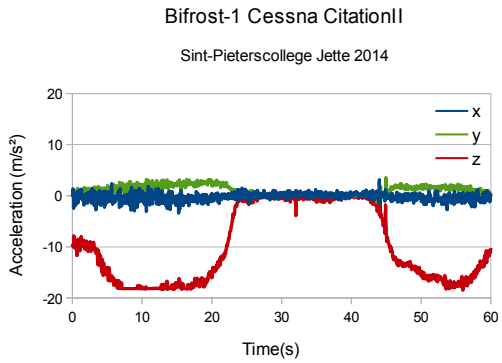

Figure 4. Acceleration along 3 axes during a parabola flown on the Cessna Citation II. The z-axis is vertical (with respect to the plane's fuselage).

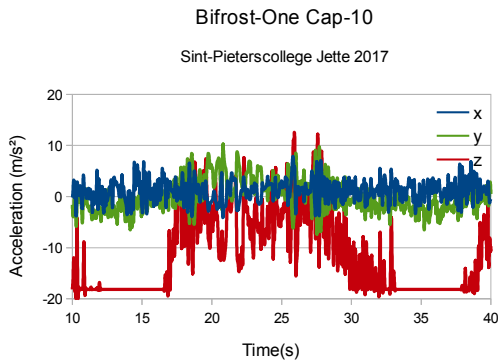

Figure 5. Acceleration along 3 axes during a parabola flown on the Cap10. The z-axis is vertical (with respect to the plane's fuselage).

A mathematical analysis of the data shows that on the Cessna Citation II the average gravity level during the parabolas is about 0,32 m/s², with a standard deviation from the mean of 0,35 m/s². For the Cap10 these values are 3,31 m/s² and 4,82 m/s², respectively. Clearly, it is not appropriate to describe the Cap10 parabolas as 'microgravity'.

6. EXPERIMENT EXAMPLE: TELEROBOTICS

Students in the final year of secondary education at Sint-Pieterscollege Jette proposed a human physiology experiment called 'telerobotics' as their project proposal for the Bifrost One campaign in 2017. It was selected.

6.1. Rationale

Whenever the day comes to send people beyond LEO (Low Earth Orbit) radiation protection will become an even bigger issue than it is on the ISS. On such deep space missions, risky EVA (Extra Vehicular Activity) may be necessary to perform repairs or even just to achieve mission goals, such as Mars exploration or asteroid sample return. While robots can be used for some tasks, they lack human decision making skills.

Figure 6. Enhancing the scientific return of exploration missions by using synergies between man and machine: robustness versus human decision making capabilities.

Therefore remote control may be mandatory in a number of situations. However, in deep space, remote control from Earth may not be a viable option because of the time delay caused by the finite value of the speed of light. Hence the astronauts themselves will have to operate their robots, which makes the reliability of their fine motor skills an essential prerequisite for mission success.

6.2. Experiment concept

The goal is to asses a test subject's ability to remotely steer a laser dot through a maze. To do this, a joystick is connected to an Arduino microcontroller that uses a 20mW radio module operating at 430MHz to send its instructions to a pan- and tilt platform that carries a small laser module, iamed at a simple maze. The whole setup is filmed and the imagery is wirelessly sent to FPV goggles using equipment used by drone pilots.

This allows the test subject to get real-time visual feedback on what happens, just as an astronaut would if he was operating a Mars rover in the field from the safety of his surface or orbital habitat. See Fig. 6.

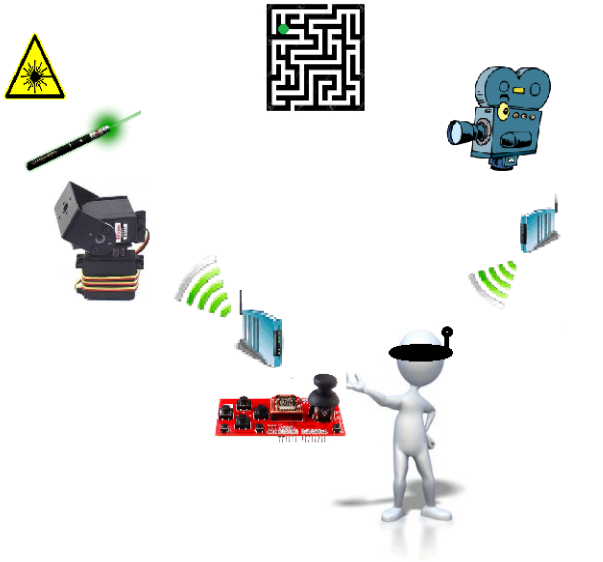

Figure 7. From the top clockwise: A maze is filmed and the images transmitted to FPV goggles, carried by a test subject using this visual feedback to manipulate a joystick that – through Arduino microcontrollers) wirelessly controls a pan- and tilt platform carrying a small laser module. The goal is for the test subject to steer the laser dot through the (simple) maze while in microgravity.

7. CONCLUSIONS

Hands-on space education projects provide youngsters with challenging opportunities to think outside the box and acquire both knowledge and skills way beyond any curriculum. Cooperation, multitasking, scheduling, reporting are skills being built in the course of such projects. Knowledge gains are more dependent on the nature of the project. With Asgard high altitude balloons most experiments require microelectronics and things like power management and data storage are important aspects. Scientific experiments are situated mostly in the fields of Earth sciences, atmospheric, solar and astrophysics. Technology experiments cover such items as inertial gondola stabilisation, solar cell perfomance and radio wave propagation.

With Bifrost parabolic flights, other sciences can be studied as well: medecine, biology, planetary geology and fluid physics. In all cases, student motivation reaches exceptional heights as the teams are well aware of the unique nature of the flight opportunity, and the interaction with other teams, each struggling the make the most of this life-changing experience.

8. REFERENCES

1. Chameleva, H., Degroote, C., Dhaese, Z., Paice, C., Plas, H., Van den Bossche, A. ,Vander Dockt, L., Vander Vost, J., de Schrijver, E., (2015) SP.ACE" 2013–2015: ASGARD Balloon and BIFROST Parabolic Flights: Latest Developments in Hands-On Space Education Projects for Secondary School Students. In Proc. 22nd 'Esa Symposium on European Rocket and Balloon Programmes and Related Research'. ESA Publications Division, European Space Agency, Noordwijk Netherlands.

EISCAT INCOHERENT SCATTER RADAR FACILITIES FOR GROUND-BASED ATMOSPHERIC, SOLAR-TERRESTRIAL AND PLANETARY SCIENCE IN THE NORTHERN AURORAL OVAL AND POLAR CAP

Carl-Fredrik Enell[1], **Craig Heinselman**[1], **Anders Tjulin**[1], **and Johan Kero**[2]

[1]*EISCAT Scientific Association, PO Box 812, SE-981 28 Kiruna, Sweden*
[2]*Institutet för rymdfysik, PO Box 812, SE-981 28 Kiruna, Sweden*

ABSTRACT

EISCAT Scientific Association is an international research organisation that at present operates two incoherent scatter radars in the northern auroral zone in Fenno-Scandinavia and one in the cusp region on Svalbard. EISCAT also operates an ionospheric heater facility and an ionosonde in Tromsø, Norway. EISCAT observations enable fundamental research in solar-terrestrial and atmospheric physics, observing direct solar photo-ionisation as well as ionospheric effects of magnetospheric events and atmospheric dynamics. EISCAT can also study solar system objects such as meteoroids.

In September 2017 EISCAT will officially start the EISCAT_3D construction project, which will become a world-leading international research infrastructure consisting of a multistatic antenna array system operating at 233 MHz as well as an e-infrastructure for data transfer and analysis. EISCAT_3D will be the first of a new generation of flexible radars that take advantage of the software defined radio approach. EISCAT_3D will be able to operate continuously and image a large volume of the ionosphere, which will provide new details of how the Earth's atmosphere is coupled to space. The system will also be a versatile monitor of extraterrestrial dust and objects like the Moon and asteroids.

Key words: EISCAT, high power large aperture radar, incoherent scatter, ionosphere, ground-based instruments.

1. INTRODUCTION

1.1. Incoherent scatter radar

The ionosphere is a remote region of the atmosphere, accessible only by sounding rockets and remotely sensing radio and optical instruments on the ground and on satellites. Out of these methods, radio remote sensing works under the largest variety of atmospheric conditions. Low power radio instruments usually utilise total ionospheric reflection at critical plasma frequencies, and thus cannot probe the whole ionospheric height profile. This leaves incoherent scatter observations by high power large aperture radars at HF, VHF and UHF frequencies (50 MHz and higher) as the only remote method able to make continuous measurements of height profiles (or volumes) of ionospheric parameters.

Incoherent scatter radars are by necessity large instruments, the most well-known facility of its kind being the Arecibo radar, also used as a radio telescope, in Puerto Rico. Several other stations exist as shown in Figure 1. These stations operate at different frequencies and use different antenna technologies, either large dishes of different designs or antenna arrays.

1.2. EISCAT

Being significantly more accessible than the Antarctic, the northern auroral oval and polar cap is a suitable place to study coupling between space and the atmosphere. Several research institutes have been active in the area for a long time. The European Incoherent Scatter Scientific Association (EISCAT) was established in 1975 and started operations with a UHF radar on the northern Scandinavian mainland in 1981 [FHW83]. Today EISCAT is a truly international organisation with member institutes (Associates) in

China China Research Institute of Radiowave Propagation (CRIRP)

Finland Suomen Akatemia (SA)

Japan National Institute of Polar Research (NIPR) and Nagoya University Institute of Space-Earth Environmental Research (ISEE)

Norway Norges Forskningsråd (NFR)

Sweden Vetenskapsrådet (VR)

UK Natural Environment Research Council (NERC)

In addition to the Associates, there are also affiliate institutes (funding EISCAT radar time but not full membership) in France, South Korea, and Ukraine.

The detailed map of northernmost Europe in Figure 2 shows the locations of existing operational EISCAT stations. Details are listed in Table 1.

The Tromsø site at Ramfjordmoen in northern Norway is the mainland transmitter site (Figure 3). The UHF radar, seen at the right side of the picture, has a 32 m parabolic dish antenna and operates at 930 MHz. From the start in 1981 until 2012, the UHF radar was tristatic with remote receivers at the Kiruna and Sodankylä sites. In 2012 the remote receivers had to be converted to the VHF frequency due to interference from mobile communications at 930 MHz, and since then the UHF radar has been monostatic.

The VHF radar operates at 224 MHz and has a 40 times 120 meter parabolic cylinder antenna in four sections, seen at the left of Figure 3. Since the conversion of the remote sites in 2012, the VHF radar has two remote receiver stations: Kiruna, Sweden, and Sodankylä, Finland (Figure 5), with 32 m dishes that are identical to the UHF antenna (except for the transmitter feed and the VHF replacement visible in the photo from Kiruna, making it the only operational tristatic incoherent scatter radar in the world.

The EISCAT Svalbard radar (ESR) is a separate system with a transmitter operating at 500 MHz [WWV+97]. It has two antennas (Figure 4), one steerable 32 m dish and another fixed field aligned 42 m dish, which can be used simultaneously in a pulse-to-pulse switching mode.

The EISCAT ionosonde at the Tromsø site is an old HF radar with a phased array receiving antenna, applying the Dynasonde pulse modulation technique and the corresponding DSND analysis software [RWZP08].

Finally but importantly, EISCAT also operates a high power HF transmitter with large antenna arrays at the Tromsø site. It is known as the EISCAT Heater [RKKS92] and with recent upgrades [RSMW16] it is capable of both artificial ionospheric heating and HF radar operation.

1.3. Access to EISCAT

EISCAT runs Common Program observations on radar World Days and during other events of interest. In addition, scientists can apply for Special Programmed (SP) observations, i.e. to run their own observations. Each Associate and Affiliate is required to set up an internal review system of their choice to consider proposals for Special Programs submitted by scientists of that Associate or Affiliate. Once granted SP time, an experiment can be requested through the online schedule system. The legacy EISCAT systems have a strict scheduling policy

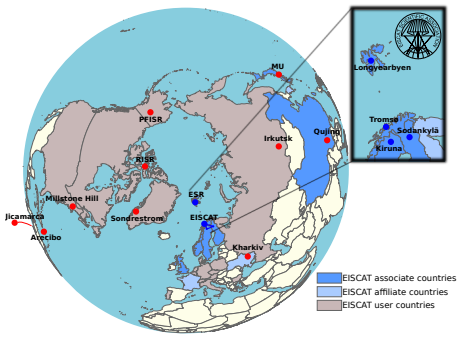

Figure 1. Incoherent scatter radar stations around the world, EISCAT sites highlighted. Most of them are in the northern hemisphere. The MU radar in Japan is a 50 MHz HF atmospheric radar with some ISR capabilities, and the Jicamarca radar in Peru is also an HF radar dedicated to phenomena at the magnetic equator. The other radars operate at VHF frequencies or higher.

since the transmitters require manual operation by specially trained engineers. When several applicants request an experiment at the same time, a priority order is assigned, meaning that the second priority applicant is allowed to measure in case the first priority applicant decides to cancel, and so on. Use of EISCAT data is embargoed. In general, only the experimenter is allowed to download and use the data for the first year after an observation.

Scientists from non-EISCAT member countries and institutes can obtain EISCAT data through collaboration. There have also been so called Timebuyer and Peer Review access programs.

2. EISCAT SCIENCE

EISCAT is used by scientists from several fields of ionospheric and atmospheric research, often during coordinated campaigns involving other ground-based instruments, satellite conjunctions, or rocket launches. The following is a selection of scientific topics, by no means complete.

2.1. Solar-terrestrial interaction and the ionosphere

The auroral oval, where the magnetospheric plasmasheet maps down to the ionosphere, was the original reason for constructing EISCAT. Although studied since the dawn of spaceflight in the 1950's, the wave-particle interactions that accelerate charged particles still hold unknown details. Due to its unique tristatic capabilities, EISCAT is suitable for measuring electric fields, plasma motion, and ion outflow. See for example [ACN12] and [OSH+08].

Figure 6 shows an example of an image [DAK+10] from Auroral Structure and Kinetics (ASK), a narrow field

Table 1. The locations and technical details of the existing legacy EISCAT instruments. [1] *The Heating facility was built by the Max Planck Institute of Aeronomy and taken over by EISCAT in 1993.* [2] *Year of upgrade to digital recording on PC.* [3] *The remote sites in Kiruna and Sodankylä were parts of the fully steerable UHF radar from the start in 1981 until September 2012, when they were converted to the VHF frequency due to interference from mobile communication in the 930 MHz band.*

Site	Latitude	Longitude	Instrument	Frequency	Power	Started
ESR	78.15 N	16.02 E	ESR	500 MHz	1 MW peak	2001
Tromsø	69.58 N	19.23 E	UHF	930 MHz	2 MW peak	1981
			VHF	224 MHz	1.6 MW peak	1985
			Heater	4–8 MHz	1.2 MW CW	1979[1]
			Dynasonde	1–12 MHz	10 kW peak	1992[2]
Kiruna	67.87 N	20.43 E	VHF Rx[3]	224 MHz[3]	—	1981[3]
Sodankylä	67.37 N	26.63 E	VHF Rx[3]	224 MHz[3]	—	1981[3]

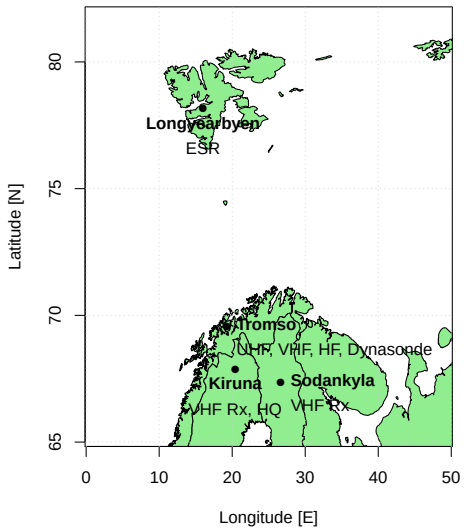

Figure 2. Detailed map of the EISCAT sites, indicating where the legacy EISCAT instruments are installed. Transmitters are located in Tromsø, Norway, and Longyearbyen, Svalbard. The organisation headquarters (HQ) is co-located with the Swedish Institute of Space Physics, which also hosts the Kiruna receiver site.

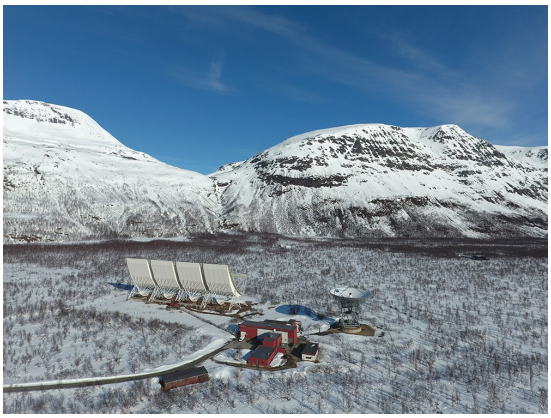

Figure 3. The main EISCAT mainland site at Ramfjordmoen near Tromsø in Norway. From left to right the VHF 120×40 m antenna, the main building, and the 32 m UHF dish can be seen. The Heating and ionosonde antenna arrays are outside this picture.

of view, high time resolution instrument co-located with EISCAT (Tromsø in this example, later on Svalbard). The circle marks the EISCAT UHF beam. This kind of small and rapidly varying structures, caused by wave-particle interactions, could not be resolved until the advent of fast imagers such as electron-multiplying CCDs (EMCCD).

Another important issue is energy deposition into the ionosphere. As mentioned EISCAT is often used together with satellite measurements of energetic particles and optical emissions with instruments on polar-orbiting satellites (examples include [TPJ13]). However, it is always difficult to compare single line of sight radar measurements and conjugate satellite instruments due to both spatial and temporal limitations, as well as possible problems with the particle instruments as addressed e.g. by [AM13]).

In Figure 7, from [PJK+04], auroral ionisation rates have been estimated by two methods: from optical emission rates [Jan01] and from EISCAT electron density variation [Kir88]. Results are shown from two seasons. Although the results fall on straight lines as they should, there are differences that may depend on background sunlight (that cause an offset in optical emission) or different atmospheric composition (affecting recombination rates).

Figure 4. The EISCAT Svalbard site with its steerable 32 m dish seen on the left, the main building in the middle, and the fixed 42 m dish to the right.

Figure 5. The EISCAT Kiruna and Sodankylä sites with their steerable 32 m dishes. The VHF conversion is visible in the photo from the Kiruna site: there is a dipole antenna in the focal point instead of the Cassegrainian subreflector (which can in fact be seen on the ground below the cable trunks to the immediate left of the antenna). The UHF feeder horn is not in use but can still be seen in the centre of the antenna.

2.2. Middle-atmospheric physics and chemistry

The energy deposited into the atmosphere by auroral precipitation may produce odd nitrogen species (NO_x = NO + NO_2) which can survive and subside in the winter polar vortex and affect middle atmospheric ozone and thus the temperature profile (e.g.[SRC+09]). Figure 8 depicts this procedure schematically.

Figure 9 shows a comparison between a time series of NO measurements from the SCISAT Atmospheric Chemistry Experiment (ACE), EISCAT Svalbard radar electron densities and electron densities modelled with the Sodankylä Ion Chemistry (SIC) model, all at an altitude of 92 km. At these lower ionospheric altitudes, NO^+ is the major ion. The nitric oxide concentration in SIC was thus forced until modelled and measured electron densities agreed during the daytime periods dominated by photochemistry, ascertaining that forced NO concentrations were consistent with the satellite measurements. In this way, EISCAT

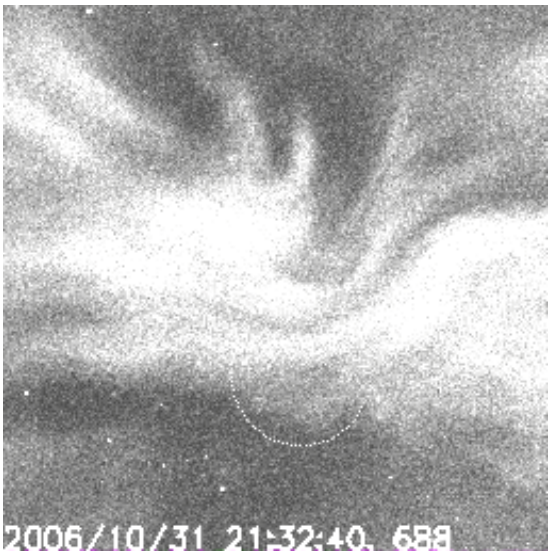

Figure 6. An image from the narrow field of view, high time resolution ASK instrument, which was at the EISCAT Tromsø site in 2008. The circle marks the UHF beam and it can clearly be seen that the aurora has fine structures on a small scale. Figure by courtesy of Hanna Dahlgren, KTH, Stockholm

measurements can be used to estimate changes in NO.

2.3. Meteors, space debris and other coherent targets

It is of great practical and theoretical importance to determine the mass index and orbit distribution of the meteoroid environment, to constrain models of Solar System formation, and to estimate the hazards meteoroids present to spacecraft and manned space missions. The mass influx of extraterrestrial material onto Earth is the source of the neutral and ion metal layers in the middle atmosphere and plays an important role in atmospheric dynamics and processes such as the formation of high-altitude clouds, possibly through coagulation of charged meteoric smoke particles acting as condensation nuclei for water vapour.

The altitude region of the lower ionosphere overlaps with the meteor zone and incoherent radar systems can therefore advantageously be used to study also radar echoes from coherent meteor plasma structures. The high power density permits numerous head echo detections from very faint meteors. Studies conducted at EISCAT pioneered the usage of modern High Power Large Aperture (HPLA) radars for meteor science [PW94]. In addition to meteors, HPLA radars can also detect small solid objects further away, such as space debris and asteroids. Real-time space debris monitoring have routinely been combined on top of normal ionospheric EISCAT work [MLL05].

A meteor head echo comes from the compact region of plasma close to and travelling along with a meteoroid and is therefore highly transient and Doppler-shifted. Its

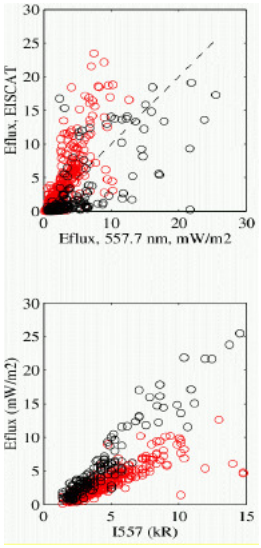

Figure 7. Scatter plot of ionisation rates calculated in the EISCAT volume by two methods: From optical auroral emission rates and from the EISCAT electron density time series. Red and black circles denote different seasons and thus there may be a variable offset caused by the daylight background. Figure from [PJK+04].

characteristics are very different from those of a meteor trail echo, which is a radar echo from the column of plasma left behind the meteoroid and that drifts with the local wind speed. The tristatic EISCAT radar offers a unique possibility to observe the same meteor head echo from three directions simultaneously, which has been used to study processes such as fragmentation [KSPW+08]. Three independently measured velocity components enable calculating accurate meteoroid trajectories, which can be transformed into accurate meteoroid orbits [SKM+08]. However, current tristatic observations are confined within a relatively small measurement volume and tristatic meteor work in principle limited to Special Program observations.

The future EISCAT_3D radar described in next section will allow multi-purpose experiments and data analysis approaches to be used as a standard. This approach will enable tristatic observations of coherent targets to run in parallel with incoherent scatter data analysis whenever the radar is in operation. In addition to meteors and space debris, this will extend the possibilities for observations of other strong coherent radar targets such as Polar Mesospheric Echoes (e.g. [BSR+08] and [MHT+16]) and to utilise them for studying atmospheric dynamics.

3. THE FUTURE OF EISCAT: EISCAT_3D

3.1. Overview

During 2018 EISCAT will start to build the next generation radar, EISCAT_3D. As the name implies, the main

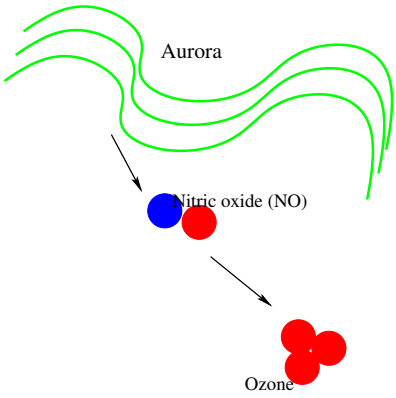

Figure 8. Effects of odd nitrogen (NO_x = NO + NO_2) in the upper middle atmosphere: Illustration of how NO_x can subside from the auroral thermosphere into the winter polar vortex and affect the middle-atmospheric height profile of ozone.

purpose of EISCAT_3D is volume imaging, which is not possible with the single-beam antennas of the old radars. [MAA+15] and [PKH+16] give comprehensive reviews of scientific topics that EISCAT_3D will be able to address. This will be accomplished by means of a distributed system (Figure 10). In the initial stage there will be three stations: a core transmitting and receiving site near Skibotn, Norway, and two additional receiver sites in Sweden and Finland.

3.2. EISCAT_3D system design

Each EISCAT_3D site will consist of almost 10000 crossed dipole antennas as shown in Figure 11. There will be 109 hexagonal subarrays of 91 crossed dipoles receiving two linear polarisations each, i.e. 182 channels per subarray.

The received radiowaves will be digitised close to the antennas without analogue mixing. The rest of the beamforming and analysis will all be done in software. On the subarray level, FPGAs will be used, transmitting up to 20 wide beams from each subarray to the central site computer. With this input, the site computer will calculate up to 200 narrow, steerable radar beams (100 directions and 2 polarisations) from the site.

The frequency chosen for the system is 233.5 MHz, i.e. close to the frequency of the legacy VHF radar. This is essentially a tradeoff between the scales of scientific targets and possible frequency allocations between commercial broadcast bands.

Figure 12 shows the calculated performance of the system. The numbers are the integration times required to measure standard incoherent scatter radar parameters at three ionospheric altitudes,calculated for a normal ionosphere and reasonable requirements on the signal to noise ratio. The aim is for EISCAT_3D to be at least an or-

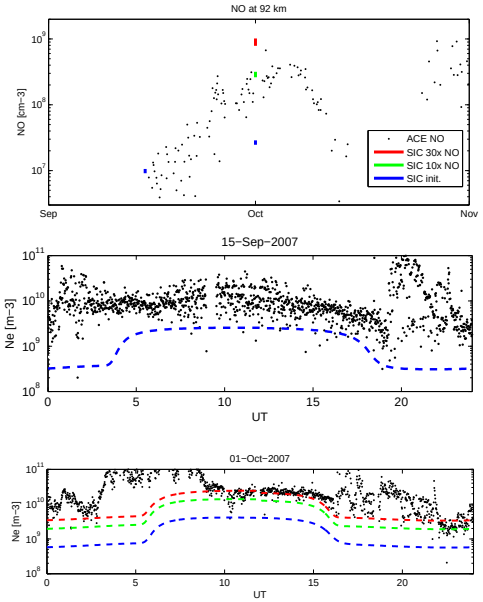

Figure 9. Comparison of measured and modelled nitric oxide concentration and electron density at 92 km. Upper plot, black dots: SCISAT ACE satellite measurements of NO. Lower plots, black dots: EISCAT Svalbard electron density. Coloured lines: SIC model electron density for different scaled concentrations of NO. Effects of article precipitation are seen in the EISCAT measurements during night time but are not modelled here. In this way the composition and chemical effects of variable NO_x concentrations can be studied. Figure by Antti Kero, Sodankylä Geophysical Observatory.

der of magnitude faster than the old radars, which will be accomplished through high transmitter power, narrow beams (although the most common targets are beam-filling, sky noise should be reduced), low noise receivers, and improved pulse coding and signal processing algorithms.

3.3. EISCAT_3D e-infrastructure

The stations will be controlled and connected by high speed Internet links over optical fibres. The rates of data output from one site at full power and resolution can be over 50 gigabytes per second, so at a minimum 100 Gb/s links buffered links are planned.

Data will be analysed and visualised at a central facility, the Operations Centre, and spare computing capacity at the sites will also be utilised for data analysis when the stations run at a low duty cycle. The data will be archived

Figure 10. Layout of the planned full EISCAT_3D system. Top: Visualisations of the fields of view and the common 3D volume. Bottom: Locations of the sites. The construction of the first phase starts in 2018 and includes the Skibotn core site and the Karesuvanto and Kaiseniemi receiver sites. Two additional locations are planned for future expansions.

at two separate locations, the Data Centres.

3.4. Scheduling of EISCAT_3D

EISCAT_3D will be much more flexible than the old EISCAT radars since it will be fully autonomous and remotely controlled. Several experiments will run simultaneously in an interleaved way and it will also be possible to trigger experiments on demand. The system will run in a low power, low duty cycle overview mode 24/7 and will thus be able to detect events and switch experiment modes accordingly by conditions rather than by time.

3.5. EISCAT_3D timeline

The project starts officially in September 2017 but has been preceded by a design study within EU FP6, a preparatory phase project in FP7 and a prototype subarray project in H2020. The prototype subarray is being constructed to test hardware compatibility and performance.

August 2017 Prototype subarray at Tromsø site

September 2017 Official project kickoff

2018 Start of site preparation

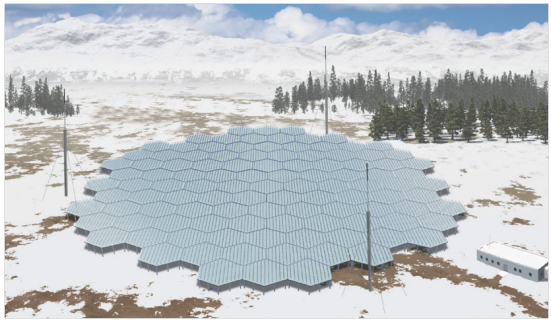

Figure 11. Design of the EISCAT_3D sites, artistic visualisation of a station. The antenna arrays will consist of 109 hexagonal subarrays with 91 crossed dipole aerials each).

2021 First measurements with the Phase 1 system

Future TBD Computing facility with hundreds of TFLOPs processing power for volume imaging

Future TBD Upgrade of Skibotn transmitters from 5 MW to 10 MW

Future TBD Remote receivers south (near Porjus, Sweden) and west (Andøya rocket range) of the core sites

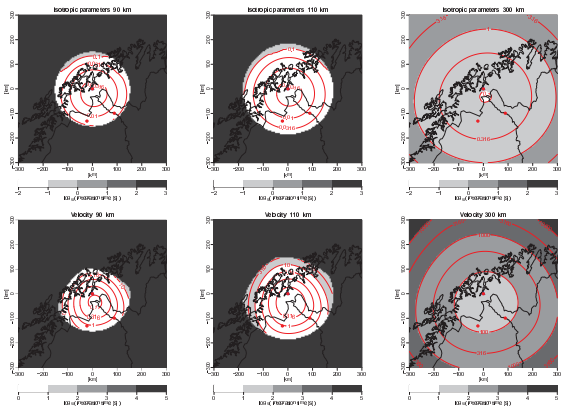

Figure 12. EISCAT_3D performance calculations, estimated as described by I.I. Virtanen, University of Oulu (in Appendix B in https://eiscat3d.se/project/fp7/handbook). The contour lines show integration times required to determine standard incoherent scatter parameters at heights 90, 110 and 300 km from a typical ionospheric signal. Upper panel: calculated for scalar parameters (electron density, electron temperature, ion temperature). Lower panel: calculated for vector velocity. The aim is to be an order of magnitude faster than legacy incoherent scatter radars, which will be accomplished by means of a large antenna area and powerful distributed transmitters.

4. SUMMARY

EISCAT incoherent scatter radars are among the most versatile instruments of their kind. The new EISCAT_3D system, which will be constructed soon and operational during 2021, will set a new standard. These instruments have multiple purposes and the best scientific use will be obtained by collaboration with other ground-based facilities (for example HF radars and the ALIS and MIRACLE imagers) and with launches of sounding rockets from ESRANGE and Andøya Rocket Range. EISCAT_3D will be much more flexible with respect to scheduling and experiment configuration than the old radars.

ACKNOWLEDGMENTS

EISCAT is an international association supported by research organisations in China (CRIRP), Finland (SA), Japan (NIPR and ISEE), Norway (NFR), Sweden (VR), and the United Kingdom (NERC).

REFERENCES

[ACN12] A. T. Aikio, L. Cai, and T. Nygrén. Statistical distribution of height-integrated energy exchange rates in the ionosphere. *J. Geophys. Res.*, 117(A16):A10325, October 2012.

[AM13] T. Asikainen and K. Mursula. Correcting the NOAA/MEPED energetic electron fluxes for detector efficiency and proton contamination. *J. Geophys. Res. (Space Phys.)*, 118:6500–6510, October 2013.

[BSR+08] E. Belova, M. Smirnova, M. T. Rietveld, B. Isham, S. Kirkwood, and T. Sergienko. First observation of the overshoot effect for polar mesosphere winter echoes during radiowave electron temperature modulation. *Geophys. Res. Lett.*, 35:L03110, February 2008.

[DAK+10] H. Dahlgren, A. Aikio, K. Kaila, N. Ivchenko, B. S. Lanchester, D. K. Whiter, and G. T. Marklund. Simultaneous observations of small multi-scale structures in an auroral arc. *J. Atmos. Sol.-Terr. Phys.*, 72:633–637, May 2010.

[FHW83] K. Folkestad, T. Hagfors, and S. Westerlund. EISCAT: An updated description of technical characteristics and operational capabilities. *Radio Sci.*, 18:867–879, 1983.

[Jan01] P. Janhunen. Reconstruction of electron precipitation characteristics from a set of multiwavelength digital all- sky auroral images. *J. Geophys. Res.*, 106:18505–18516, 2001.

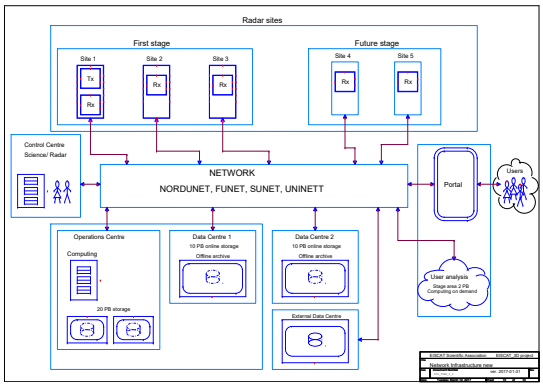

Figure 13. Design of the EISCAT_3D e-infrastructure with network, analysis facilities, data centres, data portal and control centre. Figure from the NeIC support project for EISCAT_3D.

[Kir88] Sheila Kirkwood. SPECTRUM—a computer algorithm to derive the flux-energy spectrum from EISCAT electron density profiles. Technical Report 034, Swedish Inst. of Space Physics, Kiruna, October 1988.

[KSPW+08] Johan Kero, Csilla Szasz, Asta Pellinen-Wannberg, Gudmund Wannberg, Assar Westman, and David D. Meisel. Three dimensional radar observation of a submillimeter meteoroid fragmentation. *Geophys. Res. Lett.*, 35:L04101, 2008.

[MAA+15] I. McCrea, A. Aikio, L. Alfonsi, E. Belova, S. Buchert, M. Clilverd, N. Engler, B. Gustavsson, C. Heinselman, J. Kero, M. Kosch, H. Lamy, T. Leyser, Y. Ogawa, K. Oksavik, A. Pellinen-Wannberg, F. Pitout, M. Rapp, I. Stanislawska, and J. Vierinen. The science case for the EISCAT_3D radar. *Progress in Earth and Planetary Science*, 2:21, December 2015.

[MHT+16] I. Mann, I. Häggström, A. Tjulin, S. Rostami, C. C. Anyairo, and P. Dalin. First wind shear observation in PMSE with the tristatic EISCAT VHF radar. *J. Geophys. Res. (Space Phys.)*, 121(A10):11, November 2016.

[MLL05] J. Markkanen, M. Lehtinen, and M. Landgraf. Real-time space debris monitoring with EISCAT. *Adv. Space Res.*, 35:1197–1209, 2005.

[OSH+08] Y. Ogawa, K. Seki, M. Hirahara, K. Asamura, T. Sakanoi, S. C. Buchert, Y. Ebihara, Y. Obuchi, A. Yamazaki, I. Sandahl, S. Nozawa, and R. Fujii. Coordinated EISCAT Svalbard radar and Reimei satellite observations of ion upflows and suprathermal ions. *J. Geophys. Res.*, 113(A05306), 2008.

[PJK+04] N. Partamies, P. Janhunen, K. Kauristie, S. Mäkinen, and T. Sergienko. Testing an inversion method for estimating electron energy fluxes from all-sky camera images. *Ann. Geophys.*, 22:1961–1971, June 2004.

[PKH+16] A. Pellinen-Wannberg, J. Kero, I. Häggström, I. Mann, and A. Tjulin. The forthcoming EISCAT_3D as an extra-terrestrial matter monitor. *Planet. Space Sci.*, 123:33–40, April 2016.

[PW94] A. Pellinen-Wannberg and G. Wannberg. Meteor observations with the European Incoherent Scatter UHF radar. *J. Geophys. Res.*, 99(A6):11379–11390, June 1994.

[RKKS92] M. T. Rietveld, H. Kohl, H. Kopka, and P. Stubbe. Introduction to ionospheric heating at Tromsø-I. Experimental overview. *J. Atmos. Terr. Phys.*, 55:577–599, 1992.

[RSMW16] M. T. Rietveld, A. Senior, J. Markkanen, and A. Westman. New capabilities of the upgraded EISCAT high-power HF facility. *Radio Sci.*, 51:1533–1546, September 2016.

[RWZP08] M. T. Rietveld, J. W. Wright, N. Zabotin, and M. L. V. Pitteway. The Tromsø dynasonde. *Polar Science*, 2:55–71, 2008.

[SKM+08] Csilla Szasz, Johan Kero, David D. Meisel, Asta Pellinen-Wannberg, Gudmund Wannberg, and Assar Westman. Orbit characteristics of the tristatic EISCAT UHF meteors. *Mon. Not. R. astr. Soc.*, 388:15–25, July 2008.

[SRC+09] A. Seppälä, C. E. Randall, M. A. Clilverd, E. Rozanov, and C. J. Rodger. Geomagnetic activity and polar surface air temperature variability. *J. Geophys. Res.*, 114(A10), 2009.

[TPJ13] A. T. Aikio T. Pitkänen and L. Juusola. Observations of polar cap flow channel and plasma sheet flow bursts during substorm expansion. *J. Geophys. Res.*, 118:774–784, 2013.

[WWV+97] G. Wannberg, I. Wolf, L.-G. Vanhainen, K. Koskenniemi, J. Röttger, M. Postila, J. Markkanen, R. Jacobsen, A. Stenberg, R. Larsen, S. Eliassen, S. Heck, and A. Huuskonen. The EISCAT Svalbard radar: A case study in modern incoherent scatter radar system design. *Radio Sci.*, 32(6):2283–2307, 1997.

RECENT AND FUTURE NORWEGIAN SOUNDING ROCKET PROJECTS CONDUCTED BY ANDØYA SPACE CENTER

Geir Lindahl [(1)]

[(1)] *Andøya Space Center, Norway, Bleiksveien 46, N-8480 Andenes, Norway, geir@andoyaspace.no:*

ABSTRACT

During the last couple of decades several Norwegian sounding rocket payloads have been launched from Andøya and Svalbard, where Andøya Space Center(ASC) have been responsible for project management, integration and qualification. The missions were either financed by the 6th EU Frame Program or through shared funding by the Norwegian Research Council and the Norwegian Space Center. All payloads have been based on the well-proven Hotel Payload configuration. A standardized solution, both mechanically and electronically, with good possibilities for adaptation to a wide variety of scientific needs. Both one and two stage configurations have been flown.

In the summer of 2016 the Improved Malemute Qualification/MaxiDusty mission was conducted from Andøya Space Center as a cooperation between Andøya Space Center and DLR Moraba. The mission had two main objectives; qualifying the Improved Malemute rocket engine for scientific use as well as delivering the two scientific payloads, Maxi Dusty 1 and Maxi Dusty 1b into Middle Atmosphere. Both objectives were reached with great success.

Currently, two additional Hotel Payloads are under development: Nucleus and ICI-5. The Nucleus payload is built for Nammo and are going to fly on the test flight of the Nucleus hybrid rocket engine, scheduled for launch September 2017. The ICI-5 payload, with PI Jøran Moen from the University of Oslo, is going to participate in the Grand Challenge as one of the vehicles launched from Svalbard. This paper summarizes the technical challenges and solutions of the payloads and motor configurations for the mentioned projects.

1. INTRODCUTION

Andøya Space Center have through the last decades developed a well-proven standardized module based payload platform; the Hotel Payload.

The Hotel Payload concept revolves around the idea that Andøya Space Center takes care of the project management, payload design, payload integration, qualification, trajectory calculations, telemetry, launch operations and all other supporting activities, so that the scientists can focus all their efforts into their specific scientific instruments.

The Hotel payload has traditionally been composed of five standard module sections.

- Nosecone Section
- Electronic Section
- Hotel Section
- Service Section
- Second Stage Ignition Section

The Nosecone Section is spilt open, by pyrotechnical charges at a predetermined time, exposing the underlying sensors to the environment.

The Electronic Section traditionally houses support electronic for the sensors in the nosecone.

The Hotel Section has two large deployable hatches, which are released at a predetermined time, making it possible for deployable booms to be extended out through the openings.

These three front sections are customized according to customers' requirements.

The Service Section contains support electronics that handles power distribution, data transmission to ground, timed events and attitude determination.

The Second Stage Ignition Section houses electronics for the ignition of the second stage motor.

The complete basic Hotel Payload configuration is 356mm (14inch) wide and almost 3m tall as shown in Fig. 1. The payload is qualified for a dual stage motor configuration with a VS-30 as the first stage and an Improved Orion as the second stage. With the Maxi Dusty campaign, the Hotel Payload also became qualified for an Improved Malemute as a single stage configuration. The two-stage configuration takes the payload up to an apogee of 350km and around 120km for the single stage. Typical payload weight is 135kg.

The payload can be launched from either Andøya or Ny-Ålesund, Svalbard.

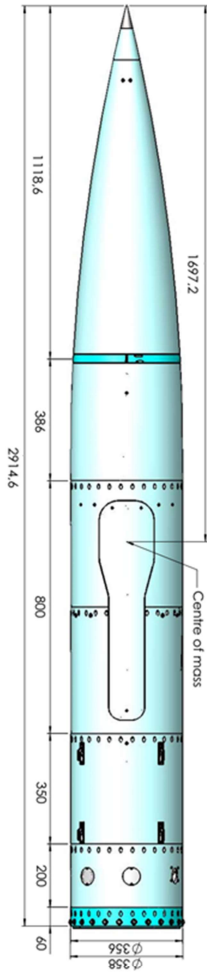

Figure 1: Hotel Payload basic configuration.

2. ICI-4

The principal investigator for the ICI-4 payload was Professor Jøran Moen from the University of Oslo. In addition to the instruments from University of Oslo the payload housed participating instruments from the Institute of Space and Astronautical Science, Japan, University of Alberta, Canada and the Laboratoire de Physique des Plasmas, France.

2.1. Objectives

The main objective was to investigate the micro-physics of plasma instabilities and turbulence phenomena associated with polar cap patches being pulled into the night-time aurora, referred to as auroral blobs.

The auroral blob phenomenon is created when polar cap patches - islands of high electron density plasma - exit the polar cap at night, i.e. when they are entering the night-time auroral oval.

The ingredients are high density F-region plasma structures, imposed by auroral precipitation, field aligned currents and flow shears. This appears to be the most violent situation for GNSS scintillations in the Scandinavian Arctic sector. This is a highly complex region of the auroral ionosphere driven by tail reconnection [1].

2.2. Payload

The payload structure was a basic Hotel Payload configuration.

ICI-4 was launched from Andøya on the 19th of February 2015, with a total payload mass of 136kg and reach an apogee of 361km. The flight was nominal.

3. MAXI DUSTY

The Maxi Dusty project consisted of two payloads, the Maxi Dusty 1 and Maxi Dusty 1b. The principal investigator for the payloads were Professor Ove Havnes from the University of Tromsø. In addition to the instruments from the University of Tromsø the payload housed participating instruments from the University of Oslo, Norway, University of Stockholm, Sweden, Graz University of Technology, Austria, University of Alberta, Canada and University of Colorado, Boulder USA.

The Maxi Dusty payloads, were middle Atmospheric research payloads, with the intent to investigate the NLC/PMSE layers at around 80km, and with an target apogee of 110km. This meant that the two stage configuration was out of the question. It was first proposed launched with the VS30 as a single stage configuration but the Scramspace incident putting the VS30 on the ground for some time, and the long lead time when it got the return to flight status, made us look for other launch vehicles. The Improved Malemute became our solution.

As this was the first time the Improved Malemute have been launched as a single stage, the Maxi Dusty payloads became the qualification flights for the Improved Malemute and for the Hotel Payload with this motor. The campaign was conducted in cooperation between DLR Moraba, who were in charge of the motor qualification and Andøya Space Center who were in charge of payload preparations and launch operations.

3.1. Objectives

There were two main objectives for the campaign. One scientific and one technical.

One of the two principal aims was to successfully flight qualify the transfer of the military surplus Patriot PAC2 MIM-104C missile into the civil-use Improved Malemute sounding rocket vehicle to serve various kinds of research applications for the scientific community. This includes the flight qualification of all vehicle hardware, including two different sets of stabilizing fins for each of the test flights, and to validate the flight dynamic modelling of this vehicle. Therefore, a comprehensive flight diagnostic package was part of the qualification effort involving standard instrumentation such as accelerometers, magnetometers, temperature sensors and additionally on-board GPS and TV imagery as well as ground based radar tracking.

The second major mission goal was the collection of scientific data in the field of Middle Atmosphere research. The scientific questions focuses on:

- Launch the, too this date, two most complete payloads to study the NLC/PMSE clouds and their cloud particles.
- Maiden flight of a new mass spectrometer, ICON, to study the evaporation gases from collected icy NLC/PMSE cloud particles to gain new knowledge on their chemical composition.
- On the MXD-1B payload: a newly developed Mother-Daughter system where 6 daughter payloads are ejected from the main (Mother) payload to study the 4D conditions around the payload trajectory.
- Fly for the first time the complete set of 3 MUDD probes to study in detail the energy, or mass distribution of fragments produced by impacting NLC particles. The fragments are most likely related to the mass distribution of meteoric smoke particles (MSP).
- First opportunity to gain new insight in the NLC/PMSE cloud physics by comparing measurements from such a diverse set of dust probes as DUSTY, MUDD, ICON and MiniMASS.
- MXD-1 and MXD-1B will have support measurements - plasma density - dust size - of exceptional quality.
- Conduct measurements to study the influence of the payload on probe measurements through aerodynamic drag and/or payload charging.
- Gain insight in the performance of various probes as a basis for probe improvement and the development of new probes [2].

3.2. Payload

The Maxi Dusty 1 payload was a basic Hotel Payload configuration except the Second Stage Ignition Section which was exchanged with a newly qualified GPS Section.

The GPS Section houses a GPS wraparound antenna, a GPS receiver and electronics to set off pyrotechnical charges at a predetermined height.

On the Maxi Dusty 1b payload the Second Stage Ignition Section was also exchanged with a GPS Section. In addition, the Hotel Section was exchanged with a newly developed 4D Space Section.

The 4D space Section houses 6 deployable daughter payloads. The daughters are released in pairs at a predetermined time. There is a two-way communication link between each daughter and the main payload.

Another minor adjustment of the two payloads was the blunted tip to reduce the apogee, speed and heat generated on the payload structure.

In order to qualify the Hotel Payload for the Improved Malemute the aerodynamical loads were calculated, structural analyses were performed and a bend down test was conducted.

The Improved Malemute Qualification flight 1/Maxi Dusty 1 was launched from Andøya on the 30th of June 2016 and a total payload mass of 134kg reaching an apogee of 114km. The flight was nominal.

The Improved Malemute Qualification flight 2/Maxi Dusty 1b was launched from Andøya, on the 8th of July 2016, with a total payload mass of 135kg reaching an apogee of 117km. The flight was nominal.

The two payloads are illustrated in Fig.2.

Figure 2: Maxi Dusty 1 to the left and Maxi Dusty 1b to the right.

4. NUCLEUS

Nucleus is a scientific sounding rocket built to demonstrate Nammo's cutting-edge hybrid motor in a flight demonstration into space. The payload is built by Andøya Space Center and is currently going through the final stages of construction and qualification. Nucleus is scheduled for launch during September 2017 from Andøya.

4.1. Payload

The payload will be a small Hotel Payload configuration, consisting of a Nosecone Section, an Electronic Section, a Service Section and a 4D Space Section. Total payload mass is estimated to be approximately 65kg. Target apogee is around 100-110km.

The launch will contain an on board camera system delivered by DLR Moraba which will capture and downstream the entire flight.

A new type of IMU, the STIM300 from Sensonor, is going to be test flown on this payload.

A new type of pyrotechnical release system to separate the nosecone will be flight qualified with this flight. The system is more or less a copy of the old system, but the expensive, ITAR regulated pressure cartridges from Holex are replaced with a squib used in airbag systems.

5. ICI-5

The ICI-5 payload is in the early design phase. The payload is going to be a basic Hotel Payload except Hotel Section which is going to be replaced with two 4D-Space Sections.

The ICI-5 payload is scheduled for launch in December 2018 from Ny-Ålesund as a part of the Grand Challenge Initiative(GCI) – Cusp Project. The GCI is a large-scale international collaboration effort targeting advancement in specific, fundamental issues in space and earth science. The core of the GCI cusp project is a series of sounding rocket missions independently conceived and developed in US, Norway and Japan. The scientific goal for the GCI cusp project is to determine multi-scale physics of heating and charged particle precipitation in the ionosphere specific to the geomagnetic cusp region.

6. REFERENCES

1. ASC-P-382 (2015) *Flight Requirement Plan ICI-4 Campaign.*
2. ASC-P-401_0.8 (2016) *Flight Requirement Plan IM Qual 1/2 (IMQ) MaxiDusty1/1b (MXD) Campaign*.

ELAHA – ELASTIC AIRCRAFT FOR HIGH ALTITUDES

CONCEPT AND CURRENT DEVELOPMENT STATE OF AN UNCONVENTIONAL STRATOSPHERIC UAV

Sven Wlach[(1)], Georg Balmer[(2)], Milan Hermann[(3)], Tilo Wüsthoff[(4)]

[(1)]*DLR - Institute of Robotics and Mechatronics, Oberpfaffenhofen, Germany, sven.wlach@dlr.de*
[(2)]*DLR - Institute of Robotics and Mechatronics, Oberpfaffenhofen, Germany, georg.balmer@dlr.de*
[(3)]*DLR - Institute of Robotics and Mechatronics, Oberpfaffenhofen, Germany, milan.hermann@dlr.de*
[(4)]*DLR - Institute of Robotics and Mechatronics, Oberpfaffenhofen, Germany, tilo.wüsthoff@dlr.de*

NOMENCLATURE

DLR	German Aerospace Center
ELAHA	Elastic Aircraft for High Altitudes
ELHASPA	Electric High Altitude Solar Powered Aircraft
HABLEG	High Altitude Balloon Launched Experimental Glider
HAP	High Altitude Platform
HAPS	High Altitude Pseudo-Satellite
IMU	Inertial Measurement Unit
UAV	Unmanned Aerial Vehicle

ABSTRACT

The group *Flying Robots* at the *DLR Institute of Robotics and Mechatronics* in Oberpfaffenhofen conducts research on solar powered high altitude aircraft. Due to the high altitude and the almost infinite mission duration, these platforms are also denoted as High Altitude Pseudo-Satellites (HAPS) or High Altitude Platforms (HAP).

After the successful flight of HABLEG [1], which was presented at ESA PAC 2015 [2], work continued with the goal to reach the stratosphere under own power with a reasonable sized platform.

In order to achieve continuous flying, the overall goal with HAP designs is to obtain a very high battery-to-structure mass ratio. This leads to very fragile aircraft which greatly influences operational availability due to the dependence on calm weather conditions. In fact, thermals and wind have led to several catastrophic failures in the past.

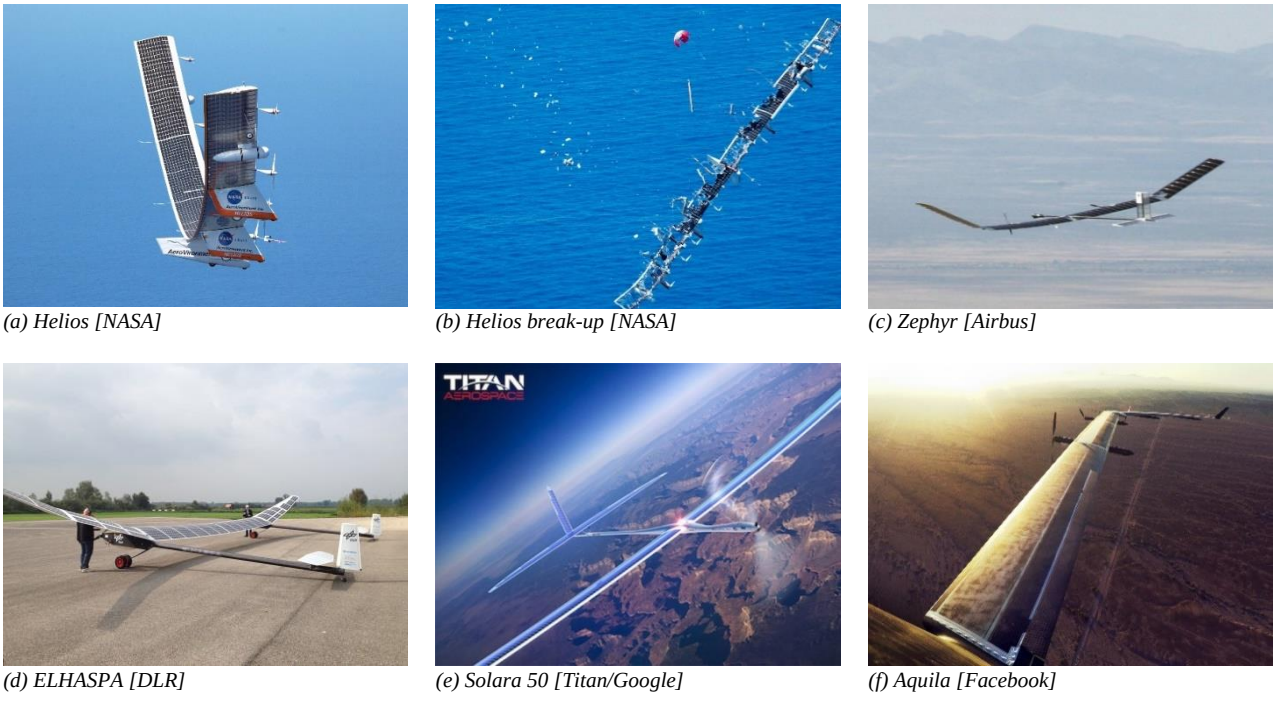

(a) Helios [NASA] *(b) Helios break-up [NASA]* *(c) Zephyr [Airbus]*

(d) ELHASPA [DLR] *(e) Solara 50 [Titan/Google]* *(f) Aquila [Facebook]*

Figure 1: Current HAP Designs

This overview paper proposes a new way of building high altitude platforms. The idea behind ELAHA (Elastic Aircraft for High Altitudes) is to build a segmented airplane with an extremely elastic wing, only elevators as control surfaces and appropriate control algorithms that allow it to survive in turbulent weather conditions.

To date, a proof-of-concept has already been flown successfully and the construction of a larger 10m wingspan version is ongoing. This paper discusses the concept, what has already been achieved and the current status of the development.

1. PROBLEMS OF CURRENT HAP DESIGNS

Fig. 1 shows a few examples of HAP designs. Of those, only the upper row, Fig. 1 (a) – (c), have actually flown in the stratosphere whereas the others only did low level flight testing so far.

Current HAP designs are built using modern fiber compound materials. The mandatory weight reduction as a key design driver currently leads to lightweight but also extremely fragile platforms. Carbon fiber, which is commonly used, has a very high tensile strength and stiffness, but is only capable of small amounts of compression before failing. This geometrically limits the achievable bending radius of a wing with a given thickness. In combination with high wingspans and low wing loadings, these fragile structures lead to tight flight envelopes in which an overspeed condition is reached rather easily. It can be stated that there were several incidents involving structural failure of existing HAP designs.

The airplanes in the lower row of Fig. 1, ELHASPA, Solara 50 [3], and Aquila [4], all encountered structural failure in consequence of piloting or autopiloting shortcomings which caused a violation of flight envelopes. We assume that a more deformable and thus forgiving wing structure in combination with high local control authority to cope with reduced stiffness can help to extend the operation boundaries and avoid getting into undesired situations.

A non-sufficient local control authority of a high aspect-ratio wing also played a role in the Helios breakup. Here, the aircraft morphed into a high dihedral state. The "procedure to reduce dihedral was to increase airspeed" [5]. This approach failed and the wing disintegrated after a successional occurrence of deficient longitudinal control stability.

Furthermore, some of the existing designs don't scale well in size. The increase in size comes with the need for an over-proportionally heavier structure diminishing the potential gain of a bigger platform. This can only be adverted by truly span-loading platforms.

2. THE CONCEPT

We propose to approach these problems with a highly elastic wing and a segmented aircraft.

By highly elastic, we mean a wing that is able to bend up to 90° from wingtip to wingtip. If, as shown in Fig. 2, a thermal updraft catches a part of the aircraft, the wing bends all the way up until the projected surface against the updraft is reduced to almost zero and thereby has no further harming influence. We refer to this, as passive safety.

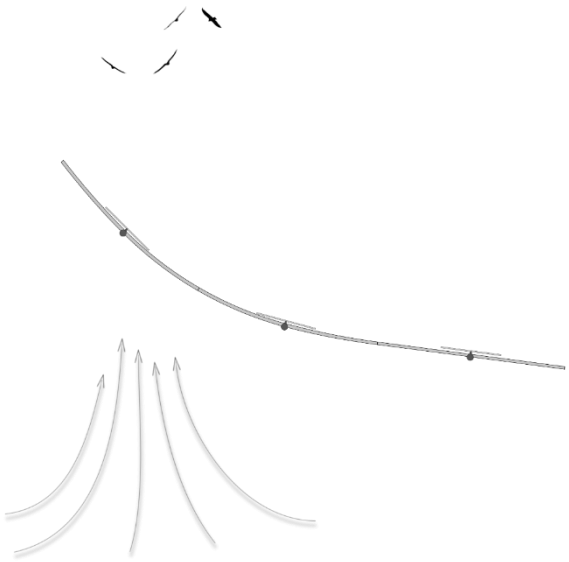

Figure 2: Thermal bending wing upwards

The airplane is made up of segments that can be joined together as needed, which can be seen in Fig. 3 and following. We distinguish between payload and propulsion segments:

Payload segment
- Build like a conventional aircraft
- Stiff enough to distribute the forces of a payload point mass over the segment wingspan
- Receives power to counter its drag, either in electrical form from the propulsion segments if it has an own engine or in form of an interface force from the neighboring propulsion segments

Propulsion segment
- Highly elastic wing
- Spanwise distribution of batteries
- High battery-to-structure weight ratio

This aircraft is controlled by wing torsion which is induced by several all-moving horizontal stabilizers. A deflection of such a horizontal stabilizer leads to a force that, with the tail boom as lever, generates a moment at the wing structure. This local change in attitude, results

in a change of the local angle of attack, which changes the local generated lift and thereby makes it possible to move a segment of the wing upwards or downwards. An appropriate control law is used to keep the wing level and locally counteract disturbances. Differential thrust is used to control heading. This setup allows for a high control authority in various conditions which we refer to, as active safety.

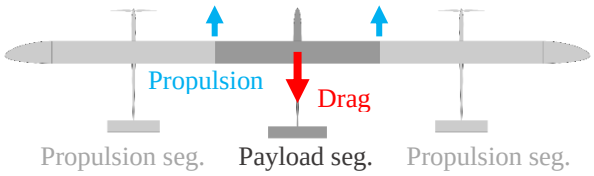

Figure 3: Segmented aircraft – propulsion forces on payload segment

The segmented approach allows the plane to be reconfigured depending on the mission. So, if for example a heavier payload segment needs more propulsive power, additional propulsion segments can be added as shown in Fig. 4. This even improves the systems overall efficiency, due to the increased aspect ratio of the wing. Here, the central property of the concept that every segment basically flies for itself plays a major role. Adding segments doesn't over-proportionally add structural weight like adding wingspan to a conventional aircraft design would.

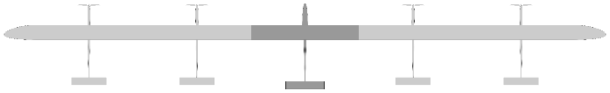

Figure 4: Aircraft with single payload and four propulsion segments

Since only two segments are needed to provide controllability, even an in-flight separation is possible, as shown in Fig. 5. This allows for a landing of separate segment groups in unfavorable weather conditions, due to the smaller wingspan. Operational-wise this makes a lot of sense, where you have better control over the launch conditions than the landing conditions, especially considering long duration missions.

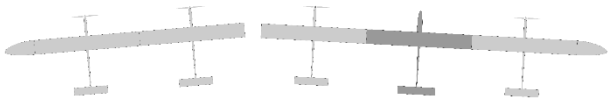

Figure 5: In-flight separation

Separation would also allow for a staged ascent. In order to lift heavy payloads to stratospheric altitudes, first, power would be drawn from batteries of two neighboring outer segments and then, upon depletion, they would be detached and returned to base while the remaining segments with the payload would continue their ascent.

An additional benefit of an elastic wing with high control authority is the possibility to morph it into different shapes. For example, it might be beneficial to partly bend the wing upwards to catch shallow sunlight that would otherwise not be captured by the solar cells due to the unfavorable angle of incidence, as it has been described by Parks [6].

Finally, since every segment flies at its own angle of attack needed to generate the necessary lift at a given common speed, the lift distribution over the entire wing, can be influenced to some degree by distributing the masses over the segments accordingly. For example, with five or seven segments, the outer left and right segment could be loaded with less batteries, thereby favorably influencing the lift distribution and subsequently the efficiency of the whole wing.

A more exotic example for benefits regarding mission flexibility arose from discussions with our friends from T-minus Engineering. A small sounding rocket with 10kg total mass and 2kg payload capability would reach an altitude of only 6km from sea level, due to a great amount of air friction losses in the dense lower part of the atmosphere. However, if launched vertically in 20km altitude, the apogee would increase drastically to 122km.

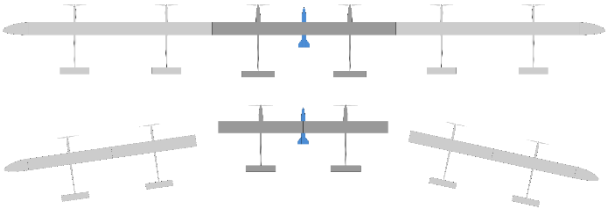

Figure 6: Air-launch of a small sounding rocket

To make this possible, the aircraft could be configured as shown in Fig. 6. Two relatively stiff built payload segments with own electric engines are joined together rigidly. Upon reaching launch altitude, the outer propulsion segments would detach. The payload segments with the rocket would then perform a dive and pull-up manoeuver, during which the rocked is fired.

It needs to be noted that there are other concepts that share some of the features just described.

One is the X-HALE project [7]. Their goal was to create a test platform to research the behavior of flexible slender wings for high altitude platforms. They also use wing torsion for control. Though their wings are quite elastic they don't bend as far as we intend ours to do.

At the aerospace fair LIMA 2017, the company UAVOS displayed an UAV named APUS that has many common features to our concept. It is also meant for high altitude flying and also relies on control by wing torsion induced

by elevators. They claim that they can save 25% of structural weight by building the aircraft this way [8]. To this date we however don't know to which extent their wings are capable of bending up- and downwards. Also they don't pursue a segmented approach.

3. PROOF OF CONCEPT

To prove the concept, we built several foam demonstrators to test the general idea of an extremely elastic wing with control by wing torsion. In several iterations different configurations were tested and basic flight control algorithms developed. Each fuselage has an IMU allowing to capture the local attitudes and use them for control. As presented during the talk, it is possible to fly this 3.6m wingspan aircraft in extremely turbulent weather conditions which shows the general validity of our approach. These demonstrators, which we refer to as ELAHA_dev, will also be in further use to develop the avionics and software for the bigger, all-composite, versions ELAHA 10 and 15.

Figure 7: ELAHA_dev flying in turbulent air conditions

4. CURRENT DEVELOPMENT

Aside from afore mentioned demonstrators, work has already begun on the 10m wingspan version, ELAHA 10, which is pictured in Fig. 8 as work-in-progress.

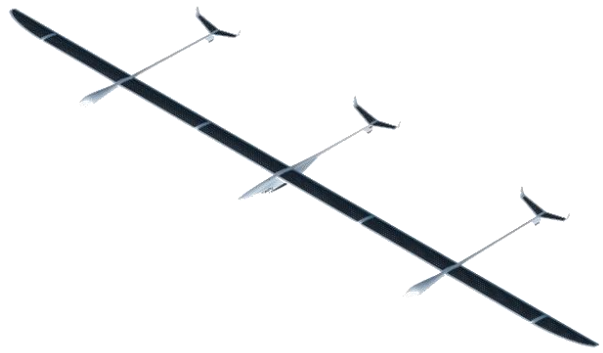

Figure 8: ELAHA 10 (Work in Progress)

The aerodynamic design of the wing segments is finished. Here, a batch analysis comprising a set of over 1500 airfoils has been conducted. The top 100 candidates of this analysis were used for another batch analysis with the goal to optimize an actual three-dimensional wing for different altitude regimes using these airfoil candidates. Then the top five candidates were individually compared for their performance at 0km, 10km and 20km altitude. The final airfoil is an optimized blend of two airfoils to improve the average performance over a broader altitude range. The base airfoils are Mark Drela's Dae51 and Dae41, originally developed for the human powered aircraft project Daedalus [9].

Based on this outer shape, the wing structure was designed [10] and molds were built, as pictured in Fig. 9. With the goal to reach the desired bending capabilities of the wing, material tests with different composite sandwich materials were made. This is necessary due to the, for aircraft structural parts, uncommonly thin laminates. Furthermore, an analysis toolchain was implemented to predict the mechanical properties of the wing structure. This toolchain was verified with several structural tests, including those of a full wing segment with an inter-segment joint, as shown in Fig. 10. The current focus lies on further refining the structure and start building the first wing segments meant for flying.

Figure 9: Mold with first finished ELAHA 10 wing-segment used for structural testing

Another focus is the development of a distributed control system. Each segment will have a microcontroller performing low-level control. The segments communicate over a bus system and will receive commands of a mission control computer running all higher control loops. Here, also the implementation of different control approaches is a strong topic. Also the in-flight reconfiguration into two individual aircraft has to be kept in mind.

Overall, the goal is to conduct a first flight with ELAHA 10 in 2018 and shortly after begin with modifications to make it high altitude capable.

If successful, the next update would integrate solar cells into the wing structure and extend the aircraft with two additional segments, resulting in a total wingspan of 15.6m. In this configuration it should already be possible to lift payloads of up to 5kg to an altitude of 20km or conduct continuous day-night cycles with a minimalist payload.

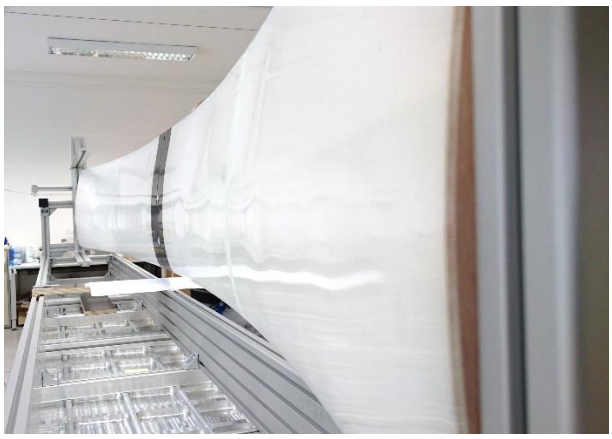

Figure 10: Structural test of ELAHA 10 wing segment

5. CONCLUSION

As we have shown in section 1, there are a number of reasons for pursuing the concept of an elastic and segmented aircraft, the most relevant reason being the paradigm “what bends doesn’t break”.

The concept also offers a great flexibility to reconfigure the airframe for different mission requirements while using a majority of identical parts.

So far, we have demonstrated the general validity of our approach by flying several demonstrators under difficult weather conditions.

The development of the larger 10m wingspan version ELAHA 10 is ongoing with the goal of a first flight in 2018.

We strongly want to encourage everyone to contact us in regard of collaborations regarding scientific or other applications that would benefit from the capabilities of a stratospheric UAV.

6. REFERENCES

[1] S. Wlach, "Development of a flying test platform for technologies of future High Altitude Pseudo-Satellites (HAPS)," Diploma thesis, University of Stuttgart, 2014.

[2] S. Wlach, M. Schwarzbach and M. Laiacker, "DLR HABLEG – High Altitude Balloon Launched Experimental Glider," in *22nd ESA Symposium on European Rocket and Balloon Programmes and Related Research*, Tromsø, Norway, 2015, pp. 385-392.

[3] "Aviation Accident Final Report, NTSB Identification: DCA15CA117," National Transportation Safety Board, 2015.

[4] "Aviation Accident Final Report, NTSB Identification: DCA16CA197," National Transportation Safety Board, 2016.

[5] T. E. Noll, J. M. Brown, M. E. Perez-Davis, S. D. Ishmael, G. C. Tiffany and M. Gaier, "Investigation of the Helios Prototype Aircraft Mishap," NASA Langley Research Center, 2004.

[6] R. Parks, "Non-planar adaptive wing solar aircraft". US Patent App. 12/211,027, 2010.

[7] C. E. S. Cesnik, P. J. Senatore, W. Su, E. M. Atkins, C. M. Sheare and N. A. Pitchter, "X-HALE: A Very Flexible UAV for Nonlinear Aeroelastic Tests," in *51st AIAA/ASME/ASCE/AHS/ASC Structures, Structural Dynamics and Materials Conference*, Orlando, Florida, 2010, doi:10.2514/6.2010-2715.

[8] UAVOS, "APUS UAV," [Online]. Available: http://www.uavos.com/media/UAVOS-press-release.docx. [Accessed 21 08 2017].

[9] M. Drela, "MIT Human Powered Aircraft and Hydrofoil info web page," [Online]. Available: http://web.mit.edu/drela/Public/web/hpa/. [Accessed 21 08 2017].

[10] M. Hermann, "Entwicklung der Leichtbauflügel-struktur eines hoch fliegenden Flugzeugs," Diploma thesis, University of Stuttgart, 2017.

DESIGN AND QUALIFICATION OF A NOVEL PYROTECHNICAL RELEASE SYSTEM FOR SOUNDING ROCKETS

VISBY, SWEDEN
11-15 JUNE 2017

Torgeir Lauritsen Grønås [(1)], Geir Lindahl [(1)], Thomas Gansmoe [(1)], Trond Aksel Olsen [(1)]
[(1)] Andøya Space Center, Beiksveien 46, N-8480 Andenes, Norway. Email: torgeirg@andoyaspace.no

ABSTRACT

Pyrotechnic devices are commonly used in sounding rockets for various separation mechanisms. The price of American manufactured squibs have in the past years increased to a point that alternatives need to be looked into. An adapter for 11mm airbag squibs have been developed and tested with good result and will be used in the Nucleus rocket. The squib has a single bridge igniter, while the Holex used today have double bridge. To avoid sacrificing redundancy, the possibility of using two airbag squibs are to be looked into. This paper describes the design, testing and conclusion of the use of airbag squibs as a possible replacement for some of today's pyrotechnics.

1. INTRODUCTION

Separation mechanisms are integrated parts of the payloads and completely necessary for separating the nosecone and doors in order for the instruments to deploy and carry out their measurements in the atmosphere. Similar mechanisms are used for separation of the payload from the motor. The separation mechanisms have traditionally a pyrotechnic device (squib) mounted at the end of a cylinder and a piston moves a knife blade that cuts one or several screws or wires causing the nose cone or doors to separate.

In later years, the price on American manufactured squibs have increased. These pyrotechnic devices used for separation mechanisms amounted in 2014 for 30% of the total hardware cost for a sounding rocket payload [2]. A more cost effective solution was favourable and the use of gas/gunpowder used in airbags were looked into.

2. CURRENT SOLUTION

The Hotel Payload uses three squibs for splitting the nose cone, two for cutting the wires for the hotel doors and one is used for cutting the wire for the doors on the 4D module. This adds up for a total of six squibs. To release the nose cone and hotel doors Holex 3702 are used. On the 4D module Holex 2800 or 2801 can be used. Fig. 1 shows the different Holex squibs used today in the Hotel Payload.

Figure 1- Holex 2800, 2801, 3702 (top to bottom). The squibs currently in use at Andøya Space Center.

The 3702 are used both in our wire cutter shown in Fig. 2 and in our bolt cutter shown in Fig.3.

Figure 2 - Heavy duty wire cutter designed by ASC.

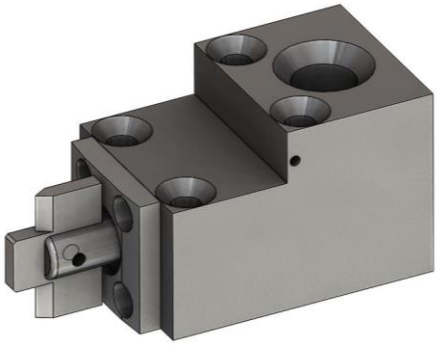

Figure 3 - Bolt cutter used in the separation of the nose cone.

3. DESIGN

The new design had one critical design requirement, to use a standard 11mm airbag squib. Before any cad model was created, a prototype was made in a manual lathe and mill from some simple hand sketches to get an idea of how it would fit together. After it was test fitted, the parts were then measured and drawn in 3D using SolidWorks. Dimensions and features were refined and a 2D production drawing with the appropriate tolerances was created.

The solutions is a simple holder for the airbag squib. It has a small o-ring behind it to prevent the pressure of escaping out the back. The squib is held in place with a small retainer that screws in using a special tool. A bigger o-ring sits on the outside and prevents pressure to escape out the threads when the entire assembly is screwed in place. Fig.4 and Fig.5 shows the adapter assembly.

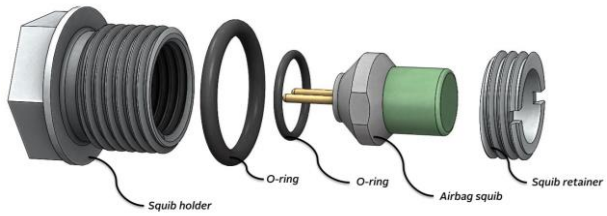

Figure 4 – Exploded view of the assembly showing the different components.

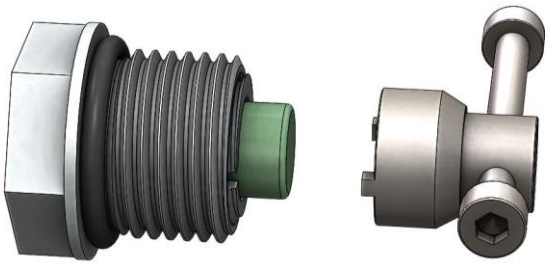

Figure 5 - The airbag squib is mounted into the holder using a special tool.

On the opposite side is a retainer for the cable connection and a corresponding connector. The one used is manufactured by Delphi, which offer a wide range of types and coding. A type called FCI was selected in this case. The retainer also short circuits the squib when the connector is unplugged.

Figure 6 - Retainer clips and connectors from Delphi.

The squibs chosen are from a Czech company called Indet Saftey Systems. The squib model is GST-61 and produces a pressure of 135 bars at $10cm^3$ [1]. This is approximately 1958 Psi and is close to the specification of the Holex 3702, which is 2000 Psi at $10cm^3$. The production of the GST-61 is coming close to its end and the GTMS will replace it. A sample batch with a pressure of 145 bars, approximately 2103 Psi, at $10cm^3$ was bought, but have not yet been tested. The all-fire and no-fire currents are different between the Holex and airbag squibs. The 3702 have an all-fire current of minimum 3,5A and a no-fire current of 1A for 5 minutes. The GST-61 and GTMS have an all-fire current of 1,2A for 2ms or 1,75 for 0,5ms. The no-fire currents is 0,4A for 10s [1].

The squibs used today all have double igniter bridge, while the airbag squibs are single bridge. To avoid sacrificing redundancy the possibility of using two airbag squibs will be looked into in the next phase of development.

4. TESTING

A few squibs was fired in open air to test the firing circuit. Then a couple of tests was done with the squib adapter that was screwed into a closed chamber. This was to ensure that the o-rings and threads would hold. A wiring cutting test have also been done with good result. Two 3mm wires were cleanly cut in this test. All the testing have been done with our existing firing circuit. The squib and adapter will be tested on the Nucleus rocket where it will be used to separate the nosecone. A test were pressure is logged should be carried out to see how consistent the results are in a batch of squibs. This and measuring the bridgewire resistance will give some indication on the quality and reliability of the squibs.

5. CONCLUSION

To use an airbag squib such as the GST-61 with a holder as a possible replacement for the Holex 3702 looks promising. All the tests were successful, but some additional testing should be carried out. Also the issue regarding redundancy will be looked into. Adding together the cost of development, manufacturing, cost of squibs and hardware, this design is an inexpensive solution.

6. REFERENCES

1. Indet Saftey Systems. (2010). ISS GTMS Data Sheet for ISN11558, 3.11.2010, DH
2. ASC. Thomas Gansmoe. (2017). BAS.02.15.5_NRS_Sluttrapport

FORWARD TO AUTOMATIC FORECASTING OF RADIATION HAZARDS FROM SOLAR COSMIC RAYS FOR SPACECRAFTS, AIRCRAFTS, AND LONG-LIVED BALLOONS

VISBY, SWEDEN, 11-15 JUNE 2017

Lev Dorman [1, 2], Lev Pustil'nik [1], Uri Dai [1], Fatima Keshtova [3], Abraham Sternlieb [1]

1. Israel Cosmic Ray & Space Weather Centre with Emilio Ségre Observatory affiliated to Tel Aviv University, Shamir Research Institute, and Israel Space Agency, ISRAEL (lid010529@gmail.com)
2. Cosmic Ray Department of Pushkov's IZMIRAN, Moscow, RUSSIA
3. Universitäten Oldenburg, GERMANY

ABSTRACT

We present method of automatically forecasting of solar cosmic ray (SCR) impact caused by solar flare and estimation of radiation hazard level. We use model of solar cosmic ray diffusion in general form and coupling functions for neutron monitors network with different altitudes and cut-off rigidities, including also space detectors like GOES-11, 12. Another observational data for estimation of energy spectra is multiplicity of CR registration by some neutron monitors. We demonstrate algorithms for automatic estimation of the event starting, determination time-evolution of SCR in space by coupling functions in the frame of spectrographic method, solving inverse problem for SCR generation in solar corona and propagation in the interplanetary space, automatic determining on the basis of CR observation data parameters of SCR generation in solar corona, escaping into solar wind, and propagation in space. We show that on the basis of these parameters it can be automatic forecasting on the basis of first about 0.5 hour data expected level of radiation hazards for full time of event (up to about 48 hours) for objects in space on different distances from the Sun, in magnetosphere at different orbits, and in atmosphere at different altitudes and cutoff rigidities. If for some objects expected level of radiation hazards will be dangerous, after about 0.5 hour from event beginning will be formatted and sent corresponding Alert. We take into account that for the first about 0.5 hour data from event beginning, when coming mostly only small flux of high energy particles – radiation hazards expected very small in comparison with more delay time when coming main part of SCR with energy ≤ 1 GeV, formatted sufficient part of radiation hazards.

1. THE MATTER OF THE PROBLEM

It is well known that in periods of great SEP (Solar Energetic Particle) events, the fluxes can be so big that memory of computers and other electronics in space may be destroyed, satellites and spaceships became dead (each year Insurance Companies paid billions dollars for these failures). Let us outlined that if it will be event as February 23, 1956 (see detail description in Dorman 1957), will be destroyed about all satellites in few hours, the price of this will be more than 10-20 billion dollars, will be total destroying satellite communications and a rose a lot of other problems. In periods of great SEP events is necessary to switch off some part of electronics for short time to protect computer memories. These periods are also dangerous for astronauts on space-ships, and International Space Station (ISS), passengers and crew in commercial jets (especially during great radiation storms).

The problem is how to forecast exactly these dangerous phenomena. We show that exact forecast can be made by using high-energy particles (about 2-10 GeV/nucleon and higher) which transportation from the Sun is characterized by much bigger diffusion coefficient than for small and middle energy particles. Therefore high energy particles came from the Sun much more early (8-20 minutes after acceleration and escaping into solar wind) and later - main part of smaller energy particles caused dangerous situation for electronics and people health (about 60 and more minutes later).

2. MAIN STEPS OF FORECASTING

As the **first step**, we use automatically working program "SEP-Start", supposed, developed and checked in the Emilio Segre' Observatory of Israel Cosmic Ray and Space Weather Center (Mt. Hermon, 2050 m above sea level, cut-off rigidity 10.8 GV).

Using of this program on many CR stations and on satellites allowed determining automatically the beginning of SEP event.

The **second step** is "SEP-Coupling" – using developed in Dorman (1957, 1958, 2004) method of coupling functions for transformation obtained at different altitudes and cutoff rigidities data on CR intensity to the space and calculation CR energy spectrum and angle distribution out of the Earth's atmosphere and magnetosphere, directly in the interplanetary space near the Earth (Dorman et al., 2006a). Before we made these complicated operations step by step on the basis of historical SEP events data during long time and determined flare energetic particle spectrum in the interplanetary space and its change with time by method of coupling functions (in scientific literature called as Dorman functions). Now we prepared algorithms and try to create program which will be made these calculations automatically after each new minute of CR data very quickly for time not more than few seconds.

The Third Step "SEP-Inverse Problem" is based on theoretically solved by Dorman et al. (2006b) about 10 years ago inverse problem and determine time of ejection energetic particles, source function and transport parameters in dependence from particle energy and distance from the Sun. Several years ago we made corresponding calculations very long time, so obtained results cannot be practically used for forecasting. Now we prepared all algorithms and try to create program which will be made these calculations automatically after each new minute of CR data very quickly for time not more than few seconds.

The Fourth Step "SEP-Forecasting" based on the theoretically solved direct problem and parameters founded in the Third Step and known coupling functions, we calculate time evolution of solar CR spectrum with time and expected total fluency (radiation hazards) in the interplanetary space for spaceships at different distances from the Sun in dependence of shielding, in the Earth's magnetosphere for satellites with different orbits, in the Earth's atmosphere for airplanes on different airlines, rackets and balloons in dependence of altitude and cutoff rigidities, and for ground at different air pressure and cutoff rigidities. Again, we checked all these mathematical procedures basing on real data of historical SEP events and it need so long time that it is not possible to use these results for forecasting of expected radiation hazards. Now we for this step also prepared all algorithms and try to create program which will be made these calculations automatically after each new minute of CR data very quickly for time not more than few seconds. To determine the quality of obtained results, after 5-10 minutes from beginning starts to work the final, Fives Step.

The Fives Step "Checking of Forecasting Quality and Alerts" starts to work at 5-10 minutes after the event beginning. In this Step we compare expected (calculated in the Fourth Step by using coupling functions CR intensity for neutron monitors on different stations and on satellites) with observed. If the difference will be small enough (smaller than 10-20%) and the radiation hazards expected to be dangerous for spaceships in the interplanetary space, for some satellites in the Earth's magnetosphere, for airplanes on some airlines, apparatuses on rackets and balloons, or for some objects on the ground, will be send corresponding Alerts with detail information on the expected radiation hazards calculated in the Fourth Step. After few minutes a new, more exact Alerts will be sent. More and more exact new Alerts will be repeated each few minutes during the dangerous event. Let us outline that Step 1 finished to work after determining the beginning of SEP event, but Steps 2 – 5 continued to work for each new minute. They will be finished to work only when the difference between consequences Alerts became smaller than statistical errors.

3. PREPARING FOR AUTOMATICALLY FORECASTING PROCEDURE AND ON-LINE DETERMINING SPECTRUM SCR IN SPACE

3.1. Automatically CR, R_C, and *h* data collection

As we outlined in the Section 2, we will use one-minute CR data, available from Internet (first of all – NMDB data): high-latitude stations with R_C < 1 GV (Oulu, Apatite, South Pole, and some other), middle-latitude stations with R_C = 2–4 GV (Moscow, Kiel, Novosibirsk, Yakutsk, Lomnitsky Stit, Yungfraujokh, and others), stations with R_C = 6–7 GV (Rome, Athens, Tjan Shan, and others), and low-latitude stations with R_C = 10–16 GV (Mt. Hermon, Mt. Norikura, Mexico, Mt. Haleakala, and others). For very small energy solar CR we will use satellite one-minute data, also available through Internet (e.g., GOES data).

Now we have planetary distribution of R_C during 1950 – 2050 in dependence of altitude and level of magnetic activity for all CR stations (Gvozdevsky et

al., 2017) and in preparing are book (Dorman et al., 2018) on R_c distribution and its time variations in the Geomagnetosphere (important in case of applications automatically forecasting procedure for satellites).

For each used CR stations we need to know also exact values of atmospheric pressure h (in units 1000 g/cm^2) at the points of each CR detector (for some stations with big atmospheric winds – with corrections for effect Bernoulli).

3.2. Calculating of coupling functions

For the polar normalized coupling function for any secondary component of type i ($i = n$ – for total neutron component, $i = m$ – for neutron multiplicities $m = 1, 2, 3, \ldots$, $i = h\mu$ – for hard muons, $i = s\mu$ – for soft muons, $i = ep$ – for electron-photon component, and so on) can be approximated by the so called in scientific literature Dorman function

$$W_{oi}(R,h) = a_i k_i R^{-(k_i+1)} \exp\left(-a_i R^{-k_i}\right), \qquad (3.1)$$

where coefficients a_i and k_i are functions from h and level of solar activity. For the normalized coupling functions at any point on Earth with cut off rigidity R_c and atmospheric pressure h will be (Dorman, 2004)

$$W_i(R_c,R,h) = \begin{cases} 0 & \text{if} \quad R < R_c \\ a_i k_i R^{-(k_i+1)}\left(1 - a_i R_c^{-k_i}\right)^{-1} \\ \times \exp\left(-a_i R^{-k_i}\right) & \text{if} \quad R \ge R_c . \end{cases} \qquad (3.2)$$

The dependence of a_n and k_n for total neutron component and a_m and k_m for neutron multiplicities m = 1, 2, 3, … on the CR station with pressure h and solar activity level characterized by the logarithm of CR intensity per one hour (we used here monthly averaged of Climax NM $\ln(N_{\mathrm{Cl}})$, available starting from 1952) can be approximated by the functions:

$$a_n = \left(-2.915h^2 - 2.237h - 8.654\right)\ln(N_{\mathrm{Cl}}) + \left(24.584h^2 + 19.460h + 81.230\right) \qquad (3.3)$$

$$k_n = \left(0.180h^2 - 0.849h + 0.750\right)\ln(N_{\mathrm{Cl}}) + \left(-1.440h^2 + 6.403h - 3.698\right), \qquad (3.4)$$

$$a_m = \left[\left(-2.915h^2 - 2.237h - 8.638\right)\ln(N_{\mathrm{Cl}}) + \left(24.584h^2 + 19.46h + 81.23\right)\right] \times \left(0.987m^2 + 0.225m + 6.913\right)/9.781, \qquad (3.5)$$

$$k_m\left[\left(0.180h^2 - 0.849h + 0.750\right)\ln(N_{\mathrm{Cl}}) + \left(-1.440h^2 + 6.403h - 3.698\right)\right] \times \left(0.081m + 1.819\right)/1.940, \qquad (3.6)$$

where multiplicities m = 1, 2, 3, …. Instead of Climax NM, one can also use monthly averages of any other CR station with appropriate recalculation of the coefficients determined by correlation between monthly data N_{CL} of Climax NM and this station for several years. For example, the regression coefficients for 6NM-64 on Mt Hermon for two years data are

$$\ln(N_{\mathrm{Cl}}) = (1.947) \times \ln(N_{\mathrm{ESOI}}) - (1.75) \qquad (3.7)$$

with correlation coefficient CC = 0.892.

For Rome 17NM-64 for many (more than 15 years)

$$\ln(N_{\mathrm{Cl}}) = 2.048 \times \ln(N_{\mathrm{Roma}}) - 1.965 \qquad (3.8)$$

with CC = 0.982. For 18 NM-64 Apatite

$$\ln(N_{\mathrm{Cl}}) = 1.178 \times \ln(N_{\mathrm{Apat}}) - 2.256 \qquad (3.9)$$

with CC = 0.992. For Athens station with 6 NM-64

$$\ln(N_{\mathrm{Cl}}) = 2.278 \times \ln(N_{\mathrm{Ath}}) - 0.828 \qquad (3.10)$$

with CC = 0.947. For Moscow station with 24 NM-64

$$\ln(N_{\mathrm{Cl}}) = 1.194 \times \ln(N_{\mathrm{Mosc}}) + 1.853 \qquad (3.11)$$

with CC = 0.985. For McMurdo station with 18 NM-64

$$\ln(N_{\mathrm{Cl}}) = 1.121 \times \ln(N_{\mathrm{McMur}}) + 2.074 \qquad (3.12)$$

with CC = 0.981. For Kiel station with 18 NM-64

$$\ln(N_{\mathrm{Cl}}) = 1.152 \times \ln(N_{\mathrm{Kiel}}) + 2.395 \qquad (3.13)$$

with CC = 0.976. For Oulu station with 18 NM-64

$$\ln(N_{\mathrm{Cl}}) = 1.1794 \times \ln(N_{\mathrm{Oulu}}) + 2.8424 \qquad (3.14)$$

with CC = 0.992. For TianShan station with 24 NM-64

$$\ln(N_{\mathrm{Cl}}) = 1.875 \times \ln(N_{\mathrm{TS}}) - 5.277 \qquad (3.15)$$

with CC = 0.975. Substituting Eqs. 3.7 – 3.15 in Eqs. 3.3–3.6, we obtain the coupling functions as a function of the level of solar activity on the basis of monthly NM data of any CR station in the World.

Because in our method of determining spectrum of solar CR out of magnetosphere can be used also other CR secondary components, let us outlined that according to Dorman (M2004), the coefficients a_i, k_i in the analytical form described by Eq. 3.1 for different CR secondary components will be as following: 1) for neutron component at $h = 312$ mb (about 10 km - altitude of many airlines) $a_n = 8.30$, $k_n = 1.45$; 2) for neutron component at $h = 680$ mb (mountains at about 3 km), $a_n = 13.62$, $k_n = 1.26$; 3) for hard muon component at sea level (average $h = 1030$ mb) $a_{h\mu} = 35.3$, $k_{h\mu} = 0.95$; and 4) for hard muon component underground at the depth 7 m w.e., $a_{h\mu} = 58.5$, $k_{h\mu} = 0.94$.

3.3. For estimation of small changes of coefficients a_i, k_i in Eqs. 3.1 and 3.2 with changing *h* and solar activity, characterized by $\ln(N_{\mathrm{Cl}})$, we obtain

$$\delta a_i = (\partial a_i/\partial h)\delta h + (\partial a_i/\partial \ln(N_{\mathrm{Cl}}))\delta \ln(N_{\mathrm{Cl}}), \quad (3.16)$$

$$\delta k_i = (\partial k_i/\partial h)\delta h + (\partial k_i/\partial \ln(N_{\mathrm{Cl}}))\delta \ln(N_{\mathrm{Cl}}). \quad (3.17)$$

3.4. Tabulating special functions $F_i(R_c,\gamma)$ for each used CR station and each component

Let us suppose that in some interval of rigidities to which are sensitive our detectors the primary solar CR variation $\Delta D(R,t)$ we describe as

$$\Delta D(R,t)/D_o(R) = b(t)R^{-\gamma(t)}, \quad (3.18)$$

where $D_o(R)$ is the differential spectrum of galactic CR at $t=0$ (for which coupling functions are defined). In Eq. 3.18 the parameters *b*(*t*), $\gamma(t)$ depend on *t* and we will try to determine them from CR ground observations. For calculating on-line expected spectrum of solar CR out of the Earth atmosphere and magnetosphere we need to know for each used CR station and each secondary component functions

$$F_i(R_c,\gamma) = a_i k_i \left(1-\exp\left(-a_i R_c^{-k_i}\right)\right)^{-1} \times \int_{R_c}^{\infty} R^{-(k_i+1+\gamma)} \exp\left(-a_i R^{-k_i}\right) dR, \quad (3.19)$$

where R_c, a_i, k_i were described above (for NM by Eqs. 3.3 – 3.6). Function $F_i(R_c,\gamma)$ can be calculated by replacing variables:

$$y = a_i R^{-k_i},\ dy = -a_i k_i R^{-k_i-1} dR. \quad (3.20)$$

$$\int_{R_c}^{\infty} R^{-(k_i+1+\gamma)} \exp\left(-a_i R^{-k_i}\right) dR = \frac{a_i^{-\gamma/k_i}}{a_i k_i} \cdot \gamma\left(\frac{\gamma}{k_i+1}; a_i R_c^{-k_i}\right), \quad (3.21)$$

where $\gamma(x; a_i R_c^{-k_i})$ is not-full gamma-function, which for $x = \frac{\gamma}{k_i+1} = n$, where *n* is natural number, may be presented as a finite sum:

$$\gamma(n; a_i R_c^{-k_i}) = \sum_{j=0}^{n-1} \frac{(a_i R_c^{-k_i})^j}{j!}. \quad (3.22)$$

Introducing Eq. 3.21 into Eq. 3.19, we obtain

$$F_i(R_c,\gamma) = a_i^{-\gamma/k_i} \gamma\left(\frac{\gamma}{k_i+1}; a_i R_c^{-k_i}\right) \times \left(1-\exp\left(-a_i R_c^{-k_i}\right)\right)^{-1}, \quad (3.23)$$

3.5. For using on-line data of pairs CR stations with different cutoff rigidities we need to tabulate special functions $\Psi_{il}(R_{c1},R_{c2},\gamma)$ for each pair of used CR stations with the same or different type of measured component, with the same or different R_{c1}, R_{c2}, and with the same or different *h*

In this case the observed ratio of CR enhancements on both stations will be

$$\delta N_i(R_{c1},t)/\delta N_l(R_{c2},t) = \Psi_{il}(R_{c1},R_{c2},\gamma), \quad (3.24)$$

where

$$\Psi_{il}(R_{c1},R_{c2},\gamma) = F_i(R_{c1},\gamma)/F_l(R_{c2},\gamma) = \frac{a_i^{-\gamma/k_i}\gamma\left(\frac{\gamma}{k_i+1}; a_i R_{c1}^{-k_i}\right)\left(1-\exp\left(-a_i R_{c1}^{-k_i}\right)\right)^{-1}}{a_l^{-\gamma/k_l}\gamma\left(\frac{\gamma}{k_l+1}; a_l R_{c2}^{-k_l}\right)\left(1-\exp\left(-a_l R_{c1}^{-k_l}\right)\right)^{-1}} \quad (3.25)$$

After tabulating $\Psi_{il}(R_{c1},R_{c2},\gamma)$ according to Eq. 3.25, we obtain on the basis of Eq. 3.24 the inverse function:

$$\gamma_{il}(t) = \Omega_{il}\left(\delta N_i(R_{c1},t)/\delta N_l(R_{c2},t)\right). \quad (3.26)$$

As some example, on Figure 1 is shown Function (3.26) for the ratio of NM Tyan Shan to NM Moscow.

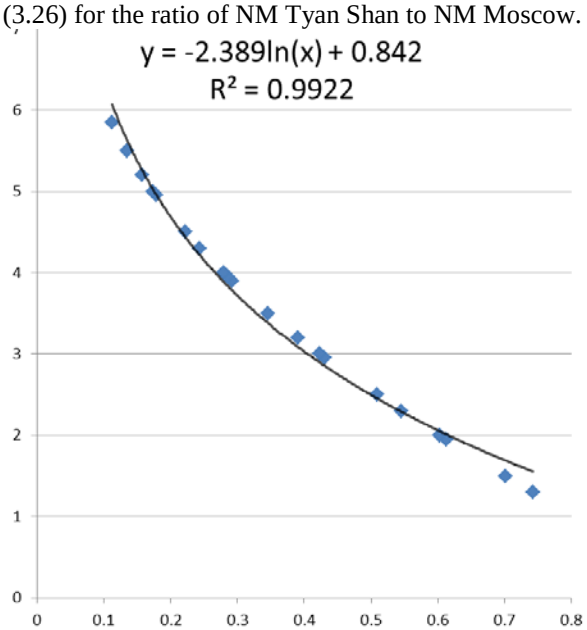

Figure 1. An example of determining $\gamma(t)$ (ordinate, y-axes) by ratio $\delta N_i(R_{c1},t)/\delta N_l(R_{c2},t)$ for NM Tyan Shan to NM Moscow (abscissa, x-axis).

After determining $\gamma(t)$ according to Eq. 3.26, function $b(t)$ can be determined from any of two equations:

$$b(t) = \delta N_i(R_{c1}, t) / F_i(R_{c1}, \gamma(t)), \quad (3.27)$$

$$b(t) = \delta N_l(R_{c2}, t) / F_l(R_{c2}, \gamma(t)), \quad (3.28)$$

and result must be the same.

3.6. Spectrum of solar CR in space

Spectrum of SCR out of the atmosphere and magnetosphere according to Eq. 3.18 will be

$$\Delta D(R,t) = b(t) D_o(R) R^{-\gamma(t)}, \quad (3.29)$$

where $\gamma(t)$ is determined by Eq. 3.26, and $b(t)$ – by Eqs. 3.26 and 3.27.

4. AUTOMATICAL DETERMINATION THE START OF SEP EVENT

4.1. The algorithms.

The determination of increasing flux we make by comparison with intensity averaged for one day (1440 minutes) from 1560 to 120 minutes before the present Z-th one-minute data. For each Z minute data, worked the program "SEP-Search". The program for each Z-th minute determines the values

$$D_{AZ} = \left[\ln(I_{AZ}) - \sum_{k=Z-1560}^{k=Z-120} \ln(I_{Ak}) / 1440 \right] \Big/ \sigma, \quad (4.1)$$

$$D_{BZ} = \left[\ln(I_{BZ}) - \sum_{k=Z-1560}^{k=Z-120} \ln(I_{Bk}) / 1440 \right] \Big/ \sigma, \quad (4.2)$$

where I_{Ak} and I_{Bk} are one-minute counting rate in the sections of neutron super- monitor *A* and *B*, and σ is the statistical error for one minute:

$$\sigma = \langle I_{Ak} \rangle^{-1/2} \cong \langle I_{Bk} \rangle^{-1/2} \quad (4.3)$$

For NM at Mt. Hermon the average counting rate in each sections $\langle I_{Ak} \rangle \cong \langle I_{Bk} \rangle$ is about 5000 per one minute, and $\sigma \cong 0.014 = 1.4\%$. If simultaneously

$$D_{AZ} \geq 2.5, \; D_{BZ} \geq 2.5, \quad (4.4)$$

the program "SEP-Search" repeat the calculation for the next Z+1-th minute and if Eq. 4.4 is satisfied again, we conclude that the onset of great SEP is estimated and will be start the next program "SEP-Research/ Spectrum" for determining the SEP spectrum $\Delta D(R,t)$ in space (see above, Eq. 3.29). If Eq. 4.4 is not satisfied, the program "SEP-Search" continue to check next minutes up to the moment when Eq. 4.4 will be satisfied at least for two nearest minutes.

4.2. The probability of false alarms

The probability of an accidental increase with amplitude more than 2.5σ in one channel will be $(1-\Phi(2.5))/2 = 0.0062\,\text{min}^{-1}$, that means in one day about 9 accidental increases in one channel). The probability of accidental increases simultaneously in both channels will be $((1-\Phi(2.5))/2)^2 = 3.845\times10^{-5}$ min^{-1} that means one in about 18 days. The probability that the increases of 2.5σ will be accidental in both channels in two successive minutes is equal to $((1-\Phi(2.5))/2)^4 = 1.478\times10^{-9}\,\text{min}^{-1}$ that means one in 6.76×10^8 minutes ≈1286 years. If this false alarm (one in about 1300 years) is sent, it is not dangerous, because the first alarm is preliminary and can be cancelled if in the third successive minute is no increase in both channels bigger than 2.5σ (it is not excluded that in the third minute there will be also an accidental increase, but the probability of this false alarm is negligible: one in 3.34×10^7 years). Let us note that the false alarm can be sent also in the case of solar neutron event (which really is not dangerous for electronics in spacecrafts or for astronauts health), but this event usually is very short (only few minutes, see in Dorman, 2010) and this alarm will be automatically canceled at the end of this event.

4.3. The probability of missed triggers

The probability of missed triggers depends very strong on the amplitude of the increase. Let us suppose for example that we have a real increase of 7σ (that for NM on Mt. Hermon corresponds to an increase of about 10 %). The trigger will be missed if in any of both channels and in any of both successive minutes if as a result of statistical fluctuations the increase of intensity is less than 2.5σ. For this the statistical fluctuation must be negative with amplitude more than 4.5σ. The probability of this negative fluctuation in one channel in one minute is equal $(1-\Phi(4.5))/2 = 3.39\times10^{-6}$ min^{-1}, and the probability of missed trigger for two successive minutes of observation simultaneously in two channels is 4 times larger: 1.36×10^{-5}, i.e. only one missed trigger per about 70000 events.

5. THE INVERSE PROBLEM FOR SEP GENERATION AND PROPAGATION

5.1. The matter of the inverse problem

In the frame of this problem we try on the basis of one minute CR observation to estimate time of SEP injection into interplanetary space, source function, and SEP diffusion coefficient. We start from the easiest model of diffusion with the diffusion coefficient which depends only from SEP energy and not depends from the distance to the Sun. Only model in which the diffusion coefficient depends both from SEP energy and from the distance to the Sun shows well agreement with observations after few scatterings of SEP (during about 20-40 minutes) with magnetic inhomogeneities in space (see in Dorman, 2006).

5.2. The inverse problem for the case when diffusion coefficient depends from particle rigidity and from the distance to the Sun.

Let us suppose, according to Parker (1965), that the diffusion coefficient

$$\kappa(R,r)=\kappa_1(R)\times(r/r_1)^{\beta}. \quad (5.1)$$

In this case the solution of diffusion equation will be

$$N(R,r,t)=\frac{N_o(R)\times r_1^{3\beta/(2-\beta)}(\kappa_1(R)t)^{-3/(2-\beta)}}{(2-\beta)^{(4+\beta)/(2-\beta)}\Gamma(3/(2-\beta))} \times\exp\left(-\frac{r_1^{\beta}r^{2-\beta}}{(2-\beta)^2\kappa_1(R)t}\right), \quad (5.2)$$

where t is the time after SEP ejection into solar wind. So, we have four unknown parameters: time of SEP ejection into solar wind T_e, β, $\kappa_1(R)$, and $N_o(R)$. Let us assume that according to ground and satellite measurements at the distance $r=r_1=1$ AU from the Sun we know $N_1(R)$, $N_2(R)$, $N_3(R)$, $N_4(R)$ at UT times T_1, T_2, T_3, T_4. Let $t_1=T_1-T_e=x$, than

$$t_2=T_2-T_1+x,\ \ t_3=T_3-T_1+x,\ \ t_4=T_4-T_1+x, \quad (5.3)$$

For each $N_i(R,r=r_1,T_i)$ we obtain from Eqs. 5.2, 5.3:

$$N_i=\frac{N_o(R)\times r_1^{3\beta/(2-\beta)}(\kappa_1(R)(T_i-T_1+x))^{-3/(2-\beta)}}{(2-\beta)^{(4+\beta)/(2-\beta)}\Gamma(3/(2-\beta))} \times\exp\left(-\frac{r_1^2(2-\beta)^{-2}}{\kappa_1(R)(T_i-T_1+x)}\right), \quad (5.4)$$

where i = 1, 2, 3, and 4. To determine x let us step by step exclude unknown parameters $N_o(R)$, $\kappa_1(R)$, β. As result, we obtain equation for determining x:

$$x^2(a_1a_2-a_3a_4)+xd(a_1b_2+b_1a_2-a_3b_4-b_3a_4) +d^2(b_1b_2-b_3b_4)=0, \quad (5.5)$$

where a_1=$(T_2-T_1)(T_4-T_1)\ln(N_1/N_3)$–$(T_3-T_1)(T_4-T_1)$ ×$\ln(N_1/N_2)$, a_2=$(T_3-T_1)(T_4-T_1)\ln(x/(T_2-T_1+x))$–$(T_2-T_1)$ ×$(T_3-T_1)\ln(x/(T_4-T_1+x))$, a_3=$(T_2-T_1)(T_3-T_1)\ln(N_1/N_4)$ -$(T_3-T_1)(T_4-T_1)\ln(N_1/N_2)$, a_4=$(T_3-T_1)(T_4-T_1)$ ×$\ln(x/(T_2-T_1+x))$–$(T_2-T_1)(T_4-T_1)\ln(x/(T_3-T_1+x))$, b_1= $\ln(N_1/N_3)$–$\ln(N_1/N_2)$, b_2= $\ln(x/(T_2-T_1+x))$ –$\ln(x/(T_4-T_1+x))$, b_3= $\ln(N_1/N_4)$–$\ln(N_1/N_2)$, b_4= $\ln(x/(T_2-T_1+x))$–$\ln(x/(T_3-T_1+x))$, d=$(T_2-T_1)(T_3-T_1)(T_4-T_1)$

As it can be seen, only coefficients a_2, a_4, b_2, and b_4 depend from x, but very weekly (as logarithm). Therefore, Eq. 5.5 we solve by iteration method: as a first approximation, we use $x_1=T_1-T_e\approx 500$ sec (which is the minimum time propagation of relativistic particles from the Sun to the Earth's orbit). Then we determine $a_2(x_1)$, $a_4(x_1)$, $b_2(x_1)$, $b_4(x_1)$ and by Eq. 5.5 we determine the second approximation x_2, and so on. After determining x, we easy determine according to Eq. 5.3 t_1, t_2, t_3, t_4, and the final solutions for β, $\kappa_1(R)$, and $N_o(R)$:

$$\beta=2-3\left[(\ln(t_2/t_1))-\frac{t_3(t_2-t_1)}{t_2(t_3-t_1)}\ln(t_3/t_1)\right] \times\left[(\ln(N_1/N_2))-\frac{t_3(t_2-t_1)}{t_2(t_3-t_1)}\ln(N_1/N_3)\right]^{-1}. \quad (5.6)$$

Then we determine diffusion coefficient at the Earth's orbit $\kappa_1(R)$:

$$\kappa_1(R)=\frac{r_1^2(t_1^{-1}-t_2^{-1})}{3(2-\beta)\ln(t_2/t_1)-(2-\beta)^2\ln(N_1/N_2)} =\frac{r_1^2(t_1^{-1}-t_3^{-1})}{3(2-\beta)\ln(t_3/t_1)-(2-\beta)^2\ln(N_1/N_3)}. \quad (5.7)$$

After determining parameters β and $\kappa_1(R)$ we can determine the source function $N_o(R)$:

$$N_o(R)=N_i(2-\beta)^{(4+\beta)/(2-\beta)}\Gamma(3/(2-\beta))r_1^{-3\beta/(2-\beta)} \times(\kappa_1(R)t_i)^{3/(2-\beta)}\times\exp\left(\frac{r_1^2}{(2-\beta)^2\kappa_1(R)t_i}\right), \quad (5.8)$$

where index i = 1, 2 or 3. Let us outline that for all i results must be the same (it can be used as control of correct calculations).

6. COMPARISON WITH OBSERVATIONS AND ESTIMATION OF EXPECTED RADIATION HAZARDS ALERTS

6.1. Comparison with observations

On the basis of found T_e, β, $\kappa_1(R)$, and $N_o(R)$ with help of coupling function we can calculate expected variation of SCR intensity with time by any detector at any place:

$$\frac{\Delta N_i(R_c,h,t)}{N_i(R_c,h,0)}=\int_{R_c(t)}^{\infty}W_i(R_c,R,h)\times\exp\left(-\frac{r_1^2(2-\beta)^{-2}}{\kappa_1(R)(T_i-T_1+x)}\right) \times\frac{N_o(R)\times r_1^{3\beta/(2-\beta)}(\kappa_1(R)(T_i-T_1+x))^{-3/(2-\beta)}}{(2-\beta)^{(4+\beta)/(2-\beta)}\Gamma(3/(2-\beta))}dR. \quad (6.1)$$

The expected variation of CR intensity for NM on the ground for the SEP event at 29 September 1989 on Mt. Gran Sasso are shown in Figure 2 and for satellites in

Geomagnetosphere in Fig. 3. Forecasting curves are shown in comparison with observation data (circles).

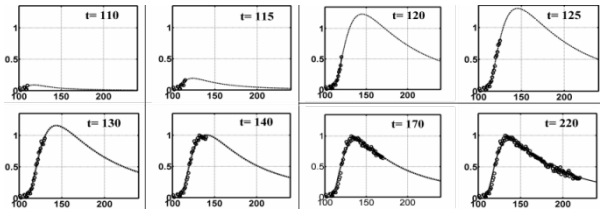

Figure 2. Calculation parameters $T_e, \beta, \kappa_1(R)$, and $N_o(R)$ according to Sections 3-5, and forecasting of total neutron intensity according to Eq. 6.2 (on the abscissa axis the time *t* is in minutes after 10.00 UT of September 29, 1989). Curves –forecasting on the basis of the first 10 minutes, then on the basis of the first 15 minutes, then on the basis of the first 20 minutes, and so on. Small circles – observation one minute data. It can be seen that after 1-st and 2-nd panels (10 and 15 minutes after event's beginning) the discrepancy between prediction and observations is too much (diffusion regime does not established), but after 3-th and 4-th panels (after 20 and 25 minutes) prediction curve became closer and closer to observations.

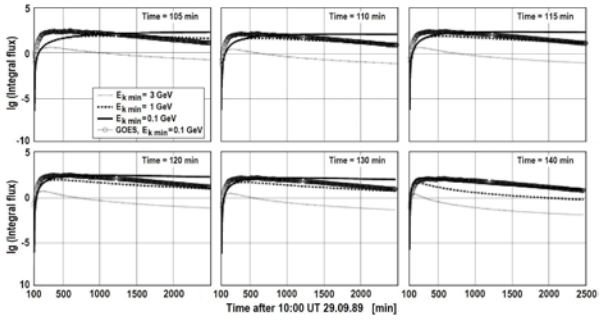

Figure 3. Combined forecasting on the basis of NM data and beginning of satellite data; comparison with GOES observations. Curves – forecasting of solar CR intensity with kinetic energy > 3 GeV, > 1 GeV, and > 0.1 GeV. Circles – observations on GOES of solar CR intensity with kinetic energy > 0.1 GeV. It can be seen that after 5 minutes it is a big difference between forecasting and observed variations of solar CR intensity with kinetic energy > 0.1 GeV (in this short time diffusion regime does not formatted), but with time the coincidence became more close and fully coincident after 40 minutes up to about two days from the beginning of event.

If expected and observation data are in good correlation, it will be mean that the determining of primary solar CR variations and solution of inverse problem are correct and we can forecast expected radiation hazards for different objects.

6.2. Forecasting of expected radiation hazards for space-crafts in interplanetary space at different distances from the Sun

In this case $R_c = 0$ and $R_{\min}$ will be determined only by shielding $R_s = R_{\min}$. The coupling function will be determined by meson-nuclear and electro-magnetic processes only in shielding *S*. The full radiation hazard during SEP event (including radiation hazards $N_G(R,r,S)$ from GCR during effective time Δt of SEP event) will be:

$$F(r) = \int_0^\infty dt \int_{R_{\min}}^\infty W(R,S) \frac{N_o(R) \times r^{3\beta/(2-\beta)} (\kappa_1(R)t)^{-3/(2-\beta)}}{(2-\beta)^{(4+\beta)/(2-\beta)} \Gamma(3/(2-\beta))}$$

$$\times N_G(R,r,S) \exp\left(-\frac{r^2(2-\beta)^{-2}}{\kappa_1(R)t}\right) dR + \int_{R_{\min}}^\infty N_G(R,r,S) \Delta t dR. \quad (6.2)$$

6.3. Forecasting of expected radiation hazards for space-crafts in the Geomagnetosphere

Let us consider space-crafts only on altitudes more than few hundred kilometers. In this case we can neglect by influence of atmosphere (i.e. to put $h = 0$), but need to take into account that $R_c \neq 0$ and $R_{\min} = \max(R_c, R_s)$. The full radiation hazard during SEP event (together with GCR) will be determined by the same Eq. 6.2, only instead of $R_{\min} = R_s$ we need to use

$$R_{\min}(t) = \max(R_c(t), R_s). \quad (6.3)$$

6.4. Forecasting of expected radiation hazards for electronics in troposphere and stratosphere on balloons and rockets, as well as for electronics and people health in air-crafts and on the ground

In this case $h \neq 0$, $R_c \neq 0$ and $R_{\min}$ will be determined by Eq. 6.3. The full radiation hazard during SEP event (including influence of GCR) will be determined by following fluency:

$$F(r) = \int_0^\infty dt \int_{R_{\min}}^\infty W(R_c(t)R,S) \frac{N_o(R) \times r^{3\beta/(2-\beta)} (\kappa_1(R)t)^{-3/(2-\beta)}}{(2-\beta)^{(4+\beta)/(2-\beta)} \Gamma(3/(2-\beta))}$$

$$\times N_G(R,r,S) \exp\left(-\frac{r^2(2-\beta)^{-2}}{\kappa_1(R)t}\right) dR + \int_{R_{\min}}^\infty N_G(R,r,S) \Delta t dR. \quad (6.4)$$

6.5. Automatically formatting corresponding Alerts when radiation hazards expected to be dangerous for electronics or/and people health

In all cases, when the calculated radiation hazards expected to be dangerous for electronics, computer memories, or/and for people health, will be immediately send automatically formatted corresponding Alerts with information on the calculated in Subsections 6.2 – 6.4 expected fluencies and levels of radiation hazards for different cases.

Acknowledgements. We use this opportunity to acknowledge Ministry of Science of State Israel, Tel Aviv University, Israel Space Agency, and Shamir Research Institute for continues support of Israeli Cosmic Ray & Space Weather Centre with Emilio Segre Observatory on Mt. Hermon.

References.

Dorman, L.I. (1957). *Cosmic Ray Variations*. Gostekhteorizdat, Moscow , pp 495. In Russian.
In English: (1958) US Department of Defense, Washington, DC.

Dorman, L.I. & Miroshnichenko L.I. (1968). *Solar Cosmic Rays*, Physmatgiz, Moscow (in Russian).
In English: (1976), NASA, Washington, DC.

Dorman, L.I. (1978). *Cosmic Rays of Solar Origin*, Moscow.

Dorman, L.I. & Zukerman, I. (2003). "Initial concept for forecasting the flux and energy spectrum of energetic particles using ground-level cosmic ray observations", *Advances in Space Research*, Volume 31, Issue 4, p. 925-932.

Dorman, L.I. (2004). *Cosmic Rays in the Earth's Atmosphere and Underground.* Kluwer Ac. Publ., Dordrecht/Boston/London.

Dorman, L.I. (2006). *"Cosmic Ray Interactions, Propagation, and Acceleration in Space Plasmas"*, Springer.

Dorman, L.I. (2008). "Natural hazards for the Earth's civilization from space", *Advances in Geosciences*, Volume 14, pp.281-286.

Dorman, L.I. (2009). *Cosmic Rays in Magnetospheres of the Earth and other Planets*, Springer, Heidelberg, Germany.

Dorman, L.I. (2010). *Solar Neutrons and Related Phenomena*, Springer, Heidelberg, Germany.

Dorman, L.I., L.A. Pustil'nik, A. Sternlieb, and I.G. Zukerman (2006a). "Forecasting of radiation hazard: 1. Alerts on great FEP events beginning; probabilities of false and missed alerts; on-line determination of solar energetic particle spectrum by using spectrographic method", *Advances in Space Research*, **37**, 1124-1133.

Dorman, L.I., N. Iucci, M. Murat, M. Parisi, L.A. Pustil'nik, A. Sternlieb, G. Villoresi, and I.G. Zukerman (2006b) "Forecasting of radiation hazard: 2. On-line determination of diffusion coefficient in the interplanetary space, time of ejection and energy spectrum at the source; on-line using of neutron monitor and satellite data", *Advances in Space Research*, **37**, 1134-1140.

Dorman, L.I., Yanke V.G., Belov A.V. et al. (2018). *Time-Space Distribution of Cosmic Ray Cut-off Rigidities in Geomagnetosphere*, Nova Science Publishers, New York (in press).

Gvozdevsky, B., Dorman, L.I., Belov A.V. et al. (2017). "The secular variations of cosmic ray cutoff rigidities, caused by century variations in geomagnetic field, and cosmic ray variations". Proc. Intern. Cosmic Ray Conf., South Korea

Mirohnichenko, L. (2015) "*Solar Cosmic Ray. Fundamentals and Applications*", Astrophysics and Space Science, Springer.

Parker, E.N. (1965). *Dynamical Processes in Interplanetary Space*, Moscow, Inostrannaja Literatura (translation from English by L.I. Miroshnichenko, editor L.I. Dorman).

Reames, D.V. (2013), "The Two Sources of Solar Energetic Particles", *Space Sci. Rev*., **175**, 53–92.

Velinov, P.I.Y.; Asenovski, S.; Kudela, K.; Lastovicka, J.; Mateev, L.; Mishev, A.; Tonev, P. (2013). "Impact of cosmic rays and solar energetic particles on the Earth's ionosphere and atmosphere", *Journal of Space Weather and Space Climate*, Volume 3, id.A14, 17 pp

RESULTS FROM THE INFLATABLE , TEXTILE AND RIGIDISABLE ANTENNA EXPERIMENT (INTEX) ON THE BEXUS 20/21 MISSION

Martin Laabs[1], Evgeniy Zakutin[1], Thilo Zirnstein[1], Justus Rischke[1], Dirk Plettemeier[1], Hannes Weisbach[2], Andreas Nocke[3], and Moritz Frauendorf[3]

[1] *Communication Laboratory, Technische Universität Dresden, Dresden, Germany, Mail: martin.laabs, evgeniy.zakurin, thilo.zirnstein, justus.rischke, dirk.plettemeier@tu-dresden*

[2] *Operating Systems Group, Technische Universität Dresden, Dresden, Germany, Mail: hannes.weisbach@tu-dresden.de*

[3] *Institute of Textile Machinery and High Performance Material Technology, Technische Universität Dresden, Dresden, Germany, Mail: andreas.nocke@tu-dresden.de, moritz.frauendorf@gmail.com*

ABSTRACT

The InTex experiment developed and tested a novel approach for inflating antenna structures for space and terrestrial applications. Instead of using polymer based or metallic foils, a hybrid textile material was utilized. The Intex experiment introduced a cotton fabric, coated with a thin PVC layer to ensure air-tightness. Since leakage is a major risk for almost all inflatable structures a UV cured epoxy rigidisation was applied. The experiment was conducted on a stratospheric balloon flight within the the BEXUS 21 mission.

Key words: antennas, inflatable, textile, polymere.

1. INTRODUCTION

During the BEXUS 21 stratospheric balloon flight, a circular Yagi antenna was inflated. It is made from a polyvinyl chloride (PVC) coated cotton fabric and metallized fleece for the conductive elements. The main objective was to prove the feasibility using a textile material instead of foil based systems and developing a rigidization technology for the textile fabric. We chose an antenna as a test vehicle for this technology since radiating structures take great advantage from inflation approaches. To prevent premature curing of the rigidization polymer, the antenna was stowed in a heated, light-tight container. At the apogee of the balloon flight the container was opened and the inflation took place. The antenna became inflated and the epoxy cured due to UV irradiation by sunlight. Afterwards, a leakage was enforced to proof the success of the stabilization approach. The experiment has been monitored by two high resolution cameras and the electrical properties as well as important environmental factors such as pressure and temperature of the antenna where measured continuously.

This paper is divided into three sections. First, selection of the cotton based textile material, the sealing approach as well as the choice of rigidization polymere will be covered. This includes a short survey about materials that were used for other experiments as well as common rigidization technologies. Secondly, the electrical and mechanical design of the antenna and the supporting mechanical as well as of the electrical structure will be explained. Finally, the results of the experiment are presented and discussed. The experiment has been carried out successfully and performed as expected. However, we noticed serious outgasing of the epoxy in the stratospheric enviroment. On the subsequent BEXUS 20[1] mission we were able to demonstrate a sealing approach to mitigate this adverse effect.

2. TEXTILE MATERIAL SELECTION

Textile fabrics offer multiple advantages over thin foils. Firstly they can be manufactured as non-planar structures, eliminating or reducing the length of seams. Secondly they are more robust against damage during handling, packing and impacts. Thirdly the textile structure provides an excellent matrix for the rigidization resin. Finally there are multiple methods for selective introduction of conducting filaments, generating a high degree of freedom for the antenna design.

Knitting is the most versatile method for textile manufacturing. It allows seamless 3D structures and selective introduction of different (e.g. conductive) filaments without strong geometric restrictions. Feature dimensions below 1 mm are possible when using

[1] BEXUS 21 was actually before BEXUS 20

thin yarn and small loop tools. Unfortunately knitted fabrics are more elastic and less airtight than woven fabrics. For dimensional stability and airtightness additional treatments are necessary. For the InTex Experiment semi-round knitted samples from a double flatbed knitting process out of a polyamid 6.6 Multifilament yarn have been evaluated. The samples have been treated with a silicone coating to ensure air-tightness and to improve dimensional stability. However - the resulting samples had a weight approx. 10 times of the finally selected cotton based fabric and exhibited a very poor adhesion to different rigidization agents. Nevertheless knitted fabric shall be considered a promising option for further research due to the unique flexibility. To achieve provide dimensional stability as well as air-tightness a transfer/hydrographics like coating of the knitted fabric could be used.

Braided fabrics are typically very dense but are limited in their geometry. Braiding of hoses is a very common technology and is very well established. Due to the regular geometry and well established processes coating does not require much additional research. Long dipole antennas for e.g. orbiter based subsurface radar applications could be easily manufactured by braiding from fully or partial conductive yarn.

If the geometry contains only single curved (so called developable) surfaces it can be easily manufactured by sewing woven fabric. Non-developable surfaces (e.g. parabolic dishes or spherical objects) often can be approximated by multiple developable surfaces. This introduces long seams which are not preferable for airtightness and weight. The material selection is based on the mission specific requirements. Typically flexibility at low and sufficient strength at high temperatures is required. This requirement excludes most thermoplastic fibres for high temperature applications. Polyamid based fabrics can be used up to approximately 350 °C. For higher temperatures only silicone and/or glass/ceramic based materials might be used. If the outgassing property of the selected material is not sufficient it might be mitigated via coating. Depending if and how the rigidization is applied, the textile material has to be compatible with the selected rigidization technique. For epoxy based systems the fibres shall be absorptive. For strain based rigidization special care has to be taken in the fabric design to not rip overstressed fibres. Foam and thermoplastic based rigidization techniques are less depending on the actual textile material selection.

In the InTex Experiment a woven cotton fabric was used. It is readily available, has low cost, weight and excellent processability. It remains flexible at high and low temperatures and provides an excellent matrix for the epoxy resin. To achieve air-tightness the fabric is coated with a thin layer of PVC. Due to proper heating of the PVC in the bonding process it is not fully absorbed into the cotton yarn. Only the surface of the PVC is bonded to approximately 1/4 of the yarn diameter. This ensure a sufficient bonding strength but also good wetting/soakablilty of the resin used for rigidization. The cross section of the coated fabric is shown in figure 1 and 2. The conductors of the antenna where made out of a commercial of the shelf (COTS) copper coated polyethylene terephthalate (PET) fleece for electromagnetic compatibility applications. All parts of the antenna where sewed together. The seams got an additional extra PVC coating to ensure air-tightness.

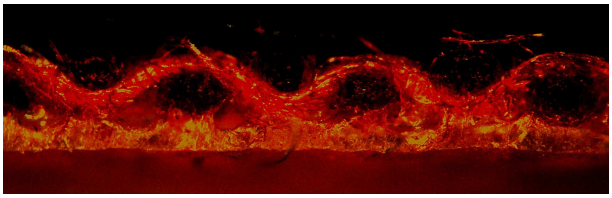

Figure 1. Cross-sectional micrograph of the PVC coated woven cotton fabric used in the InTex experiment. The lower coating is not drawn into the multifilament yarn, ensuring enough absorptivity for the rigidization resin.

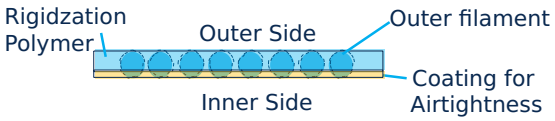

Figure 2. Cross-sectional drawing of the proposed material.

For the successor project DIANE - (Dipole Inflatable ANtenna Experiment) a polyamide fabric with thermoplastic polyurethane coating was used. It is even lighter than the cotton fabric but is not compatible with an resin rigidization.

The selection of the resin was based on low viscosity, low UV dose curing, broadband sensitivity and availability. Most of the considered UV curable epoxy resins require a thermal post-cure for their full performance. Obviously this is not possible in our application. For the experiment the OG603 UV curable acrylate from Epotek was chosen. It cures within seconds, has very low viscosity and soaks very well into the cotton fabric. For the recommended cure the resin shall be exposed to UV light with a power flux density of 100 mW/cm^2. The wavelength of the light shall be in between 240 nm and 365 nm. However, based on [AST14], the integral power flux of the sunlight from 240 nm to 365 nm in the upper stratosphere is only 23 mW/cm^2. Experiments in the lab have shown, that a curing with this reduced flux is still possible in less than 60s. During the experiment we actually noticed a very rapid cure in the stratospheric environment which indicates a much broader spectral sensitivity of the resin than specified.

3. EXPERIMENT DESIGN

The experiment flew on the BEXUS 21 mission. Since mass and power budget restrictions are not as stringent as for sounding rocket designs much monitoring equipment was included in the experiment. This includes two cameras, three pressure and four temperature sensors as well as a small vector network analyser for measuring the antenna return loss. The electronic as well as the pneumatic system are mounted inside a robust plastic box. The antenna, covered by a lid, is attached to this box as shown in figure 3.

The rough experiment sequence is as follows:

- The pressurized tank is filled with dry nitrogen before start
- During ascent into the stratosphere residual air in the antenna is vented. To prevent freezing of the resin the antenna compartment is heated to approximately 25 °C.
- After the floating phase of the balloon is reached the lid is opened by activating a burn wire
- The antenna is inflated and the return loss is measured
- A leakage is simulated after 120 s by opening the venting valve
- The return loss is measured again
- During descent the venting valve is closed to create mechanical stress due to the increasing atmospheric pressure

The experiment is monitored continuously with two cameras and observed by the ground station. In case of a failure of the communication link the experiment switch in an autonomous mode.

3.1. Antenna Design

A circular Yagi antenna was chosen as test vehicle for the textile technique. For regulative reasons the 70 cm radio amateure frequency band from 430 MHz to 440 MHz was selected since measuring the return loss during flight will also radiate little rf power. The design of the antenna is shown in figure 4. The gain of the antenna is approximately 9 dB, circular polarized. It consist of a driven, one reflecting and two directing elements. To simplify the manufacturing the driven and reflecting as well as the two directing elements have been chosen to have the same radius. In the final design the reflector was realized by the mount of the antenna. The remaining three elements consists of non-woven, electrical conductive fabric. This stripes have been taped to the PVC coated cotton fabric in the antenna. Electrical contacts to the outside where made by press-stud buttons. The antenna requires a symmetric feeding with 100 Ohm impedance. Therefore a balun was incorporated on an external press-stud-button to SMA adaptor PCB.

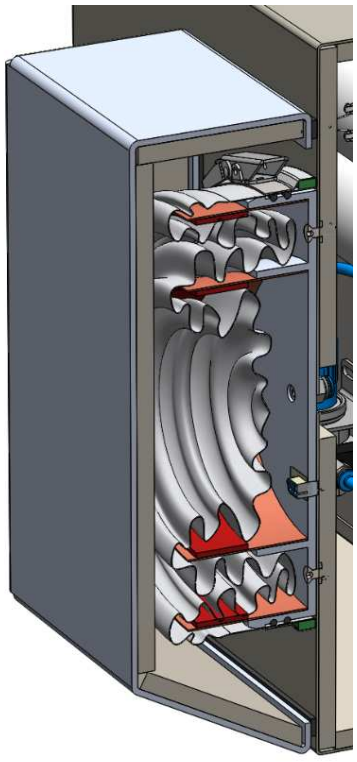

Figure 3. Cross-sectional rendering of the deflated antenna in the lid

More details about the antenna design can be found in [ML15]

3.2. Electronic Design

The purpose of the electronic system is to operate the experiment fully automatically or via remote control. Telecomanding is provided by the BEXUS service system due an Ethernet link which is fully transparent for the experiment and the corresponding ground station [Eur16]. A small ARM/Linux based computer is used for ground station communication, sensor data acquisition and actor control. To ensure correct temporal sensor data alignment, even in case of a short power outage, an independent, battery powered real-time clock was included. All sensor and camera data is stored on-board to flash memory as well as being transmitted to the ground station. However - due to limitation in the bandwidth, camera data has to be compressed further for the wireless downlink. Two webcams with integrated H.264 encoding have been selected to offload the computing power from the on-board computer. Measurement of the reflection coefficient are made with a low cost miniature vector network analyser (NWA). Beside the USB connected devices (camera and NWA) all sensors and actors where isolated galvanically from the on-board computer to prevent grounding loops and other EMI interferences. Since the housing is

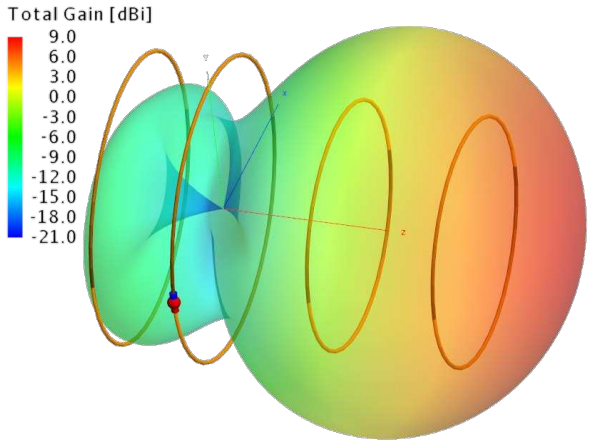

Figure 4. Antenna design with simulated radiation pattern

made from non-conductive plastic material a pure star-type grounding topology has been utilized.

3.3. Mechanical Design

In uncured, resin soaked state the antenna has to be protected from sunlight and very low as well as very high temperatures. Both is accomplished by the lid section depicted in figure 3. Thermal analysis of the structure indicated the risk of freezing of the resin during the mission. To prevent this risk heating elements where added. However - the convectional heat transfer is very limited in the stratospheric environment due to the low air density. Thereby only thermal conduction and radiation are significant. To improve the thermal conduction the antenna was pulled over two heated rings of copper resulting in a large contact area between fabric and the heat source. Additionally the outer side of the lid was isolated with foam plastic, coated with multi layer isolation (MLI) material. The lid is spring loaded and fastened with a nylon yarn. To open the lid, the nylon yarn is cut by a spring loaded heating filament. The burn wire mechanism, similar to [Thu12], is shown in figure 5. Activation of the burn wire system is accomplished by driving a high current through the thin heating filament. Care has to be taken to not melt the heating filament by excessive current. Too low current however would also lead to failure by not melting the nylon yarn. Fortunately [Thu12] gave a good starting point for the correct dimension of the heating filament and current density.

In this experiment pressurized nitrogen was used to inflate the antenna structure. It was stored at 8bar in a 660ml pressurized tank and controlled by two magnetic valves. For inflation an pressure reducing valve was utilized which limits the relative/over- pressure inside the antenna to 250 mBar. The antenna volume is approximately 15 l. Hence the pressurized air is sufficient for inflation in the high altitude environment with near vacuum. However, for ground tests a bigger pressurized tank is required. For future applications a pyrotechnical cold gas generator can provide a reliable and compact source of pressurized gas.

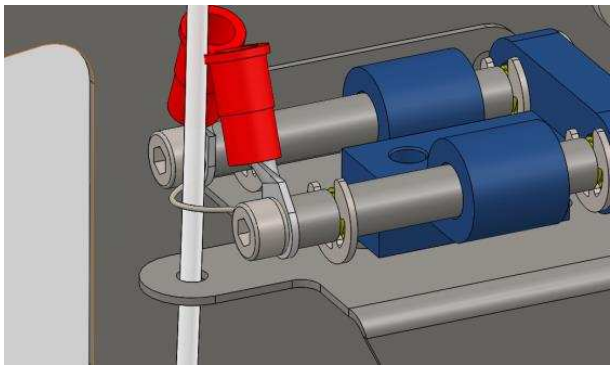

Figure 5. Burn wire mechanism for lid opening

4. EXPERIMENT RESULT

The experiment was successfully carried out on 7. October 2015. During the launch preparation a leakage of the high pressure tank was observed. Its source could not be determined but the leakage rate was relatively low. Calculation showed enough remaining pressure for a sufficient inflation process when a refill is performed directly before launch. Fortunately a late access was granted to perform this refill. The inflation was commanded at an altitude of 23.4 km under video control. After opening the lid in the shadow of the gondola and balloon (figure 6) the inflation valve was opened (figure 7). Full inflation was achieved after 3s as shown in figure 8.

Figure 6. Lid opening after burn-wire activation

No curing sensor is included in the experiment. To prove curing of the resin a slight change in reflectivity and mechanical stiffness after opening the venting valve 120 s after inflation can be exploited. However - suddenly after the antenna was exposed to the direct sunlight generation of smoke can be observed

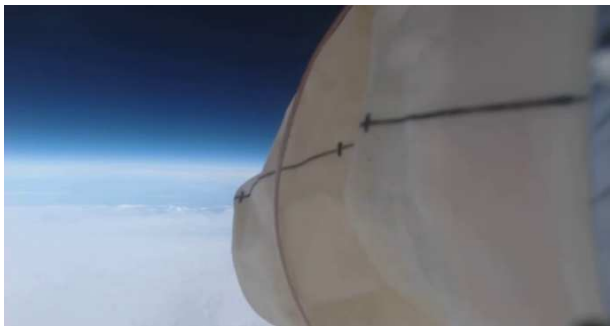

Figure 7. Inflation process after opening the inflation valve

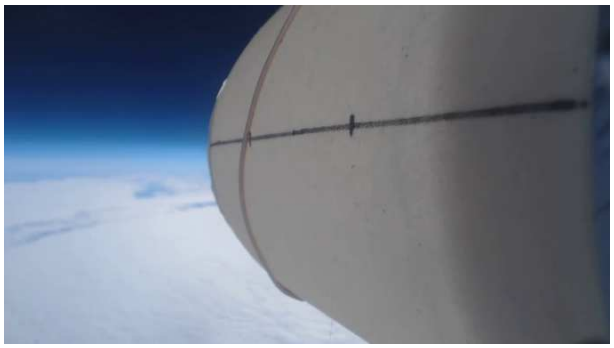

Figure 8. Fully inflated antenna with the helical wound coaxial cable

in the video. [2] Observation of this behaviour of the resin where seen in the lab when curing with very high UV power densities only. As described in section 2 the calculated power density in the specified sensitive wavelength range is barely sufficient for curing. Therefore it is assumed that the actual sensitive wavelength range is much larger than specified. In this case the absorbed power is also larger which leads to the smoking due to overexposure. The generation of this large amount of smoke is obviously problematic, especially for space mission since outgassing might lead to malfunction of other instruments. To prove the hypothesis of the increased sensitivity range of the resin and mitigate the outgasing issue a second experiment was flown on the subsequent BEXUS 20 mission. For this experiment a sample of the spare antenna was cut out and mounted on a small sample holder top side down shown in figure 9. When the structure in figure 2 is flipped over the PVC is exposed to the stratospheric environment. The transparency of 10 % to 20 % of the material was measured at the specified UV wavelength for curing. Within the lab curing experiments with the expected power density of 23mW/cm^2 where not successful in the flipped over configuration. However - after recovery of the sample flown on the BEXUS 20 mission we observed full cure of the exposed resin on the bottom side of the

[2] An image of the smoke is not included since it is barely visible in a video screenshot

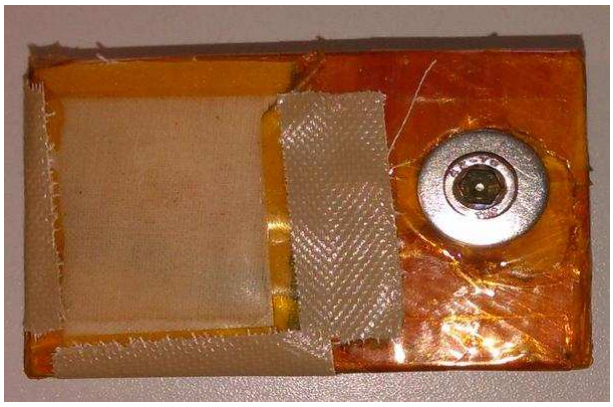

Figure 9. Flipped over textile sample holder of the 2nd experiment after recovery

PVC/cotton laminate. Figure 10 to 12 shows the cross section of the laminated material. All samples are throughout cured.

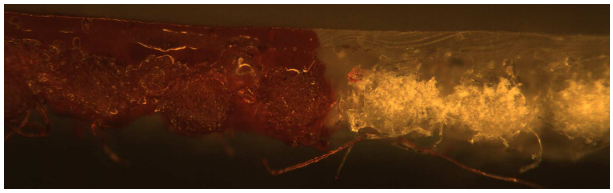

Figure 10. Sample cross section mircrograph from the upper part of the cured antenna. One half is red dyed.

Figure 10 is from the top section of the antenna. Due to the gravity the resin is slightly thicker at the bottom sample in figure 11.

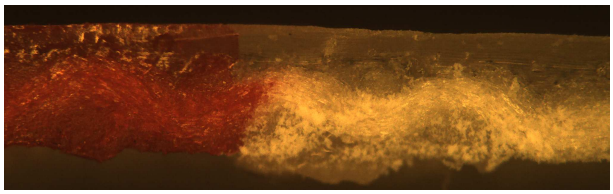

Figure 11. Sample cross section mircrograph from the lower part of the cured antenna. One half is red dyed.

Figure 12 is the cross section micrograph from the 2nd experiment from the BEXUS 20 mission. The thinner resin layer results from manual application of the resin prior mounting resulting in less resin compared to the antenna.

During the decent the antenna was surprisingly robust and even multiple collisions with the banging lid did not result in visible permanent structural damage of the antenna as shown in figure 14.

Since the venting valve was intentional closed during decent the antenna became compressed by increas-

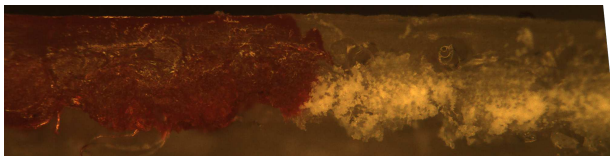

Figure 12. Sample cross section mircrograph from the 2nd experiment with flipped over exposure. One half is red dyed.

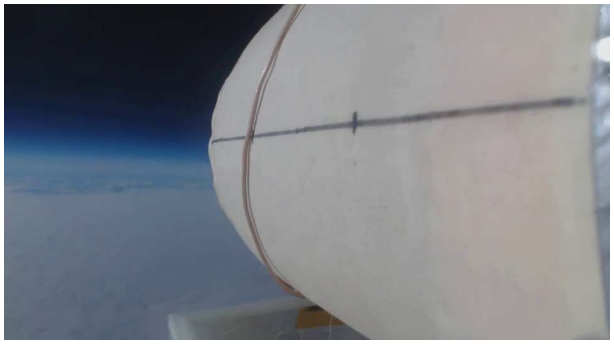

Figure 13. Lid is banging against the rigidized antenna during descent

ing external air pressure. Similar to the lid banging this did not result in visible structural damage of the antenna. However - the compression resulted in some permanent deformation of the antenna visible in figure 15 and 16. Curing of residual, uncured resin during decent is improbable because of the long flight and high UV power density which shall lead to complete cure as discussed above. Internal stress induced during curing is also not very likely since the structure was intact without internal overpressure before decent as seen in figure 14. Most probably microstructural cracks induced by the external overpressure lead to plastically deformation of the antenna. This however does not limit the application of the material since external overpressure can be avoided with a venting valve or opening.

The measured return loss of the antenna was not as

Figure 14. Compressed antenna during decent caused by increasing air pressure due to closed venting valve

Figure 15. Antenna before recovery of the BEXUS goldola

Figure 16. Cut antenna after recovery. Plastically deformation from compressing during descent are clearly visible.

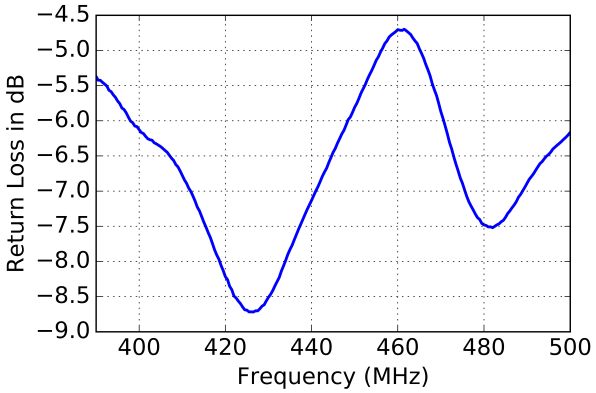

Figure 17. Measured return loss (S11) after inflation.

good as expected. The main reason is the misalignment of the antenna during mounting. This lead to the spirally wrapped coaxial feeding cable visible in figure 7 and 8. We also observed large variance of the measured return loss which do not correlate to time or internal pressure of the antenna. The utilized low cost NWA has a large temperature dependency. It was calibrated before start and switched off between every measurement for power budget reasons. This obviously lead to a large and nearly random temperature deviation between calibration and every measurement. A less temperature sensitive NWA device, automatic calibration before every measurement or a temperature controlled environment for the NWA can mitigate the effect in the future.

5. SUMMARY

Within the InTex-Experiment an inflatable antenna, based on a cotton/PVC laminate, was developed, built and tested successfully. Ridigization with a UV curable resin stabilized the antenna after inflation and maintained the structural integrity after an artificial leakage was enforced. An unexpected fast curing was observed visually. This lead to the hypothesis that the utilized resin is sensitive to a broader UV spectral range than specified. To prove this hypothesis and mitigate observed outgassing issues a second test with a flipped over sample was successfully performed, proving the feasibility of a low-outgassing laminate technology.

ACKNOWLEDGMENTS

The InTex team would like to thank the DLR, SNSB, ESA and ZARM for making this experiment possible. We would also like to acknowledge the Communication Laboratory and Institute of Textile Machinery and High Performance Material Technology of the Technische Universität Dresden for ideational and financial support and the access to all relevant facilities. For the textile coating we acknowledge the Sächsisches Textilforschungsinstitut e.V. We would like to express our thanks to our sponsors: Eurocircuits, Mouser Electronics, Festo and Fischer Elektronik. Finally we thank Dirk Plettemeier for endorsing the whole project.

REFERENCES

[AST14] ASTM. *Standard Solar Constant and Zero Air Mass Solar Spectral Irradiance Tables*. Number ASTM E490 - 00a(2014). 2014.

[Eur16] Eurolaunch. *BEXUS User Manual v.7.0*, 2016.

[ML15] A. Nocke & D. Plettemeier M. Laabs, E. Zakutin. Textile based inflatable antenna systems for space applications. In *36th ESA Antenna Workshop (ESA/ESTEC), Noordwijk, Netherlands,*, 06.-09. Oct. 2015.

[Thu12] S.; Koss S.; Oppenheimer P.; Butcher S.; Schlater J.; Hagan P. Thum, A.; Huynh. Nichrome burn wire release mechanism for cubesats. In *Proceedings of the 41st Aerospace Mechanisms Symposium, Jet Propulsion Laboratory*, May 2012.

LANGMUIR PROBES MULTI-POINTS MEASUREMENTS OF THE PLASMA PROPERTIES INSIDE AN AURORAL ELECTROJET RECORDED BY THE SPIDER SOUNDING ROCKET

Gabriel Giono[1,2] and Nickolay Ivchenko[1]

1: Department of Space and Plasma Physics, School of Electrical Engineering, KTH-Royal Institute of Technology, Stockholm, Sweden. Email: ggiono@kth.se, nickolay@kth.se

2: Leibniz Institute of Atmospheric Physics at the Rostock University (IAP), Kühlungsborn, Germany

Abstract

The SPIDER sounding rocket, flown in February 2016, released ten Free Flying Units (FFUs) in the ionospheric E region (100 to 120 km) in order to investigate the plasma properties inside an auroral electrojet. In this region, the electric fields result in a relative drift motion of electrons and ions, and the induced unstability may create electrostatic waves, in a process referred as Farley-Buneman instability.

SPIDER aimed at characterizing such non-linear coupling between the waves on various scales and the electrostatic turbulence by performing multi-points measurements of the bulk properties of the plasma and the electric field. Each FFUs was equipped with four spherical electric field probes (high impedance probes close to the floating potential) mounted on 2-meters long deployable booms, and four spherical Langmuir probes mounted on 1-meter long deployable boom. Out of the ten FFUs, six were successfully recovered after landing. However, a negative payload charging (around -0.8V) was observed as the FFUs flew through the aurora, resulting in a shift of the Langmuir probe sweeps towards the ion current. Additionally, a larger current than expected was observed, hence saturating the limiting current range of the Langmuir probes (-150 to 250 nA) for many of the bias voltage steps. Nevertheless, some interesting measurements of the current were recorded by the Langmuir probes on four of the six recovered FFUs, for positive bias from +0.1V to +0.7V.

In this paper, a detailed analysis of the Langmuir probes data is presented, showing the retrieval of the plasma properties in the ionospheric E region for two of the FFUs recovered.

Key words: Aurora, Langmuir probes, sounding rocket, SPIDER.

1. INTRODUCTION

Auroral electrojet is a strong horizontal electric current, being part of auroral current circuit. Aurora is created by energetic particles, accelerated in the Earth magnetosphere, and reaching the upper atmosphere along the magnetic field lines. Ionisation and optical emissions are produced by the energetic particles as they collide with atmospheric atoms and molecules.

The E region is the lowest part of the ionosphere, located at heights from 100 to 120 kilometres. This region holds some important scientific questions such as the so-called Farley-Buneman instability: the electric fields induce a relative drift motion between the electrons and the ions, thus creating an unstability possibly leading to electrostatic waves. The waves have been studied theoretically and by MHD simulation [1] but their multiscale interactions remain to be studied experimentally.

Characterizing the non-linear coupling between the waves on various scales and the presence of electrostatic turbulence inside of an auroral electrojet was the main scientific objective of the SPIDER sounding rocket experiment. SPIDER stands for "Small Payloads for Investigating the Disturbances in Electrojet by Rocket" and aimed at performing multi-points measurements of the bulk properties of the plasma and the electric field, by deploying ten identical disk-shape Free Flying Units (FFUs). Each FFU was equipped with four spherical electric field probes (high impedance probes, close to the plasma floating potential) mounted on 2-meters long deployable wire booms, and four spherical Langmuir probes mounted on 1-meter long deployable wire boom. All eight probes were gold coated spheres of diameter 25 mm and deployed radially using the spin of the FFU (*i.e.* conserved from the rocket spin after ejection). The SPIDER sounding rocket was successfully launched on February 2$^{\mathrm{nd}}$ 2016, and six FFUs out of the ten were recovered (*i.e.* the data was stored onboard each FFU's flash memory).

This article is focused on the data analysis of the Lang-

muir probe measurements recorded by two of the recovered FFUs, namely FFU02 and FF06. First, Section 2 presents an overview of the Langmuir probe measurements. The detailed theory used to analyse the measurements is then explained in Section 3 and the results are presented in Section 4. Section 5 summarizes the results obtained from the analysis, as well as discussing the further work to be done with the SPIDER measurements.

2. LANGMUIR PROBE MEASUREMENTS

Each FFU was equipped with four spherical Langmuir probe (LP) mounted on deployable 1-meter long wire-boom. The Digital-to-Analog Converters (DAC) on two LPs were programmed to perform "short-sweeps" from -0.12 V to $+0.12$ V while one LP was performing "long-sweep" from -3 V to $+1.5$ V. The remaining LP was fixed at -5 V. The DAC steps are shown in Figure 1.

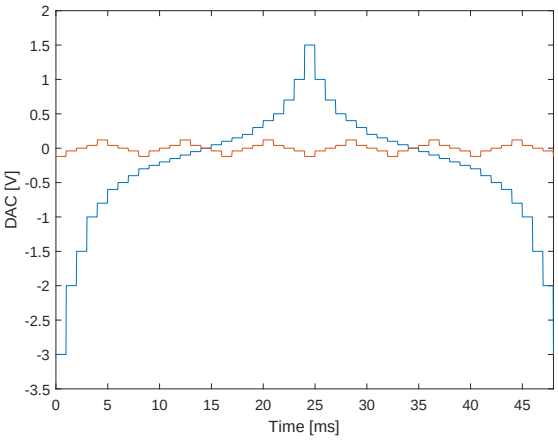

Figure 1. DAC setting for the sweeps ("long-sweep" in blue, "short-sweeps" in red). "Long-sweep" are looped every 48 ms and "short-sweep" every 8 ms. Each bias step duration is 1 ms, during which the current is sampled 32 times (0.0312 ms sampling rate).

Due to an unexpected payload charging around -0.8 V (determined using the electric field probes), the floating potential for the LPs was shifted to $\sim+0.8$ V. Hence, the sweeps from the two "short-sweeps" LPs were shifted towards the negative ion current and most of the recorded data was saturated (*i.e.* below the -150 nA minimum range of the Analog-to-Digital Converter). Only the "long-sweep" LP recorded usable data, for bias from $+0.1$ V (*i.e.* sampling the ion saturation current) to $+0.7$ V (*i.e.* foot of the exponentially increasing electron current). Figure 2 shows the current measured by the "long-sweep" LP for the different bias for the two FFUs considered in this article. Notice the number of bad data points in FFU02: these were due to short-circuits induced by a wobble-motion of the FFU (*i.e.* wobble motion creating contact between the FFU hull and the wire-boom). The same effect was seen to much larger extend in FFU03 and FFU05, making the analysis from their Langmuir probes quite unreliable, hence the focus of this article on the measurements from FFU02 and FFU06. Current-Voltage (IV) curve can be obtained by selecting the measured current from the different bias recorded at a given time, as shown in Figure 4.

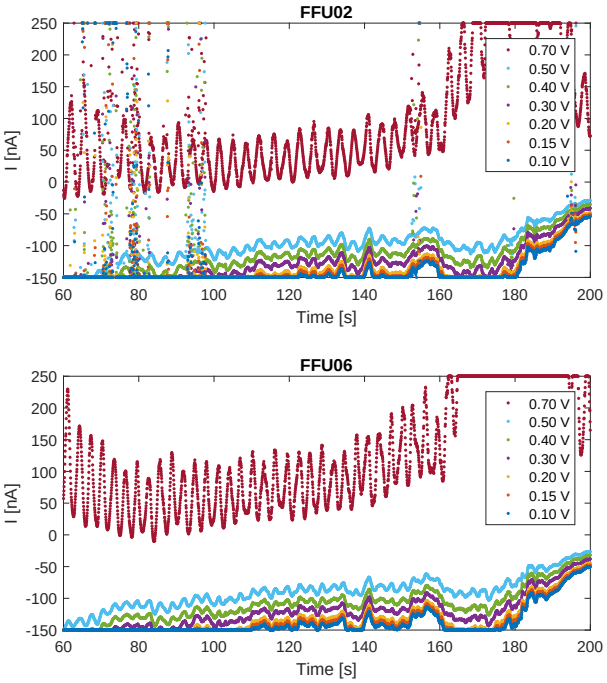

Figure 2. Langmuir probe measurements for FFU02 (top panel) and FFU06 (bottom panel), for the various unsaturated bias and from 60 s to 200 s after deployment.

3. ANALYSIS

The plasma parameters, namely the density n, the electron temperature T_e, the ion temperature T_i and the plasma potential V_p, can be retrieved from the IV curve by fitting a suitable expression for the collect current. The collected current is expressed as the sum of the electron current I_electron minus the ion current I_ion as

$$I = I_\mathrm{electron} - I_\mathrm{ion} \quad (1)$$

Since the SPIDER measurements only sampled the ion saturation and the transition part between the ion and electron saturation, the electron current can be expressed as

$$I_\mathrm{electron} = 4\pi r^2 n \mathrm{e} \sqrt{\frac{\mathrm{k_B} T_\mathrm{e}}{2\pi m_\mathrm{e}}} e^{\mathrm{e}(V-V_p)/(\mathrm{k_B} T_\mathrm{e})} \quad (2)$$

where r is the radius of the spherical probe, k_B is the Boltzmann constant and m_e is the mass of the electron. Note that the part before the exponential corresponds to the current collected by the random motion (*i.e.* thermal) of the electron, assuming a Maxwellian distribution.

On the other hand, the ion saturation current can be written in a similar fashion as

$$I_{ion} = 4\pi r^2 ne\sqrt{\frac{k_B T_i}{2\pi m_i}} I_{acc} \tag{3}$$

with the current collected by the random motion of the ion multiplied by a factor including the effect of the potential (*i.e.* attracting more ions as the potential becomes more negative) and the collection of ions as the probe moves through the plasma. Note that this latter effect was neglected for the electrons, as their mobility is much higher than the FFU speed. However, for ions, their expected thermal speed is comparable to the FFU velocity (couple of hundreds of meter per second). This factor is denoted as I_{acc}, as it corresponds to the current induced by the ions accelerated towards the probe.

The expression for I_{acc} was taken from [2] and is shown in Equation 7 (see Appendix A). This expression is the general formulation for a moving sphere and includes the balance between potential energy and thermal energy W, the Mach number M of the moving FFU and the thickness of the plasma sheath around the probe h. It is important to notice that this large expression can be greatly simplified in the two extreme sheath regimes: thin-sheath (*i.e.* $a/r \rightarrow 1$) as used in [3] and large-sheath (*i.e.* $a/r >> 1$), also referred as Orbital Motion Limit regime. The OML expression can be simplified further for large speed, *i.e.* $M >> 1$ [4, 5]. However, such assumptions cannot be used in the case of SPIDER, for which the Debye length λ_D is around 3 mm (*i.e.* sheath thickness of the order of a couple of λ_D, hence of the same order as the probe radius r) and the Mach number M is close to unity. Therefore, the general formulation shown in Equation 7 should be used, and an estimate the sheath thickness is required.

The sheath thickness h can be related to the probe's potential and the electron temperature via the Child-Langmuir relation

$$\eta = \left(\frac{3}{4}2^{3/4}\xi\right)^{4/3} \tag{4}$$

where η=$(e|V - V_p|)/(k_B T_e)$ and ξ=h/λ_D. The Child-Langmuir law provides an accurate estimation of the sheath thickness only for large value of η (>100) whereas, in the case of SPIDER, η is expected to be between 1 (at bias of -0.1 V, assuming maximum T_e around 1000 K) and 20 (at bias of -0.7 V, assuming minimum T_e around 400 K). Hence, a more accurate solution to estimate the sheath thickness in this regime is to solve the sheath equation

$$\frac{1}{2}\left(\frac{d\eta}{d\xi}\right)^2 = \mathfrak{M}^2\left[\sqrt{\left(1+\frac{2\eta}{\mathfrak{M}^2}\right)} - 1\right] + e^{-\eta} - 1 \tag{5}$$

where $\mathfrak{M} = \sqrt{(m_i v_i^2)/(k_B T_e)}$. The sheath equation can be solved only if $\mathfrak{M}^2 \geq 1$. This imposes the ion velocity v_i to be larger or equal to $\sqrt{(k_B T_e)/m_i}$ and is usually referred as the Bohm criterion. In essence, this result indicates that ions are accelerated by the probe/sheath potential to a speed higher than their thermal velocity (*i.e.* as $T_e > T_i$). Therefore, in this regime, the ion temperature cannot be retrieved from the collected current. Examination of the Bohm criterion expression of v_i reveals a very similar equation as the ion kinetic energy, where T_i is replaced by $T_e/2$. This suggests that the accelerated ions have a temperature of at least $T_e/2$. Hence, T_i was replaced by $T_e/2$ in the expression of the ion current, both in Equation 3 and Equation 7.

Solving Equation 5 comes down to numerically integrating the differential equation

$$d\eta/d\xi = \sqrt{2}\left[\sqrt{1+2\eta} + e^{-\eta} - 2\right]^{1/2} + s \tag{6}$$

The s parameter in this differential equation corresponds to the slope of the potential dV/dx at the edge of the sheath (*i.e.* at x=h). The edge of the sheath is define as where $V(x$=$h)$=0, but the negative potential from the probe at $V(x$=$0)$ extends beyond the sheath edge to the plasma potential (*i.e.* $V(x\rightarrow\infty)$=$V_p > 0$). Hence, s=dV/dx at x=h cannot be equal to zero. Accurately selecting s is a very complicated problem: knowledge on the shape of the potential around the probe cannot be simply derived from the recorded current. In theory, there is not reason for s to be fixed, as the shape of the potential could be influenced by both the plasma environment and the bias potential on the probe. However, leaving s as a free parameter when fitting the IV curve leads to some troubles: since s dictates the shape of the sheath, it competes with the plasma parameters when fitting the measurements.

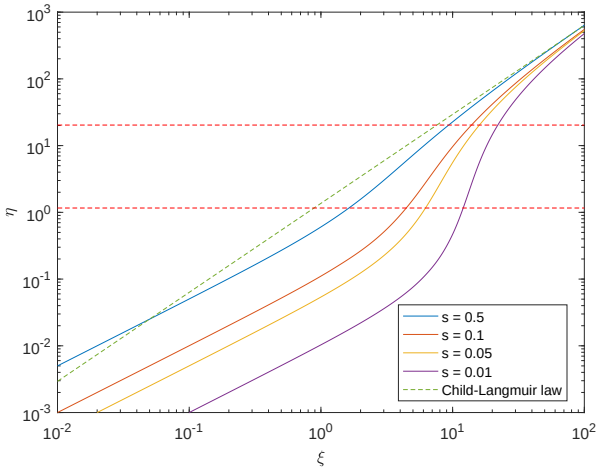

Figure 3. Sheath thickness ξ versus potential/thermal energy ratio η for various s values as well as for the Child-Langmuir law. Horizontal red dash lines shows the approximated maximum and minimum η value during SPIDER flight.

As a result, unrealistic values for both s (*i.e.* ≥ 1) and the plasma parameters are found. On the other hand, fixing s to a given value can provide consistent results for the three plasma parameters n, T_e and V_p, for all the IV curves recorded during the flight. Although the selection of a fixed s value does slightly offset the fitted plasma parameters, the temporal variations were unaffected. A s value of 0.5 was selected, as it provided consistent fitting results for all measurements, in both FFU02 and FFU06. Such s value correspond to a slight deviation from the Child-Langmuir law, as shown in Figure 3.

4. RESULTS

An example of IV curve measurement is presented in Figure 4, with the corresponding theoretical curve fitted as described in Section 3. As one can see, the fitted curve nicely reproduces the ion saturation current recorded by the LP.

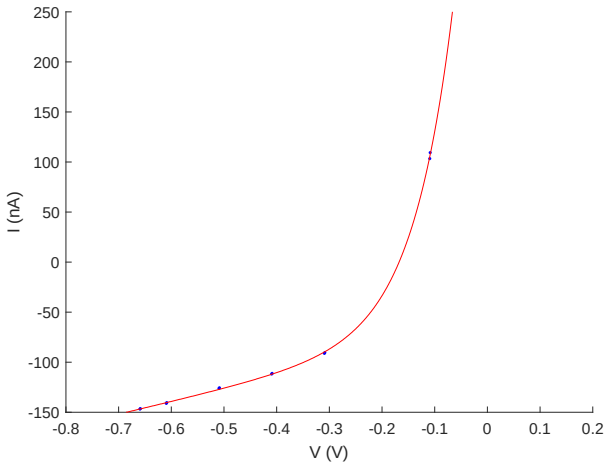

Figure 4. Example of an IV curve taken from FFU06 at 110 s. Blue dots correspond to the measured current the various bias. Red line show in fitted curve. Plasma parameter for this fitted curve are: $n = 5.42 \times 10^{11}$ *m^{-3},* $T_\mathrm{e} = 879.9$ *K and* $V_\mathrm{p} = 0.18$ *V.*

Time-series of the plasma parameters retrieved during the flight for FFU02 and FFU06 are shown in Figure 5. A very good correlation can be seen in the all parameters between the two FFUs. Note that the offset seen in the plasma potential is most likely an artefact due to how the "ground" was selected: the zero-volt of the IV curve was estimated by removing the payload charging, estimated from the Electric probe measurements. However, offsets were observed between the various electric field probes, hence inducing an uncertainty on the payload "ground". It is interesting to notice that the derived parameters are not affected by the FFU speed (parabolic trajectory peaking around 130 s), indicating that the theory used correctly takes into account to collected current due to the probe motion. On the other hand, although the effect of the FFU rotation was supposedly removed by adjusting the bias voltage of each IV curve point using the corresponding electric field measurements, some periodic fluctuations can still be seen in the retrieved parameters. Further investigation is required to determine if they are related to the FFU rotation.

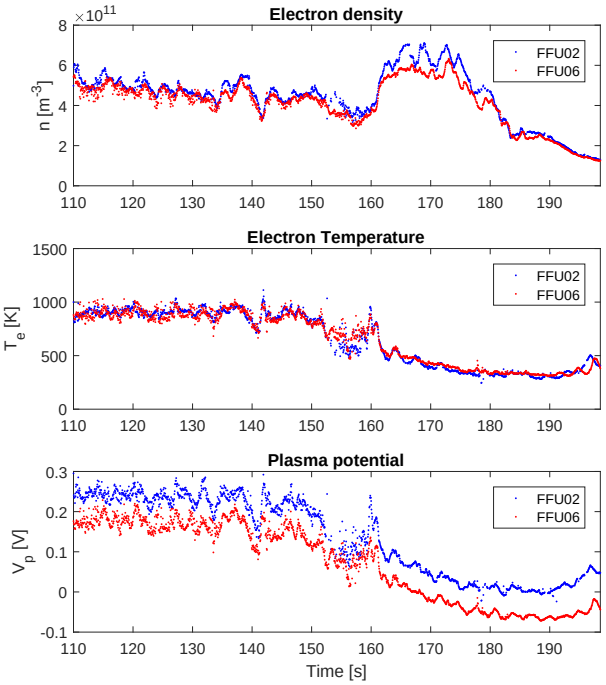

Figure 5. Results for the electron density n (top panel), the electron temperature T_e (middle panel) and the plasma potential V_p (bottom panel) for FFU02 (blue) and FFU06 (red).

Using the GPS data, n and T_e from Figure 5 can be displayed along the FFUs trajectory and compared to the coordinated EISCAT radar measurements performed during the flight, as shown in Figure 6. A similar structure of the aurora can be seen in both instruments, both in term of the electron density and electron temperature.

5. CONCLUSION

The SPIDER sounding rocket aimed at providing multi-point measurements of the plasma properties inside of an auroral electrojet. Although only a limited number of FFUs recorded usable Langmuir probe data, the results presented in this article demonstrated the feasibility of such multi-point measurements. Due to the complexity of the plasma regime encountered during the flight (*i.e.* probe radius comparable to sheath thickness and probe moving at comparable speed to the ions), the general for-

mulation for the accelerated ion current was used in order to retrieve the plasma parameters, *i.e.* the density n, the electron temperature T_e and the plasma potential V_p, from the measured IV curves recorded by two FFUs. The results show a very good correlation between the two FFUs and the coordinated EISCAT radar measurement of the aurora. The small temporal variations seen in the plasma parameters are interesting, and more work needs to be done in order to interpret them. Additionally, it is worth mentioning that the SPIDER FFUs also recorded interesting electric field measurements, which were not discussed in this article.

ACKNOWLEDGEMENT

The work was partially supported by the Swedish Government Agency for Innovation Systems (VINNOVA) contract no. 2016-04094.

A. General formulation for the accelerated ion current collected by a moving spherical probe.

The general formulation of the accelerated ion current collected by a moving spherical probe is

$$
\begin{aligned}
I_{acc} = &\left(\frac{a}{r}\right)^2\Big[\frac{\sqrt{\pi}}{2}\frac{(M^2+\frac{1}{2})}{M}\mathrm{erf}(M)\\
&+\frac{\sqrt{\pi}}{2}\frac{W}{2M}\big[\mathrm{erf}(M-\gamma W^{1/2})\\
&+\mathrm{erf}(M+\gamma W^{1/2})\big]+\frac{1}{2}e^{-M^2}\Big]\Big]\\
&-\left(\left(\frac{a}{r}\right)^2-1\right)\Big[\frac{\sqrt{\pi}}{2}\frac{(M^2+\frac{1}{2}+W)}{2M}\\
&\big[\mathrm{erf}(M-\gamma W^{1/2})+\mathrm{erf}(M+\gamma W^{1/2})\big]\\
&+\frac{M+\gamma W^{1/2}}{4M}e^{-(M-\gamma W^{1/2})^2}\\
&+\frac{M-\gamma W^{1/2}}{4M}e^{-(M+\gamma W^{1/2})^2}\Big]
\end{aligned}
\tag{7}
$$

The variables W, M, γ and a are defined as:

$$
\begin{aligned}
W &= \frac{\mathrm{e}\mid(V-V_\mathrm{p})\mid}{\mathrm{k_B}T_\mathrm{i}}\\
M &= \frac{m_\mathrm{i}v^2}{2\mathrm{k_B}T_\mathrm{i}}\\
\gamma &= \frac{1}{\sqrt{(a/r)^2-1}}\\
a &= r+h
\end{aligned}
\tag{8}
$$

where v is the speed of the FFU and m_i the mass of the ions. In SPIDER case, v was taken from the GPS and m_i as 31u (average mass of the two most common species of ions at these heights: O_2^+ and NO^+).

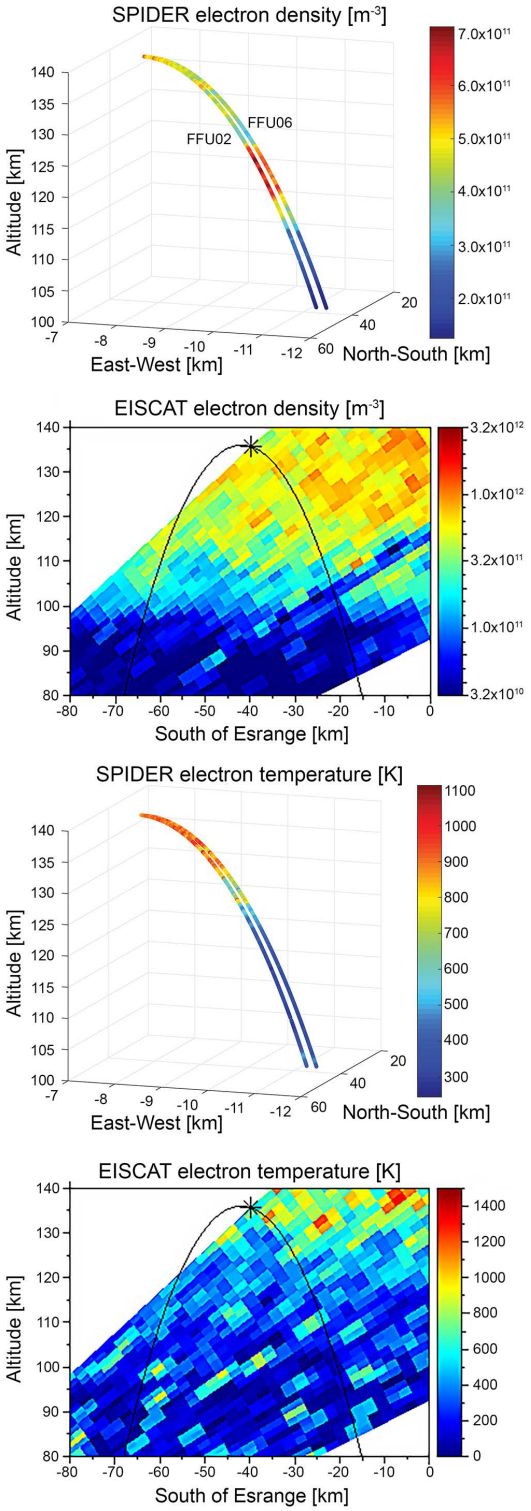

Figure 6. From top to bottom: SPIDER electron density, EISCAT electron density, SPIDER electron temperature and EISCAT electron temperature. Cross shows the position of the rocket for this EISCAT measurement.

References

1. M. M. Oppenheim and Y. S. Dimant. Kinetic simulations of 3-D Farley-Buneman turbulence and anomalous electron heating. *J. Geophysical Research : Space Physics*, 118, 2013.

2. L. E. Warthon and W. R. Hoegy. Current to moving spherical and cylindrical electrostatic probes. *NASA Goddard Space Flight Center internal report*, X-621-71-276, 1971.

3. R. C. Sagalyn, M. Smiddy, and J. Wisnia. Measurement and interpretation of ion density distribution in the daytime f region. *J. Geophysical Research*, 68, 1963.

4. A. Pedersen et al. Electron density estimations derived from spacecraft potential measurements on cluster in tenuous plasma regions. *J. Geophysical Research*, 113, 2008.

5. U. Fahleson, C. G. Falthammar, and A. Pedersen. Ionospheric temperature and density measurements by means of spherical double probes. *Planet. Space Sci.*, 22, 1974.

DETAILED PHOTOCURRENT CHARACTERIZATION FOR METEOR SMOKE PARTICLE DETECTORS ONBOARD THE PMWE SOUNDING ROCKETS

Gabriel Giono[1,2], Boris Strelnikov[1], Heiner Asmus[1], Tristan Staszak[1], Nickolay Ivchenko[2], and Franz-Josef Lübken[1]

1: Leibniz Institute of Atmospheric Physics at the Rostock University (IAP), Kühlungsborn, Germany

2: Department of Space and Plasma Physics, School of Electrical Engineering, KTH-Royal Institute of Technology, Stockholm, Sweden. Email: ggiono@kth.se

Abstract

Characterizing the photoelectron current induced by the Sun's UV radiation is crucial to ensure an accurate daytime measurement from particle detectors. This article layout the methodology used to address this problem in the case of the Meteor Smoke Particle Detectors (MSPDs), developed by the Leibniz Institute of Atmospheric Physics at the Rostock University (IAP) and to be flown on the PMWE (Polar Meosphere Winter Echoes) sounding rockets. The methodology focuses on two complementary aspects: modelling and calibration.

A detailed model of the MSPD photocurrent was created based on the expected solar UV flux, the atmospheric UV absorption as a function of height, the photoelectic yield of the material coating the MSPD as a function of wavelength, the index of refraction of these materials as a function of wavelength and the angle of incidence of the illumination onto the MSPD. Due to its complex structure, extensive ray tracing calculations were conducted to obtain the illumination's angle of incidence onto the central electrode and shielding grids for various orientation of the MSPD with respect to the Sun. Initial results of the modelled photocurrent at different heights are discussed.

An experimental setup for the calibration of the MSPD photo-current is also presented, which includes a vacuum chamber to simulate the flight condition by varying the density of molecular oxygen, a Deuterium UV light-source with wavelength range from 115 to 300 nm, and narrow-bands filters to select particular UV wavelengths.

Key words: Photocurrent, Meteor Smoke Particle, sounding rocket, Polar Mesosphere Winter Echoes.

1. INTRODUCTION

Polar mesospheric winter echoes (PMWE) are enhanced radar returns from altitudes of 55 to 85 km [1] and their formation mechanism is still under debate. Meteoric smoke particles (MSPs) at mesospheric heights are a strong candidate for explaining polar winter echoes but no direct confirmation of their presence has been made yet. The ongoing sounding rocket project PMWE led by IAP aims at measuring densities of all dusty plasma constituents including MSPs. Two sounding rockets will carry several Meteor Smoke Particle Detectors (MSPDs, described in more detail in an accompanying paper [2]), each composed of a central spherical electrode collecting the MSPs, shielded by two concentric and electrically biased grids repelling the ambient ions and electrons as shown in Figure 1.

Figure 1. Meteor Smoke Particle Detector with its central spherical electrode (26 mm radius) shielded by two concentric and electrically biased grids (35 mm and 45 mm radius).

However, understanding the photoelectron current from the electrode induced by the solar UV illumination is crit-

ical for quantifying the measurements. The presented work addresses this aspect in two distinct, yet complementary, ways: modelling and experiment calibration. In Section 2, the recipe for a detailed model of the MSPD photocurrent is presented based on the expected solar UV flux, the atmospheric UV absorption as a function of height, the photoelectic yield of the material coating the MSPD as a function of wavelength, the index of refraction of these materials as a function of wavelength and the angle of incidence of the illumination onto the MSPD. Due to its complex structure, extensive ray tracing calculations were conducted to obtain the illumination's angle of incidence onto the central electrode and shielding grids for various orientation of the MSPD with respect to the Sun. Results of the modelled photocurrent at different heights are discussed. Section 3 presents the experimental setup and method for estimating the MSPD photocurrent. The setup includes a vacuum chamber to simulate the flight condition by varying the density of molecular oxygen, a Deuterium UV light-source with wavelength range from 115 to 300 nm, and narrow-bands filters to select particular UV wavelengths.

2. Recipe for modeling photocurrent

Photocurrent is the result of the photoelectric effect [3]: photons with high enough energy, typical UV wavelength and below, eject electrons from a material when absorbed. The number of electron ejected depends on, 1) the flux of photon at different wavelengths illuminating the material and, 2) the material properties which influence its interaction with the energetic photons.

2.1. UV photons: Solar spectrum, atmospheric density and atomic absorption

The solar UV spectrum has been measured by various space-borne instruments since the beginning of the space age. Its main characteristic is the Lyman-alpha line at 121.56 nm which is more than two orders of magnitude larger than the continuum. As the continuum decreases at shorter wavelengths, only the part from 115 to 300 nm will be considered for modelling the photocurrent (the photoelectric effect is negligible for most material at larger wavelength). The reference solar UV flux considered in the model was taken from the SOLSTICE instrument onboard the SOlar Radiation and Climate Experiment (SORCE) spacecraft [4], taken on the July 30$^{\text{th}}$ 2006 (*i.e.* 11 years ago) to roughly represent a similar solar activity as expected during the launch.

In the case of a sounding rocket, the flux of photon emitted from the Sun is absorbed by the atmosphere. This effect depends on the atmospheric density n of the atomic elements (depends on the height h) and the absorption

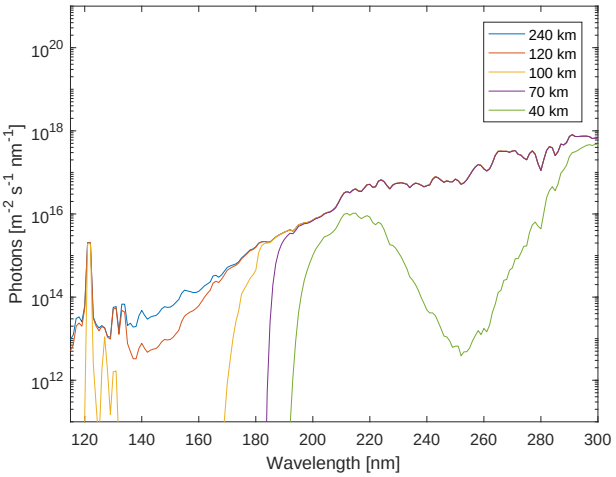

Figure 2. Spectral flux from 115 to 300 nm at various atmospheric height, for a solar zenith angle θ_z of 75°.

cross-section σ for these elements (depends on the wavelength λ), as well as the solar zenith angle θ_z which affects the atmospheric column above the height h. The main contributor for the atmospheric absorption is molecular oxygen O_2 at heights below 150 km and for wavelength below 200 nm. Ozone O_3 also contributes to UV absorption in a band from 200 nm to 300 nm at heights below 70 km. The atmospheric density as a function of heights were taken from [5] for O_2 (taken in a low solar activity scenario) and from [6] for O_3 (taken at the latitude of rocket launch site, Andøya in Norway, at 69.1144°N). The absorption cross section for O_2 was taken from [7, 8, 9] and from [10, 9] for O_3. Using these data, the amount of absorption at a given height is derived by first calculating the β coefficient at each height:

$$\beta(h, \lambda) = n(h) \times \sigma(\lambda) \tag{1}$$

The total β is obtained by simply the sum of β_{O_2} and β_{O_3}. Then, the absorption optical depth τ is calculated at each height by integrating the β coefficient from this height to the top of the atmosphere.

$$\tau(h, \lambda) = \int_{\text{h}}^{\infty} \beta(h, \lambda) \text{d}h \tag{2}$$

Finally, the number of photons at a given height is derived using the absorption equation

$$F(h, \lambda) = F(\infty, \lambda) \times \text{e}^{-\tau(h,\lambda)/\mu} \tag{3}$$

where $F(\infty, \lambda)$ is the solar UV flux at the top of the atmosphere and μ is the cosine of the solar zenith angle θ_z, assuming a plane parallel atmosphere.

Figure 2 presents the solar UV flux obtained at various heights for a solar zenith angle θ_z of 75° (expected solar zenith angle durning winter in Andøya). Results are very consistent with the similar results presented by [9].

2.2. Material interaction: photoelectric yield and reflectance

The second aspect of the photocurrent depends on the material properties, namely photoelectric yield and the reflectance. The photoelectric yield gives the probability for photon of a given energy to eject an electron from the material surface. Indeed, although all transmitted photons with sufficient energy transfers its energy to an electron, most electrons are only moved inside of the material and are not ejected, therefore not contributing to the photocurrent. Photoelectric yields were taken from [11] for four materials: gold, aluminium, stainless steel and graphite.

The reflectance of the material is also important, as reflected photons do not contribute to the photocurrent. The total $R(\lambda, \theta_i)$ is the average of the two $R_\mathrm{s}(\lambda, \theta_i)$ and $R_\mathrm{p}(\lambda, \theta_i)$ reflectances for s and p polarization, respectively, which can be obtained from the Fresnel equations

$$\begin{aligned} R_\mathrm{s}(\lambda, \theta_i) &= \\ &\left| \frac{\cos\theta_i - n(\lambda)\sqrt{1 - n(\lambda)^{-2}\sin^2\theta_i}}{\cos\theta_i + n(\lambda)\sqrt{1 - n(\lambda)^{-2}\sin^2\theta_i}} \right|^2 \\ R_\mathrm{p}(\lambda, \theta_i) &= \\ &\left| \frac{\sqrt{1 - n(\lambda)^{-2}\sin^2\theta_i} - n(\lambda)\cos\theta_i}{\sqrt{1 - n(\lambda)^{-2}\sin^2\theta_i} + n(\lambda)\cos\theta_i} \right|^2 \end{aligned} \tag{4}$$

and depends on both the refractive index of the material $n(\lambda)$ and the angle of incidence of the light onto the material θ_i. The fraction of photon transmitted into the material is given by the transmittance, which can be obtained from the reflectance as $T(\lambda, \theta_i) = 1 - R(\lambda, \theta_i)$. Values of $n(\lambda)$ for the four materials were taken from [12]. However, $n(\lambda)$ data for stainless steel has not been available and values for iron was used instead.

2.3. Illumination onto the MSPD: angle of incidence

As shown in Section 2.3, the transmittance depends on the angle of incidence θ_i of the incoming photons. Therefore, a proper knowledge of the illumination onto the MSPD is required to determine the photocurrent. Ray-tracing simulations can provide a quantitative estimation of illumination across the detector (*i.e.* down to the resolution of the grid used). However, due to its complex geometry, modelling the detector in a usual ray-tracing software was not possible and a custom MATLAB routine was created to tackle the challenge. The central electrode was modelled as a sphere and each grid wire as a torus (98 total). The ray-tracing calculations aimed at finding the intersection between a ray, modelled as a vector, and the detector surfaces which imply resolving a quartic equation for each torus. The resolution for the simulation is 0.1 mm (grid wire radius: 0.5 mm) and, due to symmetry reason, only half of the MSPD is required to be covered by the simulation, *i.e.* X from 0 to +45 mm, and Z from −45 to +45 mm. Indeed, although the MSPD design is symmetrical along two of its axis, a different inclination might result in a different illumination of the central electrode. For this reason, the calculations have to be performed for various inclination, from 0° to 90°. Due to computational load of the simulation and for practical reasons, the routine was run on one of the 24 CPUs node of the Tegner post-processing unit, belonging to the PDC supercomputer from KTH. Total computation time per inclination is about a week. Figure 3 shows the resulting illumination for inclination angle of 0°.

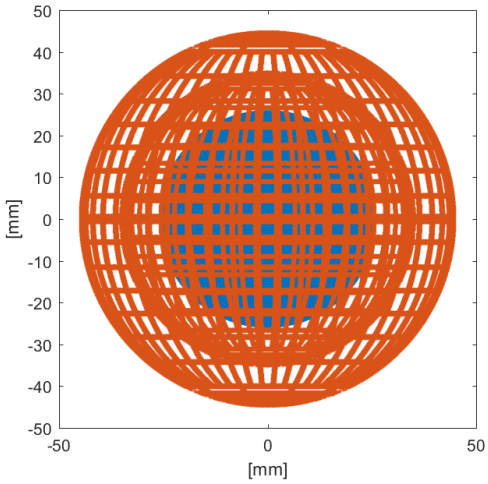

Figure 3. Illumination on the MSPD for an inclination angle of 0°. Blue shows the rays hitting the central electrode and orange the rays hitting the grids.

2.4. Resulting photocurrent

Figure 4 shows the resulting photocurrent at different height and for four different materials, based on the solar flux from Section 2.1, the material properties from Section 2.2 and the MSPD illumination at 0° from Section 2.3. Based on this results, it seems that a carbon coating would reduce the most the photocurrent at heights above 80 km.

3. Experimental measurement of the photocurrent

The second aspect of photocurrent characterization is to experimentally measure it. Ideally, one would like to have a well-calibrated and wavelength-adjustable UV light source (*i.e.* monochromator setup) to illuminate the detector and record the resulting the photocurrent at each

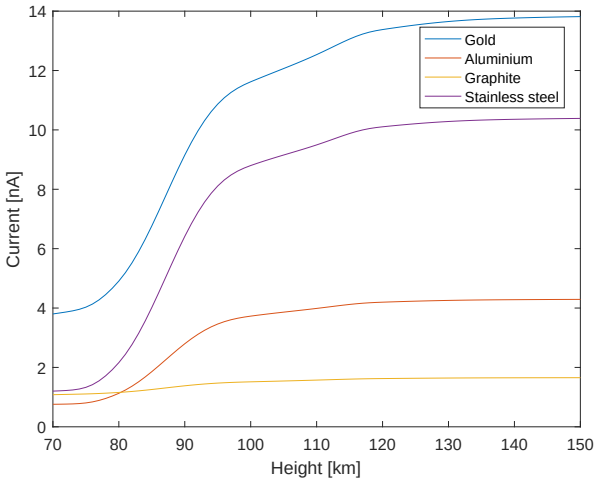

Figure 4. MSPD photocurrent at various heights for four different materials, for an inclination angle of 0° and a solar zenith angle of 75°.

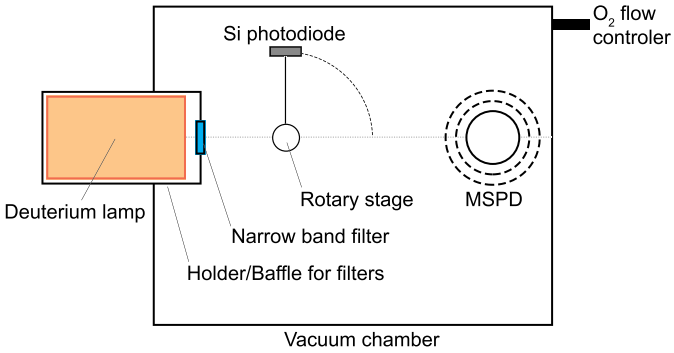

Figure 5. Layout of the experiment in the IAP large vacuum chamber.

wavelength. The approach presented in this article uses narrow-band filters to select various UV wavelength instead. This approach is not as accurate since the filters are not perfect, and the number of different filters is limited, but has the advantage of being simpler: filters can simply positioned in front of the UV light-source, and the UV flux can be easily monitored with a Si photodiode. Figure 5 shows the layout of the experiment inside of the IAP large vacuum chamber (300 mm radius and 600 mm length).

A Deuterium lamp is used to provide UV photons, from 115 to 300 nm. Its spectrum, presented in Figure 6, was measured independently by PTB (Physikalisch-Technische Bundesanstalt (PTB), the German national metrology institute located in Berlin, Germany) and at Rostock University (Germany) for the purpose of a previous experiment [13]. Similar measurements are to be performed at Rostock University to confirm the Deuterium lamp spectrum.

Four narrow-band filters were selected to sample the UV

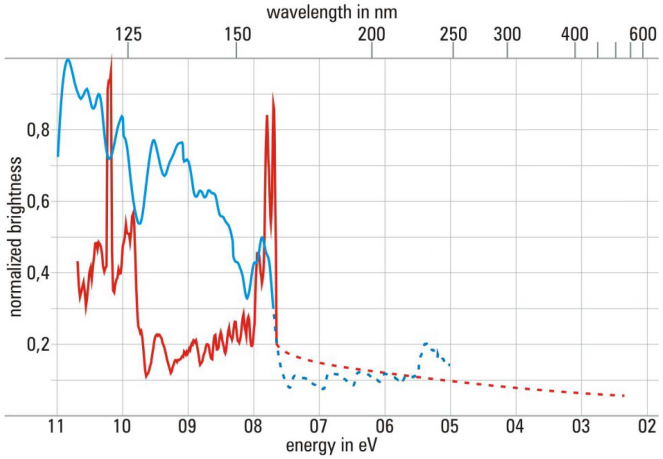

Figure 6. Deuterium lamp spectrum measured by PTB (red solid line) and at Rostock University (blue solid line). Dash lines indicate the expected spectrum. Figure adapted from [13].

region, at 121, 160, 200 and 250 nm. The transmission curve for these filters was measured by the manufacturer, and are presented in Figure 7. The actual spectral flux transmitted by the filter can be derived based on the light-source spectrum and the transmission curve. In addition, a Si photodiode mounted on a rotary stage is used to monitor the transmitted flux throughout the experiment.

The MSPD is mounted in a custom jig allowing to change its inclination with respect to the light source beam. Additionally, the density of molecular oxygen inside the vacuum chamber can be adjusted in order to simulate the effect of atmospheric absorption as a function of height. The experiment will be conducted during summer 2017, and results will be compared to the modelling results from Section 2, for the different inclination and atmospheric density.

4. CONCLUSION

Characterizing the photocurrent induced by the Sun UV photons is a crucial aspect to ensure the measurements from particle detectors launched during day-time, and this is of prime-importance when aiming at measuring the presence of meteor smoke particles in the upper-atmosphere. A dual and complementary approach to the problem was presented, by means of modelling and experimental measurements. The recipe for simulating the photocurrent on a metallic detector was explained, which includes 1) an atmospheric absorption model proving the UV flux as a function of height, 2) the material properties of the detector influencing the efficiency of the photoelectric effect and 3) detailed ray-tracing simulation to obtain a complete picture of the illumination onto the MSPD. Contribution from Rayleigh scattering was not considered in the model yet, and is to be included. The lay-

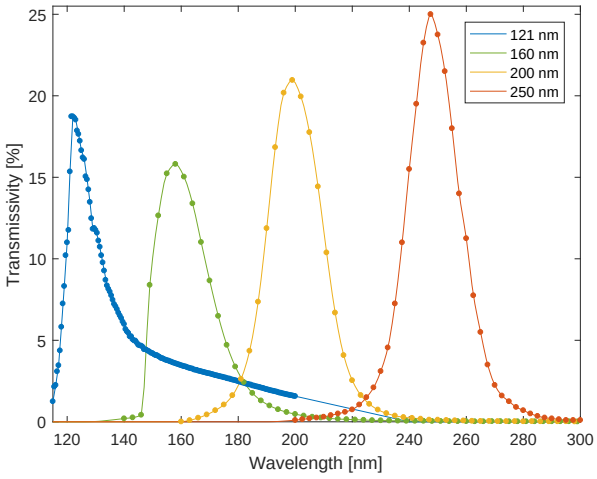

Figure 7. Transmissivity of the four VUV narrow band filters.

out for an experimental measurement of the photocurrent was also presented, using a Deuterium lamp as UV light source and narrow-band filters to select particular wavelengths. This experimental setup is to be implemented during summer 2017, and results will be compared to the modelled photocurrent.

ACKNOWLEDGEMENT

The work was partially supported by the Swedish Government Agency for Innovation Systems (VINNOVA) contract no. 2016-04094. This work was supported by the German Space Agency (DLR) under grant 50OE1402 (project PMWE). The authors thank H.-J. Heckl and T. Köpnick for building the instrument.

References

1. R. Latteck and I. Strelnikova. Extended observations of polar mesosphere winter echoes over Andoya (69N) using MAARSY. *J. Geophysical Research: Atmosphere*, 120, 2015.

2. T. Staszak, H. Asmus, B. Strelnikov, F.-J. Lübken, and G. Giono. A New Rocket-borne Meteor Smoke Particle Detector (MSPD) for D-Region Ionosphere. In *Publication Proceedings of the 23th Symposium on European Rocket and Balloon Programmes and Related Research*, Visby, Sweden, 11-15 June 2017.

3. A. Einstein. Concerning an Heuristic Point of View Toward the Emission and Transformation of Light. *Annalen der Physik*, 17, 1905.

4. G. Rottman, T. Woods, and V. George. *The Solar Radiation and Climate Experiment (SORCE)*. Springer, New York, NY, 2005.

5. COSPAR International Reference Atmosphere (CIRA-2012), 2012. http://spaceweather.usu.edu/htm/cira.

6. G. Bodeker and B. Hassler. Bodeker Scientific Global Vertically Resolved Ozone Database, 2012. NCAS British Atmospheric Data Centre, http://catalogue.ceda.ac.uk/uuid/9a2438602c2b534f54d81e54b9d98d75.

7. M. Ogawa. Absorption Coefficients of O2 at the Lyman-Alpha Line and Its Vicinity. *J. Geophysical Research*, 73, 1968.

8. A. J. Blake, J. H. Carver, and G. N. Haddad. Photoabsorption cross sections of molecular oxygen between 1250A and 2350A. *J. Quant. Spectosc. Radiat. Transfer*, 6, 1966.

9. R. E. Huffman. *Handbook of Geophysics and the Space Environment*. Air Force Geophysics Laboratory, 1985.

10. L. T. Molina and M. J. Molina. Absolute Absorption Cross Sections of Ozone in the 185- to 350-nm Wavelength Range. *J. Geophysical Research*, 14501-14508, 1986.

11. B. Feuerbacher and B. Fitton. Experimental Investigation of Photoemission from Satellite Surface Materials. *J. Applied Physics*, 43, 1972.

12. Refractive Index Database, 2016. https://refractiveindex.info/.

13. S. Ernst, S. Skruszewicz, B. Strelnikov, and M. Rapp. Absolute Calibration of Vacuum Ultraviolet Xenon Flash Lamps used for Photoionization of Meteor Smoke Particles. In *Publication Proceedings of the 20th Symposium on European Rocket and Balloon Programmes and Related Research*, volume ESA SP-700, Hyere, France, October 2011.

THE NEW OLD PROCESS OF WIND WEIGHTING

VISBY, SWEDEN
11-15 JUNE 2017

Klas Nehrman[(1)], Johan Nilsson[(1)]

[(1)]Swedish Space Corporation (SSC), Esrange Space Center P.O Drag Box 802, SE-98128 Kiruna Sweden
Email: klas.nehrman@sscspace.com
Email: johan.nilsson@sscspace.com

ABSTRACT

Wind weighting is the process of correcting for impact point displacement due to wind effects during sounding rocket launches.
At Esrange Space Center the application Storm is used for wind weighting. Storm implements the historically proven Lewis method for launcher setting corrections.
SSC developed Storm as a part of our effort to rejuvenate and future-proof our safety software suite. It has been fully operational since late 2015.
Storm depends on services provided by the application Breeze, which collects wind measurements and forecasts, refining these for usage by other applications.
These applications were designed with extensibility and maintainability in mind, while providing both internal users and customers with highly valuable visualizations of predicted and current launch conditions.

1. SCOPE

This paper will specifically focus on wind weighting and how SSC's in-house developed software suite takes on the challenge to combine the tradition of wind weighting and modern technology. As well as the challenge to be able to adapt to new and changing demands but still have certified safety software.

2. BACKGROUND

Rocket launches can have the adverse effect of exposing the general public and/or specific individuals to a risk for injury or casualty from the launch operations. Flight safety work address the quantification of the risk levels introduced from debris and vehicle systems that will have a ground impact or pose a risk to vehicles in mid-air. A key point in the work to quantify the risk levels and define the Hazard Areas for a sounding rocket launch is to decide a point to aim the vehicle at; this point is normally called the Nominal Aiming Point (NAP) or the Nominal Impact Point (NIP).
When knowing:

- the NAP
- the population density in the area affected from the chosen NAP
- the vehicle impact dispersion
- the physical characteristics of the vehicle

…risk numbers are calculated in the preparation phase for the launch.
One mean to make sure that approved risk levels are not violated by the launch is to wind weight the rocket.
Wind weighting is the operational task of aiming an unguided vehicle to the NAP, this through an atmosphere including the present wind situation. This is done by adjusting the launcher settings to an Elevation and Azimuth settings. The launcher settings are changed from its nominal ones is to compensate for the actual wind situation effect on the rocket trajectory.
By wind weighting a vehicle the NAP will be the most probable impact point!

3. WIND WEIGHTING

The process of wind weighting unguided rockets has been used to calculate wind corrected launcher setting for more than half a century. At Esrange Space Center (ESC) the wind weighting is conducted with the Lewis Method, as in [1]. One key advantage with wind weighting through the Lewis Method is that the computational power needed is very limited, this especially with respect to the way of using iterative 5 or 6 degree of freedom (DoF) simulations to find the settings to compensate for wind effects.

The Lewis Method provides the wind weighting operator some parameters/characteristics that will give the operator a feel for how the vehicle behaves. These key parameters is useful when comparing different vehicles characteristics and also to communicate a vehicle characteristics.

The Lewis Method offers a process that uses a very limited amount of computing power during countdown. This is achieved through running multiple trajectory simulations (5 or 6 DoF) well before the actual countdown. From the output of the simulations the key wind weighting parameters are established. These parameters/characteristics will be shortly explained in the following subchapters.

3.1. The wind weighting function

A specific rocket travelling upwards in the atmosphere will react on the encountered winds in its flight path. The "sensitivity" to the wind is different depending at what altitude a specific rocket is at.
The wind weighting function describes the distribution of the "wind sensitivity" versus altitude for a nominal flight scenario.

3.2. Ballistic wind

A Ballistic Wind (BW) is a wind that has constant speed and direction from ground to the end of the atmosphere. The magnitude and direction of the BW is calculated from an actual wind profile (with different wind situations at different altitudes) combined with the wind weighting function.
The purpose of this combination (calculation of BW) is to determine a constant wind (from ground to end of atmosphere) that will have the same effect on a rocket that the wind profile that varies with altitude.

3.3. The Unit Wind Effect (UWE)

UWE at ESC is defined as the impact displacement resulting from a change in the Ballistic Wind by 1 m/s. The UWE is expressed in [km/ (m/s)].

3.4. The Tower Tilt Effect (TTE)

TTE at ESC is defined as the impact displacement resulting from a one degree change in launcher elevation. It is expressed in [km/degrees]

3.5. The Launcher Correction Factor (LCF)

LCF is UWE divided by TTE and is therefore expressed in [degrees/ (m/s)]. This describes how much the launcher has to be corrected to compensate from a one m/s BW.

4. WHY A NEW PROCESS

The process to develop/validate/qualify/certify software that is used for safety applications is resource demanding. Therefore safety software is seldom replaced without good reasons.
But in the beginning of the decade the final reason to replace the then existing system at ESC occurred; The supplier of hardware support for the DEC Alpha computers that hosted many ESC's operational flight safety applications notified ESC that the equipment is soon End Of Life.
Parts of the system (hardware and software) had then been in use for more than 20 years. During these years new development, changes and additions to the system had been done. This continuous development in a system that was not designed with continuous changes in mind together with the End Of Life for the hardware lead to the decision to redo all software hosted on the DEC Alpha computers.

5. WHAT TO DEVELOP

ESC was partly forced to the decision to renew the safety application because of the limited extensibility and troublesome maintainability. That resulted in the decision that the new applications have to be designed with extensibility and maintainability as prime focus. This in turn led to a key factor in the new systems that were to be developed; all applications that will be a part of the safety system must have well defined interfaces to each other.
Therefore the system to take care of the wind weighting (which is the scope of this paper) was divided into two applications. Application one (named Breeze) that is responsible for generating a wind profile. And application two (named Storm) that calculates how to aim the launcher to compensate for the wind effect on the rocket from the above mentioned wind profile.

5.1. Wind weighting system requirements

After using a system for more than 20 years we realized that we might not know what we really would like our new system to be like. But the project group could agree on the following requirements:

- The system must support our way of work
- The applications must be user friendly
- The applications must have a modern feel at the time of roll out.
- The application must be global (the system must be able to handle a launch from any position on earth)
- The applications shall be able to run on standard a PC

Many specific functions were also identified and listed for possible implementation in the applications to be developed.

6. THE DEVELOPMENT PROCESS

The option not to have 100% in-house development of all parts of the applications was never really discussed. The challenge to be able to convey ESC way of work during operations with wind weighting into a complete new application by developers not having any operational experience was considered too big. Also, when developing a system and its applications knowledge about them is gained that is hard to obtain from only using them. It is of great importance that this thorough system knowledge is kept in-house to futureproof ESCs ability to meet new demands.

6.1. Way of work

The way of work during development was influenced by Scrum [2] and test driven development [3]. Parts of the system and its applications were developed during designated sprints that lasted for about three weeks. Before each sprint start it was decided what functionality that had the highest priority to be implemented. The functionality could either be one of those defined in the attempt to try to list functionality in the preparation phase of the project, or a new feature that had been realised important during the implementation process. The prioritized functionality was broken down to manageable parts that could be completely delivered and tested before completion of the sprint.

This way of work resulted in the fact that we after each sprint had a working application that could be verified towards our old existing system and application. This was done during the whole process to make sure that the qualification of the final delivery was quite straight forward. This also comes with the fact that any future additions to the software can be done with limited qualification work.

7. THE RESULT, SYSTEM OVERVIEW

The system for wind weighting consists of two major components; wind data processing and the actual wind weighting itself (see Fig.1). Wind data processing includes the collection of wind data as well as the processing of this wind data into a form suitable for usage by other applications. This form is referred to as wind profiles. Within our system this function is implemented by the application Breeze.

Wind weighting include applying the characteristics of how the vehicle behaves when exposed to winds during different parts of its trajectory. Using this knowledge in combination with wind profiles enables efficient calculation of how to correct the launcher settings in order to aim at the nominal impact point. This part of the wind weighting process is supported by the application Storm.

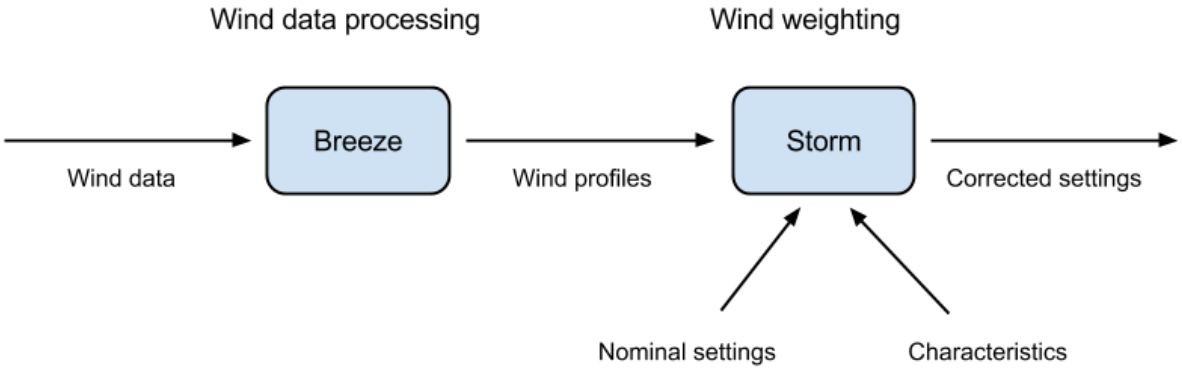

Figure 1. System overview of the wind weighting system

7.1. Breeze

Breeze collects wind data from external data sources and provides this data in a unified format to other applications (see Fig.2). The data sources are separated into categories:

- Forecast: Meteorological forecast data originating from e.g. SMHI, ECMWF, and NOAA/GFS.
- Sounding: Wind data derived from measurements during the ascent phase of a balloon.
- Static level: Continuous measurements of winds at fixed levels, such as e.g. wind towers.

Wind data from sources belonging to the above categories are processed into wind profiles, describing the wind conditions within different regions of the atmosphere. These wind profiles can also be further combined into composite wind profiles.

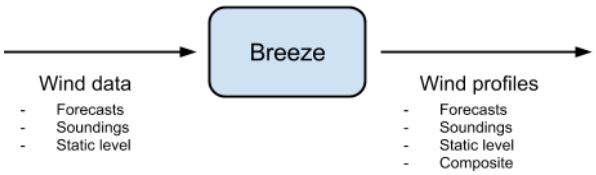

Figure 2. Breeze data flow

The Breeze application is capable of having multiple concurrent active configurations, where one configuration typically is targeted to support a specific vehicle launch. Each active configuration can support multiple connected client applications. The Breeze user interface (see, Fig. 3) is only connected to one configuration at a time but can be switched to any configuration as needed.
The architecture of Breeze enables easy integration of new data sources matching the above categories using a plugin model.

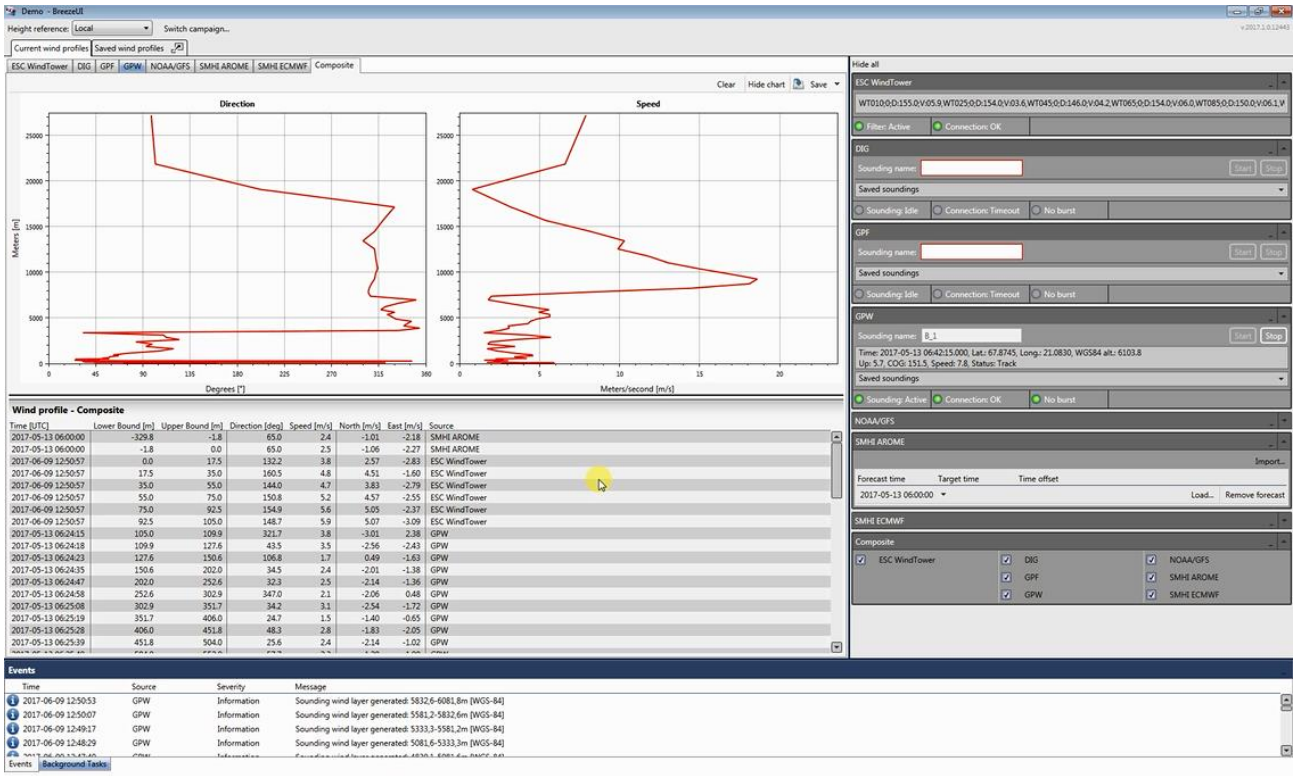

Figure 3. Breeze user interface

7.2. Storm

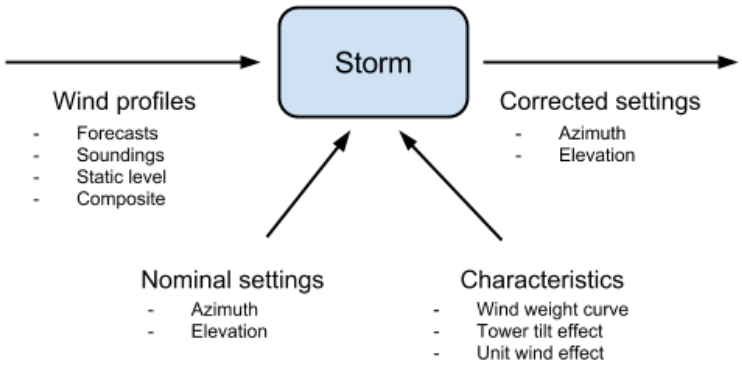

Figure 4 Storm data flow

As Storm is a wind weighting application the main task is to calculate the wind corrected launcher settings with regards to the wind profile that is read in to Storm. The corrected launcher setting is calculated as soon as an update of the wind profile has taken place in Breeze.

As seen in Fig. 4 Storm needs the wind weighting characteristics and a wind profile to calculate the corrections needed to compensate for the winds. During operation the correction is of less importance than the actual corrected launcher settings. Therefore Storm also needs the nominal settings to know what to correct from. In addition to calculate the corrected launcher settings Storm is also used to monitor that the wind situation and the launcher correction are on the right side of our limits that we have permission to launch in. How this is normally monitored is shown in Fig. 5. On the top left section there is a plot that visualizes the launcher settings. The small blue dot (the "live dot") inside the small blue circle indicates the present corrected launcher settings. The cross where the mouse pointer is indicates the nominal launcher setting; these are the wind corrected settings if no wind were present. When the "live dot" during a countdown is located inside the green sector the launcher setting are in our approved envelope.

The large circle with its origin at the nominal settings is the BW limit. If the BW is at its limit the "live dot" will be located somewhere on the circle circumference, where on the circumference is decided by the direction of the BW.

Below the settings plot is a table where saved live values are shown. These saved values are typically done for the preliminary launcher settings, final settings and launch. When saving the launcher settings several other parameters are also saved, of great importance is the wind profile that correlates to the saved correction. To have the wind profile "locked" gives the operator an opportunity to run 5/6 DoF simulations to validate the Lewis Methods proposed launcher settings, and also to look into detail for other interesting parameters such as Angle of Attack during the flight. The 5/6 DoF simulation functionalty is a plug-in to Storm and is reached through the same user interface but under the rightmost tab "Simulation".

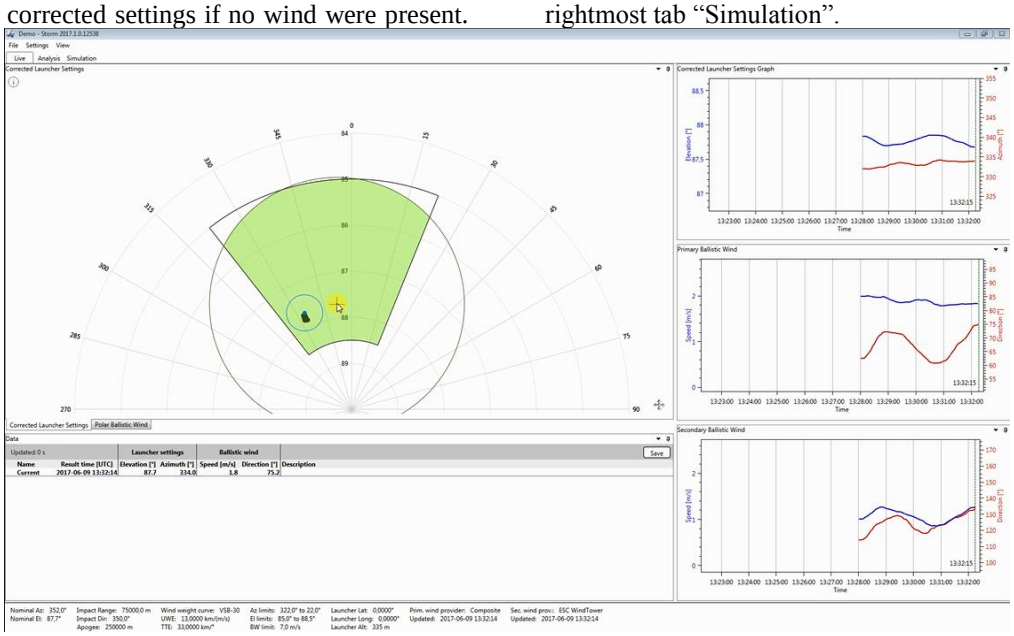

Figure 5 Storm user interface, the Live tab

Between the Live and Simulation tab is the Analysis tab, see Fig. 6. The analysis tab is used operationally to handle forecast data. This functionality to process forecast data (from a Breeze service) gives the operator the oppurtunity to plot how the wind corrected launcher settings will be during the forecasted period. See Fig. 6 middle section for an example: here the blue dots and line draws the development for the launcher settings during the forecasted period. There is one highlighted red point that can be moved in time (along the line) with the slider at the bottom of the section. At the right section more information of the highlighted point can be found, when pushing "Save" the point also moves into the Live tab. This is often done if the operator would like to compare the forecast with actual data. Another example is to move several consecutive points to the Live tab to create a trace of the expected wind evolution for the closest hours to come, this can be valuable information if in a hold situation in the countdown. Features like the ones mentioned above are very valuable for the wind weighter to be able to get to know the current and future wind situation. This knowledge is is crucial to be able to plan campaign activities in such a way all teams are ready when the wind situation is favorable for launch.

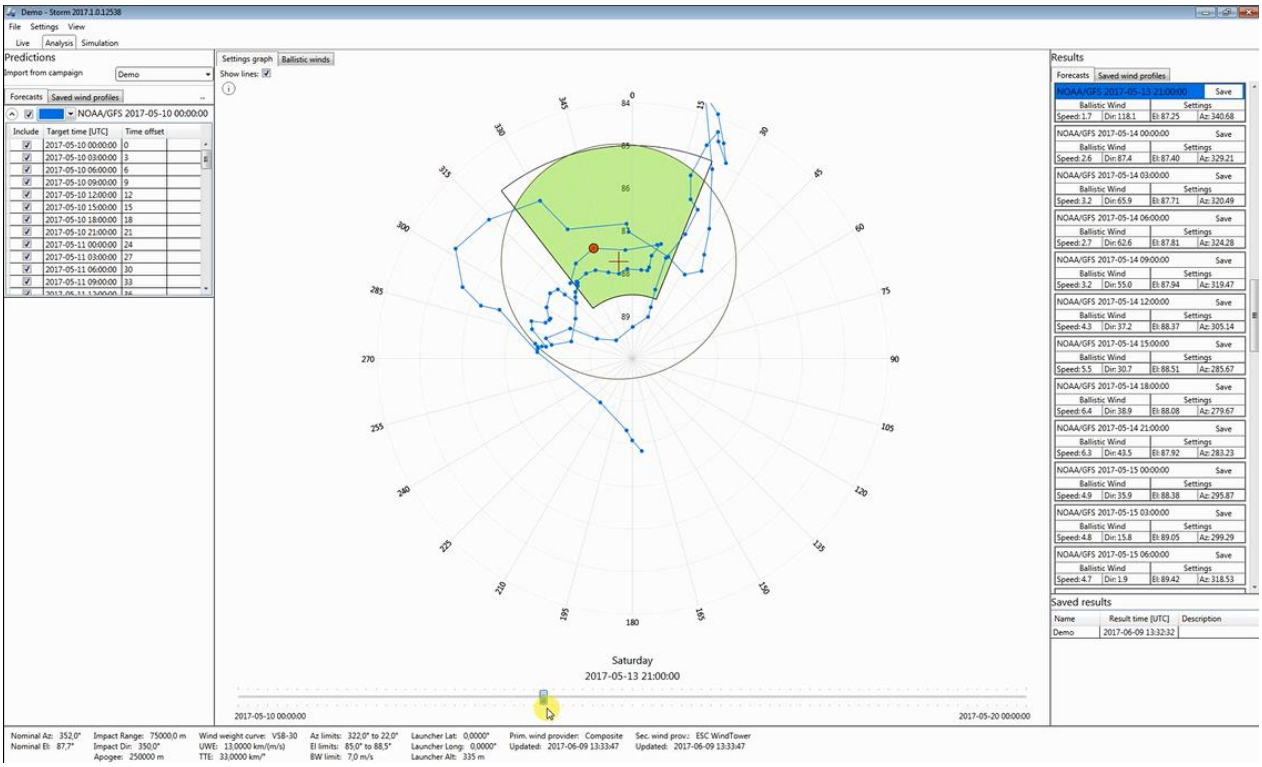

Figure 6. Storm user interface, the Analysis tab

8. ACKNOWLEDGEMENT

The authors of this paper would like to thank Mr. Martin Hedqvist for his outstanding work during the development process of the applications in question.

9. REFERENCES

1. J.V.Lewis, "The Effect of Wind and Rotation of the Earth on Unguided Rockets", Ballistic Research Laboratories Report No. 685, March, 1949
2. https://en.wikipedia.org/wiki/Scrum_(software_development)
3. https://en.wikipedia.org/wiki/Test-driven_development

SIMULTANEOUS IN SITU AND REMOTE OBSERVATIONS OF DUST IN THE POLAR SUMMER MESOSPHERE: AN OVERVIEW OF THE MAXIDUSTY CAMPAIGN

Tarjei Antonsen[1], Ove Havnes[1], Ralph Latteck[2], Josef Höffner[2], Gerd Baumgarten[2], Martin Friedrich[3], Jonas Hedin[4], and Lasse Clausen[5]

[1]*Dept. Phys. Tech., UiT - The Arctic University of Norway, 9037 Tromsø, Norway*
[2]*IAP Kühlungsborn, Germany*
[3]*IKS, TU Graz, Austria*
[4]*MISU, Stockholm University, Sweden*
[5]*Dept. Phys., University of Oslo, Norway*

ABSTRACT

The MAXIDUSTY campaign comprised two rocket payloads, launched from Andya Space Center (69°17N 16°01E) on June 30 and July 8 2016, and simultaneous radar and lidar observations of the mesosphere with focus on the altitude region between 80 and 90 km. The sounding rocket payloads were equipped with several different types of dust instruments, including impact detectors, Faraday bucket detectors, a neutral mass spectrometer, electron density probes and a photometer. The first payload, MXD-1, was launched during PMSE and NLC conditions, and the MAARSY radar provided VHF measurements coincident with the rocket flight path. The ALOMAR RMR lidar provided NLC measurements during the first flight. The second payload was launched during similar conditions, but without lidar measurements. In this work, we present an overview of the MAXIDUSTY campaign with some general results. Some preliminary key results include a thorough analysis of the Faraday impact probe MUDD, which shows that it is possible to use the size distribution of fragments of colliding mesospheric ice particles as a proxy for the size distribution of meteoric smoke particles. Results from analysis of MUDD data also confirms that the volume filling factor of meteoric material inside mesospheric ice particles can be several percent.

1. INTRODUCTION

The polar summer mesopause region, situated between $\sim$ 80 and 90 km, is the coldest environment in the terrestrial atmosphere with recorded temperatures reaching as low as 100 K [17, 9]. The low temperatures in combination with additional cooling due to gravitational wave forcing, allow for condensation of water vapour to nanoscale ice particles which are the foundation for phenomena such as the visible noctilucent clouds (NLC) and the coherent radar reflections called Polar Mesospheric Summer Echoes (PMSE) (see e.g [12, 13]). It is now consensus that effective growth into $\gtrsim$ 10 nm ice particles requires heterogeneous nucleation with condensation nuclei, for which the most likely candidate remains meteoric smoke particles (MSPs) [4, 10]. The idea that complex ions can form from meteor vapour was introduced by Rosinski & Snow [14] and further extended into the concept of MSPs by Hunten et al. [8]. The MSPs have radii $\sim$ 1 nm, and are thought to participate in a number of chemical processes in the upper atmosphere. They may influence lower atmospheric layers due to gravitational sedimentation, and are particularly effective in removing certain molecular species [11, 10, 15, 6]. Moreover, it has been confirmed by rocket and satellite measurements that ice particles around the mesopause contain up to a few percent MSPs by volume [4, 7].

The present paper gives a short review of the MAXIDUSTY (MXD) rocket campaign, which consisted of two payloads launched during the summer of 2016 with simultaneous remote measurements. The main scientific goal of the campaign was the characterization of mesospheric ice and MSP sizes, composition, charge state and multi-scale spatial structure. Such knowledge about the intrinsic dust properties is instrumental in resolving currently open questions about the interconnection between the upper mesosphere and neighboring atmospheric layers.

2. THE MAXIDUSTY CAMPAIGN

The MXD-1 and MXD-1B rocket payloads were launched from Andøya Space Center (69.29°N 16.02°E) at 09:43 UT on the 30th of June 2016 and 13:01 UT on the 8th of July 2016, respectively. MXD-1 was launched through an NLC, as detected by the RMR-lidar at the ALOMAR observatory (see Von Zahn et al. [16] for technical details). PMSE measurements were made simultaneously along the rocket trajectory by the MAARSY radar. For the MXD-1B launch, clouds obscured the NLC

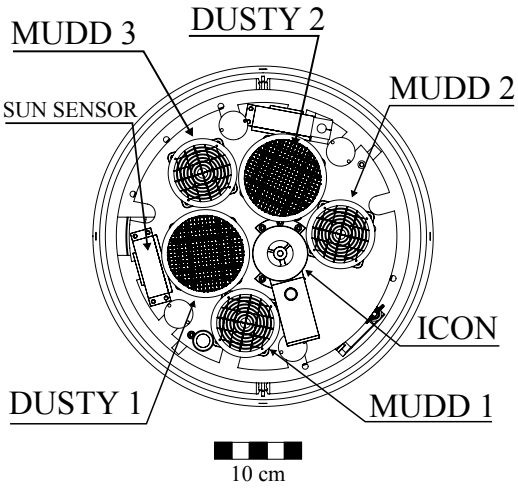

Figure 1. Top deck geometry MXD-1B.

measurements, but PMSE observations were made.

The top deck geometry of MXD-1B is shown in fig. 1. The MXD-1 top deck utilized the same geometry, but the DUSTY-2 probe was replaced by the miniMASS dust detector (UC Boulder). Both top decks were equipped with the Faraday cup probe DUSTY [5], and a triplet of MUDD (Multiple Dust Detector) probes – a Faraday impact detector measuring the size distribution of embedded MSPs inside ice particles (see [3, 1] for details). The neutral mass spectrometer ICON were included on both payloads, and is aimed towards characterizing the vapours of evaporated ice particles [2]. Electron densities were measured by two needle Langmuir probe booms (mNLP) built by the Univ. of Oslo and Faraday-rotation on both payloads. A positive ion probe and E-field probe was also included on the two rockets. Other instruments include a side-viewing photometer on MXD-1 built by MISU, and a 4D-space mother-daughter module (UIO/ASC).

3. REMOTE MEASUREMENTS

Due to lidar measurements only being available for the MXD-1 launch, we emphasize the first flight in our presentation of the remote measurements.

The PMSE profiles around the time of the MXD-1 launch are shown in figure 2. Around launch, the PMSE was moderate in strength and displayed four thin layers with highly dynamic features. Two dimensional slices from MAARSY reveal that the payload missed the strong structure around 87 km.

MXD-1 was launched through a relatively broad NLC reaching from $\sim$ 80 to 86 km, as shown in fig. 3. This NLC had a strong volume backscatter coefficient from 80 to 82 km, and a more diffuse appearance in the upper part. A useful by-product of the RMR measurements, is the derivation of dust sizes throughout the layer, which will

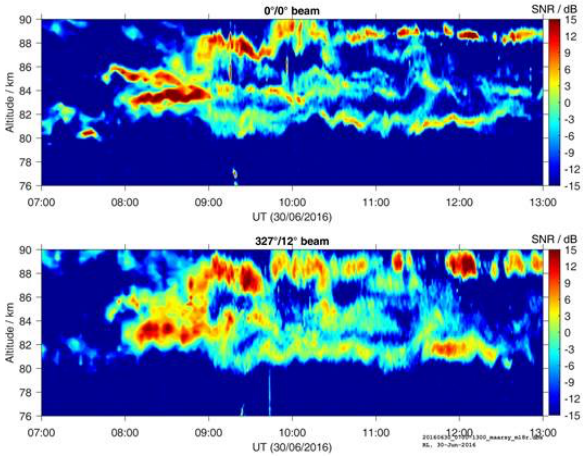

Figure 2. PMSE measured by MAARSY during MXD-1. The top panel shows the vertical beam, while the bottom panel shows the beam from the same volume as the rocket trajectory.

be compared to dust size derivations from in-situ measurements in future works.

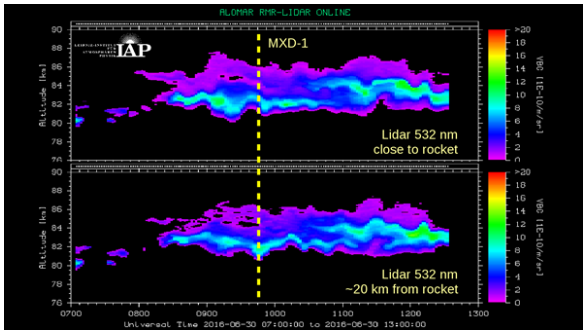

Figure 3. RMR lidar backscatter for two beams. The top panel shows the profile close to the rocket, while the top panel shows the profile $\sim$ 20 km away from the trajectory through the layer.

The mesopause region temperatures derived from the iron lidar measurements around the time of the MXD-1 launch are shown in fig. 4. The profile around the time of launch (09:43 UT) show that the entire region had very low temperatures $\sim$ 120 K. Such low temperatures can affect the nucleation and growth of ice particles, and is point of interest for further work. Other future work related to the Fe-lidar measurements will include a study on iron depletion and its connection to dust particles around the mesopause.

4. IN-SITU MEASUREMENTS OVERVIEW

The majority of the instruments aimed were aimed at detection and characterization of dust; with the exceptions of electron density probes, magnetic field sensors and sun sensors. Furthermore, the two latter sensors were mainly

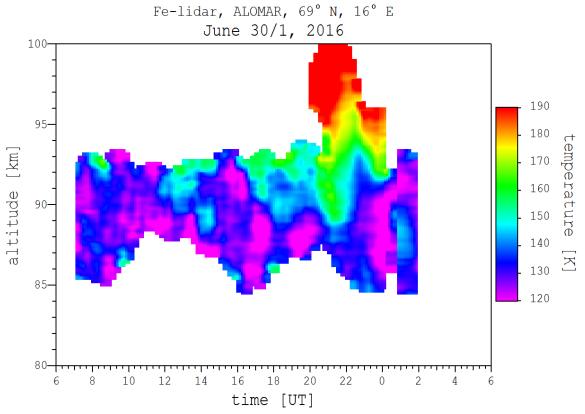

Figure 4. Temperatures around the mesopause obtained from Fe-lidar measurements.

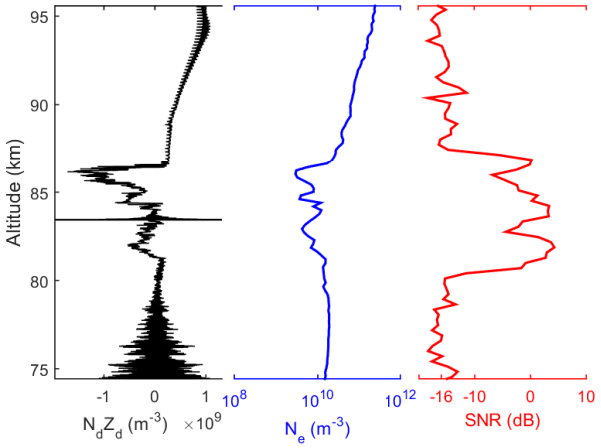

Figure 5. Comparison of number charge density from DUSTY (left), electron density (middle) and MAARSY SNR (right) for the upleg of MXD-1.

intended as orientation identifiers. We will in this section give a brief overview of the measurements obtained by the DUSTY and MUDD probes and give preliminary results on the intercomparison of these with the supporting electron density measurements and remote observations.

Figure 5 shows a comparison of the number charge density derived directly from DUSTY bottom plate currents, electron density derived from the UiO needle Langmuir probes and the MAARSY 50 MHz radar SNR. The electron profiles has a clear bite-out between ~ 81 and ~ 87 km, which is a clear indication of charged particles in that layer. This is mirrored in the number charge density. The radar SNR shows relatively good agreement with the electron profile, but has a larger spread in height. Considering that the theoretical radar scattering cross section is proportional to $\langle \Delta N_e \rangle^2$, the SNR seems to be supported by the electron density measurements. As mentioned below, there is still ongoing work related to the electron density measurements; both MXD payloads had two electron probes (Faraday rotation and Langmuir) and there is some disagreement in absolute values from the two instruments around the mesopause. Compared to earlier flights of DUSTY, the observed number density can be considered moderate. Further work will include studies of the connection between the number charge density and the radar and lidar backscatter.

In figure 6 we show the results from a novel analysis method of DUSTY currents. The method takes into account the secondary charging effects in DUSTY and yields the size and charge distributions of the mesospheric dust through an iteration scheme. The top panel shows the obtained dust radii, which agree to some extent with sizes calculated via Mie-theory from both RMR lidar and the onboard photometer (Baumgarten and Hedin, priv. comm.). Further effort will be put into obtaining dust (ice) particle properties from analysis of DUSTY currents and the comparison of these results to optical measurements. In the bottom panel we have included a calculation of collision times of free iron with dust particles, as motivated by figure 4 and the consideration of iron around the mesopause. The question of whether or not dust/ice particles play an important role in the depletion of iron in the polar mesosphere during the summer months is still open, and will be investigated further in the future.

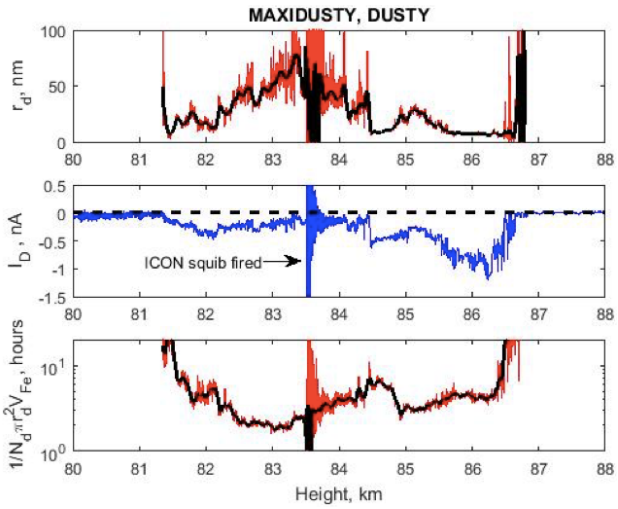

Figure 6. Derived dust radii from DUSTY (top panel), DUSTY bottom plate current (middle panel) and calculated collision time for iron atoms with a dust grain (bottom panel).

One of the key goals of the MAXIDUSTY project is to characterize the size distribution of MSPs, motivated by the finding that they are abundant inside NLC ice particles [4, 7]. For this purpose, three MUDD probes were flown on each payload. The principle of MUDD is that large ($\gtrsim 10$) nm particles will partly fragment in the collision with a fragmentation grid inside the probe, and release charged fragments of which the dominating part will be MSPs. The results of the complete analysis are

given in Antonsen et al. (2017, subm. JGR-ATM). The main result is that MSPs inside NLCs have an inverse power law size distribution similar to the theoretical distribution of free MSPs. Figure 7 show the evolution of the different channels of MUDD throughout the dust layer during MXD-1 upleg. The curves show the relative contribution to the current, with the legend noting the retarding potential (for negatively charged fragments) of each channel. The $U_R = -2V$ channel can be regarded as the total fragment current. From this picture, a size distribution can be calculated if charging probability is taken into account. As expected, the observed currents confirm that the size distribution must change with height, however the reasons for the change may be several.

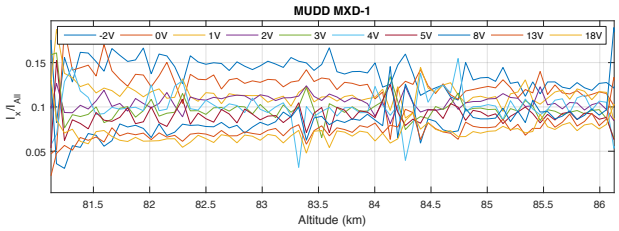

Figure 7. Ratio between MUDD currents from each retarding potential channel respectively (I_X) and the sum of all currents (I_{All}), i.e. relative contribution to the total current, on the MXD-1 payload.

5. FUTURE RELATED WORK

In this paper we have given a short overview of the MAXIDUSTY rocket project, with special emphasis on the research connected to the flights which the University of Tromsø is directly involved in. The data set from both remote and in-situ observations is enormous, and will yield important insight to physical processes and phenomena occurring around the polar summer mesopause. Ongoing and future work based on the observations will focus on, among other topics:

- MSP size distribution
- Comparison of the number charge density as obtained by the Faraday cup DUSTY and MAARSY radar measurements (50 MHz).
- Dust/ice particle size distributions from DUSTY using a novel analysis method.
- The relationship between dust/ice and iron depletion around the mesopause
- Discrepancy between two independent measurements of electron density made with Faraday rotation and Langmuir probes.
- Neutral mass spectrometer data from the mesopause region.

ACKNOWLEDGEMENTS

The MAXIDUSTY project is supported by the Norwegian Research Council and The Norwegian Space Center. We would like to thank all collaborators from cooperating institutions, and the team at Andøya Space Center for two successful launches.

REFERENCES

[1] Antonsen, T. & Havnes, O. 2015, Review of Scientific Instruments, 86, 033305

[2] Havnes, O., Antonsen, T., Hartquist, T., Fredriksen, Å., & Plane, J. 2015, Journal of Atmospheric and Solar-Terrestrial Physics, 127, 129

[3] Havnes, O., Gumbel, J., Antonsen, T., Hedin, J., & Hoz, C. L. 2014, Journal of Atmospheric and Solar-Terrestrial Physics,

[4] Havnes, O. & Næsheim, L. I. 2007, Annales Geophysicae, 25, 623

[5] Havnes, O., Trøim, J., Blix, T., et al. 1996, Journal of Geophysical Research: Space Physics, 101, 10839

[6] Hervig, M. E., Bardeen, C. G., Siskind, D. E., Mills, M. J., & Stockwell, R. 2017, Geophysical Research Letters, 44, 1150

[7] Hervig, M. E., Deaver, L. E., Bardeen, C. G., et al. 2012, Journal of Atmospheric and Solar-Terrestrial Physics, 84-85, 1

[8] Hunten, D. M., Turco, R. P., & Toon, O. B. 1980, Journal of the Atmospheric Sciences, 37, 1342

[9] Lübken, F.-J. 1999, Journal of Geophysical Research: Atmospheres, 104, 9135

[10] Plane, J. M. C. 2012, Chem. Soc. Rev., 41, 6507

[11] Plane, J. M. C., Feng, W., & Dawkins, E. C. M. 2015, Chemical Reviews, 115, 4497

[12] Rapp, M. & Lübken, F.-J. 2004, Atmospheric Chemistry and Physics, 4, 2601

[13] Rapp, M. & Thomas, G. E. 2006, Journal of Atmospheric and Solar-Terrestrial Physics, 68, 715

[14] Rosinski, J. & Snow, R. H. 1961, Journal of Meteorology, 18, 736

[15] Saunders, R. W., Dhomse, S., Tian, W. S., Chipperfield, M. P., & Plane, J. M. C. 2012, Atmospheric Chemistry and Physics, 12, 4387

[16] Von Zahn, U., Von Cossart, G., Fiedler, J., et al. 2000, Annales Geophysicae, 18, 815

[17] Zahn, U. & Meyer, W. 1989, Journal of Geophysical Research: Atmospheres, 94, 14647

A NEW ROCKET-BORNE METEOR SMOKE PARTICLE DETECTOR (MSPD) FOR D-REGION IONOSPHERE

Tristan Staszak[1], Heiner Asmus[1], Boris Strelnikov[1], Franz-Josef Lübken[1], and Gabriel Giono[1, 2]

[1] *Leibniz-Institute of Atmospheric Physics, Kühlungsborn, Germany, Email: staszak@iap-kborn.de*
[2] *KTH, School of Electrical Engineering, Stockholm, Sweden*

ABSTRACT

In this paper we introduce a new rocket-borne Meteor Smoke Particle Detector (MSPD) for the D-region ionosphere. Its geometry was optimized based on numerous combined aerodynamic and electrostatic simulations to allow for detection of tiny MSPs at altitudes below 80 km. We show results of these simulations and the derived MSP collection efficiencies as dependence of mass and altitude. The new instrument is capable of measuring tiny MSPs with radii less than 1 nm at altitudes down to ∼60 km.

Key words: MSPD; meteor smoke particle detector; farraday cup; D-region; detection efficiency.

1. INTRODUCTION

Direct rocket-borne detection of charged aerosols has ever been an essential part of in-situ investigation of the middle atmosphere or even triggered theoretical studies like e.g., positive metallic ion detection as described in [1]. There are two sorts of aerosols in the middle atmosphere: ice particles and the so called meteor smoke particles (MSP). Ice particles can form only in summer and solely in the height region of mesopause, i.e. where mean neutral air temperature drops down to ∼130 K [e.g., 2; 3; 4]. MSPs are deposited by incoming meteoroids which are evaporated in the height range 70-120 km [see e.g., 5, for a review of relevant processes].

Data from particle impact detectors on a sounding rocket [e.g., 6] gave first evidence that MSPs are related to the Noctilucent clouds (NLC) [e.g., 7], observable by naked eye at the summer polar mesopause at night. Later, charged ice particles (MSP as nucleus) were proposed as a possible explanation for strong coherent radar backscatters in the polar summer mesopause (Polar Mesosphere Summer Echoes, PMSE) from VHF radars [e.g., 8; 2; 3; 4].

Most of those instruments for in situ aerosol measurements utilized the Faraday cup principle based on the original design of [2]. However, it has been realized that due to aerodynamics this type of instrument has a severely limited altitude dependent detection efficiency for MSPs with radii less than ∼2 nm [e.g., 9; 10; 11; 12]. A suitable review of the available to date MSP measurements can be found in [13].

The MSPs were also suggested as a key player in forming the polar mesosphere winter echoes (PMWE) [e.g., 14]. However, so far there are no direct in situ measurements of MSPs in connection to PMWE. PMWE occur at altitudes from ∼80 down to 50 km and, therefor face the mentioned above aerodynamic challenge for the rocket-borne investigations.

In this paper we introduce a new rocket-borne instrument for MSP measurements developed at Leibniz Institute of Atmospheric Physics in Khlungsborn, Germany. In the following sections we subsequently consider different aspects and challenges of the in situ MSP measurements as applied to the new design of our Instrument.

2. THE NEW METEOR SMOKE PARTICLE DETECTOR (MSPD)

The Direct Monte Carlo Simulations (DSMC) technique is currently a common tool to asses the influence of aerodynamics on rocket-borne measurements [e.g., 15; 11; 16]. Such simulations supported by experimental results show, that cup-like geometries are heavily affected by aerodynamic effects [e.g., 15; 11; 12; 17]. On the one hand, they are usually mounted on the ram deck of a sounding rocket, that is behind the rocket's main bow shock where the incident flux of the measured constituents (e.g., MSPs, ions or neutral air) is already filtered. This effect is stronger at higher pressures and velocities [e.g., 15; 12; 17]. On the other hand the cup-like geometry itself is a source of particle size-dependent filtering [e.g., 11; 12; 17]. Simple cup geometries lead to stag-

nation pressures 12 times the ambient pressure at 85 km altitude. Such very dense layer of air near the measuring electrode prohibits detection of smallest MSPs of ∼2 nm radii [e.g., 12].

Motivated by the need to measure the tiny MSPs with radii less than ∼1 nm, we transferred the Faraday cup principle into a spherical design for a boom mounting sensor to minimize both these effects. Similar to a Faraday cup the new particle detector consists of a central electrode for MSP measurements surrounded by two biased shielding grids to repel electrons and positive ions. The charged heavy particles, i.e. MSPs penetrate through these shielding grids due to inertia [see e.g., 2, for more details].

A schematic of the new instrument called MSP detector (MSPD) is shown in Fig. 1. The outer and inner grids (G1 and G2) are fixed biased at -6 and +6 V relative to rocket body potential, respectively. These potentials can be changed in the range ±6 V to adjust plasma shielding properties of the sensor. The inner MSP collecting electrode can also be biased in the range -4 to +12 V to achieve desired MSP collecting capabilities, discussed below. The both grids and the inner electrode are connected to sensitive electrometers.

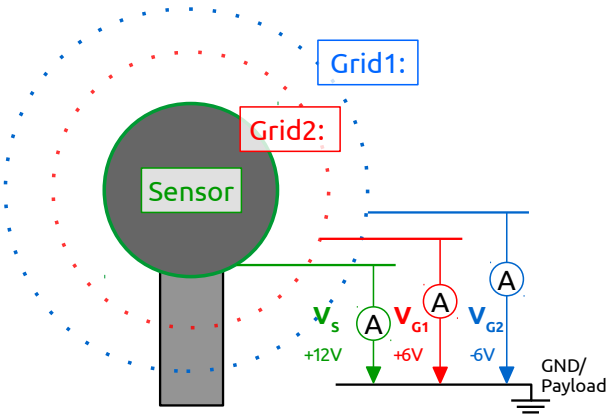

Figure 1: Meteor Smoke Particle Detector schematic of electrode potentials

During the design phase of the development of the new instrument different aspects of rocket-borne measurements of MSPs were considered and simulated and discussed in the following sections.

Aerodynamic Design Aspects

Fig. 2 shows results of DSMC simulations performed for the new spherical MSPD for two altitudes, 65 and 85 km. The instrument's cross-section is shown in black and the density increase in terms of a ram-factor, that is the ratio of local to undisturbed ambient density of air, in color. It reveals ram-factors of up to ∼3 to ∼6 at 85 and 65 km, respectively. These are much smaller ram-factors than those reported for cup-geometries at ∼85 km which are of the order of 12 and higher [e.g., 11].

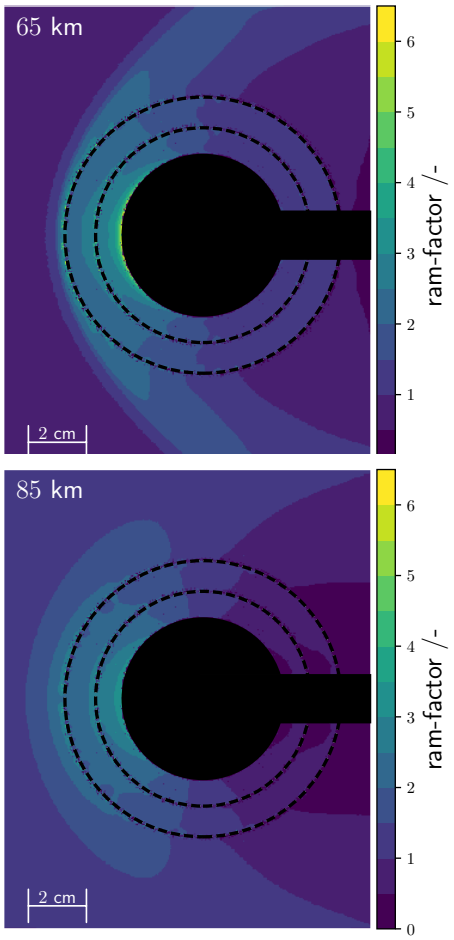

Figure 2: ram contours from 3d dsmc-simulation (OpenFoam) in sectional view trough sensor

Electrostatic Design Aspects

The charged constituents of the D-region ionosphere during day time include electrons, positive and negative ions, and positive and negative aerosols. The aerosols are solid state particles consisting of meteor material (MSPs) or of water ice in summer. Since the D-region plasma density is roughly ten orders of magnitude smaller than neutral air density, plasma constituents are collisionally dominated and must reveal the same temperature as neutral air [18; 19]. Under assumption of Maxwell distribution and a temperature of 200 K the average kinetic energy of ambient D-region plasma can be estimated as:

$$E_{kin} = \frac{1}{2} \cdot \frac{8 k_B T}{e} \approx 69 \cdot 10^{-3} eV \qquad (1)$$

The surrounding electric field maintained by the

shielding grids must ensure that none of the light plasma constituents penetrate to the interior of the MSPD. For this purpose electrostatic simulations of different grid cell geometries and sizes were done using the SIMION® package [20]. The goal was to find a compromise between effective shielding and low aerodynamic disturbance. The resulting grid specifications are summarized in Tab. 1. The simulations show that the potential drop in the middle of such a grid cell can be down to 1 V, thereby decreasing the shielding potential to 5 V. This is still high enough to effectively repel the D-region electrons.

	G_1	G_2
b [mm]	0.6	0.5
k [mm]	5.65	4.398
Tr	0.80	0.786

Table 1: Following the notation for grid structures in [16] the grids are defined as follows: b and k, define the diameter and spacing of the grid. Transmission is defined by $Tr = (k-b)^2/k^2$.

During the day time rocket flight under the sun light radiation MSPD will experience photo-effect. The induced photoelectric current depends on different factors such as material work-functions, electron yield, wavelength (changing with altitude), solar zenith and vehicle inclination angles, etc. The resulted photocurrent was simulated and is currently under investigation in laboratory and is discussed in detail in an accompanying paper by [21].

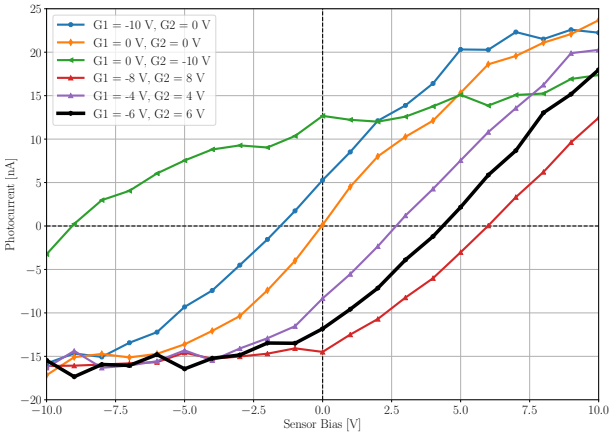

Figure 3: Photo current on sensor as a function of sensor bias (relative to ground) for different biases. Our configuration is $G1 = -6$ V and $G2 = +6$ V (solid black line)

Fig. 3 shows results of laboratory measurements of the photo current induced by a Xe-flash lamp used in another experiment [22]. The spectrum of the Xe-lamp is much different from those expected from sun at mesospheric heights and the resulted photocurents may not be considered as simulations of real flight conditions. The goal of these measurements was to asses a possibility to reduce the photocurrent by applying different potential configurations on the MSPD. One obvious effect seen in Fig. 3 is the saturations at the negative and positive ends of the graphs. This can be explained as that all photoelectrons are deflected from or attracted to the sensor surface by the electric field between the electrode and the nearest grid.

To reduce the influence of photo-current on the measurements and increase the efficiency of collecting of negatively charged MSPs the sensor potential was chosen to be +12 V.

Spatial Resolution

To make the MSPD capable of measuring MSP density fluctuations, the sampling rate of all electrometers (i.e., for the inner electrode and both shielding grids) was increased to $f_s = 4$ kHz. For a typical rocket velocity of ∼1 km/s this will result in a spatial resolution of ∼25 cm.

Measurement Ranges

In order to roughly estimate the needed MSP measurement range we took mean MSP number density values from a collection of rocket-borne MSP measurements by [13] (see their Fig. 1). Two mean MSP densities were estimated to be $N_{MSP\ 90} \approx 6.6 \cdot 10^{-07}$ m^{-1} and $N_{MSP\ 80} \approx 1.5 \cdot 10^{-08}$ m^{-1} for 90 and 80 km, respectively. The available MSP density measurements below 80 km must be taking with care because of the challenging aerodynamic effects in that altitude region.

To estimate the current range on the outer grid G1 we used recent rocket borne measurements of positive ion densities by [17]. This reveals ion densities of $N_{i\ 90} \approx 2 \cdot 10^{10}$ m^{-1} and $N_{i\ 80} \approx 2 \cdot 10^{9}$ m^{-1} for 90 and 80 km height, respectively.

The instrument current can be derived as:

$$I = N \cdot e \cdot |\vec{v}| \cdot A \qquad (2)$$

Where N is the ion or MSP number density, e the elementary charge, $|\vec{v}|$ the absolute velocity and A the sensor surface area.
For a velocity of 1000 ms^{-1} and surfaces $A_S = 0.009$ m^2 (sensor), $A_{G2} = 0.009$ m^2 (inner grid), $A_{G1} = 0.018$ m^2 (outer grid), for altitudes of 80 and 90 km we estimated:

$$I_S^{90} \approx 90\ pA \quad I_{G2}^{90} \approx 90\ pA \quad I_{G1}^{90} \approx 60\ nA$$
$$I_S^{80} \approx 210\ pA \quad I_{G2}^{80} \approx 215\ pA \quad I_{G1}^{80} \approx 6\ nA$$

where superscript indicates altitude and the subscript refers to sensor, inner, and outer grid, respectively. This shows, that to resolve one per cent density fluctuations, the electrometer must be capable of

measuring currents of ∼1 and 2 pA for 90 and 80 km altitudes, respectively.

For daylight measurements an additional photocurrent offset should be considered. To decrease this offset current and to make it less altitude dependent, we decided to make a graphite coating for the electrode's and grids' surfaces [see 21, for more details]. The expected photocurrent offset is of the order of some nA. The electrometer's noise level is less than 2 pA. Utilizing 16 bit ADC allows to cover the current range from ∼1.5 to 50 nA. The actual measurement ranges of the new MSPD are summarized in Tab. 2.

	I_{high}	I_{low}
Sensor	$\approx 50\ nA$	$\approx 1.5\ pA$
Inner (G2)	$\approx 50\ nA$	$\approx 1.5\ pA$
Outer (G1)	$\approx 2\ \mu A$	$\approx 50\ pA$

Table 2: Measurement ranges of the MSPD.

3. DETECTION EFFICIENCIES

In order to derive the detection efficiencies as a dependence of MSP-mass (sizes) and different flow conditions around the detector (e.g., due to a payload precession), numerous coupled electrostatic- aerodynamic simulations were performed. The simulations covered an altitude range from 65 to 90 km and particle masses from 250 to 60000 u. We used SIMION® software package for particle simulations in the electrostatic field of an 1:1 3d CAD model of the MSPD. The needed background fields for temperature, density, and velocity were derived using the dsmcFoam [23] solver which is a part of the OpenFoam project [see e.g., 23; 16].

Aerodynamic Simulations, Background fields

Aerodynamic simulations were performed with the Direct Simulation Monte Carlo (DSMC) method [24]. The case setup is similar to that described in [16]. We took boundary background values (temperature, O2, N2 and Ar densities) from the empirical NRLMSISE-00 model [25] and velocities for a ballistic rocket flight with an apogee of ∼115 km. We simulated the flow around the detector for an altitude range from 65 to 90 km in 5 km steps. Fig. 2 shows simulation results for two altitudes, i.e., for 65 and 85 km. It reveals two different aerodynamical regimes, i.e. continuum flow and free molecular flow, at 65 and 85 km, respectively. For continuum flow conditions we found features like a strong bow shock and large ratios of stagnation to ambient density. For free molecular flow conditions we see a bubble-like stagnation field in front of the detector with much lower ram factors. These simulated density fields were further used in the coupled electrostatic-aerodynamic simulations described below.

Coupled Electrostatic-Aerodynamic charged particle tracing

For the coupled simulations we used the SIMION® version 8.1 software package. With this tool it is possible to simulate collisions between particles and a user defined background gas. We used a hard sphere collision model with $M_{air} = 28$ u and the effective collision cross section, calculated as:

$$\sigma = \frac{\pi}{4}\left(d_{air} + d_{particle}\right)^2 \tag{3}$$

where $d_{air} = 4.19{\cdot}10^{-10}$ m is the mean diameter of an air molecules and $d_{particle}$ is the diameter of the particle (MSP). All other parameters like e.g., mean free path are calculated internally by the software.

Theoretically, the simulation volume must be chosen large enough, that it exceeds the Debye sheath around the biased outer grid of the MSPD. However, for altitudes above ∼80 km this would require huge memory usage, whereas the simulation package is only available for MS-Windows platform, i.e. it is not scalable to super-computers like e.g., OpenFoam software. For that reason we had to limit the computational volume to the available hardware configuration and make the distance between the MSPD's outer grid and the volume boundary shorter than the Debye sheath radius. To verify whether this yields reliable results we made simple test-simulations with proper volume size and appropriate background conditions. The results showed that the aerodynamical effects significantly dominate the simulation results so that the electrostatic interactions at large distances from the grid are negligible (not shown here).

The potentials setup for simulations reproduces the MSPD configuration shown in Fig. 1. The number of particles was chosen to be 6000, which leads to a statistical uncertainty of less than 2%. We simulated trajectories for both negatively and positively charged particles assuming that they are singly charged. This was done for 21 different particle masses in a range from 250 u to 60000 u. The scope of particle properties used in the simulations is summarized in Tab. 3.

m [u]	r [m]	σ [m^2]
250	$3.67{\cdot}10^{-10}$	$1.05{\cdot}10^{-18}$
500	$4.63{\cdot}10^{-10}$	$1.42{\cdot}10^{-18}$
1000	$5.83{\cdot}10^{-10}$	$1.97{\cdot}10^{-18}$
2500	$7.91{\cdot}10^{-10}$	$3.15{\cdot}10^{-18}$
5000	$9.97{\cdot}10^{-10}$	$4.57{\cdot}10^{-18}$
7500	$1.14{\cdot}10^{-09}$	$5.73{\cdot}10^{-18}$

m [u]	r [m]	σ [m^2]
10000	$1.26{\cdot}10^{-09}$	$6.75{\cdot}10^{-18}$
12500	$1.35{\cdot}10^{-09}$	$7.67{\cdot}10^{-18}$
15000	$1.44{\cdot}10^{-09}$	$8.52{\cdot}10^{-18}$
17500	$1.51{\cdot}10^{-09}$	$9.33{\cdot}10^{-18}$
20000	$1.58{\cdot}10^{-09}$	$1.01{\cdot}10^{-17}$
22500	$1.65{\cdot}10^{-09}$	$1.08{\cdot}10^{-17}$
25000	$1.70{\cdot}10^{-09}$	$1.15{\cdot}10^{-17}$
27500	$1.76{\cdot}10^{-09}$	$1.22{\cdot}10^{-17}$
30000	$1.81{\cdot}10^{-09}$	$1.28{\cdot}10^{-17}$
35000	$1.91{\cdot}10^{-09}$	$1.41{\cdot}10^{-17}$
40000	$1.99{\cdot}10^{-09}$	$1.53{\cdot}10^{-17}$
45000	$2.07{\cdot}10^{-09}$	$1.64{\cdot}10^{-17}$
50000	$2.15{\cdot}10^{-09}$	$1.75{\cdot}10^{-17}$
55000	$2.22{\cdot}10^{-09}$	$1.85{\cdot}10^{-17}$
60000	$2.28{\cdot}10^{-09}$	$1.95{\cdot}10^{-17}$

Table 3: Masses, radii and effective cross section

To convert MSP mass to radius we used a particle bulk density of 2 g cm^{-3} [26]. The initial kinetic energy is defined by MSP mass and the rocket velocity, which is a function of altitude. The simulated MSP velocities are summarized in Tab. 4.

altitude [km]	$\vec{v}$ [m/s]
65	929.8
70	876.8
75	820.4
80	759.9
85	694.2
90	621.7

Table 4: velocities at simulated altitudes for an apogee of ≈115 km

Detection efficiency definition and normalization

In the simulations particles start from a disc-like area $A_{start} = \pi \cdot 45^2$ mm^2 which corresponds to the size of the entire MSPD including shielding grids. This was done to perform a simulation for the electrode's current and currents on the grids simultaneously. This implies, that the detection efficiency of the inner grid and the sensor must be scaled by factor f which is proportional to corresponding surface areas ratio:

$$f = \frac{A_{start}}{A_{electrode}} \cdot \prod_{i}^{j} tr_i \qquad (4)$$

where $\prod_i^j tr_i$ is the product of all transparencies tr upstream the electrode of the interest. For example, for the innermost electrode the transparencies tr_i are the transparencies of the G1 and G2. The grid transparencies were derived by counting the detections of MSPs in vacuum under zero potential.

This normalization helps us to define an efficiency which only accounts for aerodynamics and electrostatics and does not depend on the detection area. The efficiency can be written as:

$$\eta = \frac{N_{detected}}{N_{start}} \cdot \frac{1}{f} \cdot 100\ \% \qquad (5)$$

Here $N_{detected}$ and N_{start} are the number of particles detected on an specific electrode and the total number of simulated particles, respectively.

Resulting detection efficiencies

Normalized detection efficiencies were derived for all electrodes, namely outer grid G1, inner grid G2, and the sensor. For consistency check also the particles splats on the simulation boundary were counted, to make sure that the sum of all detected particles is equal to the number of started particles.

In Fig. 4–8 we show 3d plots of the derived detection efficiencies versus altitude and particle mass. Fig. 4 and 5 show results for positively charged and Fig.6, 7 and 8 for negatively charged particles, respectively.

As can be seen from the Fig. 4, the outer grid detects not only positive ions (as assumed by conventional fixed biased ion probes), but also tiny MSPs. The detection rate gets lower for larger MSP, which have a higher kinetic energy, but is still on a high level of around 60 % to 80 % for altitudes above 70 km. Below 70 km we see a drastically decreasing efficiency mainly due to aerodynamic effects.

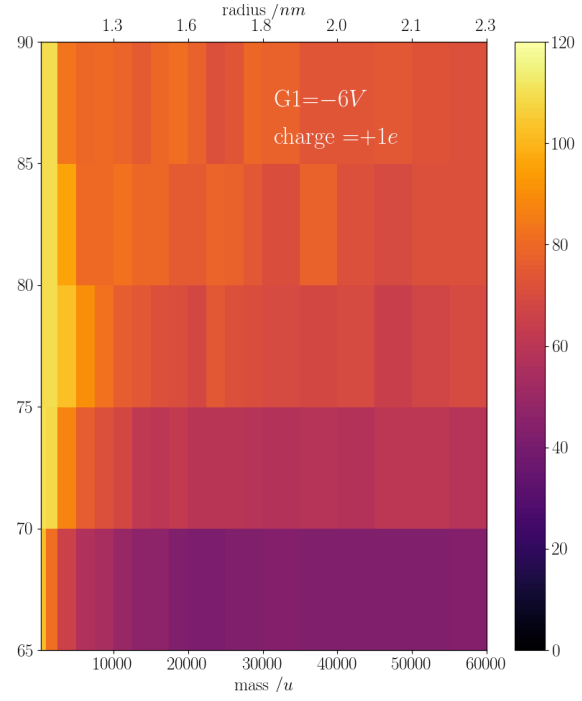

Figure 4: Efficiency for G1 (outer grid) for positively charged MSP

Interestingly, as can be seen from Fig. 5, the positively biased inner grid (G2) also detects some larger particles with a relatively high kinetic energy. Large particles have non-zero probability to hit the sensor at altitudes above 75 km where collisions with the neutral background become more unlikely and kinetic energies stay at a high level.

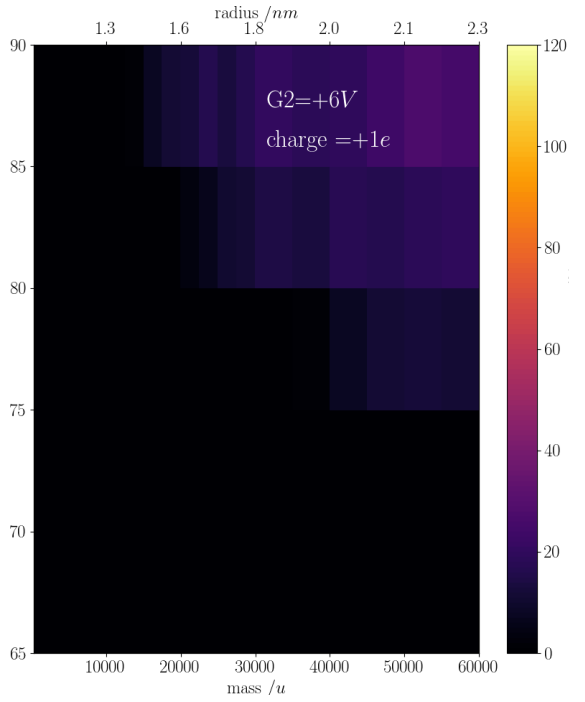

Figure 5: Efficiency for G2 (outer grid) for positively charged MS0

The detection efficiency of the sensor is 0 % for all positively charged particles and, therefore not shown here. This is due to high positive potential of +12 V in combination with the +6 V bias on the nearest grid (G2). Note, that such a configuration maintain an electric field which also decreases the influence of photocurrent from the electrode and, thereby allows to resolve smaller currents due to MSP density fluctuations.

The simulations of negatively charged particles yielded the following results. As shown in Fig. 6 the outermost grid shields smaller negative particles. Larger particles with higher kinetic energy can also be detected by the detector, though with relatively low efficiencies of maximum ∼30 % (similar to Fig. 5) and an increasing filtering effect on small particles for lower altitudes down to 70 km. Below 70 km we see a more complicated picture, with an increasing detection efficiency for small particles.

For the inner grid (G2), biased positively we see the shielding effects for small particles of the upstream inner grid G1. Again, the filtering effect above 70 km is present for small particles. Similar to the detection efficiency of the outer grid, the detection of particles

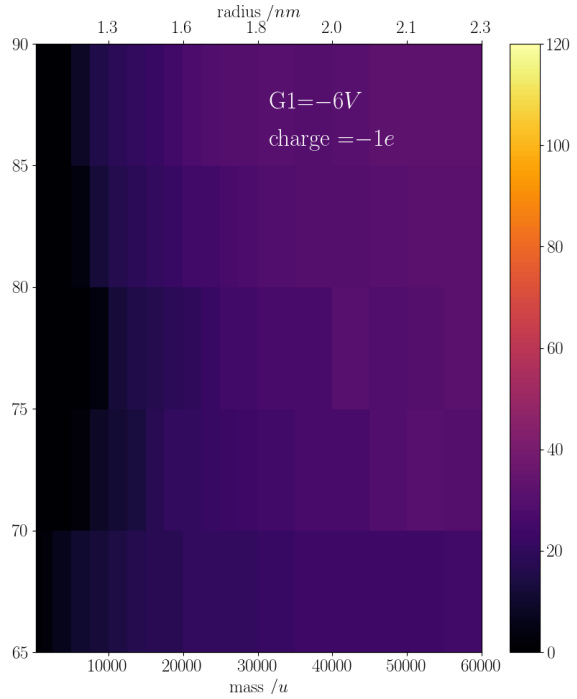

Figure 6: Efficiency for G1 (outer grid) for negatively charged MSP

enhances below 70 km, which allows a MSP detection for radii less than 1 nm.

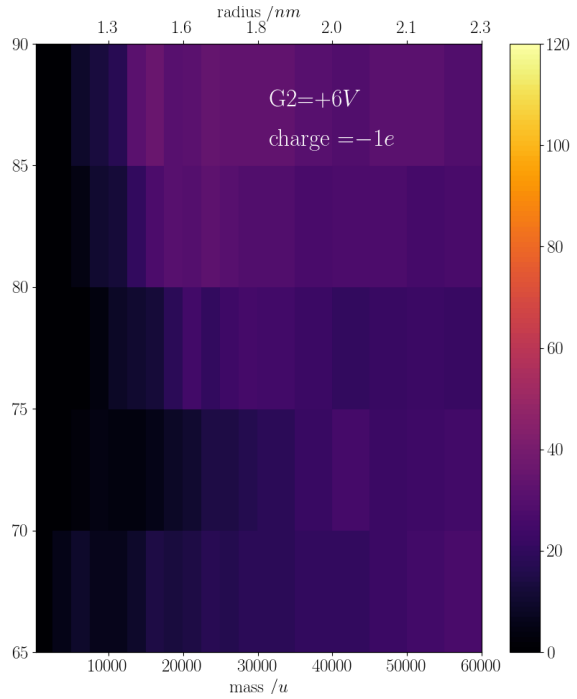

Figure 7: Efficiency for G2 (inner grid) for negatively charged MSP

It is apparent from Fig. 8, that a positively biased sensor is insensitive to very small negatively charged particles with $r \gtrsim 1$ nm at altitudes above 70 km.

The more complicated picture of detection efficiencies continues for the sensor, too. Resulting in a high probability for small MSP detection below 70 km and very low efficiencies for large (collision affected by ambient neutral gas) MSPs.

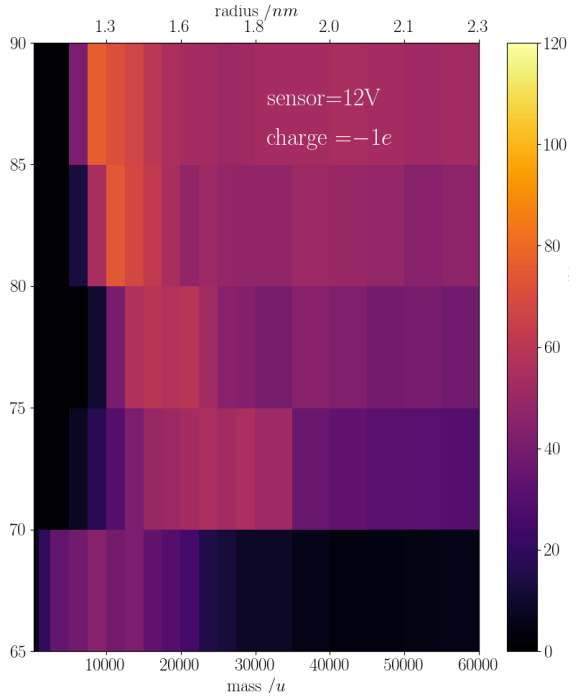

Figure 8: Efficiency for the sensor for negatively charged MSP

A maximum detection efficiency is visible at altitudes above 80 km for radii around 1.3 nm similar to the detection characteristics of the MSP sensor described in [27], but with a higher efficiency for larger particles.

4. CONCLUSION

We introduced a new Faraday cup type detector, MSPD, for in situ measurements of charged MSPs in the D-region ionosphere especially developed for low altitude measurements e.g., below 80 km.

Extensive coupled electrostatic and aerodynamic simulations demonstrated that due to improved aerodynamic properties the new MSPD must be capable of detection of tiny MSPs with radii of 1 nm and smaller. Sensitive electronics that has a small time constant allows for measuring of small MSP density fluctuations of ∼1 %. The outer grid of the MSPD is negatively biased and connected to a sensitive electrometer and, therefore works as a electrostatic positive ion probe.

The combination of different biases applied to the electrode and grids allows to adjust sensor's sensitivity to different signs of charge and masses of MSPs. The presented configuration must be more sensitive to negatively charges, however other combinations of the applied potentials are currently under investigation. By adjusting these biases we plan to find a combination of MSPDs which will be capable of measuring both negatively and positively charged MSPs with a high precision.

ACKNOWLEDGMENTS

This work was supported by the German Space Agency (DLR) under grant 50OE1402 (project PMWE). The authors thank H.-J. Heckl and T. Köpnick for building the instrument.

REFERENCES

1. Rosinski, J. & Snow, R. H. Secondary particulate matter from meteor vapors. *Journal of Meteorology*, 18(6):736–745 (1961).
2. Havnes, O., Trøim, J., Blix, T., Mortensen, W., Naesheim, L. I., Thrane, E., & Tønnesen, T. First detection of charged dust particles in the Earth's mesosphere. *Journal of Geophysical Research: Space Physics*, 101(A5):10839–10847 (1996).
3. Lübken, F.-J. Thermal structure of the Arctic summer mesosphere. 104:9135–9149 (1999).
4. Rapp, M. & Lübken, F.-J. Polar mesosphere summer echoes (PMSE): Review of observations and current understanding. 4:2601–2633 (2004).
5. Plane, J. M. C. Atmospheric chemistry of meteoric metals. *Chemical Reviews*, 103(12):4963–4984 (2003). PMID: 14664639.
6. Hemenway, C. L. & Soberman, R. K. Symposium: Small meteoric particles in the earth's neighborhood: Studies of micrometeorites obtained from a recoverable sounding rocket. *The Astronomical Journal*, 67:256 (1962).
7. Rosinski, J. Condensation products of meteor vapors and their connection with noctilucent clouds and rainfall anomalies. 26(1961) (1964).
8. Havnes, O., Melandsø, F., Hoz, C. L., Aslaksen, T. K., & Hartquist, T. Charged dust in the Earth's mesopause; effects on radar backscatter. *Physica Scripta*, 45(5):535–544 (1992).
9. Horányi, M., Gumbel, J., Witt, G., & Robertson, S. Simulation of rocket-borne particle measurements in the mesosphere. *Geophysical Research Letters*, 26:1537–1540 (1999).
10. Rapp, M., Hedin, J., Strelnikova, I., Friedrich, M., Gumbel, J., & Lübken, F.-J. Observations of positively charged nanoparticles in the nighttime polar mesosphere. *Geophysical Research Letters*, 32 (2005).

11. Hedin, J., Gumbel, J., & Rapp, M. On the efficiency of rocket-borne particle detection in the mesosphere. *Atmospheric Chemistry and Physics Discussions*, 7(1):1183–1214 (2007).

12. Strelnikova, I., Rapp, M., Strelnikov, B., Baumgarten, G., Brattli, A., Svenes, K., Hoppe, U.-P., Friedrich, M., Gumbel, J., & Williams, B. P. Measurements of meteor smoke particles during the ECOMA-2006 campaign: 2. Results. *Journal of Atmospheric and Solar-Terrestrial Physics*, 71:486–496 (2009).

13. Baumann, C., Rapp, M., Kero, A., & Enell, C. F. Meteor smoke influences on the D-region charge balance - Review of recent in situ measurements and one-dimensional model results. *Annales Geophysicae*, 31(11):2049–2062 (2013).

14. Hoz, C. L. & Havnes, O. Artificial modification of polar mesospheric winter echoes with an RF heater: Do charged dust particles play an active role? *Journal of Geophysical Research Atmospheres*, 113(19):1–7 (2008).

15. Gumbel, J. Aerodynamic influences on atmospheric in situ measurements from sounding rockets. *Journal of Geophysical Research: Space Physics*, 106(A6):10553–10563 (2001).

16. Staszak, T., Brede, M., & Strelnikov, B. Open Source Software Openfoam as a New Aerodynamical Simulation Tool for Rocket-Borne Measurements. Number June. 22nd ESA Symposium on European Rocket and Balloon Programmes and Related Research (2015).

17. Asmus, H., Staszak, T., Strelnikov, B., Lübken, F.-J., Friedrich, M., & Rapp, M. Estimate of size distribution of charged msps measured in situ in winter during the wadis-2 sounding rocket campaign. *Annales Geophysicae*, 35(4):979–998 (2017).

18. Blix, T., Svenes, K., Gumbel, J., & Strelnikov, B. In situ measurements of neutral temperature in the middle atmosphere by means of swept Langmuir probes. In Paillé, J.-P., editor, *35th COSPAR Scientific Assembly*, volume 35 of *COSPAR Meeting*, page 347 (2004).

19. Svenes, K. R., Blix, T. A., Hoppe, U.-P., Gumbel, J., & Strelnikov, B. In-situ measurements of neutral temperature in the middle atmosphere by using electrons as proxy. In Warmbein, B., editor, *17th ESA Symposium on European Rocket and Balloon Programmes and Related Research*, volume 590 of *ESA Special Publication*, pages 191–196 (2005).

20. Scientific Instrument Services, Inc. SIMION® version 8.0/8.1 user manual. User manual, Scientific Instrument Services, Inc. (2013).

21. Giono, G., Strelnikov, B., Asmus, H., Staszak, T., & Ivchenko, N. Detailed photocurrent characterization for meteor smoke particle detectors onboard the pmwe sounding rocket. In *23rd ESA Symposium on european rocket and baloon programmes and related research*, Visby, Sweden (2017).

22. Ernst, S. M., Skruszewicz, S., Strelnikov, B., & Rapp, M. Absolute Calibration of Vacuum Ultraviolet Xenon Flash Lamps Used for Photoionization of Meteor Smoke Particles. In Ouwehand, L., editor, *20th Symposium on European Rocket and Balloon Programmes and Related Research*, volume 700 of *ESA Special Publication*, pages 105–112 (2011).

23. Scanlon, T., Roohi, E., White, C., Darbandi, M., & Reese, J. An open source, parallel DSMC code for rarefied gas flows in arbitrary geometries. *Computers & Fluids*, 39(10):2078–2089 (2010).

24. Bird, G. A. Molecular gas dynamics. *NASA STI/Recon Technical Report A*, 76:40225 (1976).

25. Picone, J. M., Hedin, A. E., Drob, D. P., & Aikin, A. C. NRLMSISE-00 empirical model of the atmosphere: Statistical comparisons and scientific issues. *Journal of Geophysical Research: Space Physics*, 107(A12):1–16 (2002).

26. Robertson, S., Dickson, S., Horányi, M., Sternovsky, Z., Friedrich, M., Janches, D., Megner, L., & Williams, B. Detection of meteoric smoke particles in the mesosphere by a rocket-borne mass spectrometer. *Journal of Atmospheric and Solar-Terrestrial Physics*, 118:161–179 (2014).

27. Plane, J. M. C., Saunders, R. W., Hedin, J., Stegman, J., Khaplanov, M., Gumbel, J., Lynch, K. A., Bracikowski, P. J., Gelinas, L. J., Friedrich, M., Blindheim, S., Gausa, M., & Williams, B. P. A combined rocket-borne and ground-based study of the sodium layer and charged dust in the upper mesosphere. *Journal of Atmospheric and Solar-Terrestrial Physics*, 118:151–160 (2014).

ANDØYA SPACE CENTER TRAJECTORY AND POSITION SYSTEM (TPS)

Johan Idivuoma

Andøya Space Center, Bleiksvegen 46, NO-8480 Andenes

johan@andoyaspace.no

ABSTRACT

The Trajectory and Position System (TPS) is one of the most critical software systems during campaigns at Andøya Space Center. The main functionality of the system is to gather the payload position information from all available input sources, weight the data and present actual position, velocity vector and instantaneous impact point at real-time. Furthermore, the TPS system handles all logging of position data necessary to perform a postflight trajectory analysis, in addition to providing guiding functionality to tracking antennas.

Several input data clients are fully integrated at existing system, as for example radar, several GPS position formats and ASC telemetry antenna controllers. Since the system is fully developed at ASC, thus owning the code-base, we also have the possibility to integrate new types of clients whenever needed.

An integrated part of the TPS is the ASC developed slantrange measuring system for telemetry antennas, the Time Interval Counter (TIC). The TIC-system provides us together with the pointing angles of the telemetry antenna with the rocket position information even without radar or GPS tracking.

An overview of the Andøya Space Center TPS system will be presented. The TIC-system is covered in more detail, the basic principles are described and the accuracy of position measurements using telemetry antannas equipped with the TIC-system is compared to radar and GPS measurements.

Key words: ASC, TPS, realtime.

1. INTRODUCTION

Andøya Space Center (ASC) Trajectory and Positioning System (TPS), a real-time software system for monitoring payload position and trajectory, represents one of the most critical systems for rocket operations conducted by Andøya Space Center.

The main functionality of the system is to receive and decode position information from various positioning sources such as radar, telemetry antennas and GPS. The system merges the information from the sources and presents the current position, IIP and other key flight parameters of the moving payload as output in close-to real-time.

The TPS system is an in-house solution with the code base fully owned and developed by ASC. This makes it straightforward to fork the code base to a new version for unknown input format or specific output format if needed. Since the system runs on standard Windows PC's it is also easy to set it up on different launch locations (i.e. ASC launch site at Ny-Aalesund Svalbard).

This report presents an overview of the system. A more detailed description of positioning based telemetry antennas only will be given. The accuracy will be covered and compared to GPS measurements.

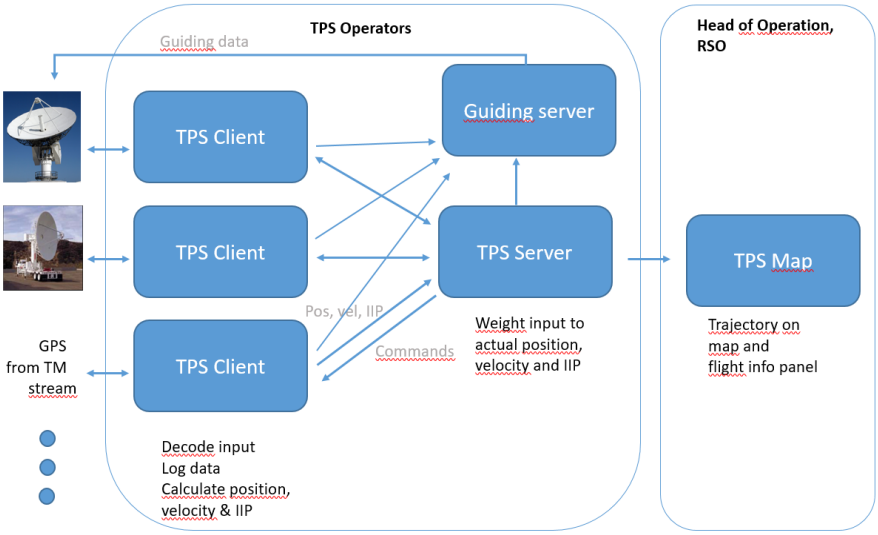

Figure 1. Schematic overview of the TPS system.

2. OVERVIEW

The TPS is a real-time client-server based system running on standard Windows PC's. The TPS Clients handles all communication with input sources, thus each input source has its own client assigned.

The TPS Server merges input from the clients to an unique current position and key flight parameters, and forward that information to the TPS Map solution and Flight information panel for presentation to the Head of operation and Safety Manager, in addition to sending information to the TPS Guiding Server which takes care of all necessary guiding of antennas.

Since the system runs on standard Windows PC's it is mobile and straightforward to set up and operate on different launch locations, i.e. ASC SvalRak launch site at Ny-Aalesund in Svalbard.

An overview of the TPS system is visualized in figure (1).

2.1. Development environment, test coverage and some notes about the realtimeness of the system

The solution is fully developed by ASC, thus owning the code base. It is developed in C++ on Windows operating system and is running on standard Windows PC's. Since it is an in-house solution new versions can be forked off to support unknown input sources or deliver customized output on a short notice.

At operations all the PC's in the system are synchronized to UT time. The logging of the input data at the clients is triggered at the arrival to minimize latency for post-processing. The timestamps of the tracking device are also logged if they are included in the communication telegram.

Since the system is thought of as a presentation tool for operators an updating frequency of 10Hz has been chosen, which compared to the human reaction time is expected to be sufficient. The system as a whole has however been tested and verified to operate at speeds up to 50 Hz, making it possible to minimize latency if needed.

The TPS system represents a critical system that usually is up and running for a long period of time with high demands of stability and accuracy. All the critical calculation units are covered by

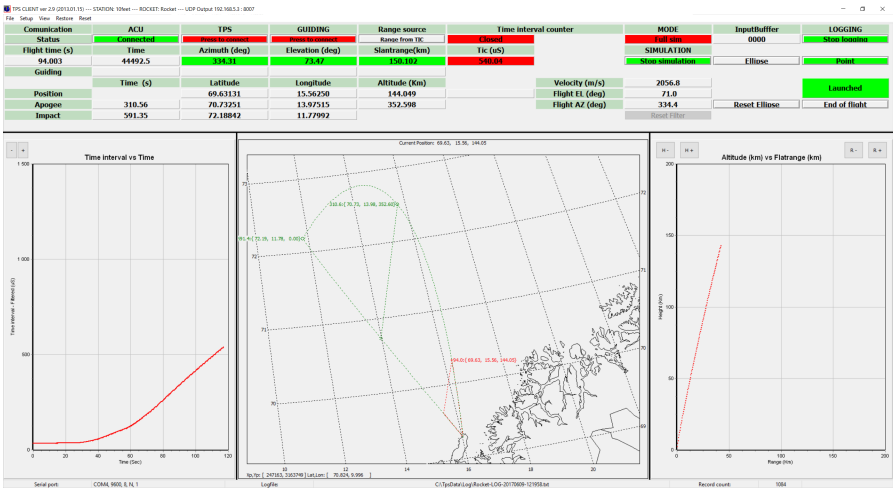

Figure 2. TPS Client GUI.

unit tests in addition to an extensive final testing regime.

The final testing consists of a simulator mode extension to the TPS Clients that based on a nominal trajectory file emulates input exactly matching the format and delivery method of the device the client is connected to. Several runs of simulated launches with the flight-ready system are performed prior to each launch and the trajectory, final apogee and impact calculations are verified to match the nominal trajectory.

2.2. TPS Client

The TPS Client is the most complex part of the system, taking care of basically all complex calculations with high demands of low latency logging and communication with the tracking devices.

Each positioning input source has its own TPS Client assigned. The client handles communication with the input device, decodes input telegrams and logs position data at arrival. Based on the position measurement history the TPS Client calculates current velocy, expected apogee and IIP position. This information is presented to the TPS operator, and sent to the TPS Server for merging and presentation.

Currently several types of GPS formats are supported in addition to DLR/Moraba RIR and ASC MPS36 radar. GPS and radar position input represents the most accurate sources available, giving accurate current position and estimation of apogee and IIP points already early in the free-flight phase.

The ASC TM antennas are also used for positioning. Here the pointing angles of the antenna are delivered by the ACU and the slant-range is calculated using the TIC-system (Time Interval Counter), an ASC developed and owned solution providing slant-range using the telemetry signal. A more detailed description of the system and accuracy of the positioning using TM antennas only will be given later in this document.

Since the decoding of input telegrams is an internal task of the client, addition of an new input format requires code changes. The system is however designed to make it possible to perform modifications of the decoding of input as straightforward as possible.

The GUI of the TPS Client can be seen in figure (2).

2.3. TPS Server and Map and Information panel

Based on pre-determined weighting of the connected TPS Clients the TPS Server merges input

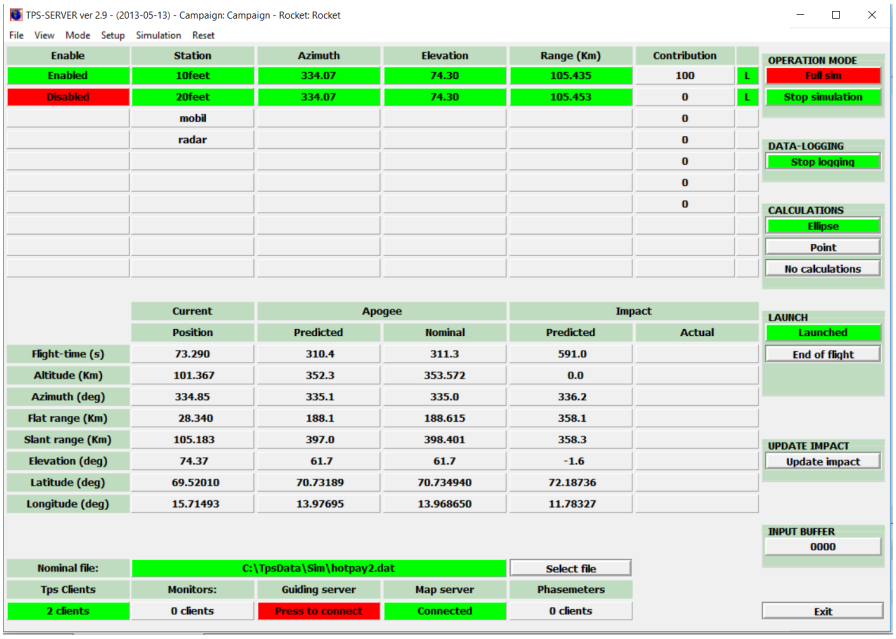

Figure 3. The TPS Server.

data to an unique current position, velocity, estimated apogee and IIP point. The information is sent to the TPS Map Server and flight information panel for presentation to the Head of operation and Safety Manager. In addition the information is sent to the TPS Guiding Server for guiding of tracking antennas if necessary.

The TPS Server also serves as a control panel for the TPS operator. From here the operator can broadcast events controlling the connected clients, for example start a simulated launch, initiate logging and trigger a launch event. During flight the operator also enables or disables client input based on presented key information using the TPS Server control panel.

The TPS Server GUI can be seen in figure (3).

The Map Server is a presentation tool only. It presents current position and trajectory on a map for the Head of operations. It also contains an information panel with current velocity, estimated apogee and IIP point. The Map Server is viewed in figure (4).

3. POSITIONING BASED ON TELEMETRY ANTENNAS ONLY

Andøya Space Center has developed a method for tracking the position of the payload using telemetry antennas only. In this section the solution is described and the accuracy of the positioning is discussed.

3.1. Pointing angles

The pointing angles of the telemetry antennas are delivered by the ACU's of the antennas through network to the TPS Clients.

The figures (5) and (6) shows measured azimuth and elevation residuals from a typical rocket flight, campaign [1]. The accuracy of the pointing angles of ASC telemetry antennas can be specified to be within $\pm 0.08^\circ$ Azimuth and $\pm 0.05^\circ$ Elevation, giving an accuracy of < 80 m per 100 km slantrange.

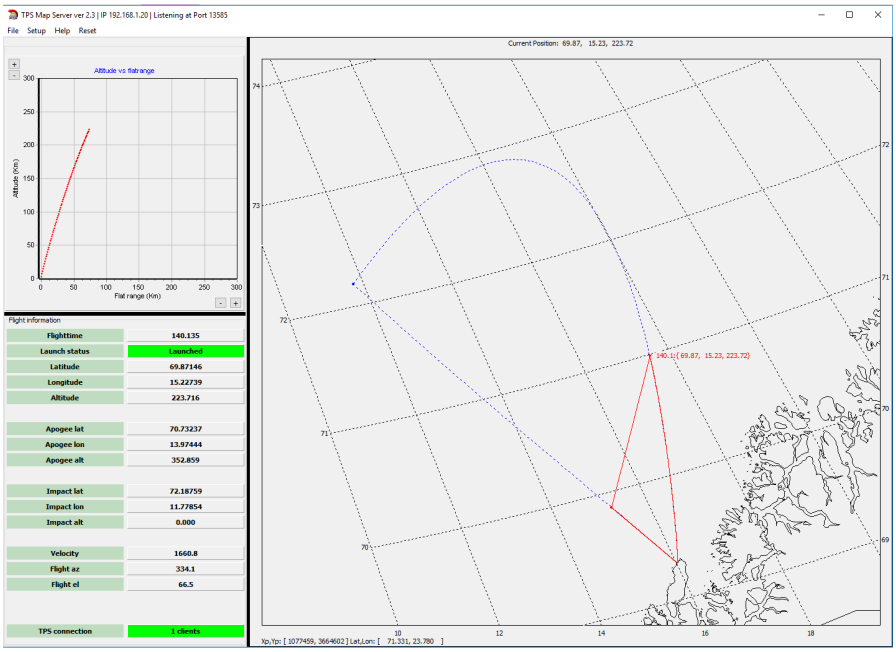

Figure 4. The TPS Map and Information panel.

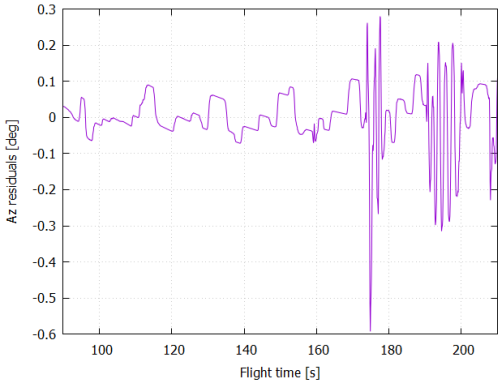

Figure 5. Typical Azimuth residuals.

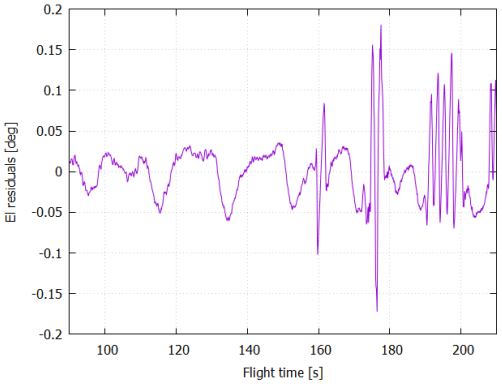

Figure 6. Typical Elevation residuals.

3.2. The TIC system

The slant range using telemetry antennas for positioning is given by the TIC system, an Andøya Space Center developed and owned technology for measuring the slant range using the telemetry signal.

The system is based on measuring the time interval between the signal sent from the payload and received by antenna.

The electronic unit takes care of synchronization and calculation of the time difference, while the TPS Client gets time differences as input in 10 Hz frequency.

As with other sources, the TIC time differences are logged at arrival for trajectory post processing.

The standard deviation of the data logged at arrival is as low as $\sigma = 3.1$ m, meaning that the precision of the signal is comparable to radar range measurements. The data histogram is plotted in figure (7), campaign [1].

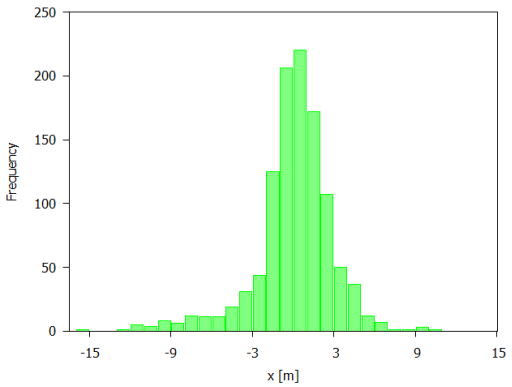

Figure 7. TIC slant range logged at arrival histogram.

The standard deviation of the data used in the TPS Client calculations, i.e. fetched at 10 Hz, is $\sigma = 60.1$ m. The data histogram is plotted in figure (8), [1].

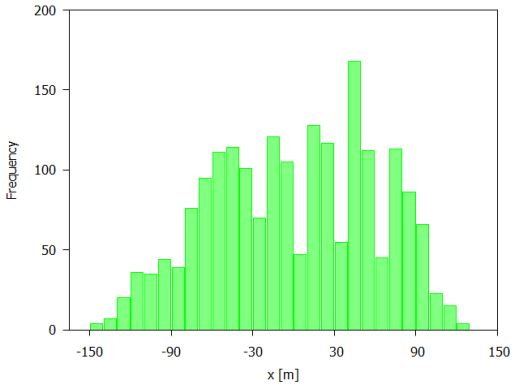

Figure 8. TIC slant range fetched by TPS calculation units at 10 Hz *histogram.*

Since the system is depending on a stable oscillator onboard the accuracy is highly depending on type of oscillator: if the onboard oscillator is drifting during flight the range measurements will be correspondingly affected, while a stable oscillator maintains the accuracy. This means that even if the *precision* of the TIC measurements is good, it doesn't automatically imply that the *accuracy* is good.

Figure (9) shows a typical drift of range measurements due to a positive drift of the onboard oscillator, campaign [2] .

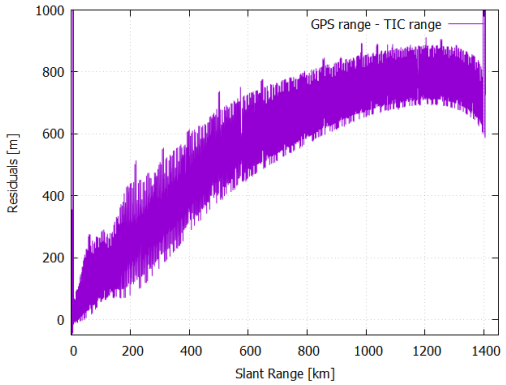

Figure 9. TIC slant range residuals indicating a positive drift.

The drift is typically within < 100 m per 100 km slant range.

3.3. Telemetry antenna positioning accuracy

The accuracy due to pointing angles using ASC telemetry antennas is within 80 m and the corresponding accuracy of the TIC measured slant range is typically within 100 m per 100 km slant range. This gives a total accuracy typically within 130 m per 100 km slant range, depending on the type of oscillator onboard. This accuracy is however expected to be improved by post flight calculations of the trajectory.

4. CONCLUSION (AND SOME PLANNED IMPROVEMENTS)

The accuracy of the TPS system is depending on the input data, accurate input gives accurate output.

If as accurate trajectory as possible is important for the operation, a GPS solution should be in-

tegrated in the payload or the cost of operating one or both the radar stations available at Andøya Space Center be accepted.

On the other hand, if inaccuracy of up to 130 m per 100 km slant range is acceptable at the quick-look files after launch and further improved by post processing logged data to an actual trajectory, the TM antennas can be used for positioning.

The TPS Clients are maintained on a regular basis due to changes in input formats. The TPS Map solution of the system is however planned to be rewritten as a next bigger development step. The main goal is to get a visually more attractive map, and the possibility to add ship positions as measured by AIS is under investigation. Also, we are investigating the possibility to add a toolset for range and bearing measurements directly on the map as an aid for the Head of operation and Safety Manager.

REFERENCES

[1] ASC, 2016, LAUNCH REPORT..., MaxiDusty1 launched 30.06.2016, [DocId ASC-R-387]

[2] ASC, 2015, Final Trajectory Report..., BBXII launched 24.11.2014

ATTITUDE CALCULATIONS BASED ON 3-AXIS MAGNETOMETER MEASUREMENTS

Johan Idivuoma

Andøya Space Center, Bleiksvegen 46, NO-8480 Andenes

johan@andoyaspace.no

ABSTRACT

Andøya Space Center Hotel Payload standard configuration includes a 3-axis magnetometer integrated in the payload. The magnetometer gives us the possibility to perform post-flight calculations of the orientation of the payload to a low cost in terms of both the device itself and integration effort.

The solution has proven to be accurate for determining the apparent spin frequency of the payload with minimal post-processing effort. The calculated orientation of the three magnetometer axes are typically less than 2 degrees from the measured values converted to angles, indicating that the accuracy is good. However, since the device itself is positioned inside a rotating metallic cylinder, we also need to correct the calculated orientation for the induced magnetic field.

We will here present the mathematical framework, including necessary coordinate systems, on which the orientation calculations are based. Uncertainties introduced by the different calculation steps and assumptions are identified and described. We will also compare the calculated orientation with data from other sources to visualize the accuracy of the calculations.

Key words: ASC, magnetometer, attitude.

1. INTRODUCTION

The Hotel Payload standard configuration of Andøya Space Center includes a 3-axis magnetometer. The magnetometer has a high sampling rate (2890Hz for the MaxiDusty payload), provides us with accurate measurements of the magnetic field vector components along the magnetometer axes and represents a low-cost solution in terms of both the cost of the device and integration effort. The magnetometer is mounted with one axis aligned with the payload longitudinal axis, and two axes orthogonal to it, thus measuring the spinning motion of the payload.

Mathematically we are modelling the payload as a spinning top, simplified by neglecting the nutation motion. We let the spin-axis be aligned with the longitudinal symmetrical axis of the payload and the precession axis, representing the coning of the payload, be aligned with the velocity vector at non-negligible atmosphere and constant above it. Together with a magnetic field model giving the magnetic field vector, it is possible to calculate the actual orientation of the payload based on the magnetometer measurements.

This article presents the mathematical framework including necessary coordinate systems to perform those calculations. The MaxiDusty 1 flight launched from Andøya in 2016 [1] will be used as an example.

2. MAGNETIC FIELD VECTOR AS SEEN FROM THE PAYLOAD

The aim of this section is to establish relations of how the magnetic field vector is seen from the payload, and thereby being measured by the magnetometer. Necessary coordinate systems are presented, and equations for expressing the magnetic field vector component along the payload longitudinal axis and (fixed to the payload) transversal axes are deduced. We will also have a look at how those equations can be used to establish a theoretically modeled coning and spinning payload that fits the magnetometer measurements.

2.1. Payload−Magnetic field coordinate systems

Let the coning axis, or precession axis in the terminology of a spinning top, be described by the vector $\vec{H}$. Furthermore, let the magnetic field vector be given as $\vec{B}$.

Let us now define the *coning axis − magnetic field* coordinate system $O_C = (\hat{X}_C, \hat{Y}_C, \hat{Z}_C)$, with origin at the payload center of gravity, as:

$\hat{Z}_C -$ along the instantaneous coning vector $\vec{H}$, positive forward in the direction of payload longitudinal axis, .

$\hat{X}_C -$ perpendicular to $\hat{Z}_C$, lying in the $\hat{Z}_C - \vec{B}$ symmetric plane, positive towards $\vec{B}$.

$\hat{Y}_C -$ normal to the $\hat{Z}_C - \hat{X}_C$ symmetric plane, fulfilling RHS.

Related to the O_C coordinate system is also the *Body* (or *Payload*) coordinate system $O_B = (\hat{X}_B, \hat{Y}_B, \hat{Z}_B)$, also with origin at the payload center of gravity, defined as

$\hat{Z}_B -$ along the payload longitudinal axis, positive forward.

$\hat{X}_B -$ perpendicular to $\hat{Z}_B$, positive down towards $\hat{X}_C - \hat{Y}_C$ symmetric plane.

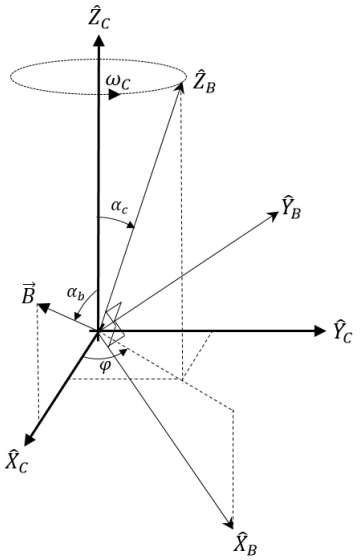

Figure 1. O_C and O_B coordinate systems.

$\hat{Y}_B -$ normal to the $\hat{Z}_B - \hat{X}_B$ symmetric plane, fulfilling RHS.

The O_C and O_B coordinate systems are visualized in figure (1).

2.2. Magnetic field vector in Body Coordinate System

Assume that the payload longitudinal axis $\hat{Z}_B$ is spinning around the axis $\hat{Z}_C$, from the $\hat{X}_C - \hat{Z}_C$ plane against $\hat{Y}_C - \hat{Z}_C$ plane, as described in figure (1).

Let us make the following definitions:

$t -$ flight time in seconds

$\alpha_b -$ instantaneous angle between $\hat{Z}_C$ and $\vec{B}$ $(0 \leq \alpha_b \leq \pi)$.

$\alpha_c -$ instantaneous angle between $\hat{Z}_C$ and $\hat{Z}_B$, coning half-angle $(0 \leq \alpha_c \leq \pi/2)$.

$\omega_c -$ instantaneous angular frequency of which $\hat{Z}_B$ is rotating around $\hat{Z}_C$ $(\omega_c > 0)$.

t_0 – the (constant) flight time $t = t_0$ for which the $\hat{Z}_B$ axis is in the $\hat{X}_C - \hat{Z}_C$ symmetric plane.

With the above definitions the magnetic field vector in O_C coordinate system is given by

$$\begin{cases} \vec{B} \cdot \hat{X}_C &= |\vec{B}| \sin(\alpha_b) \\ \vec{B} \cdot \hat{Y}_C &= 0 \\ \vec{B} \cdot \hat{Z}_C &= |\vec{B}| \cos(\alpha_b) \end{cases} \tag{1}$$

The angle φ in figure (1) becomes $\varphi = \omega_c \cdot (t - t_0)$. Performing a coordinate transformation from O_C to O_B gives the magnetic field vector $\vec{B}$ in O_B coordinate system as

$$\begin{cases} \vec{B} \cdot \hat{X}_B &= |\vec{B}| \sin(\alpha_b) \cos(\alpha_c) \cos(\varphi) - \\ & \quad -|\vec{B}| \cos(\alpha_b) \sin(\alpha_c) \\ \vec{B} \cdot \hat{Y}_B &= -|\vec{B}| \sin(\alpha_b) \sin(\varphi) \\ \vec{B} \cdot \hat{Z}_B &= |\vec{B}| \sin(\alpha_b) \sin(\alpha_c) \cos(\varphi) + \\ & \quad + |\vec{B}| \cos(\alpha_b) \cos(\alpha_c) \end{cases} \tag{2}$$

The above result can easily be obtained by transforming $\vec{B}$, given by equation (1), to a spherical coordinate system with $\theta = \alpha_c$ and $\phi = \varphi$.

The magnetic field vector component given by $\vec{B} \cdot \hat{Z}_B$ in equation (2) is of course the one measured by the axis aligned with the payload longitudinal axis of the onboard magnetometer.

2.3. Magnetic field vector as seen by payload spinning axis

Let us now assume that the payload itself is spinning around its longitudinal axis $\hat{Z}_B$, from the $\hat{X}_B - \hat{Z}_B$ plane towards $\hat{Y}_B - \hat{Z}_B$ plane.

We now make the following definitions:

$\vec{r}_s$ – a vector fixed to the payload and thus spinning with it, orthogonal to $\hat{Z}_B$ (thus residing in the $\hat{X}_B - \hat{Y}_B$ symmetric plane).

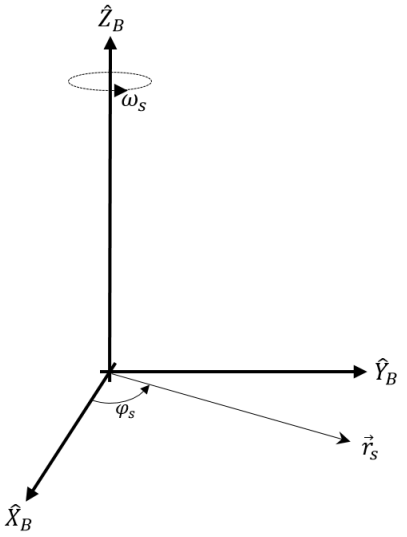

Figure 2. Payload orthogonal vector $\vec{r}_s$.

ω_s – instantaneous angular frequency of which $\vec{r}_s$ is rotating around $\hat{Z}_B$ ($\omega_s > 0$).

t_{0s} – the (constant) flight time $t = t_{0s}$ for which the $\vec{r}_s$ axis is in the $\hat{X}_B - \hat{Z}_B$ symmetric plane.

The vector $\vec{r}_s$ is shown in figure (2).

The angle φ_s in figure (2) becomes $\varphi_s = \omega_s \cdot (t - t_{0s})$. Using the definitions given above, and assuming that $|\vec{r}_s| = 1$, we can express the vector $\vec{r}_s$ in O_B as

$$\begin{cases} \vec{r}_s \cdot \hat{X}_B &= \cos(\varphi_s) \\ \vec{r}_s \cdot \hat{Y}_B &= \sin(\varphi_s) \\ \vec{r}_s \cdot \hat{Z}_B &= 0 \end{cases} \tag{3}$$

By using equation (2), the magnetic field component along the vector $\vec{r}_s$ is given by

$$\begin{aligned} \vec{B} \cdot \vec{r}_s \;=\; & \cos(\varphi_s) \Big(|\vec{B}| \sin(\alpha_b) \cos(\alpha_c) \cos(\varphi) - \\ & -|\vec{B}| \cos(\alpha_b) \sin(\alpha_c) \Big) - \\ & - \sin(\varphi_s) \Big(|\vec{B}| \sin(\alpha_b) \sin(\varphi) \Big) \end{aligned} \tag{4}$$

The magnetic field vector components measured by the transversal (spinning) axes of the on-board magnetometer are given by equation (4).

2.4. Relating magnetometer measurements to the payload orientation

Let us now assume that the quantities α_b, α_c, ω_c and ω_c are changing with flight time in a smooth and continuous way during some flight time interval T for which the quantities t_0 and t_{0s} can be assumed to be constant scalar values. We can then express the quantities as smooth and continuous functions of flight time, $\alpha_b(t), \alpha_c(t)$, $\omega_c(t)$ and $\omega_s(t)$ for $t \in T$.

Letting $B_z = \frac{\vec{B}\cdot\hat{Z}_B}{|\vec{B}|}$ and using equation (2) we get the magnetic field component along the rocket longitudinal axis as

$$B_z = \cos(\alpha_b(t))\cos(\alpha_c(t)) + \\ + \sin(\alpha_b(t))\sin(\alpha_c(t))\cdot \\ \cdot \cos(\omega_c(t)(t-t_0)) \quad (5)$$

The magnetometer axis aligned with the longitudinal axis of the payload provides us with a series of measured values of B_z. We can now use equation (5) to find the functions of $\alpha_b(t), \alpha_c(t)$ and $\omega_c(t)$ together with the scalar value of $t_0(t)$ for flight time $t \in T$ by means of a least square fit.

In the same way, we can express the relation for the payload transversal axes, measured by the magnetometer transversal axes, by letting $B_s = \frac{\vec{B}\cdot\vec{r}_s}{|\vec{B}|}$ and using equation (4) as

$$B_s = \cos(\omega_s(t)(t-t_{0s}))\Big(\\ \sin(\alpha_b(t))\cos(\alpha_c(t))\cos(\omega_s(t)(t-t_{0s})) - \\ - \cos(\alpha_b(t))\sin(\alpha_c(t))\Big) - \\ - \sin(\omega_s(t)(t-t_{0s}))\Big(\\ \sin(\alpha_b(t))\sin(\omega_s(t)(t-t_{0s}))\Big) \quad (6)$$

The transversal axes of the magnetometer gives us a series of measured values of B_s. Once the $\alpha_b(t), \alpha_c(t)$, $\omega_c(t)$ and the scalar value of $t_0(t)$ is known we can use equation (6) to find a function of $\omega_s(t)$ together with the scalar value of t_{0s} using a least square fit.

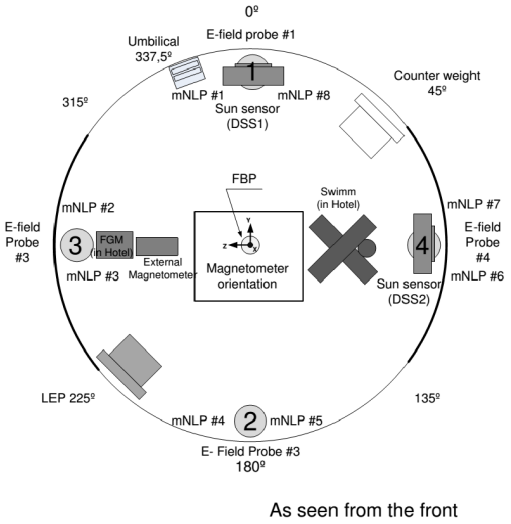

Figure 3. Magnetometer sensor in MaxiDusty 1 payload.

3. MAXIDUSTY1 PAYLOAD ORIENTATION IN O_B COORDINATE SYSTEM

As a working example the magnetometer readouts of the MaxiDusty 1 flight are used. The internal orientation of the magnetometer is in [2] described as given in figure (3).

The magnetic field components as measured by the magnetometer axes plotted in this section are normalized to unit length and transformed to aspect angles, i.e. we are working with $B_i = acos\left(\frac{\vec{B}_i}{|\vec{B}|}\right), i \in \{\text{magnetometer axes}\}$.

Figure (4) shows the magnetic field aspect angles measured by magnetometer longitudinal axis B_z together with the fitted functions $\alpha_b(t), \alpha_c(t)$ and the scalar value of t_0.

The fitted function $w_c(t)$ is presented as period time $T(t) = \frac{2\pi}{w_c(t)}$ in figure (5).

Using equation (5) with the fitted functions $\alpha_b(t)$, $\alpha_c(t)$, $w_c(t)$ and t_0 gives us the possibility to calculate theoretical values of B_z. Those values are plotted in figure (6) together with the measured aspect angles.

The payload longitudinal axis orientation is now described in the O_B coordinate system. Let us

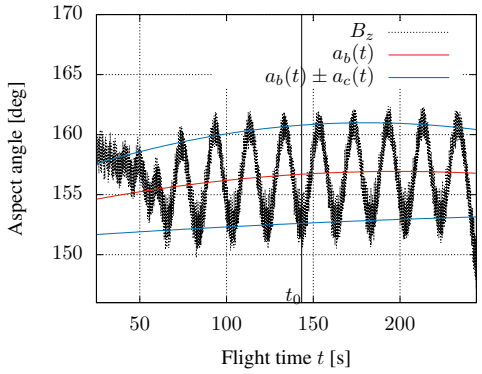

Figure 4. Magnetometer longitudinal axis measured aspect angle B_z together with the fitted functions $\alpha_b(t)$ and $\alpha_b(t) \pm \alpha_c(t)$.

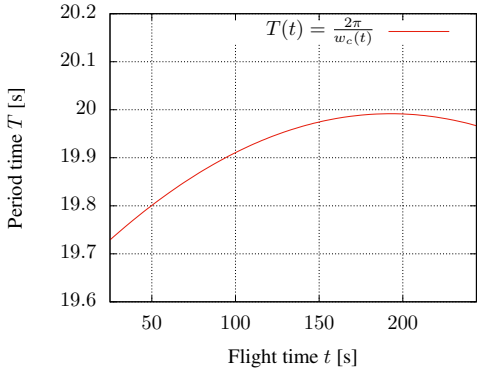

Figure 5. The longitudinal axis period time $T(t)$.

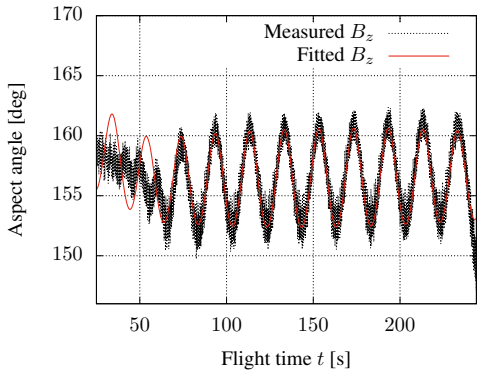

Figure 6. Measured and calculated aspect angles B_z.

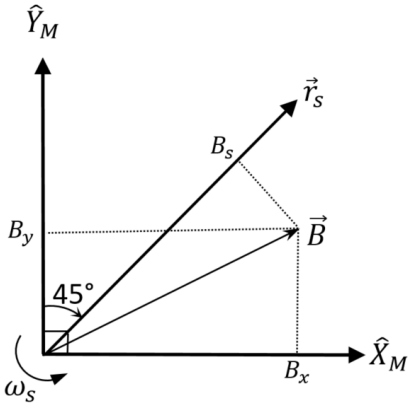

Figure 7. Spinning axes measurements along the vector r_s.

now move on to the spin-axis orientation.

Let the magnetic field components measured by the two orthogonal spinning axes $\hat{X}_M$ and $\hat{Y}_M$ of the magnetometer be B_x and B_y. We now define a new axis $\vec{r}_s$ as in figure (7), in the middle of $\hat{X}_M$ and $\hat{Y}_M$. The magnetic field component B_s along the axis $\vec{r}_s$ now becomes

$$B_s = \frac{B_x}{sqrt2} + \frac{B_y}{sqrt2} \tag{7}$$

The series of measured values given by equation (7), together with the fitted functions of $\alpha_b(t)$, $\alpha_c(t)$, $w_c(t)$ and the scalar value t_0, in equation (6) to find the unknown function $w_s(t)$ and scalar value t_{0s}.

The measured values of B_x and B_y and the calculated values of B_s are plotted together with the fitted scalar value t_{0s} in figure (8). If we assume orthogonal magnetometer axes, the aspect angle of the magnetic field vector component projected on the $\hat{X}_M - \hat{Y}_M$ plane is given by $B_{XY} = acos(\sqrt{1 - B_z^2})$. This angle is included in the plot given in figure (8).

The fitted function $w_s(t)$ is plotted as spin frequency given by $\frac{w_s(t)}{2\pi}$ together with the apparent spin frequency corrected for the coning frequency, i.e. $\left(Apparent\ spin - \frac{w_c(t)}{2\pi}\right)$ in figure (9).

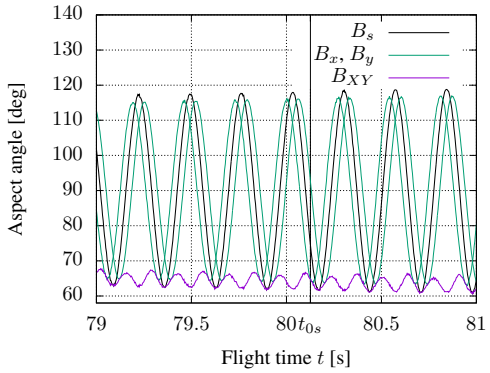

Figure 8. Magnetometer spinning axes measurements B_x and B_y, the calculated magnetic field B_s, fitted scalar value of t_{0s} and projected magnetic field aspect angle B_{XY}.

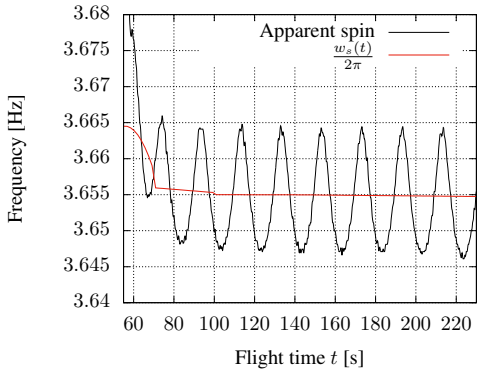

Figure 9. Measured apparent spin corrected for coning frequency (given by $\frac{w_c(t)}{2\pi}$) and fitted function $w_s(t)$ expressed as frequency, i.e. $\frac{w_s(t)}{2\pi}$.

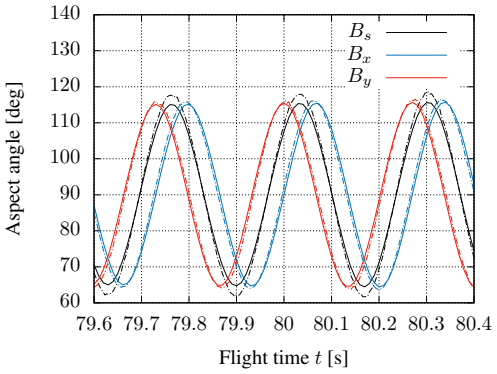

Figure 10. Measured (dashed line) and calculated (filled line) aspect angles of B_x, B_y and B_s.

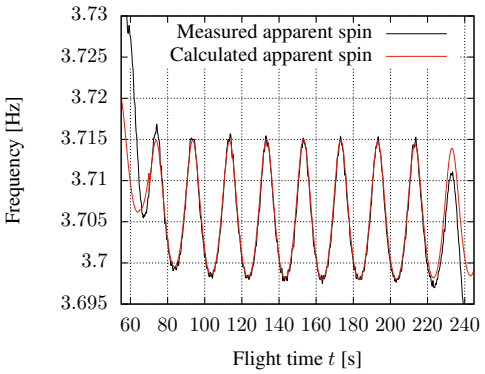

Figure 11. Measured and calculated apparent spin.

Inserting the fitted functions in equation (6) allows us to calculate theoretical values of B_s, B_x and B_y. Those are plotted together with measured values in figure (10).

With the payload spin axis orientation known in the O_B coordinate system it is possible to calculate values of the apparent spin frequency, and analysis of magnetometer spinning axes measurements provides us with the measured apparent spin axis frequency. Those frequencies are plotted in figure (11).

4. PAYLOAD ORIENTATION IN EARTH SYSTEM

Once the functions $\alpha_b(t)$, $\alpha_c(t)$, $w_c(t)$, $w_s(t)$ and the scalar values t_0 and t_{0s} are known we conceptually have everything needed to describe the payload orientation in the O_B and O_C coordinate systems as presented in section (2.1). However, in order to be able to relate the payload orientation to other objects in space we will need to present the orientation as seen from earth. In this section we will present necessary coordinate systems and transformations between O_B system and ultimately the Earth Centered Earth Fixed (ECEF) system.

Let us however begin with having a look at the payload spinning axis orientation as measured by the magnetometer.

4.1. The spinning axis orientation in the O_B coordinate system

The magnetometer is in the standard configuration placed inside the payload section, i.e. surrounded by a metallic cylinder spinning in a slowly changing magnetic field. The spinning cylinder itself generates *eddy currents* [3], giving raise to an induced magnetic field component. Even if the phenomena is complex to understand, the induced magnetic field is reduced to a surprisingly simple relation.

Let us model the payload section hosting the magnetometer as an infinitely long hollow cylinder with radius r and thickness t, spinning with angular velocity w_A in a constant magnetic field $\vec{B}$ orthogonal to the cylinder, as shown in figure (12). The field $\vec{B} = B_X$ should here be understood as the component of the magnetic field projected on the orthogonal plane of the payload, and the angular frequency w_A the *apparent* angular frequency of the payload against the magnetic field.

Inserting a Cartesian coordinate system such that the magnetic field vector is given by $\vec{B} = B_X$ and the payload is spinning from X towards Y, as shown in figure (12), the induced magnetic field is given by

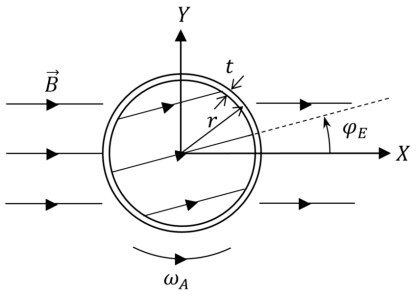

Figure 12. The induced magnetic field of the spinning payload.

$$B_Y = B_X \mu_0 \omega_A \sigma \frac{rt}{2} \tag{8}$$

where μ_0 is the magnetic constant and σ is the electric conductivity of the material.

From equation (8) it directly follows that the eddy correction angle φ_E as shown in figure (12) is given by

$$\varphi_E = atan\left(\frac{B_Y}{B_X}\right) = atan\left(\mu_0 \omega_A \sigma \frac{rt}{2}\right) \tag{9}$$

The magnetic field vector measured by the spinning axes of the magnetometer, and thus used to calculate the spin-axis orientation of the payload, of course includes the induced component as given by equation (8). The calculated spin-axis orientation is thus pointing an angle φ_E along the spin direction of the payload from the projected component of the magnetic field vector.

In terms of section (2.3), the vector $\vec{r}_s$ as visualized in figure (2) becomes by using equation (3) in the O_B coordinate system as

$$\begin{cases} X_B &= \cos(\varphi_s + \varphi_E) \\ Y_B &= \sin(\varphi_s + \varphi_E) \\ Z_B &= 0 \end{cases} \tag{10}$$

where $\varphi_s = \omega_s \cdot (t - t_{0s})$ as given in section (2.3) and φ_E given by equation (9).

In fact, an arbitrary unit vector $\vec{u}$ fixed to the payload and thus spinning with it, described by the

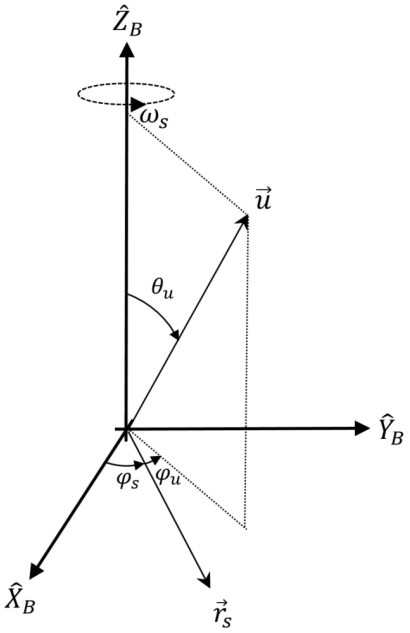

Figure 13. An arbitrary vector $\vec{u}$ in O_B coordinate system.

(constant) angle φ_u as the angle between the vector $\vec{r}_s$ and projection of $\vec{u}$ on the $\hat{X}_B - \hat{Y}_B$ symmetric plane, and θ_u as the angle between payload longitudinal axis $\hat{Z}_B$ and $\vec{u}$, as visualized in figure (13), is in the O_B system given by

$$\begin{cases} X_B &= \sin(\theta_u)\cos(\varphi_s + \varphi_E + \varphi_u) \\ Y_B &= \sin(\theta_u)\sin(\varphi_s + \varphi_E + \varphi_u) \\ Z_B &= \cos(\theta_u) \end{cases} \tag{11}$$

The arbitrary unit vector $\vec{u}$ should in terms of payload engineering be understood as the internal orientation of an arbitrary instrument with respect to the (known) orientation $\vec{r}_s$. Let us now move on to see how this vector can be expressed in the O_C coordinate system.

4.2. Coordinate transformation from O_B to O_C

Using the coordinate systems O_B and O_C as presented in section (2.1) and visualized in figure (1) the basis vector relationship between O_B and O_C are given by

$$\begin{cases} X_C &= X_B\cos(\alpha_c)\cos(\varphi) - \\ &\quad -Y_B\sin(\varphi) + Z_B\sin(\alpha_c)\cos(\varphi) \\ Y_C &= X_B\cos(\alpha_c)\sin(\varphi) + \\ &\quad +Y_B\cos(\varphi) + Z_B\sin(\alpha_c)\sin(\varphi) \\ Z_C &= -X_B\sin(\alpha_c) + Z_B\cos(\alpha_c) \end{cases} \tag{12}$$

where α_c and $\varphi = \omega_c \cdot (t - t_0)$ are as defined in section (2.1)

4.3. Moving from O_C to earth fixed coordinate system

Let us first define new coordinate systems needed to relate the orientation to earth fixed coordinate system.

Let the Earth Fixed Earth Centered (ECEF) coordinate system, $O_E = (\hat{X}_E, \hat{Y}_E, \hat{Z}_E)$ be given by

$\hat{X}_E -$ on the earth equatorial plane, pointing to the zero longitude.

$\hat{Y}_E -$ on the earth equatorial plane, pointing to the 90° longitude.

$\hat{Z}_E -$ perpendicular to the equatorial plane, pointing to the north pole.

The O_E system has its origin at center of earth and is fixed to the rotating earth.

In order to make the coordinate transformations easier to follow we also define the coning axis − inertial coordinate system $O_{CE} = (\hat{X}_{CE}, \hat{Y}_{CE}, \hat{Z}_{CE})$, with origin at payload center of mass and fixed to space described by the instantaneous coning vector and rotating earth, defined by

$\hat{Z}_{CE} -$ along the instantaneous coning vector $\vec{H}$, positive in the Z_B direction, giving $\hat{Z}_{CE} = \hat{Z}_C$.

$\hat{X}_{CE} -$ perpendicular to $\hat{Z}_{CE}$, lying in the $\hat{Z}_{CE} - \hat{Z}_E$ symmetric plane, positive down towards $\hat{X}_E - \hat{Y}_E$ symmetric plane.

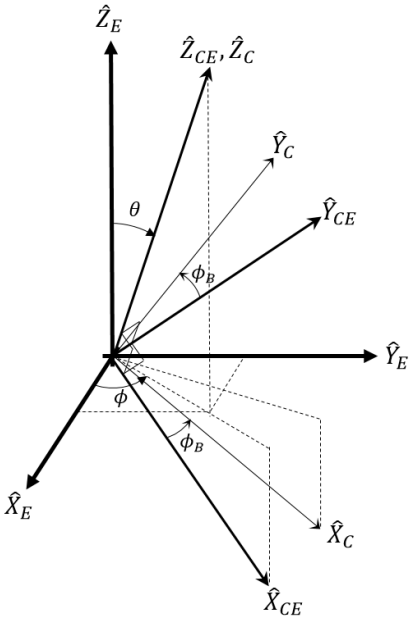

Figure 14. The coordinate systems O_E and O_{CE} with angles θ, ϕ and ϕ_B.

$\hat{Y}_{CE}$ – normal to the $Z_{CE}-X_{CE}$ symmetric plane, fulfilling RHS.

The O_E and O_{CE} coordinate systems are visualized in figure (14).

As shown in figure (14), let us now make the following definitions:

θ – the angle between $\hat{Z}_E$ axis and $\hat{Z}_{CE}$ axis,

ϕ – the angle between $\hat{X}_E$ axis and the projection of $\hat{Z}_{CE}$ to $\hat{X}_E - \hat{Y}_E$ plane, measured from $\hat{X}_E$ toward $\hat{Y}_E$.

Assuming that the coning vector $\vec{H}$ is known, $\vec{H}$ expressed in O_E coordinate system gives us the values of θ and ϕ.

Now, we can express the basis vector transformation from O_{CE} to O_E as

$$\begin{cases} X_E &= X_{CE}\cos(\theta)\cos(\phi) - Y_{CE}\sin(\phi) + \\ &\quad + Z_{CE}\sin(\theta)\cos(\phi) \\ Y_E &= X_{CE}\cos(\theta)\sin(\phi) + Y_{CE}\cos(\phi) + \\ &\quad + Z_{CE}\sin(\theta)\sin(\phi) \\ Z_E &= -X_{CE}\cos(\theta) + Z_{CE}\cos(\theta) \end{cases} \tag{13}$$

The reversed basis vector transformation, from O_E to O_{CE}, is given by

$$\begin{cases} X_{CE} &= X_E\cos(\theta)\cos(\phi) + \\ &\quad + Y_E\cos(\theta)\sin(\phi) - Z_E\sin(\theta) \\ Y_{CE} &= -X_E\sin(\phi) + Y_E\cos(\phi) \\ Z_{CE} &= X_E\sin(\theta)\cos(\phi) + \\ &\quad + Y_E\sin(\theta)\sin(\phi) + Z_E\cos(\theta) \end{cases} \tag{14}$$

Since $\hat{Z}_C = \hat{Z}_{CE} = \frac{\vec{H}}{|H|}$ and both O_C and O_{CE} are orthogonal RHS systems, the transformation from O_C to O_{CE} is just a matter of rotating O_C around its $\hat{Z}_C$ axis. We define the rotation angle as

ϕ_B – the angle between $\hat{X}_{CE}$ axis and $\hat{X}_C$ axis, measured from $\hat{X}_{CE}$ toward $\hat{Y}_{CE}$.

Recalling that the vector $\hat{X}_C$ lies in the $\hat{Z}_{CE} - \vec{B}$ symmetrical plane, the angle ϕ_B is found by transforming the known magnetic field vector $\vec{B}$ to the O_{CE} coordinate system using equation (14).

Now, the basis vector transformation from O_C to O_{CE} is given by

$$\begin{cases} X_{CE} &= X_C\cos(\phi_B) - Y_C\sin(\phi_B) \\ Y_{CE} &= X_C\sin(\phi_B) + Y_C\cos(\phi_B) \\ Z_{CE} &= Z_C \end{cases} \tag{15}$$

4.4. Finding the $\vec{B}$ and $\vec{H}$ vectors

The $\vec{B}$ is found by simply using the World Magnetic Model delivered by NOAA [5].

The function of $\alpha_B(t)$, giving the angle between the magnetic field vector $\vec{B}$ and $\vec{H}$, is known from the analysis of the magnetometer data. The vector $\vec{H}$ could, however, be pointing anywhere along the imaginary cone given by α_B around the magnetic field vector, and yet yield the same resulting magnetometer measurements. The vector $\vec{H}$ can thus not be uniquely identified using the magnetometer alone.

We can however assume that $\vec{H}$ is aligned with the velocity vector of the configuration during non-negligible atmosphere. Helped by the spin of the configuration we can also assume $\vec{H}$ to be constant in the non-rotating space above the atmosphere. These assumptions should remain valid for at least aerodynamic stable configurations.

Finding the vector $\vec{H}$ is thus reduced to finding the time of flight where the aerodynamic forces acting upon the configuration becomes negligible, and at the same time giving a constant orientation of $\vec{H}$ for the theoretical values of angle α_B to remain consistent with measurements during the above-atmosphere part of the flight.

5. MAXIDUSTY1 PAYLOAD ORIENTATION AS SEEN FROM THE EARTH

By carefully modelling the metal surrounding the magnetometer to correspond to the radius and thickness given in table (1), and using σ for the aluminium 6082-T6 alloy, the eddy correction angle φ_E calculated using equation (9) is shown in figure (15).

Table 1. Properties for calculating φ_E

property	value	unit
r	174	mm
t	8	mm
σ	$2.5974 \cdot 10^7$	Sm
μ_0	$4\pi \cdot 10^{-7}$	$\mathrm{N/A^2}$

Figure (16) shows the aspect angle of the magnetic field vector $\vec{B}$ as seen from the velocity vector $\vec{v}$ and the coning vector $\vec{H}$, together with

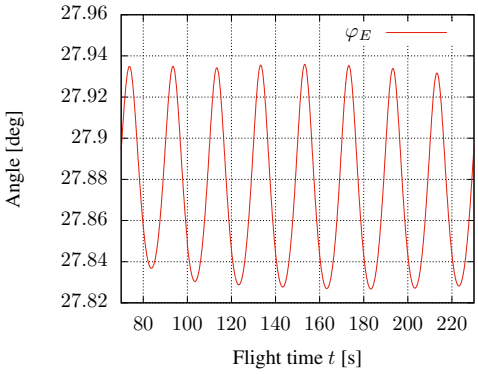

Figure 15. The eddy correction angle φ_E.

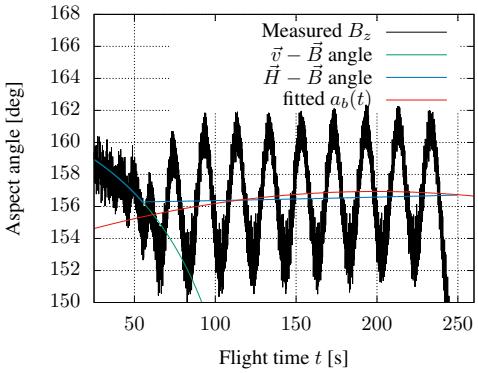

Figure 16. The aspect angle of $\vec{B}$ from $\vec{v}$ and $\vec{H}$ plotted together with $\alpha_b(t)$.

the fitted function $\alpha_b(t)$. As described in section (4.4), the coning vector $\vec{H}$ is chosen to be constant in non-rotating space after flight time $t = 55$ s, corresponding to alt $= 65$ km.

5.1. The orientation of MISU Photometer in MaxiDusty1

The MaxiDusty 1 payload included a photometer owned and developed by MISU [4]. The TM readout of the photometer shows clearly visible peaks when the photometer is pointing towards the sun and thus provide a set of measurements to compare with the calculated orientation of the photometer.

Using equation (11), (12), (15) and finally (13)

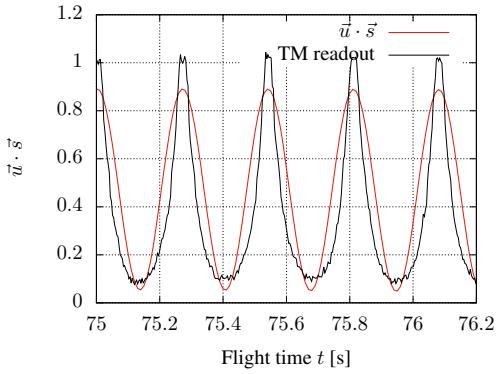

Figure 17. MISU Photometer TM readout together with $\vec{u} \cdot \vec{s}$.

gives us the orientation $\vec{u}$ of the photometer in ECEF coordinate system throughout the flight.

The sun position vector $\vec{s}$ as seen from the payload is calculated using an ASC piece of software based on Naval Observatory Vector Astrometry Software, NOVAS [6].

The scalar product $\vec{u} \cdot \vec{s}$ gives us the component of the photometer orientation aligned with the sun position vector. This scalar product is plotted together with TM readouts in figure (17).

The measured peaks of the photometer seems to match the calculated local maximum values of $\vec{u} \cdot \vec{s}$ very well.

6. ACCURACY OF THE CALCULATED ORIENTATION USING MAGNETOMETER

6.1. Residuals of the fit

The residuals of the calculated longitudinal axis B_z and spin axis B_s orientation during the flight are plotted in figure (18) and (19) respectively. The plots indicates that the accuracy of the calculated orientation is within $\pm 2^\circ$ from the one reflected by the magnetometer measurements.

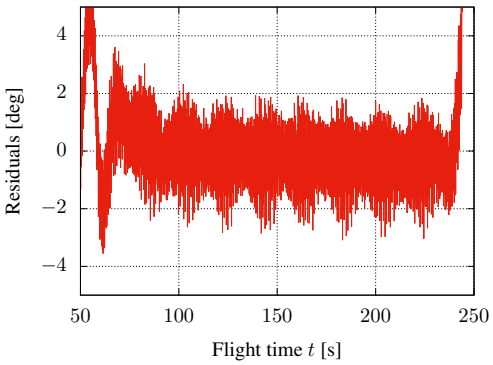

Figure 18. Longitudinal axis B_z residuals.

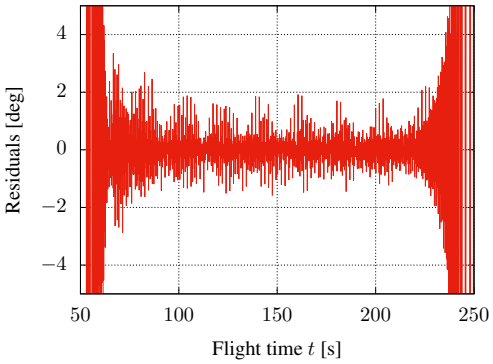

Figure 19. Spinning axis B_s residuals.

6.2. Potential pitfalls

The normalization of the magnetometer measurements, i.e. the transformation of the measured values to aspect angles, is a critical step for an accurate final result. Since the longitudinal axis orientation, i.e. the coning motion, is based on the magnetometer longitudinal axis aspect angles only, errors in normalization will be directly reflected as errors of the longitudinal axis orientation.

The transformation of the longitudinal axes orientation to an earth fixed frame also rely on the accuracy of coning axis $\vec{H}$ orientation. The assumption that $\vec{H}$ remains constant during the free-flight phase, and choosing the point of flight where the aerodynamic forces becomes too weak to align $\vec{H}$ with the velocity vector might at a first glance seem to be suspicious, but the magnetometer measurements gives indications of the validity of the assumption and helps us to choose the point of flight for which the calculated orientation during the free-flight phase matches measurements.

Since the orientation of the spin-axis is assumed to be orthogonal to the longitudinal axis, any inaccuracy of the longitudinal axis is also transformed to corresponding inaccuracy of the spin-axis orientation.

The calculated spinning axis orientation is described by angular velocity and phase of the spinning motion. However, the accuracy of the transformation of the spin-axis orientation to a fixed earth frame is depending on accurate calculations of the eddy effect. This corresponds to a phase shift of typically $25 - 30^\circ$ and thus represents the main source of inaccuracy of the absolute orientation of the spinning axis.

In reality, the magnetometer is not only surrounded by a (non-infinite) metallic cylinder but has also metallic plates, electronics and batteries rotating with it in near vicinity of the sensor, presumably giving additional induced transversal magnetic field component. Accurate calculations of the total effect is demanding and any additional sensors, as for example sun-sensors, provides useful data to correct the calculations.

7. SOME REMARKS ABOUT SUN SENSORS

By normalizing Sun sensor measurements to aspect angles and exchanging the magnetic field vector $\vec{B}$ with the Sun position vector $\vec{S}$ in the equations presented in this document, we are able to calculate the orientation of the payload based on Sun sensors instead of magnetometer using the same method.

The upside of using Sun sensors would be that we get rid of the inaccuracy introduced by the eddy effect. The $\vec{H}$ orientation would however still be based on assumptions, even if the combination of sun sensor and magnetometer conceptually gives us enough data to calculate the orientation of $\vec{H}$.

The downside is of course that the sensor has to be illuminated by the Sun in order to provide us with data, meaning that the orientation of the payload before nose-cone ejection remains unknown.

8. CONCLUSION (AND FURTHER IMPROVEMENTS)

Using the mathematical framework and magnetometer output from Hotel Payload standard magnetometer setup makes it possible to calculate orientation of the payload with a typical accuracy of $\pm 2^\circ$ for the longitudinal axis.

The spinning axis residuals typically indicates an accuracy of $\pm 2^\circ$, but the accuracy of the orientation of this axis outside the payload depends on careful correction of the induced magnetic field component due to the eddy effect.

One of the most obvious improvements is to measure the eddy effect using a spin-bench at a preflight stage when the payload is integrated, assuming that it is practically possible, and thereby create a table with correction angle versus apparent spin frequency.

It might also be worth considering to incorporate a Sun-sensor setup into the Hotel Payload and extend the theoretical framework to take both sensors into account.

REFERENCES

[1] ASC, 2016, LAUNCH REPORT..., MaxiDusty1 launched 30.06.2016, [DocId ASC-R-387]

[2] ASC, DLR Moraba, 2016, FLIGHT REQUIREMENTS PLAN..., [DocId ASC-P-401_0.8, MRB IMQ_MXD_1+2_FRP_0.8]

[3] Aubert G., Jacquinot J.-F, Sakellariou D., 2012, Eddy current effects in plain and hollow cylinders spinning inside homogeneous magnetic fields: Application to magnetic resonance, J. Chem. Phys. 137, 154201 (2012) [http://dx.doi.org/10.1063/1.4756948]

[4] MISU, Department of Meteorology, Stockholm University

[5] NOAA, 2015, The World Magnetic Model, [https://www.ngdc.noaa.gov/geomag/WMM/]

[6] NOVAS, 2011, Naval Observatory Vector Astrometry Software (C Edition C3.1), [http://aa.usno.navy.mil/software/novas/]

LIFE-CELL IMAGING OF F-ACTIN CHANGES INDUCED BY 6 MIN OF MICROGRAVITY ON A TEXUS SOUNDING ROCKET FLIGHT

Marcus Krüger [(1)], **Markus Wehland** [(1)], **Sascha Kopp** [(1)], **Thomas J. Corydon** [(2,3)], **Manfred Infanger** [(1)], **Daniela Grimm** [(1,2)]

[(1)] *Clinic for Plastic, Aesthetic and Hand Surgery, Otto-von-Guericke University, Leipziger Straße 44, 39120 Magdeburg, Emails: marcus.krueger@med.ovgu.de, markus.wehland@med.ovgu.de, sascha.kopp@med.ovgu.de, manfred.infanger@med.ovgu.de*

[(2)] *Department of Biomedicine, Aarhus University, Wilhelm Meyers Allé 4, 8000 Aarhus C, Denmark, Emails: corydon@biomed.au.dk, dgg@biomed.au.dk*

[(3)] *Department of Ophthalmology, Aarhus University Hospital, 8000 Aarhus C, Denmark*

ABSTRACT

We have recently investigated human MCF-7 breast cancer cells after exposure to a Random Positioning Machine (RPM). After 24 h small compact multicellular spheroids (MCS) were detectable; after 5 d many MCS were floating in the supernatant above the remaining adherent cells. The MCS resembled the ducts formed *in vivo* by human epithelial breast cells. Genes belonging to cytoskeleton, cell communication and apoptosis were downregulated. To elucidate the influence of RPM-exposure and possibly early mechanisms of 3D spheroid formation, we are currently preparing a sounding rocket mission. MCF-7 cells stably transfected with a green fluorescing LifeAct-GFP (and mCherry-tubulin) construct will be used to perform life-cell imaging of changes in the actin cytoskeleton during 6 min of microgravity on TEXUS-54. Observations will be made with the FLUMIAS microscope, which has already been successfully used by us in a comparable experiment with thyroid carcinoma cells.

1. BREAST CANCER

Breast cancer is the second most frequent cancer worldwide and the most common invasive cancer in women [1]. Invasive ductal carcinoma (IDC), which starts in epithelial cells of the ducts, is the most common type of breast cancer with an incidence of 80% [2]. The high mortality rate is directly related to its ability to readily metastasize.

There are several treatment options: mastectomy in combination with irradiation and/or estrogen deprivation therapy, but the risk of relapse for estrogen receptor positive breast cancer is still very high.

For our experiments, we will use progesterone and estrogen receptor positive MCF-7 cells that were isolated from a pleural effusion of a patient suffering from IDC [3].

2. BREAST CANCER CELLS IN MICROGRAVITY

In previous experiments we cultured MCF-7 cells on a Random Positioning Machine (RPM), simulating some of the effects of microgravity (μ*g*) [4]. Like with other cancer cells [5, 6] we observed multicellular spheroids after 24 h (Fig. 1B), which are associated with a modified cell environment. In the 2D environment of adherent cells there are diffuse secreted factors, defined cytoskeletal filaments, adhesion points mainly at the bottom of the cells and an extracellular matrix (ECM) layer with high stiffness (Fig. 1E). In the 3D environment of spheroids, the cytoskeletal filaments are diffuse, there are "hotspots" with highly concentrated secreted factors, adhesions in all directions and a relaxed ECM with low stiffness (Fig. 1D).

A completely new finding was the formation of glandular spheroids after 5 d on the RPM (Fig. 1C). In these spheroids, we found duct-like structures with unicellular borders and polarized cells. It seemed that MCF-7 cells attempt to resemble the ducts formed *in vivo* by human epithelial breast cells. To form such structures cells must undergo several processes: communication with other cells, communication with the ECM, directed apoptosis, and polarisation. For cell polarity, cytoskeletal filaments and associated proteins may play a significant role. For example, the polarity of epithelial cells is, among other factors, triggered by actin filaments mainly located on the apical membrane [7].

2.1. Changes of the cytoskeleton

Up to now, it is unknown how human cells sense gravity and convert this stimulus into a biochemical signal. Vorselen *et al.* suggested that the cytoskeleton may act as a "gravisensor" in cells [8]. Indeed, modifications of actin and microtubules during exposure to μ*g* are reported for many cell lines and could be a primary cause for the change in cell architecture [9-13].

In MCF-7 cells Vassy and coworkers found an alteration of microtubules after they were flown for 1.5 h in space [14, 15]. In another study, it has been shown that simulated μ*g* also impedes integrin expression and microtubule formation [16].

Furthermore, many processes observed in μ*g* like membrane blebbing, formation of stress fibres, actin

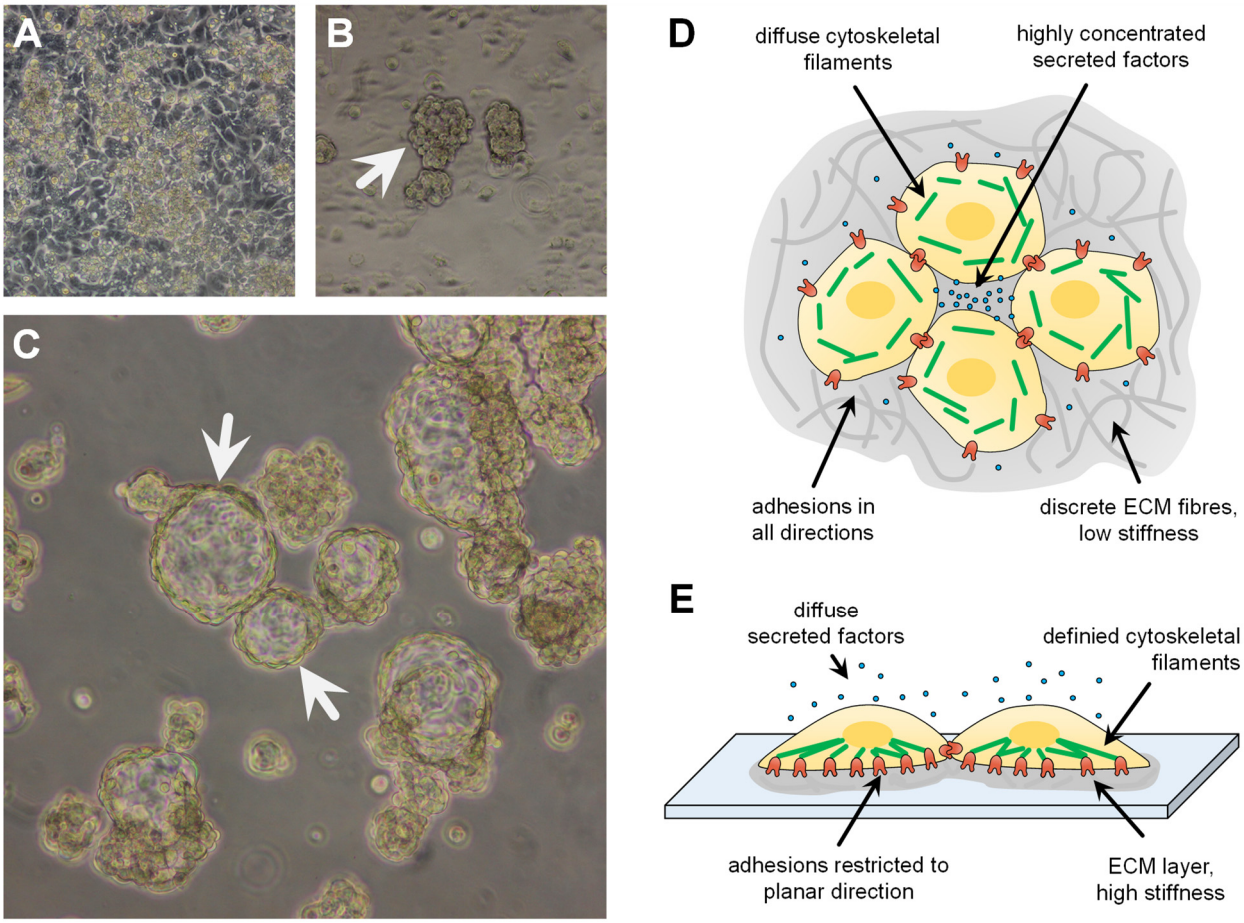

Figure 1. (A) Adherent MCF-7 cells under normal gravity. (B) Formation of multicellular spheroids after 24 h on an RPM. (C) Example for glandular spheroids after 10 d of exposure to the RPM. The illustrations on the right side show the different microenvironments of 2D (D) and 3D (E) cell cultures.

spikes, lamellipodia- and filopodia-like structures are directly or indirectly caused by cytoskeletal modifications [17, 18]. In order to clarify an active involvement of the cytoskeleton in MCF-7 spheroid formation on the RPM, we analysed the expression of different cytoskeletal genes via quantitative real-time PCR (qPCR): In the adherent cells of short-term samples (2-24 h), we did not find any alteration although membrane blebbing (2 h), stress fibres (4 h) and cytoskeletal holes (24 h) could be observed. Later, in the 5 d-spheroids, F-actin was located at the boundaries. Genes for actin, tubulin and the ERM protein family (ezrin, radixin, moesin) were downregulated [4]. The ERM protein family connects the plasma membrane with the actin cytoskeleton by binding to transmembrane receptors like CD44 or intercellular adhesion molecule 1 (ICAM-1) (both mRNA levels were reduced in spheroids as well) [19]. Consequently, variations in ERM expression could result in major modifications of cell-cell and cell-matrix adhesion.

However, the alteration of gene expression is only the last process in a long row of processes (Fig. 2B). We assume that it starts with a structural reorganisation of the cytoskeleton when entering microgravity. One option can be tensegrity (tensional integrity) after gravitational unloading (Fig. 2A) [20, 21]. After the new arrangement of cytoskeletal filaments focal adhesions (FAs) and transmembrane receptors are relocated and can influence intracellular signalling pathways towards the nucleus (i.e. MAPK/ERK, NF-κB) where gene expression is finally adjusted (Fig. 2B) [22]. Moreover, there is some evidence that the actin cytoskeleton directly interacts with stretch-activated ion channels in the plasma membrane what also can affect multiple steps in intracellular signalling [23, 24].

2.2. Changes of the extracellular matrix

The maintenance of numerous cellular processes including cell adhesion, survival, proliferation, differentiation, polarity, and migration relies substantially on ECM proteins and structure. The ECM can determine the cell behaviour and in most cases, it is remodelled to higher stiffness by cancer cells [25-27]. Especially the upregulation of fibronectin is closely connected with tumour progression and tumour cell responsiveness to therapy [28].

Cells can respond to mechanical and biochemical changes in the ECM through the crosstalk between integrins and the actin cytoskeleton [29], forming a dynamic network with an ECM-nucleus connection [30]. Integrins typically cluster within FAs next to the cell membrane and linked to the ECM. FAs are very dynamic and heterogeneous structures with respect to size, composition, and orientation to actin filaments [31]. Changes of the actin cytoskeleton can influence the dynamic regulation of integrin adhesive functions ("inside-out" signalling through talin-interaction with the cytosolic β-subunit) [32, 33]. We proceed on the assumption that integrin recruitment may be a bidirectional process [34, 35]: when cells enter µg mechanical rearrangement of ECM can force a reorganisation of FAs followed up by a remodelling of the actin cytoskeleton and *vice versa*. This results in an adjustment of gene expression leading to a modified matrix (Fig. 2B).

In our study the expression of integrin β1, which is involved in the regulation of actin cytoskeleton [36] and is able to form a fibronectin receptor, was first upregulated after 4 h in (some) adherent cells and later downregulated in the spheroids [4]. For fibroblasts it has been shown, that the fibronectin-integrin connection increases ECM stiffness and is absolutely mandatory for spheroid formation [37]. In MCF-7 spheroids that were exposed to the RPM for 5 d the *FN1* gene was finally downregulated [4]. It seems that cells of spheroids actively modify their ECM.

2.3. Influence on intracellular signalling

Intracellular signalling is crucial for cells to react on various stimuli orchestrating an appropriate response through effector molecules.

When growing on the RPM, MCF-7 cells upregulate genes for interleukin 8 (IL-8), vascular endothelial growth factor (VEGF) and the VEGF receptor Flt-1 during the first 24 h [4]. For endothelial cells, it could be demonstrated that movements of integrins and the actin cytoskeleton play important roles in regulating the shear stress-induced IL-8 gene expression [38]. IL-8 then increases cell adhesion to fibronectin. VEGF and Flt-1 can also be expressed as an answer to mechanical stress [39]. In endothelial cells, VEGF induces an accumulation of stress fibres associated with new actin polymerisation and rapid formation of focal adhesions at the surface of cells [40]. Flt-1 regulates actin reorganisation, which is essential for cell motility and migration [41].

Taken together, in the first hours in µg ECM adhesion and actin reorganisation for enhanced cell motility are genetically organised. These processes could be the first step in detachment of the cells from the surface. At least for thyroid cancer cells it could be shown that IL-8 is important for spheroid formation [42].

In the 5 d-spheroids several genes belonging to signalling pathways (*VEGFA*, *FLK1*, *PRKCA, CASP9*, and untranslated *CASP3* [43]) were downregulated [4].

Though VEGF-dependent pathways seem not to be the dominant driving force in spheroid formation [4], junctional mechanosensors like KDR (VEGFR-2) are able to regulate cytoskeletal stiffening in response to force [44]. Czeisler and Mikawa developed a model of microtubules in KDR signalling, proposing that KDR is trafficked along microtubules after VEGF activation as they found that the loss of microtubules leads to an increase in total KDR levels [45]. Protein kinase Cα influences phospholipase D altering cellular events (like

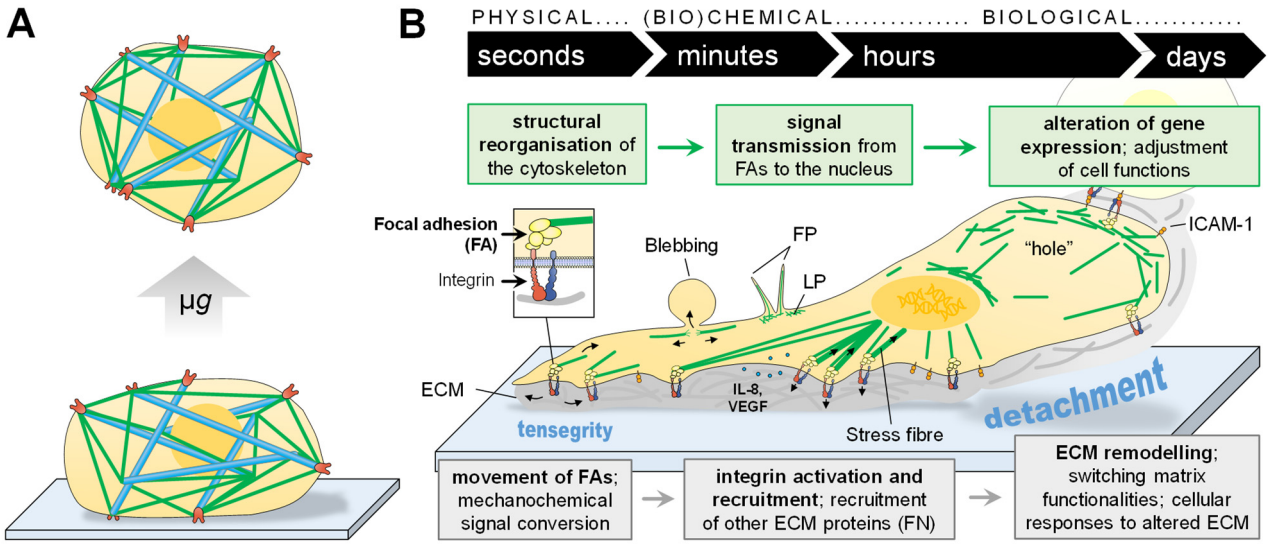

Figure 2. A) The tensegrity model for the explanation of cytoskeletal reorganisation: scheme of a cell in normal gravity (lower image) and of the same cell shortly after entering microgravity (upper image). B) Proposed model for short-term and long-term cellular processes concerning cytoskeleton (F-actin in green) and ECM under microgravity conditions. FP: filopodia-like structure; LP: lamellipodia-like structure.

invasion and migration) and initiates formation of FAs [46] and filopodia-like structures (www.cellsignal.com). Triggers and effects of caspase regulation are not completely understood, but it has been supposed that they could also play a role in the maintenance of cytoskeleton integrity [47].
It seems that in spheroids ECM adhesion, angiogenesis, tumourigenesis and leakiness of cells are reduced which – together with the temporary downregulation of ICAM-1 [48] – could result in a less aggressive phenotype. It is also interesting that proteins like VEGFA are regulated similarly to thyroid cancer cells on the RPM [49-51].
Since the actin cytoskeleton is ubiquitous in eukaryotic cell function it remains unclear where filaments are able to interfere in cell signalling [52]. A summary is given in Fig. 3. Furthermore, several studies have demonstrated a role for actin in triggering apoptosis by filament dynamics and the modulation of actin binding protein function [53, 54]. The investigation of these interactions will be a topic for future studies.

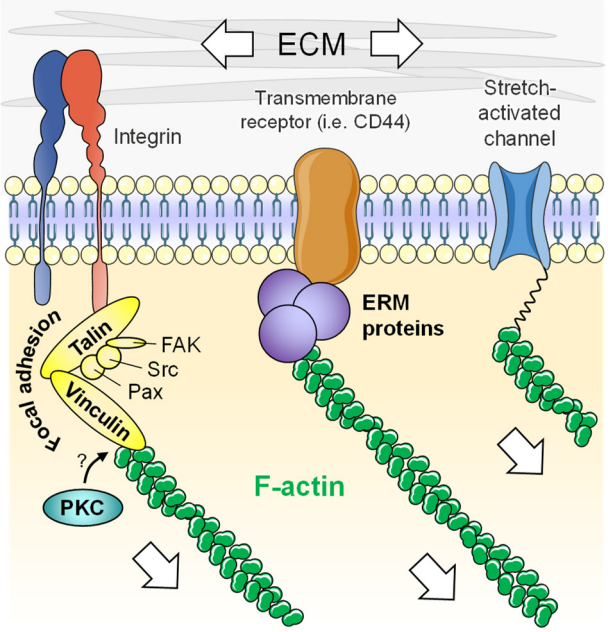

Figure 3. How rearrangement of actin filaments can directly affect cell-matrix interactions, cell shape and membrane transport which in turn influence intracellular signalling. Some parts of the figure were drawn using pictures from Servier Medical Art.

3. LIFE-CELL IMAGING ON TEXUS-54

Our focuses for the next TEXUS mission are the early mechanisms of spheroid formation of MCF-7 cells. As we will use the FLUMIAS microscope during the flight, we can observe possible alterations of the cytoskeleton shortly after entering microgravity. This has been already successfully done with thyroid cancer cells [55].

3.1. Construction of LifeAct-MCF-7 cells

To be able to detect alterations of the cytoskeleton we transfected MCF-7 cells stable with the pLAGITC vector previously used in FTC-133 cells (Fig. 4) [55]. It is composed of a sequence coding for LifeAct-GFP, which can bind to actin filaments, and mCherry-tubulin.

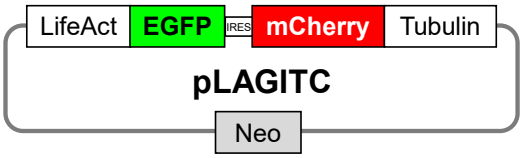

Figure 4. The pLAGITC vector.

3.2. The FLUMIAS module

The FLUMIAS (Fluorescence-Microscopic Analysis Systems for Space Application) confocal laser spinning disc fluorescence microscope was developed by FEI Munich GmbH, Germany. The technical adapted microscope module for parabolic or sounding rocket flights (installation interface, telemetry, experiment service subsystem, etc.) was designed and built by Airbus Defence and Space GmbH. The first version of FLUMIAS has already been used on the 24th DLR parabolic flight campaign and the TEXUS-52 sounding rocket mission (Fig. 5) [55].

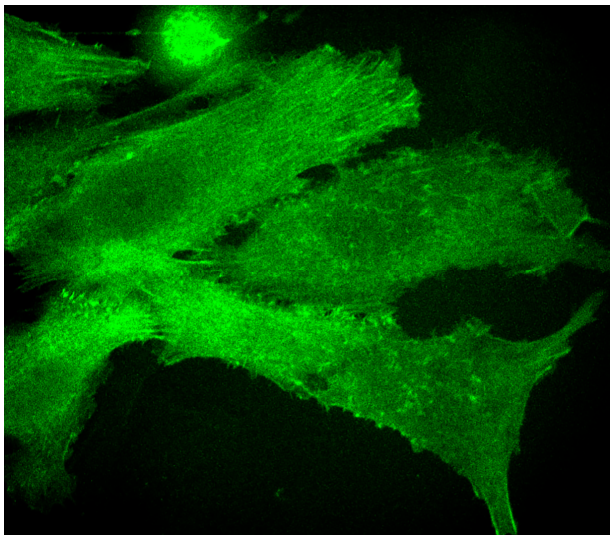

Figure 5. LifeCell image of the actin cytoskeleton in thyroid carcinoma cells expressing LifeAct. The picture was taken with the FLUMIAS module on TEXUS-52.

It was used with a setup that allows parallel scanning of thousands of sample points while eliminating out-of-focus light. This enables for fast imaging with high contrast. Contrary to the first version of FLUMIAS, the improved version will work with water immersion (40x/1.2) instead of air. This will even enhance contrast. In addition, the model used for parabolic flights will be

uncoupled from the aircraft and out-of-focus images due to vibration will be erased.

4. SUMMARY AND OUTLOOK

Gravitational unloading represents short-period mechanical stress for cells but thereafter the influence of microgravity often allows the formation of unique multicellular spheroids. Microgravity is not directly an option for cancer treatment [56] but cancer MCS are an invaluable model for the search for new drug targets. Consequently, it is important to know how cells form such three-dimensional structures.

Mechanotransduction in cells is a complex process, including rearrangement of cytoskeleton and focal adhesions, remodelling of the ECM as well as activation of mechanosensitive channels and membrane transporters (see also Fig. 3). The contribution of molecular deformation on protein function (binding properties, enzymatic activity, lifetime, etc.) has also to be enlightened in future [57, 58]. All processes finally end up in the alteration of signalling pathways and the adaption of gene expression, that clearly differs between spheroids and adherent cells. Interestingly, there are some parallels (gene expression, cytoskeletal structures) between the detachment before spheroid formation and breast cancer cell migration [59-61], where *in vivo* mechanical compression triggers cytoskeletal rearrangement.

One main focus of the next TEXUS mission will be the investigation of early-stage cytoskeletal reorganisation (actin, microtubules) when MCF-7 cells were exposed to microgravity. The investigation will be performed with life-cell imaging of a MCF-7 cell line expressing a LifeAct-GFP marker protein and with the FLUMIAS confocal laser spinning disc fluorescence microscope. TEXUS-54 will be launched from Esrange Space Center, Sweden, in November 2017.

REFERENCES

1. Ferlay, J., Soerjomataram, I., Dikshit, R., Eser, S., Mathers, C., Rebelo, M., Parkin, D.M., Forman, D. & Bray, F. (2015). Cancer incidence and mortality worldwide: sources, methods and major patterns in GLOBOCAN 2012. *Int J Cancer*. **136**(5), E359-386.
2. Arps, D.P., Healy, P., Zhao, L., Kleer, C.G. & Pang, J.C. (2013). Invasive ductal carcinoma with lobular features: a comparison study to invasive ductal and invasive lobular carcinomas of the breast. *Breast Cancer Res Treat*. **138**(3), 719-726.
3. Soule, H.D., Vazguez, J., Long, A., Albert, S. & Brennan, M. (1973). A human cell line from a pleural effusion derived from a breast carcinoma. *J Natl Cancer Inst*. **51**(5), 1409-1416.
4. Kopp, S., Slumstrup, L., Corydon, T.J., Sahana, J., Aleshcheva, G., Islam, T., Magnusson, N.E., Wehland, M., Bauer, J., Infanger, M. & Grimm, D. (2016). Identifications of novel mechanisms in breast cancer cells involving duct-like multicellular spheroid formation after exposure to the Random Positioning Machine. *Sci Rep*. **6**, 26887.
5. Grosse, J., Wehland, M., Pietsch, J., Schulz, H., Saar, K., Hubner, N., Eilles, C., Bauer, J., Abou-El-Ardat, K., Baatout, S., Ma, X., Infanger, M., Hemmersbach, R. & Grimm, D. (2012). Gravity-sensitive signaling drives 3-dimensional formation of multicellular thyroid cancer spheroids. *FASEB J*. **26**(12), 5124-5140.
6. Grimm, D., Kossmehl, P., Shakibaei, M., Schulze-Tanzil, G., Pickenhahn, H., Bauer, J., Paul, M. & Cogoli, A. (2002). Effects of simulated microgravity on thyroid carcinoma cells. *J Gravit Physiol*. **9**(1), P253-256.
7. Li, R. & Gundersen, G.G. (2008). Beyond polymer polarity: how the cytoskeleton builds a polarized cell. *Nat Rev Mol Cell Biol*. **9**(11), 860-873.
8. Vorselen, D., Roos, W.H., Mackintosh, F.C., Wuite, G.J. & Van Loon, J.J. (2014). The role of the cytoskeleton in sensing changes in gravity by nonspecialized cells. *FASEB J*. **28**(2), 536-547.
9. Hughes-Fulford, M. (2003). Function of the cytoskeleton in gravisensing during spaceflight. *Adv Space Res*. **32**(8), 1585-1593.
10. Maier, J.A.M., Cialdai, F., Monici, M. & Morbidelli, L. (2015). The Impact of Microgravity and Hypergravity on Endothelial Cells. *Biomed Res Int*. **2015**, 434803.
11. Corydon, T.J., Mann, V., Slumstrup, L., Kopp, S., Sahana, J., Askou, A.L., Magnusson, N.E., Echegoyen, D., Bek, T., Sundaresan, A., Riwaldt, S., Bauer, J., Infanger, M. & Grimm, D. (2016). Reduced Expression of Cytoskeletal and Extracellular Matrix Genes in Human Adult Retinal Pigment Epithelium Cells Exposed to Simulated Microgravity. *Cell Physiol Biochem*. **40**(1-2), 1-17.
12. Carlsson, S.I.M., Bertilaccio, M.T.S., Ballabio, E. & Maier, J.a.M. (2003). Endothelial stress by gravitational unloading: effects on cell growth and cytoskeletal organization. *Biochim Biophys Acta, Mol Cell Res*. **1642**(3), 173-179.
13. Aleshcheva, G., Wehland, M., Sahana, J., Bauer, J., Corydon, T.J., Hemmersbach, R., Frett, T., Egli, M., Infanger, M., Grosse, J. & Grimm, D. (2015). Moderate alterations of the cytoskeleton in human chondrocytes after short-term microgravity produced by parabolic flight maneuvers could be prevented by up-regulation of BMP-2 and SOX-9. *FASEB J*. **29**(6), 2303-2314.
14. Vassy, J., Portet, S., Beil, M., Millot, G., Fauvel-Lafeve, F., Karniguian, A., Gasset, G., Irinopoulou, T., Calvo, F., Rigaut, J.P. & Schoevaert, D. (2001). The effect of weightlessness on cytoskeleton architecture and proliferation of human breast cancer cell line MCF-7. *FASEB J*. **15**(6), 1104-

1106.
15. Vassy, J., Portet, S., Beil, M., Millot, G., Fauvel-Lafeve, F., Gasset, G. & Schoevaert, D. (2003). Weightlessness acts on human breast cancer cell line MCF-7. *Adv Space Res*. **32**(8), 1595-1603.
16. Li, J., Zhang, S., Chen, J., Du, T., Wang, Y. & Wang, Z. (2009). Modeled microgravity causes changes in the cytoskeleton and focal adhesions, and decreases in migration in malignant human MCF-7 cells. *Protoplasma*. **238**(1-4), 23-33.
17. Charras, G.T. (2008). A short history of blebbing. *J Microsc*. **231**(3), 466-478.
18. Zigmond, S.H. (1996). Signal transduction and actin filament organization. *Curr Opin Cell Biol*. **8**(1), 66-73.
19. Fehon, R.G., Mcclatchey, A.I. & Bretscher, A. (2010). Organizing the cell cortex: the role of ERM proteins. *Nat Rev Mol Cell Biol*. **11**(4), 276-287.
20. Ingber, D.E., Wang, N. & Stamenovic, D. (2014). Tensegrity, cellular biophysics, and the mechanics of living systems. *Rep Prog Phys*. **77**(4), 046603.
21. Ingber, D. (1999). How cells (might) sense microgravity. *FASEB J*. **13 Suppl**, S3-15.
22. Najrana, T. & Sanchez-Esteban, J. (2016). Mechanotransduction as an Adaptation to Gravity. *Front Pediatr*. **4**(140).
23. Mazzochi, C., Benos, D.J. & Smith, P.R. (2006). Interaction of epithelial ion channels with the actin-based cytoskeleton. *Am J Physiol Renal Physiol*. **291**(6), F1113-1122.
24. Mills, J.W., Schwiebert, E.M. & Stanton, B.A. (1994). The cytoskeleton and membrane transport. *Curr Opin Nephrol Hypertens*. **3**(5), 529-534.
25. Nam, J.M., Onodera, Y., Bissell, M.J. & Park, C.C. (2010). Breast cancer cells in three-dimensional culture display an enhanced radioresponse after coordinate targeting of integrin alpha5beta1 and fibronectin. *Cancer Res*. **70**(13), 5238-5248.
26. Marastoni, S., Ligresti, G., Lorenzon, E., Colombatti, A. & Mongiat, M. (2008). Extracellular matrix: a matter of life and death. *Connect Tissue Res*. **49**(3), 203-206.
27. Huang, S. & Ingber, D.E. (2005). Cell tension, matrix mechanics, and cancer development. *Cancer Cell*. **8**(3), 175-176.
28. Wang, J.P. & Hielscher, A. (2017). Fibronectin: How Its Aberrant Expression in Tumors May Improve Therapeutic Targeting. *Journal of Cancer*. **8**(4), 674-682.
29. Kim, S.H., Turnbull, J. & Guimond, S. (2011). Extracellular matrix and cell signalling: the dynamic cooperation of integrin, proteoglycan and growth factor receptor. *J Endocrinol*. **209**(2), 139-151.
30. Spencer, V.A., Xu, R. & Bissell, M.J. (2010). Gene Expression in the Third Dimension: The ECM-nucleus Connection. *J Mammary Gland Biol Neoplasia*. **15**(1), 65-71.
31. Zamir, E., Katz, B.Z., Aota, S., Yamada, K.M., Geiger, B. & Kam, Z. (1999). Molecular diversity of cell-matrix adhesions. *J Cell Sci*. **112**(11), 1655-1669.
32. Hughes, P.E. & Pfaff, M. (1998). Integrin affinity modulation. *Trends in Cell Biology*. **8**(9), 359-364.
33. Calderwood, D.A., Shattil, S.J. & Ginsberg, M.H. (2000). Integrins and Actin Filaments: Reciprocal Regulation of Cell Adhesion and Signaling. *J Biol Chem*. **275**(30), 22607-22610.
34. Schoenwaelder, S.M. & Burridge, K. (1999). Bidirectional signaling between the cytoskeleton and integrins. *Curr Opin Cell Biol*. **11**(2), 274-286.
35. Hynes, R.O. (2002). Integrins: bidirectional, allosteric signaling machines. *Cell*. **110**(6), 673-687.
36. Klahan, S., Wu, M.S., Hsi, E., Huang, C.C., Hou, M.F. & Chang, W.C. (2014). Computational analysis of mRNA expression profiles identifies the ITG family and PIK3R3 as crucial genes for regulating triple negative breast cancer cell migration. *Biomed Res Int*. **2014**, 536591.
37. Salmenperä, P., Kankuri, E., Bizik, J., Sirén, V., Virtanen, I., Takahashi, S., Leiss, M., Fässler, R. & Vaheri, A. (2008). Formation and activation of fibroblast spheroids depend on fibronectin–integrin interaction. *Exp Cell Res*. **314**(19), 3444-3452.
38. Cheng, M., Wu, J., Liu, X., Li, Y., Nie, Y., Li, L. & Chen, H. (2007). Low shear stress-induced interleukin-8 mRNA expression in endothelial cells is mechanotransduced by integrins and the cytoskeleton. *Endothelium*. **14**(6), 265-273.
39. Beckmann, R., Houben, A., Tohidnezhad, M., Kweider, N., Fragoulis, A., Wruck, C.J., Brandenburg, L.O., Hermanns-Sachweh, B., Goldring, M.B., Pufe, T. & Jahr, H. (2014). Mechanical Forces Induce Changes in VEGF and VEGFR-1/sFlt-1 Expression in Human Chondrocytes. *Int J Mol Sci*. **15**(9), 15456-15474.
40. Rousseau, S., Houle, F., Kotanides, H., Witte, L., Waltenberger, J., Landry, J. & Huot, J. (2000). Vascular Endothelial Growth Factor (VEGF)-driven Actin-based Motility Is Mediated by VEGFR2 and Requires Concerted Activation of Stress-activated Protein Kinase 2 (SAPK2/p38) and Geldanamycin-sensitive Phosphorylation of Focal Adhesion Kinase. *J Biol Chem*. **275**(14), 10661-10672.
41. Kanno, S., Oda, N., Abe, M., Terai, Y., Ito, M., Shitara, K., Tabayashi, K., Shibuya, M. & Sato, Y. (2000). Roles of two VEGF receptors, Flt-1 and KDR, in the signal transduction of VEGF effects in human vascular endothelial cells. *Oncogene*. **19**(17), 2138-2146.
42. Svejgaard, B., Wehland, M., Ma, X., Kopp, S., Sahana, J., Warnke, E., Aleshcheva, G., Hemmersbach, R., Hauslage, J., Grosse, J., Bauer, J., Corydon, T.J., Islam, T., Infanger, M. & Grimm,

D. (2015). Common Effects on Cancer Cells Exerted by a Random Positioning Machine and a 2D Clinostat. *PLoS ONE*. **10**(8), e0135157.
43. Liang, Y., Yan, C. & Schor, N.F. (2001). Apoptosis in the absence of caspase 3. *Oncogene*. **20**(45), 6570-6578.
44. Givens, C. & Tzima, E. (2016). Endothelial Mechanosignaling: Does One Sensor Fit All? *Antioxid Redox Signal*. **25**(7), 373-388.
45. Czeisler, C. & Mikawa, T. (2013). Microtubules Coordinate VEGFR2 Signaling and Sorting. *PLoS ONE*. **8**(9), e75833.
46. Hu, T. & Exton, J.H. (2004). Protein Kinase Cα Translocates to the Perinuclear Region to Activate Phospholipase D1. *J Biol Chem*. **279**(34), 35702-35708.
47. Watanabe, Y. & Akaike, T. (1999). Possible involvement of caspase-like family in maintenance of cytoskeleton integrity. *J Cell Physiol*. **179**(1), 45-51.
48. Rosette, C., Roth, R.B., Oeth, P., Braun, A., Kammerer, S., Ekblom, J. & Denissenko, M.F. (2005). Role of ICAM1 in invasion of human breast cancer cells. *Carcinogenesis*. **26**(5), 943-950.
49. Bauer, J., Kopp, S., Schlagberger, E.M., Grosse, J., Sahana, J., Riwaldt, S., Wehland, M., Luetzenberg, R., Infanger, M. & Grimm, D. (2017). Proteome Analysis of Human Follicular Thyroid Cancer Cells Exposed to the Random Positioning Machine. *Int J Mol Sci*. **18**(3).
50. Kopp, S., Warnke, E., Wehland, M., Aleshcheva, G., Magnusson, N.E., Hemmersbach, R., Corydon, T.J., Bauer, J., Infanger, M. & Grimm, D. (2015). Mechanisms of three-dimensional growth of thyroid cells during long-term simulated microgravity. *Sci Rep*. **5**, 16691.
51. Riwaldt, S., Bauer, J., Wehland, M., Slumstrup, L., Kopp, S., Warnke, E., Dittrich, A., Magnusson, N.E., Pietsch, J., Corydon, T.J., Infanger, M. & Grimm, D. (2016). Pathways Regulating Spheroid Formation of Human Follicular Thyroid Cancer Cells under Simulated Microgravity Conditions: A Genetic Approach. *Int J Mol Sci*. **17**(4), 528.
52. Carpenter, C.L. (2000). Actin cytoskeleton and cell signaling. *Crit Care Med*. **28**(4 Suppl), N94-99.
53. Desouza, M., Gunning, P.W. & Stehn, J.R. (2012). The actin cytoskeleton as a sensor and mediator of apoptosis. *Bioarchitecture*. **2**(3), 75-87.
54. Franklin-Tong, Vernonica e. & Gourlay, Campbell w. (2008). A role for actin in regulating apoptosis/programmed cell death: evidence spanning yeast, plants and animals. *Biochem J*. **413**(3), 389-404.
55. Corydon, T.J., Kopp, S., Wehland, M., Braun, M., Schutte, A., Mayer, T., Hulsing, T., Oltmann, H., Schmitz, B., Hemmersbach, R. & Grimm, D. (2016). Alterations of the cytoskeleton in human cells in space proved by life-cell imaging. *Sci Rep*. **6**, 20043.
56. Sahebi, R., Aghaei, M., Halvaei, S. & Alizadeh, A. (2017). The Role of Microgravity in Cancer: A Dual-edge Sword. *Multidisciplinary Cancer Investigation*. **1**(3), 1-5.
57. Alonso, J.L. & Goldmann, W.H. (2016). Cellular mechanotransduction. *AIMS Biophysics*. **3**(1), 50-62.
58. Hu, X., Margadant, F.M., Yao, M. & Sheetz, M.P. (2017). Molecular stretching modulates mechanosensing pathways. *Protein Sci*. **26**(7), 1337-1351.
59. Tse, J.M., Cheng, G., Tyrrell, J.A., Wilcox-Adelman, S.A., Boucher, Y., Jain, R.K. & Munn, L.L. (2012). Mechanical compression drives cancer cells toward invasive phenotype. *Proc Natl Acad Sci U S A*. **109**(3), 911-916.
60. Wirtz, D., Konstantopoulos, K. & Searson, P.C. (2011). The physics of cancer: the role of physical interactions and mechanical forces in metastasis. *Nat Rev Cancer*. **11**(7), 512-522.
61. Paszek, M.J., Zahir, N., Johnson, K.R., Lakins, J.N., Rozenberg, G.I., Gefen, A., Reinhart-King, C.A., Margulies, S.S., Dembo, M., Boettiger, D., Hammer, D.A. & Weaver, V.M. (2005). Tensional homeostasis and the malignant phenotype. *Cancer Cell*. **8**(3), 241-254.

COMPARISON OF IN-SITU BALLOON-BORNE AND LIDAR MEASUREMENT OF CIRRUS CLOUDS

Thomas Kuhn[1], **Veronika Wolf**[1], **Peter Völger**[2], **Marin Stanev**[3], **and Jörg Gumbel**[3]

[1]*Luleå University of Technology, Department of Computer Science, Electrical and Space Engineering, Division of Space Technology, 98128 Kiruna, Sweden*
[2]*The Swedish Institute of Space Physics (IRF), Polar Atmospheric Research Programme, Kiruna, Sweden*
[3]*Stockholm University, Department of Meteorology (MISU), Stockholm, Sweden*

ABSTRACT

A series of in-situ balloon-borne experiments conducted at Kiruna, Sweden (68 °N), is studying upper-tropospheric, cold ice clouds in arctic latitudes. Experiments are launched from Esrange Space Center and collect ice particles with an in-situ imaging instrument. One of the aims with these measurements is to improve satellite remote sensing of cold ice clouds. Such clouds can be observed by lidar. Therefore, when possible, concurrent ground-based lidar measurements have been carried out with two available lidar systems to accompany the balloon-borne measurements. The Esrange lidar is located at Esrange Space Center, approximately 500 m from the in-situ launch site on the balloon pad; the IRF lidar is located about 29 km to the west of Esrange Space Center (operated by the Swedish Institute of Space Physics, IRF). Here we present results from these lidar measurements and compare them to ice particle properties determined during the in-situ measurements.

Key words: Cirrus; ice clouds; lidar; ice particles; in-situ; balloon-borne; Arctic; high latitude measurements.

1. INTRODUCTION

Upper-tropospheric cold ice clouds (cirrus) play an important role in the radiative energy budget of the atmosphere [1]. They can both have a cooling as well as a warming effect as they reflect part of the incoming shortwave radiation and absorb part of Earth's outgoing longwave radiation, respectively. The net effect depends on the various cloud's macro- and microphysical properties, such as size and shape of ice particles.

Cirrus can be detected remotely by lidar and cloud radar. However, they are often thin and are consequently better observed by the more sensitive lidar while they are invisible or very weak to the cloud radar [2]. For these cases improved satellite retrieval methods will allow better ice cloud determination by space-borne lidar only. Retrieval methods for remote sensing of ice cloud properties require good knowledge of the microphysical properties of ice clouds, as for example shapes and size distributions of ice particles [1, 3]. Also radiative transfer simulations and climate models that include cloud processes need such knowledge. In-situ measurements are therefore necessary to acquire these properties.

Many in-situ measurements have already been performed by aircraft-mounted instruments. A review of some of the recent campaigns can be found for example in [4]. However, there are some problems associated with aircraft-based instruments. Shattering of larger ice particles at the inlet due to high impact speed causes many smaller fragments that may be detected erroneously as many small ice particles [5]. Instruments can now correct for this and/or avoid shattering [6], but the problem can not be eliminated entirely [7]. Also, most in-situ aircraft instruments have problems detecting and sizing ice particles smaller than about 100 µm [8] and in addition shapes of these particles remain uncertain [9]. Balloon-borne measurements do not suffer from shattering problems and smaller ice particles can be measured more accurately [10, 11]. In addition, they directly measure near to vertical profiles, which is an advantage when comparing to vertically sensing lidar measurements and for radiative transfer simulations.

Compared to mid- or tropical latitudes, only few in-situ measurements, both aircraft- and balloon-borne, exist at northerly, arctic latitudes [e.g. 12]. Furthermore, only few direct comparisons between ground-based lidar and in-situ measurements have been done [e.g 13]. Therefore, we have started balloon-borne in-situ measurements of high latitude, upper-tropospheric, cold ice clouds with concurrent ground-based lidar measurements. In the following, we describe first comparisons between these lidar and in-situ measurements of ice clouds.

2. EXPERIMENTAL METHODS

2.1. Balloon-borne in-situ measurements

2.1.1. Balloon campaign

The in-situ measurements used in this study are from an ongoing campaign of balloon-borne measurements of ice cloud particles, 'in-situ IWC' [14, 11]. A series of balloon launches has started in 2012. All balloons are launched from Esrange Space Center (67.9 °N 21.1 °E), about 30 km east of Kiruna located in northern Sweden, north of the Arctic circle. On the campaign days, balloon measurements have been carried out during morning up to around local noon. This allows for recovery by helicopter at daylight on the same day. The balloons on the campaign days considered here were launched from around 9:30 to 11:30 UTC (10:30 to 12:30 local time).

2.1.2. In-situ measurement method

The instrument carried by balloon is collecting individual ice particles on an oil-coated film. Particles are shortly after collection imaged with a high-resolution camera system that allows measurements of small ice particles. From the particle images size, area, and shape of particles with sizes down to about 20 µm can be determined. In addition to these single particle properties, ensembles are characterised by number and area concentrations and size distributions. Details of the instrument and the related image analysis methods have been described earlier [11].

The extinction coefficient $\alpha_{\text{in-situ}}$ of an ensemble of sampled ice particles in a cirrus can be determined from the image data by determining the cross-sectional area of this ensemble of particles. The sum of the individual ice particle areas is divided by the corresponding sampling volume, which yields the area concentration. The extinction cross section of an individual ice particle is given by twice its cross sectional area in the geometric scattering case that is applicable here where particle dimension is much larger than the wavelength of visible light. Hence, the local extinction coefficient is given by twice the area concentration of a representative ensemble of ice particles at that location. Then, from the extinction coefficients throughout a cirrus, along the vertical profile sampled by the balloon-borne in-situ measurements, the optical depth $\tau_{\text{in-situ}}$ can be determined by integrating over $\alpha_{\text{in-situ}}$ vertically through the cirrus cloud.

2.2. Ground-based lidar measurements

2.2.1. Lidar systems

During the campaign, when possible, the balloon-borne in-situ measurements have been accompanied by concurrent lidar measurements by at least one of the two ground-based lidars, the lidar at IRF or at Esrange Space Center. The IRF lidar is located about 1 km from the Space Campus in Kiruna, which is around 3 km east of Kiruna airport and 29 km west of Esrange Space Center. This lidar is operated by the Swedish Institute of Space Physics (IRF). It uses elastic backscattering at 532 nm wavelength to detect clouds in an altitude range of 4 km to 15 km under daylight conditions. Data from the IRF lidar has a vertical resolution of 30 m and an averaging time of 133 s. More details about the IRF lidar can be found in [15].

The Esrange lidar is located at the Esrange Space Center on a hill that is around 500 m away from the location on the balloon pad where the in-situ balloons are launched. This lidar is operated by Stockholm University. It is a Rayleigh/Mie/Raman backscatter lidar. The lidar data used in this study uses the backscatter signals from the elastic low- and medium sensitivity Rayleigh channels at 532 nm wavelength covering the atmosphere from about 4 km to 30 km altitude during daylight conditions. The backscattered light is filtered through density tuned fixed-spacer etalons for that purpose. The Esrange lidar has a vertical resolution of 150 m and a time resolution of approximately 5 min. More details about the Esrange lidar can be found in [16].

2.2.2. Cirrus analysis with lidar

The free tropospheric aerosol in the measurement region in this study has very low concentrations compared to lower latitude locations in the northern hemisphere [17]. Therefore, we assume here that the lidar backscatter is caused only by atmospheric molecular scattering and backscatter from cirrus ice particles. Below and above clouds we expect only atmospheric backscatter. Below a cloud this signal is not affected by the cloud. Hence, there the signal can be predicted from the atmospheric molecular density, which is known from the temperature profile acquired by radio sonde measurements that accompany all balloon-borne measurements.

The backscatter signal from above a cirrus cloud can also be predicted, however, the signal is now attenuated by the presence of the cirrus. This attenuation, i.e. the optical depth of the cirrus cloud layer, can be determined by independently fitting the atmospheric backscatter below and above the cloud layer. The resulting factor between these two fits is attributed to attenuation of the cirrus and equal to its transmission squared, T^2_{cirrus}, which can be converted to its optical depth τ_{lidar} by

$$\tau_{\text{lidar}} = -\ln T_{\text{cirrus}} \tag{1}$$

For this purpose, the cloud bottom and top is determined for each lidar profile. Then the expected atmospheric scattering is fitted to the signal below the cloud bottom and above the cloud top.

Different methods exist for considering the molecular background within the cirrus layer, so that the fitted signals below the bottom and above top of the cirrus can be joined to form a continuos atmospheric molecular backscattering component S_{bg} of the signal, the atmospheric background scattering. This background can then be compared to the total signal within the cirrus layer, i.e. the sum of both signal components due to cirrus (S_{cirrus}) and atmospheric background scattering (S_{bg}). The ratio between the total backscatter and the background scattering signals is called backscatter ratio, or BSR.

$$\mathrm{BSR} = \frac{S_{\mathrm{cirrus}} + S_{\mathrm{bg}}}{S_{\mathrm{bg}}} \tag{2}$$

The backscatter ratio can also be expressed in terms of the backscatter coefficients for cirrus ($\beta_{\mathrm{lidar}}^{\mathrm{cirrus}}$) and background scattering($\beta_{\mathrm{lidar}}^{\mathrm{bg}}$):

$$\mathrm{BSR} = \frac{\beta_{\mathrm{lidar}}^{\mathrm{cirrus}} + \beta_{\mathrm{lidar}}^{\mathrm{bg}}}{\beta_{\mathrm{lidar}}^{\mathrm{bg}}} \tag{3}$$

The backscatter coefficient $\beta_{\mathrm{lidar}}^{\mathrm{bg}}$ of the background atmosphere can be determined from the atmospheric molecular density and the cross section of air molecules for backscattering at 532 nm (differential Rayleigh cross section of 6.1810^{-28} cm^2 sr^{-1}). From this, together with BSR, the cirrus' backscatter coefficient $\beta_{\mathrm{lidar}}^{\mathrm{cirrus}}$ can be inferred using Eq. 3. While no assumptions were required to determine the cirrus optical depth directly from comparisons of signals above and below the cirrus layer, now assumptions are needed to determine BSR and $\beta_{\mathrm{lidar}}^{\mathrm{cirrus}}$. Within the cirrus $\beta_{\mathrm{lidar}}^{\mathrm{bg}}$ needs to be known, hence, an assumption on how exactly $\beta_{\mathrm{lidar}}^{\mathrm{bg}}$ varies in the cirrus layer is required.

Even more assumptions are required to determine the extinction coefficient of the cirrus cloud, which is therefore the most uncertain cirrus optical property to be retrieved. This is due to the fact that there are two unknowns, the backscatter and extinction coefficients, and only one received backscatter signal [18, 19]. The ratio between cirrus extinction ($\alpha_{\mathrm{lidar}}^{\mathrm{cirrus}}$) and backscatter coefficients ($\beta_{\mathrm{lidar}}^{\mathrm{cirrus}}$) is called the lidar ratio L_{cirrus}. One needs to know L_{cirrus} so that $\beta_{\mathrm{lidar}}^{\mathrm{cirrus}}$ can be converted to $\alpha_{\mathrm{lidar}}^{\mathrm{cirrus}}$. Further, an assumption on how L_{cirrus} varies within the cirrus (and over time) is required. If we assume a constant L_{cirrus}, then

$$\alpha_{\mathrm{lidar}}^{\mathrm{cirrus}} = \beta_{\mathrm{lidar}}^{\mathrm{cirrus}} L_{\mathrm{cirrus}} \tag{4}$$

This can then be compared to the extinction coefficients $\alpha_{\text{in-situ}}$ determined from in-situ ice particle image data (see Sect. 2.1.2). Here, we assume a lidar ratio $L_{\mathrm{cirrus}} = 20$ sr, which is well within the large range of lidar ratios reported in the literature [e.g. 20, 21, 22].

3. MEASUREMENT RESULTS AND ANALYSIS

3.1. Measurement days

In-situ data have been collected on eight days so far from 2012-04-04 until 2016-12-15. Accompanying lidar data, however, are not available from all these days. On some occasions lidar measurements were not possible due to different reasons such as low-altitude liquid-phase clouds that were too optically thick obscuring the cirrus atop, ongoing lidar repairs/updates, or unavailability of lidar personnel. In the following Sections 3.2 and 3.3 lidar data from two days have been considered: 2013-02-20 (IRF and Esrange lidars) and 2016-02-12 (IRF lidar). On 2016-02-12 the cirrus originated from a warm front along the Swedish–Finish border associated to a strong low-pressure system over the northern Baltic Sea. On 2013-02-20 Kiruna was affected by a strong, northwesterly wind, which led to orographic lifting and mountain lee waves, causing a cirrus layer. The wind was originated from the cold front of a low-pressure system over Spitsbergen pushing air masses against a high-pressure system dominating Scandinavia.

3.2. 2016-02-12

3.2.1. Raw signals of IRF lidar

Fig. 1 shows the raw signal as a colour plot with all profiles measured by the IRF lidar on 2016-02-12. During the time of the balloon launch, from 9:40 to 10:40 UTC (10:40 to 11:40 local time), a cirrus layer can be seen between approximately 5 km and 8 km altitude. Altitude here refers to the lidar range, i.e. the vertical distance from lidar to the cloud layer from which backscattering is received. Later, when comparing lidar and in-situ data, the in-situ altitude (above sea level) is converted to range by subtracting 0.4 km, the actual altitude of the two lidars.

This cloud layer persisted for several hours, as long as measurements were recorded with the lidar. The figure shows at about 10:40 to 11:00 UTC (11:40 to 12:00 local time) an additional lower cloud layer at approximately 2 km altitude. It can be noted how this cloud layer is disturbing the cirrus observations above because it is attenuating the lidar signal.

As an example, Fig. 2 shows a backscatter signal with background noise removed of the IRF lidar on 2016-02-12 for one profile, at 9:38 UTC (10:38 local time). One can clearly see that the signal is predominantly caused by a cirrus layer between about 5 km and 10 km. The expected signal from atmospheric molecular backscattering (atmospheric background) is also shown for reference as dashed line. A second dashed line shows the same atmospheric background but scaled by a factor that can be attributed to attenuation by the cloud, i.e. its optical depth τ_{lidar} (see Sect. 2.2.2), which for this example was 2.0.

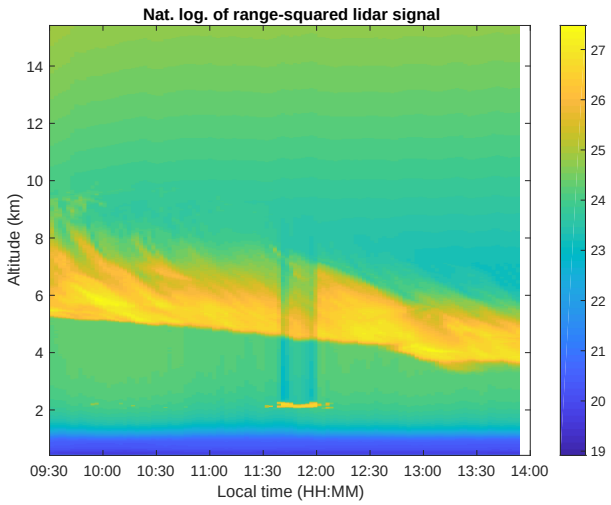

Figure 1. Raw signal of IRF lidar on 2016-02-12, range-squared.

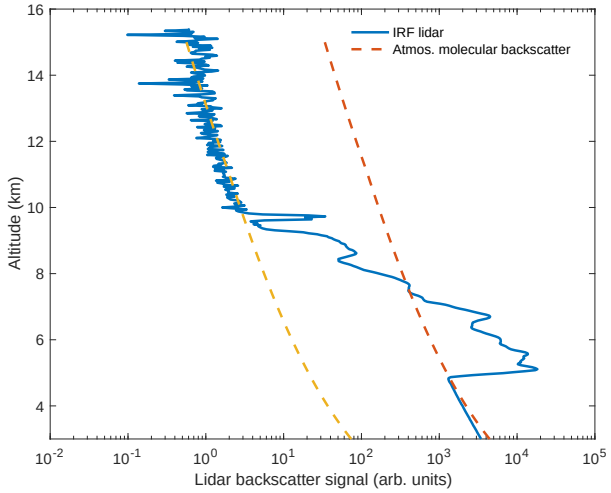

Figure 2. Backscatter signal of IRF lidar on 2016-02-12, at 9:38 UTC (10:38 local time). The atmospheric background is indicated as two dashed lines, one for the signal below and one for above the cirrus layer.

3.2.2. Collocation

The in-situ data on 2016-02-12 showed a cirrus layer between approximately 3.4 km and 7.7 km. That is a larger altitude range, and extending to lower altitudes compared to the lidar-measured cloud shown in Fig. 1. This is most likely caused by the fact that the lidar and the in-situ measurements do not happen at the same location. The IRF lidar is 29 km away from the Esrange balloon pad. Wind data from the radiosonde attached to the in-situ instrument showed that the wind from about 3 km altitude upwards came from S–SSW. At 5 km altitude it was from 209 ° at 9.1 m s^{-1}. This resulted in a closest horizontal distance between lidar observed air volume and in-situ measurement location of about 21 km at 5 km altitude. To reach this closest distance, the lidar observed air volume advected from the lidar 12 km in approximately 22 min, i.e the lidar measured at about 9:40 UTC a cloud that then advected closer to the location of in-situ measurement at the same altitude at about 10:00 UTC. Hence, lidar data from 9:40 UTC (10:40 local time) were chosen for comparison with in-situ data on that day. The balloon trajectory and the wind direction from the lidar are depicted in Fig. 3. Similarly, on 2013-02-20 an appropriate time for comparison was chosen to minimize the distance between lidar and in-situ measurements.

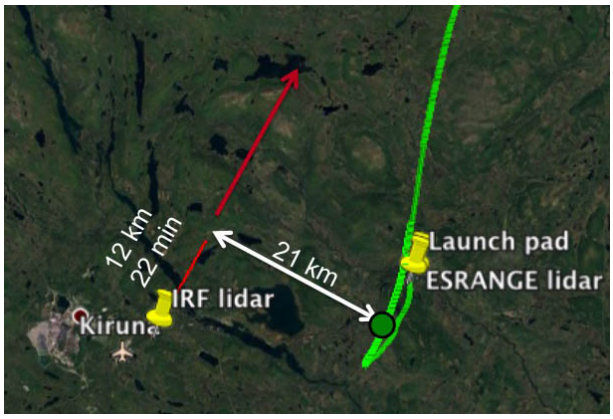

Figure 3. Balloon trajectory on 2016-02-12. The lidar location is marked as well as the wind direction at 5 km altitude, 209 °. Clouds observed at the lidar advect in this wind direction, along the red line in the figure. The location of the balloon at approximately 5 km altitude is indicated with a green circle. At this altitude it is about 21 km away (indicated with white arrow) from the line of clouds advecting from the lidar.

3.2.3. In-situ data

The cirrus cloud as measured with the in-situ instrument on 2016-02-12 extended from 3.40 km to 7.68 km altitude, with temperatures from −23 °C at the cloud bottom to −48 °C at the top. A total of 712 ice particles were analysed from this cloud. Fig. 4 shows the area size

distribution of these particles. It is determined from the number size distribution, which is multiplied, on a bin-by-bin basis, by the average area of the ice particles in the respective size bin. The total area concentration, the integral of the area distribution in Fig. 4, is 0.21 km^{-1} for 2016-02-12. Hence, the extinction coefficient, twice the area concentration (see Sect. 2.1.2), is 0.41 km^{-1}.

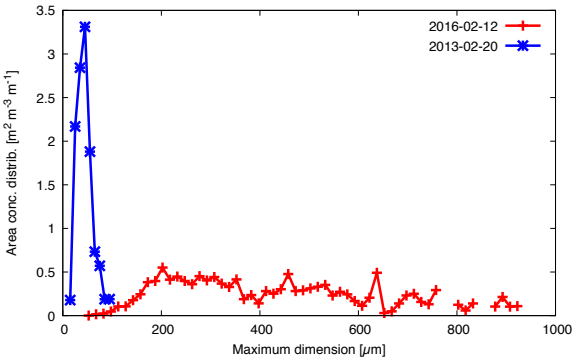

Figure 4. Area size distribution of cirrus clouds on 2016-02-12 and 2013-02-20.

When analysed in three layers, this cirrus had a lower extinction coefficient in the bottom layer, and a higher extinction in the top layer, compared to the value in the middle layer ($\alpha_{\text{in-situ}} = 0.094\,km^{-1}$ between 3.4 km and 4.5 km; 0.36 km^{-1} between 4.5 km and 5.6 km; and 0.81 km^{-1} between 5.6 km and 7.7 km). The number concentrations were 3.9 L^{-1} at the bottom, 13 L^{-1} in the middle, and 4.7 L^{-1} at the top.

The overall optical depth $\tau_{\text{in-situ}}$ of this cloud is 1.8, determined from vertically integrating the extinction coefficients or, equivalently, by multiplying the average extinction coefficient of 0.41 km^{-1} with the geometrical thickness of 4.3 km.

3.2.4. Extinction coefficient from lidar data

The extinction coefficients $\alpha_{\text{lidar}}^{\text{cirrus}}$, as described in Sect. 2.2.2, can be determined from BSR using Eq. 3 and Eq. 4. For an IRF lidar profile at about 9:40 UTC on 2016-02-12 the resulting extinction coefficient profile can be seen in Fig. 5.

Values for $\alpha_{\text{lidar}}^{\text{cirrus}}$ from lidar using BSR are generally smaller than values of $\alpha_{\text{in-situ}}$ from in-situ data (see Fig. 5). A possible explanation for this could be that the assumed lidar ratio L_{cirrus} was too small. However, the fact that lidar and in-situ instrument did not measure the cloud at the same location makes this reasoning uncertain.

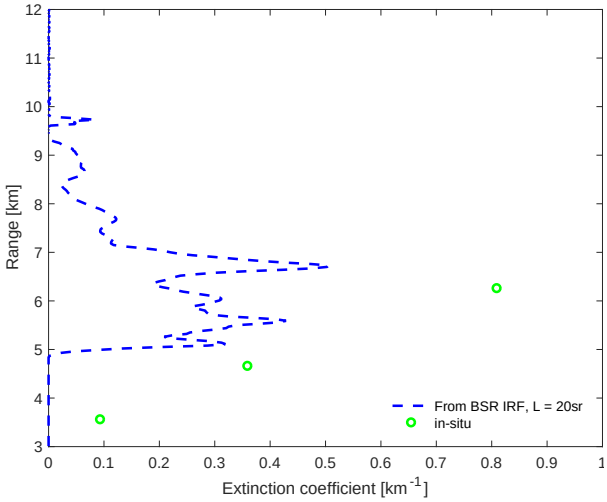

Figure 5. Extinction coefficient $\alpha_{\text{lidar}}^{\text{cirrus}}$ determined from BSR using Eq. 3 and Eq. 4 for 2016-02-12 at 9:38 UTC (10:38 local time) from the IRF lidar. For comparison, extinction coefficients $\alpha_{\text{in-situ}}$ are shown as well.

3.2.5. Optical depth

The optical depth τ_{lidar} is determined from the lidar attenuation, or transmission T_{cirrus} through the cloud as described in Sect. 2.2.2. No further assumptions have to be made for this. Alternatively, τ_{lidar} can be determined by integrating $\alpha_{\text{lidar}}^{\text{cirrus}}$ through the cloud. To first determine $\alpha_{\text{lidar}}^{\text{cirrus}}$, we had to assume the lidar ratio L_{cirrus}. Here we assumed a constant $L_{\text{cirrus}} = 20$ sr. If it was over- or underestimated, then also $\alpha_{\text{lidar}}^{\text{cirrus}}$ and with that τ_{lidar} will be over- or underestimated.

Fig. 6 shows time series of τ_{lidar} on 2016-02-12 determined using the two methods mentioned above. After about 10:30 UTC increased noise in the data due to the lower cloud observed in Fig. 1 caused problems determining τ_{lidar}. Before that, one can see that τ_{lidar} from integrating $\alpha_{\text{lidar}}^{\text{cirrus}}$ seems underestimated. This could be due to a too low assumption of L_{cirrus}, which would confirm our earlier reasoning when comparing $\alpha_{\text{lidar}}^{\text{cirrus}}$ with $\alpha_{\text{in-situ}}$ in Fig. 5.

3.3. 2013-02-20

3.3.1. In-situ data

On 2013-02-20 a cirrus was measured by the in-situ instrument between 9.0 km and 10.5 km altitude. Of all collected particles a representative sample of 279 has been analysed. These particles are from three layers within the continuous cloud: bottom, middle, and top. On this day, the particle concentrations were relatively high (86 L^{-1}, 220 L^{-1}, and 370 L^{-1} at the cloud bottom, middle, and top, respectively). Fig. 4 showed the area size distribution for the complete cirrus layer. The extinction coefficients

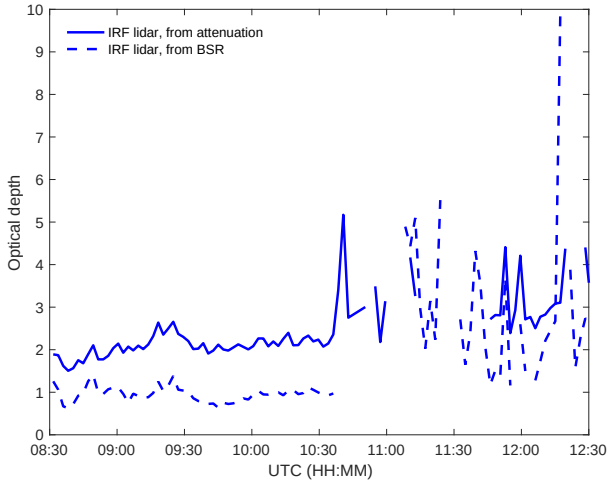

Figure 6. Optical depth τ determined from lidar measurements on 2016-02-12. Results from directly looking at attenuation of the signal from below to above the cloud and from integration of $\alpha_{\text{lidar}}^{\text{cirrus}}$, determined from BSR are compared.

in these three layers are $\alpha_{\text{in-situ}} = 0.22\,\text{km}^{-1}$ at around 9.2 km; $0.28\,\text{km}^{-1}$ at 9.8 km, and $0.26\,\text{km}^{-1}$ at 10.3 km. While number concentrations increased with increasing altitude and decreasing temperature (from $-56\,°\text{C}$ at the cloud bottom to $-66\,°\text{C}$ at the top), extinction coefficients stayed almost constant. The values for $\alpha_{\text{in-situ}}$, despite the higher number concentrations, were similar or lower than on 2016-02-12. The overall optical depth $\tau_{\text{in-situ}}$ on 2013-02-20 of 0.41, however, was smaller than on 2016-02-12 because of the cloud being geometrically thinner.

3.3.2. Extinction coefficient from lidar data

For lidar measurements on 2013-02-20, extinction coefficients $\alpha_{\text{lidar}}^{\text{cirrus}}$ determined from the BSR are shown in Figures 7, 8, and 9. On that day both lidars operated and profiles from about 11:00 UTC are shown in Fig. 9. After that time the IRF lidar was stopped due to increased stray light issues. The best time for comparison with the in-situ measurements would have been around 11:30 UTC. Profiles of $\alpha_{\text{lidar}}^{\text{cirrus}}$ from the Esrange lidar are shown for both these times.

On 2013-02-20 values for $\alpha_{\text{lidar}}^{\text{cirrus}}$ and $\alpha_{\text{in-situ}}$ were more similar than on 2016-02-12. However, the two profiles for the Esrange lidar show how much $\alpha_{\text{lidar}}^{\text{cirrus}}$ can vary in a short period of time of 30 min. Also in 4 min, from one profile to the next, $\alpha_{\text{lidar}}^{\text{cirrus}}$ may change by 50% in certain layers. The better agreement between $\alpha_{\text{lidar}}^{\text{cirrus}}$ and $\alpha_{\text{in-situ}}$ indicates that the assumed lidar ratio of 20 sr may be a better guess on this day.

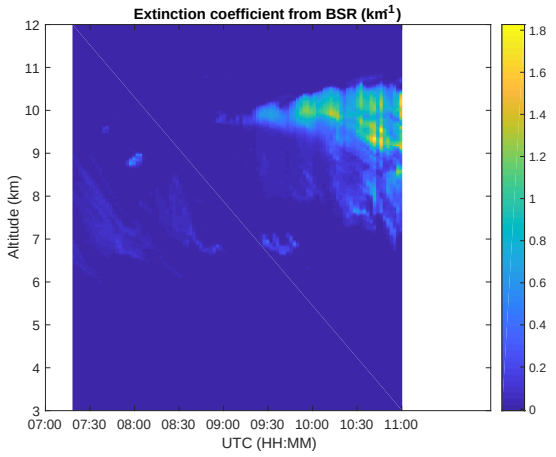

Figure 7. Extinction coefficients $\alpha_{\text{lidar}}^{\text{cirrus}}$ determined from BSR of IRF lidar on 2013-02-20.

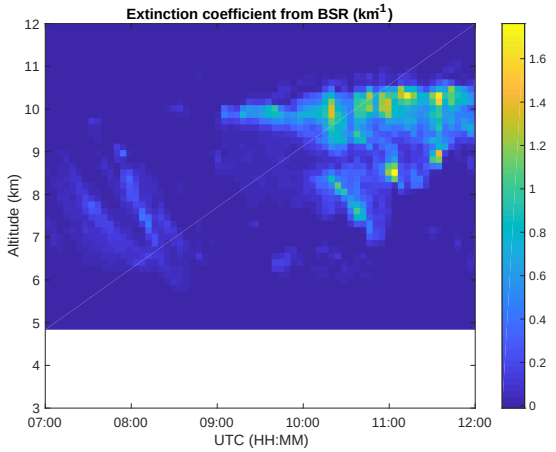

Figure 8. Extinction coefficients $\alpha_{\text{lidar}}^{\text{cirrus}}$ determined from BSR of Esrange lidar on 2013-02-20.

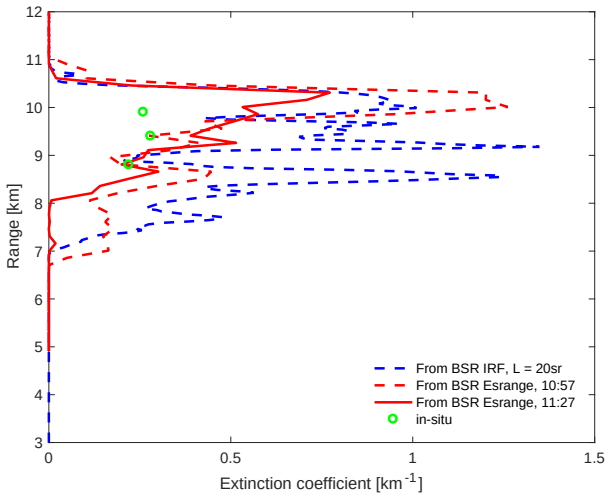

Figure 9. Extinction coefficient α_{cirrus} determined from BSR using Eq. 3 and Eq.4 for 2013-02-20 from the IRF and Esrange lidar, respectively.

3.3.3. Optical depth

Fig. 10 shows time series of τ_{lidar} on 2013-02-20 determined using the methods described in Sections 3.2.5 and 2.2.2. For both the IRF and Esrange lidar the optical

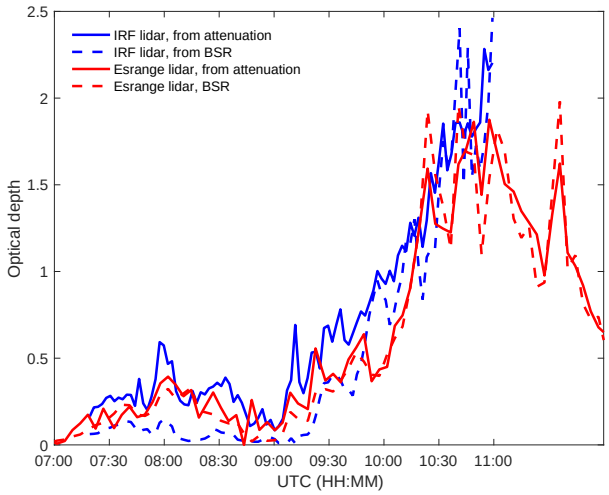

Figure 10. As Fig. 6, but for 2013-02-20.

depths from the two methods seem to agree much better on this day. This indicates that the assumed lidar ratio, as already speculated in Sect. 3.3.2, is indeed better on 2013-02-20 than on 2016-02-12. For the Esrange lidar the agreement seems very good, so that $L_{\mathrm{cirrus}} = 20\,\mathrm{sr}$ is the best lidar ratio resulting from this optical depth comparison. For the IRF lidar, $L_{\mathrm{cirrus}} = 20\,\mathrm{sr}$ also seemed a good assumption for the whole measurement period on 2013-02-20. However, in the earlier hours (7:00 to 9:30 UTC) a somewhat higher lidar ratio would have yielded a better agreement.

4. CONCLUSIONS AND FURTHER WORK

We have shown the first collocations of our ongoing balloon-borne cirrus campaign that started in 2012. A comparison between in-situ measurements and ground-based lidar measurements has been presented for two days of the campaign. In general, good agreement in extinction coefficients and optical depths from in-situ and remote sensing was observed when a suitable lidar ratio was selected. While this best lidar ratio was approximately 20 sr on a day with small particles (2013-02-20), it was larger, around 40 sr, on the other day (2016-02-12), on which larger particles were observed by the in-situ measurements. This agrees with a dependence of lidar ratio on ice particle size observed by [23].

This shows how combining our in-situ measurements with concurrent ground-based lidar measurements provide data that complement each other. While the in-situ measurements provide detailed information of the microphysical properties of the cirrus probed by balloon, the lidar serves also to characterize the temporal and spatial evolution of the cirrus that we sampled.

The comparison of extinction coefficients and optical depth, quantities derived from both in-situ data and lidar measurements is somewhat difficult because exact collocations in time and space cannot easily be achieved. The smallest collocation distances in our measurements are on the order of 20 min and 20 km. While this may be satisfactory under certain conditions, it may be too far under different conditions. Thus, a more carful analysis of the meteorological conditions on the measurement days will be necessary to evaluate how homogeneous or not cirrus layers are in spatial dimensions and how they evolve over time.

Therefore, rather than in a direct comparison of extinction coefficients, a major benefit of having concurrent lidar observations with our in-situ measurements will be in the further studies that are possible. So far we have not used the information on the polarization of the backscattered light that the lidar can provide. Depending on the shape of ice particles, the scattered light measured by lidar is more or less polarized. Thus, we will compare also the lidar depolarization ratios with the observed shapes, which could aid a determination of dominant shapes from lidar depolarization ratios. The lidar ratio will also be studied more in detail by looking at relationships between lidar ratio and cloud microphysical properties from in-situ measurements. In addition to looking at effects of particle size on the lidar ratio, we can also look at the effects of the shape on it. If the lidar ratio can be determined more directly and accurately, then this can reduce uncertainties in lidar derived quantities. In addition, one may infer certain microphysical properties such as dominant shape or size from lidar ratios. For this, the lidar ratio could be derived independently from the vibrational Raman channel [19] of the Esrange lidar. This will require night-time measurements with less stray light. Such night-time measurements would also have the additional benefit of much reduced signal-to-noise ratios in all lidar data. All this planned future work will help to provide better ice cloud properties from lidar-only measurements of cirrus at high latitudes.

ACKNOWLEDGMENTS

We thank Swedish National Space Board for funding this balloon campaign, and Andrew Heymsfield and National Center for Atmospheric Research (NCAR, USA) for their support.

REFERENCES

[1] B. A. Baum, P. Yang, A. J. Heymsfield, C. G. Schmitt, Y. Xie, A. Bansemer, Y. X. Hu, and Z. Zhang. Improvements in shortwave bulk scattering and absorption models for the remote sensing of

ice clouds. *J. Appl. Meteorol. Clim.*, 50:1037–1056, 2011.

[2] M. J. McGill, L. Li, W. D. Hart, G. M. Heymsfield, D. L. Hlavka, P. E. Racette, L. Tian, M. A. Vaughan, and D. M. Winker. Combined lidar-radar remote sensing: Initial results from CRYSTAL-FACE. *J. Geophys. Res.*, 109(D7), 2004.

[3] P. Eriksson, M. Ekström, B. Rydberg, and D. Murtagh. First Odin sub-mm retrievals in the tropical upper troposphere: ice cloud properties. *Atmos. Chem. Phys.*, 7:471–483, 2007.

[4] A. Heymsfield, C. Schmitt, and A. Bansemer. Ice cloud particle size distributions and pressure-dependent terminal velocities from in situ observations at temperatures from 0 to -86 C. *J. Atmos. Sci.*, 2013.

[5] A. V. Korolev, E. F. Emery, J. W. Strapp, S. G. Cober, G. A. Isaac, M. Wasey, and D. Marcotte. Small ice particles in tropospheric clouds: fact or artifact? airborne icing instrumentation evaluation experiment. *Bull. Amer. Met. Soc.*, 92(8):967–973, 2011.

[6] Alexei Korolev, Edward Emery, and Kirk Creelman. Modification and tests of particle probe tips to mitigate effects of ice shattering. *Journal of Atmospheric and Oceanic Technology*, 30(4):690–708, 2013.

[7] R. C. Jackson, G. M. McFarquhar, J. Stith, M. Beals, R. A. Shaw, J. Jensen, J. Fugal, and A. Korolev. An assessment of the impact of anti-shattering tips and artifact removal techniques on cloud ice size distributions measured by the 2d cloud probe. *J. Atmos. Oceanic Technol.*, 31:2567–2590, 2014.

[8] Alexei Korolev. Reconstruction of the sizes of spherical particles from their shadow images. Part I: theoretical considerations. *J. Atmos. Oceanic Technol.*, 24(3):376–389, 2007.

[9] M. T. Stoelinga, J. D. Locatelli, and C. P. Woods. The occurrence of "Irregular" ice particles in stratiform clouds. *J. Atmos. Sci.*, 64(7):2740–2750, 2007.

[10] L. M. Miloshevich and A. J. Heymsfield. A balloon-borne continuous cloud particle replicator for measuring vertical profiles of cloud microphysical properties: Instrument design, performance, and collection efficiency analysis. *J. Atmos. Oceanic Technol.*, 14(4):753–768, 1997.

[11] Thomas Kuhn and Andrew J. Heymsfield. In situ balloon-borne ice particle imaging in high-latitude cirrus. *Pure Appl. Geophys.*, 173(9):3065–3084, 2016.

[12] C. Schiller, M. Kraemer, A. Afchine, N. Spelten, and N. Sitnikov. Ice water content of Arctic, mid-latitude, and tropical cirrus. *J. Geophys. Res.*, 113, DEC 24 2008.

[13] J.-F. Gayet, I. S. Stachlewska, O. Jourdan, V. Shcherbakov, A. Schwarzenboeck, and R. Neuber. Microphysical and optical properties of precipitating drizzle and ice particles obtained from alternated lidar and in situ measurements. *Annales Geophysicae*, 25(7):1487–1497, 2007.

[14] T. Kuhn, A. J. Heymsfield, and S. A. Buehler. Balloon-borne measurements of ice particle shape and ice water content in the upper troposphere over northern Sweden. *Proc. 21st ESA Symposium on European Rocket and Balloon Programmes and Related Research*, SP-721:93–97, 2013.

[15] P. Voelger and G. Nikulin. The new lidar system at the swedish institute of space physics in kiruna: description and first measurements. *17th ESA Symposium on European Rocket and Balloon Programmes and Related Research*, ESA SP-590:321–325, 2005.

[16] U. Blum and K. H. Fricke. The Bonn University lidar at the Esrange: technical description and capabilities for atmospheric research. *Ann. Geophys.*, 23(5):1645–1658, 2005.

[17] T. Kanitz, A. Ansmann, R. Engelmann, and D. Althausen. North-south cross sections of the vertical aerosol distribution over the atlantic ocean from multiwavelength raman/polarization lidar during polarstern cruises. *J. Geophys. Res. Atmos.*, 118(6):2643–2655, 2013.

[18] J. D. Klett. Stable analytical inversion solution for processing lidar returns. *Appl. Opt.*, 20:211–220, 1981.

[19] A. Ansmann, U. Wandinger, M. Riebesell, C. Weitkamp, and W. Michaelis. Independent measurement of extinction and backscatter profiles in cirrus clouds by using a combined raman elastic-backscatter lidar. *AO*, 31(33):7113–7131, 1992. Cited By :432.

[20] J. Reichardt, S. Reichardt, M. Hess, and T. J. McGee. Correlations among the optical properties of cirrus-cloud particles: Microphysical interpretation. *JGR*, 107(21):XL, 2002. Cited By :16.

[21] R. Kuehn, R. Holz, E. Eloranta, M. Vaughan, and J. Hair. Developing a climatology of cirrus lidar ratios using University of Wisconsin HSRL observations. In *EPJ Web of Conferences*, volume 119, 2016.

[22] M. Saito, H. Iwabuchi, P. Yang, G. Tang, M. D. King, and M. Sekiguchi. Ice particle morphology and microphysical properties of cirrus clouds inferred from combined caliop-iir measurements. *JGR*, 122(8):4440–4462, 2017.

[23] J. F Gayet, G. Febvre, G. Brogniez, H. Chepfer, W. Renger, and P. Wendling. Microphysical and optical properties of cirrus and contrails: Cloud field study on 13 october 1989. *JAS*, 53(1):126–138, 1996. Cited By :78.

LAUNCH CAMPAIGN OF THE HYBRID SOUNDING ROCKET HEROS

J. Breitinger[1], C. Schmierer[1], M. Kobald[2], and S. Schlechtriem[2]

[1] *Institute of Space Systems, University of Stuttgart*
Pfaffenwaldring 29, 70569 Stuttgart, Germany
Email: jonas.breitinger@online.de, schmierer@irs.uni-stuttgart.de
[2] *German Aerospace Center (DLR)*
Langer Grund, 74239 Hardthausen, Germany
Email: mario.kobald@dlr.de, stefan.schlechtriem@dlr.de

ABSTRACT

Due to its inherent safety and easy handling, hybrid rocket propulsion offers a wide bandwidth of applications. Scientific progress in hybrid propulsion facilitated the usage of this type as an alternative to classical liquid and solid propellant based rocket motors. Especially for students, the low cost and simple availability of suitable propellants in hybrid rocket engines combined with a high achievable performance is an advantage.

DLR initiated the STERN program (Studentische Experimentalraketen) with funding from the German Federal Ministry for Economic Affairs and Energy to encourage students to design, build and launch their own rocket system. From the University of Stuttgart, the student team "Hybrid Engine Development" (HyEnD) participated in this program. Their third full scale rocket HEROS 3 broke the world altitude record for hybrid student rockets and the European student altitude record for sounding rockets in general during its nominal flight to an altitude of 32.3 km above ground level.

1. INTRODUCTION

1.1. Hybrid Engine Development

HyEnD (Hybrid Engine Development) is a student group founded in 2006. Until 2012, the group designed and tested multiple hybrid rocket engines ranging from 250 N to 2000 N thrust. In 2012, the team was selected for the STERN (Studentische Experimentalraketen, engl. student experimental rockets) program, initiated by the German Aerospace Center (DLR). HyEnD is being supported by the Institute of Space Systems (IRS) at the University of Stuttgart. During the years, around 30 students have participated in the HyEnD group. They designed and launched a demonstrator rocket, MIRAS (Mikro Rakete Stuttgart), two times in Germany. The full-scale rocket HEROS (Hybrid Engine Rocket Stuttgart) has been the most powerful rocket built by HyEnD. Extensive engine tests with the 500 N MIRAS engine [1] and the full-scale 10 kN HyRES engine for the HEROS rocket have been conducted between 2012 and 2016.

1.2. STERN

The main goal of the STERN program is the design, development and flight of an experimental sounding rocket within a time frame of three years [2]. Students are thereby encouraged to deepen their knowledge gained during their studies. Typical engineering problems, such as mechanical design, system design, fluid dynamics, combustion and heat transfer have to be solved during design. Young students shall be offered a real hands-on experience as all necessary parts are designed and most parts are manufactured by students. Various universities in Germany have been supported by DLR. Multiple reviews and extensive documentation of the activities shall ensure an approach comparable to the professional projects in space industry. This offers a valuable opportunity to gain insight into processes in the later field of work.

1.3. Hybrid Rocket Propulsion

A chemical hybrid rocket engine combines two propellants in different aggregate states. In the classical configuration, a liquid or gaseous oxidizer are utilized together with a solid fuel. The solid fuel is stored inside the combustion chamber while the oxidizer is loaded into a tank. This spatial division of the propellants lead to a very safe propulsion system.

Furthermore, hybrid rocket engines can offer an I_{sp}

greater than solid rocket motors but lower than liquid engines. In terms of complexity the hybrid rocket engine is also located between the solid and liquid propulsion systems as only the oxidizer has to be fed into the combustion chamber. Throttle-ability [3] and re-ignition capability are additional benefits of hybrid propulsion.

Additionally, a wide range of oxidizers including O_2, N_2O, N_2O_4 and many more can be selected [4]. Hydroxyl-terminated polybutadiene (HTPB) and paraffins are the most widespread solid fuels currently in use. With the discovery of liquefying fuels by Karabeyoglu in 2002 [5] a main drawback, low regression rates leading to low thrust densities, has been reduced to a point where application in sounding rockets is possible with simple fuel geometries. Paraffin is one of the best-known liquefying fuels, whereas HTPB as a classical, non-liquefying fuel is still in use. Detailed analyses of paraffin as fuel in hybrid rocket engines have been conducted recently [6], [7].

While solid and liquid rocket propulsion are still far more widespread than hybrid engines, multiple projects determine the feasibility of the last named concept for different applications. One of the most famous is the suborbital plane SpaceShipTwo by Virgin Galactic. Currently, the second SpaceShipTwo is tested [8]. Multiple student groups conducted tests and launched small experimental rockets for educational purposes in the last years, some in frame of STERN program.

2. HEROS ROCKET AND SUPPORT EQUIPMENT

HEROS (Hybrid Engine Rocket Stuttgart) consists of multiple subsystems, which have all been designed by students. With a length of 7.5 metres and a diameter of 22.3 centimetres, the single staged rocket shall reach an altitude of more than 20 kilometres. In Fig. 1, a schematic overview of the rocket's subsystems is shown. A more detailed overview of the development can be found in [9].

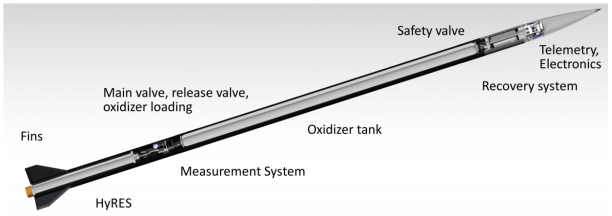

Figure 1. Overview of HEROS' subsystems

2.1. Propulsion System

HEROS' propulsion system consists of a hybrid engine, a pyrotechnical valve and an oxidizer tank. The rocket is powered by a 10 kN hybrid rocket engine called HyRES (Hybrid Rocket Engine Stuttgart), which utilizes a paraffin based fuel and nitrous oxide as propellants. Recent developments in the understanding of hybrid rocket engines led to this fuel, which offers regression rates high enough for an engine design suitable for application in this sounding rocket. Multiple full-scale on-ground tests helped to optimize the engine performance. A picture of such a test is shown in Fig. 2.

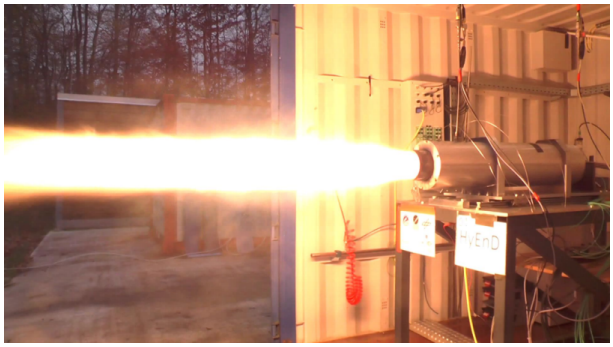

Figure 2. Engine test at DLR Lampoldshausen

Oxidizer tank and engine are connected via a self-designed pyrotechnical main valve as suitable off-the-shelf valves were too heavy. For ignition of the engine, a small portion of fuel has to be melted to react with the oxidizer and start the combustion process. The usage of small, solid model rocket motors has been established during the ground tests of the engine. They are ignited shortly before the main oxidizer valve is opened. In case of a main valve failure, only the igniters burn and melt the top layer of the fuel.

It has to be noted, that with hybrid rocket engines, an spontaneous combustion is impossible due to the spatially divided propellants: while the paraffin based fuel is stored in the combustion chamber, the oxidizer is filled into an lightweight tank, which is shown in Fig. 3. This tank consists of an aluminium liner, which is reinforced by CFRP. Aluminium was picked to avoid contact between the oxidizer, nitrous oxide, and the resin used in the CFRP structure. Up to around 80kg of nitrous oxide can be stored in the 130l tank at a pressure of 60bar. This design was developed as part of a thesis [10]. Nitrous oxide is self pressurizing, therefore an additional pressurization system is not necessary.

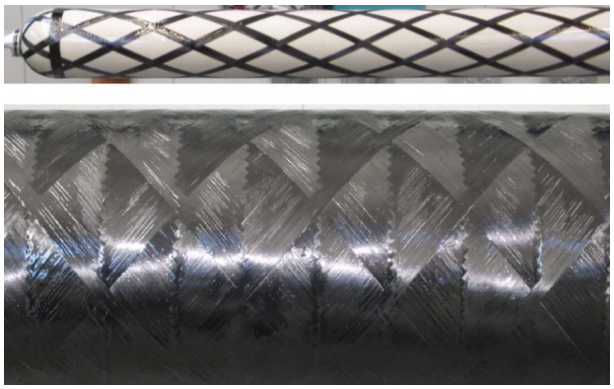

Figure 3. Oxidizer tank during (top) and after CFRP winding

2.2. Recovery System

HEROS is recovered via a two-stage parachute system. At apogee, a cluster of two drogue parachutes is ejected sideways to decelerate the rocket for main parachute deployment. At a preselected height, the main parachute is pulled out by the drogue chutes and slows the rocket down to an acceptable landing speed. All parachutes can be seen in Fig. 4. The rocket is recovered in one piece, which makes the system reusable to a certain extent.

Figure 4. Drogue cluster and main parachute

2.3. Telemetry and Electronics

A telemetry and electronics system transmits valuable data such as position, speed and system status during flight. The electronics feature a redundant architecture, combining two flight computers, multiple batteries and cable cutters to trigger the recovery system at the right moment. Due to a radio silence requirement at Esrange, the telemetry additionally has to be remotely turned off and on during countdown.

2.4. Measurement System

Engine and tank data as well as structure temperatures are monitored with a Genuino-based measurement system. This micro controller is formerly known as Arduino and was programmed with the Arduino software environment. Three Genuino micro controllers have been used in HEROS. Tank pressure, injector pressure and combustion chamber pressure are measured at a rate of 1000Hz to determine engine performance and combustion stability. At the flight tank, injector and fins, temperature measurements are conducted at 2Hz. A Bosch BNO055 IMU sensor is measuring the rockets attitude in Eulerian angles during the flight. Additionally, this sensor delivers the raw acceleration data, gravitational acceleration, magnetic field data and rotational rates. Each of them are given in 3 body axes at a frequency of more than 90Hz. Data of each Genuino is saved on Micro-SD cards during the flight and is analyzed afterwards. Temperature data, tank pressure and Genuino status signals are monitored in real-time on the launcher before lift-off and are transmitted to the GSE. Proper temperature and pressure of the N2O in the rocket tank is one of the main GO/NOGO criteria for a launch.

2.5. Ground Support Equipment

Ground support equipment is used to allow remote control of valves, heaters, on board electronics and cameras.

Nitrous oxide stored in multiple bottles is transferred to two intermediate tanks, where it is heated to optimal temperature shortly before start of the countdown. Additionally, the rocket is heated inside of a styrofoam box during countdown because of the high dependence of engine performance on temperature. A pair of heaters supplies the styrofoam housing of the rocket with hot air to keep the oxidizer temperature in a defined window. Temperature is measured at multiple points such as the intermediate tanks and different positions next to the rocket. To determine the oxidizer mass in the flight tank during all phases, intermediate tanks and rocket are weighed during the whole loading process. The mass flow between intermediate tanks and rocket is monitored as well with a Coriolis mass flow sensor. This method leads to a highly accurate measurement of the loaded oxidizer mass, which is an important parameter for engine performance evaluation and trajectory simulation verification. Ground support equipment is controlled via a Labview program.

For post flight analysis and monitoring of oxidizer loading arm status, a camera system has been developed. It consists of seven cameras, thereof three with video live-link to the control room. All cameras are protected against snow and rain. They can be switched from control room and save videos on SD cards. Fig. 6 shows a picture recorded by one of these cameras.

An aluminium rail adapted to the MRL launcher ensures correct attitude during the first tens of seconds as the HEROS rockets are passivly stabilized.

When the tower exit velocity (TEV) is reached, disturbances as wind have only small effects on the trajectory. An oxidizer loading arm acts as mechanical interface between the intermediate tanks and the rocket and is shown in Fig. 5. This arm is retracted during countdown.

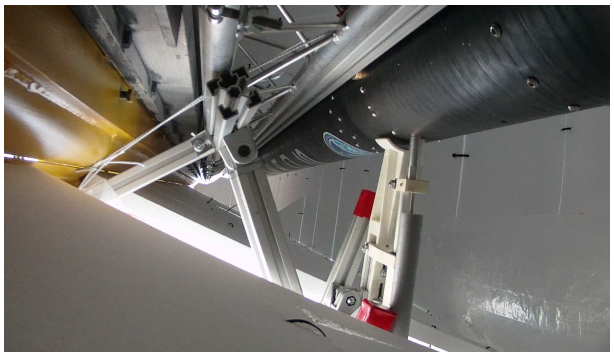

Figure 5. Oxidizer loading arm

3. LAUNCHES OF HEROS 2 AND HEROS 3

3.1. HEROS 2

HEROS 2 was launched from the MRL launcher at Esrange Space Center in Northern Sweden on 31st October 2016 at 12:00 UTC. The countdown went very smoothly: The tank filling with N_2O was quickly done and a heating system consisting of the air-heated styrofoam box on the launcher as well as heating bands around the GSE tanks ensured an appropriate temperature of the nitrous oxide. The ground and on-board electronics worked flawlessly during the countdown. A lot of great video material of the lift-off and the ascent into the clouds was recorded by the ground camera system. The lift-off is shown in Fig. 6.

However, an electronic interference right at T-0 of the countdown caused a failure of the on-board electronics and telemetry system. Without a telemetry signal it was not possible to get any information about the position during and after flight of HEROS 2. The recovery system was most likely affected by the failure as well. A helicopter team searched at the nominal impact point, but due to the weather and sight conditions it was impossible to find the rocket. The video material and sound recordings were analyzed and all evidence points to the hybrid rocket engine HyRES working nominally during the whole ascent of the rocket. In the following days the failure was investigated in detail and it was shown that an electronic interference with the main ignition impulse induced a voltage in the connecting line between the ground support computer and the rocket on-board electronics. This voltage was high enough to generate a shut-off signal in the command line.

Figure 6. Lift-Off of HEROS 2

After extensive testing, the failure could be localised and the proposed solution was accepted by Esrange safety board leading to GO for launch of HEROS 3.

3.2. HEROS 3

On 8th November, HEROS 3 was launched succesfully to an apogee altitude of 32,300 m (106,000 ft) setting a new european altitude record for student and amateur rockets and a world altitude record for hybrid rockets built by students. HEROS 3 reached apogee 89 s after lift-off and could be recovered undamaged. A picture taken by HEROS 3 at apogee is shown in Figure 7. As the thermal loads during supersonic flight and the effects of rising temperature in the CFRP fin structure could not be determined exactly before the flight, the oxidizer tank was filled to about 70% in order to keep the maximum velocity lower. Additionally, a relatively flat launcher elevation were selected by Esrange for HEROS 2 and HEROS 3 to ensure a quick movement away from the launch site. Both factors lowered the achievable apogee from the maximum possible apogee with completely filled oxidizer tank and a steeper launch angle. Launch configurations of HEROS 2 and HEROS 3 can be found in Tab. 1.

Post flight analysis has been carried out after recovery. Detailed discussion of the outcome can be found in [11]. A comparison to conducted trajectory simulations is made in [12].

4. ADVANTAGES OF HYBRID SOUNDING ROCKETS

4.1. Transport

There are no additional regulations regarding the paraffin based fuel used in HEROS. The oxidizer, however, has to be labelled as class 2.2 non-flammable and non toxic gas as well as class 5.1 oxidizing substance. According to this classification, transport regulation depending on the way of transport occur. In general, the shipping of a hybrid rocket motor together with the described propellants is less restricted in comparison to the commercial solid sounding rockets. This leads to a faster and less costly shipping process.

4.2. Handling Procedures

The inherent safety of the hybrid propulsion concept enhances the safety for personnel and facilities during launch preparations. While an accidental ignition of a solid rocket motor can be caused by a small spark, the unintended ignition of a hybrid rocket motor is nearly impossible due to its spatially separated propellants. During assembly of the rocket and integration on the launcher, the oxidizer is not loaded into the rocket's tank. There is no ignition possible until the oxidizer is loaded by remote control during the countdown. However, pyrotechnical charges in other parts of the rocket have to be handled carefully. Therefore, ESD clothing as well as anti-static wristbands were used during the integration process of the HEROS rockets, similar to the handling procedures applying for solid rockets.

Nitrous oxide has to be handled with care. At high pressure (over 40 atm), decomposition rates of nitrous oxide are relatively low for temperature below 850 K. The characteristic decomposition time reduces exponentially with rising temperatures and reaches the millisecond scale at temperatures above 1500 K [13]. Catalytic materials such as hydrocarbons [14] represent a severe danger as they increase the decomposition rate. Therefore, precautions have to be taken. The tanks, lines and valves have to be clean. Additionally, the temperature of the oxidizer is monitored at various points.

4.3. Countdown

In case of the HEROS rockets, the oxidizer is loaded remote controlled shortly before lift-off as a pressurized tank loaded with nitrous oxide presents a severe danger. Nobody is permitted to be next to the launcher in this state. In case of a launch abort, the flight tank can be depressurized remote controlled via a release valve.

4.4. Flight Performance

In general, higher Isp values can be achieved with a hybrid rocket engine compared to solid motors. However, a higher structural mass of the hybrid configuration due to tanks and piping has to be considered. Furthermore, hybrid engines can be throttled and feature shut-off and re-ignition capability. For application in sounding rockets, the first point is the most interesting one. A throttled hybrid engine may increase the achievable apogee altitude further, as the thrust can be decreased shortly after lift-off while flying in dense atmosphere and increased at high altitude.

A main benefit of solid rocket engines is the higher thrust density and lower structural mass as well as good predictability of system performance due to a great amount of flights in multiple programs. In combination with the availability of de-militarized rocket engines, these benefits lead to the fact that nearly all sounding rockets currently in use are based on solid propulsion.

5. CONCLUSION

The STERN project showed the possibility, to design, build and launch three HEROS hybrid sounding rockets within a student project in just four years. Subsystems as recovery, electronics, structure, measurement system and propulsion system have been developed by students. Compared to the more common solid propulsion systems, hybrid engines offer benefits regarding safety and therefore handling. However, more complex ground systems for oxidizer loading and temperature monitoring have to be considered. All in all, the potential of this propulsion concept has been shown and many students have been encouraged to deepen their theoretical knowledge during design and production.

ACKNOWLEDGMENTS

The HyEnD-STERN project was funded by the DLR Space Administration with funding from the Federal Ministry for Economic Affairs and Energy (BMWI) at the Institute of Space Systems at the University of Stuttgart, under the grant number 50RL1254 since September 2012.

REFERENCES

[1] Petrarolo, A., Kobald, M. & Schmierer, C. Characterization of Advanced Hybrid Rocket Engines. In *6th European Conference for Aeronautics and Space Sciences*, 2015.

[2] Lappöhn, K., Regenbrecht, D. & Bergmann, D. STERN - A Rocket Program for German Students. In *5th European Conference for Aerospace Sciences*, 2013.

[3] Whitmore, S.A., Peterson, Z. W., & Eilers, S. D. Deep Throttle of a Nitrous Oxide and Hydroxyl-Terminated Polybutadiene Hybrid Rocket Motor. *Journal of Propulsion and Power*, 30(1):78–86, January-February 2014.

[4] Altman, D. & Holzman, A. Overview and History of Hybrid Rocket Propulsion. In Martin J. Chiaverini and Kenneth K. Kuo, editors, *Fundamentals of Hybrid Rocket Combustion and Propulsion*, volume 218 of *Progress in Astronautics and Aeronautics*, pages 1–36. American Institute of Aeronautics and Astronautics, January 2007.

[5] Karabeyoglu, M. A., Altman, D & Cantwell, B. J. Combustion of Liquefying Hybrid Propellants: Part 1, General Theory. *Journal of Propulsion and Power*, 18(3):610–620, 2002.

[6] Kobald, M. *Combustion Phenomena of Advanced Hybrid Rocket Fuels*. Doktorarbeit, University of Stuttgart, 2015.

[7] Karabeyoglu, M. A., Zilliac, G., Cantwell, B. J., DeZilwa, S. & Castellucci, P. Scale-Up Tests of High Regression Rate Paraffin-Based Hybrid Rocket Fuels. *Journal of Propulsion and Power*, 20(6), November-December 2004.

[8] Flight Test Update From Mojave. http://www.virgingalactic.com/flight-test-update-from-mojave/, May 2017. [cited 19 May 2017].

[9] Schmierer, C. et al. HEROS - Sounding Rocket Development by the HyEnD Project. In *6th European Conference for Aeronautics and Space Sciences*, 2015.

[10] Fischer, U. Design of a CFRP-Pressure Vessel for a Sounding Rocket. *Studienarbeit*, 2014.

[11] Kobald, M. et al. Sounding Rocket "HEROS" - A Low-Cost Hybrid Rocket Technology Demonstrator. In *53rd AIAA/SAE/ASEE Joint Propulsion Conference*, 2017.

[12] Hertel, F., Schmierer, C. & Kobald, M. Trajectory analysis of the hybrid sounding rocket heros. In *23RD ESA Symposium on European Rocket and Balloon Programmes and Related Research*, 2017.

[13] Karabeyoglu, A., Dyer, J., Stevens, J. & Cantwell, B. Modeling of N2O Decomposition Events. In *44th AIAA/ASME/SAE/ASEE Joint Propulsion Conference & Exhibit*, 2008.

[14] Kapteijn, F., Rodriguez-Mirasol, J. & Moulijn, J. A. Heterogeneous Catalytic Decomposition of Nitrous Oxide. *Applied Catalysis B: Environmental*, September 1996.

Table 1. Launch configuration

	HEROS 2	**HEROS 3**
Length	7.5 m	7.5 m
Diameter	223 mm	223 mm
Dry mass	75 kg	75 kg
Oxidizer mass	72 kg	74 kg
Paraffin fuel mass	12.31 kg	12.48 kg
Lift-off mass	159.31 kg	161.48 kg
Launcher	MRL	MRL
Launcher elevation	80°C	80°C
Launcher azimuth	0°C	0°C
Launch Date	October 31st, 2016	November 8th, 2016
Weather conditions	Cloudy, slightly foggy	Clear sky

Figure 7. On-board picture by HEROS 3 at 32,300m apogee

USING A HABDUINO FOR TELEMETRY IN ARCTIC ATMOSPHERES AS A HANDS-ON SPACE EDUCATION PROJECT FOR SECONDARY SCHOOL STUDENTS

Sander Vuurstaek[(1)], Dirk Geeroms[(1,2)]

[(1)]Stedelijke Humaniora Dilsen, Europalaan 10, 3650 Dilsen, Belgium, sandervuurstaek@hotmail.com, +32472262821
[(2)]Hasselt University – Campus Diepenbeek, Agoralaan – Building D, 3590 Diepenbeek, Belgium

ABSTRACT

The HABduino project is an open source shield for the Arduino Uno. The main purpose of the HABduino is to send the position and altitude of a high-altitude balloon with radio telemetry.

Although the HABduino was not developed to send custom data, students from secondary school Stedelijke Humaniora Dilsen managed to adjust the code so it could send their own data from a high-altitude balloon flown above the Norwegian archipelago Svalbard.

The main scientific purpose of the project was to determine the altitude of the tropopause in an arctic atmosphere. A temperature sensor and a humidity sensor were used to achieve this goal. The measurements were sent to the HABduino via serial communication before sending them to the receiver. Two balloons were used to reduce errors.

1. LAUNCH IN SVALBARD

One obvious reason to opt for the Norwegian archipelago Svalbard as a launch site is the almost complete absence of air traffic. Another reason is the possibility to carry out a radiation experiment to study a possible correlation between atmospheric gammas and latitude, as described in [1].

Figure 1. Seven students of Stedelijke Humaniora Dilsen, known as Deezers, and their teacher after successfully tracking both payloads.
From left to right: Simon Paradijs, Deyan Marolt, Wouter Coenen, Jarne Dijkmans, Simon Rutten, Sander Vuurstaek, Bram Creusen and Dirk Geeroms.

Figure 2. Sealing the first helium filled stratospheric balloon with the help of balloon expert Steven Peterzén

In order to minimize the costs of an expedition to Svalbard, this project was executed in collaboration with two other secondary schools, i.e. Sint-Pieterscollege Jette in Belgium and St Paul's School from London. However, each school had its own scientific project.

As retrieving a balloon in the inaccessible environment of Svalbard is not to be expected, a HABduino shield was used to send the data gathered by the Arduino to a receiver.

2. PAYLOADS UNCOVERED

Each payload consists of two microcontrollers, as can be seen in Fig. 3: a first Arduino Uno is attached to the sensors and a micro SD card, a second Arduino Uno is used to drive the HABduino. Though it is possible to hook up all the sensors and the HABduino to a single microcontroller, this was not done due to memory limitations. Because two Arduinos are used, the data has to be transferred between both. This was achieved through serial communication.

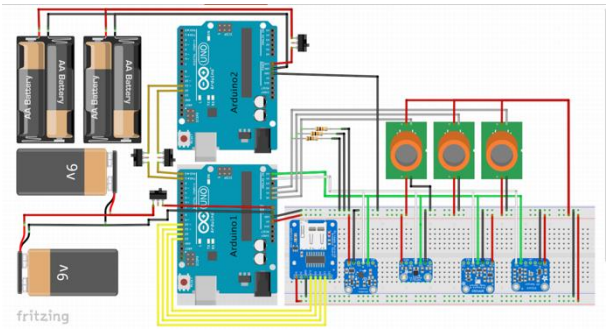

Figure 3. Schematic design of the hardware

The starting point for communicating with sensors is Arduino, an open-source electronics prototyping platform. The Arduino is based on the ATmega328-chip but makes it easier for beginners to start with microcontrollers. The Arduino programming environment is easy to use for beginners, yet flexible enough for advanced users. It is based on the Processing programming environment and can be expanded through C++ libraries. These libraries are used frequently in this project. On the one hand to make it easier to read data from sensors, on the other hand because transferring data between two Arduinos becomes straightforward.

The sensors used in this project are all manufactured by Adafruit. A major advantage of using these sensors is the availability and access to tutorials and libraries on the Adafruit website. The sensors are connected to the Arduino microcontroller by use of an I2C-bus. This makes it possible to drive the sensors with only two wires attached.

There is also a micro SD card on board so data from the sensors can be saved to the SD card as well as be transmitted. There are multiple advantages of using an SD card as a storage device: it is small, light-weight and has a capacity large enough to save a lot of data. The major disadvantage – yet very relevant at Svalbard – is that the SD-card has to be retrieved in order to collect data from it.

Figure 4. Top view of payload 1

3. HABDUINO EXPLAINED

The HABduino project is an open source shield for the Arduino Uno. The main purpose of the HABduino is to send the position and altitude of a high-altitude balloon with radio telemetry as well as data from temperature sensors soldered on to the HABduino. The biggest disadvantage is that the HABduino is not capable of transmitting data from other sensors, like the ones attached to a second Arduino microcontroller. This was overcome by a few software tweaks.

The HABduino board as well as code are fully open source and available on GitHub. The code is written in the Arduino Integrated Development Environment (IDE) and can thus easily be uploaded to an Arduino board. The original code from the developers uses a lot of interrupts – functions that run side by side with the main loop. Because the ATmega328 is a single-core microcontroller, the microcontroller first executes a command of the main loop, then a command of the interrupt, again a command of the main loop and so on. This makes it possible for the Arduino to ‘multitask’. A drawback of using interrupts is the relatively high complexity for beginners, even more so if these

beginners want to adjust the code.

The data from the second Arduino microcontroller is received through serial communication. To make things less complicated, a library called 'EasyTransfer' is used to manage the transmission of the data. This library is freely available on GitHub. It is able to send data saved in a particular structure with just the use of a simple function. The only problem that can occur using this method is that serial communication might fail while an interrupt is executing. Serial data is a stream of data and while an interrupt is running, this stream cannot be received. This issue has been solved with an if-statement in the code of the HABduino before calling the function to receive data. This means that the Arduino will first execute commands after the if-statement before continuing with the interrupts.

The HABduino stores the data string, that has to be transmitted by radio, in a buffer with the *snprintf()* function. This allows the HABduino to send character after character with the use of the earlier mentioned interrupts, while also gathering the new data for the next data string at the same time. A problem with this function is that support for floating point numbers in the *snprintf()* function has been removed from the Arduino IDE. To maintain the precision of the data, some of the values are multiplied by 100 and converted into long integers rather than just converted into integers. Later in the data processing, this change is reverted.

A disadvantage of the HABduino is the rate at which data is sent. This is caused by a relatively slow baud rate setting in the standard program. Therefore a complete data string, consisting of around 100 characters, takes roughly twenty seconds to be received.

4. RECEIVING DATA

Receiving data was achieved by a technology called Software Defined Radio (SDR). SDR makes it possible to receive and decode radio signals into characters. The only equipment needed is a laptop, a dongle named Airspy Mini and a Yagi antenna. The Yagi antenna was connected to the Airspy Mini with a standard antenna cable.

The Airspy Mini comes provided with software called SDR#. The software translates radio signals received by the Airspy Mini into a spectrum. The user is able to select a part of this spectrum that will be converted into audible sound. The sound produced is then transferred to a program, called Dl-fldigi, with the use of yet another program, Virtual Audio Cable (VAC). VAC makes use of the integrated soundcard of a laptop to record the sound from SDR# and play it back into Dl-fldigi. Dl-fldigi finally converts the sound, which consists of two alternating tones that represent a binary 0 and 1, into readable characters.

An example of a received data string looks as follows: "$$$$$D1,14:22:21,78.147637,16.041252,632,481,954, -6846,93739,2150,61669,584,5749,555,2888,1,300,0,0, 0,*F07E". The data from each sensor is separated by a comma.

One of the major drawbacks of this method is that Dl-fldigi needs a strong signal to decode correctly. This means that the transmitter, the HABduino in this case, has to send out a signal strong enough to transmit the many kilometres to the receiver. Consequently, if the balloon were farther away than expected, there is a chance that the antenna would not be able to pick up the relatively weak signal of the HABduino.

5. MEASUREMENTS

The scientific goal of this project was to determine the altitude of the tropopause in arctic conditions. Two balloons were launched with identical payloads to minimize errors. The sensors on board were a humidity sensor and a temperature sensor. The altitude data was taken from the GPS on board the HABduino. These sensors were able to determine the altitude of the tropopause because once the tropopause has been crossed, the temperature starts climbing again and the humidity drops to about 0%. Radio connection with the second balloon was lost while it was descending at an altitude of 15.6 kilometres.

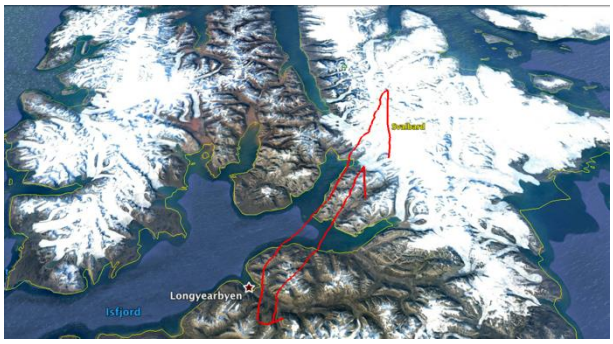

Figure 5. The trajectory of both payloads flown above the Norwegian archipelago Svalbard

The data from the GPS on board gives the opportunity to recreate the trajectory of the two balloons in Google Earth, as can be seen in Fig. 5. They were launched only a few hours apart. It was not possible to launch them simultaneously because there was no equipment available to receive data from two balloons at the same time. Both balloons followed a similar path, but the second balloon did not get nearly as far to the north as the first.

The data clearly shows that the points where the temperature starts climbing and the humidity drops to about 0% do not coincide. This is caused by tiny water drops that are still attached to the humidity sensor while the balloon is already in the stratosphere. The drops take a while to evaporate due to the rotating payload. This has no major impact on the estimation of the altitude of the tropopause because the lack of humidity in the stratosphere is caused by the change in temperature.

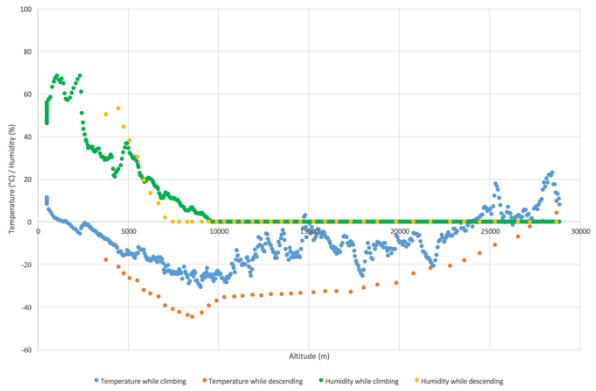

Figure 6. Temperature and humidity versus altitude of both payloads

In Fig. 6, the temperature has a lot of tiny variations. This is again caused by the rotation of the balloon. The sensor heats up when exposed to the Sun's radiation and cools down when not. While descending there were only a few minor variations because of the sunset. This is also the reason why the point where the temperature changes while descending is at a lower altitude than while the balloon was ascending.

It is only possible to make a rough estimation of the altitude of the tropopause because of two reasons: firstly the use of non-professional sensors and secondly the many variations in temperature due to the Sun's radiation. When the average of the data of both payloads is taken, the altitude of the tropopause above Svalbard on September 4, 2016 was between 9000 and 9650 meters.

6. CONCLUSIONS

This paper describes a project carried out by secondary school students. Projects of a similar difficulty level, described in [2] and [3], have been executed by students at Hasselt University. This project shows that it is also possible for even younger students to reach this level. These projects open the door for scientifically and technologically inspired students to an enormous variety of learning opportunities that are scarcely available within a regular secondary school environment.

The open-source platform Arduino was the basis of this project and once again proved to be very student friendly [2] [3].

Previous collaboration [4] between secondary schools showed that organizing the flight and trip together but letting each school fly its own experiment, might be the best approach. Hence partners involved don't need to have a similar level of technological proficiency.

Whatever the benefits of schools cooperating on expeditions abroad like these, time spending at fundraising remains one of the drawbacks.

7. ACKNOWLEDGEMENTS

This project would never have been possible without the expertise of Steven Peterzén, CEO and president of the ISTAR Group, a company that specializes in high altitude, near space balloon launches, launch site development and recovery methods. Thanks to Steven we were able to make use of the Kjell Henriksen Observatory for the integration of our two payloads.

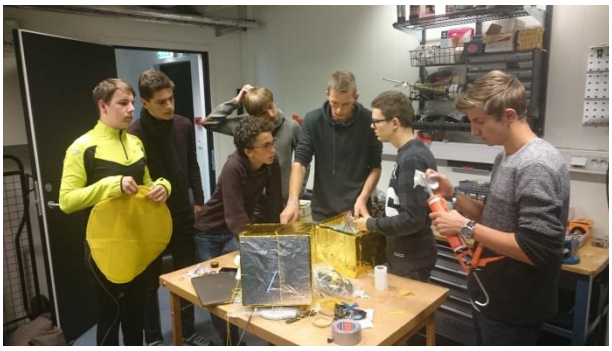

Figure 7. Hands-on work during payload integration at the Kjell Henriksen Observatory

We would also like to thank both team leaders of Sint-Pieterscollege Jette and St Paul's School London, Erik de Schrijver and Ken Zetie respectively. The presence of their teams reduced drastically the costs of our expedition to Svalbard.

8. REFERENCES

[1] Behe, N., Buggenhout, D., Chentouf, Z., Dekock, I., Smet, A., van Moll, C., Van Vreckom, E., de Schrijver, E. (2017). Secondary School Students Designing, Testing and Flying Geiger Counter Equipment to study Atmospheric Gammas over Europe and Svalbard. In *'23rd ESA Symposium on European Rocket and Balloon Programmes and Related Research'*, Visby, Sweden, 11-15 June 2017, ESA Publications Division, European Space Agency, Noordwijk, The Netherlands.

[2] Geeroms, D. et al. (2015). ARDUSAT, an Arduino-Based CubeSat Providing Students with the Opportunity to Create their own Satellite Experiment and Collect Real-World Space Data. In *Proc. '22nd ESA Symposium on European Rocket and Balloon Programmes and Related Research'*, Tromsø, Norway, 7-12 June 2015, ESA SP-730, ESA Publications Division, European Space Agency, Noordwijk, The Netherlands, pp. 643-647.

[3] Joris, T. et al. (2013). Data Logging a Water Rocket with Arduino. In *Proc. '21st ESA Symposium on European Rocket and Balloon Programmes and Related Research'*, Thun, Switzerland, 9-13 June 2013, ESA SP-721, ESA Publications Division, European Space Agency, Noordwijk, The Netherlands, pp. 201-205.

[4] de Schrijver, E. & Geeroms, D. (2011). A Novel Approach to Hands-On Space Education Outreach for Secondary School Students. In *Proc. '20th ESA Symposium on European Rocket and Balloon Programmes and Related Research'*, Hyères, France, 22-26 May 2011, ESA SP-700, ESA Publications Division, European Space Agency, Noordwijk, The Netherlands, pp. 249- 252.

TRAJECTORY ANALYSIS OF THE HYBRID SOUNDING ROCKET HEROS

Ferdinand Hertel[(1)], Christian Schmierer[(1), (2)], Mario Kobald[(2)], Stefan Schlechtriem[(1), (2)]

[(1)]University of Stuttgart Institute of Space Systems,
Pfaffenwaldring 29, 70569 Stuttgart, Germany,
E-mail: ferdinandhertel@googlemail.com, schmierer@irs.uni-stuttgart.de
[(2)]German Aerospace Center (DLR),
Im Langen Grund, 74239 Hardthausen am Kocher, Germany,
E-mail: mario.kobald@dlr.de, stefan.schlechtriem@dlr.de

ABSTRACT

HEROS is a hybrid sounding rocket designed and built by the student group HyEnD of the University of Stuttgart. The rocket was successfully launched from Esrange, Kiruna in 2016. It set a European altitude record of student rockets, by reaching 32.3 km. This paper discusses the trajectory analysis for the HEROS campaign.
Pre-flight analysis was conducted to aid the design process by predicting the impact of different configurations on the rocket's trajectory. The engine model was created with EcosimPro/ESPSS. The resulting thrust curves were validated with ground testing. ASTOS was used for the trajectory analysis. During the launch campaign, wind conditions were taken into consideration. Winds influence the landing location and can impede the recovery system. The data recorded on the rocket during flight was used to refine the simulated trajectory so that a better understanding of HEROS' characteristics could be reached.

1 INTRODUCTION

HyEnD (Hybrid Engine Development) was founded in 2006. It is a student group at the University of Stuttgart that was focused on designing and building hybrid rocket engines based on paraffin and nitrous oxide. In 2012 the German Aerospace Center Space Administration launched the STERN-program (STERN for student's experimental rockets), funded by the German Federal Ministry for Economic Affairs and Energy. The STERN project was coordinated by the German Aerospace Center Space Administration. It funded student groups from 8 Universities in Germany to design, build and fly rockets that would meet its objectives. Those objectives were to achieve an apogee of over 3 km above ground, to break the sound barrier, to have telemetry downlink and to be recoverable. Also, the project duration was set to 3 years. The participating student groups were free to define their rockets, as long as these objectives would be met. [1]
HyEnD developed two rockets during its STERN-project, MIRAS (Micro Rocket Stuttgart, a small technology demonstrator, launch mass ca. 10 kg) and HEROS (Hybrid Experimental ROcket Stuttgart, launch mass ca. 160 kg). HEROS is the rocket fulfilling the STERN objectives. Two MIRAS rockets were launched: the first in February 2015 and the second rocket in August 2015. Three HEROS rockets were built and launched. HEROS 1 was launched in October 2015. At an altitude of around 1.2 km, an engine failure occurred, so that the project objectives could not be met. In spring 2016, the German Aerospace Center - Space Administration approved a project extension until end of 2016. Within this time, HyEnD built two rockets of an improved version of HEROS. In October 2016, HEROS 2 was launched, but the electric current igniting the pyro-valve induced a voltage in the connecting line between ground support and on-board computers. This voltage was interpreted by the computers as a shut-down signal. Based on limited ground observation, nominal performance of the engine was assumed. The error in the on-board electronics could be isolated and corrected within a week, so that HEROS 3 could be launched in early November 8th 2016. HEROS 3 flew nominally, achieving an apogee altitude of 32.3 km and a maximum Mach number of ca. 2.3. By this, it set a new European altitude record for student rockets and a world altitude record for student hybrid rockets. [2]
An overview is given of the activities in the area of trajectory analysis and engine simulation that were undertaken in the context of HyEnD's STERN-project. The first part deals with the pre-flight trajectory analysis. Here, the simulation of the engine in EcosimPro/ESPSS (European Space Propulsion System Simulation) will also be discussed. In this phase, simulations of engine performance and trajectory were used as references for design and safety evaluation. After that, a description of the activities during the 2016 launch campaign follows, which were aimed at generating predictions for landing sites and weather constraints. The final part of this paper concerns with the post-flight analysis. In this phase flight data was compared with the simulations in order to get further insights into HEROS' performance.

2 PRE-FLIGHT

2.1 Transition to ASTOS

During most of the conceptual and preliminary design phases, a MATLAB SIMULINK based simulation was used for trajectory analysis. This simple simulation generated early insights into HEROS' performance and was used as a point of reference for the rocket's dimensioning. In late preliminary design, ASTOS was made available

to HyEnD by Astos Solutions GmbH. Training sessions for the students have been offered. ASTOS (AeroSpace Trajectory Optimization Software) is a commercial program designed to calculate and optimize trajectories during launch, ascent and other phases of spaceflight. Due to the larger number of features included in ASTOS, more effects are taken into consideration. Also ASTOS' user interface allowed for a more productive work environment. This enabled HyEnD to run simulations for additional scenarios, analysing a bigger number on factors that would possibly influence the trajectory. Also a standard simulation was being set up and later maintained, representing the current state of development, so that there would always be a reference for aerodynamic and thermodynamic loads.

2.2 Parameter Studies

After the initial construction of HEROS' model in ASTOS, several analyses were done on the impact of different rocket configurations. At this point, the project was in its late preliminary design and early detailed design phase, which meant that there was some uncertainty in HEROS' final attributes (especially regarding the rocket engine's performance). The impact of external pressurization of the oxidizer tank was assessed. Two configurations of HEROS featuring oxidizer pressurization with an additional tank of Helium were compared with a configuration only pressurized by the oxidizer's evaporation. The resulting altitudes and Mach numbers are given in Tab. 1. The increase in performance due to pressurization is comparatively low. This is due to the fact that an additional high pressure Helium tank increases the structural mass of the rocket. Since the Helium tank would also introduce more complexity to the system, a decision was made to remove the pressurization from HEROS' design.

Table 1: Pressurization Study

Configuration	Apogee Alt [km]	Max Mach Number
18 l at 405 bar	38.93 km	3.56
9 l at 400 bar	46.76 km	3.52
No Helium	34.67 km	2.71

The second major parameter study was aimed at identifying the impact of different levels of engine performance, structural mass and drag coefficient. The engine was represented as one of eight models listed in Tab. 2. Before the test campaign of the HyRES (Hybrid Rocket Engine Stuttgart) the engine's performance regarding maximum burn duration, solid fuel regression rate and combustion efficiency was not clear. [3]

Table 2: Engine Configurations

Nom. Thrust	Burn Duration	avg. Massflow	Isp
10 kN	15 s	4.57 kg/s	217 s
10 kN	12.5 s	4.57 kg/s	217 s
10 kN	10 s	4.57 kg/s	217 s
10 kN	12.5 s	5.14 kg/s	198 s
10 kN	10 s	5.14 kg/s	198 s
10 kN	10 s	5.7 kg/s	171 s
7.5 kN	13.3 s	4.29 kg/s	171 s
5 kN	20 s	2.85 kg/s	171 s

The second parameter taken into consideration was the structural mass of the rocket. As the concept for the oxidizer tank was not yet fully determined, there was some variation in structural mass. Also, the different engine configurations require different amounts of oxidizer; therefore the total volume of the tank was not determined. For the purposes of the parameter study, three dry masses for HEROS were assumed: 54 kg, 59 kg and 64 kg.
The third parameter analysed was aerodynamic drag. HEROS' aerodynamic model was based on a CFD simulation during the early preliminary design phase. The calculated curves of the drag coefficients over the Mach number were scaled up by 1.1, 1.05 and 1.0 and put into the simulation. After August 2015, simulations were done with aerodynamic coefficients gained with Missile Datcom.
The parameter study was executed by simulating the trajectories for all possible combinations of the given three parameters. As points of reference for comparing the different options, the apogee altitude and the maximum Mach number were taken into consideration. As HEROS' design changed significantly after this parameter study, the results became less meaningful. Their significance lies in the identification of trends. For the sake of brevity, the results will not be shown, but this method itself was applied at a smaller scale at later times to inform single design choices. In general, dry mass has little effect on the apogee altitude. There is some dependency on the drag coefficient, but the main deviation is caused by variations in combustion efficiency.

2.3 Prediction of Landing/Impact Area

To ensure safety during HEROS' flight, it was necessary to demonstrate that the rocket would touch ground within the boundaries of Esrange's designated impact area under any circumstances which still permit flight. This included both cases of a successful deployment of the parachutes or a ballistic impact.
A trajectory was simulated representing a nominal flight without any winds. After that, a wind profile that is typical for Esrange was applied to the model. This profile is given in Fig. 1. The trajectory was computed again for the same wind profile coming from north at all altitudes and the landing location was saved again. After

that, the wind profile was rotated by an increment of 10 degrees. This was repeated until a full rotation was completed, considering wind from all directions. Afterwards, the wind speeds were scaled up and down by a factor x, repeating the procedure as before. Similar analyses were done for a scenario representing a failure of the recovery system. The map in Fig. 2 shows the impact points calculated with this method.

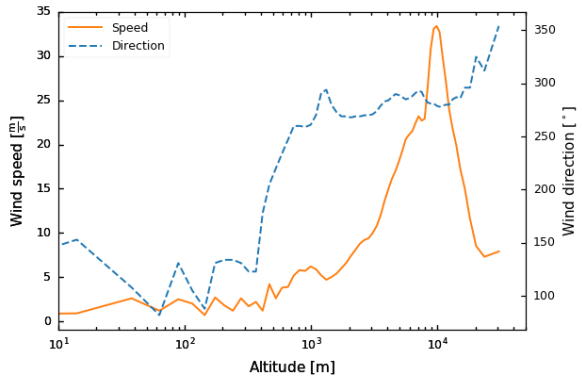

Figure 1: The nominal wind profile used in the landing area analysis.

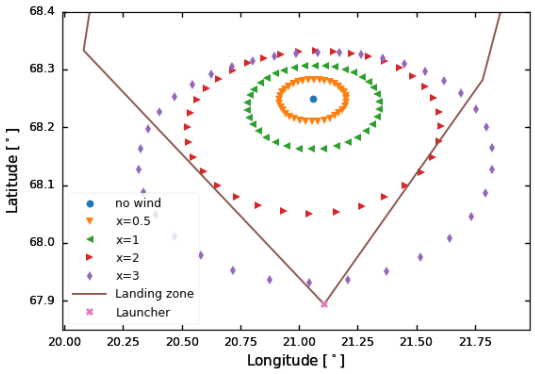

Figure 2: The ballistic impact area calculated pre-flight.

2.4 UWE, TTE and Wind-Weighting Curves

In order to calculate its suggestion for the launch tower correction Esrange needs some input data, which was generated in advance. Three variables were required: UWE (unit wind effect), TTE (tower tilt effect) and a wind-weighting curve.

1. UWE is the displacement of the impact point caused by a constant wind of 1 m/s from a given direction. It is assumed to be linear for small wind velocities.
2. TTE is the displacement of the impact point caused by a reorientation of the launch tower of 1 degree. It is assumed to be linear for small deviations from nominal attitude.
3. The wind-weighting curve is a function of the altitude describing the fraction of displacement of the impact point caused by wind. The reference is the distance between the impact point without wind and the impact point with a constant wind. As the next step, the wind speed is set to a constant value above a certain altitude. Below this altitude, it is set to 0. As a result, the displacement of the impact point will be reduced. By this, a fraction of effect of the wind below a certain point can be derived. The wind-weighting curve is a plot of this fraction over altitude. As an example Fig. 3 displays the wind-weighting curves of HEROS for a wind speed of 1 m/s and an oxidizer filling of 72.5 kg. As this curve displays, 90 percent of displacement of the impact location is caused by winds below 1000 m.

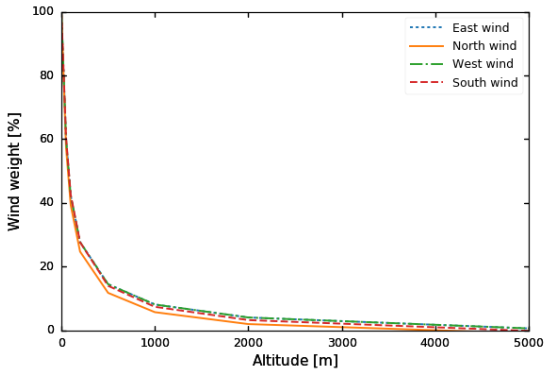

Figure 3: The wind-weighting curve of HEROS at 1 m/s wind speed and 72.5 kg oxidizer filling.

When the weather data is in, Esrange uses the wind profile and the wind-weighting curves to calculate a constant wind, which has the same effect on the rocket as the actual wind profile (called ballistic wind). This wind is multiplied with the UWE to calculate a displacement of the impact point. The last step is to calculate a launch tower reorientation using TTE to compensate the effects of wind on the impact point.

2.5 Simulation of Thrust

In the early design phase the hybrid rocket engine was preliminarily designed with analytical formulas for rocket combustion, using the combustion performance data of nitrous oxide and paraffin-based fuel [4]. There are three factors which increased the uncertainty of this analysis dominantly: Firstly, the regression rate of the propellant combination was not known very well. Over 100 small scale tests with small scale rocket engines have been done to determine the regression behavior of the used fuel with nitrous oxide. However, the upscaling from 500 N to 10000 N still changed the regression rate, and therefore the performance prediction and design

was reviewed and adapted always during the development phase. At the end of the test campaign, the regression rate behavior of the HEROS rocket engine HyRES was well known and understood. Secondly, the efficiency of the combustion was not known in the beginning. During the test campaigns the efficiency was raised from about 80 percent in the beginning of the tests to up to 99 percent in the end. This also had a huge impact on the overall performance of the engine, and this changed the estimated flight altitudes and maximum loads on the rocket during the development many times. The third unknown was the blowdown behavior of nitrous oxide during complete emptying of the tank while pressurizing only with the vaporizing of nitrous oxide itself. No additional pressurizing system was implemented. The system of equations to simulate this kind of self-pressurization is very complex. It is not enough to simulate the liquid as one volume. Instead, a discretization is needed, and a detailed model including vapor bubbles, heat exchange between tank wall, gas phase and liquid phase was necessary. Also the two-phase flow in the pipe, main valve and injector dome have an enormous impact on the total mass flow and thrust evolution during blow down. To include all these effects in the development, simulations with EcosimPro and the ESPSS library were done at the DLR Lampoldshausen. Detailed models of the tank filling process as well as the rocket engine burning in blow down mode were created. The simulations were refined and matched to the HyRES tests which were conducted partially in blow down mode too. Even when a lot of data was gathered in these tests, the simulations allowed to do parameter studies without the need for a lot of tests, which reduces development cost and duration. With this parameter studies, e.g. different initial oxidizer mass or initial oxidizer temperature, several thrust and mass flow curves could be created to be used in ASTOS simulations. This improved greatly the understanding of the rocket's reaction to different engine performances. The simulations of nitrous oxide for a hybrid rocket engine in blow down have a high accuracy, which was not found in literature up to date. The simulation of nitrous oxide in ESPSS seems to be highly promising to greatly reduce development time of such rocket engines in the future.

Fig. 4 shows the schematic layout of the used simulation model in ESPSS. The tank is modelled including the aluminium and carbon fiber walls. The tank is connected via pipe, hose, valve and orifice components to the hybrid combustion chamber. The simulated thrust, tank and chamber pressure are shown in Fig. 5. These simulation results represent the simulation of HEROS 3 flight, which was used to reconstruct the flight in the ASTOS simulation. The duration of the liquid oxidizer feeding phase was roughly 15 s which is a bit less than experienced on ground testing. It can be explained by the higher oxidizer mass flow due to the additional acceleration of the rocket, which increases the pressure at the tank outlet. After the liquid oxidizer is depleted, the remaining gaseous oxidizer in the tank can sustain thrust still for further 15 s. The thrust drops to less than 50 percent of the nominal value. In reality the transition between liquid and gas phase is less instantaneous, which is caused by the limited discretization of the simulation model and the two phase flow simulation.

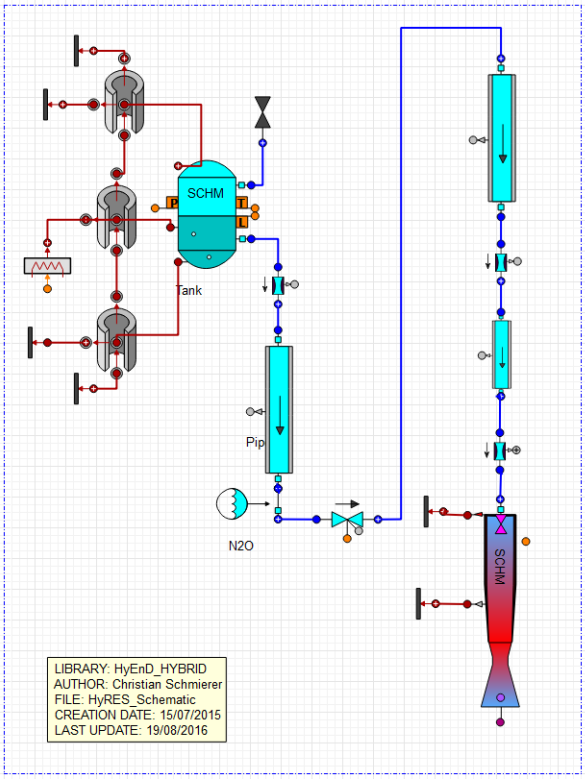

Figure 4: A depiction of the setup of HEROS' HyRES engine.

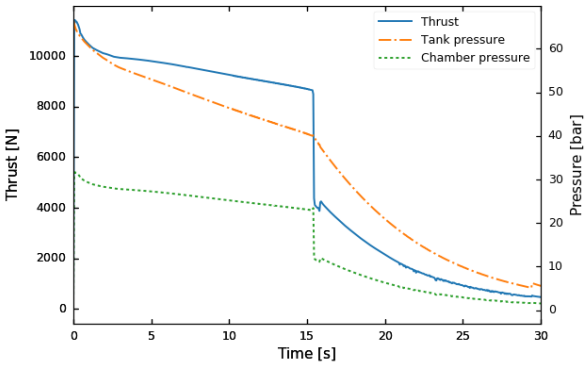

Figure 5: Thrust and pressures over time from the ESPSS Simulation.

3 LAUNCH CAMPAIGN

During HyEnD's launch campaign of HEROS 2 and 3 from October 24th 2016 to November 06th 2016 at Esrange trajectory analysis was needed for two tasks: checking if the requirements of the recovery system are met and analysing the influence of the wind on the impact point. A correction of the launch tower was derived from this wind analysis. A weather balloon was released during countdown, in order to take wind measurements. Based on those a forecast is generated for T=0.
The limiting factor for the recovery system in this context is the apogee speed. If it is too high, the shock loads during deployment of the drogue parachute exceed the specifications. As HEROS orients itself, so that it faces into the direction the airstream is coming from, wind from north results in a shallower trajectory. Thus, the increase in velocity includes a larger horizontal component, which is reflected in the apogee speed. Using the wind forecast for T=0, a trajectory is simulated using ASTOS. The altitude and speed at apogee are compared to the limits defined in the recovery system's requirements, so that a GO/NO GO decision can be made. The maximum dynamic pressure during descent is also taken into consideration, as the decelerating capabilities of parachutes near apogee are small and gravity further accelerates the rocket.
If the conditions are met for a GO, a simulation is run with changed settings, so that the trajectory of HEROS with a ballistic descent is represented. The resulting impact point is compared to the impact point that would have occurred if no winds were present. Esrange suggests a change in launch tower attitude based on separate calculations using UWE, TTE and the wind-weighting curve (see chapter 2.4). Another simulation is done with the new attitude and the impact point is compared to the two points calculated before. Based on the three calculated impact points, the final launch tower attitude is determined. A comparison and cross check with Esrange's tool was done. The purpose of this iterative approach is to work around the stronger deviation from the assumed linear dynamic behaviour HEROS has compared to other sounding rockets. An overview of the other activities of HyEnD during the launch campaign is given in [5].

4 POST FLIGHT

Due to the varying performances of HEROS 1, 2 and 3, the post flight trajectory analysis was aimed at different objectives for each rocket. For HEROS 1 and 3, flight data is available and the rocket could be recovered. Therefore a reference is given on which the trajectory analysis can be based. For the flight of HEROS 2, no data is available, so trajectory analysis functions as a method to narrow down a possible impact location.
Due to the engine malfunction of HEROS 1, the trajectory was changed significantly. During propelled flight, thrust and thus acceleration were reduced. After 7 seconds, the engine ruptured and destroyed the aft section of the rocket. This caused HEROS to become aerodynamically unstable, so the rocket diverted from its nominal attitude and decelerated quickly. Weather conditions during launch hindered visibility. Due to that, trajectory simulation was necessary, combined with flight data analysis, analysis of the rocket's structure and sound recordings, to get an insight into what happened. In this context, trajectory simulation was used to recreate a more comprehensive depiction of the events occurring during this flight.

At the ignition of HEROS 2's oxidizer pyro valve, both on-board computers where shut down by the interference with the ignition current. Due to that, no telemetry downlink occurred, so no flight data was available. Visual contact to the rocket was also cut off shortly after launch, because of clouds. These circumstances lead to the assumption that the recovery system was not activated and HEROS 2 impacted the ground. HyEnD simulated trajectories in an attempt to localize the area at which the rocket had impacted. It also applied the deviations from predicted behaviour noticed in the trajectory analysis of HEROS 3 to the trajectory of HEROS 2, but up until now the rocket could not be found.

HEROS 3 performed nominally. HyEnD received telemetry data up until a few seconds before ground contact, so the rocket's position was known accurately. HEROS 3 could be recovered within two hours. The recorded data made it possible to recreate the engine performance of the flight in an EcosimPro/ESPSS simulation and integrating these results into a model for the trajectory. A wind model based on data from a second weather balloon at T=-15 min and data from Esrange's wind tower from T= 0 were also considered. Analyzing this model, some insights into the rocket's actual parameters could be obtained. The drag coefficient was ca. 10 percent higher than calculated and the rocket's attitude was more stable than expected. This resulted in less pitch down when leaving the launch rail. Over all, good correlation between simulation and flight data can be achieved if the prerequisite of accurate wind profiles is fulfilled. Fig. 6 shows a comparison between simulation and IMU (Inertial Measurement Unit) flight data. Fig. 7 features a representation of the simulated trajectory and the GPS (Global Positioning System) flight data in Google Earth. The GPS curve begins close to apogee, because tracking before this point was disabled due to the COCOM (Coordinating Committee for Multilateral Export Controls) limits. [6]

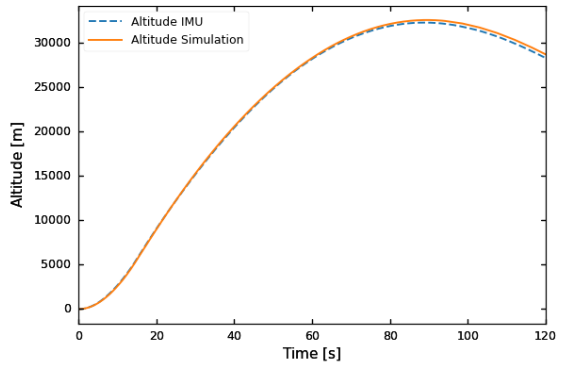

Figure 6: A comparison between simulated and measured altitude.

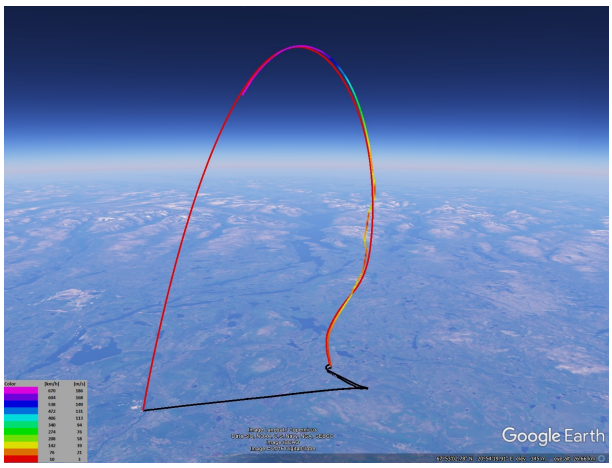

Figure 7: A depiction of the trajectory in Google Earth. Red curve: Simulation, multicoloured curve: GPS

5 CONCLUSION

During HyEnD's STERN-project, trajectory analysis and engine simulation were used in multiple contexts and benefitted the design, flight and analysis of the HEROS rocket. Trajectory analysis served as a reference for the other areas of development and for flight safety considerations.
After an introduction to HyEnD and the STERN programme, the activities done during the development phase of the rocket were reported on. Those included the provision of a general reference for vehicle design and the comparison of multiple technical implementations in a parameter analysis. Predictions on probable landing areas and a calculation of parameters required by Erange's flight safety office were done pre-flight. Engine performance simulations were done with EcosimPro and ESPSS. Comparisons with the tests done at test bench M11.5 at the DLR Lampoldshausen were done, and the models were refined with the gained data. Propulsion system simulations could be done to perform parameter studies and learn about the impact of the propulsion system's performance on the rocket's trajectory. During the countdown, trajectory analysis predicted the fulfilment of the recovery system's requirements and aided in determining the optimal launch tower orientation. Post flight, the flight data was compared to the simulation to further refine the characteristics of the HEROS rockets. Also, post flight analysis was used in an attempt to determine the position of impact of HEROS 2.
In general, HyEnD could apply trajectory and engine simulation and analysis at multiple occasions within its STERN-project. ASTOS, EcosimPro and ESPSS improved on the team's predictive capabilities.

ACKNOWLEDGMENTS

The HyEnD-STERN project was coordinated by the DLR Space Administration with funding from the Federal Ministry for Economic Affairs and Energy (BMWi) at the Institute of Space Systems at the University of Stuttgart, under the grant number 50RL1254 since September 2012.

REFERENCES

[1] Lappöhn, K., Regenbrecht, D., Bergmann, D., Schmid, M. & Rickmers, P. (2012). STERN Raketenprogramm für Studenten. *Deutscher Luft- und Raumfahrtkongress 2012*, Deutsche Gesellschaft für Luft- und Raumfahrt - Lilienthal-Oberth e.V., Berlin, Germany

[2] Kobald, M., Fischer, U., Tomilin, K., Petrarolo, A., Kysela, P., Schmierer, C., Pahler, A., Gauger, J., Breitinger, J. & Hertel, F. (2017). Sounding Rocket "HEROS" - A Low-Cost Hybrid Rocket Technology Demonstrator. *53rd AIAA/SAE/ASEE Joint Propulsion Conference*, Atlanta, GE, USA

[3] Kobald, M., Schmierer, C., & Petrarolo, A. (2015). Test Campaign of a 10000 N Hybrid Rocket Engine. *6th European Conference For Aerospace Sciences (EUCASS)*, Krakow, Poland

[4] Kobald, M. (2015). Combustion Phenomena of Advanced Hybrid Rocket Fuels. Dissertation, University of Stuttgart.

[5] Breitinger, J., Schmierer C., Kobald, M. & Schlechtriem, S. (2017). Launch Campaign of the Hybrid Sounding Rocket HEROS. *23rd ESA Symposium on European Rocket & Balloon programmes and related research*, Visby, Sweden

[6] Copenhagen Suborbitals (2014). GPS without limits. Online at *https://copenhagensuborbitals.com/gps-without-limits/* (as of May 31st 2017).

STAGE CONCEPT FOR A HOVERING THERMOSPHERE PROBE VEHICLE WITH GREEN, SAFE AND AFFORDABLE GELLED PROPELLANT ROCKET MOTORS

Pedro C. Pinto[(1)], Karl W. Naumann[(2)], Jürgen Ramsel[(3)], Tobias Meyer[(4)], Sebastian Rest[(5)]

[(1-4)] Bayern-Chemie GmbH, PO. Box 1131, D-84544 Aschau/Inn, Germany
[(1)] pedro.caldas-pinto@mbda-systems.de
[(2)] karl.naumann@mbda-systems.de
[(3)] juergen.ramsel@mbda-systems.de
[(4)] tobias.meyer@mbda-systems.de
[(5)] sebastian.rest@mbda-systems.de

ABSTRACT

This paper presents the design concept of a propulsion system for a scientific vehicle for atmospheric research. The specific property is that this vehicle can hover at a required altitude, or scan an altitude range or a lateral range to gather measurements about a selected volume of the atmosphere. The preferred altitude for those measurements is the mesosphere and the thermosphere. This region is too high for balloons but nevertheless of importance for the re-entry of space vehicles. Traditional sounding rockets that can cross this atmospheric layer upwards and downwards yield only measurements along a narrow flight path over a short period of time. Hence, a vehicle that can travel or hover at a required altitude will enhance the measuring capability significantly. As a baseline we assume that the total vehicle mass is about 400 kg which equals the standard payload mass of a VSB-30 sounding rocket assembly. Dependent on the cruise altitude, the vehicle van be launched by a one- or two-stage sounding rocket. The paper outlines the concept and the functional and performance parameters of two demonstrator vehicles, of 100 and 300 kg mass, respectively.

1. INTRODUCTION

Bayern-Chemie is a company located near Aschau am Inn, a small town around 60 Km East of Munich, Germany. Its main activity field is propulsion for tactical missiles, which includes rocket motors with solid and gelled propellants, as well as airbreathing ducted rockets. It is a 100% subsidiary of MBDA Germany, which is the German arm of the European company MBDA Missile Systems. This paper focuses on the scalability of the Throttleable Gelled Rocket Motor (GRM) as designed and tested by Bayern-Chemie as the propulsion system for future missiles [3,4], sounding rockets [5,12] and divert and altitude control systems (DACS) [6].

This article is divided in 4 sections. Section 2 concerns the current state of the gel propellant development at Bayern Chemie. In section 3, a description is given of the green GRM characteristics and performance is given. This is followed by an overview of the hovering thermosphere vehicle with a gel propellant motor and an analysis of the two proposed configurations. Finally, an overall summary of the article is given.

2. GEL ROCKET PROPELLANT TECHNOLOGY

In the last two decades a growing interest in gelled propellants, propellants or propellant combinations for rocket and ramjet propulsion applications can be observed worldwide. Gelled propellants have the potential to combine major positive properties of liquid and solid propulsion systems without combining major disadvantages. This means in detail that a gel rocket motor combines thrust variation on demand, i.e. an advantageous characteristic of liquid rocket motors, with the easy handling and storage characteristics of solid rocket motors. Also for air-breathing ramjets the use of gel propellants is advantageous because of better safety aspects in comparison to liquid propellants [7,8].
The possibility to combine these above mentioned properties is caused by the non-Newtonian rheological behaviour of gels. Gels are solid at rest and are thus easy to handle and store, similar to solid propellants. Under a sufficiently high applied shear stress, however, they can be liquefied whereas their viscosity decreases with increasing applied shear stress.
The origin for the development of a gel rocket motor (GRM) was the demand to realize a rocket motor with variable thrust, easy handling and storage characteristics and lower hazard potential than typical solid and liquid rocket motors (LRM). The requirement of environmental friendliness on propellants and exhaust, commonly designated as “green propulsion”, was also added. For the German Gel Propulsion Technology Program (GGPT) [3], the absence of toxic and thus hazardous ingredients like hydrazine and its derivatives,

N2O4 (NTO) and HNO3 (IRFNA) was an initial key requirement. The requirement of long-time storability of the propellants excluded ingredients that exhibit autocatalytic processes, are otherwise chemical unstable or are not storable under ambient temperature and pressure like N2O or cryogenic liquids.
A GRM or Gel Gas Generator (GGG) shares with the liquid rocket motor (LRM) the separation of tank and combustion chamber and with solid rocket motors (SRM) the essentially solid nature of the propellant as long as it rests in the tank. The essentially solid state of the propellant in the tank reduces the hazard potential significantly because in case of damage or an accident the gelled propellant:

- Does not spill
- Produces no large evaporation surface
- Has a much lower vapour pressure than the liquid
- Does not soak into the ground

Like for LRM, thrust control is possible by control of the gelled propellant mass flow rate. The key ingredients of an effective GRP are a balanced blend of energetic fluids mixed with small amounts of efficient gelling agents. Additives can be used to modify the combustion behavior or other properties of the GRP. If tolerable, solid particles can be suspended in the gel to increase the I_{spec} and / or the density of the GRP, because the nature of the GRP prevents sedimentation or buoyancy of incorporated particles even over long storage times. GRMs can be either bi-propellant or monopropellant systems.
The GRP is fed to the combustion chamber (CC) by a pressure feeding system because a gel cannot be pumped e.g. via turbopumps as in typical larger liquid rocket engines. For smaller liquid propulsion systems, however, pressure feeding systems are equally used. In most cases this is driven by pressurization gases, either produced by a gas generator (GG) or from a high pressure gas reservoir. For a gel rocket motor (GRM) it is advantageous that a piston within a long cylindrical tank or a membrane within a short or spherical tank separate the GRP from the pressurizing gas. The GRP is injected into a combustion chamber in such a way that a spray of small droplets is formed. The very high shear rates produced during the injection process destroy the gel structure and the GRP behaves similar to a liquid propellant (LP).
The thrust level of the GRM can be either controlled by control of the GRP mass flow or by intermittent operation, and a GRM can be shut off on demand at any time
The “solid” nature of GRP also prevents sloshing in the tank, if the tank is subjected to variable acceleration or vibration. Figure 1 shows a sketch of the principle of operation of a GRM.

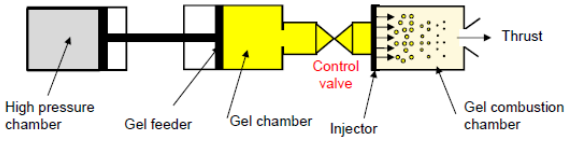

Figure 1: Principle of operation of a GRM

3. GREEN GRM CHARACTERISTICS AND PERFORMANCE

The propellant development guidelines of the German Gel Propulsion Technology program are:

- A GRP that is storable at least 10 years.
- To use ingredients not particularly toxic, carcinogen, acid or in other respects harmful for people or the environment, because the hazard potential of these materials would disqualify them for use in military applications. This disqualifies ingredients like hydrazine or its derivatives and oxidizers like dinitrogen tetroxide or nitric acid
- To develop GRP formulations that cover as widely as possible also the military relevant operational temperature range from -40 °C up to +71°C. This also excluded aqueous solutions of many oxidizer salts.

The first result of the development activities was a monopropellant throttleable GRM system, burning GRP-001 that was demonstrated by the two successful flight tests [2]. Since then, the goal of the activities has been to improve the functional and performance parameters of the motor. Key properties of the monopropellant system are:

- Stable start and combustion
- Throttleability
- Wide turn-down range
- A family of monopropellants with different gelling agents, liquid and solid ingredients and additives
- Good scalability of the GRM over the nominal thrust range of 300 to 6000 N at atmospheric pressure
- Environmental friendliness of propellant and exhaust gas
- Little primary and secondary smoke if no solid additives are used
- Good handling, transport and storage properties
- Long storage time. An environmental test program similar to that for a solid propellant rocket motor, covering 5 years of lifetime was carried out for a GRM with GRP-001 and after this program the GRM showed no degradation at a static firing test
- High degree of insensitivity. Tests with GRP-001 carried out at the Federal Institute for materials Research and Testing (BAM) yielded the rating “no explosive”. IM-tests carried out at WTD 91 showed mild burning under propellant fire, slow heating and bullet attack and no reaction under fragment

attack. A more detailed assessment of the hazard potential of different propellant systems is given in [9]

- A wide operational temperature range
- Ignition by solid propellant igniters and an external gas lancet has been demonstrated
- Monoblock solid gas generator designs for tank pressurization that allow to cover within a given time frame various thrust profiles, and a method to predict the tank pressure histories dependent on thrust course and gas generator (GG) design which can be used to optimize the ballistic behavior of the GG

A penalty to be paid for the high degree of insensitivity is that the GRM needs a comparatively powerful ignition system, which complicates the design of a GRM with repeatable ignition. Hypergolic systems and non-hypergolic bi-propellant systems are a topic of actual basic research activities, but not yet sufficiently mature to build a rocket motor.

Table 1 gives an overview on theoretical specific impulse I_{spec}, density ρ and theoretical combustion temperature T_c of the different propellants of BC's GRP family. The theoretical performance of the propellants has been validated by a campaign of performance test runs. Looking for ballistic performance, the maximum I_{spec} of GRP-002, GRP-004 and GRP-013 (for example) is comparable to that of classic moderately aluminized propellants with HTPB as binder and ammonium perchlorate as oxidizer. Other propellants like GRP-007, GRP-008, GRP-010 or GRP-019 have a low combustion temperature and are suited for the use in gas generators (GG) that pressurize volumina, e.g. tanks, produce the driving gas for mechanical assemblies or for DACS. By blending of different ingredients the combustion temperature of the gelled propellant can be adapted to the thermal sustainability of the mechanical structures, e. g. valves or other gas flow control or energy conversion systems that are subjected to the combustion products. Notice that the density of the GRP tends to be higher than that of liquid propellants which are currently in use.

Table 1: Key parameters of the GRP family

Gel	I_{spec} 70:1 [Ns/kg]	T_c [K]	ρ [g/cm^3]
001	2194	2144	1.13
002	2512	2795	1.31
003	2236	2089	1.18
004	2586	2910	1.28
005	2080	1883	1.17
006	2182	1981	1.16
007	1900	1396	1.11
008	1878	1375	1.09
009	2143	1904	1.19
013	2290	2536	1.41
014	2178	1857	1,14
015	2467	2770	1.38
016	2465	2809	1.38
017	2423	2650	1.38
018	2135	2574	1.42
019	1990	1438	1,11
026	2622	3150	1.49
039	2629	3180	1.55

4. HOVERING THERMOSPHERE PROBE VEHICLE

The concept of a GRM probe vehicle was first introduced in [11] The goal of this study is to build a GRM that can sustain a payload for high atmospheric research within a given altitude band in order to allow for extended measuring times over a desired vertical and horizontal band. Detailed knowledge of the high atmosphere is essential for the reentry of space vehicles, and not directly accessible by either orbital space craft or balloons. The guidelines are:

- Designing a probe capable or maneuvering vertically in the high atmosphere
- Achieving a sampling time of at least 1 minute
- Ground launched sounding rocket, preferably single stage
- Simple and cost-effective design
- Fast implementation, in particular of the 100 kg variant.
- Use of off-the-shelf, proven hardware and designs as much as possible

In this paper we describe two different configurations for the probe vehicle: a first, basic demonstrator of around 100 kg mass and a second, scaled-up demonstrator of 300 kg mass and a caliber of 356 mm or 438 mm.

Figure 2 shows a sketch of the proposed GRP probe vehicle and launcher, while *Figure 3* shows a close-up of the probe vehicle. To note are the spherical gas tank,

the GRP tank and the gimbaled bearing connecting the GRP tank to the motor/nozzle section, which allows for thrust control.

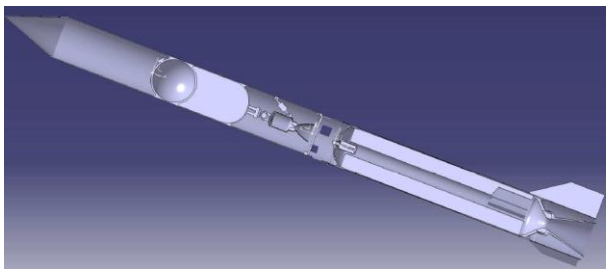

Figure 2: Sketch of the GRP Hovering Thermosphere Probe Vehicle and first stage launcher

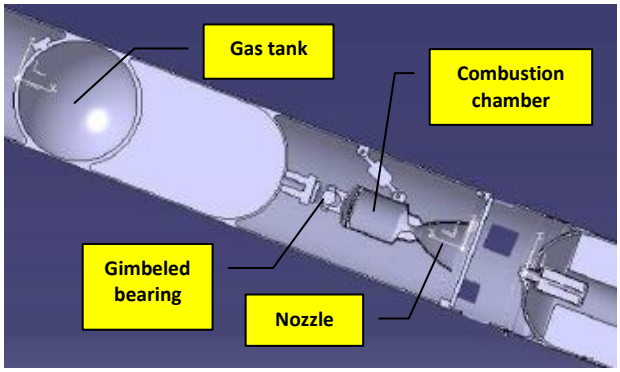

Figure 3: GRP Hovering Thermosphere Probe Vehicle

A roll control is already foreseen for the reference stage. If an attitude control should be necessary, its gas supply can be provided by the GGG of the roll control system.

Depending on the specific mission requirements, the probe vehicle can have higher or lower thrust, with more or less propellant to cover longer or shorter flight times, since the GRM tank can be loaded with a full or limited propellant load. With a reduced propellant load, the propellant mass ratio, being one of the most important figures of merit, will not be impressive, but a partial propellant load may benefit the mission, e. g. trading a higher payload mass against a shorter hovering time.

It is necessary to achieve a high enough forward velocity in order to avoid an influence of the rocket exhaust gas (*Figure 4*). This is not a problem when moving upwards, as the rocket motor is located in the rear. Otherwise, an incidence angle of up to 20° – 30° already provides a significant lateral acceleration with marginal loss of climbing efficiency.

A higher incidence angle is recommended when moving downward:

- A small vertical thrust is advantageous when accelerating downward
- By constant downward movement an incidence angle can be chosen that provides the probe the desired forward

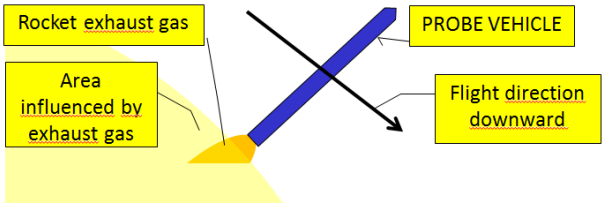

Figure 4: Exhaust gas constraint on the flight trajectory

1.1. START AND BOUNDARY CONDITIONS

The mean propellant mass flow is $m \bullet g / I_{sp} \sim 0{,}4$ kg/s per 100 kg Mass (particle-free propellant) if the following points are considered:

- Equally distributed upward (higher thrust) and downward acceleration (lower thrust).
- For 100 kg start mass and 30 kg propellant t_{op} = $30/(85 \bullet g/2500) = 90$s
- For 300 kg start mass around 90 kg propellant are needed.

In case of ascent or descent at high subsonic speeds, which is eventually advantageous for sampling, since the probes will not be affected by shock wave effects, and at constant vertical speed of 250 m/s the flight will have a duration of:

- 80s for an altitude difference of 20 km. If multiple cycles are needed then either a higher proportion of propellant is necessary or a more energetic, particle loaded, GRP needs to be considered.
- For higher average ascent/descent speeds the cycle will be of shorter duration, since the high and low thrust phases are dominant in comparison with the mid thrust phase.

The output parameters of the motor design are the (fixed) injector head and nozzle diameter. The combustion pressure can vary between 6 – 60 bar, which is roughly equivalent to the thrust variation in Vacuum.

Table 2 presents the theoretical thrust and acceleration for both 200 and 300 kg probe configurations and an acceleration of 40 m/s^2 and Table 3 the results for the same probe configurations and an acceleration of 30 m/s^2. Based on the results, a moderate ascent acceleration seems plausible. For the 100 kg probe the test GRP motor at Bayern chemie with eight injectors and maximum thrust of c.a 2.5 to 3 kN is suitable. For the 300 kg probe the flight motor at BVC with 18 injectors and a maximum thrust of c.a 6 kN can be used.

Table 2: Thrust and acceleration for the 100 kg and 300 kg probe with a total acceleration of 40 m/s^2

Parameter	m = 100 kg	m = 300 kg
Mid hover thrust	850 N	2550 N
Mid. Ascent thrust (a+g) = 40 m/s^2:	3400 N	10000 N
minimum thrust:	340 N	1000 N
average ascent acc.time from 0 – 250 m/s:	8.3 s	8.3 s
average descent acceleration:	5.8 s	5.8 s
average descent acc. Time from 0 – 250 m/s:	43 s	43 s

Table 3: Thrust and acceleration for the 100 kg and 300 kg probe with a total acceleration of 30 m/s^2

Parameter	m = 100 kg	m = 300 kg
Mid hover thrust	850 N	2550 N
Mid. Ascent thrust (a+g) = 30 m/s^2:	2550	7650 N
minimum thrust:	250 N	760 N
average ascent acc.time from 0 – 250 m/s:	12.4 s	12.4 s
average descent acceleration:	6.8 s	6.8 s
average descent acc. Time from 0 – 250 m/s:	36 s	36 s

The gel tank is a structural component of the system and can be constructed out of steel or CFK, which would mean a mass reduction of roughly 10 kg in both configurations. The Gel propellant tank membrane is of known design. The combustion chamber is made of steel with an ablative thermal protective layer and a CMC nozzle throat.

The thrust control is achieved through a propellant mass flow control valve, The motor is designed with a fixed nozzle and fixed number of injectors. The thrust vector control is achieved though a 2-axis moveable combustion chamber and the roll control through pressurized gas.

Th gas chosen to pressure the gel tank is Helium, which is available at storage pressures of maximum 70 MPa.

The basic dimensions for the 100 and 300 kg demonstrator can be found in *Table 4.*

Table 4: basic dimensions for the demonstrator

Parameter	m = 100 kg	m = 300 kg
Maximum Thrust	2500 N	6300 N
Mass propellant	30 kg	100 kg
Length complete GRM	520 mm	645 mm
Combustion chamber	265	270 mm
Nozzle(A/A*= 60)	205 mm	325 mm
External combustion chamber diameter:	90 mm	110 mm
Final diameter nozzle (A/A*= 60)	190 mm	290 mm
Length propellant tank	400 mm	1000 mm
Diameter gas tank (600 bar, spheric)	240 mm	355
Length cylindric gas tank, (600 bar, 120 mm outside diameter)	350 mm	355 mm
Total length with inline gas tank	1160 mm	2000 mm
Total length with gas tank on the sides of the CC:	920 mm	
Mass propulsion system without propellant:	30 kg (metal tank) or 20 kg (CFK tank)	60 kg (metal tank) or 50 kg (CFK tank)

5. SUMMARY

It is possible to design a hovering thermosphere probe vehicle with GRM that allows sampling the atmosphere along a given flight trajectory. In the design as described in this paper, the probe can be launched as the upper stage of a sounding rocket. The necessary technologies to develop the probe motor are known and to a certain extent tested with GRM.

6. ACKNOWLEDGEMENTS

We highly appreciate the support DLR MoRaBa in the definition of the GRM stages and for the calculation of the trajectory. Equally we thank all our colleagues that work with endeavour within the GGPT working group.

7. REFERENCES

[1] Ciezki H.K., Naumann K.W., Weiser V., "Status of Gel Propulsion in the Year 2010 with a Special View on German Activities", *Deutscher Luft- und Raumfahrtkongress 2010*, Hamburg, Germany, August 31 – September 2, 2010

[1] Stierle, R., Schmid, K., Ramsel, J., Naumann, K. W., "Free-Flight Demonstration of the Gelled Propellant Rocket Motor of MBDA-Bayern-Chemie", *4th European Conference for Aeronautics and Space Sciences*, St. Petersburg, Russia, July 4 – 8, 2011

[2] Ciezki, H.K., Negri, M., Gernoth, A., "Advanced

Liquid and Gelled Propellants for Rocket and Ramjet Propulsion," Int. Journal of Energetic Materials and Chemical Propulsion, Vol. 14, No. 2, 2015, pp. 85–123

[3] Schmid, K., Ramsel, J., Naumann, K.W., Stierle, R.; Weiser V., "Raketenmotore mit Gel-Treibstoffen – Stand der Technologie bei Bayern-Chemie", *Deutscher Luft- und Raumfahrtkongress 2012*, Berlin., Germany, September 10-12, 2012

[4] Naumann K.W., Ciezki H. K., Stierle R., Schmid K., Ramsel J., "Rocket Propulsion with Gelled Propellants for Sounding Rockets", *20st ESA Symposium on European Rocket and Ballon Programmes and Related Research*, Hyères, France, June 22-26, 2011.

[5] Naumann K. W., Ramsel J., Niedermaier H., Caldas-Pinto P., Hopfe N., Scheutzow S., Riemäcker C. M., Thumann A, "The Application of Rocket Motors and Gas Generators with Gelled Propellants for BMD Interceptors", *AAAF 10th Int. Conf. on Missile Defence*, Mainz, Germany, June 17-20, 2014

[6] Ciezki H.K., Naumann K.W., Weiser V., "Status of Gel Propulsion in the Year 2010 with a Special View on German Activities", *Deutscher Luft- und Raumfahrtkongress 2010*, Hamburg, Germany, August 31 – September 2, 2010

[7] Madlener, K. and H.K. Ciezki. 2009. Some Aspects of Rheological and Flow Characteristics of Gel Propellants with Regard to Propulsion Application. In: *45th AIAA Joint Propulsion Conference*. Paper no. AIAA-2009-5240, August 2-5, 2009, Denver, Colorado, USA.

[8] Sackheim R. L., Masse R. K; "Green Propulsion Advancement: Challenging the Maturity of Monopropellant Hydrazine", AIAA Journal of Propulsion and Power, Vol. 30, N0. 2, pp. 265 – 276, March-April 2014.

[9] K.W. Naumann, H.K. Ciezki, P. Caldas Pinto, J. Ramsel, T. Meyer, S. Rest, A. Thumann, G. Kurth "Green Gelled Propellant Throtteable Rocket Motors for Affordable and Safe Micro-Launchers", *7th European Conference for Aeronautics and Space Sciences*, Milan, Italy, July 3 – 6, 2017

[10] Naumann, K. W., Caldas-Pinto, P., Ramsel, J., Niedermaier, H., Risse, S., Thumann, A. "Green, Highly Throttleable Gelled Propellant Rocket Motors – State and Application Potentials", *52nd AIAA Joint Propulsion Conference August 2-5, 2009, Salt Lake City, USA.*

[11] Naumann, K. W, Ciezki, H., Caldas Pinto, P., Ramsel, J., Niedermaier, H., Rest, S.. "A Modular Sounding Rocket Concept with Green, Safe and Affordable Gelled Propellant Rocket Motors

", *23rd ESA Symposium on European Rocket and Ballon Programmes and Related Research*, Visby, Sweden, 2017

FRENCH BALLOON ACTIVITIES 2015 – 2018

VISBY, SWEDEN
11-15 JUNE 2017

Vincent Dubourg, Philippe Raizonville, André Vargas,
Philippe Cocquerez, Stéphane Louvel, Frédéric Thoumieux, Muriel Saccoccio, Frederi Mirc
CNES, Centre National d'Etudes Spatiales, Toulouse, 31401, France
Tel : +33561273523 E-mail : vincent.dubourg@cnes.fr
Tel : +33561273047 E-mail : philippe.raizonville@cnes.fr
Tel: +3361273493 Email: andre.vargas@cnes.fr

ABSTRACT

The French Centre National d 'Etudes Spatiales (CNES) goes on supporting a significant balloon program and infrastructure, for scientific and technological purposes.
Designed to be mobile, the CNES balloon systems and operation means can be deployed and operated worldwide, at several latitudes. The extended range of vehicles and payload gondola service provided by CNES allows addressing several kinds of missions such as astronomy, atmospheric physics and chemistry, meteorology, and technology.
The main achievement of the past 7 years was to deeply renovate the CNES balloons command and control systems and flight operation processes to comply with more stringent Safety constraints and with growing performance and reliability requirements. This is done for zero pressure balloons (ZPB), and in progress for the other product lines.
Since 2014, 18 successful scientific flights of ZPB have been carried out from Timmins (Canada), Kiruna (Sweden), and Alice Springs (Australia).
In the field of long duration balloons, CNES decided, in June 2016, the development of the STRATEOLE 2 project, for the study of the low stratosphere in equatorial regions. Based on the use of fleets of small super pressure balloons (SPB) flying up to 3 months each, the program consists in two launch periods in late 2020 and 2023. The related infrastructure will be available no later than end of 2018, paving the way to a new capacity for long duration flights in general.
A synthesis of the activities of the past two years is presented: the 3 CNES ZPB campaigns, the EUSO Balloon payload flight under the US SPB, the development status of the FIREBALL UV payload.
The SPB system for STRATEOLE 2 is described, as well as the Aeroclipper tropospheric vehicle, and perspectives for new developments and collaborations are addressed.

1. INTRODUCTION

CNES has developed and operates both stratospheric and tropospheric balloons. To study the stratosphere, up to 40 km, CNES implements two types of balloons: the Zero Pressure Balloon (ZPB) and the Super Pressure Balloon (SPB). For the boundary layer in-situ measurements, two kinds of balloons are used: the Boundary Layer Pressurized Balloon (BLPB) and the Aeroclipper which is a semi tethered balloon, in gross lift deficit, for the study of the ocean-atmosphere interface with the capability to penetrate into tropical cyclones. This paper presents:
- The ZPB campaigns: Timmins (Canada) 2015, Kiruna (Sweden) 2016 and Alice Springs (Australia) 2017.
- The EUSO and FIREBALL payloads achievements,
- The Strateole-2 project using SPB flotillas of long duration balloons, which is currently in detailed definition and development phase.
- The improvement of the AeroClipper for the study of cyclone genesis.
- The perspective of the HEMERA initiative, proposed to H2020 Infraia 02-2017 Program, for a European increased collaboration on balloon infrastructures.

2. ZERO PRESSURE BALLOON CAMPAIGNS

2.1 The NOSYCA system architecture

The NOSYCA system, as shown in figure 1, ensures a fail-safe design for all critical functions of the aerostat. It is composed of:
- A flight segment with two housekeeping gondolas, the Operational Gondola (OG) for controlling the aerostat during the flight, and the Envelop Gondola (EG) to track the balloon envelop during descent after the flight train separation (cut off), and a payload gondola (PLG).
- A ground segment including a S Band station, a nominal and an emergency control center, and mission control centers.

The IP board to ground interface has a high bit rate of 1.0 Mb/s via S Band, of which 0.95 Mb/s are dedicated to science telemetry. The use of TCP/IP enables the scientists to access their payload in real time through a standard internet link. As shown below (see figure 1), each control center is connected with Iridium data transmission services. Depending on the scientific mission altitude profile and on the flight duration, the ground segment can use several stations, remotely controlled.
The ground network architecture allows the operation team to control one flight, and to prepare and check in parallel payloads at ground for the next flight. Furthermore, the ground stations and the control centers are installed into sea containers in order to be easily transported and operated anywhere in the world.
This system is now fully operational and has allowed to conduct 4 successful ZPB campaigns and 18 flights from 3 different sites during the last 3 years.

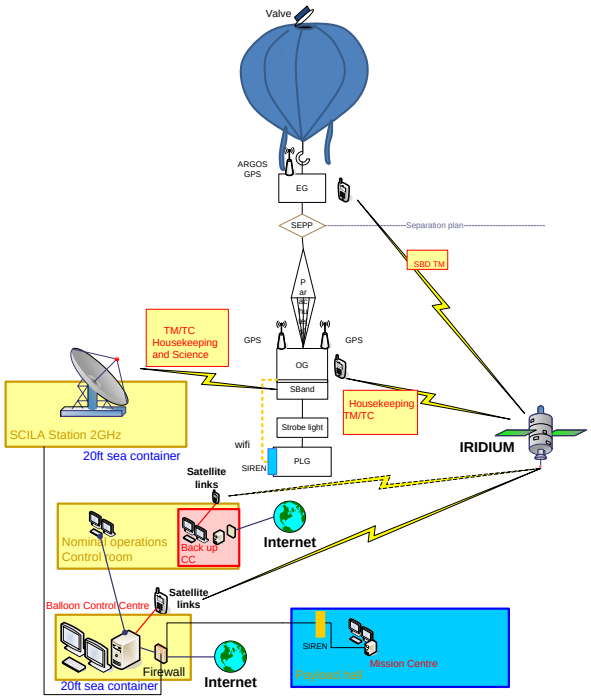

Figure 1. The NOSYCA system architecture

2.2 The Timmins 2015 STRATOSCIENCE campaign

The Timmins 2015 launch campaign, named "Strato-Science", was the second ZPB campaign with the NOSYCA system; it took place from August 12th to September 30th during the turnaround period. Six flights were scheduled, 4 of them for the French and European scientific community, two for the Canadian community, in the framework of the arrangement between CNES and the Canadian Space Agency (CSA). During the campaign, all the flights have been successful. The scientific payloads (see [1], [2], [3], [4], [5], [6], [7]) and the technological gondola were the following:

- The "Greenhouse Gases" gondola with 3 x Pico-SDLAs (laser diode sensor for CH4, CO2 and H2O measurements), a lightweight model of Pico-SDLA (H2O) developed for Strateole-2 project, 2 AMULSE (miniaturized instrument for CH4 and CO2 measurements) and 3 AirCore ultra-light spectrometers to study the chemical composition of the stratosphere.

- The "H2O" gondola with SAWfPHY (H2O measurements) developed for the Strateole-2 project, 4 Pico-SDLA, AMULSE (CH4 measurements) and a lightweight model of AirCore.

- The technological GOLD gondola for the qualification of the parachute system for heavy payloads (750 kg to 1100 kg).

- The BIT (Balloon-borne Imaging Test-bed) gondola, a Canadian pointed gondola (Toronto University) accommodating a 0.5 meter visible light telescope, whose maiden flight objectives were mainly technological.

- The CNES CARMEN pointed gondola, hosting LOAC (French atmospheric Light Optical Aerosol Counter (*)) and 4 Canadian instruments: MAESTRO (Environment Canada), and Paris-IR, DA2 and SPS-B which are the 3 instruments of PARABLE (PAyload for Remote sounding of the Atmosphere using Balloon Limb Experiments) from the Toronto University.

- The PILOT telescope (see below), which flew during 21 hours at a ceiling of 39 km (see [10] and [11]).

Timmins 2015 operation summary is as follows: ZPBs of 100 000 m3 to 800 000 m3 were used; the payload masses varied from 227 kg to 1058 kg; the flight durations, all compliant with the missions requirements varied from 4h30 to 23h54. The campaign of 2015 was the opportunity to qualify and use a new kind of auxiliary balloon (BAX) for the handling of the payload at launch. This BAX is unique; it remains in the flight train until recovery (See figure 2 below).

Figure 2. Auxiliary balloon (on the right)

(*) For the purpose of regular measurements of the aerosol profile in the atmosphere, about 90 flights of the LOAC, using meteorological balloons, took place since 2014 from the French Aire sur l'Adour CNES site.

2.3 The Kiruna KASA 2016 campaign

It was the first time the NOSYCA system was operated from the Esrange Balloon Facility in Kiruna (Sweden). In particular, the new S-band antenna of the site was used for high-rate RF communication link. The campaign also took place from August 17th to September 8th; two flights were on schedule; the first one, named CLIMAT, for the French and European scientific community, the second one shared with the Canadian community. The two flights have been successful. The scientific payloads were the following:

- The CLIMAT gondola with 3 Pico-SDLAs (CH4, CO2 and H2O measurements), a lightweight model of

Pico-SDLA (H2O) developed for the Strateole-2 project, 2 AMULSE, and 3 AirCore payloads to study the chemical composition of the stratosphere. CLIMAT had a mass of 260 kg.

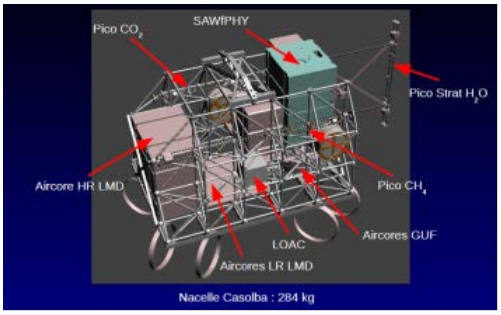

Figure 2. CLIMAT, the Greenhouse Gas gondola schematic view of the various payloads

- The BANA gondola, with 3 LOAC and 1 bi-gas AMULSE (CH4 & CO2 measurements) for the French contribution, The technological Canadian instruments were a Fabry-Perot high-resolution spectrometer for O2 measurements, and an instrument for high-precision atmospheric pressure and temperature measurements. BANA had a mass of 200 kg.

- Operation summary: Balloons of 100000 m3 and 150000 m3 were used. The logistic effort to organize a campaign at Esrange was limited due to the relatively short distance to France, and to the fully equipped facilities available on site.
See below the vertical profile of the CLIMAT flight, with a piloted slow descent from 33 km to 17 km, as well as its horizontal trajectory: the flight trains landed in the very center of the target area.

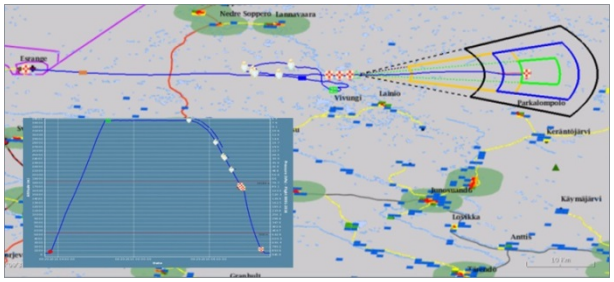

Figure 3. CLIMAT trajectory and flight profile

2.4 The Alice Springs AUSTRAL 2017 campaign

CNES had not launched any balloon from Australia since the 2 flights of 1988 from Charleville. An attempt in 1992 did not succeed due to strong low levels jets preventing any launch. The choice of Alice Springs for the 2017 ZPB campaign was due to the requirement of PILOT to observe the galaxy from the southern hemisphere for its second flight. The campaign took place from March 11th to April 20th: three flights were foreseen, one being shared with our Canadian partners. The three flights were successful. The payloads were:
- CLIMAT: the Greenhouse Gas gondola (see above).

-The CNES CARMEN pointed gondola, hosting a sun-pointed tray for the calibration of 60 solar cells, mainly for the European Space Agency, French LOAC and 2 Canadian instruments: ALI (Aerosol Limb Imager) from the University of Saskatchewan, and WLPC (Wyoming Laser Particle Counter), from the University of Wyoming.

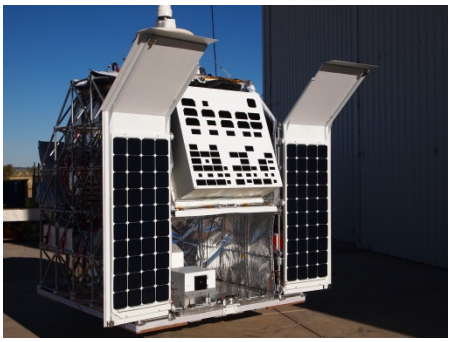

Figure 4. The CARMEN gondola with the pointed-tray of solar cells in the upper middle. (Credit CNES/CNRS - S. Chastanet)

- The PILOT gondola (see below), which flew during 33h40min, a record !

Figure 4. The PILOT gondola – system test with diurnal stellar sensor (ESTADIUS). (Credit CNES/CNRS - S. Chastanet)

2.5 The PILOT gondola (see [8] and [9])

PILOT (Polarized Instrument for Long wavelength Observation of the Tenuous interstellar medium) is a balloon-borne astronomy experiment built to study, in the submillimetric and far infrared wavelengths, the polarized emission arising from dust grains present in the diffuse interstellar medium in our galaxy. By the analysis of the alignment properties of the dust grains with the galactic magnetic field, these measurements will permit to make cartography of the direction and intensity of the magnetic field on a large scale, and also to know the magnetic properties of the grains themselves.

PILOT detects not only the polarized emission of the dust grains, but also the intensity of the emission. That allows completing the former observations yielded by instruments like Pronaos (balloon), Archeops (balloon) and Planck (satellite). The PILOT instrument comprises a 0.9 m primary mirror and a photometer for observations in channel at 240 microns wavelengths. PILOT uses bolometer arrays, developed for the PACS instrument on board the Herschel satellite. The cryogenic cooling system for the detectors reaches a temperature of 0.3 K.
The PILOT instrument has been developed by the French IRAP (Astrophysics and Planetology Research Institute) and IAS (Space Astrophysics Institute), with the support of CNES for providing the pointed gondola. This measurement duration requirement imposes to be able to make observations during daytime (and nighttime) in the stratosphere, with an attitude restitution of about 5 seconds RMS. That is why the CNES has developed a daytime attitude stellar sensor named ESTADIUS.
To comply with the mission objectives of PILOT, three flights are foreseen. The first two flights took place respectively from Timmins in 2015 and from Alice Springs in 2017. The location place for the third flight is not yet defined. For each flight, a minimum duration of 20 hours is required.

2.6 CNES participation to the NASA/CSBF 2017 balloon campaigns

- EUSO SPB at Wanaka 2017 (New-Zealand): The EUSO-SPB payload (see [12], [13], [14]), a UV fluorescence telescope, has been developed by French CNRS IRAP, LAL, APC labs and 11 international labs; CNES participated in the design and in the qualification of the scientific gondola. The instrument, looking downwards to the Earth surface from the balloon at float, monitors a wide area for the detection of UV fluorescence events induced by energetic cosmic rays entering the atmosphere. The technological flight of EUSO-Balloon, during the CNES 2014 Timmins ZPB campaign, was successful.

The NASA SPB, after two validation flights of 32-days and 46-days, hosted the EUSO gondola, with improved detectors, for its 2017 flight; EUSO-SPB was launched from Wanaka on April 24th, and the flight ended 12 days later close to the Pâques Island in the Pacific. 60 Tera bytes of data have been collected and will be analyzed by the scientific community. Figure *5* below shows the Timmins 2014 EUSO gondola inserted into the new structure for CSBF services accommodation (mainly energy and satellite communication link) for the 2017 long duration flight performed by NASA/CSBF.

Figure 5. System testing of EUSO-Balloon gondola in SPB flight configuration

- FIREBALL at Fort Sumner 2017 (USA): FIREBall (the Faint Intergalactic Redshifted Emission Balloon – see [15]) is a balloon-borne 1-m telescope coupled to an ultraviolet fiber-fed spectrograph. FIREBall is designed to study the faint and diffuse emission of the intergalactic medium.

As part of an international collaboration, CNES has designed and manufactured the FIREBall pointing gondola platform (see figure *6*), with its flight services, to accommodate the instrument developed by LAM (Astrophysics Laboratory of Marseille) and NASA (University of Columbia and Caltech). The 1600 kg gondola hosts the UV telescope equipped with a spectrograph. The performance objective of the gondola is to maintain 3 axis inertial pointing of the instrument line of sight (right ascension, declination and polar angle) with 1 arcsec accuracy during a few hours.

After the first flight in 2009, the instrument was improved to gain a significant sensitivity factor. The 2nd flight is scheduled during the fall 2017 at Fort Sumner, New Mexico. NASA/CSBF will perform the balloon operations.

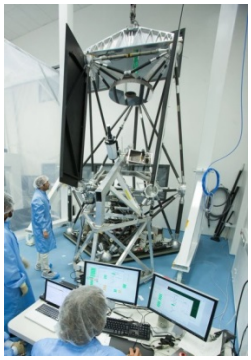

Figure 6. Integration of the FIREBall gondola

3. The Strateole-2 project

3.1 Introduction

Further to several international launch campaigns in the last decade, namely VORCORE-STRATEOLE-1 (McMurdo, 2005 – [16]), AMMA (Niger, 2006) and CONCORDIASI (McMurdo, 2010, see *Figure 7*, [17], [18] , [19]), CNES started the renovation of the small Super Pressure Balloons (SPB) system, to carry up to 50 kg at hook, for long duration flights in the low stratosphere (three months at about 20 km).

The envelope of the SPB is already qualified. Before the next scientific mission Strateole-2 using SPBs in the tropical regions, a new TT & C system will be qualified to be compliant with the new safety rules applicable at CNES.
Below are presented the CNES new long duration flight system, as well as an overview of the Strateole-2 project, today in phase B/C (detailed definition and manufacturing phase).

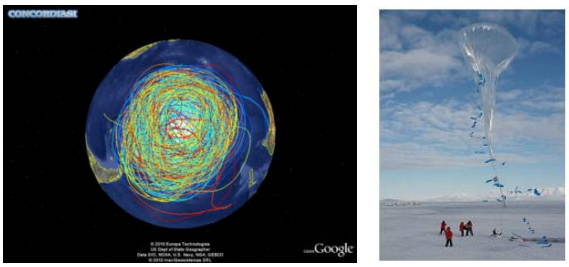

Figure 7. CONCORDIASI 2010: 19 flights, 69 days in average per flight, 1316 cumulated days of flight

3.2 Overview of the Strateole-2 project

- The scientific objectives:

The Strateole-2 program was proposed by the French LMD-CNRS laboratory, backed by French and international scientific communities and agencies. In France, the labs LPC2E, GSMA, CNRM, LATMOS, DT-INSU are participating, with CNES for the project management and the funding. Regarding international partnerships, collaboration with the USA is established, with NSF (National Science Foundation) and several research institutes in the field of atmospheric science: the Laboratory for Atmospheric and Space Physics in Boulder, the Scripps Institution in San Diego and the NorthWest Research Associates/CoRA in Boulder. Other countries like Italy (CNR-ISAC), India (NARL) and Russia (TSAO) are also participating.

The Strateole-2 project aims at improving our knowledge of coupling processes between the troposphere and the stratosphere in the deep tropics. Strateole-2 will provide information relevant to horizontal and vertical transport in the Tropical Tropopause Layer, penetrating convection, dehydration, cirrus occurrence, gravity-wave generation, propagation and driving of tropical stratospheric oscillations (QBO, SAO), which are all critical dynamical and physical processes in tropical and global climate. Strateole-2 will furthermore provide near-real time observations to improve weather analyses and forecasts in the tropics during the campaigns, and contribute to the validation of the Aeolus space borne wind lidar.

In order to document the UTLS (Upper Troposphere/Lower Stratosphere) under different stages of the QBO, two scientific campaigns will be conducted, scheduled about three years apart. They will involve stratospheric balloons as a research platform carrying several types of instruments, both for in situ and remote measurements in the atmosphere. These measurements will be performed in association with space borne observations (e.g. IASI, Aeolus space borne wind lidar), as well as with radiosonde soundings and other ground-based observations conducted from several stations in the tropics (like from NARL, India).

The main period of interest for Strateole-2 extends from early October to late March, i.e. the boreal winter season. As a 2 month-long time period is needed to release the ~20 balloons per campaign, the balloon launch window will thus take place in the October-December –period. Once launched, the balloons will then nominally fly for 3 months, behaving as quasi-Lagrangian tracers of air parcel motions, which is a valuable property for the study of transport mechanisms. The launch site, selected for the campaigns, is Mahe / Seychelles [4° 40’ S], where the pre-Concordiasi campaign took place in 2010: see in Figure 8 the 3 SPB trajectories, with a flight duration of about 3 months at around 60 hPa flight level.

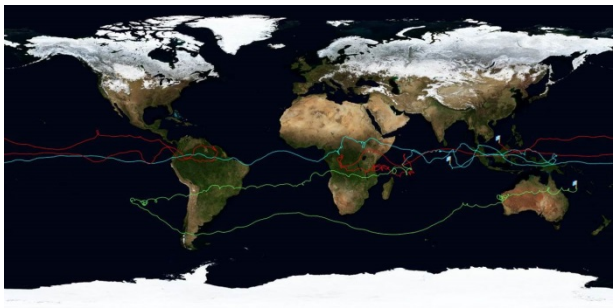

Figure 8. Trajectory of the 3 SPBs during the Pre-Concordiasi campaign (2010)

- The scientific instruments are:

-TSEN (LMD) to perform in-situ meteorological accurate measurements of temperature, and pressure.
-SAWfPHY (LMD), a lightweight frost point hygrometer.
-B-BOP (LMD), an ozone photometer.
-ROC (Scripps, USA), an improved dual frequency GPS receiver, which will be used for position and occultation measurements, giving information on waves dynamics,

and on temperature and moisture variations under the balloon.
-BOL-DAIR (LATMOS), a radiometer for the measurements of upwelling infrared flux and albedo.
-BeCOOL (LATMOS & CNR-ISAC), nadir pointing lidar measurements will permit to detect cirrus.
-Pico-SDLA (GSMA): measurements of water vapor and carbon dioxide based on laser absorption spectroscopy in an open atmospheric cell.
-LPC (LAPS), an aerosol counter.
-LOAC (LPC2E), an aerosol optical counter.
-RAChuTS (LASP), a package deployed 2 km below the balloon, combining several instruments for measurements of water vapor (FLASH-B / TSAO), of temperature and pressure (light version of TSEN / LMD & FLOAT / LASP) and an aerosol profiler (RACHuTS / LASP).

- Technical descriptions of the campaigns:

Two main types of flights will be performed:

- Flights in the upper part of the Tropospheric Layer (~70 hPa / ~120 g/m3) with mainly in-situ measurements (notably trace species and particles), and "in situ" profiling down to a few km below the balloons (denominated "TTL").

- Flights higher up in the lower stratosphere (~50 hPa / ~90 g/m3) with mainly remote sensing measurements, denominated "STRAT" for Stratospheric.

TTL flight configurations:
TTL - 1: GPS + TSEN + SAWfPHY + LOAC + LAOC + B-BOP.
TTL - 2: GPS + TSEN + Pico-SDLA + FLOAT.
TTL - 3: GPS + TSEN + LPC + RACHuTS.

STRAT flight configurations:
STRAT - 1: GPS + TSEN + ROC + BeCOOL + BOL-DAIR.
STRAT - 2: GPS + TSEN.

Before the two scientific campaigns, an in-flight validation campaign will be conducted, with the dual purpose of validating the CNES system and the science system. A unit of each one of the flight configurations will be flown (i.e. 5 flights). This campaign will take place from the same location as for the science flight campaigns (Victoria Airport, Seychelles), and tentatively at the same period of the year (November).

The two scientific campaigns will then include 20 flights each, they will be scheduled three year apart, and each campaign will include 10 TTL flights and 10 STRAT flights.

The fight domain will extend to [20°S, +15°N] latitude limits, pending the flight authorization from every over-flown country.

Each scientific campaign will take place during well-established QBO wind regime in the flight altitude range. The expected dates for the campaigns are late 2018 for the validation campaign, late 2020 and late 2023 for the 1st and the 2nd scientific campaigns.

3.3 The SPB envelope:

The SPB is a spherical balloon, of which only the balloon size will have to be adapted to Strateole 2 flight altitudes: the study gives a diameter of 11 m for the low flight level and 13 m for the high flight level, the envelopes weighing respectively 29 kg and 40 kg. The material is a complex multilayer film of polyester and polyamide, yielding the capacity to withstand a burst super pressure of 20 hPa to 28 hPa. Designed to keep a constant volume at float, this balloon flies at constant level, depending on its diameter and of the total floating mass. Manufactured in a cleanroom with strict quality control, and softly handled during launch, this type of balloon reaches flight durations (depending on gas leakage), of more than 3 months.

3.4 The new long duration flight system

- General information and requirements:

The CNES strategy to renovate its long duration flight system, is to realize a cost effective mix between the previous TT&C system used for CONCORDIASI (named ISBA) and the new NOSYCA system developed for the zero pressure balloons (ZPB). Several upgrades to the former system are being implemented:

- The lessons learned from CONCORDIASI showed that several electronic components (RAM,…) were sensitive to the atmospheric radiation environment, the new design implements more radiation-resistant components.
- The ground and onboard systems shall be fully compliant with CNES safety rules: a few residual single point failures will be eliminated.
- A second real-time RF link will be implemented as secondary terminating system instead of the previous end-of-flight timer system.
- A third real-time RF communication link will be dedicated to scientific payloads.
- The mass budget shall be optimized; in particular, more efficient and enduring solar panels shall be qualified. A mass balance in the range 20-25 kg should be allocated to the operational gondola and the flight chain.
- The mass allocated to scientific instrumentation is 10 kg, excluding payload gondola structure and services masses (power, thermal-control & communication).
- The communication links will provide a worldwide coverage for bidirectional communications, permitting real time monitoring and controlling of the balloon flights.
- The system shall have the capacity to monitor 25

flights in parallel. The launch rate should be at least 3 per week. The payload telemetry volume per day shall reach some megabytes. Some data will be processed and disseminated within less than 3 hours, for assimilation in the numerical weather prediction models. In a first version, it is not foreseen to reuse the flight equipment, as most of the flight systems should not be recovered.

- Architecture definition:

The architecture definition for the SPB system of Strateole 2 is described below (see Fig. 9):
The SPB balloon has a diameter of 11.0 m or 13.0 m, is filled with helium, accommodating an instrumentation package for measuring the gas temperature and the internal overpressure.
The flight chain will comprise a pyrotechnical release mechanism, a parachute, an operational gondola (EUROS) for flight control, a ballast tank and a scientific payload gondola (ZEPHYR).
The control center (nominal and redundant) are located in Toulouse and in Aire sur l'Adour.
The independent mission center will be located in Paris.

The ZEPHYR payload gondola and the mission center will be developed by the scientific team lead by LMD-CNRS.

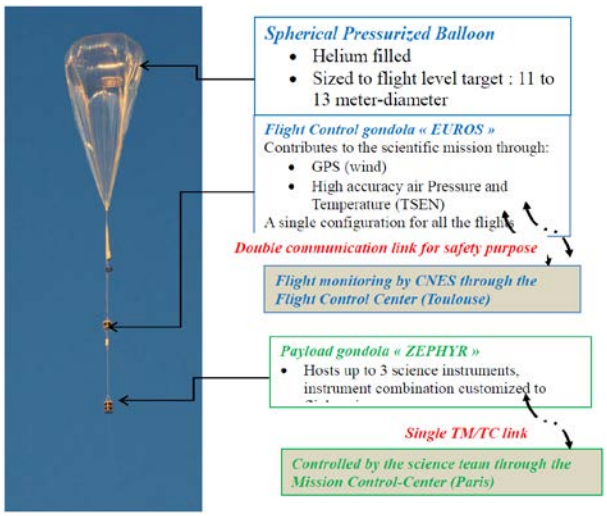

Figure 9. Architecture of Strateole-2 SPB system

Figure 11. The EUROS gondola

- The EUROS gondola design

The operational gondola EUROS includes 2 independent sub-systems for flight control (one nominal and one secondary for safety purposes), mainly in terms of Control Processor Unit (CPU), communication link, pyro-cutter for flight termination and power supply. The 2 CPU cards are packaged with the Input / Output (IO) card to constitute the On-Board computer (OBC).

Nominal sub-system:

-A permanent power supply card (MC2) using solar panels to charge a battery set, and some accumulators to power the pyro cutters dedicated to flight termination.
- A GPS receiver for localization.
- Air traffic control (ATC) devices: one ADS-B altitude reporting radar transponder (TRIG TT 26) and one strobe light.
- A flight termination command system (independent arming and activation commands of pyro-cutters).
- Actuators: one gas valve and a ballast tank.
- A global coverage communication system via satellite, based on Iridium real-time modem (CLS/A3LA-R).
- An active thermal control system.
- A housekeeping instrumentation system for the measurement of air and gas temperature, external pressure and overpressure.
- A telemetry storage and transmission system.
Secondary sub-system: It is working in listening mode and giving health status periodically or on demand, only activated in case of main gondola failure. It comprises:
- Specific accumulators as rescue power supply for all the functions including pyro cutters.
- A connection to the battery or solar panels of the main gondola.
- A GPS receiver for redundant localization.
- A flight termination command system (independent arming and activation commands of pyro-cutters).
- A global coverage communication system via satellite, based on Inmarsat or on Inmarsat modem (SkyWave/IDP-680) in Short Burst Data mode.
- A thermal control system.

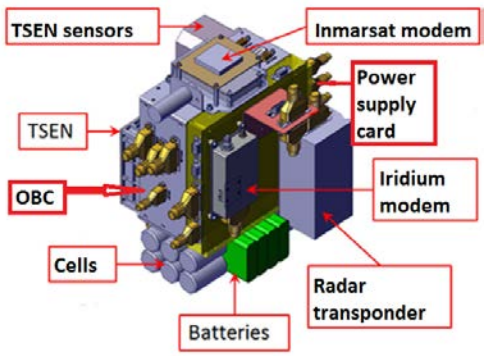

Figure 12. The EUROS equipment

- Ground segment design:

The Ground segment is composed of a nominal and a redundant flight control center with the following functions and performances:
- Control and command in real time of a flotilla of 25 balloons.
- Onboard recording with maximum sampling and transmission with programmable sampling rate.
- Downloading and display of the trajectories and trajectory forecasts.
- On the main gondola, monitoring of the onboard functional chains, and of the telemetry flows, remote control and command of the flight via the actuators and measured parameters, telemetry storage, and scientific data dispatching to the mission and control centers.
- On the secondary gondola, monitoring of the onboard functional chains, and good health check, active mode implementation when needed, telemetry flow monitoring, flight termination activation.

It is also foreseen to decline from the NOSYCA heritage, a system bench (for system validation and operational team training) and an Integration & Testing bench for gondola preparation before flight.

4. The AeroClipper balloon system

- The AeroClipper system overview

With climate change, cyclones should become more and more frequent, that is why scientists have a strong will to improve the knowledge of such phenomena. The AeroClipper Balloon, whose development started at CNES some years ago, could be the adequate vehicle to make measurements of air temperature, humidity, and pressure some meters above the sea surface, up to the core of cyclones. Indeed, the 2007 VASCO balloon campaign, with the capture of 2 AeroClippers by DORA cyclone (see Ref. 20), demonstrated that it is possible to introduce an atmospheric surface layer balloon in the eye of a cyclone in order to monitor surface parameters in near real time. These balloons also give direct observations of the surface wind and of thermodynamic parameters in the vicinity of the cyclone during the phase of convergence into the eye. The monitoring of tropical cyclones in near real time requires an adaption of the AeroClipper and the definition of a new strategy to launch this balloon system on a trajectory crossing the cyclone surface convergence area.

The Aeroclipper is a quasi-tethered balloon, in buoyancy deficit, carrying a guiderope, pushed by the winds at the sea surface. The basic principle is that the guiderope can host two gondolas, one in the water, the second in the atmosphere at a height of about 30 m. This aerostat allows to measure in parallel sea and atmospheric parameters.

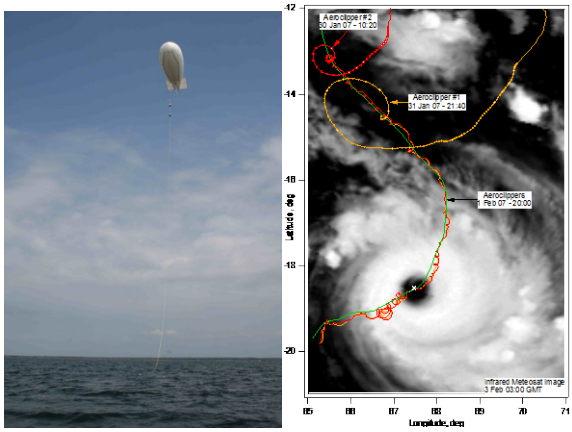

Figure 13. AeroClipper during VASCO Captured by DORA cyclone (2007)

2) On-going developments for the 'cyclone' configuration:

The aerodynamic behavior of the vehicle has already been validated by system tests in 2012, but in a configuration without an operational flight train, whose gondolas must be upgraded to comply with new performance and safety requirements. The development activities of the AeroClipper vehicle, in cyclone configuration with limited instrumentation, started in 2015. These works concern the flight segment, mainly the housekeeping and scientific gondolas. To minimize costs, these gondolas were directly derived from those of the Boundary Layer Pressurized Balloon (BLPB), what will allow to reuse the ground segment of the BLPB as is (see [21]).

The main components of this system are:
- A blimp balloon, filled with helium, with a maximum volume of 40 m3 (mass ~ 22 kg).
- A set of 2 housekeeping gondola for drift control and monitoring (mass ~ 3 kg), accommodated inside the balloon. The monitoring of the flight is performed in real time, by using the Iridium satellite communication system.
- A scientific atmospheric gondola (mass ~ 4 kg).
- A guiderope with a length of 30 m (mass ~ 12 kg, i.e. 0.4 kg by meter).

With about 10 meters of guiderope floating on the surface of the ocean, the balloon drifts at the altitude of 35 m. The house-keeping gondola is accommodated inside the balloon, and the scientific atmospheric gondola is located just below the balloon.

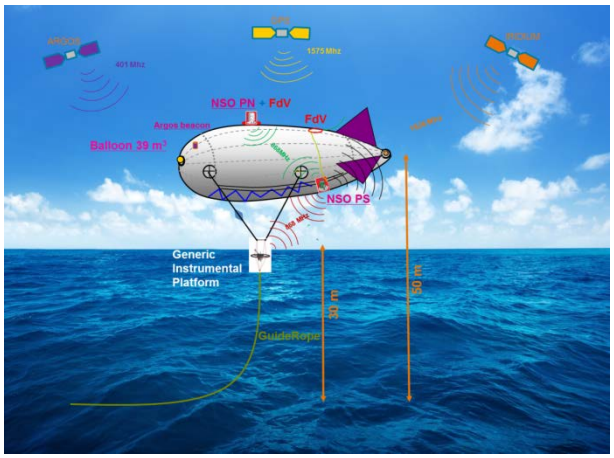

Figure 14. The AeroClipper in 'cyclone' configuration

Evolutions of BLB gondola for AeroClipper control

Main house-keeping gondola:
- Nominal GPS receiver.
- Data management: acquisition and on-board storage.
- Communication with ground segment via Iridium satellite system Short Burst Data mode.
- Frequency: 2 minutes or 30 minutes (power supply saving purpose).
- 'Flight' termination management.
- Balloon technology measurements: gas temperature & balloon overpressure.
- Wireless communication with redundant house-keeping gondola.

Redundant house-keeping gondola:
- Redundant GPS receiver.
- 'Flight' termination management.
- Atmospheric (technologic) measurements: atmospheric pressure and temperature.
- Wireless communication with main house-keeping gondola

Flight termination device (FdV):
- Heating wire to open a polyurethane membrane.
- Two termination devices activated by each house-keeping gondola (main & redundant).
- Nominal activation of flight termination device: 'Real Time' remote control via Iridium.
- Backup activation of flight termination device (loss of communication link): crossing of geographical barriers (positioning by GPS), and Programmable end of life time.

A Generic Instrumentation Platform (GIP) has been developed for scientific instrumentation which is the following:

- Vaisala meteorological station:
- Atmospheric pressure, temperature and moisture.
- Wind speed.

Radiometer: Sea Surface Temperature (SST) remote measurement.
Load / force sensor: restitution purpose of the GIP altitude.
Optional: Laser altimeter accommodated in the GIP. A thermometer is foreseen at the bottom part of the guiderope for in-situ SST measurement.

- The Guam validation campaign:

To validate this configuration, 3 AeroClippers will be released at sea from the North-East Coast of Guam Island in October 2017 for maximum navigation duration of 30 days. The AeroClipper moving under the action of the wind, it is impossible to precisely predict its trajectory up to 30 days in advance. Thus possibly, according to the evolution of the weather conditions, the AeroClippers could approach the Economic Exclusive Zone (EEZ) and the Continental Shelf (CS) of the countries bordering the experimentation basin. Pursuant to articles 248 and 249 and following provisions of the Montego Bay convention (United Nations convention on the Law of the sea), we asked for authorization to allow the AeroClipper navigations in the Exclusive Economic Zone and on the Continental Shelf of the bordering countries. In all cases and in particular before entering territorial waters of the bordering countries, the AeroClipper navigation will be stopped (emptying of the balloon and sinking of the system) either by emitting a real time remote control command via the Iridium satellite communication system, either automatically by the house-keeping gondola (end of life timer or crossing of geographical barriers).

5. HEMERA

HEMERA is the name of the European initiative to provide integrated access to balloon-borne platforms for innovative research and technology, submitted to the H2020 INFRAIA-02-2017 Program.
If selected, HEMERA will integrate a large Starting Community in the field of tropospheric and stratospheric balloon-borne research, in order to make existing balloon facilities available to all scientific teams in the European Union and associated states. The complementarity of the HEMERA members' capabilities in the field of balloon systems and operations will allow an easy and enhanced service to the scientific community; a wide range of scientific and technical themes would be addressed, such as astronomy, atmospheric physics and chemistry, climate research, fundamental physics, biology, space research and technology.
If approved, the HEMERA project will set up a large consortium dealing with balloon-borne research, which will encompass 13 Partners from 7 countries. HEMERA will be complementary to national programs in order to :
- Provide coordinated balloon access to the troposphere and stratosphere for scientific and technological research, in response to the scientific user needs;
- Attract new users to enlarge the community using the

balloon infrastructure and foster scientific and technical collaboration;
- Enlarge the fields of the science and technology research conducted with balloons;
- Improve the balloon service offered to scientific and technical users through innovative developments;
- Favor standardization, synergy and industrialization through joint developments, with greater cost-effectiveness.

6. CONCLUSION

After qualification of a new command and control system for the Zero Pressure Balloons, CNES, with the CSA and SSC support, and their scientific partners have successfully implemented three scientific campaigns: Timmins 2015, Kiruna 2016 and Alice Springs 2017.

Two payloads, the EUSO and FIREBall gondolas, were developed in a context of international cooperation. EUSO was successfully launched on April 24th from Wanaka (New Zealand) by NASA/CSBF. The FIREBall flight should take place before the end of the year, also launched by NASA/CSBF from Fort Sumner, New Mexico.

A new important work is going-on with the renovation of the long duration balloons infrastructure for the Stratéole-2 project, now in development phase at CNES and in the partner labs. The very long duration capability with SPBs will be available in early 2019.

Finally, the upgrade of the AeroClipper system in its cyclone version is in progress, with a technical and scientific validation campaign planned in October 2017, paving the way to the availability of an operational tool for the survey of cyclones.

For the next years several technical developments are planned, in particular to reduce the flight train mass for small ZPB payloads, making easier the launch of small balloons, in particular in the inter- tropical region.

European and international collaborations will also be intensified to make the balloons services available to a wider community.

REFERENCES

1.Renard J.-B., F. Dulac, G. Berthet, T. Lurton, D. Vignelles, N. Verdier, and Al.: LOAC: a small aerosol optical counter/sizer for ground-based and balloon measurements of the size distribution and nature of atmospheric particles - Part 1. Principle of measurements and instrument evaluation. Atmos. Meas. Tech. Discuss., 8, 1203-1259 (2015).

2. Renard J.-B., F. Dulac, G. Berthet, T. Lurton, N. Verdier, and Al.: LOAC: a small aerosol optical counter/sizer for ground-based and balloon measurements of the size distribution and nature of atmospheric particles – Part 2: First results from balloon and unmanned aerial vehicle flights. Atmos. Meas. Tech. Discuss., 8, 1261-1299 (2015).

3.Berthet G., J.-B. Renard, M. Ghysels, G. Durry B. Gaubicher, N. Amarouche: Balloon-borne observations of mid-latitude stratospheric water vapour: comparisons with HALOE and MLS satellite data, J Atmos Chem, 70, 197-219, doi:10.1007/s10874-013-9264-7 (2013).

4.Ghysels M., G. Durry, N. Amarouche, J. Cousin, L. Joly, E. D. Rivière, L. Beaumont, A lightweight balloon borne laser diode sensor for the in situ measurement of CO2 at 2.68 µm in the upper troposphere and the lower stratosphere, Applied Physics B, Volume 107, Issue 1, pp 213-220, DOI: 10.1007/s00340-012-4887-y (2012).

5.Olivier Membrive, Cyril Crevoisier, Colm Sweeney, François Danis, Albert Hertzog, Andreas Engel, Harald Bönisch, Laurence Picon : AirCore-HR: A high resolution column sampling to enhance the vertical description of CH4 and CO2, Atmos. Meas. Tech. Discuss., doi:10.5194/amt-2016-236, 2016, Manuscript under review for journal Atmospheric Measurement. Techniques. Published: 26 September 2016.

6.Lilian Joly, Rabih Maamary, Georges Durry and Al. : Atmospheric Measurements by Ultra-Light SpEctrometer (AMULSE) Dedicated to VerticalProfile in Situ Measurements of Carbon Dioxide (CO2) Under Weather Balloons: Instrumental Development and Field Application, Sensors 2016, 16, 1609; doi:10.3390/s16101609.

7.Rabih Maamary, Lilian Joly, Michel Ramonet, François-Marie Bréon, Georges Durry and Al. : “Atmospheric Measurements by Ultra-Light SpEctrometer” (AMULSE) dedicated to vertical profile measurements of greenhouse gases (CO2, CH4) under stratospheric balloons: instrumental development and field application, Geophysical Research Abstracts Vol. 18, EGU2016-13468, 2016 EGU General Assembly 2016.

8. J-Ph. Bernard, P. Ade, Y. André, , I. Ristorcelli, L. Rodriguez, O. Simonella, M. Saccoccio, and Al.: PILOT: a balloon-borne experiment to measure the polarized FIR emission of dust grains in the interstellar medium, Proc. SPIE, volume 9153, 91531H, Millimeter, Submillimeter, and Far-Infrared Detectors and Instrumentation for Astronomy VII, (August 2014).

9. Y. Longval, R. Misawa, P. Ade, Y. André, P. de Bernardis, J-P Bernard and Al. : The optical performance of the PILOT instrument from ground end-to-end tests, ICSO 2014, International Conference on Space Optics.

10. Bernard, J.-Ph., P. Ade, Y. Andre, Mirc F. and Al.: Inflight performance of the PILOT balloon-borne experiment, Proc. SPIE volume 9914, 9914OW,

Millimeter, Submillimeter, and Far-Infrared Detectors and Instrumentation for Astronomy VIII, (June 2016) .

11.Muriel Saccoccio, Jean-Philippe Bernard; Yves André; Isabelle Ristorcelli, Stephane Louvel and Al : Operations and results of the PILOT balloon borne telescope flight, SpaceOps 2016 - 14th International Conference on space operations, SpaceOps 2016 - 14th International Conference on Space Operations, American Institute of Aeronautics and Astronautics.

12. Louvel, S., Evrard J., Montminy S., Assessment of the Last Two STRATO SCIENCE Campaigns in Timmins, Canada, Space Ops conference, AIAA 2016, 16-20 May 2016.

13.The JEM-EUSO Collaboration (81 Institutes & 12 countries : Bulgaria, France, Germany; Italy, Japan, Republic of Korea, mexico, Russia, Spain, Switzerland, USA), The EUSO-Balloon Pathfinder, Experimental Astronomy, November 2015, Vol 40, Issue 1, pp 281 - 299.

14.P. von Ballmoos, A. Santangelo, J.H. Adams, J. Evrard, G. Medina-Tanco, B. Mot, E. Parizot, G. Roudil, and Al; A balloon-borne prototype for demonstrating the concept of JEM-EUSO, Advances in Space Research, Volume 53, Issue 10, 15 May 2014, Pages 1544–1550.

15.B. Milliard, D. C. Martin, D. Schiminovich, J. Evrard, M. Matuszewski, S. Rahman, S. Tuttle, R. McLean, J.M. Deharveng, F. Mirc, R. Grange, R. Chave, FIREBALL: The Faint Intergalactic medium Redshifted Emission Balloon -- Overview and 1st Science Flight Results, SPIE, 2010, SPIE Vol. 7732 773205.

16.Hertzog, A., Cocquerez, Ph. & al., Stratéole/Vorcore "Long-duration, superpressure balloons to study the Antarctic lower stratosphere during the 2005 winter, J. Atmos. Ocean. Technol., 24, 2048-2061, 2007.

17.Vincent, R. A., and A. Hertzog, The response of super pressure balloons to gravity wave motions, Atmos. Meas. Tech., 7, 1043-1055 (2014).

18. Jewtoukoff, V., R. Plougonven, and A. Hertzog, Gravity waves generated by deep tropical convection: estimates from balloon observations and mesoscale simulations, J. Geophys. Res., 118, 9690-9707, doi: 10.1002/jgrd.50781 (2013).

19. Plougonven, R., A. Hertzog, and L. Guez, Gravity waves above Antarctica and the Southern Ocean: consistent momentum fluxes in mesoscale simulations and stratospheric balloon observations, Q. J. R. Meteorol. Soc., 139, 101-118, DOI:10.1002/qj.1965 (2013).

19. Duvel J.-Ph., C. Basdevant, H. Bellenger, G. Reverdin, A. Vargas et J. Vialard, The Aeroclipper: A New Device to Explore Convective Systems and Cyclones, Bull. Am. Meteorol. Soc., 90, 1, 63-71, doi: 10.1175/2008BAMS2500.1 (2009).

20. Mongis, J., Denis, I., Chatain, Ch., Gagne, JM., "Nosyca: a new system for balloon operations", 20th ESA Symposium on European Rocket and Balloon Programmes and Related Research, SP-700, Hyères, France, 22-26 May 2011.

21. Dubourg, V. and Levesque, D., "Operating a new French balloon system from a new Canadian launch site", AIAA Balloon Systems Conference, AIAA 2013-1335, Daytona Beach, Florida, USA, 25-28 March 2013.

22. Strzepez, A., Landrodie, P., Marigo, J., Salas-Solano, S. and Tourraille, JM., "Simulation means supporting Nosyca Project", Space Ops conference, AIAA 2014-1693, Pasadena, CA, USA, 5-9 May 2014.

23. Dubourg, V., Cocquerez, P., Huens, T., Verdier, N. and Vassaux, D., "The French balloon program 2012 – 2015", AIAA Balloon system conference, AIAA 2014-2706, Atlanta, GA, USA, 16-20 June 2014.

24. Vargas, A. and Levesque, D., "Qualification of the new French balloon system and of the new Canadian launch site", AIAA Balloon system conference, AIAA 2014-2707, Atlanta, GA, USA, 16-20 June 2014.

25. Dubourg, V., Vassaux, D., Vargas, A., Cocquerez, P., Louvel, S., Douchin, F., Saccoccio, M. and Mirc, F., "The French balloon program 2013– 2016", 22nd ESA Symposium on European Rocket and Balloon Programmes and Related Research, SP-730, Tromso, Norway, 7-12 June 2015.

26. Lafrance, S., Montminy, S. and Louvel, S., "CSA's Stratos Program: bringing a New Mid-latitude Stratospheric Balloon Base", IEEE aerospace conference, Yellowstone, MT, USA, 5-12 March 2016.

FLY A ROCKET! A NORWEGIAN-ESA EDUCATIONAL PROGRAMME – PILOT CYCLE REPORT AND CONCLUSIONS

CHRISTOFFER STAUSLAND[(1)], ALEXANDER KINNAIRD[(2)], JESSICA KORZENIOWSKA[(2)], MARIANNE MOEN[(3)]

(1) NAROM, Norwegian Centre for Space-related Education (Norway), Tel: +47 76144661, E-mail: christoffer@narom.no

(2) European Space Agency, Education and Knowledge Management Office (Netherlands), Tel: +31 715656565, E-mail: flyarocket@esa.int

(3) Norwegian Space Center (Norway), Tel: +47 22511817, E-mail: marianne.moen@spacecentre.no

ABSTRACT

"Fly a Rocket!" is a new European student programme initiated to give first and second year university students an introduction to rocketry and related fields, with emphasis on learning by doing.

The programme pilot cycle was realised in late 2016 and early 2017. The programme is a collaboration between the European Space Agency's (ESA's) Education Office, the Norwegian Centre for Space related Education (NAROM) and the Norwegian Space Centre (NSC). Funding was provided by ESA, NAROM and NSC. Additionally ESA was responsible for participant selection and NAROM for the online course and campaign realisation.

The pilot cycle started with an online pre-course in November 2016, followed by a rocket campaign at Andøya Space Center (ASC) in March 2017, and ending with a technical report delivered by the students as a group in July 2017. In this paper the cycle is presented and the conclusions are given. Section 1 will give a brief introduction to why the programme was initiated and shortly about the general overview of the rocket campaign which forms the basis of the programme. The educational objectives are described in Section 2. In Section 3 the "Fly a Rocket!" programme is explained more in detail, and in Section 4, the results and conclusions are given.

1. INTRODUCTION

ESA Education has long experience with providing great teaching resources with emphasis on space for high school students, with Cansat being the most well known, and for graduate students with the REXUS and BEXUS rocket and balloon programs. There has been, though, a gap where first and second year university students has not had a dedicated programme. ESA want to fill this gap with "Fly a Rocket!", which aim to give students insight into rocketry, both for students that have already started their space studies and for students in other fields as a recruitment opportunity. A large number of applicants to the cycle confirms the need for such a programme.

The programme is open to all students from an ESA member state, with a target audience of 1st and 2nd year bachelor students studying, but not limited to, engineering, physics, mathematics or other technical subjects. The programme is a hands on activity for University students, which offers opportunities for young university students, who have not necessarily defined their career, and may not have considered space research and engineering as an option. The programme, specifically the campaign week, aims to take students through a full sounding rocket life cycle, from design and development to launch operations and results analysis, albeit in a very condensed timescale.

It is believed that the programme enable students to make informed decisions about careers and continued study with STEM subjects and particularly space research and engineering, further motivating to the potential candidates for more advanced programmes of the ESA Education office such as spin, drop and fly your thesis and REXUS/BEXUS. This programme provides a unique hands on and early experience for University students.

2. EDUCATIONAL OBJECTIVES AND GOALS

One of the strong point of the programme is the practical part. This means that there is a high level of things the students will experience and which is not possible to experience anywhere else. The learning process is therefore made in a practical way. This is not only more encouraging, but also better the learning of the concepts. In addition, the program shows and allows to play with the scientific method in an active way, and this is very valuable pedagogically. The experience gives very valuable insights about how to work in a real project, as

all the practical steps are reproduced, like a real scientific project.

The condensed learning objectives are:

- Background information of the physics and technical aspects of rockets and rocket flights
- The use of rockets, balloons and ground based instruments as a technology platform to study processes in the atmosphere
- Basics of measuring with electronics onboard a highly accelerated platform and in low pressures and temperatures
- Work on a real rocket project as a team and interact with industry experts and other students from many different nations
- Data comparison with models
- Reproduce a scientific project: scientific objective, building and testing instrumentation, collecting data, analysis, and conclusions

The involved students will gain experience in several areas but it is also important to be aware of the fact that they will be a part of an international working group which enrich the experience. This is also an example about what happens in reality in space science projects. Space is a place without frontiers, where international collaboration is crucial to reach the objectives. The program aims to train the students also in this aspect.

3. PROGRAMME DETAILS

The application process, the pre-course and the campaign phases of the pilot cycle is described in more detail in this section.

3.1 Application and selection process

In October, 2016, the Call for applications resulted in a total of 493 applications for the total of 20 openings, which is a much higher number than any previous course/campaign at NAROM. ESA selected the 20 participating students from 20 different ESA member states and collaborating nations, and an additional 3 students on waiting list. All the invited students accepted their invitation.

The application from the students consisted of a single document where the student would describe his/hers motivation for joining the programme, what outreach would be done if accepted, a tie-breaker with a suggestion of the name of the rocket, and a technical task were the student had to suggest an additional payload on the rocket.

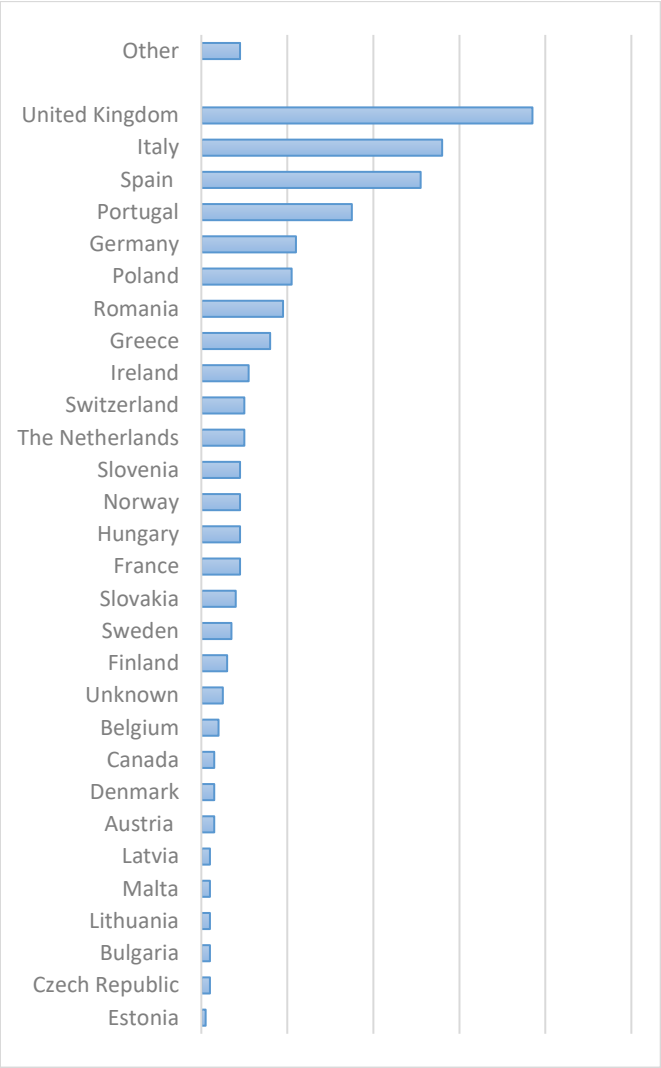

Figure 1: Number of applicants sorted by nationalities

Figure 1 shows the number of applicants sorted by nationalities. Note that some of the students had dual citizenship, and that some of the students had undetermined or non-eligble nationalities and hence not included.

3.2 Online pre-course

In NAROM's and ESA's experience, the students involved were expected to be highly motived, and NAROM developed an online based pre-course to use this motivation to increase the knowledge of the students on rocket related subjects prior to the campaign and to encourage promotion of STEM subjects. The pre-course was split in two parts: an online text which introduce both rocketry and satellite orbits, in addition to a very brief overview of the technical parts of the NAROM student rocket. The text uses real ESA and Norwegian

Figure 2: Students of the "Fly a Rocket!" pilot cycle, with the rocket the students built

projects as examples on the different subjects. The subjects of the online text is:

- *Rocketry*: rocket principle, types of rocket engines, rocket thrust equation
- *Rocket dynamics*: rocket degrees of freedom, forces acting on the rocket, simulations on rocket trajectories
- *Satellite orbits*: Kepler's laws, the six orbital parameters, detailed analysis of orbits in a plane
- *NAROM student rocket* (as a small introduction)

The online text will be made available to the public at Sarepta.org before the end of 2017. The second part of the pre-course is two assignments with questions from the online text that the students are expected to answer and hand in, with individual feedback to each of the students from NAROM professionals. The students are invited to a closed group on Facebook to communicate with each other and to collaborate about the hand-ins. Parts of these assignments was made deliberately challenging to push the students, which has a wide range of different backgrounds, to help each other to solve the assignments. The students was given a long time to solve the two assignments so they could work on them when it suited them the best.

3.3 Rocket campaign week

The campaign week was in the end of March, 2017 and centered around the launch of a 2.7 meter long carbon fiber Mongoose 98 rocket launched to an apogee of 8.5 km with a flight time of 90 seconds. No recovery is done.

The campaign started with introductory lectures before the students were divided into groups of 3-6 persons to do more in-depth work, such as: payload integration, electronics assembly, rocket trajectory simulations and setting up the telemetry station. Each group was "experts" on the work that they did, so everyone took an integral and important part of the project/campaign. Two days was used to prepare the rocket before flight.

The work towards the launch went great, and the students showed great knowledge and, maybe more important, eagerness to learn new things. On launch day, the fourth day of the campaign week, everything that the students had done during the week was "go for launch" and after a pre-launch meeting with ASC the countdown started. Such a countdown always start with ASC releasing a weather balloon to measure the winds over the launch site, and it was quickly seen that the winds was not favorable. After a long hold in the countdown where the students remained at their stations in case of a possible change in winds, the launch attempt was delayed until the next day. The students then analyzed data from an earlier rocket flight with a similar configuration and prepared presentations for the next day. On the last day of the campaign week the wind was still not favorable, and the students presented their results from the earlier flight to each other while ASC kept monitoring the winds, before cancelling the operation in the afternoon and the students prepared to leave for home. Figure 2 shows the students together with the rocket that they built.

What should be emphasized is that the students did most of the work during the pre-launch phase, rocket operation and post-launch analysis, with the crew from ASC and NAROM involved only for help and guidance.

For instance, one of the students was Head of Operation which leads the countdown and talked on the intercom which is distributed all over the space center. All such similar tasks was done by the students.

3.4 Student report and launch

In the last phase of the pilot cycle, the students made one report together of the campaign week with the results from the data they had from the earlier student rocket launch. The report was submitted to ESA in early May.

Volare-1 (*to fly* in Italian), the name the students had given to the rocket, was launched at a later opportunity on May 31, see Figure 3, with the countdown operation (which was led by NAROM and ASC) and launch was streamed online to the students. After the launch, the students generated a new report based on data from their own rocket.

Figure 3: Launch of "Volare-1", the "Fly a Rocket!" pilot cycle rocket on May 31st, 2017 from Andøya Space Center

4. SURVEY, IMPROVEMENTS AND CONCLUSIONS

ESA did an extensive survey with the students shortly after the students returned from the campaign week, which this section is partly based on. ESA and NAROM also noted possible future improvements during the cycle.

The Call for Application period worked generally good, though the students would have enjoyed a better ratio between the genders.

The pre-course phase was new to both ESA and NAROM, and is seen as important for the success of the programme as it boosted the professional level for the campaign quite a lot. It was seen, however, that the students struggled with the harder part of the assignments, and the collaboration between the students could have been better. The difficulty of the assignments could be decreased or collaboration between the students done in another way. Collaboration is seen as a very important part of "Fly a Rocket!", both for making the students more familiar with each other, and also for getting experience with international collaboration in general. The pre-course failed to encourage the promotion of STEM subjects and failed to increase participant's knowledge of Norwegian and ESA projects, which was one of the objectives of the pre-course.

The campaign period got good student feedback, but some of the students thought that some of the topics could be taught more in-depth and advanced. It should be noted that the balance between in-depth discussions and making all the students able to follow is always difficult, and NAROM always attempt to find the proper level of all of their activities. The students were very satisfied with the very international atmosphere, but they requested also more exposure to Norwegian culture.

Generally, NAROM, ESA, NSC and all of the students were very satisfied with the pilot cycle, with the feedback from the students being "very high levels of satisfaction and [they] would recommend the project and ESA Education office activities." The pilot cycle is now being reviewed by all parties, and additional cycles are being considered.

BEXUS 23 OSCAR: SOLAR CELL I-V MONITORING SYSTEM FOR SPACE ENVIRONMENTS

S. Nagels [1] [2], I. Cardinaletti [1] [3], R. Cornelissen [4], D. Scheurs [1] [3], T. Vangerven [1] [3], J. Vodnik [1] [3], J. Hruby [1] [3], M. Nesladek [1] [3], J. V. Manca [4], and W. Deferme [1] [2]

[1] Hasselt University, Istitute for Materials Reseach (IMO), Wetenschapspark 1, 3590 Diepenbeek, Belgium
wim.deferme@uhasselt.be
[2] Flanders Make vzw, Oude Diestersebaan 133, 3920 Lommel, Belgium
wim.deferme@uhasselt.be
[3] IMEC vzw – Division IMOMEC, Wetenschapspark 1, 3590 Diepenbeek, Belgium
wim.deferme@uhasselt.be
[4] Hasselt University, XLAB, Agoralaan gebouw D, 3590 Diepenbeek, Belgium
jean.manca@uhasselt.be

ABSTRACT

Novel thin film solar cells exhibit unprecedented specific power, which is a key figure of merit for space applications. To get a first indication of their possible degradation in space environments, the OSCAR ('Optical Sensors based on CARbon materials') team has built a solar cell performance monitoring system and deployed it on the BEXUS 23 flight. This paper reports the design, testing and performance of said system. Our system performed impeccably over its 4h mission course, maintaining communication and reliably reporting solar cell I-V curves. It forms a guideline for anyone who needs to measure millivolts and microamperes in similar conditions, monitor solar cells on remote locations or wants to follow up on degradation of thin film solar cells in space.

1. INTRODUCTION

1.1. Background

Solar energy is consistently used for powering long-term spacecraft missions ever since the launch of the Vanguard 1C satellite in 1958 [1]. Alternatives such as batteries and RTG's are undesirable either due to short depletion time or public health risks on reentry. Specific power – watts per kg – remains the main selection parameter since launch costs are mainly calculated on a per kilogram basis. Thick, rigid gallium-arsenide cells pose the current de facto standard because they are known for their reliability and high power per square meter. However, based on specific power, they are trumped by new generations of thin film solar cells (i.e. polymer, small molecule, perovskite). Usage of these novel cells in aerospace applications is still non-existent due to their unknown reliability. This is exactly the property OSCAR ('Optical Sensors based on CARbon materials') monitored during the BEXUS23 flight.

1.2. Monitoring reliability of solar cells

Each solar cell is characterized by its I-V curve. This curve typically resembles a dark current elbow shape which shifts down under the influence of light-generated current – also known as 'photocurrent' – and shows the currents and corresponding voltages at which the solar cell operates [2]. Along this curve, a specific point can be found for which the output power is highest. This point on the I-V curve is called the maximum power point (MPP). Together with the open circuit voltage V_{oc} and the short circuit current I_{sc}, the MPP can be used to calculate the solar cell's power conversion efficiency. By observing changes in I_{sc}, V_{oc} and MPP over time, we can monitor how the solar cells behave over the course of our flight.

Six different kinds of solar cells were selected for the experiment, each with its own range of currents and voltages as depicted in Tab. 1. Current ranges are taken from dark current beyond the 1 sun V_{oc} up to 50% over the photocurrent reached at 1 sun.

Table 1 – Solar cell samples included in our experiment along with their operating voltage and current ranges.

#	Cell Type	Voltage [V]		Current [mA]	
		min	max	min	max
A	IPV	0.00	7.00	-119	411
B	$MAPbI_3$	0.00	1.00	-6.75	3.50
C	$PBDTTPD:PC_{71}BM$	0.00	1.00	-3.00	14.0
D	$PCPDTQx(2F):PC_{71}BM$	0.00	0.85	-3.00	3.50
E	$F4\text{-}ZnPc:C_{60}$	0.00	0.85	-1.07	2.80
F	$DCV5T:C_{60}$	0.00	1.00	-1.05	2.10

The monitoring system should be able to take measurements within these ranges at optimal measuring resolution. 20 equidistant voltages should be applied from the devices' voltage range while measuring the corresponding current.

1.3. Implications of space environment

Since the experiment had to go into space, both mechanical dimensions and weight became a constraint. The flight we designed for had a cruising altitude of 25km and floating time of 2h. Temperatures would reach as low as -70ºC, pressures 10mbar and the gondola would be rotating. Furthermore, we would have a 100W EBASS and a 10W E-Link transmitter emitting lots of interference at respectively 30m and less than 1m from our measuring setups. All these factors had to be taken into account when designing our measuring setup.

2. DESIGN

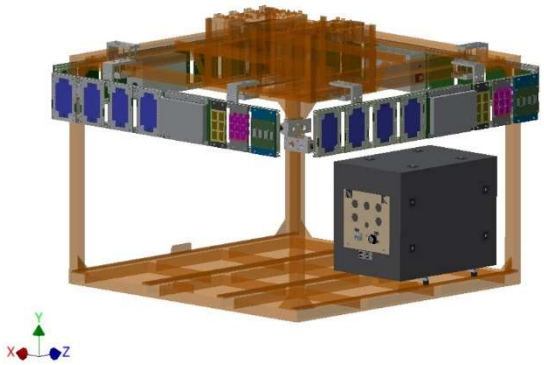

Figure 1 – Mechanical design of the OSCAR project on the BX23 gondola. Each side is equipped with an I-V measuring panel. Sample positions indicated in blue (type A), yellow (types B-C-D) and pink (types E-F).

2.1. System level design choices

We decided to place identical but independent measuring units on all 4 sides of the gondola. By doing this, we make sure at least one panel is in direct sunlight at any given time. Each of these panels contains 64 devices: 8 UHasselt PBDTTPD:$PC_{71}BM$, 8 UHasselt PCPDTQx(2F):$PC_{71}BM$, 8 IMEC $MAPbI_3$, 24 IAPP F4-ZnPc:C_{60}, 12 IAPP DCV5T:C_{60} and 4 Infinity PV cells. Measuring a point from the I-V curve requires first the application of a voltage step from the cell's operating range (through DAC) and secondly analog read of this applied voltage as well as its corresponding solar cell current (through 2 separate ADC's). A single circuit capable of measuring a solar cell I-V curve thus consists of at least 1 DAC for applying voltage and 2 ADC's respectively for measuring voltage and current.

2.2. Measuring board level design choices

To perform measurements with the highest possible precision, we had to match the solar cell I-V ranges to the selected Arduino Due microcontroller board's analog in- and outputs. It provided 2 12bit DAC (0.55 to 2.75V output) and 12 12bit ADC (0 to 3.3V input) channels. If we combine the number of chosen samples, their I-V ranges and the number of ADC channels at hand, three sample groups can be made. Each sample group corresponds to a (number of) measuring circuit(s) with fixed gain and offset values to match the broad, bipolar range of the solar cell signals to the limited, unipolar range of signals with which the microcontroller can work. Tab. 2 shows all three sample groups along with their current and voltage ranges.

2.3. Single measuring circuit design

Since channels were limited, we chose our measuring strategy to use a single DAC channel which supplies 20 equidistant voltages from its output range to all subcircuits. From there on, 6 differential amplifier circuits offset and rescale this voltage according to Eq. 1:

$$V_O = (R_2 / R_1) * (V_2 - V_1) \quad (1)$$

In this way the applied voltage then corresponds to the requested voltage range for each of the sample groups it is applied to. Within each sample group circuit, both this applied voltage as well as the corresponding solar cell current are then measured through each their own ADC channel. For the solar cell current signal, a transimpedance amplifier first performs a conversion from current to voltage following Eq. 2.

$$V_O = -R * I_{in} \quad (2)$$

Then a matching is performed again by shifting and rescaling differential amplifier circuits according to Eq. 1, be it this time of the current and voltage signals from the solar cell to the input of the microcontroller's ADC. Each measuring circuit supports up to 16 devices through an analogue multiplexing stage.

Table 2 – Sample groups with their corresponding measuring ranges and theoretical resolutions, respectively for voltage and current.

#	Voltage [V]		V LSB [mV]	Current [mA]		I LSB [µA]
	min	max		min	max	
A	0.00	7.00	1.709	-300	500	170.9
BCF	0.00	1.00	0.244	-6.00	14.0	4.883
DEdiode	0.00	0.85	0.208	-5.00	5.00	2.441

Compromises were made in current measuring resolution where needed in order to group certain solar cell types together. Since we scale the current and voltage ranges to the complete input voltage of the 12bit ADC's, we can calculate the theoretical measuring resolutions. These are depicted along with the voltage and current measuring ranges in Tab. 2.

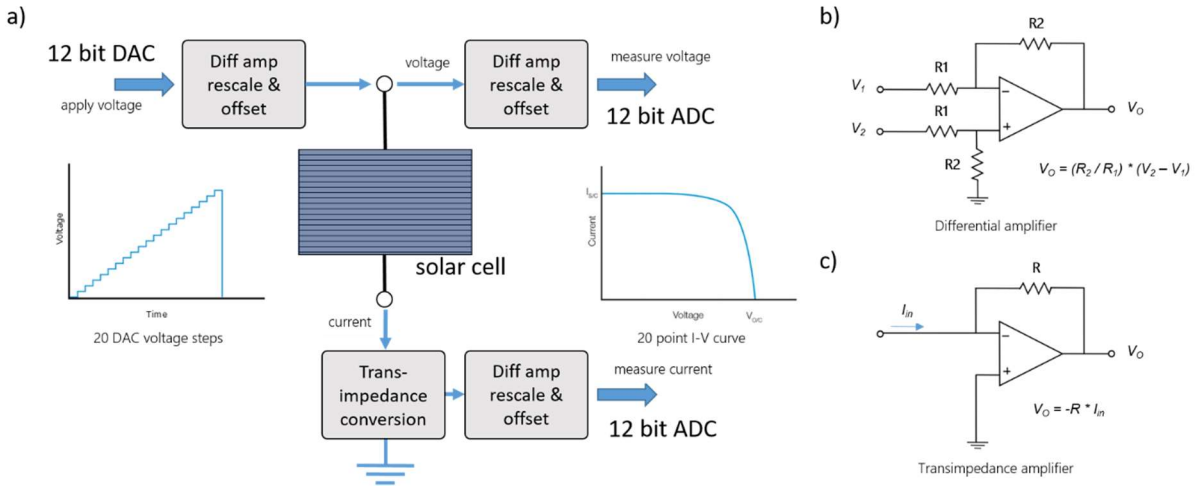

Figure 2 – a) High level circuit description of a single sample group measuring circuit (multiplexing stage not shown for the sake of clarity) b) Basic differential amplifier rescale & offset circuit c) Basic transimpedance amplifier circuit.

As can be derived from Tab. 2, solar cell sample groups were named according to the letter designations of the cell types from Tab. 1. Furthermore a reference silicon photodiode was included in the DE sample group, hence 'DEdiode'.

2.4. Software flow panels

A simple state machine is used for the control software running on the measurement boards. This enables us to recover to a certain state from intermittent power interruptions.

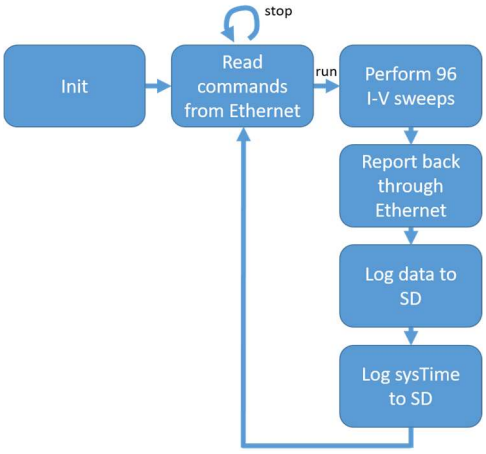

Figure 3 – Measuring panel software flow chart

Upon powering up, the system checks in its non-volatile memory (SD card) which was the last recorded previous state and total runtime and recovers it to SRAM. In a first loop step, pending commands from ground station (GS) are handled. When the system is on halt, this will be the only loop step. From the moment on a 'run' command is received, the system goes into active state, records this state change in flash, and subsequently measures a 20 point I-V curve for each of the 96 channels, sends these measurement values down to ground station, creates a local back-up of the data in flash and logs current system runtime to flash.

2.5. Ground station software

The GS consists of a LabVIEW program which is able to send commands to the measuring panels, receive and log their sent down data and display the last reported I-V sweeps for each panel.

3. IMPLEMENTATION

Figure 4 – Fully populated measuring panel with measurement board's metallic enclosure removed.

3.1. Electromechanical co-design

A single I-V panel consists out of one measuring board accompanied by 7 sample contacting PCB's: 4 on the left and 3 on the right as shown in Fig. 4. Connecting traces run from the measuring board through PCI-e edge connectors across the contacting boards to spring loaded contacts. The samples are placed on top of these spring loaded contacts and held in place by Teflon brackets. This whole stack, PCB–sample–bracket, is then screw fastened with bolts and T-nuts to a frame of strut profiles. By implementing in this way, we employ our circuit boards both for carrying the electrical connections as well as the mechanical load of the samples and their brackets. By relying solely on PCB's and edge connectors, we create very robust connections throughout the entire system and a minimum build and

(dis)assembly time. Not a single wire connection was used to implement the measuring panels.

3.2. Shielding considerations

A typical BEXUS experiment is inherently bound to radio frequent transmission: be it of housekeeping data, experiment communications, air traffic transponder or post cut down GPS tracker. All these RF transmitters are promising culprits of electromagnetic interference (EMI) noise in our measuring setup. Tab. 3 lists all different sources with characteristics most important to our setup.

Table 3 – Inherent sources of EMI on board the BEXUS 23 flight. ATC stands for Air Traffic Transponder.

EMI source	TX freq. [MHz]	Power [W]	Distance [m]
E-Link	2400 – 2500	10	< 1
E-BASS	402.2	100	30
ATC	1090	200	30
GPS tracker	1615	0.1	< 1

Aside from these inherently present EMI sources, only a single experiment on board transmits RF signals. This is the diamond based magnetometer which forms the second part of the OSCAR experiment. It transmits microwaves in the range of 2700 to 3000 MHz at 0.063W and less than 1m from the measuring panels.

All in all we can conclude that some form of EMI shielding is adequate considering the amount of EMI sources, their power and proximity. For this reason, all connecting boards have fully copper poured ground planes on the top and bottom layers which are stitched together with vias every 10mm ($\lambda/10$ for f = 3GHz) around the edges of the board. It effectively creates a Faraday cage around the traces which connect measurement board to samples and thus reduces the surface susceptible to EMI to the contact points and samples themselves. The measuring board is completely enclosed in a metallic enclosure which acts as a shield. The PCB copper pour shielding layers, strut profile frame and measuring board enclosure are all connected through to the ground terminal of the measuring board's isolating DC/DC converter. Each frame is furthermore mounted with electrically isolating rubber bumpers to the gondola.

3.3. Measuring board overview

Our measuring board has an Arduino Due at heart and is surrounded by 6 measuring circuits, each supporting 16 devices through analog multiplexers. ADG1406 multiplexers were used because of their +-15V rail to rail operation, 300mA continuous current support, 3V logic compatible inputs and 9.5Ω on resistance. Sample group A however exceeds the current supported by ADG1406 and is therefore outfitted with G3VM-61 MOSFET relays with 500mA continuous current support and 1Ω on resistance on each multiplexing channel. The relays are driven one at a time by the 16 multiplexer channels and, when selected, connect to the measuring circuit.

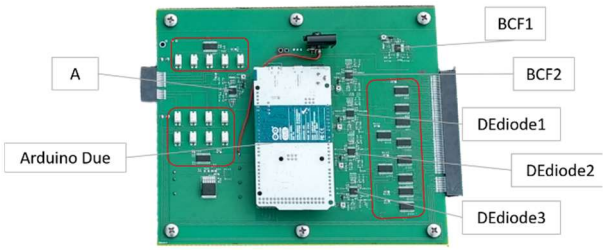

Figure 5 – Indication of measuring board subcircuits and microcontroller board. Multiplexing stages in red outlined shapes. Notice the white MOSFET relays included at sample group A's measuring circuit.

4. FLIGHT

The BEXUS23 gondola ultimately launched on the 7th of October 2016 at 07:07:26 UTC. It reached its cruising altitude of 32km after about 2h flight time and remained at this altitude for just over 2.5h. Air pressure dropped steadily with altitude and reached a minimum of 6hPa. Temperatures dropped to a minimum of -56.8°C in the tropopause.

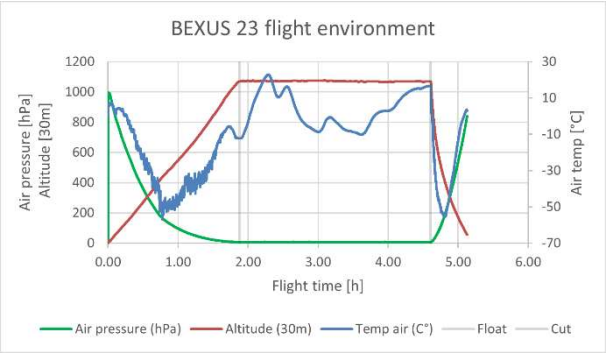

Figure 6 – BX23 flight data. Air pressure shown in green, altitude in red and air temperature in blue. Float phase starts at 1h52m. Cut-down performed at 4h36m into the flight. Courtesy of the Swedish Space Corporation (SSC).

The system performed steadily over the entire course of the flight until at 4h15m flight time I-V measurements shown at ground station appeared corrupted and shortly after communications were also lost. Post flight failure analysis however proved this was caused by battery drainage. This also fits the systems behavior: as battery voltage drops, at some point the +-15V DC/DC converters fail which power the OPAMP measuring circuits. This results in false measurement data but it is still sent down to ground

station by the communications link. As the voltage drops lower, it ultimately dips below the logic level voltage of the Arduino and communication is lost. All in all we attained almost double the flight time which we designed for.

5. RESULTS

All data show consistent I-V measurements, yielding a data set of 192000 I-V characteristics acquired at a steady interval throughout the whole flight.

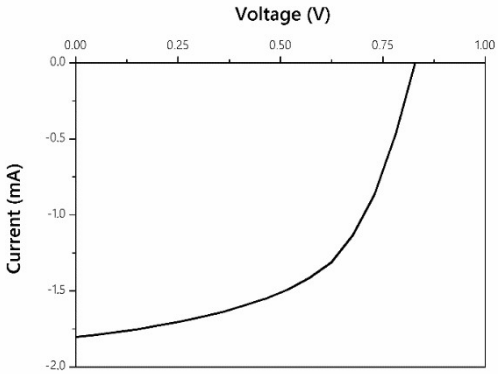

Figure 7 – Example I-V curve acquired in the stratosphere through the BCF circuit.

The main focus of this communication however lies with the measuring system itself. The performance thereof is monitored by adding a reference resistor to one of the MUX channels of each measuring circuit. Assuming the value of this resistor remains unchanged during flight, every observed change in its I-V curve can then be traced back to an inconsistency in the monitoring system's performance. Since the I-V curve of a resistor is a straight line with the slope indicating value of resistance, observing the evolution of this measured slope over time in this case indicates system behavior. Slopes were derived from the 20 point I-V curves by performing linear regression and taking the regression coefficient. To make up for the different resistor values used on BCF vs DEdiode sample group measuring circuits, the relative change ($\Delta val/val_0$) of regression coefficient is plotted as a function of sweep number. Sample group A's measuring circuit was not equipped with a reference resistor. Its performance is therefore not monitored separately.

Fig. 8 depicts this evolution of reference resistor measurements throughout time for the BCF1, BCF2, DEdiode1, DEdiode2 and DEdiode3 measuring circuits. The measured resistance is clearly not the constant value which would be expected for a steady measuring setup performance when assuming unchanged resistance value. On plain sight, all 5 graphs exhibit the same trend of rises and falls. Furthermore, deeper analysis proves a fixed gain difference between the graphs of BCF circuits when compared to DEdiode.

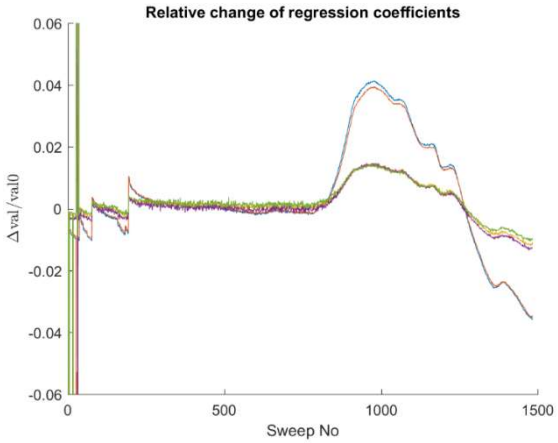

Figure 8 – Relative change of regression coefficients as a function of sweep number. BCF1 in red, BCF2 in blue, DEdiode1 in yellow, DEdiode2 in green and DEdiode3 in red.

6. CONCLUSIONS

The OSCAR project successfully designed, built and launched a solar cell performance monitoring system for space-like environments. The system performed steadily throughout its 4h flight time and reported an extensive amount of data on novel thin film solar cells exposed to the conditions of a stratospheric balloon flight. The measuring setup itself indicates similar drifts on each of the subcircuits. Moreover, this drift varies between sample group measuring circuits with a fixed gain, indicating a shared external influencing parameter with different levels of significance between BCF and DEdiode. This could be justified from the usage of different reference resistors with different thermal coefficients for each. The influencing parameter would in this case be ambient temperature and not have its biggest influence on the measuring setup itself, but on the resistors used to monitor its behavior. A follow-up experiment to assess this prediction would consist of comparing 2 cases where we again perform the same measuring system performance monitoring in a climate chamber. The measurement board would, for each BCF and DEdiode measuring subcircuit, be externally connected to a resistor identical to its internal reference resistor via the edge connector. In the first case both the measuring board with internal reference resistors as well as the externally connected resistors would be thermally cycled. In the second case only the externally connected resistors would be thermally cycled while the measurement board and reference resistors are kept stable. A comparison between both should clearly indicate the influence of temperature on the measurement board and its subcircuits on their own.

7. REFERENCES

[1] R. L. Easton and M. J. Votaw, “Vanguard I IGY satellite (1958 beta),” *Rev. Sci. Instrum.*, vol. 30, no. 2, pp. 70–75, 1959.

[2] F. A. Lindholm, J. G. Fossum, and E. L. Burgess, “Application of the Superposition Principle to Solar-Cell Analysis,” *IEEE Trans. Electron Devices*, vol. 26, no. 3, pp. 165–171, 1979.

OVERVIEW OF THE DIPOLE INFLATABLE ANTENNA EXPERIMENT (DIANE) WITHIN THE REXUS 21 MISSION

Evgeniy Zakutin [(1)], Martin Laabs [(1)], Thilo Zirnstein [(1)], Timo Fuckner [(1)], Ulrich Nordmeier [(1)], Nadin Rößler [(1)], Dirk Plettemeier [(1)], Tina Heidrich [(2)]

[(1)] Communication Laboratory, Technische Universität Dresden, Dresden, Germany, Mail: {evgeniy.zakutin, martin.laabs, thilo.zirnstein, timo.fuckner, ulrich.nordmeier, dirk,plettemeier}@tu-dresden.de
[(2)] Institute of Textile Machinery and High Performance Material Technology, Technische Universität Dresden, Dresden, Germany, Mail: tina.heidrich@tu-dresden.de

ABSTRACT

Inflatable structures attract for its unique characteristics. Low mass and superior volume packaging efficiency – those are not all, but the most significant advantages of such structures. Extremely light constructions can be fabricated out of thin films or various airtight textiles. Being a promising technology for future space applications, inflatable structures generally is a constantly developing theme, huge subject of discussions with lots of opened questions yet. As such constructions can be inflatable antennas having a huge potential in this field. Inflatable antennas can have wide range of application, beginning with ground penetrating radar used during space body flyover and ending with plasma probes and solar orbiter missions.

Key words: antenna, dipole, inflatable, oscillation.

1. INTRODUCTION

Today's tiny satellites use mechanical antenna stripes, which after deployment bring the satellite itself to excessive dynamical vibrations. Forces, moments and vibration profiles of the huge mechanical antennas for space can be estimated with mechanical laws on Earth. Inflatable structures, in their turn, can cause unexpected dynamics during inflation. It is possible to simulate the inflating process on computer, but verification of the simulation of the real deployment process it is not reasonable due to the earth gravity. The rocket parabolic flight during the REXUS 21 campaign provides a relative simple opportunity to conduct and observe this verification in reduced gravity environment.

For this reason, the Dipole Inflatable Antenna Experiment (DIANE) will be conducted within the REXUS 21 campaign. Being a successor of the InTex experiment held on BEXUS 21 mission [1], DIANE experiment is focused on developing of a first 7m long inflatable dipole antenna for application on miniaturized satellites like a CubeSat, as well as on big space vehicles. The deployment process of the antenna, stowed and stored in volume of 0.2 dm^3 within a CubeSat, is being recorded by two lateral cameras for future analysis and comparison with computer simulated model. Recorded video footage helps us to understand the dynamical behavior of gas inflated structures and extend it for other applications.

The paper also describes the process of fabrication of antenna structure out of thin Nylon fabric coated with Thermoplastic polyurethane (TPU). The mechanical and electrical properties of selected materials, the antenna itself, supporting structure design and tests are covered as well. Almost all inflatable constructions are subject of structure stability and pressure loss issues. For this experiment, no rigidizing technology was implemented due to the focus on the dynamic inflation behavior and the short experiment duration. However, suitable technologies for rigidizing are proposed for further experiments and applications.

Design and manufacture an inflatable antenna, made of thin and compact folded air-tight textile or film, inflate the antenna in microgravity environment and establish the downlink connection with ground station – these are the primary objectives of the experiment.

Investigation of electromagnetic waves distribution in ionosphere is being conducted during the flight as a secondary objective.

2. EXPERIMENT DESIGN

The DIANE experiment (Dipole Inflatable Antenna Experiment) is focused on developing an inflatable antenna with application in space (Fig. 1). A CubeSat 5U chassis was chosen for its convenient and compact design. The experiment consists of two main units: supporting stage with ejector and the CubeSat 5U unit. The experiment is located under the rocket nosecone to have an obstacle-free access to space environment after nosecone separation. CubeSat unit contains gas system with pressure sensors, transmitting board and antennas itself, stowed in dedicated sections atop of the module and covered by the hatches. The stage with ejector represent a supporting structure for the experiment module. Ejection of the CubeSat module is required due to safety reasons during the rocket's parachute deployment. On the lateral walls of the stage there are

two cameras, recording the deployment process. Under the rocket's bulkhead there is the main board serving as an interface between the rocket and experiment, and used for managing all tasks on the experiment.

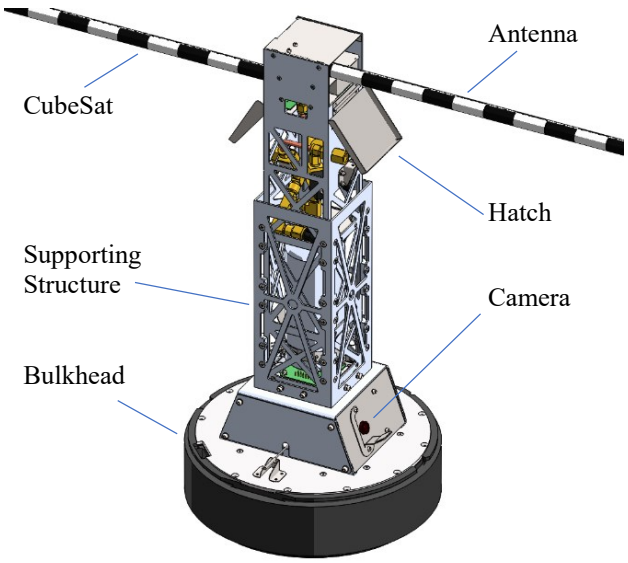

Figure 1. 3D model of the experiment.

As for gas generating system, it was too expensive to utilize space qualified Cool Gas Generators (CGG) or use any sublimating powders for this experiment for several reasons, mainly because of short experiment duration. Therefore, a simple pressure system, made of gas storage bottle and magnet valve was designed. Gas bottle stores the nitrogen under 4.5 bar, what is sufficient to inflate 2-liter antenna volume with approx. 2 bar of inner pressure. Fig. 2 shows the scaled overview of fully deployed antenna.

Figure 2. Scaled overview of fully deployed antenna out of CubeSat 5U module.

3. ANTENNA DESIGN

The antenna structure is made of air-tight nylon fabric, coated with TPU (thermoplastic polyurethane) with an overall layer thickness of 0.16 mm. There is no machine available on the market to sew a round dense nylon hose with diameter of 20 mm – it is too fine to fabricate it. Therefore, antenna hose was manufactured by welding a patch line atop of the butt seam, melting together TPU coated sides of the nylon structure. For this purpose, a welding device was built with round inlay bars made of Teflon, to feed nylon and stripe into it, fix with center part and heat the welding region only (Fig. 3). One semi-antenna represents a continuously welded hose 3.5 m long.

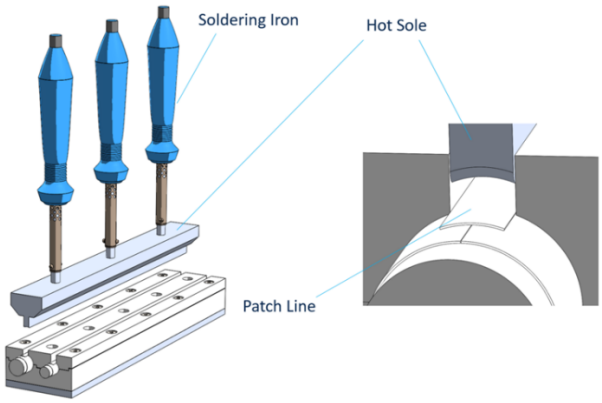

Figure 3. Welding device.

The steel rope with diameter of 0.45 mm fed through the whole hose, attached and glued on the other free end of the structure and acts as a conducting antenna element (Fig. 5). The free end of the hose is sealed by melting the nylon structure. Both semi-antennas are connected to the transmitting board and acting as a dipole antenna. The operating frequency of the DIANE experiment is 21.1 MHz and belongs to the radio amateur band. A special coded message is being sent by antenna to receive it on the ground station.

During the preparation of the experiment several methods of structure folding were studied. Final and simplest one was proposed is to fold the structure in zig-zag way. Whole antenna is stowed in dedicated volume of 0.2 dm^3 (50x31x62 mm) and weights about 44 grams (Fig. 4).

Both antennas are attached to the adapter and were pre-evacuated before being folded. Gas evacuation helps to fold and pack the structure inside of the storage volume.

Antennas are attached to the adapter, pulled over the gas nozzle and glued around it. The total length of both antennas in inflated state is 7 meters. The hose structure is designed and tested to withstand the fourfold hoop stress.

Figure 4. Folded antenna structure.

Figure 5. Conducting element.

4. RESULTS

4.1. Dynamic behavior

Main and most valuable source of information is the video footage, recorded during the flight. It clearly shows the deployment process. Analyzing the video frame by frame allows us to calculate different mechanical parameters, as well as to see the dynamic behavior of the structure during deployment (Fig. 6).

At the time when the hatches are opened t=0, deployment process occurs (Fig. 6, a). First two seconds after opening antenna stretches freely in reduced gravity environment (Fig. 6, b). Both antennas were shot out of the storage volume quickly because of the pressure difference inside of the structure, gained by ascending. It was not possible for us to evacuate the air from antenna structure completely. Then after 10 seconds when the magnet valve was opened and both antennas were fully inflated, the structure begins to oscillate (Fig. 6, c). Relatively long structures under the pressure could be considered as usual cantilevers, neglecting their shell nature. In 30 seconds after the hatches were opened the oscillation process ceases and antenna is fully stabilized (Fig. 6, d).

The oscillation was mitigated by two main reasons. Firstly, on the operating altitude of 89 km where the experiment was conducted, the presence of the rest atmosphere is still observed. On the video it is clearly to see the deflection of the structure because of the air drag due to residual tumbling of the rocket. Second reason is the inner friction inside of the nylon structure. This feature of textile-based space structures can be taken as an advantage as it helps to stabilize the swinging.

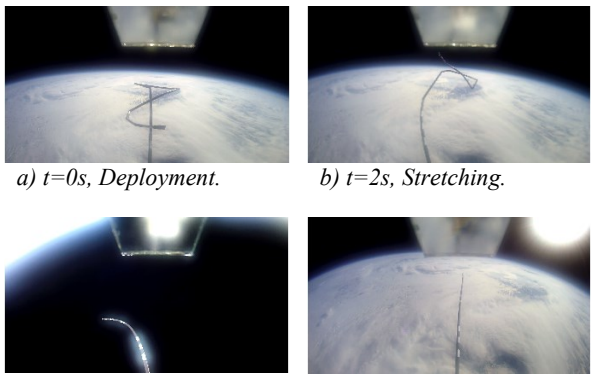

a) t=0s, Deployment. *b) t=2s, Stretching.*

c) t=10s, Oscillation. *d) t=30, Stabilization.*

Figure 6. Antenna deployment sequence.

Underdamper oscillation can be described by the following equation:

$$x(t) = Ae^{-\zeta t}cos\omega t \qquad (1)$$

Where $A=x(0)$ is the initial amplitude; $\zeta=\delta/T$ is the damping ratio; $\omega=2\pi/T$ is the angular frequency; and $\delta=ln(x_0/x_1)$ is logarithmic decrement, the natural log of the ratio of the amplitudes of any two successive peaks.

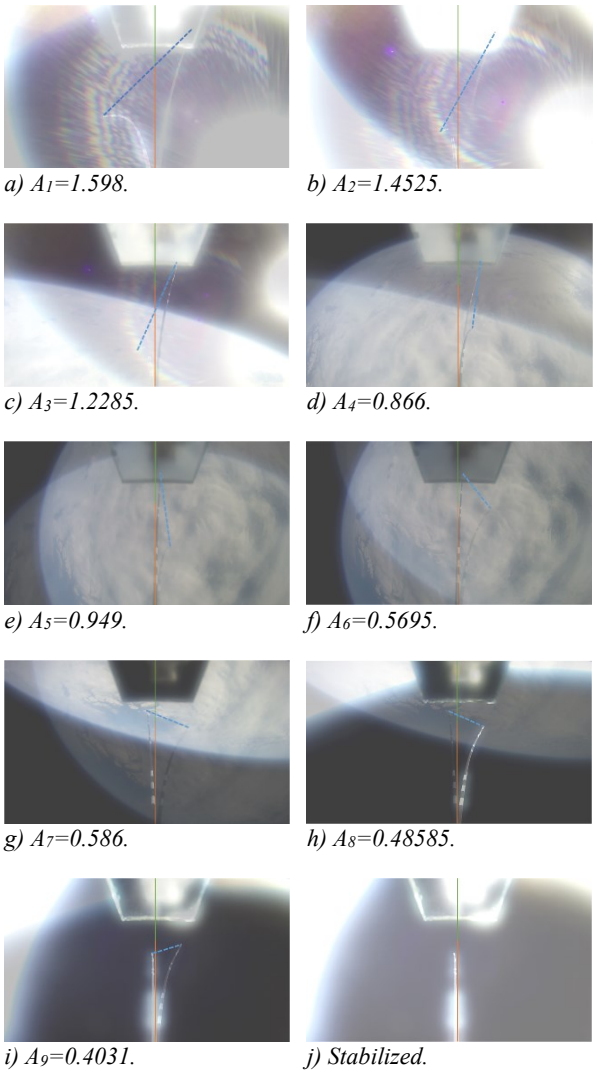

a) A_1=1.598. *b) A_2=1.4525.*

c) A_3=1.2285. *d) A_4=0.866.*

e) A_5=0.949. *f) A_6=0.5695.*

g) A_7=0.586. *h) A_8=0.48585.*

i) A_9=0.4031. *j) Stabilized.*

Figure 7. Sample compare and amplitude determination.

Analyzing the sequence of video frames overlapping each other, where the antenna's end is in extreme positions, it is possible to define the initial and all following amplitudes of the oscillation process by drawing a connection line between antenna ends (Fig. 7). It is hard to estimate the real amplitude value, because of perspective view, lens curvature and the constant changing of the oscillation plane due to the rest rocket rotation. Therefore, the amplitude is given in "units" and it is not affecting any following calculations.

Knowing the period T=3.58 s and calculating of all other parameters we can determine the damping ration ζ=0.07. Using the Eq. 1 the dynamic behavior can be recreated on the diagram (Fig. 8). Measured amplitude is marked with blue points, whereas the calculated orange curve approximately aligns the points and clearly shows the oscillating behavior. It helps to predict the time of full

damping of the structure. In our case it is about 30 seconds, what can be verified by video footage. These parameters are important to know, if the antenna is being developed for the real space mission to foresee the influence of the excessive vibrations on the satellite.

Another important moment observed on the video is a possibility of structure knotting during the inflation process. As it was already mentioned before, the antenna was shot out of the storage volume because of the rest of inner pressure built up inside of the structure during the rocket ascending. This can be avoided by slow and controlled gas inflation process, if antenna structure is completely gas evacuated. If not, then by using the valves with vent hole to mitigate pressure difference.

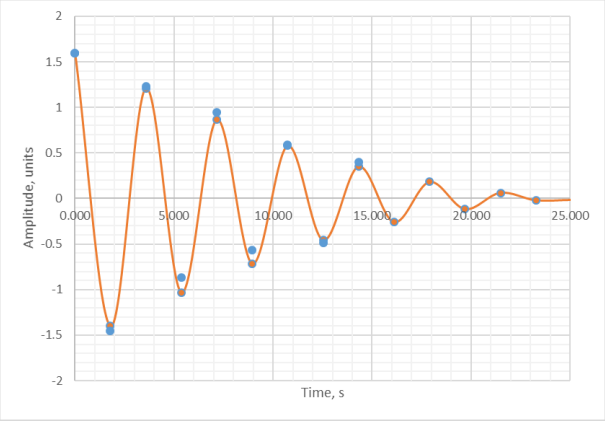

Figure 8. Damped oscillations. Measured amplitude is showed by blue points. Orange curve is calculated.

4.2. Wave propagation study

Figure 9. Radius of the direct wave propagation path.

Secondary objective of the experiment was the investigation of distribution of electromagnetic waves in ionosphere, between layers E and D. Transmitting the amateur radio signals on this operating altitude of 89 km is of interest of wave propagation by direct radiating path or by indirect way, reflecting between these layers.

There are several issues, including weak transmitting signal, unknown parameters of radio amateur equipment, uncalibrated base station and its cheap radio amateur components, unknown alignment of antenna to the Earth surface due to residual rocket spin rate, sun activity – that make estimation harder.

It was not possible to receive the signal beyond the direct path area in Netherland on the WebSDR station. However, excepting our ground station, two verified reports were received from other amateur radio operators inside of the direct wave propagating area, furthest one within 856 km range (Fig. 9).

5. APPLICATIONS

Good overview of possible applications for inflatable structures is given in InTex paper [1]. It covers different types of antennas that can be made of textile materials.

The technologies used in MARSIS radar antenna [2] and tubular space booms [3] allow to design and fabricate the straight structures only. However, textile-based inflatable antennas have a potential to be made of any form, for example, broadband logarithmic-periodic Yagi.

The long dipole antennas have specific area of application, e.g. satellites, where the low radio frequencies are required. The inflatable beams could be used as a supporting structure for deployment of solar cells or space sails.

The DIANE experiment was the first challenging attempt to demonstrate that the long inflatable antennas can be designed for CubeSat missions, opening for this class of satellites a new horizon for applications, such as flyovers near the comets and meteorites as probes to scan the surface and receive an initial information about the certain celestial body. The research group in MIT is also studying the application of inflatable antennas for the CubeSat, developing the volumetric inflatable structures, such as parabolic antenna [4].

6. SUMMARY

Primary objectives of the DIANE experiment were completely fulfilled. The deployment of a long inflatable antenna was successfully performed during the REXUS 21 mission. The downlink connection was established and two verified signal receptions were received at 856 km distance [5]. The experiment also demonstrates the large and long constructions are capable to be folded and stowed in a small volume. Inflatable structures in common case the way lighter and compacter comparing to rigid and mechanically deployable structures. In combination with appropriate rigidization method this

technology has a huge potential for aerospace application. Further investigations will cover the studies of pressure loss, appropriate rigidization methods as well as the numerical simulation of antenna deployment process. Preparing a proper finite element model helps us to extend the properties and loads to other more complex antenna designs mentioned in [1], taking into account the inner friction inside of the textile structure, since it has a beneficial effect on mitigation of oscillation. Having the such model will allow us to predict the behavior of the antenna without conducting an experiment in reduced gravity environment.

7. ACKNOWLEDGEMENT

Team DIANE wants to thank the DLR, SNSB, ESA, and ZARM for making this experiment possible. We would also like to acknowledge the Communication Laboratory and Institute of Textile Machinery and High Performance Material Technology of the Technical University of Dresden for ideational and financial support and the access to all relevant facilities. For the material tests we acknowledge the Institute of Textile Machinery. We would like to express our thanks to our sponsors: Mouser Electronics, WiMo and International Space Education Institute e.V. Finally, we thank Dirk Plettemeier for endorsing the whole project.

8. REFERENCE

1. Laabs, M., Zakutin, E., Plettemeier, D., Nocke, A., Frauendorf, M.: *Textile based inflatable antenna systems for space applications.* In: Proceedings. 36th ESA Antenna Workshop, ESTEC, Noordwijk (The Netherlands), October 06-09, 2015

2. Northropgrumman, (2015), Product Document, Online at *http://www.northropgrumman.com/BusinessVentures/AstroAerospace/Products/Documents/pageDocs/DS-412-FlatFoldTube.pdf*

3. Herzl, G. G. (1970). *Tubular Spacecraft Booms: Extendible, Reel Stored*. Lockheed Missiles & Space Company.

4. Babuscia, A., Corbin, B., Knapp, M., Jensen-Clem, R., Van de Loo, M., & Seager, S. (2013). Inflatable antenna for cubesats: Motivation for development and antenna design. *Acta Astronautica*, *91*, 322-332.

5. DIANE Project, Home of DIANE REXUS Team, Online at *http://dianeproject.de/* (as of 21 August 2017).

DEVELOPING STUDENT LEADERSHIP IN SPACE SYSTEMS ENGINEERING VIA THE G-CHASER STUDENT ROCKET

VISBY, SWEDEN
11–15 JUNE 2017

Sven G. Bilén [(1)], Timothy J. Kane [(1)], and Timothy F. Wheeler [(1)]

[(1)] The Pennsylvania State University, School of Electrical Engineering and Computer Science, University Park, PA 16802 USA, Email: sbilen@psu.edu

ABSTRACT

The G-Chaser Student Rocket Program represents an exciting opportunity for engineering and science students to participate in the Grand Challenge Initiative–CUSP Project, an international research campaign to study the cusp of the earth's magnetic field. Penn State's participation in G-Chaser provides its students and faculty with an excellent opportunity to work with renowned atmospheric scientists from around the world and to develop continuing research collaborations with the science teams on the other Grand Challenge Initiative rockets. This paper reports on some of the formative activities of Penn State's contribution to G-Chaser, called the Polar Atmospheric Winter Student Sounding-rocket payload (PAWSS).

1. GCI–CUSP PROJECT

The Grand Challenge Initiative–CUSP Project (GCI–Cusp) will advance the understanding of the space physics of the Earth's cusp region through coordinated experimental and theoretical research [1]. GCI–Cusp will bring together ground-based instruments, modelling, sounding-rocket investigations, and satellite-based instruments. Seven scientific payloads from Norway, USA, and Japan (see www.grandchallenge.no) are to be launched in December 2018 and January 2019 from Andøya, Norway. Fig.1 provides a pictorial overview of the participating missions and organizations.

Figure 1. Missions and organizations included as part of the GCI–CUSP Project (figure: K. Blix).

1.1. Student participation

An integral aspect of the GCI-Cusp Project is the participation of an international cadre of students who will contribute a dedicated student rocket (called G-Chaser) as well as be involved in space plasma model development. The G-Chaser student rocket payload will be comprised of five-to-seven instruments built by students primarily from Norway and the U.S. In the U.S., participants have been selected from proposals submitted by universities with sounding rocket experience through the RockSat-X Program administered by the Colorado Space Grant Consortium (see spacegrant.colorado.edu/national-programs/rs-x-home). Penn State has been selected to participate and plays a critical role because of our extensive experience with international student rocket programs. The ESPRIT rocket program (Fig. 2) was of a similar scale as the G-Chaser rocket, also encompassed a collaboration with three Norwegian universities, and flew successfully from Andøya in July 2006. Over a dozen papers at conferences were published, most with students as lead authors. It was the success of the ESPRIT program that inspired the Norwegian Andøya Space Center to propose a student rocket be included in the CGI–Cusp campaign.

Figure 2. International ESPRIT team with rocket ready for launch in 2006.

2. PENN STATE'S G-CHASER COURSE

At Penn State, we established a companion course to our

overall effort in order to facilitate student engagement in G-Chaser. Offered as a special topics course, the objectives of our G-Chaser course are formulated to solidify the pedagogical impacts of the project. Since the student participants are of varying levels of experience, varying years at university, and come from several disciplines, the class provides a support structure, i.e., a means for ramping up new student participants and for keeping the various elements of the project team coordinated.

As there are several ways to meet the broad objectives of our project mission, the class is where features of those approaches are discussed and decisions are made as to which ones we will serve us better. A widely diverse set of skills is needed to meet our success criteria. For instance, before their involvement with G-Chaser, students would not be expected to have a command of systems engineering, data analysis, and rocketry investigation techniques—all important to the success of G-Chaser. Rather, through the class, they are introduced to the particular aspects of those topics that will be pertinent to our work on this project.

Beyond the immediate impact of, say, hands-on experience, a project like G-Chaser presents an opportunity to have a profound and lasting impact on the development of these students into space engineers and scientists—an important need in our nation's future [2]. For this reason, the class is designed to keep the broader contexts of space engineering and science firmly in the minds of these students. For example, a student might benefit greatly from designing a circuit for this sounding rocket environment. Yet, the more lasting impact might be in his or her interaction with atmospheric scientists from around the world who are involved in the associated GCI–Cusp Project. It is in the class that the importance of the international collaboration can be emphasized. While taking responsibility for a small part of the overall payload, the student will be exposed to a wide range of people and skills that could inspire life-changing self-discovery. The class provides a setting where we can keep a focus on these broader contexts and encourage them to participate on many different levels.

Designing a class to meet these broad objectives—keeping a disparate set of students on a rigid design/build schedule while encouraging broad participation and self-discovery—is a challenge that we are addressing in the following ways:

- Although there is significant responsibility (and hours) required, the class is low stakes (only one credit). After taking the class three times (for a total of three credits), students may petition their departments for using the credits as an elective that satisfies degree requirements.
- There is an emphasis on individual professional development in the class. At the beginning of each semester, the students are asked to prioritize which aspects of the class and project are important to their development and then to identify semester goals related to those priorities. The students deposit evidence of their progress toward those goals into a folder as the semester progresses. In this way, a metric for progress can be established for each student, whether she is a senior electrical engineering student or he is a sophomore astrophysics student.
- The class is run by a team of three professors, each with experience in sounding-rocket research. In this way, students are exposed to a variety of perspectives and skills related to sounding-rocket research.
- The activities of the class are supported by the facilities (and social structure) of Penn State's Student Space Programs Lab (SSPL, [3,4]). Project-wide communication can happen in the class, but the students are responsible for their own work in SSPL. Class time is important if only because it is a set point on everyone's schedule.

The basic approach to the class was developed during ESPRIT [5]. ESPRIT was a previous collaboration between Penn State and three Norwegian universities. That payload, comprised of ten student-built experiments, was launched from Andøya in July 2006. ESPRIT (and the two prior SPIRIT student rockets) [13,14], showed that multi-year rocket programs have a large impact on student development. They provide opportunities for students to grow and mature with the project and to acquire both technical and leadership skills and a commitment to careers in space engineering and science [2].

During spring 2017, we concluded the first semester of the G-Chaser class. The allure of a Norwegian–American collaboration was significant. The class was oversubscribed and had to be capped at 30 students. The students who responded were diverse, representing seven majors, approximately equal numbers from each class level, and about one-third of the students were female. Furthermore, there was an even split between engineering students and those interested in the science issues. This means that a close collaboration with the scientists on the various GCI missions will be well-received. Even with normal turnover from one semester to the next, we have reason to be optimistic that there will be a strong group to see the project through to its conclusion.

Over the course of the first semester (Spring 2017), the structure of the program began to take shape and student leaders have begun to emerge. We are fortunate to have strong leaders at different class levels, so smooth transitions (always a concern) are expected as students graduate.

Coursework in the first semester included introductory treatments of atmospheric science and sounding-rocket research techniques. The primary deliverable for the semester was a Mission Concept document that was delivered for review by the RockSAT XN program. The Mission Concept required the students to develop a mission statement along with prioritized mission objectives (see Section 3). It should be noted that this stage of a project development is not commonly conducted by students. Usually, they begin their design effort with a mission statement that is delivered to them. With G-Chaser, however, the students energetically debated where our strengths lie as a program (and as a team), how we might contribute to the GCI–Cusp Project, and how G-Chaser fits into the larger vision for student projects at Penn State. As a result of these discussions, the science, engineering, and educational goals were developed and we have decided to contribute the following instruments described in Section 3.2.

G-Chaser will be a program of high significance for Penn State and the students on the project. The high degree of international collaboration, long duration of the project and the opportunities to interact with Grand Challenge scientists will have a high impact on the development of these students' careers.

3. POLAR ATMOSPHERIC WINTER STUDENT SOUNDING ROCKET

The Polar Atmospheric Winter Student Sounding-rocket payload (PAWSS) is the name of Penn State's contribution to G-Chaser. PAWSS will provide *in-situ* atmospheric measurements to be integrated with ground-based measurements to support the investigation of polar mesospheric and lower ionospheric phenomena. Data will benefit the scientific community studying Polar Mesospheric Winter Echoes (PMWEs). As currently formulated, the primary and secondary objectives are:

Primary Objectives:

- Provide *in-situ* measurements of the mesosphere and lower ionosphere
- Integrate ground-based and *in-situ* data to provide a clear picture of the region of interest
- Develop students as scientists and engineers prepared to work in a global environment
- Modernize and test scientific instrumentation for atmospheric measurements for use on future missions

Secondary Objectives:

- Investigate the phenomenon of Polar Mesospheric Winter Echoes
- Utilize and improve legacy technology from the Student Space Programs Lab
- Foster international collaboration through research on atmospheric phenomena and technological development

Currently, we anticipate three instruments to be part of the PAWSS payload. These include (1) a Langmuir probe (LP), which will be used to measure electron density, such that density structures in the atmosphere can be resolved with high local resolution; (2) a total electron content (TEC) receiver, which will be used to measure absolute/calibrated TEC in a column by measuring Faraday rotation of a polarized RF signal; and (3) a lidar, which will measure neutral dynamics and from which data are used to measure turbulent neutral structures

1.1. PAWSS science

PMWEs are theorized to have their origin in either neutral turbulence, through the presence of aerosol particles, or generated by infrasound waves from the ground [8]. Ground-based lidar measurements taken in January 2002 during a solar proton event suggested the presence of aerosol particles within the PMWE region [9]. Alternately, Lübken et al. [10] analysed rocket data (launched through PMWE regions) from Andøya Rocket Range in 2005 and concluded that turbulence was the prime cause of PMWEs.

Penn State, and more recently, SSPL has a long history of work developing and flying LPs. Thus, developing and flying an instrument for G-Chaser fits into the long-term strategy for SSPL. In the spirit of collaboration with CGI–Cusp, this will be a useful chance to compare our measurements with those of the University of Oslo (UiO), which will place LPs on several payloads.

Another electron density measurement with a long history in sounding rocket research is Faraday rotation–derived total electron content (TEC) [11]. A second international collaboration with M. Friedrich (U. Gratz) will update his hardware-based receiver to a modern software-defined receiver. The benefit in doing so is that the measurement technique is not limited by obsolete components and it can be adjusted for each site rather quickly.

Rocket-borne lidar was first flown on the RONALD payload from the Andøya Rocket Range on 12 October 1997 [12], but no significant turbulent activity was observed in the relative neutral densities (see Fig. 3).

Following the latter example, the PAWSS lidar will measure the neutral dynamics of the atmosphere (based on Rayleigh scattering), as well as be sensitive to aerosol presence. The lidar will operate in conjunction with the other scientific payloads on the G-Chaser Student Rocket and ground-based resources such as the RMR lidar at the Alomar Observatory. This synergistic approach will allow for measurement of atmospheric dynamics from lower atmospheric sources to the heights where the waves break and induce neutral turbulence [13].

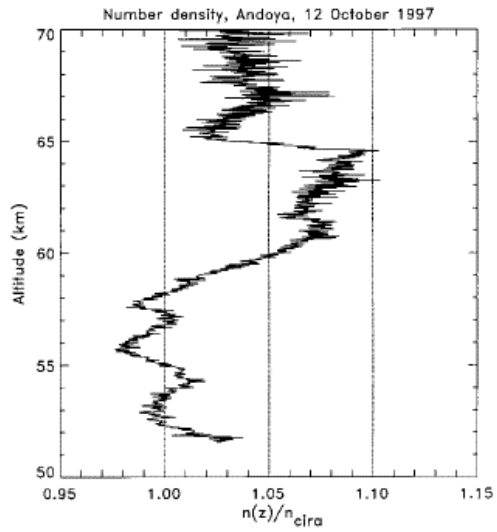

Figure 3. Measured number density profile, normalized to CIRA (from [12])

This system will be in many ways similar to TROLL (on RONALD [12]), but optical technology has come quite a ways since then, allowing for significant improvements. Engineering trade-offs between the physics and new technologies will allow for optimization of signal-to-noise ratio, by the use of the lidar equation [14]:

$$N_{\text{photons}} = \eta \frac{A_R}{4\pi} \int_{r0}^{r1} \frac{1}{z^2} dz \beta_R \frac{P_0}{(hc/\lambda)} \qquad (1)$$

Aperture area A_R (set up in either a binocular or Cassegrain configuration) is limited by deck size and real estate, though obviously we will maximize it to the best of our ability. The Rayleigh backscatter β_R increases dramatically (as wavelength to the fourth power) if we operate at shorter wavelengths. Limited to how low we can go by detector capability (though not by atmospheric absorption, like ground-based systems), we will operate using relatively new blue laser diode arrays, around 450 nm. A newer detector technology called MPPC (multi pixel photon counter) will also be utilized, which not only increases our sensitivity but expands the dynamic range. In addition to enabling the overall PAWSS system, this payload development will test these new technologies and determine if they are applicable for sounding rocket research.

The significance of the rocket-borne lidar is that this was entirely a student idea. Fortunately, one of our faculty team has experience with lidars and can guide the students in their enthusiasm for exploring this measurement technique. Student rockets are an excellent platform for trying such high-risk, high-payoff new technologies. The students have expressed excitement that they have this chance to improve sounding rocket practice. It has given them an evident sense of purpose in the larger context of the GCI–Cusp. Whether the lidar data are substantive or not, the students feel that they are playing an important role with this initiative.

1.2. PAWSS payload engineering

The engineering of the PAWSS payload is still in its early stages and much is subject to change. PAWSS will be provided a single full-height RockSat-X deck for payload accommodation. A notional view of payload configuration is given in Fig. 4. Items for consideration include the requirements that the lidar system, being heavier, shall be placed towards the middle of the deck with an unobstructed line of sight towards the outside. Antennas (tape measures) for the TEC receiver and the LP boom shall be placed close to the outer edge for deployment. Dimensions and masses for each of the components are yet to be obtained.

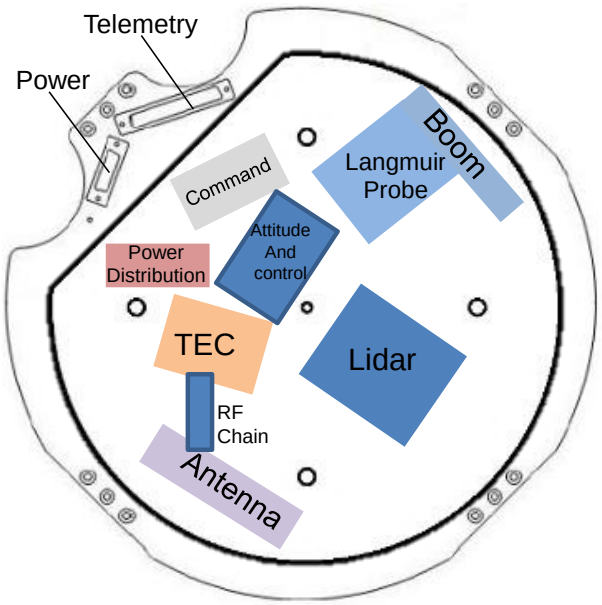

Figure 4. Notional deck layout for PAWSS.

During the fall, the students will prepare for the following design reviews. See Table 1 for the complete schedule.

Table 1. RockSAT XN Schedule

May 19–24, 2017	Conceptual Design Review
September 2017	Preliminary Design Review
November 2017	Critical Design Review
December 21, 2017	Final Down Select—Flights Awarded
February 2018	Subsystem Testing Review Experiment Decks and Connectors Sent to Teams
March 2018	Integrated Subsystem Testing Review
April–May 2018	Full Mission Simulation Review
June 2018	Integration Readiness

	Review
	Testing and Environmental with Wallops Flight Facility
July 2018	Launch Readiness Review
August 2018	Final Integration at Wallops
September 2018	Rocket shipped to Andøya Space Center, Norway
January 2019	Launch from Andøya

4. SUMMARY

The G-Chaser Student Rocket Program represents an exciting opportunity for engineering and science students to participate in an international research campaign to study the cusp of the earth's magnetic field. Penn State's participation in G-Chaser provides its students and faculty with an excellent opportunity to work with renowned atmospheric scientists from around the world and to develop continuing research collaborations with the science teams on the other GCI–Cusp Project rockets.

Student-built rocket payloads are extraordinarily effective pedagogical tools and represent an engaging, innovative educational tool, as there is a significant real-world application, problem-based learning, and hands-on nature to them. Additionally, students are exposed to a complete life-cycle—conceive, design, build, fly, analyse, report—and must employ systems engineering processes to ensure success. Based on our experience with Esprit, we can attest that an international student rocket program is also well-suited to participatory cultural experiences and education for the formation of competent engineers who are globally engaged. Even basic engineering training provides a confidence and an enthusiasm for this research that is seen to span national boundaries. G-Chaser is well-positioned to take full advantage of this enthusiasm and to encourage long-term friendship and collaboration among the students and faculty participants.

5. ACKNOWLEDGEMENTS

We are grateful for support from the Penn State College of Engineering Global Engineering Leadership Program (GELP) and the Pennsylvania Space Grant Consortium. We also wish to recognize the dedicated students who showed the way with ESPRIT and those who are part of G-Chaser.

6. REFERENCES

1. Blix, K., "The Grand Challenge Initiative Cusp Project," 23rd ESA Symposium on European Rocket and Balloon Programmes and Related Research, Visby, Sweden, 11–15 June 2017.
2. Bilén, Sven G., Mieke Schuurman, Lisa Brown, Timothy Wheeler, and Julio Urbina, "Addressing Aerospace Workforce Needs: The Impact of Hands-On Space Systems Project Experiences on Career Choices," 2008 ASEE Annual Conference, Pittsburgh, PA, 22–25 June 2008.
3. Bilén, Sven G., and Brian C. Schratz, "The Penn State Student Space Programs Lab: Training the next generation of space systems engineers," 2008 ASEE Annual Conference, Pittsburgh, PA, 22–25 June 2008.
4. DeVore, Steven M., Allen T. Kummer, Brian C. Schratz, and Sven G. Bilén, "The Student Space Programs Laboratory: Fostering student space Systems education and research within a university environment," 19th ESA Symposium on Rocket and Balloon Programmes, Bad Reichenhall, Germany, 7–11 June 2009.
5. Wheeler, Timothy F., Sven G. Bilén, Kenneth Haugland, and C. Russell Philbrick, "A broader vision: Space projects and international collaboration," 18th ESA Symposium on Rocket and Balloon Programmes, Visby, Sweden, 3–7 June 2007.
6. Bilén, Sven G., C. Russell Philbrick, Timothy F. Wheeler, John D. Mathews, Robert G. Melton, and David B. Spencer, "An overview of space science and engineering education at Penn State," *IEEE Aerospace and Electronic Systems Magazine*, Vol. 21, No. 7, pp. S-23–S-27, 2006.
7. Marra, Rose M., and Timothy F. Wheeler, "The impact of an authentic, student-centered engineering project on student motivation," 2004 FIE Annual Conference, Savannah, GA, 20–23 October 2004.
8. Kirkwood, S., "Polar mesosphere winter echoes – A review of recent results," *Advances in Space Research*, Vol. 40, No. 6, pp. 751–757, ISSN 0273-1177, http://dx.doi.org/10.1016/j.asr.2007.01.024, 2007.
9. Stebel, K., Blum, U., Fricke, K.-H., Kirkwood, S., Mitchell, N. J., and Osepian, A., "Joint radar/lidar observations of possible aerosol layers in the winter mesosphere," *J. Atmos. Solar-Terr. Phys*., Vol. 66, pp. 957–970, 2004.
10. Lübken, F.-J., Strelnikov, B., Rapp, M., Singer, W., Latteck, R., Brattli, A., Hoppe, U.-P., and Friedrich, M., "The thermal and dynamical state of the atmosphere during polar mesosphere winter echoes," *Atmos. Chem. Phys*., Vol. 6, pp. 13–24, 2006.
11. Martin Friedrich, *Handbook of the Lower Ionosphere*, Verlag der Technischen Universität Graz, 2016.
12. Eriksen, T, U.-P. Hoppe, E.V. Thrane, and T.A. Blix, "Rocketborne Rayleigh lidar for *in situ*

measurements of neutral atmospheric density," *Applied Optics*, Vol. 38, No. 12, 1999.

13. Gerrard, A.J., T.J. Kane, S. Eckermann, and J.P. Thayer, "Gravity waves and mesospheric clouds in the summer middle atmosphere: A comparison of lidar measurements and ray modeling of gravity waves over Sondrestrom, Greenland," *J. Geophys. Res*., Vol. 109, No. D10, D10103 10.1029/2002JD002783 22 May 2004.

14. Kovalev, V.A. and Eichinger, W.E., Elastic Lidar: Theory, Practice, and Analysis Methods," Hoboken, NJ: John Wiley & Sons, Inc. 2004.

HORIZON ACQUISITION FOR ATTITUDE DETERMINATION USING IMAGE PROCESSING ALGORITHMS – RESULTS OF PATHOS ON REXUS 20

Bastian Klein, Liviu Stamat, Moritz Aicher, Kevin Chmiela, Jonas Ehnle, Elke Heidemann, Felix Klesen, Florian Kunzi, and Dominik Wagner

Team PATHOS

Chair of Computer Science VIII – Julius Maximilian University of Würzburg c/o Prof. Dr. Hakan Kayal
Sanderring 2, D-97070 Würzburg, Germany
Email of corresponding authors: liviu.stamat@pathos-rexus.eu, bastian.klein@pathos-rexus.eu

ABSTRACT

The aim of Position-vector Acquisition Through Horizon Observation System (PATHOS) was to further develop a new concept for a two-axis horizon sensor operating in the visible spectrum of light as proposed by HORACE[1] and test this sensor system under space-like conditions, proving its usability as an Attitude Determination Sensor. The PATHOS system thus offers increased algorithm performance and a miniaturized version of HORACE. The REXUS[2] 20 rocket provided a suitable testing platform for the sensor system and the data collected during flight show the speed (~12fps) and reliability of the implemented image processing approach. This gives a first insight on the robustness of the system under high-spin conditions. Furthermore, the size of the sensor and its performance during flight prove its suitability for small satellite missions.

Key words: PATHOS; Position-vector Acquisition Through Horizon Observation System; Attitude Sensor; Attitude Determination; REXUS 20;

1. INTRODUCTION

Most satellite missions make use of an Attitude Determination and Control System during their flight in order to ensure a successful mission. While the sensors used in such systems employ a great number of different physical concepts as well as different references for attitude determination, there is a need of a sensor system that can still prove reliable even in case of an emergency high-spin situation, such as one following the satellites impact with space debris. As an answer to this need, the HORACE [1] experiment, successfully launched on REXUS 16 proposed a static horizon sensor operating in the visible spectrum of light, which was designed to maintain a sufficient performance during level the tumbling of the rocket, simulating the conditions which resemble a high spin rate scenario of a small satellite. This paper presents an advanced version of that sensor system, mainly aiming to miniaturize it, improve the efficiency of its image processing algorithm and prove its suitability under space-like conditions.

During the life cycle of the Position-vector Acquisition Through Horizon Observation System (PATHOS) project, the original system was studied and a new setup was proposed in the scope of the REXUS/BEXUS programme[3] [2], consisting of a simulated satellite environment and two identical, independent PATHOS sensors running an improved version of the image processing algorithm and its required software requirements. This platform was successfully launched on March 15 2016 06:30 (UTC+1) from Esrange, Sweden. The parabolic flight of the rocket with a peak of 77km fulfilled all the testing requirements for PATHOS, including the minimum required altitude and the uncontrolled tumbling motion to test the systems behavior in different working conditions.

The following sections offer an overview of the PATHOS experiment setup as well as a detailed discussion regarding the results of the flight of the PATHOS system on REXUS 20, including outlook possibilities.

2. GENERAL APPROACH

The starting point in the design of the PATHOS system was the experimental HORACE setup, since as their successors, our constraints in terms of sensor characteristics and motivation remained the same. One of our main objectives was therefore the optimization of the system in terms of size, weight and power

[1] Horizon Acquisition Experiment
[2] Rocket Experiments for University Students
[3] Rocket and Balloon Experiments for University Students

consumption. While the general idea remained unchanged – a visible spectrum camera captures images of the rockets surroundings and these images are processed by an algorithm that provides attitude data – we aspired to separate the simulated satellite environment and the PATHOS system entirely. This leads to a significant decrease in size and weight of the sensor system itself, thus also making the test outcome even more significant for small satellite missions. Furthermore it allows for an accurate measurement of the power requirements of the PATHOS system itself.

Our second main objective was to attempt to improve the image processing algorithm, in order to increase the number of frames processed per second. This is a very important figure with regard to the behavior of the system in a high-spin scenario, as a too low frame rate would render the sensor unreliable at higher spin rates.

Furthermore, due to the hosting possibilities of the REXUS 20 rocket [2], the decision has been made for two completely independent systems to be flown in the same module – with two different downlink channels – thus doubling the amount of experimental data collected and adding a vital failsafe to the experiment in case one of the systems happens to fail during flight.

3. EXPERIMENT OVERVIEW

3.1. Electrical & Mechanical Setup

The PATHOS experiment setup makes use of both off-the-shelf components, such as the On-Board Computer (OBC), the computer module of the Image Processing Board (IPB) and the Optical Sensor as well as components designed specifically for the mission, more precisely the Power Distribution Unit (PDU).

Simulation of the satellite environment for each of the two PATHOS systems is achieved by a Technology Systems TS-7700 embedded computer with Ethernet, I2C and SPI support. This computer is running the flight software and is responsible for managing flight modes and communication with the PATHOS system. The PDU acts as the electrical interface between the REXUS Service Module and our experiment. It realizes the connection between them and consists of a pair of DC/DC converters, limiting the 24V to 36V of unregulated voltage coming from the Service Module to a constant 5V voltage needed for the operation of the PATHOS experiment. Each of the two flown experiments has its own interface port and as such, its own PDU. The PDU also forwards rocket signals to the OBC and downlink data from the OBC to the Service Module. Additionally, an IMU-3000 Inertial Measurement Unit is fitted in with the OBC, supplied by the OBC and has its readings saved on the OBC.

One PATHOS system consists of one IPB and one camera. The chosen camera, a CMOS digital image sensor CASPA VL with a resolution of 752x480 pixels up to 60 frames per second seemed the perfect choice for our needs due to its small size (25.7mm x 39mm), low-light sensitivity with automatic exposure time and the known compatibility with the computer module of the IPB. The two are connected via a flat band cable and are housed together in the same structure, thus creating the core system of our experiment, also referred to as the PATHOS system. This system runs the image processing algorithm and its required interfacing software on a Yocto Linux operating system, a custom-build distribution for embedded systems. The camera records images in a YUV format, thus lowering the pixel information and as such the processing times required per image.

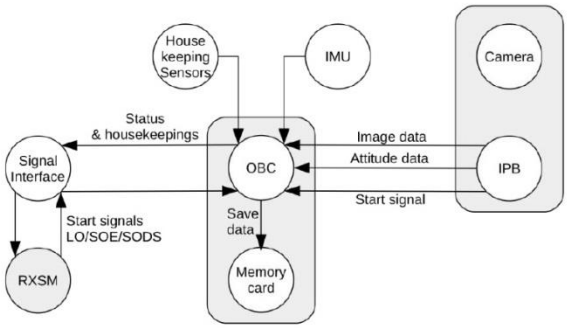

Figure 1: Block diagram providing an overview of one PATHOS experimental unit [3]

Our sensitive electronics are protected from the harsh space environment by means of individual aluminum housings and protected from electrical interference with themselves and other experiments via added aluminum tape on the inner walls of each of the housings. All the boards and housings are mounted individually on one single bulkhead, which is fitted horizontally to the middle of the REXUS ring module. For ease of access, we use both sides of the bulkhead, thus having the OBC and PATHOS system on the lower side of the bulkhead and the PDU on its upper side. Two circular holes are carved in the ring and covered with protective glass so

the camera can record images of the rockets surroundings. The two independent PATHOS experiments are placed symmetrically to the middle axis of the REXUS rocket so as to avoid inflicting unnecessary inertial movement to the rocket.

3.2. Optical Design

The optical design of PATHOS has two main requirements: first, during the experimental phase, at least one camera should be able to see the horizon in its field of view for as long as possible; that means keeping the horizon in view for as long as possible. Thus the decision was made to place the cameras adverse to one another so that if one camera was pointing into the vastness of space, the other would have the horizon in its field of view. The lenses for the cameras have also been chosen accordingly to offer a wide-enough field of view without however lowering the image quality by introducing any distortions or fish-eye effects, which would render the image processing algorithm to yield false results.

Another optical specification is that PATHOS cameras are mounted as close as possible to the modules protective windows. This offers an inherent advantage in terms of lens flare reduction caused by light refracting through the protective window and then the lens, as well as a wider field of view for the camera. Furthermore, the protective borosilicate windows used in the module have their frames anodized in black and the window sheet specially coated to reduce stray light and accompanying reflexes or lens flares.

3.3. Software Design

The PATHOS software can be broken down into three parts: the flight software, the image processing algorithm and the ground station software. As the algorithm is basically the scientific part of the mission, this subsection handles the other two software components.

The PATHOS flight software was running on each of the flown OBCs. It comes with three different operation modes, each one designed for a specific mission-related reason: Stand-by, Flight Mode, and Shutdown. The Stand-by mode is the mode in which the system boots up. It verifies successful boot-up and sends that information to the ground station. Flight mode is triggered at T+300s by the two rocket signals “Start of Experiment” (SOE) and Start of Data Stream (SODS) and thus the system begins the actual mission: Housekeeping is recorded and the PATHOS system begins processing images. Processed images, as well as the time-stamped results are saved, while the processing results are also sent to the ground station via downlink, along with housekeeping data. At T+570, the Shutdown mode is triggered, ensuring safe shutdown of all the software components and thus avoiding the risk of data loss. Another important part of the flight segment is the interface program that link camera images to the algorithm. It is a C++-based application that starts with the Image Processing Board (IPB) and requests camera images, processes them into an algorithm-suitable format, and finally saves these images along with their corresponding results. Image saving occurs once every 10 images in order to reduce overhead (non-algorithm-related processing times).

The ground station software was programmed in the QT [4] environment, which provides a good C++-based graphical user interface (GUI) programming environment. The Ground Station kept track of housekeeping data received from the rocket module, processing and displaying them for better readability and also informed the user about the image processing algorithm status by making use of a shared result code that was sent down by the space segment. The user was also able to use the ground station for testing the system, such as testing rocket signal reception.

4. ALGORITHM

4.1. Basic Idea

The image processing algorithm ran on PATHOS’ Image Processing Board (IPB) was the third iteration of the one operated by HORACE [5]. It receives an image from the interface software and makes use of the contrast between the orbited body and the dark space surrounding it to detect its horizon, thus being able to calculate a 2D vector from the center of the image to the center of the body and provide roll and pitch angle measurements of the spacecraft in relation to it. For this task, it requires images with a good contrast, as well as the presence of the horizon in the image.

4.2. Image Processing Approach

The image processing algorithm employed by PATHOS functions in the same main steps as the one operated by

HORACE, but with some important changes. These steps are described as the Threshold Filter, the Line Detection, the Vector Calculation and the Horizon Line Division.

4.2.1. Threshold Filter

PATHOS makes use of a static Threshold Filter, this means that every Y value of a pixel – which holds the value of the pixels brightness, from 0 to 255) is compared against a fixed threshold value. In this case, the output of this filter is either a 1 for white or a 0 for black, as shown in Eq. (1).

$$Y'(p_i) = \begin{cases} 1, if\ Y(p_i) > 100 \\ 0, \qquad\qquad else \end{cases} \tag{1}$$

The difference to the previous version of the algorithm is that PATHOS does not account the Threshold Filter as a main step, but rather as a function called every time a new pixel is checked for brightness. This saves processing time, as the image is only ran through once instead of twice.

4.2.2. Line Detection

The PATHOS Line Detection step is an improved version of the one used by the HORACE algorithm. It is essentially a topological search which outputs only one line in the end, by looking for pixels that satisfy the criteria for a border pixel and then following the neighboring border pixels in a border until the first one is reached again, then moving on to the next border pixel, thus finding another border. The longest border found is then selected as the one most likely to describe the horizon line.

An important difference in the PATHOS Line Detection step is the way the image is being processed. Instead of running through the image in a standard fashion, checking every pixel in order, this step starts by only searching the outermost pixels of the image – the uppermost and lowermost rows and the rightmost and leftmost columns. If a border pixel is found in this process, the image continues to be processed as described above. If none of these pixels satisfy the border pixel criteria, the image is discarded on account of having no horizon present. This is made possible on a REXUS flight by knowing the fact that the peak altitude reached is around 80km, which means the camera is not far enough from Earth to see the whole planet in any one image, as such the presence of the horizon is easily discovered by checking just the outermost pixels of the image.

4.2.3. Vector Calculation

The Vector Calculation step in the PATHOS algorithm runs as the one in the HORACE algorithm. It first uses the data of all pixels in one line to perform a circle fit by the least square method and then uses the calculated coordinates of the circle center to calculate a vector to it from the center of the image. Since disturbances which may alter the horizon line – such as lens flares or the Sun itself – have to be taken into account, the radius of the found circle is used as a means to check whether it fits between the maximum and minimum expected radius of the orbited body, based on the characteristics of the optical system.

4.2.4. Horizon Line Division

The Horizon Line Division step replaces the Division step employed by the HORACE algorithm [5]. As such, instead of dividing the complete image into four parts if the horizon detection proves unsuccessful due to obstructing artifacts, the PATHOS algorithm takes only the horizon line outputted by the Line Detection step and divides it iteratively in half until a result is achieved, or the line is too small to offer a reliable detection that remains representative for the initial image.

5. RESULTS AND DISCUSSION

The flight of the two PATHOS systems in March 2016 was a complete success and thus offered us with a great deal of useful in-flight-processed image data and information regarding the behavior of the system. Based on this data, a qualitative analysis has been undertaken to verify the suitability of the horizon sensor for a future space mission.

Considering the fact that this sensor has a minimum altitude required for reliable operation, we have observed this altitude to be roughly 40km. Thus, with the help of DLR MORABA we have chosen the timeframe when the rocket was above this altitude threshold to be between T+47s and T+224s. Therefore, only data collected during this time window will be analyzed.

5.1. Frame Rate

The first important figure regarding the behavior of our experiment is the frame rate the system was able to process. By analyzing the image data, we calculated the values for the frame rate and the time needed per frame as shown in Table 1.

	Minimum	Average	Maximum
	Frame Rate [fps]		
System 1	9	12.28	16
System 2	8	12.58	23
	Time per Frame [ms]		
System 1	42.8	62.3	189.3
System 2	42.8	67.1	258.6
	Overhead [ms]		
System 1	4.8	22.1	392.0
System 2	4.8	21.0	441.9

Table 1: Calculated frame rates and processing times for the two PATHOS systems on REXUS 20

Table 1 also shows the needed overhead per frame, which represents all non-algorithm-related processing times related to the processing of the frame, such as preprocessing and saving.

5.2. Detection Types

We have defined five different types of detections based on the test scenarios used in the development of the algorithm, which remain valid for the collected scientific data, as shown in Figure 2:

- Correct Detections – A horizon is present in the image and successfully detected or no horizon is present and none is detected;
- Correct Detections with offset – A horizon is present in the image and it is detected but with a slight offset to the actual horizon line;
- False Detections – A horizon is visible in the image but the detected horizon does not correspond to the actual horizon line;
- False Negatives – A horizon is visible in the image but not detected by the algorithm;
- False Positives – There is no horizon in the image but the algorithm detects one.

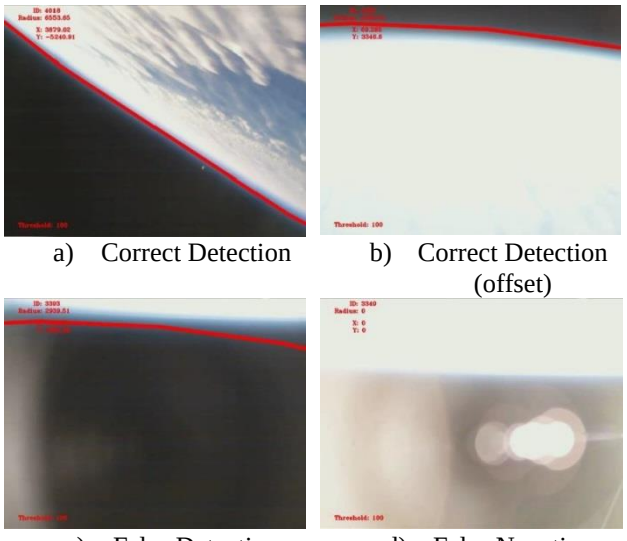

a) Correct Detection b) Correct Detection (offset)

c) False Detection d) False Negative

Figure 2: Types of detections encountered by PATHOS during its flight on REXUS 20

There have been no recorded false positives for either of the two PATHOS systems. Out of the total number of images considered for this evaluation, System 1 has 48.7% of them with a visible horizon while System 2 has 49.3% of the same. Out of all images with a visible horizon, System 1 has a correct detection percentage of 57.8% and System 2 has a correct detection percentage of 59.0%. As far as false detections go, System 1 encountered 6, while System 2 has encountered 18. As far as false negatives go, System 1 has a false negative percentage of 20.0%, whereas System 2 has a false negative percentage of 19.3%.

5.3. High-spin Evaluation Phase

With the help of DLR MORABA we were able to choose a timeframe for the high-spin phase of our evaluation above the 40km mark. However, due to the rocket's high velocity, this time window lasted a mere 19 seconds, which any decision as to whether or not the horizon sensor is reliable enough to be used in such conditions less trustworthy. Quantitatively, however, the frame rate of the systems seems unaffected and the detection rate is greater than for the rest of the flight. This improved detection rate is also due to the fact that the rocket maintains an almost perpendicular position to the horizon line during its ascent, which could provide an easier case of detection. The frame rates for this 19 second window are almost identical to the ones calculated for the rest of the flight.

5.4. Power Consumption

The power consumption levels for each PATHOS system as recorded by the current sensors throughout the flight are shown in Figure 3. It is worth noting that PATHOS needs less power as opposed to HORACE, but there does not seem to be any correlation between the algorithm activity and the IPB's power consumption. The observed reduction in power between the two experiments is related to PATHOS using an embedded system with an ARM microprocessor subsystem and SD Flash Cards for storage, as opposed to an Intel ATOM chipset with Solid State Drives for storage.

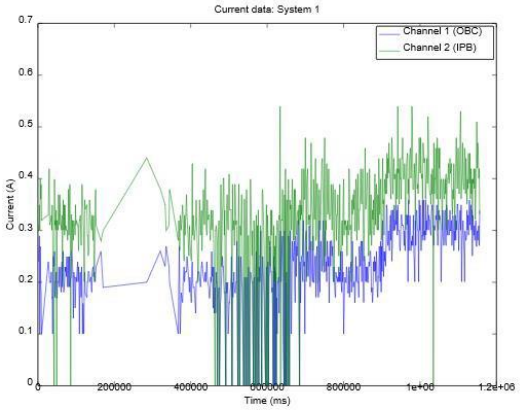

a) System 1

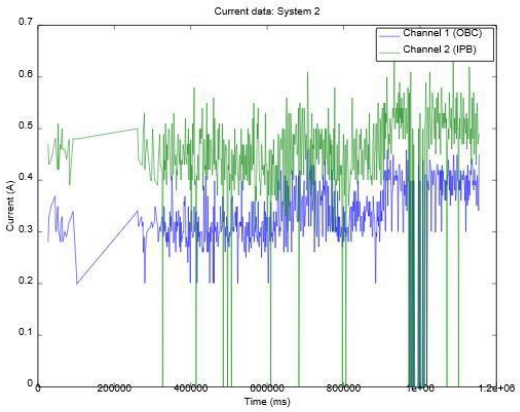

b) System 2

Figure 3: Power consumption of the two PATHOS systems during their flight on REXUS 20

5.5. Discussion

While the PATHOS experiment is still an early step in the process of qualifying the proposed sensor technology for small satellite missions, the results obtained during the PATHOS experimental flight correlated with the HORACE simulations show how much potential this horizon sensor has. The frame rate of roughly 12 fps is a strong reason for the system to be considered for a high-spin emergency situation, especially since so far it is only limited by the on-board calculation power available to it. While the trustworthiness of the high-spin evaluation phase may be lowered by its short time window, the quality of the individual images taken during that time remains the same as for the rest of the flight, which speaks strongly in favor of the applicability of this sensor to such conditions.

As far as detection rates are concerned, there is one most important algorithm component that needs to be considered for revision and improvement: the threshold filter. While the algorithm's functionality has been proven during the PATHOS experimental flight by its correct detections and the lack of false positives, one fifth of the frames still result in false negatives and even though it is true that this type of detection does not harm the system by providing incorrect readings, they are also not wanted, as lighting conditions in space are often unfavorable for a visible-spectrum camera. Furthermore, the 6 and 18 false detections encountered by the system are clearly the effect of an insufficiently mature threshold filter and while they can easily be transformed into false negatives by using pixel data on both sides of the line to determine the expected curvature, this is just a workaround, not a fix. Thus, work is still needed on the threshold filter in order for this horizon sensor to be considered in a professional environment.

Last but not least, the low power requirement and size of the PATHOS system are both advantages when it comes to its inclusion in a small satellite mission.

6. FURTHER WORK & OUTLOOK

All the objectives of the PATHOS project – to offer a new approach and an improved version of this static horizon sensor using a visible-spectrum camera – could be reached and the project was a great success. However, there is still room for improvement and a way

to go before this sensor can be fitted into a space mission. Thus, the next important steps as far as the implementation of this horizon sensor is concerned would be the quantitative qualification of the system by flying it alongside one or more accurate attitude determination sensors as reference, as well as an improved approach for a more autonomous and reliable Threshold Filter, which is so far the most important component of this system.

Another future option that might be of significance in terms of size, weight and most importantly processing speed would be implementing the PATHOS system as an embedded system without an operation system as a layer between the algorithm and the hardware.

7. CONCLUSION

Analysis of the recorded in-flight data of both PATHOS systems shows a very successful first test of the system in space-like conditions, in which the Image Processing Algorithm as well as the entire PATHOS system performed nominally and as expected. The change in flight hardware lead to successfully avoiding the unfortunate malfunction that degraded HORACE's in-flight data and also proved that the system can operate with a low standard VGA image resolution. Maintaining a false positive rate of 0% and achieving a frame rate of roughly 12 frames per second offer strong insight towards the fact that the horizon sensor discussed in this paper is robust enough to be considered for further testing and qualification towards small satellite applications.

Another important aspect to be taken into account during this evaluation is the educational benefit that PATHOS offered, thanks to being developed in the scope of the REXUS/BEXUS programme. The opportunity for Bachelor students to be able to experience the life cycle of a space mission first-hand is an invaluable experience for their future space careers. Furthermore, acquiring these insights as part of a controlled space mission environment with a mainly educational goal where failures – while not encouraged – are "allowed", offers the student one of the best career-related experiences one could receive during their studies, thus greatly outweighing deficiencies related to the scientific result alone.

ACKNOWLEDGEMENTS

We would firstly like to thank Prof. Dr. Hakan Kayal and his staff for the supervision provided throughout the entire project, as well as for providing us with a controlled work environment and access to financial support and the chair's resources and facilities. Secondly, we would like to thank the German Aerospace Center (DLR) and the Swedish National Space Board (SNSB) for offering us the opportunity presented by the REXUS/BEXUS programme, and for allowing us to take part in it, thus making the PATHOS project become reality. Last but not least, our thanks go to the staff of all other agencies associated with the REXUS/BEXUS programme, the European Space Agency (ESA), the Center of Applied Space Technology and Microgravity (ZARM), DLR Mobile Rocket Base (DLR MORABA) and SSC Esrange for their continuous professional support, as well as to all our other supporters and partners, personal or professional, who helped a great deal in making PATHOS happen.

REFERENCES

[1] T Rapp, J Barf, M Bergmann, et al., "HORACE Student Experiment Document v5.0," 2014.

[2] S Mawn, A Schmidt, H Hellmann, et al. (2014) REXUS User Manual v7.13.

[3] D Wagner, M Aicher, J Ehnle, et al., "PATHOS Student Experiment Document v5.0," 2016.

[4] Qt Company. (2017) Cross-platform application & UI development framework. [Online]. http://www.qt.io

[5] J Barf, T Rapp, M Bergmann, et al., "HORIZON ACQUISITION FOR ATTITUDE DETERMINATION USING IMAGE PROCESSING ALGORITHMS – RESULTS OF HORACE ON REXUS 16," in *22nd ESA Symposium*, Tromsø, 2015, pp. 627 - 634.

[6] J. Barf, "Development and Implementation of an Horizon Sensing Algorithm based on Image Processing Technologies," 2014.

LOW COST NAVIGATIONAL DATA RECORDING PAYLOAD FOR SERA SOUNDING ROCKETS

L. Strizic, G. Antoja, H.H. Hristov, A. Jegatheesan, A. Pontoni, T. Seth, and H. Woo

Luleå University of Technology, Box 848, 981 28 Kiruna, Sweden, Email: lukstr-5@student.ltu.se

ABSTRACT

The Vibrations Inherent System for Tracking and Analysis (VISTA) project is a low-cost Global Positioning System (GPS) receiver that flew on the Supersonic Experimental Rocket ARES-III (SERA-III) sounding rocket as part of the Projet Etudiant de Recherche Spatiale Européen Universitaire et Scientifique (PERSEUS) project.

On April 26, 2017, SERA-III was successfully launched from the European Space and Sounding Rocket Range Space Center (ESC) launch base near Kiruna, Sweden. Raw GPS data was recorded by VISTA throughout its flight and was processed after recovery.

Key words: GPS; sounding rocket; Software-Defined Radio; trajectory analysis.

1. INTRODUCTION

The PERSEUS project (Projet Etudiant de Recherche Spatiale Européen Universitaire et Scientifique) is an initiative of CNES (Centre National d'Études Spatiales) to promote innovative technical solutions in the aerospace domain with industrial and educational applications, realized by university students. One of the projects under PERSEUS is SERA (Supersonic Experimental Rocket ARES), whose objective is to provide a platform to test and validate other technologies developed in the frame of PERSEUS, through a supersonic flight. VISTA (Vibrations Inherent System for Tracking and Analysis) is a payload provided by an international team of students studying at LTU (Luleå Tekniska Universitet) in Kiruna, Sweden. The VISTA team designed a payload to record the trajectory of the SERA-III rocket throughout its flight using Global Positioning System (GPS) technology. Rather than using standard GPS receivers which are software-limited, according to Coordinating Committee for Multilateral Export Controls (CoCom) regulations, to stop output of data when they reach high acceleration or altitude, the experiment recorded raw GPS data during the entire flight which was later post-processed on the ground.

The rocket was successfully launched from the European Space and Sounding Rocket Range Space Center (ESC) near Kiruna on April 26, 2017 and the VISTA payload was recovered on the same day. Preliminary post-processing of the data on payload recovery showed that its performance was nominal. Post-processing was performed using a Software-Defined Radio (SDR) written in MATLAB by Colorado Center for Astrodynamics Research (CCAR).

This paper presents the final design of the VISTA payload that flew on the SERA-III rocket and the results of the experiment.

2. MECHANICAL DESIGN

The flight model of the payload was designed in accordance with the requirements provided by CNES. Some of the key requirements were: the payload should not exceed $500g$ in mass; should be limited to a cube of $80mm$x$80mm$x$80mm$ size; should withstand mechanical stresses up to $15G$ of acceleration and launch vibrations of up to approximately $1000Hz$ since the SERA-III rocket was fitted with 3 engines each having a vibrationnal frequency of 300-$600Hz$.

2.1. Design description

The design underwent multiple iterations to accommodate the electronic components used in the experiment. Tab. 1 shows the list of electronic and mechanical components used and their masses. The table also shows that the payload was well below the $500g$ limit, thereby meeting the mass budget requirements. The final CAD design of the payload can be seen in Fig. 1.

The outer structural support was 3D printed using Polylactic acid (PLA) plastic to keep the payload light-weight without jeopardizing the structural integrity of the payload. Inside the structure, the space was accommodated for securing the electronic components on the walls of the plastic using zip ties. The outer portion of the payload consisted of 3 separate aluminum panels, suitably bent where necessary and attached to the plastic using

Table 1. Component mass budget

Payload components	**Mass(g)**
SiGe GN3S	10
Raspberry Pi	9
SMA connector on the wall	8
D-subs x 2	16
Batteries x 2	72
Wires	8
3D printed plastic support structure	55
Aluminium box	94
Fittings	28
TOTAL	**300**
External antenna (not part of the mass budget)	150

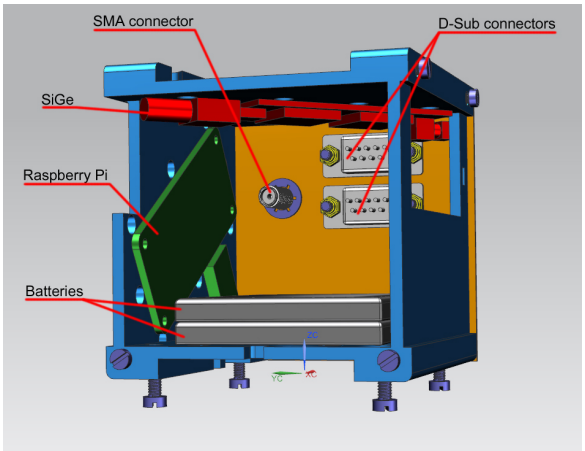

Figure 1. Isometric view of CAD model

helicoils and screws. The panels also served the purpose of mounting the D-subminiature (D-sub) and SubMiniature version A (SMA) connectors. The remaining space inside the plastic casing was used for cable and wire management as seen in Fig. 2. The side window on the plastic was used for easier access to the electronics and the connections during the assembly process. The entire payload was affixed to the rocket's interface plate by using M4 screws bolted into the plastic structure that contained a hexagonal nut. Any gaps left were sealed with aluminium tape to prevent signal interference between the payload and the rocket.

2.2. Testing and validation

In order to validate that the payload would survive stresses and loads up to 15G acceleration and up to 1,000Hz vibrational frequency during the initial, high-acceleration phase of the flight, a software simulation and a mock up shaker test were conducted. A simple response simulation was conducted on NX NASTRAN only on the lightest part of the payload, i.e. the plastic casing, using the aforementioned material properties, boundary conditions and constraints. The analysis revealed that the eigenfrequency for only the first mode of vibration was

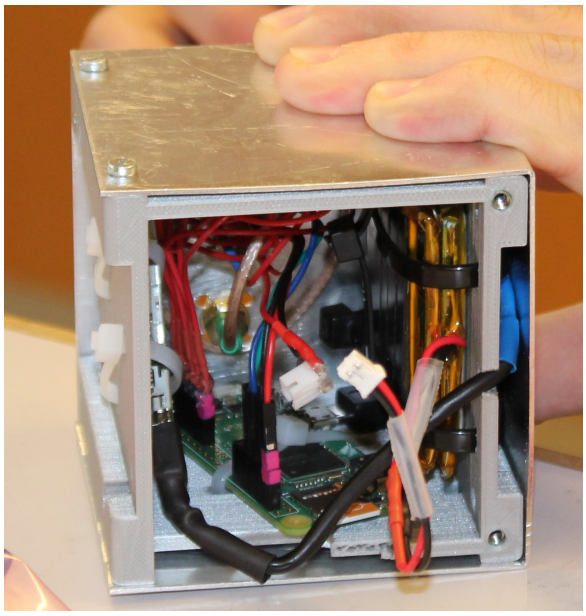

Figure 2. Flight model before integration into rocket

1,217 Hz as seen in Fig. 3, which was well above the threshold frequency.

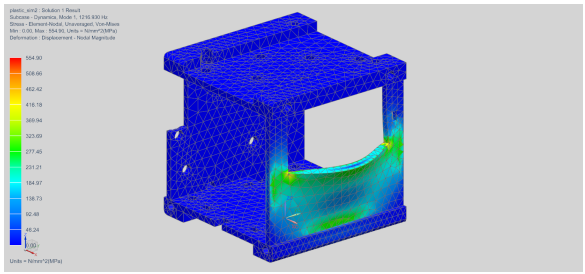

Figure 3. Mode 1 frequency vibrations on NX Nastran

According to electronics test documentations provided by CNES, their components were normally tested at 1G. A crude shaker test using dummy weights was performed to check if vibrations caused any damage to the structure under loading and whether the fittings might loosen. The shaker test was conducted at a facility in Institutet För Rymdfysik (IRF) in Kiruna. The test was setup for Sinusoidal vibration at 1G between a frequency range of 5-2kHz as shown in Fig. 4. Before starting with the tests, preliminary software settings were made. Two sensors, one attached to the shaker's mounting plate and the other to the payload, were used to monitor the constant acceleration given by the user i.e. 1G and the variation in acceleration and frequency on the structure respectively. The same test was performed twice, once the payload was mounted in a horizontal position, and after that in a vertical position. Post-testing, it was seen that there was no change in the structure of the payload under loading conditions and the fittings remained intact.

In order to check if any damage would occur to the payload during descent phase of the rocket, a basic drop test

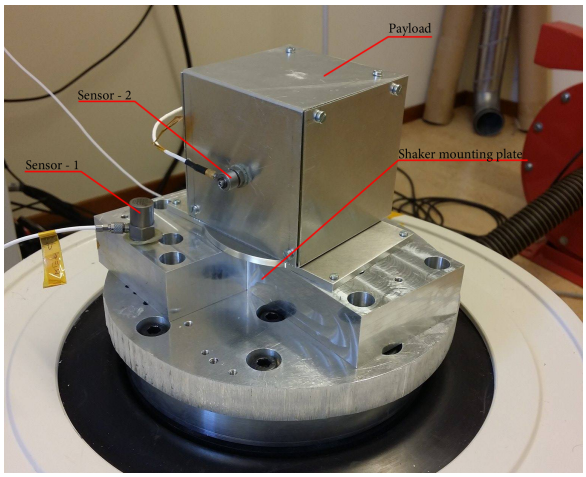

Figure 4. Test setup with dummy payload mounted on shaker table

was conducted. The payload with all its components secured was dropped from the 3rd floor of the university building (approximately 8-10m high). Post-test, it was noted that there was no broken parts or damage to the components, the fittings remained intact and there was no disconnection of wires or misplacement of the SD card. Right after the drop test, a successful data recording test was performed, showing that the internal payload components survived on impact as well.

3. ELECTRONICS DESIGN

A well-tested and proven GPS RF front-end was used: the SiGe GN3S Sampler, developed and designed by the Colorado Center for Astrodynamics Research (CCAR), at the University of Colorado in Boulder.

The SiGe GN3S used a SE4120 GPS Application Specific Integrated Circuit (ASIC) and a Cypress FX2 Universal Serial Bus (USB) controller. It also included a mini USB connector for connecting it to a Personal Computer (PC).

To accommodate the relatively high computational requirements for communication over USB, a Raspberry Pi Zero was picked, which is a complete computer based on the Broadcom BCM2835 platform, featuring a $1GHz$ single-core ARM11 CPU and 512 MB of Random Access Memory (RAM). Subsequently, a standard Raspbian GNU/Linux distribution was used as the operating system on the Raspberry Pi, and a tailored USB on-the-go (OTG) adapter was used to interface with the SiGe GN3S. With the Raspberry Pi acting as a regular PC, it was possible to reuse the original software written for the SiGe GN3S, with only the changes needed to accommodate for the limited resources on such a platform, achieved by removing unnecessary features and doing performance improvements. A block diagram of the payload is shown in Fig. 5.

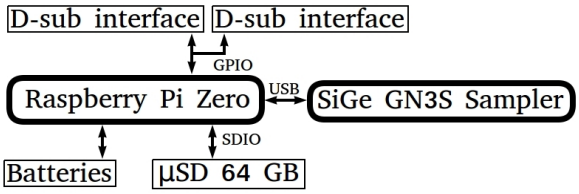

Figure 5. Block diagram of the payload's electronics.

Both D-sub interface specifications utilized Raspberry Pi's General Purpose Input Output (GPIO) pins. It is worth noticing that the electrical interfaces of the payload were not decoupled from those of the rocket but were instead referenced to the rocket's signal ground.

Rocket	
J1	
Wire 1	Status +
Wire 2	Init +
Wire 3	Ignit +
Wire 4	LOa
Wire 5	---
Wire 6	StatusReturn
Wire 7	InitReturn
Wire 8	IgnitReturn
Wire 9	LOb

Ground Station	
J2	
Wire 1	Power+
Wire 2	Batt+
Wire 3	Batt-/GND
Wire 4	RX
Wire 5	TX
Wire 6	---
Wire 7	---
Wire 8	---
Wire 9	---

Figure 6. Signals of the ground station and rocket interface.

Signals that were sent through the D-sub interfaces are shown in Fig. 6. Status+ and StatusReturn signals were used to signal the rocket that the payload was on and ready to fly. Init+ and InitReturn were signaled by the rocket, indicating that its on-board computer was on, but were ignored in the design as they were not relevant to the function of the payload. Ignit+ and IgnitReturn signalized the ignition of the rocket's engine. LOa and LOb were shorted while the rocket was on the ground and open during flight. To turn the payload on, Power+ and Batt+ needed to be shorted. Batt+ and Batt- were connected to the positive and negative poles on the battery, respectively, and were used for charging the payload without taking it apart and disconnecting the batteries. This also facilitated in recharging the batteries after integration on the rocket. RX and TX provided a Universal Asynchronous Receiver/Transmitter (UART) interface to Raspbian's shell and were used to control the payload without taking it out of the rocket.

A 64-gigabyte microSD card and two 2,000mAh batteries were finally used, in order to make sure that there was enough room and power for many hours of recording. After almost three hours of operations, around 30GB of data were recorded and the payload consumed less than half of its batteries' maximum charge.

4. POST-PROCESSING OF DATA

The SERA-III launch campaign was held from April 24 to April 28 at the ESC, a launch base of the Swedish Space Corporation (SSC) situated in northern Sweden near Kiruna. Four members of the VISTA team joined the other Supersonic Experimental Rocket ARES-III teams there.

The SERA-III sounding rocket was launched on April 26, 2017. The flight was successful, although the first stage of the rocket unexpectedly broke off from it. The rest of the rocket was recovered a few hours after touchdown and the payloads extracted from it intact. The raw GPS data recorded by VISTA was post-processed using a Software-Defined Radio (SDR) developed by CCAR and which had been previously tested and used with the SiGe GN3S module.

The SDR analysed the first few milliseconds of the input data file, created by the SiGe GN3S, to see which satellites were in the field of view which, due to the short timespan of the mission, were unlikely to disappear from the field of view. Once all the satellites in the field of view had been identified, the satellite tracking was started and one by one, pseudo-ranges for each satellite were calculated and stored for further obtaining the position solution once the tracking was done.

For faster post-processing, most of the data recorded before lift-off, while the rocket was still on the launch pad, was discarded. The SDR was ran with a file containing data starting only a few minutes before launch. After running the post-processing software, it was concluded that at the moment of lift-off seven satellites were visible in the sky, namely satellites 3, 6, 14, 19, 25, 31 and 32 as seen in Fig. 7. Furthermore, the SDR provided navigation solutions every $10ms$ and plotted, over time, their variations with respect to their mean value in Universal Transverse Mercator (UTM) coordinates as well as the position of the acquired satellites in polar coordinates (also Fig. 7).

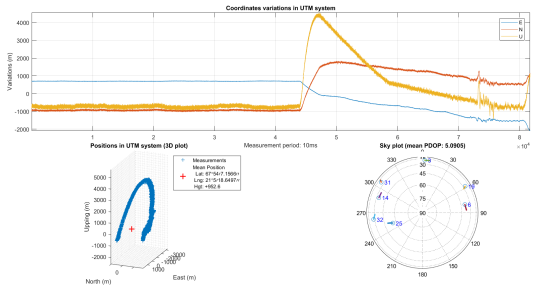

Figure 7. Variations of the positions calculated by the SDR, in UTM coordinates

The data was rather noisy, even before lift-off when the rocket was standing on the launch pad. During this period the standard deviation was around $68m$ in height, but averaging the values resulted in coordinates that Google Maps indicated to be only a few meters from where the rocket actually was. For further post-processing we used the navigation solutions converted to latitude, longitude and height by the SDR and smoothed them with a moving average. Fig. 8 shows the raw height computed by the SDR, over which its smoothed (averaged) form has been plotted. The different phases of the flight are easily visible on this figure: the high acceleration phase lasted around $31s$, at which moment the drogue parachute opened and the rocket started its descent phase. The second, main parachute opened at around T+$148s$ and the descent velocity of the rocket subsequently decreased. The moment when the rocket touched the ground was not easy to make out because the data was very noisy around that time.

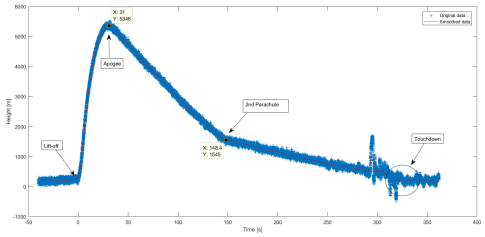

Figure 8. Height recorded by the payload: in blue, the navigation solutions calculated by the SDR; in red, the same data after a smoothing function (moving average) was applied to it.

The velocity and acceleration were computed using the smoothed positions data set and were plotted in Fig. 9. As its name suggests, SERA-III was indeed supersonic: a maximum velocity of about $350m \cdot s^{-1}$ was reached at T+$9s$. The maximum acceleration was reached at T+$5s$, measured at $7G$.

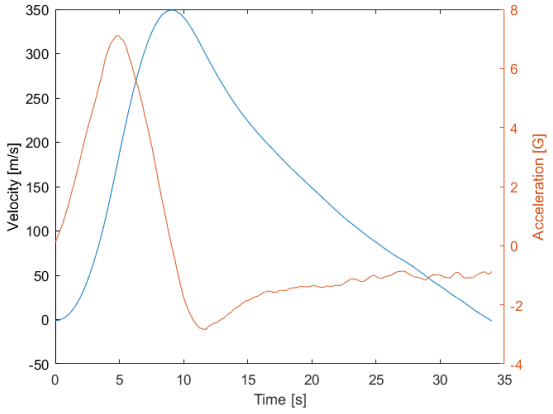

Figure 9. Velocity and acceleration of the rocket during the first 34s of flight.

According to our data, the rocket landed at the location $67°54'24.5"N\ 21°03'06.5"E$, which is $2.7Km$ away from the launch pad in the north-western direction (see

Fig. 10), trajectory that hints at rather strong winds coming mostly from the eastern direction.

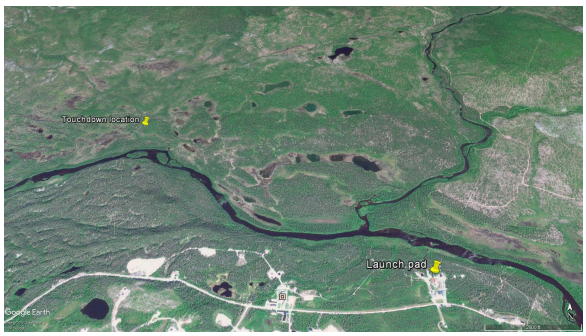

Figure 10. Google Earth Pro image of the launching area. The two yellow pointers indicate the launching pad and touchdown positions recorded by the payload.

The data was afterwards imported into Google Earth Pro in order to visualize the trajectory in 3D (Fig. 11), where once again the effects of possibly strong winds may be appreciated.

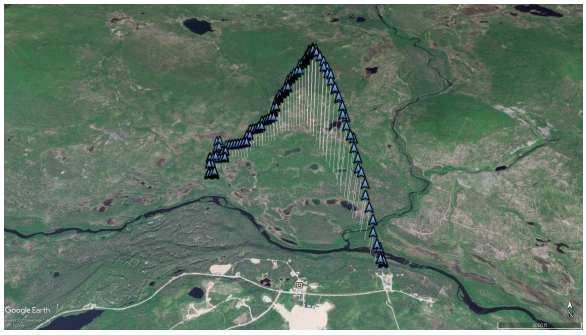

Figure 11. 3D trajectory of the rocket visualized in Google Earth Pro. It should be noted that only 1 out every 100 values was used for plotting this trajectory.

Most of the results from post-processing the data recorded by VISTA were consistent with the different sensors installed by CNES on the rocket. However, the maximum acceleration was found to be slightly lower than that recorded by CNES, of $9.73G$.

5. CONCLUSION

The objective of the VISTA experiment was to record the trajectory of the SERA-III sounding rocket using GPS, which was carried out successfully. The VISTA team designed a payload using low-cost, off-the-shelf, well-documented and field-tested components to achieve the stated objectives while complying with the requirements provided by CNES. The flight was successful and the recorded data was consistent with the expected flight dynamics as well as with the data recorded by other sensors of the rocket, to a certain degree.

The results of VISTA experiment are also valuable for future SERA missions as they now have a working solution to build and improve upon.

ACKNOWLEDGMENTS

The authors would like to thank CNES for giving us an opportunity to build a payload for their SERA-III rocket. Particularly, the SERA teams present at Esrange contributed to a smooth and successful launch campaign guided by ESC. We express our gratitude towards Luleå University of Technology and Swedish National Space Board for providing us with project funding and access to technologies and labs during payload development. Lastly, we would like to thank Dr. Thomas Kuhn, our project supervisor, for guiding us throughout the course of the project.

WOLF: A REXUS STUDENT EXPERIMENT TO DEMONSTRATE AN ACTIVE WOBBLING CONTROL SYSTEM FOR SPINNING FREE FALLING UNITS

A. Buzdugan, F. Franzen, F. Giuliano, G. Guerra, H. Hultin, E. Von Keyserlingk, P. C. Kotsias, J. Olsson, K. Papavramidis, D. Rozenbeek, G. Giono, G. Tibert, and N. Ivchenko

Royal Institute of Technology (KTH), 100 44 Stockholm, Sweden, wolf-team@kth.se

ABSTRACT

WOLF (WObbling controL system for Free falling unit) is a student experiment developed in the frame of REXUS/BEXUS programme, scheduled for launch in March 2018 on board of the REXUS24 sounding rocket. The primary objective of the project is to demonstrate a system to suppress the wobbling of Free Falling Units (FFUs) ejected from a spinning rocket. Multiple FFUs ejected from a single carrier provide means of multipoint measurements in the upper atmosphere, where spin stabilisation is a common attitude control scenario. Lateral rates introduced by rocket coning, ejection tip-off or other effects result in wobbling of FFUs, while for many missions flat spin is required. A reaction wheel based control system is proposed to suppress the wobbling. A single reaction wheel, with rotation axis perpendicular to the nominal spin axis of the FFU, actuated with a control law based on the phase of the FFU wobbling is effective in reducing the lateral rates during short flight time of the rocket. An analytical model of the motion of a cylindrically symmetric FFU is put forward, and verified by numerical simulation and a prototype test with a gravity-offloaded system, representative of the FFUs. The experiment to demonstrate the system in flight is based on two identical FFUs, launched inside a rocket module. Both FFUs will carry the wobble control system, a parachute based recovery system and a wire boom deployment system. After dewobbling the FFUs, the wire booms with spherical probes will be deployed and the deployment process will be recorded. The electrical characteristics of the probes will be monitored and compared with models of photoelectric current from various probe surfaces. Additionally, the rocket dynamics will be observed with an inertial measurement unit (IMU) and a magnetometer.

Key words: WOLF; Free Falling Unit(s); REXUS; Wobble control.

1. INTRODUCTION

Since aircraft and balloons are limited to altitudes of typically less than 40 km and orbital spacecraft have a minimum altitude of well above 100 km, the only viable solution to access the middle atmosphere and lower ionosphere is the use of sounding rockets. Free flying payloads ejectable from sounding rockets can be used to make multi-point in-situ measurements, e.g. [1, 2, 3].

A series of student rocket experiments with free-flying payloads have been conducted at Royal Institute of Technology, KTH, Sweden [4]. All experiments were carried out on a standard Improved Orion REXUS vehicle, and released before the despin of the vehicle, following a ballistic trajectory until deploying a parachute for safe landing and subsequent recovery. SQUID experiment [5] ejected an FFU axially from underneath the nose cone for demonstration of a wire boom deployment system. In the RAIN experiment [6] two FFUs were ejected radially to collect aerosol samples throughout the upper and middle atmosphere. MUSCAT experiment [7] ejected four active falling spheres for characterisation of atmospheric density and temperature profiles. Subsequent experiments, such as ISAAC [8] and SCRAP [9], and later SLED, realised different experiments with similar hardware concept, where two disk-shaped FFUs are ejected radially from the rocket. The FFU design is modular, with the upper module having same function (recovery system and trajectory logging) and similar design, while the lower modules were different.

Based on the concept of ejectable FFUs developed and demonstrated in the REXUS programme, a research sounding rocket was proposed and realised in the Swedish national sounding rocket and balloon programme. The experiment, Small Payloads for Investigation of Disturbances in Electrojet by Rockets (SPIDER), aimed at characterisation of Farley-Buneman turbulence in the E region of the ionosphere on multiple scales. Ten FFUs, conceptually similar to the ISAAC FFUs [8] were ejected from the same carrier, reaching an apogee of over 130 km. Each of the FFUs had eight spherical probes on radial wire booms, with four of them used for measuring the electric field vector in the spin plane by double probe method [10].

The SPIDER sounding rocket was launched on February 2, 2016 from Esrange Space Centre. The payloads were successfully ejected, and most of them were recovered. However, the FFUs experienced a wobbling motion,

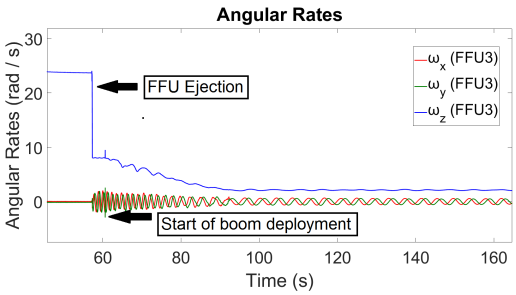

Figure 1. Components of angular rate vector in the FFU body frame recorded during SPIDER flight by one of the FFUs.

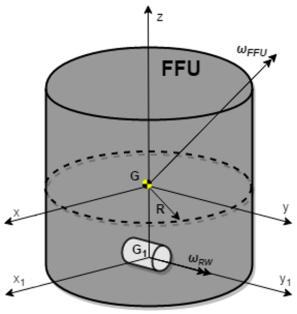

Figure 2. Orientation of the FFU and the reaction wheel.

probably induced during ejection (see Figure 1). The wobbling motion of the FFUs complicates the attitude reconstruction of the units, and compromises the electric probe measurements on the spinning payloads.

The WOLF REXUS experiment sets out to address the issue of payload wobbling, aiming to demonstrate a system to suppress the wobbling and to ensure flat spin motion on cylinder-shaped FFUs. The system will be important for future experiments with electric field booms, but also generally applicable for payloads that require spin stabilisation and benefit from flat spin. The experiment also addresses the questions of the FFU ejection effect on the main rocket attitude dynamics, and develops a more robust recovery and localization system to be used on FFUs of this class.

This paper presents the status of the experiment after the Critical Design Review. We start with presenting an analytical model of the FFU rotational motion with a reaction wheel, formulate the concept of active control for reducing the lateral rates, which is then simulated numerically. A prototype test is conducted with a gravity offloading system to demonstrate the concept. We proceed then to discuss the experiment setup, focusing on the major modifications compared with the previous experiments with similar FFUs. The secondary objectives of the experiment (characterising of the probe photoemission, monitoring the effect of the FFU ejection on the dynamics of the rocket, characterising of the probe dynamics during and after deployment) are presented as well.

2. MODEL AND NUMERICAL ANALYSIS

The dynamics of a rigid body is described by Euler's equations. For an axially symmetric body (with moments of inertia about two principal axes equal), the motion is particularly simple, reducing to a combination of spin and coning (see e.g. the presentation in [11]). We consider an FFU with a controllable reaction wheel perpendicular to the spin axis, and describe its dynamics, formulating a simple control law.

2.1. Analytical model for rotation of an FFU with a reaction wheel

We consider an FFU with an axisymmetric moment of inertia. A reaction wheel with an axisymmetric moment of inertia is part of the FFU, mounted with its spin axis perpendicular to the spin axis of the FFU (see Figure 2).

If gravity torques and drag forces are neglected, no external torques are assumed to act on the FFU, then the total angular momentum is conserved. Represented in FFU body frame, the Euler's equations [12] are

$$\dot{\vec{L}} + \vec{\omega_{\mathrm{FFU}}} \times \vec{L} = 0, \tag{1}$$

where $\vec{\omega_{\mathrm{FFU}}}$ is the angular velocity of the FFU and $\vec{L}$ is the angular momentum of the FFU, given by

$$\vec{L} = I^{\mathrm{TOTAL}} \cdot \vec{\omega}_{\mathrm{FFU}} + I^{\mathrm{RW}} \cdot \vec{\omega}_{\mathrm{RW}} \tag{2}$$

Here, I^{TOTAL} is the moment of inertia of the whole FFU, including the reaction wheel:

$$I^{\mathrm{TOTAL}} = \begin{bmatrix} A & 0 & 0 \\ 0 & A & 0 \\ 0 & 0 & C \end{bmatrix} \tag{3}$$

and I^{RW} is the moment of inertia of the reaction wheel in its principal principal axes (parallel to the FFU parallel axes by assumption):

$$I^{\mathrm{RW}} = \begin{bmatrix} \alpha & 0 & 0 \\ 0 & \beta & 0 \\ 0 & 0 & \alpha \end{bmatrix} \tag{4}$$

The second term in equation 2 describes the contribution of the rotation of the reaction wheel with respect to the FFU to the total angular momentum (the contribution of the reaction wheel rigidly rotating with the FFU is included in the first term). While the angular velocity of the FFU can have arbitrary orientation, $\vec{\omega}_{\mathrm{FFU}} = (\omega_{\mathrm{x}}, \omega_{\mathrm{y}}, \omega_{\mathrm{z}})$, the reaction wheel is constrained to rotate about its axis fixed in the FFU frame, and $\vec{\omega}_{\mathrm{RW}} = (0, \omega_{\mathrm{s}}, 0)$.

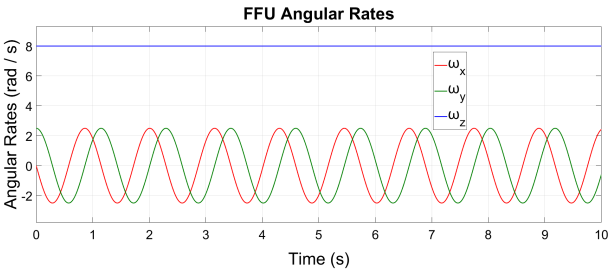

Figure 3. Numerical simulation of torque-free precession of a thin disk.

Substituting equation 2 into equation 1 yields

$$I^{\mathrm{TOTAL}} \cdot \dot{\vec{\omega}}_{\mathrm{FFU}} + I^{\mathrm{RW}} \dot{\vec{\omega}}_{\mathrm{RW}} + \vec{\omega}_{\mathrm{FFU}} \times (I^{\mathrm{TOTAL}} \cdot \vec{\omega}_{\mathrm{FFU}} + I^{\mathrm{RW}} \cdot \vec{\omega}_{\mathrm{RW}}) = 0 \tag{5}$$

Using equations 3 and 4 this can be written in components:

$$\begin{bmatrix} A\dot{\omega}_{\mathrm{x}} \\ A\dot{\omega}_{\mathrm{y}} \\ C\dot{\omega}_{\mathrm{z}} \end{bmatrix} + \begin{bmatrix} 0 \\ \beta\dot{\omega}_{\mathrm{s}} \\ 0 \end{bmatrix} + \begin{bmatrix} (C-A)\omega_{\mathrm{y}}\omega_{\mathrm{z}} \\ (A-C)\omega_{\mathrm{x}}\omega_{\mathrm{z}} \\ 0 \end{bmatrix} + \begin{bmatrix} -\beta\omega_{\mathrm{z}}\omega_{\mathrm{s}} \\ 0 \\ \beta\omega_{\mathrm{x}}\omega_{\mathrm{s}} \end{bmatrix} = 0 \tag{6}$$

This can be re-arranged as

$$\dot{\omega}_{\mathrm{x}} - \frac{(A-C)}{A}\omega_{\mathrm{y}}\omega_{\mathrm{z}} = \frac{\beta}{A}\omega_{\mathrm{z}}\omega_{\mathrm{s}} \tag{7a}$$

$$\dot{\omega}_{\mathrm{y}} - \frac{(C-A)}{A}\omega_{\mathrm{x}}\omega_{\mathrm{z}} = -\frac{\beta}{A}\dot{\omega}_{\mathrm{s}} \tag{7b}$$

$$\dot{\omega}_{\mathrm{z}} = -\frac{\beta}{C}\omega_{\mathrm{x}}\omega_{\mathrm{s}} \tag{7c}$$

This set of three non-linear coupled differential equations describes the time evolution of the angular velocity of the FFU, if the angular velocity of the reaction wheel $\omega_{\mathrm{s}}(t)$ is known. If the reaction wheel is disabled, equation 7 reduces to the known torque-free motion of a spinning top with constant ω_z. The perpendicular component of the angular rate rotates about the FFU z axis:

$$\omega_{\mathrm{x}}(t) = |\omega_{\mathrm{FFU}}^{perp}| cos(\lambda t + \phi_0) \tag{8a}$$

$$\omega_{\mathrm{y}}(t) = |\omega_{\mathrm{FFU}}^{perp}| sin(\lambda t + \phi_0) \tag{8b}$$

$$\omega_{\mathrm{z}}(t) = \Omega = const \tag{8c}$$

where ϕ_0 is the initial phase. The angular velocity λ is

$$\lambda = \left(\tfrac{C-A}{A}\right)\Omega. \tag{9}$$

For an oblate body with $C > A$, as is the case for disk-shaped FFUs, the lateral rate vector rotates in the same sense as the spin.

If the reaction wheel rotates, it will affect the dynamics of the whole FFU through the terms on the right hand side of equation 7, which contribute to the component of angular acceleration $\vec{\alpha} = \dot{\vec{\omega}}$ of the FFU:

$$\alpha_{\mathrm{RW}} = \begin{bmatrix} \frac{\beta}{A}\omega_{\mathrm{z}}\omega_{\mathrm{s}} \\ -\frac{\beta}{A}\dot{\omega}_{\mathrm{s}} \\ -\frac{\beta}{C}\omega_{\mathrm{x}}\omega_{\mathrm{s}} \end{bmatrix} \tag{10}$$

The y component of α_{RW} is related to spin acceleration of the reaction wheel, while the other two components are related to torque needed to rotate the spinning reaction wheel with the FFU. To reduce the lateral rates, α must be directed opposite to $\vec{\omega_\perp} = (\omega_x, \omega_y)$. While this is not possible to achieve precisely in general case, based on the free motion of the FFU, the control law is proposed as

$$\omega_s(t) = -S\,\cos\phi, \tag{11}$$

where S is the maximum and $\phi = \tan^{-1}(\omega_y/\omega_x)$ is the phase of the lateral rate vector. As the FFU is dewobbled, its spin rate will increase slightly, so the phase should be updated based on observed angular rate components in the body frame.

2.2. Numerical simulation

The model defined by equations 7 was built up in Matlab/Simulink interface, which is used in modeling of dynamical systems and control problems. The input of the model is the velocity profile of the motor and the outputs are the angular rates of the FFU. The parameters of the FFU and the reaction wheel enter the model as the coefficients (gains).

The result of a simulation of force-free precession of a thin disk with $C = 2A$, and an initial condition of $\vec{\omega} = (0, 2.5, 8)$ rad/s is shown in Figure 3. The precession of the FFU is reproduced, with ω_z being constant, and $\vec{\omega_\perp}$ rotating in the xy plane in the positive sense, as the analytical model shows.

To evaluate the effectiveness of the proposed control law, a SIMULINK model was created. The inertia of the cylindrical FFU is estimated as $A = 0.0128$ kg m^2 and $C = 0.0216$ kg m^2, assuming a mass of 3 kg, radius of 0.12 m and height of 0.09 m. The effectiveness of actuation is linear with the ratio of the reaction wheel moment of inertia about its axis, β, to the FFU moment of inertia about its spin axis A. For a representative reaction wheel the ratio β/A was assumed at $1.8{\cdot}10^{-3}$. The maximum spin rate of the reaction wheel was set to 300 RPM.

Figure 4 shows the response of the FFU to the applied control. The lateral rates are reduced during the actuation, while the spin rate of the FFU is slightly increased, due to angular momentum conservation.

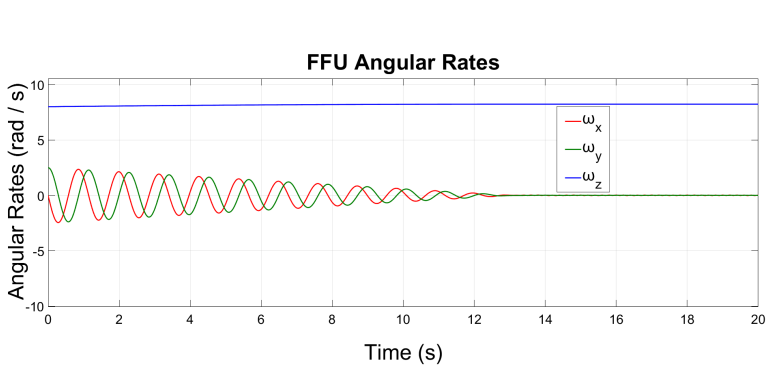

Figure 4. Left: time history of the FFU angular rates with dewobbling control. Right: hodogram of $\omega_\perp$ during RW operation.

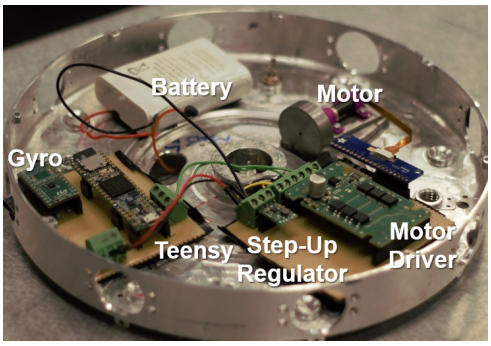

Figure 5. Prototype implementation.

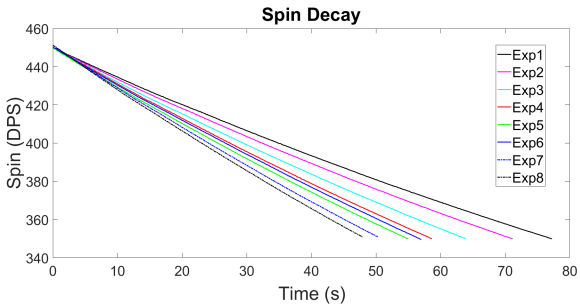

Figure 6. Decay of the prototype spin rate in eight consecutive tests.

3. PROTOTYPE TEST

Evaluating the dewobbling system requires supporting the FFU prototype in a way allowing free rotation in all three axes with low friction. This is achievable with a gimbal, a spherical air bearing, or a single string suspension near the centre of mass. Suspension based systems provide a simple way of removing the gravity effects (e.g. [13]). A prototype, see Figure 5, was suspended on a 1.85 m long string (Savage-Gear Silencer SPE 8-Braid fishing line of 0.09 mm thickness, with 4.7 kg rating). The hull of a BDU (heritage from SPIDER) was used to mount the prototype components, and the setup was balanced using placticine weights. The mass of the prototype was 0.355 kg, of which 0.047 kg is the reaction wheel. The moment of inertia A was $13{\cdot}10^{-4}$ kg m^2, and the wheel moment of inertia β was $5{\cdot}10^{-6}$ kg m^2. A Faulhaber 0824006B brushless DC motor with integrated spur 21.9:1 gearhead was used for actuation, operated by a dedicated Faulhaber SC2402P motor driver. The control algorithm is performed by a PJRC Teensy3.6 microcontroller board, based on measurements of a STM L3GD20H angular rate sensor. All electronics were powered by a SAFT MP144350 3.75 V Li-ion battery, boosted to 5 V by a POLOLU U1V11F5 regulator board. Angular rate readings were stored in a SANDISK 8GB microSD card.

External torques in the string suspension test originate from gravity, aerodynamic drag and string torsional stiffness. To reduce gravity torque, the prototype was suspended at its centre of mass. The air drag damps the spin of the prototype, and winding of the fishing line produces return torque.

The prototype was spun up by a spin table with adjustable height. By ramping up the spin rate to the desired value, and lowering the spin table, the suspended prototype was left in a state close to flat spin. To evaluate the effects of the air drag and filament twisting, a number of flat spin decay sequences were recorded consequently, starting with the same initial spin rate (with no actuation). Overlaid spin rate decay time histories are shown in Figure 6, with the first one starting with untwisted fishing line. The spin rate decays faster as the twisting of the string increases, yet the decay is dominated by the air drag. The total twisting of the string of over 100 turns between the first and the last amounts to a decay rate somewhat smaller than the air drag. This results in highly reproducible experiments, dominated by the air drag.

To demonstrate dewobbling of the prototype, lateral rates were induced by the reaction wheel. A short disturbance was introduced, followed by a period with the positive feedback control law, increasing the wobbling amplitude. Two scenarios were run at this point: disabling the reaction wheel or operating with the negative feedback con-

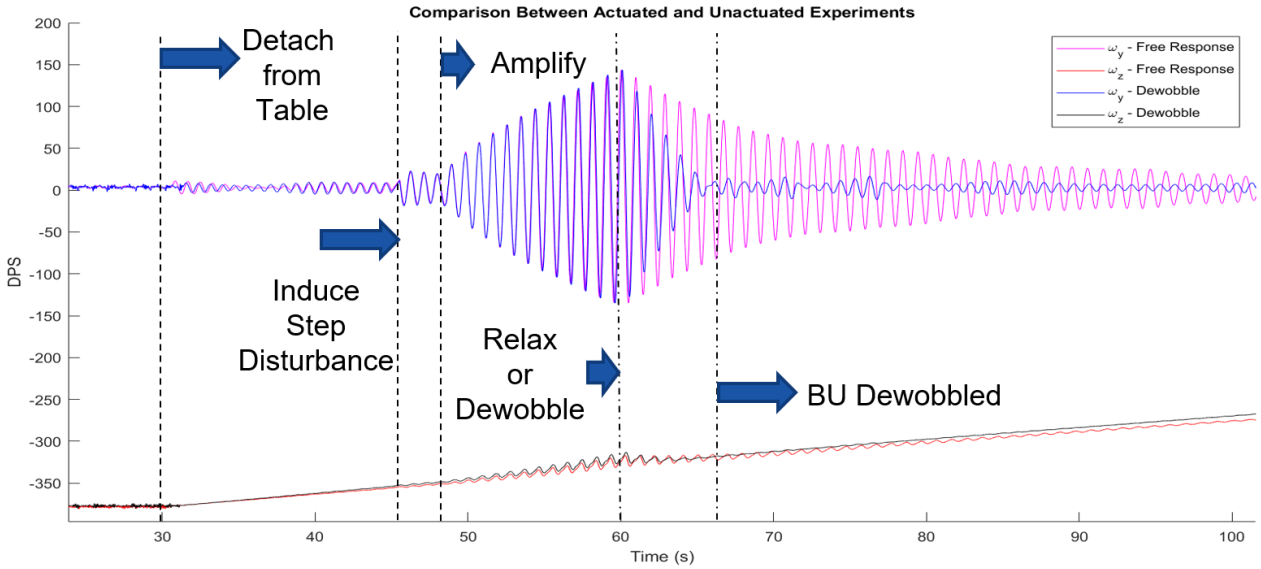

Figure 7. Time history of natural damping and active dewobbling tests.

trol. The former scenario includes air drag damping of the prototype rotation, while the latter scenario demonstrates the effect of the actuation. Figure 7 presents a comparison between the runs, with the main experimental steps annotated. Until 60 s the two time histories overlay, indicating high repeatability of the test. With actuation, the lateral rates are reduced after 6 s, while with the damping of the unactuated system is considerably slower, taking over 40 s to achieve the same amplitude.

4. EXPERIMENT OVERVIEW

The primary objective of the WOLF experiment is to demonstrate a wobbling control system based on the concepts above. The layout of the experiment largely follows the solution from the REXUS experiments, starting with the ISAAC experiment [8], and the SPIDER experiment, here we focus on the major changes compared to those.

4.1. Experiment concept and timeline

The experiment hardware consists of one Rocket Mounted Unit (RMU) and two Free Falling Units (FFUs), see Figure 8. A spring-based ejection system in the RMU keeps the FFUs constrained inside the FMU, and releases them at 65 km altitude. The dewobbling system is activated immediately after ejection, followed by the deployment of the wire booms. The FFUs deploy a parachute at 5 km altitude, and land for subsequent recovery. Each FFU consists of three modules: the bottom unit (BU), the Boom Deployment Unit (BDU), and the Common Unit (CU). The BU contains the dewobbling system and the electronics for deployment of the wire booms and for measurement of the electric probes. The BDU contains the wire boom deployment system, probes and miniature cameras for recording the process of the boom deployment. The CU records the general flight data including raw GPS data, accelerations, angular rates, and atmospheric pressure. Each of the units has a diameter of 240 mm and a height of 30 mm, the total height of the FFU being 94 mm.

4.2. Dewobbling system

The system to suppress FFU wobbling closely follows the prototype setup described in Section 3. The wheel itself is supported by a steel shaft, mounted in both ends in ball bearings press-fitted in the support structure. The motor is attached to the structure by means of a cap and screws, and is connected to the reaction wheel by a coupler. The mass of the reaction wheel is 94 g and its moment of inertia is $9{\cdot}10^{-6}$ kg m^2. To achieve higher speeds of the reaction wheel, a gearbox with smaller transmission ratio of 9.4:1 will be used.

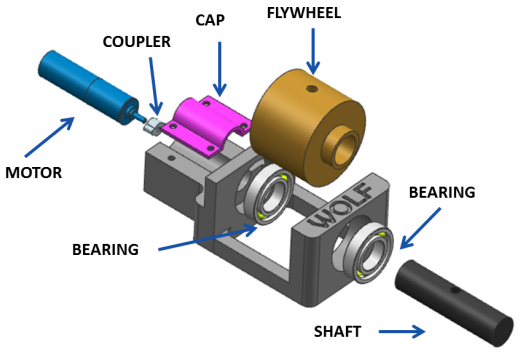

Figure 9. Reaction wheel assembly exploded view.

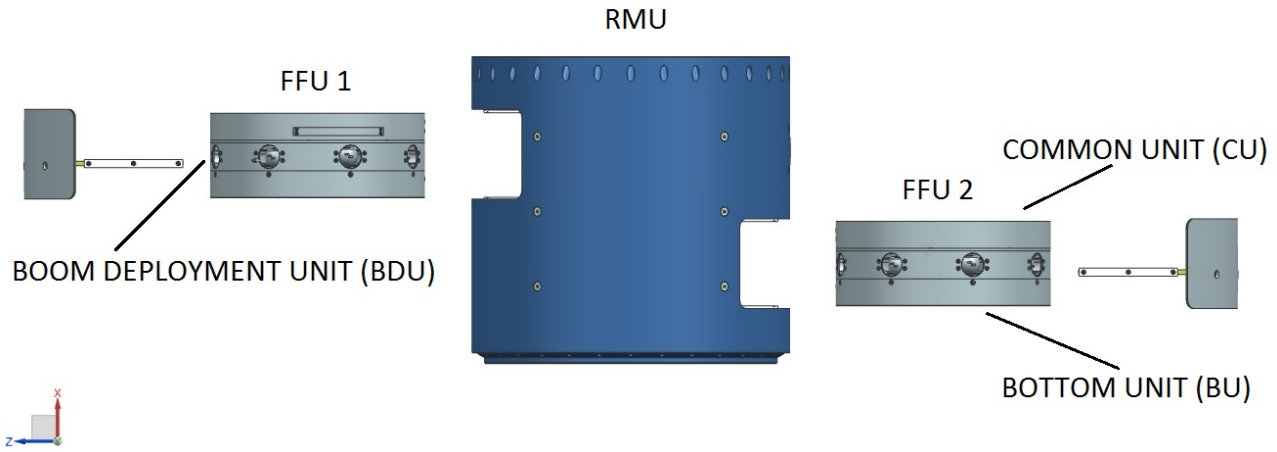

Figure 8. FFUs ejected from RMU.

4.3. Wire booms and probes

The wire boom deployment system is heritage from the SPIDER experiment, with spherical probes of 25 mm diameter at the tips of thin wire booms. SPIDER experiment used four electrical probes (operated in high impedance mode, measuring the voltage of the probes at a preset value of bias current) on 2 m long wire booms and four Langmuir probes (operated in low impedance mode, measuring current to the probe biased at a adjustable potential with respect to the body of the FFU) on 1 m long wire. In WOLF only the Langmuir probes will be used, and the locations of the four electrical probes will be used for miniature cameras to record footage of the boom deployment.

In the stowed configuration, the wire booms are wound on a common spool that connects to the BU electronics through a flat cable and the probes are constrained by a disk, holding them down to the bottom of the BDU structure. The disk prevents rotation of the spool by pins engaging in the spool holes. The disk is spring-loaded and constrained by a polymer filament, which is cut by a thermal cutter initiating the boom deployment. The rotation of the spool is controlled by a dedicated piezoelectric motor and optical system for monitoring the spool rotation angle.

While the relatively low altitude of the REXUS flights combined with launch not related to any specific geophysical conditions limit scientific value of the data to be collected on the Langmuir probes, they could be used for a measurement technology experiment. As REXUS rockets are flown during day-time, the probes onboard WOLF FFUs could be utilized to record the photoelectron current induced by solar UV radiation and its dependence on altitude and probe surface material. Estimating the photoelectron current is important in case of particle detectors, e.g. the Meteror Smoke Particle Detector, for which a model of the photocurrent as a function of altitude and material coating was developed [14]. WOLF spherical probes will have surface of several materials (gold, graphite, nickel, etc.) and will provide useful measurements to test this model of photoelectron current. Probes will be operated in voltage swept mode (measuring the probe current at varied voltage) using the hardware and firmware inherited from the SPIDER experiment.

4.4. Localisation and recovery system

While the recovery system has been reliable in the experiments with smaller FFUs [6, 7], it has not performed equally well on experiments with larger FFUs and SPIDER. An analysis of the recovered units revealed mechanical damage to CU electronics, possibly during parachute deployment. The WOLF CU is modified to make it more robust. The electronics in the WOLF design are mechanically separated from the parachute by a flat lid (see Figure 10). The rim of the CU structure extends as a cylindrical wall, to which the lid attaches. The parachute is placed between the lid and the ejectable cover, held onto the CU with a polymer filament. The filament is cut by a thermal cutter, releasing the spring-loaded cover and exposing the parachute to the air flow.

While the FFUs store all measurement data onboard, and thus do not rely on continuous radiolink to the ground, RF systems are used for localisation of the FFU. The FFUs store raw L1 GPS data for post-flight trajectory reconstruction (see [15]). During the parachute descent phase, a commercial GPS module provides the position of the FFU, which is transmitted during a VHF link and sent to Globalstar satellite network. Most KTH REXUS experiments used separate off-the-shelf antennas for the GPS and Globalstar, but in MUSCAT experiment a custom designed combined GPS/Globalstar antenna was successfully implemented [7].

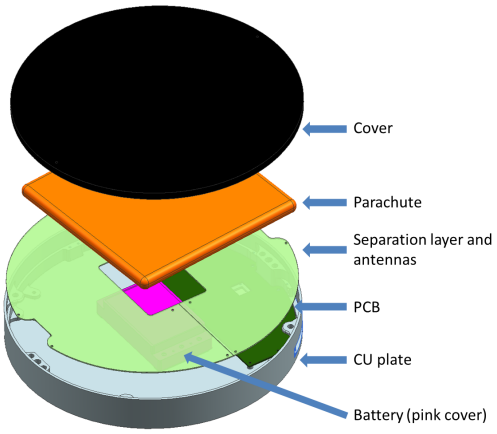

Figure 10. CU overview.

.

In WOLF experiment, we extend the raw GPS data logging to the new L5 data signal to improve post flight trajectory reconstruction. Thus, the CU utilizes three radio frequencies, Globalstar (1615 MHz), GPS L1 (1575.42 MHz) and GPS L5 (1176.45 MHz). As the range of commercially available small L1 antennas is yet very limited, and the antennas must comply with the space limitation of the CU, it was decided to pursue a custom antenna solution for WOLF.

The antennas reside within the same volume of the CU as the parachute. Any protruding part of an antenna may cause the parachute to catch onto it and endanger the experiment. For this reason, patch antennas were chosen due to their flat design and easy integration on the lid that separates the parachute from the electrical components underneath.

Three single fed patch antennas are laid out on the lid, Figure 11. Circular polarization is achieved by truncating two opposite corners of each patch. Feeding to the patch is done using probes through the substrate, which is 1.6 mm thick FR-4. CST Microwave Studio was used to model and simulate the antennas. The simulated results for the L1 patch are shown in Figure 12, the other patches show similar behavior.

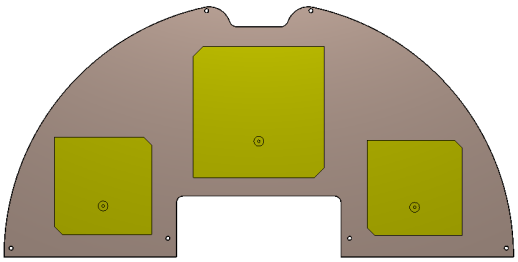

Figure 11. Top view of the patch antennas on the CU lid separating the electronics from the parachute.

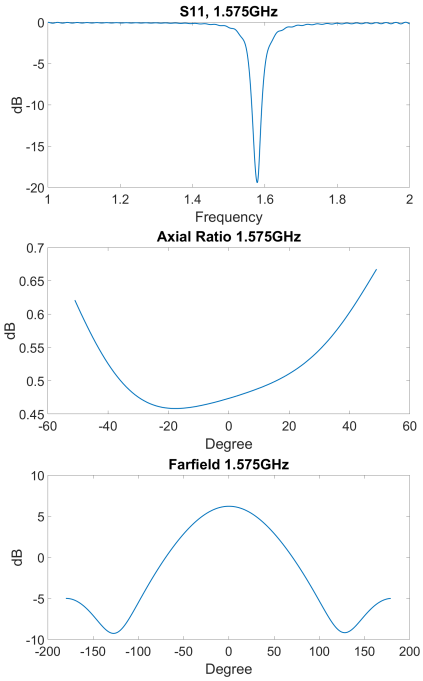

Figure 12. Modelled performance of the L1 antenna, top to bottom: S11, axial ratio and direction diagram.

4.5. Ejection effect on the rocket dynamics

One of the secondary objectives of the WOLF experiment is to characterize the effect of the FFU ejection on the dynamics of the main rocket. The ejection of the FFUs is initiated simultaneously and they are ejected in opposite directions. The difference in position along the rocket axis will however generate a lever arm that will impart a tip-off angular momentum onto the rocket. To evaluate the amount of the tip off and to provide a reference dataset for the ejection process of the FFUs of this class, WOLF will record high resolution attitude data. We use STIM300 inertial measurement unit, measuring angular velocity vector at 2000 samples per second, and SMILE magnetometer [16] measuring vector magnetic field at 250 samples per second.

5. SUMMARY

The demonstration of a wobbling suppression system would help to improve the performace of future experiments with spinning FFUs, in particular those involving the electric double probes. Such a system can be implemented with a single reaction wheel mounted perpendicular to the FFU spin axis. Here we exhibited the effectiveness of the system by numerical simulation and a prototype test and WOLF experiment will provide a real flight demonstration of the system. It will also provide data to monitor the disturbance on the main rocket introduced by the ejection of the FFUs and it will validate several improvements to the CU design.

ACKNOWLEDGMENTS

The REXUS/BEXUS programme is realised under a bilateral Agency Agreement between the German Aerospace Center (DLR) and the Swedish National Space Board (SNSB), through a collaboration with the European Space Agency. EVK participation in the 23rd ESA Pac symposium was supported by SNSB. GG was partially supported by the Swedish Government Agency for Innovation Systems (VINNOVA) contract no. 2016-04094.

REFERENCES

[1] D Pietrowski, KA Lynch, RB Torbert, G Marklund, N Ivchenko, A Ranta, M Danielides, and MC Kelley. Multipoint measurements of large DC electric fields and shears in the auroral zone. *Geophysical Research Letters*, 26(22):3369–3372, NOV 15 1999.

[2] M. R. Mella, K. A. Lynch, D. L. Hampton, H. Dahlgren, P. M. Kintner, M. Lessard, D. Lummerzheim, E. T. Lundberg, M. J. Nicolls, and H. C. Stenbaek-Nielsen. Sounding rocket study of two sequential auroral poleward boundary intensifications. *Journal of Geophysical Research (Space Physics)*, 116:A00K18, December 2011.

[3] E. T. Lundberg, P. M. Kintner, K. A. Lynch, and M. R. Mella. Multi-payload measurement of transverse velocity shears in the topside ionosphere. *Geophysical Research Letters*, 39:L01107, January 2012.

[4] N. Ivchenko and G. Tibert. Sounding rocket experiments with ejectable payloads at KTH. In *21st ESA Symposium: European Rocket and Balloon Programmes and Related Research, 913 June 2013, Thun, Switzerland*, ESA Special Publications, pages 503–510, 2013.

[5] M. Alaniz, S. Belyayev, D. Bergman, G. Casselbrant, M. Honeth, J. Huang, N. Ivchenko, M. Laukkanen, J. Michelsen, V. Pronenko, M. Paulson, G. Schlick, G. Tibert, and M. Valle. The SQUID Sounding Rocket Experiment. In Ouwehand, L, editor, *20th ESA Symposium on European Rocket and Balloon Programmes and Related Research*, volume 700 of *ESA Special Publications*, pages 159–166, 2011. 20th ESA Symposium on European Rocket and Balloon Programmes and Related Research, Hyere, FRANCE, MAY 22-26, 2011.

[6] W. Reid, P. Achtert, N. Ivchenko, P. Magnusson, T. Kuremyr, V. Shepenkov, and G. Tibert. Technical Note: A novel rocket-based in situ collection technique for mesospheric and stratospheric aerosol particles. *Atmospheric Measurement Techniques*, 6:777–785, March 2013.

[7] M. T. Bordogna, L. Fidjeland, M. Fjällid, M. Galrinho, A. Haponen, A. Hou, N. Ivchenko, D. Kristmundsson, O. L. Lárusdóttir, M. Lejon, M. Lindh, E. Lozano, P. Magnusson, A. Myleus, B. Oakes, and Tibert. G. MUSCAT Experiment: Active Free Falling Units for in Situ Measurements of Temperature and Density in the Middle Atmosphere. In *Proceedings of the 21st ESA Symposium on European Rocket and Balloon Programmes and Related Research*, volume 250 of *ESA Special Publications*, pages 575–582, 2013.

[8] G. Balmer, A. Berquand, E. Company-Vallet, V. Granberg, V. Grigore, N. Ivchenko, R. Kevorkov, E. Lundkvist, G. Olentsenko, J. Pacheco-Labrador, G. Tibert, and Y. Yuan. ISAAC: A REXUS Student Experiment to Demonstrate an Ejection System with Predefined Direction. In L. Ouwehand, editor, *22nd ESA Symposium on European Rocket and Balloon Programmes and Related Research*, volume 730 of *ESA Special Publication*, page 235, September 2015.

[9] R. Bergstrom, M. Crimella, N. Ivchenko, A. Karlsson, H. Lindberg, L. Persson, N. Schlatter, G. Tibert, and S. Westerlund. Scattering of Radar Waves on Areosols in Plasmas. In L. Ouwehand, editor, *22nd ESA Symposium on European Rocket and Balloon Programmes and Related Research*, volume 730 of *ESA Special Publication*, page 87, September 2015.

[10] U. Fahleson. Theory of Electric Field Measurements conducted in the Magnetosphere with Electric Probes. *Space Science Reviews*, 7:238–262, October 1967.

[11] Y. Zheng, K. A. Lynch, M. Boehm, R. Goldstein, H. Javadi, P. Schuck, R. L. Arnoldy, and P. M. Kintner. Multipoint measurements of field-aligned current density in the auroral zone. *Journal of Geophysical Research (Space Physics)*, 108:1217, May 2003.

[12] H. Curtis. *Orbital Mechanics for Engineering Students*. Elsevier, 2010.

[13] H. Mao, P. L. Ganga, M. Ghiozzi, N. Ivchenko, and G. Tibert. Deployment of Bistable Self-Deployable Tape Spring Booms Using a Gravity Offloading System. *Journal of Aerospace Engineering*, 30(4), JUL 2017.

[14] G. Giono, B. Strelnikov, H. Asmus, T. Staszak, N. Ivchenko, and F.-J. Lübken. Detailed Photocurrent Characterization for Meteror Smoke Particle Detectors onboard the PMWE sounding rocket. In *Publication Proceedings of the 23th Symposium on European Rocket and Balloon Programmes and Related Research*, Visby, Sweden, 11-15 June 2017.

[15] Y. Yuan, E. Linden, and N. Ivchenko. Post-flight trajectory reconstruction of suborbital free-flyers using GPS raw data. *Journal of Geodetic Science*, 7:94–104, 2017.

[16] Å. Forslund, S. Belyayev, N. Ivchenko, G. Olsson, T. Edberg, and A. Marusenkov. Miniaturized digital fluxgate magnetometer for small spacecraft applications. *Measurement Science and Technology*, 19(1):015202, January 2008.

RaCoS - A COLD GAS RATE CONTROL SYSTEM ON BOARD OF REXUS 22

Florian Wolz, Marion Engert, Dennis Kaiser, Tobias Wahl, and Tobias Zaenker

Team RaCoS
Chair of Computer Science VIII – Julius Maximilian University of Würzburg c/o Prof. Dr.-Ing. Sergio Montenegro
Josef-Martin-Weg 52, Raum 2.011, D-97074 Würzburg, Germany
Email of corresponding author: Florian.Wolz@RaCoS-REXUS.de

ABSTRACT

RaCoS (Rate Control System) is a payload part of REXUS[1] 22 which was launched in March 2017 at Esrange Space Center. The experiment's purpose was to reduce and control the angular rate of the REXUS sounding rocket in the roll axis by using a cold gas system propelled by nitrogen. In order to achieve the experiment's objective, the angular rate of the roll axis is measured and used by the control algorithm, which calculates the opening times of the valves.
Unlike most existing systems, RaCoS is lightweight and was inexpensive to build. This was achieved by using commercial off-the-shelf components, which also includes industrial, but non-space grade solenoid valves, common pressure hoses, carburetor jets instead of laval nozzles and a paintball composite pressure tank. The complete system and the underlying theory for dimensioning and choosing the parts needed are described as well as the composition of the mechanics, electronics and pneumatics.

Key words: RaCoS, REXUS 22, RCS, rate control system, cold gas thruster, space propulsion, solenoid valve, nozzle, nitrogen.

1. INTRODUCTION

Most spin-stabilized sounding rockets take advantage of a yo-yo system which is deployed directly before motor separtion during the ascent phase of a ballistic flight. The yo-yo system consists a two masses attached to wires which are spirally coiled around the rockets longitudinal axis. Both masses have to be exactly calculated since they are related to each individual charasteristics of each rocket. The yo-yo system releases both masses and the attached wires will be uncoiled before the steel wires will be cut and the spin frequency induced to the spin-stabilized flight will be significantly reduced. In practice, the yo-yo system is not capable of reducing the spin rate in the roll axis to zero due to errors in the measurements and calculations of the yo-yo masses. A maximum residual rate of 30 $^\circ/s$ is possible (cf. Schüttauf et al. 2016, p. 27). Various residual rates of the roll axis can be found in figure 1 after yo-yo despin and motor seperation.

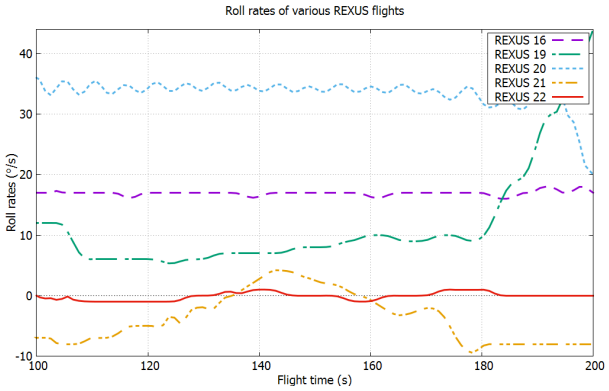

Figure 1: Residual roll rates of REXUS rockets after yo-yo despin & motor seperation from T+100 s to T+200 s.

Accordingly, for a better quality of weightlessness, a rate control system was developed and integrated in the payload of REXUS 22 to reduce the residual rate in the roll axis after the yo-yo despin and motor seperation.
RaCoS succesfully reduced the angular rate in the roll axis from 142 $^\circ/s$ to 1.5 $^\circ/s$ on the flight of REXUS 22, which was launched on March 16, 2017 13:00 UTC from Esrange Space Center in northern Sweden. The sounding rocket reached an altitude of 84 km.

2. SCIENTIFIC APPROACH

2.1. Computations

To dimension the system, computations regarding the nozzle diameter, the pressure at the nozzle inlets and the tank pressure were performed. The formulas were taken from Ley et al. (2011), Braeunig (2012), Nakka (2015) and Hall (2015).

[1] Rocket Experiments for University Students

2.1.1. Nozzle Design

To calculate the thrust of the system, the exit velocity of the nitrogen was needed. To calculate it, the local Mach number at nozzle exit had to be determined. This was done with Eq. 1.

$$N_m = \sqrt{\frac{2}{k-1} \cdot \left(\left(\frac{p_c}{p_a} \right)^{\frac{k-1}{k}} - 1 \right)} \tag{1}$$

k: Specific heat ratio (Nitrogen: 1.4)
R: Gas constant (8.3126 $J/(molK)$)
M: Molecular mass (Nitrogen: 0.028 kg/mol)
p_c: Pressure at nozzle inlet
p_a: Ambient pressure ($< 30\ Pa$)

The pressure at the nozzle inlet was set to 300 kPa for the first calculations. In flight configuration, a pressure of 500 kPa was used. For the given values, N_m is greater than 1. Due to the use of convergent nozzles, the Mach number is limited to 1, so in the following, $N_m = 1$.
The exit velocity was calculated from the Mach number with Eq. 2.

$$v_e = N_m \cdot \sqrt{k \cdot \frac{R}{M} \cdot T_t} \tag{2}$$

T_t is the temperature at the nozzle exit/throat and was calculated from the temperature at nozzle inlet with Eq. 3.

$$T_t = \frac{T_C}{1 + {N_m}^2 \cdot \frac{k-1}{2}} \tag{3}$$

As the inlet temperature was not exactly known, values for $T_{C1} = 260\ K$ and $T_{C2} = 320\ K$ were calculated. For T_{C1}, $T_{t1} = 202\ K$ and $v_{e1} = 285\ m/s$. For T_{C2}, $T_{t2} = 249\ K$ and $v_{e2} = 316\ m/s$.
The mass flow is defined by the smallest area of the nozzle and the corresponding pressure with Eq. 4

$$q = \frac{A_t \cdot p_t}{\sqrt{\frac{R \cdot T_t}{M \cdot k}}} \tag{4}$$

A_t: Nozzle exit/throat area
p_t: Nozzle exit/throat pressure

The nozzle diameter was set to 1 mm for the first calculations. As the theoretical thrust values could not be reached in tests, the flight was performed with 1.7 mm nozzles. The exit area A_t for a nozzle with an exit diameter of 1 mm is about $7.9 \cdot 10^{-7}\ m^2$; for a diameter of 1.7 mm, it is $2.3 \cdot 10^{-6}\ m^2$. The throat pressure p_t was calculated from the inlet pressure with Eq. 5.

$$p_t = p_c \cdot \left(1 + {N_m}^2 \cdot \frac{k-1}{2} \right)^{-\frac{k}{k-1}} \tag{5}$$

For an inlet pressure of 300 kPa, $p_t = 158.5\ kPa$. Therefore, the mass flow q at a nozzle diameter of 1 mm for temperature T_{t1} is $q_1 = 0.60\ g/s$. For T_{t2}, $q_2 = 0.54\ g/s$.
For an inlet pressure of 500 kPa, $p_t = 264.1\ kPa$. Therefore, the mass flow q at a nozzle diameter of 1.7 mm for temperature T_{t1} is $q_3 = 2.9\ g/s$. For T_{t2}, $q_4 = 2.6\ g/s$.
The force of the nozzles can then be calculated with Eq. 6.

$$F_N = q \cdot v_e + A_t \cdot (p_t - p_a) \tag{6}$$

For both q_1, v_{e1} and q_2, v_{e2}, $F_{N1} = 0.3\ N$. For q_3, v_{e1} and q_4, v_{e2}, $F_{N2} = 1.44\ N$.

With the force of the nozzles calculated, the influence on the angular rate in the roll axis can be determined. The radius of the rocket is $r = 0.178\ m$. With Eq. 7, the torque of the two nozzles can then be determined. The result is $M_1 = 0.107\ Nm$ for F_{N1} and $M_2 = 0.512\ Nm$ for F_{N2}.

$$M = 2 \cdot F_N \cdot r \tag{7}$$

The average moment of inertia of past REXUS rockets was 2.12 $kg \cdot m^2$. With these values, the angular acceleration can be computed with Eq. 8. For M_1, a_1 is 0.050 $\frac{rad}{s^2}$. For M_2, a_2 is 0.242 $\frac{rad}{s^2}$. The actual moment of inertia of the rocket during flight was $2.482\ kg \cdot m^2$, which would result in an accelaration of 0.043 and 0.207 $\frac{rad}{s^2}$ instead.

$$a = \frac{M}{J} \tag{8}$$

As the angular rate after the yo-yo de-spin was expected to not exceed 30 $^\circ/s$ (which is about 0.5 rad/s), the maximal de-spin time, calculated with Eq. 9, is equal to $t_1 = 10\ s$ for a_1 and $t_2 = 2\ s$ for a_2.

$$t = \frac{v}{a} \tag{9}$$

2.1.2. Tank Design

The total mass of the needed gas can be calculated as the product of the mass flow through the two nozzles and the corresponding opening time with Eq. 10. For both t_1 ans q_2 (1 mm nozzles at 300 kPa inlet pressure) and t_2 and q_4 (1.7 mm nozzles at 500 kPa inlet pressure), $m_{t1} = 0.0108\ kg$.

$$m_t = 2 \cdot t \cdot q \tag{10}$$

The total mass of the gas in the tank can be determined with Eq. 11.

$$m_{ta} = \frac{M \cdot V_{ta} \cdot p_{ta}}{R \cdot Z \cdot T_{ta}} \tag{11}$$

V_{ta}: Tank volume (0.7 l)
p_{ta}: Tank filling pressure
T_{ta}: Tank filling temperature
Z: Compressibility factor

For $p_{ta1} = 60\ bar$ at $T_{ta} = 300\ K$ ($Z_1 = 0.9977$), $m_{ta1} = 0.0473\ kg$. For $p_{ta2} = 100\ bar$ at $T_{ta} = 300\ K$ ($Z_2 = 1.0050$), $m_{ta2} = 0.0782\ kg$. For $p_{ta3} = 200\ bar$ at $T_{ta} = 300\ K$ ($Z_3 = 1.0571$), $m_{ta3} = 0.1487\ kg$.

As the tank was emptied by opening all valves, the maximum time to empty the tank was calculated with Eq. 12.

$$t_{te} = \frac{m_{ta}}{4 \cdot q} \tag{12}$$

For m_{ta1} and q_2 (60 bar tank pressure, 1mm nozzles), $t_{te1} = 22\ s$. For m_{ta2} and q_2 (100 bar tank pressure, 1mm nozzles), $t_{te2} = 36\ s$. For m_{ta3} and q_4 (200 bar tank pressure, 1.7 mm nozzles), $t_{te3} = 14\ s$.

The maximum up-spin is reached if two associated nozzles are permanently open. For this configuration, the maximum spin-up time can be calculated with Eq. 13.

$$t_{tm} = \frac{m_{ta}}{2 \cdot q} \tag{13}$$

With m_{ta1} and q_2, $t_{tm1} = 44\ s$. With m_{ta2} and q_2, $t_{tm2} = 72\ s$. With m_{ta3} and q_4, $t_{tm1} = 28\ s$.

The maximal obtainable up-spin can then be determined with Eq. 14.

$$v_{max} = t_{tm} \cdot a \tag{14}$$

For m_{ta1} and q_2, $v_{max1} = 127\ °/s$ ($0.35\ Hz$). For m_{ta2} and q_2, $v_{max2} = 208\ °/s$ ($0.58\ Hz$). For m_{ta3} and q_4, $v_{max3} = 394\ °/s$ ($1.10\ Hz$).

The pressure was set to 200 bar during flight to ensure sufficient nitrogen.

3. Experiment Setup

3.1. Mechanical Design

The process of designing the mechanical setup of the experiment was a more complicated one than expected. The module ring already had many bores since it had previously been used on the former REXUS experiment MOXA. During the designing phase, it was not possible to get the module ring. For the construction of the setup the CAD of the module ring was used. There were some limitations for the setup, which are summarized as follows:

- Two bores for the outlet of the nozzles had to be on a parallel of a tangent, the other two bores had to be placed parallel to those two
- Due to the launcher rail it is not allowed to place bores on and near the 180 ° line
- The valves had to be placed in an upright position to stay closed during the ascend phase of the rocket due to high acceleration forces
- The used module ring had a height of 170 mm deducting the upper and lower height limit of 30 mm, which should stay free of any components
- The new bores may not overlap the already existing bores
- The minimal bending radius of the pressure hoses had to be considered

A late access for refilling the pressure tank was needed. For this, the former late access hatch was used, which was already in the module ring hence it was used on REXUS 16. In the CAD model of the former used module, not all bores were depicted. The missing bores had to be transfered to the digital model by using photos which was not precise since some bores were not centered and drilled manually.
The views of the system are shown in figure 2 and 3.

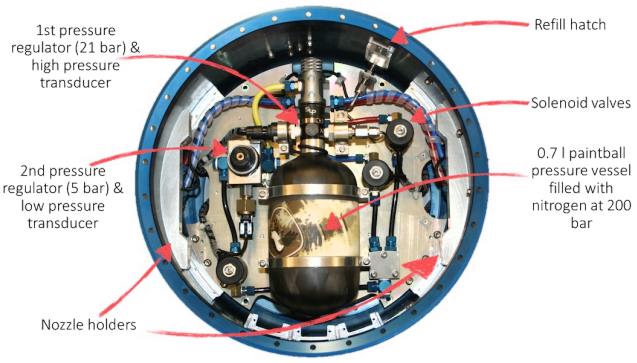

Figure 2: Top view of the setup

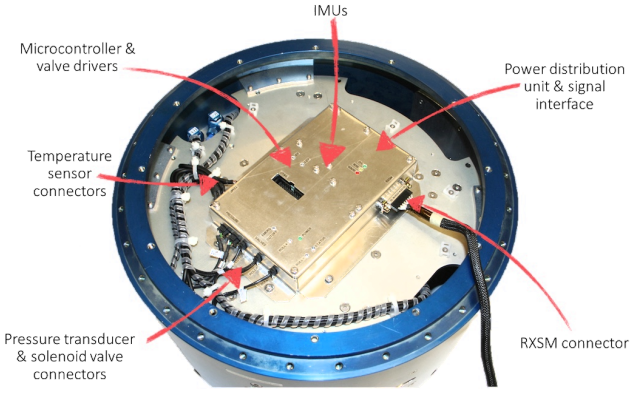

Figure 3: Bottom view of the setup

The most challenging part was to implement the pneumatic system into the module since the length of the hoses for the Roll+ and Roll- nozzels had to be the same. Otherwise the thrust in both direction wouldn't be equal or one nozzle would reach more thrust than the corresponding counterpart which would lead to an influence in other axes and not only in the roll axis. These constraints were implemented by integrating pneumatic splitters like T-piece adapters into support structures which were placed

in the center between both nozzle holders to split the gas-flow in half for each of the two connected nozzles.
Nevertheless this placement was not ideal for quick maintenance or replacing defective components.
The diameter of the composite pressure tank was 100 mm which dominated and defined the height of the module ring. The pneumatic components were placed in the upper part of the bulkhead due to the restricted alignment of the solenoid valves which have to be fixated in an upright position. The electronics were attached in an aluminium box which was placed on the bottom side of the bulkhead. Customized brackets for fixation of the bulkhead to the module ring were developed to gain more space and to use both sides of the bulkhead for mounting of the components.

3.2. Electrical Design

The electronics of the flight segment can be seperated in four main parts namely the *power distribution unit*, *data acquisition unit*, *communication interface* and the *valve drivers* (Figure 4).
The power distribution unit consists of two Traco DC/DC converters which are directly connected by ripple filters with the 28 V RXSM power lines. A TEL 5-2411 is used to provide 5 V for the communication interface, A/D converter, temperature sensors and the microcontroller. Followed by a low-dropout linear regulator LM1117-3.3 which supplies 3.3 V to support the microcontroller and the microSD mass storage device. The Traco TEN 30-2412 DC/DC converter supplies 12 V for the three valve drivers respectivly for the solenoid valves which are remotly controlled by the microcontroller. The temperature rise of the DC/DC converters, especially the Traco TEN 30-2412 when all active solenoid valves draw 21 W in the blow-down mode, lead to the decision of a mechanical surface enlargement which acts like a heatsink.
The main component is the data acquisition unit which is an ARM Cortex M4 32-bit RISC STM32F405RGT7 microcontroller. The microcontroller has a JTAG interface which is used for in-system programming. The microcontroller provides some in- and outputs for registrating the state and triggering each valve, the RXSM signal, triggering the 12 V DC/DC converter and to give optical feedback via LEDs. The SPI interface is used to communicate with two redundant InvenSense 9-DoF MPU-9250 ineratial measurement units as well as the microSD card. The I2C bus is handling the data communication for the 12-bit ADS1015 A/D converter to get the pressure readings of the tank and the pneumatic system. To maintain the temperatures inside the system, a GPIO pin is used to implement the 1-Wire protocol to hook up six digital DS18B20 temperature sensors. The temperature sensors are placed on both nozzle holders, in each valve and inside the heatsink of the power distribution unit. A serial interface was used to establish a communication link between the groundstation and the flight segment. An additional serial debug connection is used for debugging.
The communications interface is used to convert the serial TTL signal to RS-422 by using a MAX488 converter

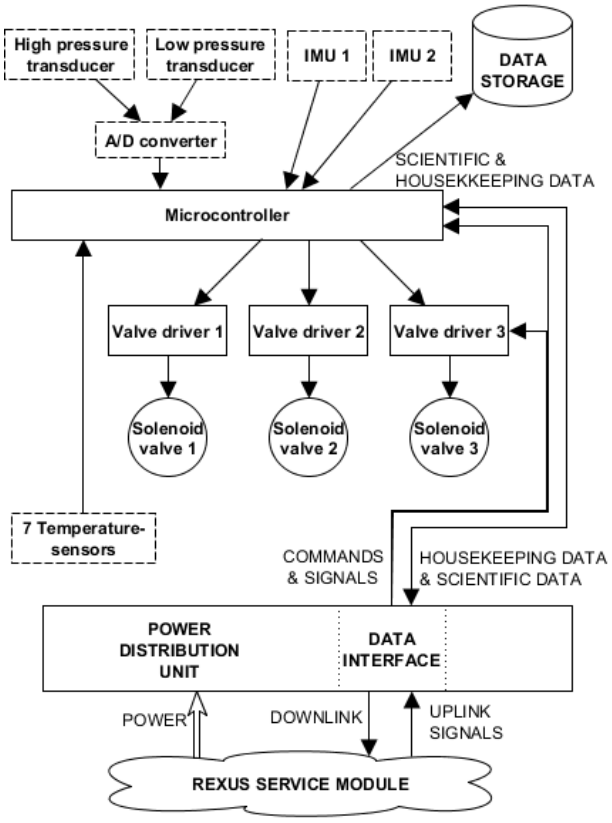

Figure 4: Electronic concept of RaCoS

chip, since a RS-422 up- and downlink capability is provided by the RXSM. The Lift-off signal, as well as the SOE and SODS signals are electrically isolated by using PC817 optocouplers. The SODS signal is responsible for activating the pneumatic operation of RaCoS and is directly connected with the microcontroller in series. Therefore an accidental operation is impossible since the emergency cutoff valve would not be opened and the gas flow is cut.
The valve drivers are triggered by PC817 optocouplers, followed by a field effect transistor IRF640 which energizes the solenoid valves, each with 12 V and 0.6 A. To eliminate the effects of a high inductive load and protect the components from reverse voltage spikes a bypass diode is used.
During the flight a total of around 1.2 Wh was used by RaCoS which can be splitted into the different modes of operation. In idle mode RaCoS needs about 0.3 W whereas during the main despin 14 W were needed. After that the average consumption was 1.12 W to T+201 s. In the blow-down mode the average consumption resulted in 20.2 W when all three solenoid valves, each one with 7 W, were opened.

4. SOFTWARE

4.1. On-board Software

The on-board-software consists of major parts, which are essential for the operation. These are the controller, the housekeeping, the health-watchdog, the inertial data fusion unit, the telemetry and telecommand-module and a storage controller.

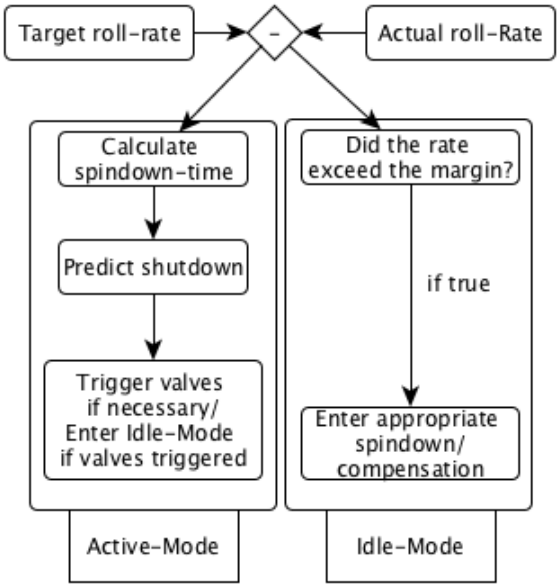

Figure 5: Control modes block diagram

The controller consists of the main controller and a shutdown prediction (Figure 5). The main controller is a 3-state-controller with an adaptive hysteresis, which is connected to the prediction-module. For a correct shutdown-prediction the predictor needs to be calibrated in advance, which is done by a $1\ s$ measurement-pulse at the beginning of the operation.
The predictor divides each thruster action into three parts. The first part is the startup, which means the buildup of thrust at the nozzles, resulting in an increasing thrust over time. The second part is the operation after startup, so the thrust and pressure at the nozzles is constant. The third part is the shutdown, which means the release of pressure after closing the valves, resulting in a remaining amount of thrust until the hoses and nozzles are empty. Additionally, there is a system delay which is also considered by the prediction.

The controller also needs reliable data of the spin rate, which is handled by the inertial data fusion unit, consisting of a simple sensor-read with a unit conversion and a sensor fusion. After reading the values of the two IMUs with a rate of $100\ Hz$, the sensor fusion calculates an average over the last five samples and calculates the sensor noise by comparing these values. This is an effective low-pass-filter and an addition to the low-pass already implemented on-chip on the IMU. These averages and noises are calculated per axis per IMU.
After this the sensor fusion calculates a weighted average of the two IMUs per axis with noise as weight-criteria. Because there is a possibility of both IMUs suffering from high noise, there is also a simulation of the IMU-values, supporting the IMUs. This simulation consists of a linear extrapolation because there is no oscillating behavior on the roll axis and linear influence of the experiment.

The calculated noise consists of an accumulation of the difference of the last five values to its direct neighbour and never exceeded $9.0867\ ^\circ/s$. The best measurements had a noise of $0.007629\ ^\circ/s$ which is a good performance for MEMS-IMUs. Also important for accurate measurements is a wide measurement-range with a high accuracy. This always results in a tradeoff between range and accuracy, but can be minimized by autoscaling. In this case the IMUs had a software-side autoscaling feature, which switches the measurement-range of the IMUs dependent on the actual roll-rate to minimize the occurrence of sensor saturation.
In theory, the sensor should switch its measurement range to the next higher range level at the cost of accuracy if it is near to the actual measurement limit. This prevents the sensor getting into saturation until the limit of the sensor is reached. In the actual flight software a software bug limited the switching feature to $500\ ^\circ/s$. This had no influence on the system performance or accuracy during operation, so the system was still fully functional.

To ensure everything works well, the housekeeping monitors temperature and pressure of the system components, the pressure regulator as well as the remaining tank pressure. This is necessary because the second pressure regulator needs a remaining pressure on the high-pressure side to work well, and this state needs to be maintained until blow-down-mode. This mode is part of the major operating modes during the full timeline to ensure a safe behavior.
After power-on the system stays in standby-mode, which only monitors the IMU- and housekeeping-data, downlinks and saves them. With recieving of LO the system sets the internal launch-time and remains in standby-mode. The system waits for SODS at T+71 s and shortly after SOE at T+72 s the system enters flight-mode.
At the beginning the controller calculates the prediction and after this the main operation starts by de-spinning the rocket. The main operation ends with $230\ s$ after LO. Then the system enters blow-down-mode which opens all valves to release pressure. This mode stays active until 2 bar remaining tank pressure and enters safe mode afterwards for power saving and to prevent overheating of the solenoid valves.
For testing purposes the system can enter a test-mode, which prevents the system to fully deplete the tank because of the second pressure regulator blocking after refill in case the tank is empty.

4.2. Groundstation Software

The ground station software was written in C++ with Qt as GUI (Figure 6). All telemetry data (temperatures, pressures, angular rate, acceleration, valve states) were displayed in a single window, so every system could be checked at once. Critical states were indicated by red colour, alarming states by yellow. The course of the roll rate of the rocket was displayed in a graph.
The menu bar has three submenus. The first one allowed to send commands to the flight segment during testing and before lift-off. The user is then asked to confirm the transmission of this command by retyping the command and confirm in an opening window. Alternatively, the dedicated command bar below the graph could be used to enter a command. If a command was sent successfully, it was indicated by the text field on the right of the command bar.
The second one allowed to connect and disconnect to and from the available serial ports on the groundstation computer.
The received data was stored on the ground station's hard drive for later analysis. It is possible to display old data by opening these files with the GS using the third submenu button. Opening old data files is not allowed while the GS is connected to a COM port.
At the bottom-left corner, the current mode of the GS-Software is displayed. Possible modes are "Disconnected", "Connected to <COM-name>" or "History Data: <FILENAME>".

Figure 6: Groundstation Software

5. Testing

To ensure the functionality of RaCoS a multitude of tests which accumulated to 28 different testing scenarios were planned. These had to be undergone before launch. Some examples are as follows (ascending complexity):

- component tests (sensors, electronics)
- software tests (different modes, bug fixing)
- subassembly tests (mechanical, pneumatics)
- full-fledged flight computer tests (timeline, countdown procedures)
- whole module in vacuum chamber and thermal chamber in accordance to the REXUS manual
- whole system tests (mainly pneumatic system)
- whole system despin tests, which presented a special kind of problem concerning the evaluation, as the system performs differently under atmosphere and therefore the observed system performance diverged from the calculated behaviour in vacuum

One noteworthy test was the vacuum test[2], referenced above as one of the system despin tests in which the whole system was placed inside a pressure chamber, the ZARM drop-tower, and tested to the vacuum conditions according to REXUS manual (cf. Schüttauf et al. 2016, p. 58) as well as to achievable system performance. The resulting vacuum reached down to a pressure of 60 Pascal and RaCoS ran through different spin-up and spin-down cycles, which resulted in satisfactory findings concerning the performance, illustrated by values of 4.5 s for up- and 2.5 s for downspin of respectively $30\ ^\circ/s$.
Another test was the air-bearing test[3] at DLR Oberpfaffenhofen, in which the system was mounted via special construction on the bearing with a counterweight at the other side, was spun up manually in one or more axis and had to perform normal system operation, respectively spin down from $30\ ^\circ/s$ to near to $0\ ^\circ/s$ whilst under influence from the other axis. This test also resulted in success as in all conditions the system was able to get as close to $0\ ^\circ/s$ as was possible with this major setup.

6. External Support

We were supported by the German Aerospace Center (DLR) and the Swedish National Space Board (SNSB) as well as the European Space Agency (ESA), the Swedish Space Corporation (SSC) and the Center of Applied Space Technology and Microgravity (ZARM) which provided amongst others general technical support.

As specialised testing equipment was not widely available, a great many companies were approached to support the cause and to help achieve better testing results (as well as financial support overall) – which in total sums up to approximately 140 companies that had been written to. Of course, not all of them accepted or replied to the plea, in detail $47\ \%$ have not answered. Afterall a noteworthy success rate of over $10\ \%$ was accomplished, which meant that tests could be performed more professionally, provide qualitative better measurements and in the end cumulated to a lot of well needed special equipment which not only helped the testing but also helped with building the system, expanding it and supplying the

[2] RaCoS Spinup test in vacuum and atmosphere: https://www.youtube.com/watch?v=Jb2PAsQshy0
[3] REXUS 22 RaCoS air-bearing test: https://www.youtube.com/watch?v=Yx1gSbgJPr8

team with extra funds to take more team members to the official testing appointments and milestones at the DLR in Oberpfaffenhofen or ZARM in Bremen.

7. Results and Discussion

During the flight, all experiment objectives could be reached. The rate in the roll axis was successfully detected, reduced and kept near to zero during operation (Figure 7).

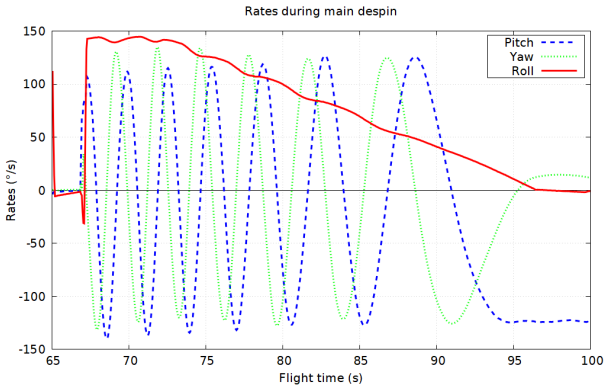

Figure 7: Rates during main despin

The recorded values for the angular rates show that after the YoYo-despin of the rocket at T-65 s, the remaining roll rate was about 5 $°/s$. At T-68 s, a problem at the motor separation caused the rocket to spin up to 144 $°/s$ in the roll axis, and up to 140 $°/s$ in pitch and yaw axis. At T-73 s, RaCoS changed to flight mode and started triggering its nozzles (Figure 8). Over a time of 24 s, the roll rate was reduced to below 1 $°/s$ with the first major pulse. A rate of 108 to 124 $°/s$ in the pitch axis and 29 to 61 $°/s$ in the yaw axis remained. During the remaining operation, RaCoS managed to keep the roll rate below 2 $°/s$ until T+210 s (Figure 9). Then, the re-entry of the rocket caused the rocket to spin up again due to strong atmospheric drag. The tank pressure dropped from 195 bar to 107 bar. The pressure difference equals a gas consumption of 75 g.

At T+230 s, the blow-down mode was entered and the remaining gas in the tank was emptied to 2 bar. The gas release during blow-down mode was from 85 bar at T+230 s to 8 bar at T+256 s, resulting in a pressure drop of 3 bar/s over 26 s. According to the computations, the pressure drop should have been about 14.5 bar/s. Thereafter, the release got slower and reached 2.5 bar at T+272 s. The blow-down mode was supposed to change to secure mode after the tank pressure had fallen below 2 bar for power saving purposes. However, the pressure did not fall below this border up until T+400 s. The pressure drop is shown in Figure 10.

The prediction for the despin-time of the on-board computer did not work correctly. During the test pulse, an

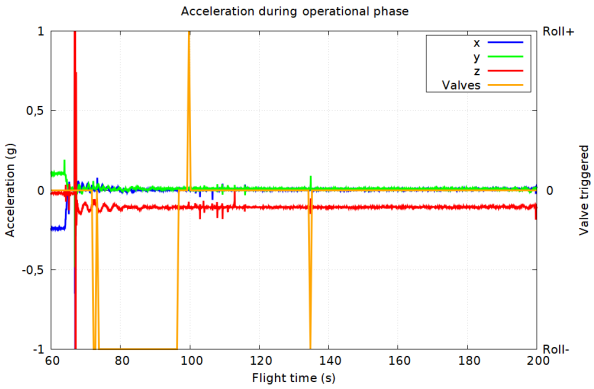

Figure 8: Acceleration during operational phase with nozzle triggers

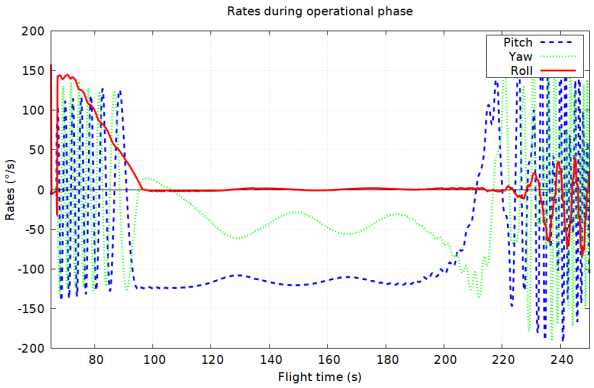

Figure 9: Rates during operational phase

influence of 2.8 $°/s^2$ was measured by the controller. The actual angular acceleration of the main pulse was 5.8 $°/s^2$. This deviation caused the controller to predict a despin time of 49 s instead of the correct 24 s. The reason for this discrepancy could be the fluctuation of the roll rate which can be observed in the plot of the roll rate (Figure 11). A constant update of the predicted influence during despin would have been necessary to achieve more accurate values.

The influence of the pulses differs from the computed theoretical values. With 5 bar pressure and 1.7 mm nozzles, the theoretical thrust of the system is 1.44 N per nozzle, resulting in a torque of 0.512 Nm and an angular acceleration of 11.8 $°/s^2$. The difference was already observed during testing.

After the flight a checkup of the system revealed a pressure leak in the sealing of the high pressure side of the second pressure regulator. The leakage was significant and was hearable since 21 bar were leaking. A significant leakage before or during flight was not detected and the refill procedure before launch in a late-access went well and did not notice any leakage. Investigation of this issue revealed that the second pressure regulator is under certain circumstances shock sensitive which could lead to leakage since the top cover gets loose and reveals the

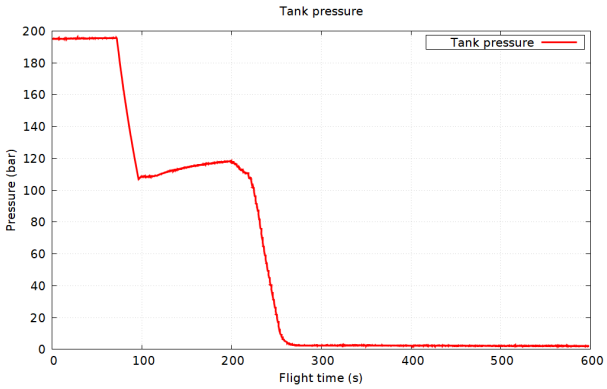

Figure 10: Tank pressure

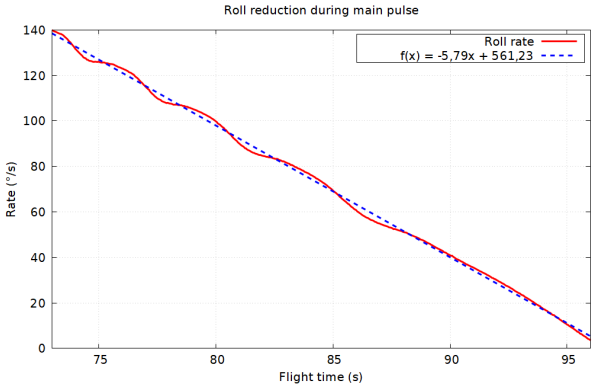

Figure 11: Roll rate reduction

sealant. The fact, that no leakage occured during flight lead to the assumption, that the leakage was induced during the landing phase when the payload hit the ground.

8. Further Work & Outlook

The experiment aimed to reduce the angular rate in the roll axis to gain experience in developing, building and commissioning a pneumatic and electronic system as well as basic knowledge in control engineering of a space related project. The gained scientific data showed that the system's performance could be improved due to the fact, that the achieved residual rate in the roll axis fluctuated between $\pm 1.5\ ^\circ/s$. A better resolution of the residual rate can be achieved by using faster solenoid valves and an overdrive during the operation. The nozzles and the pressure can be optimized since more time and equipment was needed to tune both components better. A possible reflight with a three axis cold gas rate control system could be implemented by adding four nozzles and solenoid valves to the existing system. The control algorithm has to be adapted and a direct activation of the solenoid valves by use of pulse-width modulation is conceivable. A second pressure regulator could be dropped by using industrial grade high pressure regulators which directly output the needed pressure for the nozzles. To fit into a $170\ mm$ module, all nozzles could be built with integrated manifold solenoid valves which will save costs and space. A central pressure supply tube around the bulkhead could supply each valve. RaCoS did not use a inlet filter because of a lack of space but may not be waived in a new system.

9. Conclusion

The malfunction of the launcher which accelerated the payload in the roll axis after the de-spin and motor seperation at T+71 s to 142 $^\circ/s$ was a worst-case scenario for RaCoS. Nevertheless the rate control system performed very well under this condition and decelerated the payload to $1.5\ ^\circ/s$. The reached residual rate in the roll axis was the lowestest compared to other REXUS flights and showed the potential of RaCoS (Figure 1). However, the residual rate can be improved and the system can be extended to a three axes rate control system which could even perform attitude control and improve and extend the milli-g phase during flight.

Acknowledgments

We want to thank Prof. Dr.-Ing. Sergio Montenegro from the Chair of Aerospace Information Technology at University of Würzburg for providing access to the chair's facilities, laboratories and resources. Furthermore we want to thank the German Aerospace Center (DLR) and the Swedish National Space Board (SNSB) for the participation in the REXUS/BEXUS programme which made this experiment possible and the European Space Agency (ESA), Center of Applied Space Technology and Microgravity (ZARM) as well as DLR Mobile Rocket Base (MoRaBa), Swedish Space Corporation (SSC) and Esrange for their outstanding and professional support.
Additionally we want to thank all other sponsors, supporters and partners from industry or public institutions who supported us in various ways to conduct this experiment in a professional way which wouldn't be possible without them.

References

Braeunig, R. A. 2012, Basics of Space Flight: Rocket Propulsion, http://www.braeunig.us/space/propuls.htm

Hall, N. 2015, Interactive Nozzle Simulator, https://www.grc.nasa.gov/www/k-12/airplane/ienzl.html

Ley, W., Wittmann, K., & Hallmann, W. 2011, Handbuch der Raumfahrttechnik, 4th edn. (München: Hanser)

Nakka, R. 2015, Nozzle Theory, http://www.nakka-rocketry.net/th_nozz.html

Schüttauf, K., Markgraf, M., Drescher, O., et al. 2016, REXUS User Manual v7.14, EuroLaunch

NEW TELECOMMAND SYSTEM AT ESRANGE SPACE CENTER

Håkan Eriksson

Swedish Space Corporation (SSC), Esrange Space Center P.O Box 802 SE-98128 Kiruna Sweden
Email: hakan.eriksson@sscspace.com

ABSTRACT

The new telecommand system at Esrange Space Centre was installed in autumn of 2016, and it replaces an old telecommand system that has been in use since 1988.
For sounding rocket microgravity operations, both Scientific and Range Safety commands are used.
The system can and must be able to handle the two cases simultaneously and independent of each other.
For FTS operation the system is designed to meet RCC 319-92 Standard, Flight Termination System Commonality Standard.
The new system is designed for fully redundancy and higher output power compared to the old system.

1. BACKGROUND

In 2014 the discussion started to invest in a new telecommand system, replacing an old system from 1998 which most of the hardware was obsolete.
The control and monitor computer was a PS2.
Communication between transmitter site and telemetry station was using dupline, (2 wire peer to peer communication).
The old system used 5 IRIG-tones for FTS commands.
Output power was limited to 250 Watts.
2016 decision was taken to invest is a system from WV communication INC, the first campaign with the new system was Maxus -9 in spring of 2017, both FTS and scientific operations was used with good results.

2. GENERAL DESCRIPTION

The new telecommand system is a dual system for both FTS operation and scientific commands.
The system is fully redundant and controlled via network and fibre optics.

For the FTS system 20 IRIG tones can be used, the system is also prepared for using 8 Hi Alpha secure tones.

The scientific baseband system is prepared for three (3) different locations at Esrange Space Center, launching area, scientific centre and balloon pad. At these locations a special patch panel is available for inserting the signals into the transmitter system.

Figure 1 Patch panel for scientific baseband signals

One scientific unit with two (2) exciters modules mounted in a mobile rack for easy transportation between locations.
The exciters can handle both digital and analogue baseband signals such as CPFSK, GMSK and Fm signals with or without ALC.

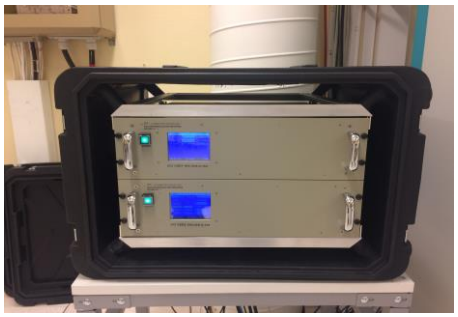

Figure 2 Scientific exciter unit

For operation of a mission, the mission is set up in the workstation located in telemetry station.
The system can be run as a single mission or with two missions linked together in one mission.

FTS operations are operated by the safety officer, ARM and Terminate of the vehicle.

For the scientific system ones the signals are confirmed and calibrated no operations are needed, telecommand operator is monitoring the signals during mission.

3. SYSTEM OVERVIEW

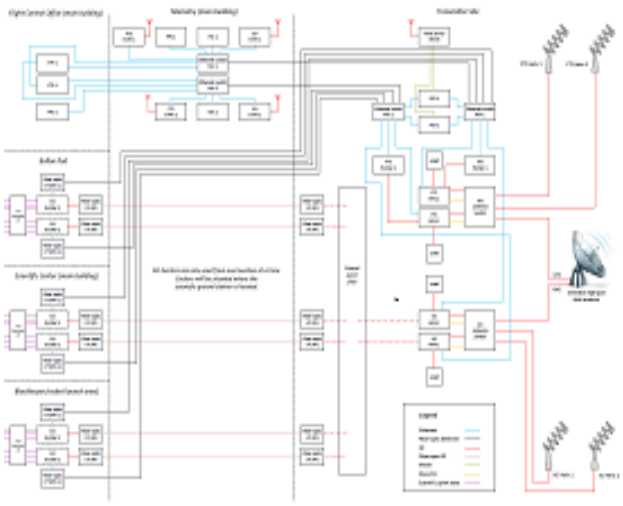

Figure 3 System Block Diagram

The system is located at Esrange Space Center at tree (3) different locations.

On the left side scientific equipment with its tree possible locations

In the middle main building with safety and telemetry stations

On the right side transmitter site with all transmitter equipment

The system consists of:

4 Helix antennas, 2 each for FTS and SCI use.
2 FTP, Flight Termination Panels
2 FCP, Flight Control Processor
2 FTS, Status and Control Panels
1 FPS Workstation, Linux OS
2 FTS Command Exciter/Encoder with IRIG and Hi Alpha
2 FTS Command Verification Receiver/Decoder with IRIG and Hi Alpha
2 FTS HPA Amplifier 1000 W 410 – 450 MHz
2 SCI Exciter with FM & CPFSK Modulation
2 SCI Verification Receivers with FM & CPFSK Demodulation
2 SCI HPA Amplifier 500 W 410 – 450 MHz
2 Antenna Switch over Units 2 in – 3 out

Figure 5 Transmitter rack at transmitter site

The system is located at Esrange Space Center at three (3) different locations.
1: Main building
2: Launching area
3: Transmitter site

At main building we have operation and control equipment both in Safety room and in telemetry station.

FTP panels in Safety console where FTS commands are executed by Flight Safety Officer.

Figure 6 FTP Panel

FTS equipment in telemetry station for setup and monitor of missions, from the workstation missions are planned and from FSC the mission is operated, switch on /off carrier etc.

Figure 7 FSC status and monitor unit

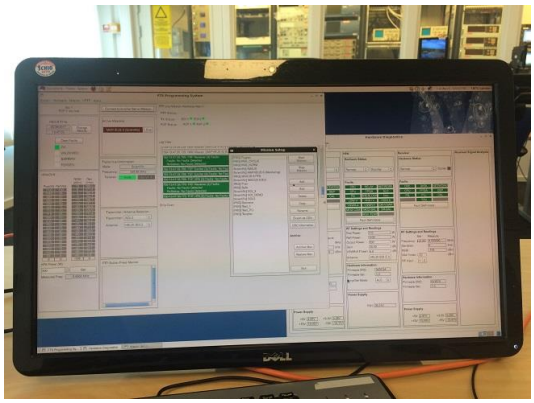
Figure 8 Linux Workstation

At launching area the interface for SCI commands are located.


Figure 9 Scientific exciter unit

4. CONCLUSION

With the new telecommand system, Esrange Space Centre is well prepared for future sounding rockets and balloon missions.
The system is easy to configure for different missions and if in the future there is needs for more secure and control functions for FTS operations, it is possible to upgrade the system for EFTS operations, one module in the FTS Command Exciter/Encoder.

EFTS Enhanced Flight Termination System.

5. REFERENCE

RCC Range Commander Council

1. RCC 319-92
2. RCC 319-10
3. RCC 313-01

NEW TELEMETRY STATION AT ESRANGE SPACE CENTER

Kjell Larsson

Swedish Space Corporation (SSC), Esrange Space Center P.O Box 802, SE-98128 Kiruna Sweden
Email: kjell.larsson@sscspace.com

ABSTRACT

The reconstruction of the telemetry station for sounding rockets and balloons at Esrange has been going on since 2012. There are many reasons why it was needed: to get a higher security level on the optical cables, computers, network switches, to get a more efficient signal distribution to customers, switching of telemetry data, to manage simultaneous campaigns and to get a quiet control room for the operators, especially during long balloon flights.

1. INTRODUCTION

TMS -Telemetry server room with six racks was created for our computers, network switches and optical fiber cables. The analogue TV-receivers were moved to the common TV- center together with DLR. A room for balloon sounding and a RF – laboratory was built. TMR -Telemetry receiver station was constructed and all equipment was moved behind a glass wall. The signals are routed logically from left to the right: Antennas, RF-matrix, receiver, analogue video matrix, analogue video, digital matrix, digital RS422/TTL, TM over IP network. The telemetry data distribution to customers are analogue video, digital RS422/TTL or via network. We use HDD recording with chapter10 format for recording of: RF- IF, video and digital sources. TMC -Telemetry control room are equipped with three ACU -Antenna Control Unit's. The EMP antenna is on the roof of the main building. The Datron antenna is on Keops hill and a new Orbit antenna is situated on radar hill. From the control room we can easily switch antennas and distribution of telemetry signals via the switch operator location. Vaisala metrological soundings can be monitored from the TM-station as well.

2. OLD TM-STATION BACKGROUND

The working environment was noisy and there were unclear structure on equipment and signal paths.
Signal switching and distribution possibilities were limited. The location of optical fiber was a safety issue and there were not enough available room in the server racks. The station gave an aging impression.

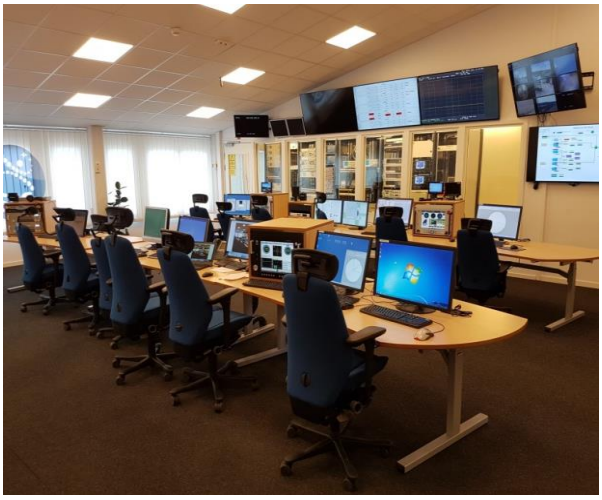

Figure 1. The new TM-station.

Figure 2. The old TM-station.

3. OBSTACLES ALONG THE WAY

The campaign scheme was fully booked. The TM-station is an important asset point at Esrange with a lot of connections. Many cables were tangled to each other. Twenty six optical cables had to be moved and had to have enough length to reach the new server room.

4. SO HOW DID WE PROCEED?

The easiest way would have been to close down the station for a time, remove all cables and equipment and rebuild the station. But that decision was not in our hands. We had to rebuild the TM-station between the campaigns and projects, and do it step by step.

Figure 3. Old TM-station. Equipment in different racks.

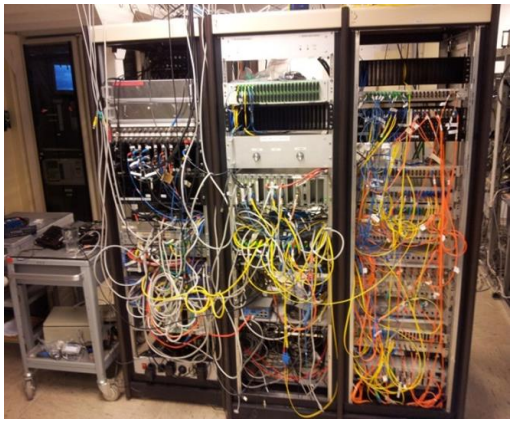

Figure 4. Distribution racks in old station.

5. CONSTRUCTION

Figure 5. TMR; New data floor. Nine new telemetry racks, 44RU.

Figure 6. TMC; A new ceiling with dimmable LED-lights was installed.

Figure 7. TM-equipment moved to the other side of the glass wall.

6. STATION LAYOUT

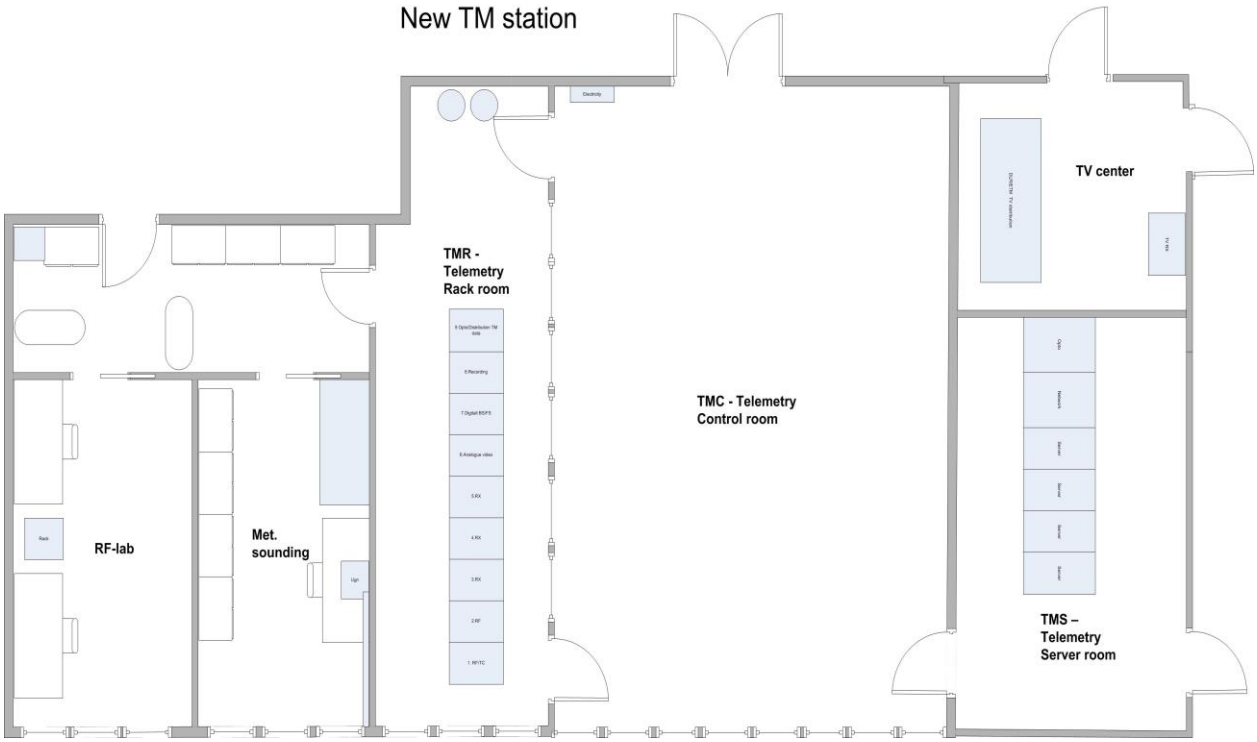

Figure 8. Telemetry station overview.

- A server room with six racks was created
- TMC-Telemetry Control room was constructed
- TMR-Telemetry rack room was built and all equipment was moved behind a glass wall
- A RF-lab and a metrological sounding room was built.

7. PREPARATIONS FOR THE NEW DATA FLOOR

- Old cables were removed
- Cable ladders were installed

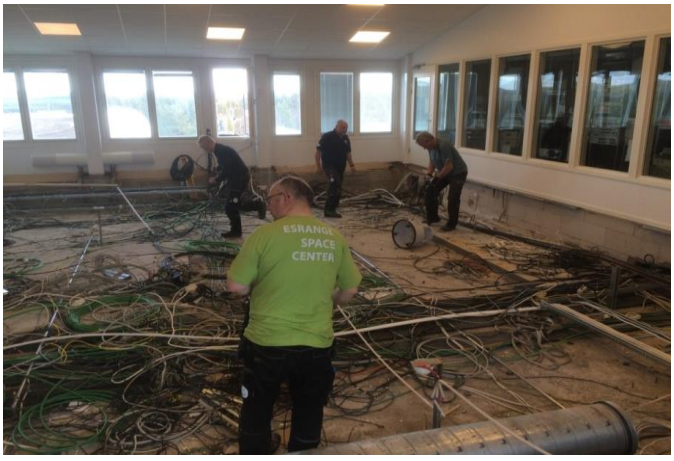

Figure 9. Old data floor.

8. A NEW TM-ERA WAS CREATED!

- The environment is quiet
- The tables are adjustable
- The floor has carpet covered tiles
- There are cable ladders under the floor
- It is easy to install new cables

9. TM-FRONT TABLES OPERATORS

From left:

- EMP antenna control
- Switch operator control and receiver monitoring
- Keops antenna control

Figure 10. TM -Front tables operators.

10. TM-REAR TABLES OPERATORS

From left:

- Telecommand control
- GPS extraction
- Slant range
- Orbit antenna control
- Office computer

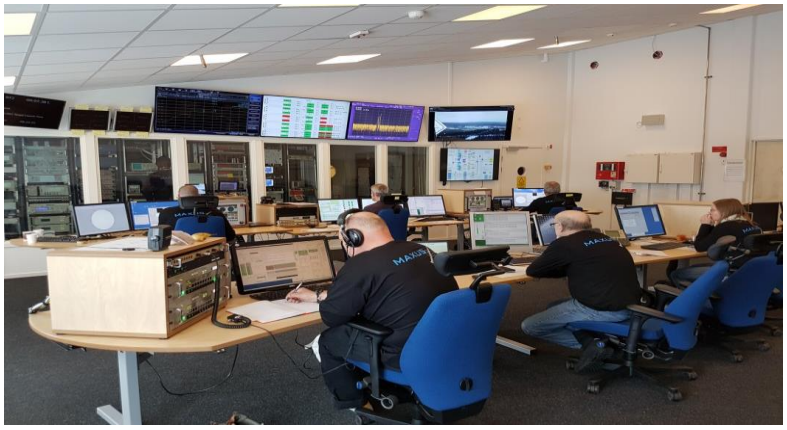

Figure 11. TM -Rear tables operators.

11. STRUCTURE IN THE NEW STATION

-Straight signal routing in the racks from left to right
-Flexibility where it is needed; via matrix switches
-New RF-matrix
-New digital matrix
-Video matrix
-Fixed connections for equipment that shall always be connected
-Extended remote control and monitoring

12. SWITCH MATRICES

-Connection of signal paths that are static during the whole campaign
-Are used for data switching between different signal sources
-Data switching are mostly done with the digital matrix

13. NEW DIGITAL MATRIX

- 64 inputs x 64 outputs
- Data and clock
- TTL (BNC) and RS422 (TRB twinax)
- 30 Mbit/s

Figure 12. New digital matrix.

14. NEW RF-MATRIX

- One equipment for each polarization
- Synchronized control of both polarizations
- 12 inputs x 12 outputs
- Frequency specification 200–2400 MHz

Figure 13. New RF-matrix.

15. DIGITAL MATRIX GUI

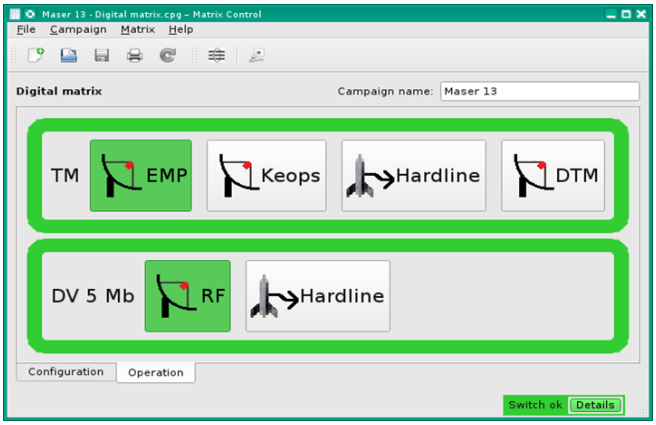

Figure 14. Digital matrix in operational mode.

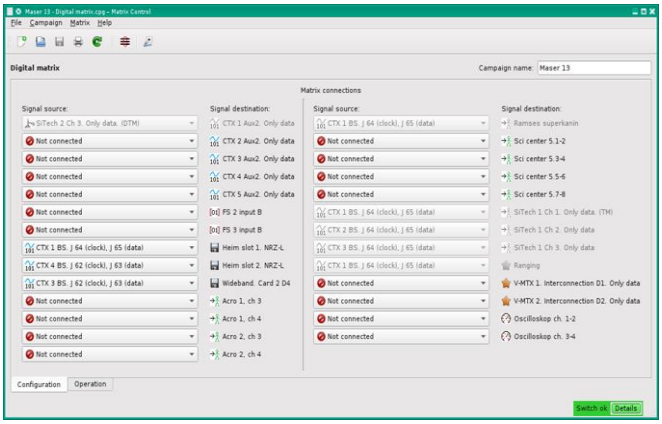

Figure 15. Configuration mode of the digital switch matrix.

16. SIGNAL STATUS OVERVIEW

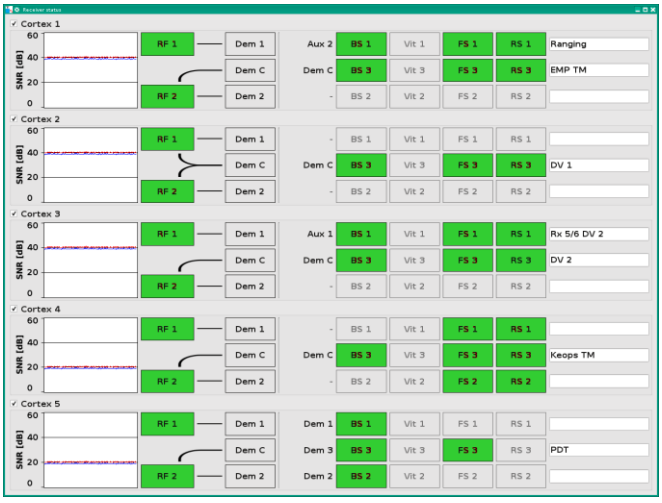

Figure 16. Monitoring of receivers, bitsync's and framesync's lock status.

17. ESRANGE NEW TM-STATION

Figure 17. The new TM-station.

Figure 18. RF-lab.

Figure 19. Met. sounding preparation.

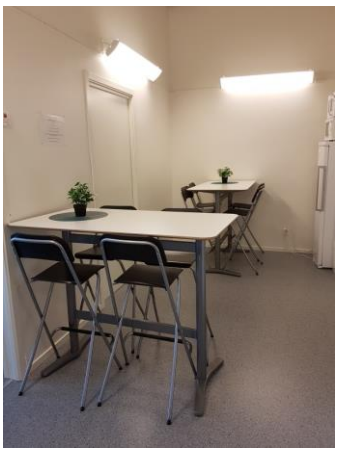

Figure 20. Lunch room.

SIGNON ON BEXUS 23

VISBY, SWEDEN
11-15 JUNE 2017

Bruno Correia [(1)], Américo Duarte [(1)], David Leite [(1)], Nuno Moreira [12)], Sérgio Cunha [(2)]

(1) *Students of Faculty of Engineering of University of Porto, Rua Dr. Roberto Frias, 4200-465 Porto, Portugal, bruno.correia@fe.up.pt*

(2) *Endorsing Professor of Faculty of Engineering of University of Porto, Rua Dr. Roberto Frias, 4200-465 Porto, Portugal, sergio@fe.up.pt*

ABSTRACT

The SIGNON experiment flew on BEXUS 23 at 7th of October of 2016, from Esrange Space Center in Kiruna. The goal of SIGNON experiment was to use radio signals of opportunity to obtain navigation information during a stratospheric BEXUS* flight. For this purpose, a software defined radio (SDR) receiver, tuned to these signals of opportunity, was used. Post-processing by correlation with equivalent data gathered by a small set of reference stations in known locations allowed to compute distances between transmitting stations and the balloon and, consequently, to obtain the balloon trajectory.

1. INTRODUCTION

Electromagnetic waves are everywhere. Their wavelength defines the behavior while interacting with the environment. The band from roughly 10 MHz to 1 GHz is here emphasized. These frequencies correspond to wavelengths from 30 cm to 3 m, which interact with environment objects with dimensions of the same order of magnitude, that correspond to antennas that are neither too large nor too small and are not significantly affected by the atmosphere.

Although GPS is a proven radio signals based navigation system, its use in orbital conditions is not straightforward. It's not very energetically and cost efficient as their low dynamics counterparts. Navigation based on other signals may provide more effective solutions in certain applications.

SIGNON team intended to capture and analyze signals from FM-B (Frequency Modulation Broadcasting from 88MHz to 108Mhz), DTTV (Digital Terrestrial Television from 450Mhz to 650Mhz) and ADS-B (Automatic Dependent Surveillance Broadcast from 1090MHz). The first signals are used in radio communication and commercial radio; the second are used to broadcast digital television; the last one code messages issued by aviation transponders that include their location.

The first two are particularly interesting because the ground stations transmit them continuously with significant power, reaching long distances with enough signal to noise ratio (SNR) to enable decoding them.

During the BEXUS 23 campaign four antennas were used to capture the signals. A SDR receiver was used to collect raw samples that were stored in a solid-state disk for post-processing. There were reference stations in known locations along the flight path, with clear reception for all signals.

2. SIGNALS OF OPPORTUNITY

As mentioned in this paper, there were three types of signals of opportunity of interest: FM-B, DTTV and ADS-B. Each one of these signals has different properties which allowed for comparison between the behaviour and their resolution.

FM-B signals exhibit a low bandwidth and high-power transmission, so they reach the largest distances. Although considered low when compared to the other signals, their spectrum span about 100 KHz, which provides correlation accuracy in the order of hundreds of meters. DTTV signals have slightly lower power and significantly larger bandwidth, 8MHz. Although reaching shorter distances, their correlation peak is accurate to few tens of meters. ADS-B signals are composed by several short pulses, providing an accuracy equivalent to DTTV or slightly better. They are interesting because, although issued by moving aircraft, the signal encodes transmitter coordinates and availability of airplanes flying in the neighborhood has almost global coverage. Also, all aircraft share the same frequency, allowing the reception of multiple stations without retuning.

The resolution of a given signal is given by:

$$\frac{Velocity\ of\ light}{Bandwidth} \quad (1)$$

The bandwidth definition that is used in calculations

*BEXUS - Balloon EXperiment for University Students – is a programme promoted and sponsored by ESA, DLR, SNSB, ZARM, MORABA and SSC, that aims to fly experiments in a stratospheric balloon.

refers to the frequency range in which the signal spectral density is nonzero or above a -3dB threshold value relative to the peak power. Using as example a DTTV signal that has 8MHz bandwidth, the correlation peak width that SIGNON expected to achieve is:

$$\frac{Velocity\ of\ light}{Bandwidth} = \frac{3\times10^8}{8\times10^6} = 37{,}5m \quad (2)$$

The peak instant can be obtained with an accuracy of one tenth of the peak width, leading to a resolution of better than 4 meters,

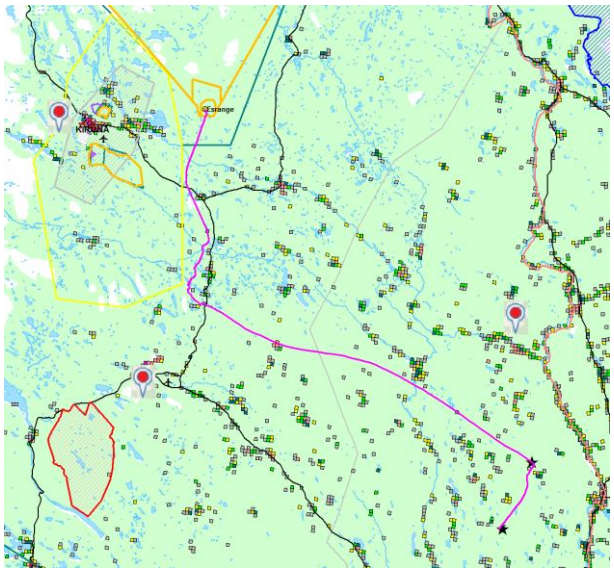

Figure 1: Plot of BEXUS 23 balloon path given by the organization, and some suitable DTTV stations in Sweden. The purple line is the trajectory of the balloon, and the red and blue markers are the DTTV transmitters.

The FM-B stations distribution is similar to that of DTTV stations, with the advantage of being more powerful transmitting stations.
The ADS-B availability will vary a lot with the part of the globe that is being considered. In this specific case, there weren't so many aircraft passing by.
Focusing on DTTV, once this signal has weaker power, here is it the link budget:

1	Effective Tx power Pt	100 W	20 dBW
2	Tx antenna gain	+3 dBi	23 dBW
3	Tx antenna misaligment	–1 dB	22dBW
4	Free space losses fc=550 MHz dist=100 Km	–127 dB	–105 dBW
5	Rx antenna gain	+4 dBi	–101 dBW
6	Rx antenna misaligment	–3 dB	–104 dBW
7	Cable losses	–1 dB	–105 dBW
8	Noise level T=290 K BW=8 MHz	–135 dBW	–135 dBW
9	SNR at antenna	(7) – (8)	30 dB
10	Figure of merit of RX chain	3 dB	
11	SNR at receiver	(9) – (10)	27 dB
12	Min SNR	26 dB	
13	Link margin	(11) – (12)	1 dB

Table 1: SIGNON link budget for DTTV

3. RECEPTION AND SYNCHRONIZATION

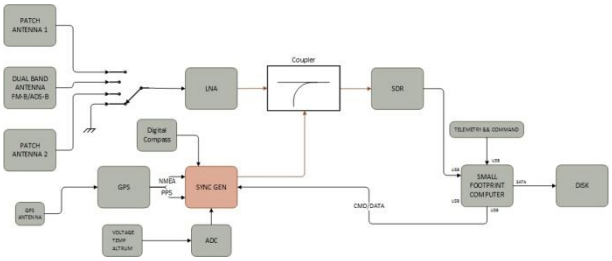

Figure 2: Hardware description of SIGNON experiment

The SIGNON experiment was composed by:
RF front-end and synchronization – composed by 3 antennas to receive signals, 2 patch antennas for DTTV and a dual-band antenna for FM-B and ADSB. Signals flowed through a low noise amplifier(LNA). The synchronization board, SyncGen, had a thermally controlled crystal oscillator (TCxO), a phase lock loop (PLL) and a micro-controller. This board synchronized the received signals with the Pulse Per Second given by a GPS receiver that would provide an accurate timestamp for the signals.

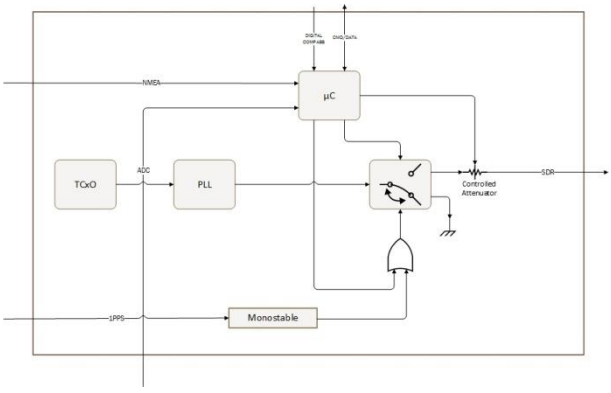

Figure 3: SyncGen hardware

Regarding the synchronization part, there was a PCB composed by a microcontroller, a PLL controlled trough SPI by the microcontroller, and a 1ppm TCxO that supplied the reference for the PLL. The output of the PLL

passed by a controlled attenuator and then was added to the RF chain through an ON/OFF RF switch. This switch was both actuated by the GPS PPS signal and by the microcontroller. At the coupler, this signal was added to the one that comes from the LNA was received by the antennas.
Between the antennas and the LNA there was a switch that was also controlled by the microcontroller, which allowed to choose which antenna was to be selected to receive the desired signals.
On the ground SIGNON had reference stations placed on strategic locations along the flight path, where the transmitters of the selected signals can be recorded with excellent SNR. These stations consisted of boxes, with the exact same design and content as the one that flew in the BEXUS gondola. The maxim distance to the actual flight path was 100km making the location easy to choose from wind forecast data available one day prior to the flight. The correlation between the signals received by the flying set-up with those received by the stations on the ground enabled to measure the differential range between stations, which ultimately provided position estimates of the balloon.

The data processing for the data collected in the gondola was divided in the following steps:
- The gondola trajectory was obtained from the GPS signal.
- Then the data processing was divided according to the three kinds of signals: FM-B, DTTV and ADS-B:

For FM-B:

1. Find timestamps;
2. Sample the signal;
3. Gather sub-intervals;
4. Correlate the gondola signal with counterparts from reference station;
5. Determine correlation peak instants, with sub-sample precision;
6. Calculate residual error.

For DTTV:

1. Synchronize signal with symbols;
2. Identify pilot frequencies;
3. Decode Signal;
4. Find and correct digital errors;
5. Correlate with decoded signal;
6. Identify correlation peak instants;
7. Calculate residual error;

For ADS-B

1. Find initial flags of transmitted packets
2. Decode packets;
3. Find and use packages that contain coordinates;
4. Correlate signal to obtain packet time;
5. Calculate residual error.

4. RESULTS

After the processing is concluded, some results were taken by SIGNON team. Unfortunately, only a small portion of the flight data was in acceptable conditions for processing. However, in the next figures it's possible to see some examples of SIGNON correlation results.

The processing of the signals of opportunity that the team used are based on correlating the received signals, with those received by reference stations. The sharpness of the correlation peak is given by the inverse of the bandwidth of the signal (multiplied by the speed of light to convert into distance accuracy). Figure 4 and 5 illustrate the correlation of respectively DTTV and FM-B signals, where the horizontal scales have been converted into distance by multiplying by the speed of light.

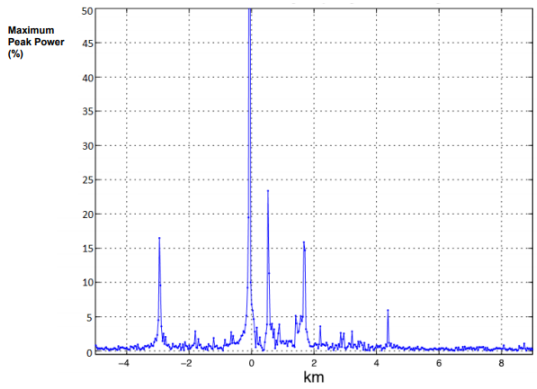

Figure 4: Correlation of received DTTV signals with the digitally regenerated transmitted signal.

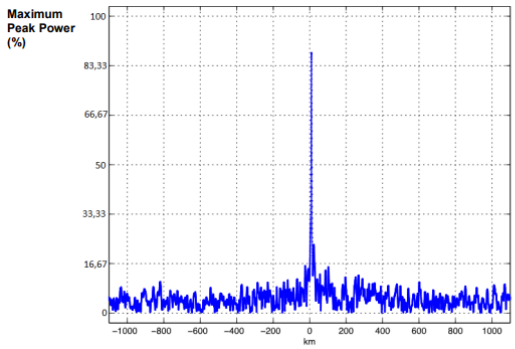

Figure 5: Correlation between FM-B signals.

DTTV signals exhibit a constant average power spectrum along their bandwidth. This makes best use of the spectrum for correlation. Being digitally coded with forward error correction data included enables reconstruction of the originally transmitted signals. Consequently, correlation between the received signals with the digitally reconstructed version allows to accurately detect the transmitter peak.

5. CONCLUSIONS

Summing up, the main objective of SIGNON was to use signals of opportunity like FM, DTTV and ADSB to do navigation. This way of doing navigation is an alternative to GPS that can be a very expensive device to include in a small satellite, once that a normal GPS receiver does not work because, in a LEO satellite environment COCOM restrictions are applicable. Although the results were not the SIGNON team wished, with them, we could understand feasibilities at high altitudes and understand practicalities of this concept.

6. REFERENCES

RX_REF_REXUS_UserManual_v7-14_21DEC16
http://rexusbexus.net/rexus/rexus-user-manual/

XRMON-SOL MICROGRAVITY EXPERIMENT MODULE ON MASER 13

Jianning Li [(1)], Y. Houltz [(1)] , K. Henriksson [(1)], A. G. Murphy [(2)], R. Mathiesen[(3)], A. Vaerneus [(1)], C. Lockowandt [(1)], D. J. Browne [(2)]

[(1)] Swedish Space Corporation, P.O. Box 4207, SE-171 04 Solna, Sweden, Jianning.li@sscspace.com
[(2)] School of Mechanical & Materials Engineering, University College Dublin, Belfield, Dublin 4, Ireland
[(3)] Department of Physics, Norwegian University of Science and Technology, NO-7491 Trondheim, Norway

ABSTRACT

The XRMON-SOL microgravity experiment observed spatially isothermal equiaxed solidification of an Al–Cu alloy in microgravity on board the MASER 13 sounding rocket, launched in December 2015. It is the first time that isothermal equiaxed solidification of a metallic alloy has been observed in situ in space, providing unique benchmark experimental data.

The experiment used a newly developed isothermal solidification furnace in the re-used module of the MASER 12 experiment XRMON-GF. A grain-refined Al–20 wt%Cu sample was fully melted and solidified during 360 s of microgravity and the solidification sequence was recorded using time-resolved X-radiography. Equiaxed nucleation, dendritic growth, solutal impingement, and eutectic transformation were thus observed in a gravity-free environment.

This paper describes the technology development of the experiment module

1 BACKGROUND

1.1 XRMON project under MAP programme

The XRMON (X-Ray Monitoring) project under the ESA MAP (Microgravity Applications Promotion) programme was established to conceive and perform in situ X-ray radiography observations of metallurgical processes under microgravity and terrestrial conditions. Under the programme, a series of experiment modules and facilities have been developed and advanced experiments of metallurgical processes have been performed with X-ray radiography observations under microgravity conditions. These include:

- ✓ XRMON-Metal Foam: Study of metallic foams, MASER 11 2008, two parabolic flight campaigns in 2007 and 2009
- ✓ XRMON-Diffusion: MAXUS 8 sounding rocket in 2010
- ✓ XRMON-Gradient Furnace: MASER 12 sounding rocket in 2012
- ✓ XRMON Laboratory Set-up in 2012
- ✓ XRMON Parabolic Flight Facility: Four flights during 2013-2016
- ✓ XRMON-SOLidification Furnace: MASER 13 sounding rocket in 2015
- ✓ XRMON-Diffusion 2: MAXUS 9 sounding rocket in 2017
- o XRMON-Gradient Furnace 2: MASER 14 sounding rocket, under pre-study

1.2 XRMON-GF Experiment Module

Within the above activities, XRMON-GF was the first ever sounding rocket experiment with in situ X-ray monitoring of alloy solidification during flight [1]. The consequent XRMON Laboratory Set-up, XRMON-PFF and XRMON-SOL inherited the same overall system design of the XRMON-GF module. All of them use (with or without adaptation) the same compact X-ray imaging system developed under XRMON-GF project.

The XRMON-GF module was designed with the aim of being possible to be re-used. XRMON-SOL is the first re-fly of the XRMON-GF module, albeit with a very different experimental furnace design. The following chapter will focus on describing the adaption made to the module to accommodate the XRMON-SOL experiment and the design improvement implemented after the XRMON-GF project.

1.3 XRMON-GF Furnace

The XRMON-GF Furnace, developed under XRMON-GF project, is a gradient furnace of Bridgman type with two identical heaters for the “hot” and “cold” zones (Figure 1). It was designed for columnar solidification experiments [2].

The furnace has been accommodated in XRMON Laboratory Set-up and XRMON-PFF. Nearly isothermal solidification experiments have been performed by applying the same temperature to both heaters in XRMON-GF furnace. Experiments have been performed by using these 2 set-ups both on ground and in Parabolic Flight [3].

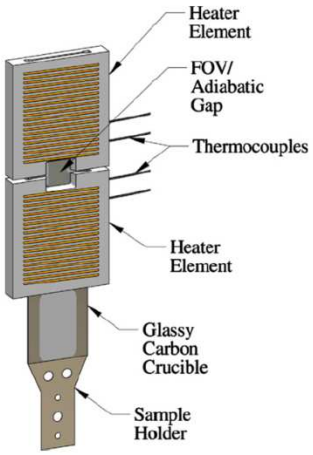

Figure 1. Schematic layout of the XRMON-GF furnace

However, a temperature gradient has been observed in the sample when attempting to perform isothermal solidification with the XRMON-GF furnace. The furnace design does not enable a temperature field which is isothermal in the Field of View (FoV); this is needed for equiaxed solidification [2].

2 XRMON-SOL EXPERIMENT MODULE

2.1 XRMON-SOL Furnace

The major activity in the XRMON-SOL project was to develop the XRMON-SOL furnace for equiaxed solidification experiment.

Based on the experience of XRMON-GF furnace, a completely new furnace, XRMON-SOL, was needed. It was to have rotational symmetry. It was designed to have one heater body (Ø70 mm) with eight heaters arranged so that 4 heaters form the inner ring and 4 heaters form the outer ring (Figure 2). Heating wire is wound as coils on the heater body. The inner ring heaters and the outer ring heaters are displaced by 45° so that the outer ring heater will guard the gap between inner ring heaters to minimize the heat leakage through the gap.

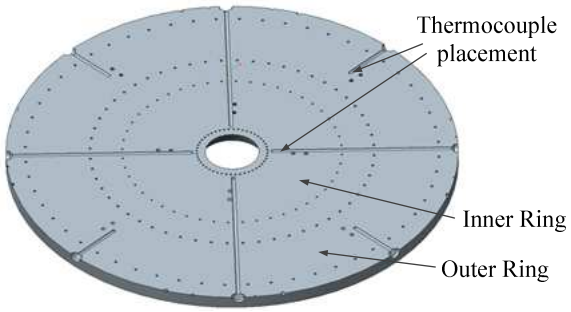

Figure 2. Cross-section of heater body showing placement of thermocouples

Eight thermocouples are used and one is placed in each heater zone. Figure 2 shows also the placement of thermocouples.

After heater wires and thermocouples have been assembled (Figure 3), a sample holder with sample compartment is placed on top of the heater body. The alloy sample is placed between 2 glassy carbon crucible sheets and placed in the sample compartment (Figure 4). The sample has a diameter of 23 mm and the sample thickness is 0.2 mm. A sample lid is placed to cover the sample compartment and to hold the sample in place (Figure 5). Heater body, sample holder and sample lid are made from a special unidirectional sintered ceramic, to achieve good thermal conductivity and X-Ray transparency.

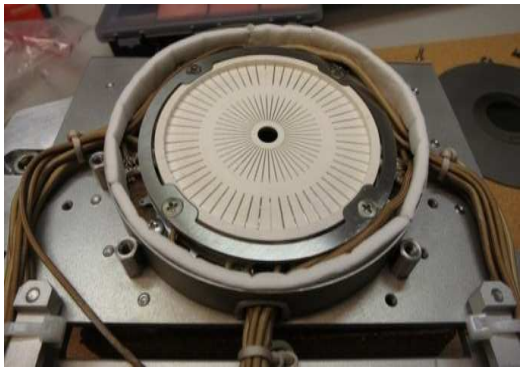

Figure 3. Heater has been assembled

Figure 4. Sample holder and the flight sample, photo was taken after payload retrieval

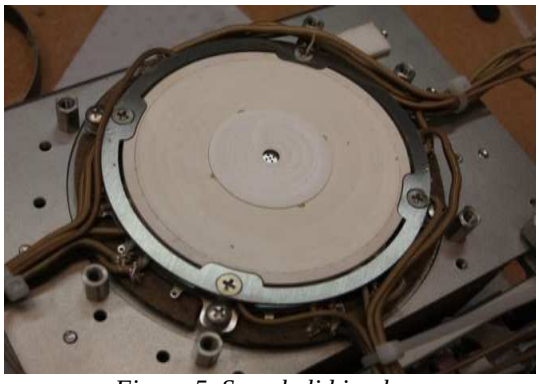

Figure 5. Sample lid in place

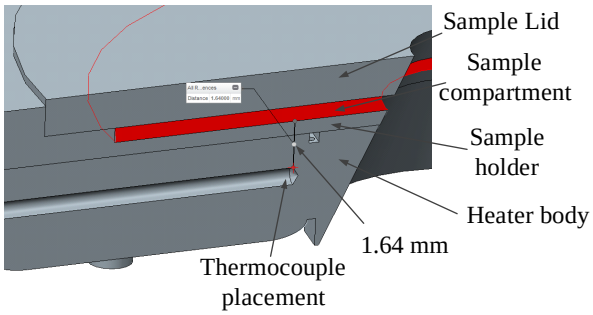

Figure 6. Part of cross-section of heater body, sample holder and sample lid showing placement of inner ring thermocouples

Efforts have been made to place the inner ring thermocouples as close as possible to the sample. Figure 6 shows part of the cross-section of heater body, sample compartment and sample lid. It shows that the inner zone thermocouples are placed less than 2 mm from the sample.

Figure 7 shows the complete assembled XRMON-SOL furnace. The furnace lid is made out of a tungsten alloy, with glassy carbon thermal shielding, in the X-ray window. It is insulated towards the furnace.

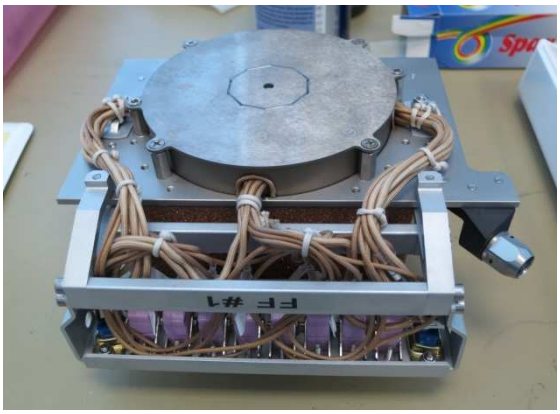

Figure 7. Flight furnace complete assembled

2.2 Furnace Temperature Regulation

Heaters and thermocouples are numbered according to Figure 8. Heaters 1 to 4 are inner ring heaters and heaters 5 to 8 are outer ring heaters.

For fine-tuning of solidification process, all 8 heaters are individually regulated. For the simplicity during operation, only two target temperatures (regulation set-points) are used. The inner ring heaters use the inner ring set-point and the outer ring heaters use the outer ring set-point. Hence a temperature offset could be set for each heater. The offset could be used to compensate the eventual temperature difference caused by tolerance of the furnace or the sample. Offset of all heaters were set to zero during the flight, which means the furnace and the sample were manufactured very precisely to provide isothermal condition.

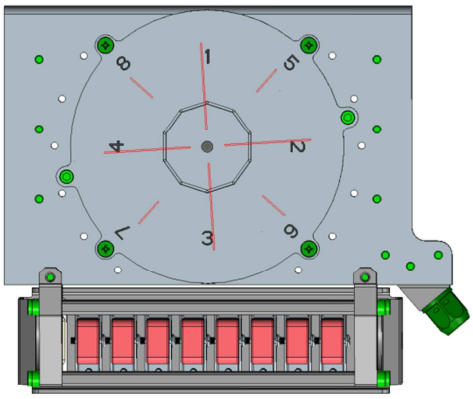

Figure 8. Heater and thermocouple numbering

A new design of sensor board and PWM control board has been implemented since XRMON Laboratory Set-up.

The multiplexer before thermocouple amplifier on the sensor board was removed, as multiplexing the thermocouple amplifier limits the sampling frequency. Instead, each thermocouple gets a dedicated thermocouple amplifier. Microcontroller was also upgraded from an 8-bit MCU to a 32-bit MCU. The sampling frequency had been increased and a better software filter was used. The 24-bits temperature data from output of the software filter was used in the temperature control loop.

Also the 8-bit microcontroller on the PWM control board has been upgraded to 32-bit microcontroller. After the upgrade, PWM resolution was increased from 1000 in XRMON-GF module to 10000. The PWM frequency could be decreased from 1250 Hz to 25 Hz which dramatically reduces the switching loss of the output driver.

To adapt to this improvement, XRMON-GF sensor board was replaced by XRMON-PFF sensor board. XRMON-GF PWM board was replaced by a new PWM board that has 8 PWM outputs. The new PWM contains 2 microcontrollers to control 4 PWM outputs each. A general time synchronization mechanism via CAN bus has been implemented. The synchronization accuracy is less than +/- 2 µs. Based on time synchronization, the 8 PWM outputs are divided into 4 groups with 2 outputs in each group. The groups has PWM phase shift at 0^o, 90^o, 180^o and 270^o. Each group drives 1 inner ring heater and 1 outer ring heater. In this way, the power consumption is more equally distributed.

Table 1 shows the temperature control error the first 50 s after lift-off when the furnace temperature was set to

540 °C. It shows that the temperature control is very accurate and stable for all heater zones.

Table 1. Furnace temperature control error, from lift-off to 50 s in flight, set temperature 540 °C

	Mean (°C)	Std (°C)
TC1	-0.002	0.027
TC2	-0.001	0.026
TC3	-0.004	0.029
TC4	-0.003	0.031
TC5	-0.018	0.025
TC6	-0.010	0.030
TC7	-0.015	0.029
TC8	-0.013	0.030

2.3 X-Ray Imaging

Although the same X-Ray and X-Ray camera were used, the sample placement for XRMON-SOL has been adapted to the FoV requirement of XRMON-SOL.

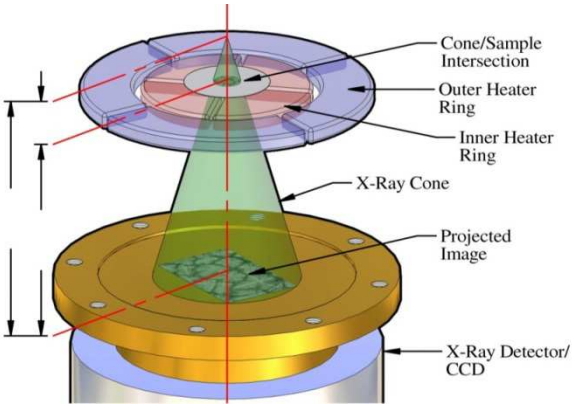

Figure 9. X-Ray image projection illustration

Figure 9 illustrates the relation between X-Ray source, the sample and the camera. The distance from the source to sample is 5.7 mm and the distance from the source to CCD sensor is 46.9 mm. This gives magnification factor 8.2. Consider that the effective pixel of the CCD sensor is 18 µm (CCD size 24x36 mm, 2012x1340 pixels @ 2x2 binning), the virtual pixel size is 2.2 µm in the sample. The actual spatial resolution [4], which is a function of the scintillator pitch (50 µm) and the source size (3 µm), was calculated as ~ 6.3 µm.

2.4 XRMON-SOL module

After the above mentioned modifications (include the entirely new furnace design) and a few other improvements, the XRMON-GF module became XRMON-SOL module. It is worthwhile to mention that in order to meet requirements on general payload mass reduction, the total mass was reduced from 103.7 (XRMON-GF) to 99.3 kg. Extensive testing has been performed to verify the performance of the furnace and the module [5].

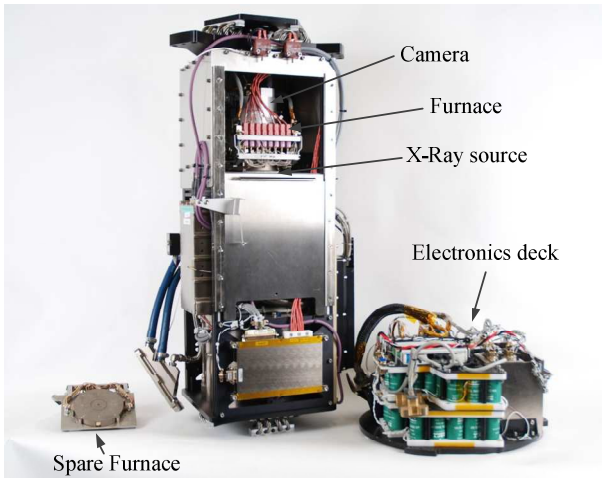

Figure 10. XRMON-SOL Module

3 XRMON-SOL FLIGHT ON MASER 13

MASER 13 sounding rocket, with XRMON-SOL on board, was launched on Dec. the 1st, 2015. It reached apogee of 261.7 km and provided good microgravity levels about 10^{-4} g for 359 seconds.

XRMON-SOL module was controlled by a pre-configured time-tagged tele-command queue. XRMON-SOL experiment was nominal during the count-down and the flight. No manual intervention was need.

Figure 11 shows the flight time line by using the actual furnace temperature data during the flight. Time 0 is the rocket lift-off time which was 2015-12-01 05:00:00 UTC. The microgravity time is from 89 s to 448 s. Because of the accurate furnace temperature control, time line could simply be defined by the inner ring and outer ring set-point. The alloy was melted and re-solidified within the microgravity time window.

The experiment started at T-15 min, heating the sample to 540 °C at the rate of 2 K/s. At 60 s after lift-off (Figure 11), heating to 650 °C at 2 K/s was commenced. After an initial holding/stabilisation period of about 20 s, the sample was cooled to standby temperature of 625 °C at 0.9 K/s and 1.1 K/s on the inner respect the outer heater ring. After a second holding/stabilisation period, the first stage of the solidification experiment commenced at 180 s by applying cooling rate of -0.05 K/s to all eight heaters simultaneously. At 359 s, the second stage of solidification, i.e. the eutectic transformation, started by increasing the cooling rate to -1 K/s on the inner ring and the -1.5 K/s on the outer ring. All heaters were switched off at 435 s.

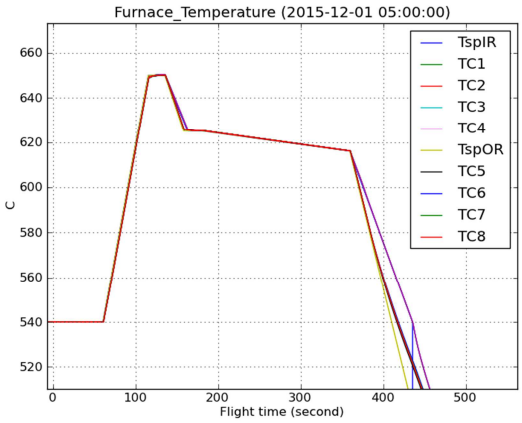

Figure 11. Experiment temperature profile / Time line

Because of the slow cooling rate of -0.05 K/s, it is important to identify the actual solidification temperature of the sample. Missing one degree means loss of 20 s of microgravity time. Therefore, sample conditioning was planned at the beginning of launch campaign. Sample conditioning uses a tele-command queue similar to the flight tele-command queue, but with bigger temperature and time margin. Sample solidification start temperature and eutectic transformation temperature (where all remaining liquid disappears) could be identified via the X-ray image. Then the new standby temperature and time to start the first and the second solidification stages could be calculated. The flight tele-command queue was updated accordingly.

It is important that nucleation of solid would not occur until the planned start of the first solidification stage. Therefore it is critical that the actual temperature should not drop below the standby temperature before the slow cooling of -0.05 K/s had been applied. The temperature regulation had been fine-tuned to avoid over/under shoot (Figure 12).

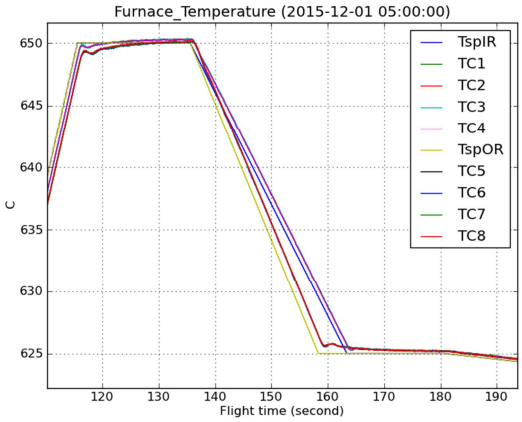

Figure 12. Standby temperature, commenced temperature and actual temperature

The uncompressed 12-bit X-Ray image was saved at 3 frames/s on board. Compressed image was down-liked live at 1 frame/s during the flight. The compression ratio is about 10 which is less than that of XRMON-GF. The down-linked images were already deducted by a reference image taken after sample melting. Figure 13 shows some examples of down-link images. Study [6] shows that observable solidification within the FOV occurred between 241 s and 425 s and eutectic transformation between 414 s and 425 s.

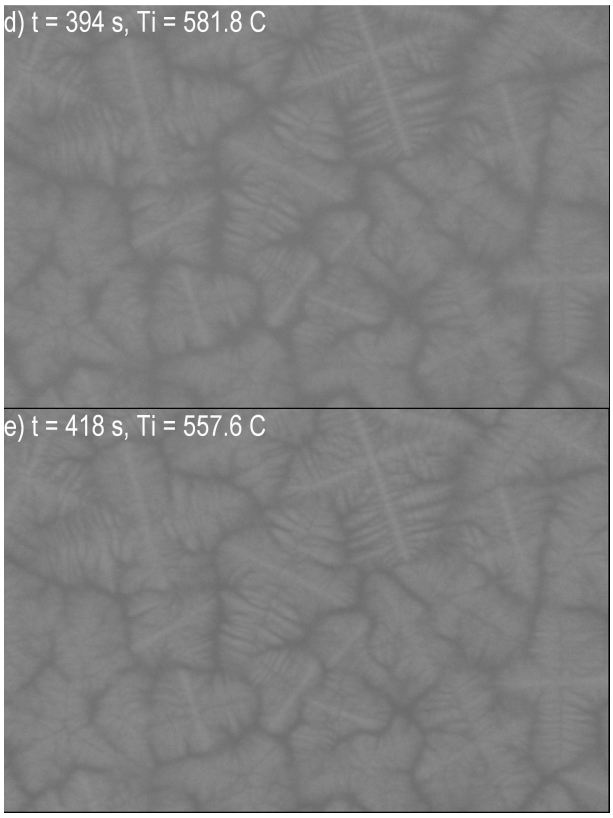

Figure 13. Example of live down-linked X-Ray image for monitoring durng the flight. a) & b) Solidification stage 1; c) start of Solidification stage 2; d) Solidification stage 2; e) eutectic transformation

Digitally enhanced images have been published [6] with open online access to the video sequence from the sounding rocket experiment. The XRMON-SOL project on equiaxed solidification was a scientific and technical success, and further quantitative examination of the results is being carried out by the UCD team.

4 ACKNOWLEDMENTS

The authors wish to acknowledge the funding for development of XRMON-SOL furnace and module through ESA's ELIPS (European Life and Physical Sciences in Space) programme. The research work is supported by the ESA-MAP project XRMON.

5 REFERENCES

1. Y. Houltz, J. Li, H. Nguyen-Thi, G. Reinhart, G. Salloum Abou Jaoude, R. Mathiesen, D.J. Browne, A.G. Murphy , G. Zimmmith (2013). “The XRMON-GF Microgravity Experiment Module on MASER 12 and its Continuation”. *21st ESA Symposium on European Rocket & Balloon Programmes and Related Research*, ESA SP-721, pp. 275-283.
2. Mirihanage, W.U., Dai, H.J., Dong, H.B., Browne, D.J., "Computational modelling of columnar to equiaxed transition in alloy solidification", *Advanced Engineering Materials*, 15(4), 2013, pp.216-229.
3. A. G. Murphy, J. Li, O. Janson, A. Verga, and D. J. Browne, “Microgravity and Hypergravity Observations of Equiaxed Solidification of Al-Cu Alloys using *In-situ* X-radiography recorded in Real-time on board a Parabolic Flight,” *Mater Sci Forum*, vol. 790–791, pp. 52–58, 2014.
4. C. Rakete, C. Baumbach, A. Goldschmidt, D. Samberg, C. G. Schroer, F. Breede, C. Stenzel, G. Zimmermann, C. Pickmann, Y. Houltz, C. Lockowandt, O. Svenonius, P. Wiklund, and R. H. Mathiesen, “Compact X-Ray Microradiograph for *In Situ* Imaging of Solidification Processes: Bringing *In Situ* X-Ray Micro-Imaging from the Synchrotron to the Laboratory”, *Rev Sci Instrum*, vol. 82, no. 10, pp. 105108 –105108–10, 2011.
5. A. G. Murphy, R. H. Mathiesen, Y. Houltz, J. Li, C. Lockowandt, K. Henriksson, G. Zimmermann, N. Melville, D. J. Browne, “XRMON-SOL: isothermal equiaxed solidification of a grain refined Al–20 wt%Cu alloy”, *J. Cryst. Growth* 440(2016) p38–46.
6. A. G. Murphy, R. H. Mathiesen, Y. Houltz, J. Li, C. Lockowandt, K. Henriksson, N. Melville, D. J. Browne, “Direct observation of spatially isothermal equiaxed solidification of an Al–Cu alloy in microgravity on board the MASER13 sounding rocket”, *J. Cryst. Growth* 454(2016) p96–104.

BOOSTER – BALLOON FOR SCIENCE AND TECHNOLOGY FROM ESRANGE

Ella Carlsson Sjöberg[1], Peter Dalin[1], Johan Kero[1], Uwe Raffalski[1], Martin Wiesser[1]
Swedish Institute of Space Physics, Box 812, 981 28 Kiruna, Sweden, ella@irf.se
Tel:+46 980 790 00, Fax: +46 980 790 50, E-mail: ella@irf.se

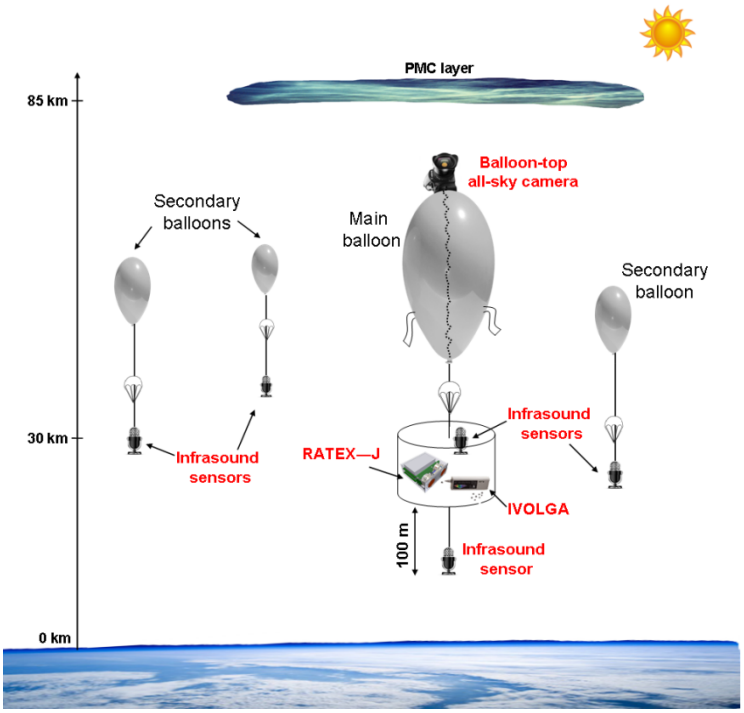

Figure 1. Conceptual image of the balloons and the location of the experiments (not to scale).

1. ABSTRACT

BOOSTER is a balloon flight with four balloons in a formation: one main balloon and three smaller ones. The balloons will carry four different experiments in the stratosphere for up to two days. BOOSTER will give insight in atmospheric and magnetospheric physics and also serve as a technology demonstrator for future planetary missions and for developing Esrange's future capabilities with regards to formation flying and the in-situ measurements of wind profiles.

2. THE BOOSTER PROJECT

The BOOSTER project will consist of four balloons, one main balloon and three smaller ones in order to conduct triangulation with infrasound sensors. Esrange has never attempted to launch several balloons simultaneously before and the BOOSTER project will hence be a part of Esrange's capability development within the New Esrange project. Esrange has also a need to develop a capability to produce wind profiles *in situ* in order to better estimate the flight pattern of their balloons. The IVOLGA experiment could besides measuring greenhouse gases also measure wind profiles, which will be helpful for the determination of wind directions and velocities.

The balloons will all together carry four different experiments in the stratosphere for two days in the late summer stratospheric zonal wind turnaround period. Figure 1 displays a conceptual design of BOOSTER.

The main balloon will carry the All-sky camera on a platform on top of the balloon, pointing towards zenith. The experiments IVOLGA, RATEX-J and one infrasound sensor box will be located on the gondola. 100 m below the gondola a wire will be extended to carry another infrasound sensor box. The three smaller balloons will also have infrasound sensor boxes. It is not important to fly in an exact formation. The exact positions of the balloons are needed at all times in order to conduct a successful triangulation of the infrasound. This information is stored as part of the data.

3. RATEX-J

3.1. Jupiter's radiation environment

The ESA's mission to Jupiter (JUICE) will carry the Particle Environment Package (PEP), a comprehensive set of instruments investigating the plasma and neutral gas environment around Jupiter and is built under the lead of IRF in Kiruna.

PEP sensors use among others, multi-channel plates (MCPs) and channel electron multipliers (CEMs) as particle detectors. They are employed on a large number of plasma instruments, for example on ASPERA-3 and ASPERA-4 onboard Mars and Venus Express [12].

However, the harsh Jovian environment with its penetrating radiation is a major problem for MCPs and CEMs: high fluxes of penetrating radiation and in addition secondary particles generated in the shielding material around the detectors result in substantial background signals with the potential of completely saturating detectors. Consequently, the actual science measurement cannot be performed any-more. Additionally, the lifetime of the detectors depends on the total extracted charge and decreases in a harsh radiation environment.

Very limited data is available about the efficiency of MCPs and CEMs to electron radiation above some 1MeV. Preliminary results indicate that there might be a significant difference in efficiency between MCPs and CEMs for penetrating radiation [8], which could influence future instrument design.

Obtaining the correct energetic particle spectrum in ground based facilities like accelerators is difficult. Only a few accelerators are available in Europe in the energy range of interest and none have directly usable particle beam properties for our applications.

At an altitude of 20-30 km above Earth, secondary particles generated from cosmic ray background radiation prove to have a shape of the energy spectrum that is comparable of what is expected behind the radiation shielding on a spacecraft in orbit around Jupiter (Figure 2).

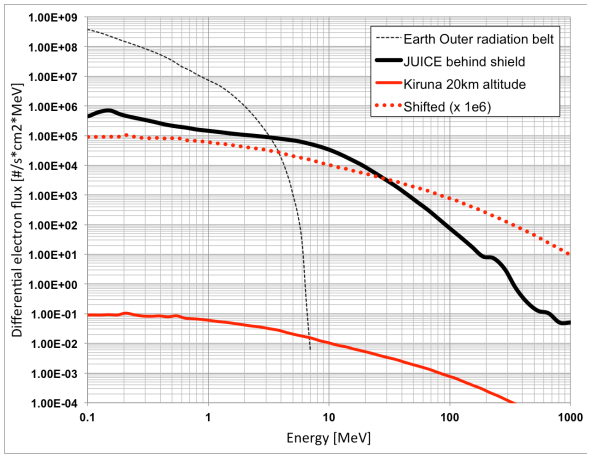

Figure 2. Energetic electron energy spectrum at 20 km altitude (solid red line) compared to the energy spectrum at Jupiter behind radiation shielding (solid black line). For shape comparison with the Jovian spectrum, the Kiruna spectrum is shifted upwards by a factor of 10^6. Good agreement is obtained especially above 3 MeV. Above this energy, not even a spacecraft in Earth orbit crossing the outer radiation belt (thin dotted line) will experience significant fluxes.

The remaining difference is that the particle fluxes at these altitudes are about six orders of magnitude lower than what is expected at Jupiter. However, even with these lower fluxes, detection rates will be of the order of one per second - sufficient to obtain statistically significant results in less than one hour.

3.2. RATEX-J: Instrumentation

The RAdiation Test EXperiment for Jupiter (RATEX-J) is an experiment setup dedicated to investigate the response of MCPs and CEMs to high energetic penetrating radiation. Apart from the MCPs we use so far in our plasma instruments, we also plan to test a promising new MCP technology: Atomic Layer Deposition MCPs [15] are mechanically flexible and robust, show lower background rates and their surface coating can be chosen independently to optimize it for our purpose.

RATEX-J was originally built for deployment on a CubeSat and was subsequently used for initial radiation sensitivity measurements in ground-based accelerators (e.g. the Microtron at KTH). It became immediately clear however that a better reproduction of the expected energy spectrum is needed.

RATEX-J uses different particle detectors, classical MCPs, ALDs and CEMs. All of them are placed behind a semiconductor detector. The semiconductor detector serves as coincidence detector (as electrons are likely to trigger coincidences, while photons do not), as spectrometer to monitor and characterize the respective radiation field, and as dosimeter. RATEX-J includes detector stacks (front-end electronics, pulse height analysis, high voltage supply and a simple data processing unit. This setup allows flexibility and mobility of the unit).

For the use on the BOOSTER balloon we integrate the RATEX-J into a small vacuum system. Where applicable, we will use expertise and remaining hardware from the MEAP/PBACE balloon flight in 2009 [22, 1] to reduce cost and testing efforts.

The total experiment mass including a small vacuum system with pumps is currently estimated to 20 kg and the power consumption to 25 W. Optional, the power system may be included into RATEX-J resulting in a mass of 70 kg and no requirements towards platform power.

RATEX-J contains its own onboard computer and requires limited telemetry and command capabilities in the first phase of the BOOSTER balloon flight.

4. INFRASOUND IN THE ATMOSPHERE

Acoustic waves with frequencies below 20 Hz are not perceived by the human ear as a sound. These

frequencies, down to a fraction of a Hz, are known as infrasound. Since acoustic attenuation is proportional to frequency squared, infrasound from various sources is detectable over long distances. Continuous recording of infrasound with a network of small aperture microphone arrays in Sweden started in October 1973 at Kiruna Geophysical Observatory, which later became IRF. Infrasound recordings in Sweden are the longest continuous time series of its kind in the world. It has provided data on long distance infrasound propagation from industrial sources, meteoroid entries, supersonic jets, sprites and volcanoes, to name a few [11].

Figure 3 [10] shows the current distribution of sensor arrays and sites of repeating explosions in the European Arctic. The combination of the wide range of sources together with the dense sensor network is unique and offers unprecedented ground coverage. IRF operates the four microphone arrays located in Kiruna, Sodankylä, Jämtön and Lycksele as well as a temporary microbarometer array deployed in Kiruna 2016-2018 together with CEA, France, in the frame of the EU-H2020 Design Study Project ARISE2. The IS37 and ARCES/ARCI stations are operated by the Norwegian ARISE2 partner NORSAR. Modelling of infrasound propagation from sources as the Aitik querry (Figure 3) is a hot topic within ARISE2 in order to evaluate and improve numerical weather forecast models [19]. Analysis and evaluation of balloon borne flight data in comparison with registrations on the ground will strongly benefit from the ARISE2 network of instruments and leading experts.

4.1. Balloon borne measurements of infrasound

Infrasound generated by e.g. ocean waves (microbaroms), thunderstorms and severe weather propagates into the mesosphere and thermosphere where its energy is dissipated. The amount of energy from microbaroms is estimated to be up to 0.3W/kg, leading to a heating rate of 30K/day in the thermosphere between 110 and 140 km in certain situations [16] and to fluctuations in the mesopause temperature of 0.1–1.0 K [14]. Fluctuations up to 10 K are expected if the source strength is in the order of about 100 Pa, typical for volcanic activity, earthquakes and larger explosions. However, the three-dimensional acoustic wave field above the ground is still virtually unexplored and the acoustic energy flux from the lower to the upper atmosphere has never been measured directly. Balloon-borne infrasound measurements are limited to a small set of flights conducted 2014-2016 [4] following a longer series of flights conducted in the 1960:s [21]. The recent flights have served as a technological testbed and demonstrated the feasibility of a stratospheric sensor network able to place observational constraints on upgoing waves.

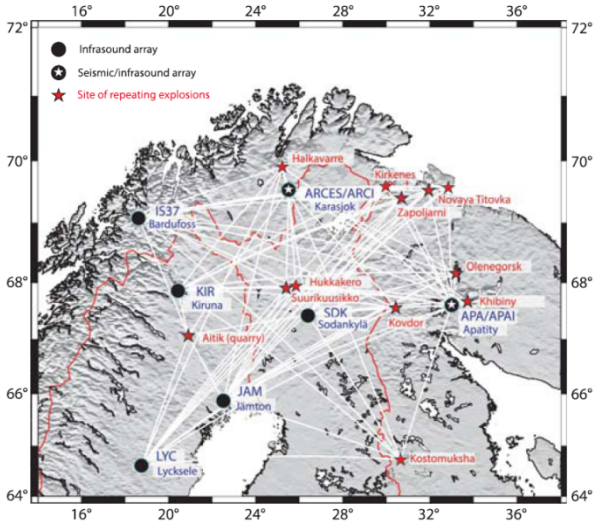

Figure 3. Sensor arrays and sites of repeating explosions in the European Arctic [10].

4.2. Infrasound: Instrumentation

We propose constructing a 100 m long vertical baseline using one infrasound sensor box on the gondola together with an independent box hanging on a wire below. In addition we will launch an array of three independent sensors located on a free-floating formation of three separate small/medium sized balloons. Such a formation flight has never been tried and is the natural next step in the technological development of state-of-the-art balloon borne infrasound measurements [4]. We will explore the three-dimensional acoustic wave field and catch up- and down going rays in the stratospheric duct from known sources.

The design of the sensor boxes and instrumentation has been developed and improved throughout flights conducted 2014-2016 in order to eliminate noise and interference present on the first flights [4]. The data acquisition system will consist of the Omnirecs Datacube3, a 3-channel 24-bit logging system designed for seismic applications. Acoustic data will be collected using three InfraBSU sensors [13]. Each instrumentation package will be time synchronized using continuous GPS with an accuracy of approximately 1.25 ms. The digitizers will record horizontal and vertical location at 1 Hz, acoustic data at 200 Hz.

Based on previous flights, the payloads will be reusable with limited amount of maintenance. In order to maximize scientific return we propose a second launch of three infrasound boxes on small/medium sized balloons from Esrange in the second half of August when three payloads recovered from the first launch are prepared for a new flight. The Finnish Defence Forces has a two-week annual blast campaign from late August to early September at Hukkakero (Figure 4) to destroy

expired ammunition. Blast weights of the order of ~20 tons of TNT occur once per day. Seismic as well as infrasound detections of these blasts are recorded at all ground stations in the European Arctic [10]. Simultaneous registration on the balloon formation will serve as an excellent case study.

5. All sky camera: Introduction to PMCs

The atmosphere between the ground and the exosphere (at about 400 km altitude) is a huge medium in which waves of different scales can be excited and propagate. Waves play a significant role in the energy budget of the Earth's atmosphere. A prominent role of wave activity is, e.g., that of creating the polar summer mesosphere. This is the region where the temperatures fall to the lowest values of the entire terrestrial atmosphere. The extremely low temperatures (130°K and less) are far from radiative balance. If radiative processes controlled the thermal structure of the mesosphere, one would expect warm summers and cold winters (the polar mesosphere is illuminated by the Sun 24 hours a day in summer and vice versa in winter). However, observations made in the 1950's [20] showed exactly the opposite result: low summer temperatures and warm winter ones. This is a result of dynamical processes due to complex wave activity in the middle atmosphere. The key role in these processes is supposed to belong to gravity wave propagation and breaking. There is also a strong influence of planetary waves on global scales as well as of turbulent eddies of a few meters. This dynamical forcing drives the polar summer mesosphere to around 60° below radiative equilibrium temperatures. This is a very approximate description and even today details of the dynamical forcing are not well known. Study of the wave regime in the middle atmosphere is still in its infancy and is, therefore, the goal of this project.

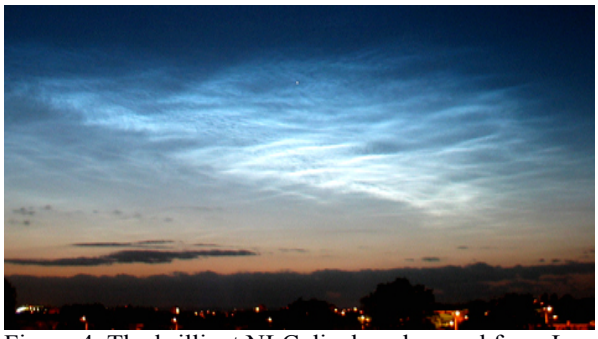

Figure 4. The brilliant NLC display observed from Lund (Sweden) on 16-17 June 2004. Gravity waves of different scales are seen.

Polar Mesospheric Clouds (PMCs) or Noctilucent Clouds (NLCs) (Figure 4) are the highest clouds in the Earth's atmosphere, observed around the summer mesopause of 80-85 km altitude, the coldest place in the atmosphere. These clouds are comprised of small water-ice particles because of the extremely low temperatures in the summer mesopause. These particles scatter sunlight and thus NLCs are readily seen against the dark twilight sky. NLCs are visible during the summer months of each hemisphere, mid-May to late August in the Northern Hemisphere and mid-November to late February in the Southern Hemisphere [9].

At present observations of PMCs/NLCs are carried out both from space [2, 6] and from the ground [5, 7]. Each technique has its advantages and disadvantages. Some types of observations can only be carried out from space and some only from the ground. Satellite-borne instruments make it possible to get an overview of the distribution of PMC fields around the globe in the latitude range of 60°-85° for both hemispheres in summer time. These measurements are not dependent on weather conditions in the troposphere. At the same time, satellites capable of PMCs observations make only about 15 orbits per day around the globe, which implies a very large gap of 900-1500 km between mapped points in the latitude range of 70º-55º, and the spatial resolution is limited to 5 km. Moreover, due to rotation of the Earth sun-synchronous satellites measure PMCs and mesopause environment every 1.5 hours at the same latitude circle, meaning that PMC spatial dynamics cannot be separated from their temporal variability and vice versa.

Ground-based photographic observations of NLCs, on the other hand, are able to give much more detailed information with a spatial resolution of about 100 meters and temporal resolution of minutes and even seconds. However, these observations cover a smaller area and they are limited to nighttime (excepting lidar measurements). Besides, observations from the Earth surface are strictly dependent on weather conditions. Thus, there is no single technique, which is best for obtaining comprehensive information on PMC/NLC characteristics. Satellite observations should be accompanied by ground-based ones and vice versa.

We propose a novel technique to investigate PMCs using an automated all-sky camera pointing at zenith and placed on the top of a balloon, flying between 26 and 30 km altitudes, where the sky is almost black due to significantly decreased Rayleigh scattering of sunlight of the atmosphere. This technique will allow us to register the PMC layer 24 hours a day during summer time, with unprecedented scale-length of about 1700 km. At the same time, due to usage of a high-resolution camera the spatial horizontal resolution of PMC images will be high and compared with that of ground-based NLC observations (~60 m looking at zenith). Since the balloon will be about stationary relative to the ground (flight in August) it will be possible to separate spatial variability of PMCs from their temporal dynamics. A

wide spectrum of waves (gravity waves and tides) propagating through the summer mesopause can be studied by using balloon-top all-sky PMC images.

5.1. Open questions and problems

Under realization of the balloon-top experiment the following questions will be answered:

- What is the characteristic horizontal scale of PMC fields at 60-76°N?
- How much is the temporal dynamics of PMCs important versus their spatial variability?
- How much is the wave activity important in the formation/destruction of PMC fields?
- What is the characteristic gravity wave spectrum at the summer mesopause at 60-76° N?
- How the propagation of the solar thermal tide and mesospheric fronts influence the formation/destruction of PMC fields?

The results of the sub-project will provide quantitative information on characteristic scales of PMC fields, which is important for estimating the total ice budget at the summer mesopause. The wind regime and wave activity (gravity waves and solar tides) will be characterized at sub-polar and polar latitudes 60-76°N. Special emphasis will be addressed to the impact of wave processes on the formation/destruction of PMCs and their dynamics in space and time. It has the potential to significantly advance our understanding of the physics of layered phenomena at the summer mesopause.

Balloon-borne PMC observations will be combined with the ground-based NLC observations conducted at Kiruna (67.8°N). The common-volume balloon-borne/ground-based observations will allow us to estimate the PMC/NLC height hence providing information on their dynamics in 3-D space. Also, balloon-borne optical observations will be analyzed together with the Esrange VHF radar data, which is continuously operating and capable of registering Polar Mesospheric Summer Echoes (PMSE). The common-volume PMC/PMSE observation will provide information on significance of neutral dynamics versus electrically charged ice component. There will be obtained fundamental information on the above-mentioned physical properties of PMC in space and time, which can be further used in modeling of the summer mesopause environment.

5.2. All sky-camera: instrumentation

The balloon-top instrument will be composed of an automated compact light-weight high-resolution camera equipped with a wide-angle (fisheye) lens.

The camera will be powered via a cable going from the main power source (located in the gondola) throughout the balloon to the top. The same technique will be utilized for the data transfer from the camera to the main computer. All these technical aspects have been discussed at the official meeting between IRF scientists and Esrange engineers, who have confirmed principal possibility of the camera operation on the top of balloon.

Detection of greenhouse gases and determination of wind profiles

6. The IVOLGA instrument

Tunable diode laser (TDL) spectroscopy goes back to the 70s and is known for high sensitivity gas analysis in laboratory environment. IVOLGA uses a gas flow guided through a probe cell where the absorption of the laser light can be analyzed and addressed to chemical compounds and their abundances in the gas flow.

The same TDL can be used for laser heterodyne spectroscopy where the probe cell is the entire volume of the atmosphere between the sun and the sensor (occultation geometry) [17, 18].

The Russian Multi-channel Diode Laser Spectrometer (M-DLS) for investigation of the Martian atmosphere is a highly compact, light-weighted, low-power device originally developed for the ExoMars-2020 landing platform.

IVOLGA, a precursor of M-DLS has been designed and developed by the Moscow Institute of Physics and Technology (MIPT). For test purposes it was installed and operated at the institute's rooftop during some weeks in 2016.

IVOLGA measures the Doppler broadening of IR absorption lines of atmospheric CH_4 and CO_2 in the near infrared (NIR) regime around 1.65 μm (~6057 cm^{-1}). Although the tuning range of the laser allows for observation of only these two trace gases, the extremely high spectral resolution of this laser heterodyne technique ($l/dl \approx 10^7 - 10^8$) enables not only vertical profiles of these gases but also wind observations due to Doppler shift of the signatures.

6.1. Background rationale for IVOLGA

- CH_4 and CO_2 are of great importance in the Mars atmosphere. CH_4 is the basic building block of all organic chemistry. 90% of CH_4 on Earth is produced by living organisms. Measuring CH_4 on Mars basically means searching for life on Mars. CO_2 is the key species for a habitable Mars environment.

- A test of IVOLGA on a balloon platform at float altitude 30 km will resemble environmental conditions close to those for the instrument working on a Mars platform (~6 mbar) as is planned for the joined ESA-Russian ExoMars 2020 mission.

Flying IVOLGA will:

- provide a serious technology test for the ExoMars 2020 mission,
- enable IRF to involve into basic planetary atmospheric science on Mars,
- strengthen the scientific collaboration with the highly reputable Russian research institute MIPT,
- build up a strategic co-operation with Russia regarding future balloon missions involving long duration (or even circumpolar) flights over Russia.

• IVOLGA is suitable for any other planetary mission but also suitable to fly on balloon platforms.

• CH_4 has 28 times the Global Warming Potential per molecule (GWP) of CO_2 in Earth's atmosphere. Both are strong drivers for climate change on Earth and continuous observation is needed.

• Remote wind measurements are difficult to perform. With the extremely high resolution of IVOLGA it will be possible to resolve wind speed and direction in the atmosphere

• Since the instrument is light-weighted it will be very suitable as piggy-back payload on a lot of balloon flights in the future.

This instrument needs a gimbal technique allowing tracking the sun during the flight. Such gimbal technique is both a challenge and a strong motivation for SSC/Esrange to develop such technique, even for future balloon flights with similar requirements.

7. SUMMARY

BOOSTER is a balloon flight proposed to fly in the fall of 2018 with four balloons: one main balloon and three smaller ones in formation, which is the first time for Esrange. The balloons will carry four different experiments in the stratosphere for two days. BOOSTER will give insight in atmospheric and magnetospheric physics and also serve as a technology demonstrator for future planetary missions.

8. REFERENCES

1. Abplanalp, D. et al., A neutral gas mass spectrometer to measure the chemical composition of the stratosphere, *Advances in Space Research*, 44(7):870 – 878, 2009.
2. Bailey, M.S., et al., Phase Functions of Polar Mesospheric Cloud Ice as Observed by the CIPS Instrument on the AIM Satellite, *J. Atmos. Solar-Terr. Phys*., 71, 2009.
3. Bowman, D. C. & Lees, J. M., Infrasound in the middle stratosphere measured with a free-flying acoustic array, *GRL* 42, 10, 2015.
4. Bowman, D. C., Infrasound from ground to space, Thesis (Ph.D.)-The University of North Carolina at Chapel Hill, 2016.
5. Dalin, P., et al., Ground-based observations of noctilucent clouds with a northern hemisphere network of automatic digital cameras, *J. Atmos. Solar-Terr. Phys*., 70, 11-12, 1460-1472, doi:10.1016/j.jastp. 2008.04.018, 2008.
6. DeLand, M. T., and G. E. Thomas (2015), Updated PMC trends derived from SBUV data, *J. Geophys. Res. Atmos*., 120, 2140-2166, doi:10.1002/2014JD022253.
7. Fiedler, J., G. Baumgarten, and F.-J. Lübken, NLC observations during one solar cycle above ALOMAR, *J. Atmos. Sol. Terr. Phys*., 71, 424–433, 2009.
8. Funsten, H. et al. (2015), Particle Measurements in Challenging Environments, presentation at MTSSP, Boulder, CO, USA
9. Gadsden, M., and W. Schröder, Noctilucent clouds, 165 pp., Springer-Verlag, New York, 1989.
10. Gibbons, S.J., et al., The European Arctic: A Laboratory for Seismoacoustic Studies, *SRL* 86(3), 917–928, 2015.
11. Liszka, L., Infrasound: a summary of 35 years of infrasound research, number 291 in 'IRF Scientific Reports', 2008.
12. Lundin, R., S. Barabash, and the ASPERA-3 team: ASPERA-3: Analyser of space plasmas and energetic neutral atoms, *ESA SP-1291*, 199-215, 2009.
13. Marcillo, O., et al, Implementation, characterization, and evaluation of an inexpensive low-power low-noise infrasound sensor based on a micromachined differential pressure transducer and a mechanical filter. *JAOT*, 29:1275-1284, 2012.
14. Pilger, C. & Bittner, M., Infrasound from tropospheric sources: Impact on mesopause temperature? *JASTP*, 71, 816-822, 2009.
15. Popecki, M., et al. (2015), Next Generation Microchannel Plates, presentation at MTSSP, Boulder, CO, USA.
16. Rind, D., Heating of the lower thermosphere by the dissipation of acoustic waves. *J. Atmos. Terr. Phys.*, 39, 445-456, 1977.
17. Rodin, A., Klimchuk, A., Nadezhdinskiy, A., Churbanov, D., and Spiridonov, M., High resolution heterodyne spectroscopy of the atmospheric methane NIR absorption, *OSA*, Vol. 22 (11), DOI:10.1364/OE.22.013825, 2014.
18. Rodin, A. V., et.al., M-DLS laser and heterodyne IR spectrometer for studies of the Martian atmosphere from ExoMars-2018 landing platform, Proc. *Of SPIE*, Vol. 96080B-1, 2015.
19. Smets, P.S.M. et al., Probabilistic infrasound propagation using realistic atmospheric perturbations, *GRL*, 42, 6510–6517, 2015.

20. Stroud, W. et al., Rocket-grenade observation of atmospheric heating in the arctic, *J. Geophys. Res*., 64, 1342-1343, 1959.
21. Wescott, J. W., Acoustic detection of high-altitude turbulence. *Technical report*, The University of Michigan, 1964.
22. Wieser, M. et al., The mars environment analogue platform long duration balloon flight. *Advances in Space Research*, 44(3):308 – 312, 2009.

MIRKA2-RX – AN EDUCATIONAL PRECURSOR MISSION FOR A RE-ENTRY BASED CUBESAT MISSION

VISBY, SWEDEN
11-15 JUNE 2017

Martin Siedorf [1,2], M.T. Koller [2], J.P. Baumann [2], A. Behnke [2], J. Franz [2], D. Galla [2], B. Gäßler [2], F. Grabi [2], N. Müller [2], A. Papanikolaou [2], J. Rieser [2], F. Schäfer [2], V. Schöneich [2], H. Seiler [2], V. Starlinger [2], A. Stier [2], A. Tabelander [2], F. Vardar [2], S. Wizemann [2], G. Herdrich [3], A. S. Pagan [3], M. Ehresmann [2, 3], C. Montag [3], R. Laufer [4,5]

[1] University of Stuttgart, Germany, siedorf@ksat-stuttgart.de
[2] Small Satellite Student Society KSat e.V., University of Stuttgart, Germany, contact@ksat-stuttgart.de
[3] Institute for Space Systems, University of Stuttgart, Germany, herdrich@irs.uni-stuttgart.de
[4] Space Lab, University of Cape Town, South Africa, rene.laufer@uct.ac.za
[5] CASPER, Baylor University, USA, rene_laufer@baylor.edu

ABSTRACT

The paper presents the results of the experiment MIRKA2-RX (Micro Return Capsule 2 REXUS). The experiment is a precursor mission to the CubeSat project CubeSat Atmospheric Probe for Education (CAPE) and was launched in March 2016 with the sounding rocket REXUS 19 in Sweden. The Micro Return Capsule 2 (MIRKA2) was ejected at the apogee of the rocket's trajectory. A mirror system of the capsules electronic remained in the rocket and collected additional sensor data. The experiment qualified the separation mechanism LOTUS (Low Orbit Technical Unit Separator), the aerodynamic behaviour, and the electronics of the capsule during its flight in micro gravity and subsequent return. Additionally, the results of the follow-up missions MIRKA2-HyEnd and MIRKA2-ICV are explained and discussed. These experiments are built, designed and constructed by students from the University of Stuttgart and members of KSat, in collaboration with the Institute of Space Systems (IRS).

1. INTRODUCTION

CubeSats, i.e. pico and nano satellites, became an easy and cost-efficient platform for spaceflight technology demonstrations and scientific purposes [1]. Additionally, the short duration of such a project allows students to participate in project and development cycles and gain hands-on spacecraft engineering experience.

Atmospheric entry is an important aspect of many space missions. Numerical simulations and tests in plasma wind tunnels are partial qualification methods. But do not allow to obtain full flight qualification.

Therefore, the Institute of Space Systems (IRS) initiated the CubeSat Atmospheric Probe for Education (CAPE) project [2, 3]. The project is supported by the Small Satellite Student Society of the University of Stuttgart (KSat e.V.). CAPE is a platform for CubeSat experiments and electric propulsion and for qualification and testing of experimental heat shield materials. The CubeSat consists of two main modules. The Service and Deorbit Module (SDM) [4] equipped with a pulsed plasma thruster will provide orbit control. Thereby, secondary experiments can be performed. The second module is the Micro Return Capsule (MIRKA2), which will be separated from the SDM at about 120 km altitude above ground. The capsule will perform an atmospheric entry and during it record data about the quality and performance of the heat shield material. All data needs to be transferred to the Iridium Satellite Constellation before demising in the ocean. The SDM will demise during re-entry. The mission scenario is shown in Fig. 1.

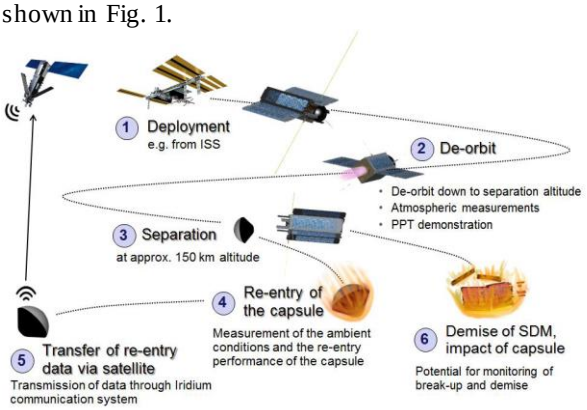

Figure 1: Mission Scenario of CAPE

One big step towards the CAPE mission was achieved by participating in the Rocket and Balloon Experiments for University Students program (REXUS/BEXUS) [5] of the German Aerospace Centre (DLR) and the Swedish National Space Board (SNSB). The precursor project was the Micro Re-entry Capsule 2 – REXUS

(MIRKA2-RX) [6]. It aimed for increasing the technical readiness level (TRL) of the separation system and the capsule components and overall setup. The integrated capsule is attached to the separation mechanism during launch and ejected at the apogee of the rocket's trajectory. The capsule will transmit recorded data to the Iridium network after the ejection. A mirror system of the capsule's electronics remains on the rocket and transmits its recorded data via a communication emulator to the onboard computing Unit (OBU). After return of the module and the capsule, both are to be recovered. The mission scenario with event times is shown in Fig. 2.

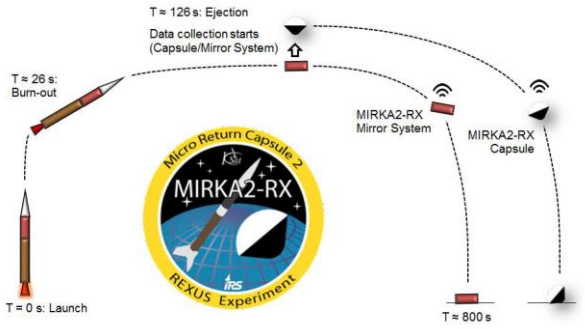

Figure 2: Mission Scenario MIRKA2-RX

The mission objectives were:

Primary

- Qualification of the separation system for a miniaturized capsule in a micro gravity environment
- Qualification of the electronic system of the capsule
- Qualification of the Iridium communication link

Secondary

- Acquisition of scientific data for aerodynamic behaviour of the capsule
- Recovery of the capsule

2. EXPERIMENT SETUP

The setup of the experiment is placed in one REXUS module and consists of three main parts. The separation mechanism with its holding construction, the capsule itself and the electronics box behind it. The arrangement of the components is shown in Fig. 3.

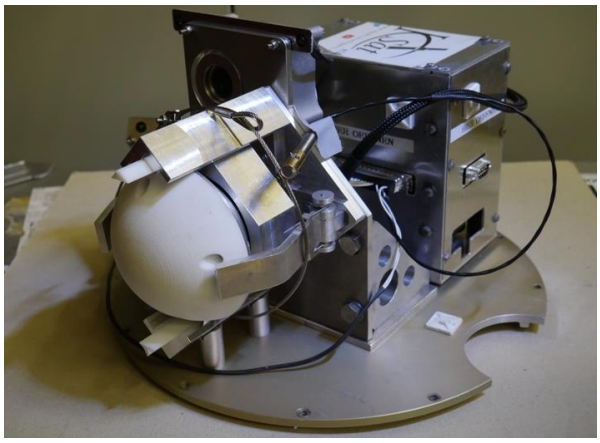

Figure 3: MIRKA2-RX setup

2.1. Separation Mechanism

The separation mechanism developed for this mission is called Low Orbit Technical Unit Separator, or LOTUS [7]. Its purpose is secure the capsule during the launch and maintain deactivation. Securing the capsule is achieved with two clamps, pushing the capsule into the carrier. The clamps are held together by a wire, going around the construction. At predetermined time, the pyrocutter board sends a signal to cut the wire via a pyrocutter. The spring-loaded clamps open and the carrier pushes the capsule with its four springs along the two guide rails out of the construction. The carriage accelerates the capsule up to a calculated speed, but is held back by a stopper in the construction. The process is illustrated in Fig. 4.

The capsule deactivation during the launch and first mission phase is achieved by a pin, going inside the capsule and pushing a deactivation button. The pin is pulled during the separation and activates the capsule.

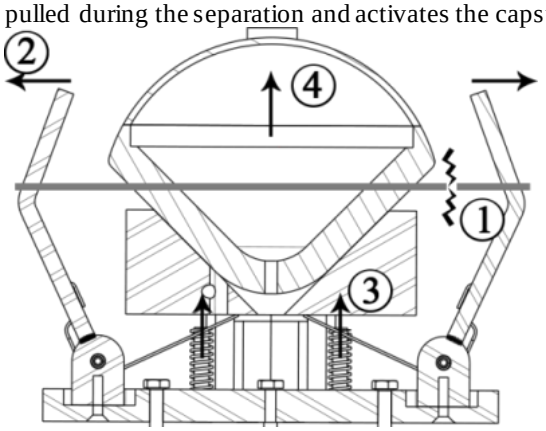

Figure 4: Separation process of LOTUS

2.2. Capsule

The capsules consist of a carbon fibre heat shield dummy, as the expected temperatures are significantly lower than during an actual atmospheric entry. At the back shell a Wound Highly Porous Oxide Ceramic Matrix Composite (WHIPOX), developed by the DLR [8] is utilized to enable data transfer from the capsule

inside to an Iridium constellation satellite. The capsule is equipped with two four-layer PCB's with three separate microcontrollers, the Iridium transmitter and the GPS module [9]. Additional sensors, such as pressure sensors, an IMU, a thermopile sensor and thermocouples are placed inside to assess the state of the capsule and its environment. The system is powered by high energy density batteries. The detailed assembly is shown in Fig. 5.

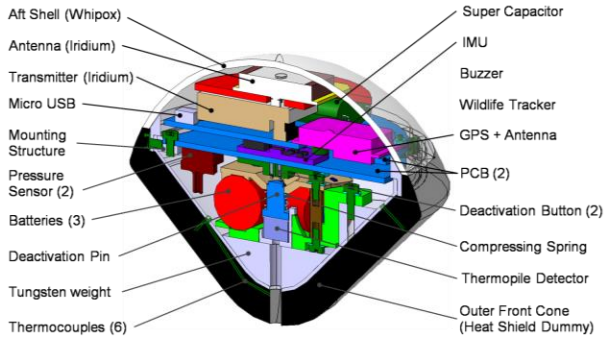

Figure 5: Capsule components

2.3. Electronic Box

The electronic box is placed behind the separation mechanism as seen in Fig. 3 and houses the mirror system of the capsule's electronics, the on-board computing unit (OCU) and the pyrocutter board.
The OCU handles the triggering of the pyrocutters and controls the video cameras. One of the two cameras has a live TV link to the ground station. The two pyrocutter for the hatch are activated by the service module of the rocket directly. The third pyrocutter of LOTUS is activated by the charged stored in the capacitors from the pyrocutter board and triggered by the OCU.
The mirror system of the capsule is a full duplicate of capsule's electronics, with exception of the Iridium transmitter, which is replaced by an emulator. The transmitted data is additionally stored on an on-board SD memory card.

3. MINATURIZATION

The big challenge for the project was the small size constraints of the capsule, which severely limits the component choice and related available performance. The capsule and the separation mechanism needs to fit inside one CubeSat Unit of 10 x 10 x 10 cm^3. LOTUS uses a spring and clamp system, which was especially custom tailored to fit these constraints. Although cutbacks on redundancy were necessary in comparison to the initial design. The structure of the capsule itself could be utilized, because some parts could be produced as integrated components.
The fitting of the capsule electronic and sensory system was challenging, but finally achieved by custom-designed printed circuit boards. Most of the components are commercial of the shelf (COTS) to fit the cost constraints and are mostly not space qualified.

4. RESULTS

The launch of REXUS 19 with the MIRKA2-RX experiment was conducted on March 18th, 2016 at 05:10:00 UTC. With good weather conditions and a nominal launch procedure, the experiment modules were recovered and the stored data could be analysed [10, 11].
The capsule did not collect data during the free fall phase, as activation during the ejection was not achieved. After the impact of the capsule on the snowy ground in Kiruna, Sweden the activation was triggered due to inertia of the deactivation button. After this, GPS position and other data were sent and the capsule was subsequently recovered.

4.1. LOTUS Data

The separation of the hatch before de-spin of the rocket was successful. The ejection of the capsule was performed nominally. From video footage, an ejection velocity of 0.775 m/s was calculated [12, 13]. A superimposed image of the capsule ejection is shown in Fig. 6. The ejection mechanism did not produce a measurable rotation on the capsule.

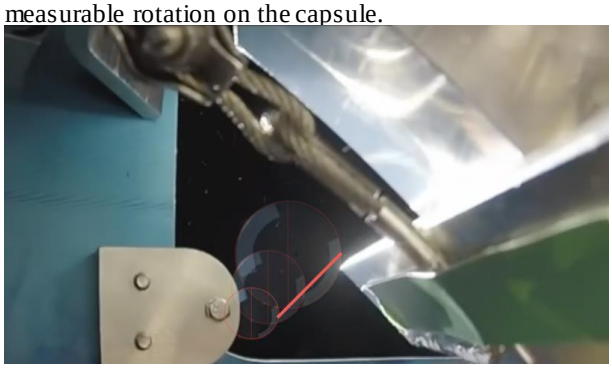
Figure 6: Capsule ejection, superimposed images

4.2. Capsule Data

The capsule electronics did not suffer visible damage, from launch loads, ejection and finally the impact in soft snow. According to the impact whole in the snow, the capsule did fall almost vertically and had a tilt angle of about 2°.
During the free fall of the capsule, the deactivation button was jammed and the capsule remained passive. The system activated during impact in the snow and jerk on the deactivation mechanism inside the capsule. This resulted in no measured data during the free fall phase. The gathered data of the capsule and the mirror system over the complete mission are visualized in Fig. 7.

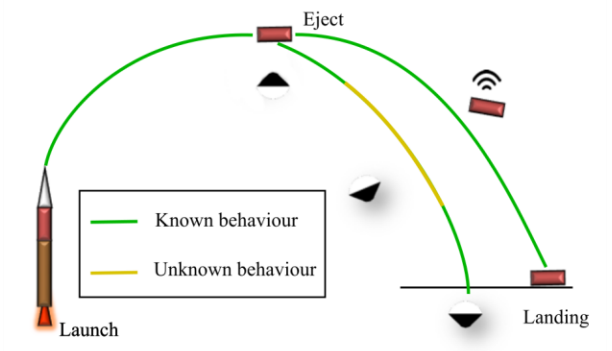

Figure 7: Known behaviour of MIRKA2-RX

Nevertheless, the capsule communication system was able to transmit 64 messages via the Iridium network after activation. The run-time during these messages was about 30 min, before the transmitting stopped due to lack of power.

The on-board protocol showed 67 transmitted short burst data (SBD) messages. The three missing messages were probably neglected due to bad satellite connections. A missing message due to problems in the satellite network itself are neglected due to the high reliability of the inter satellite communication.

With the size of one SBD message with 340 Bytes, the data rate can be calculated. The plot is shown in Fig. 8. The average data rate is 14 b/s with a maximum at 42 b/s and 5 b/s as minimum.

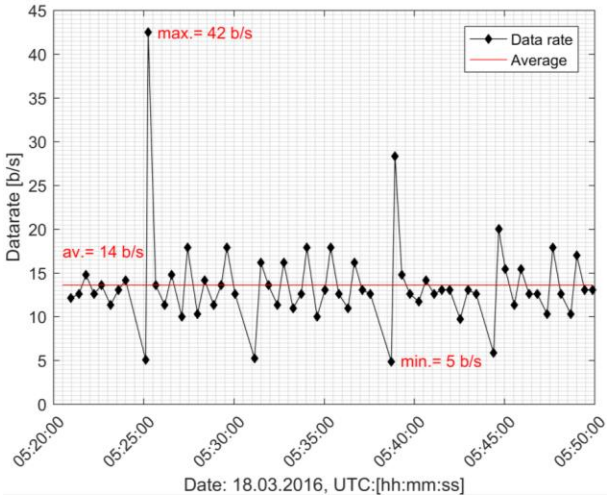

Figure 8: Capsule transmission rate

The battery voltage was measured by the voltage controller and is shown in Fig. 9. During the first 19 minutes, a constant degradation of voltage is, as expected, observed. After this time, a sharp voltage drop and high fluctuations occur. The measurements after message 44 must be assessed with reservations, as the voltage drops below 3.3 V. By this the output voltage of the microcontrollers is not guaranteed and sensor supply might be insufficient. This point can also be seen in the differing on-board times between each microcontroller. As one of them shows a slightly lower run-time duration.

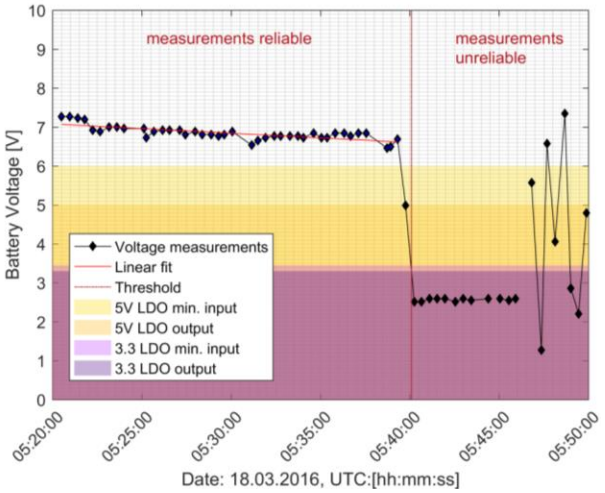

Figure 9: Capsule battery voltage over time

The cause of the dropped voltage was the low voltage supplied by the batteries, the high discharge current for transmission and the low temperature environment. The internal temperatures are plotted over the time in Fig. 10. The thermocouples 1 - 5 are placed on and within the heat shield dummy. Thermocouple 6 is placed below the WHIPOX back shell. The outside structure adopted a temperature between -16°C to -19°C due to the free fall. The temperature graph shows a logarithmic rise, which is in accordance with thermodynamic expectations. Thermocouple 6 had a temperature of 8°C at begin of the measurement.

The Temperature of the boards stayed at approximately -5°C to +2°C. The waste heat of the microcontroller was thermally distributed by the boards with its almost 2 complete copper layers. Concluding from Fig. 10, no strong influence from the structural temperature on the electrical system is seen.

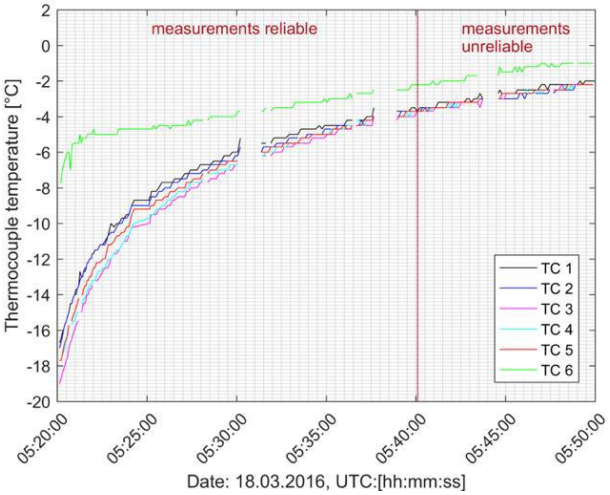

Figure 10: Thermocouple temperature over time

4.3. Mirror System Data

The mirror system was started with the ejection of the capsule at the apogee. The following data shows different data sets than the capsule data due to the different trajectory and movement of the sounding rocket module.

Fig. 11 shows the analog pressure sensor data over the height together with the altitude of the rocket and the calculated pressure, using the ICAO 1976 International Standard Atmosphere model [14]. The maximum pressure of the sensor at 18 km altitude is a fragment of the sensors effective pressure range.

The IMU roll rate data are plotted in Fig. 12 together with the attitude and the roll rate of the REXUS 19 IMU sensor. Both graphs of the roll rate are mostly in agreement with each other.

The gaps in the sensor data in the mirror system appear due to the simulated satellite connection and the thereby low data sampling frequency of 24 seconds.

The self-calibration of the IMU at activation during microgravity was an uncertain factor, but the magnetorquer calibrated correctly and the resulting sensor quality is acceptable.

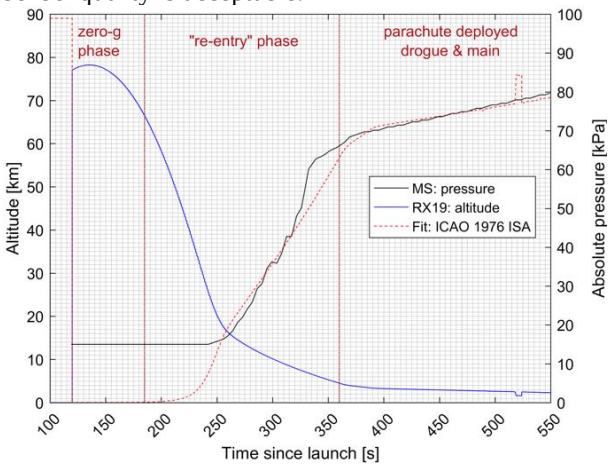

Figure 11: Analog pressure sensor data

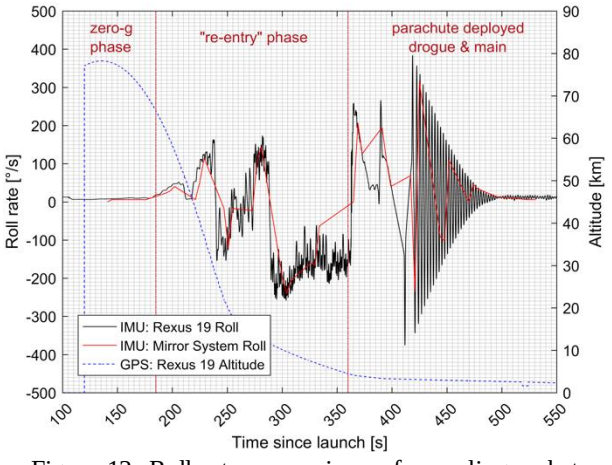

Figure 12: Roll rate comparison of sounding rocket module and MIRKA2-RX mirror system

5. SUCCESSOR MISSIONS

5.1. MIRKA2-HyEnD

The project MIRKA2-HyEnD was a collaboration of KSat and the Hybrid Engine Development (HyEnD) student team at the University of Stuttgart. HyEnD developed and built the two sounding rockets HEROS II and HEROS III, as part of the Student Experimental Rockets (STERN) program of the DLR.

The capsule electronics were flown with HEROS III and tested during ultrasonic flight conditions. The electronics of the capsule were improved with a new GPS receiver.

The launch of the rocket HEROS III was conducted in November 2016. The flight of HEROS III was successful and the IMU and GPS output of the capsule could be validated by comparison with the rocket measurements. The recorded Global Navigation Satellite System (GNSS) data for GPS are plotted in Fig. 13.

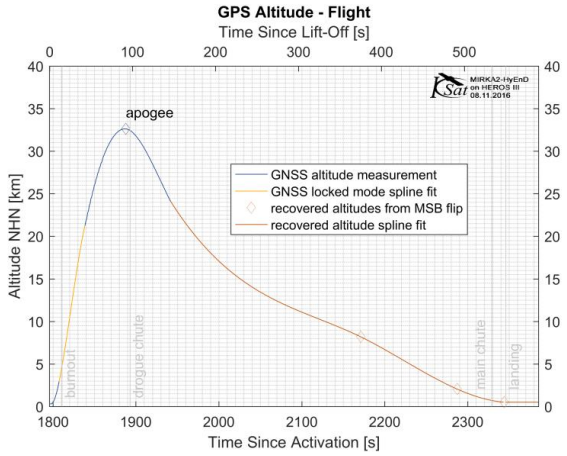

Figure 13: GPS data of HEROS III by the capsule electronics

The activation of the system was secured by manual trigger prior to lift-off. The Iridium transmission stopped before the launch, about four minutes after activation. Therefore, no in-flight Iridium communications verification was achieved during this mission. Post mission analysis concluded that it is likely that the transmitter picked up radio frequency interference or an electromagnetic distortion and self-deactivated on that account. A retry of the communication initialization after a single time failure has been not yet implemented and led to a termination of transmission attempt.

The power was supplied by the HEROS III rocket electrical system and made a five-hour runtime possible until manual deactivation.

The experiment data from the SD memory show that the GPS performance is suitable for future missions. The thermocouple data is considered useless, due to integration errors.

5.2. MIRKA2-ICV

The project MIRKA2-ICV (In-flight Communication Verification) aims to remove the knowledge gap of in-flight capsule transmission performance left open from previous missions. The project is a communication experiment of IRS and KSat e.V. in collaboration with a high-altitude balloon experiment from the SpaceLab of the University of Cape Town in South Africa.
The mission scenario was to launch a weather balloon with the capsule mounted on the lower side of the payload compartment. At approximately 20 – 25 km altitude, the MIRKA2 capsule would be separated and during free fall, recorded data would be sent to the Iridium network.
The balloon was launched on 21st July 2017 in South Africa. The sent messages stopped after three received SBD messages and further post-flight analysis will be done after the recovery of the balloon module.
For this mission, the design of the MIRKA2-RX electronics was further improved. The capsule contained only one microcontroller with now higher performance to simplify the electronics boards. The arrangement of the sensors was identical. Heat shield dummy material were aluminium alloy in order to enable simple manufacturing and lower the production costs. The back shell was made from 3D-printed polyamide with similar characteristics as WHIPOX concerning the transmission of communication frequencies.
The separation mechanism LOTUS was replaced by a simple holding mechanism with one wire going through the back shell of the capsule. The wire should be cut by a burning wire and gravity would accelerate the capsule towards the ground. This mechanism is not planned to be utilized during the CAPE mission as it is unsuitable for use in micro-gravity.
The deactivation mechanism of MIRKA2-RX is replaced by two pads placed on the outside of the back shell. The pads will have electrical contact with two spring pins in the holding mechanism. The MIRKA2-ICV capsule and the DokPot for programming are shown in Fig. 14.

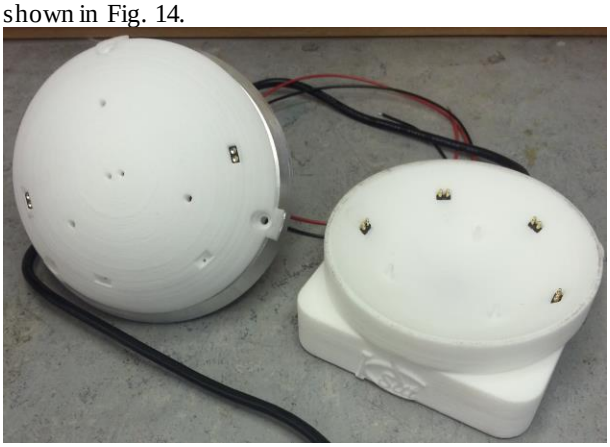

Figure 14: MIRKA2-ICV capsule and DokPot

The deactivation pins are short-circuited and the capsule is thereby deactivated. Additionally, six more pads are attached on the outside of the back shell, to provide a software interface with the microcontroller and external power supply. The interface allows software changes on the fully integrated capsule. Additionally, the interface makes late access to the software of the microcontroller possible and provides access during the launch to the data of the capsule without a satellite connection.

6. QUALIFICATION FOR CAPE

Separation mechanism
The separation mechanism LOTUS withstood the vibration loads of the rocket during launch and ejected the capsule as planned. However, the ejection velocity was smaller than expected, which is critical to the mission scenario for CAPE, as the re-entry parameters of the MIRKA2 capsule are dependent. With the lower separation velocity of the capsule, the re-entry angle will be lower, the re-entry time higher and with this the integral heat loads will increase, which might exceed thermal limitations of electronic components.
An improvement of the separation mechanism ejection velocity should be considered. Nonetheless, the LOTUS prototype in its current state is considered as qualified. Furthermore, the pyrocutter and the related pyrocutter board worked as planned and can be seen as qualified.

Activation
The activation during the ejection process of the MIRKA2-RX flight did not trigger. Analysis after capsule recovery have concluded that the deactivation button was jammed.
The design configuration is therefore unsuitable for the CAPE mission.
The activation method of MIRKA2-ICV proved more viable during ground tests but the in-flight activation is still on-going analysis. The results will be discussed in a follow-up publication.

Power supply
The capsule sent data for almost 30 minutes enabled reliable measurements for 20 minutes before the link to the satellite network was lost.
The planned re-entry phase for CAPE will take 45 minutes maximum but the capsule will not transmit messages during the full duration. The power supply system is therefore seen as qualified.

Thermocouples
During the MIRKA2-RX mission several thermocouples produced reasonable temperature data sets for several points inside the capsule. The different temperature rises of the heat shield dummy temperature to the WHIPOX temperature indicate correct behaviour due to the different thermal characteristics.
This shows the capability of MIRKA2 to record temperature with the implemented thermocouple setup.

Pressure sensor
The pressure sensor on MIRKA2-RX and MIRKA2-HyEnD provided additional pressure data for both trajectories. Due to the expected stagnation point pressure, the sensor will be changed for the CAPE mission to gain better pressure resolution during lower altitude of the capsules trajectory.

IMU
The IMU data gathered during MIRKA2-RX is acceptable in comparison to the sounding rocket reference IMU data. For a complete qualification in micro-gravity, a higher sampling rate needs to be utilized, to improvement the movement behaviour analysis.

Data transmission
The communication of the Iridium module with the satellite network has been demonstrated to be able to operate during slow movements or still positions on ground level, when an Iridium satellite is visible.
The low sampling rate is software defined to accommodate the low bandwidth associated with the Iridium transmitter. Additionally, a compression algorithm was not used in either of the missions and needs to be implemented to gain a higher effective data rate.
Successful free flight data transmission was not yet demonstrated with the missions MIRKA2-RX, MIRKA2-HyEnD and MIRKA-ICV.

7. CONCLUSION

During the MIRKA2-RX project several subsystems for CAPE were tested and critical design aspects were shown to be suitable designed. The separation mechanism LOTUS, the pyrocutter board and the mirror system of the capsule were successfully tested and were operated nominally. The electronics of the capsule performed nominally, even though the activation did not occur with the ejection.
During MIRKA2-HyEnD new electronic components were tested in ultrasonic flight and increased the technical readiness level of multiple components, beside the communication method.
During the MIRKA2-ICV project, a new activation method was developed and the electrical system of the capsule was simplified. A simple holding mechanism for balloon release missions was tested and can be utilized for further balloon projects.
Moreover, the missions were a great success concerning the educational aspect and the collaborations with other student groups, universities and industry partners.

8. ACKNOWLEDGEMENTS

The team of the experiments and the authors would like to thank SNSB and DLR for the Opportunity and the support of MIRKA2-RX, which was made possible due to the REXUS Program. Members of the Institute of Space Systems (IRS) of the University Stuttgart and Thales Alenia Germany supported the development, the design process and the qualification.
We also would like to thank the STERN team and the HyEnD group for the additional rocket launch in the MIRKA2-HyEnD project.
Furthermore, we thank the team from the University of Cape Town for the cooperation and the support in the MIRKA2-ICV project.
Several key components were made available, thanks to the following supporters: DLR Stuttgart – head shield dummy, DLR Cologne – WHIPOX cap, NamTrack – Tracking beacon, Multiband Antennas – Iridium Components, Laser Components – Thermopile, CadSoft – EAGLE.

9. REFERENCES

1. Heidt, H., Puig-Suari, J., Moore, A., Nakasuka, S., & Twiggs, R. (2000). A new Generation of Picosatellite for Education and Industry Low-Cost Space Experimentation. In AIAA/USU Small Satellite Conference Proceedings V-5.
2. Ehresmann, M., Pagan, A. S., Herdrich, G., Laufer, R., Galla, D., Franz, J., Friedrich, L., Gäßler, B., Grabi, F., Schöneich V., Hießl, R., Koller, M.T., Kumpf, P., Müller, N., Papanikoloau, A., Rieser, J., Schäfer, F., Seiler, H., Siedorf, M., Starlinger, V., Stier, A., Tabelander, A., Wizemann, S., Vardar, F., (2015). CubeSat-sized Re-entry Capsule MIRKA2. In 10th IAA Symposium on Small Satellites for Earth Observation, Berlin.
3. Pagan A.S., Herdrich G., Laufer R., J.-P., Behnke, A., Belser, V., Ehresmann, M., Galla, D., Franz, J., Friedrich, L., Gäßler, B., Grabi, F., Schöneich V., Hießl, R., Koller, M.T., Kumpf, P., Müller, N., Papanikoloau, A., Rieser, J., Schäfer, F., Seiler, H., Siedorf, M., Starlinger, V., Stier, A., Tabelander, A., Wizemann, S., Vardar, F. (2015). Cubesat Atmospheric Probe for Education (CAPE). In 10th IAA Symposium on Small Satellites for Earth Observation, Berlin.
4. Schöneich V., Pagan, A. S., Herdrich, G., Laufer, R., Baumann, J.-P., Behnke, A., Belser, V., Ehresmann, M., Galla, D., Franz, J., Friedrich, L., Gäßler, B., Grabi, F., Hießl, R., Koller, M.T., Kumpf, P., Müller, N., Papanikoloau, A., Rieser, J., Schäfer, F., Seiler, H., Siedorf, M., Starlinger, V., Stier, A., Tabelander, A., Wizemann, S., Vardar, F. (2015). Service and Deorbit Module for CubeSat Applications. In 10th IAA Symposium on Small Satellites for Earth Observation.
5. Schmidt, A. (December 2014). REXUS User Manual, EuroLaunch, Version 7.11.
6. Galla, D., Baumann, J.-P., Behnke, A., Belser, V., Ehresmann, M., Franz, J., Friedrich, L., Gäßler, B., Grabi, F., Hießl, R., Koller, M.T., Kumpf, P., Müller, N., Papanikoloau, A., Rieser, J., Schäfer, F., Schöneich, V., Seiler, H., Siedorf, M., Stier, A., Tabelander, A., Wizemann, S., Vardar, F., (June 2016). Student Exchange Documentation MIRKA2-RX. Version 5.
7. Siedorf, M. (2016). Design, construction and test of the low orbit technical unit separator LOTUS. Bachelor thesis IRS-16-S-012 Institute of Space Systems, University of Stuttgart, Stuttgart.
8. Göring J., Hackemann S., Kanka B., WHIPOX®: Ein faserverstärkter oxidkeramischer Werkstoff für Hochtemperatur-Langzeitanwendungen, Mat.-wiss. u. Werkstofftechnik page 28, 2007, doi:10.1002/mawe.200700191
9. Koller M. T. (2015). Development of the electronic system for the MIRKA2 micro return capsule. Bachelor thesis IRS-15-S-077, Institute of Space Systems, University of Stuttgart, Stuttgart.
10. Ehresmann, M., Pagan, A. S., Montag, C., Herdrich, G., Laufer, R., Baumann, J.-P., Behnke, A., Belser, V., Ehresmann, M., Franz, J., Friedrich, L., Gäßler, B., Grabi, F., Hießl, R., Koller, M.T., Kumpf, P., Müller, N., Papanikoloau, A., Rieser, J., Schäfer, F., Schöneich, V., Seiler, H., Siedorf, M., Stier, A., Tabelander, A., Wizemann, S., Vardar, F., (2016). Micro return capsule 2 – Rexus Experiment Results. In 4S Symposium, Malta.
11. Galla, D., Pagan, A. S., Montag, C., Herdrich, G., Laufer, R., Starlinger, V., Baumann, J.-P., Behnke, A., Belser, V., Ehresmann, M., Franz, J., Friedrich, L., Gäßler, B., Grabi, F., Hießl, R., Koller, M.T., Kumpf, P., Müller, N., Papanikoloau, A., Rieser, J., Schäfer, F., Schöneich, V., Seiler, H., Siedorf, M., Stier, A., Tabelander, A., Wizemann, S., Vardar, F. (2016). MIRKA2-RX – a REXUS Flight Experiment in Preparation for the Atmospheric Entry CubeSat Mission CAPE. In 7th Nano Satellite Conference, Bulgaria.
12. KSat e.V., MIRKA2-RX Capsule Ejection 1. Video, 2016, Link: https://www.youtube.com/watch?v=V7-P_HCwBiw
13. KSat e.V., MIRKA2-RX Capsule Ejection 2. Video, 2016 Link: https://www.youtube.com/watch?v=idRL7uG6_LU
14. ICAO, 1976 International Standard Atmosphere, International Civil Aviation Organization, 1976.

REXUS19 - LIME (LINK MADE EARLY) - INVESTIGATION OF AN ATTITUDE-DEPENDENT SATELLITE COMMUNICATION SCHEME

Severin Haas[1], Hannes Zöllner[1], Stefan Biereigel[1], Wolfgang Büttner[1], Gabriel Buchard[1], Tobias Eickhölter[1], Andreas Koch[1], René Krummel[1], Eric Langner[1], Fabian Lami[1], Jan Maass[1], Julian B. Oberender[1], Robert Plumbaum[1], Carlo Spanke[1], Patrick Theis[1], and Sebastian Weiss[1]

[1] *University of Applied Science Jena, Germany*

ABSTRACT

Small satellites – such as CubeSats – impose strict mass and mechanical constraints on attitude control systems. Especially in the early phases of their mission, communications can be a difficult because of the slowly damped rotation of such satellites. The LiME experiment proposes a dynamic scheme for the communication of CubeSats - based on current satellite attitude. Satellites could use simple directional antennas and only transmit with high data rates while the main lobes are pointing towards their ground station. This scheme may help to improve data throughput and link stability in early mission phases. If transmissions are disabled when the satellite antennas do not point to a ground station, reduced power consumption can be achieved, which is also a critical budget constraint for small satellites.

Key words: LiME, REXUS/BEXUS, CubeSat, attitude determination.

1. INTRODUCTION

The LiME-experiment was built by a team of young engineering students from the University of Applied Science Jena, Germany.
The experiment was tested during the flight of REXUS19, which was launched from the Esrange Space Center, located near the city of Kiruna, Sweden.
The REXUS/BEXUS (**R**ocket/**B**alloon **E**xperiments for **U**niversity **S**tudents) programme is realized under a bilateral Agency Agreement between the German Aerospace Center (DLR) and the Swedish National Space Board (SNSB). The Swedish share of the payload has been made available to students from other European countries through a collaboration with the European Space Agency (ESA).
EuroLaunch, a cooperation between the Esrange Space Center of SSC and the Mobile Rocket Base (MORABA) of DLR, is responsible for the campaign management and operations of the launch vehicles. Experts from DLR, SSC, ZARM and ESA provide technical support to the student teams throughout the project.

1.1. Experiment scheme

The general experiment idea was to analyze the conditions and behaviour of small satellites after ejection from their launcher platform. To achieve this goal, a platform capable of attitude determination on small PCBs, which were to be ejected from a REXUS rocket was developed. These small PCBs (referred to as FFUs – Free Falling Units – from now on) try to model satellites after ejection from a launcher and therefore also implement the basic communication subsystems needed. The measurements taken by the attitude determination sensors were transmitted to the ground station. The Rocket Module serves as a carrier for the FFUs until ejection and provides the possibility to record and store transmissions from the FFUs as it is in direct proximity during the flight. The ground station tries to represent a typical CubeSat ground station, being capable to receive, analyze, visualize and store received data. The FFUs were ejected following de-spin of the rocket. The small remaining body rates of the rocket were analyzed and decided to be representative of usual CubeSat deployments.
The developed experiment scheme can be seen in figure 1. As soon as ejection has happened, the FFUs constantly take sensor measurements, do necessary pre-processing and transmit them to the ground station.

2. EXPERIMENT DESIGN

The experiment setup is outlined in figure 2. The experiment consists of several individual smaller experiment components like an ejection mechanism, the FFU electronics and software as well as the ground station. The different parts of the experiment are outlined in the following sections and their design is described afterwards.

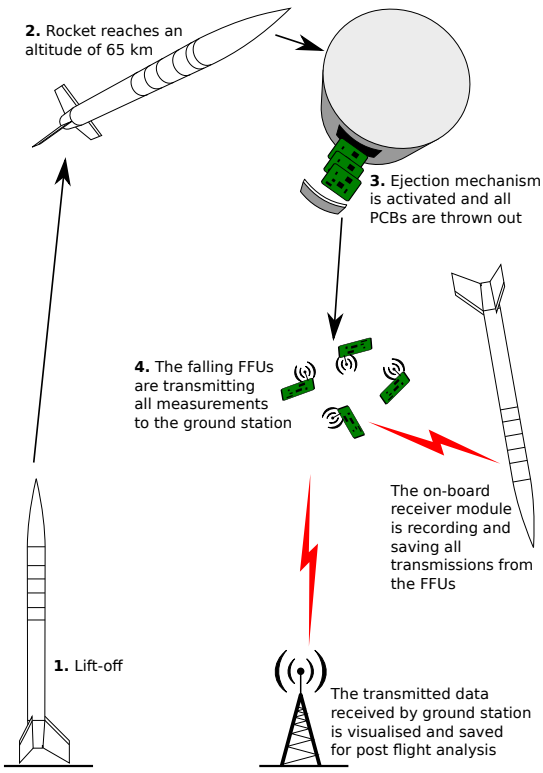

Figure 1. Experiment scheme

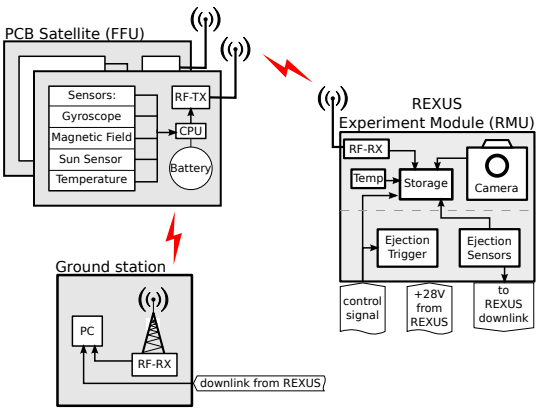

Figure 2. LiME experiment block diagram

2.1. Free-falling units

The satellite models, which are the main experiment payload were named FFU. They were designed to be good physical models for small CubeSats after ejection into space, having similar size and mass properties. From an electronics point of view, they are small embedded systems comprised of the various subsystems a satellite has to include on board. Each is equipped with a transmitter for downlink telemetry and payload information, an inertial measurement unit (IMU) for ongoing determination of satellite attitude and a microprocessor for controlling all operations on-board. Four FFUs were used to gather sufficient (statistically representable) data from their transmissions. After the mission, the FFUs were not recovered. The environmental impact is estimated to be unproblematic.

2.1.1. Sensors

The FFU includes three types of sensors for the IMU (attitude determination): Magnet field sensors, sun sensors and gyroscopes. Magnet field and gyroscope sensors are MEMS types, which makes them very power efficient and small. For the sun sensors, six commercial photo diodes were used together with an analog front-end measuring the photoelectric current. The magnet field sensors, which are sensing earths magnetic field, and the sun sensors, which measure the incidence angle of the sun, are used for constant attitude determination. The gyroscope was used for improvement of the measurements. The photoelectric currents from the sun sensors are converted to voltages by operational amplifiers and digitized by the microcontroller AD-converter. The MEMS sensors are connected via dedicated SPI interfaces to the microcontroller.

2.1.2. Transmitter and antenna

The RF transmitter unit is comprised of a stable reference frequency oscillator, a PLL and a VCO to transmit in the 13 cm amateur radio band. The PLL divider register is used for digital frequency modulation of the carrier from the microcontroller. The output of the transmitter is amplified by MMIC amplifiers to 100 mW (20 dBm) and fed to the antenna.
The antenna was implemented directly onto the PCB. A HB9CV antenna design was chosed to be implemented, which gives a very good forward/backward radiation relation and can achieve a gain of up to 6 dBi in the forward direction. To increase the usable transmission angle deviation, it also gives a relatively big 3 dB-width of at least 70° in every cutting plane.

2.1.3. Rocket control unit

The rocket control unit (RCU) is the main controlling and interfacing unit in the rocket module. It houses the control logic and is responsible for all communication handling inside the rocket module and the communication link to the ground station provided by the REXUS service module. Using the RCU it was possible to talk to all four FFUs before launch and read telemetry such as battery voltages and temperatures from them. The RCU was also used to trigger the camera recording, which was supposed to film the rocket launch, and the on board SDR to record all telemetry sent out by the FFUs directly from the rocket.

2.2. Ejection mechanism

For the LiME experiment a special ejection mechanism (see figure 3) was developed to fulfil the required functionality.
The FFU PCBs were screwed to gliding blocks (see figure 4). The gliding blocks are guided by the gliding rods and trenches. Springs between the gliding block and the rod mount push the notch of the gliding block towards the nose of the hatch. The hatch cover is held back by a retaining rope. It is a single rope with crimped threads on both sides and screws at the ends of the rope are used to adjust the rope force. To eject the FFUs, a pyrocutter cuts through the retaining rope. For reliability reason two pyrocutters were used to cut the rope. As soon the rope has been cut, the hatches and the FFUs are free to move. Due to the force of the springs, the gliding blocks are moving on the gliding rods and are ejected from the rocket module.

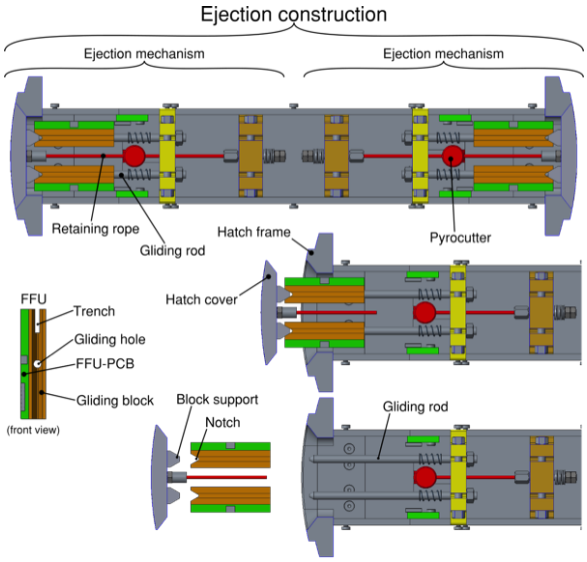

Figure 3. Ejection mechanism description

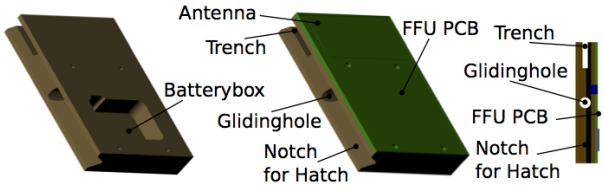

Figure 4. FFUs gliding block side view

2.3. Ground station

Initially the team assembled their own ground station, to record the RF transmissions from the FFUs. It consisted of a bladeRF SDR with an additional LNA working in the 13 cm amateur radio band and a helical antenna. The filter and the LNA were installed directly next to the antenna in a weather-proof box to keep system noise figure low. A long low-loss coax cable leads to the ground station.
During the launch the team was additionally able to use one receiver provided by DLR MORABA connected to their S-band tracking antenna. The flight trajectory of the rocket closely matched the FFUs trajectories after ejection for the important experiment duration, which is why the antenna could be used.

3. RESULTS

The experiment as a whole worked as specified with only the camera staying inoperative during the entire flight. No deviations between planned and actual/recorded sequence of events could be noticed. Team SLED provided their video recordings to us, so the FFU separation (figure 5) could be analyzed successfully. A video clip of the ejection is published at [1]. During the flight, every part of the IMU delivered data as planned.

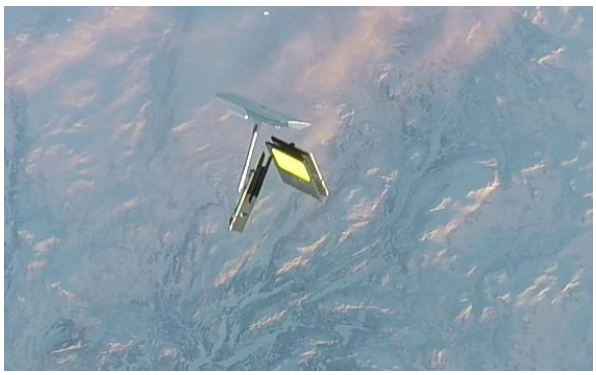

Figure 5. Separation of two FFUs with hatch above them

To gather all sensor data for further analysis, the

raw data was sent to the ground station, no attitude determination was done onboard the FFUs. The data fusion and actual attitude determination was done post-flight and correlated with the signal strength. It showed that the received signal strength fluctuation remained in close correlation with the attitude measurement of each FFU throughout the flight, the results of which can be seen in figure 6. The rotation rate of the FFUs could be measured to approximately equal 0.6 Hz, which is also a typical value for CubeSats after deployment. From the

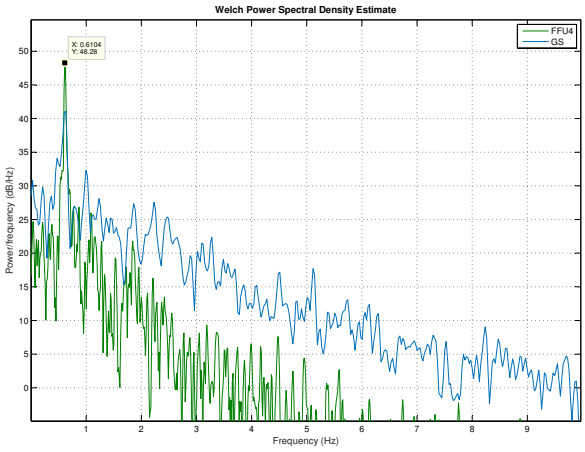

Figure 6. Correlation between the received signal strength and the measured movement.

received and processed attitude data of the FFUs from the ejection altitude of approximately 65 km downwards till loss of signal were analyzed in detail. Exact IMU accuracy figures cannot be given, as time constraints made an exact calibration impossible before launch. However, it can be concluded that the IMU worked as planned and the scheme could have successfully been applied for transmissions. Data analysis did reveal that the fraction of time during which the antenna main lobe points toward the ground station is relatively small and that there might be bad attitude states which would lead to long times between transmissions.

The gathered insights might be useful for future experiments in this area of research. Despite the positive findings obtained from the experiment, post-flight analysis showed that the scheme proposed by the LiME experiment does not seem to be overly aspirational for a CubeSat implementation. The time frame available for transmitting with a high data rate from the satellite is very small. To achieve higher data rates, high antenna gains have to be realized which lead to narrow antenna beamwidths. In comparison to a more or less non-directional antenna system, the amount of data transmitted will be almost the same. It is also complicated to integrate directional antennas into a CubeSat form factor.

For further information about the experiment the final report can be found at [2].

ACKNOWLEDGEMENTS

We want to thank the whole REXUS/BEXUS team for their support during the project. Without this help, the experiment couldn't have been carried out as it was. We also want to thank DLR MORABA for recording the telemetry data from our FFUs during the flight. The additional data that could be gathered from their recording allowed us to do far more extensive data analysis than what would have been possible using only the experiment ground station.

CONTACT

One can reach the LiME team via the following channels:

Via Mail: lime@lstsrv.org
Website: www.rexus-lime.de

REFERENCES

[1] LiME REXUS19 flight
`https://vimeo.com/163750496`

[2] RX19_LiME_SED_v5-1_01Sep16
`http://rexusbexus.net/wp-content/uploads/2017/07/RX19_LiME_SED_v5-1_01Sep16.pdf`

UB-SPACE ON REXUS 21: TEST DATA ACQUISITION FOR RELATIVE NAVIGATION WITH A CAMERA SYSTEM FOR A 360 DEGREE ROUND VIEW FROM A SOUNDING ROCKET

Amina Zaghdane[1], Maren Hülsmann[1], Lars Flemnitz[1], Julian Schröder[2], and Oliver Dorn[3]

[1]*University of Bremen, Germany, Email:Amina.Zaghdane@gmail.com, Maren.Huelsmann@ub-space.de, Lars.Flemnitz@ub-space.de*
[2]*City University of Applied Sciences Bremen, Germany, Email: Julian.Schroeder@ub-space.de*
[3]*Leibniz Universität Hannover, Germany, Email: Oliver.Dorn@ub-space.de*

ABSTRACT

Space debris is a growing challenge in space flight. Yet, no promising solution has been implemented to remove the amount of debris surrounding our planet. By using systems which are able to navigate autonomously, it is possible to detect and remove space debris, such as defective satellites. One important step within the removal procedure is the relative navigation during the final approach of the collecting vehicle to the target. To this day mainly visualisations are used to test camera-based relative navigation systems due to the lack of real images.

The UB-SPACE experiment on the REXUS 21 sounding rocket provides a freely accessible test data set of an uncooperative object in the space environment for camera-based relative navigation of space vehicles. The data shall in particular serve as an enhancement for the preparation of missions aiming at space debris removal, on-orbit servicing, formation flight, docking manoeuvres and other tasks where the approach to an uncooperative object in space is required.
A satellite-like Free Falling Unit (FFU) is ejected and observed from the rocket via 360 degree camera view. In addition, an IMU and sun sensors are used for attitude determination of the rocket. The acquired data enables a pose estimation of the FFU relative to the rocket by means of image processing.

This paper presents the experiment design and the acquired data with emphasis on the camera system which allows a 360 degree view from the sounding rocket with six cameras.

Key words: relative navigation; vision-based navigation; uncooperative objects; ADR; camera system; REXUS.

1. INTRODUCTION

Proximity navigation is an important aspect in a wide range of applications, e.g. debris removal, on-orbit servicing, docking or formation flight, where a target space vehicle or object is approached by a space vehicle. Especially with uncooperative objects involved, vision-based approaches are applied for relative navigation.

Several demonstrator missions attempting this issue were already conducted such as the PRISMA mission [2], enabling different formation flight and proximity operation tests and the AVANTI experiment within the FireBIRD mission [3], to demonstrate the approach to an uncooperative target at far distance.
Others are planned, e.g. the vision-based navigation experiment RemoveDebris [4], with the aim to demonstrate active debris removal technologies by releasing and recapturing two CubeSats.
All mentioned missions prove the feasibility of autonomous vision-based navigation solutions.
Nevertheless, there is no freely accessible test data of real manoeuvres available which can be used for testing algorithms prior to a mission. In particular not for uncooperative objects in close distance. This is what the experiment UB-SPACE is addressing.
The objective of the experiment is to provide a freely accessible test data set of an uncooperative object in space for camera-based relative navigation of space vehicles, including:

- Camera recordings of the object
- Sensor measurements for pose determination of the rocket
- Reference sensor measurements of the uncooperative object

It shall serve the preparation of future space missions and support the efforts to enable more complex autonomous manoeuvres. The provided data is specifically meant for

testing algorithms for detection and identification of uncooperative objects in close distance and their pose estimation.

2. UB-SPACE EXPERIMENT

2.1. Experiment Concept

A passive FFU is ejected from the rocket during flight. Once ejected, the distance of the FFU to the rocket increases over time. This process is recorded by cameras and sensor units and stored onboard the rocket.

Inside the Rocket Mounted Unit (RMU), six cameras with integrated storage are arranged outwardly such that a 360 degree view around the rocket is possible. For the ejection, a special mechanism is installed inside the RMU in which center the FFU is placed. The attitude determination of the RMU is realised using an Inertial Measurement Unit (IMU) and two sun sensors in addition to the GPS of the rocket. To ensure a closed rocket during the launch the opening from which the FFU is ejected is covered with a hatch. This is hold in place by steel wires. Before the FFU can be ejected the hatch is detached some seconds prior to the despin of the rocket using pyro cutters. The FFU is then ejected shortly after the motor is separated.

The FFU is equipped with an IMU to determine its attitude. The recorded data is send to the RMU via WIFI. In addition the FFU is covered in gold foil and each side is marked with a unique LED pattern for later pose determination.

Over the entire duration of the experiment, the cameras inside the RMU record images of the FFU.

2.2. Mechanical Design

The mechanical design is divided into the RMU and the FFU. The RMU contains every component which remains inside the rocket module after the ejection of the FFU.

Two important subunits within the RMU are the ejection mechanism and the sensor system, see Fig. 2 for details.
The image acquisition equipment, part of the sensor system and mainly consisting of six GoPro Hero 4 Black Edition, serves to record an omni directional view orthogonal to the z-axis of the rocket. This camera arrangement is chosen due to the remaining rotation of the rocket which could cause a single camera pointing in one direction to lose the target object fast of the field of view.
At 150 degree, the cutting for the camera window starts. The centre of each oval camera cutting is 60 degree away

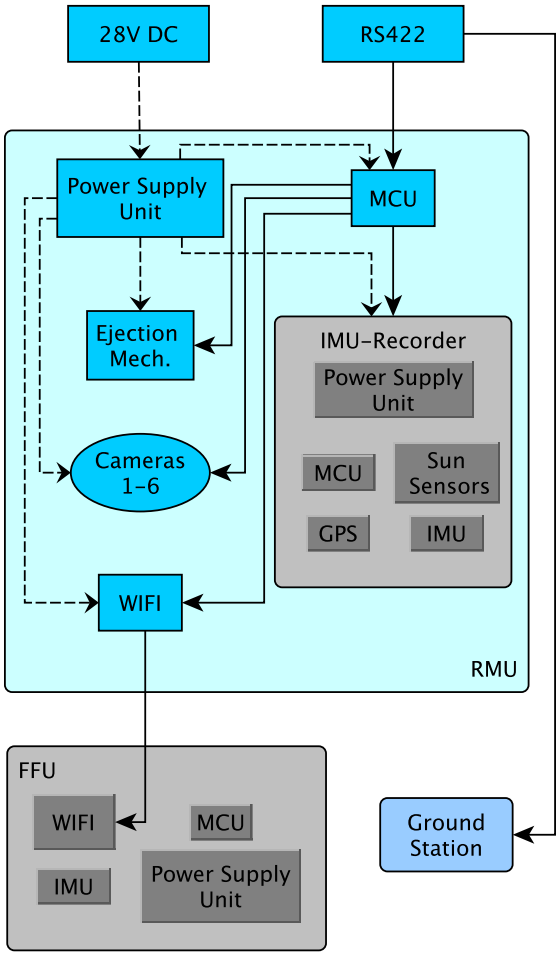

Figure 1. Experiment setup

from the previous one. Furthermore, the system consists of two sun sensors mounted to the inner wall of the module. The cuttings for the sun sensor are positioned at 60 degree and 240 degree. Every single cut out is stabilised by a frame support construction.

The ejection mechanism consists of two lead screws which are separately powered by two stepper motors (NEMA 11), one for each lead screw. Each motor provides a torque that ensures an ejection speed of 30 mm/s. The carrier module that is part of the ejection mechanism conveys the FFU through the hatch out of the module. Besides, if one motor is not working, a safe ejection is ensured.

The FFU is an aluminium 3D printed cube with an edge length of 60 mm. It consists of two parts, the body and the cap. Inside the FFU four PCBs are stacked with a distance of approximately 11 mm. To ensure a connection, between the RMU and the FFU spring loaded connectors are be used. At the backside of the FFU 12 target connectors connect to spring loaded pins on the carrier module. This enables a wired communication

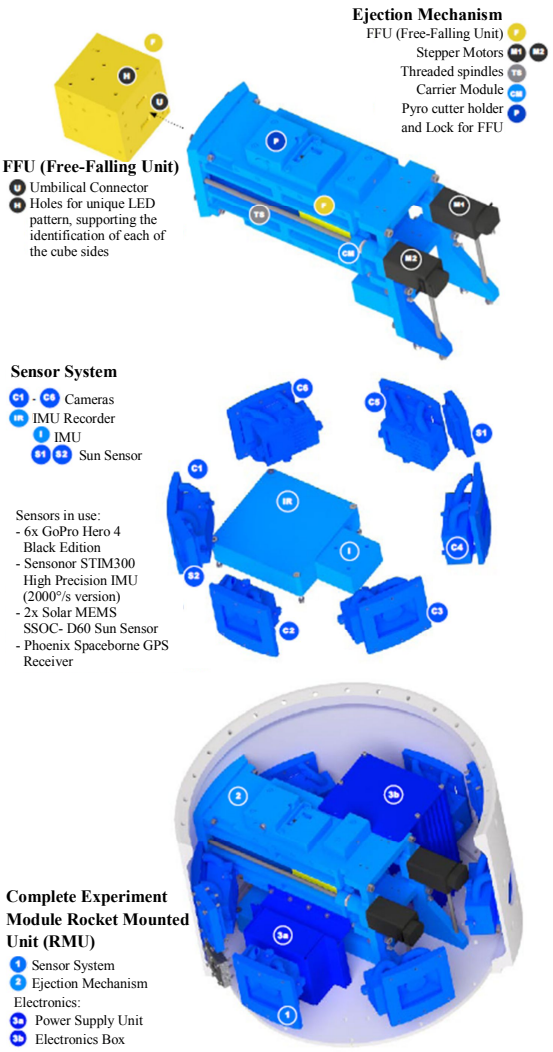

Figure 2. System design

prior to ejection. On each of the six surfaces of the FFU LED markers are placed. The LED pattern of each side of the cube consists of six LEDs, uniquely arranged on a 4x4 grid. This pattern enables to identify each side individually for the determination of the orientation of the FFU.

2.3. Electronics Design

The electronics design of the experiment can be split up in two main parts. On one hand, there is a microcontroller responsible for the sequence control of the experiment. It is controlling all actuators and the cameras. On the other hand, there is a microcontroller interfacing all sensors and recording all arising data.

All actuators of the experiment are connected to their microcontroller via GPIO. The ejection mechanism consists of four motors, two stepper and two servo

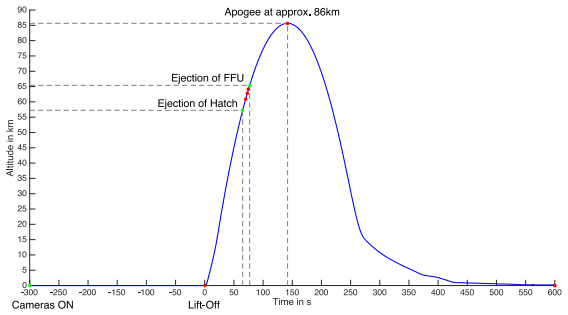

Figure 3. Experiment event timeline

motors. The servo motors drive the locks that hold the FFU in place during ascent. Their absolute position (locked / unlocked) is simply given by a PWM signal, generated by one of the timers of the microcontrollers. The stepper motor controllers are interfaced similar. However, the PWM signal adjusts the speed of the motors. Thereby, the ejection speed of the FFU is set by software. In addition, one GPIO is used to determine the motors' rotational direction.
The six GoPro cameras have been modified, so the shutter button can be activated via GPIO. A wire has been soldered to the gate of the dedicated transistor. However, modifying the cameras only has been a fallback option. Previously, it was planned to utilise the I2C bus of the camera. Eventually controlling the cameras via GPIO worked. A single pulse has been sufficient to turn on the cameras and start the recording. The video data is stored on the memory cards of the cameras.

The second microcontroller is responsible for data acquisition. Both sun sensors, the IMU and the GPS receiver are connected to it via serial buses. Each measurement is supplemented with a timestamp and stored on a memory card. The dataset of every sensor is stored in separate files.

More details concerning the experiment design can be found in [1].

3. RESULTS

The experiment was launched on March 15th, 2017 at 11:43 CET from Esrange Space Center aboard the rocket REXUS 21 in the course of the ninth REXUS/BEXUS cycle.

The event timeline (Fig. 3) illustrates the procedure of the experiment. The cameras are powered at T-300, after Yo-yo-despin (T+70), nosecone separation (T+73) and motor separation (T+74), the FFU is ejected at T+77.

Figure 4. Cam 3, T+65: Hatch

Figure 5. Cam 1, T+71: Yo-yo

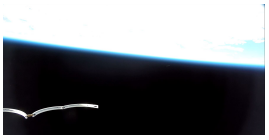

Figure 6. Cam 1, T+72: Yo-yo, motor mounting ring

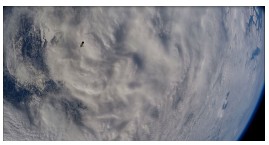

Figure 7. Cam 1, T+81: Motor

Figure 8. Cam 1, T+83: FFU ejection and motor

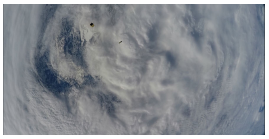

Figure 9. Cam 4, T+88: FFU and motor

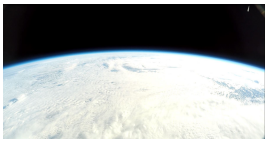

Figure 10. Cam 2, T+94: Nose-cone

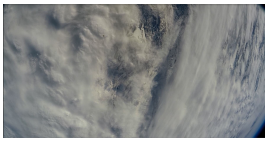

Figure 11. Cam 2, T+97: FFU and motor

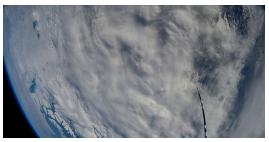

Figure 12. Cam 1, T+119: DIANE antenna and motor

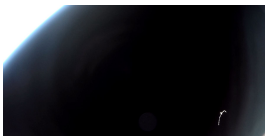

Figure 13. Cam 2, T+199: DIANE

3.1. Acquired Data

All cameras recorded during the experiment, however some stopped before the final shut-off instruction, see Tab. 1 for exact shut-off times:

Table 1. Shut-off times of all cameras

Camera	1	2	3	4	5	6
Shut-off time, T+	174	548	549	548	401	23

The experiment succeeded in acquiring image series showing several uncooperative objects. The cameras recorded with a resolution of 1080p and a rate of 60 frames per second. Several uncooperative objects were recorded in addition to the FFU. See Fig. 4 to Fig. 13 for example images of visible uncooperative objects.

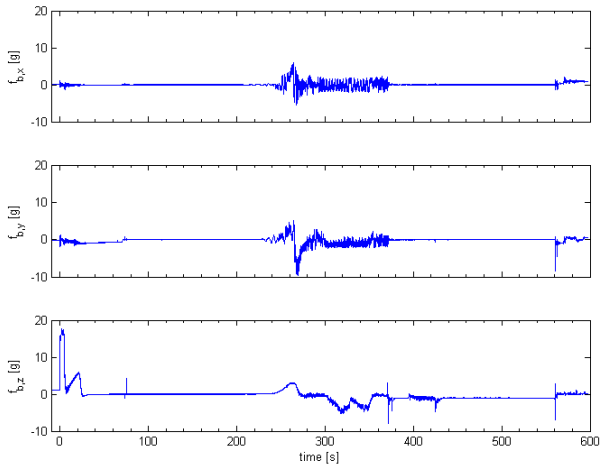

Figure 14. Acceleration

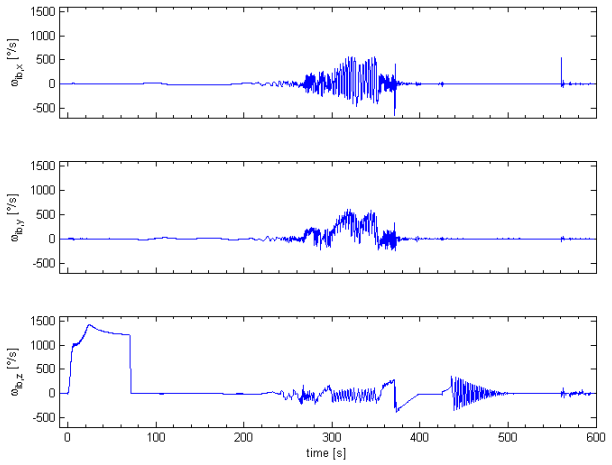

Figure 15. Angular rate

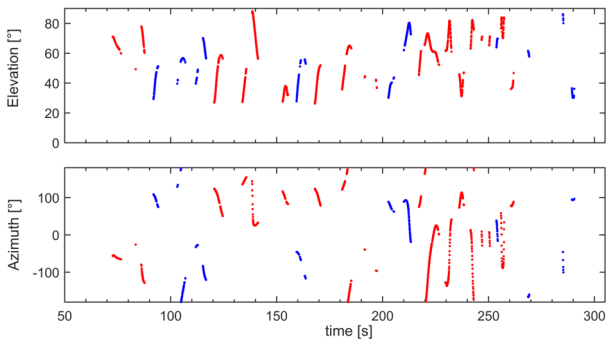

Figure 16. Sun sensor measurements

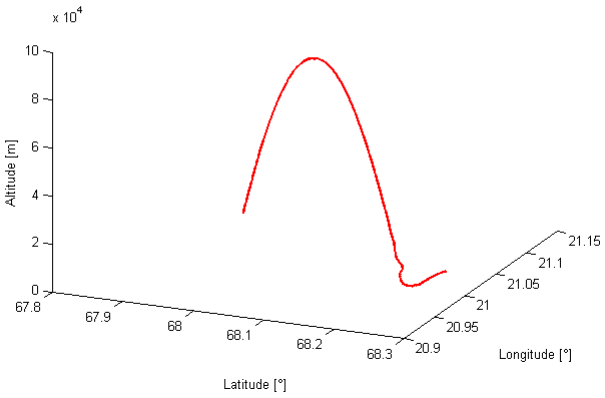

Figure 17. Rocket trajectory from GPS recordings

For attitude determination of the rocket a combination of different sensors is used. The acquisition of measurements of the accelerometer, gyroscope, sun sensors and GPS was successful, see Fig. 14, 15, Fig. 16 and Fig. 17, respectively.

The acceleration of all three axis is shown in Fig. 14, with the initial variations in the x- and y- axis attributable to the spin and a slightly off-centre position. The strong central deflections, starting around T+240 result from re-entry into the atmosphere.
In Fig. 15, the angular rate of the roll-axis z reaches its maximum at about $1400^\circ/s$ which corresponds to 3.9Hz. The sun sensor measurements are shown after despin of the rocket in Fig. 16, red representing the first sun sensor and blue the second.
The GPS track is visualised in Fig. 17.

3.2. Camera System

Tab. 2 shows first results for the intrinsic calibration using CalLab [5] with Levenberg-Marquardt as underlying method. The order of the distortion parameters in kc is chosen as in Bouguet's toolbox [6].

The actually given field of view for each camera is shown in Fig. 18. Provided that every camera is recording, a 360° round view is achieved. This holds true for the first 23 seconds after launch, see Tab. 1. The overlapping of the field of views starts at approximately 220 mm distance from the external skin of the rocket.

Table 2. Intrinsic calibration

Camera		1	2	3
Focal length	f_x	880	875	867
	f_y	887	887	874
Principle Point	c_x	1025	976	922
	c_y	549	541	557
Skew	α_c	0.0007	0.001	0.0004
Distortion kc	k_1	-0.2614	-0.2556	-0.2585
	k_2	0.0931	0.0844	0.0879
	p_1	-0.0013	-0.0027	-0.0027
	p_2	0.0172	0.0098	-0.006
	k_3	-0.0176	-0.014	-0.0153
RMS Error		0.4218	0.4775	0.443

Camera		4	5	6
Focal length	f_x	873	878	871
	f_y	880	885	878
Principle Point	c_x	923	900	959
	c_y	548	537	548
Skew	α_c	0.0006	0.0005	0.0007
Distortion kc	k_1	-0.2561	-0.2568	-0.2551
	k_2	0.086	0.0865	0.0838
	p_1	-0.0002	-0.0006	-0.002
	p_2	-0.0057	-0.0145	0.0004
	k_3	-0.0149	-0.0149	-0.0139
RMS Error		0.423	0.4248	0.4245

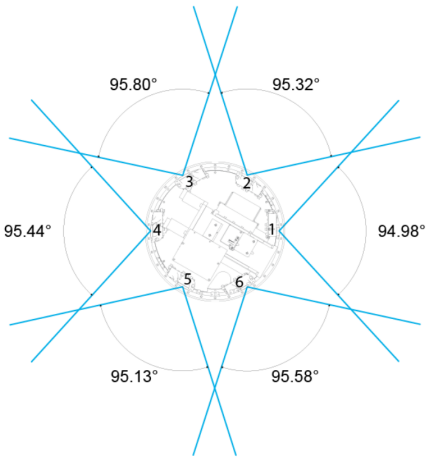

Figure 18. Field of view angle for each camera

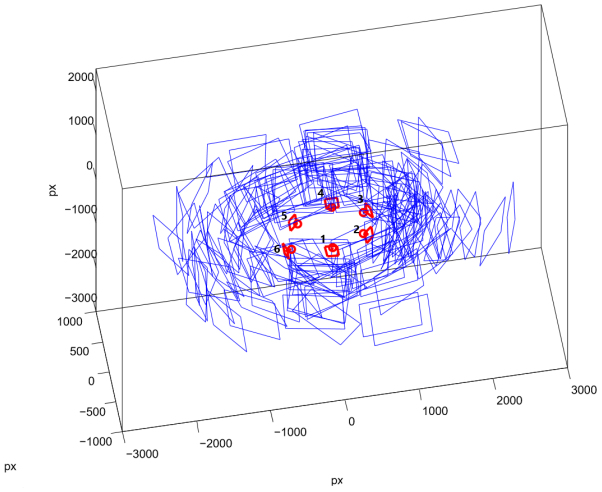

Figure 19. Extrinsic calibration

A first result indicating the poses of the cameras in relation to the neighbouring cameras is shown in Fig. 19 in red, combined with the positions of the calibration pattern in blue, leading to this result. This result was obtained using the calibration toolbox of Bo Li et al. [7]. It is noticeable that the result is not yet sufficiently accurate since the alignment of camera 1 and 6 does not correspond to the real setting.

4. CONCLUSION

Most of the objectives of the experiment have been completed successfully. The ejection mechanism achieved its purpose by releasing the FFU with a controlled speed. Moreover, video material of uncooperative objects in space was acquired. To the extent of our knowledge the camera system used for this objective is the first one allowing a 360 degree round view to fly on a sounding rocket. With the IMU, sun sensor and the camera recordings, an ample amount of data is available for an accurate attitude determination of the rocket.
Unfortunately, no wireless connection between RMU and FFU could be established, the consequence being that no sensor measurements of the uncooperative object are available. This makes it impossible to provide reference position and attitude information of the object.
A re-flight using the existing experiment set-up with an added functional wireless connection between RMU and FFU would enhance the quality of the acquired data significantly with relatively low additional effort.

5. OUTLOOK

To prepare the data for utilisation a few preprocessing steps have to be accomplished. Presently only the preflight camera calibration results are available. These will be checked against the post flight results. For the extrinsic camera calibration a correction is necessary, for instance by exploiting known design induced constraints. Furthermore, the determination of the absolute position and orientation of the rocket from a combination of recordings of sun sensors, IMU, GPS receiver and cameras is still outstanding, as well as the determination of the pose of the FFU relative to the rocket from the camera recordings.

The full data set will be made freely accessible.

ACKNOWLEDGEMENTS

The experiment was performed within the framework of the REXUS/BEXUS programme.
The REXUS/BEXUS programme is realised under a bilateral Agency Agreement between the German Aerospace Center (DLR) and the Swedish National Space Board (SNSB). The Swedish share of the payload has been made available to students from other European countries through the collaboration with the European Space Agency (ESA). Experts from DLR, SSC, ZARM and ESA provide technical support to the student teams throughout the project. EuroLaunch, the cooperation between the Esrange Space Center of SSC and the Mobile Rocket Base (MORABA) of DLR, is responsible for the campaign management and operations of the launch vehicles.
The realisation of the experiment is supported by the Navigation and Control Systems Department of the Institute of Space Systems and by the Space Flight Technology Department of the German Space Operation Center (GSOC) of the German Aerospace Center (DLR).
Special thanks to Stephan Theil, Benjamin Braun, Markus Markgraf, Christian Mietner, René Schwarz, Hans Krüger, David Heise, Michael Dumke and the entire REXUS/BEXUS team for the support during the whole project which was indispensable for its success.

REFERENCES

[1] M. Hülsmann, A. Zaghdane, L. Flemnitz, M. Braschkies, O. Dorn, and J. Schröder, UB-SPACE: Image Processing for Determination of relative Satellite Motion, Student Experiment Documentation Version 5, 2017.

[2] S. Persson, S. D'Amico, and J. Harr, Flight Results from PRISMA Formation Flying and Rendezvous Demonstration Mission, 61st International Astronautical Congress, Prague, CZ. 2010.

[3] G. Gaias, J.-S. Ardaens, and T. Terzibaschian, Paving the way for future on-orbit serviving missions: The AVANTI experiment, 25th International Symposium on Space Flight Dynamics, 2015.

[4] J. L. Forshaw, G. S. Aglietti, T. Salmon, I. Retat, C.Burgess, T. Chabot, A. Pisseloup, A. Phipps, C. Bernal, F. Chaumette, A. Pollini, and W. H. Steyn, The

RemoveDebris ADR Mission: Preparing for an International Space Station Launch, 7th European Conference on Space Debris, 2017.

[5] K. H. Strobl, W. Sepp, S. Fuchs, C. Paredes, M. Smisek, and K. Arbter, DLR CalDe and DLR CalLab, Institute of Robotics and Mechatronics, German Aerospace Center (DLR), http://www.robotic.dlr.de/callab/

[6] Bouguet, J. Y. Camera Calibration Toolbox for Matlab. Computational Vision at the California Institute of Technology.

[7] Bo Li, Lionel Heng, Kevin Koeser, and Marc Pollefeys, A Multiple-Camera System Calibration Toolbox Using A Feature Descriptor-Based Calibration Pattern, IROS 2013.

DEVELOPMENT OF ULTRA-SENSITIVE PORTABLE 3D MAGNETOMETER BASED ON DIAMOND NV-CENTERS FOR OSCAR (BEXUS 23)

Jaroslav Hruby [1,2], Jelle Vodnik [1], Tim Vangerven [1,2], Ilaria Cardinaletti[1,2], Rob Cornelissen [1,3], Dieter Schreurs [1,2], Steven Nagels [1,2], Michel De Roeve[3], W. Deferme[2], Jean V. Manca[3], and Milos Nesladek[2]

[1] OSCAR Student team, Hasselt University, Agoralaan 1, 3590 Diepenbeek, Belgium
[2] IMO-IMOMEC, Hasselt University, Wetenschapspark 1, 3590 Diepenbeek, Belgium
[3] X-LAB, Hasselt University, Agoralaan 1, 3590 Diepenbeek, Belgium
Email: bexus.oscar@gmail.com
jaroslav.hruby@uhasselt.be
milos.nesladek@uhasselt.be

ABSTRACT

Ultra-high sensitivity magnetic measurements are already used in many fields, such as navigation, healthcare, geology, mining, solar wind measurements and other space applications. The quantum measurement techniques open new possibilities of exploitation, providing unmatched sensitivity [1,2,3] The idea behind the OSCAR (Optical Sensors based on Carbon materials) project was to test the feasibility of conceptually novel magnetometer based on colour centres in diamond [1], in an aerospace environment during a stratospheric balloon flight. The important disadvantages of this kind of sensor are the high sensitivity and the intrinsic stability of diamond in harsh environments [1]. The diamond magnetometer serves as a three-dimensional compass. The complete device design satisfies the requirements of low mass, low power consumption, and high reliability imposed by the space industry for the launch on the BEXUS balloon. Ongoing work is focused on a fully electrical method for the diamond sensor readout, potentially leading towards further miniaturization.

1. INTRODUCTION

1.1. Why magnetometry

Sensing the magnetic field is of great importance in a large variety of applications. The range of magnetic sensors goes from the familiar compasses used for navigation purposes, to probes employed in geological studies and mining or in the biomedical sector. Magnetometers are also fundamental in space-related applications, such as the measurement of the solar wind. So far, however, high sensitivity magnetometers required cryogenic temperatures [2] to be operated and were therefore not fit for a large variety of applications: for example, when cost or space were limited, or in high temperature environments.

1.1. What was the aim of this project

The primary aim of our project was to construct a portable magnetic field sensor exploiting the Zeeman splitting between the different electronic spin sublevels of a colour centre in diamond, detected optically through the ODMR (Optical Detection of Magnetic Resonance) method. A secondary aim was to use this device like a compass detecting the movement of the gondola attached under the BEXUS stratospheric balloon. Thirdly, we wanted to prove the viability of this technology in harsh space-like conditions. And lastly, we aimed at developing a workflow for testing and verification of the next generation of diamond based magnetometers working on an electrical readout principle.

1.2. Why diamond

Diamond is a robust material, well known for its strength and toughness. It is very stable against temperature, pressure, chemical, and mechanical stress. It is also a very radiation-hard material due to its wide band gap. Diamond contains, in its crystalline lattice, opto-magnetic defects called Nitrogen-Vacancy (NV) centres (see Figure 1). NV centres-point defects in diamond lattice - are photo luminescent and when excited with green light with wavelength of 532 nm, they emit red light which is stable and resistant to photo-bleaching. The photoluminescence transitions associated with the $|\pm1\rangle$ spin sublevels of NV ground state present lower intensity than the transitions associated with the $|0\rangle$ sublevel. Under green illumination, the ground state is polarized into the $|0\rangle$ spin sublevel. The application of a microwave field with resonant frequency drives electrons from the $|0\rangle$ to the $|\pm1\rangle$ spin sublevels, and leads therefore to a drop of the luminescence intensity. The presence of an external magnetic field induces a splitting between $|\pm1\rangle$ spin sublevels (Zeeman effect), resulting in a splitting between the microwave resonant frequencies. From this effect, it is possible to determine the magnitude of the magnetic field, since in the weak magnetic field regime the splitting between the spin sublevels depends linearly on the projection of the magnetic field along the NV axis (see Figure 1). It was demonstrated that NV

centres can be used for ultra sensitive measurement of magnetic field [1,4]. The NV centres are located in four different orientations within the diamond lattice, thus enabling 3D sensing of magnetic field with a single sensor.

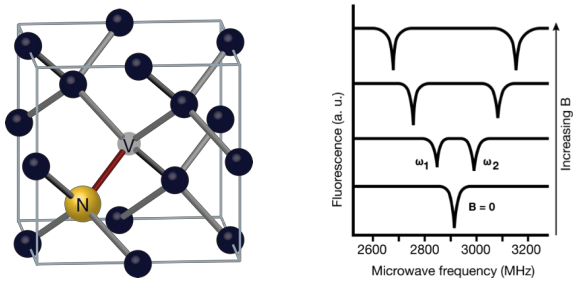

Figure 1. (left) Nitrogen-Vacancy (NV) centre in the diamond crystal lattice (right) Zeeman splitting of NV-based magnetometer.

1.3. What is OSCAR project

Within the framework of the REXUS/BEXUS programme, our OSCAR (Optical Sensors based on CARbon materials) project proposed to study the degradation of organic solar cells in the stratosphere and to prove the concept of a prototype diamond magnetometer as space magnetometer, by testing its performance during a stratospheric balloon flight. The tested device was designed to maintain the total weight, volume, and power consumption of the sensor as low as possible. At the same time, we developed a measurement protocol (further described below) to allow for constant tracking of the changes in the magnetic field during flight.

1.4. Flight conditions and flight route

The launch took place on October 7th, 2016, with a countdown initiated at 3:30 AM, and lift-off around 9 AM local time. In the few hours previous to lift-off, the last tests were performed on the ground, at a temperature close to 0 °C. The temperature decreased to a minimum of about -56 °C, roughly 15 km above ground. After reaching 32.3 km of altitude, the temperature remained between 23 and -13 °C, and the experiment kept running for more than 2 hours.
The resulting fall occurred over 5 hours after lift-off, several km away.
Throughout the whole flight, the entire experimental load experienced continuous rotations, which were quite fast during the ascent phase, and became slower (nevertheless without ceasing) during floatation at 32.3 km. The entire flight trajectory is shown in figure 2.

Figure 2. Balloon flight trajectory is shown as purple solid line.

2. METHODS

2.1. Device construction

The stratospheric balloon flight imposed severe limitations on the total weight, dimensions, and power consumption of the mounted experiment. Moreover, our sensor needed to be designed keeping in mind the expected operational temperature range, pressure, and mechanical vibrations.

As demonstrated in figure 3, the device base consists of a laser mount with heat sink, necessary to stabilize the temperature of the employed green laser (532nm, 50mW) operating in mild vacuum. The lower part of the device body hosts the lenses used for focusing the laser on the diamond sensor, placed on top of a sample holder with embedded microwave antenna. The lenses to collect the red light emitted from the NV-rich diamond are located in the top part of the device, together with a set of filters to filter out the green excitation light. The filtered red signal is then focused on an avalanche photodiode (APD) detector.

The device also consists out of readout electronics circuitry, microwave generator and switch, and micro-controller unit with Ethernet connection and flash memory, for data management, storage and transmission to the ground station.
For the sake of miniaturization and specificity of our use, we developed the entire readout and control circuitry. Namely, we designed and built our own laser driver, to provide steady laser operation, and a lock-in amplifier tailored for our needs of operation. The main benefit of this approach was the dramatic reduction of footprint, power consumption and weight, while boosting the performance (in our specific operating range).

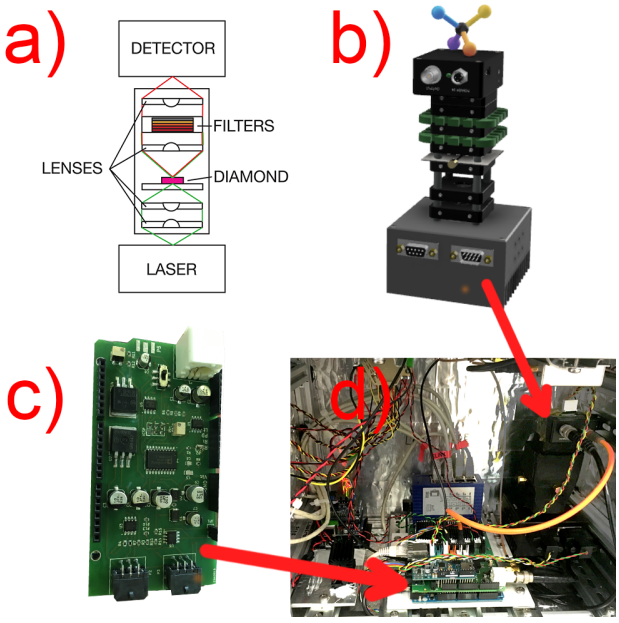

Figure 3. Shows in section a) device construction, b) 3D model of the device with schematic representation of four orientations of NV centre axis respectively to the device and the colours which are used through all results. Section c) shows readout board specifically developed for this use. Section d) provides view of the internal master box layout.

In order to enable the lock-in detection of the APD output signal, we were driving the microwave switch with 5 kHz TTL pulses. In this way, we modulated the microwave signal and detected only the portion of the photoluminescence light which was directly affected by the microwave modulation. In this configuration, magnetic resonances appear as positive peaks in the photoluminescence spectrum (see Fig. 5).

Weight (including electronics)	1,5 kg
Power consumption	8 W
Laser power	50 mW
MW power	+18 dBm
MW range	2,82 – 2,92 GHz
Operating temperature range	-40 – +50 °C

Table 1. Device characteristics summary.

2.2. Measurement routine and calibration

Each measurement cycle consisted in the measurement of the red photons emitted over a microwave sweep in the range of 2820 to 2920 MHz (in steps of 50 kHz) and in the data transmission part. For each sweep cycle, data collection took roughly 20s and data transfer to the ground station took about 16s, due to the limited available bandwidth. The consequence of this measurement routine was a low sampling rate, which had an impact on the collection of flight data, especially during the lift-off phase.

In order to analyse the data, the first step was to recognise the peaks in our optical readout, in order to determine their position with respect to the frequency of the applied microwave field. An example graph of acquired data and peak detection is shown in figure 5. The four pairs of peaks correspond to the projection of the magnetic field along the four NV centre axis in the diamond crystal.

We performed calibration measurement, where we positioned the sensor on a rotational mount in a way that one of the NV centre axis (see Fig. 3) was perpendicular to the Earth's magnetic field and we were spinning the device around this axis. By this approach we identified, isolated and measured all four NV centre axes of diamond. We then associated them to the orientation of the measurement device. After the calibration, we knew what the contribution of the magnetic field along each axis was, and we knew how the axes were oriented. This allowed us to reconstruct the resulting magnetic field vector from the acquired data.

In order to develop an automated calibration mechanism, we first modelled the expected output. When we isolated one axis by making it perpendicular to the Earth's magnetic field, we expected the projection of the magnetic field along this axis to be equal to 0. Then, if we spin the device 360° around this axis, the change in the magnetic field along the rest of the axes will be a sine function, where the functions representing each axis will be 120° phase shifted to each other, due to the geometry of the lattice.

2.3. Reconstruction of magnetic vector from data

First, we constructed a simplified 3D atomistic wire model of a NV centre. Then, we mapped the intensity of the magnetic field along each NV axis (Fig. 4a). From those intensities, we calculated the resulting magnetic field vector (Fig. 4 – red dashed line). From the resulting magnetic field vector, we determined yaw, pitch and roll angles, based on the following allocation of planes to the model. Plane XY (Fig. 4c) is the top plane, which we used for the calculation of the heading/yaw angle, YZ (fig. 4d) is the front plane, which we used for the calculation of the roll angle, and XZ (Fig. 4e) is the left plane, used for the calculation of the pitch angle. Since we are currently working on a further development of this step, the shown results are not yet final.

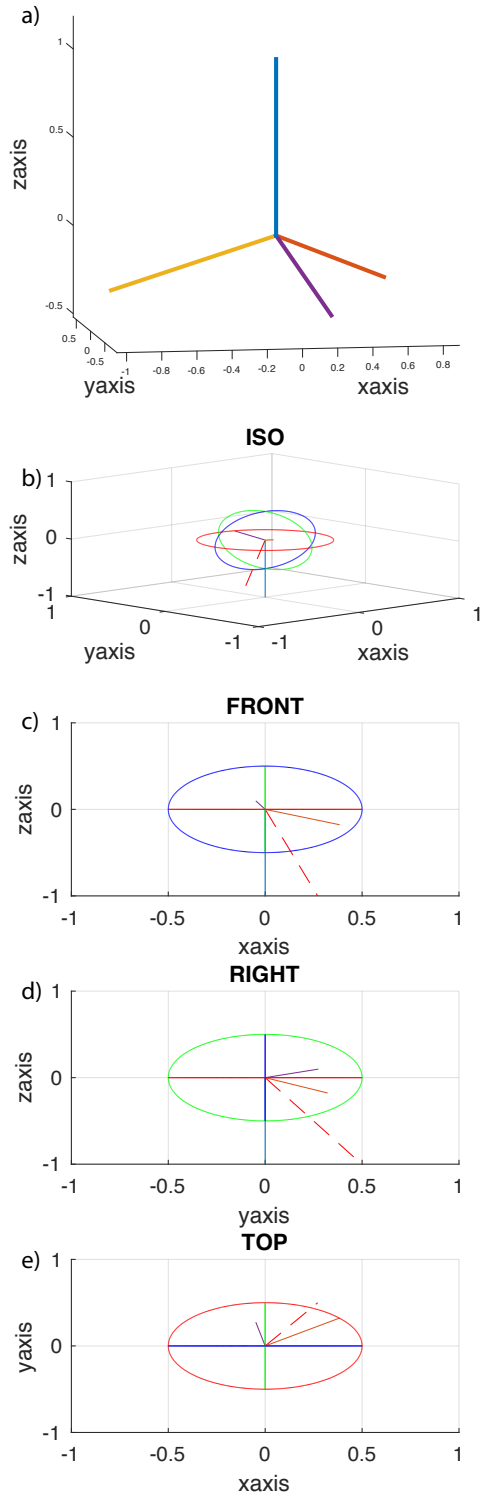

Figure 4. Shows preview of the reconstruction of magnetic vector from 4 different orientations of the NV centre. The simplified atomistic 3D wire model of NV centres axes (a) and resulting vector of the magnetic field is represented by red dashed line.

3. RESULTS AND DISCUSSION

3.1. Raw data

The first step towards fulfilling the aims of the project was to develop a device capable of measuring the magnetic field with high sensitivity and stability through a diamond crystal, exploiting the ODMR signal. Figure 5 shows a preview of the raw magnetic resonance performed by diamond magnetometer and showing 4 sets o resonance peaks, each of the of particular orientation of magnetic field. Data were acquired by our miniaturized system. With this step, we already greatly reduced the background noise of the setup, approaching the sensitivity which is characteristic for a setup on an optical table. Furthermore, we were able to detect some hyperfine structures in the resonances coming from coupling of NV electron spin with the nuclear spin of ^{14}N atoms, on top of the peaks resulting from the Zeeman splitting. This proves the very high resolution of the portable magnetometer.

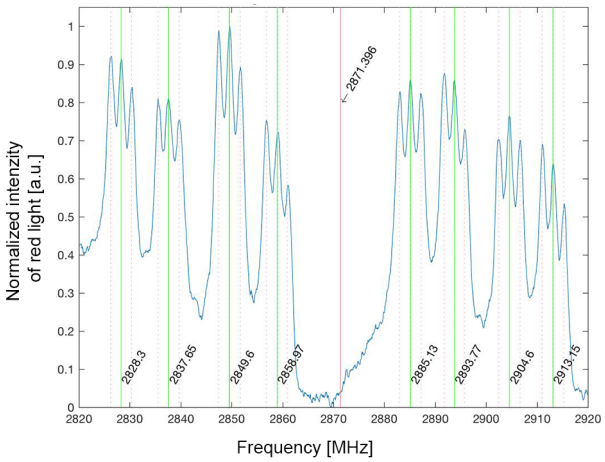

Figure 5. Preview of a raw ODMR data from single sweep acquired by the measurement system. Green solid lines represent central peak position, red dotted line hyperfine peak detection and red solid line represent centre of the data set. The intensity drift is caused by charge and discharge of time-constant capacitor of the lock-in amplifier.

3.2. Calibration data

In order to understand better the behaviour of our diamond magnetometer, and hence to correctly analyse the data, we performed its detailed calibration and extensive testing, as mentioned in previous sections. Figure 6 shows the results of this calibration. It is worthwhile to note that the measured data correspond with the modelled data. This means that the device can indeed work as a compass, as reacts to the magnetic field along all three dimensions of space.

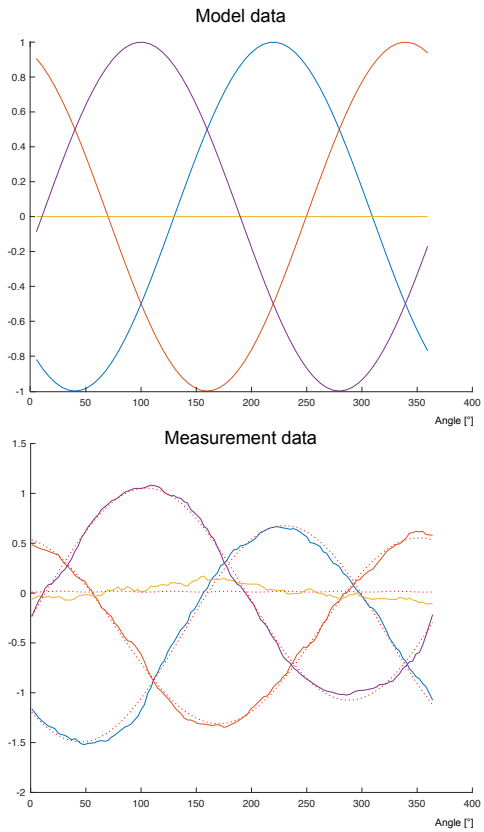

Figure 6. Shows data preview from calibration of the device. The model data shows expected behaviour of measurement data. Each of the colours corresponds with the appropriate NV centre axis. The difference between model and measured data was caused by slight tilt of yellow axis, which was not perfectly perpendicular to the magnetic field of the Earth.

3.3. Flight data

We also proved the viability of using this kind of device in harsh space like conditions. Before the flight, we tested our device in a vacuum chamber, and at temperatures in the range of -40 to +50°C.

During flight, the device was mounted on a gondola attached to a stratospheric balloon, which reached an altitude of 32.2 km. Between the flight preparations and the actual flight, we were measuring for a total of 8h. On Figure 7, we present data divided into three segments: preparation, lift-off and float phase.

During the preparation phase the balloon (and thus also the gondola) was standing still for the majority of the time. The only source of movement was the transportation of the gondola to the sweet spot, for the final communications testing, and to the launch position itself.

During the lift-off phase, the gondola was spinning rapidly and we discovered that a main drawback of our measurement device which was the slow sampling rate. The third and last part of the flight was the float phase, during which the gondola rotated at a much slower pace and we were able to measure exploitable data again.

The slow sampling rate was caused by two main issues, the rate at which we were performing the sweep (1 sweep = 20s) and the rate at which the raw data were transmitted towards ground station (16s).

Except for this drawback, the device was operating well, and we were able to notice slow rotations in the data, which were also confirmed by a video from a camera mounted on the gondola. Due to the complexity of the measurement and to the huge amount of data, we still need to continue with further analysis in order to extract more information from flight data.

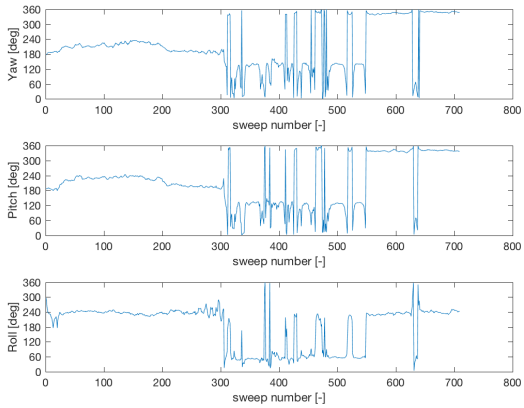

Figure 7. Flight result data shows almost no change while on the ground (sweep number ~0-300), rapid rotations and changes in lift of phase (sweep number ~300-550) and stabilization of rotation during float phase (sweep number ~550-700).

4. CONCLUSIONS

We successfully designed, built, calibrated and tested a portable diamond magnetometer, and verified its proper operation in harsh space-like conditions. We were able to use the device as a compass and measure the rotation of the gondola mounted under the stratospheric balloon. By successfully meeting the aims of this project, we enabled further development of portable diamond based magnetic field sensors and we developed testing and measurement protocols, which can also be used in the next iterations of diamond magnetometer development.

The main advantages of this device are its 3D sensing capability, its potential for high sensitivity sensing and its robustness in various environments.

The drawback was measurement slow sampling rate, which can be addressed in future iterations (for example by not streaming raw data to ground station and by performing the calculations on board).

5. OUTLOOK

In 2015, it was demonstrated by our research group that the magnetic resonance of NV-centres in diamond can be measured by probing the photocurrent instead of the optical read-out [3]. This direct photo-electric read-out of NV centres, called Photocurrent Detection of Magnetic Resonance (PDMR), is based on the detection of charge carriers promoted to the conduction band of diamond by two-photon ionization of NV centres under green illumination. Minima are detected in the measured photocurrent at resonant microwave frequencies, due to the spin-dependent ionization dynamics of the NV centres. This detection technique only requires the fabrication of electrodes on the diamond chip by standard lithography and avoids the complexity of optical detection. By using this technique, the diamond sensor serves as its own detector.

With our first optical readout based prototype, we revealed several limitations of this system, such as low readout speed, bulkiness, high power consumption, mechanical complexity and low long term stability caused by the optical components. Advances in the field of photoelectric readout (PDMR) will allow us to fabricate a device which will overcome the aforementioned limitations, mainly in terms of a further reduction of mass, power consumption, and complexity. Moreover, we foresee an improvement in sensitivity and system stability.

The precision of this device, combined with its small dimensions, can provide a perfect solution for aerospace applications. For example, in satellite missions, for accurate altitude determination, it is essential to know how the satellite is oriented in the inertial space. To do so, low Earth orbit satellites can use a magnetometer to read the magnetic field of the Earth and compare it with a geomagnetic reference field (i.e. IGRF). For this, it is necessary to know the position of the spacecraft at the exact moment (GPS, laser ranging or combined). Then, by taking the reference field in that position and comparing it with the readout from the magnetometer, a rotational matrix can be calculated. In a final step, the rotational matrix is used to determine the precise orientation of the satellite.

6. REFERENCES

1. Rondin, L. et al., Magnetometry with nitrogen vacancy defects in diamond, Rep Prog Phys 77 (2014)

2. Fagly, R.L. et al., Superconducting quantum interference device instruments and applications, Review of scientific instruments 77, 101101

3. Tiporlini, V. et al., High Sensitivity Optically Pumped Quantum Magnetometer, Scientific World Journal, 858379, (2013)

4. 2006Wolf, T. et al., Subpicotesla diamond magnetometry, Phys Rev X. 2015;5(4):041001.

5. Bourgeois, E. et al., Photoelectric detection of electron spin resonance of nitrogen-vacancy centres in diamond, Nature Communications 6, 8577 (2015)

INSTRUCTIONS TO AUTHORS FOR THE PREPARATION OF PAPERS:

FINDINGS OF THE PREDATOR (PRESSURE DIFFERENCE DEPENDENCY ON ALTITUDE VERIFICATOR) EXPERIMENT – BEXUS 23

VISBY, SWEDEN
11-15 JUNE 2017

Bc. Jan Lukacevic [(1)], Pavel Paces, Ph.D. [(2)], Bc. Zuzana Tumova[(3)], Ondrej Trojan[(4)], Bc. Michal Gabriel[(5)], Milos Hampl[(6)]

[(1)] Faculty of Mechanical Engineering, Czech Technical University in Prague, Technická 4, 16636, Prague, Email: jan.lukacevic@fs.cvut.cz
[(2)] Faculty of Electrical Engineering, Czech Technical University in Prague, Technická 4, 16636, Prague, Email: pacesp@fel.cvut.cz
Faculty of Electrical Engineering, Czech Technical University in Prague, Technická 4, 16636, Prague, Email: zuzkatum@gmail.com
Faculty of Electrical Engineering, Czech Technical University in Prague, Technická 4, 16636, Prague, Email: trojaon@gmail.com
Faculty of Electrical Engineering, Czech Technical University in Prague, Technická 4, 16636, Prague, Email: gabriel.michal4@gmail.com
Faculty of Nuclear Sciences and Physical Engineering, Czech Technical University in Prague, Technická 4, 16636, Prague, Email: miloshampl@hotmail.cz

ABSTRACT

The aim of The PREDATOR Experiment is to verify a new pressure difference method of which implementation would lead to introduction of new, more precise measurement devices used in the aircraft navigation systems. PREDATOR (PREssure Difference dependency on Altitude verificaTOR) is a verification experiment that has been developed and conducted by a student team consisting of undergraduate and graduate students from the Czech Technical University in Prague within the REXUS/BEXUS programme and is fully supported by the European Space Agency. Objective of the experiment is to verify a new measurement method using a specific arrangement of the pressure sensors in a particular setting enabling to determine the limits and feasibility of a measurement method. If successfully implemented, such method has a wide range of use for further improvement of current AHRS (Altitude Heading Reference System) in aircraft and can improve future navigation systems.

The experiment is based on a previous research at Czech Technical University and it has been tested in conditions of a scientific laboratory, in a natural environment using UAV and small commercial aircraft. The article widely focuses on findings of the final experiment conducted during a flight that happened in September 2016 at Esrange Space Center near Kiruna. Currently gathered measurement data so far suggest the validity of the method and will be further examined in order to be presented in detail during 23rd ESA PAC Symposium.

KEYWORDS: navigation systems, verification, measurement methodology, pressure sensors,

NOMENCLATURE

P	Pressure [Pa]
ρ	Density [kg/m^3]
g	Acceleration of gravity [m/s^2]
h	Height [m]
$R_{specific}$	Specific gas constant for dry air [J kg−1 K−1]
T	Absolute temperature of gas [K]

ACRONYMS/ABBREVIATIONS

IMU……Inertial Measurement Unit
GPS……Global Positioning System
UAV……Unmanned Aerial Vehicle
ESA……..European Space Agency
SNSB…….Swedish National Space Board
DLR……..German Aerospace Center
SSC……Swedish Space Corporation
ISA……..International Standard Atmosphere

1. INTRODUCTION

The PREDATOR experiment aims at verification of a measurement method. Motivation for such experiment originated in identifying multiple issues with contemporary aircraft systems. If the new method proves be valid, there might be a possibility for a further research and development of new sensors and complex navigation systems.

Aircraft navigation systems used in current aircrafts use various methods to process multisensory input. One of the ways is to process data using Quadratic Linear Estimation[1]. To resolve a position of an aircraft, a common framework of Euler angles has been established. These angles describe roll, pitch and yaw of an aircraft. In order to determine these angles, sensors such us accelerometers and magnetometers are used. In combination with the Global Positioning System (GPS) signal, the input data from aforementioned sensors is processed and used to resolve an actual position of the aircraft. Quality of the GPS signal received influences the overall quality of the output, therefore if the signal is lost, the precision of measurement decreases. Due to the nature of Quadratic Linear Estimation, an error occurs and grows in time (respectively, the travelled distance).

To compensate this, additional data input from an independent source can be used and one of such can be developed using the tested measurement unit. The basic principle this method is built upon acknowledges the fact the atmospheric pressure is dependent on altitude. If the pressure sensors are suitable positioned on the aircraft, this provides with an information of the respective Euler angles.

2. THEORY

In accordance with the International Standard Atmosphere (ISA) model which elaborates on specifics of atmospheric viscosity, temperature, density, as well as pressure, with an increasing altitude, the value of atmospheric pressure decreases [2]. To decide upon the success rate of the measurement method at particular heights, the ISA model has been used for comparison. Using the mathematic apparatus of ISA model, it can be calculated an operational range of given measurement method as the model divides the atmosphere into layers which follow a linear distribution of a temperature. The remaining values are calculated using a concurrent solution of the vertical pressure variation [2] in Eq. 1

$$\Delta P = -\rho g \Delta h \qquad (1)$$

And the ideal gas law in molar form, which create relations between density, pressure, density and temperature:

$$P = \rho R_{specific} T \qquad (2)$$

Using Eq. 1 and Eq. 2 in a combination with a local weather forecast as well as the long and mid-term meteorological measurements in the launch area, it can be calculated an estimated maximum operational range of the measurement method validity. As such, this has been estimated to be working at altitude between 10 and 12 km. The variation can be explained by current weather conditions on site.

Due to the nature of the measurement (as explained in detail in the Section 3) and working conditions of pressure sensors, it has been expected that the actual operational range of the method would differ from the calculated one. This would be mainly caused by safety constrains of the balloon gondola and instability of the local weather. Additionally, the resolution of pressure sensors used for the experiment poses certain limitations and it is a factor determining a precision of the measurement.
In theory, upon reaching the altitude of 10 or 12 kilometres, the experiment setting will reach the point when it loses the precision. This is caused by a fixed distance between pressure sensors and the difference of pressure at the altitudes between the sensors will be lower than is a relative precision of sensors and their absolute resolution.

3. METHODOLOGY OF RESEARCH

The entire PREDATOR Experiment is a part of more extensive research. Although the core of the experiment realised within the BEXUS programme is the test of the measurement device during the stratospheric balloon flight, it has been preceded by laboratory measurement and testing of the technology using an Unmanned Aerial Vehicle.

3.1 Laboratory measurement

The laboratory measurement was the basis for a basic validation of the method. Using a pair of pressure sensors[3], the theory behind the experiment has tested in a following way: Sensors has been manually moved to different altitudes to determine a minimal measurable distance between two sensors. The measurement took place in the summer of 2015, with stable atmospheric pressure and humidity and a constant temperature of 27°C/80°F, therefore not distorting the outcomes of the measurement.

Measured pressure difference is visually interpreted in Fig. 1 (in Appendix). The measurement, which took a total of 150 seconds, has been split into three sequences with different characteristics. The initial 50-second-long sequence aimed at testing of the coherence between two

chosen sensors, therefore it has been divided into two sub sequences. During the first 25 seconds Sensor 1 has been repeatedly moved 1 metre above and below the level of Sensor 2 and in the following sub sequence, the same has been repeated with the opposite configuration. The second 50-second-long-sequence utilised a movement of both sensors opposite to each other, hence both sensors have been moved in opposite vertical directions. This resulted in the absolute altitude difference of 2 metres which significantly propagates in the Fig. 1. The last 50-second-long-sequence was used for reference and recalibration so none of the sensors has been moved and they remained in the same static altitude.

3.2 UAV measurement

The test conducted using Unmanned Aerial Vehicle (UAV) has been held in an open-air field with a west wind of 25km/h/15.5mph and temperature 18°C/64°F [3].

The initial laboratory measurement has been followed by an open space in flight conditions measurement. This has been achieved using the UAV. Two previously used pressure sensors have been inserted into protected chambers located on opposite sides of the aircraft wing. This small-scale model of an aircraft was used to determine the extent to which it is possible to resolve a roll angle on the experimental basis via the pressure difference between sensors placed on each side of the wing.

In the Fig. 2 (in Appendix) is represented the pressure difference development throughout the flight (marked with a yellow line) and the total of 3 other characteristics. One of which is the trajectory input provided by the Autopilot. The Horizon detection shows the roll angle using the combination of camera and picture recognition software. Third, supportive characteristic, is the pressure border which simply suggests a tilt of the aircraft either to the left or right side.

3.3 Stratospheric balloon measurement

To ultimately determine the maximum altitude and working range for chosen measurement method and the overall validity of the method, a stratospheric balloon flight has been chosen. The test flight was realised within the BEXUS 23 campaign in October 2016 at Esrange Space Center near Kiruna. The initial conditions at the launch site were 6.05°C of air temperature and 996.56 hPa of atmospheric pressure on the ground level (333 metres above sea level). As the conditions dynamically changed, a section 4.1. elaborates on them.

The Experiment used following design features:

3.3.1 Mechanical design

In order to maximise the amount of measured data, the construction and interfaces comprise durable off-the shelf polycarbonate boxes which serve as enclosures both for pressure sensors as well as communication and memory units.

Figure 3 Experimental assembly on ground

The pressure sensors are located on the mounting rod outside of the gondola and connected with the control & memory unit inside the gondola. There are 6 enclosures in various sizes used for the experiment. Five of these protect the pressure sensors that are set apart by 462 millimetres to maintain as big vertical distance as possible. Within each of the enclosures is a specially design case surrounded by thermal insulation form a lightweight polyethylene foam. Each of the box has an inbuilt connecting interface connector allowing a simple connection with the main box using 6 cored FEP

insulation cables. The aforementioned aluminium alloy mounting rod is attached to the gondola by polycarbonate crossbars which was designed to break off upon landing to transform the kinetic energy of the impact into deformation, hence protecting both gondola and the experimental set-up itself. The enclosure placed inside of the gondola, has a particular thermal design. It is insulated from the inside using layers of polyethylene foam which provides good insulation in flight, however, to avoid overheating prior the flight, a custom made polyethylene cradle filled with dry ice (200g) has been inserted underneath the main box.

3.3.2 Electronics design

The core of the measurement is conducted using 5 pressure sensors Memscap TP3100. These are all connected with the PC Advantech ARK-1503. To process signals on different logic levels, an RS232-to-TTL converter is in use. Apart from these components, the experiment comprise 4 bare Printed Circuit Boards (PCBs) in the main box (Altitude Heading Reference System - AHRS, Power supply, Converter and 5V regulator). The experiment is using an integrated gondola power supply [4].

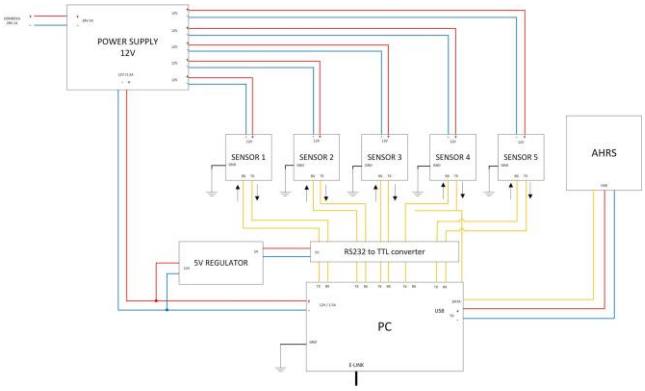

Figure 4: Power scheme of the experiment

2.3.3 Software design

The measurement control software is running on simplified Linux OS distribution Fedora. On this OS, a control program, gathers the data, saves them into internal memory (SD card) and sends the measured data immediately to ground station via E-link to ensure potential data recovery. It has been calculated that it is required to maintain a sampling frequency from the pressure sensor to the PC of 10 μs. Apart from measuring the pressure in each sensor, it also records the temperature at each of the sensors. The programme is autonomous with optional manual control. This has been used to switch off the experiment during the float phase to protect the experimental set-up from overheating. Program consists of several separate processes, in which the original process is forked after Ethernet initialization. Scheme of the process communication using pipes is shown in the Fig. 6 (in Appendix).

4. RESULTS

4.1. Flight data

For reference, flight data from the EBASS unit [4] installed on the balloon payload has been recorded. The ground altitude was 333 metres above the sea level, the maximum reached altitude 32290 metres above the sea level. The temperature development can be seen in the Fig. 5, it varied between -58.6°C during the ascent and 22.9°C during the float phase as the sunlight heated the gondola up. This also reflected on the result of actual measurement. The ground level pressure was 996.5 hPa and the minimum temperature during the float phase was 5.6 hPa.

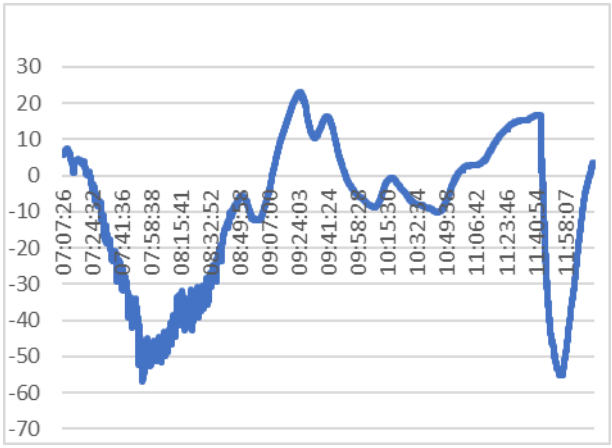

Figure 7: Development of an air temperature during the flight

4.2. Measured data

In the flight data analysis, the input from all 5 sensors has been successfully recorded, although the quality of input varies throughout the flight. This is mainly caused by adaptive self-calibration of the sensors and instable flight conditions. Although it has been expected to encounter turbulences and other weather phenomenon and it was considered in the experimental set-up, it significantly affected the quality of the outcomes. Initially, it has been expected to use the data from both ascent and the descent, however some of the sensors from unforeseen reasons conducted recalibration during the float phase and dramatically distorted the descent phase data output. Therefore it has been decided to focus mainly on the ascent data.

This fraction of data can be seen in the Fig. 8 and it is marked with the red rectangle.

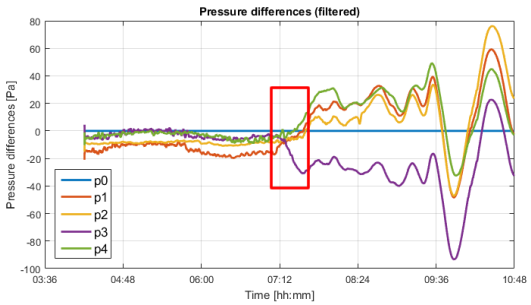

Figure 8: Pressure differences of the ascent phase

To interpret the data correctly, it is important to understand the actual sensor set-up and naming. Naming of the sensors has been done in a following way:

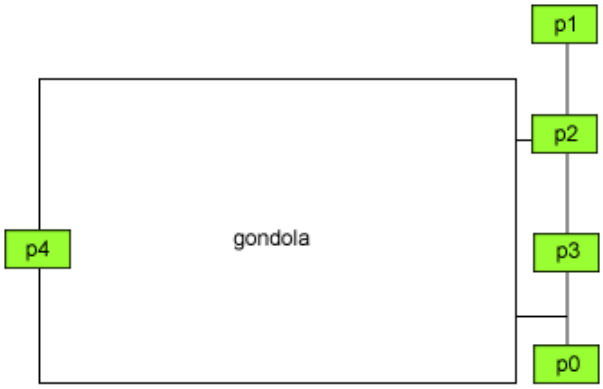

Figure 9: Sensors set-up during the inflight configuration

Furthermore, some of the sensors provided instable in-flight data. On multiple occasions, several sensors deviated from the expected progress of the pressure difference, as they overlapped or went completely off their expected trajectory. Despite repeated filtering of the data which was required as the sensors are unnecessarily precise, sensors provided dissatisfying results. This can be seen in Fig. 10:

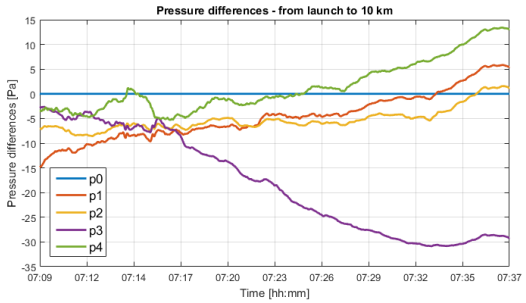

Figure 10: Pressure differences during the first 10 km

By the process of elimination, sensors p2, p3 and p4 have been filtered out. The only sensors which provided adequate input were the most distant ones, namely p0 and p1. These behaved according to the pre-flight calculations, therefore provided the most viable output data which could be further analysed. These two sensors have been compared in Figure 11, where the input of sensor p0 has been used as a reference and the progression of the pressure difference between p0 and p1 is represented using a red line. The represented sequence is from the ascent phase.

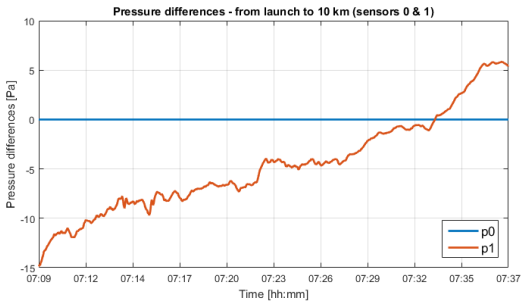

Figure 11: Pressure difference between p0 and p1

It can be seen that at 7:34 both lines cross. At this moment, the pressure difference becomes the same as the absolute resolution of chosen pressure sensors. Using comparison of the EBASS data and data from the pressure sensors it has been calculated that the maximum working range of the measurement method is approximately 8 kilometres of altitude. This is less than in theory which expected the altitude of 10 to 12 kilometres above the ground.

4.3. Explanation of the results

The measured experiment results differ in various aspects from the expectations and preliminary calculations which determined theoretical values. There are multiple factors influencing the results and possible explanations for such measurement record.

- Use of MEMSCAP TP 3100 – these military sensors primarily used by US Air Force seemingly provide extremely high precision, however, their working principle and detail preprogramed setting is classified, therefore certain unforeseen situations can happen. One of which is an adaptive filtering and uncontrollable internal independent calibration of each sensors. This obviously results in loss of relevance of results in case of using multiple sensors for a comparative measurement and analysis.
- Weather effects – from the EBASS data as well as data provided by other experimental teams located on the same gondola it is known that the balloon flew through turbulences which reflected in majority of cases equally on all sensors, however they could be a trigger for some of the aforementioned changes in sensors behaviour. Also, due to a placement of sensors in an extensive spatial configuration, each of

the sensors (despite the effort trying to minimise this effect), has been exposed to different sunlight – and thus – temperature conditions. Temperature usually promotes widely in the behaviour of the membrane pressure sensors as it can affect the elasticity and tension of the membrane. Certain differences in temperature recorded by the sensors can be seen in Fig. 12

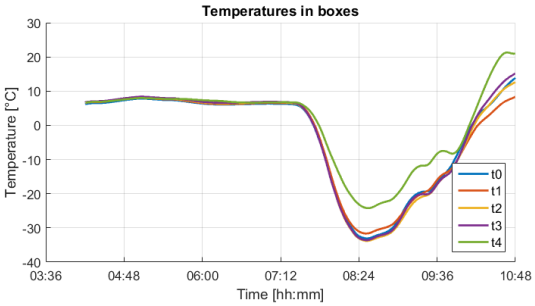

Figure 12: Temperatures in enclosures

Furthermore, the local weather conditions, 200 km above the polar circle could potentially explain the difference in expected working range of the method and the empirical results.

5. CONCLUSIONS

The PREDATOR Experiment conducted in several phases provided the research of aircraft navigation systems and their position resolution methods with valuable input. Despite the difficulties with the technical configuration and challenging weather conditions, the measurement method using pressure sensors has been proven as valid.

This however does not go without limitations and constrains. One of the major condition is the way the data is analysed and processed. The success rate of the method validity varies immensely depending on the length of the continuous data sample. To illustrate this, a following chart can be used:

Minimal Interval Length	Method Validity Success Rate	Success Rate within 0.5x-1.5x of calculated result
1	48.9%	20.0%
5	29.1%	3.2%
10	29.1%	3.2%
15	20.1%	2.0%
20	14.2%	1.3%
25	10.9%	0.8%
30	9.3%	0.6%
35	5.3%	0.1%

Figure 11: Method Validity Success Rate

Depending on the interval length of the measured sample upon which we decide on the method validity, the success rate varies a lot. The longer the analysed sample is, the lower the success rate is. This is caused both by having very incoherent results from overly sensitive sensors. Even after flattening and filtering out the raw measurement data, the outputs do not provide the desired reliability. The success rate of the method validity decreases as the analysis spans over greater and greater length of a sample. To improve the outcomes of the research in future instances, certain suggestions and recommendations should be followed:

- The data analysis method shall be reconsidered, this way, it is extremely dependent on high quality, smooth input from pressure sensors which degrades with any disturbance, such as turbulences and uneven weather effects on each of the sensors.
- To improve the quality of the input, different pressure sensors shall be used. Although TP3100 seemingly provide very high precision of the results, each sensor has its own specific behaviour which is not suitable for experiments that require comparative analysis. Furthermore, the high resolution of the sensors degrades the quality of input in case of other-than-ideal conditions.
- The experiment should be tested again in a modified configuration which would counter the aforementioned atmospheric effects.

In conclusion, this very promising measurement method has been proven valid with certain limitations. It is a satisfying and motivating result which opens opportunities for further testing and potential development of new, functional devices which may add another layer of information to future aircraft navigation systems.

6. ACKNOWLEDGEMENT

The project was supported by the research program no. SGS15/212/OHK3/3T/13, “Safe and Safety Elements in Aerospace and Space Technology II”, of the Czech Technical University in Prague.

7. REFERENCES

[1] Kalman, R.E. (1960). "A new approach to linear filtering and prediction problems" Journal of Basic Engineering. 82 (1): 35–45. doi:10.1115/1.3662552. Retrieved 2008-05-0

[2] International Organization for Standardization, Standard Atmosphere, ISO 2533:1975, 1975.

[3] O.Trojan, P. Paces, Static Pressure Measurement And Horizontal Roll Angle Comparison During UAV Flight (not published yet)

[4] REXUS/BEXUS Organisers, KINNAIRD A. BEXUS User Manual. 2014

8. APPENDIX:

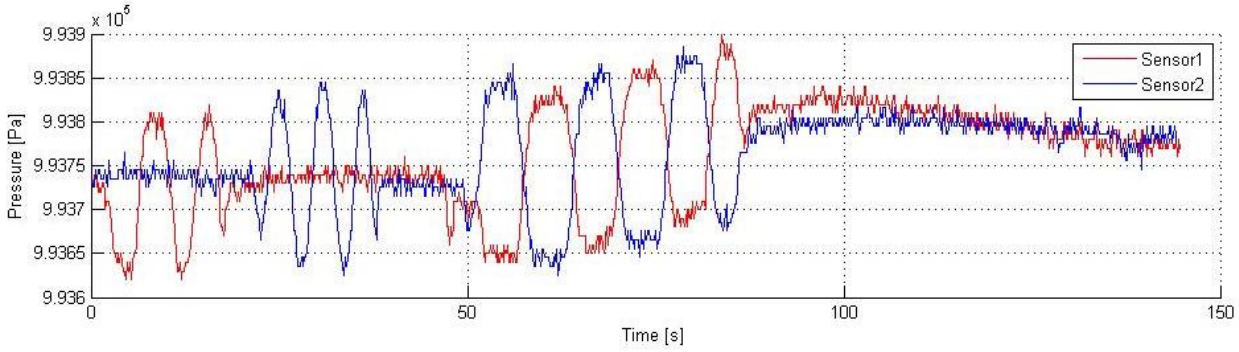

Fig. 1. Pressure difference measurement in a laboratory conditions [3]

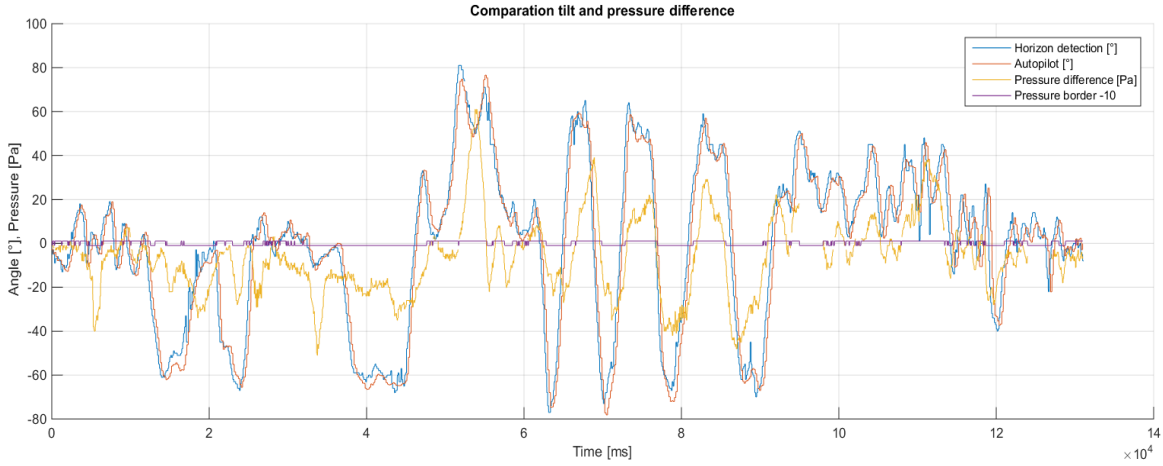

Fig. 2 Pressure difference measurement on UAV [3]

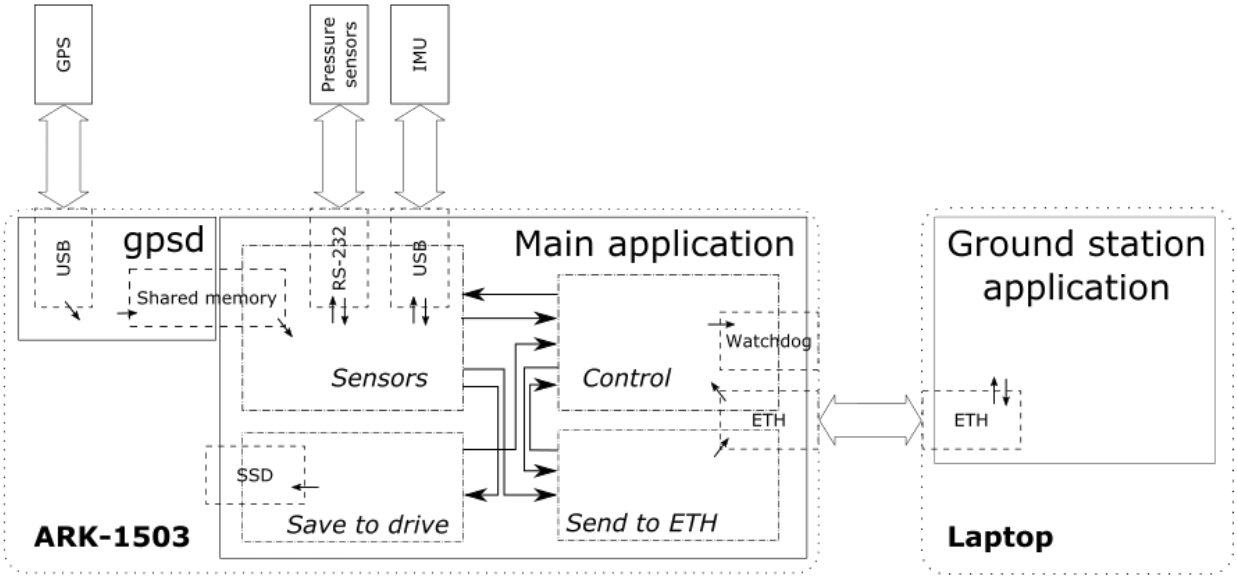

Fig.6 Program scheme

XRMON-DIFF 2 MICROGRAVITY EXPERIMENT MODULE ON MAXUS 9

A. Værnéus [(1)], Y. Houltz [(1)] , O. Jansson [(1)], M. Lindh[(1)],
F. Kargl [(2)], E. Sondermann[(2)],

[(1)] Swedish Space Corporation, P.O. Box 4207, SE-171 04 Solna, Sweden, alf.vaerneus@sscspace.com
[(2)] DLR, Institut für Materialphysik im Weltraum, Linder Höhe, 51147 Köln, Florian.Kargl@dlr.de

ABSTRACT

The XRMON-DIFF 2 microgravity experiment performed in-situ monitoring of diffusion process of metal alloys (AlTi and SiGe) in different concentrations on board the MAXUS 9 rocket launched in April 2017. The purpose is to demonstrate to industry how diffusion measurements (especially for technically important alloys) should be performed on earth, and how deliberate µg-experiments serve as calibration of terrestrially obtained results.

The experiment used a custom designed furnace, providing the ability to achieve a controlled start of the diffusion process, using a shearing mechanism. The samples were melted prior to launch, and the diffusion process was started in a controlled manner once microgravity conditions were achieved. The whole diffusion process and events were monitored using high-resolution X-radiography.

This paper describes the technology development of the experiment module

1 BACKGROUND

1.1 XRMON project under MAP programme

The XRMON (X-Ray Monitoring) project under the ESA MAP (Microgravity Applications Promotion) programme was established to conceive and perform in situ X-ray radiography observations of metallurgical processes under microgravity and terrestrial conditions. Under the programme, a series of experiment modules and facilities have been developed and advanced experiments of metallurgical processes have been performed with X-ray radiography observations under microgravity conditions. These include:

- ✓ XRMON-Metal Foam: Study of metallic foams, MASER 11 2008, two parabolic flight campaigns in 2007 and 2009
- ✓ XRMON-Diffusion: MAXUS 8 sounding rocket in 2010
- ✓ XRMON-Gradient Furnace: MASER 12 sounding rocket in 2012
- ✓ XRMON Laboratory Set-up in 2012
- ✓ XRMON Parabolic Flight Facility: Four flights during 2013-2016
- ✓ XRMON-SOLidification Furnace: MASER 13 sounding rocket in 2015
- ✓ XRMON-Diffusion 2: MAXUS 9 sounding rocket in 2017
- o XRMON-Gradient Furnace 2: MASER 14 sounding rocket, under pre-study

1.2 XRMON-DIFF Experiment Module Legacy

The XRMON-DIFF 2 module is a partial reflight of the XRMON-DIFF module, flown on MAXUS 8 2010. Major modifications include a new furnace design to be compatible with the alloys of greatest interest for the Science Team. In addition, a shearing mechanism was introduced, providing a controlled start of the diffusion process. To be compatible with the new furnace system a significant update of several support systems in the module was introduced. However, the principle concept, including the X-Ray monitoring system, was re-used.

1.3 XRMON-DIFF Furnaces

The furnace assembly of the predecessor XRMON-DIFF consist of three furnaces. The PIs delivered graphite crucibles containing diffusion couples samples. With a heater insulated with Al2O3 tubes the crucibles were heated and the temperature monitored with two thermocouples at two different positions in the crucible. Alumina felt insulation was winded around the crucible in order to reduce the heat radiation together with a Ti foil. The complete crucible was mounted tight in a quarts glass tube with feed troughs in top and bottom, this assembly is named Diffusion Couple Assembly, DCA.

The DCAs were mounted in the experiment assembly with connections for vacuum and cooling gas in the bottom part. Valves for the cooling gas are controlled during the experiment sequence. Before flight, valves for vacuum access are used for evacuation of the DCA cavities.

These furnaces were flown on MAXUS 8, March 2010.

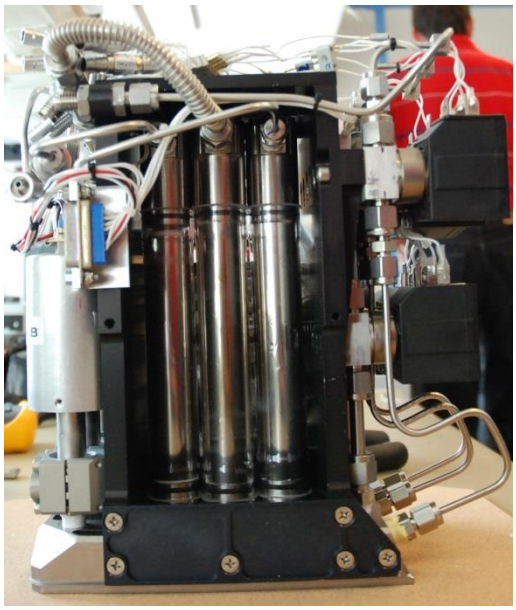

Figure 1. The DCA's of the XRMON-DIFF module

2 XRMON-DIFF 2 EXPERIMENT MODULE

2.1 XRMON-DIFF 2 Furnace

The furnace used in XRMON-DIFF 2 is developed at DLR, Cologne, and is a modified version of a previously used [1] shear-cell type furnace, in detail described in [2], illustrated in fig. 2. For the XRMON-DIFF 2 experiment, the furnace comes in two configurations, one with a graphite-based crucible and one with an alumina crucible, the latter compatible with temperatures up to 1600°C

Figure 2. Shear cell furnace used in the XMRON-DIFF 2 module

The furnace principle components are the crucible, with support for three sample rods, and the heaters, one at each side of the crucible. This furnace has been shown to provide very good isothermal conditions upon constant power input. The bottom part of the crucible is movable, enabling the shearing to take place by pushing it with a shearing rod.

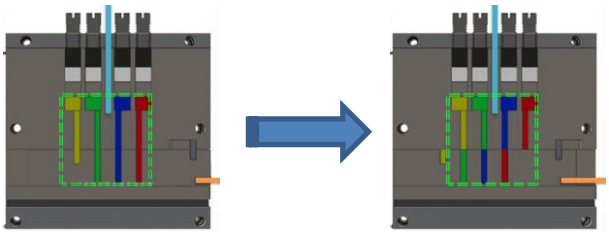

Figure 3. Shearing concept

The heater wires, made out of Mo-Lanthanoxid (ML), are connected to the power sub-system, further described in 2.4. The crucible has also support for insertion of two thermocouples, thereby positioned close to the alloys of interest, representing the experiment temperature.

The samples integration into the furnace can be done well in advance of the experiment execution.

2.2 Diffusion Vacuum Assembly (DIVA)

The furnace integration is a multi-layer assembly, to provide the appropriate environmental conditions for the samples. The full assembly, the DIVA, is designed by SSC to contain two shear cells as described above.
The first layer in the DIVA assembly is a thermal insulation layer out of graphite foam, which introduces a 40mm thick layer around the furnaces, illustrated in figure 4. These 40mm provides a thermal gradient of 1560°C - ~150°C on the outside when operated in the module. The heat loss at target temperature is in the range 250-300W.

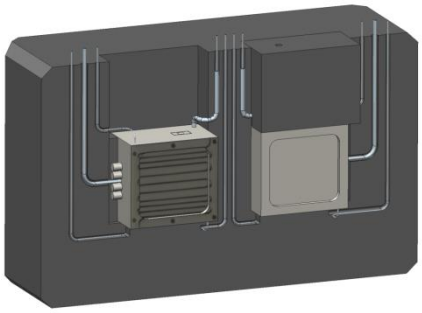

Figure 4. Shear cell furnace used in the XMRON-DIFF 2 module

On top of the thermal insulation layer is the electrical interconnection section, where heater wires and thermocouples are connected to the supporting sub-systems, illustrated in figure 5.
The second layer of protection provides a pressure-tight compartment, enabling the assembly to be evacuated, which is required during heating.
In the bottom part of the DIVA, two DC motors are located, used for the shearing movement of each shear cell. The motor shaft is connected to a Niobium rod to transfer the force to the shearing slide in the crucible

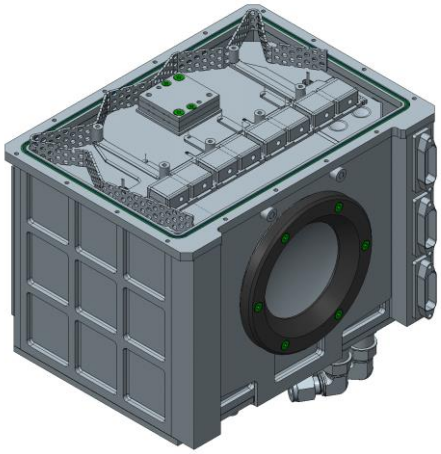

Figure 5. Furnaces and insulation foam inserted into the DIVA, with the electrical connectors visible.

When fully assembled, the DIVA is not necessarily fixed to the module, due to the slide-in interface used for insertion and removal of the unit from the module, via a late-access hatch in the outer structure of the module.
The DIVA also contains a cooling loop, connected to the module cooling system once installed in the module. This is necessary for a proper heat transfer from the furnace heating during operation.

2.3 X-Ray Imaging

Although the same X-Ray source and X-Ray detector were used, the sample placement for XRMON-DIFF 2 has been adapted to the FoV requirement of the two shear cells in the DIVA

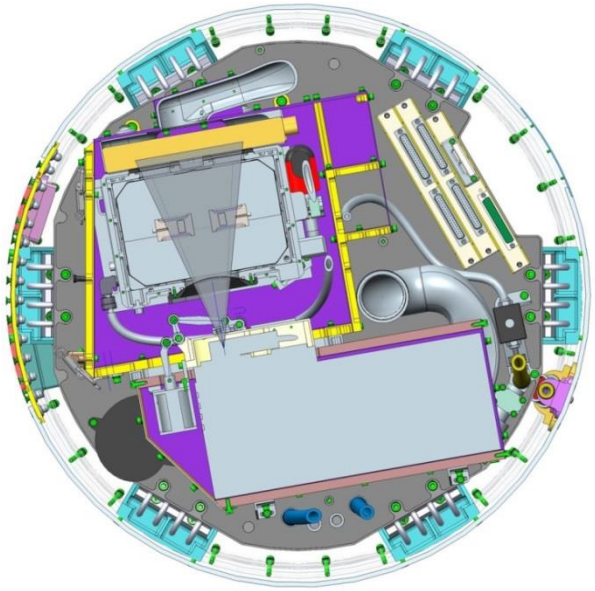

Figure 6. X-Ray image projection illustration

Figure 6 illustrates the relation between X-Ray source, the sample and the detector.
The X-ray unit is a 10W Hamamatsu L8031-01 Tungsten target microfocus source. In order to obtain a 5um focal point it should be operated below 7W (60kV 115 uA). In this application operation at full power may be feasible.
Images are recorded by a digital X-ray flat-panel detector, Hamamatsu C7942CA-02 . The detector active area is 120x120 mm, 2400x2400 pixels, 50 x 50 µm pixels,12-bit image depth, max 2 f/s.
The distance from the source to sample is 140 mm and the distance from the source to the flat panel sensor is 224 mm. This gives magnification factor 1.6.
Both the X-Ray units and the DIVA is, when operated, enclosed in a radiation-proof containment, providing safe operation for the personell.

2.4 XRMON-DIFF 2 Electronic System

The experiment system is controlled, supported and monitored by the on-board electronic and power system. The experiment sequence is primarily controlled by the on-board Power Control and Distribution Unit (PCDU). By sending commands to the supporting Electronic Control Boards (via a CAN network), the PCDU controls the individual components in the system. Similarly, sampled sensor data is packed in CAN data messages and transmitted from the Electronic Control Boards to the PCDU for storage and transmission to ground via the telemetry system.
A separate Image Control Computer (ICC) controls the X-ray tube and the digital X-ray flat-panel detector, connecting to the PCDU over network interface. This system stores images in real-time on a Solid State disk drive.
Two custom-designed power boards are used to provide up to 1kW to each furnace in the DIVA. This board implements an external-internal power switch, providing glitch-free transfer from external to internal power, even when operated at full power.

2.5 XRMON-DIFF 2 Module

As the XRMON-DIFF 2 module in principle is a reflight of its predecessor, the layout of the module is similar, however with a few modifications.
The physical properties of the module are:

Diameter: 640mm
Total height: 669mm
Total mass: 104kg

Figure 7. XRMON-DIFF 2 Module with late-access hatch open and DIVA installed.

3 XRMON-DIFF 2 FLIGHT ON MAXUS 9

MAXUS 9 sounding rocket, with XRMON-DIFF 2 on board, was launched on April 7th, 2017. It reached apogee of 678.3 km and provided good microgravity levels about 10^{-4} g for 707 seconds.
XRMON-DIFF 2 module was controlled by a pre-configured time-tagged tele-command queue. XRMON-DIFF 2 experiment was nominal during the count-down and the flight. No manual intervention was needed.
Figure 7 shows the flight time line by using the actual furnace temperature data during the flight.
The experiment started at T-13 min, heating the first sample from the preheating condition of 700°C up to target temperature at the rate of 1.5 K/s. At T-9 min, the second furnace final heating was started.
The samples in the two furnaces did melt at approximately T-2min, and were fully molten upon launch.

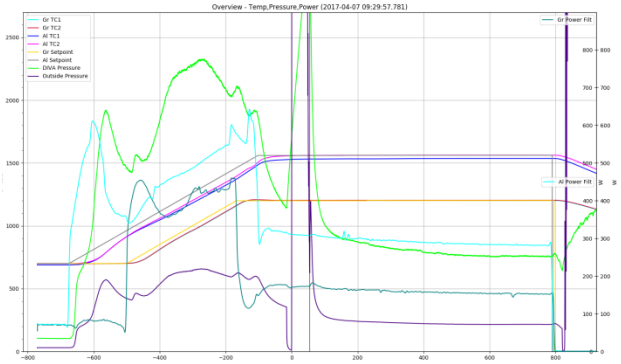

Figure 8. Experiment temperature profile / Time line

At T-1min the power was switched to internal, at a time when the power output was close to constant. The vacuum pump on ground, used for evacuating the experiment assembly, was stopped at T-15s after the closure of a vacuum valve in the module. This valve was opened again at T+55, a time when the outside atmospheric pressure was well below the pressure within the DIVA.

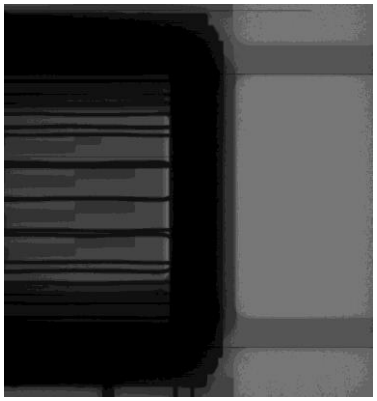

Figure 9. X-Ray image of ongoing shearing in alumina furnace

50 s after microgravity start, the shearing of the alumina furnace was initiated and successfully finalised. The same occurred for the graphite furnace 120s after microgravity start.
Once the shearing of the two furnaces were finalised, the observation period starts. The X-Ray images in combination with the experiment temperatures provides the vital information about the experiment execution.
The observation phase continues throughout the rest of the microgravity period. Just befor the end of microgravity the heating of the furnaces were shut off. Also other vital sub-system, especially the X-Ray equipment, were shut off before re-entry occurred.
All flight events were nominal and no manual interaction with the module was needed during flight.

Upon publication of this paper, the scientific analysis of the results are still ongoing.

4 ACKNOWLEDMENTS

The authors wish to acknowledge the funding for development of XRMON-DIFF 2 furnace and module through ESA's ELIPS (European Life and Physical Sciences in Space) programme. The research work is supported by the ESA-MAP project XRMON.

5 REFERENCES

1. Martin Siegl, Florian Kargl, Frank Scheuerpflug, Jörg Drescher, Christian Neumann, Michael Balter Matthias Kolbe, Matthias Sperl, Peidong Yu and Andreas Meyer, "Material Physics Rockets Mapheus-3/4: Flights and Developments", Proc. 21st ESA Symposium on European Rocket and Balloon Programmes and Related Research.

2. Neumann, C., Sondermann, E., Kargl, F., & Meyer, A. (2011). Compact high-temperature shear-cell furnace for in-situ diffusion measurements. Journal of Physics: Conference Series 327, 012052.

BALLOONS AND SOUNDING ROCKETS – PLATFORMS FOR DROP TESTS

Gunnar Florin [(1)], Christian Lockowandt [(1)], Mattias Abrahamsson [(1)]

[(1)] SSC, P.O. Box 4207, 171 04 Solna, Sweden, Email: gunnar.florin@sscspace.com

ABSTRACT

Stratospheric balloons and sounding rockets can provide an ideal in-flight platform for performing re-entry and other high speed tests off different types of vehicles and techniques. They are also ideal platforms for testing different types of recovery systems such as airbrakes and parachutes.

This paper expands on some examples of platforms and missions for drop tests from balloons as well as sounding rockets launched from Esrange Space Center, a facility run by Swedish Space Corporation SSC in northern Sweden.

1. INTRODUCTION

With an increasing interest in Europe to test and validate re-entry systems of various kinds in-flight, an increased demand on flight opportunities from Esrange Space Center can be expected.

Stratospheric balloons that are launched from Esrange has a capacity to lift a mass up to 2 tonnes and can reach an altitude of 40 km, equivalent to an atmospheric pressure of 3 mbar. The payload or test object (re-entry vehicle, parachute system, etc.) that shall be tested can be equipped with telemetry and tele-command system for real time monitoring and control during the complete flight and free fall.

Sounding rockets launched from Esrange can also be used in a similar way for reaching high altitudes, although with a lower mass test objects. Rockets with different capacities can be launched to any altitude up to 700 km, and can carry experiment payloads up to 300 kg.

2. ESRANGE SPACE CENTER

Esrange Space Center (67.9°N - 21.1°E) is operated by SSC. From Esrange are launched circumpolar balloons as well as sub-orbital sounding rockets. With its large impact zone of 5200 km^2 and 6100 km^2 restricted air space in non-inhabited area 40 km from the town of Kiruna in northern Sweden above the polar circle, Esrange is an ideal site for performing challenging re-entry missions tests.

Esrange was inaugurated in 1966, and has since then launched over 1000 rockets and balloons. The largest balloons lift over 2 tonnes of payload to 42 km altitude and largest rockets lift 800 kg payload to 700 km apogee. Over the decades, drop tests of various bodies have been performed in the Esrange area. Hereafter is described a few of them as well as some upcoming ones.

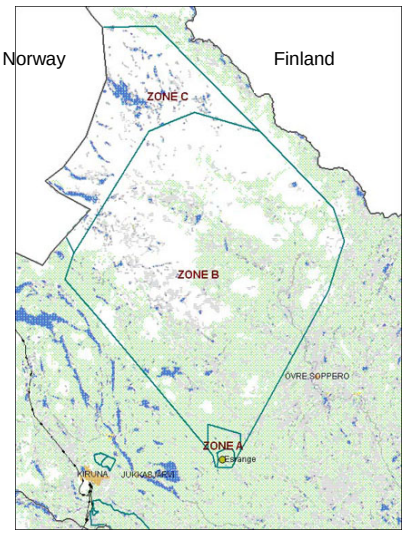

Figure 1. Esrange Impact Zones, 5200 km2.

3. D-SEND

D-SEND is a JAXA project with goal to design a silent supersonic transportation system that is economically viable and eco-friendly for travels in the 21st century.

1.1. D-SEND #1

Figure 2. SSC's vehicle 'Hercules' preparing to release D-SEND #1 drop bodies

In first phase, drop bodies with shaped nose cones were in 2011 released from a balloon at 20 km altitude. A system of blimp-carried microphones at 1 km altitude, positioned at various spots in the impact area, measured

the effect of the turbulence to the sonic boom signatureBy these drops, the validity of low sonic boom axisymmetric design by a balloon drop test was confirmed.

The gondola and drop bodies were manufactured and provided by SSC, in accordance with JAXA's design

1.2. D-SEND #2

In the second phase, an experimental supersonic 8 meters long unmanned airplane was released on July 24, 2015 from a balloon at 30.5 km altitude. The aircraft glided at a flight-path angle of 47.5 degrees and speed of 1.39 Mach over the blimp system that measured the sonic boom where the generated boom signature went down vertically towards the systems.

Figure 3. SSC's vehicle 'Hercules' holding JAXA's D-SEND #2 aeroplane. Photo by JAXA.

4. ERC

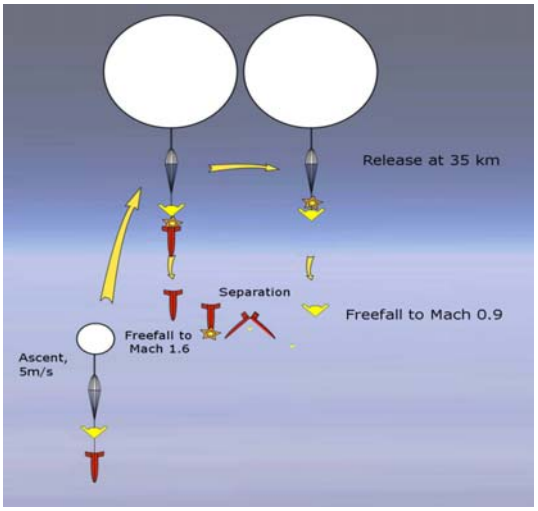

Figure 4. Sketch of the ascent, release and descent phases of ERC drop bodies. Sketch by Vorticity.

A series of drop tests by balloon were to be carried out at Esrange in summer 2015 with the objective of performing full end-to-end dynamic stability tests of re-entry capsules, validating the designs and acquiring detailed aerodynamic characterization of Earth Return capsules of different shapes.

Small ~60 kg bodies, developed by Vorticity (UK) under ESA contract, were dropped over Esrange impact area from stratospheric balloons at 35 km altitude.
The mission consisted of successful drops of nine bodies, from three balloons, carried out during two campaign periods in June and August 2015. The balloon system, flight train, service system and separation systems were provided by SSC.

Figure 5. Launch of the balloon with ERC drop bodies.

5. SHARK

SHARK - Sounding Hypersonic Atmospheric Re-entering 'Kapsule' – is a drop body for test of Ultra High Temperature Ceramics (UHTC), developed by CIRA, Italy. It was accommodated on Maxus 8 sounding rocket micro gravity mission with the objective to prove the possibility to set up a low cost experimental space platform and execute a re-entry test flight by dropping a capsule from a sounding rocket.

Figure 6. Flight model of SHARK capsule

With its high trajectory apogee of 700 km, MAXUS programme served as perfect platform for carrying out SHARK re-entry test flight. The accommodation of SHARK was decided quite late in the project of MAXUS 8 – little more than six months before launch.

Figure 7. MAXUS 8 rocket (left) and payload (right).

The requirements from MAXUS towards SHARK were well defined: SHARK must be not interfere with the MAXUS mission, its diameter must be limited to 290 mm, height 250 mm and mass below 20.0 kg.

Respecting these constraints, SHARK capsule could be accommodated in the volume of the motor adapter, but mounted onto the aft end segment of the payload, namely the re-entry cone.

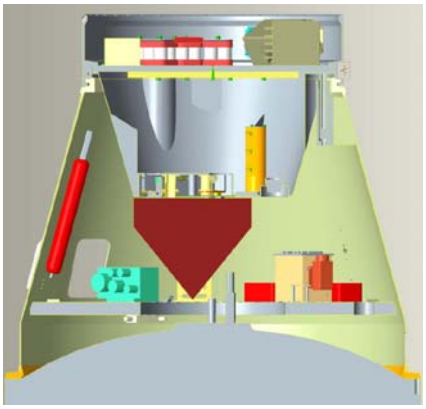

Figure 8. Cross-cut of motor adapter volume with SHARK inside the volume, mounted on re-entry cone.

An in-house designed separation system using a three-spring system with wire-held hooks and explosive wire cutter was used to achieve controlled separation of the SHARK capsule.

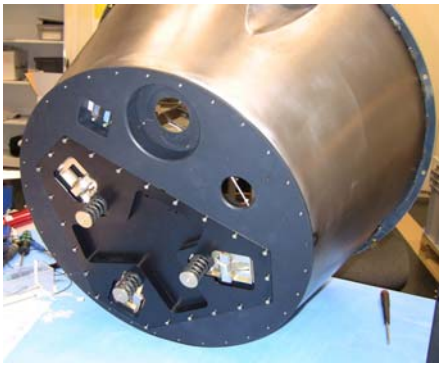

Figure 9. Three-spring separation system of SSC.

With the short time available for development of SHARK, the capsule was delivered to the project at shortly before the start of the launch campaign. It required a minimum of interaction from the MAXUS project side The separation should be activated 5 seconds after motor separation, and the separation speed was designed to be 1 m/s. The robust SSC separation system had already been used for separation of small satellites.

Figure 10. Flight integration of SHARK, mounted on the MAXUS 8 re-entry cone at Esrange Space Center.

SHARK lifted off with MAXUS 8 on March 26, 2010, only 9 months after its introduction to the MAXUS project. Separation of SHARK occurred 91 sec after ignition, at a ~150 km altitude, at a speed of 3 km/s and 88° flight path angle. SHARK reached apogee of over 700 km during its ballistic flight

The capsule had no parachute system, and in spite of a robust system of localisation based on a satellite emergency locator system, It was hard to localise SHARK after the flight in the arctic and snow-covered impact area. SHARK was localised in the field three months after launch. The prediction of the landing site was pretty accurate and the capsule was found at less than 3 km from the estimated landing site.


Figure 11. SHARK at impact site.

The SHARK mission was a great success, and opened the door to using sounding rockets as in-flight platforms for drop capsules. SHARK will be followed by Supe-MAX capsule on MAXUS 9, for test of a super-sonic parachute.

6. SUPERMAX

SUPERMAX – 'Supersonic parachute test bed demonstrator' on MAXUS – is a supersonic parachute test bed demonstrator for conducting a supersonic parachute free flight test, where MAXUS offers a better test facility than currently operating wind tunnels. The system was developed by Vorticity, UK. It was accommodated on Maxus 9 sounding rocket micro gravity mission with the aim to demonstrate Europe's capability to conduct a supersonic parachute test using a piggy-back payload on a sounding rocket flight, and to deploy a parachute at supersonic speeds (Mach 1.4 to 2.0)

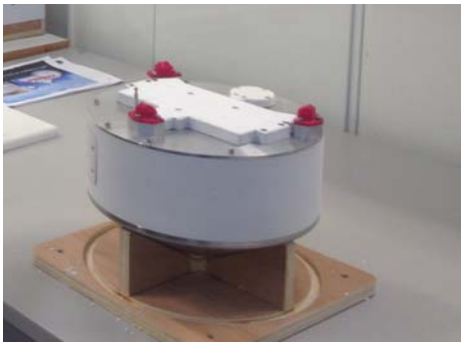

Figure 12. SUPERMAX capsule. Photo by Vorticity.

With its high trajectory apogee of 700 km, MAXUS programme served as an very interesting platform for carrying out SUPERMAX validation flight, providing the opportunity to reach high mach values. The accommodation process of SUPERMAX benefited from the experiences made for SHARK accommodation on MAXUS 8. The SHARK boundary conditions –

volume, attachment points, operations – were also applied for SUPERMAX. Mass limit was set to 15 kg.

Figure 13. MAXUS 9 rocket ready for launch.

Respecting these constraints, SUPERMAX capsule could be accommodated in the volume of the motor adapter, but mounted onto the end-cone in aft end segment of the payload.

The in-house SSC designed separation system using a three-spring system with wire-held hooks and explosive wire cutter was again used to achieve controlled the separation of the capsule. The separation was to be activated 5½ seconds after motor separation, and the separation speed was again designed to be 1 m/s.

In the wake of analyses made after the MAXUS 8 flight, where the end-cone was lost during re-entry, the end-cone 'lid' had undergone a designed modification, in order to better withstand the thermo-aerodynamic re-entry forces. The changes consisted of change of material to high strength structural and bracing to cope with the aerodynamics loads, as well as application of ablative cork on all surfaces subjected to high thermal loads during the re-entry phase. The interface to the drop body remained nevertheless unchanged. Separation tests and mechanical fit-checks using a representative mock-up proved to be a valuable step in the acceptance process.

Figure 14. Flight integration of SUPERMAX completed, mounted on the MAXUS re-entry cone.

SUPERMAX lifted off with MAXUS 9 at 11.30 AM (LT) on April 7, 2017.

Figure 15. SUPERMAX (middle right) released from MAXUS payload, after motor (lower right) separation. Also in picture: one of the three separation spring (left).

Separation of SUPERMAX occurred 91.4 sec after

ignition, at a ~163 km altitude, at an upward speed of 3 km/s and 88° flight path angle. SUPERMAX reached an apogee of 680 km during its ballistic flight.

The capsule had a robust system of localisation based on GPS data, with position transmitted in real time to the ground station. Hence, localising SUPERMAX, having impacted 6 km from MAXUS payload impact site, was easy, and the object was retrieved together with the payload a couple of hours after flight.

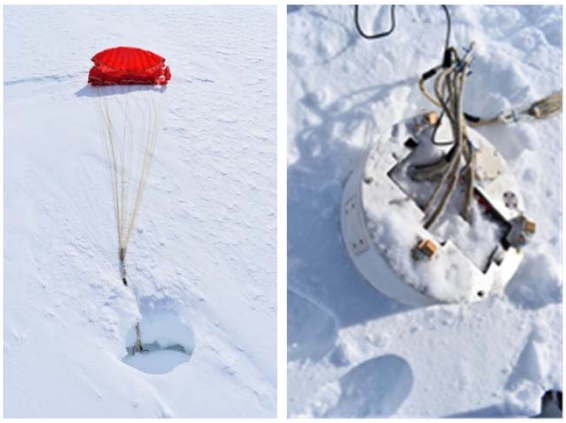

Figure 16. SUPERMAX at impact site. Photo by Vorticity.

The SUPERMAX mission was a great success, and confirmed the using of sounding rockets as in-flight platforms for drop capsules. SUPERMAX will be followed by Mini-Irene (Italian Reentry NacElle) capsule, an ESA project under CIRA contract, in 2018/2019 on a sounding rocket flight to 260 km apogee, for flight demonstration of a deployable heat shield aimed at a drastic reduction of Ballistic coefficient.

7. HADT

PAS HADT (Parachute System High Altitude Drop Test) balloon flights will take place in May/June 2018 and July/August 2018.

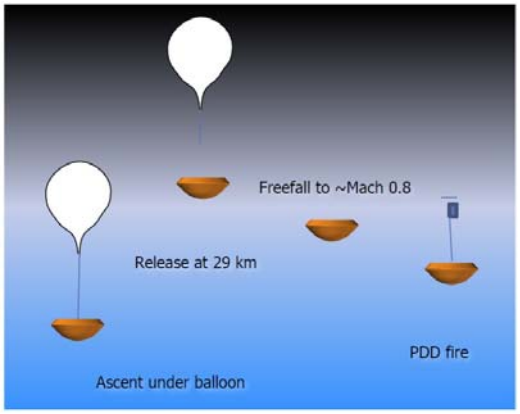

Figure 17. Visualisation of balloon ascent phase and PAS descent after release. Sketch by Vorticity.

The mission contains drops of two bodies with parachutes from balloons floating at 29 km altitude. One body weighs 800 kg and the other 2000 kg. The objective of the mission is to qualify the parachute system designs to be used within ExoMars program. The drop bodies have been design by Vorticity (UK) and the mission is carried out under ESA contract

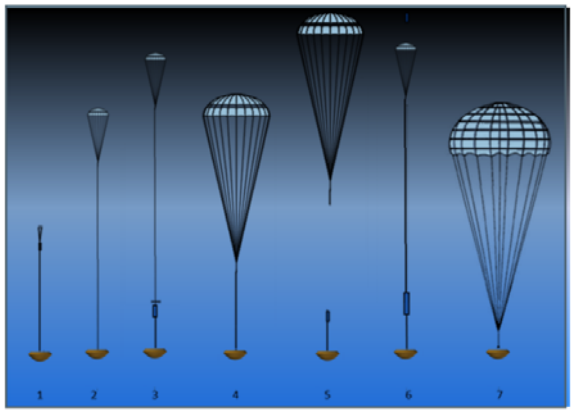

Figure 18. Visualisation of parachute qualification test after release from balloon. Sketch by Vorticity.

8. OTHER EXAMPLES OF USING SOUNDING ROCKET AS IN-FLIGHT PLATFORM

MASER 13 sounding rocket – a microgravity mission launched in December 2015 from Esrange Space Center - accommodated a payload data transmitter system using SOQPSK modulation, demonstrating the feasibility to enhance the band width of the payload by 2-4 times to 20 Mbps.

MASER 13 also accommodated in the payload adapter a small Inertial Measurement Unit Breadboard, with the objective to test performance in representative launch, ascent and planetary descent/re-entry environment. This system's flight model is subject to flight on MASER 14 in 2019.

9. A SOUNDING ROCKET DEDICATED TO DROP TESTS

Using in-flight test platforms for carrying out drop tests has the disadvantage of bringing in dependency on the main mission in terms of interface requirements, requirements on scheduled deliveries and trajectory constraints.

SSC has identified the possibility to create sounding rocket missions dedicated to drop tests – or any other activity that requires high altitudes.

As a first iteration, a low cost example of such mission would be the use of a 1500 mm 14" (355 mm) diameter module structure to send 50 kg of experiment payload to 100 km apogee, all propelled by an Improved Orion single stage rocket motor.

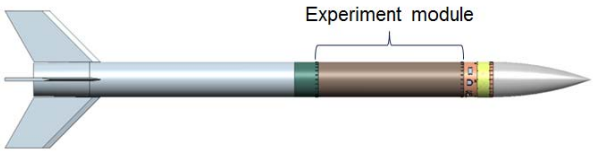

Figure 19. Sounding Rocket dedicated to drop tests.

Once motor separation has occurred, the experiment can be initiated. There are several possibilities & solutions that can be imagined for carrying out the missions, some of them are;

- Ejecting a re-entry body from the inside of the experiment structure
- Splitting the experiment module open late in the descent phase, to release the experiment once the speed is high (as practiced in drop tests from balloons)
- Using nose-cone and service module as ballast mass for super-sonic parachute tests

With several yearly missions, running cost would be low. First launch could take place in less than a year from mission order, and thanks to land recovery, the flown object(s) would be back with experimenters within a couple of hours after flight.

10. CONCLUSIONS

With its unique position in unpopulated area and with a high level of infrastructure, Esrange Space Center is an excellent site for carrying out re-entry tests using sounding rockets and balloons, be it as piggy-back flights on already planned missions, or using balloon and sounding rocket platforms dedicated to carrying re-entry test bodies.

MASER 13 SOUNDING ROCKET MISSION – WORTH WAITING FOR

G. Florin[(1)], A. Værnéus[(1)], J. Li[(1)], M . Inga[(1)], M. Lundin[(1)], J. Thorstenson[(1)]

[(1)] Swedish Space Corporation, P.O. Box 4207, SE-171 04 Solna, Sweden, gunnar.florin@sscspace.com

ABSTRACT

After 23 days of waiting for proper launch conditions, MASER 13 sounding rocket was launched on 1 December 2015 from Esrange Space Center, Sweden. The five experiments on board were of different disciplines; 2 biology experiments, SPARC and GRAMAT studied root growth, using A. Thaliana; XRMON-SOL studied isothermal equiaxed solidification of an Al–Cu alloy melted in a small high-temperature furnace; CETSOL-MEDI investigated formation of equiaxed crystals in liquid solution; CHYPIE-MARCHE experiment studied fluid dynamics with the objective to observe hydrodynamic instabilities generated by chemical reactions. The payload also accommodated technical experiments, making use of MASER as an in-flight test platform.

The mission was carried out under ESA contract.

1 THE MASER SYSTEM

The MASER system accommodates 4 to 5 dedicated 17" experiment modules of high complexity and offers real-time digital television monitoring as well as control capabilities during the flight of the scientific experiments. MASER programme has provided thirteen successful MASER flights of 6-8 minutes of microgravity. With the 2015 Cryofenix mission, SSC introduced the possibility to provide low gravity levels to experiments, in this case 1.75 mg and 7 mg, by applying thrusts of 7 N and 28 N.

In the unpopulated area north of Esrange Space Center rocket payloads can descend with no danger of causing harm. Despite its remote location, the town of Kiruna with its airport is only 45 km away, and provides all the logistic support needed for a launch site.

2 MISSION DESCRIPTION

MASER 13 was launched on 1 December at 06:00 LT from Esrange Space Center in northern Sweden. The mission was accomplished by SSC and its sub-contractors for the European Space Agency (ESA).

The two stage VSB-30 solid fuel rocket motor propelled the MASER 13 payload from Esrange Space Center in northern Sweden on the dark and foggy polar night "morning" of 1 December 2015. In less than a quarter of an hour the payload with its four experiment modules travelled 262 km upwards, and landed safely back on Earth, 62 km down-range assisted by its parachute system. It took only 45 seconds for the sounding rocket to leave the atmosphere. Once it ran out of propellant and the motor thrust exhausted, the mission had only just begun for the scientists watching on ground. They had about six minutes of precious minutes of weightlessness to run their experiments and collect data during the ballistic free fall conditions.

Figure 1. Dark night launch of MASER 13 from Esrange Space Center

The duration of the microgravity phase was 6 minutes, during which the five experiments were carried out, see Table 1.

Table 1. Scientific experiments flown on MASER 13

Experiment name	Investigator(s)	Module	Title
GRAMAT	K. Palme et al. FRIAS, Albert-Ludwigs-Universität Freiburg	BIM-3	Isolation of mRNA from microgravity and ground control samples to identify gravity related gene expression
SPARC	G. Scherer/K Palme et al. Institut für Zierpflanzenbau, Universität Hannover	BIM-3	A Specialized Phospholipase A, and Relocalization in auxintransporting cells in microgravity
CETSOL-MEDI	L. Sturz et al. ACCESS e. V. Aachen	MEDI	Multiple Equiaxed Dendrite Interaction
CHYPI-MARCHE	A. de Witt et al. Université Libre de Bruxelles	CDIC-3	Chemo-hydrodynamic patterns and instabilities
XRMON-SOL	D. Browne University College of Dublin	XRMON-SOL	In-site X-ray monitoring of advanced metallurgical processes under microgravity and terrestrial conditions

The GRAMAT and SPARC experiments required careful planning of the launch window and recovery operations, making good use of the laboratories in the launching area before and after flight. XRMON-SOLidfication Furnace had requirements on pre-heating prior to lift-off, as did also CETSOL-MEDI furnace. CHYPIE-MARCHE required high resolution video images during the filling

phase for careful monitoring and control of the solution filling.

All experiments, apart from the biological GRAMAT and SPARC experiments, used systems for optical monitoring. The X-ray diagnostics system of XRMON-SOL used on-board storage of the scintillator CCD images. MEDI and CDIC-3 modules used digital video cameras, and during the flight the images from the in total 6 cameras were stored and also transmitted to ground in compressed format by the Digital Video System (DVS) and the MASER Service Module, occupying 10 Mbps dedicated bandwidth. In addition to the experiment cameras, there were one analogue camera recording the deployments of the recovery parachutes and two on-board flight observation cameras, filming the complete flight. As the flight took place in the night with no sunlight available, the images of these latter cameras were however mostly black.

100 % scientific success rate was attributed to the MASER 13 flight.

2.1 Using MASER 13 as platform for in-flight technological experiments

Thanks to significant mass saving measures implemented for BIM-3, CDIC-3 and XRMON-SOL modules, it was possible to make benefit of the MASER 13 vehicle as a platform for in-flight experiments, accommodating two technological experiments; A Payload Data Transmitter (PDT) demonstrating performance of SOQPSK modulation technique and a breadboard of an Inertial Measurement Unit (IMU-BB) for testing its overall performances in a representative launch, ascent and planetary descent/re-entry environment.

2.2 Design for landing and recovery in wet areas

MASER missions are carried out in the cold season from November to May. Although there is a thick snow cover and frozen lakes in the Esrange impact area throughout May, there is in late spring an increased probability that the payload may land in wet areas such as rivers, marshlands and lakes. Likewise, in early November – when lakes, rivers and marshlands should be covered with a thick ice layer – it may be that the freezing of wet areas is delayed some weeks.

As a means to be able to launch and perform recovery within the planned campaign period without being impaired by unfavourable recovery ground conditions, i.e. wet landing, the MASER payload was carefully designed to mitigate the risk of damage to the payload in case of landing it wet areas. The design adaptation included water-tight compartments so that the payload would float in water, and also careful design of the electrical system so that there would be no risk of electrical short-circuit that would lead to loss of scientific data.

For the recovery operation, a local group with expertise, experience and equipment in the field of operations in cold waters had been contracted, to be deployed on short notice in case the payload was found to have plunged into a lake or a river. When the payload finally was launched, it landed on solid ground, and the "wet recovery" operation team was never required to assist to operations.

3 CAMPAIGN AND FLIGHT PREPARATIONS

The launch campaign at Esrange Space Center was planned to last only 8 days, from 2nd to 9th November, with launch on 8th November. Nevertheless, campaign activities began three days ahead with preparations of the biological lab facilities and biological sample preparations and start of the plants' life cycles.

All four laboratories of Esrange were used by the experiment teams during the campaign. The biological experiments required the two class S1 laboratories for preparation and post-flight handling of the samples.

The count-down attempts were associated with some strict boundary conditions, related to the preparation of the biological samples, and the application of day/night regime for the plants. In order to mitigate the risks for unwanted and unplanned holds in the narrow count-down window, a full dress rehearsal involving ground stations as well as scientific preparations was carried out, following the same time scheme as foreseen for hot preparations and count-down.

4 RECOVERY OPERATIONS

4.1 Recovery preparations

The launch campaign eventually became a thrill. Indeed, the planned first launch attempt day of MASER 13 was November 8, 2015. But, alas, unfavourable wind conditions seconded by bad recovery weather – fog, snow and severe risk of icing for the recovery helicopter – firmly grounded the rocket for twenty-three consecutive days until December 1. Eventually, as an alternative and back-up solution to recovery by helicopter, a small campaign team, having extensive experience of manoeuvring snow mobiles in the terrain, made their way with two machines to the impact area a day before the last possible launch days, for an attempt of early recovery of the biological samples. For the return transport of the precious biological samples, the team brought along a ruggedized custom-made temperature controlled transport box that in very short time had been manufactured by the campaign team.

In view of the continuously decreasing period of day light, and the critically limited availability of biological samples for the SPARC and GRAMAT experiments, the decision was eventually taken to make a final launch attempt on December 1, in spite of thick fog in the region that prevented payload recovery by helicopter, relying on the possibility that the snow mobile team

would reach the payload in due time to recover the sensitive biological material.

With landing position information provided by the Launch Safety Officer, the snow-mobile retrieval team carefully made their way to the communicated impact point, a mist-covered flat, high-ground area, only 5 km off a semi-major snow mobile track and at 17 km reachable distance of the snow mobile team's starting point. The valuable biological samples could in less than eleven hours after launch be returned in excellent condition to the Science Team. The following day, the complete payload was returned by helicopter under blue sky.

4.2 Flight and recovery

At lift-off, there was heavy fog over Esrange and throughout the impact area. The flight was flawless. Microgravity conditions were however reached 14 seconds later than predicted, as the yo-yo de-spin system experienced partial malfunction, leaving an unusually high residual roll rate of 0.8 Hz. The cold gas rate control system reduced the roll rate to zero Hz in 29 seconds. During microgravity phase, no further rate control correction pulses were needed. Highest angular rate was 0.8°/sec (pitch).

The payload reached the expected apogee of 262 km and the microgravity phase was 359 seconds (6 minutes) long. Micro-g levels during microgravity phase were lower than 0.1 mg, except for some spikes around 0.2 mg. The deceleration forces at re-entry were low, 17 g at the most, but the shock forces at impact on ground were unusually hard, likely due to hard, icy ground.

Recovery by helicopter could not be deployed on the launch day. An SSC snow mobile team had been stationed in Pulsujärvi sami village in the impact area, ready to attempt bio sample recovery by snow mobile. The payload landed near a sami snow mobile track only 17 km from Pulsujärvi. The snow mobile team covered the distance carefully through the fog, and reached the payload in less than 3½ hours after landing.

Payload recovery by helicopter was performed at the end of the short period of daylight the following day on December 2, in good flight conditions.

5 MISSION OBJECTIVES

5.1 Payload configuration

The scientific payload consisted of the experiment modules CDIC-3, MEDI, BIM-3 (with SPARC and GRAMAT experiments) and XRMON-SOL listed from aft end towards the top, with centre of mass positioned at the level of BIM-3 LAU with its experiments cell, Figure 3.

In addition to the experiment modules there were the nose cone and recovery system at the forward end, followed by the balancing ring which housed the GPS receiver.

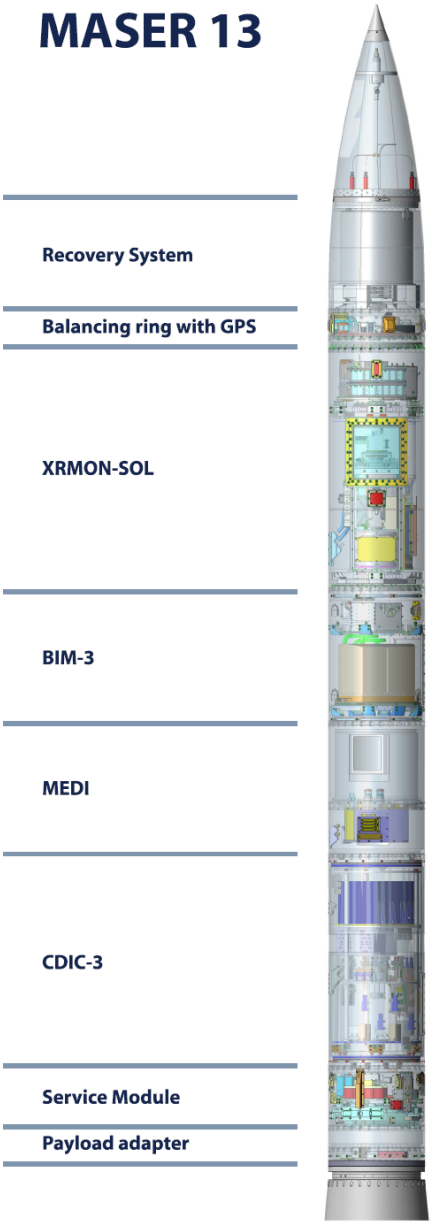

Figure 2. MASER 13 payload configuration

Quite some efforts were spent on mass-reducing measures for the experiment modules. Thereby the mass budget allowed for accommodation of two technological experiments; a Payload Data Transmitter (PDT) accommodated within the CDIC-3 volume, demonstrating performance of SOQPSK modulation technique; and a breadboard of an Inertial Measurement Unit (IMU-BB) accommodated in an extended volume of the payload adapter, for testing its overall performances in a representative launch, ascent and planetary descent/re-entry environment.

The mass of the scientific experiment modules, 282 kg, constituted 70 % of the total payload, which had a

length of 5.30 m and a lift-off mass of 406 kg.

5.2 BIM-3

The BIM-3 (Biology In Microgravity) experiment module is designed for biological experiments. The experiment module is designed and manufactured by Swedish Space Corporation and RUAG Space Nyon. BIM-3 experiment module is a reflight (however with modifications to meet the specific requirements of the experiments) of BIM-2 flown in spring 2012, which in turn was based on the design of the BIM experiment module flown on of MASER 10 in 2005.

BIM-3 experiment module contained 2 plant biology experiments SPARC and GRAMAT "Gravity perception/signal transduction pathways & auxin-transporting proteins" of Prof. K. Palme Univ. of Freiburg. Both experiments study the root growth mechanisms of the plant A. Thaliana.

The SPARC experiment objectives were to study auxin-transporting proteins and change of subcellular localization.

The GRAMAT experiment main objectives are to share light on the following questions:

- Does gravity drive the expression of particular classes of genes?
- Conversely, does microgravity inhibit/induce particular classes of genes?
- Does gravity influence the expression of the same genes in different plant organs, like roots and shoots?

The BIM-3 experiments are performed in 48 experiment units. Plants, cultivated in a day-night regime, grow in microgravity conditions, and also in a 1 g reference centrifuge on-board the module, and are exposed to a fixative just before end of microgravity conditions.

There was also a reference cultivation on-ground. The experiment units were prepared few hours before launch and are integrated in late access unit systems. The flight system is installed in the module via a hatch. The ground system with the reference experiment units is placed in an incubator.

5.2.1 BIM-3 Experiment System

The experiment system is accommodated in the Late Access Unit. The tasks of the experiment system are to accommodate seedlings in sealed cassettes in a controlled temperature environment. The system provides nutrition to the seedlings and performs fixation of the seedlings after the micro-gravity phase, according to the pre-defined timeline.

The experiment units were prepared few hours before launch and are integrated in late access unit systems.

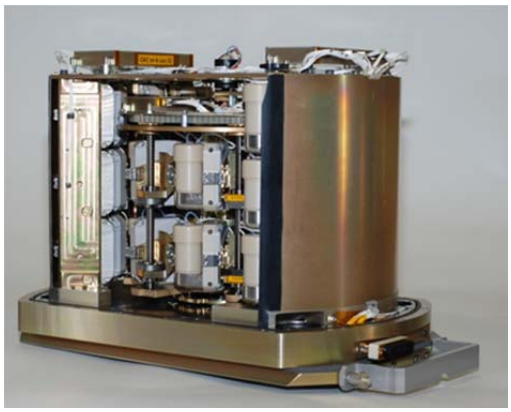

Figure 3. BIM-3 Late Access Unit without its hood

Figure 4. BIM-3 module with Experiment System.

Because of the sensitivity to low temperature the samples were to be retrieved s from the module already at the landing site. This turned out to be a contributing factor for the long campaign duration.

5.2.2 BIM-3 Flight preparations

The experiments required carefully planned and detailed preparation schemes. In total, there were 26 seedling preparation 26 days, with 56 cassette inserts per day, with 40 seedlings in each cassette. By this, nearly 60,000 seedlings were prepared during the campaign!

Figure 5. Forty seedlings in an experiment cassette.

5.2.3 BIM-3 Flight Result

The experiment system performed excellently during ground operations as well as during the whole sequence in microgravity, with the centrifuge spin-up and the activations of each experiment cassette carried out as pre-programmed.

In parallel with the experiment activations during flight, the 1g Ground Reference Unit placed in an incubator at Esrange, was operated and – for equal g-force direction

as the on-board centrifuge samples – physically turned when the flying centrifuge started, and was turned back when it stopped.

Contrary to what we consider as normal recovery operations by helicopter, Gramat and SPARC had to rely on land recovery of the specimen by a team of snow mobiles, as adverse weather conditions had for several weeks prevented launch and helicopter recovery in the same day. Even though timely, successful recovery of the specimen was not guaranteed, the decision was taken to opt for this last opportunity to launch before the daylight would be too short to allow for helicopters to later retrieve the payload.

Figure 6.Recovery team finally arrived at landing site.

Within four hours after launch, the Late Access Unit was successfully retrieved from the payload, and inserted in a special-made box with heat packs to maintain the specimen sufficiently warm, and twelve hours after lift-off, the samples were safely returned to the science team at Esrange.

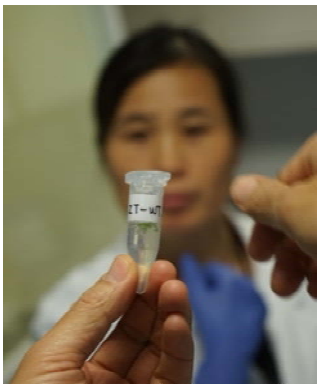

Figure 7. Returning bio samples to Science Team

At post-flight inspection, all experiment cassettes were confirmed to have been functional, and all samples had been successfully fixated. Visual inspection of the BIM-3 module after flight showed no visible mechanical damages.

5.3 MEDI

MEDI (Multiple-Equiaxed-Dendrite-Interaction) houses the CETSOL-MEDI experiment, of PI L. Sturz, ACCESS e.V., Aachen, Germany. Scientific Team Coordinator is Gerhard Zimmermann, ACCESS e.V., Aachen, Germany.

The general objective of the CETSOL project is to improve the understanding of the physical phenomena that govern the formation of the columnar-to-equiaxed transition (CET) in alloy solidification and its consequences for casting soundness. For that purpose, both experimental investigations of the formation of columnar and equiaxed dendritic solidification and the CET, as well as numerical models are being developed.

Figure 8.a Columnar dendritic growth

Figure 8.b Equiaxed dendritic growth

The MASER 13 experiment MEDI is based on previous work, experience and results from TEXUS experiments TRACE focusing on the columnar-to equiaxed transition in the same alloy system, but with different concentrations of (d)Camphor and lower optical resolution.

The scientific objectives for MEDI are to investigate, characterize and validate models for single equiaxed dendrite growth & multiple equiaxed dendrite interaction in 3D and in-situ; to perform microgravity experiments to avoid melt convection and crystal sedimentation; and also identify gravity effect by comparison to reference experiments on ground

The experimental concept of MEDI encompasses:

- Decrease of thermal gradient and cooling rate to obtain purely equiaxed growth
- Determination of temperature field by thermocouples
- Determination of equiaxed dendrite density in time (overview image)
- Determination of single equiaxed dendrite 3D orientation in space and growth rate (detail image)
- Determination of effect of interaction of (some) adjacent crystals in morphology&speed

5.3.1 MEDI Flight Result

The module worked flawlessly during the flight. From

scientific point of view, the preliminary results are said to clearly indicate the soundness of the experimental concept and the complementary results obtained from both length scales at the cell size and the size of individual and groups of equiaxed dendrites.

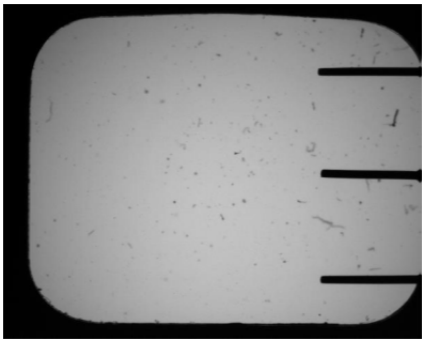

Figure 9.a t=90s after Lift-Off: in µg period.

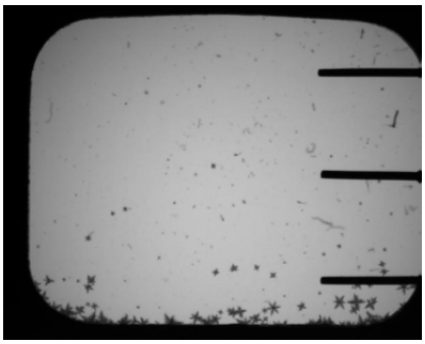

Figure 9.b t=270s after Lift-Off

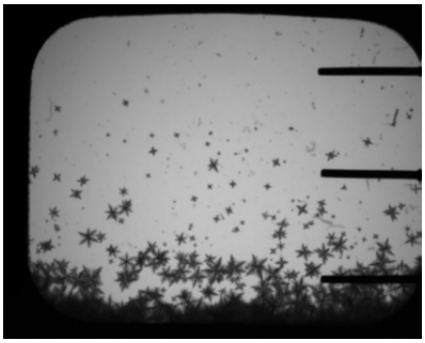

Figure 9.c: t=370s after Lift-Off.

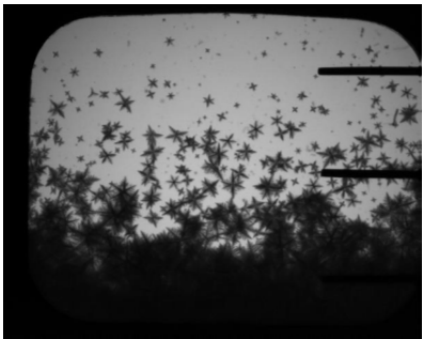

Figure 9.d: t=460s after Lift-Off, µg period ended.

The Figure 9.a-d above show the evolution of the experiment in time. Due to the small temperature gradient, first crystals appear at the bottom of the experimental cell, grow and form a network, while new equiaxed crystals nucleate and grow in the undercooled region. Sedimentation and motion of the equiaxed crystals are clearly suppressed in microgravity

5.4 CDIC-3

CHYPIE-MARCHE is a fluid experiment where a chemical reaction is triggered in a homogeneous fluid mixture (arsenoid-ion-diotate) by a short electronic pulse, which results in a chemical front propagation in the fluid cell containers. The fluid mixture had tracers particles added for PIV, Particle Image Velocity measurements.
The experiment was performed in two experiment cells, 50x10mm, with an optical depth of 5 respective 10 mm and observed through a Fourier-transform and PIVoptical systems by four high-resolution cameras.
The images are stored on-board, but also transmitted to ground in compressed format, as the automatic fillings of the cells have to be completed by manual filling commands by the science team members.

5.4.1 Overall design

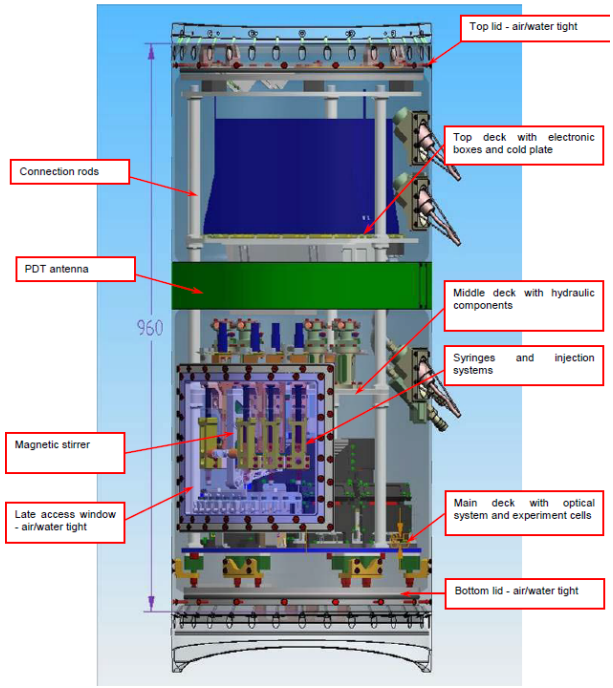

Figure 10. CDIC-3 Module assembly

The 73 kg 690 mm module had, in order to promote buoyancy, been designed as air/water tight by means of o-ring seals. Considerable mass savings efforts had reduced the module mass by more than 5 kg.

In addition to generic subsystems, the module contains advanced optical system, an advanced liquid system for

performing the experiment, laser light sources, digital video system.
One late access window was implemented on the outer structure in order to access four syringes and 11 valves in the launch tower and to perform the needed operations on the hydraulic circuit on ground.

Figure 11 Detail of CDIC-3 late access window

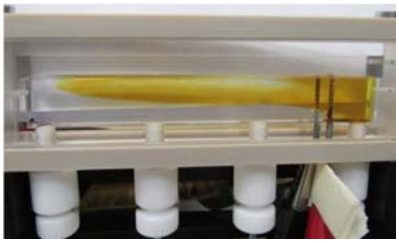

Figure 12. One of the two CDIC-3 experiment cells, on ground, with chemical reaction on-going

5.4.2 Flight results

The CDIC3 experiment performed as expected during filling and microgravity phases, and all requirements were fulfilled apart from delta temperature inside both cells which was higher than expected, but was said not to impair the research. The experiment was monitored and controlled from the Science Center room at Esrange during in real time during the flight.

6 XRMON-SOL

XRMON-SOL microgravity experiment observes spatially isothermal equiaxed solidification of an Al–Cu alloy in microgravity. It the fourth sounding rocket flight within the ESA - MAP research project entitled XRMON (X-Ray Monitoring). It was the first time that isothermal equiaxed solidification of a metallic alloy had been observed in situ in space, providing unique benchmark experimental data.

The experiment used a newly developed isothermal solidification furnace in the re-used module of the MASER 12 experiment X XRMON-GF. A grain-refined Al–20 wt%Cu sample was fully melted and solidified during microgravity phase and the solidification sequence was recorded using time-resolved X-radiography. Equiaxed nucleation, dendritic growth, solutal impingement, and eutectic transformation were thus observed in a gravity-free environment.

6.1 Overall design

The major design activity was the development of the isothermal furnace. Based on the experience of XRMON-GF furnace, the XRMON-SOL furnace is designed to have one heater body (Ø70 mm) with eight heaters arranged so that 4 heaters form the inner ring and 4 heaters form the outer ring (Figure 13). Heating wire is wound as coils on the heater body. The inner ring heaters and the outer ting heaters are displaced by 45º so that the outer ring heater will guard the gap between inner ring heaters to minimize the heat leakage through the gap.

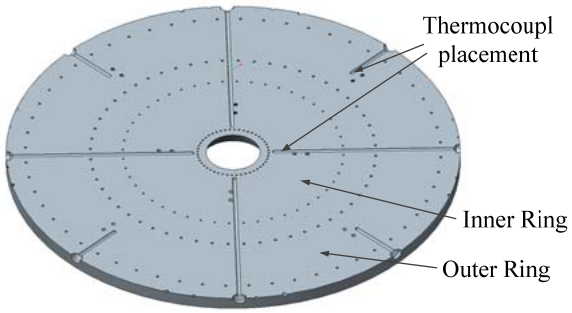

Figure 13. Cross-section of heater body showing placement of thermocouples

Eight thermocouples are placed in each heater zone. Figure 13 shows also the placement of thermocouples.

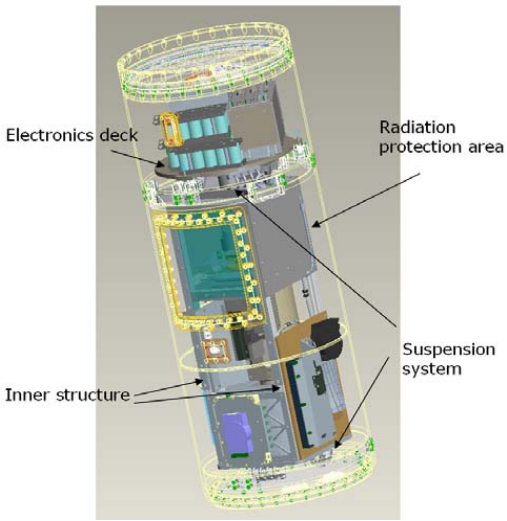

Figure 14. XRMON-GF/ XRMON-SOL Module assembly

XRMON-SOL re-uses XRMON-GF module (Figure 14). It is a 115 cm tall module of 99.3 kg mass. The cooling subsystem has been simplified and cooling fluid flow has been improved.

The module accommodates a compact oil-free micro-focus transmission type X-ray tube that was designed with intention for using on ISS. The X-ray camera is an industry CCD camera integrated with a 5 cm thick fibre optical plate to protect the sensor from radiation. A scintillator plate placed in front of the optical fibre

converts X-ray to visible light.

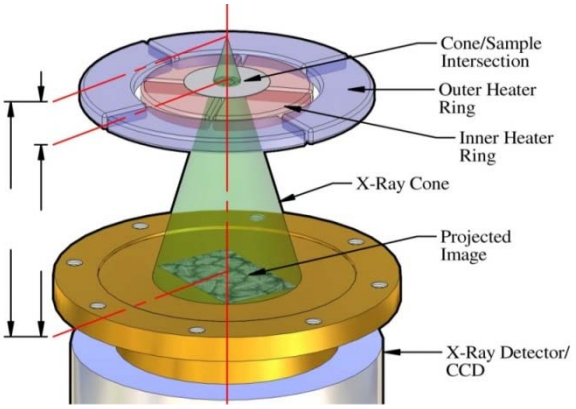

Figure 15. X-Ray image projection illustration

As illustrated in Figure 15, the CCD sensor is larger than the observation area of the sample. The magnification factor is 8.2. With the effective pixel of the CCD sensor of 18 µm (CCD size 24x36 mm, 2012x1340 pixels @ 2x2 binning), the virtual pixel size is 2.2 µm in the sample. The actual spatial resolution, which is a function of the scintillator pitch (50 µm) and the source size (3 µm), is calculated as ~ 6.3 µm.

Uncompressed images were stored on-board by the Digital Video System with a frame rate of 3 frames per second. During count-down and at the beginning of the flight, compressed images were down-linked in real time at a speed of one frame every three seconds in order to give enough down-link bandwidth to CDIC experiment. 110 seconds into the flight, the down link image rate was increased to one frame per second.

6.1.1 Flight results

The performance during flight was flawless. The experiment was controlled by pre-configured tele-command queue with manual intervention.

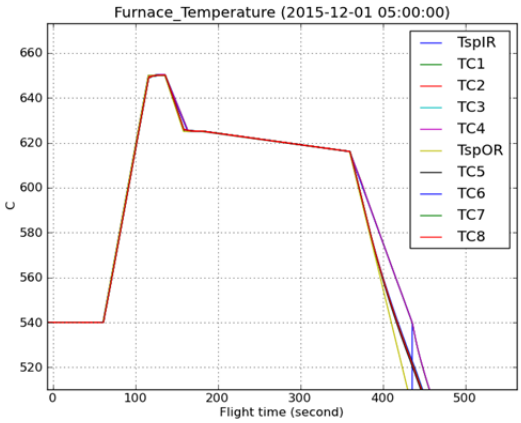

Figure 16. Furnace temperature during the flight

Figure 16 shows the furnace temperature during the flight. The sample was heated to 650 °C at 2 K/s 60 s after lift-off. After a stabilisation period, the sample was cooled to standby temperature of 625 °C at about 1.0 K/s. After a second stabilisation period, the first stage of the solidification experiment commenced at 180 s by applying cooling rate of -0.05 K/s to all eight heaters simultaneously. At 359 s, the second stage of solidification, i.e. the eutectic transformation, started by increasing the cooling rate to -1 K/s on the inner ring and the -1.5 K/s on the outer ring. All heaters were switched off at 435 s.Equiaxed nucleation, dendritic growthand eutectic transformation could be observed live during the flight (Figure 17). The uncompressed image was downloaded after the flight. Study of uncompressed image has been published. It shows that observable solidification within the Field of View occurred between 241 s and 425 s and eutectic transformation between 414 s and 425 s.

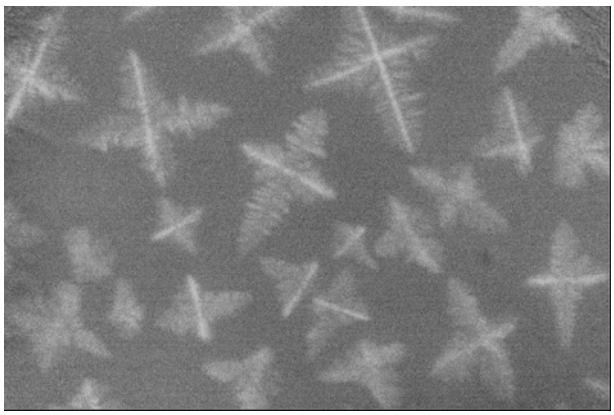

Figure 17. Live X-ray image of a growing equiaxed structure of Al-Cu alloy, t=316 s, T=618.3 °C

7 UPCOMING MASER MISSION

MASER 14 is scheduled for launch in 2019. Two experiments are by ESA selected for the mission, and there is volume available for 2-3 additional experiments, provided by other organisations.

XRMON-GF2 is a reflight of XRMON-GF flown on MASER 12 in 2011, but with different experiment sample. XRMON-GF investigates directional solidification on metallic alloys by using gradient furnace.

ARLES is an experiment studying droplet evaporation, accommodated in a new experiment module.

8 ACKNOWLEDMENTS

The authors wish to acknowledge the funding for the development and flight of MASER 13 sounding rocket through ESA's ELIPS (European Life and Physical Sciences in Space) programme.

IN SITU X-RAY STUDIES OF DIRECTIONAL SOLIDIFICATION OF METAL ALLOYS IN MICROGRAVITY CONDITIONS

H. Nguyen-Thi[(1)], G. Reinhart[(2)], D.J. Browne[(3)], G. Zimmermann[(4)], R. Mathiesen[(5)], F. Kargl[(6)], W.H. Sillekens[(7)]

[(1)]Aix-Marseille Univ/CNRS/IM2NP, Campus Saint-Jérôme, Case 142, 13397 Marseille cedex 20, France, E-Mail: henri.nguyen-thi@im2np.fr
[(2)]Aix-Marseille Univ/CNRS/IM2NP, Campus Saint-Jérôme, Case 142, 13397 Marseille cedex 20, France, E-Mail: guillaume.reinhart@im2np.fr
[(3)]University College Dublin, Belfield, Dublin 4, Ireland, E-Mail: david.browne@ucd.ie
[(4)]ACCESS e.V., Intzestrasse 5, 52072 Aachen, Germany, E-Mail: g.zimmermann@access-technology.de
[(5)]Norwegian University of Science and Technology, 7491 Trondheim, Norway, E-Mail: ragmat@phys.ntnu.no
[(6))]Institut für Materialphysik im Weltraum, Deutsches Zentrum für Luft- und Raumfahrt (DLR), 51170 Köln, Germany, E-Mail: florian.kargl@dlr.de
[(7)]ESA/ESTEC, Keplerlaan 1, PO Box 299, NL-2200 AG Noordwijk, The Netherlands, E-Mail: wim.sillekens@esa.int

ABSTRACT

The performance of structural metallic materials is associated with the solidification microstructures, which are strongly dependent on gravity effects. Experimentation in a microgravity environment is a unique way to suppress these effects and to provide benchmark data for testing current theories of grain and microstructure formation. This contribution presents a summary of results obtained for directional solidification of Al-Cu alloys within the framework of the XRMON project. It is focussing on *(i)* the first ever microgravity experiment on solidification with in situ monitoring of metal alloys performed on board a sounding rocket and *(ii)* solidification experiments performed on board parabolic flights, where the effects of varying gravity level have been studied.

1. INTRODUCTION

The most common solidification microstructure is the dendritic grain, which can be either columnar or equiaxed [1]. The grain structure is called columnar if the growth is preferentially oriented in a direction close to the heat flux, whereas equiaxed grains are growing in all space directions, leading to a material with more isotropic macroscopic mechanical properties and a more homogeneous composition field. Depending on the application, one type of grain structure is usually preferred, e.g. equiaxed grains in automotive components and columnar grains in turbine blades. Elsewhere, an important issue is to clarify the role of convection on macrosegregation and on microstructure formation during the solidification process.
The coupling between gravity effects and solidification has been the subject of a great deal of experimental, theoretical and numerical work. The main conclusion of all these studies is that gravity is the major source of various disturbing effects, which can significantly modify or mask important physical mechanisms on Earth (1g) [2]. Numerous experiments in microgravity conditions have shown that the microgravity (µg) environment is a unique and efficient way to eliminate buoyancy and convection to provide benchmark data for the validation of purely diffusive models and numerical simulations [3, 4]. In addition, a comparative study of solidification experiments at 1g and µg can also enlighten the effects of gravity [5, 6].

1.1. In situ characterization during solidification of metallic alloys

As most of the phenomena involved during solidification are dynamic, in situ and real-time X-ray imaging should be retained as the method of choice for investigating the solidification front evolution of metallic alloys grown from the melt [7], in particular on the effects induced by gravity [2]. In this non-destructive technique, the contrast in the recorded image is due to local changes in the amplitude of the X-ray beam transmitted through the sample. A (monochromatic) X-ray beam illuminates the sample and a 2D-detector (photographic film or CCD camera) is placed close to the sample to record the transmitted beam. In alloy systems, contrast mainly results from segregation of the chemical species and is generally weak and therefore difficult to reveal with conventional X-ray sources.
Recent developments of more powerful laboratory X-ray sources, as well as modern X-ray detectors, have opened up new perspectives for the application of X-ray radiography to microgravity experiments. Indeed, it has become conceivable to design facilities dedicated to the study of alloy growth processes with in situ characterization on board microgravity platforms.

1.2. Microgravity relevance

On Earth, gravity has important additional effects on the solidification process. Firstly, gravity induces natural convection in the melt, due to density variations following the local temperature and concentration [4].

The main impacts of convective flows on the solidification microstructure are the macroscopic deformation of the solid/liquid interface, the micro- and macro-segregation in the sample, and the modification of the primary arm spacing (Fig.1a). Secondly, due to solute rejection during the liquid to solid transition, growing grains and surrounding liquid have generally different densities. Consequently, buoyancy force can act on the solid grains, which lead to their sedimentation or flotation in the liquid phase (Fig.1b). Therefore, equiaxed microstructures on Earth and in microgravity are dramatically different. Thirdly, gravity is at the origin of mechanical effects, in particular on the secondary arms. It has been shown that these mechanical effects can induce the bending of secondary arms when they are long enough (Fig.1c). In some cases, the bending phenomenon can precede the dendrite fragmentation [8]. Finally, a less addressed issue related to gravity is the hydrostatic pressure in the melt, despite its strong impact on the human body during space travel. It is well known that hydrostatic pressure applied during solidification significantly reduces the formation of porosities. On the contrary, under microgravity conditions, the liquid shape is only determined by the surface tension and the wetting behaviour of the melt on solid surfaces. Hence, the loss of hydrostatic pressure in the melt can cause shrinkages or the formation of voids along the sample during microgravity experiments [9]. Therefore, a deeper understanding of gravity effects on solidification microstructure formation is of great importance for scientists and industrialists alike.

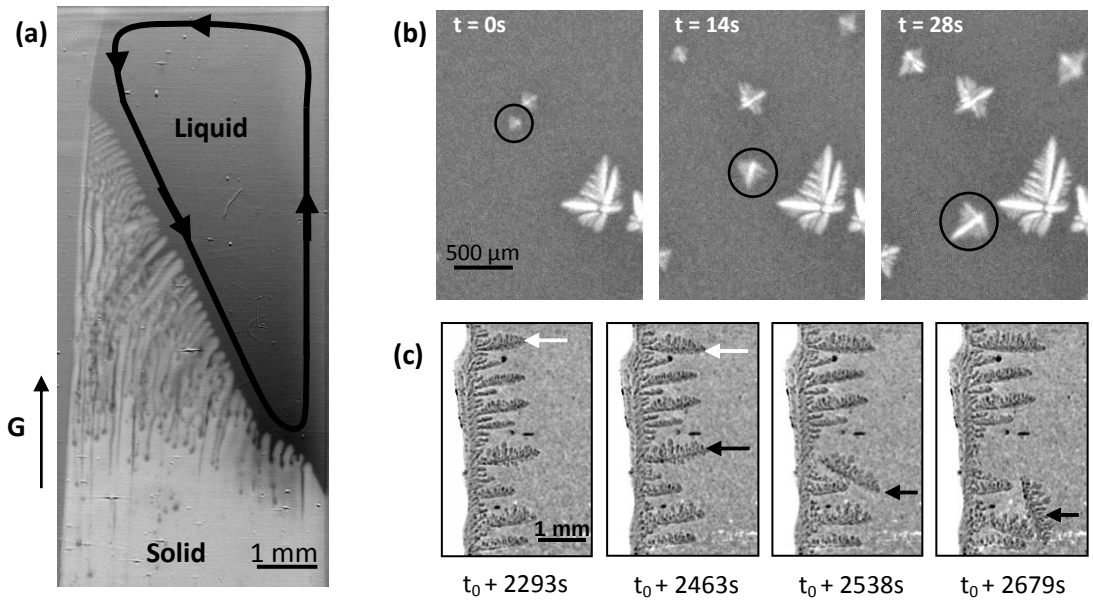

Figure 1. *In situ observation of gravity effects during direction solidification: (a) Deformation of the solid–liquid interface due to convection during directional solidification of Al–4wt.% Cu (cooling rate is 0.3 K/min, temperature gradient is 35.5 K/cm); (b) Sequence of radiographs recorded during Al-10wt.% Cu equiaxed solidification showing the sedimentation of equiaxed grains; (c) Radiographs showing bending and fragmentation of secondary arms during the development of a columnar dendrite of Al-7wt.%Si (cooling rate is 0.5 K/min, temperature gradient is 15 K/cm)*

1.3. XRMON project

Since 2004, the European Space Agency (ESA) has been supporting investigation of gravity effects on solidification by promoting in situ X-ray monitoring of the solidification of aluminium alloys on microgravity platforms and on earth. The ESA-MAP (Microgravity Application Promotion) entitled XRMON (In-situ X-ray monitoring of advanced metallurgical processes under micro gravity and terrestrial conditions) aims to develop and perform in situ X-ray radiography experiments on metallurgical processes related to solidification phenomena, as well as solute diffusion in liquid metals, in microgravity and terrestrial environments [10]. The specific research subjects are closely linked to subjects of interest in several other active MAPs, but nevertheless unique as they deal with in situ X-ray studies which are not included in the other running projects.

Within the framework of the XRMON project, we have designed and developed new facilities dedicated to the study of Al-based alloy solidification on board microgravity platforms, with in situ X-ray radiography. The aim of this paper is to give an overview of the in situ X-ray studies of metal alloy solidification, carried out in sounding rocket and during ESA Parabolic Flight campaigns. The presented experiments mainly focussed on directional solidifications, and equiaxed growth experiments [11, 12] are out of the scope of this paper.

2. XRMON-GF (Gradient Furnace) and XRMON-PFF (Parabolic Flight Facility) apparatus

The XRMON-GF set-up was developed within the framework of the XRMON project by SSC (Swedish Space Corporation) to perform directional solidification with in situ X-ray radiography observation in microgravity conditions. The gradient furnace is of Bridgman type, with two identical heaters for the "hot" and "cold" zones (Fig.2a) that are independently regulated by a PID-regulator. This furnace enables directional solidification with thermal gradients within the range of 5-15 K/mm. The heater gap has a "hole" of 5mm x 5mm for the X-ray radiation transmission. Solidification of the sample is made by cooling the two heaters at the same cooling rate *R* to keep a temperature gradient *G* constant.

The experiment samples were made of Al-10wt.% Cu and Al-20.wt% Cu. The high amount of solute was chosen to ensure a high contrast between the grown solid and the surrounding liquid phase but also to have a short solidification interval which could enable us to visualize the whole mushy zone in the Field-of-View (FoV). The sample dimensions were 50 mm (length) x 5 mm (width) and 150 µm in thickness (drawn in white in Fig.2b). The sample was enclosed in a crucible, made of two 150 µm thick glassy carbon (Sigradur K) sheets, which were sewn together with a 200 µm silica thread along the long edges and left open in the short ends.

The X-ray diagnostic device comprises two main parts: The X-ray source and the camera (Fig.2c). A microfocus transmission-type X-ray tube with 3 µm focal spot was used in order to meet the spatial resolution requirement (roughly 5 µm) and a sufficient photon flux to ensure a good image contrast. The two peaks in energy are K_α = 17.4 keV and K_β = 19.6 keV, which are adapted to Al-20wt.% Cu alloys. It is worth noting that, contrary to synchrotron sources, which provide a parallel beam, microfocus sources deliver a cone-beam. This leads to a geometrical magnification of the image, depending on the respective source-sample and source-camera distances. In our geometry, the magnification is about 5 and, a pixel size of the camera of 20 µm corresponds to a "real" pixel (i.e. at the level of the sample) of 4 µm.

The camera system comprises a digital camera (Vosskühler 11000) with a 24x36 mm CCD-sensor adapted for X-ray usage by the integration of a 50 mm thick fiber optical plate that protects the sensor from radiation. A scintillator plate placed in front of the optical fiber converts X-ray radiation to visible spectrum light [13].

To perform directional solidification experiments during ESA parabolic flight campaign, a duplicate of the XRMON-GF was built, named XRMON-PFF (Parabolic Flight Facility). This facility is quite similar to the XRMON-GF, with only minor changes to be fitted in the Airbus A300 Zero-G operated by Novespace (www.novespace.fr) [14].

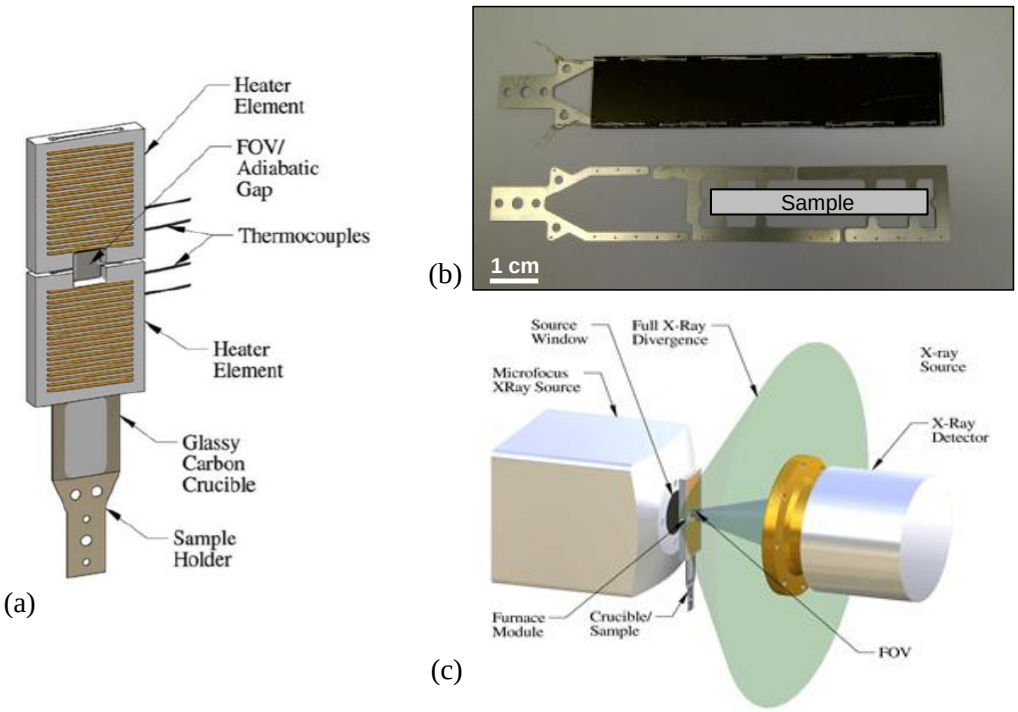

Figure 2. (a) *Sketch of the Bridgman furnace, (b) Pictures of the crucible-sample system and (c) X-ray device facility.*

3. INFLUENCE OF GRAVITY ON DENDRITE FRAGMENTATION

The first solidification experiment in microgravity using the XRMON-GF facility was successfully carried out during the MASER-12 sounding rocket mission on February 13th, 2012 at Esrange (Sweden). The initial objective of this microgravity experiment was to demonstrate the new opportunities that X-ray radiography offers for future microgravity experiments. In addition, some interesting results were obtained and described in details elsewhere [13, 15].

Since the microgravity duration during a MASER sounding rocket is limited to 6 min, a suitably adapted experimental timeline was defined [13]. After a short stabilization period (about 20 s), the sample directional solidification was triggered by applying successively three increasing cooling rates to both heaters (0.15 K/s $\rightarrow$ 0.7 K/s $\rightarrow$ 3 K/s). Two ground-reference tests were carried out with the same experimental profile and on a fresh sample, for two different sample orientations: in the first reference test, the growth direction was perpendicular to the gravity vector, while it was parallel and in the opposite direction to the gravity vector in the second ground-reference test.

Fig.3 displays two sequences of radiographs recorded during the solidification experiment in microgravity conditions and for the reference experiment at normal gravity. These sequences of radiographs unveil the time evolution of the interface pattern during the slowest cooling rate (R = 0.15 K/s), with a temperature gradient of about 15 K/mm between the heaters.

The sample in the field of view (FoV) was fully liquid at the end of the melting phase and then nucleation of the first solids occurred below the field of view. After a while, dendrite tips appeared at the bottom of the FoV (left column in Fig.3) and formed a very disordered dendritic pattern (second column in Fig.3). Gradually the grain competition gave a more regular array of dendrites (third column in Fig.3).

During the columnar solidification in microgravity conditions, nucleation of one equiaxed grain ahead of the columnar front is visible (Fig.3a2, bottom right), most likely on a small heterogeneity of the sample oxide layer. This grain slightly rotated during the solidification, which clearly showed that it was not stuck on the sample walls. However, due to the microgravity environment, this equiaxed grain remained at the same altitude and were progressively engulfed by the columnar front and then completely incorporated into the columnar microstructure.

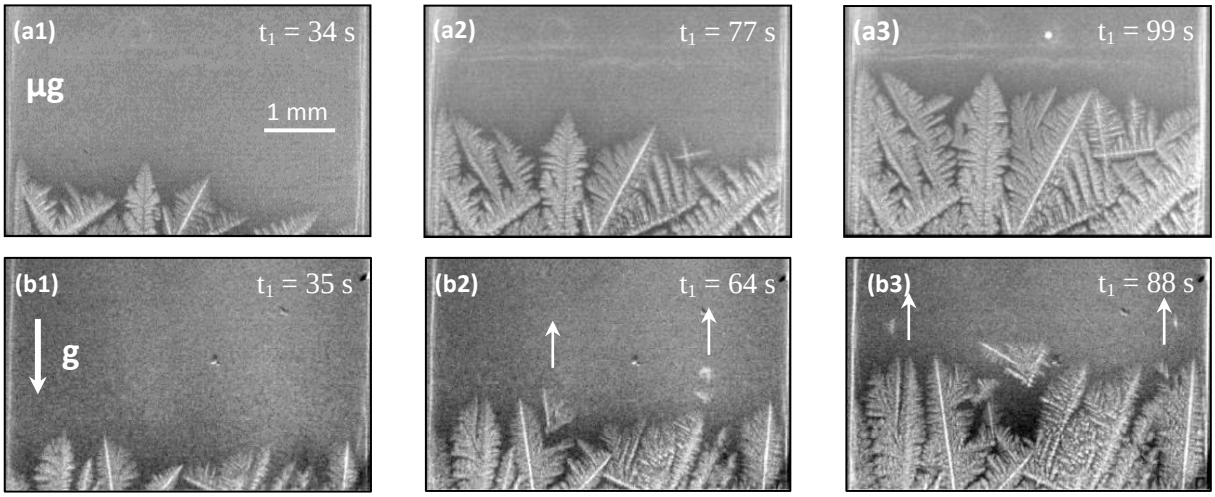

Figure 3. *Columnar solidification of Al-20wt.% Cu with a temperature gradient of about 150 K/cm between the two heaters and a cooling rate of 0.15 K/s on both heaters: (a1-a3) in microgravity conditions, (b1-b3) sample in vertical position (same reference time for the three experiments).*

For the upward solidification experiment on Earth, the most important feature is the multiple fragmentations in the mushy zone region (Fig.3b2 and Fig.3b3, indicated by arrows), in particular at the top of the columnar front. The fragmentation density in this region is about twenty times larger than in the deep mushy zone as displayed in Fig.4 For the microgravity experiment, dendrite fragmentations also occurred in the whole mushy zone but the difference between the top of the mushy zone and the deep mushy zone is less marked than for 1g-experiment (only 5-6 times larger). These measurements are qualitatively in agreement with recent results of others groups [16, 17]. This dramatic difference of behaviour between μg and 1g experiments may be attributed to two effects: *(i)* the presence of gravity-driven convection in the inter-dendritic liquid regions in the top of the mushy zone, where the liquid fraction is relatively high [17, 18] or/and *(ii)* the buoyancy force acting on secondary arms of dendrites [19, 20].

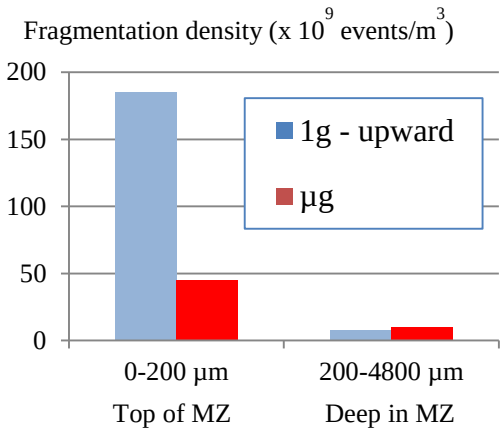

Figure 4. *Fragmentation density measured for 1g (blue bars) and µg (red bars) experiment, respectively for the top and deep regions of the mushy zone.*

For 1g conditions, most fragments moved upward after their detachment, due to the buoyancy force because the solid density is lower than the density of the surrounding liquid. Some of those fragments were free to float to the hot region of the sample (white arrows in Fig.3). During their upward motion, the size of the dendrite fragments decreased because they gradually melted, forming a final white cloud, which corresponded to the melting of the aluminium-rich dendritic fragment. It is worth noting that these dendrite fragments could not promote columnar-to-equiaxed transition, because they were carried up too far into the liquid where they were re-melted. In addition, a strong segregation along the sample occurred during solidification because all Al-enriched dendrite fragments were transported by buoyancy forces into the upper part of the sample and mixed in the liquid phase after melting. In absence of gravity, dendrite fragments moved towards the cold part of the mushy zone after their detachment, carried by the liquid movement induced by the sample shrinkage.

4. COLUMNAR-EQUIAXED TRANSITION TRIGGERED BY GRAVITY LEVEL VARIATION

Directional solidification experiments on refined Al–20 wt.%Cu and refined Al–10wt.%Cu samples were also carried out during several ESA Parabolic Flights (PF) campaigns. The succession of periods with different gravity levels offered by parabolic flight allowed the investigation of the effects of gravity level variations on the columnar-to-equiaxed transition. Experiments were carried out in the XRMON-PFF apparatus for a wide range of cooling rates and a constant temperature gradient. As mentioned in Section 2, this facility is simply a duplicate of the XRMON-GF used during the MASER-12 experiment, which has been adapted to the Airbus A-300 and then A-310, operated by Novespace (Bordeaux-France). Solidification is induced by the power-down method, which consists of applying the same cooling rate on both heater elements to keep a constant temperature gradient during the process. X-ray radiography was successfully used to observe the microstructure evolution following the variations of gravity level. The solidifications of two samples were carried out, an Al–20 wt.%Cu sample and Al–10 wt.%Cu sample, both inoculated with AlTiB grain refiners.

According to the parabolic trajectory of the plane, the gravity level changes during each parabola approximately from 1g → 1.8g → 0g → 1.8g →1g (Fig. 5), with approximately 24s and 22s at 1.8g and 0g, respectively [21]. During the course of the flight, the parabola is repeated a total of 31 times. In this section, we present the solidification experiments for the refined Al–20wt.%Cu sample alloy at slow cooling rate R = 0.05 K/s that extended over five parabolas.

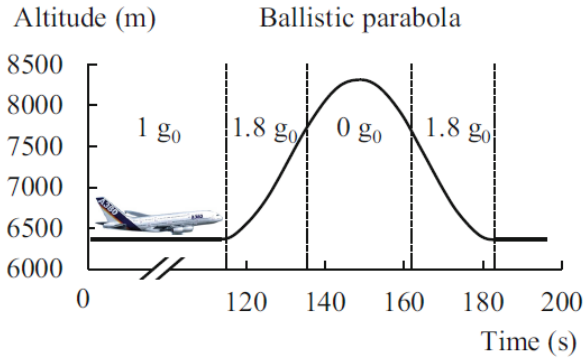

Figure 5. *Parabola profile, showing the gravity level variations during the course of the plane.*

Figure 6 displays a sequence of radiographs recorded during a part of the solidification experiment of refined Al-20.wt% Cu sample under varying gravity level. During the 1g period, a development of a columnar microstructure was observed at the bottom of the field of view (Fig.6a). Fragmentation phenomena continuously occurred along the solid/liquid interface, and the dendrite fragments floated from the bottom to the top due to buoyancy force (Fig.6b). During their upward motion, the fragments gradually melted and eventually disappeared, like in experiments performed in terrestrial laboratory conditions. In this parabolic flight experiment, a few grains additionally nucleated on the crucible wall.

The most striking effect was observed at the step-change of gravity level. Indeed, when the gravity level suddenly increased to 1.8g at the beginning of the parabola, a sudden nucleation of a large number of equiaxed grains ahead of the columnar front was observed (Fig.6c and Fig.6d). This explosive nucleation

phase was obviously provoked by the sharp increase of the gravity level. The activation of refining particles ahead of the columnar front was likely triggered by an increase of the magnitude of liquid undercooling ahead of the columnar front, which is itself due to a decrease of the liquid composition ahead of the columnar structure. Indeed, the increase of the hydrostatic pressure of the melt when the gravity level changed from 1g to 1.8g generates a downward flow of Cu-poorer liquid toward the columnar front, which modifies the liquid composition ahead of the columnar front [14]. After their nucleation, the equiaxed grains started to float and then melted when they reached the hot region of the liquid (Fig.6d and Fig.6e). Some grains remained stuck between the sample walls, because their size was too large compared to the sample thickness (Fig.6f).

As soon as the gravity level reached 0g, the equiaxed grains stopped moving upward because the buoyancy force vanished (Fig.6e and Fig.6f). During the microgravity period, the grains were dissolved due to an upward copper-enriched fluid flow, which is visible in Fig. 6f as a dark region in the liquid ahead of the microstructures. This is particularly visible for the big dendrite fragment stuck on the right side of the sample. This upward fluid flow is due to vanishing of the hydrostatic pressure in absence of gravity.

After the reduced gravity period, the gravity level increased again to 1.8g and the explosive nucleation phenomenon occurred again (Fig.6g and Fig.6h), but in a less intensive manner. All these phenomena were repeated in the following parabolas. It is worth noting that these observations were also made in the experiment with the same sample, the same temperature gradient but at a higher cooling rate (R = 0.15 K/s) [14].

Moreover, the same phenomena were observed during the solidification experiment on refined Al-10.wt%Cu sample, which confirms the reproducibility of the observations. However, contrary to the Al-20wt.%Cu sample, the nucleated equiaxed grains moved slightly downwards and formed a closely-packed layer of equiaxed grains ahead the columnar front. This change in the behaviour of equiaxed grains is expected for an alloy of composition Al-10wt.%Cu, since the density of the solid is higher than the density of the liquid [22] Therefore, a columnar-to-equiaxed transition is achieved at this alloy composition. During the subsequent increase of gravity level from 0g to 1.8g period, the explosive nucleation phenomenon occurred again [14].

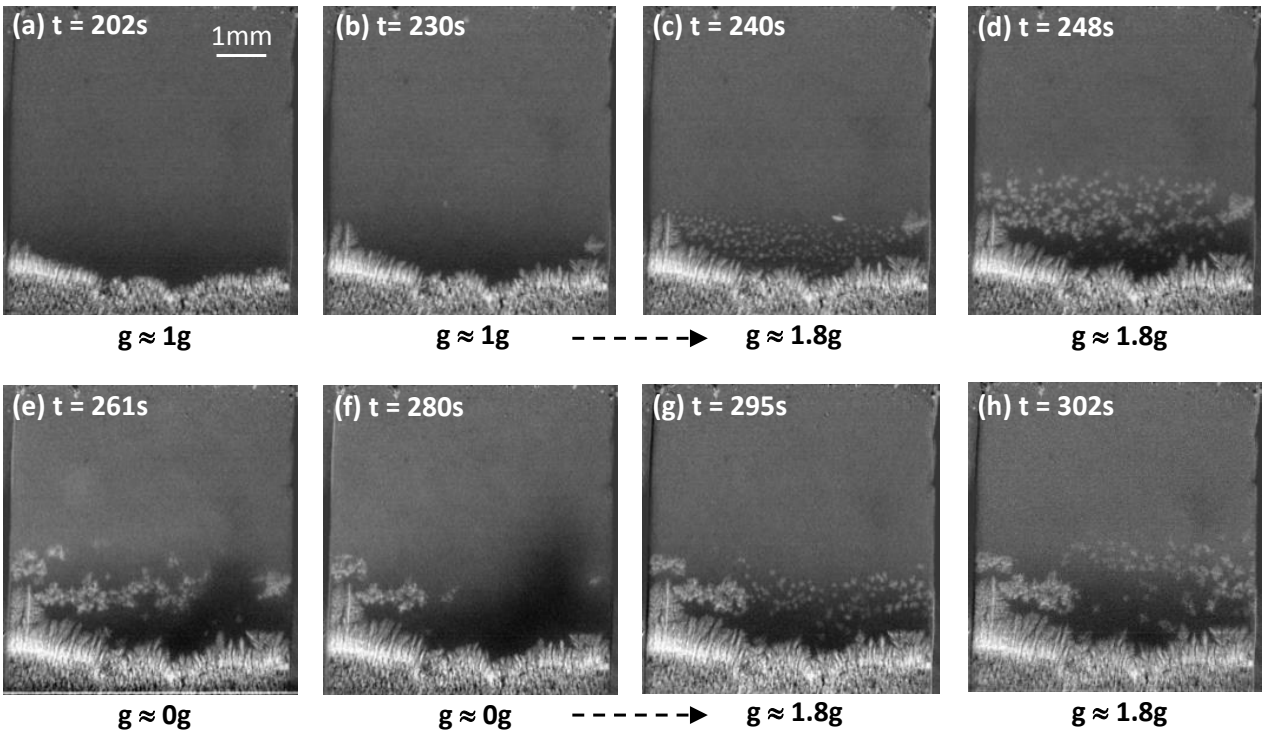

Figure 6. *Sequence of radiographs recorded during the solidification of a refined Al–20.wt.% Cu for a low cooling rate (R_1 = 0.05 K/s) and temperature gradient (G = 15 K/mm) under varying gravity level (parabolic flight). The gravity vector (in $1g_0$ and $1.8g_0$ periods) points vertically downwards relative to the field of view.*

5. CONCLUSIONS

X-ray radiography (or X-radiography) was used during Al–Cu solidification experiments carried out in terrestrial conditions and on board of microgravity platforms (sounding rocket and parabolic flight campaigns).

The MASER 12 solidification experiment was the first solidification experiment with in situ and real-time characterization by X-ray radiography on metallic alloys in microgravity conditions. The results obtained during the MASER 12 mission, as well as the two ground-reference tests, were very promising and validated the experimental set-up in terms of thermal behaviour and X-ray imaging, which were very challenging issues at the beginning of the project. From a scientific point of view, these results demonstrate the capability of the X-ray device developed within the framework of the XRMON project to provide a real-time diagnostic technique during solidification or melting of Al-based alloys.

It was observed that gravity level variations can have a significant impact on the microstructure formation. The variation of g-level induces a variation of the liquid composition ahead of the solid/liquid interface which affects the constitutional undercooling. For a refined alloy, this undercooling increase can provoke an explosive nucleation of equiaxed grains ahead the columnar front, yielding a composition-dependent columnar-to-equiaxed transition.

6. ACKNOWLEDMENTS

The authors are grateful to ESA for financial and practical support for this work, particularly through their Microgravity Applications Promotion (MAP) programme (XRMON: current contract number 4200020288/06/NL/VJ, and originally AO-2004-046), and their PRODEX programme. The space hardware and XRMON furnaces development was funded through ESA's ELIPS (European Life and Physical Sciences in Space) programme. We are also grateful for support from the French National Space Agency (CNES) and Enterprise Ireland. Thanks are also due to Dr. Andrew Murphy, Dr. Georges Salloum-Abou-Jaoude and Dr. Lara Abou-Khalil for their active participation in this research; without them many of these results would not have been achieved.

7. REFERENCES

1. Dantzig J.A. and Rappaz M. (2009) *Solidification*, EPFL Press: Lausanne (Suisse)
2. Nguyen-Thi H., Bogno A., Reinhart G., Billia B., Mathiesen R.H., Zimmermann G., Houltz Y., Löth K., Voss D., Verga A. and De Pascale F. (2011) Investigation of gravity effects on solidification of binary alloys with in situ X-ray radiography on earth and in microgravity environment, *Journal of Physics: Conference Series*, **327**, 012012
3. Akamatsu S. and Nguyen-Thi H. (2016) In situ observation of solidification patterns in diffusive conditions, *Acta Materialia*, **108**, 325-346
4. Nguyen-Thi H., Reinhart G. and Billia B. (2017) On the interest of microgravity experimentation for studying convective effects during the directional solidification of metal alloys, *Comptes Rendus Mécanique*, **345**, 66-77
5. Nguyen Thi H., Dabo Y., Drevet B., Dupouy M.D., Camel D., Billia B., Hunt J.D. and Chilton A. (2005) Directional Solidification of Al-1.5wt% Ni alloys under diffusion transport in space and fluid flow localisation on Earth, *J. of Crystal Growth*, **281**, 654-668
6. Drevet B., Nguyen Thi H., Camel D., Billia B. and Dupouy M.D. (2000) Solidification of Aluminum-Lithium Alloys near the Cell/Dendrite Transition - Influence of Solutal Convection, *J. Crystal Growth*, **218**, 419-433
7. Nguyen-Thi H., Salvo L., Mathiesen R.H., Arnberg L., Billia B., Suery M. and Reinhart G. (2012) On the interest of synchrotron X-ray imaging for the study of solidification in metallic alloys, *Comptes Rendus Physique*, **13**, 237-245
8. Reinhart G., Nguyen-Thi H., Mangelinck-Noel N., Baruchel J. and Billia B. (2014) In Situ Investigation of Dendrite Deformation During Upward Solidification of Al-7wt.%Si, *JOM*, **66**, 1408-1414
9. Drevet B., Camel D., Malmejac C., Favier J.J., Nguyen Thi H., Li Q. and Billia B. (1995) Cellular and Dendritic Solidification of Al-Li Alloys during the D2-Mission, *Adv. In Space Res.*, **16**, 173-176
10. Browne D.J., García-Moreno F., Nguyen-Thi H., Zimmermann G., Kargl F., Mathiesen R.H., Griesche A. and Minster O. (2017) *Overview of In Situ X-Ray Studies of Light Alloy Solidification in Microgravity*, Magnesium Technology 2017, K. N. Solanki, et al. (Eds), The Minerals, Metals & Materials Society, 581-590
11. Murphy A.G., Mathiesen R.H., Houltz Y., Li J., Lockowandt C., Henriksson K., Melville N. and Browne D.J. (2016) Direct observation of spatially isothermal equiaxed solidification of an Al-Cu alloy in microgravity on board the MASER 13 sounding rocket, *Journal of Crystal Growth*, **454**, 96-104
12. Murphy A.G., Mathiesen R.H., Houltz Y., Li J., Lockowandt C., Henriksson K., Zimmermann G., Melville N. and Browne D.J. (2016) XRMON-SOL: Isothermal equiaxed solidification of a grain refined Al-20 wt%Cu alloy, *Journal of Crystal Growth*, **440**, 38-46
13. Nguyen-Thi H., Reinhart G., Salloum-Abou-Jaoude G. , Mathiesen R.H., Zimmermann G., Houltz Y., Voss D., Verga A., Browne D.J. and Murphy A.G. (2013) XRMON-GF: A novel facility for

solidification of metallic alloys with in situ and time-resolved X-ray radiographic characterization in microgravity conditions, *Journal of Crystal Growth*, **374**, 23-30
14. Abou-Khalil L., Salloum-Abou-Jaoude G., Reinhart G., Pickmann C., Zimmermann G. and Nguyen-Thi H. (2016) Influence of gravity level on Columnar-to-Equiaxed Transition during directional solidification of Al – 20 wt.% Cu alloys, *Acta Materialia*, **110**, 44-52
15. Murphy A. G., Reinhart G., Nguyen-Thi H., Salloum-Abou-Jaoude G. and Browne D. J. (2013) Meso-scale modelling of directional solidification and comparison with in situ X-ray radiographic observations made during the MASER-12 XRMON microgravity experiment, *Journal of Alloys and Compounds*, **573**, 170-176
16. Gibbs J.W., Tourret D., Gibbs P.J., Imhoff S.D., Gibbs M.J., Walker B.A., Fezzaa K. and Clarke A.J. (2016) In Situ X-Ray Observations of Dendritic Fragmentation During Directional Solidification of a Sn-Bi Alloy, *Jom*, **68**, 170-177
17. Liotti E., Lui A., Vincent R., Kumar S., Guo Z., Connolley T., Dolbnya I.P., Hart M., Arnberg L., Mathiesen R.H. and Grant P.S. (2014) A synchrotron X-ray radiography study of dendrite fragmentation induced by a pulsed electromagnetic field in an A1-15Cu alloy, *Acta Materialia*, **70**, 228-239
18. Ruvalcaba D., Mathiesen R.H., Eskin D.G., Arnberg L. and Katgerman L. (2007) In situ observations of dendritic fragmentation due to local solute-enrichment during directional solidification of an aluminum alloy, *Acta Materialia*, **55**, 4287-4292
19. Reinhart G., Buffet A., Nguyen-Thi H., Billia B., Jung H., Mangelinck-Noel N., Bergeon N., Schenk T., Hartwig J. and Baruchel J. (2008) In-Situ and real-time analysis of the formation of strains and microstructure defects during solidification of Al-3.5 wt pct Ni alloys, *Metallurgical and Materials Transactions a-Physical Metallurgy and Materials Science*, **39A**, 865-874
20. Billia B., Bergeon N., Nguyen Thi H. and Jamgotchian H. (2004) Cumulative moments and microstructure deformation induced by growth shape in columnar solidification, *Phys. Rev Lett.*, **93**, 126105
21. Pletser V., Rouquette S., Friedrich U., Clervoy J.-F., Gharib T., Gai F. and Mora Ch. (2015) European parabolic flight campaigns with Airbus ZERO-G: Looking back at the A300 and looking forward to the A310, *Advances in Space Research*, **56**, 1003-1013
22. Ganesan S. and Poirier D.R. (1987) Densities of Aluminum-Rich Aluminum-Copper Alloys during Solidification, *Metallurgical Transaction A*, **18A**, 721-723

Making the case for Sounding Rocket guidance systems

Albert Thuswaldner[(1)], Gunnar Florin[(2)]

[(1)]RUAG Space AB, ASJ-Vägen 9, SE-581 88 LINKÖPING, SWEDEN, albert.thuswaldner@ruag.com
[(2)]SSC, Swedish Space Corporation, P.O. Box 4207, SE-171 04 Solna, gunnar.florin@sscspace.com

ABSTRACT

Guidance systems have been used successfully on hundreds of sounding rocket missions for over 40 years. The primary reason for adding a guidance system was mission requirements which aimed for a much higher apogee while at the same time the level of impact dispersion had, for safety reasons, to be kept in check. For missions launched over a land based range like Esrange and White Sands Missile Range this is of paramount importance.
There are other compelling reasons to include a guidance system as well, related to the guided vehicles' reduced sensitivity to wind, which has a positive effect on the planning of the launch campaign. Being virtually unconstrained by the wind conditions means that launch can be conducted on the planned date, and additional campaign days at launch site becomes exceptional. Moreover, scientists can with high confidence plan their stay at launch site to be present for launch and post-launch activities. Biological experiments that require short turn-around time have significantly higher chance of success.
Guided sounding rocket missions need additional system solutions compared to an equivalent unguided mission; besides the obvious need for a guidance system, a Safety Operation system including thrust termination system has to be put in place as well as additional flight trajectory tracking means to fulfil safety requirements.
RUAG Space currently provides three types of sounding rocket guidance, navigation and control systems: The S19L - to be superseded by the electrical version S19E, which uses aerodynamic canard control, the thrust vector control system GCS and the cold gas Spinrac system for exo-atmospheric impact point control and payload pointing. Over time, all these systems have become more capable, their mass and cost have decreased.
Esrange safety requirements call for use of guided vehicles for missions with 1-sigma dispersion values larger than approximately 20 km – typically for apogees above 270 km. The first four missions within SSC's MASER programme, providing 7 minutes of microgravity, were guided missioins attaining 300 km apogee. Also missions not obliged to be guided would benefit from the use of guidance system, as campaign duration would be shortened, and follow-on missions would not risk to be shifted to later dates, as often is the case with preceding extension of launch campaigns due to high winds.
This paper aims at taking a holistic view on guided sounding rocket missions, further discuss the benefits of guided vehicles and how the additional system solutions can be put in-place in a cost-effective manner.

1. THE BEGINNING

Almost fifty years ago, the advantages of using sounding rockets as a research tool started to become obvious. Using military surplus motors kept the cost low, as did the philosophy to avoid unnecessary overhead. This provided short and efficient research programs, with valuable feedback of scientific results to the users.

The good economy of sounding rocket based research made the scientific community ask for launches of ever heavier experiments to ever higher apogees, that is longer flight/experiment time. At the same time, however, the scientific instruments became more sophisticated, and recovery of increasingly complicated and thus expensive science tools came in high demand. Recovery also paved the way for re-use after refurbishment, thereby effectively off-loading the cost of the scientific payload modules.

Land recovery is by far the easiest way to get a payload back in good shape after a suborbital flight. This however, presents new challenges:

- One must be able to predict the nominal impact point with reasonable precision in spite of varying wind conditions during launch.
- The statistical dispersion around that point must be contained inside the rocket range.

To achieve good impact point prediction, wind profile measurements were performed prior to launch, and the actual launcher settings were calculated by means of wind weighting. The statistical dispersion was lowered by increasing the length of the launcher rail, and by spinning the vehicle up to mitigate the influence of motor thrust misalignment. Even with these measures taken to their maximum performance, apogees beyond 250 km were questionable from range safety point of view at land recovery ranges.

For this reason, the S19 Boost Control System was invented at the RUAG Space facility in Linköping, at that time in the beginning of the 1970ies part of Saab.

In cooperation with NASA and SSC, the first flight ever of an S19-guided single stage Black Brant VC rocket took place at Wallops Flight Facility on 10 Jan, 1976. The flight was a perfect success, and the S19 was recovered from the Atlantic (but re-used only as a museum object, since no efforts had been made to make the unit waterproof).

The S19 was upgraded from prototype to commercial status already in 1977, and the first flight was followed by a second one in 1978 from Esrange. This time, a two stage configuration was being used with even higher wind tolerance than on the maiden flight. During subsequent years Esrange saw many guided scientific flights with apogees up to over 400 km. The upgraded system is seen in Fig 3.

Figure 1. Maiden S19 flight from Wallops FF

Figure 2. Prototype S19 recovered from the Atlantic Ocean.

Figure 3. The operative version uses a lightweight magnesium structure and upgraded internal equipment

2. THE BENEFIT OF GUIDANCE

The first and foremost benefit of using a boost guidance system in a sounding rocket application is the reduced sensitivity to wind during the accent phase.

There is this and additional benefits with guidance systems:

- Reduced sensitivity to wind
- Reduced dispersion - allow for a much higher apogee.
- Reduced sensitivity to disturbances other than wind
- Being able to launch at the designated time:
    - Minimize extra campaign days
    - simplify experiment preparation for certain kinds of experiments (biological)
    - Scientists will be more likely to be able to remain during the launch.

Compared with having no guiding system aboard the sensitivity is reduced by one order of magnitude. This is illustrated by the wind limit example in Fig 1. below.

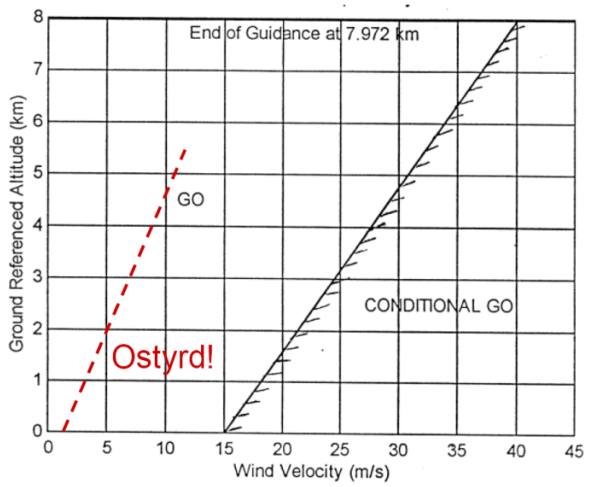

Figure 4. Example of a comparison of wind limits for a vehicle configuration with and without (red) guidance system.

What also should be noted in the figure above is that the wind limit for a guided configuration is not fixed. Beyond the limit, the possibility to launch the guided vehicle still exists, pending an analysis where the actual wind conditions are used as input. In all, the probability for a launch on time increases significantly.

With a guidance system onboard, the rocket is normally launched on the first day regardless of the wind situation, reducing range and personnel costs. Thus there is an economical factor to consider for using a guidance system as it can act as an insurance against potential launch delays. Launch delays cost real money considering all the personnel that need to be at standby. One launch day cost in the order of tenths of thousands of euros.

Data from Esrange shows that historically there has been launch delays in many of the unguided sounding rocket campaigns. Table 1 below shows a number of these flights, the number of days of delays and reason for the delay.

Mission	Days	Date	Note
Texus 42	1	2005-12-01	Inferred from data in EUK167-E50
Texus 43	4	2006-05-11	cancelled due to strong winds.
Texus 44	8	2008-02-07	due to strong winds and/or bad recovery situations.
Texus 45	11	2008-02-21	due to strong winds and/or bad recovery situations.
Maser 11	8	2008-05-15	due to strong winds and/or bad recovery situations.
Texus 46	7	2009-11-22	Bad recovery situation (and sometimes also strong winds)
Texus 47	4	2009-11-27	Bad recovery situation (and sometimes also strong winds)
Average	6		

Table 1. Summary of launch delays for a number of VSB-30 flights from Esrange.

The data provided in table 1. above was provided by SSC in [1]. A more complete list of flights need to be gathered to be able to perform a full analysis. This analysis would also need to carefully consider the exact cause of the delays, and which were related strong winds at the launch pad.

The end result of such an analysis could get a good estimate on what the real economic savings that could be achieved by adding a guidance system. To then form the business case also the associated costs need to be considered.

3. THE PREREQUISITS FOR GUIDANCE

The prerequisites or associated costs comes from the fact that a guided vehicle requires more hardware and supporting systems compared to an unguided vehicle.

In principal the following is required.

- Guidance system
- Safety Operation System including:
    - Flight Termination system and Thrust termination system (2nd stage motor)

- Radar transponder (2nd stage motor)
- Two independent live-feed tracking sources

The scheme of the Saftey Operation system is dictated by Range safety requirements of the specific Range where the launch would take place.

To complete the business case mentioned earlier a deeper analysis of the Range safety requirements to possible solutions that could make lower the overall cost for introducing guidance systems.

One of the possible ways to reduce the overall cost would be to consider replacing the radar tracking of the second stage with a GPS transponder. Also the other alternatives to the Trust termination system which is part of the flight termination system could be considered.

4. RUAG SPACE GUIDANCE SYSTEMS

Today RUAG Space provides three types of sounding rocket guidance, navigation and control systems to the market world-wide. These three systems are:

- S19E – an aerodynamic canard control system
- GCS – a thrust vector control system
- Spinrac – an exo-atmospheric impact point control and payload pointing.

The fourth generation member of the S19 Family of the S19L has been a work horse for many years racking up about 50 successful flights to date. This system is centred on the LN200 Inertial Measurement Unit and a dedicated Guidance processing unit GPU. The 5th generation S19E retained these core units but replaces the pneumatic servo system with a electro mechanical servo system.

The S19E retains the overall performance of its predecessor, but due to the higher energy density of modern battery technology compared to low pressure cold gas tanks, the possibility exists to extend the guidance time far beyond the 18-20 seconds that the older S19 systems could achieve.

The real benefit with the S19E system is however its lower price tag, lower weight and much simplified operations characteristics.

Figure 4. S19E – The 5th generation S19

The Guidance, Navigation and Control system for the Maxus was named GCS, and initially based upon the RIINS inertial navigation system built by Inertial Science Inc.). The GCS controlled the Thrust Actuator on the Castor IVB motor which has been used throughout the whole Maxus program. Going through a number of upgrade cycles the current 4th generation GCS shares the same electronics as the S19E.

The GCS utilises trajectory and impact point guidance and can easily be adapted to any TVC based rocket motor configuration other than the MAXUS vehicle.

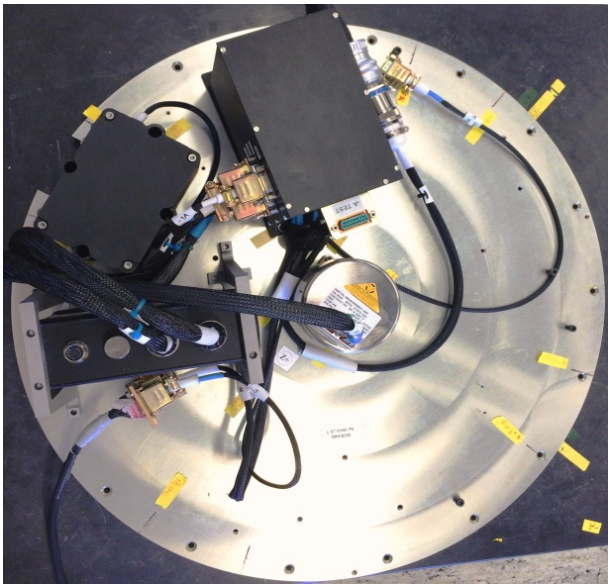

Figure 5. GCS for Maxus 9 – The 4th generation GCS

Figure 5. The 4th generation Spinrac

The Spinrac system is an elegant solution to solve the specific problem to remove the coning and repoint the sounding rocket during exo-atmospheric conditions in one single seamless movement. In this way the system is very efficient and requires far less amount of cold gas than had that been performed by a traditional RACS system.

The Spinrac has typically been used on extreme high altitude three-stage sounding rockets up to 1000 km where the third stage is ignited outside the atmosphere.

5. COMMON FEATURES

RUAG Space guidance, navigation and control systems provide the following major advantages:

- Significantly improved impact dispersion performance, as compared to unguided vehicles, allows for high apogee / long duration flights at geographically limited rocket ranges.
- High wind tolerance provide highly relaxed launch conditions, and the rocket can be launched when the scientist wants to, not when the weather situation so dictates. Typically, a Terrier-BBVC vehicle guided by the S19E can be safely launched into a wind profile of 10-15 m/s at ground level, increasing to 50 m/s at 10 km of altitude. The wind limits of the GCS guided Maxus are similarly high.
- High reliability. Considering the full flight record of flown RUAG guidance systems the total reliability is greater than 99%.
- Recent systems provide an excellent single-screen overview of a multitude of system status and ready-to-launch data during countdown and flight.
- Situational awareness data for Range Safety, including heading, position and velocity data as well as in-flight instantaneous impact point prediction.
- Navigational and pointing data for scientists and other users, for use on-line or during post flight data reduction exercises.
- System interfaces have become more standardized, such as RS232 and RS422 data interfaces.
- Minimum battery capacity is 20 minutes. This means that navigational and attitude data remain available not only during guidance, but throughout the flight.
- Recent systems share the basic electronics between each other which makes it possible to reuse many of the components between these and be able to have multiple guidance systems for various rocket types at a low cost.
- Finally, the cost of the newer systems is lower thanks to less complicated solutions. The same holds true for their refurbishment cost.

7. CONCLUSION

Guidance systems provides a degree of certainty to a sounding rocket project as it significantly increases the probability to launch on-time.

There are steps that can be taken to enable cost-effective guided sounding rocket launches.

RUAG will continue being a partner in enable efficient sounding rocket operations.

8. REFERENCES

1. Ridderström, C. (2002). TN4 □ Implementation of a guidance system to Maser rockets, RUM1221-S8, SSC

JAPANESE SOUNDING ROCKET ACTIVITY IN 2015-2017

Takumi Abe [(1)], Nobuaki Ishii [(2)]

[(1)] Institute of Space and Astronautical Science, Japan Aerospace Exploration Agency, 3-1-1, Yoshinodai, Chuo-ku, Sagamihara 252-5210, Japan, E-mail: abe.takumi@jaxa.jp
[(2)] Institute of Space and Astronautical Science, Japan Aerospace Exploration Agency, 3-1-1, Yoshinodai, Chuo-ku, Sagamihara 252-5210, Japan, E-mail: ishii.nobuaki@jaxa.jp

ABSTRACT

Japanese sounding rockets have been used to achive various objectives such as thermospheric, ionospheric and magnetospheric physics, microgravity experiment, demonstration of various instrument and technique, and advanced engineering experiments. In the years of 2015-2016, three rockets were launched from Uchinoura Space Centre (USC) in Japan, and another rocket will be launched from Ny-Ålesund in Svalbard, Norway in December 2017. In this presentation, we will introduce recent activities of Japanese sounding rocket.

1. INTRODUCTION

In Japan, the Institute of Space and Astronautical Science (ISAS) of Japan Aerospace Exploration Agency (JAXA) has been continuing sounding rockets experiments for various objectives. In the recent years, we are operating three different types of the rocket; S-310, S-520, and SS-520. Tab. 1 shows a list of Japanese sounding rocket experiment in the period from 2015 to early 2017. One S-310 rocket was launched for a purpose of the ionospheric study in 2016, while one S-520 rocket was launched for a microgravity experiment in 2015. In January 2017, SS-520 rocket was used to put a nano satellite into orbit. In this paper, we give a brief description of the recent activity with Japanese rockets during 2015-2017.

Table 1. List of Japanese rocket experiments during 2015-2017.

Rocket	Objective	Launch Date
S-520-30	To investigate nucleation process of cosmic dust under microgravity	Sept 11, 2015
S-310-44	To elucidate electron heating process in the Sq current focus in the mid-latitude ionosphere	Jan 15, 2016
SS-520-4	Demonstration of nanosatellite launch by using SS-520 rocket	Jan 15, 2017

2. S-520-30 ROCKET EXPERIMENT (SEPTEMBER, 2015)

The S-520-30 sounding rocket was launched from Uchinoura Space Center (USC) on September 11, 2015, with the objective of clarifying the nucleation process of oxide-based cosmic dusts. It is important to understand initial characters of oxide dust, because it is a building block of solar system bodies. Homogeneous nucleation process of mimic dust was tried to partly reproduce on μ-gravity environment during the ballistic flight of the rocket so that one can obtain physical parameters and reveal the formation process of cosmic dust particles. In the experiment, oxides was evaporated under the micro-gravity environment, and onboard instruments directly measured the generation and growth process of oxide particles that were condensing after the evaporation.
This experiment was conducted by using two new instruments; 1) a dual-wavelength interferometer, 2) an on-site measurement instrument of floating dust infrared spectra. The first instrument is to simultaneously measure temperature and density of gas with high precision and without any contact by taking advantage of the fact that refraction indices of each light wavelength are different in a transparent sample. The second one was developed to directly measure infrared spectra which are information that we can gain through studying lights in the infrared region of a celestial body. Detailed results from this experiment were published in the literature [1,2].

3. S-310-44 ROCKET EXPERIMENT (JANUARY, 2016)

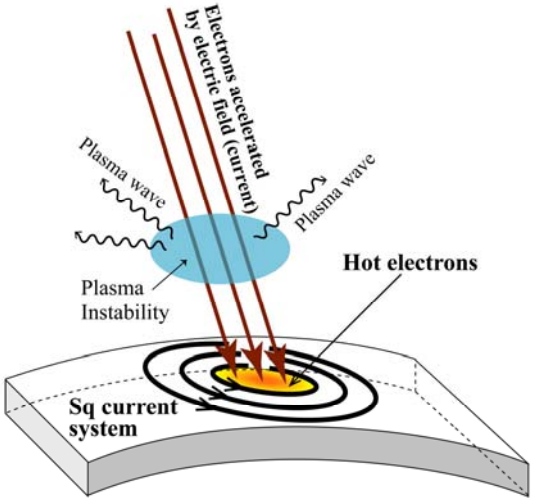

Figure 1. Schematic drawing of phenomena occurring in the Sq current focus

On January 15, 2016, sounding rocket "S-310-44" equipped with a suite of five science instruments was launched from the USC. The objective of this experiment was to elucidate a generation mechanism of the ionospheric electron heating in the Sq current focus. According to the previous study [3], precipitating electrons accelerated by the potential difference along the magnetic field lines which connects between the Sq current focus in the north hemisphere and that in the south hemisphere may be a possible heat source to increase electron temperature in the lower ionosphere. If this is true, plasma instability may be generated by the precipitating electrons. Fig. 1 shows a schematic illustration of phenomena which are thought to exist in the Sq current focus. The five instruments were selected so that these phenomena can be revealed by their measurements, and enables us to make *in-situ* measurements of thermal electron energy distribution, electric field, electron density perturbation, plasma wave, and magnetic field in the Sq current focus of mid-latitude ionosphere. These are thought to be key parameters to understand the unresolved phenomena. Fig. 2 shows a picture of the payload section of "S-310-44" rocket, which was covered by nose cone at the time of rocket launch.

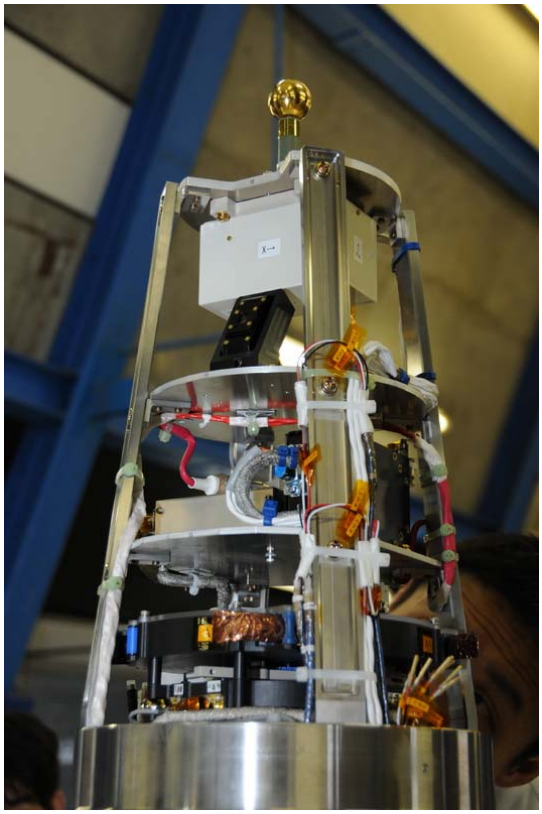

Figure 2. Payload section of "S-310-44" rocket

The energy distribution of thermal electrons may contain information how these particles get energy via dynamic and/or energetic process. The electric field data

Figure 3. Launch of S-310-44 rocket

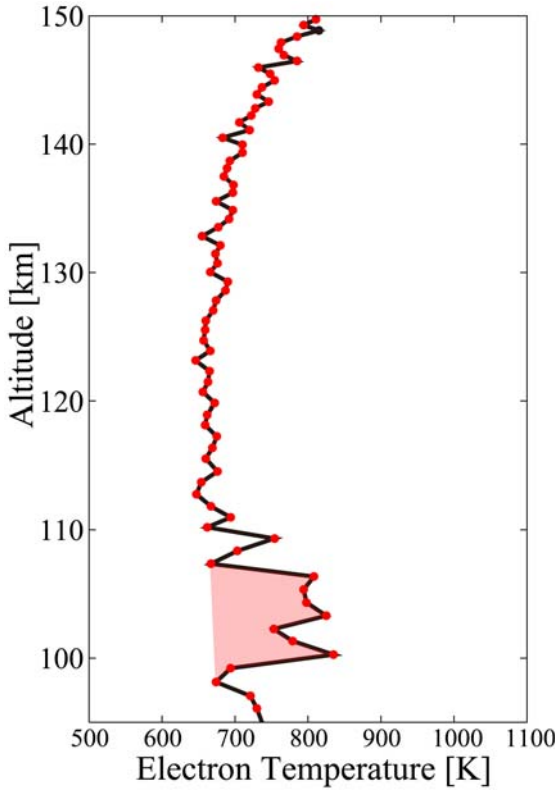

Figure 4. Electron temperature profile from the FLP instrument on "S-310-44" rocket

can become evidence if the electrons are accelerated by the field-aligned potential difference. If plasma instability exists in this region, the electron density perturbation may be detected as a result of development of small-scale disturbance. The rocket was launched from USC at 1200 LT on January 15, 2016.

Fig. 4 shows altitude profile of the electron temperature derived from the Fast Langmuir Probe (FLP) measurement on rocket. This indicates that the electron temperature increased by about 200 K with respect to the background in the altitude range from 100 to 110 km. Furthermore, this confirms that the temperature increase

is a phenomenon that is most frequently generated in the Sq current focus and that the actual rocket trajectory was near-by.

Another significant feature is that the electron energy distribution obtained by the FLP in the high temperature region unlikely seems *Maxwellian* distribution and suggests a possible existence of *non-Maxwellian* component. Electron current incident to a spherical probe of Fixed Bias Probe (FBP) was applied to power spectrum analysis to determine a dominant frequency of small-scale electron density perturbation. The calculated power spectrum indicates that the amplitude in the frequency range of several hundred Hz increased at 96-112 km altitude in the ionospheric E region. This suggests that the strong electron density perturbation was existing in the broad frequency range at this altitude range. In addition to such a broad band increase of the amplitude, a strong peak was found to exist in the frequency between 1.0 kHz to 1.5 kHz and the peak frequency increases with altitude up to 122 km. In contrast, the peak frequency decreases with altitude above 122 km. Such a change in the peak frequency seems to be related with the number density of thermal electrons. Surprisingly, the dynamic power spectrum from HF band plasma wave receiver also has similar feature of the peak frequency and its trend.

4. SS-520-4 ROCKET EXPERIMENT (JANUARY, 2017)

At 08:33 JST on January 15, 2017, SS-520-4 rocket was launched from the USC. The objective of this experiment was to develop rockets and satellites using civil engineering technology and to demonstrate a launch of nanosatellite with about 3 kg mass. SS-520-4 rocket is a three-stage rocket that is a modification of the SS-520 two-stage rocket. The launch was conducted as a part of Japanese government's program for development of launch vehicles and satellites in public-private partnerships.

In the actual sequence, the first stage motor was ignited as planned, and the overall system including ground systems for telemetry and tracking radar, etc. was normal for initial 20 sec after the launch. However, data transmission from the telemeter ceased at 20.4 sec after the launch. As a result, data on Quick-Look display screen were lost, and it was not possible to confirm telemetry information.

Unfortunately, the situation did not improve afterwards, and the status of the overall system was not ascertained. Therefore the second stage motor ignition command was not sent, and it was not possible to put the nanosatellite into the expected orbit.

5. NEAR-FUTURE EXPERIMENTS

In winter of 2017, we will launch sounding rocket "SS-520-3" in Svalbard, Norway, to investigate the generation mechanism of the ion upflow/outflow in the ionospheric cusp region. In particular, we will focus on the interaction between plasma wave and particles which is believed to play an important role to significantly energize the ionospheric ions. Fig. 5 is a schematic illustration of the ion upflow originated from the ionospheric cusp together with the expected rocket trajectory. Lowest altitude of the interaction between plasma wave and particles is thought to be below ~1000 km altitude, above which energized ions can be probably observed. To get an overall picture of such causal relationship, we have selected instruments so as to make a comprehensive measurement of thermal plasma, low-energy electrons and ions, electric and magnetic fields, and plasma wave, as shown in Tab. 2. The ground-based instruments will also be operated to monitor a position of the cusp and a condition of the cusp ionosphere during this experiment.

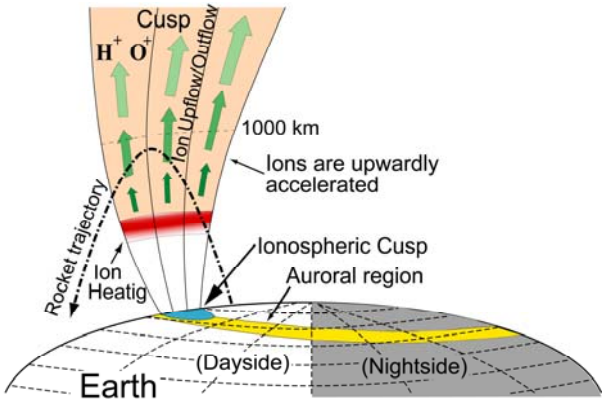

Figure 5. Schematic illustration of the ion upflow From the ionospheric cusp region

Table 2. List of science instruments on "SS-520-3" rocket

Instrument	Responsible Institute
Digital Flux Gate Magnetometer (DFG)	ISAS/JAXA
Low Frequency Analyzer System (LFAS)	RISH/Kyoto Univ.
Thermal ion Spectrum Analyzer (TSA)	ISAS/JAXA, Nagoya Univ.
Low Energy Particle Experiment (LEP)	ISAS/JAXA
Ion Mass Spectrometer (IMS)	ISAS/JAXA
Fast Langmuir Probe (FLP)	ISAS/JAXA
Multi Needle Langmuir Probe (NLP)	Univ. of Oslo
Plasma and Wave Monitor (PWM)	Tohoku University
Sun Aspect Sensor (SAS)	Tokai University

6. ACKNOWLEDGEMENTS

We are very grateful to all the staff of ISAS for the rocket launch. We would also like to thank Profs. Inatomi, Kimura, Yoshida, Habu, and Saito for providing information for the present paper.

7. REFERENCES

1. Ishizuka, S., Kimura, Y., Yamazaki, T., Hama, T., Watanabe, N. & Kouchi, A. (2016). Two-step Process in Homogeneous Nucleation of Alumina in Supersaturated Vapor, *Chemistry of Materials*, **28**(23), 8732–8741, DOI: 10.1021/acs.chemmater.6b04061.

2. Ishizuka, S., Kimura, Y. & Yamazaki, T. (2016). In Situ FT-IR Study on the Homogeneous Nucleation of Nanoparticles of Titanium Oxides from Highly Supersaturated Vapor, *Journal of Crystal Growth*, 450 (15), 168-173, DOI: 10.1016/j.jcrysgro.2016.06.036

3. Oyama, K.-I., Abdu, M.A., Piel, A. and Thiemann, H. (1993). Electron heating associated with the Sq current focus, *ISAS Research Note*, No. 534.

ESRANGE SPACE CENTER - LATEST HIGHLIGHTS AND FUTURE PLANS

Mattias Abrahamsson [(1)]

[(1)] SSC, Esrange Space Center, PO Box 802, SE-98128 Kiruna, Sweden, Email: mattias.abrahamsson@sscspace.com

ABSTRACT

After the last ESA-PAC meeting in Tromsö, in the summer of 2015, several rocket and balloon campaigns have been performed at Esrange. The majority of these have been within the national programmes of the EASP countries, and have been presented by the representatives of the countries. The ERC drop test campaign, the Swiss SMARTFISH campaign, the Japanese D-SEND flight, the US BARREL campaign and the commercial ISOBAR flight will all be presented. The newest upgrades of the Esrange facility and the future plans will also be spoken about.

1. INTRODUCTION

Since the last ESA-PAC meeting in Tromsö in the summer of 2015 there have been several rocket and balloon campaigns performed at Esrange.
The majority of the campaigns are presented in the national presentations of the EASP countries, but a number of the campaigns are campaigns from users outside the EASP countries. In this paper we will present some of the more interesting campaigns from these users, as well as one of the EASP campaigns..

2. EASP CAMPAIGNS

From summer 2015 to summer 2017 there have been 24 rockets and 46 balloons launched. Of these, all 24 rockets and 21 balloons were in EASP campaigns. These will not be further discussed as they are presented in the national programmes by SNSB, DLR and CNES.

2.1. EASP rockets

2015-06-30	04:55:00	MAPHEUS 5
2015-10-02	05:39:00	O-STATES 1
2015-10-19	14:09:00	O-STATES 2
2015-10-22	08:45:00	STERN Faust
2015-10-22	14:45:00	STERN Hero
2015-10-27	13:55:09	STERN Decan1
2015-10-29	08:55:00	STERN Decan 2
2015-12-01	06:00:00	MASER 13
2016-01-23	08:30:00	TEXUS 53
2016-02-02	21:09:00	SPIDER/LEEWAVES
2016-03-15	05:30:00	REXUS 20
2016-03-18	05:10:00	REXUS 19
2016-04-14	06:00:00	STERN Aquasonic
2016-04-16	09:57:00	STERN Zephyr
2016-04-28	12:00:00	SERA-2
2016-07-19	06:05:00	ROTEX-T
2016-10-31	12:00:00	STERN HyEnd 1
2016-11-08	09:30:00	STERN HyEnd 2
2017-01-23	03:30:00	MAIUS
2017-03-15	10:43:00	REXUS 21
2017-03-16	13:00:00	REXUS 22
2017-04-07	09:30:00	MAXUS 9
2017-04-26	13:30:00	SERA-3
2017-05-13	09:20:00	MAPHEUS 6

2.2. EASP balloons

2015-10-07	09:31:00	BEXUS 21
2015-10-10	09:17:00	BEXUS 20
2015-10-19	14:30:00	SMARTFISH 1
2015-10-19	16:00:00	SMARTFISH 2
2015-10-20	10:30:00	SMARTFISH 3
2015-10-21	14:40:00	SMARTFISH 4
2015-10-22	11:27:00	SMARTFISH 5
2015-10-22	13:31:00	SMARTFISH 6
2015-10-23	10:52:00	SMARTFISH 7
2015-10-24	10:44:00	SMARTFISH 8
2015-10-24	13:50:00	SMARTFISH 9
2016-01-14	13:32:00	LTU
2016-02-12	10:30:00	LTU
2016-03-15	08:26:00	LTU
2016-06-02	08:50:00	ANDA
2016-07-12	03:17:00	POGO+
2016-08-29	03:48:00	CNES/KASA
2016-09-03	04:43:00	CNES/KASA
2016-10-05	13:34:00	BEXUS 22/23
2016-10-07	07:08:00	BEXUS 22/23
2016-12-15	10:02:00	LTU

3. NON-EASP CAMPAIGNS

From summer 2015 to summer 2017 there have been 25 balloons flown outside EASP campaigns.

2015-06-14	20:34:00	ERC 1
2015-06-21	15:36:00	ERC 2
2015-07-24	02:43:00	D-SEND#2C
2015-08-05	06:03:00	ERC 3
2015-08-10	13:52:00	BARREL 3A
2015-08-13	04:30:00	BARREL 3B
2015-08-17	12:08:00	BARREL 3C
2015-08-19	06:03:00	BARREL 3D
2015-08-21	07:05:00	BARREL 3E
2015-08-25	06:39:00	BARREL 3F
2015-08-25	08:58:00	BARREL 3G
2016-08-13	22:25:00	Barrel 4A
2016-08-16	20:02:00	Barrel 4B
2016-08-19	10:00:00	UMich 1
2016-08-19	11:30:00	UMich 2
2016-08-19	13:00:00	UMich 3
2016-08-20	13:15:00	UMich 4
2016-08-21	10:48:00	Barrel 4C
2016-08-21	17:48:00	Barrel 4D
2016-08-24	11:25:00	ISOBAR test flight
2016-08-24	17:23:00	Barrel 4E
2016-08-28	18:33:00	Barrel 4F
2016-08-29	18:50:00	Barrel 4G
2016-08-30	18:14:00	Barrel 4H
2016-09-05	12:05:00	ISOBAR

4. HIGHLIGHTS FROM CAMPAIGNS

Below are some highlights from the EASP- and non-EASP campaigns that we would like to point out.

4.1. ERC

The ERC campaign was a drop test campaign from balloon in June and August 2015 by Vorticity LTD, for a technical test for ESA, where SSC provided operations. The goal was to test various drop body designs for an Earth Return Capsule (ERC). During each flight three different payloads were released at different altitudes for free-falling tests in the Esrange rocket impact area, which is where such tests can be performed. Special wind conditions during June made only two flights possible, and a third flight was made in August. All flights gave good results to the scientists.

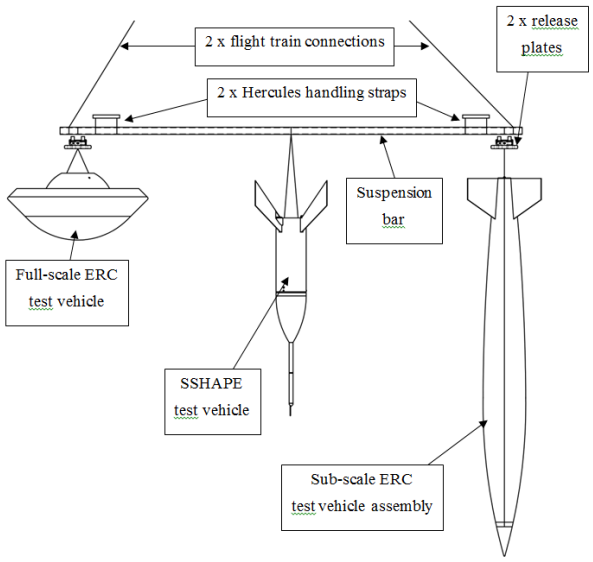

Figure 1. ERC drop configuration

4.2. D-SEND #2C

The goal of the D-SEND project performed by JAXA at Esrange was to provide sonic boom data by recording the sonic boom from an autonomous gliding vehicle that was released from 30 km altitude. The vehicle reached M1.4 in free-fall after which it flew past a number of microphone arrays, both on the ground and suspended under tethered airships.

Figure 2. D-SEND vehicle

SSC provided operations for the balloon, with one flight performed already in 2013. The flight in August 2015 was flawless and provided good results to the scientists.

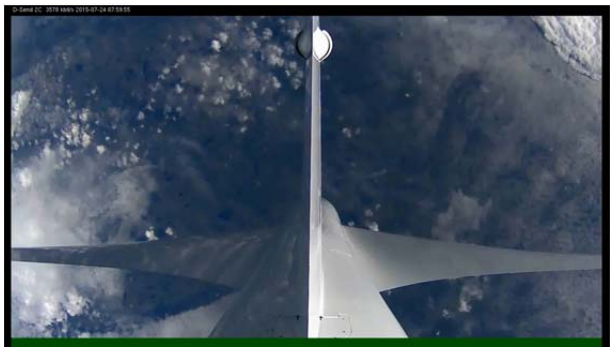

Figure 3. D-SEND vehicle at drop altitude

4.3. SMARTFISH

The SMARTFISH campaign was a Swiss drop test campaign from balloon in October 2015 by Meteolabor AG, for a technical test for ESA, where SSC provided operations.
One of the most interesting things with this campaign was the fact that the drop tests were performed so late in the year that the winds at altitude were going eastwards, away from the Esrange area where landings are performed. This meant that the launches of the balloons had to be performed west of Esrange, in the mountain range, to allow the balloons to drift into the Esrange area while gaining altitude.

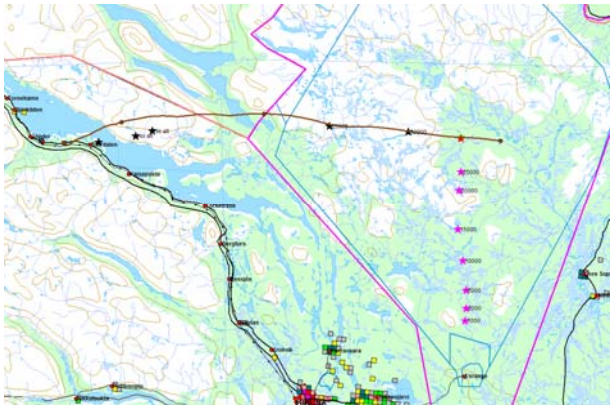

Figure 4. Flight trajectory of SMARTFISH launched from outside Esrange base

Figure 5 Launch of SMARTFISH

4.4. BARREL 2015 and 2016

The first BARREL campaign at Esrange was performed in August 2015 by Darthmouth college for NASA, with operations from SSC. A second campaign was then performed in August 2016.
The goal of the project was to measure X-rays produced by fast-moving electrons high up in the atmosphere. The project had already flown two campaigns in the southern hemisphere in Antarctica. The flights at Esrange were made during turn-around wind conditions and this produced long flight times at float, with a longest flight duration of 36 h. BARREL got good data, also making joint measurements with satellites.

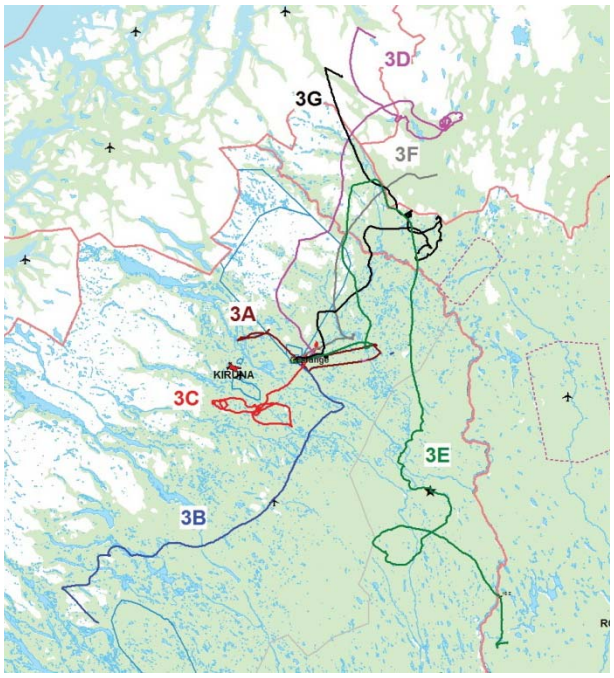

Figure 6. Trajectories of BARREL in 2015

NAME	DATE	DURATION
Barrel 3A	Aug 10, 2015	7h 26m
Barrel 3B	Aug 13, 2015	12h 55m
Barrel 3C	Aug 17, 2015	15h 25m
Barrel 3D	Aug 19, 2015	6h 45m
Barrel 3E	Aug 21, 2015	36h 11m
Barrel 3F	Aug 25, 2015	25h 46m
Barrel 3G	Aug 25, 2015	24h 12m

The table above shows the corresponding flight times to the map in Figure 6.

4.5. ISOBAR

A very special project was made in September 2016 when SSC was asked to fly a payload for a Swedish advertisement company. The payload consisted of a COTS mobile telephone that was to send streaming video data from a balloon, with the intention to achieve the altitude record of such a feat. SSC provided a very light gondola construction, and operations. The balloon reached 18,4 km, streaming good data throughout the flight.

Figure 7. COTS telephone flying on the ISOBAR flight

4.6. CHALMERS UAV

Chalmers University tested a UAV system at Esrange in 2016, before going on a research trip to Papua New Guinea. The goal of the UAV flight was to validate the functionality of a helicopter drone system that was to be used for scientific measurements of volcano gasses. The tests were performed at Esrange in a very short time, showing the flexibility of using Esrange also for this type of missions.

Figure 8. UAV coming in for landing at Esrange

5. UPDATES

Esrange is continuously upgrading equipment and systems. Since the last report three major upgrades have been performed.

5.1. TM station

The Esrange telemetry station has been completely upgraded to provide a better working environment.

Figure 9. The new TM room

5.2. NOSYCA antenna

In 2010 CNES put in a request to SSC to acquire and deploy a NOSCYA ground station as part of the EASP agreement. SSC responded with a solution of fusing NOSCYCA ground station equipment – SCLIA with an L/S-band 3.7m antenna. The antenna has been housed on top of the radar hill, inside the old radar antenna dome.

5.3. Ground instruments

Both the ESRAD atmospheric radar and the SkiYMet meteorite radar has been upgraded over the last years.
ESRAD can now work in an bi-static mode. The SkiYMet has been refurbished and taken over by SSC, while the data is still handled by Uni Bath.

6. ROCKET MOTOR TEST FACILITY

Among the many plans for the future that exists at Esrange, one of the most interesting is the one for a rocket motor test facility.
The facility would be placed by the launching area and provide instrumented possibilities to fire rocket motors with up to 50 000 kg thrust, and lengths up to 7 m.
This includes the VS and VSB configurations currently mostly used today.

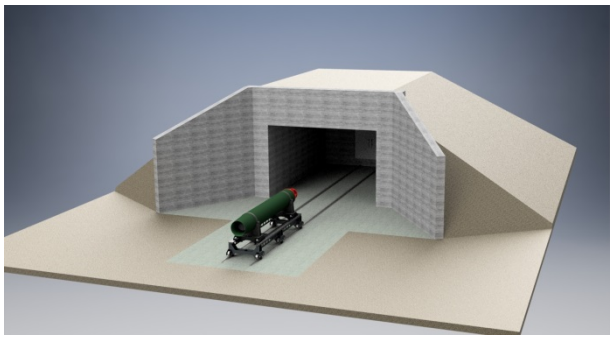

Figure 9. The new TM room

7. CONCLUSION

Since the 22nd ESA-PAC symposium, Esrange has continued to provide unparalleled possibilities for scientists needing sounding rocket and stratospheric balloon operations, as well as developing systems and facilities for the future needs of the community.

ETHERNET FOR SOUNDING ROCKETS

Markus Wittkamp and Rainer Kirchhartz

Deutsches Zentrum für Luft- und Raumfahrt (DLR), Mobile Rocket Base, markus.wittkamp@dlr.de

ABSTRACT

The standard interface for experiment computers for forwarding low to medium data rates to the Service Module on a Sounding Rocket payload is still the asynchronous UART protocol on a RS422 physical layer. This interface is well known, easy to implement and debug. However, it is limited in speed and signal integrity when it comes to high bit rates. Further, the UART protocol cannot be routed without additional layers of communication, since it was designed to serve as a point to point protocol.

A common interface to overcome these problems is Ethernet together with the TCP/IP family of protocols. Some experimenters are already using this stack in their laboratory.

This paper presents a communication system which provides Ethernet on-board a Sounding Rocket to provide the flexibility of this standard system to the experiments. The architecture is based on a pair of gateways to adapt to the existing TM/TC systems without modifying them. The system requires transparent octet-streams on both TM and TC. It replaces the Ethernet frame and forwards data of the IP communication layer.

Due to the nature of IP based communication, the messages can be routed within networks and Firewalls might be used at the Gateways on both ends to protect the TM/TC connections from unwanted packets.

Within the paper we describe the details of the architecture, show an reference implementation of the two Gateways and results of tests during the MAIUS flight.

Key words: Ethernet, Gateway, Sounding Rocket, TM/TC, MAIUS.

1. INTRODUCTION

Modern Payload Systems on Sounding Rockets or Balloons require more flexibility on data distribution on board. Some of these systems also provide several different data streams and not all of them are directed to the ground stations but to other subsystems. These systems might depend on each other, they are able to cooperate and receive information from other systems.

One solution to realise such a scenario is to use the already known and commonly used TCP/IP family of protocols together with Ethernet. Compared to interfaces like UART on RS422, this stack of protocols was designed to handle very large networks, not just point-to-point connections. When it comes to higher data rates, Ethernet also works better in terms of EMC[1] and usability. The system is also more easy to install by using managed or unmanaged switches. Since the system is forming a star-topology, at least parts of the data-paths can be shared between devices and therefore the topology reduces the total number of wires in the harness and provides access-points to the network for monitoring and debugging of the network traffic at the same time.

From a communications engineering point of view, the UART protocol with start- and stop-bits, together with RS422 is operating on the physical layer (OSI Layer 1) [1, Chapter 9.1.4]. A message protocol using frames of octets can be treat as a communication system on the link-layer (OSI Layer 2). If such a protocol includes a destination address, a routing logic can be defined to forward single messages to a destination within a network of computers. This is a property of the network layer (OSI Layer 3).

The IP protocol, specified in [2] was designed as a network layer protocol, whereas Ethernet is providing only layer 1 and 2. TCP and UDP are transport protocols, related to the transport layer of the OSI model (layer 4).

This forms a stack of protocols where each protocol depends on the layer below. Technically a message on a specific layer is embedded in the next layer below, until the whole stack reaches the physical layer. That also means each protocol has to add the specific information for its layer and therefore the size of the message grows with each layer. However, a protocol on a specific layer usually does not need any information of any other layer. This allows to replace protocols with different, compatible ones of the same layer and adapt the stack to fit to different purposes.

To connect an onboard network with the ground stations, the IP data can be forwarded within the already existing

[1] EMC: Electro Magnetic Compatibility

up- and downlink infrastructure. Ethernet itself is not a suitable protocol for this task, since it already defines the physical layer and was not made for RF links. Further, the protocol specifies several services at layer 2 which are not required for forwarding of IP messages to a ground-station.

The subject of this paper is the description of the architecture and the implementation of the link to the existing up- and downlink infrastructure.

2. ARCHITECTURE

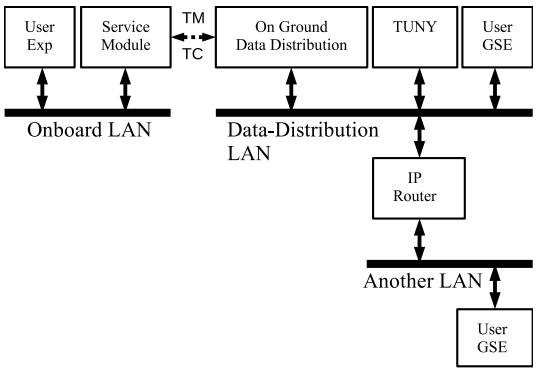

Figure 1. Dataflow overview of the connection between onboard LAN and the ground segment using standard TM/TC links.

For a short overview on the architecture of the proposed solution, Figure 1 is showing a typical scenario for a LAN[2] on a payload. One ore more user-experiments sharing this network and wants to send IP packets to a receiver in a different network on ground. It is assumed that the TM/TC-system within the service module already provides transparent up- and downlinks for streaming of octets.

In order to forward data to ground, the Ethernet protocol has to be replaced by a different and more robust one to make the new system compatible to that octet streaming service. The whole process doesn't modify the IP header nor any other information included in the packet. It basically adds synchronisation words and a protecting CRC[3].

On the ground segment the packets containing the IP data can be extracted and forwarded to their destination via IP routers as figure 1 shows.

The system has to know the length-information of the embedded IP packet for synchronisation purposes, because IP packets are variable in length. To avoid redundancy, it reads this information directly from the IP header and validating it with the IP header checksum. So it actually depends on the IP packet format and IP is not changeable anymore. Any other information in the IP header or the embedded payload within the IP packet doesn't matter for the forward process.

OSI Layer	Ethernet, TCP/IP	*IpOverDynStreams*-Stack
4	TCP, UDP, etc.	
3	IP	
2	Ethernet	*IpOverDynStreams*
1		TM/TC

Table 1. Layer Stack of TCP/IP together with Ethernet and IpOverDynStreams

This architecture results in two gateways, one on each end of the TM/TC-system. The gateways basically convert the packets from Ethernet to the internal format which was called "IP over Dynamic Streams" or *IpOverDynStreams* and back. To be more precise, the overall system is forming a layer 3 router, composed of two protocol-converters for the octet-streams on layer 2 and the actual routing logic. Table 1 shows an overview of the OSI layers to compare the TCP/IP stack with the one of the *IpOverDynStreams*.

Each of these gateways might be equipped with additional packet filtering firewalls. Such a firewall is checking both the IP- and the layer above, usually TCP or UDP, against a mission specific set of rules to forward or reject packets. This can be used to protect the up- and downlinks from unwanted packets, e.g. due to failures on a client firmware.

Due to the fact that the IP protocol itself doesn't need a response, the system can also be used in a one-way configuration, if one of the up- or downlink systems fails or simply doesn't exist by design.

3. IMPLEMENTATION

As stated in the architecture description above, the system is a composition of several sub-components: the *IpOverDynStreams* protocol on layer 2 to protect the IP packet and a gateway located in the service module close to the TM/TC system and another one in the ground segment.

The reference implementation has been done on a MFC2 computer board [3] which provides a Blackfin 561 processor together with a MAC chip for Ethernet as well as the interfaces for up- and downlink. An instance of the LwIP-stack [4] is running as a thread on the RODOS kernel [5] on the processor. This open source network stack is used to control the Ethernet port as well as the gateway to the telemetry. It is also responsible for all kind of communication on layer 3 (IP) and 4, like TCP and UDP (see also Table 1). To the LwIP stack the gateway behaves as any other network interface, since it uses the same software interface. The layers below the IP layer are performed using hardware driver. For Ethernet the MFC2

[2]Local Area Network
[3]Cyclic Redundancy Check

provides a dedicated Ethernet MAC controller. The hardware for sending and receiving octet-streams is implemented as FPGA-logic[4].

As for Ethernet, a MTU[5] size is used to determine maximum buffer sizes and optimise the link-layer protocol on the up- and downlink.

3.1. IP over Dynamic Streams

Name	Offset	Length	Description
Sync	0	4	Const.: `0xfafbfcfd`
x/IP	4	...	start of IP packet
IP-tl	4	2	total length of IP
...	...	...	
State	*see text*	2	reserved for future use
CRC	*see text*	2	CCITT 16 polynomial

Table 2. Definition of the IpOverDynStreams-Format. The grey marked area shows the embedded IP packet.

The format of the layer 2 protocol to forward and protect IP data on RF-links of the telemetry and telecommand links is shown in table 2. As usual for this kind of protocols, all fields are transmitted in big-endian format, the network order of bytes.

Synchronisation To find the start of a *IpOverDynStreams* message, a four-byte synchronisation constant is leading the octets of the message.

Message Length The problem with IP messages is that the actual length is not known in advance. To overcome this, the "Total Length"-field of the IP packet is used directly. For IP version 4, this field is located at offset zero, relative to the IP packet, which is offset 4 in the *IpOverDynStreams* packet, because of the 4 byte synchronisation constant. The total length of the IP packet is the only information needed to forward it on layer 2.

State and CRC With the length of the message, the position of the State and the CRC field can be calculated immediately: It is the total length of the IP packet plus the size of the leading and trailing fields of the additional headers. Therefore the total length of a message is the size of the IP packet plus 8 octets.

The State-field is reserved for future use. It should be set to zero.

To avoid unnoticed errors during the transport process, a CRC 16 is appended to the message. The CCITT polynomial $x^{16}+x^{12}+x^5+1$ is used to calculate this checksum. It will be initialised with 0xffff.

[4]FPGA: Field Programmable Gate Array
[5]MTU: Maximum Transfer Unit

3.2. Service Module Gateway

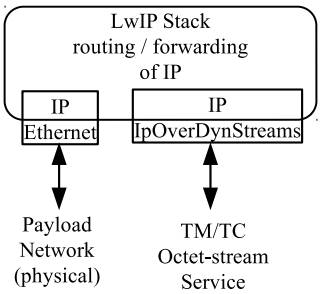

Figure 2. Routing and Forwarding Process within the LwIP stack.

LwIP Stack The on board side of the system is based on the already mentioned LwIP stack. This stack provides a rich set of functions to an application level program. Beside of this, it can handle more than one network interface and is able to forward traffic between these interfaces.

The LwIP stack itself is not subject of this paper, it is well documented in [4]. But the network interface to the TM/TC system in figure 2 uses the functions of that stack. It communicates with it by an internal software-interface for reading and writing of IP data. Since the stack was written in C, this communication is basically a passing of pointers to data-structures within the memory of the processor without copying of data (zero-copy policy).

To forward data in the scenario of this paper, it needs at least two interfaces, one to Ethernet and another one to the TM/TC system. Both of them need a full set of data: an IP Address, a Gateway address, the network mask, MAC Address, etc. One of the interfaces becomes the default gateway to the LwIP stack. Figure 2 is showing the process. It can be assumed that the default gateway points to the TM/TC system, because most other networks will be on ground instead of on payloads.

The routing logic of the stack will select a specific network interface either if it points directly to the destination network of the IP packet or it was defined to be the default gateway. This is a common way to forward packets. In this scenario the gateway will get all packets that cannot be forwarded to directly connected onboard networks.

All network interfaces controlled by the stack have to implement the same (software-) interface. Where other interfaces implementing drivers to control Ethernet chips, the interface to the TM/TC system was specially designed to connect the internal interface of the stack to the octet-streaming service. In case of the reference implementation, the streaming service consists of a set of registers and FIFOs[6] to exchange data directly with the TM/TC system.

[6]FIFO: First in, First out buffer

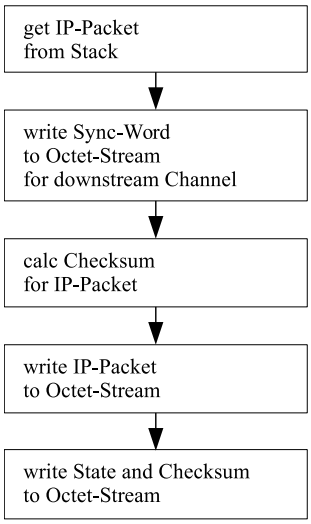

Figure 3. Flowchart of the transmitting process.

TX process Figure 3 is showing a simplified flowchart of the process of sending data to the TM/TC system, which is called the downlink direction. The stack is calling a *write* function of the gateway driver and passing a pointer to an IP packet.

The first step is to send the constant synchronisation word to the octet-stream of the TM/TC system. The next step is to calculate the CRC of the IP packet part of the message (see table 2) and the state information and write both out to the octet-stream. Finally the result of the CRC is written to the stream.

RX process Since the driver doesn't know in advance how many octets are to read for the current packet, the process is split into two parts, as Figure 4 shows in a simplified flowchart.

The first part of the process is waiting for the synchronisation words and then read the IP header of the packet. A check of the header is performed with the checksum field of the header, to ensure the integrity of the length information. If this fails, the driver will drop the already received octets and start a new read process.

With a verified IP header, the length information is known and the number of bytes left to read can be computed. The system is then changing its state, starting another read process to get the rest of the packet and start waiting for the next receive-interrupt to proceed. This interrupt is generated as soon as the requested number of octets are received in the hardware-buffer in the TM/TC system. They are not yet available to the processor.

The second part of the read process is starting with reading the rest of the IP packet from the buffer of the TM/TC system, including the tailing fields of the *IpOverDynStreams* message. When the full packet has been read, the CRC is checked and compared with a locally computed one. If this fails, the driver drops the packet and will restart the process.

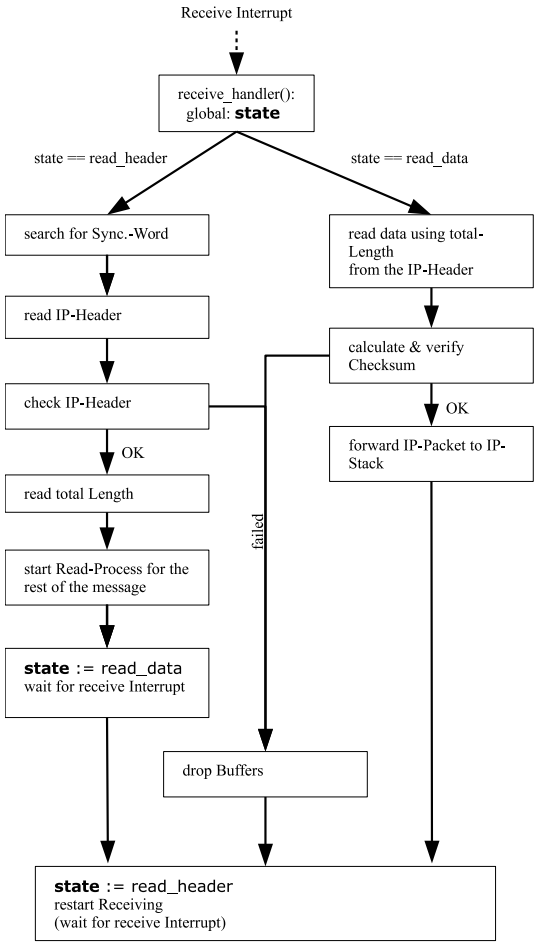

Figure 4. Flowchart of the receiving process.

If the CRCs are equal, a pointer to the IP packet is passed to the LwIP stack for further processing. The additional fields of the *IpOverDynStreams* are not needed anymore.

The receive process will restart immediately with a fresh buffer to get the next packet.

3.3. TUNY

On ground, the gateway was implemented as a Linux program, it was called *TUNY*. The Linux kernel provides an interface to its routing mechanism either on IP level (tun) or directly on Ethernet (tap) [6]. A program running with root-privileges is able to open such a driver and communicate on the selected layer. The driver becomes available as a virtual network device.

Since the gateway is acting on layer 3, a *tun*-type interface has been chosen to extract and inject IP packets to the kernel. An overview is given in figure 5. On the other

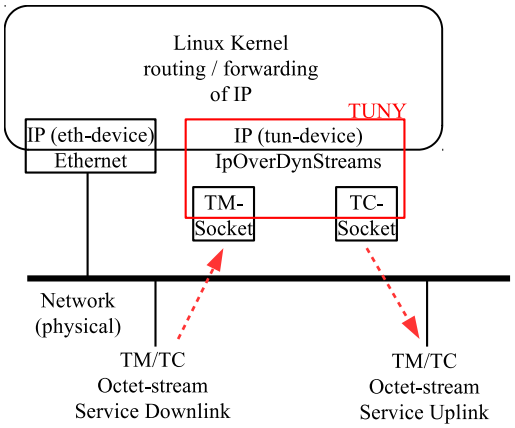

Figure 5. Routing and Forwarding Process of TUNY.

end of the communication, the program is reading and writing the octet-stream from and to the TM/TC data distribution in the ground segment using standard application level sockets.

Interface to the Linux Kernel The virtual interface *tun* allows the kernel to pass IP packets to *TUNY*. It behaves like drivers for Ethernet-cards or other devices but on layer 3 only. Therefore it needs the full set of information: IP address, network mask and gateway settings. [6] provides a documentation of the driver.

TUNY registers such a device on the kernel and provides network settings for it. The kernel is using the device from that point on until *TUNY* is closing the driver for exit.

Interface to the TM/TC system *TUNY* is designed to connect to the octet-streams for up- and downlink by UDP/IP. That implies the TM/TC-system on ground is already providing such an interface, as the reference implementation does. Figure 5 shows that connectors as sockets at application level, one for each direction of dataflow. The dataflow itself is marked with dashed lines.

This architecture of *TUNY* allows most flexible network designs in the ground segment. The network can even be distributed over several physically separated segments as long as a route exists and is known to forward the packets.

TX, Uplink process The uplink-process on ground is quite similar to the downlink process on the payload and analogously to the simplified flowchart in figure 3. *TUNY* is reading an IP packet from the *tun* device, adds the fields of the *IpOverDynStreams* packet including CRC and send it as an octet-stream to the uplink-socket. The socket forwards the octet-stream to an instance of e.g. a telecommand-encoder.

RX, Downlink process As the uplink process, also the downlink is working similar as the receiving process on board (Figure 4). The receiving UDP socket on application level (Figure 5) is reading the incoming packets byte-by-byte and searching for the synchronisation constant of the *IpOverDynStreams* header.

The next step is to read and verify the IP header to get the total-length of the packet. With the knowledge of that length, the rest of the packet can be read and the CRC can be checked.

If the packet was received without errors, the fields of the *IpOverDynStreams* are removed and the IP packet is passed to the *tun* device to be forwarded towards its destination within the ground segment by the Linux kernel. In case of receiving errors, the process is dropping the buffer and continue searching for the next packet header.

4. RESULTS AND MEASURES

4.1. Functional Test: ICMP

A first test of all IP network related implementations is the use of the ICMP protocol [7]. The popular command *ping* sends so called *ECHO Requests* to a receiver which answers with *ECHO Reply*. Further, the request frequency of the command can be adjusted and the program provides a switch to append an optional payload of almost any size. With this tool it is possible to generate arbitrary load on a network.

The response time for the command in this scenario is mainly affected by the speed and the load of the uplink. For the test the speed was set to 230.4 kBit/s for a shared uplink of 16 transparent octet-streams simultaneously. In result the response time was about 18 ms to several 100 ms, depending on the load of the link.

4.2. Performance during Flight of MAIUS

The main experiment on MAIUS was connected to a local network on board the payload. The implementation presented in this paper has been used during flight to forward the data to the ground segment and transport telecommands the other way.

Figure 6 shows the load of the octet-stream over flight-time. This curve is generated by the telemetry statistic module of the telemetry generator. In this case, the statistic is generated by counting bytes over a full second and writing the result to a housekeeping message. The message is generated synchronously to the measure. Depending on the operational state, the experiment computer is generating burst of different types, length and contents. As the figure shows, the sum of octets of this messages ranges from zero to over 80 kByte/s.

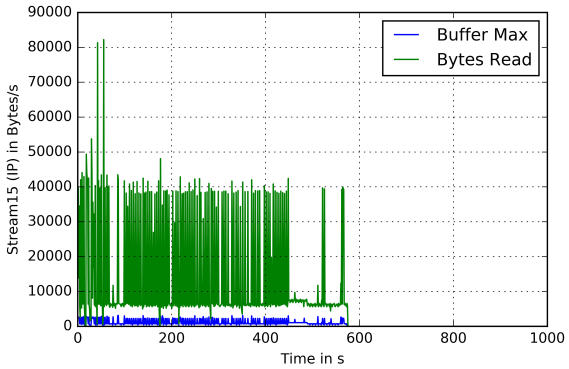

Figure 6. Load of the octet stream reserved for IP data during flight of MAIUS.

The blue curve in figure 6 shows the maximum number of bytes used from the telemetry buffers within the second of sampling. This is merely a measure of burst sizes to the octet buffer to the telemetry system. The maximum value for the buffer was 3130 Bytes. It shows that the telemetry system was filled with a quite high octet-rate, compared to the rate of reading octets from that buffer to the actual telemetry transfer frame.

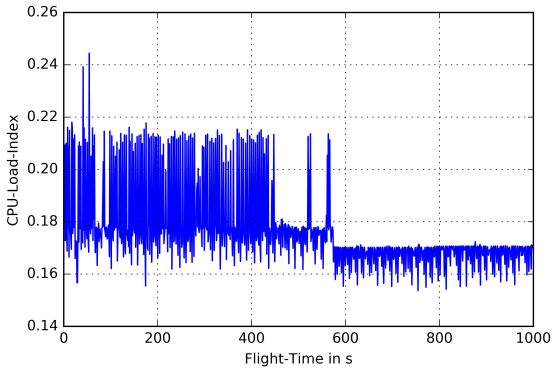

Figure 7. CPU Load Index on MAIUS during flight.

A descriptive plot of the load-index of the CPU is shown in figure 7. It shows the same period of time as in figure 6, to demonstrate the correlation of network load to CPU load. This index is derived from a counter running in the idle thread of the RODOS kernel. It's proportional to the CPU load; 100% of load results in an index value of 1. The index is computed once a second and is also part of the already mentioned housekeeping message.

Beside the handling of the LwIP stack and forwarding of data from the payload to the ground segment, the CPU was used for short, periodic tasks with high frequencies. As expected, this generates a base load to the processor with the additional load induced by network traffic on top. The system performed well during the flight of MAIUS, no data was lost and the CPU and buffer load was as expected.

5. CONCLUSION

Within this paper an architecture and an implementation of a set of routers was shown to forward IP data on up- and downlinks on sounding rockets or balloons. This provides a solution to replace serial RS422 connections with Ethernet networks to provide higher data rates and more flexibility to the users.

The architecture fits easily to existing octet-streaming TM/TC systems. It has been used successfully for the MAIUS mission and will be used also for future projects.

REFERENCES

[1] Dietmar Lochmann. *Digitale Nachrichtentechnik*. Verlag Technik, 3. auflage edition, 2002.

[2] Jon Postel. Internet protocol. Technical report, University of Southern California, 1981. `https://tools.ietf.org/html/rfc791`.

[3] Markus Wittkamp and Anderson Cattelan Zigiotto. A very high performance multi purpose computing card for tm/tc and control systems. *European Test and Telemetry Conference (ETTC'09), Toulouse*, 6 2009.

[4] Adam Dunkels and Leon Woestenberg. Lightweight ip stack. `http://www.nongnu.org/lwip/2_0_x/index.html`.

[5] S. Montenegro and F. Dannemann. RODOS - Real Time Kernel Design for Dependability. In *DASIA 2009 - Data Systems in Aerospace*, volume 669 of *ESA Special Publication*, page 66, May 2009.

[6] Maxim Krasnyansky. Universal tun/tap device driver, 2000. Part of the linux documentation at kernel.org `https://www.kernel.org/doc/Documentation/networking/tuntap.txt`.

[7] Jon Postel. Internet control message protocol. Technical report, University of Southern California, 1981. `https://tools.ietf.org/html/rfc792`.

CNES SUPER PRESSURE BALLOONS UPGRADE FOR STRATEOLE-2 CAMPAIGN

VISBY, SWEDEN
11-15 JUNE 2017

Stéphanie VENEL [(1)], Philippe COCQUEREZ [(1)], Albert Hertzog [(2)], Riwal Plougonven [(2)], Eric d'Almeida [(3)]

[(1)] CNES, 18 Av E. Belin, 31401 Toulouse, France, Emails: stephanie.venel@cnes.fr, philippe.cocquerez@cnes.fr
[(2)] LMD, Ecole Polytechnique, F-91128 Palaiseau Cedex, France,
Emails: albert.hertzog@lmd.polytechnique.fr, riwal.plougonven @lmd.polytechnique.fr
[(3)] LATMOS, 11 boulevard d'Alembert, 78280 Guyancourt, France, Email: eric.dalmeida@latmos.ipsl.fr

ABSTRACT

The French Space Agency, CNES, has developed, since about twelve years ago, super pressure balloons (SPB) that float on constant density (isopycnic) surfaces in the lowermost stratosphere for typically three months, and are able to carry 40 to 50 kg payloads. These SPB have been successfully deployed in small flotilla (~20 balloons) during several scientific campaigns all over the world in different configuration sizes from 8.5 to 12 m diameter, mainly to document the chemistry and dynamics of the atmosphere, to study gravity waves, and to provide in-situ atmospheric profiles thanks to the NCAR Driftsonde payload.

The SPB housekeeping gondola used from 2006 to 2011 has been upgraded in order to increase the flights' safety and to improve its performance with up to date equipment. The Flight Control Center has also been redesigned. These modifications take into account the experience acquired during the last SPB campaigns, mainly during Concordiasi, which released 19 balloons over Antarctica from September 2010 to January 2011. After a successful critical design review, the project is now conducting the qualification phase.

This new system is developed for Strateole-2, a project dedicated to studying the coupling processes between the troposphere and the stratosphere in the deep tropics, using both in situ and remote instruments designed for SPB. Strateole-2 includes two measurement campaigns, three years apart to study both phases of the Quasi-Biennial Oscillation. During Strateole-2, the scientific payloads will be fully autonomous, yet common technical solutions will be shared with the CNES housekeeping gondola, such as the renewable power system.

This paper will describe the Strateole-2 project and the developments in progress for the SPB system upgrade.

1. CNES SUPER PRESSURE BALLOON SYSTEM

1.1. Balloon system overview

Super Pressure Balloons are sealed spherical balloons, typically 12-meter diameter (see Fig. 1). The closed and stiff envelope of these balloons means they rise and expand to their full volume where the gas density matches the density of the surrounding air, and drift with the wind along constant density surfaces.
They fly during typically 2 to 3 months, carrying an overall 40-50 kg suspended load, and flotilla of 20 to 25 balloons can be deployed.
They thus allow "quasi Lagrangian" observation of the lowermost stratosphere and are acting as observation platforms for remote sensing of the troposphere.
Also, they just need mobile and light launch infrastructure.

Figure 1. Super Pressure Balloon

1.2. Typical missions

The first scientific mission with SPB was Strateole/Vorcore from September 2005 to February 2006, see [1]. 27 balloons, 8.5 and 11-m diameters, were launched from McMurdo, Antarctica, and flew into the stratospheric polar vortex. Long-duration flights were successfully achieved, 16 of those flights lasting for more than 2 months.
The collected dataset (more than 150 000 independent observations) provides a thorough high-resolution sampling of the polar lower stratosphere in the Southern Hemisphere from its wintertime state up to the establishment of the summer circulation in December–January.

During the international African Monsoon Multidisciplinary Analysis (AMMA) project in 2006, eight 12-m diameter SPB carrying NCAR driftsondes gondolas capable of dropping meteorological sondes were deployed over West Africa and the tropical Atlantic, see [2]. The goals of this deployment were to test the Driftsonde technology and to study the African easterly waves, which are often the forerunners of hurricanes. Between 29 August and 22 September 2006, 124 sondes were dropped across Africa into the Atlantic between about 10° and 20°N, where almost no in situ vertical information exists.

13 driftsondes have then been flown during the 2010 Concordiasi campaign (see [3] and [4]) together with 6 other gondolas carrying instruments dedicated to in situ measurements, mostly for ozone, aerosols, air temperature and air pressure. 12-m diameter SPB were launched from McMurdo, Antarctica, and flew into the stratospheric polar vortex (see Fig. 2) from September 2010 to February 2011, cumulating 1300 days of flight.

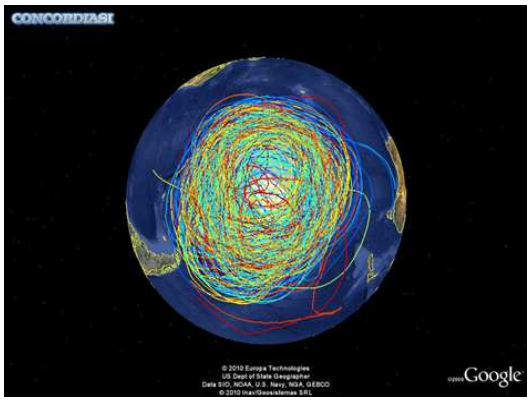

Figure 2. Trajectories of the 19 Concordiasi super pressure balloons from September 2010 to January 2011

Preceding this campaign, during the pre-Concordiasi campaign, 3 SPB were also launched from Seychelles Islands in the Indian Ocean and flew quite along the equator from February to May 2010, see Fig. 3.

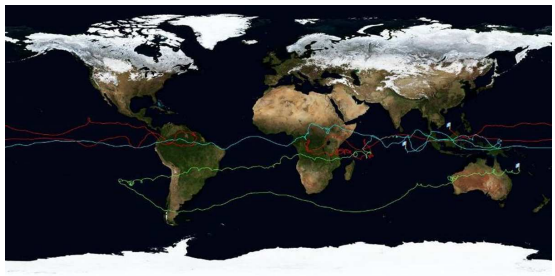

Figure 3. Trajectories of 3 SPB, pre-Concordiasi 2010

The analysis of the achieved in situ measurements allows e.g. an unprecedented investigation of the whole gravity wave range up to the highest frequency waves, see [5] and [6], as well as the identification of deficiencies in state-of-the-art weather analysis and forecasts near the equator (see [7]).

2. STRATEOLE-2 PROGRAM

2.1. Concept and Science

Strateole-2 is built on a heritage from the previous CNES long-duration balloon projects, Vorcore, AMMA and Concordiasi. This international project led by CNES and LMD involves several research groups in France, USA and Italy.

The objectives of Strateole-2 (see [8]) are to explore dynamical and physical processes that control the transport of trace gases and momentum between the equatorial Upper Troposphere and Lower Stratosphere (UTLS). The balloon campaigns will provide fine scale measurements of water vapour, temperature and aerosol/ice at the balloon flight level as well as within a couple of kilometers below it, thus documenting air composition and investigating the formation of cirrus in the upper Tropical Tropopause Layer (TTL). The balloons themselves provide unique measurements of the whole spectrum of equatorial waves from high-frequency buoyancy waves to planetary-scale equatorial waves, providing information needed to improve their representation in climate models. The balloons will sample the whole equatorial band from 20°S to 15°N, thus complementing in an original way the widespread (but limited resolution) space borne observations and the high-resolution (but geographically restricted) airborne and ground-based measurements.

Other Strateole-2 science objectives include contributions to operational meteorology and satellite validation.
Wind analyses and forecasts have notably large errors in the tropics associated with the lack of balance between tropical winds and temperatures and sparse wind measurements (e.g. [7]). Strateole-2 balloon flights will provide unprecedented, accurate wind observations in the equatorial UTLS, in particular over oceanic areas that are otherwise devoid of any wind measurements.

These meteorological measurements will be disseminated in real time for operational use by all operational centers and for research aimed at reducing tropical analysis errors in future forecast systems.
They will furthermore contribute to the validation of ADM-Aeolus wind products. ADM-Aeolus, due to be launched by late 2017, is an innovative ESA mission, designed to perform the first space borne wind lidar measurements providing unprecedented global coverage.

2.2. Instruments and flight configurations

The Strateole-2 instrumentation includes in situ measurements of pressure, temperature and winds every 30s, ozone, aerosols, water vapour and carbon dioxide, plus remotely sensed cloud structure with a microlidar and directional radiative fluxes (see Fig. 4). Instruments providing profiles will include GPS radio-occultation temperatures, and novel reel-down devices suspended as far as two kilometers below the balloon which are designed to explore the fine-scale distribution of temperature, aerosol/ice and humidity.

Instrument	Institution	Purpose	Measurement type	Altitudes	Raw measurement quantities	Geophysical quantities
GPS (Euros)	CNES	Wind (through position)	in-situ	flight level	every 30 s	3D positions, horizontal winds
TSEN	LMD	Air Pressure and Temperature	in-situ	flight level	every 30 s every 1 s	temperature pressure
RACHuTS	LASP (USA)	Local Profiler Air Temp., Water Vap., Cloud Detection	in-situ	flight level down to 2 km below	3/4 profiles per night	temperature, H2O mixing ratio, Cloud detection
FLOATS	LASP (USA)	Local Profiler : Air Temperature	in-situ	flight level down to 2 km below	2 profile every 5-10 min	temperature
BOL-DAIR	LATMOS	Up-Welling Infrared Flux	in-situ	flight level	every 1 min	total upwelling flux, total long wave flux
SAWfPHY	LMD	Water Vapor (through dew-point)	in-situ	flight level	every 10-15 min	H2O mixing ratio
Pico-SDLA	GSMA	Water Vapor and Carbon Dioxide (through light absorption)	in-situ	flight level		H2O & CO2 mixing ratios
B-Bop	LMD	Ozone Photometer	in-situ	flight level	every 10-15 min	O3 mixing ratio
LPC	LASP (USA)	LASP Particle Counter	in-situ	flight level	every 8 min	size resolved (8 bins) aerosol number concentration
LOAC	LPC2E	Optical Particle Counter	in-situ	flight level		size resolved particle #
BeCOOL	LATMOS & CNR (Italy)	Nadir Cloud détection trough Long Distance Lidar	remote (nadir)	flight level down to ~5 km below	1 profile every 5-10 min	attenuated backscatter
ROC	Scripps I. O. (USA)	Atmospheric Sounding through GPS Radio-Occultation High accuracy position through GPS	remote (limb)	flight level down to z~4 km	tens of profiles per day	high-precision 3D positions temperature

Figure 4. List of Strateole-2 instrumentation

Ten super pressure balloons will fly near 20 km altitude, just above the TTL, and ten others near 18 km altitude, within the TTL. Each balloon will carry up to four instruments.

For the lower level at the tropical tropopause (air density of 125 g/m^3), three different combinations of in-situ sensors will fly onboard a 11-m diameter balloon. Fig. 5a describes these combinations. Except for the GPS and TSEN instruments, which are hosted inside the CNES housekeeping gondola named EUROS, all the instruments lay in the scientific gondola named ZEPHYR.

For the upper level in the lowermost stratosphere (air density of 95 g/m^3), there are two flight configurations, see Fig. 5b. The one called STRAT2 only uses GPS and TSEN through EUROS and will fly with a 11-m diameter balloon. The other ones fly with a 13-m diameter balloon.

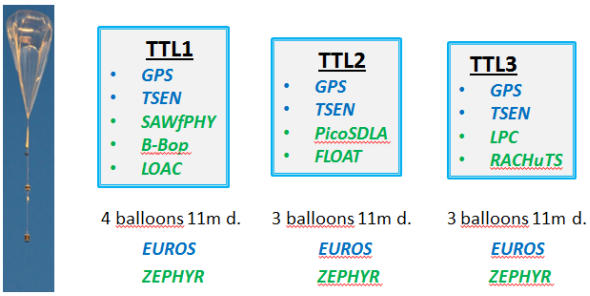

Figure 5a. 10 flights in the tropical tropopause

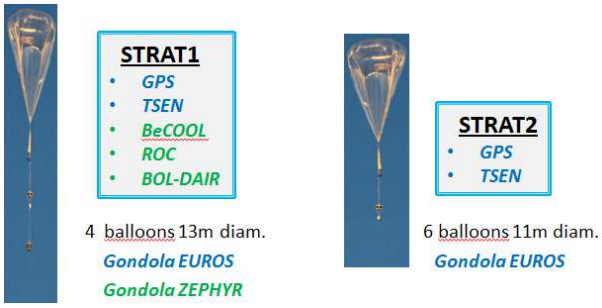

Figure 5b. 10 flights in the lowermost stratosphere

2.3. STRATEOLE-2 campaigns

The SPB will be launched from Seychelles Islands in the Indian Ocean.

The Strateole-2 research program will begin with a five balloons technology validation campaign in boreal fall-winter 2018-2019, followed by 20 balloon flights in boreal fall-winter 2020-2021. A final 20 balloons campaign in 2023-2024 will drift in the opposite direction due to the shifting phase of the Quasi-Biennal Oscillation (QBO), a dominant periodic east-west oscillating feature in tropical lower stratospheric winds.

3. SPB UPGRADES FOR STRATEOLE-2 PROGRAM

3.1. Upgrades needed

SPB upgrade is required after Concordiasi (2010):

- to meet higher safety standard,
- to correct anomalies,
- to reduce the weight of the suspended assembly,
- to simplify flight-control / payload development and operations.

For this upgrade, we benefit from systems recently developed for other types of balloons or flight systems, such as the large zero pressure balloons (ZPB) on-board software, or the software library of the Flight Control Center for fine axis pointing gondolas.

The new SPB system has to meet more strictly enforced safety standards, since it is considered as potentially lethal for ground population. This means that it shall fully meets the criteria that no single point failure might lead to potentially catastrophic event and the compliance with that criteria shall be extensively documented.
Mainly, the on-board software is developed with “safety critical validation rules”, and will be common to all CNES Stratospheric balloons. A secondary flight control command line (instead of a timer and Argos downlink) is implemented through a dedicated telecom link, using Inmarsat SBD for Strateole-2. Also the flight Control Center is redeveloped, meeting the above failure tolerance criteria and using Iridium RUDICS service as the nominal communication link.

Lessons learned from Concordiasi showed that several electronic components (RAM…) are sensitive to the atmospheric radiation environment, causing many transitory or permanent interruptions of the control boards for power or payload management (once per week…). The new design implements more radiation resistant electronic components, software protection for vital data, and equipment design will be validated in radiation chambers.

On several Concordiasi flights we also experienced loss of solar power slightly before the specified 3-month duration. New more enduring (UV) solar panels, and with a better power/weight ratio are under qualification process. These solar panels will be used both for EUROS and ZEPHYR, with different number of cells because of the different power need, together with the new energy management system.

Special care is given to minimizing the mass with an overall suspended weight target of 42 kg instead of 50 kg for Concordiasi while allowing +25% to the scientific instruments, i.e. a 10 kg mass allocation instead of 8 kg.

For Strateole-2, see Fig. 6, it has been decided to fully segregate :
- the CNES Flight Control System (as a sort of stratospheric carrier) composed of :
  - the EUROS gondola,
  - two Control Centers located in Toulouse and in Aire-sur-l’Adour, France,
  - CNES operational staff,
- from the Science Payload System composed of :
  - the ZEPHYR gondola,
  - the ZEPHYR Mission Control Center in Paris,
  - Science laboratories operational staff.

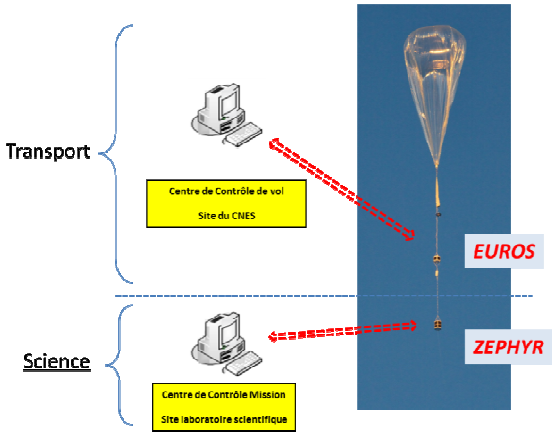

Figure 6. Flight Control System vs. Payload Control System

This allows a parallel development of both segments. In particular, safety issues are solved once for ever on the CNES Flight Control System which does not depend on the potentially evolving scientific payloads. Procurement, assembly, tests are also conducted without impact from one system on the other one, except common procurements such as solar panels, energy management systems or batteries.

The Flight Control System is developed by CNES and the ZEPHYR Payload System is developed by the scientific team composed of LMD, LATMOS, DT-INSU and IPSL. Both systems are aimed to be used for future SPB or ZPB missions.

3.2. Development status and overall schedule

Concerning the CNES Flight Control System, a Critical Design Review (CDR) has been conducted in March 2017. It is currently under qualification phase.
Assembly, integration and test of 7 flight models (for 5 flights) will take place the first semester of 2018.

The CDR of the Zephyr Payload Control System and of the Strateole-2 project has been conducted in May 2017. The steering board held mid-July has authorized the start of the qualification phase.
The Payload platform will be qualified first quarter of 2018, and instruments will be available also first quarter of 2018. Assembly, integration and test of the 4 payload configurations will take place second quarter of 2018. The Mission Control Center will be validated in July 2018.

4. REFERENCES

1. A. Hertzog, Ph. Cocquerez et al. (2007). Stratéole/Vorcore - Long-duration, Superpressure Balloons to Study the Antarctic Lower Stratosphere during the 2005 Winter, *Journal of Atmospheric and Oceanic Technology*, 24, p. 2048-2061.

2. Ph. Drobinski et al. (20013). Driftsonde Observations to Evaluate Numerical Weather Prediction of the Late 2006 African Monsoon, *Journal of Applied Meteorology and Climatology*.

3. F. Rabier et al. (2012). The Concordiasi field experiment over Antarctica: First results from innovative atmospheric measurements, *Bulletin of the American Meteorological Society*, doi: 10.1175/BAMS-D-12-00005.1

4. S. A. Cohn et al. (2013). Driftsondes : Providing In-Situ Long-Duration Dropsonde Observations Over Remote Regions, *Bulletin of the American Meteorological Society*, BAMS-D-12-00075.

5. V. Jewtoukoff et al. (2013). Gravity waves generated by deep tropical convection: estimates from balloon observations and mesoscale simulations, *Journal of Geophysical Research, 118, 9690-9707,* DOI: 10.1002/jgrd.50781, 2013.

6. V. Jewtoukoff et al. (2015). Comparison of Gravity Waves in the Southern Hemisphere Derived from Balloon Observations and the ECMWF Analyses, *Journal of the American Meteorological Society*, DOI: 10.1175/JAS-D-14-0324.1

7. A. Podglajen et al. (2014). Assessment of the accuracy of (re)analyses in the equatorial lower stratosphere, *J. Geophys. Res. Atmos.*, 119, 11,166-11,188, DOI: 10.1002/2014JD021849.

8. Jennifer S. Haase, (submitted 2017). Stratéole-2 - Around the world in 84 days, *EOS*

SWEDISH SPACE ACTIVITIES – GENRAL OVERVIEW WITH A FOCUS ON BALLOONS AND ROCKETS

Kristine Dannenberg

Swedish National Space Board, Box 4006, SE-171 04 Solna, Sweden, Email: dannenberg@snsb.se

ABSTRACT

The paper gives a brief overview of Swedish space activities with a focus on balloon and rocket projects, launched from Esrange Space Center. This includes projects within the Swedish national balloon and rocket programme and/or within international collaboration. Several on-going national balloon and rocket projects are described in brief. Sweden is also a major player in sounding rocket activities within the ELIPS programme of the European Space Agency (ESA) and the new programme E3P (European Exploration Envelope Programme), as provider of launch services and developer of modules for microgravity experiments. Another important activity, described below, is the student programme REXUS/BEXUS, carried out within the framework of a bilateral agreement between DLR and SNSB, in collaboration with ESA. It should also be noted that several other balloons and rockets have been launched from Esrange Space Center during the reporting period. The present paper focuses, however, on the projects led by Swedish Principal Investigators and activities with a major involvement of Swedish scientists and engineers.

1. INTRODUCTION

Swedish space research comprises many different fields, such as astronomy, space physics, astrobiology, Earth observation, atmospheric research, space physiology, space radiation and microgravity research. The major part of Swedish space research activities is supported by SNSB (Swedish National Space Board), within its national programme for space research and Earth observation. The annual budget available for space research and related activities is around 20 M€, which also includes Swedish national balloon and rocket programme as well as the new national initiative for development of small low-cost innovative research satellites. Along with the participation in Swedish national programmes, many Swedish researchers utilise flights offered by ESA programmes and/or data provided by ESA satellites and other international space missions.

In 2012, a dedicated national programme for balloon and rocket projects was established by SNSB in order to allow Swedish scientists to utilise balloon and rocket flights from Esrange on regular basis. National activities within this field are of strategic importance as they provide unique opportunity of combining basic science with instrument development as well as possibility to use a dedicated platform for the experiment. In addition, the smaller scale of the balloon and rocket projects allows close cooperation between the research groups, technicians and Swedish industry. Another advantage is the fact that the time-frame from the start of the project to publishing the results is relatively short, which is especially attractive for young researchers and PhD students.

The establishment of the national balloon and rocket programme allows issuing regular calls for balloon and rocket projects. Swedish national balloon and rocket programme programme is also open for projects carried out in international collaboration.

The balloons and rockets are launched from Esrange Space Center, a unique Swedish and European facility, situated above the polar circle 40 km East of Kiruna at lat. 67° 53'N, long. 21° 04'E, with a rocket impact area of 5600 km^2. Landing sites for short duration balloons include northern Scandinavia whereas long duration balloons usually land in northwest Canada. The flight to Canada usually takes 5-6 days and allows to perform experiments that require longer observation time, e.g. within astrophysics. Such a flight was performed for the Swedish experiment PoGO+ that was successfully flown from Esrange to the Victoria Island (Canada) in July 2016. The PoGO+ flight is described in more detail in the following chapter.

2. SWEDISH EXPERIMENTS ON BALLOONS AND ROCKETS

Currently, several balloon and rocket research projects within various research fields are ongoing within the national balloon and rocket programme. Most of the projects are in the data analysis phase. In the beginning of 2017 several proposals for new balloon and rocket projects were received in response to a new call issued by SNSB, and are under evaluation.

A major Swedish balloon project is the astrophysics experiment PoGO+ (Polarized Gamma-ray Observer) for measurements of the polarisation of gamma-rays from extreme astrophysical objects, such as the Crab Nebula. The project is led by Mark Pearce, KTH (Royal Institute of Technology), in cooperation with international scientists. PoGO+ is an upgrade of the previously flown experiment PoGOLite.

Figure 1. The PoGO+ team at Esrange in June 2016. (photo Kristine Dannenberg)

The PoGO+ payload, with a mass of around 2 tons, carried by a one million m^3 large balloon, was launched from Esrange in July 2016. During the flight, PoGO+ followed the winds and passed Sweden, Norway, and Greenland, landing on the Victoria Island in Canada, after six days of successful flight.

Figure 2. PoGOLite has safely landed in Canada (photo courtesy of SSC)

The flight was a great success both technically and scientifically. The analysis of the scientific results is ongoing and the first results have recently been published in the Scientific Reports by Nature, see http://www.nature.com/articles/s41598-017-07390-7.

A movie about the flight of PoGO+ has been published on youtube, https://www.youtube.com/watch?v=esIdQqWbA5M

Another balloon project, ongoing within the Swedish national programme, is In-situ IWC (In-situ Ice Water Content), led by Thomas Kuhn from Luleå Tehnical University. This project deals with ice clouds and studies of ice water content. The aim of the project is to improve remote sensing measurements of ice clouds and to refine parameterizations of cloud ice to be used in radiative transfer models. Several balloon launches have taken place already and more are foreseen in near future in order to perform ice cloud studies at different atmospheric conditions. The volume of the balloons carrying experiments is 500 m^3, enabling several launches during each campaign.

At the moment three rocket projects are ongoing within the national balloon and rockets programme with launches executed in autumn 2015 and beginning of 2016.

The O-States (Oxygen Species and Thermospheric Airglow in The Earth's Sky) rocket project is led by Jörg Gumbel from Stockholm University and deals with the studies of the lower thermosphere using O_2 atmospheric band emissions. The scientific objective of the O-States experiment is to provide information about atomic oxygen and temperature at altitudes 100-250 km by means of dayglow emission spectra of O_2. Two rocket launches at different atmospheric conditions were executed in October 2015 with the same payload that was refurbished at Esrange during less than one week.

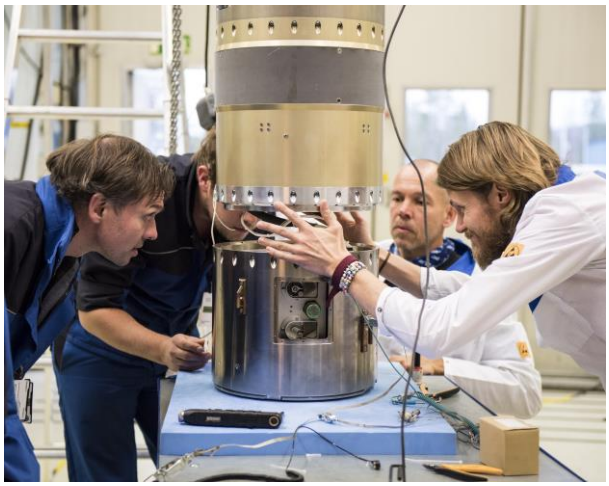

Figure 3. The SSC and DLR Moraba teams integrating the O-States payload (photo Kristine Dannenberg)

Another rocket project, SPIDER (Small Payloads for Investigation of Disturbances in Electrojet by Rockets), deals with the study of turbulence in the auroral electro-jets. PI of the SPIDER project is Nickolay Ivchenko from KTH (Royal Institute of Technology). During the flight of SPIDER, several autonomous free-flying payloads were released, based on the technology studied and developed within several REXUS student projects at KTH, being an excellent illustration of synergies between student projects and projects carried out by senior scientists. The launch of the SPIDER rocket took place in early February 2016. Another rocket project LEEWAVES shared the same rocket and studied atmospheric gravitational waves. The LEEWAVES project is carried out by Jörg Gumbel (SU) and Nickolay Ivchenko (KTH).

3. THE REXUS/BEXUS STUDENT PROGRAMME

SNSB takes an active part in the student rocket and balloon programme REXUS/BEXUS (Rocket and Balloon Experiments for University Students). The programme is a joint undertaking of DLR (German Aerospace Center) and SNSB in collaboration with ESA. Two REXUS rockets and two BEXUS balloons are launched from Esrange every year.

This year the programme celebrated its 10 years anniversary. During this period around 1200 students have participated in the activities, 36 REXUS rockets and BEXUS balloons have been launched from Esrange carrying 130 experiments, from various European universities.

Figure 4. Launch of BEXUS-21 in October 2015 (photo Kristine Dannenberg).

Responses to the regular questionnaire, distributed by to the programme participants, show that most of the students are highly satisfied with their participation in the REXUS/BEXUS programme. In many cases, the programme has also been an important stepping-stone to a professional career in the space field.

An annual REXUS/BEXUS call for proposals is being issued each summer offering an opportunity to carry out European student experiments on real rockets and balloons. The call is open to students from ESA member states and cooperating states. During each cycle of the programme student teams undergo similar steps as in real space projects, from the experiment proposal and preliminary design review to flight acceptance review.

The duration of the BEXUS balloon flights is 2-3 hours at 26-30 km altitude. The REXUS rockets reach altitudes of around 90 km.

Figure 5. The members of the Swedish SCRAP team examine their module after landing of REXUS in spring 2015 (photo Kristine Dannenberg)

The recent call was opened in June with a deadline in mid-October, and similarly to previous years, the proposals will be evaluated by experts during autumn and the selection of the new student teams will be finalised in December.

4. PARTICIPATION TO THE ESA ELIPS and E3P PROGRAMMES

Besides national activities, Sweden contributes to many ESA programmes. The ELIPS programme, for Life and Physical Sciences experiments in Space, has been one of the major optional programmes with Swedish participation, and Swedish industrial activities are mainly focused on MASER and MAXUS sounding rockets. Currently, sounding rocket activities are part of the new ESA programme E3P, European Exploration Envelope Programme.

The most recent rocket launches within the ELIPS-4 programme , MASER-13 and MAXUS-9, took place, in December 2015 and April 2017 respectively.

Figure 6. Per Baldemar, ground safety manager of SSC, with Olle Norberg, Director General of SNSB, and David Parker, ESA Director of Human Spaceflight and Robotic Exploration during a visit to Esrange in September 2016
(photo Kristine Dannenberg)

The rockets carried several experiment modules for microgravity research, involving X-ray modules XRMON-SOL and XRMON-Diff2, developed by SSC.

In addition to MAXUS and MASER, a number of other sounding rockets such as TEXUS rockets are also being launched from Esrange, within the framework of German national sounding rocket programme and/or in cooperation with ESA and other space agencies.

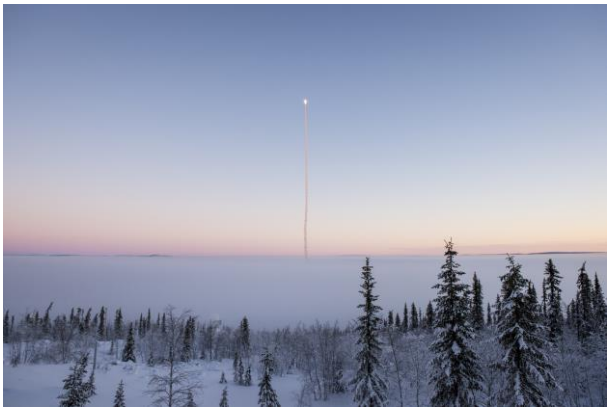

Figure 7. The launch of Texus-53 in February 2016
(photo Kristine Dannenberg)

DESIGN AND 2016 FLIGHT PERFORMANCE OF "POGO+" – A BALLOON-BORNE HARD X-RAY POLARIMETER

M. Kiss, on behalf of the PoGO Collaboration

KTH Royal Institute of Technology, Department of Physics, 106 91, Stockholm, Sweden. E-mail: mozsi@kth.se

ABSTRACT

In 2016, during a one-week balloon flight from the Esrange Space Center, Sweden, to Victoria Island, Canada, the polarization of hard X-rays ($\sim$20$-$180 keV) from the Crab system and Cygnus X-1 was successfully measured using the "PoGO+" polarimeter. The main constituents of the payload are presented here, along with a description of the observation strategies employed and the resulting pointing performance.

Key words: instrumentation – polarimeter; energy – hard X-rays; targets – Crab, Cygnus X-1; techniques – Compton polarimetry; scientific ballooning – structural design, attitude control.

1. INTRODUCTION

PoGO+ is a balloon-borne telescope for measuring the polarization of hard X-rays from the Crab system (pulsar and nebula) and Cygnus X-1 (an X-ray binary system). Polarimetry can provide information about the observed targets not obtainable through spectral and temporal studies, e.g. locations of emission, relations between geometries, magnetic fields, etc. The energy range of the instrument is approximately[1] 20$-$180 keV. PoGO+ is an upgraded version of the PoGOLite "Pathfinder" [1], which conducted a near-circumpolar two-week maiden flight from the Esrange Space Center, Sweden, in 2013. Despite a hardware failure, which allowed only three days of scientific operations, a statistics-constrained measurement of the polarization of X-rays from the Crab system was reported [2]. Experience from this flight allowed the development of the upgraded "PoGO+" instrument, with a significant improvement in polarimetric sensitivity due to numerous detector optimizations [3].

The two-tonne PoGO+ payload was launched from the Esrange Space Center at 03:17 UT on July 12th 2016 and was terminated as foreseen over Victoria Island, Canada, at 22:26 UT on July 18th. Both the Crab and Cygnus X-1 were successfully observed during each visibility and flight altitudes exceeding 40 km were achieved. Polarimetric results for the Crab system have already been reported [4] and Cygnus X-1 results will follow shortly.

Here, the performance of the instrument and the pointing system is presented. Observation strategies used for the two relevant targets are also described.

[1] As the energy range is defined relative to the detected flux, there is a moderate dependence on the spectrum of the observed source.

2. THE POGO+ POLARIMETER

Fig. 1 illustrates the design of the PoGO+ polarimeter. In the front part of the detector, copper collimators limit the field-of-view to $\sim 2^\circ$. The collimated photon flux from a source impinges on an array of 61 plastic scintillators arranged in a compact honeycomb structure. This detector array sits in the bottom of an anticoincidence well made of BGO scintillators, which shields the active volume from charged particles and photons hitting the instrument from the side or from the bottom. The wall of this shield is segmented into 30 pieces, allowing anisotropies in the background flux to be characterized. Polyethylene covers the sides and the bottom of the polarimeter, strongly reducing the background caused by atmospheric neutrons. Two LiCAF-based neutron detectors are mounted on opposing sides of the detector array, allow this background component to be monitored in-flight. The $61 + 30 + 2$ detector elements are read out by identical Hamamatsu R7899 photomultiplier tubes, coupled to a set of front-end electronics boards which sample and digitize the detector signals. To mitigate systematic effects from intrinsic differences between detector elements, the entire detector array is rotated around the field-of-view at a rate of $1^\circ/\mathrm{s}$. The full assembly weighs $\sim$600 kg. A detailed description of the polarimeter and its constituents is provided in [1].

Events comprising hits in two separate plastic scintillators are used to reconstruct the azimuthal scattering angles of interacting photons. The characteristics of the scattering angle distribution allows the polarization of the source flux to be determined. This provides two observational parameters complimenting spectral and temporal information, namely the polarization fraction and the polarization angle. The measurement of polarization is positive-definite, thus, to unambiguously

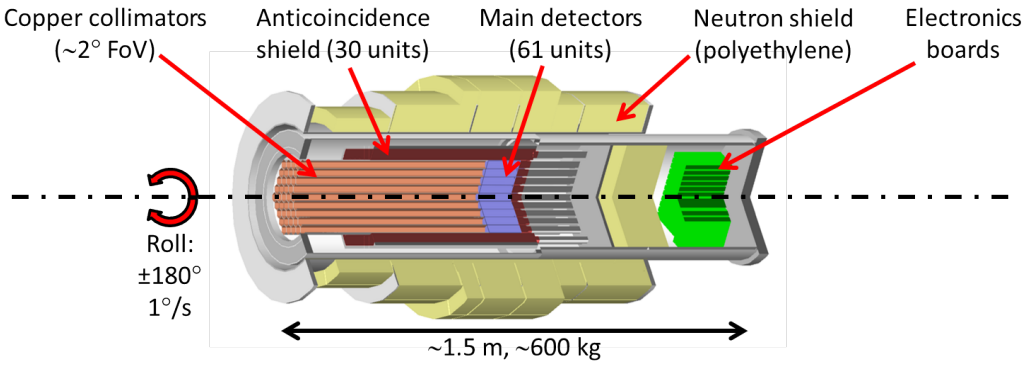

Figure 1. Sketch showing the design of the PoGO+ polarimeter.

demonstrate that a polarization measurement is intrinsic to the measured source flux and not resulting from the detector array itself, the instrument has been extensively tested and characterized, with both polarized and unpolarized sources. The modulation[2] for an unpolarized flux of 59.5 keV photons irradiating the detector array is thus found to be $(0.10 \pm 0.12)\%$, while the response for a $\sim$100% polarized flux at 53.3 keV is $(37.83 \pm 0.73)\%$ [5].

3. GIMBAL UNIT AND ATTITUDE CONTROL

In order to avoid performance degradation due to detector shadowing, the in-flight pointing must be kept on-target to within 0.1°. This is achieved using a custom attitude control solution, developed by DST Control [6], Sweden, which consists of a mechanical structure and an array of attitude sensors. The structure, called the gimbal unit assembly, is shown in Fig. 2.

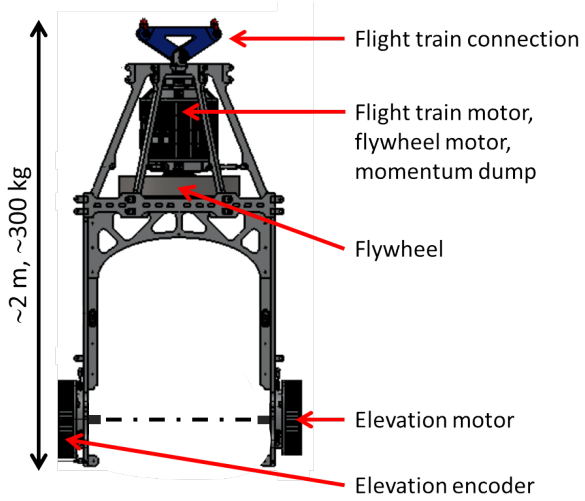

Figure 2. Sketch showing the gimbal unit assembly.

[2]A measure of anisotropy in the reconstructed scattering angle distribution from the detector.

Coarse pointing in azimuth is achieved using a flight-train motor which acts directly on the connection to the balloon rigging. A flywheel provides fine-pointing in azimuth and allows cable friction and torsion to be counteracted. In case the flywheel becomes saturated, momentum can be dumped to the balloon through the flight train connection. Digital direct drive torque motors[3] are used throughout, providing excellent heat dissipation and electromagnetic compatibility. The gimbal unit assembly including the motors and controllers are free from ITAR restrictions and the total weight is $\sim$300 kg. A detailed description of the attitude control system and gimbal configuration is presented in [7].

The attitude information is provided by the following set of sensors and equipment:

Differential GPS: Two GPS antennas separated by a $\sim$10 m baseline and a Trimble receiver provide a pointing precision of approximately 0.1° even in the absence of additional attitude information.

Magnetometer: A three-axis magnetometer provides a precision on the order of 1° in case the GPS fails.

Optical star tracker camera: An off-the-shelf CCD and custom-made lens system with thermal design mitigating the need for refocusing. The star tracker is mounted co-axially with the polarimeter and can identify optical guide stars of magnitude $\sim$4–5 in daytime conditions at float altitude. Its field-of-view is $5.0° \times 3.7°$ and the assembly weighs about 5 kg, with a length of 1 m, including the baffle.

Sun tracker: A small, free-moving gimbal assembly housing a position-sensitive device which tracks the direction to the sun. The gimbal spins around its axis to locate the sun, then locks the sun in the center of its field of view and feeds its orientation relative to the mechanical structure, thus providing azimuth information for the pointing.

[3]Motors act directly on the corresponding axles, without the use of gearboxes, and the power amplifier and servo controller are integrated with the armature windings.

Inclinometer: An inclinometer is mounted on the main gimbal structure and provides pitch and roll information, allowing e.g. pendulum swings of the payload under the balloon to be accounted for.

Inertial measurement unit: A micro-mechanical inertial measurement system provides redundancy for the attitude information. While other attitude sensors are available, the system is continuously corrected for drift. If other systems are temporarily unavailable, the inertial measurement system can retain attitude information for some time, until normal operations can be restored.

Signals from the various attitude sensors are processed by an attitude control unit. After a user-based selection of operation mode, e.g. azimuth/elevation pointing, zero-velocity, etc., the system feeds velocity set-points for the various motors, allowing the requested pointing solution to be maintained and targets tracked on the sky.

4. GONDOLA STRUCTURES AND SYSTEMS

The gondola, developed by SSC Esrange, is a dome-like structure hanging off the gimbal unit assembly. It houses ancillary hardware such as batteries and communications equipment, provides thermal and mechanical protection for the polarimeter, and also supports the solar panels. The structure uses light-weight materials, such as honeycomb composite panels, aluminum rib-structures and glass-fiber booms. In order to simplify post-flight recovery, the gondola is designed to be separated into an upper and a lower part. The upper part holds the gimbal unit assembly, including the polarimeter, while the lower part houses the batteries and other electronics. Including all equipment and auxiliary electronics, the total weight is about 950 kg, and the "wing-span" of the solar panel arrays is $\sim$10 m. An additional 450 kg of ballast is carried during the flight, resulting in a total payload launch weight of just below two tonnes. Fig. 3 shows an illustration of the gondola, with the gimbal unit assembly and polarimeter held inside.

5. OBSERVATION STRATEGIES

Different observation strategies are employed for the two main targets, the Crab and Cygnus X-1. When pointing at large angular separation from the sun, such as during Cygnus observations, the star tracker camera can be used, which has been extensively tested and successfully used during the flight of the PoGOLite Pathfinder. Based on the known offset of the relevant guide star from the target of interest, propagated as a function of time during the observation, the star tracker provides automatic tracking in both azimuth and elevation. For Crab observations, due to the relatively close proximity to the sun, the sun tracker is used instead. In this configuration, the azimuthal pointing is obtained from the known offset between the sun and the Crab, while the elevation is derived from an angular encoder on the polarimeter elevation axle. In this mode, the star tracker camera is only used for monitoring. The sun tracker was added for the 2016 flight of PoGO+ and thus did not have the same flight heritage, but nevertheless performed flawlessly throughtout the flight.

As X-ray polarimetry relies on reconstructing an angular modulation in detector count rates, anisotropies from the background environments themselves, caused e.g. by albedo neutrons, must be well characterized and treated properly. In order to track temporal evolution of measurement backgrounds, source observations are thus interspersed with pointings to background fields, separated by 5° in the horizontal plane. Transition occurs automatically approximately every 15 minutes, alternating between the East and West directions. Equal amount of time is thus spent observing the source and the background fields, which is a necessity to prevent the background subtraction from deteriorating the statistical precision of the polarimetric results.

6. IN-FLIGHT PERFORMANCE

The described observation strategies worked very well throughout the flight, allowing the two targets to be observed successfully at each opportunity. In total, about 25 hours of on-source data was recorded for the Crab and 34 hours for Cygnus, which rises higher in the sky, with approximately equal time spent also on the corresponding background fields of each target.

The pointing error/offset can be determined from the sampled angular separation between the expected position of the optical guide star and its actual recorded position[4]. The offset in both the horizontal (azimuth) and vertical (elevation) direction follow Gaussian distributions, while the resulting total angular offset[5] follows a Rayleigh distribution, as expected. The peak of this Rayleigh distribution is at $\sim$0.05° and at $\sim$0.02° for the Crab observation and Cygnus X-1 observation, respectively, i.e. well within the 0.1° design requirement.

The alignment of the polarimeter axis and the reconstructed pointing direction (as derived from the optical guide star) is confirmed through an observed increase in event count-rate when pointing on-source as opposed to off-source. In this case, an excess of about 1 Hz is observed for the Crab, in agreement with expectations from simulations conducted prior to the flight [5]. For the Crab measurements, which feature a periodic emission component resulting from the spin of the Crab pulsar, an in-

[4]When tracking using the star tracker, this offset is produced automatically. The same information is stored also while using the sun tracker, although in this case, the data is used only for monitoring, not for attitude feedback and control.

[5]Obtained by taking the square root of horizontal (azimuth) offset and vertical (elevation) offset added in quadrature.

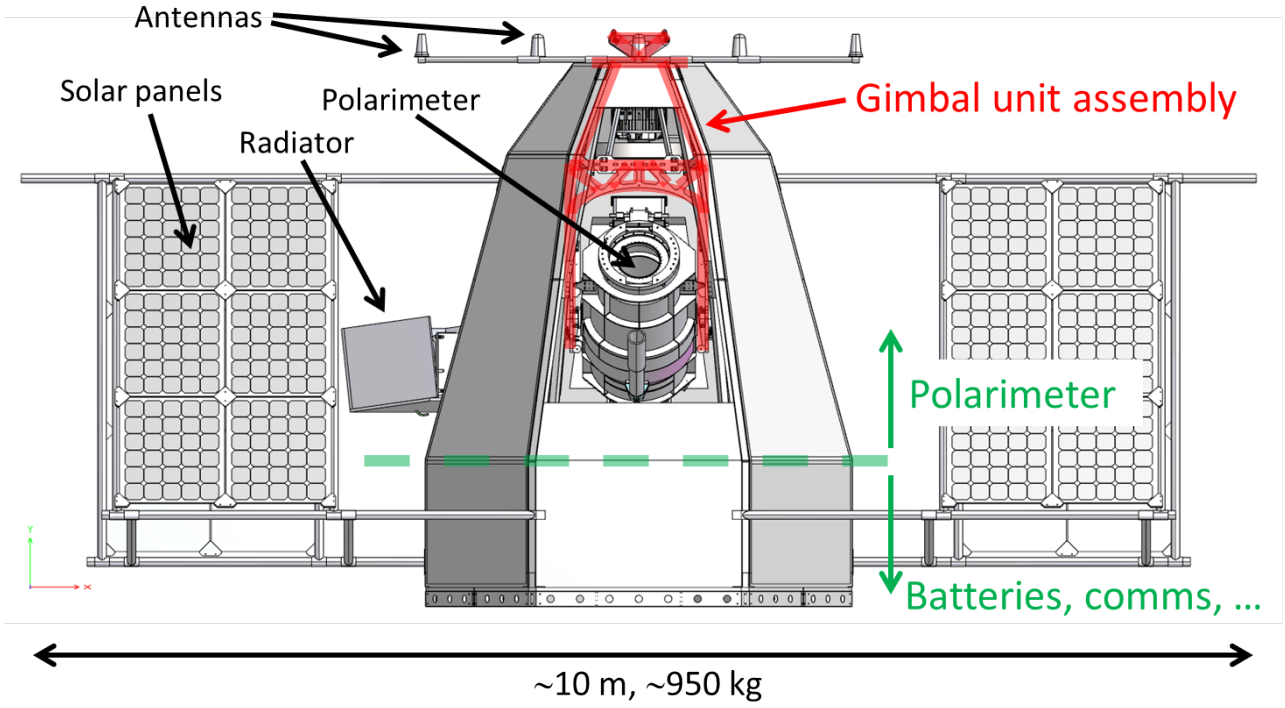

Figure 3. Sketch showing the PoGO+ gondola. The structure can be separated at the seam indicated in green, facilitating the post-flight recovery. Ballast and crash-pads mounted underneath the gondola are not shown.

dependent confirmation is additionally provided by the reconstructed light-curve. This curve, folded by the pulsation period of approximately 33 ms, is shown in Fig. 4 and can only arise from photons emitted from the Crab system interacting in the detector array. These photons can be used for polarimetry, producing the results as reported in [4].

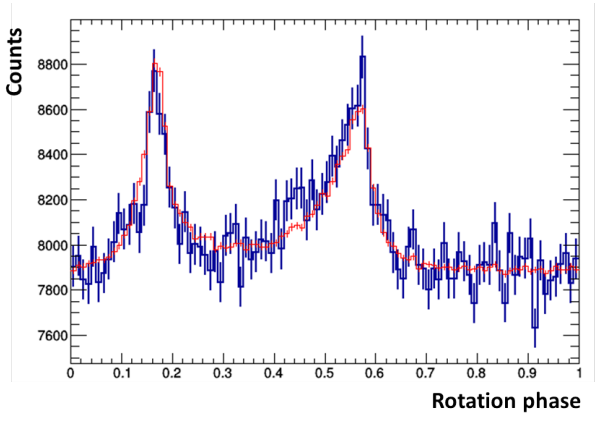

Figure 4. Crab light-curve as observed by the PoGO+ instrument during the 2016 flight (blue) and a reference light-curve derived from publicly available X-ray data recorded with the Suzaku satellite (red). The abscissa corresponds to time, folded by the pulsar spin period.

ACKNOWLEDGMENTS

This research was supported in Sweden by The Swedish National Space Board, The Knut and Alice Wallenberg Foundation, and The Swedish Research Council. In Japan, support was provided by Japan Society for Promotion of Science and ISAS/JAXA. SSC are thanked for providing expert mission support and launch services at the Esrange Space Centre. DST Control developed the PoGO+ attitude control system under the leadership of J.-E. Strömberg. Contributions from past Collaboration members and students are acknowledged. In particular, we thank M. Kole, E. Moretti, G. Olofsson and S. Rydström for their important contributions to the PoGOLite Pathfinder mission from which PoGO+ was developed.

REFERENCES

[1] Chauvin, M., et al. (2016) *Exp. Astron.* **41**, 17.

[2] Chauvin, M., et al. (2016) *MNRAS Lett.* **456**, L84.

[3] Chauvin, M., et al. (2016) *Astropart. Phys.* **82**, 99:

[4] Chauvin, M., et al. (2017) *Sci. Rep.* **7**, 7816.

[5] Chauvin, M., et al. (2017) *Nuc. Inst. Met. A* **859**, 125.

[6] DST Control, Åkerbog. 10, SE-582 54 Linköping.

[7] Strömberg, J.-E., 2011, Proc. 20th ESA Symposium on European Rocket & Balloon Programmes.

PERSEUS

EUROPEAN SPACE RESEARCH PROGRAM FOR STUDENTS

Jean Oswald, Anne Galeon, Hélène Hingre, Rémi Delpy, Aymeric Legrand, Sylvain Pernon

CNES Launcher Directorate, 52 rue Jacques Hillairet, 75612 Paris Cedex, France : jean.oswald@cnes.fr,
CNES Launcher Directorate, 52 rue Jacques Hillairet, 75612 Paris Cedex, France : anne.galeon@cnes.fr
MI-GSO, 110 – 114 rue Jules Guesde 92300 Levallois-Perret, France : hhingre@mi-gso.com
GAREF, 6 Rue Emile Levassor 75013 PARIS, France : perseus.etudes@garef.com
GAREF, 6 Rue Emile Levassor 75013 PARIS, France : perseus.aetna@garef.com
Université Rennes 1, 2 rue de Thabor 3506 Rennes, France : sylvain_pernon@yahoo.fr

ABSTRACT

PERSEUS is a french acronyme for “Projet Etudiant de Recherche Spatiale Européen Universitaire et Scientifique”. The PERSEUS project provides the opportunity for motivated students to pool their knowledge to the development of Nano Satellite Launcher. Their applicative work refers to a subscale of a Nano Satellite Launcher which corresponds to a more or less powerful experimental rocket. They can work either through the classical pedagogic frame proposed by their university, either in a space association or as researchers in a laboratory. The CNES (French Space Agency) with the help of partners (AJSEP, ArianeGroup, Bertin Technologies, GAREF, IPSA, ISAE-Supaero, MI-GSO, ONERA, Planètes Sciences, ROXEL, UEVE) is coordinating all these activities in order to achieve a complete life cycle of prototypes: objectives, studies, development realization, reviews, ground or flight test and exploitation.

1. INTRODUCTION

The PERSEUS project was launched 12 years ago [9]&[10]. It was organized on three main objectives. The first one is innovation and testing promising technologies applicable for space launch system. The second is to rely on students to practise the first objective and, at the same time, to keep their motivation for space through their graduation. The third objective is to provide a frame to students which enable them to build a set of ground and flight demonstrators in order to confirm or disprove the technology potential.

The number of students who get involved every year is about 250. They are mainly involved through pedagogic activities and can extend their participation through space association within their university. An integrated team (EPIP) located at Evry University (UEVE) coordinates all the activities.

2. THE PERSEUS NETWORK

Twelve partners have signed this agreement with CNES. Some groups can be identified, Universities (IPSA, ISAE-Supaero and UEVE), space associations of experimented amateurs (GAREF and Planètes Sciences), some small and medium enterprises (Bertin Technologies, MI-GSO, ROXEL), an institution (ONERA) and even an industry, ArianeGroup, through the AJSEP association, has joined the project. Partner’s members within or in association with the integrated team provide an efficient support to the teachers in charge of the students supervision [2]&[6].

An adaption of the management rules used in space industry has been carried out for the student projects. These management rules teach the students that a minimum of documentation is required and reviewed by a group of expert at predefined date. The required documentation must be compliant with the pre-set level of realisation of the demonstrators for this date. The levels range from the objectives, preliminary definition, critical definition qualification, flight up to of course flight data exploitation. This last point which is essential to correctly define the new objectives is unfortunately not deeply analysed by students and has to be finalized by the PERSEUS Team.

The PERSEUS project has a large turnover of students, this was chosen to promote innovation with purpose, but the counterpart is that a lack of knowledge about launch system constraints is obvious. In order to reduce this drawback, the PERSEUS project has developed specific spots:

- Several formations are given to the students, specially about management, organization (MI-GSO) and system loop initiation and electrical integration (GAREF)
- The teachers in university and the lead students in association are invited to transmit their knowledge to the new generation in order to progress on the demonstration realizations rather than starting from zero each year!
- A collaborative portal (hosted by MI-GSO partner) is dedicated to documentation, reference documentations as well as working documents accessible to all the PERSEUS community.
- At last in complement to demonstrator realizations an annual seminar is held at Paris in winter, where all the students are invited to present their own work (oral and poster forms) to the industrial and scientific community. So they can understand easily their contribution to the global project and defend their work face to senior experts.

3. FLIGHT DEMONSTRATIONS

The flight demonstration is the most impressive realization of the PERSEUS project.

3.1. At the beginning Subsonic regime

During the 10 first years of the project almost 20 rockets named ARES [5] (diameter 160 mm, height 2.5 m and GLOW between 15 and 20 kg) were launched, mainly during the French National campaign called C'Space organized by CNES. Two rockets were also launched in the Netherlands in cooperation with DARE students from Delft University. These rockets were propelled by small hybrid engines at the beginning and then replaced by solid Pro54-5G and Pro75-3G Cesaroni engines. Step by step, a global architecture, and an exhaustive avionics, was developed, improved and operated by students. These demonstrators reach an altitude of altitude 2 km and a subsonic Mach number of 0.6.

Figure 1: ARES rocket with canard fins for roll control

These regular launches of ARES enable to test a lot of technologies such as:

- sandwich composite structure for the tube and the fins, a patent was filed
- Aluminum 3D additive process with laser fusion for fins, or rocket top head including pressure canals [7].
- Thin circular antenna for full 3D clear emission of telemetry

3.2. Supersonic regime with SERA

Based on this constant progression, our students have been working on supersonic rocket named SERA [4]. Their performance enables to demonstrate that the PERSEUS project masters the classical dimensioning cases encountered for the development of an operational space launcher during its atmospheric phase, that is to say: lift off, Qmax, transonic regime and acceleration not higher than 10g.

Three SERA rockets has already been launch from SSC site at Kiruna end of April respectively in 2014, 2016 and 2017. SERA 1&2 have the same diameter than ARES, a height of 3 m and a GLOW of 26.5 kg. A Pro98-6G green 3 engine was used. On SERA3 a cluster of three Pro98 engines was used which required to increase the size of the rocket, the diameter is 250 mm, a height of 5 m and as consequence a GLOW of 80 kg. The altitude reached by the SERA rocket is about 5 km with a maximum supersonic Mach number of 1.3.

The work performed by SCUBE, OCTAVE, ISS and CLC student associations from ISAE-Supaero, UEVE, IPSA and Centrale Lyon can be highlighted. The GAREF partner is among else in charge for the ground installation and telemetry.

Figure 2: SERA rockets on MRL

A Swedish payload developed by students from Luleå Technology University was embedded on each SERA rocket the payloads are respectively named MADS, TAPAS and VISTA [3]. They have carried out experiments such as magnetic field measurements during ascent, or more recently trajectory rebuilding with rough GPS measurement. As SERA3 was a more powerful rocket a second payload which use another IMU from the Tech For Space Association (TFS) was embedded.

3.3 Airborne launch : The composite EOLE / RSS / ARES

Following previous CNES/ONERA studies on airborne launch with the purpose of optimizing the global system a lack of modelization of the separation and release system of the rocket from the carrier was identified. So it was decided to have a carrier, named EOLE, in order to be a flying test bench for release and separation system (RSS) which could be developed by students.

This project is coordinated by ONERA partner. EOLE was built and piloted by an experimented small company Aviation Design [8]. The RSS was defined and build by UEVE and UR1. The rocket developed in order to be carried by EOLE is an adapted ARES type rocket, developed in cooperation with students from CLC, GAREF and IPSA. The EOLE span is 6.7 m, propelled by two AMT Titan turbojet of 40 daN thrust. The maximum payload weight is 43 kg for a MTOW of 150 kg. A patent was filed. Under the authority of the French DGAC, The EOLE carrier has performed several Visual Line Of Sight (VLOS) with and without the ARES rocket at the Saint Yan aerodrome in the center of France. The last flight of 2014 was performed in full automatic mode except the remote piloted take-off and landing. The next step is to perform the flight at 4 km of altitude Beyond Visual Line Of Sight (BVLOS) in order to be able to automatically release the rocket and ignite it safely. These flights could be done at Kourou Space Center (CSG), opening the way for other tests on future separation and release system developed by students.

Figure 3: EOLE carrying an ARES rocket

3.3 Mini-Apterros

One year ago, a new type of small demonstrators was proposed to the students within the PERSEUS Project. It deals with reusability of a first stage of the rocket. Two developments need specific attention for such a vehicle. The first one is having an engine with thrust modulation (it will be discussed in the next item) and the second one is the GNC solution which is not obvious. So the specification of a little vehicle based on UAV technologies was fixed. The thrust has to be under the main core of the demonstrator which lay on the ground on several legs. The stabilization must be mastered with the orientation and modulation of the thrust as for a first stage of launcher. The weight is limited to 10 kg and the electric propulsion should not exceed 15 kW. For the safety aspect it should only fly in the bird cages which are dedicated to UAV flight test. Four student teams have worked on this

concept, Scube, SATURN, Octave and CLC. After one year of work none of the demonstrator was able to perform a first flight or jump. But the enthusiasm of the students for this activity makes the project to be confident for having a flight next year.

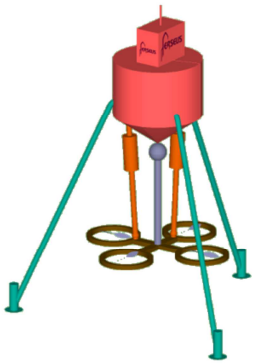

Figure 4: Sketch of the Mini-Apterros demonstrator

4. BI-LIQUID PROPULSION

4.1 LOX-Ethanol

The first bi-liquid engine built is a classical bi liquid engine using liquid Oxygen and Ethanol [1], able to propel an evolution of SERA rocket up to10 km. This MINERVA project is coordinated directly by the PERSEUS integrated team. Classical triplet injectors (F-O-F) were designed in order to atomize the fuel and oxidant mixture in a chamber insulated with ablative protection. The rate flow of the 7 injectors was defined in order to have a 5 kN engine thrust. The estimated chamber pressure is fixed at 10 bar and the combustion time is 20 s. The estimate efficiency is 0.95 for a vacuum ISP of 295 s.

Three parts were separately developed. The ground facilities consisting in two Skids were built and are operated by the ROXEL Partner. One Skid is dedicated to Lox feeding another is dedicated to alimentation of Fuel. Both were developed with the support of the CNES R&T department. These two skids have been qualified and are waiting for the engine. The third part which is the engine itself was defined through a synthesis of student works. The achievement was made entirely by a small enterprise (STIM) which has contributed by its expertise to the finalization of a design compatible with the conventional manufacturing processes.

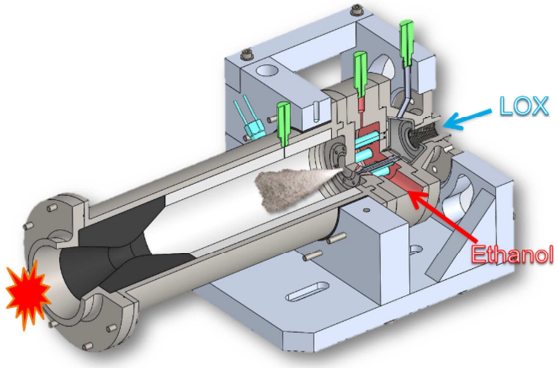

Figure 5: Overview of the first biliquid engine for ground fire test.

Several water tests were performed at the Martel facilities in Poitier. Theses rather simple tests enable to check the correct rate flow, the mixing plume shape and any leakage in the injection dome.

Figure 6: water test of the injecting plate.

Since June 2016, 6 fire tests were achieved with the thrust chamber. The first 3 tests were realized with 4 seconds of combustion were dedicated to prove the repeatability of the ignition sequence and to determine the degradation rate of different systems (thermal protection, injection plate, carbon throat). Then, 2 fire tests were successfully achieved with 20 and 22 seconds of combustion time.

Figure 6: fire test of MLE5K-1sa LOX/Ethanol

4.1 LOX-Methane

As mentioned previously in the Mini Apterros section §3.3, the need to have an engine with thrust modulation becomes mandatory to be able to perform a demonstrator of a reusable first stage. That is why it was decided first to switch to Liquid Methane propellant instead of Ethanol. The main reason is that Methane is a more suited fuel for reusable engine. Of course some adaptions of the present engine will the done in order to be tested with Lox/LCH4, but they are not so important. The second adaption will enable modulation, for that the impact injectors will be abandoned in favor of Pintle injectors. For that a new design of the engine is underway and the ignition test should be feasible by the end of 2018.

5. PROPULSIVE STRUCTURE

A specific activity, PEGASE, is performed within the PERSEUS project in the Bordeaux area. The AJSEP Partner linked to ArianeGroup partner is coordinated it. They are working on tanks for the liquid engine and on nozzle for the solid engine. One can notice that an important supervising was offer in that case at the school project level, which leds in significant results: a tremendous progression of the devices (tank, nozzle, insulated protection,…) defined and built by the students each year. The high level management was expressed through competition between projects on same objectives but with different constraints (economical, weight and innovation).

Tanks

The tank activity is applied to fuel and oxidant tanks for biliquid stage. A tank potentially candidate for Lox storage on this stage was already built by students and could be tested by ROXEL partner in order to verify the compliance with Lox during the whole life cycle. An improvement of the students manufacturing process is on going in order to reduce the level of leakage which regularly postponed of one year the test of the tank.

Propellant mass ratio

The purpose of these activities is to optimize the propulsive stage in order to reduce the propellant mass ratio. The starting point is the existing solid stage. It is a serious pedagogic objective, which enables development of firing test structures which will be operated by ONERA. In this facilities new combustion chamber, nozzle and internal insulation developed by students will be tested.

6. AVIONICS

An electrical architecture driven by the GAREF partner has been developed. The main features of this architecture are:

- Telemetry at 2,235GHz with 5Mb/s rate compatible of professional launch site such as Kiruna in Sweden or Kourou in French Guyana
- Two IMU with MEMS enabling 3D measurements : accelerations, gyrometers, magnetometers
- GPS is also available but the loss of signal at lift off due to high acceleration rate must be bypassed before using it properly.
- On board experimental measurements such as pressure, temperature, vibration, acoustic,…sent by telemetry in the limit of the capacity of the bandwith
- Video streaming
- Precise datation up to 1/1000s of each event
- Non-intrusive detection of ignition order
- USB and RS485 on board network
- Command of each event
- On board batteries
- A set of ground installation in order to check the rocket behavior during the chronology, including the hot count down.

This architecture has the advantage that students can easily contribute and can propose evolution. They have appropriated this architecture. Moreover, a lot of specific measurements can be performed during flight in order to investigate a specific physical phenomena (aerodynamic, thermic,...). This architecture was optimized and used for the SERA flight. The flight electrical heart device was submitted to sinusoidal and vibrational tests.

Figure 7: the electrical heart of SERA

In order to completely fulfill the main objectives of the PERSEUS project, some improvements are planned such as introducing a CAN network. The development of an Iron Bird seems to be necessary to check new items develop by students before integrating them into the rocket.

7. CONCLUSION

The PERSEUS project has developed a network of heterogeneous partners gathering youths and experts, associations and industries. This network has generated significant demonstrators :

- supersonic rockets (SERA),
- liquid LOX/Ethanol engine (MINERVA),
- demonstrators of reusable first stage (APTERROS)
- airborne demonstrators (EOLE)

These demonstrators were finalized mainly because the space dream can express itself through student's activities relayed by the supervision of the teachers, the engineers and the senior experts.

All the part of the launch system are analyzed, developed and tested within the PERSEUS project. Structural, propulsion, avionics, etc…The performance of the demonstrators which are in constant progression is also a good way to keep this project attractive for students.

The number of partners will increased by the arrivals of ESTACA and ESILV. This is a proof of the pedagogic interest of this project for High engineering school and will reinforce the attractiveness of the project for students.

8. PERSEUS CHALLENGE

In order to stimulate these activities while keeping the main development of the project compatible, a PERSEUS Challenge was initiated :

"5-50-500", for the 5 next years, the PERSEUS Project should be able to develop a demonstrator of a reusable first stage able to :

- Reach an altitude of 5 km
- A dry mass of 50 kg
- With a Lox/LCH4 engine of 500 daN of thrust

It's really a challenge to be able to achieve that within the PERSEUS Project because a lot of developments are still necessary. But challenge is part of students motivation, so combined with the attractiveness for space activities, the PERSEUS project meet the challenge.

Web site: http://www.perseus.fr

Contact: perseus@cnes.fr

9 REFERENCES

[1] R. Delpy, J. Oswald - PERSEUS Project 5kN LOX/Ethanol rocket engine fire tests– 7th EUCASS 2017 – Milan Italy 2017

[2] H. Hingre, J. Oswald – PERSEUS European Space Research Program for Students– 6th EUCASS 2015 – Krakow Poland 2015

[3] G. Antoja, M. Baker, H. Hristov, A. Jergatheesan, E. Martinez, M. Nyström, A. Pontoni, T. Steh, L. Strizic, H. Woo –Low cost Navigation data recording payload for SERA sounding Rockets -- 23rd ESA PAC symposium – Visby Sweden 2017

[4] C. Dupond, S. Pernon, J. Oswald - SERA 1 the first supersonic rocket developed in the frame of perseus project – 22nd ESA PAC symposium – Tromsø Norway 2015

[5] C. Dupond, S. Pernon, J. Oswald - ARES rockets demonstrators of French Space Agency PERSEUS project 21nd ESA PAC symposium – Thun – Switzerland 2013

[6] H. Hingre, R. Bec, J. Oswald, S. Pernon - European University and Scientific Space Research Program PERSEUS (Projet Etudiant de Recherche Spatiale Européen Universitaire et Scientifique) 4th Eucass 2011 - Saint Petersburg – Russia

[7] J. Korwin, B. Hugues - ARES EVE5: an OCTAVE's experimental rocket for PERSEUS project - IAC Toronto 2014

[8] J. Ledogar, J. Hermetz, H. Sohier, J. Oswald, E. Rantet - EOLE, an innovative flying test scale demonstrator for air-launch-to-orbit autonomous systems – ICAS 2012

[9] J.-M. Astorg, R. Bec, C. Bernard-Lépine, K. de Groote, F. Amouroux – PERSEUS A Nanosatellite Launch System Project Focusing on Innovation and Education– IAC 2007 Hyderabad, India.

[10] R. Bec, C. Bernard-Lépine, K. de Groote and F. Amouroux - PERSEUS A Nanosatellite Launch System Project Focusing on Innovation and Education 2nd EUCASS 2007 Brussels, Belgium

10 ACRONYMS

3P : Plateau Projet PERSEUS
AJSEP : Association Jeunesse Sciences Espace Passion
APTERROS : Advanced Propulsion Technology for Experimental Reusable Rocket and Operating System
ARES : Advanced Rocket for Experimental Studies
CLC : Space Association of Students from Ecole Centrale de Lyon
EPIP : Equipe Projet Intégrée PERSEUS (PERSEUS integrated team)
IMU : Inertial Measurement Unit
ISS : Space Association of Students from IPSA
MEMS : MicroElectroMechanical Systems
MINERVA : Moteur INnovant Experimental pour les Recherches sur les Vehicules Aerospatiaux
GLOW : Global Lift Off Weight
MTOW : Maximum Take Off Weight
OCTAVE : Space Association of Students from Evry University (UEVE)
PEGASE : Projet Etudiant Girondin Activités Sciences Espace
PERSEUS : Projet Etudiant de Recherche Spatiale Européen Universitaire et Scientifique
RSS : Release and Separation System (DSL in French)
SERA : Supersonic European Rocket ARES
SCUBE : Space Association of Students from ISAE-Supaero
STIM : Société de Tolerie Industrielle et Mécanique
SSC : Swedish Space Corporation
SATURN : Space Association of Students from Rennes 1 University
UEVE : Université d'Evry Val d'Essonne
UR1 : Universités de Rennes 1

ARION 1: THE NEXT EUROPEAN AND REUSABLE SOUNDING ROCKET

Francisco García, Raúl Torres

PLD Space
Nicolas Copérnico 7, 03202 Elche, Spain
Email: francisco.garcia@pldspace.com, raul.torres@pldspace.com

ABSTRACT

In the Q1 of 2019 the European sounding rocket, ARION 1 will have its maiden flight. ARION 1, a liquid-propelled sounding rocket that is being developed by PLD Space, will lift-off from the launch facilities that the company has in the South of Spain, concretely in Huelva.

PLD Space, a Spanish start-up company stablished in 2011, has been focused during the last years in the development of liquid-propulsion rocket engines that will power their rockets. After having tested successfully the first rocket engine in their propulsion test facilities at Teruel´s Airport, PLD Space is concentrating its efforts in developing the entire ARION 1 sounding rocket.

ARION 1, the first-ever reusable sounding rocket in Europe, will be able to provide around 5 minutes of microgravity conditions after reaching an apogee of 150 km in a nominal mission. This sounding rocket, will have the capability of carrying up to 100 kg of payload, exposing the experiments, scientific and technological payloads to low accelerations due to the liquid-propulsion technologies.

With this paper, PLD Space wants to introduce the ARION 1 sounding rocket, its capabilities as well as the advantages of a liquid-propelled based sounding rocket with respect to other traditional space launch systems.

ARION 1 aims to be the sounding rocket reference in Europe, providing affordable, flexible and simple access to space to Industry, Space Agencies, Research centres and Academia.

1. CURRENT OUTLOOK TO SOUNDING ROCKETS IN EUROPE

Today´s sounding rockets in Europe are only used under a complex Institutional market, providing few launch opportunities to experimenters and scientists.

These launch opportunities are offered under National and Institutional sounding rocket programmes, or a combination of both, involving usually different space agencies, companies and institutions of different countries. The consequences of the current European sounding rocket offer are a set of disadvantages:

- Complex management of the Projects and complex procurement chain
- Difficulties when interacting with key responsible people; duplication of roles and responsibilities
- Bureaucratic procedures in order to fulfil the requirements of the different parties and entities involved
- No standardisation of Payload servicing offer

As said before, all these issues lead to very few sounding rocket launch opportunities along the year. Only experimenters and scientist from Germany have more than a couple of launches per year[1]. The rest of scientific community in Europe have to rely on Institutional Programmes managed by the European Space Agency.

As a comparison of the low number of scientific missions using sounding rocket, we can compare this number of launches with the NASA Sounding Rocket Programme.

Taking as reference all the sounding rockets launched in Europe under European programmes from 2010 until 2016, we can see that just NASA [1] launched in the same period of time more than the double of them. And we are not counting commercial services provided by companies like Up Aerospace or Blue Origin.

In fact, this commercial approach, which has been taken by some American companies, is the one that PLD Space believes that will boost the fields of experimentation, research and technology validation via sounding rockets. PLD Space aims to offer an end-to-end service to simplify access to space while cutting-down management costs.

Furthermore, these European programmes are relying on existing solid rocket engines based on missiles, which are imported from outside Europe.

1 http://www.dlr-gsoc.de/moraba2015/index.php/missions-kalender.html

PLD Space proposal; ARION 1 is a 100% European sounding rocket that will be powered with a liquid-propellant engine developed and tested entirely in Spain.

2. ARION 1 VEHICLE DESIGN

ARION 1 launch vehicle is a one-stage TVC guided sounding rocket propelled with a liquid motor using Kerosene and Liquid Oxygen (KeroLOX) as propellants.

ARION 1, with a gross lift-off weight of approximately 2400 kg, is capable of lifting up to 100 kg to an apogee of 150 km, providing a microgravity environment to the payloads up to 5 minutes.

The vehicle diameter is 0.7 meters, the total length is approximately around 12.5 meters and it is made mostly using aluminium alloys.

ARION 1 will be the first reusable sounding rocket in Europe. PLD Space is developing a recovery strategy based on the use of a system of parachutes that will ensure a smooth splash down in the Atlantic Ocean.

2.1 Propulsion

PLD Space has been since 2014 developing from scratch, the liquid engine that will powered ARION 1 during 120 seconds.

PLD Space started first testing in its own Test Facilities located in the industrial Airport of Teruel (Spain), a first version of the engine; a calorimetric model used to understand the behaviour of the combustion and the performance of the engine.

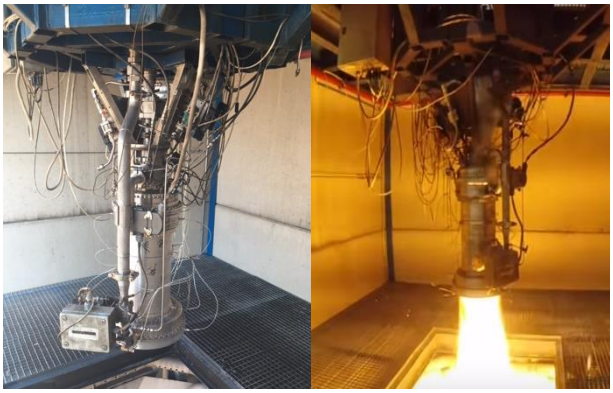

Figure 1. ARION 1 regenerative cooling engine

After more than 45 hot firings, PLD Space has started testing the next version, a regenerative cooling engine (Figure 1) that will be the same version, in terms of functionality, that the one that will flight on board of ARION 1.

ARION 1 liquid engine is pressured-fed and has a net thrust of 30 kN at sea level.

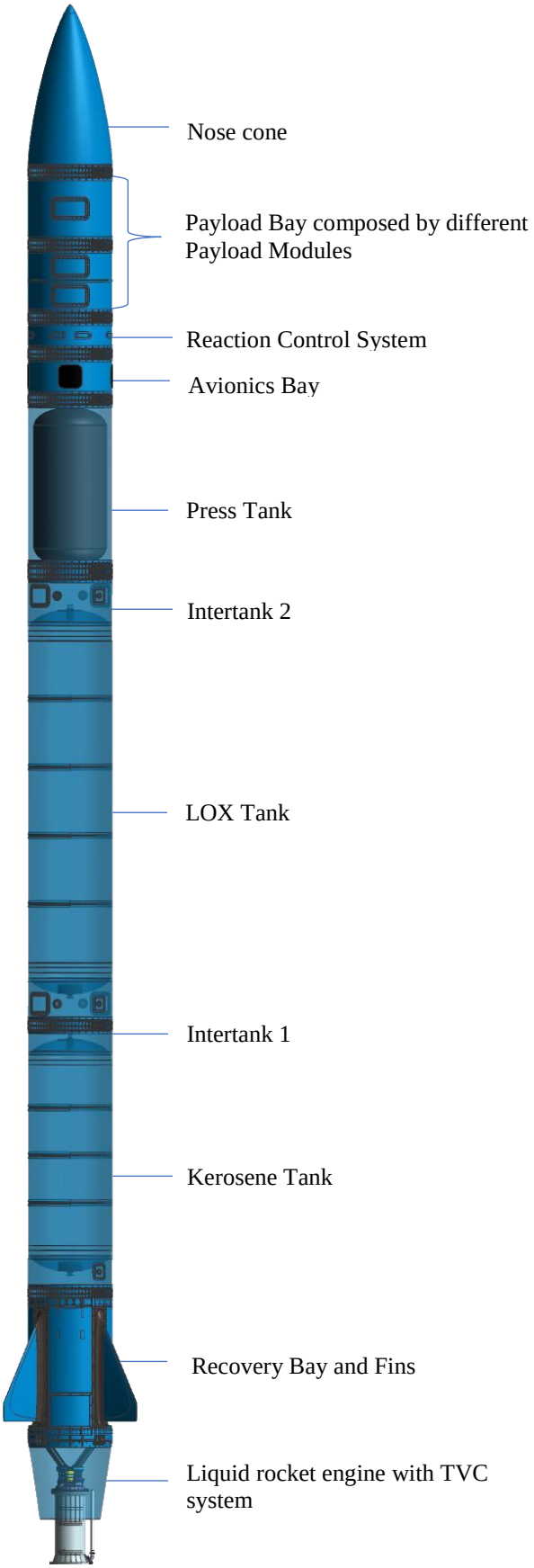

Figure 2. ARION 1 sounding rocket

2.2 GNC

The guidance, navigation and control (GNC) system of ARION 1 is responsible of obtaining navigation data, guide ARION 1 and perform all the necessary control loops to follow a pre-designated nominal trajectory.

The GNC system counts with various inertial measurements units as well as gyroscopes to determine the attitude of the rocket. In order to position itself, the rocket also uses a GPS System.

ARION 1 counts with a Reaction and Control System (RCS) based on Nitrogen cold-gas thruster. The RCS is used to control not-desired roll rates during the entire flight as well as to flip the rocket when it starts the descend phase, ensuring there is a nose-first re-entry position.

ARION 1 is also equipped with a Thrust Vector Control (TVC) system that maintains the desired pitch and yaw attitude. This TVC will used two electro-mechanical actuators that will make gimbal the nozzle in two axes.

2.3 TM/TC

On board the Avionics section, the Telemetry and Telecommand (TM/TC) System provides reliable communications with ground segment as well as data transmission for the vehicle and FTS

The TM/TC System will ensure successful real-time downlink of the data gathered and generated by the vehicle during all the flight as well as the experiments on board of the Payload Bay.

2.4 FTS

ARION 1 counts with an independent Flight Termination System that will ensure there are no major incidents, in case of vehicle malfunction or anomaly, by actively terminating the flight of the sounding rocket.

INTA (in English, National Institute of Aerospace Technology), who is the Range Authority in "El Arenosillo" (ARION 1 Launch Site), will provide the FTS receivers that will be on board of ARION 1.

Figure 3. One of the optronic systems at "El Arenosillo"

"El Arenosillo" range centre counts with all the necessary ground segment elements required to proper function the FTS.

3. LAUNCH SITE

PLD Space will use the already existing facilities of INTA; the "El Arenosillo" test range located in the south of Spain, concretely in the province of Huelva.

Figure 4. A replica of the INTA 300 sounding rocket, one of the most launched rockets from "El Arenosillo" in the original launch ramp.

INTA has been using this launch site since 1996. Up to now, more than 550 sounding rockets have been launched from this site, sometimes in collaboration with other countries.

PLD Space is planning to develop its own mission control centre as well as its own hangar in order to preserve the rocket in optimal conditions, as well as to carry-out all the final integration operations prior to launch.

Figure 5. Aerial view of "El Arenosillo" range centre

PLD Space, with the support INTA as Range Authority in charge of the FTS, will operate the rocket and manage all launch and recovery operations from its facilities inside "El Arenosillo" range centre.

Currently, sounding rockets in Europe are only launched from sites located in much northern countries, being closed to the artic and making sometimes difficult execution of the launch campaigns.

One of the advantages of launching from “El Arenosillo" in the South of Spain is the availability of good weather conditions along the year; every year there are more than 300 sunny days when PLD Space could potentially launch ARION 1.

4. PAYLOAD SERVICE

The aim of PLD Space with ARION 1 is to offer the same commodities and microgravity conditions that usually are provided under the National and Institutional sounding rocket programmes.

With an apogee of 150 km, and to a maximum payload of 100 kg, ARION 1 will provide to experimenters and scientist up to 5 minutes of high quality microgravity conditions.

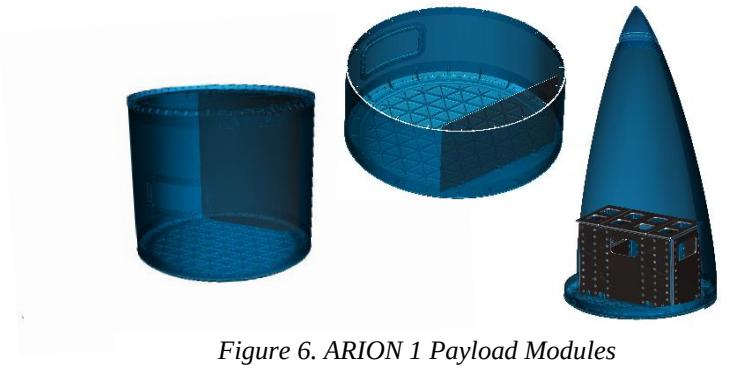

Figure 6. ARION 1 Payload Modules

ARION 1 Payload Bay can be composed by either four single modules, two double modules or the combination of two single modules and one double module. Experiments or technology demonstrators can be also placed inside the fairing on the Rack Modules, using the standard CubeSat platform (6U and 12U slots).

Type of Module	Single	Double	Rack
Diameter (mm)	584	584	-
Height (mm)	283	566	340
Max. Weight (kg)	25	50	16
Power (V)	12-24	12-24	12
Data Storage/SSD (Gb)	128	128	32
Max. Downlink rate (Mbps)	4	4	4
Environmental Control	Yes	Yes	No

Table 1. Characteristics of the different modules & rack

All modules have standard interfaces for power and data recording and transmission connections, as well as a standard isogrid plate (in the case of the single and double module) to mount the base of the experiment.

5. ARION 1 MISSION OPERATIONS

As described at the beginning of this paper, ARION 1 aims to be the reference of the sounding rockets in Europe providing simple, flexible and affordable access to space.

To do so, PLD Space will manage the end-to-end of the mission except the development of the experiment or technology demonstrator, simplifying the interfaces and the management of the Projects.

Furthermore, as said before, PLD Space will operate the sounding rocket using its own mission control, and will be in charge as well of all the recovery and refurbishing operations to ensure ARION 1 is ready to fly again.

With this approach, PLD Space retains control on the cost of the different operations, being able to cut it down and to optimise in the future its operations.

5.1 Launch operations

Once the rocket has been tested vertically at Teruel Airport, ensuring that the propulsion system, as well as the Avionics, and GNC systems work as expected, the rocket will be moved to the PLD Space HQ (in Alicante) to seal it, and to finally move it to “El Arenosillo” by road.

In order to simplify transporting and launching operations, PLD Space is developing a trailer that will be used for these two purposes.

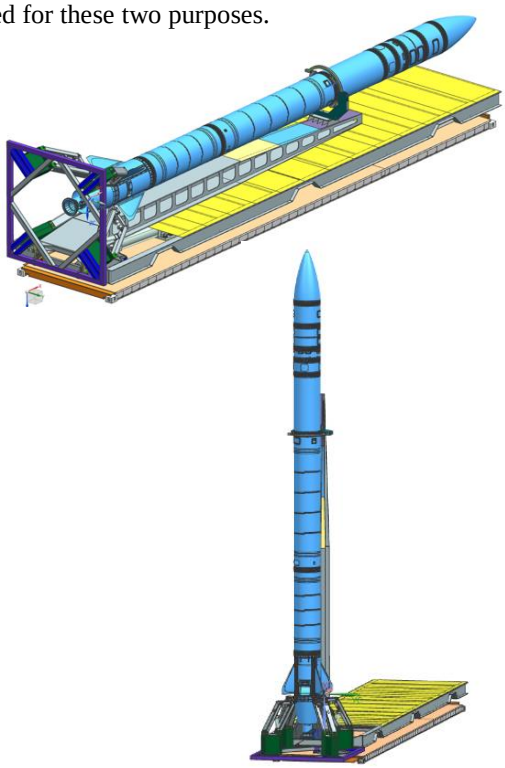

Figure 7. ARION 1 Transporter/Launch Ramp trailer

Moved by a truck, the trailer (Figure 7) will be used to move the rocket around PLD Space different sites but also as a key facility during ARION 1 launch; the trailer will incorporate the different elements and systems needed during pre-launch operations (i.e. propellants loading) as well as all electrical interfaces to ensure proper understanding of the rocket health and behaviour.

In what regards the Payload Bay and nose-cone, PLD Space will be in charge, together with some customer representative people, of integrating the different experiments on board of the Payload Bay and always after having passed the necessary tests at PLD Space premises.

Once everything has been integrating, the Payload Bay and nose-cone, will be sealed and will travel to "El Arenosillo" where the final matting of the rocket will occur.

5.2 Recovery operations

Once the rocket has deployed its parachutes to softly land on the Atlantic Ocean, around 30 km from the coast, PLD Space will start the recovery operations.

PLD Space will use a towing vessel to pick-up the rocket from the water and to transport it to the closest harbour of "El Arenosillo"; Mazagón harbour which is just few kilometres away from it.

Once the rocket has arrived to the harbour, it will be moved to "El Arenosillo" where the first cleaning and refurbishing operations will take place.

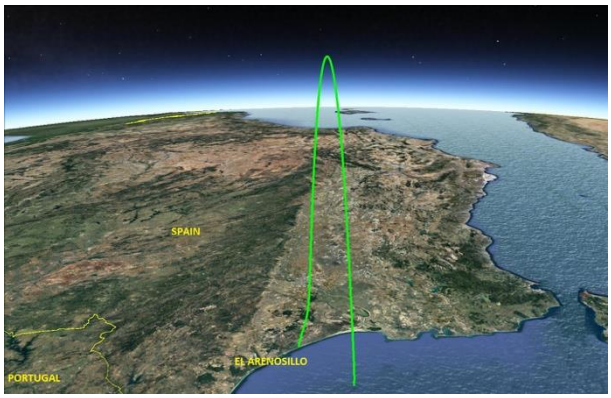

Figure 8. ARION 1 flight profile

6. FUTURE PLANS

PLD Space expects to have successful tests flights of ARION 1 during Q1 and Q2 of 2019. Following these flights, PLD Space will start providing to Research Institutes, industrial companies, and academia its launch services.

Furthermore, PLD Space has conceived ARION 1 since the beginning as the technological demonstrator of a much bigger rocket; ARION 2, an orbital launch vehicle.

ARION 2 will be a three-stages and reusable liquid rocket that will be able to put 150 kg of payload into a Low-Earth Orbit.

ARION 2 main subsystems; propulsion, avionics and GNC, structures and recovery will be based on all the developments that have been proven successful in ARION 1. Hence, ARION 1 can be at the same time the perfect test-bed of PLD Space in order to develop in a more reliable and fast way a Micro-launcher.

PLD Space expects to have the maiden flight of ARION 2 in Q1 of 2021.

7. CONCLUSIONS

As it has been described along the paper, ARION 1 stands out as the only European sounding rocket, that is capable to provide similar microgravity time and conditions than current European sounding rocket programmes.

Furthermore, PLD Space has designed ARION 1 to simplify all the operations; from integration to launch in order to accelerate mission timing and also in order to reduce the cost of the mission.

PLD Space advocates for standardisation and this is why, it has developed a set of payload modules that can be used for different purposes under the same constraints, allowing flexibility and simplicity when looking for launch opportunities.

All these aspects will contribute to increase PLD Space capabilities to offer launch services. In fact, PLD Space estimates 8 launches of ARION 1 per year, once the company has proved that it works as expected.

ARION 1, while setting the principles of reusability in Europe, aims to be the sounding rocket reference, providing affordable, flexible and simple access to space to Industry, Space Agencies, Research Centres and Academia.

8. REFERENCES

[1] National Aeronautics and Space Administration. NASA Sounding Rockets Annual Report 2016, pp64. Online at: www.sites.wff.nasa.gov/code810/download_archive.html

HUMAN CELLS IN SPACE

Daniela Grimm [1,2], **Thomas Juhl Corydon** [1,3], **Sascha Kopp** [2], **Marcus Krueger** [2], **Manfred Infanger** [2], **Markus Wehland** [2]

[1] *Department of Biomedicine, Aarhus University, Wilhelm Meyers Allé 4, DK-8000 Aarhus C, Denmark, Emails: dgg@biomed.au.dk, corydon@biomed.au.dk*
[2] *Clinic for Plastic, Aesthetic and Hand Surgery, Otto-von Guericke-University, Leipziger Straße 44, 39120 Magdeburg, Emails: sascha.kopp@med.ovgu.de, marcus.krueger@med.ovgu.de,* manfred.infanger@med.ovgu.de*, markus.wehland@med.ovgu.de*
[3] *Department of Ophthalmology, Aarhus University Hospital, 8000 Aarhus C, Denmark*

ABSTRACT

It is a dream of mankind to conquest space. Important steps to realize this dream were parabolic flights, rocket flights, unmanned Bion flights, or travels to space stations. A long-term stay in space can cause various medical problems. To investigate the different microgravity-related diseases, scientists examine the health of astronauts or focus on the mechanisms of microgravity-dependent molecular and cellular changes.
Altered gravity conditions influenced apoptosis, altered the cytoskeleton, signal transduction, differentiation, growth, cell adhesion, migration, cell cycle and cell adhesion. Short-term microgravity induced alterations of the cytoskeleton in various cell types. The cytoskeletal alterations were confirmed by the compact fluorescence microscope (FLUMIAS) for fast live-cell imaging of FTC-133 cancer cells under real microgravity (TX52 mission).
Knowledge of the underlying mechanisms of microgravity-dependent changes is an important topic for improving Space Medicine and developing new treatment strategies or countermeasures for humans in space.

1. INTRODUCTION

Research in microgravity is an important part of Space Medicine. Astronauts suffer from various health problems after a long-term stay in orbit [1-5].
Bone loss and fractures, muscle atrophy, cardiovascular problems, problems occurring because of immune system function changes together with a disturbed wound healing, a disruption of the biological clock, nephrolithiasis, as well as ocular problems (choroidal folds, optic disk edema, globe flattening, and hyperoptic shifts) have been described [3, 4, 6].
To clarify the mechanisms of the observed health changes, studies in the field of basic sciences have increased enormously. In this presentation, the field of Life Sciences will be introduced. Studies involving signal transduction, cellular differentiation, gene expression, apoptosis, cytoskeleton, and cell adhesion were performed. In addition, studies in cancer research, regenerative medicine, OMICs investigations, immunology, muscle and bone research, metabolism in space, cardiovascular research, stem cell research, and ophthalmology in space were of interest. A newer area is translational research: Tissue engineering, multi-cellular (tumour) spheroids, "space" pharmacology, and wound healing processes under unloading conditions.

2. PLATFORMS FOR RESEARCH IN REAL MICROGRAVITY

The most important platform for Space experiments is the International Space Station (ISS). The ISS serves as a space environment research laboratory. Since 1998 this manned station is maintained in a nearly circular orbit with a minimum mean altitude of 330 km. It provides a platform for long-term experiments in microgravity with an additional centrifuge for a 1*g* control. However, flight opportunities for research projects on the ISS are very rare and costly. Another important option for studies in Space had been the US Space Shuttle flights, until NASA had withdrawn from the program in 2011. It provided research for several days. Today private companies transport experiments to the ISS. Unmanned satellites and spaceships are a good possibility to perform experimental cell research in Space. However, as these are unmanned, a complex automation of the experiments is required. These flight options can be used for experiments with cells, plants, small animals or microorganisms. When a long duration of real microgravity is not necessary, sounding rockets are the platform of choice. These rockets transport a payload, like an experimental cell culturing and fixation device or a microscope, in a sub-orbital flight, reaching apogees of up to 1500 km. They reach microgravity for some minutes, but also require a fully automated setup. Examples for sounding rockets are TEXUS and MAXUS, which were developed by Airbus Defence and Space (formerly Astrium), Bremen, Germany [7].
For astronaut training purposes and for the preparation of Spaceflights, parabolic flights are necessary and are an example for a real µ*g*-condition achievable on Earth [8-11]. A parabolic flight consists of a test parabola and then of 30 parabolas, which can provide 22 s of real µ*g*. Parabola one starts with a static 1*g*-phase, which is followed by a pull-up of the plane and initiation of a 20 s-long hypergravity phase of 1.8*g*. When the aircraft

reaches an ascent angle of 47°, thrust is annulled and the aircraft follows parabolic trajectory in free fall, resulting in 22 s of μ*g*. This is followed by the interception of the aircraft and additional 1.8*g* for 20 s after which the aircraft stays in static 1*g* again [10].

Finally, the drop tower at the University Bremen (ZARM) provides up to 9 s of microgravity. The payload is enclosed by a capsule and is catapulted in an evacuated tube (~1 Pa) to a height of nearly 110 m and falls back to the ground.

All these real microgravity platforms are rather expensive to use and many research groups were competing for an opportunity, which renders them unsuitable for high-throughput investigations.

Therefore, researchers use the method of microgravity simulation/modelling in their laboratories for the preparation of a future Space mission. Thus, devices were constructed to simulate conditions of microgravity on Earth [12-14].

Examples are the 3D random positioning machine (RPM), the 2D fast rotating clinostat (FRC) or the rotating wall vessel (RWV). They have been used for culture of adherently growing cells like keratinocytes [15], chondrocytes [16], osteoblasts [17], endothelial cells [18, 19], epithelium cells [6], fibroblasts [20, 21], cancer cells [13, 22-24] and in suspension proliferating lymphocytes [25] for various time periods.

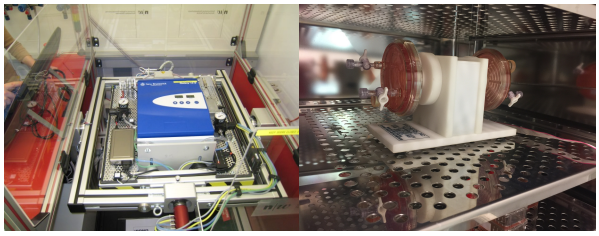

Figure 1. Left side: Incubator RPM and right side: Rotating Wall Vessel for Tissue Engineering.

3. HARDWARE FOR CELL CULTURE IN SPACE

Many Space experiments investigating cells in orbit on the ISS or on unmanned Spacecrafts like the Sino-German Shenzhou-8/SimBox mission [26-28] had been flown in the last years.

The materials of the hardware have to be biocompatible with the cells. In advance biocompatibility experiments have to be performed in detail to check the viability of the cells and their proliferation status [27, 29].

Several hardware types had been developed. Examples are hardware containers for lymphocytes [30], macrophages [26], endothelial cells [29] and thyroid cancer cells [27].

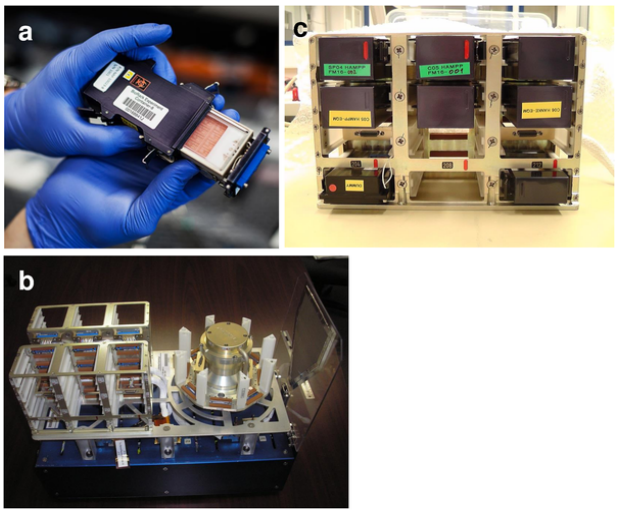

Figure 2. "NanoRacks Astrium Centrifuge" (U.S. National Laboratory) containing Biorack type I standard CELLBOX EUE type IV (Photos: Jesper Rais). (a) Biorack type I container with inserted CELLBOX EUE type IV. (b) "NanoRacks Astrium Centrifuge" with static and centrifuge slots. (c) "NanoRacks Astrium Centrifuge" with integrated EUE inserts [26].

4. RESULTS OF SPACE EXPERIMENTS

4.1. Multicellular Spheroids

Three-dimensional (3D) growth was observed by exposing cells to Space conditions or to devices simulating microgravity conditions on Earth (so-called ESA ground-based facilities). A part of the cells initially growing as a monolayer detaches from the bottom of the culture flask. These cells assemble and form 3D spheroids, cartilage pieces or tubes resembling the tissues from which the cells have been derived [31-33]. However, a confluent monolayer of cells revealed to hamper the initiation of 3D aggregates [24, 34].

Changes of the secretome, proteome and gene expression pattern were induced by microgravity conditions [27, 28, 35, 36].

In 1997 Freed *et al.* [37] cultured cartilage pieces on the Mir Space station. Compared with the Earth group, Mir-grown constructs were more spherical, smaller, and mechanically inferior.

Stamenković et al. [38] cultured porcine chondrocytes during the Flight 7S (Cervantes mission) on the ISS. A weaker extracellular matrix staining of ISS neocartilage tissue was noted compared with both Earth-cultivated tissues.

Thyroid cancer cells (FTC-133 cell line) were flown in Space during the Shenzhou-8/SimBox mission. Many cells assembled to larger spheroids compared to Earth-engineered spheroids [27]. Epidermal growth factor and connective tissue growth factor are involved in the aggregation process [27].

In addition, thyroid cancer cells and breast cancer cells

grow as MCS floating in the supernatant after RPM-exposure [13, 22, 23]. Various different cell types were cultured on the Rotating Wall Vessel [39] and revealed a 3D growth behaviour, such as fibroblasts, prostate cancer cells, breast cancer cells and others.

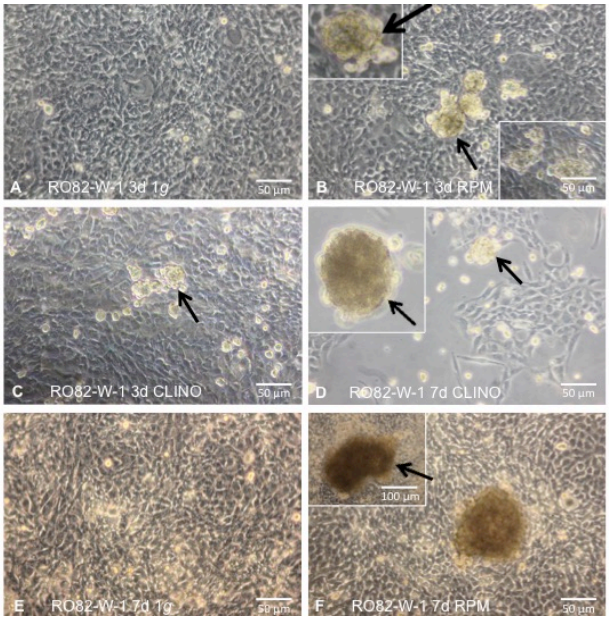

*Figure 3. Phase contrast microscopy: A) Follicular thyroid cancer cells cultured for 3 d at static 1*g*. The cells proliferated as 2D monolayer. B) RO82-W-1 cells incubated for 3 d on the RPM. The arrows show 3D aggregates (multicellular spheroids; MCS). The inserts show swimming 3D spheroids in the supernatant. C) MCS formed on the CLINO after 3 days. D) RO82-W-1 cells cultured for 7 days on the CLINO. The arrows show 3D spheroids. The insert demonstrates a floating spheroid in the supernatant. E) RO82-W-1 cells cultured for 7 days at static 1*g*-conditions grow as well as a confluent monolayer. F) 7-day-old MCS (arrows) could be detected and adherent RO82-W-1 cells [13].*

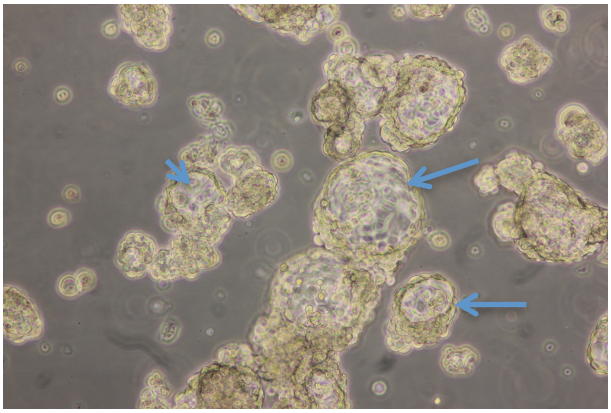

Figure 4. Phase contrast microscopy of 10-day RPM-exposed MCF-7 breast cancer cells. Glandular structures are visible (blue arrows).

4.2. Apoptosis of cells cultured under microgravity

The appearance of apoptosis in human T lympho-blastoid cells (Jurkat), flown on the Space Shuttle was described by Lewis *et al.* in 1998 [40]. At 4 h, 30% of flown, compared to 17% of ground, cells showed apoptosis. In parallel, a time-dependent increase of the apoptosis-associated Fas/APO-1 protein in static flown, but not the in-flight 1*g*-samples or ground controls, confirmed microgravity-associated apoptosis [40].
Alteration of the gravity vector is an external apoptosis inducer. Clinorotation-induced apoptosis was found in cultured glial cells [41], but not in chondrocytes exposed to the RPM [42].
FRTL-5 thyroid cells were exposed to real microgravity during the TX44 mission (launched February 7, 2008, from Kiruna, Sweden) [43].
At an altitude of 264 km, the culture media were injected with or without TSH in the different samples, and weightlessness prevailed on board for 6min and 19 s. Control experiments were performed, in parallel, in an on-board 1*g*-centrifuge and on ground in the Kiruna laboratory. Apoptotic thyrocytes were found in microgravity samples without TSH treatment. TSH revealed a cell-protective effect [43]. In addition, apoptosis was also detectable in ML1 thyroid cancer cells exposed to the random positioning machine for some days [44].
Investigations, using a compact Spinning-disc Fluorescence Microscopy Analysis System (FLUMIAS) and FTC-133 cancer cells expressing the LifeAct-GFP marker protein on the TX52 sounding rocket mission revealed a detaching cell, which may be apoptotic. This finding has to be confirmed in future experiments [7].
Early activation of 5-lipoxygenase plays a central role in the initiation of the apoptotic program [30]. During the ROALD experiment, human lymphocytes were cultured in real microgravity on the ISS [30]. DNA fragmentation was seen after 24 h and 48 h in ISS-0*g* samples compared with ISS-1*g* or ground control samples [30]. Cleaved PARP was already detectable after 4 h [30].

4.3. Alterations of the Cytoskeleton

Various researchers reported about cytoskeletal changes in a microgravity environment, during spaceflight, rocket flight, or parabolic flight missions and on ground-based facilities [10, 45].
Alterations of the microtubule cytoskeleton were demonstrated in Jurkat cells, glial cells, endothelial cells, chondrocytes and other cells exposed to real or simulated microgravity [8, 9, 16, 40, 46].

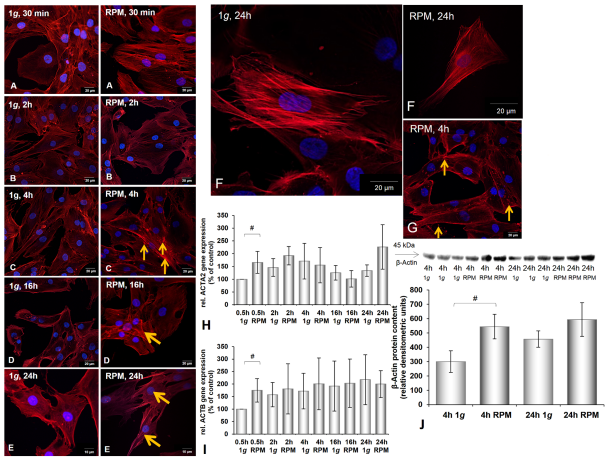

Figure 5. Integrity of nuclei counter-stained by Hoechst 33342, distribution of F-Actin, ACTA2 *and* ACTB *gene expression, and Western blot analysis of beta-actin of chondrocytes cultured at 1g or on the RPM. A–E: Integrity of nuclei counter-stained by Hoechst 33342 and distribution of F-Actin in human chondrocytes cultured at 1g or on the RPM for different times (30 min (a), 2 h (b), 4 h (c), 16 h (d), 24 h (e)). After 30 min and 2 h stress fibres were visible in RPM samples (A, B). After 4 h accumulations of F-actin were visible in the outer cellular membrane (C, G). The cells were smaller after 24 h RPM exposure (F). H, I:* ACTA2 *and* ACTB *gene expression: Early up-regulation of these mRNAs was found after 0.5 h. J: Western blot analysis of beta-actin: Beta-actin clearly increased after 4 h incubation on the RPM. Data are given as mean ± standard deviation; #P<0.05; *P<0.005 [16].*

In addition, intermediate filaments and the F-actin cytoskeleton were altered by microgravity in various cell types [6, 7, 10, 22, 46]. Notably, such alterations seem to occur immediately after entrance to µg conditions [7, 8].

A human cell can sense microgravity with signalling across transmembrane adhesion receptors linking to the cytoskeleton, to the extracellular matrix and to other cells [47].

The altered actin cytoskeleton is connected to various membrane proteins, and may therefore influence cell polarity, or adhesion and migration behaviour.

Taken this together, the microtubules lose their radial organization, can be shortened, and can be more curved and bent [40]. They are regularly localized more perinuclearly. The actin stress fibres are reduced in number, length and thickness. Actin is often redistributed and has either a more perinuclear or more cortical localization [9, 16]. Focal adhesion proteins no longer align well with the stress fibres, but appear as bigger clusters without radial orientation in the cortical layer, which results in reduced cell spreading [45]. Intermediate filaments such as vimentin form clusters, and larger meshes appear in the network, and the localization is more perinuclear [16, 45, 46].

5. SUMMARY

In summary, when human cells are exposed real and simulated microgravity, they alter their phenotype and grow as monolayer or assemble to 3D aggregates, depending on their tissue of origin. They exert an early induction of apoptosis and an altered cytoskeleton. The cytoskeletal changes can be detected already after 22 s of real microgravity as realized during a parabolic flight. Moreover, the cells showed an altered differentiation, migration and cell adhesion as well as changed in proliferation and the composition of the extracellular matrix.

6. CONCLUSIONS

Alterations at the molecular level in cell biology, gene expression and signal transduction in different cell types suggest the health concerns observed in astronauts may be partly due to microgravity.

Microgravity is an invaluable tool for exploring new targets in anticancer therapy and can be simulated in some aspects in ground-based facilities.

A scaffold-free formation of three-dimensional aggregates by thyroid cancer cells with altered expression of *EGF*, *CTG*F and other genes in space.

Subsequent analyses of space samples revealed a scaffold-free formation of 3D structures in space [27, 29, 37, 38].

REFERENCES

1. White, R.J. & Averner, M. (2001). Humans in space. *Nature*. **409**(6823), 1115-1118.
2. Cogoli, A. (2004). Strategies of cell biology experimentation in space. *J Gravit Physiol*. **11**(1), 111-116.
3. Pietsch, J., Bauer, J., Egli, M., Infanger, M., Wise, P., Ulbrich, C. & Grimm, D. (2011). The effects of weightlessness on the human organism and mammalian cells. *Curr Mol Med*. **11**(5), 350-364.
4. Grimm, D., Wise, P., Lebert, M., Richter, P. & Baatout, S. (2011). How and why does the proteome respond to microgravity? *Expert Rev Proteomics*. **8**(1), 13-27.
5. Grimm, D., Grosse, J., Wehland, M., Mann, V., Reseland, J.E., Sundaresan, A. & Corydon, T.J. (2016). The impact of microgravity on bone in humans. *Bone*. **87**(44-56).
6. Corydon, T.J., Mann, V., Slumstrup, L., Kopp, S., Sahana, J., Askou, A.L., Magnusson, N.E., Echegoyen, D., Bek, T., Sundaresan, A., Riwaldt, S., Bauer, J., Infanger, M. & Grimm, D. (2016). Reduced Expression of Cytoskeletal and Extracellular Matrix Genes in Human Adult Retinal Pigment Epithelium Cells Exposed to

Simulated Microgravity. *Cell Physiol Biochem*. **40**(1-2), 1-17.
7. Corydon, T.J., Kopp, S., Wehland, M., Braun, M., Schutte, A., Mayer, T., Hulsing, T., Oltmann, H., Schmitz, B., Hemmersbach, R. & Grimm, D. (2016). Alterations of the cytoskeleton in human cells in space proved by life-cell imaging. *Sci Rep*. **6**(20043).
8. Grosse, J., Wehland, M., Pietsch, J., Ma, X., Ulbrich, C., Schulz, H., Saar, K., Hubner, N., Hauslage, J., Hemmersbach, R., Braun, M., Van Loon, J., Vagt, N., Infanger, M., Eilles, C., Egli, M., Richter, P., Baltz, T., Einspanier, R., Sharbati, S. & Grimm, D. (2012). Short-term weightlessness produced by parabolic flight maneuvers altered gene expression patterns in human endothelial cells. *FASEB J*. **26**(2), 639-655.
9. Aleshcheva, G., Wehland, M., Sahana, J., Bauer, J., Corydon, T.J., Hemmersbach, R., Frett, T., Egli, M., Infanger, M., Grosse, J. & Grimm, D. (2015). Moderate alterations of the cytoskeleton in human chondrocytes after short-term microgravity produced by parabolic flight maneuvers could be prevented by up-regulation of BMP-2 and SOX-9. *FASEB J*. **29**(6), 2303-2314.
10. Ulbrich, C., Pietsch, J., Grosse, J., Wehland, M., Schulz, H., Saar, K., Hubner, N., Hauslage, J., Hemmersbach, R., Braun, M., Van Loon, J., Vagt, N., Egli, M., Richter, P., Einspanier, R., Sharbati, S., Baltz, T., Infanger, M., Ma, X. & Grimm, D. (2011). Differential gene regulation under altered gravity conditions in follicular thyroid cancer cells: relationship between the extracellular matrix and the cytoskeleton. *Cell Physiol Biochem*. **28**(2), 185-198.
11. Wehland, M., Ma, X., Braun, M., Hauslage, J., Hemmersbach, R., Bauer, J., Grosse, J., Infanger, M. & Grimm, D. (2013). The impact of altered gravity and vibration on endothelial cells during a parabolic flight. *Cell Physiol Biochem*. **31**(2-3), 432-451.
12. Herranz, R., Anken, R., Boonstra, J., Braun, M., Christianen, P.C., De Geest, M., Hauslage, J., Hilbig, R., Hill, R.J., Lebert, M., Medina, F.J., Vagt, N., Ullrich, O., Van Loon, J.J. & Hemmersbach, R. (2013). Ground-based facilities for simulation of microgravity: organism-specific recommendations for their use, and recommended terminology. *Astrobiology*. **13**(1), 1-17.
13. Svejgaard, B., Wehland, M., Ma, X., Kopp, S., Sahana, J., Warnke, E., Aleshcheva, G., Hemmersbach, R., Hauslage, J., Grosse, J., Bauer, J., Corydon, T.J., Islam, T., Infanger, M. & Grimm, D. (2015). Common Effects on Cancer Cells Exerted by a Random Positioning Machine and a 2D Clinostat. *PLoS One*. **10**(8), e0135157.
14. Warnke, E., Pietsch, J., Wehland, M., Bauer, J., Infanger, M., Gorog, M., Hemmersbach, R., Braun, M., Ma, X., Sahana, J. & Grimm, D. (2014). Spheroid formation of human thyroid cancer cells under simulated microgravity: a possible role of CTGF and CAV1. *Cell Commun Signal*. **12**(32).
15. Ranieri, D., Proietti, S., Dinicola, S., Masiello, M.G., Rosato, B., Ricci, G., Cucina, A., Catizone, A., Bizzarri, M. & Torrisi, M.R. (2017). Simulated microgravity triggers epithelial mesenchymal transition in human keratinocytes. *Sci Rep*. **7**(1), 538.
16. Aleshcheva, G., Sahana, J., Ma, X., Hauslage, J., Hemmersbach, R., Egli, M., Infanger, M., Bauer, J. & Grimm, D. (2013). Changes in morphology, gene expression and protein content in chondrocytes cultured on a random positioning machine. *PLoS One*. **8**(11), e79057.
17. Prodanov, L., Van Loon, J.J., Te Riet, J., Jansen, J.A. & Walboomers, X.F. (2014). Nanostructured substrate conformation can decrease osteoblast-like cell dysfunction in simulated microgravity conditions. *J Tissue Eng Regen Med*. **8**(12), 978-988.
18. Grimm, D., Infanger, M., Westphal, K., Ulbrich, C., Pietsch, J., Kossmehl, P., Vadrucci, S., Baatout, S., Flick, B., Paul, M. & Bauer, J. (2009). A delayed type of three-dimensional growth of human endothelial cells under simulated weightlessness. *Tissue Eng Part A*. **15**(8), 2267-2275.
19. Grimm, D., Bauer, J., Ulbrich, C., Westphal, K., Wehland, M., Infanger, M., Aleshcheva, G., Pietsch, J., Ghardi, M., Beck, M., El-Saghire, H., De Saint-Georges, L. & Baatout, S. (2010). Different responsiveness of endothelial cells to vascular endothelial growth factor and basic fibroblast growth factor added to culture media under gravity and simulated microgravity. *Tissue Eng Part A*. **16**(5), 1559-1573.
20. Beck, M., Tabury, K., Moreels, M., Jacquet, P., Van Oostveldt, P., De Vos, W.H. & Baatout, S. (2012). Simulated microgravity decreases apoptosis in fetal fibroblasts. *Int J Mol Med*. **30**(2), 309-313.
21. Ulbrich, C., Leder, A., Pietsch, J., Flick, B., Wehland, M. & Grimm, D. (2010). The impact of vascular endothelial growth factor and basic fibroblast growth factor on cardiac fibroblasts grown under altered gravity conditions. *Cell Physiol Biochem*. **26**(6), 1011-1022.
22. Kopp, S., Warnke, E., Wehland, M., Aleshcheva, G., Magnusson, N.E., Hemmersbach, R., Corydon, T.J., Bauer, J., Infanger, M. & Grimm, D. (2015). Mechanisms of three-dimensional growth of thyroid cells during long-term simulated microgravity. *Sci Rep*. **5**(16691).
23. Kopp, S., Slumstrup, L., Corydon, T.J., Sahana, J., Aleshcheva, G., Islam, T., Magnusson, N.E.,

Wehland, M., Bauer, J., Infanger, M. & Grimm, D. (2016). Identifications of novel mechanisms in breast cancer cells involving duct-like multicellular spheroid formation after exposure to the Random Positioning Machine. *Sci Rep*. **6**(26887).
24. Bauer, J., Kopp, S., Schlagberger, E.M., Grosse, J., Sahana, J., Riwaldt, S., Wehland, M., Luetzenberg, R., Infanger, M. & Grimm, D. (2017). Proteome Analysis of Human Follicular Thyroid Cancer Cells Exposed to the Random Positioning Machine. *Int J Mol Sci*. **18**(3),
25. Maccarrone, M., Battista, N., Meloni, M., Bari, M., Galleri, G., Pippia, P., Cogoli, A. & Finazzi-Agro, A. (2003). Creating conditions similar to those that occur during exposure of cells to microgravity induces apoptosis in human lymphocytes by 5-lipoxygenase-mediated mitochondrial uncoupling and cytochrome c release. *J Leukoc Biol*. **73**(4), 472-481.
26. Tauber, S., Lauber, B.A., Paulsen, K., Layer, L.E., Lehmann, M., Hauschild, S., Shepherd, N.R., Polzer, J., Segerer, J., Thiel, C.S. & Ullrich, O. (2017). Cytoskeletal stability and metabolic alterations in primary human macrophages in long-term microgravity. *PLoS One*. **12**(4), e0175599.
27. Pietsch, J., Ma, X., Wehland, M., Aleshcheva, G., Schwarzwalder, A., Segerer, J., Birlem, M., Horn, A., Bauer, J., Infanger, M. & Grimm, D. (2013). Spheroid formation of human thyroid cancer cells in an automated culturing system during the Shenzhou-8 Space mission. *Biomaterials*. **34**(31), 7694-7705.
28. Ma, X., Pietsch, J., Wehland, M., Schulz, H., Saar, K., Hubner, N., Bauer, J., Braun, M., Schwarzwalder, A., Segerer, J., Birlem, M., Horn, A., Hemmersbach, R., Wasser, K., Grosse, J., Infanger, M. & Grimm, D. (2014). Differential gene expression profile and altered cytokine secretion of thyroid cancer cells in space. *FASEB J*. **28**(2), 813-835.
29. Pietsch, J., Gass, S., Nebuloni, S., Echegoyen, D., Riwaldt, S., Baake, C., Bauer, J., Corydon, T.J., Egli, M., Infanger, M. & Grimm, D. (2017). Three-dimensional growth of human endothelial cells in an automated cell culture experiment container during the SpaceX CRS-8 ISS space mission - The SPHEROIDS project. *Biomaterials*. **124**(126-156).
30. Battista, N., Meloni, M.A., Bari, M., Mastrangelo, N., Galleri, G., Rapino, C., Dainese, E., Agro, A.F., Pippia, P. & Maccarrone, M. (2012). 5-Lipoxygenase-dependent apoptosis of human lymphocytes in the International Space Station: data from the ROALD experiment. *FASEB J*. **26**(5), 1791-1798.
31. Grosse, J., Wehland, M., Pietsch, J., Schulz, H., Saar, K., Hubner, N., Eilles, C., Bauer, J., Abou-El-Ardat, K., Baatout, S., Ma, X., Infanger, M., Hemmersbach, R. & Grimm, D. (2012). Gravity-sensitive signaling drives 3-dimensional formation of multicellular thyroid cancer spheroids. *FASEB J*. **26**(12), 5124-5140.
32. Aleshcheva, G., Bauer, J., Hemmersbach, R., Slumstrup, L., Wehland, M., Infanger, M. & Grimm, D. (2016). Scaffold-free Tissue Formation Under Real and Simulated Microgravity Conditions. *Basic Clin Pharmacol Toxicol*. **119 Suppl 3**(26-33).
33. Grimm, D., Wehland, M., Pietsch, J., Aleshcheva, G., Wise, P., Van Loon, J., Ulbrich, C., Magnusson, N.E., Infanger, M. & Bauer, J. (2014). Growing tissues in real and simulated microgravity: new methods for tissue engineering. *Tissue Eng Part B Rev*. **20**(6), 555-566.
34. Riwaldt, S., Pietsch, J., Sickmann, A., Bauer, J., Braun, M., Segerer, J., Schwarzwalder, A., Aleshcheva, G., Corydon, T.J., Infanger, M. & Grimm, D. (2015). Identification of proteins involved in inhibition of spheroid formation under microgravity. *Proteomics*. **15**(17), 2945-2952.
35. Riwaldt, S., Bauer, J., Pietsch, J., Braun, M., Segerer, J., Schwarzwalder, A., Corydon, T.J., Infanger, M. & Grimm, D. (2015). The Importance of Caveolin-1 as Key-Regulator of Three-Dimensional Growth in Thyroid Cancer Cells Cultured under Real and Simulated Microgravity Conditions. *Int J Mol Sci*. **16**(12), 28296-28310.
36. Pietsch, J., Sickmann, A., Weber, G., Bauer, J., Egli, M., Wildgruber, R., Infanger, M. & Grimm, D. (2011). A proteomic approach to analysing spheroid formation of two human thyroid cell lines cultured on a random positioning machine. *Proteomics*. **11**(10), 2095-2104.
37. Freed, L.E., Langer, R., Martin, I., Pellis, N.R. & Vunjak-Novakovic, G. (1997). Tissue engineering of cartilage in space. *Proc Natl Acad Sci U S A*. **94**(25), 13885-13890.
38. Stamenkovic, V., Keller, G., Nesic, D., Cogoli, A. & Grogan, S.P. (2010). Neocartilage formation in 1 g, simulated, and microgravity environments: implications for tissue engineering. *Tissue Eng Part A*. **16**(5), 1729-1736.
39. Ingram, M., Techy, G.B., Saroufeem, R., Yazan, O., Narayan, K.S., Goodwin, T.J. & Spaulding, G.F. (1997). Three-dimensional growth patterns of various human tumor cell lines in simulated microgravity of a NASA bioreactor. *In Vitro Cell Dev Biol Anim*. **33**(6), 459-466.
40. Lewis, M.L., Reynolds, J.L., Cubano, L.A., Hatton, J.P., Lawless, B.D. & Piepmeier, E.H. (1998). Spaceflight alters microtubules and increases apoptosis in human lymphocytes (Jurkat). *FASEB J*. **12**(11), 1007-1018.
41. Uva, B.M., Masini, M.A., Sturla, M., Bruzzone, F., Giuliani, M., Tagliafierro, G. & Strollo, F. (2002).

Microgravity-induced apoptosis in cultured glial cells. *Eur J Histochem*. **46**(3), 209-214.
42. Ulbrich, C., Westphal, K., Pietsch, J., Winkler, H.D., Leder, A., Bauer, J., Kossmehl, P., Grosse, J., Schoenberger, J., Infanger, M., Egli, M. & Grimm, D. (2010). Characterization of human chondrocytes exposed to simulated microgravity. *Cell Physiol Biochem*. **25**(4-5), 551-560.
43. Albi, E., Ambesi-Impiombato, F.S., Peverini, M., Damaskopoulou, E., Fontanini, E., Lazzarini, R., Curcio, F. & Perrella, G. (2011). Thyrotropin receptor and membrane interactions in FRTL-5 thyroid cell strain in microgravity. *Astrobiology*. **11**(1), 57-64.
44. Grimm, D., Bauer, J., Kossmehl, P., Shakibaei, M., Schoberger, J., Pickenhahn, H., Schulze-Tanzil, G., Vetter, R., Eilles, C., Paul, M. & Cogoli, A. (2002). Simulated microgravity alters differentiation and increases apoptosis in human follicular thyroid carcinoma cells. *FASEB J*. **16**(6), 604-606.
45. Vorselen, D., Roos, W.H., Mackintosh, F.C., Wuite, G.J. & Van Loon, J.J. (2014). The role of the cytoskeleton in sensing changes in gravity by nonspecialized cells. *FASEB J*. **28**(2), 536-547.
46. Uva, B.M., Masini, M.A., Sturla, M., Prato, P., Passalacqua, M., Giuliani, M., Tagliafierro, G. & Strollo, F. (2002). Clinorotation-induced weightlessness influences the cytoskeleton of glial cells in culture. *Brain Res*. **934**(2), 132-139.
47. Ingber, D. (1999). How cells (might) sense microgravity. *FASEB J*. **13 Suppl**(S3-15).

SOUNDING ROCKET AND BALLOON ACTIVITIES AND RELATED RESEARCH IN SWITZERLAND 2015–2017

Marcel Egli

Lucerne University of Applied Sciences and Arts, Institute of Medical Engineering,
"Space Biology Group", CH-6052 Hergiswil, Switzerland
Email: marcel.egli@hslu.ch

ABSTRACT

In Switzerland balloons, sounding rockets, and the height-altitude research stations of Jungfraujoch and Gornergrat remain attractive as research platforms for studies in microgravity, astrophysics, astronomy and atmospheric science. Because the two research stations in the Alps are offering alternative access to the upper atmosphere, particularly for long-duration studies, these places have been visited frequently by scholars to find answers to their unique scientific questions. The data gathered there however cannot replace measurements taken by balloons or sounding rockets and therefore Swiss researchers participate in such missions often.

One example of a balloon mission conducted by a Swiss consortium during the indicated time period is the "Integrated Vehicle Health Management System Demonstrator" or also called "Smartfish". A balloon was used to deliver the "Smartfish" to the target altitude. During the several drops conducted at ESRANGE, the system worked perfectly and thus proved its usability.

Besides enabling research access to the upper atmosphere, balloon and sounding rockets do also represent an excellent opportunity for students to get involved in space experiment and through this to acquire new skills. The "CEMIOS" project, which was proposed and conducted by students from the Lucerne University of Applied Sciences and Arts, is a good example of how Swiss students can profit from educational programs like REXUS/BEXUS. Goal of the "CEMIOS" project was to determine potential changes of the ion flux through the membrane of living cells under microgravity conditions. A compact electro-physiological experiment, applying a patch-clamp technique, was built to comply with the space requirements and to fit into the sounding rocket. The launch took place in spring 2016 and although the cells did not survive the flight, the students learned a lot by participating.

This report provides a short overview on Swiss projects within the framework of sounding rocket and balloon activities and related research performed between 2015 and 2017. A few studies are presented in more detail as examples of the current work Swiss research groups were engaged in.

1. INTRODUCTION

The interest of Swiss researchers in conducting sounding rocket and balloon experiments is constantly high, also in the current time period of 2015 to 2017. Like in the previous years, many experiments were conducted in the framework of the Esrange Andoya Special Projects (EASP) program, in which Switzerland is participating as member state.

This short report provides information on the experiments Swiss researchers have been conducting either on sounding rockets or on balloons. Two studies are presented below as examples of the many investigations of Swiss contributors that took place on these two research platforms. The first experiment is a feasibility study in which an Unmanned Automated Vehicle (UAV) was tested by dropping it from a stratospheric balloon. The second experiment is a student project called "CEMIOS" in which membrane properties of living cells were characterized under microgravity conditions during a sounding rocket flight.

The particular topography of Switzerland enables an alternative access to the upper atmosphere, besides using sounding rockets or balloons. There are two high-altitude research stations maintained on mountains in the heart of the Swiss Alps, the "Jungfraujoch" and the "Gornergrat" facility. Both of them are located above 3'000 m altitude and are offering permanent observation possibilities of the atmosphere either by manually operated or by remotely controlled instruments.
The investigations conducted at these high-altitude research stations can be regarded as related research to sounding rocket or balloon studies and are thus mentioned in this report. A selection of five experiments are presented in more details below, which illustrate the large variety of research topics carried out at these stations. They range from atmospheric physics to medicine. Additional information on the projects as well as the other activities at the high-altitude research stations can be found online at http://www.hfsjg.ch/reports/.

2. INTEGRATED HEALTH MANAGEMENT SYSTEM DEMONSTRATOR (iHMSD)

K. SCHAFROTH, H. PFLUGSHAUPT, R. KESSLER, M. MAAG,
METEOLABOR in collaboration with CSEM and EPFL, Switzerland

A Swiss consortium developed a high speed Unmanned Automated Vehicle (UAV) to validate this technology demonstrator as an integrated health management system capable of performing Earth atmosphere re-entries. The particular goal was to make the final approach of re-entry vehicles (like the space shuttle for example) less prone to structural failure, GPS failure etc.
The tasks of the study included the preliminary design of an entire iHMSD (Integrated Health Management System Demonstrator) mission, which comprised not only the HMS subsystems but also the HMS demonstration vehicle. The functional specifications of the HMS were analyzed as well as the mission scenarios in the framework of additional tasks.
Within just 11 months, the consortium was able to demonstrate controlled flights with the HMS (called "Smartfish"), a 1.2 kg heavy glider that finds its way to a predefined landing spot from an altitude of 32 km automatically.

Figure 1. The airborne "Smart fish" during a test flight Credits: Swedish Space Corporation SSC.

The flight principle of the "Smartfish" is based on a tuna fish. This means that a stable flight position is maintained by the particular shape of the glider, without the involvement of complicated steering movements.

During the iHMSD tests flight phase a total of 31 glider missions were flown:

- 9 helicopter and 13 balloon missions in Switzerland
- 9 balloon missions in Sweden

In addition, about 50 propelled RC flights were performed. These flights allowed to develop and test a variety of functions much faster than in a glider configuration.
The test flight results obtained in Switzerland were very encouraging. Unfortunately, legal issues of getting flight permissions from the authorities prevented the team to perform more and higher flights on Swiss territory.
The high-altitude flights were then performed at ESRANGE, Kiruna, Sweden. The time point in October 2015 was quite adverse because of the rainy weather conditions and specifically strong winds. During the Swedish missions, the glider got exposed to wind speeds of almost 200 km/h, which is equivalent to a hurricane of category 4. Nonetheless, several very successful missions were carried out with the iHMSD vehicle, reaching maximum speeds of almost Mach 0.9.
The strong autumnal winds in the north of Sweden created a variety of problems originally not foreseen and also failures. These included broken hotwire cables as well as landings at off target positions. In order to cope with the extreme situation, the team struggled passionately to improve the original, good working system on site.

3. CELLULAR EFFECTS OF MICROGRAVITY INDUCED OOCYTE SAMPLES (CEMIOS)

S. WÜEST, T. PLÜSS, M. FELDER, B. FLEISCHLI, Ch. HARDEGGER, L. RÜDLINGER, C. KOMOTAR, D. FRAUCHIGER
Lucerne University of Applied Sciences and Arts and University of Bern

Prolonged exposure to microgravity has severe effects on human physiology. Muscle wasting (muscle atrophy) is among the well-known adaptation processes initiated by microgravity exposure. Extensive research has demonstrated that living cells possess multiple mechanisms to detect external mechanical forces like gravity. However, the exact mechanism by means of which cells can detect gravity and translate this information into a biological signal (mechano-transduction) is still unknown. Previous studies have shown that mechano-sensitive ion channels could be among the key players involved.
A student team from the Lucerne University of Applied Sciences and Arts and the University of Bern got selected to examine potential effects of microgravity on mechano-sensitive ion channels on board a REXUS sounding rocket. The goals of the proposed study were first to design and build hardware that allows electro-physiological measurements necessary to monitor ion channel activities of *Xenopus laevis* oocytes during a sounding rocket flight. Such hardware did not exist before because this kind of measurements have never been conducted. The second goal was to follow the gating

properties of ion channels under microgravity conditions and thus to determine whether these membrane structures are indeed responding to changes in gravity.

Figure 2. "CEMIOS" flight hardware in ground based test configuration.

The hardware design was based on previously published principles. However, it had to be built from scratch in order to meet the specific requirements of sounding rocket flights and the related high integration demands. The electrical measurements were based on principles similar to the patch clamp technique. Medium exchange possibilities required to keep the oocytes alive were realized via a particular fluidic system driven by pressured air.

Figure 3. Late access insertion: The rocket was loaded with the living cells through the late access hatch shortly before launch. This assured best possible biological material for the experiments.

The flight took place in March 2016 with the REXUS 20 rocket. Its weight was 545.8 kg and measured 5.96 m in length, which is particularly long and heavy for REXUS rockets in general. Therefore, the apogee of 77.5 km was lower than under normal conditions. The weather conditions were ideal at that day so no environmental complications occurred during the flight.

The post-flight analysis showed, however, that all recording chambers were emptied as the rocket reached the microgravity phase. A closer analysis of the flight data suggests that the oocytes were ripped apart a few seconds after the launch of the rocket. This first attempt of using sounding rockets as a research platform for electrophysiological recordings thus demonstrated the method's limitation.

4. INVESTIGATION OF FREE TROPOSPHERIC NUCLEATION

F. BIANCHI, E. HERRMANN, J. TRÖSTL, C. FREGE, U. MOLTENI, J. LAMPILAHTI
Department of Physics, University of Helsinki

This project consists of a field study at the Jungfraujoch with state-of-the-art instruments to elucidate the various processes and mechanisms governing new particle formation (NPF) in the free troposphere at a molecular level. From 2 years extensive measurements with a neutral cluster air ion spectrometer we expect to gain an overview of the new particle formation events over quite a long-time period. So far, we have done 4 months of measurements. With this instrument, we are able to detect aerosols below 5 nm (0.8 nm - 45 nm mobility diameter for ions and 3 - 45 nm for neutral particles). We installed the NAIS at the Jungfraujoch East ridge in July 2016 with the help of the Paul Scherrer Institute (PSI) colleagues. This is a new location which became available only in the recent months. Since the installation the instrument is working properly and we were already able to detect several nucleation events. As mentioned already, in this mode, the instrument can measure down to 0.8 nanometers. This extremely good sensitivity is quite useful to detect nucleation from the earliest step where the first cluster is formed. In Fig. 4 we can see that there are some similarities between positive (bottom panel) and negative (top panel) ions but also differences. In both polarities, the nucleation event is quite clear and it starts well before 12. Here, the nucleation is observed earlier than in the neutral case because the cut off of the instrument is lower. All the polarities show clearly and in a similar way the nucleation event, however, there are also some differences, especially between positive and negative ions. For example, the red band around 1 nm visible in the positive ions is totally missing in the negative one. In the next upcoming weeks, we will further investigate this feature, however we are already quite confident that it is mainly due to some instrument artefact. At the moment, the measurements are working very well and in the next two years we hope to get more exciting results and hopefully we can couple the actual setup with extra instrumentation.

Some of the results have already been published in the top scientific journal "Science" in 2016.

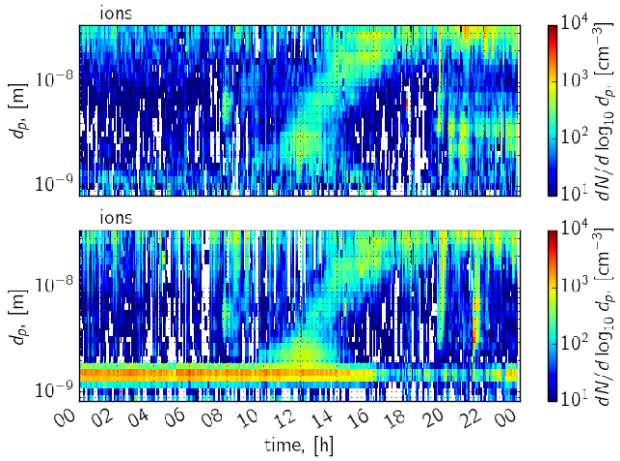

Figure 4. Ion size distribution measured by the NAIS. Negative ions displayed in the top panel and positive ions in the bottom one during a nucleation event recorded at the Jungfraujoch station.

5. DEVELOPMENT OF AN AIRBORNE SENSOR FOR THE RELIABLE DISCRIMINATION OF VOLCANIC ASH PARTTICLES FROM WATER DROPLETS OR ICE CRISTALS

E. WEINGARTNER, Z. JURANYI, D. EGLI, P. STEIGMEIER, H. BURTSCHER
University of Applied Sciences Northwestern, Switzerland

The DUWAS (DUal Wavelength Ash Sensor) is a new instrument that allows in-situ monitoring of refractory particles such as mineral dust or volcanic ash. A special feature of the employed technique is that the measurement is not biased by the presence of hydrometeors (i.e. cloud droplets or ice particles). Operated on an airplane, this technique can be used to quantify the exposure to hazardous volcanic ash. At aviation altitudes, water droplets and ice crystals are often present in a size similar to ash (> 1 micrometer) and their concentrations can reach the levels that are considered as the limits of the different volcanic ash contamination zones. An important difference to other laser based in-situ techniques is that the new method can quantify the volcanic ash exposure within water or ice clouds. Other techniques have difficulties in distinguishing ash particles from cloud droplets or ice crystals. The new aerosol detection method is based on dual-wavelength light scattering. The requirement that the sensor can distinguish cloud droplets and ice crystals from the hazardous refractory ash particles is achieved by comparing the light scattering properties of individual aerosol particles simultaneously at two different wavelengths, i.e. at λ = 660 nm (visible) and at λ = 2750 nm (infrared, IR). The envisaged component-specific particle differentiation makes use of the different scattering behavior of the aerosol components. Calculations have shown that the unique behavior of the refractive index of water at the IR wavelength of λ = 2750 nm allows distinguishing water droplets from other aerosol particles (such as volcanic ash). At the absorption band of water (in our case at λ = 2600 – 3400 nm), water droplets or ice crystals scatter much less radiation compared to their scattering further away from the absorption band. Mineral particles do not have such a distinct feature at 2750 nm. In the visible, water and volcanic ash show similar scattering intensities. Therefore, we calculate the ratio of the measured scattered light intensities at these two wavelengths.

The development of the DUWAS started in 2014, and its correct operation was first tested in the laboratory with various well-defined aerosols and water droplets. In December 2015, we installed the DUWAS at the High Altitude Research Station Jungfraujoch (3'580 m AMSL). The instrument was placed outdoors on the terrace of the research facility (see Figure 5A), where it was fully exposed to the harsh weather conditions prevailing at this site. The station is often engulfed in clouds (supercooled, mixed-phase and ice clouds) and during the campaign, the ambient temperatures were often below -20°C with extraordinary high wind speeds (up to 100 km/h). During the outdoor operation, intermittently small amounts of dust and ash particles were manually injected into the DUWAS sampling line to test its proper functioning. Figure 5B shows the measured R-value distributions for hydrometeors, dust and ash particles at the Jungfraujoch. The distributions are well separated; one even sees two distinct peaks present at the same time (green dashed line) when test dust particles were injected during cloudy conditions. This analysis shows that the DUWAS can clearly differentiate dust or ash particles from ambient cloud droplets and ice particles. In a next step, the DUWAS was tested in summer 2016 on-board of the research aircraft METAIR-DIMO. We installed the instrument in the measurement pod of the airplane, and a flow channel was designed and implemented such that the ambient aerosol (ca. 100 km/h) was isokinetically directed to the DUWAS detection volume. Overall, four flights were conducted over the Swiss Plateau, and the ambient aerosol was characterized out-of-clouds as well as within natural cloud edges.

These airborne measurements confirm the findings from the Jungfraujoch: In flight, the DUWAS was able to discriminate cloud particles from other super-micrometer sized dust-like particles that were present at low concentration as a "natural background" in our ambient atmosphere. Calculations show that the instrument would be capable of measuring volcanic ash concentrations that are considered dangerous for air traffic.

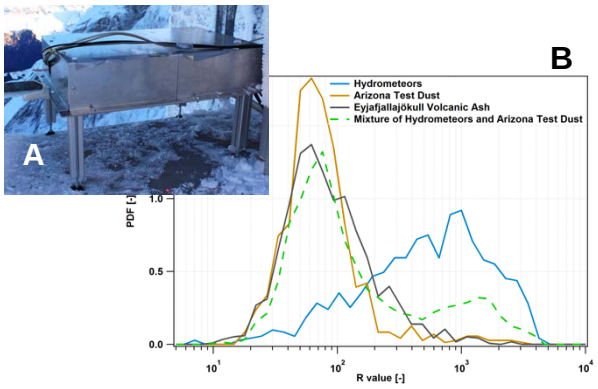

Figure 5. A: Picture of a demonstrator, placed at the Jungfraujoch research station. B: Distributions of droplets and ice crystals in contrast to Arizona test dust and ash particles sampled of the Eyjafjallajökull volcano.

Based on all these tests we plan to further develop the sensor. As a university, we are looking for future collaborations with companies that are interested in commercializing this new technique. A patent application on this method has been filed.

6. STUDY OF SOLAR AND GALACTIC COSMIC RAYS

R. BUETIKOFER
Physics Institute, University of Bern

The Physics Institute at the University of Bern, Switzerland, operates two standardized neutron monitors (NM) at Jungfraujoch: an 18-IGY NM (since 1958) and a 3-NM64 NM (since 1986). NMs provide key information about the interactions of galactic cosmic radiation (GCR) with the plasma and the magnetic fields in the heliosphere and about the production of energetic CRs at or near the Sun (solar cosmic rays, SCR), as well as about geomagnetic, atmospheric, and environmental effects. They ideally complement space observations. The NMs at Jungfraujoch are part of a worldwide network of standardized CR detectors. By using the Earth's magnetic field as a giant spectrometer, this network determines the energy dependence of primary CR intensity variations in the GeV range. Furthermore, the high altitude of Jungfraujoch provides good response to solar protons ≥ 3.6 GeV and to solar neutrons with energies as low as ~250 MeV. Neutron monitors play also an important role in the space weather domain.
In 2016, operation of the two NMs at Jungfraujoch was pursued without major problems. No technical modifications were necessary. The recordings of the NM measurements are published in near-real time in the neutron monitor database NMDB (www.nmdb.eu). Figure 1 shows the relative monthly count rates of the IGY neutron monitor at Jungfraujoch (lower panel) since it was put into operation in 1958. The GCR are always present, and their intensity shows a variation of about 11 years in anti-correlation with the solar activity characterized by the monthly mean total sunspot number. Figure 6A shows the superposition of the 13-month smoothed monthly total sunspot numbers over the solar activity cycles from cycle 20 through cycle 24. The starting point is each time the lowest smoothed monthly total sunspot number between two solar activity cycles. The duration of the last solar activity cycle (cycle 23, blue curve in Figure 6B) was with more than 12 years longer than the typical length of around 11 years. In contrast, the length of the current activity solar cycle (cycle 24, red curve in Figure 6B) will probably be shorter, maybe less than 10 years, although the gradient of the curve may still decrease significantly in the next months and the duration of cycle 24 become longer than expected. The maximum smoothed monthly sunspot number during cycle 24 was about 35% smaller than during cycle 23, i.e. the solar activity was not very high in the current solar activity cycle. In consequence, no large drops of the galactic cosmic ray intensity near Earth were observed by the worldwide network of neutron monitors. These so-called Forbush decreases are caused by traveling coronal mass ejections (CMEs) beyond the Earth's orbit. In addition, the neutron monitors so far only observed one clear solar energetic particle (SEP) event during the current solar activity cycle. This SEP event on 17 May 2012 was however only observed by high latitude neutron monitor stations, i.e. it was not seen by the two neutron monitors at Jungfraujoch.

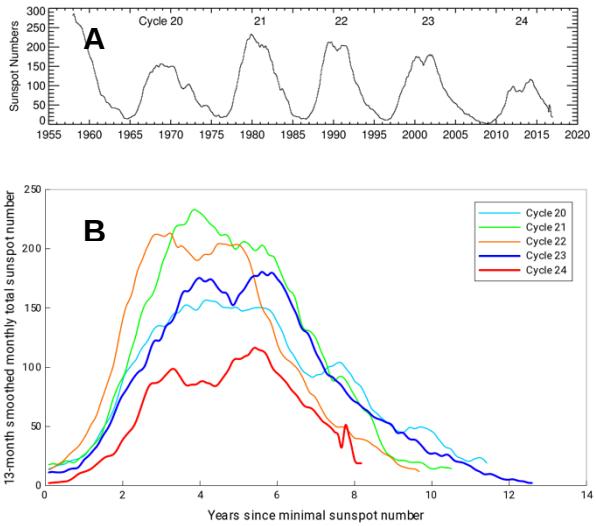

Figure 6. A: Smoothed total sunspot numbers since 1955 (reference). B: Superposition of smoothed total sunspot numbers of the solar activity cycles 20-24.

7. ISOTOPIC COMPOSITION OF N_2O AT JUNGFRAUJOCH HIGH ALTITUDE STATION

R. BÜTIKOFER, J. MOHN, L. YU, E. HARRIS, CH. ZELLWGER
Laboratory for Air Pollution and Environmental Technology, Empa

N_2O is a strong greenhouse gas with a global warming potential 298 times larger than of CO_2, and in addition it is the strongest ozone depleting substance emitted in the 21st century. N_2O concentrations are rising at a rate of 0.2-0.3% per year globally due to anthropogenic emissions. Anthropogenic sources of N_2O are dominated by disperse and highly variable agricultural soil emissions, which, combined with the long lifetime of N_2O, makes source apportionment – and thus mitigation – challenging. Although the total global source and sink strengths for N_2O are relatively well-constrained, individual source contributions and the factors causing seasonality and inter-annual variability in N_2O concentration and growth are poorly known. Isotope measurements combined with modelling show great potential to unravel sources and processes, however currently data is sparse and precision is often limiting for interpretation.
This project aims to continue monitoring the mixing ratios and isotopic composition of N_2O at the Jungfraujoch high altitude research site using biweekly/weekly sampling with high precision offline analysis at Empa. In 2015-16, this project was extended to include analogous measurements from the Cape Grim (Tasmania) air archive, to compare isotopic trends at Jungfraujoch to this important Southern hemisphere baseline site. Isotopic composition of the flask samples is measured at Empa using preconcentration unit coupled to quantum cascade laser absorption spectroscopy (QCLAS), and mole fraction is measured directly using QCLAS in the GAW-WCC laboratory at Empa.
The results in Figure 7 show a distinct trend in N_2O mixing ratio of +1.2 ppb y-1, higher than the global average of 0.73 ppb y-1.

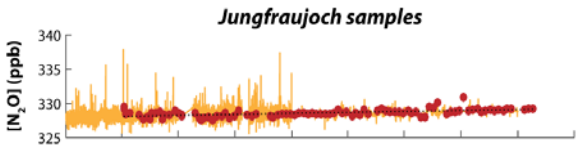

Figure 7. N_2O mixing ratio at Jungfraujoch from in situ measurements (orange) and flask samples (red).

Continuing these measurements and comparing them with seasonal and long-term trends from Cape Grim will provide exciting new insights into the global N_2O budget. In addition, the data are critical to provide an N_2O background to interpret isotope data from other sites in Switzerland.

8. THE IMPACT OF HIGH ALTITUDE ON CANCER

M. THIERSCH and M. GASSMANN
Institute of Veterinary Physiology, University of Zurich

High altitude represents a challenging environment that requires precise adaptation of the human body. Of note, even "adapted" highlanders (e.g. the South American Quechua, Fig. 8) might develop severe high altitude related diseases like chronic mountain sickness (CMS). It is surprising, nevertheless, to find that humans populating such an inhospitable environment display reduced cancer mortality compared to those living at low altitude and that this effect is independent of ethnicity and socio-economical environment. Although the reasons and the underlying mechanisms remain a matter of speculation, it seems very likely that the systemic adaptation to hypoxia activates pathways that prevent cancer formation and/or delay tumor growth. Elucidating these mechanisms will lead to the development of new (hypoxia-based) therapeutic approaches and related drugs and may be a valuable contribution to fight cancer. In our project, we analyze the impact of acute exposure to high altitude and isobaric hypoxia (Zurich, hypoxia chamber) on cancer progression, chemotherapy efficacy and tumor metabolism in comparison to low altitude. To test our hypothesis, we generated allograft mouse models with murine lung and breast cancer cells and kept these mice either at low altitude (Zurich, 400 m), at high altitude (Jungfraujoch research station, 3'580 m) or in an isobaric hypoxia chamber (Zurich).

Our analyses are ongoing and so far the following conclusions can be made:

1) no difference in tumor growth of the primary tumor
2) tumors at JFJ might respond better to chemotherapy (to be verified)
3) mitochondrial respiration in tumors of mice kept at JFJ is reduced (in complex II)
4) anemia of cancer, comorbidity and a poor prognosis factor, can be rescued in the lung cancer model, but not in the breast cancer model in JFJ or hypoxia exposed mice

Still ongoing analyses:

1) metabolomics – analyzing the changes of different metabolites
2) histology (blood vessel formation [tumor perfusion] and quantifying the size of hypoxic

tumor areas [tumor hypoxia correlates with aggressiveness])

3) metastasis in liver and lung (repetition animal experiment with labeled cells in 2017)

Figure 8. Quechua people of South America (picture from https://www.pinterest.com).

9. ACKNOWLEDGEMENT

I would like to thank all of the contributors from the different institutions for providing the input necessary to write this report. Furthermore, I gratefully acknowledge the support of the Swiss Space Office (SSO) of the State Secretariat for Education, Research and Innovation (SERI), as well as of the International Foundation High Altitude Research Stations Jungfraujoch and Gornergrat (HFSJG).

THE PACKMAN RADIATION AND ENVIRONMENTAL INSTRUMENT FOR SPACE WEATHER STUDIES.

María-Paz Zorzano[1,2], Javier Martín-Torres[1,3], Thasshwin Mathanlal[1], Abhilash Vakkada Ramachandran[1], and Álvaro Soria-Salinas[1]

(1) Atmospheric Sciences Group, Department of Computer Sciences, Electrical and Space Engineering, Lule University of Technology, 971 87 Lule, Sweden.

(2) Centro de Astrobiolog'ıa (CSIC-INTA), Torrej'øn de Ardoz, Madrid, Spain

(3) Instituto Andaluz de Ciencias de la Tierra (CSIC-UGR), Armilla, Granada, Spain

ABSTRACT

To date, there is a missing gap of information regarding the amount, energy, time variability, and type of space radiation that reaches the lower layers of the atmosphere, as well as on its geographic and altitude distribution, and thus there is not a complete understanding about the role of space weather on the Earth's atmosphere, and of its potential impact on infrastructures and climate. The PACKMAN (PArticle Counter k-index Magnetic ANomaly) instrument is a small, robust, light and scalable instrument that monitors continuously gamma, beta, alpha radiation and muons. This instrument includes environmental sensors to monitor pressure, temperature, relative humidity, and magnetic perturbations and includes data archiving, GPS and communication capabilities. Our present research is focused on Arctic and Subarctic regions. To generate this data base we designed an open source, autonomous system, with Commercial Off The Shelf (COTS) components that can monitor continuously a set of critical variables at multiple latitudes and heights in the atmosphere (in balloons). Through the deployment of multiple ground-based PACKMAN units we shall generate a network of surface instruments that acquires the same observational data set. The PACKMAN instrument system development has been completed and 'flight qualified' through test and demonstration (both on ground and space). We have demonstrated the technology readiness level (TRL) of TRL-8 of the flight-model of PACKMAN within a stratospheric balloon campaign. In the future we intend to launch similar PACKMAN units within balloon platforms in a set of predefined campaigns (circumpolar, and tropospheric soundings) to investigate in-situ the vertical profiles of radiation in the atmosphere in the polar region. The joint analysis of the measurements from these campaigns, both in-situ and on ground, with existing orbiter instruments (such as GOES in LEO orbit) will improve our understanding of the role of space radiation, from galactic cosmic rays to solar energetic particles, on the Earth atmospheric physics and chemistry. This network will provide real-time, open-policy access to a standardised data set of radiation and environmental measurements, at multiple sites. Besides its basic scientific use, the data of this project shall be used to educate and engage the public, or other industrial actors on space weather research.

Key words: Space Weather; Atmosphere; Environmental; Radiation; Detector; Balloon; Arctic; Geomagnetic field.

1. INTRODUCTION

The atmosphere of the Earth is continuously bombarded by space energetic charged particles [1]. The majority of energetic particles (EPs) originate from outer space and are known as cosmic rays (CRs), consisting mostly of protons. These particles penetrate into the Earth's atmosphere and can influence a variety of atmospheric processes [2, 3]. It has been known for a long time that the intensity as well as the energy spectrum of the galactic cosmic rays is modulated by solar activity, and thus the cycle of Galactic Cosmic Rays and the radiation from the Sun are generally anti-correlated with some time lag. In addition, the solar activity variability affects the solar energetic particle (SEP) rate reaching the Earth and, in the case of large storms, it also affects the geomagnetic field in the polar regions, and possibly the penetration depth and distribution of charged particles, but its influence on Earths climate is to-date unknown. SEP are less energetic and consist mainly of protons, electrons and alpha-particles (and small amounts of 3He and heavy ions up to Fe). They have their origin on the Sun and precipitate into the atmosphere both driven by solar wind conditions and intrinsic magnetospheric processes. The multitude of processes and their dynamical variability leads to high variations in spatial, temporal, flux and energy distributions of the precipitating particles. SEP have been monitored for years from instrumentation on orbiters such as the Geostationary Operational Environmental Satellite (GOES) platform. The GOES Space Environment Mon-

itor archive is a key component of the National Space Weather Program that is used to provide timely and reliable space environment observations and forecasts of NOAA (National Oceanic and Atmospheric Administration) because SEPs are known to affect spacecraft and, in the case of large solar storms, they can also penetrate the atmosphere, cause damage on the Earth electronic components and networks and affect the geomagnetic field in the polar and sub-polar regions. GOES monitors on orbit electrons, protons, magnetic field perturbations and X-rays fluxes. The local magnetic perturbation on the Earth surface, k-index, is used to monitor SEP and cosmic ray activity and give alerts about geomagnetic storms. Recent balloon measurements suggest, that contrary to what was expected before, SEP can penetrate the atmosphere and reach the troposphere at mid-latitudes, see [4]. This may produce atmospheric ionisation and enhance cloud nucleation affecting the Earth climate. During a SEP event associated with a solar flare on April 11, 2013, the vertical ionisation rate profile was measured using a balloon-borne detector, which showed enhanced ionisation with a 26 per cent increase at 20 km. It was evident from this experiment that the Geiger count rates were increased during the high SEP event, reaching a maximum of 67 cpm, with an enhancement from the maximum height reached (25 km) down to 10 km, indicating penetration of energetic particles well into the troposphere. However, no neutrons detection were detected at the surface; and thus, the primordial energetic particles did not have such an extremely high intensity as those of galactic cosmic rays (GCRs). This demonstrates that, SEPs are not only capable of reaching altitudes in the lower atmosphere at mid-latitudes but that the atmospheric electrical parameters near the surface may also undergo substantial associated changes. This solar-terrestrial coupling through SEP activity may have implications for a number of atmospheric processes, including ionisation variability and its influence on lower atmosphere cloud processes.

To date, there are very scarce balloon measurements of atmospheric radiation profiles and very few surface radiation detectors are devoted to monitoring continuously the amount of radiation reaching the surface. This impedes having an adequate knowledge of the impact of space weather phenomena on terrestrial infrastructures and climate. The role of latitude and local geomagnetic anisotropies on the amount of radiation that reaches the surface has also been very poorly investigated. To mitigate this, we have designed a low-cost robust space weather station that can be operated anywhere on the planet surface as well as on the lower atmosphere and near space environment. The purpose of this project was to develop an open source, autonomous space weather station, with Commercial Off The Shelf (COTS) components, that can monitor continuously a set of critical variables at multiple latitudes on the surface of the Earth and on rockets and balloons. The final goal is to generate a network of instruments operating simultaneously at multiple latitudes and heights, providing an open access data base that can be used to understand the interaction of space radiation with environmental variables of the Earth surface such as the geomagnetic field and its variability, and atmospheric variables such as pressure, temperature, density and relative humidity and eventually with long-term climate deviations.

Some previous attempts have demonstrated the feasibility of this project. For example a team of researchers of the Massachusetts Institute of Technology (MIT), [MIT project], have recently proposed the construction of a Desktop Muon Detector for undergraduate laboratory practices with low-cost components. The concept was only devoted to the laboratory demonstration of the detection of muons using silicon photomultipliers and plastic scintillators. Our instrument includes also commercially available technologies, but allows for continuous monitoring of alpha, beta, gamma and muon charged particles as well as to monitor the environment (namely the magnetic field perturbations and pressure, temperature and humidity). Our innovative low-cost instrument measures in a continuous way, archives data and finally, because its communication capabilities, can send data remotely from any location to a common data base. The BEXUS, European programme for student experiments on balloons had a two instruments to study the cosmic ray induction into the Earths atmosphere by flying the Instrument aboard the balloons. The Timepix@space on BEXUS-7 and CRIndIons on BEXUS-9 campaigns focussed on the cosmic ray measurements using Timepix detectors that are USB-powered particle trackers based on Medipix technology developed at CERN. The USB interface was developed at Institute of Experimental and Applied Physics of Czech Technical University in Prague. Both campaigns used the Medipix detectors for studying the energetic particles. The Medipix detectors are photon counting and particle tracking pixel detectors. They are unfortunately not open source which is a requirement of our concept, in order to engage multiple agents in a distributed network of space weather stations. We shall use instead two Geiger Muller tubes that can also be operated in coincidence mode which are sensitive to these energetic particles and stand advantageous in terms of lower cost and availability. The concept of using coincidence detectors was instigated by the physics lab open source community and shows the coincidence detectors designed by physics lab using SBM-20 Geiger Tube and a Theremino micro-controller device. The PACKMAN uses a more sensitive LND-712 Geiger and utilises the interrupt service routine (ISR) of Raspberry Pi for performing the coincidence computing. These Geiger counters have demonstrated recently their utility for balloon campaigns for cosmic rays and muon detection [6].

Finally, a similar distributed network of surface operation low-cost monitoring sensors has been recently implemented by uRADMonitor [uRAD- project]. The uRADMonitor global environmental network consists of a set of a distributed set of automated monitors, that measure CO2, radiation, temperature, pressure and relative humidity. The uRADMonitor project relies on civic attitude at a global level. Individuals purchasing a detector and adhering to the network contribute with data to a worldwide initiative. The measurements of each new node are transmitted automatically, via the Internet, using a cable

Ethernet connection and finally a server works as the centralised system that receives and processes environmental data showing online a graphical representation of the observations. The radiation data however are not available in open format and the magnetic field perturbation which is usually taken as proxy for solar activity is not included in the set of variables.

Our instrument shall, furthermore, be operative within a space environment and in balloons, to provide comparable measurements to the surface instruments. With this concept in mind we have defined the instrument functional requirements. As we shall see in the following sections, the system development phase has been completed and qualified through test and demonstration in a representative space and ground environment reaching a proven Technological Readiness Level (TRL) of 8.

2. INSTRUMENT FUNCTIONAL REQUIREMENTS AND IMPLEMENTATION

The PACKMAN is designed to be an space weather station that can operate autonomously and acquire data that are logged in a file in a sequential manner at predefined rate and that are then stored in a card for later data submission. The instrument shall acquire environmental observations of Pressure (P), Relative Humidity (RH), Temperature (T), and magnetic flux variation simultaneously in three axes, with a particle count detector and Global Positioning Sensor that gives information about geolocalization and time stamp. These sensing units are divided into three different conceptual modules:

- Module-I includes two LND-712 Geiger counters. The LND-712 is a highly sensitive thin end window alpha-beta-gamma detector. Alpha particles, are emitted during radioactive decays and consist of two protons and two neutrons (essentially the nucleus of a helium-4 atom). Due to their charge and mass, alpha particles interact strongly with matter, and only travel a few centimetres in air. Beta radiation takes the form of either an electron or a positron (a particle with the size and mass of an electron, but with a positive charge) being emitted from an atom. Due to the smaller mass, it is able to travel further in air. Gamma radiation, unlike alpha or beta, does not consist of any particles, instead it consists of a photon of energy being emitted from an unstable nucleus. Gamma rays can be stopped by a sufficiently thick or dense layer of material, where the stopping power of the material per given area depends mostly (but not entirely) on the total mass along the path of the radiation, regardless of whether the material is of high or low density. However, as is the case with X-rays, materials with high atomic number such as lead or depleted uranium add a modest amount of stopping power over an equal mass of less dense and lower atomic weight materials (such as water or concrete).

  In addition to the independent counts per minute of each Geiger tube, the data are also analysed for coincident events. In a future implementation, a lead plate of about 2mm may be inserted in the slots that surround the second Geiger tube to shield it away from alpha and beta particles. It shall ensure that the counts received correspond only to muons. This can then be compared with the unscreened Geiger to differentiate particle types. The energy of the particles determines the thickness of the lead plate to be used. A Raspberry Pi is used in the coincidence detection mode using GPIO (General Purpose Input Output) pins configured as interrupt service routine (ISR). The ISR is used to monitor the rising edge of both the Geiger tube outputs.

- Module-II of the PACKMAN uses three FGM-3 fluxgate Magnetometers, placed perpendicularly along the three axis. The FGM-3 devices are very high sensitivity magnetic field sensors operating in the 50 microtesla range (0.5 oersted). They are simple, essentially three terminal devices, operating from a single +5volt supply, the connections being ground, +5v and output. The output is a robust 5 volts rectangular pulse whose period is directly proportional to the field strength, giving a frequency which varies inversely with the field. The typical period swing for the full range of an FGM-3 is from 8.5 ms to 25 ms (120 KHz to 50KHz), a clear indication of its high sensitivity. The fluxgate magnetometers are not calibrated and the sensor recorded data are the fluxgate frequencies of the three magnetometers. Calibration is not included in the scope of the project. We will show instead how the time variation of frequency changes is used to investigate the geomagnetic field variations dB/dt and thus to detect solar activity. The Atmel Atmega328P-PU microcontroller is used in the Module-II for the Magnetometers. It is a 8-but micro-controller and has a 16 Mhz crystal oscillator that serves as the clock. The micro-controller interrupts is capable of operating at every 0.0625 microseconds. The Internal timer interrupt of the micro-controller is used to determine the frequency of the FGM-3 magnetometers. The frequency level that can be measured is in the range of 1 Khz to 8 Mhz, which covers the range of frequency that we would like to measure. Using an I2C interface the Atmega micro controller is linked to Module III.

- Module-III of the PACKMAN instrument contains generic atmospheric parameter measuring sensors such as Temperature, Humidity, Pressure, and a Global Positioning System(GPS) module to have the time stamp for the measurements. This module receives the data through I2C from module II, and using serial communication it communicates the data to the Raspberry PI which stores the data on to a SD card, serving as a data logger. The characteristics of the sensors used in the environmental module package are summarised in table 1 and 2.

  There are three temperature measuring sensors in

Table 1. PACKMAN sensors specifications

Variable	Senso	Operating Range	Resolution
T	DS18B20	-55C to 125C	$\pm$ 0.5 C
T	SHT10	-40C to 123.8 C	$\pm$ 0.5 C
T	BMP280	-40C to 85 C	$\pm$ 0.01 C
P	BMP280	30 to 110 10^3 Pa	0.16 Pa
RH	SHT10	0 to 100 %	$\pm$4.5 %
Radiation	LND-712	NA cpm	NA cpm
Magn.Flux	FGM-3	$\pm$ 50 μT	NA

Table 2. PACKMAN management units

Utility	Model
Time/place/stamp	MTK 3339
Microcontr., usb port	Arduino Mega 2560
Magn.-to-Freq.	Atmega328P- PU

Module-III. The DS18B20 sensor is mounted along with the Magnetometer module to determine the temperature of the triaxial magnetometer setup because it is highly temperature dependent. In satellites, the fluxgate magnetometers are placed on a long boom projected away from the satellite body with a heater to maintain the boom at a controlled temperature. The Cassini-Huygens mission had a 1W heater on the 11m boom to maintain the temperature of the triaxial fluxgate sensors. On Earth surface-based magnetometry for Auroral monitoring stations, the fluxgate sensors are buried deep in the ground 1m to 2m in the soil to maintaining a a constant operating temperature.

Finally, a GPS module MTK3339 is used to provide time stamp to the sensor readings taken. It is a -165 dBm sensitivity, 10 Hz update, 66 channel modules that has a built-in GPS antenna. An Arduino Mega 2560 is used in this module unlike using dedicated micro controllers as used in Module-I and Module-II because of the advantage of using the Arduino Mega 2560 built in Serial communication to USB for connecting to a computer.

- Within its current implementation the PACKMAN is a low-cost, light and robust instrument that can operate with a 12V power supply such as a battery, drawing an average power of 0.45Ah. The dual voltage regulation protects the circuitry from sudden voltage surges. The power consumption of the instrument is 5.4W per hour. With a 55AH GEL Battery, the instrument can run for approximately 5 days. With a solar panel coupled to charge the battery we can easily have a week of autonomous data. The mass of the hardware is 600 g and its modular arrangement allows portability of the instrument. The indoor measurements can be used without any additional cover, while for outdoor runs, an external cover protection is needed to prevent water seepage and control sudden temperature changes. The data is stored on a SD card which can have a maximum capacity of up to 32 GB. At a data frequency of 60 Hz, the data generated per day amounts to 90 KB average. The volume required to install all the electronic components and sensors is roughly 15cm x 20 cm x 15 cm.

3. EARTH SURFACE OBSERVATIONS

We shall next present a few examples of operation of PACKMAN. Two units of PACKMAN have been installed in the Arctic and sub-artic region for continuous indoors operation. One is installed at the LTU Space Campus in Kiruna (67° 51 N, 20° 13E, with an elevation of 532 m) and at the LTU University Campus in Lule (65° 35'N, 22° 9'24E and an elevation of 8 m above sea level). Both locations are separated by circa 270 km. Kiruna is 145 km north of the Arctic circle, whereas Lule is about 100 km south of the Arctic circle.

The PACKMAN data includes information about the ambient temperature and RH within the labs where they operate. This information is not useful for the research presented here. However the ambient pressure, the two geiger tubes and the fluxgate frequencies shall be here shown to illustrate the operation and data interpretation. Two geiger tubes are placed in parallel, recording the counts per minute. A synchronous flag is added when both detect a particle event within a period of 100 ms or less. These events may be produced by highly energetic particles.

On Sunday 09/07/2017 the planetary k_p index went above the 4 threshold, reaching a value of 5 for some hours, indicating a solar storm. The k-index, and by extension the Planetary K-index, k_p, are used to characterize the magnitude of geomagnetic storms. K_p is an excellent indicator of disturbances in the Earth's magnetic field and is used to decide whether geomagnetic alerts and warnings need to be issued for users who are affected by these disturbances. The principal users affected by geomagnetic storms are the electrical power grid, spacecraft operations, users of radio signals that reflect off of or pass through the ionosphere, and observers of the aurora. The PACKMAN fluxgate magnetometers are used to detect temporal disturbances in the Earth's magnetic field by comparing instantaneous values with respect to the last 12 minutes average measurements. The time sequence of deviation measurements for the fluxgate frequencies in the three axis, f_x, f_y and f_z, are compared in Figure 1 with the absolute magnetic field measurements provided by the proton magnetometer of the IRF (Space Campus of Kiruna). Both sensing devices detect the magnetic perturbation produced by the solar geomagnetic activity.

The geiger counters detect the number of particles per minute. Figure 2 shows the particle count measured by the geigers and compares with the neutron counts of the

nearby observatory of Oulu, in Finland. There was no extraordinary cosmic event which would have led to increases in neutrons. We may perhaps observe a reduction of neutrons (gamma ray) during the increase of Solar activity from 2 to 4 AM, this is called Forbush decrease and we also see it somehow in the cpm of the geigers.

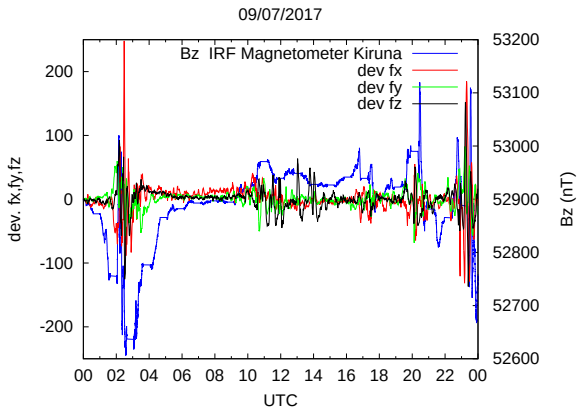

Figure 1. Comparison of PACKMAN fluxgate magnetometers with the absolute magnetic field measured by the IRF proton magnetometer during the solar storm of 09/07/2017, both operated at the Space Campus in Kiruna. The onset of the solar storm is detected at 02:00 with the geomagnetic perturbation that is sensed at the surface of Earth in high latitude regions such as Kiruna.

By operating two geiger tubes we can study the synchronous counts (assuming that they are produced by highly relativistic particles like muons) and see changes associated to both the solar induced perturbation and the atmospheric total column of air, i.e. the density (and pressure), see Figure 3. It is the density that conditions the evolution of arriving cosmic ray showers that reach the surface, so we need to take into account this parameter for the balloon campaign.

Figure 4 compares the radiation counts per minutes and the synchronous counts of two PACKMAN units monitoring space weather at different sites, namely Kiruna and Lule, during the onset of another Solar Storm, that reached a kp=6, on 16/07/2017. Overall the total particle count and the synchronous particle counts are lower in Lule. This is understandable due to multiple concurrent effects: 1) the higher atmospheric pressure, i.e. longer particle traverse path due to the proximity to the sea level and 2) the closeness of Kiruna to the magnetic pole. Figure 5 shows, for the same day, the vertical magnetic field

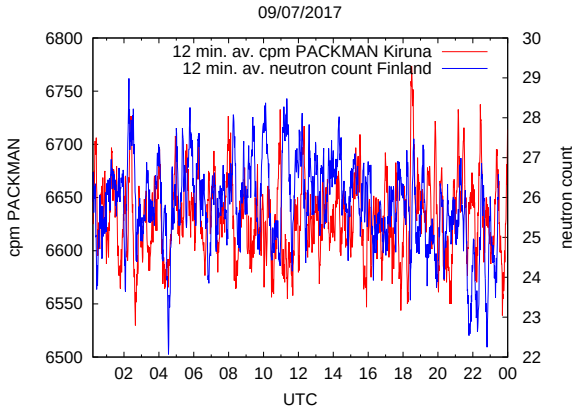

Figure 2. Comparison of PACKMAN radiation counts with the neutron data count of the Neutron Monitor in Oulu, Finland, during the onset of the solar storm of 09/07/2017. The intense solar activity at 02:00 produces a Forbush decrement of galactic cosmic rays and this is observed as a reduction in particle counts at the surface of Earth, in Kiruna by PACKMAN, and of neutrons in Oulu.

variation as measured by both PACKMAN units and by a magnetometer located in Abisko. The three instruments show the periods of large solar activity. Finally, in Figure 6, we compare for the same day, the on-orbit measurement of X-flares of high-energy ionising photons, with the surface based measurements of synchronous counts in Kiruna, and in Figure 7, the synchronous particle count of the storm of 09/07/2017 with on-orbit measurements of protons and electrons.

4. BALLOON CAMPAIGN: TROPOSPHERE AND STRATOSPHERE RADIATION PROFILE.

A balloon flight model of PACKMAN was included as scientific payload in a stratospheric balloon flight managed by Zero2Infinity SL during the night and early morning of the 29th to 30th August 2017, see Figure 8. Zero 2 Infinity is a Spanish company that provides access to space by lifting payloads into Near Space using balloon technology for scientific and commercial purposes. Additionally, the company is currently developing a balloon based launch vehicle to put payloads up to 75kg in orbit. This company runs a program, called ELE-

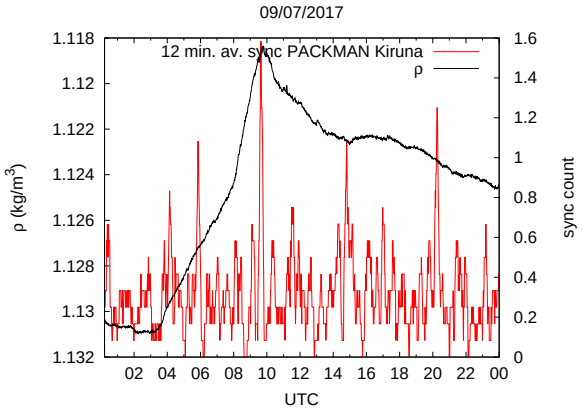

Figure 3. PACKMAN measurements of synchronous particle counts and atmospheric density at the surface, during the solar storm of 09/07/2017. The rate of cosmic rays at ground level varies in time due to changes in both the incident flux at the top of the atmosphere (which can be modulated by the magnetic field of the sun as during the period around 02:00) and changes in atmospheric gas density variations, which are in turn related to the pressures and temperatures. The maximal count of synchronous particles is detected during the hours of minimum atmospheric densities.

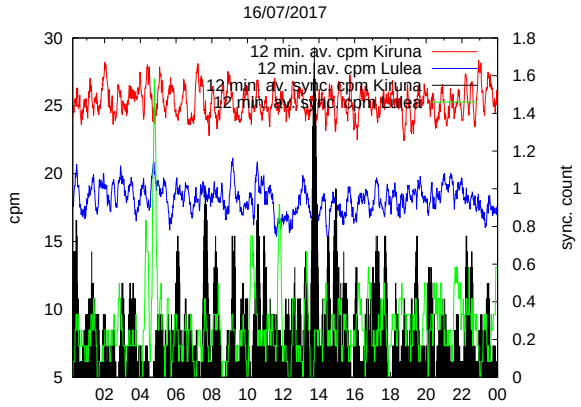

Figure 4. PACKMAN measurements of synchronous particle counts and total particle counts per minute at two sites on the surface of Earth, Kiruna and Lule, during the solar storm of 16/07/2017. The amount of radiation reaching Lulea is lower, as expected, because it is at the sea level and because is further away from the magnetic pole.

VATE, which provides a platform for testing of commercial satellites components and for Earth observation science. Zero2Infinity has been successfully lifting heavy commercial payloads into Near Space using their balloon technology since 2009. The balloon was released from Cordoba Airport, Spain, (37°50 N/ 4° 50 W, elevation 91 m), at night-time, during a period of low solar activity (kp=2). Cordoba is an ideal location for operation of these stratospheric campaigns because of the steady and gentle wind regime that allows for accurate forecast of traverse trajectory and landing points. The balloon landed after 5 hours, the scientific payload was recovered and the hardware was fully operative.

The weight of the flight model hardware was 600 g, this model included also an Inertial Module Unit to provide ancillary information to the data acquired during the flight. PACKMAN was framed within two boxes to hold the structure, prevent from damage during landing and provide partial thermal insolation, see the inset in Figure 8. This flight campaign was aimed at providing a reference example of reduced space weather effects on the atmosphere: i.e. at a mid-latitude, far from the polar geomagnetic field enhanced interaction with space weather activity, at the night-side with no X-flares solar activity and during a period of reduced solar activity. A twin model of PACKMAN was operating simultaneously from the ground surface.

An example of the preliminary observations acquired during the ascent, floating and descent phases is shown in Figure 9. PACKMAN captured the Pfoltzer maximum of radiation within the heights of 15 km to 20 km. Within this region the radiation counts per minute are about 20 times greater than at sea-level, as expected the radiation counts descend as we approach the surface and the pressure increases. For completeness the temperature sensed within the PACKMAN box is included to demonstrate the thermal range of operation of the hardware. The maximal height of floatation was about 28 km, with minimal pressures measured were about 16 mbar (1600 Pa). The minimal external temperatures in the stratosphere, as sensed by an additional external temperature sensor, were of the order of -65° C.

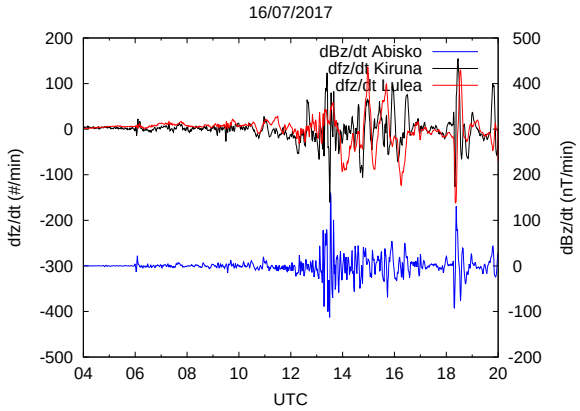

Figure 5. Comparison of dB/dt as measured by the magnetometer of Abisko, and the frequency change of the two PACKMAN fluxgate magnetometers during the onset of the solar storm of 16/07/2017. The magnetometers detect unequivocally the solar storm perturbation of the geomagnetic field.

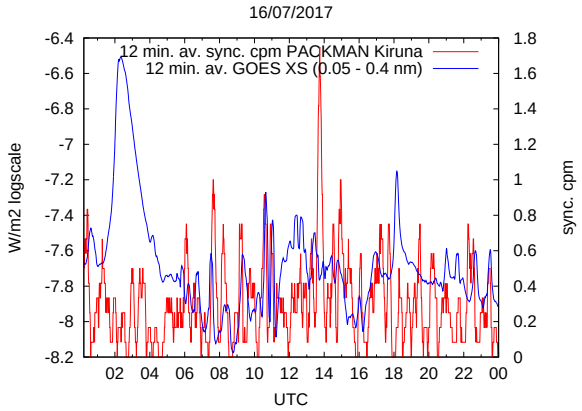

Figure 6. Comparison with the X-ray solar emission as measured by GOES at the top of the atmosphere, with the surface detection of synchronous particles by PACKMAN in Kiruna during the solar storm of 16/07/2017.

4.1. Summary

The purpose of this work was to demonstrate the utility of having a network of small-sized, detectors of the PACKMAN instrument which can be operated simultaneously to provide real time cosmic ray monitoring, covering ground based observations over a wide area (Polar Circle region to mid-latitudes). A critical and complementary observation is the one from atmospheric vertical soundings, using the same hardware, and measuring simultaneously ideally in a long duration (several days) circumpolar campaign, but also on shorter stratospheric and tropospheric sounding balloons campaigns. We have illustrated through some examples, that PACKMAN can unequivocally detect the onset of a solar storm and can provide meaningful records of particle counts, synchronous high energy particle detections, pressure and/or density anti-correlations. We have demonstrated the successful operation of the flight-model of PACKMAN instrument in an space operational environment. Through these testing campaigns, the technology has been proven to work in its final form, both for ground and space operation, and under expected conditions. This demonstrates that our space weather station has a TRL-8 and is ready for exploitation.

The radiative dose from solar and galactic cosmic radiation is caused from muons, neutrons, and electrons, and this dose varies in different parts of the world based largely on the geomagnetic field and elevation as we have seen by comparing data at different sites. Future balloon campaigns will be devoted to investigating in a systematic way the vertical profiles of radiation in the Arctic region where space radiation interacts strongly with the atmosphere. The purpose is to investigate the variability of the Pfolzer layer in height, extension and in magnitude of ionisation, during different stages of solar activity.

The advantage of PACKMAN is that it is robust, light and scalable and easy to be operated by a non-expert user. This will allow us to generate a network of instruments that provide similar data set at multiple sites and simultaneously. The observations acquired by PACKMAN will be used in future to provide open access, real time information, for: 1) education and public awareness of space weather phenomena; 2) to compare with Earth climate observations; 3) to provide realtime information of space weather variability for potential damage to infrastructures (telecommunications, power generation facilities, aviation, transport, etc); 4) to monitor natural radiation sources at multiple environments and 5) to monitor the variability of the Pfolzer maximum during different stages of solar activity.

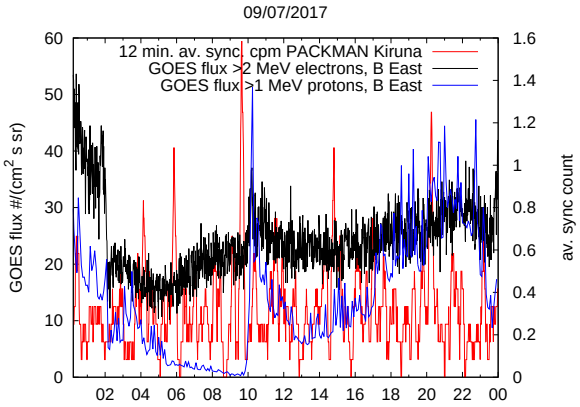

Figure 7. Comparison with the electron and proton flux as measured by GOES at the top of the atmosphere, with the surface detection of synchronous particles by PACKMAN in Kiruna during the solar storm of 09/07/2017.

Figure 8. Image of the balloon being prepared for launch by Zero2Infinity staff at the Cordoba airport runway, 29/07/2017. Inset: Detail view of the PACKMAN flight model and box for flight.

ACKNOWLEDGMENTS

We acknowledge the support and dedication of Zero2Infinity SL and the access to their balloon platform and operation. Part of the results presented in this paper have been compared with data collected at magnetic observatories. We thank the national institutes that support them and INTERMAGNET for promoting high standards of magnetic observatory practice (www.intermagnet.org). We acknowledge also the IRF institute and GOES for the open access policy of their data.

REFERENCES

[1] I. A. Mironova et. al., Space Science Reviews, 194, 1-96 (2015).

[2] G. A. Bazilevskaya, Adv. in Space Res, 35, 458-464 (2005).

[3] G. A. Bazilevskaya et. al., Space Science Reviews, 137, 149-173 (2008).

[4] K. A. Nicoll, R. G. Harrison, Phys Rev Lett., 112, 225001 (2014).

[MIT project] (https://dspace.mit.edu/handle/1721.1/104037)

[6] S. K. CHAKRABARTI, D. BHAWMICK, S. CHAKRABORTY, S. PALIT, S.K. MON- DAL, A. BHATTACHARYYA, S. MIDYA and S. CHAKRABARTI, 2013, Study of the Properties of Cosmic rays and Solar X-rays by Low Cost Balloon borne experiments, Ind. J. Physics, DOI:10.1007-s12648-013-0424-z .

[uRAD- project] (https://www.uradmonitor.com)

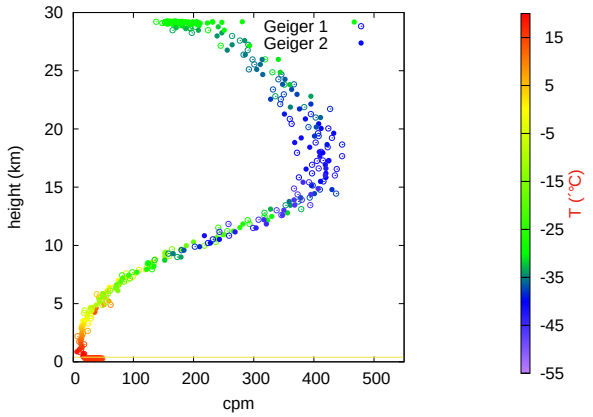

Figure 9. Vertical radiation profile observed during the release, ascent, flotation and descent of the flight-model of PACKMAN on the night of the 29th to 30th/07/2017 in Cordoba (Spain).

ALBEDO MEASUREMENT USING PHOTODIODES ON A HIGH-ALTITUDE BALLOON

VISBY, SWEDEN
11-15 JUNE 2017

BEXUS 25: The IRIS Project
E. Athanasiou, L. Jonsson, H. König, A. K. Larsén, G. Ledo López, G. Ljugné, E. Martín Nieto, O. Peláez Mercadal, F. Piette, A. Svenson, A. Tiainen, I. Wagner, A. Wallgren

Department of Computer Science, Electrical and Space Engineering, Luleå University of Technology, Rymdcampus 1, 981 92
Email: iris.bexus@gmail.com

ABSTRACT

The surface albedo of Earth was named as one of the Essential Climate Variables (ECV) by the Global Climate Observing System in 2003. The reason for this is strong impact of albedo in terms of radiative forcing. Especially the effects of the albedo in the arctic, e.g. with the ice-albedo feedback loop, play an important role and need to be investigated further. The land surface albedo is usually investigated using satellite measurements. In the last years many improvements to the estimation of albedo using satellite measurements have been made. Especially the development of bidirectional reflection distribution models, that were developed alongside MODIS, have contributed a great deal to the improvement of albedo estimation. However, the estimation is not perfect and still needs improvement. Bond Albedo is defined as the ratio of incident and outgoing radiation. Therefore, we are planning to take direct albedo measurements with a high-altitude balloon as part of the BEXUS 25 mission. In order to take the measurement, we employ two sensor boxes with multiple photodiodes. One of the sensor will be looking upwards, while the other will be looking downwards. This will allow us to find the ratio of incident and outgoing light. We will take measurements in the entire visible range as well as in the IR up to 2.5µm. Additionally, we will have photodiodes for more specific spectral ranges, such as green light around 500nm. This will allow us to obtain more information about the surface properties. For example, the red edge can be observed using the red and NIR spectral bands. With these direct albedo measurements the albedo estimates by satellites should be improved. The experiment is made in a straightforward way, so that it can be easily flown more than once and on smaller balloons as well. That would give more data and more accuracy for the improvement of satellite models and could also lead to long-term measurements of arctic albedo measurements. Which could give more clarity about possible long-term trends.

1. INTRODUCTION

IRIS consists of an apparatus which aims to measure the incoming radiation from the Sun and Earth's reflection, otherwise stated the albedo, in order to determine local albedo variations, throughout the troposphere and the stratosphere. IRIS will be mounted on a High-Altitude Balloon, in order for the experiment to meet its scientific objectives. The supreme aim is to firstly estimate and then contribute to the elimination of the error accumulated in remote sensing measurements.[6]
The Arctic circle can be considered and studied both as an independent or an integrated system. As in all climate systems, ocean, landmass and atmosphere are linked with a direct and complex interaction. The Arctic's characteristics and basic climatic features are influenced by the Albedo and Earth's thermal emissivity creating a domino effect between the surface energy budget, the atmospheric heat budget and circulation, the hydrologic cycle and vegetation mosaic.[2][3]

The albedo is a non-dimensional, unit-less quantity, which indicates the quality of reflectance a surface can return. The bond albedo specifically, is a measure of the ratio of incident to reflected radiation. It is considered as a fundamental atmospheric parameter that has deep implications on the energy balance and consequently on climate change. The energy budget is directly affected by the albedo, as it holds a key role in the process by which our planet achieves an equilibrium between the solar radiation which enters the atmosphere and then is afterwards re-emitted in considerably longer wavelengths.[2][7]

Variety and quality of the local vegetation, atmospheric composition, type of clouds found throughout the troposphere and stratosphere, the Solar Zenith Angle (SZA) and the wavelength of incoming light from the Sun, as well as, atmospheric extinction are all factors that influence deterministically the albedo. Hence, it is of great interest to further investigate thoroughly into how they influence the temperature equilibrium of our planet,

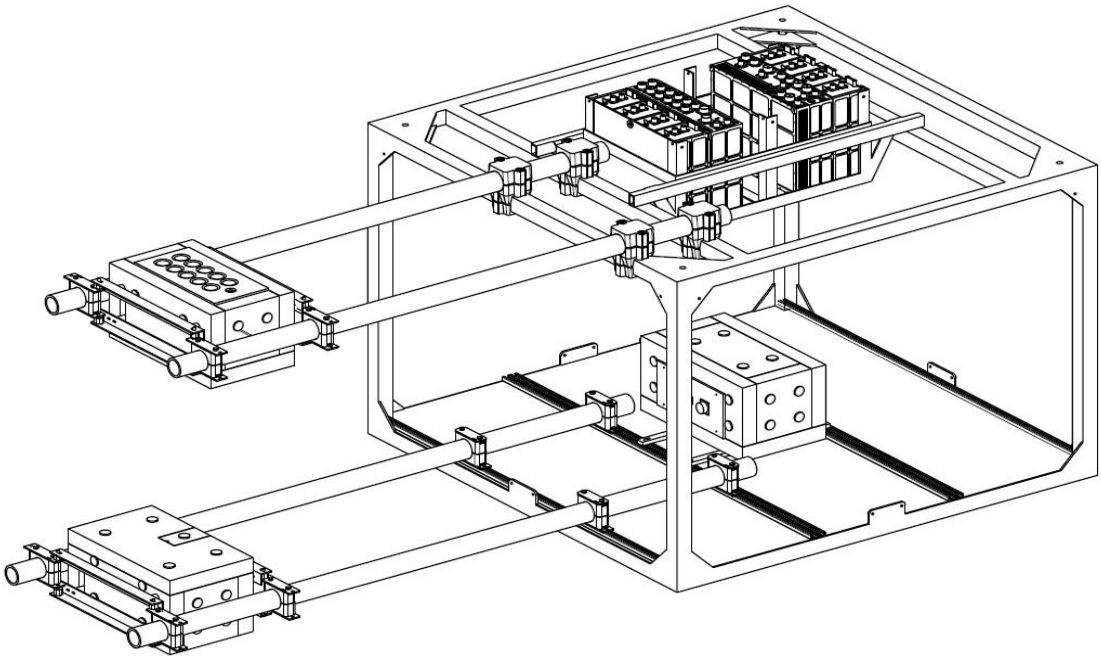

Figure 1: Mechanical design of the experiment

such as the relation between the chlorophyll levels and albedo variations and as the variations and distinguishment between snow and/or cold cloud albedo. [3][4][5]

In order for IRIS's scientific objectives to be met, a high-altitude balloon (HAB) is required. The balloon launches in October 2017 from launched from the European launch site ESRANGE (67°52′59″N21°07′00″E), which is situated near the town of Kiruna in Sweden, 200 kilometres north of the Arctic Circle. It will reach an altitude of approximately 30 km, where ambient temperature can drop to minimum value of -60 degrees C and pressure 5.5894E+2. The flight time duration is strongly depended on the speed of wind, and its three parts are estimated to last; ascent phase is ~1h30, float time 3h and descent ~30mins. After traversing through the atmosphere over the Lapland to Finland, the experiment is expected to be collected from Finland, where a helicopter by the SSC is expected to collect and return the experiment to the ESRANGE.[1]

2. MECHANICS

IRIS consists of three boxes: the "brain box" -which contains the data storage device and the main control unit- and two identical "sensor boxes" that incorporate the optical system that will perform the measurements; namely, a set of 10 photodiodes - and their associated filters and lenses - and a video camera, all mounted on the same side of the box.

All three boxes have the same dimensions, and whenever possible, the components have been used. The desired result leads to the simplification of the design and allows many spare parts to be used as redundancies.

The brain box will be placed within the gondola, directly attached to the gondola frame. On one side of the gondola there will be four parallel polycarbonate booms (PC) which will hold the two sensor boxes, as can be seen on the sketch below: this material was chosen so that the booms will break in case of hard landing, thus protecting the gondola from shock forces that could deform it. The booms will be held respectively from the top and the bottom faces of the gondola with clamps, and their sensor boxes will be attached to them so that their sensor arrays are facing upwards and downwards -respectively- to effectively measure the radiation reflected from each direction. Each of the three boxes is made up by an aluminium frame covered by Styrofoam thermal insulation, which helps keeping the internal electronic components within their operational temperature ranges. By mounting the sensor boxes on the booms, measurements taken by the top sensor array will be less affected by interference from the presence of the balloon; while the bottom one would not be affected, it should also be mounted on a boom to place it as close as possible to the parallel and horizontal position of the top sensor array.

In addition to the thermal insulation, one electrical heater mounted on a radiator, is located inside each box, along with a thermometer, forming up an active thermal control

system meant to provide control over the internal temperature of the boxes as the conditions of the surrounding environment change during the flight. The two sensor boxes and their booms are also covered by a layer of reflective material, to reduce the amount of heat received from the Sun. Computer simulations, namely in the MATLAB environment, were used to design this thermal control system.

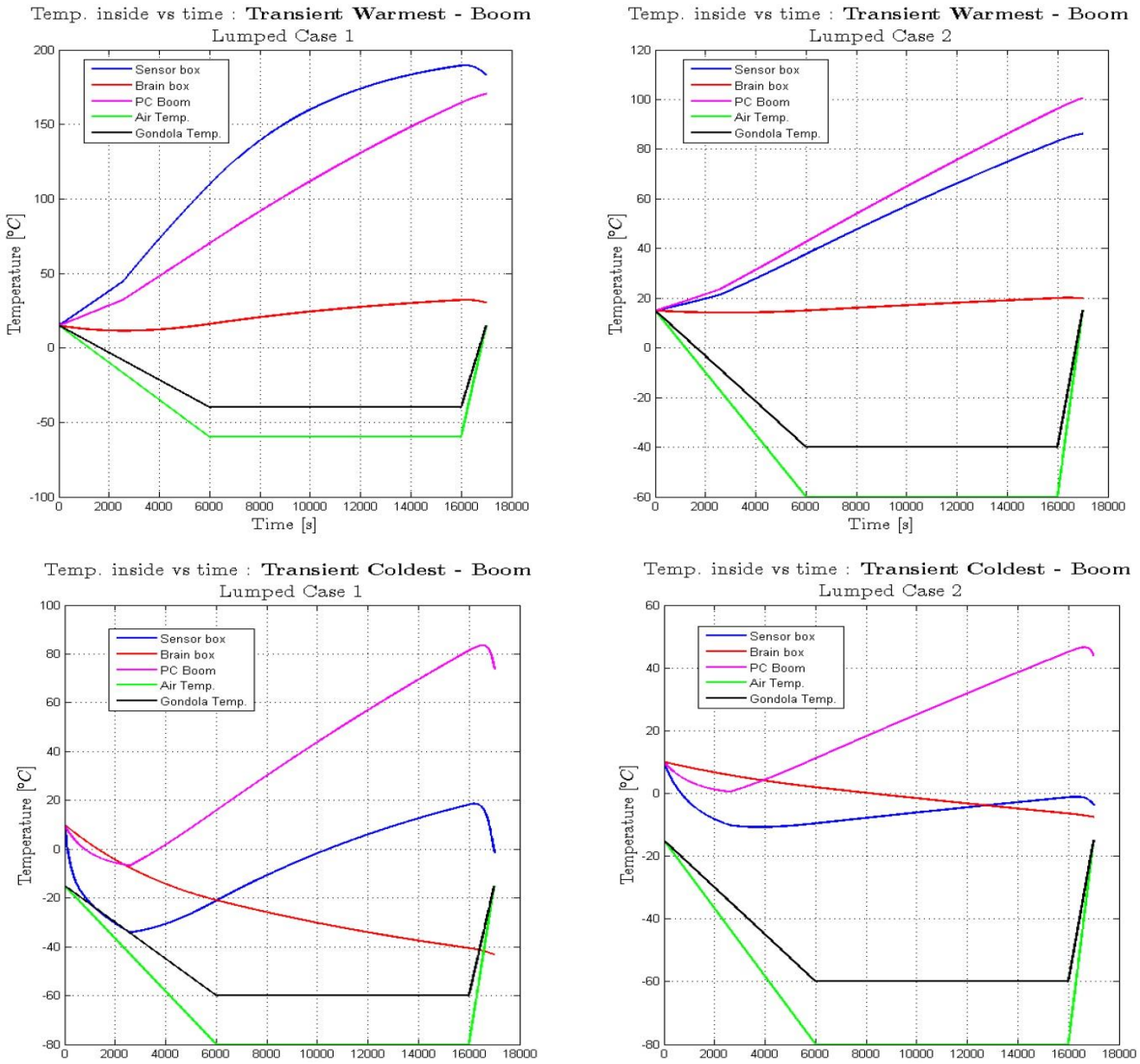

Figure 2: Thermal Simulations

For these, two cases -coldest and warmest- were considered, where external temperatures and relevance of each type of heat transfer -radiative, convective and conductive- varied between the two cases. The purpose of these calculations was to estimate the interior temperature of the different boxes of the experiment during the whole flight, for both cases. To facilitate the calculation of transient analysis, two subcases of "lumped analysis" were studied for both the coldest and the warmest cases: one where the inner aluminium plates and the electronics they hold have infinite thermal conductivity (which results in uniform temperature), and one where each whole box is one single solid of infinite thermal conductivity. Therefore, the solution for each case rests between the results of both subcases. Some of the results obtained are shown on the graphs in fig. 2.

3. OPTICS

The optical system is a critical part of the design to fulfil the requirements of the experiments. As it is desired to

measure the terrestrial (bond) albedo, it is necessary to distinguish between the incoming and the reflected solar irradiance. In order for this this goal to be achieved, two identical optical systems are needed: The area observed by each optical system is considered to be semi-spherical. One which looks upwards and observes the upper semi-sphere, measuring the incoming radiation, and a second one facing downwards which measures the reflected radiation from the Earth's surface in the lower semi-sphere. Another part of the requirement is to measure the albedo in different wavelength bands. The different bands will allow a detailed estimation of the changes of the albedo. Specifically, it can reveal how different surfaces, as well as the present atmospheric conditions can affect the albedo.

For the scientific requirements to be met, the light is captured using a combination of lenses, filters and photodiodes. These components are located in the two sensor boxes on the booms, as detailed in section 2. Two broadband photodiodes will be used without filters to give an overview over the whole solar spectrum in two parts, from 400-1100nm and from 1000nm to 2500nm. These two bands cover the most parts of the solar spectrum, especially the most energetic parts. In addition to the broadband several other channels covering multiple smaller wavelength bands are installed using lenses and filters. The small bands used are for Aerosols (430-440nm), blue channel (450-500), green channel (510-590nm), red channel (610-690nm), Near-Infrared (NIR) channel (850-890nm), two more IR channels (1350-1390nm and 1550-1650nm) as well as a mid-IR (MIR) channel (2000-2500nm). The different channels will allow an investigation of various phenomena, such as calculating the vegetation index using the red and the NIR bands as well as confirming reflective properties of snow, such as a drop in reflectivity in the IR spectrum compared to clouds. The photodiodes used in the visible as well as the NIR spectrum are of the silicon type while the IR photodiodes are two types of Indium-Gallium-Arsenide photodiodes.

The outermost part of the optical system is the lenses. The lenses are fisheye lenses that significantly increase the field of view of the whole system. A large field of view, just short of 180 degrees is required. Such a large field of view is required because the light from all directions needs to be captured. Especially during launch time in October the sun can be very low above the horizon. In fact, it does not rise more than 15 degrees above the horizon in the second half of October (include latitude and other details). Therefore a lot of light might come from closely above the horizon with a low elevation angle and this needs to be detected by the optical system. A full 180 degree field of view is not required because the ratio between the upper field of view and the lower one is measured. The light captured by both parts at 180 degrees should be very similar and thus will not contribute to any difference between the total irradiance measured by the system, e.g. the difference between the light coming from 179 degrees SZA and 181 degrees should be rather similar and thus not produce any differences in the ratio. The fisheye lenses are designed and assembled using a combination of different simpler lenses. The lenses are designed in a way that allows for the inclusion of optical filters, as it is required for the narrow bands. The filters require a nearly perpendicular incidence angle (around 90 degrees). Otherwise the center-wavelengths of the filters could be shifted towards shorter wavelengths. Therefore the light is collimated before passing through the filter. Afterwards it is focused onto the photodiode using another lens.

4. ELECTRONICS

The start of the electronical equipment is at the photodiodes. Depending on the irradiance, the photodiodes generates a certain amount of electrical current. The current is passed through an operational amplifier, that is used as a current to voltage converter and that signal is then converted to a digital value using a single ended 15-bit ADC. This value is transferred via a I2C-bus to the microcontroller that is present in each of the two sensor boxes. For this experiment, an Arduino Nano in each sensor box was sufficient. Along with the irradiance, the temperature between the photodiodes are also measured, this is to ensure that any temperature variations in the photodiodes current is taken into consideration. The microcontroller also manages the temperature inside the box by utilizing the mentioned temperature sensors along with a heater.

The center box or "Brain Box" consists of a Raspberry Pi ver2 B+, that is chosen due to its computational power, low power consumption and for not having any wireless options such as Bluetooth and WiFi which with some bad luck could disturb other experiments. When needed, the "brain box" will call for data from the two sensor boxes, and it is received by using an ordinary USB connection, which is somewhat altered for easier cable management. The "Brain box" also handles the two cameras that are used, a GPS, two different temperature sensors along with a barometer to get a rough estimation of the altitude. The data gathered are stored on a normal SD-micro card, that is used by the Raspberry Pi. For safety, some of the data will also be sent down using the downlink to the ground station. If something were to cause the Raspberry Pi to crash during the flight, an external watchdog was also implemented into the design.

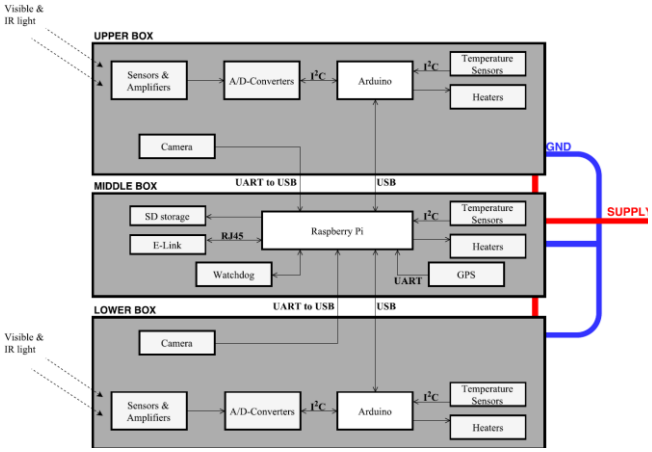

Figure 3: Electronics Design

5. SOFTWARE

As mentioned, the experiment will feature two Arduino Nano microcontrollers, a Raspberry Pi computer and different peripherals (GPS, cameras). The Arduino nano microcontrollers will collect the analog data and relay it to the Raspberry Pi, which will then sort and store the information in different files.

The connection with the Raspberry Pi will be done through USB 2.0 in the hardware level, and will feature NMEA 2000-like protocol to communicate on the software level. This is the same protocol GPS peripheral uses. For collecting the video input, the cameras will be connected directly to the Raspberry Pi collecting images and storing them in the SD card.

A fraction of the data will be relayed back to ground segment for tracking, monitoring and pre-process some of the information. Additionally, the ground station can issue commands to the Raspberry Pi in the event of malfunction. In the event of the data being corrupted or not stored properly, the transmitted data will help in recovering some of it for later analysis.

Both the Arduino Nano microcontrollers and the Raspberry Pi feature big enough buffers to ensure the data collection rate and transmission is fast enough to ensure the design data rates for the experiment.

6. EXPECTED RESULTS AND DATA ANALYSIS

The data from the sensors will be used to compute the irradiance that comes in from the sun and that is reflected from the surface and lower part of the atmosphere. After data retrieval, by comparing the values of each of the symmetrical sensor layouts, positioned on the top and bottom booms, the bond albedo can be calculated. The measurements during the ascent phase will indicate the change of the albedo during the change in altitude.

The scattering and reflectance of the light around the area of each optical system is considered homogeneous. However, the non-homogeneity of the several types of soil causes distortions, thus it is hard to distinguish between the represented data, obtained from the satellite measurements. This is because the homogeneity of the ground is directly connected with the variability of the ground topography. The more homogeneous the ground is, the less variable the ground topography is, providing more compatibility between the in-situ and the remote sensing measurements. As a consequence, factors such as the spatial resolution, the monitored area overlapping, and radiometric corrections are some of the main factors that influence the quality of satellite albedo measurements. For this reason Bidirectional Reflectance Distribution Function (BRDF) models are used to more effectively simulate the observed surface and eliminate the data drift error accumulated in the measurements due to the distortions caused by the non-homogeneity of the types of the surfaces measured.

A model for atmospheric radiative transfer analysis (RT) will be used to produce the results from the different radiative components that are coming in onto the surface, as well as the outgoing reflected flux, at the according radiation conditions. These RT models are important for satellite measurements, as they are used for the retrieval of the data. By comparing the measured values with the model results, both the model and the in-situ measurements can be evaluated. If the obtained measurements and the modelled values are in disagreement, further data analysis could reveal where the error is located and eventually contribute to the improvement of the model. An improved radiative transfer model will help to also improve the accuracy of satellite measurement evaluation.

7. CONCLUSION/OUTLOOK

Albedo has been named as a climate essential variable. As such it is vitally important to have good coverage of measurements as well to improve already existing methods. In this paper a student experiment has been presented which is supposed be kept simple and robust.
The design of the experiment has been finished and is now under construction. The launch will happen in October, then it will be shown if the design. Furthermore the data analysis plan has to improve for a possible comparison with satellite data. Because this experiment should provide high quality data over a small spatial and temporal range. This can be combined with the global repeated coverage by satellites to improve the overall coverage of albedo measurements.

8. REFERENCES

1. REXUS/BEXUS Organizers. RXBX_

   SED_guidelines_v5-2, December 17, 2015

2. John Turner. Polar meteorology, understanding global impacts, 2007.

3. I. Filella and J. Penuelas. The red edge position and shape as indicators of plant chlorophyll content, biomass and hydric status., 1994

4. Nea Kuusinen et al. Boreal forest albedo and its spatial and temporal variation. PhD thesis, University of Helsinki, 2014.

5. Fanglin Yang et al. Dependence of land surface albedo on solar zenith angle: Observations and model parameterization. Journal of Applied Meteorology and Climatology, 47:2963–2982, 2008.

6. Ying Qu, Shunlin Liang, Qiang Liu, Tao He, Suhong Liu and Xiaowen Li. Mapping Surface Broadband Albedo from Satellite Observations: A Review of Literatures on Algorithms and Products. Remote Sensing**,** 2015,7,990-1020;doi:10.3390/rs70100990

7. Ann R. Webb, I. M. Stromberg, H. Li, and L. M. Bartlett. Airborne spectral measurements of surface reflectivity at ultraviolet and visible wavelengths. Journal of Geophysical Research: Atmospheres, pages 4945–4948, 2000.